Fundamental Processes in Sputtering of Atoms and Molecules (*SPUT92*)

Symposium on the Occasion of the 250th Anniversary of the Royal Danish Academy of Sciences and Letters

Copenhagen, 30 August - 4 September, 1992

Invited Reviews

Edited by Peter Sigmund

1742

Matematisk-fysiske Meddelelser **43**

Det Kongelige Danske Videnskabernes Selskab
The Royal Danish Academy of Sciences and Letters

Commissioner: Munksgaard · Copenhagen 1993

Abstract

The contributions to this volume are based on invited review lectures presented at a symposium on fundamental processes in sputtering (*SPUT92*), attended by 82 active researchers in the field. Eight contributions cover recoil processes, or 'collisional sputtering', and six contributions cover electronic processes, or 'electronic sputtering'. The last two contributions cover two of six application areas presented at *SPUT92*, and an introductory chapter was added by the editor. The book emphasizes developments over the past decade and offers comprehensive reviews on most active research areas in the field of sputtering by particle bombardment, with the emphasis on fundamental physical and chemical processes.

Figures were reproduced with the kind permission of the American Institute of Physics, Elsevier Science Publishers, Gordon and Breach Science Publishers, the Institute of Physics, Plenum Press, Scanning Microscopy Inc., Springer Verlag, Wiley & Sons, and numerous authors.

Printed in Denmark by Bianco Lunos Bogtrykkeri A/S
ISSN 0023-3323 ISBN 87-7304-249-8

Preface

The Royal Danish Academy of Sciences and Letters celebrated its 250th anniversary in 1992. It was decided that corner stones of this anniversary should be a number of international research symposia. In 1989 I proposed a symposium on 'Fundamental Processes in Sputtering of Atoms and Molecules' (*SPUT92*) which was accepted by the academy board and received with enthusiasm by the scientific community. Due to limited space in the academy building, participation was by invitation only.

SPUT92 was held from 30 August to 4 September 1992 with 82 registered participants. The program consisted of invited summary lectures as well as oral and poster contributions on current research. In addition, a public session was arranged in which six specially invited lecturers reported on applications of sputtering.

Summary lectures were planned to represent the state of the art in research on fundamental processes in sputtering. In particular, major developments since the appearance of the monographs edited by R. Behrisch in 1981-83[1] were intended to be covered in these lectures as well as the written records. Speakers were given a generous deadline to submit manuscripts without tight limitations on length. I am glad to note that most invited speakers were able to set aside the necessary time and labor. All contributions were vigorously refereed, and there was given generous time for major and minor revision. As a result, I believe that the present volume fulfills the above goal as well as can be expected.

Authors were not asked to write tutorials for novices in the field, but many of them provided self-contained presentations that can be read without excessive recourse to earlier literature. Nevertheless, there is a certain amount of ground knowledge that may be difficult to identify and to extract for a newcomer. I have therefore written a brief introduction to sputtering as a reading help for those who wish to use this book as an introductory text. That chapter is the only contribution that is not based on a lecture presented at *SPUT92*.

Original research contributions reported at *SPUT92* have not been included in this volume. Authors were encouraged to submit their papers to a special topical issue on Fundamental Processes in Sputtering which has been published recently[2].

I received generous help from numerous individuals and organizations in working on the symposium and this publication. I like to mention first of all the staff of *SPUT92*, Karen Cauthery, Pia Sigmund, Mads W. Sckerl, and Ole Vorm, the staff of the academy, Pia Grüner, Ella Mortensen, Else Løvdal Nielsen, Henrik Caspersen, and Jørgen Maes, the members of the organizing committee, H. H. Andersen, P. Roepstorff, J. Schou, and B. U. R. Sundqvist, and the members of the international advisory committee, F. Besenbacher, G. Betz, W. Heiland, Y. Le Beyec,

---

[1] These volumes are currently out of print but will be available again shortly.

[2] Nuclear Instruments and Methods B **82** no. 2, 207 - 388 (1993)

J. K. Nørskov, E. S. Parilis, M. T. Robinson, K. G. Standing, M. Szymonski, and H. F. Winters. The symposium and this publication were generously funded by The Novo-Nordisk Foundation, The Carlsberg Foundation, The Danish Natural Science Research Council (SNF), and IBM Denmark. Special thanks are due to the authors and reviewers for their efforts, to Karen Cauthery for competent conversion of authors' textfiles into LaTeX, to Tove Nyberg for assistance with illustrations, to Andreas Närmann for invaluable help in software problems, and to Poul Lindegård Hjorth, editor of this journal, for patiently listening to and generously following my wishes concerning unusual procedures in the production of this volume.

Odense, September 1993
Peter Sigmund

Contents

General:

Recoil Processes:

Electronic Processes:

Applications:

Introduction to Sputtering

Peter Sigmund
Physics Department, Odense University
DK-5230 Odense M, Denmark

Synopsis

The main purpose of this brief tutorial is to give some guidance and reading help to the nonexpert who wants to utilize the present volume as an introduction to the field of sputtering. That field has a long history, yet the present book has been planned to cover primarily developments over the past ten years. Some basic terminology is introduced and a rough classification of the field is given. A few central references to the older literature have been listed and commented on. They are not meant to be comprehensive, but many of them are classics in the field or important sources of background information. The main function of these references should be to provide access to well-established knowledge which, more or less explicitly, enters as a common background into many of the contributions in this volume. In addition, a few hints on key applications of sputtering have been included.

1 The Phenomenon

Sputtering is the erosion of material surfaces by particle impact. The variety of materials for which sputtering has been or can be observed is virtually unlimited. The standard source of bombarding particles in the laboratory is a collimated ion beam with a well-defined energy, but both electrons and photons as well as neutrons and other particles may give rise to sputter phenomena. In applications of sputtering, and wherever the phenomenon occurs in nature, a very wide variety of bombardment conditions must be envisaged.

Sputtering is a phenomenon on the atomic scale. By this is meant that one can identify an individual sputter event, i.e., the emission of a number of atoms or molecules from a material surface initiated by a single bombarding particle. It is the physics of this individual sputter event which is the most fundamental process in sputtering and the main subject of many of the contributions to this volume. A sputter event is a priori statistical in nature. However, after bombardment with a great number of particles, macroscopic effects such as a change in weight will be observed, and a crater may be visible on the target area facing the beam. Such macroscopic phenomena are quasi-deterministic and allow the operational definition of terms such as erosion rate and sputter yield that will be discussed below.

Not all particle-induced erosion is called sputtering. If an intense beam deposits energy at a rate high enough to heat the entire target surface to near or above the boiling point, the resulting erosion by evaporation is not classified as sputtering. Clearly, this cannot be considered as a superposition of microscopic erosion effects caused by individual bombarding particles. Nonetheless, part of the observed erosion may well be caused by sputtering.

Sputtering is a ubiquitous phenomenon whenever energetic particles interact with materials, and the effect has many applications. Therefore, the term is utilized in different meanings by different communities. Those who use sputtering as a means of etching, cleaning, or polishing materials may use sputtering synonymously with 'bombarding with an ion beam'. The community of researchers and engineers who use sputtering instead of evaporation in the deposition of thin films use sputtering synonymously with 'sputter-depositing'. Historically, the term came up early in this century to illustrate the elementary event which was thought to resemble what happens when a stone falls on a water surface.

2 Quantification

Until little more than a decade ago, weight-change measurements were the main experimental tool in the quantification of sputter processes. For most of a century, such measurements were performed by literally weighing a target on a more or less sensitive scale before and after exposition to a source of energetic ions. Such measurements provide the 'sputter rate', i.e., the change in coverage [atoms per unit area] per unit time. They allow a comparison between sputter properties of different materials. When the bombarding beam is well defined and the current measurable, one may convert sputter rates into 'sputter yields', i.e., the mean number of target atoms (or molecules) sputtered per incident beam particle.

The key quantity characterizing the beam is the fluence, i.e., the number of incident particles per area. The fluence is the integral over time of the particle current density. Measurements of sputter parameters at low fluences are of prime interest in the study of fundamental sputter processes.

The sensitivity of weight-change measurements was greatly improved when targets deposited on a quartz crystal microbalance were inserted into the vacuum chamber. The fact that target preparation, ion bombardment, and measurement of sputter effects all can be performed in situ without breaking the vacuum removed a major source of experimental error, allowed for measurements at low fluences, and reduced the time needed to collect a given amount of data by several orders of magnitude.

Tabulations of sputter rates and yields for elemental targets were compiled regularly, starting with Crookes (1891). A critical and comprehensive compilation of elemental sputter yields along with an extensive discussion of requirements for reliable measurements may be found in a review by Andersen & Bay (1981).

Several alternative techniques are available for experimental determination of sputter rates and yields. Sputtered material may be deposited on a collector and quantified by weight change of a quartz crystal microbalance, by surface analytical techniques, by means of radioactive tracers, by dissolution and chemical analysis, and the like. Most of these techniques also provide differential information on the angular emission pattern of the sputtered particles as well as the chemical composition of the sputtered material in case of a multicomponent target such as an alloy, a compound, or an isotopic mixture. Pertinent data and techniques have been reviewed by Hofer (1991).

Direct analysis of the flux of sputtered particles is also possible. It is important to note that for a very wide variety of target materials, the vast majority of sputtered atoms or molecules is emitted as neutrals, although not necessarily in the ground state. Moreover, typical energies of sputtered particles lie in the lower eV region. Therefore, efficient use of conventional detection techniques for fast particles requires post-ionization and/or acceleration of sputtered particles. Typical tools for postionization are electron beams, gas discharges, and laser beams.

Laser beams have proven to be a very versatile tool for experimental research in sputtering. Sputtered atoms or molecules may be excited resonantly. For a reasonably narrow absorption line, the Doppler shift corresponding to the translational velocity of an ejected atom lies outside the resonance. Therefore, laser resonance fluorescence provides direct information on the velocity spectrum of emitted particles. By suitable combination of lasers, such information may be gained for several species present in and emitted from a multicomponent target. This information is state-specific. By use of apertures or appropriate optical techniques, also dependencies on emission angle may be studied. By means of multiphoton ionization, the detection sensitivity may be increased by many orders of magnitude. Pertinent information may be found in reviews by Hofer (1991), Gruen et al. (1983), and the contribution by WINOGRAD to the present volume. The review by Hofer (1991) also presents information on non-laser-based techniques for determining energy spectra of sputtered particles. Most of them rely on flight-time measurements.

Observation of eroded surfaces provides valuable information on sputter processes, but until recently, such information was available only on a rather large length scale. It has been known for a very long time (Günterschulze & Tollmien,

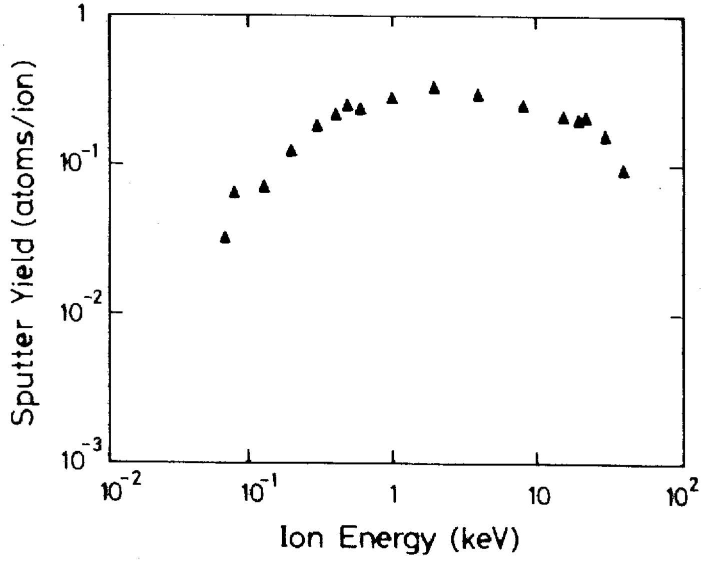

Figure 1. Sputter yield versus beam energy for He^+ on Cu. From Roth (1980).

1942) that metal surfaces develop peculiar topographies during prolonged sputtering: A sputtered crater may contain cones, pyramids, and ridges with dimensions ranging from several microns down to a few hundred Ångströms or less (Carter et al., 1983). Formation of surface structures on such a scale is unquestionably a high-fluence phenomenon dependent also on other material properties than those governing the individual sputter event. Observational techniques have now been refined to a stage where inspection of craters formed by individual ion impact down to atomic size is possible. Recent work in this rapidly developing field has been summarized by TSONG & BEDROSSIAN in this volume.

Surface analytical techniques such as Rutherford backscattering, Auger spectroscopy, or ion-surface scattering may be applied to the study of a bombarded target surface. Such measurements provide insight into near-surface changes in chemical composition of a multicomponent target caused by sputtering and other processes initiated by bombarding ions. Pertinent experimental techniques as well as data on 'partial sputter yields', i.e., sputter yields for individual species, have been summarized by Betz & Wehner (1983). A follow-up with the emphasis on the theory of compositional changes is given by LAM and myself in the present volume.

This brief survey is by no means complete: Not all experimental techniques utilized in sputter research have been mentioned, and the catalogue of measurable

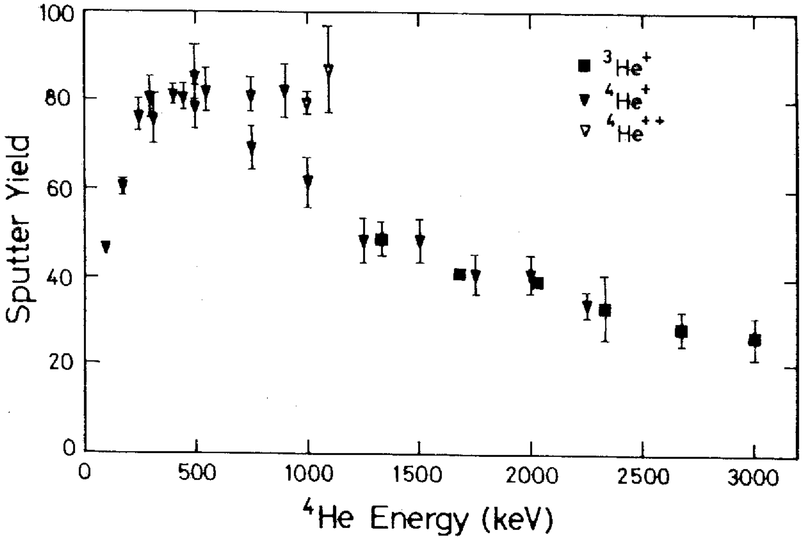

Figure 2. Sputter yield versus beam energy for He$^+$ on solid Ar. From Besenbacher et al. (1981).

parameters is not comprehensive. Nevertheless, an attempt has been made to give an indication of the level of detail at which sputter phenomena have been and can be studied experimentally. For a more comprehensive picture, the reader is referred to the experimentally-oriented contributions to Behrisch (1981, 1983a) and Behrisch & Wittmaack (1991) as well as the present volume.

3 Main Observations

The lowest recorded sputter yields have been measured for neutron bombardment: Values of $\sim 10^{-5}$ sputtered metal atoms per incident fast neutron seem common (Behrisch, 1983b). Very high sputter yields, of the order of 10^3 or more atoms or molecules per ion, have been reported for bombardment of insulating targets with swift ion beams at fission-fragment energies on the one hand, and for bombardment of conducting targets by large clusters with lower energies on the other. Pertinent summaries are found in the contributions of JOHNSON & SCHOU and ANDERSEN, respectively, in this volume.

There is usually a threshold value for the beam energy above which sputtering sets in. Conversely, sputter yields tend to decrease at high energies. The physics of the threshold is governed by energy and momentum conservation laws of the processes leading to sputtering. The decrease at high energies reflects a general property of the pertinent collision cross section, e.g., Rutherford's law in case of charged-particle bombardment.

Figures 1 and 2 show sputter yields versus projectile energy measured for He^+ bombardment of copper and solid argon, respectively, at normal incidence. While the two curves have qualitatively similar appearances, the difference in both ordinate and abscissa scale is astonishing. It indicates that we deal with entirely different mechanisms of sputtering in the two situations. Inspection of pertinent data on ion penetration shows that the energy dependence of the sputter yield of Cu resembles the behavior of the energy lost to elastic collisions, the 'nuclear stopping power' of a moving ion. Conversely, the sputter yield for the argon target follows the behavior of the electronic energy loss, or 'electronic stopping power'. This difference is crucial to all modern research in sputtering. It was not recognized until the end of the 1970s because until then, well-controlled sputter experiments were performed mainly on metallic targets where sputtering by elastic collisions, 'collisional sputtering', dominates. Up till now, electronic sputtering has been identified unambiguously only on certain insulators. Although that field has been summarized at regular intervals, the paper by JOHNSON & SCHOU in the present volume is probably the most comprehensive survey of both experiment and theory as well as the interface to collisional sputtering.

Sputter yields have of course been measured as functions of the angle of incidence of the beam. For polycrystalline and amorphous materials, the sputter yield tends to increase with increasingly oblique incidence up to a certain maximum, and to decrease at glancing incidence. The behavior reflects that of the expected density of energy deposition in the pertinent surface layer where processes occur that lead to sputtering. In case of crystalline materials the behavior is more complicated, and several pronounced minima and maxima in the dependence of the sputter yield on the angle of incidence are usually found. Minima are observed for bombardment along closely-packed directions where ions may be steered into open channels without undergoing collision events that are dramatic enough to cause emission of atoms or molecules from the surface. Most pertinent experimental work on single as well as polycrystals dates back to more than a decade ago and has been reviewed by Roosendaal (1981) and Andersen & Bay (1981), respectively.

Several material and beam properties determine the absolute magnitude of the sputter yield at a given energy and direction of incidence. In general, sputter yields increase with increasing volatility of the bombarded material. This is intimately related to the fact that energy spectra of sputtered atoms are dominated by 'low' energies, i.e., energies very near the threshold energy that allows an atom or molecule to be emitted. The physics of the effective surface binding energy in sputtering is a somewhat delicate subject, to which viable theoretical approaches

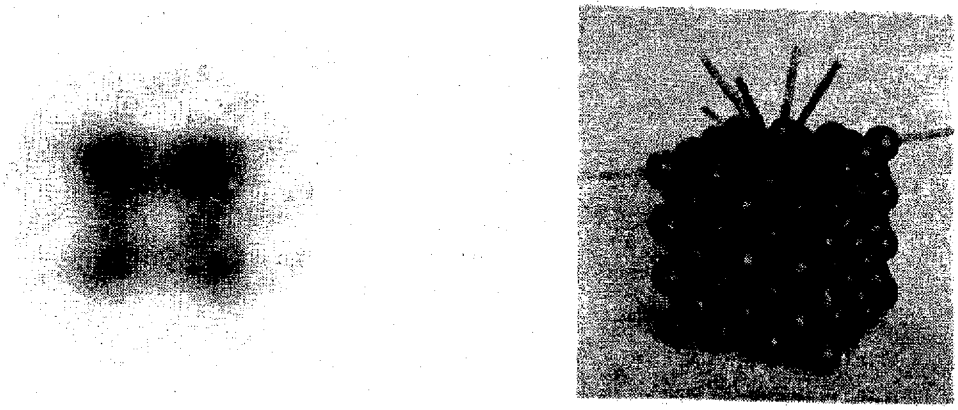

Figure 3. Emission pattern measured on a (100) Ag crystal bombarded by 100 eV Hg ions. From Wehner (1955).

have been developed only very recently, cf. contributions by NIEMINEN, ROBINSON, and SIGMUND & LAM to this volume. There is, however, clear evidence to support the notion that the effective surface binding energy does not differ dramatically from the heat of sublimation. In collisional sputtering, the maximum attainable energy of a sputtered atom may come close to the maximum transferable energy in an elastic collision between a beam particle and a target atom. In electronic sputtering, an upper limit could be set by the energy stored in an individual electronic excitation. In either case, this maximum may exceed the surface binding energy by orders of magnitude. If so, available energy tends to be shared, either collisionally via 'collision cascades' or electronically via 'ionization cascades'. One implication of this cascading process is the possibility of sputter yields $\gg 1$. Another implication is the dominance of low energies in the spectrum of emitted particles, and hence the dominating influence of the surface binding energy on the magnitude of the yield.

Closely related to energy spectra is the subject of angular distributions of sputtered particles. Dramatic effects are observed first of all under bombardment of single crystals. In fact, the observation of 'spot patterns' of ejected material by Wehner (1955), which closely reflect the crystal structure of the bombarded target (fig. 3), may well be considered to signalize the beginning of modern research in sputtering. Distributions in energy and emission angle of particles sputtered from elemental materials have been reviewed by Hofer (1991). Crystal lattice effects specifically are addressed by WINOGRAD in the present volume.

Reliable measurements on the state of aggregation as well as the state of excitation of the flux of sputtered material have become possible, and systematic trends are coming up slowly. Atoms, molecules, clusters, and large aggregates have all been identified in the sputtered flux from a variety of materials under a variety of bombardment conditions. In addition to the (usually) dominating neutral component, both positively and negatively charged species are well known to contribute. In fact, even though the charged component is a minority, it has been analysed in much greater detail for many systems since standard mass spectrometric techniques can be applied. This is particularly true for organic materials, as seen in HÅKANSSON's and ENS' reviews in this volume. The matter becomes more complicated in case of the neutral flux where recording a mass spectrum may require postionization which is a violent process from the point of view of molecular stability. Nevertheless, with increasing sophistication of experimental techniques, a trend is visible toward the recognition that molecules and clusters may constitute a very substantial fraction of all emitted material. This, in turn, sets question marks with experimental techniques that rely on the assumption that the majority of the sputtered material is ejected as atoms. Emission of molecules and clusters from inorganic materials has been summarized by URBASSEK & HOFER in the present volume. For organic materials, emission of molecules and molecular fragments is the prime subject of investigation, and atoms play only a very minor role. Therefore, the contributions by REIMANNN, HÅKANSSON, ENS, and KARAS to this volume all deal with this subject.

Very little is known about the neutral component in the sputtered flux from organic targets. Conversely, detailed studies are available for the ionization mechanism of particles – mostly atoms – sputtered from metals. This research — triggered by the needs of secondary-ion mass spectrometry (SIMS), a surface-sensitive analysis technique relying on sputtered ions — has been omitted because it is the subject of a whole conference series on Inelastic Ion-Surface Collisions. Major reviews on ionization probabilities of sputtered atoms may be found in IISC (1983, 1987).

4 Theoretical Models

Most of the theoretical modelling of electronic sputter processes has been done rather recently and is summarized in several contributions to this volume. REIMANN's contribution presents an illuminating overview, even though it addresses primarily sputter processes involving large molecules. I find it hard to imagine a better introduction to this complex of problems and, therefore, shall make no attempt to compete. The paper by JOHNSON & SCHOU emphasizes processes in condensed gases, in particular noble gases: This is the only class of material where there has been achieved a general consensus about some of the processes responsible

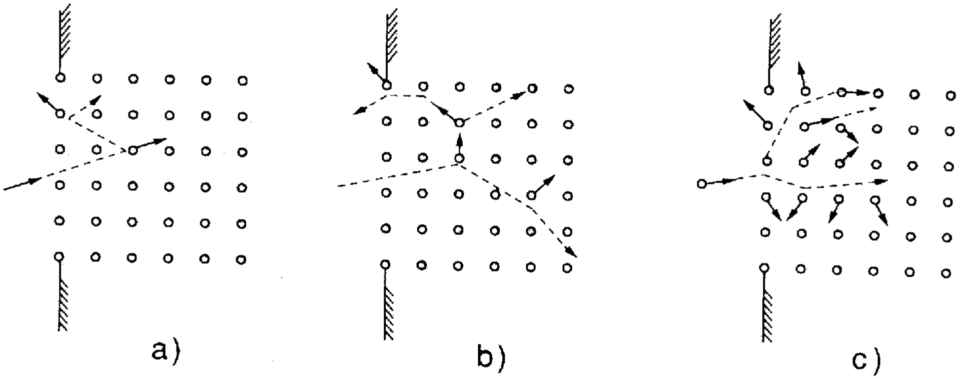

Figure 4. Three representative cases of collisional sputtering. a) Low-yield regime; b) Linear cascade; c) Spike regime. From Sigmund (1981).

for sputtering. SZYMONSKI discusses ionic crystals: Electronic sputtering from these materials has been discussed for several decades. A review of earlier work was given by Townsend (1983). Attempts to model laser-induced sputter processes on more general considerations are discussed by HAGLUND & KELLY.

There appears to be a general consensus that electronic sputter processes are heavily material-dependent not only quantitatively but even qualitatively. Therefore, very little can be said about electronic sputtering in general, and the shape of a yield curve like the one shown in figure 2 cannot be said to be universal.

The situation is very different with regard to collisional sputtering: If an adequate amount of kinetic energy can be transferred to a target atom by an incident projectile, this energy is shared with other atoms in secondary collisions. Some of those may lead to ejection of atoms. The quantitative details of this sequence of events depend more or less sensitively on all bombardment parameters, but the qualitative features are rather independent of the material. The physics of these collision cascades has been investigated for many years, and most of the fundamental concepts were well established decades ago. This knowledge enters more or less implicitly into several contributions in this volume, including those dealing with electronic sputtering processes. A brief introduction may therefore be appropriate.

Fig. 4 shows three prototypes of collisional sputtering. Fig. 4a illustrates a low-yield event which could represent the case of a heavy metal bombarded by a low-energy (< 1 keV) H^+ ion. The maximum energy transferable to a target atom is only a few electron volts, but the projectile has a high probability for wide-angle deflection according to the cross section for elastic scattering on an appropriately screened Coulomb interaction potential. Therefore, a projectile ion may return to the surface and transfer an adequate amount of energy to a target atom to enable it to overcome surface binding forces. The sputter yield for this type of event will usually be < 1, possibly $\ll 1$.

With increasing ion energy, the cross section for wide-angle scattering decreases but the maximum transferable energy increases. Sputter yields increase initially, as is seen in figure 1. This increase is caused by formation of collision cascades, i.e., the efficient dissipation of primary recoil energy amongst target atoms so that a large number of them have energy enough to be emitted. It is, then, a matter of the configuration in space how large a portion of those recoil atoms is close enough to the target surface to be ejected. Atoms recoiling from lattice sites remote from the surface cannot be ejected but tend to form defects, i.e., vacancies and interstitials and their conglomerates.

Figure 4b illustrates a 'linear collision cascade'. The main feature here is a comparatively long mean free path between energy-dissipating collision events. This has the effect that only a small fraction of the atoms occupying any simply connected volume is set in motion with a noticeable energy. The main characteristic of a linear cascade is an approximately linear dependence of the number of participating target atoms on the available kinetic energy. This is extremely useful for providing pertinent theoretical estimates on sputtering.

Figure 4c illustrates the opposite extreme of a 'collision spike'. Here the mean free path between recoil-generating collisions is so small that essentially every atom in a certain volume is set in motion. The spike volume is determined primarily by the range of the ion which depends on energy in a well-defined manner. Therefore, the number of atoms set in motion cannot be expected to be proportional to the available energy in this case.

The distinction between a linear cascade and a spike is ultimately a matter of definition of the critical energy above which an atom may be said to be in motion: If that energy is chosen high enough, any cascade will be linear. Conversely, that energy can be chosen small enough so that every cascade takes on the properties of a spike. With regard to sputtering, a reasonable choice of the threshold energy would appear to be the surface binding energy U which is typically a few electron volts. This topic has been discussed extensively by the present author (Sigmund, 1977).

Linear cascades and spikes show a different behavior with regard to sputtering. In case of a linear cascade, sputtering is little more than the intersection of a collision cascade with a target surface: The processes leading to transport of an atom toward the surface and subsequent ejection are essentially the same as those that characterize the development of the cascade as a whole. Conversely, transport of matter, energy, and momentum must proceed more collectively in case of a spike. There is, in fact, no unanimous agreement about the hierarchy of processes in a spike and the respective contribution to the sputter yield. One school of thought advocates heat transport and subsequent evaporation to be the dominating feature. Other schools operate with shock waves (or pressure pulses). Some of those features have been discussed by REIMANN, JOHNSON & SCHOU, and ANDERSEN in this volume.

Experimentally, the linearity of a cascade may be verified by bombardment with polyatomic ions. Incident molecules tend to dissociate upon impact with the target surface, and the fragments tend to follow their individual, stochastic trajectories. These trajectories are, however, confined to roughly the same target volume. In the cases illustrated in figs. 4a and 4b, the number of target atoms set in motion by a diatomic molecule will, to a good approximation, be twice as large as for monoatomic bombardment at the same projectile speed. Conversely, in case of fig. 4c, about the same number of atoms will be set in motion for monoatomic or diatomic bombardment. In the absence of competing transport processes, one expects an unchanged sputter yield per projectile atom for the low-yield case and the linear cascade, and a lower sputter yield per projectile atom in the case illustrated in figure 4c.

Pertinent measurements have been performed long ago and are summarized in ANDERSEN's contribution to this volume. For ions of low mass and atomic number, sputter yields per incident atom tend to remain constant, thus confirming linear-cascade behavior. For ions of high mass and atomic number, as well as large polyatomic ions, sputter yields per incident atom tend to be larger than for monoatomic bombardment. This suggests that additional transport mechanisms beyond energy dissipation in linear cascades must contribute to sputtering in case of high density of energy deposition.

5 Theoretical Tools

A complete, quantal calculation of a sputter event has never been performed on any system. It is not even evident whether anybody at present judges such a calculation to be necessary or desirable.

A convenient way of splitting up the physics of a sputter event is a three-stage process consisting of

I) slowing-down and energy dissipation of the primary particle,

II) cascade processes and transport, and

III) particle escape from the surface.

There is no strict separation between the three stages, and the separation may not even be visible in a given calculation, but different input is clearly required. At any rate, it is desirable to know where to look for inadequate input when there is poor agreement between theory and experiment.

The physics of the first stage (I) belongs to the field of particle penetration phenomena which is highly developed. Pertinent cross sections for elastic collisions and electronic excitation or ionization are available for all projectiles at all energies, although data tend to be less reliable in the lower keV range and below, especially for projectiles of high mass and atomic number. The classics in the field are Bethe's theory of the stopping power of a light ion (Bethe, 1930) and the LSS theory of heavy-ion ranges (Lindhard et al., 1963). Numerous reviews are available. I should like to mention Fano (1963), Inokuti (1971) and Sigmund (1975) on electronic stopping, and Sigmund (1972, 1983) on range theory.

Particle stopping and scattering as well as related processes like sputtering are multiple-collision phenomena. The stochastic nature of these processes suggests the use of bookkeeping techniques which are familiar from numerous branches of physics. Similar techniques are needed in the description of the second stage, but the merits of different approaches depend on the pertinent energy range as well as the required job. Bookkeeping procedures may be roughly classified into four categories,

- Linear transport theory,
- Monte Carlo simulation,
- Binary collision simulation,
- Molecular dynamics simulation.

Linear transport theory and Monte Carlo simulation are equivalent in principle. In either case, collision statistics is governed by Poisson's law, with binary-collision cross sections and continuous (frictional) forces being the primary input. The relative merits of the two techniques are easily identified: There are virtually no limits on the variety of quantities that can be evaluated by Monte Carlo simulation for a given geometry. Conversely, atomistic input is predominantly available in the form needed for transport calculations, i.e., stopping power, energy loss straggling, etc., while fully differential cross sections — which enter into genuine Monte Carlo simulations — are more sporadically tabulated. Most of the computation time in standard Monte Carlo simulation codes is wasted on insignificant collision events. Despite this, their statistical accuracy is usually higher than that of the other two simulation methods.

Binary-collision simulations differ from Monte Carlo simulations by the introduction of a prescribed target configuration. Such simulations are useful whenever crystal lattice effects are judged to be important. For the slowing-down stage, this is vital in attempts to predict the dependence of the sputter yield on angle of incidence.

Molecular-dynamics simulations operate on the basis of Newton's equations which are solved simultaneously for the projectile-target many-body system. Computational capacity restricts the applicability of this technique to fairly low primary-beam energies with regard to the treatment of the slowing-down stage (I). For medium-mass ions such as argon, such simulations have rarely been performed at energies exceeding 5-10 keV. For lighter ions at similar energies, penetration depths and pathlengths become exceedingly high and impose even narrower limits on accessible energy.

The three simulation techniques have been reviewed extensively in the contributions by ROBINSON and NIEMINEN to this volume. A contribution about transport theory has not been solicited since most of the fundamental concepts have been developed long ago. They are still valid and have been summarized repeatedly (Sigmund, 1972, 1981, 1987). More recent work is mentioned in proper context in several contributions to this volume.

In stage II, cascade processes and transport, it is necessary to distinguish between electronic and collisional sputtering. In electronic sputtering, energy may be dissipated first electronically and, after having been transferred into nuclear motion, also collisionally. Therefore, both ionization cascades and collision cascades may be important, as may be transport of electronic excitation as well as kinetic energy of atoms and matter. The pertinent collection of theoretical tools depends heavily on the material. As far as transport of atoms is concerned, molecular-dynamics has proved to be a useful tool in addition to classical hydrodynamics. Binary-collision-type of models, regardless of which kind, tend to be less useful in view of the extremely low energies (less than 1 eV per atom) that are frequently involved. As far as ionization cascades and excitation transport are concerned, pertinent theory is available from fields like luminescence physics and radiation dosimetry. References may be found in the contribution by JOHNSON and SCHOU.

In collisional sputtering, the description of stage II is conceptually very simple. The accuracy of the output is limited mainly by the degree of reliability of the pertinent cross sections for elastic collisions or the equivalent interatomic potentials utilized in the calculations. In a collision cascade, particles are followed down to very low energies, and since the number of participating atoms increases with decreasing energy, cross sections at the lowest energies enter with the highest statistical weight. Most important are cross sections in the range from the surface binding energy up to a few tens eV, and these are just about the least well-known ones.

The strength of analytical sputter theory (Sigmund, 1969, 1981) lies in the recognition of two pertinent energy ranges, one of the order of the primary energy and another one of the order of the surface binding energy. The major uncertainty about the interaction potential can, therefore, be condensed into one single parameter, which happens to be closely related to the depth of origin of sputtered atoms. Some of these points are reviewed in my contribution with LAM to the present volume.

In simulations of sputter events, atoms may achieve any amount of energy from a certain maximum downward. Hence, definite assumptions must enter about interaction forces at any achievable energy. Some progress has been made in the theory of interatomic potentials in particular in metals, including many-body interaction potentials, and this progress is extensively discussed in the contributions by NIEMINEN and ROBINSON. The main strength of many-body potentials is their capability to quantitatively characterize bulk and surface binding forces.

There are some conceptual differences in the characterization of collision cascades between the four available techniques which have been discussed by Andersen (1987) in a very illuminating overview. Comparisons between different simulation codes have been reviewed in ROBINSON's contribution.

As in the case of stage I, the range of applicability of transport theory and Monte Carlo simulation is restricted to materials where lattice structure is not of primary importance. Inspection of fig. 3 indicates that the crystal lattice structure might play a significant role in the development of a collision cascade. In fact, experimental results of the type shown in fig. 3 had a major influence on the direction of research in sputtering for more than a decade starting in 1955. Random collision events were considered only to govern primary interactions, and the dominating means of energy and mass transport was thought to be linear collision sequences, with or without replacement, on close-packed lattice rows. The first molecular-dynamics simulations in the pertinent energy range appeared to confirm the qualitative picture (Gibson et al., 1960). It has since then become clear — as is documented in ROBINSON's contribution — that those simulations overestimated the statistical significance of linear collision sequences. There are two main reasons for this. Firstly, the range of starting directions sampled in a limited number of simulation runs was confined to a single close-packed lattice plane. Secondly, starting energies were not sampled from a representative recoil spectrum. This kind of lesson has probably been learned repeatedly in the history of computational physics.

It was mentioned above that the absolute magnitude of the sputter yield depends on the surface binding energy. A rough, inverse relationship between measured sputter yields and the heat of sublimation has been known for a very long time (Behrisch, 1964), but accurate knowledge of surface binding forces for sputtering was lacking. The standard model was a planar surface potential (Thompson, 1968), similar to the one used in electron emission. More detailed models were based on bondbreaking arguments. Accurate theoretical predictions of forces between atoms and solid surfaces are now becoming available (Daw & Baskes, 1984; Finnis & Sinclair, 1984, Jacobsen et al., 1987) and may be utilized either directly in dynamic simulations, or indirectly as input into transport calculations or non-dynamic (Monte Carlo or binary-collision) simulations.

6 Theoretical Results

Many well-established results from sputter theory will be quoted more or less explicitly by the authors of the present volume. There are, however, a few central relationships which it may be useful to be aware of from the beginning.

The first is the so-called $(\text{energy})^{-2}$ law which dates back to Robinson (1965). This fundamental property of linear collision cascades shows up on numerous occasions, expected or unexpected, rigorous in some connections, approximate in others. For detailed discussion, the reader is referred to Sigmund (1972, 1981). The most rigorous result refers to the 'recoil density', which may be defined as the mean number of atoms recoiling with an energy in the interval $(\epsilon, d\epsilon)$ as the result of the slowing-down of a primary ion of energy E in an infinite, monoatomic, random medium. That quantity is given by

$$F(E,\epsilon)d\epsilon \sim \Gamma \frac{\nu(E)}{\epsilon^2} d\epsilon \text{ for } E \gg \epsilon, \tag{1}$$

where $\nu(E)$ is the portion of the initial energy E which is not transferred into electronic excitation, and Γ is a constant depending somewhat on the atomic interaction potential. The important feature is that the detailed nature of the elastic-scattering cross section only enters into the factor Γ but not into the dependence on recoil energy ϵ. While the above result has been derived on the basis of linear cascade theory, i.e., for long quasi-free flight paths and point particles, the simple analytical form suggests it to be more general. In fact, recoil spectra extracted from computer simulations confirm this behavior, even for crystalline targets and at quite low primary energies.

While the recoil density is a central quantity in sputter theory, it is only indirectly related to measurable energy spectra of sputtered atoms. Nevertheless, the latter spectrum is also frequently denoted as an $(\text{energy})^{-2}$ distribution. The spectra differ because of the effect of (bulk and) surface binding forces as well as the fact that the flux of sputtered atoms has contributions from several atomic layers beneath the surface, the relative significance of which depends on energy but decreases rapidly with increasing depth of origin. The recognition of both features dates back to Thompson (1968).

Consider first the effect of a planar surface potential U. If the energy spectrum of atoms arriving at the target surface were given by ϵ^{-2}, an atom moving at an angle θ to the surface normal would be emitted at an angle θ' and energy ϵ' given by the relations

$$\epsilon' = \epsilon - U; \; \epsilon' \cos^2\theta' = \epsilon \cos^2\theta - U, \tag{2}$$

and the energy spectrum of sputtered atoms would read

$$Y(\epsilon') \propto \frac{\epsilon'}{(\epsilon' + U)^3} \tag{3}$$

for an isotropic flux of atoms within the target. This 'Thompson spectrum' is the common reference standard for measured energy spectra of sputtered atoms (Gruen et al., 1983). It has frequently served as a tool for 'experimental' determination of surface binding energies. The main objection to this scheme is that the Thompson formula implies a cosine distribution of the sputtered flux which is rarely observed experimentally.

The contribution from deeper layers to the sputtered flux can be evaluated easily (Thompson, 1968; Sigmund, 1981). If surface binding is ignored, this results in the expression

$$Y(\epsilon)d\epsilon \propto \frac{1}{\epsilon S(\epsilon)} \tag{4}$$

for the spectrum of sputtered particles, i.e., one factor ϵ has been replaced by the stopping cross section $S(\epsilon)$ of a moving target particle. At low energies, $S(\epsilon)$ is not too far from $\propto \epsilon$, hence the difference is hard to identify. At high energies, $S(\epsilon)$ decreases with increasing energy, and the denominator in eq. (4) will vary very slowly. As a result, one expects the spectrum to level off. This behavior, expected to be observable in sputter experiments at high-energy heavy-ion accelerators such as GSI or GANIL, is worth remembering. Such extreme experimental conditions are not foreseen in conventional computer simulation codes.

7 Sputtering in Nature, Science, and Technology

A monograph with such a title has never been written to the author's knowledge but could be very stimulating reading. As in other parts of this introduction, I shall try to provide a few keywords and key references rather than go into a detailed listing or even discussion of occurrences and applications of sputter phenomena.

There is no doubt that sputter phenomena have played and still play a major role in stellar and planetary processes. Observational studies refer to planetary bodies such as meteorites, the Moon, and Jupiter's satellites. Sputter erosion of the Moon by solar-wind bombardment was first mentioned by Wehner et al. (1963). Interest in this type of phenomenon was greatly intensified by the discovery of electronic sputtering from water ice (Brown et al., 1978) as well as the observation of isotopic anomalies in meteorites and lunar samples. Pertinent reviews have been provided by Johnson (1990) on the former complex of problems and by TOMBRELLO in this volume on the latter.

While appearances of sputter phenomena on planetary bodies exposed to external irradiation are commonly thought to be restricted to those that do not carry an atmosphere, it was demonstrated that planetary atmospheres also may erode by sputtering due to the action of the solar wind and solar flares (Haff et al., 1978). Several features of conventional collision cascade theory apply to this system, and 'surface' binding energies equivalent to escape velocities from the gravitational field may even be comparable in magnitude with those encountered in conventional sputtering.

Sputter phenomena are an inevitable by-product of radioactivity. Heavy recoil atoms from α decays may cause violent sputter events which are responsible for the high volatility of radioactive materials (Riehl, 1963). Emitted α or β rays may give rise to pronounced electronic sputtering along with other radiation effects, dependent on the pertinent material. Such processes have been intensely studied in connection with the isolation of radioactive waste (Chakoumakos et al., 1987; Matzke, 1992).

As mentioned above, sputter yields for bombardment with (fast or thermal) neutrons are very small, but sputter rates may be substantial in the presence of high neutron fluxes such as in fission and fusion reactors (Behrisch, 1983b). Specifically for fusion reactors, the problem of plasma-wall interaction has a substantial component of sputter-related processes which has been the subject of major national and international research programs (Engelmann, 1986). Typical candidates for first-wall materials are metals, alloys, and carbon-based materials. Mostly collisional sputtering is of concern here because it is unavoidable, while chemical erosion effects are expected to be controlled. Electronic sputtering, on the other hand, is a key process connected with the injection of fuel into the fusion plasma in the form of pellets of solid hydrogen (Chang, 1991).

Probably the earliest technological application of sputtering is the deposition of thin films by collection of the sputtered flux from one or several bombarded materials. Wright (1877) produced films of hitherto unseen smoothness of a large number of metallic elements and pointed at important applications such as coating of astronomic mirrors and the like. This area has developed to major technological importance, reaching from coatings on large glass windows, photographic lenses, and razor blades to contacts on integrated circuits. More recently, production of alloys and compounds such as conventional low-temperature and ceramic high-temperature superconductors has come into focus (Geerk et al., 1989).

Sputtering has long been useful as a tool of etching, polishing, and cleaning material surfaces. This topic has been discussed by TAGLAUER in this volume.

A sputter gun is a standard piece of equipment on ultrahigh vacuum systems. It is utilized universally as a tool of initial sample preparation, in particular surface cleaning, and secondly for analytic purposes.

Sputtering as an analytic tool has revolutionized several scientific disciplines. In sputter profiling, sputtering is utilized as an etching technique in conjunction with any technique to determine the bulk or surface composition of a material. Originally, the technique was developed to determine depth profiles of implanted radioactive tracers (Lutz & Sizmann, 1964). Presently, Auger lines form the standard signal in the technique, as described by TAGLAUER in this volume.

Analysis of the composition of the sputtered flux from a material provides information on its composition. In case of an inhomogeneous material, analysis of the sputtered flux as a function of irradation time or fluence provides information on the depth profile. Standard techniques go under the headings of secondary-ion mass spectrometry (SIMS), secondary neutral mass spectrometry (SNMS), accelerator mass spectrometry (AMS), plasma desorption mass spectrometry (PDMS), and fast atom bombardment (FAB). TAGLAUER's contribution focuses on several analytic aspects related to inorganic materials. Applications related to biological materials are connected to the contributions by ENS, HÅKANSSON, and KARAS to this volume. All these techniques are extremely useful but have severe problems with regard to quantification. Indeed, there are problems both in the relation between the composition of the sputtered flux and the composition of the bombarded material, and in the relation between the composition of the sputtered flux and the measured signal. The wide application of these techniques provides a major stimulus to theoretical and experimental research on fundamental processes in sputtering.

Acknowledgements

Thanks are due to R. F. Haglund, P. Håkansson, R. E. Johnson, N. Q. Lam, C. T. Reimann, M. T. Robinson, J. Schou, E. Taglauer, and T. A. Tombrello for comments and suggestions on the manuscript. This work has been supported by the Danish Natural Science Research Council (SNF).

References

Andersen HH, 1987: Nucl. Instrum. Methods B **18** 321

Andersen HH and Bay HL, 1981: in Behrisch (1981), p. 145

Behrisch R, 1964: Ergebn. Exakt. Naturwiss. **35**, 295

Behrisch R, 1981: *Sputtering by Particle Bombardment I*, Top. Appl. Phys. **47** (Springer, Heidelberg)

Behrisch R, 1983a: *Sputtering by Particle Bombardment II*, Top. Appl. Phys. **52** (Springer, Heidelberg)

Behrisch R, 1983b: in Behrisch (1983a) p. 179

Behrisch R and Wittmaack K, 1991: *Sputtering by Particle Bombardment III*, Top. Appl. Phys. **64** (Springer, Heidelberg)

Besenbacher F, Bøttiger J, Graversen O, Hansen JL and Sørensen H, 1981: Nucl. Instrum. Methods **191**, 221

Bethe H, 1930: Ann. d. Physik **5**, 325

Betz G and Wehner GK, 1983: in Behrisch (1983a) p. 11

Brown WL, Lanzerotti LJ, Poate JM and Augustyniak WM, 1978: Phys. Rev. Lett. **40**, 1027

Carter G, Navinček B and Whitton JL, 1983: in Behrisch (1983a) p. 231

Chakoumakos BB, Murakami T, Lumpkin GR and Ewing RC, 1987: Science **236**, 1556

Chang CT, 1991: Phys. Repts. **206**, 143

Crookes W, 1891: Proc. Roy. Soc. London **50**, 88

Daw MS and Baskes MI, 1984: Phys. Rev. B **29**, 6443

Engelmann F, 1986: in *Physics of Plasma-Wall Interactions in Controlled Fusion*, D. E. Post & R. Behrisch, editors (Plenum, New York) p. 15

Fano U, 1963: Ann. Rev. Nucl. Sci. **13**, 1

Finnis MW and Sinclair JE, 1984: Phil. Mag. A **50**, 45

Geerk J, Linker G and Meyer O, 1989: Mater. Sci. Repts. **4**, 193

Gibson JB, Goland AN, Milgram M and Vineyard GH, 1960: Phys. Rev. **120**, 1229

Gruen DM, Pellin MJ, Young CE, Mendelsohn MH and DeWald AB, 1983: in IISC (1983) p. 42

Günterschulze A and Tollmien W, 1942: Zeits. f. Physik **119**, 685

Haff PK, Switkowski ZE and Tombrello TA, 1978: Nature **272**, 803

Hofer WO, 1991: in Behrisch & Wittmaack (1991) p. 15

IISC, 1977: *Inelastic Ion-Surface Collisions*, N. H. Tolk, editor (Academic Press, New York)

IISC, 1981: *Inelastic Particle-Surface Collisions*, W. Heiland and E. Taglauer, editors, Springer Ser. Chem. Phys. **17**

IISC, 1983: *Inelastic Ion-Surface Collisions*, P. Sigmund, editor, Phys. Scr. **T6**

IISC, 1987: *Inelastic Ion-Surface Collisions*, D. M. Gruen, editor, Nucl. Instrum. Methods B **27** no. 1

Inokuti M, 1971: Rev. Mod. Phys. **43**, 297

Jacobsen KW, Nørskov JK and Puska MJ, 1987: Phys. Rev. B **35**, 7423

Johnson RE, 1990: *Energetic Charged Particle Interactions with Atmospheres and Surfaces*, (Springer, Berlin)

Lindhard J, Scharff M and Schiøtt HE, Mat. Fys. Medd. Dan. Vid. Selsk. **33**, no. 14

Lutz H and Sizmann R, 1964: Zeits. f. Naturforsch. **19a**, 1079

Matzke HJ, 1992: Nucl. Instrum. Methods B **65**, 30

Riehl N, 1963: Dechema-Monographien **45**, 77

Robinson MT, 1965: Phil. Mag. **12**, 145

Roosendaal H, 1981: in Behrisch (1981) p. 219

J.Roth, 1980: in Varga et al. (1980) p. 773

Sigmund P, 1969: Phys. Rev. **184**, 383; **187**, 768

Sigmund P, 1972: Rev. Roum. Phys. **17**, 823, 969, 1079

Sigmund P, 1975: in *Radiation Damage Processes in Materials*, edited by C. H. S. Dupuis, NATO ASI Series, Ser. E no. 8 (Noordhoff, Leiden) p. 3

Sigmund P, 1977: in IISC (1977) p. 121

Sigmund P, 1981: in Behrisch (1981) p. 9

Sigmund P, 1983: Phys. Scr. **28**, 257

Sigmund P, 1987: in IISC (1987) p. 1

Thompson MW, 1968: Phil. Mag. **18**, 377
Townsend PD, in Behrisch (1983a) p. 147
Varga P, Betz G and Viehböck FP, 1980: *Symposium on Sputtering* (Inst. f. Allg. Physik, Vienna)
Wehner GK, 1956: Phys. Rev. **102**, 690
Wehner GK, Kennight C and Rosenberg DL, 1963: Planet. Space Sci. **11**, 885
Wright AW, 1877: Amer. J. Sci. **13**, 49; **14**, 169

Computer Simulation of Sputtering

By Mark T. Robinson
Solid State Division, Oak Ridge National Laboratory
Oak Ridge, Tennessee 37831-6032, USA

Synopsis

In 1986, H. H. Andersen reviewed attempts to understand sputtering by computer simulation and identified several areas where further research was needed: potential-energy functions for molecular-dynamics modelling; the role of inelastic effects on sputtering, especially near the target surface; the modelling of surface binding in models based on the binary-collision approximation; aspects of cluster emission in molecular-dynamics models; and angular distributions of sputtered particles. To these may be added kinetic-energy distributions of sputtered particles and the relationships between molecular-dynamics and binary-collision models, as well as the development of intermediate models. Many of these topics are discussed. Recent advances in binary-collision modelling include the explicit evaluation of the time in strict binary-collision codes and the development of intermediate codes able to simulate certain many-particle problems realistically. Developments in molecular-dynamics modelling include the wide-spread use of many-body potentials in sputtering calculations, inclusion of realistic electron excitation and electron-phonon interactions, and several studies of cluster-ion impacts on solid surfaces.

Contents

1 Introduction

Computer simulation has long been an important tool in studying the complex interactions of energetic ions with condensed matter which underlie such physical processes as particle reflection (backscattering) and penetration, ion implantation, radiation damage, and target erosion (sputtering). These are processes important to such technologies as controlled fission and fusion power generation, laser isotope separation, semiconductor device manufacture, plasma processing, and others. Moreover, they are the basis for the use of ion beams in more narrowly scientific areas, such as secondary-ion mass spectrometry, surface structure determination, the location of defects and impurities in solids, and so on. For these and other reasons, the interactions of ions with solids have been studied for many years by experimental, theoretical, and computational techniques.

The methods of computational physics are useful for the direct simulation of experiments, but also supply important tools for testing the assumptions of analytical theory. In addition, the computational physicist has an almost unlimited access to the atomistic details, the mechanisms whereby the initial disturbances are linked to experimental observables. The elucidation of these mechanisms is an important objective of computer simulation.

At the conference on sputtering in Spitz an der Donau, Austria, in 1986, H. H. Andersen (1987) presented a critical review of the status of the computer simulation of atomic collisions in solids, with a special emphasis on sputtering. Besides giving an admirably balanced and objective view of the state of the art at the time, Andersen pointed to a number of topics in need of further study. It is my purpose to examine the progress made in the past few years in addressing topics which he highlighted. A comprehensive review of the literature is not attempted: for this and for reviews of the subject from a variety of viewpoints, consult Robinson (1981), Yurasova & Eltekov (1982), Harrison (1983, 1988), Andersen (1987), Sigmund (1987b), Biersack (1987), Dodson (1989), Mashkova & Molchanov (1989), Barrett (1990), Eckstein (1991), and Smith & Webb (1992). These cover the literature rather completely up to about 1991.

This review is restricted to the low-dose sputtering of single-component targets under circumstances where atomic ejection is not a result of electron excitation effects. For a review of the electronic sputtering of inorganic insulators, see the companion article by Johnson & Schou (1993).

2 Recent Developments in Computer Hardware

Since 1986 there have been dramatic changes in computer hardware, which greatly alter the prospects for computer simulation. The developments include the introduction of scientific workstations which put what was once supercomputer power on (or next to) the desktop and major advances in parallel computing. Such developments make vector processors of the Cray type obsolete and revolutionize the environment in which simulation is done. Many of the controversies of the past are no longer interesting, since they can now be addressed in a simple manner by direct computation instead of by mere argument.

Several manufacturers have introduced machines based on so-called reduced-instruction-set computing (RISC). Using a simplified repertoire of commands, such machines achieve much higher speeds than were common heretofore. Moreover, manufacturing improvements make the new systems available at startlingly low cost and eliminate significant constraints on computer memory. To illustrate, Table 1 shows the time required by a set of MARLOWE (Robinson & Torrens 1974, Robinson 1989) test problems on some contemporary machines (Robinson 1992a). The IBM RISC System/6000, Model 320H, costs little enough in typical configurations that it can be viewed as a single-user workstation. Some models in this series support up to 512 megabytes of memory. The Cray X-MP, costing many times more, is less than twice as fast on MARLOWE and cannot compete in cost effectiveness. The situation depends strongly on the individual program, but few codes

Table 1: MARLOWE Test Problem Execution Times on Comtemporary Computers (Robinson 1992c)

Computer	Time (seconds)[a]
Cray X-MP 14	270
IBM RISC System/6000	
Model 320H	444
Model 560	222
Hewlett-Packard HP/9000	
Model 730	223
Digital VAX 6420	1141
IBM 3090-150E	458

[a] The time is the total for a set of 14 test problems

are likely to achieve time reductions exceeding five merely through vectorization.

A closely related development is the introduction of 'massively parallel' machines, such as the CM-5 from Thinking Machines Corp. and the Paragon from Intel. The former, a so-called SIMD (single instruction multiple data) machine, may be thought of as an extension of vectorization to a level a hundred times that of a Cray. The latter, an MIMD (multiple instruction multiple data) machine, resembles a network of workstation class machines, each operating more-or-less autonomously on parts of a complex task and communicating among each other by passing messages. It is also possible to use an actual network of workstations as a parallel-computing environment.

The challenging tasks are to identify the architecture appropriate to each computational application and to construct programs that use the architecture efficiently in solving the problem. Parallel computing is not simply an extension of previous practices, but, like vector processing, demands new computational techniques and new ways of formulating problems. Work on parallel implementations of classical-dynamical models is well-advanced at several institutions. It will be interesting to see these developments come to fruition in studies of (for example) sputtering in the next few years.

3 Computer Simulation Models

A rather complete list of the programs used to simulate sputtering processes is given in the report of a round-robin collaboration (Sigmund et al. 1989). It is difficult to develop a fully satisfying taxonomy of such codes for each has characteristic features which differentiate it from nominally similar ones. However, for the purposes of this review, four main categories of model are identified: the scheme and the notation used are those of the round-robin report.

First are codes which integrate the classical equations of motion of a large number of particles simultaneously, commonly called molecular-dynamics (MD) models. They are used widely in physics; for reviews, see Abraham (1986), Hoover (1986), and Allen & Tildesley (1987), among others. The best-known MD models for sputtering applications are those of D. E. Harrison, Jr. (Harrison 1983, 1988, Harrison & Jakas 1986a). The hallmark of the MD models used to simulate atomic-collision processes is that they integrate the equations of motion of many atoms until the energy added in an initial disturbance is dissipated or until some other condition is met. Various sorts of boundary conditions are used: cyclic, dissipative, fixed, free, and so on. Two-body interaction potentials were used originally, but several groups now use many-body potentials. Inelastic effects may be included. The MD models are particularly effective in working out detailed mechanisms. Questions still remain, however, about the sizes of the numerical crystallites required (event containment) and about the statistics of such calculations. Nieminen (1993) discusses the present status and future prospects of molecular-dynamics modelling.

Next are two sorts of codes using the binary-collision approximation (BCA) to solve the equations of motion of projectiles which are assumed to interact with the target atoms one at a time. This is appropriate at high kinetic energies, but breaks down at low ones. The two types of BCA codes are differentiated by the structures of the solid targets. In one group, as in the MD codes, the target has a definite structure: these are termed BC models. Besides conserving energy and momentum, such codes also conserve particles (as do MD codes), since it is easy to arrange that target sites emit only one atom. The principal example of BC codes is MARLOWE (Robinson 1989, 1992a). Such BC programs may provide an approximate treatment of overlapping collisions which occur at nearly the same time, designed to preserve the crystal symmetry which often accompanies them (Robinson 1989, 1993).

Aleatory (stochastic) methods are used in the second group of BCA codes to determine the locations of target atoms, to select impact parameters or scattering angles, and so forth. In general, such Monte Carlo (MC) codes conserve energy and momentum in single collisions, but do not conserve the number of particles. The targets are structureless: there are no correlations between the positions of target atoms except those imposed by the density of the substance. The principal examples of such programs are the family of TRIM codes (Biersack 1987).

There is unfortunate confusion in the literature between the two kinds of BCA codes, in part a result of the habit of some writers of referring improperly to the

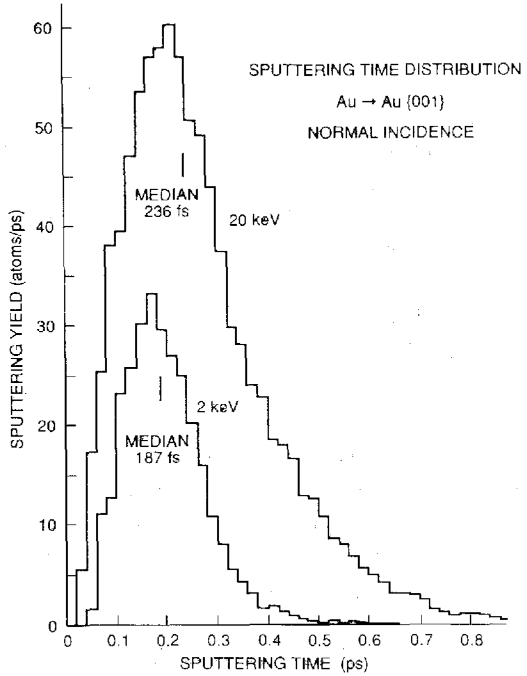

Figure 1. The distribution of sputtering times for 2 keV and 20 keV Au atoms, normally incident on Au {001} surfaces (Robinson 1992c). The potential is the Molière potential used earlier (Robinson 1992b). The median ejection times are indicated. The reference plane for the sputtering time was located 0.253 nm (0.62 of the lattice constant) in front of the target surface.

BC models as ‘Monte Carlo’ codes. Contrary to some statements (see, for example, Harrison & Jakas 1986a, Harrison 1988, Dodson 1990), aleatory methods play no part in determining target atom locations, impact parameters, scattering angles, and the like, in BC programs like MARLOWE.

In general, BCA codes (both BC and MC types) ignore the temporal aspects of cascade development, but it was shown recently (Robinson 1989) that the time of a collision may be evaluated explicitly in such codes, a result used to modify MARLOWE so that collisions are correctly ordered in time (Robinson 1990, 1992b, 1993). It is thus possible for BC codes to calculate things which had been thought of as the sole province of MD codes. To illustrate, Fig. 1 shows sputtering-time distributions obtained with MARLOWE for the self-sputtering of gold at two initial kinetic energies (Robinson 1992c). The histograms are similar to those reported by Harrison (1988) for other systems. The median ejection times for Au are a little greater than he reported for Cu and Rh, mainly because of the greater mass of Au. Other MARLOWE studies of temporal aspects of sputtering are reported elsewhere (Hou et al. 1993).

There are also codes of intermediate type, combining aspects of MD models with those of BCA models. Yamamura describes two interesting models of this type: one is the 'dynamic' MC code DYACAT (Yamamura 1982, 1988, 1990, 1991), based on the earlier MC program ACAT (Takeuchi & Yamamura 1983); the other is the 'dynamic' BC code DYACOCT (Yamamura et al. 1989), based on the BC program ACOCT (Yamamura & Takeuchi 1987). Both codes include collisions between moving projectiles and keep track of the time properly. At each encounter, they locate the potential target atom for which the collision time is least and a collision diameter is derived from the parameters of this encounter. If only one target is found within the collision diameter, the BCA is applied in the usual way, including the necessary modifications for moving target atoms. However, if several targets are present, the codes integrate the equations of motion of the entire group of particles, including the interactions of the projectile with all targets, but ignoring the interactions of the targets with each other. With these modifications, Yamamura's codes remain comparatively fast, but are still able to deal with many situations where MD codes were previously required. For example, DYACAT was used to study cluster bombardments (Yamamura 1990, 1991).

The QDYN program (Harrison & Jakas 1986a) is also an intermediate code, but one much closer to full MD models than are Yamamura's. The motion of an atom is ignored until it is struck by an already moving atom with a force exceeding a minimum value. This feature resembles aspects of quasistable MD codes (Schlaug 1966, Torrens 1973, Schwartz et al. 1976, Heinisch et al. 1979), although the older programs used energy criteria instead. In either case, completeness in the model is surrendered to achieve speed.

An alternative procedure for accelerating MD calculations is to truncate the interaction potential severely, including only repulsive forces between atoms separated by less than the equilibrium nearest-neighbor distance in the target, and adjusting matters so that there is no force between atoms on their equilibrium sites. Such metastable MD models permit quite speedy calculations and were once widely used (see Robinson 1981 for references), but their lack of restoring forces restricts them to problems in which the equilibrium state is not important. A recent example of such a code is that of Shulga (1991).

Hybrid codes are also possible. For example, Webb et al. (1986) describe QDRIM, a code which combines a TRIM-like treatment of deeply penetrating particles with a QDYN treatment of the region near the surface. Another hybrid approach is that of Pan & Hou (1992), who used MARLOWE for the collisional phase of cascade development and an MD model to follow the aging of the nascent defect distribution. A problem with such hybrid models is to obtain the proper temporal matching: since slow and stopped particles are present in simulated cascades almost from the beginning (Robinson 1990), it is not clear that the matching can always be achieved satisfactorily.

In view of the great advances in computing hardware mentioned above, a comment is in order concerning the relationships between MD codes and BCA codes. The former now follow collision cascades involving 10^4 to 10^6 atoms for simulated times up to a few picoseconds. Nevertheless, there will long be computations too massive for widespread study by MD, where swifter, but more approximate, computational methods are useful. Such applications include achieving precise statistics, where large numbers of cascades must be evaluated; cascade studies in complex materials, such as noncubic compounds, where it is difficult to determine equilibrium potentials reliably; and high-energy cascade studies. In addition, the fast response of BCA codes will remain useful for interpreting experimental data in surface physics studies and for rapid surveys of new topics. On the other hand, for cascade studies in highly symmetrical crystals containing atoms of very different masses, as, for example, Au-Cu alloys or UO_2, MD codes may be required to simulate accurately such processes as linear collision sequences along mixed atomic rows.

4 Interatomic Potentials

The interatomic potentials used in simulations of atomic collisions in solids may be divided into two groups. In close encounters, the change in potential energy is determined almost entirely by the positions of only two atoms, the other atoms of the target being merely spectators. In such encounters, a spherically-symmetrical, pairwise, repulsive interaction potential is appropriate, reflecting the essentially atomic nature of the distribution of electrons about the nuclei. Most BCA models use only these potentials although potentials with attractive parts are easily employed (Eckstein et al. 1992). At distances approaching or exceeding the normal separations of atoms in crystals, however, several atoms contribute significantly to changes in the potential energy. The electron distributions reflect the binding of the atoms in the target. Such binding effects may be supplied by the boundary conditions on a numerical crystallite, by spherically-symmetrical potentials with attractive regions, by many-body potentials, or by combinations of these. The two interaction ranges are considered separately.

4.1 Potentials for Close Encounters

Pairwise potentials for close encounters are often taken as the internuclear Coulomb repulsion, screened by a function describing the distribution of atomic electrons about the two nuclei. The very difficult problem of accurately evaluating the screening function must be approximated in various ways. First, dynamical effects on the electrons of the relative motion of the nuclei are neglected: this is the well-known Born-Oppenheimer approximation. Failure of this approximation in fast collisions probably cannot be distinguished from electron promotion and other inelastic effects discussed later. Second, the possible formation of molecular states from the atomic states of the colliding atoms must be considered. One important line of development assumes that the electron densities about the colliding atoms experience no redistribution, but may simply be superposed (Gombás 1956, Gordon & Kim 1972), with corrections to the kinetic energies of the electrons as well as corrections for electron exchange and correlation. These corrections are based on the properties of a uniform gas of free electrons of the same density. The atomic electron distributions may be taken from the Thomas-Fermi statistical model of the atom (Gombás 1956) or more accurate atomic wavefunctions may be used (Gordon & Kim 1972). When the two atoms approach each other slowly, however, there may be time for the electrons to form molecular states: see Dodson (1990, 1991) and Nakagawa (1990) for discussions of bonding effects in slow encounters. Instead of merely superposing the atomic electron distributions, so-called ab initio methods may be used to treat the molecular problem.

Molière (1947) proposed a numerically convenient approximation to a screening function derived from the Thomas-Fermi statistical model of the atom (Gombás 1956), which has the screening length

$$a_{\mathrm{TF}} = \left(\frac{9\pi^2}{128}\right)^{1/3} \frac{a_{\mathrm{H}}}{Z^{1/3}} \tag{1}$$

where Z is the atomic number of an atom and a_{H} is the Bohr radius (52.9 pm). Firsov (1957) and Lindhard et al. (1968) used the statistical model as a basis for developing approximate interatomic potentials. They expressed their results compactly by using the atomic Thomas-Fermi screening function with a screening length given by Eq. (1) with

$$\begin{aligned} \text{Firsov: } Z &= \left(Z_1^{1/2} + Z_2^{1/2}\right)^2 \\ \text{Lindhard: } Z &= \left(Z_1^{2/3} + Z_2^{2/3}\right)^{3/2} \end{aligned} \tag{2}$$

Ziegler et al. (1985) applied a local-density model which uses atomic electron distributions based on self-consistent Hartree-Fock atomic wavefunctions and includes free-electron corrections to the electron kinetic energy and for exchange and correlation (Gordon & Kim 1972; see Gombás 1956 and Ziegler et al. 1985 for additional references) to determine interatomic potentials. The resulting potentials should describe rather accurately the interactions of isolated pairs of atoms in their ground states. Ziegler et al. (1985) used the potentials computed for a large number of atom pairs as the basis for fitting a 'universal' (ZBL) potential for which they propose a screening length given by Eq. (1) with

$$\text{ZBL: } Z = \left(Z_1^{0.23} + Z_2^{0.23}\right)^3$$

The dependence of this screening length on the Z_i is weaker than those in Eq. (2). The need for a weaker dependence had already been noted (Robinson 1981, Eckstein 1991) and, in fact, the Molière potential is often used with screening lengths other than those in Eq. (2). The ZBL and Molière screening functions are both sums of exponentials:

$$\begin{aligned} V(r) &= \frac{Z_1 Z_2 e^2}{r}\phi(\frac{r}{a}) \\ f(x) &= \sum_{j=1}^{m} \alpha_j \; e^{-\beta_j x} \end{aligned}$$

$$\begin{aligned} \text{Moliere}: m &= 3; \\ \alpha &= \{0.35, 0.55, 0.10\}; \\ \beta &= \{0.3, 1.2, 6.0\} \\ \text{ZBL}: m &= 4; \\ \alpha &= \{0.02817, 0.28018, 0.50986, 0.18179\} \\ \beta &= \{0.2016, 0.4029, 0.9423, 3.2\}\ . \end{aligned}$$

These potentials are 'universal' in the sense that no explicit Z-dependence remains in the screening function. The ZBL potential is used to establish the approximate treatment of atomic scattering used in the TRIM codes (Biersack 1987) and is available in MARLOWE (Robinson 1992a). It is also used as the core portion of the interatomic potential in several MD codes (Valkealahti & Nieminen 1987, Diaz de la Rubia & Guinan 1990, Chou & Ghoniem 1991).

The ZBL potential is a reasonable description of the interactions of isolated pairs of atoms, especially those from the first half of the periodic table, as long

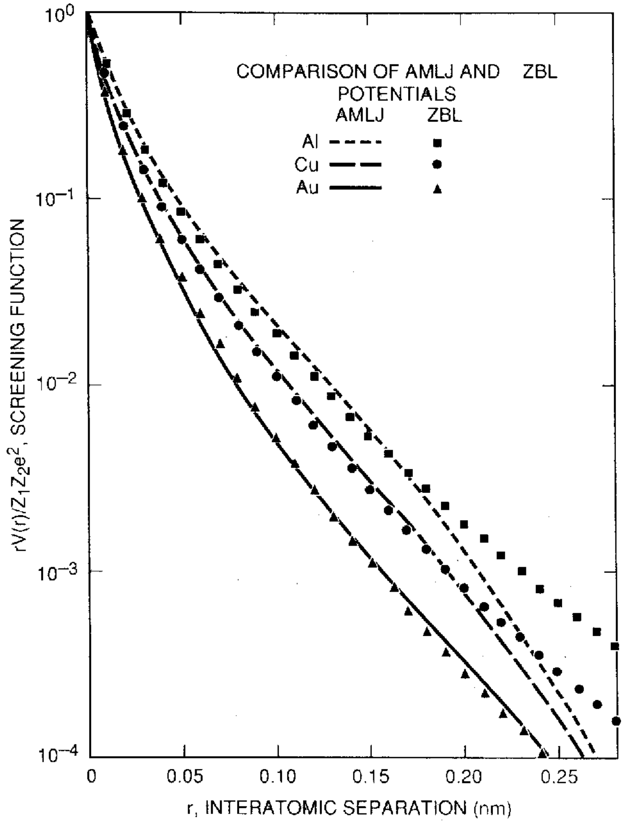

Figure 2. A comparison of the AMLJ (Nakagawa & Yamamura 1988, Nakagawa 1991) and ZBL (Ziegler et al. 1985) screening functions for Al, Cu, and Au atom pairs. The nearest-neighbor distances in the three crystals are 0.286, 0.256, and 0.288 nm, respectively.

as they remain in their ground-states (and as long as binding effects can be ignored). For heavier atoms, relativistic corrections should be included in the atomic wavefunctions, using, for example, the method of Tucker et al. (1969); tables of wavefunctions and electron densities are available for all atoms (Carlson et al. 1970, Lu et al. 1971).

Nakagawa & Yamamura (1988) used the relativistic electron densities of Carlson et al. (1970) in a statistical local-density calculation of the interactions of many pairs of atoms similar to the work of Ziegler et al. (1985). The atoms were confined to Wigner-Seitz cells representing the densities of the appropriate solids. An average modified Lenz-Jensen (AMLJ) potential was used to summarize the results. The screening function is

$$\phi(r) = e^{-\alpha_1 r + \alpha_2 r^{3/2} - \alpha_3 r^2}$$

with (Nakagawa 1991):

$$\begin{aligned} \alpha_1 &= \frac{1.706}{a_\mathrm{H}} \left(Z_1^{0.307} + Z_2^{0.307}\right)^{2/3} \\ \alpha_2 &= \frac{0.916}{a_\mathrm{H}^{3/2}} \left(Z_1^{0.169} + Z_2^{0.169}\right) \\ \alpha_3 &= \frac{0.244}{a_\mathrm{H}^2} \left(Z_1^{0.0418} + Z_2^{0.0418}\right)^{4/3} \end{aligned}$$

[Note that the original paper (Nakagawa 1991) uses atomic units and thus omits a_H from these formulas.] The AMLJ screening function is not 'universal': the three parameters show different Z-dependences so that the shape of the function varies with the atoms involved in the encounter. This behavior reflects the differing importance of the components of the total energy for different atom pairs, especially the density corrections to the electron kinetic energy and the exchange energy. The two screening functions are compared in Fig. 2 for Al, Cu, and Au atom pairs. They agree well for small separations, but significant differences appear at separations approaching the nearest-neighbor distances, especially in the lighter elements. These differences probably originate mainly in electron kinetic energy corrections resulting from confinement of the atoms in Wigner-Seitz cells. Evidently, relativistic corrections are small. The AMLJ potential is more efficient computationally than the ZBL: preliminary MARLOWE calculations (Robinson 1992c) required about 20% less time with the AMLJ potential than with the ZBL.

Several attempts have been made to establish interatomic potentials on a more fundamental basis. SCF methods were used to study potentials for Al-H (Sabelli et al. 1978) and Al-Al (Sabelli et al. 1979) interactions. In both cases, the changing symmetry of the ground-state with separation was followed, giving a clear picture of the effects of electron promotion on the potential. In the Al-Al potential, a 'kink' appears in the screening function near $2a_H$. For larger separations, the SCF potential is in excellent agreement with the local-density potential of Wilson et al. (1977).

Ab initio methods were used to evaluate potentials for a number of pairs of atoms for use in sputtering calculations. A potential was obtained for the interaction of Ar^+ with Cu, at separations from about 40 to about 140 pm, using the $^1\Sigma^+$ state of CuAr^+ as the basis (Broomfield et al. 1988). Figure 3 compares a screening function derived from this work with those for the ZBL potential and a Molière

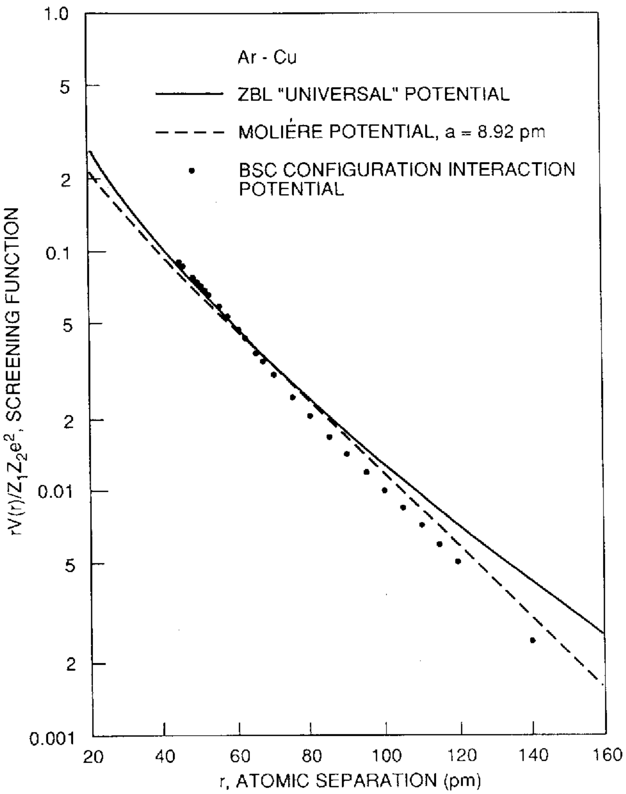

Figure 3. Screening functions for Ar-Cu collisions. The configuration-interaction potential of Broomfield et al. (1988) is compared to the ZBL 'universal' potential (Ziegler et al. 1985) and to a Molière potential with the screening length 8.92 pm (Hou & Robinson 1979).

potential with a screening length used in earlier sputtering calculations (Hou & Robinson 1979; Shulga 1982 made a similar choice). As the figure shows, the three potentials agree closely with one another. This result supports the use of the ZBL potential, but also makes it clear that the strategy of using the screening length as a fitting parameter in the Molière potential has merit. Similar potentials were calculated for Ar^+-Si and Si-Si (Stansfield et al. 1989) and for Cu-Si and Cu-Cl (Broomfield et al. 1990). Similar consistency was found between these potentials and the ZBL. In the Ar-Cu system, an avoided level crossing was noted at about 40 pm (that is, at about 1.8 keV), within which the model became unphysical and other level crossings were also mentioned. Similar crossings were found in the Ar-Si and Si-Si systems also. Such crossings signal that changes in the ground-state of the system must be expected and that electrons are likely to be promoted to excited states during an encounter (Fano & Lichten 1965, Lichten 1967, 1980, Barat & Lichten 1972).

Keinonen et al. (1991) reported potentials for K-Cl, Na-Cl, and Cl-Cl interactions, calculated for atomic clusters using density-functional theory. Their potentials also agree reasonably well with the ZBL ones.

Hsieh et al. (1992) used LCAO-MO calculations on small clusters to test a hybrid many-body potential with a Molière core. They obtained reasonable agreement for Cu-Cu and Ni-Ni interactions at energies up to 100 eV or so, but above this, their potential was more strongly repulsive than the Molière. It is not clear to what extent this results from many-body effects on the interaction between the closely-separated atoms, nor what changes would occur if the cluster were allowed to relax.

O'Connor & Biersack (1986) compared the ZBL, Molière, and other potentials with a large number of empirical potentials and found the ZBL to be the most suitable, although some of the others are sometimes useful. Other comparisons, with generally similar results were made by Chang et al. (1986, 1987) and by Chini & Ghose (1989). When a uniform beam of swift atoms is scattered from a target atom by a repulsive interaction, there is a conical region behind the target into which the beam atoms cannot penetrate. The size of this so-called shadowcone can be measured experimentally (see Eckstein 1991, p. 22, and Aono 1984). Chini and Ghose (1989) cite the Born-Mayer potentials of Andersen & Sigmund (1965) as giving good agreement with experimental shadowcones. Kato et al. (1988) find the ZBL potential to give a better account than does the Molière for experimental shadowcones observed in the scattering of 1 keV rare gas ions from a TaC (001) surface, especially when suitable account is taken of the effects of the image potential in accelerating the incident particle. The inclusion of image-potential effects might alter the other comparisons also. The AMLJ potential was compared (Nakagawa & Yamamura 1988, Nakagawa 1991) with experimental range data in Si using the ACAT code (Takeuchi and Yamamura 1983). The agreement was as good or better than O'Connor and Biersack (1986) found for the ZBL potential. Eckstein et al. (1992) compared range, sputtering, and ion reflection data, calculated for several two-body potentials with a version of the BCA code TRIM.SP (Biersack & Eckstein 1984), modified to integrate the two-body equations of motion instead of using the usual TRIM scattering approximations. The potentials were the Molière with the Firsov screening length, the ZBL, the so-called KrC potential (Wilson et al. 1977) with the Firsov screening length, and an ab initio Si-Si potential with an attractive region (Heinemann et al. 1990, Hackel et al. 1990; see also Eckstein 1991). Calculations were made for 0.1 to 10 keV Si on amorphous Si targets. Sputtering yields and reflection coefficients with the three repulsive potentials differed from those for the ab initio potential for ions incident at near grazing angles where large impact parameters are important. Otherwise, good agreement was found among the four potentials. These results support the otherwise universal use of purely repulsive potentials in BCA calculations.

The local-density method used in the ZBL and AMLJ calculations is restricted to atoms in their electronic ground-states, as were the other calculations cited. There is ample evidence (Kessel & Everhart 1966, Garcia et al. 1973, Grizzi & Baragiola 1987, Yu 1991) of inelasticity in atomic collisions in the gas phase, as well as in sputtering. Excited atoms emerging from such encounters have altered electron-density distributions and will interact according to an altered, usually more repulsive, potential-energy function in later collisions. Such effects are most important for the primary particle: since calculated sputtering yields are especially sensitive to the potential describing the interactions between the incident ions and the lattice atoms (Harrison 1981a, 1983, 1988, Broomfield et al. 1988), inelastic effects on this potential are likely to be significant. This sensitivity is explained by the result from analytical theory (Sigmund 1981) that sputtering yields closely follow the elastic stopping cross section of the incident particles. It is unlikely that the corresponding effects on interactions among the target atoms are important, as the great majority of them interact only at quite low energies, where inelastic effects will not greatly alter the electron-density distributions.

4.2 Many-Body Potentials

At the time of Andersen's (1987) review, almost all MD calculations in the atomic collisions field had been performed with pair potentials and models of this type are still used. One set of models uses a repulsive potential of the Born-Mayer type with crystal (meta)stability supplied by truncating the potential or by using boundary constraints (Averback et al. 1988, 1991, Caro et al. 1990, Diaz de la Rubia et al. 1987, 1989, Pan 1992, Pan & Sigmund 1990, Shulga & Sigmund 1990, 1991, Shulga 1991). In another set of models, the potentials are typically Morse potentials, splined to a suitable repulsive potential for close approaches between the atoms (Antonov et al. 1990, Averback et al. 1988, Betz et al. 1991, Broomfield et al. 1988, 1990, Diaz de la Rubia et al. 1989, Diaz de la Rubia & Guinan 1990, Harrison et al. 1987, Lo et al. 1987, Mazzone 1988, Pelletier et al. 1992, Shapiro et al. 1988, Shapiro & Fine 1989, Shapiro & Tombrello 1987, 1990a,b, 1991a,b, 1992a,b, Smith & Harrison 1989). Harrison (1983, 1988) discusses the use of Morse potentials.

For some purposes, pair-potential models are satisfactory and they are, moreover, more efficient computationally than more elaborate potentials. There are, however, many drawbacks (Finnis & Sinclair 1984, Carlsson 1990). First, purely repulsive models lead inevitably to close-packed structures and so are restricted to fcc metals. Second, in all pair-potential models, the proper relationships of the elastic constants can be achieved only through boundary conditions on the numerical crystallite. Such measures allow calculations for bcc metals, but are not altogether satisfactory, especially if the target has a free surface. Moreover, pair-potential models are not able to give a good account of selvage effects (relaxations, reconstructions), potentially important in sputtering, or of other defect properties, important in cascade studies as well as in more general solid-state contexts. Consequently, many-body potentials have been developed to better represent the properties of solids.

Two main classes of many-body potentials have been developed for use in studies of transition metals and semiconductors. The theory underlying these potentials and the relationships between them are reviewed in detail by Carlsson (1990). The basic idea is to express the configurational energy of a solid as the sum of two terms:

$$E_{\mathrm{C}} = \frac{1}{2}\sum_{i\neq j} V_2(\mathbf{R}_i,\mathbf{R}_j) + \sum_i U\left[\sum_j g_2(\mathbf{R}_i,\mathbf{R}_j)\right]$$

where the $\mathbf{R}_i$ are the positions of the atoms, V_2 is a pair potential, g_2 is a pair function describing the local environment of atom i in terms of the positions of its neighbors, and U is a function describing how the energy of atom i depends on its environment. It is possible to go further and allow U to depend on three- or more-body environmental terms, thus introducing angular forces into the picture, and this is generally required for substances with strongly-directional covalent bonds or for certain problems involving differences between similar structures. The pair potential is often taken as an exponential (Born-Mayer) repulsion, but any of the potentials discussed above could be employed. Furthermore, there is some arbitrariness in the division of E_C between V_2 and U: any term in U that is linear in the appropriate environmental parameter (see below) can be described by a pair potential.

One class of many-body potential is based on a tight-binding (TB) analysis (Cyrot-Lackmann 1968, Ducastelle 1970). When a solid is formed, the partly-filled atomic valence orbitals broaden into bands: this broadening supplies the attractive part of the bonding energy. It is assumed further that the valence-band electronic density of states on a particular site can be given in terms of radial contributions from the neighboring atoms. The binding function U is then expressed in terms of the moments of the density of states. Since the first moment vanishes (Carlsson 1990), the simplest approximation limits the model to the second moment, which becomes the environmental parameter, describing the width of the band, but ignoring its detailed shape. By adding higher moments to a TB model, various angular terms can be included in the interaction potential.

Another class of many-body potential is based on the so-called embedded-atom method (EAM) (Daw & Baskes 1984, Foiles et al. 1986). The solid is regarded as being assembled one atom at a time: the bonding energy is the energy gained by embedding one atom in the background electron density of all the other atoms. This density is the environmental parameter in the EAM. To make the treatment tractable for simulations, it is assumed that the bonding energy associated with a particular atom is determined by the local background electron density at the site of the embedded atom and it is further assumed that this density can be constructed as a superposition of radial functions centered on the other atoms. Angular terms can be added to EAM potentials by including gradients and higher derivatives of the electron density. It should be mentioned that the substantial formal similarities between the EAM and TB approaches (Carlsson 1990) often makes a distinction between them unnecessary or even impossible (see, for example, Johnson 1991).

Much like the EAM is so-called effective-medium theory (Jacobsen et al. 1987), useful in modelling various bulk and surface properties of metals. Each atom is embedded in a uniform electron density provided by its neighbors. The neighbor densities are averaged over the region occupied by the embedded atom. The parameters of the potential are then evaluated in the local-density approximation. Effective-medium potentials have not been used so far in atomic-collision calculations. See Carlsson (1990) for comparisons of the EAM and effective-medium theory.

Both the TB and EAM potentials may be parameterized and the parameters fit to such experimental data as the lattice constant, the cohesive energy, the bulk modulus, the elastic constants, the vacancy-formation energy, properties of the diatomic molecule, and surface properties. It is not possible to fit all experimental data with great precision and compromises are usually necessary, tailored to the needs of the particular simulation. Furthermore, fitting the parameters of many-body potentials to elastic-constant data in crystals without inversion symmetry poses special problems because of the effects of inhomogeneous strains (van Midden & Sasse 1992).

The EAM was originally applied to fcc metals, but Johnson & Oh (1989) and Adams & Foiles (1990) have described EAM models suitable for bcc metals. Suitable EAM potentials cannot be found for most of the hexagonal metals (Pasianot & Savino 1992), but TB potentials of the Finnis & Sinclair (1984) type are available (Igarashi et al. 1991), although these have been criticized (van Midden & Sasse 1992). A modified EAM was described recently by Baskes (1992).

Typical recent examples of EAM potentials are given by Garrison et al. (1988), Chen et al. (1990), and Guellil & Adams (1992). Recent TB potentials are given by Igarashi et al. (1991), Loisel et al. (1991), and Gades & Urbassek (1992). Like the pair potentials, both EAM and TB potentials may be combined with one of the repulsive potentials discussed above. Hsieh et al. (1992) use a cubic spline to connect a Molière core to the two-body part of an EAM potential; over the same range of separation, they smoothly remove the many-body part.

The EAM was used for simulations of low-energy hydrogen-atom reflection from metals by Baskes (1984), but was used first in sputtering simulations by Garrison and her coworkers (Garrison et al. 1988, Lo et al. 1988, Wucher et al. 1992, Wucher & Garrison 1992a,b, 1993). It is used in simulations of displacement cascade development (Diaz de la Rubia & Guinan 1990, 1991; Chou & Ghoniem 1991; Proennecke et al. 1991) and in studies of cluster impacts (Hsieh et al. 1992), as well as in other sputtering simulations (Gades & Urbassek 1992, Karetta & Urbassek 1992). Diaz de la Rubia & Guinan (1990) also use TB potentials of the type developed for bcc metals by Finnis & Sinclair (1984).

Angular forces are required to stabilize structures with strongly-directed chemical bonds, such as the diamond-structure semiconductors. A tight-binding analysis (Carlsson 1990) can be used to show how the inclusion of third- and fourth-moments in the evaluation of the bonding energy leads to terms depending on the positions of three or four atoms and thus introduces forces depending on the angles between the bonds. However, most simulation work uses not only empirically-fitted parameters, but also empirical dependences on bond angles.

A potential proposed by Stillinger & Weber (1985) combines two- and three-body terms. The former is a generalized Morse potential; the three-body term involves the lengths of three interatomic vectors and the angles between them. It was used in sputtering simulations by Stansfield et al. (1989). Tersoff (1986, 1988a,b,c) has proposed alternative potentials, also using a generalized Morse potential, but here the parameters are made functions of the local environment, including bond lengths and angles. The hazards in such empirical potentials are illustrated by Tersoff's first potential for Si (Tersoff 1986), which proved not to have the diamond lattice as its ground state (Dodson 1987a), a problem later corrected (Tersoff 1988a). Several alternative Si potentials have been proposed (Brenner & Garrison 1986, Baskes 1987, Dodson 1987a, Biswas & Hamann 1987). Similar potentials have been developed for C (Tersoff 1988b, Brenner 1990) and GaAs (Smith 1992). Several simulations of sputtering and related topics have used such potentials (Dodson 1987b,c, 1990, Dodson & Taylor 1987, Smith et al. 1989, 1990, Mowrey et al. 1991, Smith & Webb 1991, 1993). Several studies, summarized by Carlsson (1990), examined reconstructions of Si surfaces using the potentials cited, with mixed success. One must express some concern, therefore, that the assumed angular dependences are not accurate near surfaces and may be unsatisfactory for sputtering simulations in some cases.

An empirical potential has been proposed for MD calculations in the high-temperature perovskite superconductor $YBa_2Cu_3O_{7-\delta}$ (Chaplot 1988, 1989, 1990). This potential was used for low-energy radiation-damage studies (Cui et al. 1992). Kirsanov & Musin (1991) reported some low-energy radiation-damage calculations in this material using a Morse-type pair-potential with boundary constraints. Mention must also be made of potentials for use with alkali halides (Catlow et al. 1977) and for the interactions of rare-gas atoms with alkali halide ions (Ahlrichs et al. 1988). These potentials may be described as combining Born-Mayer repulsive interactions with attractive terms of the van der Waals power-law type. They have been used in recent studies of cluster impacts (Cleveland & Landman 1992).

5 Inelastic Energy Losses

Besides losing energy in scattering from the atoms of the target, energetic particles also lose energy by exciting electrons, both those of the medium and those of the particles themselves. Stoneham (1990) has reviewed the effects of ion-electron energy exchanges on collision-cascade development in a general way. In metals and semiconductors, the inelastic energy loss is calculated from the dynamic response of a uniform electron gas to the passage of a charged particle, a topic reviewed by Echenique et al. (1990). The theory accounts very well for the stopping of protons in matter over a wide range of kinetic energy, from a few keV to many MeV. The effective-charge theory of Brandt & Kitagawa (1982) allows this treatment to be extended to other particles. At low projectile kinetic energies, however, experimental data do not exist for testing a theory of electronic stopping and the situation is ambiguous. Finally, at the very lowest energies allowance must be made for the ordinary electron-phonon interaction, the importance of which was emphasized by Flynn and Averback (1988).

At several points in the following discussion, the inelastic energy losses are related, either explicitly or by implication, to the local density of electrons in the stopping medium. There are two problems with this formulation. First, such losses involve the excitation of target electrons that are not local to the track of the projectile: one would expect to integrate the excitations over the target electron density in a region surrounding the projectile track, with a weighting function to describe the losses as a function of the distance to the electrons in question. Second, the inelastic energy losses involve excitations of the projectile electrons themselves: again an integral over the excitations is required, this time using the electron-density distribution in the projectile. Thus, significant reservations must be expressed about formulations that do not include such integrations, but restrict themselves to the local density (see Sigmund 1991, Mikkelsen et al. 1992).

5.1 Inelastic Energy Losses in BCA Models

Some BCA simulation models treat inelastic energy losses as depending on the energy of a projectile and on the pathlength it traverses, but not on the particular surroundings of the trajectory segment. There are, therefore, no correlations between the elastic and the inelastic energy losses. Such models may be said to use 'nonlocal' inelastic losses, since no properties local to the particular path segment enter the calculation. At low energies, the nonlocal electronic stopping cross section usually takes the form (Fermi & Teller 1947, Lindhard & Scharff 1961)

$$S_{\mathrm{e}}(E) = kE^{1/2} \tag{3}$$

where E is the projectile kinetic energy and the parameter k is derived from experiment, from the well-known LSS theory (Lindhard & Scharff 1961, Lindhard et al. 1968), or otherwise. This form is included as an option in both MARLOWE (Robinson 1989) and TRIM.SP (Biersack 1987). It may be used alone or mixed in some proportion with local inelastic energy losses. In at least one case (Cowern & Biersack 1983), a version of TRIM included electronic energy-loss straggling using an approximate treatment by Bohr (1915).

An alternative formulation of the inelastic stopping problem follows Firsov (1959) in making the energy lost inelastically in a collision depend on how closely two atoms approach one another, providing a strong correlation between the elastic and the inelastic energy losses in individual encounters. Firsov assumed the relative energy in the collision to be high enough that the projectile was undeflected and used an asymptotic form of the Thomas-Fermi screening function (Gombás 1956), obtaining for the inelastic loss in a single collision

$$Q(p,E) = \frac{\alpha E^{1/2}}{(1+\beta p)^5}$$

where p is the impact parameter and α and β are numerical parameters.

Firsov's formula may be corrected approximately for scattering by replacing p with $R(p,E)$, the apsis in a collision (Robinson & Torrens 1974). The asymptotic Thomas-Fermi screening function may be replaced by an exponential function, which has a more realistic behavior at large distances (Oen & Robinson 1976). The result may be written

$$Q(p,E) = kE^{1/2}\frac{\gamma^2}{2\pi a^2}e^{-\gamma R(p,E)/a} \tag{4}$$

where a is a screening length and γ is a parameter, taken originally as 0.3 to connect Eq. (4) with the Molière potential. Under the conditions of the impulse approximation, this formulation gives the stopping cross section of Eq. (3), which

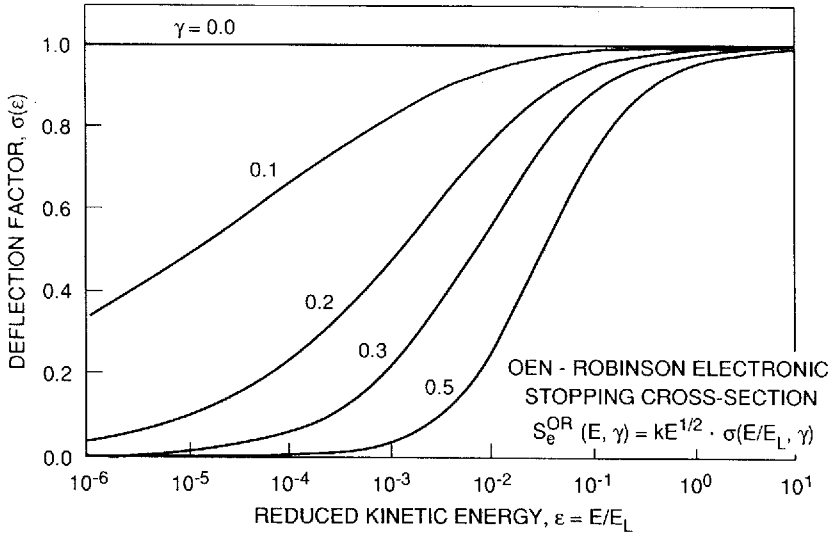

Figure 4. The deflection factor in the OR electronic stopping cross section model, evaluated for the Molière potential (Robinson 1992c). The original OR work (Oen & Robinson 1976) used $\gamma = 0.3$.

is proportional to the projectile velocity, but for lower energies, it falls more rapidly than implied by Eq. (3). The OR stopping cross section is

$$S_e^{\mathrm{OR}}(E) = 2\pi \int_0^\infty pQ(p,E)dp = kE^{1/2}\sigma(\epsilon)$$

The deflection factor is

$$\sigma(\epsilon) = \int_0^\infty u e^{-(\gamma/a)R(au/\gamma,\epsilon)}du,$$

where $\epsilon = E/E_{\mathrm{L}}$ is the usual reduced energy and

$$E_{\mathrm{L}} = \frac{Z_1 Z_2 e^2}{a}\frac{m_1+m_2}{m_2}\ ,$$

with Z_1e and Z_2e the nuclear charges of the projectile and target atoms, respectively, and m_1 and m_2 their masses. Figure 4 shows $\sigma(\epsilon)$ for the Molière potential, with several values of γ. The OR model cuts off the electronic energy losses at low projectile velocities in a plausible manner. The original connection between the OR model and the Molière potential is not essential: any potential can supply a

and $R(p, E)$, k can be determined as in the nonlocal model, and γ can be used as a free parameter with the nominal function of making the inelastic energy loss follow the electron density in the target atom. Lennard et al. (1992) used the OR model with modified constants to fit the stopping of low-velocity ^{27}Al ions in carbon. The effects on electronic stopping of the impact parameter cutoff used in BCA codes is discussed elsewhere (Oen & Robinson 1976, Robinson 1993).

Another method of treating inelastic energy losses in a local manner is to relate the stopping cross section to the local electron density at the position of a projectile. Two models of this kind were designed specifically for low-energy ion implantation in Si. Azziz et al. (1985, 1987) used linear response theory (Echenique et al. 1990) to calculate the energy transferred to an electron, viewed as an oscillator, as a function of impact parameter. A method outlined by Ferrell & Ritchie (1977) was used to average the loss over the electron distributions of the two colliding particles. The final loss calculated for B-Si collisions as a function of impact parameter was said to agree well with both the Firsov and OR models and the energy dependence of the inelastic stopping cross section was similar to the LSS function. Klein et al. (1990) used the proton stopping cross section of Echenique et al. (1981) and the effective-charge theory of Brandt & Kitagawa (1982), but used a local electron density for Si based on a muffin-tin approximation. Both Azziz et al. (1985, 1987) and Klein et al. (1990) modified MARLOWE to use their stopping cross section formalisms and both claim improved agreement between simulation and experiment for B implantation distributions in Si. Some doubt must be expressed about the validity of response functions derived for the uniform electron gas for modeling the response of the very nonuniform electron distributions in atoms.

Kaneko (1990a,b) developed a wave-packet theory for inelastic energy losses which shows losses that decrease with impact parameter less rapidly than they do in the OR model when applied to Pb. However, changes in the screening length and proper accounting for deflections would alter the comparisons. Unlike most other workers, Kaneko also discussed the impact parameter dependence of the straggling of the electronic energy loss. Inclusion of straggling is important in comparing simulations with experiment, especially at higher energies.

Murthy & Srinivasan (1993) used a different scheme to study the implantation of 7 MeV He^{++} in Si under channeling conditions. They modified MARLOWE to use the nonlocal electronic energy-loss formulation of Burenkov et al. (1980), coupled with a function describing the electron density in various important channels in Si. See Logan et al. (1992) for details.

5.2 Inelastic Energy Losses in MD Models

Nonlocal inelastic energy losses can be included in MD models by adding to the equations of motion a frictional term based on Eq. (3):

$$M\ddot{\mathbf{x}} = \mathbf{F} - \beta\dot{\mathbf{x}} \tag{5}$$

where M is the mass of an atom, $\mathbf{F}$ represents the conservative forces, $\beta = nk(M/2)^{1/2}$, and n is the target density. The frictional force represented by Eqs. (3, 5) is directed along the instantaneous trajectory of the projectile. The relaxation time for inelastic energy losses, M/β, is ~ 0.5 ps for typical cases, assuming the LSS theory for k. Only a few programs (Valkealahti & Nieminen 1987, Jakas & Harrison 1984, Harrison & Jakas 1986b) include nonlocal inelastic energy losses, mainly on the ground that they are insignificant at low initial kinetic energies.

Caro & Victoria (CV) (1989) describe an MD model for metals which includes local electronic effects. They identify two regimes: at relatively high kinetic energies, there are inelastic energy losses described by Eq. (5) with β depending on the local electron density in the spirit of the OR model; at low energies, there are interactions between slowly moving atoms ('phonons') and conduction electrons which equilibrate the excess kinetic energy of the atoms with the electrons and permit the ordinary metallic heat conductivity to carry the energy away from the cascade region (see Flynn & Averback 1988). To model the electron-phonon interaction, they turn to Langevin's equation of motion, well-known in the theory of Brownian motion and other areas of statistical physics (Chandrasekhar 1943, Uhlenbeck & Ornstein 1930, Wang & Uhlenbeck 1945; see Wax 1954). This takes the form

$$M\ddot{\mathbf{x}} = \mathbf{F} + \boldsymbol{\eta}(t) - \beta\dot{\mathbf{x}} \tag{6}$$

where $\boldsymbol{\eta}(t)$ is a random force and β now measures the strength of the coupling of the atomic system to the heat bath represented by the electrons. Each component of $\boldsymbol{\eta}(t)$ obeys a Gaussian distribution with mean value zero and variance $2\beta k_B T$, where k_B is Boltzmann's constant and T is the temperature of the reservoir. In the regime where Eq. (6) applies, M/β is the relaxation time for electronic heat conduction, ~ 10 ps. Equations (5) and (6) are similar, but the frictional coupling parameters differ by more than an order of magnitude.

CV unify the treatment of the two regimes empirically by setting

$$\beta = A \ \ln[\alpha\rho^{1/3} + b] \tag{7}$$

where ρ is the local electron density, A and b are fitting parameters, and

$$\alpha = (3\pi^2)^{1/3} \, a_{\mathrm{H}} = 3.0937 \, a_{\mathrm{H}} \quad .$$

The value of A is near $(h/3)(Z/\pi a_{\mathrm{H}})^2 = 8 \times 10^{-12} Z^2$ g/s. The electron density in Eq. (7) is derived from the many-body interaction potential used for the conservative forces, such as an EAM potential with allowance made for the repulsive potential at small interatomic separations.

The CV model provides an empirical treatment of electronic effects in cascade simulations in much the same spirit that the empirical many-body potentials do for the conservative forces. The model is used in the MOLDYCASK code (Diaz de la Rubia & Guinan 1990, 1991, Proennecke et al. 1991), but has not been applied to sputtering studies. Since the time scale for electron-phonon interactions is generally much greater than that for sputtering, it is likely that a CV model including only the local electron density dependence of the electronic stopping cross section would suffice for most sputtering simulations, subject always to the caveat expressed above about the use of local densities for this purpose.

5.3 The Effects of Inelastic Energy Losses in Sputtering

As Andersen (1987) pointed out, it has long been realized that the LSS model (Lindhard et al. 1963, 1968) implies substantial losses of energy to electronic excitations, even at very low kinetic energies. The role of these low-energy inelastic losses in displacement damage was discussed by Robinson & Oen (1982). They pointed out that the so-called modified Kinchin-Pease (or NRT) model (Norgett et al. 1975) incorrectly discounts electronic energy losses occurring below the cascade multiplication threshold in calculating the damage energy. An approximate correction can be made by defining $L = 2E_d/\kappa$, where E_d is the displacement threshold and κ is the displacement efficiency, and then writing the mean number of defects as

$$< \nu > = \frac{\hat{E}(E)}{\hat{E}(L)}, \qquad L \leq E \leq \infty$$

where $\hat{E}(E)$ is the conventional damage energy from the LSS treatment. The correction factor $L/\hat{E}(L)$ can increase the estimated damage by 20% or more.

Several claims were made during the past decade that inelastic energy losses play a major role in determining sputtering yields. This conclusion was reached on the basis of BC (Robinson 1983), MC (Harrison 1988, Jakas & Harrison 1984, Harrison & Jakas 1986b, Biersack & Eckstein 1984, Eckstein & Biersack 1984), and MD (Harrison 1988, Jakas & Harrison 1984, Harrison & Jakas 1986b) simulations as well as on a numerical transport-theory calculation (Jakas & Harrison 1985), so appears quite general. It was based, however, on simulations with nonlocal electronic stopping and, in at least one case (Robinson 1983), an artifact in the simulation was partially responsible.

Table 2: The Effect of 'Last Flight' Electronic Energy Losses on Self-Sputtering Yields in Polycrystalline $\alpha - U$ (Robinson 1983, 1992c).

	Sputtering Yield (atoms/ion)			
Incident Energy E (keV)	Local Energy Losses	Nonlocal Electronic Energy Losses		Final Path $\langle z \rangle$(nm)
		'Last Flight'	No 'Last Flight'	
0.5	1.703±0.018	0.703±0.011	1.037±0.014	0.378
1	3.324±0.039	1.591±0.025	2.157±0.029	0.290
3	7.463±0.123	3.657±0.054	4.872±0.091	0.272
5	10.600±0.190	5.203±0.111	6.757±0.129	0.247
kn = 2.625 $\text{eV}^{1/2}$/nm		U_s= 5.37 eV	p_c = 0.240 nm	

A large difference was found in the self-sputtering yields of polycrystalline α-U calculated with nonlocal and local loss models, using MARLOWE Version 11.7 (Robinson 1983): nonlocal losses were evaluated even for trajectory segments which did not end in a collision, but extended beyond the reach of the potential at the target surface. In contrast, local losses were evaluated only for trajectory segments ending in collisions. It can be shown that, when the planar model (Robinson 1981, Hofer 1991) is used to describe surface binding, the inclusion of 'last flight' inelastic energy losses is equivalent to increasing the surface binding energy U_s. The effective surface binding energy is

$$U_\text{eff} = U_\text{s} \left(1 + \frac{kn \ \langle z \rangle}{2U_\text{s}^{1/2}} \right)^2 \tag{8}$$

The electronic stopping cross section is $kE^{1/2}$, n is the target density, and $\langle z \rangle$ is the average length of the last flight segment. The effects of such 'last flight' losses are shown in Table 2, which compares yields calculated with local inelastic energy losses, with nonlocal losses calculated as in MARLOWE Version 11.7, and with nonlocal losses calculated as in MARLOWE Versions 12 and 13, where they are omitted on 'last flights'. The table also shows the mean path deduced from the two nonlocal-loss calculations using Eq. (8). As expected, $\langle z \rangle$ is somewhat greater than p_c, the impact parameter cutoff, which determines how far an atom must move away from the crystal surface plane before it no longer interacts with target atoms.

Table 2 shows how sensitive simulations can be to seemingly unimportant details. The difference between the local- and nonlocal-loss models is much greater for U than for lighter elements: here ϵ ranges from $\sim 10^{-6}$ to $\sim 10^{-3}$, so that the stopping cross section in the local model is never more than 20% of the nonlocal value. Even so, about one-third of the difference is accounted for by the 'last flight' effect. For the sputtering of Ni by Ne (Eckstein & Biersack 1984), the difference between the two models is less, but the role of 'last flights' is even greater. Both MARLOWE and TRIM.SP were modified some years ago to eliminate the 'last flight' effect.

At the present time, it is not possible to establish unambiguously whether or not low energy particle interactions in solids are dominated by electronic energy losses as implied by some of the simulations cited above. It is clear that if such losses continue to the lowest energies, as implied by the LSS theory, they must eventually be dominant (see Jakas & Harrison 1985). If the electronic stopping process is to go over into the ordinary electron-phonon interaction at thermal energies, however, the cross section must finally be an order of magnitude lower than the LSS value: see the discussion of the CV model above. What is needed is a detailed theoretical analysis of the transition between the electronic-stopping regime and the electron-phonon regime. This remains one of the most difficult and obscure problems in particle-solid interaction theory at the present time.

6 Surface Modelling

The surface of an irradiated target has a decisive influence on the number of particles sputtered and on their distributions in direction and kinetic energy. This is clear from experiments (Hofer 1991), especially those on single crystal targets, which show characteristic angular distributions. The surface is also responsible for transforming the energy distribution of atoms recoiling inside the target, more-or-less proportional to E^{-2}, into one characteristic of sputtered atoms, with a maximum near half the surface binding energy (Sigmund 1981, Thompson 1968). Thus, some attention must be given to modelling the target surface in a realistic manner. There are four issues to resolve: the magnitude and detailed nature of the surface binding, the fate of atoms which fail to surmount the binding barrier, target selvage effects, and the effects of prolonged irradiation. Surface binding is inherent in stable MD models, especially those with realistic many-body potentials, but must be considered carefully in BCA models; there are problems also in MD models using only pair potentials, since these are known (Robinson 1981) not to deal correctly with the target selvage. Geometrical changes in selvages include relaxations of near-surface atoms away from their ideal crystal positions and, even more drastically, reconstruction of the crystal surface. Relaxation effects and reconstruction of some metal surfaces have been studied with EAM models (Foiles et al. 1986, Chen et al. 1986, Foiles 1987) and the reconstruction of one Si surface has been accounted for with many-body potentials (Abraham & Batra 1985, Khor & Das Sarma 1987). There are also undoubtedly selvage effects on interaction potentials, inelastic energy losses, and surface binding energies. Nevertheless, such selvage effects are generally ignored in sputtering simulations, on the ground of their likely low significance (Harrison 1988). While caution in this area is suggested, the large uncertainties in other areas make the position tenable for the present.

6.1 Surface Binding Models

As is well-known (Robinson 1981), the cohesive energy of a solid, U_0, is the energy required to disperse its atoms into a dilute, monatomic, gas-like state. For materials evaporating exclusively as atoms, U_0 is the thermodynamic heat of vaporization, corrected to 0 K and zero pressure. For substances containing molecular species in the gas phase, further corrections are needed as well. The energy necessary to remove one atom from an interior (bulk) location in a solid to infinity is $2U_0$, excluding relaxation effects around the residual vacancy. The energy necessary to remove an atom from an average surface site (a 'half-lattice' position) is thus $U_s = U_0$, again ignoring relaxations. These energies are thermodynamic quantities, which apply only when the processes are carried out reversibly: there is no particular reason for the values to be the same when processes are carried out rapidly, as always occurs in sputtering, at least outside the thermal spike regime. It may be noted in passing that a bulk binding energy in a BCA simulation plays somewhat the role of the attractive force in an MD simulation.

In metals, and to a lesser degree in semiconductors, it is plausible to divide the total binding energy into two portions, one localized to the lattice site, the other associated with the crystal as a whole, a model consistent with electrostatic models of a metal surface (Finnis & Heine 1974, Landman et al. 1980). This model is used in both the BC code MARLOWE and the MC code TRIM.SP: the bulk binding energy is often ignored or taken as a small value (Robinson 1983, Eckstein & Biersack 1984), although the value U_0 is indicated by the foregoing discussion and is often used too (Robinson 1990, 1992b). At the surface, the value $U_s = U_0$ is used: since this surface binding energy is regarded as not being localized in interatomic bonds, it is treated as a sort of work function, affecting only the component of a projectile's motion normal to the target surface. This is the well-known planar binding model, widely used in analytical theory (Sigmund 1981, Thompson 1968) as well as in BCA codes.

There are several issues that are not fully resolved. First, U_s ought to depend on the orientation of the crystal surface, but in most calculations this is ignored (appropriately in MC codes). Second, both bulk and surface binding energies ought to depend on the surroundings of an atom: atoms in surfaces or adjacent to defects would be affected. This is not only an issue in prolonged bombardments: in some single cascades, large numbers of atoms can be ejected and changes in binding are surely associated with such events. There is evidence from MD simulations

(Shapiro & Tombrello 1990b, 1991b) that lowering of the surface binding energy by surface disorder is responsible for part of so-called nonlinear effects in sputtering. Thompson (1981) discusses several reasons for such effects. Yamamura (1988) uses a damage-dependent surface binding model in his DYACAT code. Third, both bulk and surface binding could depend on the direction in which an atom recoils. There has been speculation (Garrison et al. 1987, Kelly 1987, Oliva et al. 1987) that U_s should be greater than U_0, but these ideas are based on models in which the surface binding is localized in surface sites or depend on pair-potential calculations by Jackson (1973, 1975), which gave unphysical surface relaxations. See also comments of Andersen (1988).

Recent MD calculations by Gades & Urbassek (1992) have studied the ejection of atoms from a Cu {001} surface using pair potentials and many-body potentials of two types. With a Morse potential, they find the binding energy of an atom in an intact {001} surface to be about 31% greater than U_0, in excellent agreement with calculations of Jackson (1973,1975) and of Lo et al. (1988). However, both EAM and TB potentials gave surface binding energies only about 16% greater than U_0. The EAM result is somewhat lower than was found by Lo et al. (1988). The definition of the surface binding energy differs slightly among these calculations and the two EAM potentials were fit to slightly different data. Gades and Urbassek explain the difference between the pair-potential and many-body potential results in terms of a strengthening of bonds in the target surface, as compared with those in the interior of the target. See Carlsson (1990) for a detailed discussion of bond strengthening at surfaces. The explanation is reminiscent of that of Finnis & Heine (1974) for the inward relaxation of many metal surfaces.

Finally, something must be said about the surface binding model and temporal aspects of sputtering, especially the ejection time. It has been pointed out (Karetta & Urbassek 1992, Hou et al. 1993) that it is difficult to define the time at which an atom is ejected from a target unambiguously and that correlations between the ejection time and other quantities such as the kinetic energies of the sputtered atoms are strongly affected by the definition. The detailed spatial nature of the surface binding process is also an issue. While the energy lost to surface binding is not dependent on the spatial shape of the barrier, the time spent in traversing it is very sensitive to the shape.

6.2 Surface Binding and Sputtered-Atom Energy Spectra

When the planar binding model is used, sputtered atoms lose an energy U_s in passing the binding barrier and, since this energy comes entirely from the velocity component normal to the target surface, experience a refraction as well. The energy and direction of the sputtered atom are

$$\begin{aligned} E &= E_0 - U_\mathrm{s} \\ \mu &= \sqrt{\frac{E_0\mu_0^2 - U_\mathrm{s}}{E_0 - U_\mathrm{s}}} \end{aligned} \tag{9}$$

where $\mu = \cos\vartheta$, ϑ is the angle between the (outward) surface normal and the atom's velocity, and subscript 0 denotes values before passing the barrier. If the particle flux incident on the binding barrier is isotropic and follows an E_0^{-2} energy spectrum, the sputtered atoms are distributed as

$$p(\epsilon, \mu) = \frac{2S_0}{U_\mathrm{s}} \frac{\epsilon\mu}{(\epsilon+1)^3} \tag{10}$$

where $\epsilon = E/U_\mathrm{s}$ and S_0 is the total flux density incident on the barrier in $0 \le \mu_0 \le 1$, $1 \le \epsilon_0 \le \infty$. Equation (10) is the familiar Thompson model (1968): it has a maximum at $\epsilon^* = 1/2$; the sputtered flux is isotropic (the factor μ is just its projection onto the barrier); and the total flux density of sputtered atoms is $S_0/2$.

Equation (10) can be generalized in a simple way. Sigmund (1981) retained the isotropic flux incident on the barrier, but replaced the energy dependence with the $E_0^{-2(1-m)}$ spectrum appropriate to Lindhard's treatment of scattering (Lindhard et al. 1968), where m is the characteristic power-potential index. Garrison (1986), on the other hand, retained the E_0^{-2} spectrum, but considered the effects of flux anisotropy as a means of obtaining improved agreement with experiments (Baxter et al. 1986) which showed the maximum in the sputtered-atom energy spectrum to vary with direction. These treatments can be unified by specifying the flux incident on the barrier as

$$p_0(\epsilon_0, \mu_0) = (l-1)(k+2)\frac{S_0}{U_\mathrm{s}}\frac{\mu_0^{1+k}}{\epsilon_0^l} \qquad 0 \le \mu_0 \le 1, \quad 1 \le \epsilon_0 \le \infty$$

which may be transformed to give the sputtered flux as

$$p(\epsilon, \mu) = (l-1)(k+2)\frac{S_0}{U_\mathrm{s}}\frac{\epsilon\mu}{(\epsilon+1)^{l+1}}\left(\frac{\epsilon\mu^2+1}{\epsilon+1}\right)^{k/2} . \tag{11}$$

Sigmund's result is obtained by setting $l = 2(1-m)$ and k = 0 and Garrison's by letting $l = k = 2$. Except for the case k = 0, Eq. (11) describes an energy spectrum which depends on the emission direction, or, mutatis mutandis, an angular distribution which varies with the particle energy. Eckstein (1987) has reported TRIM.SP calculations which show sputtered-atom energy spectra which vary with the direction of emission. The maximum in the energy spectrum is a function of k, l, and μ. Suffice it to say that for $\mu = 1$ (along the target normal), the maximum occurs at $\epsilon^* = 1/l$; for $\mu = 0$, it occurs at $\epsilon^* = 1/(l + k/2)$; and for a range of cases tested, it is a monotonic function of μ. Finally, the fraction of particles incident on the barrier which successfully escape is $(2 + k)/(2l + k)$. This formula, with $k > 0$, can account for BCA simulations which show that substantially more than half the particles incident on the binding barrier with $\epsilon_0 \geq 1$ actually are sputtered. This result is evidently due primarily to the angular distribution of the incident flux and underscores the weakness of the assumption of isotropy.

Whatever the validity of the assumption of isotropic particle fluxes in structureless media, it cannot be satisfactory for atoms ejected from crystalline targets. The focusing effects of the lattice (Lehmann & Sigmund 1966) will alter the angular distributions of the ejecta, as is well known. These effects are clearly displayed by the BCA calculations of Whitlow & Hautala (1987) and of Hou & Eckstein (1990).

The calculations of Gades & Urbassek (1992) reflect on the validity of the planar binding model: they evaluated the refraction of atoms ejected from intact $\{001\}$ surfaces in Cu at various angles to the surface normal. They find the refraction in a Morse potential to be less than predicted by the planar binding model, whereas the many-body potentials show a greater refraction. Thus, in a Thompson-like model, $\epsilon^* < 1/2$ for the pair potentials and $> 1/2$ for the many-body potentials. These results are consistent with the sputtering simulations of Lo et al. (1988). However, the initial angular and energy distributions of the ejected atoms are decisive in determining the final distributions, so this property alone cannot be used to assess the potentials experimentally.

Another aspect of the planar binding model must also be dealt with by BCA codes. Since some of the atoms incident on the binding barrier have insufficient energy to escape from the target surface, some account of their fates must be given. One possibility, used in TRIM.SP (Biersack & Eckstein 1984), is to allow these atoms to reflect from the barrier and to re-enter the target for further collisions. Another possibility, used in MARLOWE (Robinson 1992a), is to consider such particles as adatoms trapped at the target surface. Since adatom kinetic energies are mostly quite small, the two procedures differ little. A more accurate model could be developed by comparisons with MD calculations.

6.3 Surface Topography and Sputtering Simulation

Sputtering experiments are often performed at doses (fluences) high enough to permit gravimetric determination of the yield. The resulting changes in topography are well-known (Carter et al. 1983, Scherzer 1983). Recent experiments with the scanning tunneling microscope show how topographic features develop even at low doses from the dynamics of surface vacancies and adatoms (Michely et al. 1991) produced during low-energy ion irradiation of noble-metal surfaces (Michely et al. 1990; Michely & Comsa 1991, 1993; Tsong 1993). Eventually, such features merge into rough surfaces of various kinds (Carter et al. 1983, Scherzer 1983, Eklund et al. 1991). Accounting for the effects of these changes in topography in computer-simulation models is not well advanced.

Yamamura and his coworkers (Yamamura et al. 1987a,b, Yamamura & Muraoka, 1989) used the MC program ACAT (Takeuchi & Yamamura 1983) to study the effects of surface roughness on sputtering simulations. A rough surface was introduced into TRIM (Biersack & Eckstein 1984, Haggmark & Biersack 1981). Several models of roughness were used in these calculations, all on a fairly fine scale. Calculations were made of the dependence of the sputtering yield on the angle of incidence of the ions. This dependence is marked by a maximum yield at an angle of 60° or so from the normal. The angle of the maximum was significantly increased when the surface was roughened, mainly because there was less reflection of the incident particles. The results were in better agreement with experiment than was achieved for smooth targets for 1.05 keV Ar^+ on Ta (Yamamura et al. 1987a) and for 1 keV D on Ni (Haggmark & Biersack 1981). The angles of maximum yield and the effects of roughness on them must depend significantly on the masses of the incident and target particles, crystal orientation, incident energy, and other variables.

The reflection of H atoms from Ni surfaces (Ruzic & Chiu 1989) and the sputtering of graphites by H and C atoms (Ruzic 1990) were studied with a version of TRIM modified to include surface roughness described in terms of fractals. A related fractal surface was also used (Ruzic & Chiu 1989) in a few reflection calculations with an MD code (Baskes 1984) based on the EAM. The fractal TRIM reflection calculations showed a decrease in the reflection coefficient as soon as the fractal dimension D increased above 2, with a minimum around $D = 2.2$, and an increase for larger roughness. The effect was small at normal incidence and most important at grazing incidence. The effect of roughness on the sputtering yield was also small at normal incidence, but, at oblique incidence, the yield increased for small roughness, passed through a maximum, and decreased again for large roughness. The effects were the greatest at the lowest energies.

None of these models of rough surfaces addresses the dynamical evolution of target surfaces during sputtering, although Ruzic's fractal surface model could probably be developed to do this and seems to show promise as part of a model of more realistic surfaces for use in MD and BC calculations. Gades & Urbassek (1992) point out that surface binding energies calculated for intact crystal surfaces are not especially relevant to sputtering under realistic conditions, since atoms in the roughened surfaces will have a statistical distribution of coordination number and thus will approximate better to the $U_s = U_0$ model.

7 Comparisons of Simulation Models

A few recent investigations compare one simulation model with another or supply information that is relevant to such comparisons. These are useful for understanding the relationships among the different models.

Webb et al. (1986) examined the frequency of encounters between moving particles in cascades, using the QDYN code. A collision was said to occur if the potential energy between two particles exceeded a threshold value. They focused on encounters that were 'nonlinear', that is, in which both colliding atoms were already moving. The number was small at the start of a cascade, but increased to a plateau after 100 to 150 fs, a time corresponding approximately to that at which the maximum number of atoms is in motion, and most particles already have very low energies. In 5 keV Ar^+ bombardments of Cu ~18% of encounters were nonlinear if the threshold was taken as 0.5 eV, ~9% for a threshold of 1 eV, and ~6% for a threshold of 2 eV. These results support the assumption of most BCA codes that encounters between moving particles can often be safely neglected.

Wucher et al. (1992) compare experiments, MD simulations, and BCA simulations of the sputtering of Ni {111} surfaces by 1.1 keV Ar^+. They observed angular distributions of energy-selected sputtered particles. Ejection near a <001> direction was found to be significantly energy-dependent, the maximum moving from a polar angle of 36.3° for 10 eV recoils to 49.4° for 55 eV recoils. Their results are said to be in quantitative agreement with a calculation for Cu (Robinson 1981), based on approximations used in MARLOWE, namely the BCA, the treatment of simultaneous collisions, and the planar surface binding model. The Gibson II Born-Mayer potential (Gibson et al. 1960) was used to describe the interactions of the atoms. The MD simulations of Wucher et al. (1992) used an EAM potential splined to a Molière core (Garrison et al. 1988) and gave a smaller change of the position of the <001> feature with recoil energy. The difference between the two calculations can be attributed partly to different potentials and partly to including the full cascade development in the MD simulation: there are many ways for particles to reach the ejection direction other than the perfectly focused <001> process assumed in the BCA calculation. It must be mentioned that studies of the sputtering of Au {111} surfaces by 0.6 keV Xe^+ with MARLOWE gave quite different results (Hou & Eckstein 1986, Eckstein & Hou 1991). Ejection of target atoms into directions interpreted by Wucher et al. as <011> and <001> directions, are interpreted in terms of other kinds of processes. The differences between these two sets of results is hard to understand. The mass ratios Xe/Au and Ar/Ni are similar, as are the penetration depths of the ions: for 0.6 keV Xe atoms, the mean penetration into Au {111} targets is $0.867 \pm 0.009\ a_0$ (just over two layers), where a_0 is the lattice constant of Au, 0.4078 nm; for 1.1 keV Ar, the mean penetration into Ni {111} is $1.239 \pm 0.009\ a_0$ (just over three layers), where the lattice constant is 0.3524 nm (Robinson 1992c). Explanations based on traditional focusing processes seem unlikely, but more research is clearly needed.

Chang et al. (1988) compared three methods of simulating the interaction of energetic ions with crystal surfaces, paralleling early work of Karpuzov & Yurasova (1971). One calculation used a full MD treatment of the interaction of Ne ions with Rh {111} and {001} surfaces. A second used a method introduced by Karpuzov and Yurasova in which interactions of the ion with all target atoms are included, but those of the target atoms with each other are ignored. The third was a BCA calculation in which the ion was allowed to interact only with the nearest target atom. In the latter two cases, the scattering of Ar ions from Ni surfaces was also studied. The Molière potential with the Firsov screening length was used for Ne-Rh and Ar-Ni interactions; the Rh-Rh interactions were described by a Morse potential splined to a Molière core. Chang et al. report angular and energy distributions for backscattered particles. In agreement with Karpuzov and Yurasova, they find very close agreement between the first two models, except at low energies (100 eV Ne on Rh {001}) where deviations begin to appear. Substantial differences are reported for the BCA model, however. These depend in a complex way on the incidence conditions (energy, polar and azimuthal angles) and on the surface. The conclusions agree generally with those of Karpuzov and Yurasova, who mainly analyzed trajectories. Both comparisons show the severe limitations of a BCA model which does not include any correction for nearly simultaneous encounters of projectiles with several target atoms. Comparisons using, for example, the MARLOWE approximations (Hou & Robinson 1976, Robinson 1989, 1993) could further illuminate this issue.

Shulga et al. (1989) used an MD simulation to examine the trajectories of particles during the scattering of heavy atoms from diatomic molecules made up of lighter atoms, using the example of Xe on Cu_2. In such cases, the first atom of the molecule may move out ahead of the heavy projectile, clearing the way for it by displacing the other member of the molecule before the heavy particle arrives. Comparisons of trajectories where the interactions of the target atoms with each other were included with those in which they were suppressed showed the importance of such effects. Smith & Webb (1992) have also noted the importance of time in the proper ordering of collisions. They show examples of how some BCA models can go astray, as compared with MD models.

The most extensive comparison of computer simulation models is the recent round-robin evaluation of the ejection probability of low-energy atoms near the surfaces of crystals (Sigmund et al. 1989). This work compared six MD codes (Harrison 1988, Valkealahti & Nieminen 1987, Baskes 1984, Shulga 1980, Chakarov & Karpuzov 1988, Shapiro & Tombrello 1987), four BC codes (Robinson 1989, Yamamura & Takeuchi 1987, Hautala 1984, Shulga 1983), and eight MC codes (Takeuchi & Yamamura 1983, Vicanek & Urbassek 1988, Hautala 1980, Betz et al. 1971, Kang et al. 1985, Ishitani et al. 1983, Cui & Li 1985, Biersack & Eckstein 1984). The task was to calculate the probability of ejection of atoms from the surface region of Cu targets as a function of depth within the target and the initial direction and kinetic energy of the recoil. The Gibson II Born-Mayer potential (Gibson et al. 1960) was used for most calculations. The planar surface binding model was used in most BCA calculations. There were substantial discrepancies among the results of the various codes for the relatively simple process examined. Some of these were merely statistical, while others could be traced to the details of the programs themselves. The lattice models, that is, the MD and BC codes, agreed among themselves reasonably well, although the neglect, or, rather, the very approximate treatment, of many-body effects in the latter caused differences to increase at low energies. The lattice models differed systematically from the MC models, however. The former agreed that no ejection of atoms occurred from below the second or third layer of the targets (never from depths as great as 0.4 nm), for primary energies up to 50 eV. The MC codes, on the other hand, showed ejection from depths of 0.4 to 0.5 nm, even at energies as low as 10 eV. Moreover, there were considerable variations among the different programs. Much of the variation was traced to detailed features of the individual models: the original work (Sigmund et al. 1989) should be consulted for these and other topics. The general differences between the lattice models and the MC models result from the statistical nature of the latter. Their rough surfaces and lack of translational symmetry result in emission from depths greater than is possible in the lattice codes. Similar effects would appear in the lattice models if thermal displacements of the atoms from their lattice sites were introduced.

8 The Statistics of Sputtering

No sputtering experiment has been carried out at a dose rate small enough to allow the observation of fluctuations in the yield of ejected particles between different incident ions. A few observations of small pits on sputtered surfaces (Merkle & Jaeger 1981) are regarded as resulting from single ion impacts, but these presumably record only extreme fluctuations. Simulations easily record detailed distributions of sputtering yields and allow evaluation of the mean yield and of higher moments. Attention to the statistics of sputtering and to the closely-related topic of correlations between the ion impact point and the yield allow statements to be made about mechanisms which influence the yield and about conditions which are likely to favor the ejection of molecular clusters or the development of pits and other topographic features on the irradiated surface. In addition, from the statistics of yield fluctuations, the precision of computations may be assessed directly in objective terms.

8.1 The Number of Displaced Atoms

Statistical studies of many aspects of collision cascade development are accessible to computer simulation and, in some cases, allow assessment of analytical models. For example, Kinchin & Pease (1955a,b) evaluated the mean number of Frenkel-defect pairs produced in a structureless medium by a primary recoil of initial kinetic energy E as

$$\langle \nu \rangle = \frac{E}{2E_d} \qquad E > 2E_d$$

where ν is the number of defects, E_d is the displacement threshold energy, and $<>$ indicates averaging. Hard-core scattering was assumed and electronic energy losses were ignored. Leibfried (1958, 1965) showed that the corresponding variance was

$$\sigma^2 = <(\nu - \langle \nu \rangle)^2\rangle = (4 \ln 4/3 - 1)\,\langle \nu \rangle \qquad E > 4E_d \tag{12}$$

where the numerical factor has the value 0.150728. Only the high-energy forms of these equations are shown; for more details see Leibfried (1965). Equation (12) shows that the variance is only 15% of the Poisson value. The smallness of the variance was confirmed by computer simulation (Robinson & Torrens 1974), but the energy dependence in Eq. (12) is overwhelmed by damage-energy straggling.

8.2 The Sputtering Yield

In striking contrast, sputtering yields are distributed over a wide range and the mean often bears little relationship to the most probable yield. Studies of the statistics of sputtering are available from MC codes (Eckstein 1988, 1991; Hou & Eckstein 1992; Conrad & Urbassek 1990), BC codes (Robinson 1983), and MD codes (Harrison 1981b, 1988, Harrison & Webb 1982, Harrison et al. 1987, Smith & Harrison 1989, Stansfield et al. 1989). Systematic differences are found between yield distributions from monocrystalline targets and from polycrystalline and structureless targets. The latter show a mode (most probable value) in the vicinity of the mean and a broad distribution that can be fit by a negative binomial distribution (Eckstein 1988, 1991), although there is disagreement about this (Conrad & Urbassek 1990). In monocrystal targets, on the other hand, BC and MD calculations

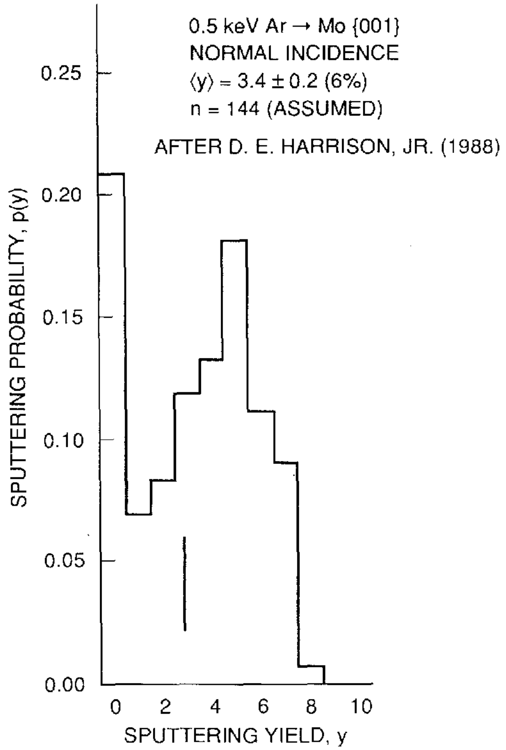

Figure 5. The sputtering yield distribution for 0.5 keV Ar on a Mo {001} surface. The data are taken from Fig. 14 of Harrison (1988). The figure is constructed on the assumption that there were 144 incident particles in the sample: with this choice, there is one count in the right-most channel. A vertical line in the histogram marks the mean yield.

agree in finding a significant probability that the incident particle ejects no target atoms at all, a probability that increases with the incident kinetic energy and is unquestionably associated with channeling of the incident beam in low-index axial and planar channels of the target. The remainder of the distribution in monocrystal targets resembles that found in structureless and polycrystalline ones.

Let $p(y)$ be the probability, normalized to unity, that an incident ion ejects exactly y atoms from a target. The sputtering yield is the mean value

$$Y = \langle y \rangle = \sum_{y=0}^{\infty} y p(y) \;;$$

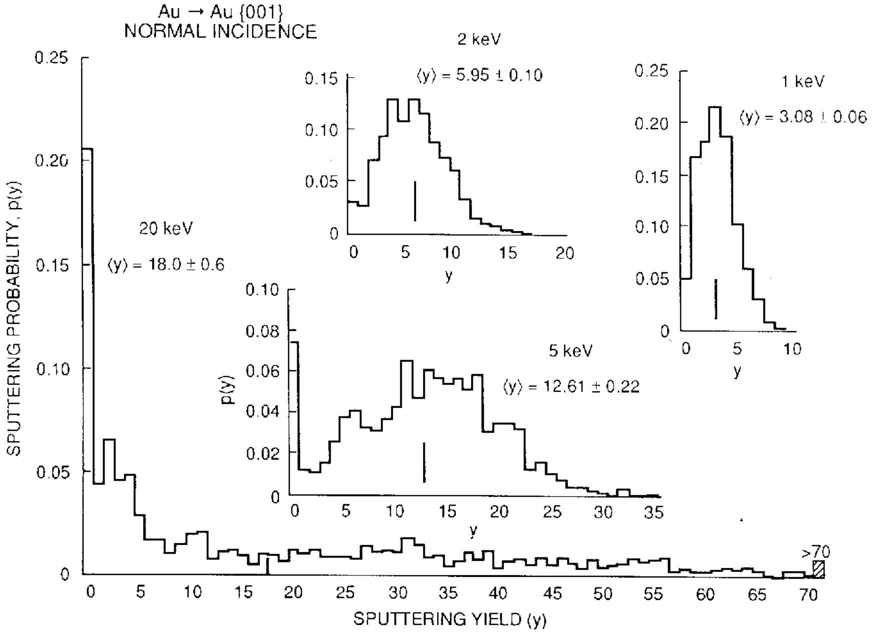

Figure 6. Sputtering yield distributions for Au atoms normally incident on a Au {001} surface, evaluated with MARLOWE (Robinson 1992c). A vertical line in each histogram marks the mean yield.

other moments are similarly defined. The variance of the yield is

$$\sigma^2 = \langle (y - \langle y \rangle)^2 \rangle \ ;$$

other central moments are similarly defined. If y is a random variable, $\langle y \rangle$ is expected from the central limit theorem (Feller 1957) to obey a normal distribution with variance $\sigma^2/(n-1)$, where n is the number of incident ions. This prediction of the central limit theorem applies to the distribution of mean values $<y>$, each from an independent sample of n incident ions. No assumption is required about $p(y)$, the distribution of single-ion yields. These results allow an assessment of the precision attained in calculations, especially important with MD models, where the sample sizes are generally small.

Figure 5 shows a yield distribution calculated by MD for 0.5 keV Ar atoms normally incident on a Mo {001} surface (Harrison 1988). The usual procedure in Harrison's calculations was to divide the asymmetric surface cell into a number (here deduced to be 144) of equal parts and to select an impact point randomly

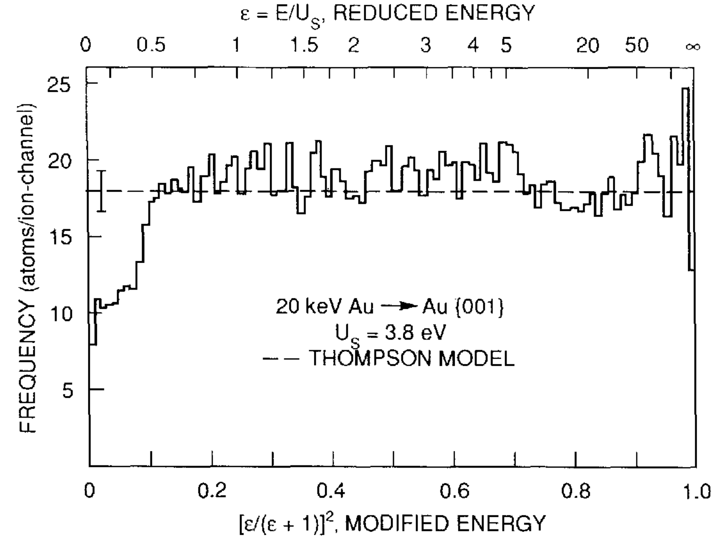

Figure 7. The energy spectrum of sputtered atoms evaluated with MARLOWE (Robinson 1992c) for 20 keV self-sputtering of Au {001}. The prediction of the Thompson (1968) model is shown by the horizontal dashed line; the statistical uncertainty of this value is shown.

within each one. The incident particles were then launched on trajectories aimed at these impact points. It is stated (Harrison 1988) that different sets of impact points selected in this manner gave results which agreed always to 'within 10% and almost always within 5%.' As Fig. 5 shows, however, the standard error of the yield, evaluated on the assumption that y is a random variable, is 6%. It is concluded that the precision of such MD calculations is just that which would be deduced for a sample selected by ordinary aleatory methods. In conventional sampling theory (see, for example, Feller 1957), one would expect the means of replicate samples of the type shown in Fig. 5 to deviate by less than 6% about two-thirds of the time and to deviate by more than 12% less than 5% of the time. This is simply a quantification of the quotation cited. Thus, Harrison's method of ensuring uniformity of irradiation actually gives results no better than do purely aleatory methods, although it may reduce the risks of large fluctuations associated with small sample sizes. This being the case, the question (Andersen 1987) whether the yield is a smooth or a chaotic function of the impact point is less important than it might be otherwise. It has, indeed, never been shown what the situation really is and this could bear on several issues, especially those involving correlations of the impact point with quantities other than the yield.

Figure 6 shows the incident-energy dependence of yield distributions evaluated with MARLOWE (Robinson 1992c) for Au normally incident on Au {001}. Each sample included 1000 incident particles. The larger samples give better precision than was achieved in Fig. 5, but the results are similar. The <001> axial channel opens rapidly above 2 keV; by 20 keV, fully 20% of the incident particles cause no sputtering at all. The occurrence of events in which the number of ejected atoms is much larger than the mean value should be noted. At 20 keV, yields extend to values > 90 with a small incidence. While nothing is known about such events from these calculations, it is natural to look at them as likely sources of cluster emission and surface pit formation, which was observed in MD simulations (Harrison 1988, Stansfield et al. 1989, Wucher and Garrison 1992), although most of these were restricted to rather low kinetic energies.

It would be desirable to have detailed studies of correlations of the sputtering yield with the impact point of the incident particle, beyond delimiting the channels by low- or non-yield situations. Harrison (1988) has reported a correlation of this kind for 0.5 keV Ar on a Rh {111} surface, but the results are very hard to interpret (see his Fig. 11). Such studies could determine whether the yield is indeed a smooth or a chaotic function of the impact point (Andersen 1987) and should be useful in understanding other kinds of correlations.

Other kinds of correlations can also be studied. As an example, Hou & Eckstein (1992) have reported correlations of the single-particle yield y [see Eqs. (27-29)] with the total number of atoms displaced in a cascade, the sputtered energy distribution, and the surface deposited energy, using the TRIM.SP code. They used these results to discuss the connection between the surface deposited energy and the yield.

8.3 Other Distributions

In view of what was said above about the precision of sputtering yield calculations, it is appropriate to make a few remarks about the precision of calculated sputtered-atom energy spectra, angular distributions, and the like. It should be clear that definitive data about such distributions can be obtained only from computational samples of sufficient size. With small samples, especially when the yield is small, only very approximate distribution functions can be obtained. However, some questions can be addressed more reliably by careful selection of the statistic to be examined.

For example, the validity of the Thompson model for the angle-averaged energy spectrum of the sputtered particles may be tested by constructing a histogram based, not on the sputtered atom's kinetic energy, but on the dimensionless modified energy variable $[\epsilon/(\epsilon+1)]^2$, where $\epsilon = E/U_s$. Since

$$d\left(\frac{\epsilon}{\epsilon+1}\right)^2 = \frac{2\epsilon d\epsilon}{(\epsilon+1)^3}$$

it follows that such a histogram will have equal counts in each channel (except the last) if the Thompson model is obeyed and will deviate otherwise. Figure 7 shows such a modified-energy histogram for the self-sputtering of Au {001} at 20 keV, evaluated with MARLOWE (Robinson 1992c). The number of atoms with energies $< U_s/2$ is significantly less than predicted by the Thompson model, but this is compensated by a slight excess at energies up to about 6 U_s; a small deficit appears around 10 U_s and an excess at the highest energies. These features can be seen much more clearly in the modified histogram than would be possible in a simple energy spectrum. Such techniques can often be used to improve the reliability of interpreting noisy data.

9 Cluster-Ion Impacts

There has been an interest in sputtering by molecules since experiments demonstrated that the yield per atom is often greater for diatomic ions than for monatomic ones, especially for high-energy heavy ions on heavy targets (Andersen & Bay 1981, Andersen 1993). Shapiro & Tombrello (1990b, 1991b) simulated impacts of some monatomic and diatomic ions on Cu and Au crystals using the SPUT2 code (Shapiro et al. 1988). At incident kinetic energies of 5 keV/atom, they found statistically significant nonlinearities in the yields for Kr and Xe ions on Cu {001} and for Kr, Xe, Au, and U ions on Au {001} and {111}, but not for Ar and Cu ions on Cu {001}. They attributed these results to collision spikes involving encounters between moving recoils, with a secondary contribution from changes in the surface binding energy caused by collisional disruption of the surface. Broomfield et al. (1990) simulated the sputtering of Cu {001} by $SiCl_4$ ions at incident energies up to 800 eV. Above the very low energy of $\sim$ 50 eV, they found nonlinearities in the yield, attributed to lowering of the surface binding energy by disruption of the target surface. Taken together, these simulations suggest that sputtering nonlinearities result from surface disruption and from spike effects, the relative importance of the two mechanisms depending on the targets, the atoms in the incident clusters, the energies of the particles, and the sizes of the clusters.

There is much current interest in the impacts of large cluster ions on solid surfaces. The incident particles are singly-charged clusters of as many as several hundred or even a few thousand atoms, with initial kinetic energies from < 1 eV/atom to $\sim$ 1 keV/atom or more. The interest in such particles stems from their potential uses in forming thin films by the ionized cluster beam (ICB) technique (see Brown et al. 1991 for a review); from claims of nuclear fusion during impacts of large, slow D_2O clusters on deuterated solid targets (Beuhler et al. 1989, 1990; Bae et al. 1991; but see Fallavier et al. 1990 for negative results and Beuhler et al. 1992 for withdrawal of the original claim); and from interest in other impact phenomena (Beuhler & Friedman 1986). Such impacts have also been suggested as a means of carrying out exotic chemical reactions in the clusters (Cleveland & Landman 1992). Sigmund (1989) discussed some of the features that can be expected in cluster impacts, but simulation methods are especially attractive for assessing the possibilities. The atomistic simulation of cluster impacts is feasible as long as the events can be contained adequately. This suggests limits ~10 eV/atom for clusters of a few hundred atoms or clusters of a few tens of atoms at 1 keV/atom. For extremely large clusters, it would surely be more effective to use models based on macroscopic mechanics.

The first simulation of ICB deposition appears to be that of Mueller (1987), a two-dimensional calculation using Lennard-Jones potentials. Incident kinetic energies ranged from 0.1 to 1.5 in units of the well-depth in the potential. Since well-depths are ~ 1 eV, these calculations correspond to very low energies. Biswas et al. (1988) and Kwon et al. (1990) used the empirical many-body potential of Biswas & Hamann (1987) in simulations of Si-cluster impacts on Si {111} surfaces. The clusters were mainly amorphous Si_{33} with energies from 0.23 to 1.4 eV/atom. The emphasis in this work was on film growth and the conditions for obtaining amorphous or epitaxial films. The energies are low enough that there is little penetration of cluster atoms into the targets.

Yamamura (1988) developed DYACAT for cluster impact studies, applying it initially to the sputtering of amorphous C by Ar clusters with 10 to 200 atoms at an initial energy of 100 eV/atom. He later studied the ICB deposition of Ag clusters with 100 to 500 atoms on amorphous C at energies of 6 to 10 eV/atom (Yamamura 1990); the atomic kinetic-energy spectra during impacts of Ag and Al clusters with 10 to 500 atoms on amorphous C and Au, at energies up to 1 keV/atom (Yamamura 1991); and the angular distributions of sputtered atoms during irradiation of Al and Ag by 1- to 500-atom clusters of Ag and Al, respectively (Yamamura & Muramoto, 1993). In these calculations, there is often substantial penetration of cluster atoms into the substrate. As the incident particles slow down in the targets, the atoms at the front of the cluster slow down before the arrival of the trailing parts. As a result of collisions between cluster atoms, some are accelerated to speeds well in excess of the initial values. In addition, lattice atoms are displaced and run ahead of the advancing cluster atoms. This is the 'clearing the way' effect (Sigmund 1989). One consequence is that the rates of energy loss of many cluster atoms is substantially less than that of isolated atomic particles.

In addition, there are substantial nonlinearities in sputtering yields, even at low kinetic energies, and significant cratering of the targets on a scale larger than the sizes of the clusters. These effects are largest when the incident atoms are heavier than the target atoms. Yamamura's calculations show the distortion of the cluster as it impacts a surface at low energy, but cannot deal effectively with spreading of the cluster or its conversion to a surface film.

Sigmund and his coworkers used a metastable MD model (Shulga 1980, Shulga et al. 1989) for studies of cluster impacts. Born-Mayer potentials with the parameters of Andersen & Sigmund (1965) were used, truncated to avoid premature 'explosion' of the clusters and targets under the conditions of the calculations, which addressed primarily the slowing down of cluster atoms in thin polycrystalline targets. The systems studied included 0.1 and 1 keV/atom Au_{13} impacting Si (Shulga & Sigmund 1990); 0.1 keV/atom C clusters with 1 to 17 atoms on Au (Pan & Sigmund 1990); 0.1 and 1 keV/atom Cu_{13} on Cu (Shulga 1991); 0.1 keV Cu_{13} on Au (Shulga & Sigmund 1991) and 0.1 and 1 keV/atom Au clusters with 1 to 34 atoms on Au (Pan 1992). These calculations show that, when the incident atoms are heavier than the target atoms, the front runners (it is difficult to avoid an analogy with the linemen in rugby or American football) accelerate some target atoms to speeds greater than that of the incident atoms, allowing later atoms in the cluster to penetrate more deeply into the target before encountering target atoms. The average energy loss per atom of the incident clusters is less than experienced by atomic particles. Similar effects persist even in the equal-mass cases. When the cluster atoms are lighter than the target atoms, their backscattering leads to collisions among cluster atoms which can be described as collision cascades occurring in the clusters. In addition, target atoms can be hit by more than one cluster atom. At all mass ratios, combinations of these effects cause broadening of energy spectra and the generation of particles moving faster than expected from two-body kinematics. There are significant effects on particle reflection and sputtering, but these calculations cannot deal completely with the latter.

The SPUT2 code (Shapiro et al. 1988) has been used to study cluster impact phenomena. The atomic interactions were based on Morse potentials splined to Molière cores. Since the clusters and the targets are stable, such simulations are suitable for problems where metastable models cannot be used. Studies were made of impacts of 1 keV/atom Al, Cu, Au, and composite clusters with 32 or 63 atoms on Al, Cu, and Au {001} targets (Shapiro & Tombrello 1990a, 1991a). Evolution of the systems was followed for 0.5 ps, long enough to make clear many features of the impacts, but not long enough to produce reliable estimates of sputtering yields. As the cluster hit the target, the atomic density in the primary impact-zone rose rapidly to about twice its initial value and then fell rapidly, reaching its original value in ~30 fs. As material was ejected from the target or driven into it, the density in the primary impact-zone then fell to about 25% of its original value over 100 fs. Potential-energy spectra of the atoms showed that during the first 60 fs some were accelerated to energies considerably higher than expected from two-body kinematics, in agreement with the results of the Sigmund group, and the associated 'clearing the way' was also seen. An interesting feature of these calculations was seen in distributions of the sites from which the sputtered atoms originated. These showed few atoms to come from the core of the impact zone, but, instead, there was a ring of emission surrounding the core, closely resembling the splash seen when heavy objects impact liquids.

The excitation of core electrons was studied during impacts of 0.2 to 1 keV/atom Al and composite clusters with 32, 63, or 108 atoms on Al $\{001\}$ targets (Shapiro & Tombrello 1992a,b). The composite clusters consisted of three layers (38 atoms) of Al backed by two layers (25 atoms) of Au. A critical approach distance was used to define L-shell excitation in the Al atoms. During the initial rapid compressional phase, significant excitation was found above a threshold energy of ~0.4 keV/atom for Al clusters and ~0.11 keV/atom for composite clusters. Intermediate-size clusters produced core excitations most efficiently. This was attributed to greater 'clearing the way' effects with the largest clusters. The authors suggest experimental studies of Auger emission from core excited states as a probe of the early compressional phase of cluster-ion impacts.

Studies were made at 1 to 10 eV/atom of the final shapes and penetration depths of 63 atom Al and Au clusters on Au $\{001\}$ (Pelletier et al. 1992). The simulations extended for 2 ps after impact. The barycenter of the Al clusters never penetrated the gold target at these low energies, but the most energetic Au cluster did penetrate slightly. All clusters were flattened substantially. At low energies, the films were in good registry with the substrate, but at higher energies, the registration was poor and there was much damage to the target.

Studies have also been carried out of Cu, Ni, and Al clusters of 4 to 92 atoms impacting the same metals at energies up to 1 keV (Hsieh & Averback 1990, Averback et al. 1991, Hsieh et al. 1992). EAM potentials with Molière cores were used in these calculations. The simulations extended to as long as 20 ps after the impact. The behavior depended sensitively on the size and energy of the cluster, the masses of the cluster and target atoms, and the properties of the substrates as modelled by the EAM potential. An important feature of these calculations is that they show very little mixing between the atoms of the cluster and those of the substrate. This behavior supports the idea of using macroscopic modelling of many aspects of cluster impacts. As a 326 eV Cu_{92} cluster begins to impact a Cu surface, the substrate is initially compressed, but, after ~0.7 ps, begins to rebound; the maximum expansion occurs at about 1 ps; after ~2.4 ps, the atoms begin to relax towards their final positions; and, by ~5.5 ps, all atoms have settled onto lattice sites. Little damage is produced in the targets. At the end of the impact, a ridge of substrate atoms appears on the surface, surrounding the impact zone. The interpretation is that the shear stress generated in compressing the substrate exceeds the critical shear strength of the target and, during the subsequent expansion, atoms flow out onto the surface. A 326 eV Cu_{92} cluster impacts a Ni target in a similar way, but penetrates less far into the substrate and the ridge of substrate atoms is less pronounced. This is consistent with the greater strength of Ni. When the cluster energy is increased to 1 keV, the plastic response of the substrate is more pronounced, but there is still little mixing of cluster and substrate atoms during the compression phase. There is also evidence of local melting in this impact and a few vacancies appear in the substrate when the melted zone is quenched. When smaller clusters of the same energy were used, such as 326 eV Cu_{13} or Cu_4, craters were produced at the target surfaces. A few interstitial atoms were produced deep within the substrate by the smallest cluster.

By combining results for various clusters and substrates, it was possible to deduce a sort of 'phase diagram,' with two variables: the kinetic energy per cluster atom and the cluster cohesive energy, each normalized to the cohesive energy of the substrate. When the former is > 10, implantation of the clusters and radiation damage to the substrate occur. When it is $\sim$1, the clusters remain intact, forming a 'glob' of material on the surface if the substrate is hard, or penetrating it if it is soft. At intermediate energies, the cluster breaks up on hitting hard substrates, spreading out over the surface, dissociating, and being reflected from it. Intermediate-energy clusters penetrate soft substrates and induce local melting. These results are generally consistent with those cited earlier, but each group has concentrated on a different aspect of the cluster impact problem. It would be interesting to make more detailed comparisons of impacts simulated by different investigators, in order to rationalize the various viewpoints more completely and to understand how much the differences in modelling affect the results.

Mention must also be made of a recent simulation of the impact of a 561-atom Ar cluster on a rock-salt surface at an energy of $\sim$ 1.9 eV/atom (Cleveland & Landman 1992). The Ar atoms interacted with each other through Lennard-Jones potentials with a well-depth of 10.3 meV, and with the atoms of the substrates through the potentials of Ahlrichs et al. (1988); the substrate atoms interacted with each other through the potentials of Catlow et al. (1977). The authors describe their event in terms similar to those used by Hsieh et al. (1992). The Ar cluster retains its identity up to about 0.5 ps, but then disrupts. As in earlier calculations, a compression of the substrate and the cluster is observed for $\sim$ 0.5 ps, followed by an expansion. Whether it is appropriate to describe such a short pressure pulse as a 'shock' may be argued, but its occurrence is clear enough.

Finally, some interesting simulations have been reported for buckminsterfullerene (C_{60}) molecules incident on hydrogen-covered diamond surfaces (Mowrey et al. 1991) and graphite (Smith & Webb 1993). In the former case, the potential was of the Tersoff type, with special modifications to fit various chemical effects (Brenner 1990); the latter calculations used a carbon potential of Tersoff (1988b). An interesting feature of both calculations is that at incident energies $\lesssim 4$ eV/atom, the C_{60} molecules rebound from the surface intact, although with substantial internal energy. Whether these would eventually fragment, as seems to occur for sputtered metal clusters (Wucher & Garrison 1993) is not yet settled, although it seems likely.

10 Concluding Remarks

I have tried in this review to consider several of the incomplete issues raised by Andersen (1987) in his earlier survey. The current situation with respect to potential functions has been discussed, both for close approaches between atoms and for separations near the normal bonding distances in solids. Methods of determining the former from ab initio calculations appear to be more-or-less in hand and empirical potentials for the latter are well-advanced. The role of electron excitations in slowing swift particles has been outlined and methods of including such effects in simulation codes have been discussed. It was pointed out that the role of electronic energy losses at low energy is still ambiguous and that more work is needed to clarify the part played in sputtering by electron-phonon interactions. The modelling of crystal surfaces has been discussed, as well as the influence of the surface on sputtered particle angular and energy distributions. It was pointed out that the effects of prolonged irradiation need to be included in simulations intended to model real experimental situations.

Limited comparisons of codes of different types have been presented. More work in this area would be very desirable. This could relate MD, BC, MC, and intermediate codes in the way done in the recent round-robin collaboration (Sigmund et al. 1989), but should be applied to a variety of problems. The statistics of sputtering were discussed: it is to be hoped that more attention will be given to statistical aspects of MD simulations, since they are usually run with very small sample sizes. Finally, recent work on cluster impacts was surveyed with the idea of giving some of the flavor of this recently active field. Further work in this area appears warranted.

Several topics in the computer simulation of of ion-solid interactions have been omitted. Many are reviewed elsewhere in this volume. One such topic is the ejection of molecular species during sputtering, which is reviewed by Urbassek & Hofer (1993). The related topic of the ejection of very large molecules by swift ion bombardment is reviewed by Reimann (1993).

No attention has been paid to the sputtering of multicomponent targets, technologically a very important topic. In addition to the issues raised in simulating the sputtering of single component materials, there are additional major issues in multicomponent ones. The most significant are concerned with the selective sputtering of the components and the accompanying changes in composition, binding energies, and the like. In prolonged irradiations, diffusion effects may be superadded. A recent example of work in this field is given by Baretzky et al. (1992). See Betz & Wehner (1983) and Lam & Sigmund (1993) for reviews of multicomponent sputtering and Sigmund (1987a) for some analysis of the subject.

Acknowledgements

I have had invaluable help in preparing this article from discussions with several colleagues, sometime in person, sometimes by electronic communication. I especially want to thank Gerhard Betz, Wolfgang Eckstein, S. H. Liu, Mark Shapiro, Peter Sigmund, Roger Smith, and Roger Webb. It would not have been possible to complete work on the manuscript successfully without the advice and invaluable assistance of Marc Hou.

This research was sponsored by the Division of Materials Sciences, U. S. Department of Energy under Contract No. DE-AC05-84OR21400 with Martin Marietta Energy Systems, Inc.

References

Abraham FF, 1986: Adv. Phys. **35**, 1

Abraham FF and Batra IP, 1985: Surface Sci. **163**, L752

Adams JB and Foiles SM, 1990: Phys. Rev. B **41**, 3316

Ahlrichs R, Boehm HJ, Brode S, Tang KT and Toennies, JP, 1988: J. Chem. Phys. **88**, 6290

Allen MP and Tildesley DJ, 1987: *Computer Simulation of Liquids* (Clarendon Press, Oxford)

Andersen HH, 1987: Nucl. Instrum. Methods B **18**, 321

Andersen HH, 1988: Nucl. Instrum. Methods B **33**, 466

Andersen HH, 1993: K. Dan. Vidensk. Selsk. Mat. Fys. Medd **43**, 127

Andersen HH and Bay HL, 1981: *Sputtering by Particle Bombardment I*, edited by R. Behrisch (Springer, Berlin) 145

Andersen HH and Sigmund P, 1965: Nucl. Instrum. Methods **38**, 238

Antonov SL, Ivanov IN, Orlikovsky AA, Vasil'chenko VYu and Yurasova VE, 1990: Nucl. Instrum. Methods B **48**, 553

Aono M, 1984: Nucl. Instrum. Methods B **8**, 374

Averback RS, Diaz de la Rubia T and Benedek R, 1988: Nucl. Instrum. Methods B **33**, 693

Averback RS, Diaz de la Rubia T, Hsieh H and Benedek R, 1991: Nucl. Instrum. Methods B **59/60**, 709

Azziz N, Brannon KW and Srinivasan GR, 1985: Materials Research Society Symposia Proceedings **45**, 71

Azziz N, Brannon KW and Srinivasan GR, 1987: Phys. Stat. Sol. (b) **142**, 35

Bae Y, Lorentz DC and Young SE, 1991: Phys. Rev. A **44**, R4091

Barat M and Lichten W, 1972: Phys. Rev. A **6**, 211

Baretzky B, Moeller W and Taglauer E, 1992: Vacuum **43**, 1207

Barrett JH, 1990: Nucl. Instrum. Methods B **44**, 367

Baskes MI, 1984: J. Nucl. Mater. **128/129**, 676

Baskes MI, 1987: Phys. Rev. Lett. **59**, 2666

Baskes MI, 1992: Phys. Rev. B **46**, 2727

Baxter JP, Singh J, Schick GA, Kobrin PH and Winograd N, 1986: Nucl. Instrum. Methods B **17**, 300

Betz G and Wehner GK, 1983: *Sputtering by Particle Bombardment II*, edited by R Behrisch (Springer, Berlin) 11

Betz G, Dobrozemsky R and Viehboeck FP, 1971: Int. J. Mass Spectrom. Ion Phys. **6**, 451

Betz G, Pellin MJ, Burnett JW and Gruen DM, 1991: Nucl. Instrum. Methods B **58**, 429

Beuhler RJ and Friedman L, 1986: Chem. Rev. **86**, 521

Beuhler RJ, Friedlander G and Friedman L, 1989: Phys. Rev. Lett. **63**,1292

Beuhler RJ, Friedlander G and Friedman L, 1992: Phys. Rev. Lett. **68**, 2108

Beuhler RJ, Chu YY, Friedlander G, Friedman L and Kunnmann, W,1990: J. Phys. Chem. **94**, 7665

Biersack JP, 1987: Nucl. Instrum. Methods B **27**, 21

Biersack JP and Eckstein W, 1984: Appl. Phys. A **34**, 73

Biswas R and Hamann DR, 1987: Phys. Rev. B **36**, 6434

Biswas R, Grest GS and Soukoulis CM, 1988: Phys. Rev. B **38**, 8154

Bohr N, 1915: Phil. Mag. (6) **30**, 581

Brandt W and Kitagawa M, 1982: Phys. Rev. B **25**, 5631

Brenner DW, 1990: Phys. Rev. B **42**, 9458

Brenner DW and Garrison BJ, 1986: Phys. Rev. B **34**, 1304

Broomfield K, Stansfield RA and Clary DC, 1988: Surface Sci. **202**, 320

Broomfield K, Stansfield RA and Clary DC, 1990: Surface Sci. **227**, 369

Brown WL, Jarrold MF, McEachern RL, Sosnowski M, Takaoka G, Usui H and Yamada I, 1991: Nucl. Instrum. Methods B **59/60**, 182

Burenkov AF, Komarov FF and Kumakhov MA, 1980: Phys. Stat. Sol. (b) **99**, 417

Carlson TA, Lu CC, Tucker TC, Nestor CW, Jr and Malik, FB, 1970: U.S.A.E.C. Report ORNL-4614

Carlsson AE, 1990: Solid State Physics **43**, 1

Caro A and Victoria M, 1989: Phys. Rev. A **40**, 2287

Caro A, Victoria M and Averback RS, 1990: J. Mater. Res. **5**, 1409

Carter G, Navinšek B and Whitton JL, 1983: *Sputtering by Particle Bombardment II*, edited by R Behrisch (Springer, Berlin) 231

Catlow CRA, Diller KM and Norgett MJ, 1977: J. Phys. C: Solid State Phy. **10**, 1395

Chakarov IR and Karpuzov DS, 1988: unpublished

Chandrasekhar S, 1943: Rev. Mod. Phys. **15**, 1

Chang CS, Knipping U and Tsong IST, 1986: Nucl. Instrum. Methods B **18**, 11

Chang CS, Knipping U and Tsong IST, 1987: Nucl. Instrum. Methods B **28**, 493

Chang CC, Winograd N and Garrison BJ, 1988: Surface Sci. **202**, 309

Chaplot SL, 1988: Phys. Rev. B **37**, 7435

Chaplot SL, 1989: Phase Transitions **19**, 49

Chaplot SL, 1990: Phys. Rev. B **42**, 2149

Chen SP, Voter AF and Srolovitz DJ, 1986: Phys. Rev. Lett. **57**, 1308

Chen SP, Voter AF, Albers RC, Boring AM and Hay PJ, 1990: J. Mater. Res. **5**, 955
Chini TK and Ghose D, 1989: Nucl. Instrum. Methods B **42**, 293
Chou SP and Ghoniem NM, 1991: Phys. Rev. B **43**, 2490
Cleveland CL and Landman U, 1992: Science **257**, 355
Conrad U and Urbassek HM, 1990: Nucl. Instrum. Methods B **48**, 399
Cowern NEB and Biersack JP, 1983: Nucl. Instrum. Methods **205**, 347
Cui FZ and Li HD, 1985: Nucl. Instrum. Methods B **7/8**, 650
Cui FZ, Xie J and Li HD, 1992: Phys. Rev. B **46**, 11182
Cyrot-Lackmann F, 1968: J. Phys. Chem. Solids **29**, 1235
Daw MS and Baskes MI, 1984: Phys. Rev. **29**, 6443
Diaz de la Rubia T and Guinan MW, 1990: J. Nuclear Mater. **174**, 151
Diaz de la Rubia T and Guinan MW, 1991: Phys. Rev. Lett. **66**, 2766
Diaz de la Rubia T, Averback RS, Benedek R and King WE, 1987: Phys. Rev. Lett. **59**, 1930
Diaz de la Rubia T, Averback RS, Hsieh H and Benedek R, 1989: J. Mater. Res. **4**, 579
Diaz de la Rubia T, Averback RS, Benedek R and Robertson IM, 1990: Radiat. Eff. **113**, 13
Dodson BW, 1987a: Phys. Rev. B **35**, 2795
Dodson BW, 1987b: Phys. Rev. B **36**, 1068
Dodson BW, 1987c: Appl. Surface Sci. **29**, 334
Dodson BW, 1989: Mater. Res. Soc. Symposium Proc. **128**, 137
Dodson BW, 1990: Nucl. Instrum. Methods B **44**, 273
Dodson BW, 1991: Nucl. Instrum. Methods B **59/60**, 481
Dodson BW and Taylor PA, 1987: J. Mater. Res. **2**, 805
Ducastelle F, 1970: J. Phys. (Paris) **31**, 1055
Echenique PM, Nieminen RM and Ritchie RH, 1981: Solid State Comm. **37**, 779
Echenique PM, Flores F and Ritchie RH, 1990: Solid State Physics **43**, 229
Eckstein W, 1987: Nucl. Instrum. Methods B **18**, 344
Eckstein W, 1988: Nucl. Instrum. Methods B **33**, 489
Eckstein W, 1991: *Computer Simulation of Ion-Solid Interactions* (Springer, Berlin)
Eckstein W and Biersack JP, 1984: Nucl. Instrum. Methods B **2**, 550
Eckstein W and Hou M, 1988: Nucl. Instrum. Methods B **31**, 386
Eckstein W and Hou M, 1991: Nucl. Instrum. Methods B **53**, 270
Eckstein W, Hackel S, Heinemann D and Fricke B, 1992: Z. Phys. D **24**, 171
Eklund EA, Bruinsma R, Rudnick J and Williams RS, 1991: Phys. Rev. Lett. **67**, 1759
Fallavier M, Kemmler J, Kirsch R, Poizat JC, Remillieux J, and Thomas JP, 1990: Phys. Rev. Lett. **65**, 621
Fano U and Lichten W, 1965: Phys. Rev. Lett. **14**, 627
Feller W, 1957: *An Introduction to Probability Theory and Its Applications, Vol. 1* (Wiley, New York, Second Edition)
Fermi E and Teller E, 1947: Phys. Rev. **72**, 399
Ferrell TL and Ritchie RH, 1977: Phys. Rev. B **16**, 115
Finnis MW and Heine V, 1974: J. Phys. F **4**, L37
Finnis MW and Sinclair JE, 1984: Phil. Mag. A**50**, 45
Firsov OB, 1957: Zh. Eksp. Teor. Fiz. **33**, 696 [Sov. Phys.-JETP **6** (1958) 534]
Firsov OB, 1959: Zh. Eksp. Teor. Fiz. **36**, 1517 [Sov. Phys.-JETP **36** (1959) 1076]
Flynn CP and Averback RS, 1988: Phys. Rev. B **38**, 7118
Foiles SM, 1987: Surface Sci. **191**, L779
Foiles SM, Baskes MI and Daw MS, 1986: Phys. Rev. B **33**, 7983
Gades H and Urbassek HM, 1992: Nucl. Instrum. Methods B **69**, 232
Garcia JD, Fortner RJ and Kavanagh TM, 1973: Rev. Mod. Phys. **45**, 111
Garrison BJ, 1986: Nucl. Instrum. Methods B**17**, 305

Garrison BJ, Winograd N, Lo DY, Tombrello TA, Shapiro MH, and Harrison DE, Jr, 1987: Surface Sci. **180**, L129

Garrison BJ, Winograd N, Deaven DM, Reiman CT, Lo DY, Tombrello TA, Harrison DE, Jr and Shapiro MH, 1988: Phys. Rev. B **37**, 7197

Gibson JB, Goland AN, Milgram M and Vineyard GH, 1960: Phys. Rev. **120**, 1229

Gombás P, 1956: *Handbuch der Physik*, edited by S. Fluegge (Springer, Berlin), Vol. XXXVI, pp. 109-231

Gordon RG and Kim YS, 1972: J. Chem. Phys. **56**, 3122

Grizzi O and Baragiola RA, 1987: Phys. Rev. A **35**, 135

Guellil AM and Adams JB, 1992: J. Mater. Res. **7**, 639

Hackel S, Fricke B, Heinemann D, Kolb D and Yang L, 1990: Report GSI-90-1, p. 165

Haggmark LG and Biersack JP, 1981: J. Nucl. Mater. **103/104**, 345

Harrison DE, Jr, 1981a: J. Appl. Phys. **52**, 1499

Harrison DE, Jr, 1981b: J. Appl. Phys. **52**, 4251

Harrison DE, Jr, 1983: Radiat. Eff. **70**, 1

Harrison DE, Jr, 1988: CRC Critical Reviews in Solid State and Materials Science **14**, S1

Harrison DE, Jr and Jakas MM, 1986a: Radiat. Eff. **99**, 637

Harrison DE, Jr and Jakas MM, 1986b: Nucl. Instrum. Methods B **15**, 25

Harrison DE, Jr and Webb RP, 1982: J. Appl. Phys. **53**, 4193

Harrison DE, Jr, Avouris P and Walkup R, 1987: Nucl. Instrum. Methods B **18**, 349

Hautala M, 1980: Radiat. Eff. **51**, 35

Hautala M, 1984: Phys. Rev. B **30**, 5010

Heinemann D, Rosen A and Fricke B, 1990: Phys. Scr. **41**, 692

Heinisch HL, Schiffgens JO and Schwartz DM, 1979: J. Nucl. Mater. **85/86**, 607

Hofer WO, 1991: *Sputtering by Particle Bombardment III*, edited by R Behrisch and K Wittmack (Springer, Berlin, etc) 15

Hoover WG, 1986: *Molecular Dynamics* (Springer, Berlin)

Hou M and Eckstein W, 1990: Phys. Rev. B **42**, 5959

Hou M and Eckstein W, 1992: J. Appl. Phys. **71**, 3975

Hou M and Robinson MT, 1976: Nucl. Instrum. Methods **132**, 641

Hou M. and Robinson MT, 1979: Appl. Phys. **18**, 381

Hou M, Eckstein W and Robinson MT, 1993: Nucl. Instrum. Methods B **82**, 234

Hsieh H and Averback RS, 1990: Phys. Rev. B **42**, 5365

Hsieh H, Diaz de la Rubia T, Averback RS and Benedek R, 1989: Phys. Rev. B **40**, 9986

Hsieh H, Averback RS, Sellers H and Flynn CP, 1992: Phys. Rev. B **45**, 4417

Igarashi M, Kanta K and Vitek V, 1991: Phil. Mag. B **63**, 603

Ishitani T, Shimase A and Hosaka S, 1983: Jap. J. Appl. Phys. **22**, 329

Jackson DP, 1973: Radiat. Eff. **18**, 185

Jackson DP, 1975: Can. J. Phys. **53**, 1513

Jacobsen KW, Nørskov JK and Puska MJ, 1987: Phys. Rev. B **35**, 7423

Jakas MM and Harrison DE, Jr, 1984: Phys. Rev. B **30**, 3573

Jakas MM and Harrison DE, Jr, 1985: Phys. Rev. B **32**, 2752

Johnson RA, 1991: Phil. Mag. A **63**, 865

Johnson RA and Oh DJ, 1989: J. Mater. Research **4**, 1195

Johnson RE and Schou J, 1993: K. Dan. Vidensk. Selsk. Mat. Fys. Medd. **43**, 403

Kaneko T, 1990a: Surface Science **236**, 203

Kaneko T, 1990b: Nucl. Instrum. Methods B **48**, 83

Kang HJ, Kawatoh E and Shimizu R, 1985: Jap. J. Appl. Phys. **24**, 1409

Karetta F and Urbassek HM, 1992: J. Appl. Phys. **71**, 5410

Karpuzov DS and Yurasova VE, 1971: Phys. Stat. Sol. **47**, 41

Kato M, Williams RS and Aono M, 1988: Nucl. Instrum. Methods B **33**, 462
Keinonen J, Kuronen A, Tikkanen P, Boerner HG, Jolie J, Ulbig S, Kessler EG, Nieminen RM, Puska MJ and Seitsonen AP, 1991: Phys. Rev. Lett. **67**, 3692
Kelly R, 1987: Nucl. Instrum. Methods B **18**, 388
Kessel QC and Everhart E, 1966: Phys. Rev. **146**, 16
Khor KE and Das Sarma S, 1987: Phys. Rev. B **36**, 7733
Kinchin GH and Pease RS, 1955a: J. Nucl. Energy **1**, 200
Kinchin GH and Pease RS, 1955b: Rep. Prog. Phys. **18**, 1
Kirsanov VV and Musin NN, 1990: Physics Lett. A **143**, 420
Kirsanov VV and Musin NN, 1991: Physics Lett. A **153**, 493
Klein KM, Park C and Tasch AF, 1990: Appl. Phys. Lett. **57**, 2701
Kwon I, Biswas R, Grest GR and Soukoulis CM, 1990: Phys. Rev. B **41**, 3678
Landman U, Hill RN and Mostoller M, 1980: Phys. Rev. B **21**, 448
Lehmann C and Sigmund P, 1966: Phys. Stat. Sol. **16**, 507
Leibfried G, 1958: Nukleonik **1**, 57
Leibfried G, 1965: *Bestrahlungseffekte in Festkörpern* (Teubner, Stuttgart) 153
Lennard WN, Xia Y and Geissel H, 1992: Nucl. Instrum. Methods B **67**, 44
Lichten W, 1967: Phys. Rev **164**, 131
Lichten W, 1980: J. Phys. Chem. **84**, 2102
Lindhard J and Scharff M, 1961: Phys. Rev. **124**, 128
Lindhard J, Nielsen V, Scharff M and Thomsen PV, 1963: K. Dan. Vidensk. Selsk. Mat. Fys. Medd. **33**, no. 10
Lindhard J, Nielsen V and Scharff M, 1968: K. Dan. Vidensk. Selsk. Mat. Fys. Medd. **36**, no. 10
Lo DY, Shapiro MH, Tombrello TA, Garrison BJ and Winograd N, 1987: Materials Research Society Symposia Proceedings **74**, 449
Lo DY, Tombrello TA, Shapiro MH, Garrison BJ, Winograd N and Harrison DE, Jr, 1988: J. Vac. Sci. Technol. A **6**, 708
Logan LR, Murthy CS and Srinivasan GR, 1992: Phys. Rev. A, **46**, 5754
Loisel B, Lapujoulade J and Pontikis V, 1991: Surface Sci. **256**, 247
Lu CC, Carlson TA, Malik FB, Tucker TC and Nestor C W, Jr, 1971: Atomic Data **3**, 1
Mashkova ES and Molchanov VA, 1989: Radiat. Eff. **108**, 307
Mazzone AM, 1988: Nucl. Instrum. Methods B **33**, 776
Merkle KL and Jaeger W, 1981: Phil. Mag. **44**, 741
Michely T and Comsa G, 1991: Phys. Rev. B **44**, 8411
Michely T and Comsa G, 1993: Nucl. Instrum. Methods B **82** 207
Michely T, Besocke KH and Comsa G, 1990: Surface Sci. Lett. **230**, L135
Mikkelsen HH, Meibom A and Sigmund P, 1992: Phys. Rev. A, **46**, 7012
Molière G, 1947: Z. Naturforsch. **2a**, 133
Mowrey RC, Brenner DW, Dunlap BI, Mintmire JW, and White CT, 1991: J. Phys. Chem. **95**, 7138
Mueller K-H, 1987: J. Appl. Phys. **61**, 2516
Murthy CS and Srinivasan G R, 1993: Phys. Rev. B, **47**, 1256
Nakagawa ST, 1990: Radiat. Eff. **112**, 1
Nakagawa ST, 1991: Radiat. Eff. **116**, 21
Nakagawa ST and Yamamura Y, 1988: Radiat. Eff. **105**, 239
Nieminen RM, 1993: K. Dan. Vidensk. Selsk. Mat. Fys. Medd. **43**, 81
Norgett MJ, Robinson MT and Torrens IM, 1975: Nucl. Engineer. Design **33**, 50
O'Connor DJ and Biersack JP, 1986: Radiat. Eff. **62**, 14
Oen OS and Robinson MT, 1976: Nucl. Instrum. Methods **132**, 647
Oliva A, Kelly R and Falcone G, 1987: Nucl. Instrum. Methods B **19/20**, 101

Pan Z, 1992: Nucl. Instrum. Methods B **66**, 325

Pan Z and Hou M, 1992: Nucl. Instrum. Methods B **67**, 401

Pan Z and Sigmund P, 1990: Nucl. Instrum. Methods B **51**, 344

Pasianot R and Savino EJ, 1992: Phys. Rev. B **45**, 12704

Pelletier JD, Shapiro MH and Tombrello TA, 1992: Nucl. Instrum. Methods B **67**, 296

Proennecke S, Caro A, Victoria M, Diaz de la Rubia T and Guinan MW, 1991: J. Mater. Res. **6**, 483

Reimann CT, 1993: K. Dan. Vidensk. Selsk. Mat. Fys. Medd. **43**, 351

Robinson MT, 1981: *Sputtering by Particle Bombardment I*, edited by R Behrisch (Springer, Berlin) 74

Robinson MT, 1983: J. Appl. Phys. **54**, 2650

Robinson MT, 1989: Phys. Rev. B **40**, 10717

Robinson MT, 1990: Nucl. Instrum. Methods B **48**, 408

Robinson MT, 1992a: MARLOWE User's Guide (Version 13), unpublished

Robinson MT, 1992b: Nucl. Instrum. Methods B **67**, 396

Robinson MT, 1992c: unpublished calculations

Robinson MT, 1993: Radiat. Eff, to be published

Robinson MT and Oen OS, 1982: J. Nucl. Mater. **110**, 147

Robinson MT and Torrens IM, 1974: Phys. Rev. B **9**, 5008

Ruzic DN, 1990: Nucl. Instrum. Methods B **47**, 118

Ruzic DN and Chiu HK, 1989: J. Nucl. Mater. **162-164**, 904

Sabelli NH, Kantor M, Benedek R and Gilbert TL, 1978: J. Chem. Phys. **68**, 2767

Sabelli NH, Benedek R and Gilbert TL, 1979: Phys. Rev. A **20**, 677

Scherzer BMU, 1983: *Sputtering by Particle Bombardment II*, edited by R Behrisch (Springer, Berlin) 271

Schlaug RN, 1965: Thesis, University of California, Berkeley (University Microfilms, Inc, Ann Arbor, Michigan, 1966)

Schwartz DM, Schiffgens JO, Doran DG, Odette GR and Ariyasu RG, 1976: *Computer Simulation for Materials Applications*, edited by RJ Arsenault, JR Beeler, Jr and JA Simmons. Nucl. Metall. **20**, 75

Shapiro MH and Fine J, 1989: Nucl. Instrum. Methods B **44**, 43

Shapiro MH and Tombrello TA, 1987: Nucl. Instrum. Methods B **18**, 355

Shapiro MH and Tombrello TA, 1990a: Phys. Rev. Lett. **65**, 92

Shapiro MH and Tombrello TA, 1990b: Nucl. Instrum. Methods B **48**, 557

Shapiro MH and Tombrello TA, 1991a: Nucl. Instrum. Methods B **58**, 161

Shapiro MH and Tombrello TA, 1991b: Nucl. Instrum. Methods B **62**, 35

Shapiro MH and Tombrello TA, 1992a: Phys. Rev. Lett. **68**, 1613

Shapiro MH and Tombrello TA, 1992b: Nucl. Instrum. Methods B **66**, 317

Shapiro MH, Tombrello TA and Harrison DE, Jr, 1988: Nucl. Instrum. Methods B **30**, 152

Shulga VI, 1980: Radiat. Eff. **51**, 1

Shulga VI, 1982: Radiat. Eff. **62**, 237

Shulga VI, 1983: Radiat. Eff. **70**, 65

Shulga VI, 1991: Nucl. Instrum. Methods B **58**, 422

Shulga VI and Sigmund P, 1990: Nucl. Instrum. Methods B **47**, 236

Shulga VI and Sigmund P, 1991: Nucl. Instrum. Methods B **62**, 23

Shulga VI, Vicanek M and Sigmund P, 1989: Phys. Rev. A **39**, 3360

Sigmund P, 1981: *Sputtering by Particle Bombardment I*, edited by R Behrisch (Springer, Berlin) 9

Sigmund P, 1987a: Nucl. Instrum. Methods B **18**, 375

Sigmund P, 1987b: Nucl. Instrum. Methods B **27**, 1

Sigmund P, 1989: J. Phys. (Paris), Coll. C-2 **50**, 175

Sigmund P, 1991: *Interaction of Charged Particles with Solids and Surfaces*, NATO ASI Series, Vol. 271, edited by A Gras-Marti et al. (Plenum, New York), 73

Sigmund P and Lam NQ, 1993: K. Dan. Vidensk. Selsk. Mat. Fys. Medd. **43**, 255

Sigmund P, Robinson MT, Baskes MI, Hautala M, Cui FZ, Eckstein W, Yamamura Y, Hosaka S, Ishitani T, Shulga VI, Harrison DE, Jr, Chakarov IR, Karpuzov DS, Kawatoh E, Shimizu R, Valkealahti S, Nieminen RM, Betz G, Husinsky W, Shapiro MH, Vicanek M and Urbassek HM, 1989: Nucl. Instrum. Methods B **36**, 110

Smith R, 1992: Nucl. Instrum. Methods B **67**, 335

Smith R and Harrison DE, Jr, 1989: Phys. Rev. B **40**, 2090

Smith R and Webb RP, 1991: Nucl. Instrum. Methods B **59/60**, 1378

Smith R and Webb RP, 1992: Nucl. Instrum. Methods B **67**, 373

Smith R and Webb RP, 1993: Proc. Roy. Soc. Lond. A **441**, 475

Smith R, Harrison DE, Jr and Garrison BJ, 1989: Phys. Rev. B **40**, 93

Smith R, Harrison DE, Jr and Garrison BJ, 1990: Nucl. Instrum. Methods B **46**, 1

Stansfield RA, Broomfield K and Clary DC, 1989: Phys. Rev. B **39**, 7680

Stillinger FH and Weber TA, 1985: Phys. Rev. B **31**, 5262

Stoneham AM, 1990: Nucl. Instrum. Methods B **48**, 389

Takeuchi W and Yamamura Y, 1983: Radiat. Eff. **71**, 51

Tersoff J, 1986: Phys. Rev. Lett. **56**, 632

Tersoff J, 1988a: Phys. Rev. B **37**, 6991

Tersoff J, 1988b: Phys. Rev. Lett. **61**, 2879

Tersoff J, 1988c: Phys. Rev. B **38**, 9902

Thompson DA, 1981: J. Appl. Phys. **52**, 982

Thompson MW, 1968: Phil. Mag. **18**, 377

Torrens IM, 1973: J. Phys. F **3**, 1771

Tsong IST and Bedrossian P, 1993: K. Dan. Vidensk. Selsk. Mat. Fys. Medd. **43**, 209

Tucker TC, Roberts LD, Nestor CW, Jr and Carlson TA, 1969: Phys. Rev. **178**, 998

Uhlenbeck GE and Ornstein LS, 1930: Phys. Rev. **36**, 823

Urbassek HM and Hofer WO, 1993: K. Dan. Vidensk. Selsk. Mat. Fys. Medd. **43**, 97

Valkealahti S and Nieminen RM, 1987: Nucl. Instrum. Methods B **18**, 365

van Midden HJP and Sasse AGBM, 1992: Phys. Rev. B **46**, 6020

Vicanek M and Urbassek HM, 1988: Nucl. Instrum. Methods B **30**, 507

Wang MC and Uhlenbeck GE, 1945: Rev. Mod. Phys. **17**, 323

Wax N, 1954: *Selected Papers on Noise and Stochastic Processes* (Dover, New York). Includes reprints of Chandrasekhar (1943), Uhlenbeck & Ornstein (1930) and Wang & Uhlenbeck (1945)

Webb RP, Harrison DE, Jr and Jakas MM, 1986: Nucl. Instrum. Methods B **15**, 1

Whitlow HJ and Hautala M, 1987: Nucl. Instrum. Methods B **16**, 370

Wilson WD, Haggmark LG and Biersack JP, 1977: Phys. Rev. B **15**, 2458

Wucher A and Garrison BJ, 1992a: Surface Sci. **260**, 257

Wucher A and Garrison BJ, 1992b: Phys. Rev. B **46**, 4855

Wucher A and Garrison BJ, 1993: Nucl. Instrum. Methods B **82**, 352

Wucher A, Watgen M, Moessner C, Oechsner O and Garrison BJ, 1992: Nucl. Instrum. Methods B **67**, 531

Yamamura Y, 1982: Nucl. Instrum. Methods **194**, 515

Yamamura Y, 1988: Nucl. Instrum. Methods B **33**, 493

Yamamura Y, 1990: Nucl. Instrum. Methods B **45**, 707

Yamamura Y, 1991: Nucl. Instrum. Methods B **62**, 181

Yamamura Y and Muramoto T, 1993: Nucl. Instrum. Methods B, to be published
Yamamura Y and Muraoka K, 1989: Nucl. Instrum. Methods B **42**, 175
Yamamura Y and Takeuchi W, 1987: Nucl. Instrum. Methods B **29**, 461
Yamamura Y, Moessner C and Oechsner O, 1987a: Radiat. Eff. **103**, 25
Yamamura Y, Moessner C and Oechsner O, 1987b: Radiat. Eff. **105**, 31
Yamamura Y, Yamada I and Takagi T, 1989: Nucl. Instrum. Methods B **37/38**, 902
Yu ML, 1991: *Sputtering by Particle Bombardment III*, edited by R Behrisch, and K Wittmaack (Springer, Berlin) 91
Yurasova VE and Eltekov VA, 1982: Vacuum **32**, 399
Ziegler JF, Biersack JP and Littmark U, 1985: *Stopping Powers and Ranges of Ions in Matter* (Pergamon, New York), pp. 25ff

Perspectives of Molecular Dynamics

By Risto M. Nieminen
Laboratory of Physics, Helsinki University of Technology
SF-02150 Espoo, Finland
and
Center for Scientific Computing, P.O. Box 405
SF-02101 Espoo, Finland

Synopsis

A brief, tutorial summary of recent developments in molecular dynamics simulations is given, with a view of their application to the interaction of energetic ions with solid substrates. In particular, the following topics are discussed: (i) interatomic potentials, (ii) ensembles and phase space sampling, and (iii) description of inelastic processes.

1 Introduction

Molecular Dynamics (MD) simulation is a widely used technique for modelling complicated physical phenomena, with applications ranging from galaxy dynamics to protein folding. In materials science, MD simulations consist of calculating numerically the trajectories of a number of interacting atoms over a given time interval. The technique allows one to model the complex dynamical behavior of materials, provided that the relevant spatial and temporal correlations can be contained within the finite size and time span of the simulation. Physical properties, including thermodynamic quantities (for an excellent treatise, see Allen and Tildesley 1987), can then be calculated as appropriate temporal averages of the simulation data. Statistical analysis of the simulation sequences yields information on the dynamic properties of the system.

Ion-solid and ion-surface collisions, including sputtering processes, constitute a complicated set of problems well amenable to molecular dynamics simulation. In fact, a computer simulation (Gibson et al. 1960) of radiation damage induced by an energetic primary-knock-on atom was one of the earliest applications of the MD technique in materials physics. An MD study of the sputtering process entails all the important and challenging ingredients of a meaningful simulation: atomic interactions, non-equilibrium (energy transfer) aspects, ensemble averaging, dissipation and boundary conditions. Below, I shall discuss current issues related to these from the viewpoint of sputtering. An extensive treatment of simulation of ion-solid interactions has recently been published (Eckstein 1991). A comprehensive review of computer simulation of sputtering by Robinson is included in this volume (Robinson 1993). Recent MD simulations of sputtering have been summarized and compared in the round-robin study of Sigmund et al. (1989). Several groups are now actively applying the MD techniques to sputtering and related processes (Garrison et al. 1998, Hsieh and Averback 1990, Shapiro and Tombrello 1992, Karetta and Urbassek 1992, Wucher and Garrison 1992).

2 Atomic Interactions: The Potential Problem

Depending on the physical circumstances one wants to simulate, the number of atoms included in an MD study ranges from a few tens to hundreds of thousands, and the relevant simulation time span is from femtoseconds up to nanoseconds. One is faced with a compromise as regards the number of atoms, the simulation time, and the description of the interatomic force laws.

At high energies (small interatomic separations), the atom-atom interaction is dominated by the two-body (dimer) term. At lower energies, especially near the equilibrium, the pair potential approximation is usually totally inadequate (except in the case of inert gas systems): the total energy of the condensed state cannot be expressed as a sum over pairwise interactions. It is customary to say that there is a volume or density dependence in the total energy. For a simple metal such as Al, in fact most of the cohesive energy is in the 'electron gas' term due to delocalised conduction electrons, with only a weak dependence on structure and interatomic distances.

There is no well-defined rule to determine when the two-body description becomes invalid. In fact the proper strategy of choosing the potential depends critically on what one wants to simulate. For the most energetic atoms in the collision cascade, with their kinetic energies large compared to the cohesive energy, it is often valid throughout the relevant time span. For example, the scattering trajectories of primary hyperthermal ions (energies above a few tens of eV) can be well calculated from pairwise summed repulsive interactions. The scattered ions mainly bounce off the surface. However, if one in the same situation is interested in such follow-on events as damage production in the substrate, many-atom interactions between the substrate atoms are necessary. Pairwise force laws cannot be used for quantitatively reliable calculations of such quantities as defect formation and

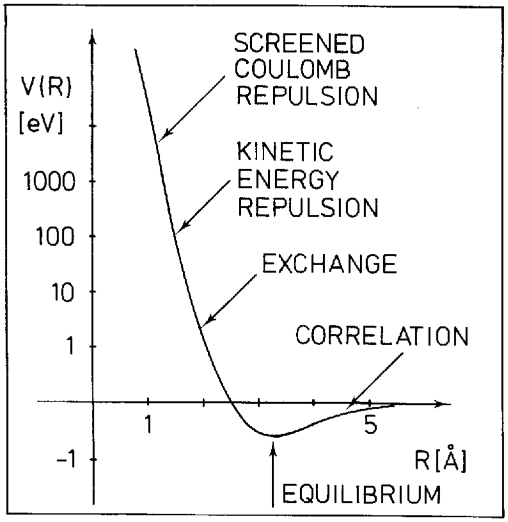

Figure 1. Schematic presentation of the interatomic potential, with the main physical effects indicated for each energy region.

migration energies or, in the case of sputtering, binding energies of surface atoms.

2.1 Two-Atom Potentials

The generic form of a two-body interatomic potential is depicted in Fig. 1. First of all, it is important to recognize the difference between the adiabatic and diabatic potential. The former corresponds to the situation where, according to the Born-Oppenheimer principle, the electrons remain at their instantaneous ground state with respect to the nuclear separation. The adiabatic potential allows for charge transfer between the interacting atoms. In the case where the incoming ion is in molecular form, it also allows for its eventual dissociation. The diabatic potential describes the case where the collision takes place at such speed that the electrons have no time to adjust to the ground state, but are constrained. The diabatic potential energy is always higher than the adiabatic one.

Again, there is no quantitative, general rule as to which potential is the physically relevant one. It is intuitive to think that one should use the diabatic description, corresponding to the initially chosen charge states for the atoms, at high kinetic energies which are large compared to the electron ionisation energy or affinity (velocities large compared to Bohr velocity).

Fig. 1 also shows schematically the major physical origin of the adiabatic two-atom interaction at various separations. The two-atom problem can be essentially regarded as exactly solved (numerically). The two most popular approaches to this problem are known as the Hartree-Fock (HF) method and density-functional theory (DFT) (see, for example, Jones and Gunnarsson 1989) . They only differ in the way they treat the electron-electron interactions. HF treats the electronic exchange (Pauli principle) exactly but neglects the remaining correlations. They can be reintroduced using sophisticated perturbation theory (configuration interaction, CI). DFT treats exchange and correlation on the same approximative level, usually within the so-called local density approximation (LDA). Except near the two-body attractive minimum, they give for the present purposes identical results. At the minimum, DFT-LDA usually leads to overbinding while HF gives underbinding. By increasing the sophistication of correlation treatments, both approaches can be pushed near 'chemical' accuracy, i.e. binding energies of even larger aggregates than dimers can be calculated to a small fraction of an eV. The proponents of both methods use the description ab initio for each of the techniques.

There are by now several computer programs available which provide the HF or DFT numerical solution. Examples of commercially supported programs are the Gaussian92 (trademark of Gaussian, Inc., Pittsburgh, Penn., USA), DMol (trademark of Biosym, Inc., San Diego, Calif., USA) and the UniChem (trademark of Cray Research, Inc., Eagan, Minn., USA) program packages. Thus, for accurate two-atom potentials, there is no need to resort to analytic, statistical or empirical approximations so popular in the past literature. For example, one can evaluate exactly the so-called 'screening function' in the high-energy region where the intra-nuclear Coulomb repulsion dominates.

The electronic structure programs can also be used to evaluate the diabatic potentials. This requires that the electronic state be constrained, for example to a fixed electronic configuration (charge state) for the constituents. While the powerful variational property is strictly valid for the ground state only, it can be extended to the total energies of the lowest excited states of a given symmetry.

2.2 Many-Atom Interactions

Let us now return to the general case where there are several interacting atoms present in the relevant region. Again, in the adiabatic case the electrons adjust themselves to the ground state corresponding to the given nuclear coordinates. In DFT, the total electron density $n(\mathbf{r})$ is the key variable, the 'glue'. The Hohenberg-Kohn theorem (Hohenberg and Kohn 1964) underpinning DFT guarantees that the total energy E is a unique functional of $n(\mathbf{r})$ and that $E\{n(\mathbf{r})\}$ is minimised at the ground state. This guarantees the applicability of the important and useful variational principle. Moreover, the interatomic forces can be exactly calculated using the Hellmann-Feynman theorem.

2.2.1 First-Principles Molecular Dynamics

First-principles MD is a method where one actually solves for the electronic (ground) state at each time step with its nuclear coordinates, and calculates the exact forces as derivatives of the total energy functional with respect to nuclear coordinates. It sounds like a formidable task, but with clever algorithms (Car and Parrinello 1985; for a recent review, see Galli and Parrinello 1991) it is now possible to carry out this task, at least for modest-size systems near their equilibrium.

The key idea is , instead of exact solution of the electronic degrees of freedom ('diagonalisation') at each timestep for nuclear motion, to solve for all the degrees of freedom in unison ('iterative diagonalisation'). This is accomplished by casting the problem into the form of global optimisation of the total energy functional in the space of both the nuclear coordinates $\mathbf{R}_i$ and the electronic wavefunctions ψ_i. The search in the phase space is done through classical equations of motion, where the driving forces are the Hellmann-Feynman forces for the nuclear coordinates, and the deviation from exact diagonality for the electronic amplitudes. An arbitrary inertia parameter ('mass') can be assigned the electronic equations of motion, and the associated fictitious kinetic energy ('electron temperature') can be adjusted to obtain optimal convergence and closeness to the Born-Oppenheimer surface. This process is called 'simulated annealing'; alternative techniques can be preconditioned conjugate gradients (Stich et al. 1989). The real temperature is naturally associated to the nuclear kinetic energy, as in classical MD.

The Car-Parrinello technique is usually implemented using plane waves as the basis set for expanding the electronic eigenstates. This set of functions is convenient for dynamic simulations as its resolution is uniform, i.e. no a priori assumptions of the relevant atomic positions need to be made. Moreover, the plane wave expansion (Fourier analysis) can be made efficiently using the Fast Fourier Transform. The drawback is that rapidly varying electronic states cannot be described by feasible numbers of Fourier terms. The technique is thus usually coupled to the pseudopotential method (Heine and Weaire 1970, Bachelet et al. 1982), where the electronic core states are projected ('pseudized') out. This seriously hampers its usefulness for atoms with deep pseudopotentials such as transition and noble metals with d-like electrons. There have recently been suggestions (Vanderbilt 1990, Laasonen et al. 1991) on how to define 'ultrasoft' pseudopotentials for these materials to make them feasible for plane wave -based methods.

Even with the pseudopotential method, the Car-Parrinello technique is computationally heavy, requiring thousands of plane waves for each eigenstate and thus a huge number of degrees of freedom to be optimised. Thus far most of its implementations have been restricted to a few tens of atoms moving gently near the equilibrium. Its most spectacular successes have been with obtaining true ground state geometries and energies in complicated low-symmetry situations, such as the (7×7) reconstruction on the Si(111) surface (Stich et al. 1992, Brommer et al. 1992) . A few studies of true dynamics, such as diffusion processes and phonon densities of states have been reported (Galli et al. 1989, Buda et al. 1989) . However, with advances in large-scale computing, such as massively parallel processing, one can expect significant advances in near future. A low-energy sputtering process involves a fairly small number of atoms. If the relevant time span (bond breaking, atomic transport) is not too long (say, 1 psec) one can imagine attacking sputtering with first-principles MD soon.

2.2.2 Tight-Binding Molecular Dynamics

Significant savings in computing requirements can be obtained with simplified descriptions of the electronic total energy. The tight-binding (TB) Hamiltonian (see, for example, Harrison 1980) is a well-tested approximation for several condensed matter systems. It retains the quantum-mechanical nature of the electronic kinetic energy, but replaces the electron-ion and electron-electron interactions with a simple operator. The electronic states are represented in terms of a small set of localised basis functions, which leads to a much less heavy diagonalisation problem. The number of atoms in TB-MD can be an order of magnitude larger than in a comparable Car-Parrinello simulation. The TB-MD technique has recently been applied for several problems in semiconductor physics (Laasonen and Nieminen 1990, Virkkunen et al. 1991, Wang et al. 1991).

2.2.3 Approximate Many-Atom Energy Functionals

A major simplification of MD results from making the approach totally classical. The overwhelming majority of MD work to date falls into this category. I have already stressed the fact that two-body classical potentials cannot be expected to work in general. Another demonstration of this comes from exact calculations for total energies of ordered atomic structures with different symmetries and coordination numbers (Goodwin et al. 1990). The obtained formation energies show a strong nonlinearity as a function of coordination number, while a pairwise interaction model should give a straight line. In fact, the curvature seems to follow a square-root behavior obtained from a simple tight-binding model.

Another way of looking at the many-atom interactions is to estimate the energy by building, atom by atom, the aggregate of the desired structure. For example, one can estimate the cohesive energy by 'embedding' an atom to an existing vacancy in the medium. The vacancy contains some electron density from the neighboring atoms. To a first guess, the embedding energy can be approximated by the energy required to immerse the atom into an electron gas (Puska et al. 1981) with that average density. This energy has a nonlinear dependence on the total density, and thus cannot be reduced back to a superposition of pairwise terms from the individual atoms.

The above is the physical motivation to a class of classical many-atom energy functionals. These include the Effective-Medium Theory (EMT (Jacobsen et al. 1987); the Embedded Atom Model (EAM) (Daw and Baskes 1983, 1984); the Finnis-Sinclair-potential and its extensions (Finnis and Sinclair 1984, Ackland et al. 1987); and the Glue Model (Ercolessi et al. 1986, 1988). In all of these, one can write the total energy in the generic form

$$E_{\text{tot}} = \sum_i F(n_i) + \frac{1}{2}\sum_{i,j} \phi(R_i - R_j) + E_{\text{bs}}. \tag{1}$$

Above, F is a (nonlinear) function of the electron density n_i at the site of atom i, arising from the neighboring atoms interacting with it. This term contains the density or volume dependence of the total energy, it depends on the coordination number but is less sensitive to the structure. The second term is a (pairwise) summation of potentials ψ of electrostatic origin. This term also contains the short range core repulsion necessary to stabilise the structure. The third term is a correction term, in some formulations associated with the single-particle eigenvalues (the band-structure energy).

The many-atom descriptions of the form sketched in Eq. (1) were first developed for close-packed fcc crystals, and contained nearest-neighbor interactions only. They have subsequently been made more general in the sense that other crystal symmetries have been included, and that interactions beyond nearest neighbors have been included (Häkkinen and Manninen 1989). The latter feature is of course necessary in order for the model to distinguish between hcp and fcc structures and to calculate stacking fault energies. For recent summaries, see Jacobsen's review (Jacobsen 1988) for the EMT model and Baskes' article (Baskes 1993) for the EAM model.

Many-atom potentials can also be derived through perturbation theory, based for example on the idea of pseudopotentials and dielectric screening (Moriarty 1982). Summaries of all the recent ideas and results for many-atom interactions have been published in two workshop proceedings (Nieminen et al. 1990, Haydock et al. 1991).

2.3 Empirical Many-Atom Potentials

For directionally bonded materials such as tetrahedrally coordinated solids, several classical, empirically motivated many-atom potential models have been proposed. Famous examples include the Stillinger-Weber potential for Si (Stillinger and Weber 1985), the carbon potentials suggested by Tersoff (Tersoff 1989) as well as several models suggested for hydrogen-bonded substances such as water (Schweizer and Stillinger 1984). Their utility in MD simulations for ground state properties varies. In general, one should be aware of the limited general applicability of empirically determined potentials outside the particular set of properties used to fit their parameters: it is sometimes difficult to 'cheat' quantum mechanics.

One final remark on the atomic force laws is in order. In sputtering simulations, considerable attention has been paid to modelling of the substrate surface. This is natural, as the ejection energy and angular distribution of the sputtered particles depend on the surface geometry and energetics. A proper MD model should contain the surface structure and binding inherently, without any extra assumptions or explicitly introduced surface potentials.

3 Ensembles and Phase-Space Sampling

The traditional and simplest way of performing MD simulations is to use the microcanonical (constant-NVE) ensemble, i.e. to solve the equations of motion for a fixed number of atoms in constant volume and with conserved total energy. Extended systems are simulated by using periodic boundary conditions in one or more dimensions. The standard algorithm for the numerical solution of the equations of motion is the velocity-Verlet method in one of its disguises. The technical issues of MD simulation have been presented in several texts (Heermann 1986).

3.1 Constant-Pressure and Constant-Temperature Simulations

In many cases, the microcanonical ensemble is not, however, the physically correct one to perform the simulations in. The MD method can be extended to other ensembles. The constant-NpH simulation corresponds to the case where the pressure p and enthalpy H are conserved, and the cell volume can change dynamically. The relevant equations of motion were first presented by Andersen (Andersen 1980), and can be efficiently implemented for MD simulations. Nosé and Klein (Nosé and Klein 1983) developed an extension to the canonical (constant-NVT) ensemble, where the temperature T is kept constant. The standard implementation of this method nowadays involves the equation of motion for the so-called Nosé-Hoover

(Hoover 1985) thermostat.

The physically most appealing ensemble is one where both pressure p and temperature T are the pre-chosen thermodynamical variables. Nosé (Nosé 1984a, 1984b) presented the extension to the constant-NpT case. Unfortunately, the set of equations of motion becomes rather cumbersome in this case, and the method has not yet been extensively applied in practical simulations.

3.2 Constrained Molecular Dynamics

An often occurring situation in MD simulations is that one wants to impose constraints on a given subset of degrees of freedom. For example, in a simulation for a molecular system it may make sense to keep the bond lengths fixed, but allow the positions of molecules and their angular orientations to evolve freely under the intermolecular and intramolecular forces. An especially useful technique to treat holonomic constraints has been presented (Ryckaert et al. 1977) . This constraint dynamics approach uses a set of Lagrange multipliers to represent the forces required to keep the desired distances (or angles) constant. The constraint forces are updated at each timestep and are correct to the same order of accuracy as the integration algorithm.

3.3 Heating and Boundary Effects in Sputtering Simulations

Also in sputtering simulations, the choice of the ensemble is of some importance. For short-time collision dynamics and ejection processes, the microcanonical ensemble seems the obvious choice. However, for longer time scale effects such as structural relaxation, damage production and annealing, and eventual equilibration, other ensembles are more appropriate. For example, swelling and eventual blistering of the sputtered surface requires volume relaxation, i.e. the constant-pressure ensemble.

The incident ion deposits kinetic energy into the substrate. While some of this energy is dissipated to the electronic degrees of freedom (see Ch. 4 below), the temperature (the ion kinetic energy) in the substrate rises. In MD simulations with accumulating dose, this eventually leads to unphysical heating of the sample. Moreover, if periodic boundary conditions are used, the hot and damaged region has periodic images throughout the surface.

A possible way to avoid unphysical heating is to embed the simulation unit cell into an unperturbed and cool substrate. This can be accomplished by defining a 'skin' region for the unit cell where the ion velocities are repeatedly scaled so that its mean temperature corresponds to the desired bulk temperature. The ion positions at the cell boundary can be fixed at their unperturbed values. This technique corresponds to the presence of a heat bath which 'dissolves' the deposited kinetic energy, and corresponds to rapid heat diffusion out of the sputtered region in a real physical system. However, care should be taken to choose the simulation conditions such that no spurious effects are introduced, for example by reflection (Laakkonen and Nieminen 1990) of the heat pulse due to the cascade off the skin. It is advisable to carefully test the simulation setup for the size of the unit cell and the cooling strategy so that they do not affect the phenomena from which one is gathering statistical information through the simulation.

Another possibility for introducing heat bath effects is to augment the deterministic MD equations with Langevin-type viscous forces affecting the atoms near the cell boundary (Tully 1980). The friction coeffients can be adjusted so as to mimic the desired heat dissipation into the substrate.

3.4 Free-Energy Simulations

MD simulations can also be used to obtain entropic contributions, e.g. free energies. The standard simulation produces a trajectory in the phase space, corresponding to a fixed total or kinetic energy for the Hamiltonian H. A direct evaluation of the Helmholtz free energy F would require the computation of a configurational integral, which is very hard due to the rapidly varying integrand. A practical free energy calculation can be based on the idea of coupling constant integration (Squire and Hoover 1969) . One chooses as a reference Hamiltonian H_0 one for which the free energy F_0 is known e.g. the ideal gas or the harmonic solid. Then the free energy for the real system is

$$F = F_0 + \int_0^1 d\lambda \left\langle \frac{\partial U(\lambda)}{\partial \lambda} \right\rangle \tag{2}$$

where $H(\lambda) = H_0 + U(\lambda)$ so that $\lambda = 0$ corresponds to the reference system while $\lambda = 1$ corresponds to the real system. The brackets denote the thermodynamic (canonical) average. By performing a series of MD simulations for selected values of the coupling constant λ, one can estimate the free energy.

3.5 Hybrid Monte Carlo -Molecular Dynamics

A fundamental limitation of the MD technique is the explicit dependence of the calculated sequences and averages on the chosen time step. On the one hand, this implies the possibility of numerical instabilities for the algorithm. On the other hand, for canonical simulations the MD technique can be extremely inefficient in the sampling of the phase space (long simulations are very costly). Monte Carlo (MC) methods in statistical physics are based on a stochastic process, where atom positions are updated randomly and the new configurations are accepted using the Metropolis criterion. Even if the updates are usually done locally, the canonical minimum can be found effectively, except near phase transitions where critical slowing down renders the algorithm very slow. The other obvious drawback of the MC method is that there is not a real 'clock' in the system, i.e. no quantitative dynamics can be obtained.

The hybrid MC-MD algorithm (Mehlig et al. 1992) is one which combines some of the appealing features of both methods. Like in MD, one generates new configurations through a deterministic algorithm (equations of motion). However, the timestep can be chosen large so that truncation errors introduce a nonconservation of the total energy. After a while, the new configuration (with a new total energy) is checked using the standard Metropolis criterion. If the algorithm for the equations of motion is time reversible and preserves the phase space volume, one can show that the canonical distribution is obtained. The algorithm is effective as most of the updates are global (as in MD), yet large drifts in the internal energy are possible. Even if the interpretation of real time is not clear in this method, it seems to provide an interesting alternative for MD simulations requiring very long time scales.

4 Non-Equilibrium MD: Electronic Cooling

Energetic ions transfer energy to the electronic subsystem as well. The phenomenon of electronic stopping is important and much studied in ion implantation. Electronic excitations can lead to direct desorption of surface atoms ('electronic sputtering') (Avouris et al. 1987) , which can simply be thought as being due to the transfer between the adiabatic and diabatic potential energy curves, induced by the incoming ion. In collisional sputtering, ion-electron energy transfer shows up in two ways. Firstly, the trajectory and the range of the primary ion is affected by the inelastic losses to electrons. Secondly, the kinetic energy of the substrate atoms having undergone collisions decreases. The latter is particularly important in such cases where dense 'thermal spikes' are formed near the end of the cascade. The spike can cool much faster if the energy-loss channel to electrons is open. The faster cooling rate has an effect on such phenomena as defect production and mixing, and can also affect sputtering.

Quantitative theories of electronic cooling of collision cascades have recently been presented. The key ingredient in these theories is the energy loss rate for a swift ion, a problem first discussed by Bohr (Bohr 1913), Fermi and Teller (Fermi and Teller 1947), Lindhard (Lindhard 1954) and subsequently dealt with by several investigators. In the case where the ion is traversing an electron-gas-like metal with a velocity small compared to the electron Fermi velocity, one can rigorously show that the stopping power (energy loss per unit distance) is proportional to the ion velocity:

$$-\frac{dE_{\mathrm{kin}}}{dx} = \alpha(Z,n)\sqrt{E_{\mathrm{kin}}}. \qquad (3)$$

The proportionality constant $\alpha(Z,n)$ can be related to the scattering cross section of Fermi surface electrons off a stationary ion, a quantity which can be calculated exactly using density-functional theory (Puska 1990). It is important to realise that $\alpha(Z,n)$ depends in a nonlinear fashion on both the ion nuclear charge Z and the electron density n. Note that the same or closely related constant appears in such diverse physical quantities as impurity resistivity, vibrational lifetimes, electron-phonon coupling and spin-lattice relaxation time.

Calculated values for the 'friction parameter' $\alpha(Z,n)$ have been tabulated by Puska and Nieminen (Puska and Nieminen 1982) . The electronic friction can (and should) be implemented in sputtering MD simulations by simply adding a velocity-dependent damping term to the equations of motion.

A problem closely related to the electronic stopping power is the energy transfer rate from a collection of mobile atoms to electronic (single-particle) excitations. Let us consider the ionic motion as being described by the dynamic structure factor $S(\mathbf{q},\omega)$ for fluctuations. This can include both single-ion motion and collective (phonon-like) excitations. Using the Fermi Golden Rule, one can write the energy exchange rate $\dot{U}$ between the ionic and electronic systems as (see, for example, Koponen 1992)

$$\begin{aligned} \dot{U} &= \frac{2\pi}{n}\int_0^{\infty} d\omega \sum_{\mathrm{k,k'}} \hbar\omega\delta(\varepsilon_{\mathrm{k}} - \varepsilon_{\mathrm{k'}} - \hbar\omega)|T_{\mathrm{q}}|^2 \cdot \\ & \qquad [f_{\mathrm{k}}(1-f_{\mathrm{k'}})S(\mathbf{q},\omega) - f_{\mathrm{k'}}(1-f_{\mathrm{k}})S(-\mathbf{q},-\omega)], \qquad (4) \end{aligned}$$

where one has assumed a monovalent metal for simplicity. Above, ε_k denotes the electron single-particle energy with wavevector $\vec{k}$, and f_{k} is the Fermi distribution function. By interpreting $\mathrm{T_q}$ as the t-matrix for electron-ion scattering, the nonlinear screening effects are included in Eq. (4) and it can therefore be made consistent with Eq. (3).

Stoneham (1990) has recently reviewed the consequences of electron-ion coupling for collision cascades in solids. Based on the ideas of Flynn and Averback (1988), Finnis et al. (1991) have recently made a quantitative study of the thermal excitation of electrons in energetic displacement cascades. Using both a continuum (diffusion) model for the cascade and an MD simulation with explicit friction forces derived from a thermal model, they showed that electron-phonon coupling has a pronounced effect on cascade cooling. For example, the 2-keV cascade quenches much faster in Ni than Cu, basically due to the much higher density of electronic states near the Fermi level. Koponen and Hautala (1993) have carried out related studies of the effect of electronic cooling on ion-beam-induced mixing.

Caro and Victoria (1989) have described a similar scheme of adding a velocity-dependent damping term to the equations of motion. They suggest an empirical interpolation formula, based on the local electron density encountered by the moving ion, for obtaining the energy-dependent electron-ion coupling throughout the whole cascade history. In effect it interpolates between the 'stopping region' (Eq. (3) and 'thermal region' (Eq. (4)).

The experimental verification of the electronic effects in collision cascades is still controversial, and the quantitative importance of the ion-electron energy exchange is not settled. The effects manifest themselves indirectly in defect product rates, defect mobility and short-term annealing. It would be highly desirable to devise novel experiments to establish the electronic cooling effect unambiguously.

Recently, the inverse process where energy is transferred from the electronic subsystem to the ions, has been investigated. This is accomplished experimentally by picosecond laser-pulse irradiation of metallic surfaces (Herman & Elsayed-Ali, 1992). Häkkinen & Landman (1993) have carried out MD simulations of the associated superheating, melting, and annealing for Cu surfaces, using the methods outlined above.

5 Algorithms and Implementation

MD simulations are typically at the forefront of computational physics. Ambitious projects require supercomputer resources. The computational cost of classical MD with short-range forces scales linearly with the number of particles N. (Long-range Coulomb forces require special Ewald summation techniques). The time-step δt for numerical solution should be chosen so that the most energetic ions do not move too much (compared to typical atom distances) during δt. In practical sputtering simulations, δt is in the average of the order of 10^{-15} s. Let us assume that one needs 100 floating-point operations per atom and time-step to calculate forces and update the position and velocity. A modern vector supercomputer processor can execute up to the order of 10^9 floating-point operations per second. This implies that one can simulate $10^{-8}/N$ real-time seconds for every computer-second. For a unit cell of 10^3 atoms, this means that each computer second corresponds to 10 ps of real time. Assuming that one needs 100 simulation histories to get acceptable statistics, the cost for simulating a 1 nsec real-time physical process is of the order of 3 CPU-hours on a supercomputer.

For first-principles MD, the numbers are much worse. First of all, the time step is determined by the quantum resolution and is typically around 10^{-16} s, a factor of 10 shorter than in the classical case. The ionic (classical) part scales as discussed above, but the electronic part is much more costly. The computational cost is for large systems proportional to N^3. This arises from the need to orthogonalise the wavefunctions. Moreover, the proportionality constant can be very large as it depends on the number of basis functions M required to represent each (occupied) eigenstate. (The iterative Car-Parrinello technique saves one from explicit full matrix construction and diagonalisation. The Fast Fourier Transform takes of the order of $M \ln M$ operations to go between the real and reciprocal space.) The numbers add up such that even with a 10^9-flop/s supercomputer one is limited to around 100 atoms, and that one computer-second translates to roughly one timestep.

Parallelisation of MD computing, both classical and quantum, is an area of active research and development. It is natural to think that since the physics in Nature takes places in parallel, one should be able to write such algorithms and programs which can effectively utilise the architecture of a (massively) parallel supercomputer. Early experiences show considerable promise that within the next few years one can widen the scale of MD simulations by an order of magnitude. This will bring more dynamic phenomena within the reach of first-principles MD simulation.

6 Conclusions

MD simulation techniques have progressed in a spectacular way during the last decade. The sophistication and accuracy of representing atomic interactions has reached a level, where structural, thermodynamic, and energetic properties can be reproduced and predicted reliably. It is also possible to investigate (with classical force laws) dynamic phenomena over time scales in tens of nanoseconds.

MD is basically a deterministic simulation technique, whereby thermodynamic ensemble averages are replaced by temporal averages. Their equivalence assumes the satisfaction of the ergodic principle, and requires that proper care is taken to avoid spurious effects arising from boundary and initial conditions, truncation errors etc. The statistical analysis of the 'computer experiments' should be made properly. The reliability of the assumed force laws should always be critically examined for the physical phenomenon in question. One should be aware of the dangers of over-interpretation of incomplete or unreliable data, just as in the case of real experiments. With those caveats in mind, it is easy to comprehend the enormous possibilities the MD techniques provide in modelling complicated materials phenomena and processes, such as sputtering.

Acknowledgments

I am grateful to Martti Puska, Mikko Hautala and Ismo Koponen for many useful discussions.

References

Ackland GJ, Tichy G, Vitek V and Finnis MW, 1987: Phil. Mag. **A56**, 705

Allen MP and Tildesley DJ, 1987: *Computer Simulation of Liquids* (Clarendon, Oxford)

Andersen HC, 1980: J. Chem. Phys. **72**, 2384

Avouris PH, Kawai R, Lang ND and Newns DM, 1987: Phys. Rev. Lett. **59**, 2215

Bachelet GB, Hamann DR and Schlüter M, 1982: Phys. Rev. **B26**, 4199

Baskes MI, 1993: Phys. Rev. B (to be published)

Bohr N, 1913: Phil. Mag. **25**, 10

Brommer KD, Needels M, Larson BE and Joannopoulos JD, 1992: Phys. Rev. Lett. **68**, 1355

Buda F, Chiarotti G,Car R and Parrinello M, 1989: Phys. Rev. Lett. **63**, 294

Car R and Parrinello M, 1985: Phys. Rev. Lett. **55**, 2471

Caro A and Victoria M, 1989: Phys. Rev. **A40**, 2287

Daw MS and Baskes MI, 1983: Phys. Rev. Lett. **50**, 1285

Daw MS and Baskes MI, 1984: Phys. Rev. **B29**, 6443

Eckstein, W, 1991: *Computer Simulation of Ion-Solid Interactions* (Springer, Heidelberg)

Ercolessi F, Tosatti E and Parrinello M, 1986: Phys. Rev. Lett. **57**, 719

Ercolessi F, Parrinello M and Tosatti E, 1988: Phil. Mag. **A58**, 213

Fermi E and Teller E, 1947: Phys. Rev. **72**, 399

Finnis MW and Sinclair JE, 1984: Phil. Mag. **A50**, 45

Finnis MW, Agnew P and Foreman AJE, 1991: Phys. Rev. **B44**, 567

Flynn CP and Averback RS, 1988: Phys. Rev. **B38**, 7118

Galli G and Parrinello M, 1991: in *Computer Simulation in Materials Science*, eds. M. Meyer and V. Pontikis (Kluwer)

Galli G, Martin RM, Car R and Parrinello M, 1989: Phys. Rev. Lett. **63**, 988

Garrison BJ, Winograd N, Deaven DM, Reiman CT, Lo DY, Tombrello TA, Harrison DE Jr., and Shapiro MH, 1988: Phys. Rev. **B37**, 7197

Gibson JB, Goland AN, Milgram M and Vineyard GH, 1960: Phys. Rev. **120**, 1229

Goodwin L, Needs RJ and Heine V, 1990: J. Phys. **CM 2**, 351

Harrison WA, 1980: *Electronic Structure and the Properties of Solids* (Freeman, San Francisco)

Haydock R, Inglesfield JE and Pendry JB (eds.), 1991: *Bonding and Structure of Solids* (The Royal Society, London)

Heermann DW, 1986: *Computer Simulation Methods in Theoretical Physics* (Springer, Heidelberg)

Heine V and Weaire D, 1970: Solid State Phys. **24**, 250

Herman JW and Elsayed-Ali HE, 1992: Phys. Rev. Lett. **68**, 2952

Hohenberg P and Kohn W, 1964: Phys. Rev. **136**, B864

Hoover W G, 1985: Phys. Rev. **A31**, 1695

Hsieh H and Averback RS, 1990: Phys. Rev. **B42**, 5365

Häkkinen H and and Landman U, 1993: Phys. Rev. Lett. **71**, 1023

Häkkinen H and Manninen M, 1989: J. Phys. **CM 1**, 9765

Jacobsen KW, 1988: Comment. Cond. Matt. Phys. **14**, 129

Jacobsen KW, Nørskov JK and Puska MJ, 1987: Phys. Rev. **B35**, 7423

Jones RO and Gunnarsson O, 1989: Rev. Mod. Phys. **61**, 689

Karetta F and Urbassek HM, 1992: J. Appl. Phys. **71**, 5410

Koponen I, 1992: Thesis, University of Helsinki, Department of Physics

Koponen I and Hautala M, 1993: Nucl. Instrum. Methods B, in press

Laakkonen J and Nieminen RM, 1990: Phys. Rev. **B41**, 3978

Laasonen K and Nieminen RM, 1990: J. Phys. **CM 2**, 1509

Laasonen K, Car R, Lee C and Vanderbilt D, 1991: Phys. Rev. **B43**, 6976

Lindhard J, 1954: Kgl. Danske Vidensk. Selsk. Mat. Fys. Medd. **28/8**, 1

Mehlig B, Heermann DW and Forrest BM, 1992: Phys. Rev. **B45**, 679

Moriarty J, 1982: Phys. Rev. **B26**, 1754

Nieminen RM, Puska MJ and Manninen M (eds.), 1990: *Many-Atom Interactions in Solids* (Springer, Heidelberg)

Nosé S, 1984a: J. Chem. Phys. **81**, 511

Nosé S, 1984b: Mol. Phys. **52**, 255

Nosé S and Klein M, 1983: Mol. Phys. **50**, 1055

Puska MJ, 1990: in *Many-Atom Interactions in Solids*, R.M. Nieminen, M.J.Puska and M.Manninen (eds.), (Springer, Heidelberg)

Puska MJ and Nieminen RM, 1982: Phys. Rev. **B25**, 67

Puska MJ, Manninen M and Nieminen RM, 1981: Phys. Rev. **B24**, 3037

Robinson MT, 1993: Kgl. Dan. Vidensk. Selsk. Mat. Fys. Medd. **43**, 27

Ryckaert JP, Ciccotti G and Berendsen HJC, 1977: J. Comput. Phys. **23**, 327

Schweizer KS and Stillinger FH, 1984: J. Chem. Phys. **80**, 1234

Shapiro MH and Tombrello TA, 1992: Phys. Rev. Lett. **68**, 1613

Sigmund P, Robinson MT, Baskes MI, Hautala M, Cui FZ, Eckstein W, Yamamura Y, Hoska S, Ishitani T, Shulga VI, Harrison DE Jr., Chakarov IR, Karpuzov DS, Kawatoh E, Shimizu R, Valkealahti S, Nieminen RM, Betz G, Husinsky W, Shapiro MH, Vicanek M, and Urbassek HM, 1989: Nucl. Instrum. Methods **B36**, 110

Squire DR and Hoover WG, 1969: J. Chem. Phys. **50**, 701

Stich I, Car R, Parrinello M and Baroni S, 1989: Phys. Rev. **B39**, 4997

Stich I, Payne MC, King-Smith RD, Lin J-S and Clarke LJ, 1992: Phys. Rev. Lett. **68**, 1351

Stillinger F and Weber T, 1985: Phys. Rev. **B31**, 5262

Stoneham AM, 1990: Nucl. Instrum. Meth. **B48**, 389

Tersoff J, 1989: Phys. Rev. **B39**, 5566

Tully JC, 1980: J. Chem. Phys. **74**, 1975

Vanderbilt D, 1990: Phys. Rev. **B41**, 7892

Virkkunen R, Laasonen K and Nieminen RM, 1991: J. Phys. **CM 3**, 7455

Wang CZ, Chan CT and Ho KM, 1991: Phys. Rev. Lett. **66**, 189

Wucher A and Garrison BJ, 1992: Phys. Rev. **B46**, 4855

Sputtering of Molecules and Clusters: Basic Experiments and Theory

By Herbert M. Urbassek
Fachbereich Physik, Universität, PF 3049
D–67653 Kaiserslautern, Germany
and
Wolfgang O. Hofer
Forschungszentrum Jülich
Institut für Plasmaphysik, EURATOM Association
D–52425 Jülich, Germany

Synopsis

A review is given of experimental and theoretical results on the sputtering of clusters obtained after the last Symposium on Sputtering (1986). We shall restrict ourselves mostly to collisional emission from electrically conducting, elemental solids upon energetic particle bombardment.

After a short historical survey, the size distributions of sputtered clusters will be presented and compared with those of other surface emission phenomena such as (thermal and laser-induced) sublimation and field evaporation.

The interpretation and in particular the pronounced dependence of the size distributions on the charge state are still controversially discussed in the literature. Also, the extent to which cluster fragmentation influences experimentally determinable emission distributions is not yet finally settled. The key quantities here are the cluster binding and ionization energy and the internal kinetic energy distribution in the cluster. These quantities are only poorly known. But there are also experimental difficulties to overcome, such as the effect of post-ionization on cluster stability, the comparatively long flight time in the particle spectrometer, and discrimination in heavy-particle detection.

Cluster fragmentation also has a direct bearing on one of the fundamental questions in sputtering, namely the fraction of atoms in the sputtered flux that is ejected in a bound state.

Kinetic energy distributions display an E^{-2} decay at high emission energies E for a wide class of sputtered molecules. This applies if strongly bound molecules are emitted which are only weakly bound to their surroundings. Such a soft decay is taken as evidence that the molecule has been emitted by a single strong collision of a recoil atom in the collision cascade set up by the bombarding particle. This feature is often observed in the emission of molecular reaction products in reactive ion etching.

The spectra of dimers sputtered from elemental metals, on the other hand, show a steeper decay with emission energy, which has been measured to lie between an E^{-3} and an E^{-5} asymptotic by different researchers. Such a steep fall-off is indicative of more than one collision being active

in emitting the cluster. In this area, recent molecular-dynamics computer simulation experiments have been performed with appropriate metallic many-body potentials and good statistics to give more details of the emission mechanism.

1 Introduction and Historical Survey

When a solid surface is bombarded by energetic atoms or ions, particles are emitted (sputtered) from the surface. In the sputtered flux, not only atoms and monatomic ions are found, but also polyatomic molecules and clusters.[1] The sputtering of molecules and clusters is a ubiquitous phenomenon. It has been found under ion bombardment of metals, semiconductors, and insulators; for elemental targets, alloys, and compounds; for molecular crystals, bio-organic, and polymeric materials.

Clusters containing an impressingly high number of atoms have been found in sputtering experiments. Fig. 1 gives an example for a metallic target, both for charged and neutral sputtered clusters.

The sputtering of clusters is interesting in itself: While the sputtering of atoms is for most systems a consequence of the momentum imparted to a (near-) surface atom in the collision cascade set up by the bombarding ion (Behrisch, 1981; Behrisch, 1983; Behrisch & Wittmaack, 1991), the emission of large clusters from strongly bonded materials has been tentatively connected to the collective or correlated emission of several atomic species (Hofer, 1980; Merkle & Jäger, 1981; Andersen, 1989; Hofer, 1991). Thus, the mere existence of large clusters in sputtering is certainly one of the important open problems in sputtering physics.

The sputtering of clusters has also found a number of interesting applications: The significance of the ion-bombardment induced desorption of organic and biomolecules has been discussed elsewhere in this Volume. Cluster emission is invariably observed in secondary ion (SIMS) and sputtered neutral mass spectrometry (SNMS) experiments and has been used in connection with surface analysis (Schou & Hofer, 1982; Oechsner, 1990; Downey et al., 1992). When surfaces are bombarded by reactive ions or by inert ions in a reactive environment, the total sputter rate can be increased, since molecular, more volatile, reaction products are more easily emitted than the unreacted material. This application of molecular sputtering is used as reactive ion etching (RIE) (Oostra & de Vries, 1987). Finally, cluster sputtering has been used as a cluster source. Since sputtered clusters are internally quite hot, this application has been comparatively rare (Thum & Hofer,

---

[1] The choice of words is somewhat fuzzy in the literature. We shall use the term 'cluster' in a broad sense to mean any aggregation of atoms. By 'molecules' we mean more specifically those strongly bonded atomic aggregations which already existed in or on the solid before bombardment, such as in molecular crystals, or which are formed under ion bombardment by chemical reactions, such as in reactive ion etching.

1979; Magnera et al., 1985; Begemann et al., 1986; Fayet et al., 1986).

The emission of clusters from solid surfaces was discovered about 50 years ago (Hahn et al., 1942; Mattauch et al., 1943). This was in an RF-spark between carbon electrodes, and hence clusters originated from sublimation. In the fifties, Honig (1953; 1954) continued this work and performed fundamental research on thermal emission from group IV elements. Later he (Honig, 1958), Krohn (1962), and others turned to sputtering as a source of ions for mass spectrometry, and their work must be considered as the first detection of the phenomenon of cluster sputtering (Hofer, 1991). Of course, in these measurements only cluster ions were detected.

Several researchers tried to detect neutral particles. Post-ionization with electron beams was the preferred method then. With the notable exception of Woodyard & Cooper (1964) this failed because of background problems caused by the residual gas. Woodyard & Cooper found a surprisingly high fraction of sputtered clusters (dimers and trimers) in the flux of neutral particles. This irritating uncertainty on one of the fundamental questions in sputtering, namely the fraction of bound particles in the sputtered flux, persisted for the next two decades and is only now in the process of being clarified.

Mass distributions[2] of cluster ions were first reported by Blaise & Slodzian (1968) and Hortig & Müller (1969). With the broad use of the SIMS analysis technique, such distributions became available for many elements and multicomponent targets. When assuming that the charged and neutral distributions follow a similar behavior, all these results pointed towards an appreciable (20-30%, in some cases even more) bound particle flux. This picture changed somewhat when Gerhard & Oechsner (1975) published the first neutral-cluster intensity ratios, i.e., dimer-to-atom and trimer-to-atom ratios. Although this investigation was carried out on a much broader experimental and theoretical basis than that of Woodyard & Cooper (1964), the choice of experimental parameters as well as unknown instrumental influences on cluster dissociation prevented an assessment of bound particle fluxes in the collision-cascade regime. The picture changed when Gnaser & Hofer (1989) found in a direct-comparison experiment the mass distributions of neutral clusters to fall off much more steeply with cluster size than for charged clusters. This holds down to cluster/atom intensity ratios of about 10^{-4}, thus covering the vast majority of the flux of sputtered particles. Still lower intensity ratios became accessible with the laser-ionization technique (Coon et al., 1991; Wucher et al., 1993). At this low level, the emission processes are hardly representative of the general phenomenon of sputtering but they are highly interesting in the elucidation

---

[2] Following a general practice, we use the terms mass, abundance, and cluster-size distribution synonymously. (As-measured) mass spectra should, ideally speaking, be corrected for instrumental effects in order to yield mass distributions. This is only seldomly done, however.

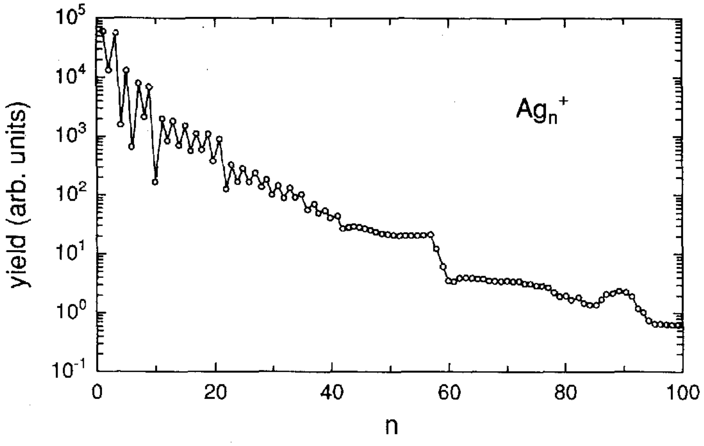

Figure 1a. Experimental data on sputtered Ag cluster abundance distributions. Ionized clusters Ag_n^+ sputtered by 10 keV Xe^+ ions (Katakuse et al., 1985). The intensity drops at Ag_9^+, Ag_{21}^+, and Ag_{41}^+ should be noted. They are associated with 'magic' numbers of binding electrons, for which jellium-type calculations yield binding energy maxima for 8, 20, and 40, respectively, 5s electrons.

of cascade-fluctuation effects as well as for specific cluster-emission events. Information available from cluster-size distributions will constitute a major part of this review.

Cluster abundance distributions are not stable during the first 10 μs or so after the clusters' genesis. The importance of fragmentation has been first shown by Ens et al. (1983) for ionically bound clusters, and by Dzhemilev et al. (1985) and Begemann et al. (1986) in the case of metal clusters. These studies showed that the cluster abundance distribution strongly changed its characteristics with the time spent after cluster formation, cf. fig. 2. The consequence of cluster fragmentation is that practically all mass spectra measured so far do not represent the emission distribution in sputtering. Rather they come near to the stationary distribution, depending strongly on the experimental technique employed for mass analysis.

In the early seventies, a number of groups started measurements of the energy spectra of charged clusters (Dennis & MacDonald, 1972; Staudenmaier, 1972; Herzog et al., 1973). This work was followed by Bernhardt et al. (1976) who were the first to monitor neutral dimer kinetic energy distributions. It was only recently that kinetic energy distributions of larger neutral clusters be measured (Brizzolara & Cooper, 1989; Coon et al., 1991; Wucher et al., 1993).

Information on the internal energy distribution of sputtered clusters has been

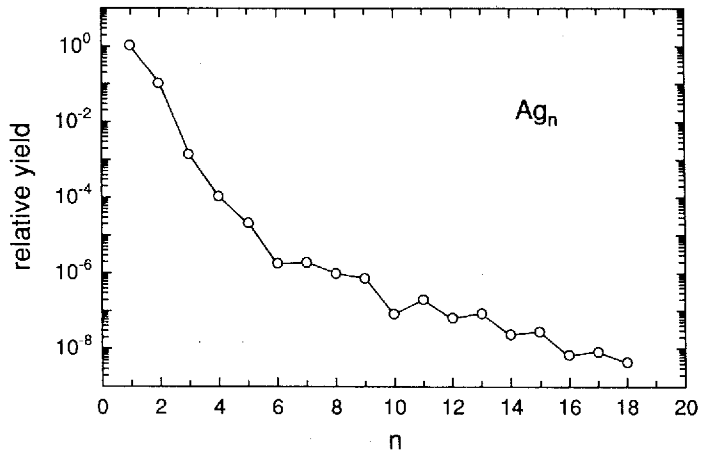

Figure 1b. Same as fig. 1a for neutral clusters Ag$_n$ sputtered by 5 keV Ar$^+$ ions (Wucher et al., 1993).

determined only for a small number of systems. Apart from the early work of Thomas & Efstathiou (1984) and Snowdon & Heiland (1984) on molecules emitted from N-bombarded Si, and of de Jonge et al. (1986a) on sulphur, the experiments by Fayet et al. (1986) on sputtered alkali dimers are particularly noteworthy.

In parallel with these experiments, theoretical models were developed and computer simulations were performed with the aim of clarifying the mechanisms underlying cluster emission. Already quite early, the two dominant models describing cluster emission were developed: The idea that clusters may be 'emitted as such' from the ion-bombarded surface seems to go back to Honig's work (1958), cf. also Staudenmaier (1972). The 'association' of individually energized[3] recoils was formulated by Gerhard (1975) and Können et al. (1974). Since then, the controversy about these two models has accompanied the discussion. As we shall note at the end of the present review, this discussion is based more on lack of care in the proper choice of words than on physically realistic and experimentally discernible distinctions.

Computer simulation in this field was pioneered by the work of Harrison & Delaplain (1976). While early studies used pair potentials even for metallic targets (Harrison, 1988), modern simulations employ many-body potentials, which are believed to be more realistic. Also, in order to obtain a representative picture of

---

[3] We are intentionally avoiding the term 'sputtered' or 'ejected' for particles which are still on their way out of the interaction region of the solid.

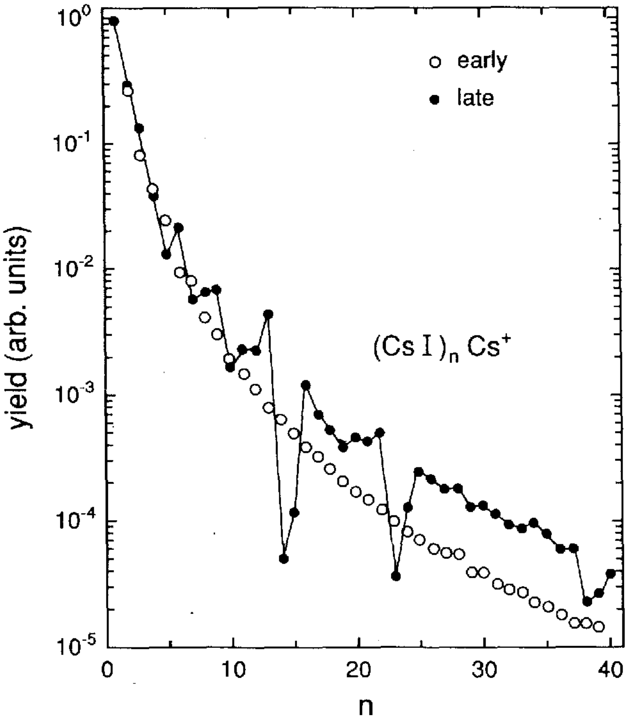

Figure 2. Relative yield of $(CsI)_nCs^+$ clusters sputtered by 3.6 keV Xe^+ ions from a CsI target. Early (late) distribution taken at 0.17 μs (750 μs) after ion bombardment; these times apply for an $n = 13$ cluster. Data taken from Ens et al. (1983).

the emission mechanism, a large number of ion impact and cluster emission events, of the order of 10^3 or more, are simulated (Wucher & Garrison, 1992a).

In our review, we shall concentrate on the work done in the field of sputtering of clusters and molecules after the Symposium on Sputtering in Spitz, Austria, 1986 (Betz et al., 1987). As the historical survey just given shows, considerable work had been performed before this date; it was reviewed by Kelly (1984), Oechsner (1985), de Vries (1987), Urbassek (1987), and Hofer (1986; 1991). In the present review, we shall restrict ourselves mostly to collisional emission from electrically conducting, elemental solids upon energetic particle bombardment. Sputtering of molecules from more complex materials, such as (bio-) organic solids, polymers, or cryogenic ices, have been covered elsewhere in this Volume (Reimann, 1993). We shall focus on situations in which the bombarding ion establishes a linear collision cascade (Sigmund, 1981). Ion bombardment induced spikes will not be considered here, even though experimentally observable emission of large chunks of matter, as reviewed by Hofer (1991), and described with recent references by Baranov et al. (1992), is often assumed to occur in a spike scenario.

2 Cluster-Size Distributions

Fig. 1 shows measured cluster abundance distributions for a metallic target, both for charged and neutral sputtered clusters. For both cases, a strong overall decay of the cluster abundance with the number n of atoms contained in the cluster can be observed. This reflects the cluster-formation probability which decreases with increasing number of atoms. In a direct comparison of the abundance distribution of charged and neutral clusters sputtered under identical conditions from the same element, two differences between ionized and neutral clusters became apparent (Gnaser & Hofer, 1989):

(i) neutral clusters show a stronger decay with atom number n than charged clusters;

(ii) the conspicuous even-odd alternations of charged clusters of monovalent elements are absent in the distribution of the neutrals.

Both findings were confirmed and extended by Franzreb et al. (1991a).

Cluster abundance distributions have been interpreted from the very beginning in terms of the clusters' electronic structures (Joyes, 1971; Leleyter & Joyes, 1973; Rodriguez-Murcia & Beske, 1978; Joyes & Sudraud, 1985). Because of spin-pairing of binding electrons, clusters with an even number of valence electrons possess an increased stability, which is enhanced both with respect to fragmentation and ionization. Thus, clusters containing an even number of binding electrons show both an enhanced dissociation energy and a larger ionization potential. It became customary to interpret cluster abundance in terms of stability against fragmentation/dissociation. This was probably influenced by the success with covalently bonded clusters (Dörnenburg et al., 1961), where indeed the binding energy controls the mass distribution – of course, apart from the kinetics of cluster formation which prescribes a monotonically decreasing dependency. However, it is also true that there remained a latent awareness that the ionization energy, too, must be an important parameter for the understanding of abundance distributions, in particular for charged clusters (Leleyter & Joyes, 1973). This issue was taken up and emphasized recently (Franzreb et al., 1991a).

Fig. 3 displays quantum-chemical data for the variation of the binding energy of a cluster with the number of atoms it contains. The binding energy of a charged cluster is definitely higher than that of a neutral cluster. This applies

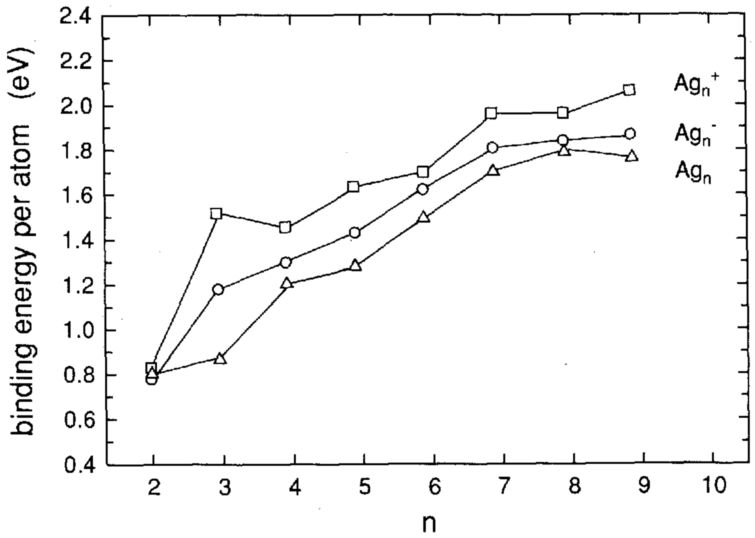

Figure 3. Binding energy per atom of charged and neutral Ag clusters. Quantum-chemical calculations due to Bonacic-Koutecky et al. (1993a,b). For comparison: Bulk sublimation energy of Ag: 2.96 eV.

both if iso-nucleonic clusters (vertical lines) and iso-electronic clusters (e. g., $Ag_4 \rightarrow Ag_5{}^+$) are compared. Interestingly, these calculated binding energies do not display the odd-even alternations as pronouncedly as earlier, simplified calculations where an oscillatory structure in the dependence of the binding energy was intimated. Binding-energy considerations, therefore, cannot explain the odd-even oscillations in the mass spectra of charged clusters of monovalent metals. The monotonically decreasing neutral-cluster intensities, on the other hand, are in keeping with calculated binding energies.

The question why the abundance distribution of charged clusters alternates while that of neutral clusters does not,[4] appears to be connected to the behaviour of the ionization energy, rather than to the binding energy (Franzreb et al., 1991a): As the experimental data plotted in fig. 4 show, the ionization energy of clusters indeed shows these oscillations. The comparison of charged and neutral cluster abundancies hence motivates the following assumption about the ejection process: First the cluster is formed in the neutral state. In a second step it is ionized while it leaves the interaction range with the surface.

---

[4] The origin of the slight alternations visible in fig. 1b for neutral clusters is not clear; it may, in fact simply stem from the detection method, viz. single-photon ionization (Wucher, 1993).

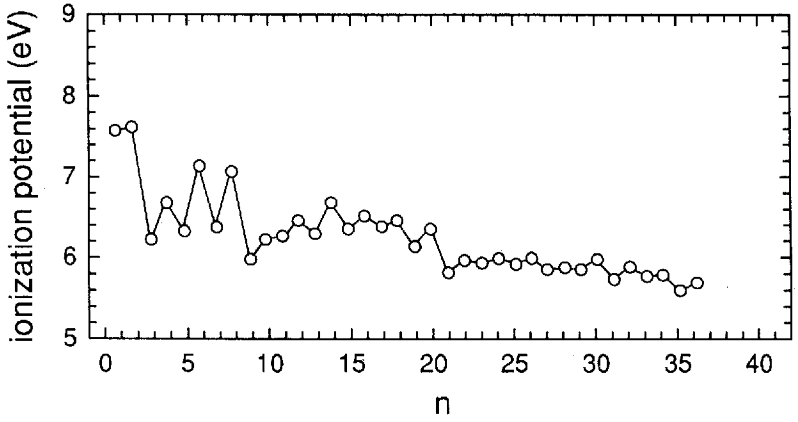

Figure 4. Ionization potential of neutral Ag clusters, measured by electron impact ionization (Jackschath et al., 1992). For comparison: Work function of Ag: 4.26 eV.

This sequence of processes is the same as in the ionization of clusters stemming from gas-agglomeration sources. Such cluster sources are in frequent use in cluster research: Material of which clusters are to form is evaporated into an inert-gas cell, where agglomeration takes place. Collisions with inert-gas atoms mediate the agglomeration and cool the clusters by dissipating the heat of condensation. Further cooling can be achieved by adiabatic expansion in a supersonic nozzle. For such a system, Powers et al. (1983) reported a smooth, monotonically decreasing size distribution of neutral Cu_n clusters. Characteristic odd-even intensity alternations appeared only in the cluster-ion spectra. For this to occur, it was important to carry out the ionization with energies near the ionization threshold; only then is the process selective and allows intensity modulation according to the ionization potential, cf. fig. 4. The intensity oscillations in the mass spectra of cluster ions are, therefore, a kind of artifact caused by ionization of neutral clusters in the threshold region of the ionization cross section.

In the above gas-agglomeration experiments, cluster formation and ionization are well separated in space and time. In sputtering, the situation is more complex: Firstly, the knock-on collision, cluster formation, and ionization all take place within 5 Å from the surface atomic layer. There is, thus, no clear separation of cluster formation and ionization. For this reason, ionization takes place long before the clusters had time to dispense of their excess energy. In surface emission of clusters, hot clusters are ionized. Remarkably, however, ionization makes for a stabilization of the cluster, cf. fig. 4.

The cluster ionization process directly depends on the bonding and electronic structure of the cluster: For metallic targets, often the electron tunneling model (Yu, 1991) of atomic ion formation in sputtering is extended to cluster-ion emission (Franzreb et al., 1991a; Makarenko et al., 1991); this implies, as we discussed above, that the cluster formation and ionization processes can be separated in time from one another. Similar considerations also apply to negative-ion formation (Abdullaeva et al., 1991; Wada et al., 1991). Other mechanisms dominate the sputtering of non-metallics, and in particular of compound targets, where the charge state of the cluster and its emission mechanism may be closely connected (Yu, 1981; Yu, 1982; Klimovskii, 1987).

Theoretical results on the mass distribution of sputtered clusters are not readily available. Computer simulation does not provide sufficient statistics to study representative ensembles of clusters containing more than 2 or 3 atoms. Analytical models hence use statistical, bond-counting considerations (Dunlap, 1982; Dunlap et al., 1983) which invariably lead to an exponential decay of cluster abundance with mass. A collective model of large cluster formation predicts a slower decay if clusters are formed in an equilibrium process in the vicinity of the critical point of the liquid-gas phase transition (Urbassek, 1989). A power-like dependence has indeed been observed in charged clusters sputtered from ion-bombarded rare-gas solids (Orth et al., 1981; Jonkman & Michl, 1981; Urbassek, 1988b).

Cluster abundance distributions from metallic targets have for a long time been believed to obey the dependence $Y_n \propto Y^n$ with cluster size n (Gerhard, 1975). Such a relationship stems from statistical considerations, which imply that clusters originate from a fixed 'active' area, viz. the intersection of the collision cascade with the target surface. Recently, Gnaser & Oechsner (1991; 1993) and Wurz et al. (1991) checked this law by varying the total yield Y via the bombarding energy of the ions inducing sputtering and measuring the emission-angle integrated dimer and trimer yields. For bombarding energies below 1 keV they verified the law for a variety of metals and alloys. However, recent experiments (Franzreb et al., 1991b) and computer simulations (Wucher & Garrison, 1992b) cast doubt on its validity for higher bombarding energy. Note, however, that by varying the bombarding energy, also the area is changed, from which particles are emitted, and hence the above law, $Y_n \propto Y^n$, need in principle not be fulfilled. An experiment using equi-velocity (light) clusters as projectiles might be better suited to test this law (Sigmund, 1993).

Finally, we note that it has been known for a long time that the sputtering of clusters is due to the effect of a single ion impact, rather than to the combined effect of several ions; a notable exception will occur for (heavy) cluster bombardment. It has also been noted frequently that there exist considerable statistical fluctuations in the collision cascades and hence in the sputtering yield. This must have a major importance on the cluster abundance.[5] As for instance Cooper & Hamed (1984) note, dimer emission may be observed in situations where the total average sputter yield is substantially below 1; nevertheless, a non-vanishing probability for the emission of two atoms from the same collision cascade must have existed. Or, as Wittmaack (1979) observed, $\mathrm{Si}_n{}^+$ clusters up to $n = 8$ appear under average yield conditions of $Y \cong 1\,\mathrm{atom/ion}$. One might indeed expect that the cluster size distribution reflects the fluctuations of the individual collision cascades. The average yield or an average of the deposited energy in the near-surface region are of little help when the observable shows such a large statistical variance as that of the cluster-size distribution.

Hence, at low bombarding energies, data on the monomer and dimer yield may give direct experimental information on the statistics of the sputter yield. A complete theoretical prediction of cluster abundancies taking these fluctuations into account and going beyond Gerhard (1975) does not yet exist.

2.1 Odd-even Alternations, Magic Numbers

Alternating cluster ion intensities are a general feature of clusters composed of atoms with an odd number of valence electrons. Although the effect is best documented for monovalent elements such as the alkali and noble metals, it is evident also for group III elements such as Al. In sputtering of alloys, the odd-electron atom imposes the alternations on the abundance distribution of composite cluster ions (Joyes et al., 1986).

The alternation effect exists both for negative and positive cluster ions, and in the latter case as well for multiply charged clusters (Joyes & Sudraud, 1985). In all cases, the intensity maxima correspond to an even number of valence electrons in the cluster.

It is interesting to note that alternating cluster ion intensities appear to be a general feature of clusters originating from surfaces of (metallic) solids or liquids. The effect is by no means confined to sputter ejection. It is well discernible in the charged flux of particles from a liquid-metal ion source (LMIS) (Joyes & Sudraud, 1985; Bhaskar et al., 1987), and also in the cluster-ion abundance from laser irradiated solids (Fürstenau & Hillenkamp, 1981). Interesting in this context is also the fact that the alternation effect for metal clusters decreases with increasing laser power, i.e., when cluster formation shifts from the surface into the adiabatically expanding vapour cloud in front of the target. Here, another cluster formation and ionization mechanism takes over. This corresponds to neutral cluster formation in

---

[5] This has often been noted in the literature (Staudenmaier, 1972; Staudenmaier, 1973; Sigmund, 1977; Wittmaack, 1979; Winograd et al., 1978; Winograd et al., 1979; Sigmund, 1987; Eckstein, 1988; Conrad & Urbassek, 1990).

supersonic nozzle beams.

The phenomenon of magic numbers in abundance distributions has recently attracted much attention in cluster research. Similar to atomic nuclei, agglomerates containing a certain ('magic') number of constituents manifest themselves by an enhanced abundance compared to their neighboring species. This effect is generally explained in terms of increased stability, i.e. binding energy. As the bulk of these magic-number studies of clusters has been carried out by non-surface emission methods, there is little uncertainty in this interpretation caused by interference from the ionization process. The origin of the enhanced stability may be quite different in differently bound clusters, however: While in ionically bound clusters the geometric ('crystal-') structure is assumed to play an important role (Campana et al., 1981), the binding in clusters composed of metal atoms is purely electronic. Therefore, the magic numbers of $n = (2), 8, 20, 40, \ldots$ given for metal clusters refer to the number of binding electrons. The number of atomic constituents thus varies with the charge state of the cluster (e. g. $Ag_9{}^+$, Ag_8, $Ag_7{}^-$ for the magic number 8 in figs. 1a and 3). We note in passing that these agglomerates are still far from evincing bulk metallic characteristics. This can be seen, for instance, in the differences to the bulk sublimation energy and the work function given in figs. 3 and 4, respectively.

Magic numbers can readily be identified in sputtered cluster-ion abundance distributions, cf. fig. 1a. Actually, the fact that sputtered clusters have a rather high internal energy and are thus subject to larger fragmentation rates (see below), increases the intensity contrast between loosely and tightly bound clusters in the mass spectra; cold clusters would not reflect their differences in binding energy in mass spectra. In general, however, the enhanced internal energy of sputtered clusters is considered as a disadvantage in cluster research. It also limits the applicability of sputtered-cluster sources in this field. For the phenomenon of sputtering, magic-number clusters have hardly any significance due to their vanishingly small fraction in the total flux of ejected particles.

No magic number characteristics have as yet been detected in the flux of sputtered neutral clusters. As with the odd/even alternations, the spectrum of neutral clusters is poorer in information than that of the charged species. This may again be a consequence of the close coupling of cluster formation and ionization in emission from surfaces. In nozzle-type experiments, by contrast, identification of magic-number clusters both in the neutral and the charged state seems to be the role.[6]

---

[6] The actual measurement always requires ionized clusters. The difference to sputtered clusters is that post-ionization is performed here on cool clusters. It would be interesting to carry out on sputtered clusters a post-ionization experiment at a cluster lifetime $> 100\,\mu s$, i.e., after fragmentation has left the clusters at lower internal energy.

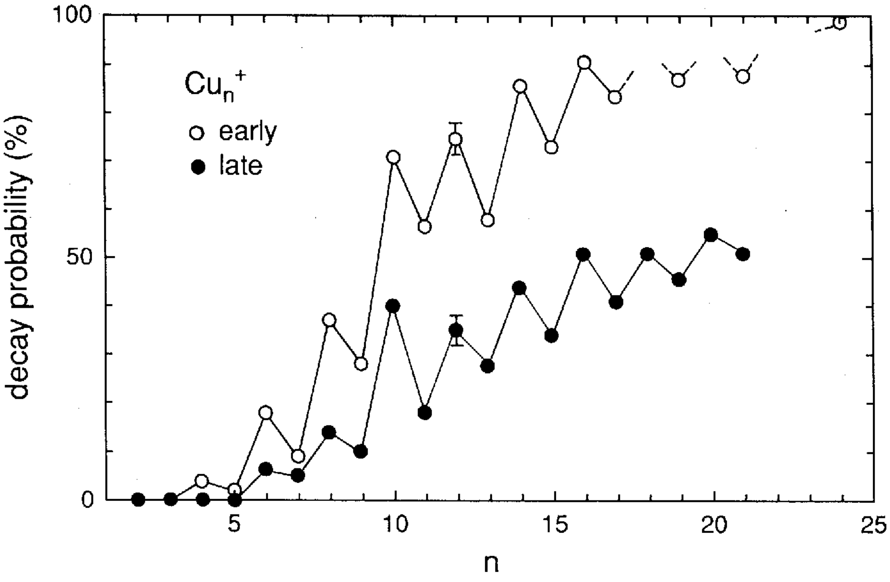

Figure 5. Decay probability of $Cu_n{}^+$ clusters sputtered by 21 keV Xe^+ bombardment. Decay is observed on two groups of clusters ('early' and 'late') which differ by the time after which decay is monitored. Early clusters decay with considerably higher probability than late clusters. Data taken from Begemann et al. (1986).

2.2 Fragmentation

Sputtered clusters are not stable right after the ejection process. Collisional ejection leaves the agglomerates with a high amount of internal energy. This causes fragmentation during a time span of 10 μs or more after the clusters' generation. The mass spectra change with time during this period, as was first demonstrated by Ens et al. (1983) for ionically bound clusters, cf. fig. 2. Here it was shown that the cluster abundance distribution strongly changed its characteristics with the time spent after cluster formation. While the 'early' distribution shows no alternations, these do form during the flight (cf. fig. 2). Apparently, characteristic structures in such mass spectra evolve as the clusters approach their stability distribution.

For metallic systems, cluster fragmentation has been investigated mainly at the Academy of Science in Tashkent by Dzhemilev & Verkhoturov (1985) and Dzhemilev et al. (1987; 1990; 1991) and at the University of Bielefeld by Begemann et al. (1986; 1986; 1987). Fig. 5 represents results obtained with $Cu_n{}^+$ clusters by the latter group. The two curves shown therein correspond to time intervals opened after different times after sputter ejection. The 'early' time interval is opened typically 50 ns after ejection, the 'late' at about 500 ns. The recording time is given by the drift time of the clusters in the time-of-flight (TOF) spectrometer. It is more than an order of magnitude longer than the 'late' delay time. 'Late' and 'early' mass spectra thus differ by the amount of clusters which have undergone fragmentation before entering the spectrometer. The decay probability plotted on the ordinate is the fraction of clusters of a given size that has undergone fragmentation during the flight through the spectrometer. In short, the main findings of these investigations, as far as they are relevant for sputtering, are:

- Small clusters attain their stability configuration quickly. After some 100 ns, no ${Cu_n}^+$ clusters up to n = 5 but a small fraction of quadrumers are subject to decay. During this time, the clusters have moved no farther than $10 - 100\,\mu$m from the surface; conventional mass spectrometers will all yield the same mass distribution. If it is allowed to transfer these results to neutral clusters, it can be stated that the majority of the sputtered flux, i.e., the flux of $n = 1 - 5$ species, is stable against fragmentation once it has cleared off the surface.
- The main form of fragmentation is the emission of neutral atoms. This is the most effective way of reducing the internal energy in the cluster. Klots (1985; 1991) used such data to shed light on the fragmentation kinetics and to correlate it with thermodynamic cluster properties. While his calculations put the emphasis on cluster stability considerations derived from binding energies, his approach could be broadened to include the structure visible in cluster ionization potentials.
- The fragmentation pattern shows odd-even oscillations for monovalent metals. Cluster ions with an even number of valence electrons show less fragmentation. Interpreted in terms of stability, this does not seem to be in agreement with the calculations shown in fig. 3, as there are no oscillations in the binding-energy curves. It should be appreciated, however, that these calculations pertain to cold clusters, while sputtered clusters are internally hot. Nevertheless, there is an inconsistency between fragmentation data and calculated binding energies for cluster ions.
- Among the larger clusters, ${Cu_9}^+$ is a particularly stable one. It is a magic-number cluster, as it contains a 'closed shell' for 8 binding electrons. All clusters composed of more electrons (atoms) show higher decay probabilities.

These results are strongly supported by recent molecular-dynamics calculations of keV Ar→Ag sputtering, using up-to-date metal potentials (Wucher & Garrison, 1992b). There it was found that the majority of the emitted trimers and virtually all the larger clusters fragmented spontaneously in the first nanosecond after emission.

This behaviour could be clearly traced back to the high internal energies with which clusters are 'born'. It is of course to be expected that stable quadrumers and even larger clusters should be detectable in such simulations; computer time restrictions, however, severely impede the simulation of sufficiently many atom impacts to obtain statistical information on large stable clusters.

Thus, fragmentation is a clear sign of the metastable character of sputtered clusters. It must be taken as a warning that measured abundance distributions may only be used with caution to represent the initial, i.e., ejection, cluster distribution. Furthermore, cluster fragmentation underlines the importance of cluster stability for abundance distributions.

3 Energy and Angular Distributions

Kinetic-energy spectra of cluster ions have been measured by many groups. Without exception, they show with increasing cluster size a faster decline of the high-energy tail, cf. fig. 6a.

In the last decade, results for neutral clusters have been obtained as well. The data displayed in fig. 6b have been obtained in an SNMS system using electron ionization, and show similar features as stated for charged clusters above.

In the following, we shall turn to a more detailed description of the characteristics of sputtered dimers. As mentioned in the Introduction, substantial work in this area was performed before the report period, i.e., up to the mid-eighties. We wish to mention in particular the experimental and theoretical work of Snowdon and coworkers as summarized by Snowdon et al. (1986); of Haring, Oostra, de Vries, and others of the FOM-group, which was summarized by de Vries (1987); and of the computer simulation studies of Harrison and coworkers, summarized by Harrison (1983; 1988). Due to these efforts, a considerable body of information on possible mechanisms of the sputtering of dimers and their properties has accumulated. Progress since then is characterized by further detailed experimental information on the one hand, and improved molecular-dynamics simulations on the other, and will now be described.

3.1 Emission of (Preformed) Molecules

Probably the simplest case of cluster sputtering is realized in a solid where (preformed) molecules exist. These are characterized by the condition that the dissociation energy D of the diatomic molecule is large compared to its binding energy U to the surroundings. This case is by definition realized in molecular solids; it may be realized in systems of chemically reactive sputtering, or in the ion-induced

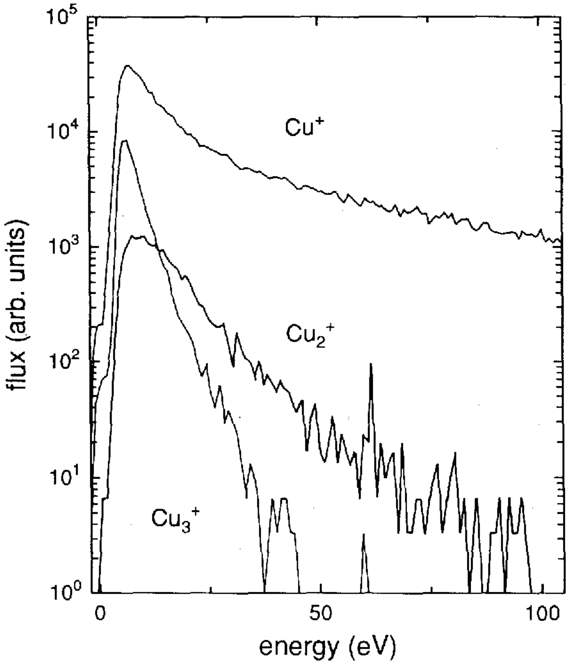

Figure 6a. Kinetic-energy distributions of clusters sputtered from a polycrystalline Cu sample. Ionized clusters Cu_n^+ from 5.5 keV Cs^+ bombardment. Data due to Gnaser (1992)

desorption of molecular adsorbate layers (Taglauer et al., 1980; Sagara & Kamada, 1982).

Measurements on elemental, diatomic molecular solids, such as solid N_2, have only very recently been performed with keV heavy ions (Pedrys, 1993). Under low-energy ion bombardment, a Thompson distribution for the kinetic energy of sputtered N_2-molecules was observed, but with an apparently lowered value of the surface binding energy U as compared to the measured sublimation energy. This may indicate that the surface binding force acts in a more complex manner on dimers, where several more degrees of freedom are active during emission than for atomic particles (Urbassek, 1992).

Otherwise, most measurements have been made on chemically transformed solids, i.e., under conditions of chemically reactive sputtering. Fig. 7 displays the kinetic energy distribution of molecules sputtered under such conditions. The E^{-2}-like decay of the distribution at high energies is strong evidence for the so-called single-collision emission mechanism, in which the molecule emission is induced by

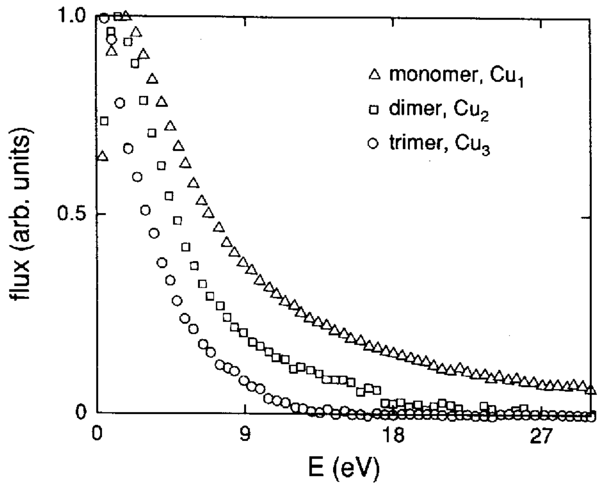

Figure 6b. Same as fig. 6a for neutral clusters Cu_n from 1 keV Ar^+ bombardment. Data taken from Brizzolara & Cooper (1989).

a single collision with a recoil particle of the collision cascade. Under these conditions, the usual argumentation of collision cascade physics applies which predicts an E^{-2} tail of the kinetic energy distribution (Sigmund, 1981). This behaviour has also been found in the emission of monoxide molecules sputtered from oxides or oxygenated surfaces (Wucher & Oechsner, 1987). As above, we note that the nature of the surface binding energy U may be more complex in the case of molecules than in that of atoms.

This so-called single-collision mechanism has been discussed in the literature repeatedly, starting with Benninghoven (1973), and followed by Oechsner et al. (1978), Sigmund et al. (1986), de Jonge et al. (1988), and others. It has been given various names such as 'direct emission', 'intact ejection', 'emission as such', etc. This mechanism allows molecules to receive a high amount of relative kinetic energy $E_{\rm rel}$ without dissociation. This is possible up to $E_{\rm rel} = D$. Since the center-of-mass and the relative energy which the molecule receives in an energetic collision are correlated, dimers with considerable center-of-mass energy can be emitted. Thus, for a homonuclear dimer the E^{-2} distribution will be valid up to a center-of-mass energy of around D. For higher energies, the collision ejecting the molecule will also impart to it such a large amount of internal energy that it breaks up. We note that the emission process at small emission energies $E \lesssim U$ may deviate from this simple picture. At these low energies, the laws underlying collision cascade physics need not necessarily apply any more. Thus, for instance, the molecule moves so

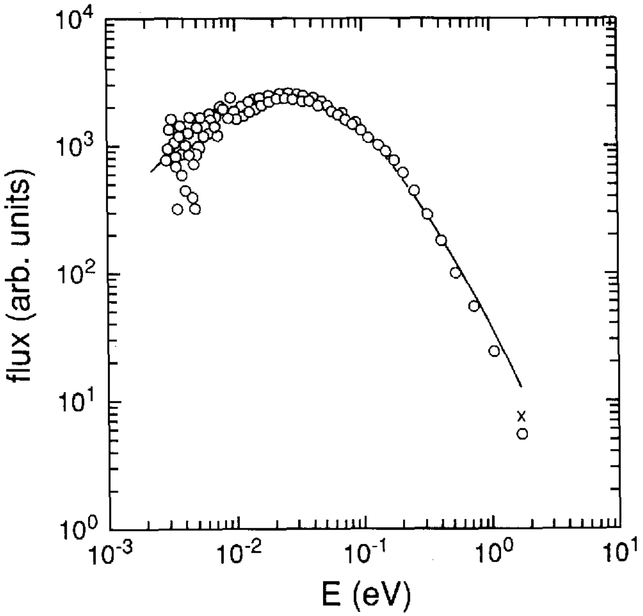

Figure 7. Kinetic-energy distribution of molecules sputtered by 3 keV Ar^+ bombardment from a Si surface in an SF_6 atmosphere at 50 K. The signal is due to both sputtered SiF_3^+ radicals and postionized SiF_4 molecules. Data taken from Oostra et al. (1986).

slowly – the binding energy U is typically below 1 eV – that several recoils may hit it.

The physics underlying the single-collision picture is sufficiently simple that detailed studies of the internal – i.e., rotational and vibrational – degrees of freedom were possible (Snowdon, 1985; Sigmund et al., 1986; de Jonge et al., 1988). A straightforward application of the ideas underlying the single-collision picture gives the following results (Sigmund et al., 1986):

(i) both rotational and vibrational excitation obey an E^{-2} law;

(ii) internal energy is positively correlated with the kinetic energy;

(iii) rotational and vibrational energy are anti-correlated with each other.

De Jonge et al. (1986a; 1986b; 1987), as summarized in de Jonge (1988), performed a detailed experimental study of the internal degrees of freedom of a sputtered dimer for a case where the single-collision mechanism could be assumed to apply. The system chosen was elementary sulphur, which is unfortunately rather a complex system. The S_8-rings, which form elemental sulphur in equilibrium,

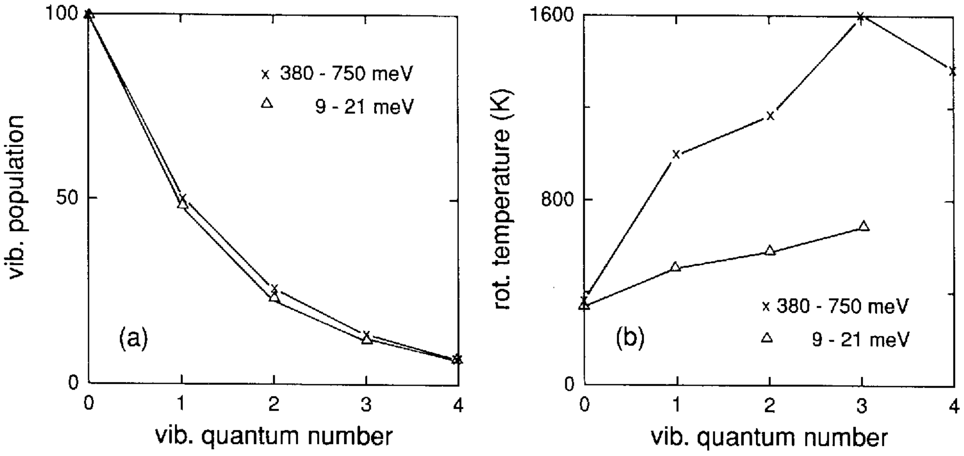

Figure 8. Internal energies of S_2-molecules sputtered by 5 keV Ar^+ ions from sulphur. Measurements are for slow and fast molecules, of kinetic energy $E_{\mathrm{kin}} = 9\text{–}21\,\mathrm{meV}$, and 380–750 meV, respectively. a) Population of vibrational levels. b) Mean rotational energy (expressed as a temperature) of molecules sputtered in a specified vibrational level. Data taken from de Jonge et al. (1987).

decompose under ion bombardment; S_2 is the majority species in the sputtered flux (Chrisey et al., 1988). It is assumed that S_2 is also the near-surface majority species in an ion-bombarded sample under steady-state conditions, and that it does not form only during emission or by fragmentation of sputtered S_8-rings. Thus, the single-collision mechanism can be assumed to apply.

Fig. 8 displays the results of such a measurement. It seems that the vibrational distribution decays exponentially rather than like an inverse power – although this is somewhat hard to decide upon the basis of the 5 data points taken. While rotational energy indeed increases with the kinetic energy of the sputtered molecules, vibrational energy appears to be independent of it. And rotation and vibration are positively correlated in contrast to item (iii) above.

These results are in conflict with the simple picture given above. However, at least a qualitative explanation of the measured data was given by de Jonge et al. (1988) and Urbassek (1988a). These authors showed that an improved modeling of the atom-molecule (or molecule-molecule) collision ejecting the molecule is necessary in order to understand the excitation of the internal degrees of freedom of sputtered molecules and their correlation with the kinetic energy.

3.2 Cluster Emission from Elemental Materials

In the majority of elemental materials, such as in metals, the dissociation energy D of a dimer is smaller than the bulk sublimation energy U, or at the most of comparable magnitude. In this case, a single collision which transfers enough center-of-mass energy to a dimer to eject it usually imparts also enough internal energy to destroy it. Thus, unless the surrounding material strongly quenches the internal degrees of freedom, the single-collision mechanism will not work.

Here, a different prototypical mechanism has been proposed (Können et al., 1974; Gerhard, 1975): Consider two atoms ejected in an ion-induced collision cascade from the target. If their momenta are sufficiently aligned and of comparable magnitude, and the trajectories of the two atoms are sufficiently close to each other, the two atoms are bound to each other and form a dimer. Since these conditions impose strong restrictions on the phase space available for dimer formation, a considerably stronger high-energy decay of the kinetic energy E is found than for atomic emission. Calculations[7] show that the distribution decays according to E^{-5} for $E \gg U, D$.

As an extension of the early papers by Können et al. (1974) and Gerhard (1975), theoretical modelling was able to provide more information on emitted dimers. We mention here the angular distribution, the internal – i.e., rotational and vibrational – excitation, and the kinetic-energy distribution at and below the surface binding energy (Snowdon, 1985; Snowdon et al., 1986; Snowdon & Haring, 1987; Haring et al., 1987; Hoogerbrugge & Kistemaker, 1987). However, these quantities depend crucially on the detailed interplay between the intramolecular potential and the surface binding forces. Here, assumptions had to be introduced the validity of which is hard to check by experiment. Realistic molecular-dynamics simulations may improve the modelling.

Experiments show that the kinetic-energy distributions of dimers sputtered from metals are indeed steeper than the E^{-2} decay of the monatomic distribution (Bernhardt et al., 1976; Brizzolara & Cooper, 1989; Coon et al., 1991). However, they approach an E^{-5} law only very slowly, if at all. In the energy window accessible to experiments ($E \lesssim 20U$), the distribution appears to be better characterized by an E^{-3} or E^{-4} decay, as is demonstrated in several papers presented at SPUT92, cf. also fig. 9 below. It is being discussed whether such a behaviour is in agreement with the simple statistical model described above (Urbassek & Gades, 1993).

Molecular-dynamics simulations have for a long time been performed[8] to shed light on cluster emission from metallic targets. Modern simulations use many-body

---

[7] Many of the published calculations contain errors which have their origin in a confusion between phase space density and flux (Haring et al., 1987; Urbassek, 1987).

[8] For reviews, see Harrison (1983; 1988).

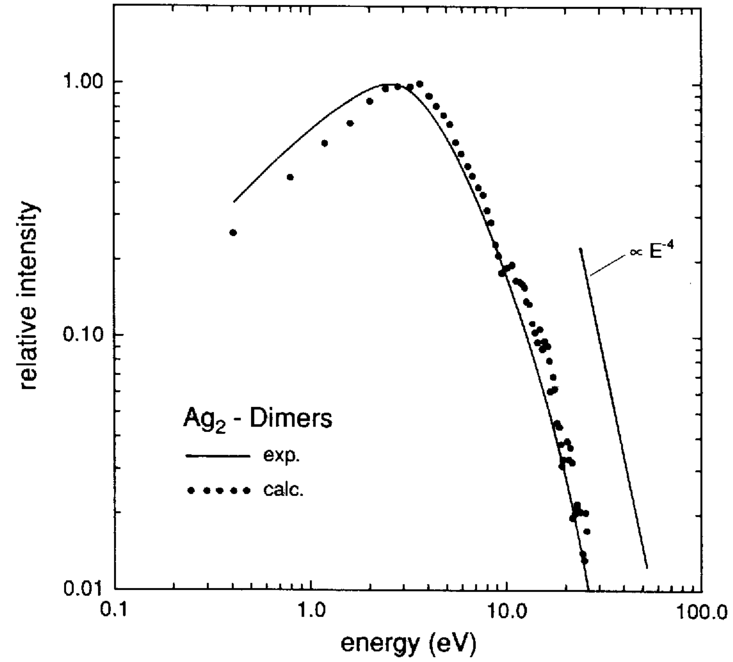

Figure 9. Kinetic-energy distribution of neutral Ag_2 dimers sputtered by 1 keV Ar^+ ions from polycrystalline Ag. Line: experiment. Dots: simulation. Data taken from Wucher & Garrison (1992a).

potentials, such as the one given by Foiles et al. (1986), and explore the relevant phase space with sufficient statistics to give representative results for dimers emitted from metals. The use of many-body potentials appears important in cluster sputtering studies since the metallic bond cannot be described in terms of pairwise binding potentials, and a proper description of the attractive forces is without doubt of prime importance for the phenomenon of cluster sputtering. In particular, the difference in potential energy, and also in the equilibrium distance, of a dimer before and after ejection can considerably affect the emission characteristics, such as the internal energy, of sputtered clusters. Furthermore, any simulation employing a pair potential derived from bulk properties will underestimate considerably the dimer dissociation energy and hence the sputtered dimer abundance ratio.

Fig. 9 shows molecular-dynamics results for the kinetic-energy distribution of sputtered Ag_2 dimers; they are seen to be in good agreement with experiment. The E^{-4} decay indicated in the figure fits the data over some part of the spectrum. However, such simulations allow to extract more data than have been measured up

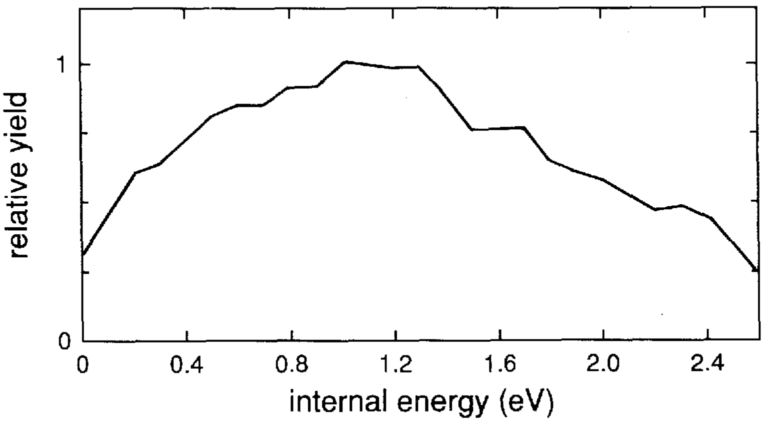

Figure 10. Internal-energy distribution of neutral Ag_2 dimers sputtered by 5 keV Ar^+ ions from Ag (111), as obtained from a molecular-dynamics simulation (Wucher & Garrison, 1992b). Fragmentation products are not taken into account here.

to now. As an example, fig. 10 displays the internal energy distribution of sputtered Ag_2 dimers. It is seen that sputtered clusters are hot, and with only little structure in the distributions. This corroborates the finding of section 2.1 above.

From such simulations it was furthermore found that for keV bombardment of metals, sputtered dimers stem predominantly from nearest-neighbour sites, and that a true double-collision mechanism[9] is responsible for the majority of dimers formed (Karetta & Urbassek, 1992; Betz et al., 1993). The so-called push-and-stick mechanism (Bitensky et al., 1992) is active to a small percentage.

Wucher & Garrison (1992b) demonstrated by molecular-dynamics simulation that fragmentation of large clusters will alter the distribution of dimers which are detected at a macroscopic distance ($\gtrsim$ 1 mm) and time ($\gtrsim$ 1 μs) after formation: Even though dimers cannot decay in a classical molecular-dynamics simulation in which the electronic degrees of freedom are not taken into account, dimer fragments formed from larger clusters will contribute slow and cool dimers, hence shifting the kinetic-energy distribution to smaller energies, and cooling the internal-energy distribution. Thus, the outcome of a molecular-dynamics simulation stopped several picoseconds after ion impact will not give the same distribution as that measured experimentally.

---

[9] Each of the two atoms, which eventually are to form a dimer, has been knocked on by a different recoil atom.

3.3 Angular Distribution

Cluster emission from polycrystalline surfaces is believed to follow a $\cos^n \vartheta$ distribution, where ϑ is the polar angle of emission, and $n \cong 1 - 2$ (Snowdon & Haring, 1987). Strong deviations from such a smooth distribution must be expected for the desorption of molecules adsorbed on surfaces, and for cluster emission from monocrystalline targets. In the latter case, experiment shows enhanced emission of dimers and trimers along the close-packed lattice directions (Hofer & Gnaser, 1987; Gnaser & Hofer, 1989). We can take this as a natural consequence of momentum alignment. Whatever the reason is for this alignment – focusing collision sequences in the collision cascade or directly induced by the projectile (Karetta & Urbassek, 1992) – any alignment of the recoils' momenta results in a reduction of their relative kinetic energy and, therefore, in an enhanced chance of fulfilling the cluster binding conditions. The striking similarity of the atom and dimer angular distributions observed from single crystals in these experiments appears hard to reconcile with a statistical emission model.

Otherwise, the lattice structure seems to have little effect on cluster emission. The abundance distributions of sputtered Si and Ge clusters at least show no influence of whether the target is in the crystalline or the amorphous state (Gnaser & Hofer, 1989). Abundance distributions in sputtering are, therefore, controlled by the short-range distance-distribution of the atoms in the solid; this is known not to be too dissimilar in crystalline and amorphous solids. As an application of this finding, we note that there is no memory effect of the target's structure in mass distributions. So far, this can be stated only for sputtering in the collision-cascade regime. For the 'softer' erosion techniques, such as sublimation by lasers or electric arcs, influences of the target structure on the mass distribution have been reported.

4 Conclusions

Since the last Symposium on Sputtering in Spitz, Austria, 1986, hardly any area in the field of sputtering has seen an advancement similar to that of cluster emission. This is primarily due to our capability of carrying out controlled measurements with neutral clusters as well as of simulating the ejection process by computers.

Let us first consider those particles which constitute the majority flux of sputtered particles. The emission of atoms, dimers, trimers and quadrumers make up more than 99% of that flux. Conventional methods such as the ionization by electrons and standard mass spectrometry are sufficient for studies of these particles. Larger neutral clusters require the outstanding sensitivity of the laser-ionization technique. It was only recently that this technique was applied to sputtered clusters. Right from the start it has resulted in the identification of clusters as large as

Cu_{15} and Ag_{18}. Although the amount of material emitted in this form is negligible, the ejection process of such agglomerates is interesting in itself.

As far as the phenomenon of sputtering is concerned, several of the long-standing key issues are in the process of being solved now.

- The fraction of bound atoms in the sputtered flux appears to be in the $10-20\%$ range for cascade sputtering. This is low compared to the corresponding number for ionic particles. The reason is, firstly, the steep fall-off in the neutrals' abundance distribution; this is expected to be connected with their reduced binding energy. Secondly, the effect of alternating abundances in the spectra of cluster-ions of monovalent elements is less pronounced or even absent with neutrals; this again reduces the bound-to-monomer emission ratio. It is important to keep in mind, however, that clusters fragment during the first several microseconds after emission. The bound-atom fraction immediately after emission may hence be larger than the measured one. As to sputtering physics, it is clearly the first quantity which is of main interest, since the solid is not involved in the fragmentation process which changes the cluster distribution after emission.

- The energy distribution of sputtered clusters is in the center of interest presently. Several contributions at this conference were concerned with it. Such experiments are plagued with a multitude of instrumental problems and artifacts. The most recent experiments indicate deviations of the measured kinetic-energy distributions from existing analytical theories. Measured distributions appear to be flatter than predicted, and approach those expected for the emission of atoms, or the single-collision ejection of preformed, adsorbed molecules. The origin of these discrepancies is at present unclear.

- Even more complicated is the determination of the distribution of internal energy. Very few experimental data exist for elemental solids. All information available now points towards a high amount of rotational and vibrational energy stored in the cluster. Rather detailed investigations of fragmentation of cluster ions show this energy to be reduced by the 'boiling off' of neutral atoms. This process takes place over a time period of $10\,\mu s$ and more. Great caution is required, therefore, in the interpretation of mass spectra from instruments with different detection time windows with respect to ejection.

  We have no information on the fragmentation of neutral clusters. Similar conditions as those with cluster ions are expected. Therefore, here too, measured mass spectra may be far from the ejection distribution. To what extent this holds, depends not only on the clusters' transit time in the spectrometer but also on the energetics of the ionization process. Furthermore, it may be decisive when after ejection clusters are post-ionized, because the ionization cross section depends on the state of internal energy, and cluster stability depends on both the charge and excitation state.

- The angular distribution of sputtered clusters is largely unknown. For clusters emitted from polycrystalline surfaces, and for not too oblique emission angles, a cosine distribution around the surface normal can be assumed. This need not hold for the emission of preformed molecules.

  Pronounced preferential emission is observed from single-crystal surfaces along low-index crystallographic directions. This must be understood as evidence that momentum alignment of recoil atoms or even correlated emission is an important feature in cluster formation.

- Clusters may contain a factor of 3 to 10 more atoms than the average sputtering yield. It is quite generally agreed that this is connected to the statistical variation of the individual cascades. It is unlikely that reaction kinetics based on an average quantity of such poor statistical significance as that of the mean sputtering yield will lead to an understanding of the elementary emission process.

  Computer simulations of the yield per individual cascade show very large fluctuations. These have to be taken into account in any theoretical treatment of cluster sputtering. Simulation by molecular dynamics appears to be predestined to this problem. However, to simulate a sufficient number of atom impacts to put large-cluster emission on a sound statistical basis is a formidable task.

Apart from yielding information on the physics of sputtering, several features of cluster emission upon ion-bombardment of solids are of interest on their own. Strictly speaking, all characteristics typical of cluster-ion emission are of minor relevance to sputtering. However, it was the observation of cluster-ion emission (in SIMS), which has triggered research on sputtering of clusters and which has provided first information on every single quantity discussed in the above chapters. Even in those cases where the information turned out not to be representative of the neutrals, which contribute the majority flux in sputtering, it is still of great importance in the general field of charged-particle emission from solid or liquid surfaces. This is equally true for emission processes of a collisional or a thermal nature, a combination of both – or of quite a different nature such as by electrohydrodynamic forces. As paradigms to such effects may serve the odd-even oscillations in ionized cluster-size distributions of monovalent elements, or the enhanced abundance of magic-number clusters.

We should like to close this review with a word on the two extreme models of cluster emission which have dominated the debate for a long time, i.e., emission as such vs. the association of independently emitted recoils in the transition region between the surface and vacuum. Most workers in this field will agree that these two models should not be interpreted in an extreme sense. Neither does association of independently energized atoms mean that they recombine in vacuum, nor does ejection as such mean that the atoms of the cluster have the same neighboring geometry as they had while they were in the solid; ejection as such is not meant as an ejection of preformed particles. If a rearrangement of atoms in the cluster-to-be is allowed during its passage through the surface, the two models mean the same thing. What is excluded, is a combination of atoms which had not remained in their mutual attraction field before they left the solid.

Acknowledgements

We gratefully acknowledge discussions with G. Betz, V. Bonacic-Koutecky, S. Coon, K. Franzreb, H. Gades, H. Gnaser, M. Vicanek, and A. Wucher. Many of these, as well as P. Sigmund and M. Ferguson, gave us critical comments on the manuscript. H. Gnaser is thanked for providing fig. 6a.

References

Abdullaeva MK, Atabaev BG and Dzabbarganov R, 1991: Nucl. Instr. Meth. **B62**, 43

Andersen HH, 1989: Vacuum **39**, 1095

Baranov IA, Novikov AC, Obnorskii VV, Tsepelevich SO, Kozlov BN and Pilyugin II, 1992: Nucl. Instr. Meth. **B65**, 177

Begemann W, Meiwes-Broer KH and Lutz HO, 1986: Phys. Rev. Lett. **56**, 2248

Begemann W, Dreihöfer S, Meiwes-Broer KH and Lutz HO, 1986: Z. Phys. **D3**, 183

Begemann W, Dreihöfer S, Meiwes-Broer KH and Lutz HO, 1987: In *The Physics and Chemistry of Small Clusters*, edited by P Jena (Plenum, New York), p. 269

Behrisch R, ed., 1981: *Sputtering by particle bombardment I* (Springer, Berlin)

Behrisch R, ed., 1983: *Sputtering by particle bombardment II* (Springer, Berlin)

Behrisch R and Wittmaack K, eds., 1991: *Sputtering by particle bombardment III* (Springer, Berlin)

Benninghoven A, 1973: Surf. Sci. **35**, 427

Bernhardt F, Oechsner H and Stumpe E, 1976: Nucl. Instr. Meth. **132**, 329

Betz G, Husinsky W, Varga P and Viehböck F, eds., 1987: *Symposium on Sputtering* Nucl. Instr. Meth., Vol. 18, p. 321 ff

Betz G, Kirchner R, Husinsky W, Urbassek HM and Rüdenauer F, 1993: Radiat. Eff. Def. Sol. **25**, in press.

Bhaskar ND, Frueholz RP, Klimcak CM and Cook RA, 1987: Phys. Rev. **B36**, 4418

Bitensky IS, Parilis ES and Wojciechowski IA, 1992: Nucl. Instr. Meth. **B67**, 595

Blaise G and Slodzian G, 1968: C. R. Acad. Sci. B **266**, 1525

Bonacic-Koutecky V, Cespiva L, Fantucci P and Koutecky J, 1993a: Z. Phys. D **26**, 287

Bonacic-Koutecky V, Cespiva L, Fantucci P and Koutecky J, 1993b: J. Chem. Phys. **98**, 7981
Brizzolara RA and Cooper CB, 1989: Nucl. Instr. Meth. **B43**, 136
Campana JE, Barlak TM, Colton RJ, DeCorpo JJ, Wyatt JR and Dunlap BI, 1981: Phys. Rev. Lett. **47**, 1046
Chrisey DB, Boring JW, Johnson RE and Phipps JA, 1988: Surf. Sci. **195**, 594
Conrad U and Urbassek HM, 1990: Nucl. Instr. Meth. **B48**, 399
Coon SR, Calaway WF, Burnett JW, Pellin MJ, Gruen DM, Spiegel DR and White JM, 1991: Surf. Sci. **259**, 275
Cooper CB and Hamed HA, 1984: Surf. Sci. **143**, 215
de Jonge R, 1988: Comments At. Mol. Phys. **22**, 1
de Jonge R, Baller T, Tenner MG, de Vries AE and Snowdon KJ, 1986a: Nucl. Instr. Meth. **B17**, 213
de Jonge R, Baller T, Tenner MG, de Vries AE and Snowdon KJ, 1986b: Europhys. Lett. **2**, 449
de Jonge R, Benoist KW, Majoor JWF, de Vries AE and Snowdon KJ, 1987: Nucl. Instr. Meth. **B28**, 214
de Jonge R, Los J and de Vries AE, 1988: Nucl. Instr. Meth. **B30**, 159
de Vries AE, 1987: Nucl. Instr. Meth. **B27**, 173
Dennis E and MacDonald RJ, 1972: Radiat. Eff. **13**, 243
Dörnenburg E, Hintenberger H and Franzen J, 1961: Z. Naturforschg. **16a**, 532
Downey SW, Emerson AB and Kopf RF, 1992: Nucl. Instr. Meth. **B62**, 456
Dunlap BI, 1982: Surf. Sci. **121**, 260
Dunlap BI, Campana JE, Green BN and Bateman RH, 1983: J. Vac. Sci. Technol. **A1**, 432
Dzhemilev NK and Verkhoturov SV, 1985: Izv. Akad. Nauk SSSR, Ser. Fiz. **49**, 1831 (Bull. Acad. Sci. USSR, Phys. Ser. **49**, 160)
Dzhemilev NK, Rasulev UK and Verkhoturov SV, 1987: Nucl. Instr. Meth. **B29**, 531
Dzhemilev NK, Verkhoturov SV and Veriovkin IV, 1990: Nucl. Instr. Meth. **51**, 219
Dzhemilev NKH, Goldenberg AM, Veriovkin IV and Verkhoturov SV, 1991: Int. J. Mass Spectr. Ion Proc. **107**, R19
Eckstein W, 1988: Nucl. Instr. Meth. **33**, 489
Ens W, Beavis R and Standing KG, 1983: Phys. Rev. Lett. **50**, 27
Fayet P, Wolf JP and Wöste L, 1986: Phys. Rev. **B33**, 6792
Foiles SM, Baskes MI and Daw MS, 1986: Phys. Rev. **B33**, 7983
Franzreb K, Wucher A and Oechsner H, 1991a: Phys. Rev. **B43**, 14396
Franzreb K, Wucher A and Oechsner H, 1991b: Fresenius J. Anal. Chem. **341**, 7
Fürstenau N and Hillenkamp F, 1981: Int. J. Mass Spectr. Ion Phys. **37**, 135
Gerhard W, 1975: Z. Phys. **B22**, 31
Gerhard W and Oechsner H, 1975: Z. Phys. **B22**, 41
Gnaser H, 1992: Private communication
Gnaser H and Hofer WO, 1989: Appl. Phys. **A48**, 261
Gnaser H and Oechsner H, 1991: Nucl. Instr. Meth. **B58**, 438
Gnaser H and Oechsner H, 1993: Nucl. Instr. Meth. **B 82**, 347
Hahn O, Straßmann F, Mattauch J and Ewald H, 1942: Naturwissenschaften **30**, 541
Haring RA, Roosendaal HE and Zalm PC, 1987: Nucl. Instr. Meth. **B28**, 205
Harrison Jr. DE, 1983: Radiat. Eff. **70**, 1
Harrison Jr. DE, 1988: Crit. Rev. Solid State Mater. Sci. **14**, S1
Harrison Jr. DE and Delaplain CB, 1976: J. Appl. Phys. **47**, 2252
Herzog RFK, Poschenrieder WP and Satkiewicz FG, 1973: In *Ion Surface Interaction, Sputtering and Related Phenomena*, edited by R Behrisch, W Heiland, W Poschenrieder, P Staib and H Verbeek (Gordon and Breach, London), p. 173; also published as: Radiat. Eff. **18**, 199
Hofer WO, 1980: Nucl. Instr. Meth. **170**, 275

Hofer WO, 1986: In *Erosion and Growth of Solids Stimulated by Atom and Ion Beams*, edited by G Kiriakidis, G Carter and JL Whitton (Nijhoff, Dordrecht), p. 1

Hofer WO, 1991: In *Sputtering by particle bombardment III*, edited by R Behrisch and K Wittmaack (Springer, Berlin), p. 15

Hofer WO and Gnaser H, 1987: Nucl. Instr. Meth. **B18**, 605

Honig RE, 1953: J. Chem. Phys. **21**, 573

Honig RE, 1954: J. Chem. Phys. **22**, 126

Honig RE, 1958: J. Appl. Phys. **29**, 549

Hoogerbrugge R and Kistemaker PG, 1987: Nucl. Instr. Meth. **B21**, 37

Hortig G and Müller M, 1969: Z. Phys. **221**, 119

Jackschath C, Rabin I and Schulze W, 1992: Z. Phys. **D22**, 517

Jonkman HT and Michl J, 1981: J. Am. Chem. Soc. **103**, 733

Joyes P, 1971: J. Phys. **B4**, L15

Joyes P, van der Walle J and Colliex C, 1986: Ultramicroscopy **20**, 65

Joyes P and Sudraud P, 1985: Surf. Sci. **156**, 451

Karetta F and Urbassek HM, 1992: Appl. Phys. **A55**, 364

Katakuse I, Ichihara T, Fujita Y, Matsuo T, Sakurai T and Matsuda H, 1985: Int. J. Mass Spectr. Ion Proc. **67**, 229

Kelly R, 1984: Radiat. Eff. **80**, 273

Klimovskii YA, 1987: Zh. Tekh. Fiz. **57**, 1951 (Sov. Phys. Tech. Phys. **32**, 1173)

Klots CE, 1985: J. Chem. Phys. **83**, 5854

Klots CE, 1991: Z. Phys. **D21**, 335

Können GP, Tip A and de Vries AE, 1974: Radiat. Eff. **21**, 269

Krohn Jr. VE, 1962: J. Appl. Phys. **33**, 3523

Leleyter M and Joyes P, 1973: In *Ion Surface Interaction, Sputtering and Related Phenomena*, edited by R Behrisch, W Heiland, W Poschenrieder, P Staib and H Verbeek (Gordon and Breach, London), p. 185; also published as: Radiat. Eff. **18**, 105

Magnera TF, David DE and Michl J, 1985: Chem. Phys. Lett. **83**, 2594

Makarenko BN, Popov AB, Shaporenko AA and Shergin AP, 1991: Radiat. Eff. Defects Solids **116**, 15

Mattauch J, Ewald H, Hahn O and Straßmann F, 1943: Z. Phys. **120**, 598

Merkle KL and Jäger W, 1981: Philos. Mag. **A44**, 741

Oechsner H, 1985: In *Symposium on Physics of Ionized Gases, SPIG 1984*, edited by MM Popovic and P Krstic (World Scientific, Singapore), p. 571

Oechsner H, 1990: Int. J. Mass Spectr. Ion Proc. **103**, 31

Oechsner H, Schoof H and Stumpe E, 1978: Surf. Sci. **76**, 343

Oostra DJ and de Vries AE, 1987: Nucl. Instr. Meth. **B18**, 618

Oostra DJ, Haring A, de Vries AE, Sanders FHM and van Veen GNA, 1986: Nucl. Instr. Meth. **B13**, 556

Orth RG, Jonkman HT, Powell DH and Michl J, 1981: J. Am. Chem. Soc. **103**, 6026

Pedrys R, 1993: Oral contribution at *SPUT92*

Powers DE, Hansen SG, Geusic ME, Michalopoulos DL and Smalley RE, 1983: J. Chem. Phys. **78**, 2866

Reimann CT, 1993: Mat. Fys. Medd. Dan. Vid. Selsk. **43**, 351

Rodriguez-Murcia H and Beske HE, 1978: Adv. Mass Spectrom. **7**, 598

Sagara A and Kamada K, 1982: J. Nucl. Mater. **111&112**, 812

Schou J and Hofer WO, 1982: Appl. Surf. Sci. **10**, 383

Sigmund P, 1977: In *Inelastic ion-surface collisions*, edited by NH Tolk, JC Tully, W Heiland and CW White (Academic Press, New York), p. 121

Sigmund P, 1981: In *Sputtering by particle bombardment I*, edited by R Behrisch (Springer, Berlin), p. 9

Sigmund P, 1987: Nucl. Instr. Meth. **B27**, 1

Sigmund P, 1993: Private communication

Sigmund P, Urbassek HM and Matragrano D, 1986: Nucl. Instr. Meth. **B14**, 495

Snowdon K, 1985: Nucl. Instr. Meth. **B9**, 132

Snowdon KJ and Haring RA, 1987: Nucl. Instr. Meth. **B18**, 596

Snowdon KJ and Heiland W, 1984: Z. Phys. **A318**, 275

Snowdon KJ, Willerding B and Heiland W, 1986: Nucl. Instr. Meth. **B14**, 467

Staudenmaier G, 1972: Radiat. Eff. **13**, 87

Staudenmaier G, 1973: In *Ion Surface Interaction, Sputtering and Related Phenomena*, edited by R Behrisch, W Heiland, W Poschenrieder, P Staib and H Verbeek (Gordon and Breach, London), p. 181; also published as: Radiat. Eff. **18**, 181

Taglauer E, Heiland W and Onsgaard J, 1980: Nucl. Instr. Meth. **168**, 571

Thomas EW and Efstathiou L, 1984: Nucl. Instr. Meth. **B2**, 479

Thum F and Hofer WO, 1979: Surf. Sci. **90**, 331

Urbassek HM, 1987: Nucl. Instr. Meth. **B18**, 587

Urbassek HM, 1988a. Habilitationsschrift, TU Braunschweig, Germany

Urbassek HM, 1988b: Nucl. Instr. Meth. **B31**, 541

Urbassek HM, 1989: Radiat. Eff. Defects Solids **109**, 293

Urbassek HM, 1992: J. Phys.: Condens. Matter 4, 4871

Urbassek HM and Gades H, 1993: In preparation

Wada M, Tsuda H and Sasao M, 1991: Jap. J. Appl. Phys. **30**, L2133

Winograd N, Harrison Jr. DE and Garrison BJ, 1978: Surf. Sci. **78**, 467

Winograd N, Foley KE, Garrison BJ and Harrison Jr. DE, 1979: Phys. Lett. **73A**, 253

Wittmaack K, 1979: Phys. Lett. **69A**, 322

Woodyard JR and Cooper CB, 1964: J. Appl. Phys. **35**, 1107

Wucher A, 1993: Private communication

Wucher A and Garrison BJ, 1992a: Surf. Sci. **260**, 257

Wucher A and Garrison BJ, 1992b: Phys. Rev. **B46**, 4855

Wucher A and Oechsner H, 1987: Nucl. Instr. Meth. **B18**, 458

Wucher A, Wahl M and Oechsner H, 1993: Nucl. Instr. Meth. **B 82**, 337

Wurz P, Husinsky W and Betz G, 1991: Appl. Phys. **A52**, 213

Yu ML, 1981: Phys. Rev. **B24**, 1147; 5625

Yu ML, 1982: Appl. Surf. Sci. **11/12**, 196

Yu ML, 1991: In *Sputtering by particle bombardment III*, edited by R Behrisch and K Wittmaack (Springer, Berlin), p. 91

Nonlinear Effects in Collisional Sputtering under Cluster Impact

By Hans Henrik Andersen
The Niels Bohr Institute, Ørsted Laboratory,
Universitetsparken 5, DK-2100 Copenhagen Ø, Denmark

Synopsis

Experimental evidence for peculiar sputtering effects under cluster impact of metals is discussed. It is emphasized that these effects, seen mainly as excessive yields, are also found for heavy single-atom impacts on heavy target materials and are connected with high energy-deposition densities in the surface region. The data are discussed in relation to a number of explanations put forward and found to be compatible only with spike effects and to some extent with lowering of surface energies due to emission of clusters. Recent computer simulations of cluster impacts will also be discussed. A number of cases where experimental data are badly missed will be pointed out and some experiments suggested.

1 Introduction

When a solid target is sputtered with a molecule or a cluster of atoms the sputtering yield may deviate from the sum of the yields of the individual atoms at the cluster velocity (Andersen & Bay, 1974). Such experimental nonlinear effects which in practice nearly always manifest themselves as enhanced yields, are the topic of the present review. An extensive review of such effects has not been given since that of Thompson (1981a; see also 1980). He discussed the phenomenon in the broad context of sputtering, radiation damage, gas desorption and ion beam mixing and suggested a number of explanations for the observed phenomena. Few systematic experimental investigations have been presented since 1981, but a number of scattered data and ideas relevant for the subject have appeared. I shall here discuss only the collisional sputtering aspects of cluster impact but shall try to cover the experimental side of this topic completely to allow a discussion of the problems raised by Thompson in his 1981 review. Nonlinear phenomena are also seen in electronic sputtering but these effects will not be discussed here. For a general discussion of electronic sputtering see Townsend (1983) and for a discussion of some of the electronic nonlinear effects see Johnson & Schou (1993).

Nonlinear effects may also be defined from a theoretical viewpoint. The analytical theory of collisional sputtering (Sigmund 1969, 1981) is established through solving of a Boltzmann transport equation describing the collision cascade. As an essential step in obtaining a solution of this equation, it has been linearized. Physically this means that moving atoms within the collision cascade are supposed to collide only with resting atoms, i.e., a moving atom will always loose and never gain energy through a collision. The solution of the linearized equation shows that the energy spectrum of the atoms set in motion within the cascade is approximately proportional to the inverse square of their starting energy. Hence at sufficiently low recoil energy any atom within the cascade volume has been set in motion and the linearity assumption breaks down. If this breakdown occurs at an energy that is very low compared to energies characteristic for the sputtering process, e.g. the sublimation energy, no consequences are expected for the sputtering yield. The higher the energy density within the cascade, the higher the breakdown energy. A way to enhance the energy density is through cluster bombardment. Hence nonlinear experimental effects may be directly related to the behaviour caused by the breakdown of the linearized Boltzmann equation.

The main theoretical result for the sputtering yield is

$$Y = 0.042\ \alpha(M_2/M_1)\frac{S_\mathrm{n}(E, Z_1, Z_2)}{U_\mathrm{s}\text{Å}^2}, \tag{1}$$

where α is a numerically calculated function of the target-to-projectile atom mass ratio M_2/M_1. S_n is the nuclear stopping cross section, which is a function of the projectile and target atomic numbers Z_1 and Z_2 and the projectile energy E. Note that this energy enters essentially through S_e. Finally, U_s is the surface binding energy, for metals mostly taken to be the sublimation energy.

Eq. (1) is usually considered to give a good fit to experimental sputtering yields if the projectile energy is above a few keV and if the energy density deposited at the target surface is not too high. There may, however, be several reasons for deviations from eq. (1), most of them non-related to the present review. Andersen & Bay (1981) discussed the region of applicability in connection with their yield-data graphs. For a number of elements, where the absolute yields are not well represented by eq. (1), the projectile-energy dependence is nevertheless given by S_n, except for large S_n in heavy targets, i.e. where the deposited-energy density is high.

When the energy spectrum of recoil atoms is modified by slowing down and by escape from the solid, the spectrum of sputtered atoms is found to be

$$\frac{dY}{dE_1} \simeq \frac{cE_1}{(E_1 + U_3)^3}, \tag{2}$$

the Thompson spectrum (Thompson, 1968). Also from this formula we expect minor deviations non-related to our present topic (Sigmund 1981, 1987), but it is clear from the discussion above that if the yield is influenced by nonlinear effects, such effects must also appear as a significant deviation from eq. (2) for small E_1.

It is not intuitively clear whether nonlinear effects will cause the yield to decrease or to be enhanced. On the one hand, within the nonlinear cascade fewer atoms are set in motion than within the linear cascade. On the other hand the moving atoms cannot get rid ot their energy. Hence the cascade will live longer. As already mentioned above, we usually find an increase. We must expect these 'extra' sputtered atoms to be of low energy, thus adding a low-energy component to the spectrum.

The connection between experimental and theoretical nonlinear effects was mentioned above. Note that we observe nonlinearities experimentally. Thompson (1981b) on the other hand argued against the use of the term nonlinear effects. It appears that this argumentation is based on the misconception that nonlinear effects should also imply that collisions may not be treated as binary (see also Johar & Thompson, 1979 for a similar statement). I maintain that linear as well as nonlinear cascade theory may be based on binary collisions, and shall hence continue to use the term 'nonlinear'.

The spatial region where a very dense collisional cascade is propagating is usually called a spike. A number of different adjectives like 'thermal', 'collisional', 'displacement', etc. have been connected with the spike. I shall only use the pure word as such. Sputtering from spikes has of course also been modelled. Sigmund (1974), Sigmund & Claussen (1981) and Johnson (1987) presented theories for sputtering from such spikes, while Sigmund & Szymonski (1984) also discussed what happens after the collisional part of the spike has passed (t $> 10^{-11}$ sec). Collective mechanisms like gas flow (David et al., 1986; Urbassek & Michl, 1987) and shock waves (Carter, 1979; Kitazoe & Yamamura, 1980; Bitensky & Parilis, 1987) have also been treated. Common to most theoretical treatments is the concept of a spike lifetime considerable longer than that of the linear cascade (Sigmund, 1974, 1975, 1977). Some aspects of these theories are discussed by Johnson & Schou (1993), but as only very few experimental data allow anything like a detailed quantitative comparison, I shall not discuss which spike theories may be most relevant. Experimental data do, on the other hand, allow to rule out a number of non-spike theories as discussed below.

Before presenting experimental data, we need eventually to discuss some nomenclature for clusters. Usually a distinction is made between clusters and molecules: Clusters are homatomic, molecules heteroatomic. But this is not consistent with chemical usage: We talk about the O_2^* or O_3 molecule. Sizewise, Harrison & Edwards (1985) proposed a hierarchy of names. With 2-10 atoms they speak about clusters, for 10-100 atoms of aggregates, for 100 to 10000 atoms of ultrafine particles and for larger sizes simply of particles. Kofman et al. (1990) remark that this classification is not fully established. This is certainly true within the ion-beam communities. Here the terms atoms, dimers and trimers are used for conglomerates of two and three identical atoms but anything containing from 2 to 10000 atoms may be called a cluster. For even larger sizes, we talk about particles. This nomenclature is essentially in agreement with the one advocated by Beuhler & Friedman (1986) and Mathew et al. (1986). Finally, it is worth mentioning that Hayashi (1987) calls attention to the fact that the term aggregate ought to be reserved for irregularly shaped objects.

2 The Experimental Data

In this section a number of experimental data relevant for the elucidation of cluster-impact effects on sputtering will be presented. The data, the method by which they are obtained, and the motivation for treating them in this section will be discussed. Whether the data allow to discern between different theories of nonlinear effects will, in contrast, first be treated in the general discussion section below.

As mentioned in the introduction, nonlinear effects on sputtering yields were postulated to occur before dimer irradiations were performed. Sigmund (1969) showed comparisons between sputtering data and theoretical predictions. While experimental yields from Ar irradiation of Cu, Ag, and Au followed the theoretical predictions rather well, yields from Kr irradiations of Ag of Au showed a moderate enhancement around the yield maximum (via eq. (1) expected to occur at the same energy as the maximum in S_n), while yields from Xe bombardment showed a moderate enhancement in copper and a strong one ($\sim$ factor 2) in Ag and Au. Due to the difficulties of the Sigmund (1969) theory to reproduce the yields of low-yield materials, similar comparisons are difficult to make for those, and fewer data exist. It seems, however, that such enhancements of yields under atomic bombardment are not found for low-yield (high surface-binding-energy) materials (Andersen & Bay, 1981; Thompson, 1980). Enhancements are seen for high-yield materials if the stopping power is high (high Z_1; close to maximum in S_n) and the recoil ranges are short (high Z_2) as seen in fig. 1. Hence, enhanced yields are seen for high energy deposition in the surface region. (See also Sigmund, 1987).

The above statement is strongly corroborated by the systematic relative-yield

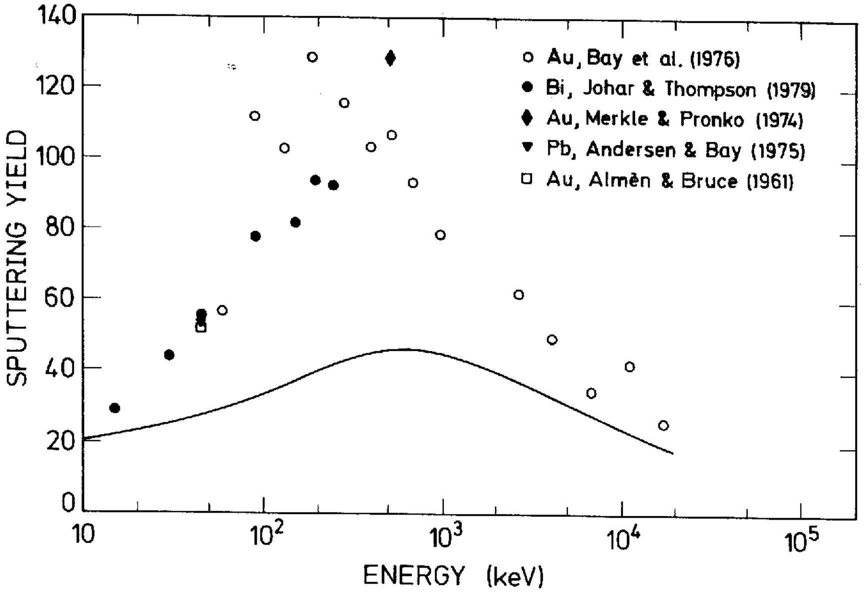

Figure 1. Gold sputtering yields under bismuth, lead, and gold bombardment. The full line represents eq. (1).

measurements performed by Andersen & Bay (1972, 1973, 1975). Their data are presented in fig. 2. Again it is seen that while the Sigmund theory predicts the Z_1 dependence of the yield at 45 keV well for silicon and nicely for copper, strong enhancements of heavy-ion yields relative to Ar sputtering are seen for silver and gold. The enhancements comprise in both cases a factor of 2.5 for the heavy projectiles.

Based on the reviews by Thompson (1980, 1981a), Zalm & Beckers (1984) conjectured that nonlinear effects should show up whenever Y exceeded 7[1]. Therefore they measured yields of zinc (U_s = 1,35 eV) bombarded by low-energy (0.2 - 20 keV) Xe atoms. The yields covered the region from 3 to 28 and closely follow the energy dependence of the nuclear stopping power, which is surprising as the energy extends well below the point where collision-cascade theories are expected to apply. The data fit nicely together with the 45 keV point obtained by Almen & Bruce (1961). That the $Y = 7$ limit does not apply for lighter targets may also be seen from the Kr yield of copper (Andersen & Bay, 1981; fig. 4.16). The energy

---

[1] On the other hand, Sigmund & Claussen (1981) stated $Y_{rmlinear} > 10$ as a necessary condition for significant nonlinear sputtering. This is in good agreement with the experimental data of Oliva-Florio et al. (1979, 1987)

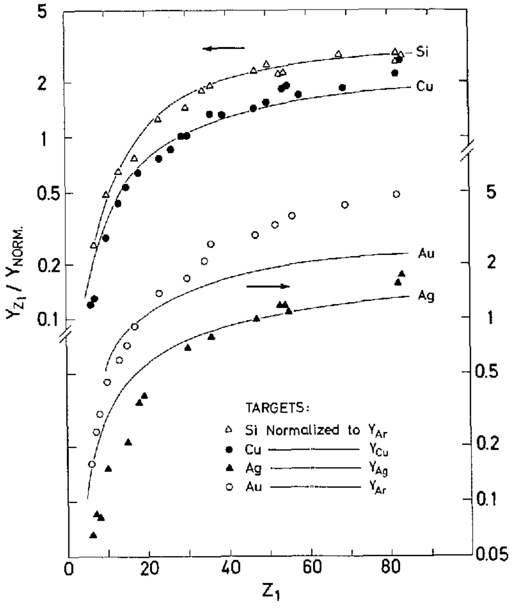

Figure 2. Relative Si, Cu, Ag, and Au sputtering yields for 22 different ions at 45 keV. Data from Andersen & Bay (1972, 1973 and 1975).

dependence follows that of S_n strictly from 2 to 1000 keV, while the yield rises to 14. Obviously the condition of short recoil ranges has not been taken into account in the argumentation of Zalm & Beckers. Notwithstanding, yield measurements for a very-high yield material like Zn would be most interesting for higher Xe energies. Such measurements are difficult as Zn is no easy target material to work with. Zalm and Beckers demonstrate by their careful measurements how such a task may be accomplished experimentally.

Nonlinear effects may be seen for light elements at low energies provided the binding energy is low enough. This is the case for condensed rare gases. The energies must be kept low to ensure collisional sputtering as these targets are otherwise sputtered heavily electronically. Fig. 3 shows data for 1-5 keV Ar, Kr and Xe sputtering of neon by Balaji et al. (1989). The yields rise much faster than proportional to S_n (an apparent slope of 1 would correspond to $Y \propto (S_n)^6$. In this case the surface binding energy is extremely low (40 meV). Balaji et al. also performed measurements on argon, krypton and xenon, where the increase of the

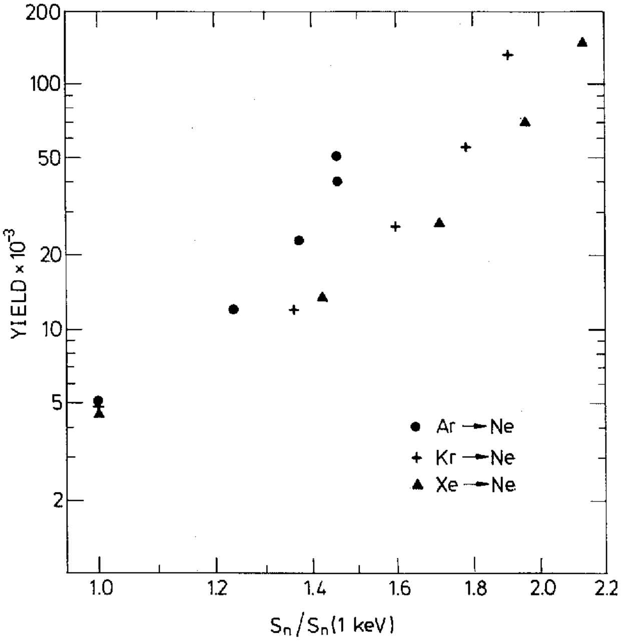

Figure 3. Sputtering yields for condensed neon bombarded by 1 - 5 keV rare gas ions as a function of the relative nuclear stopping $S_n(E)/S_n(1\text{keV})$. The horizontal scale has been stretched by a factor of 6. A slope of 1 would hence correspond to $Y \propto (S_n)^6$. Yield data are from Balaji et al. (1990).

yield with S_n is somewhat slower. Further data at slightly higher energies are given by Schou et al. (1992), and a more detailed discussion of the argon yields is given by Johnson & Schou (1993).

The evidence discussed above and mostly known prior to 1974 prompted Andersen & Bay (1974) to attempt a direct experimental proof of the existence of nonlinear effects. Silicon, silver and gold were bombarded with the dimers Cl_2, Se_2 and Te_2 and the corresponding monomers at the same energy per atom. While no significant enhancement was found for Cl_2 irradiation, Se_2 yielded in all cases an enhancement, the larger the heavier the target. An example is shown in Fig. 4. It is important that the measurements be performed alternately with monomers and dimers. In this way neither chemical effects nor topographic changes of the surface will influence the measured enhancement factors.

A few cluster bombardments were reported earlier. Grønlund & Moore (1960) bombarded silver with H and H_2 at low energies. In hindsight it is not surprising that they saw no enhancement with such light projectiles. In contrast, Rol et al.

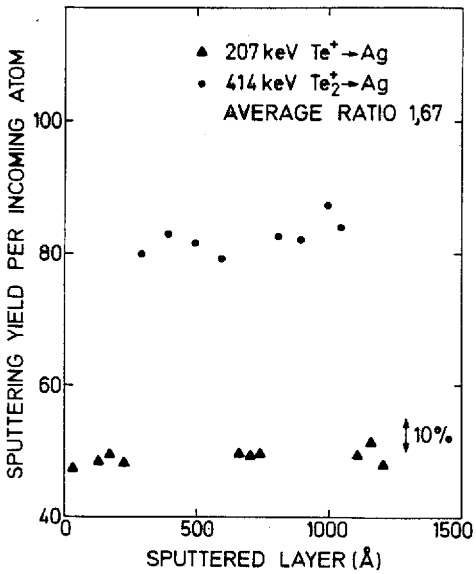

Figure 4. Sputtering yield per atom of a polycrystalline silver target for 207 keV Te^+ and 414 keV Te_2^+ ion bombardment as a function of sputtered-layer thickness. (From Andersen & Bay, 1974).

(1960) irradiated copper with 5-25 keV KJ^+ and found a 15% enhancement over the sum of the atomic yields. For N_2 irradiations they saw no particular effects. They were mildly puzzled by the KJ^+ results. It is not clear whether chemical effects could have influenced their results, but they appear reasonable in view of later data. Andersen & Bay (1975) also measured the enhancement factor for Te_2 and Se_2 on gold as a function of energy. The enhancement factors stay approximately constant over a factor of ten in energy from the stopping maximum and downwards. Above the stopping maximum, the enhancement factors decrease rapidly with increasing energy.

The energy dependence at low energy was studied by Oliva-Florio et al. (1979). They used 1-50 keV Xe and Xe_2 on Au. Their results are reproduced here as Fig. 5. The energy dependence appears to fit nicely to other experiments. The nonlinear effects are seen to persist down to a reduced energy $\varepsilon = 0.0015$ ($E = 2$ keV). Maybe there is even a cross-over giving rise to the enhancement factors being below 1.0 at lower energies. As mentioned in the discussion section, such a result would not be unreasonable. The measurements were later followed up (Oliva-Florio et al., 1987) with Ar_2 measurements on Au and Xe_2 measurements on Cu, all in the energy

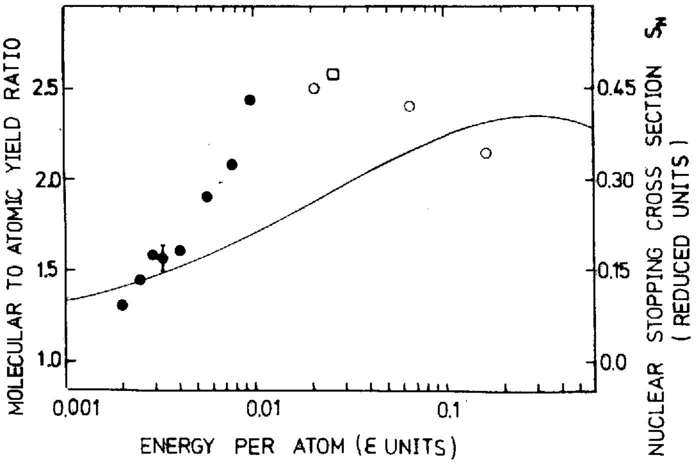

Figure 5. Nuclear stopping powers (full curve) and yield-enhancement factors for molecular irradiations of gold. Filled circles Xe_2 (Oliva-Florio et al., 1979). Open circles Te_2 (Andersen & Bay, 1974), square Sb_2 (Thompson & Johar, 1979) From Oliva-Florio et al. (1979).

interval described above. Ar_2 on Au showed a weak nonlinear effect (enhancement factor ~ 1.2) while the Xe_2 on Cu showed an enhancement factor nearly as large as on Au. With the Cu result perhaps on the high side, the results fit nicely into the trend of other measurements discussed in this section.

Johar & Thompson (1979) and Thompson & Johar (1979 and 1981) carried out a large systematic series of measurements of cluster effects. They bombarded Ag, Au and Pt with P, As, Sb and Bi monomers, dimers, and, for Sb, trimers over the energy range 10-250 keV. For Sb_3 enhancement factors as large as 10 were found. Further, in the 1981 paper they published results on the influence of the bombarding angle. The enhancement factors decreased slightly for incidence angles far away from the target normal, but due to the variation of the yield with incidence angle, yields close to 2000 were reached. The yields are depicted in Fig. 6 as a function of surface-deposited energy. Note that F_D is calculated through a Monte-Carlo procedure. This may be most reasonable for large incidence angles, but published calculations for gold at perpendicular incidence (Thompson, 1981b) show agreement with analytical values at 100 keV yet nearly a factor-of-two below at 1000 keV. All qualitative arguments indicate that the influence of the surface (the main reason for discrepancies between analytical and MC calculations) should decrease with increasing projectile energies rather than the opposite. Hence some doubt remains with respect to the MC calculations. The data from the

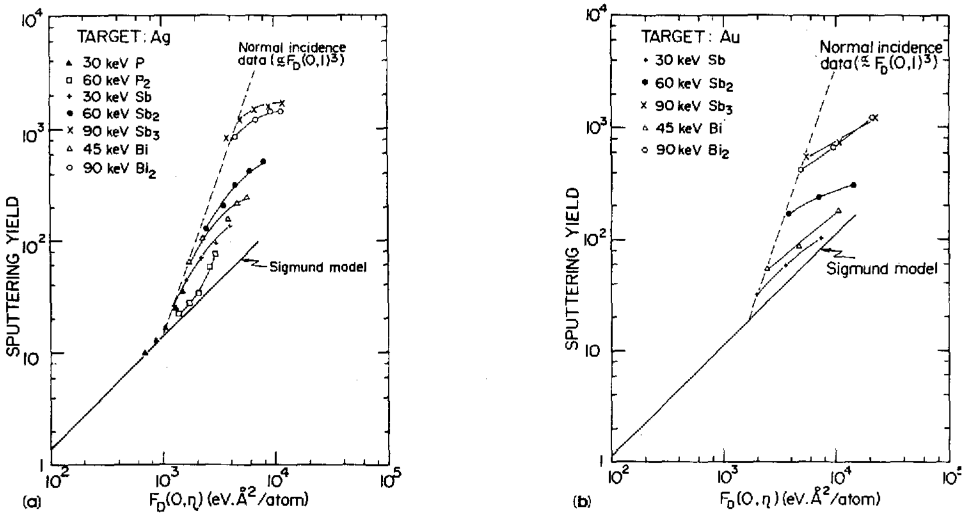

Figure 6. Measured sputtering yields of silver and gold bombarded with mono- and polyatomic ions at different energies and incidence angles as a function of surface-deposited energy, calculated by Monte Carlo methods. (From Thompson & Johar, 1981).

group have been treated in detail by Thompson (1980, 1981a,b). A number of his interpretations will be scrutinized in the discussion section below.

Hofer et al. (1983) mainly studied the influence of temperature on yield to be discussed below, but they also determined the silver yield from 100 keV Sb^+ and 200 keV Sb_2^+ impact. The enhancement factor (~ 1.5) is in good agreement with other experimental data.

Merkle & Jäger (1981) (see also their preliminary report, Jäger and Merkle (1978)) bombarded gold foils with 10 to 500 keV Bi^+ and Bi_2^+ ions and observed the foils by transmission electron microscopy (TEM). Some of their results are shown in Figs. 7 and 8. They observe craters in the surface of the foil and ascribe these craters to high-yield events. Within the resolution of the microscope only 1.5% of the incident Bi_2^+ ions at 100 keV/atom give rise to visible craters, but these craters contained some 40% of the sputtered atoms. Note also the facetted shape of the craters in fig. 7, a feature we shall return to in the discussion section. Fig. 8 shows the distribution of crater sizes. The yields from individual cratering events do of course scale as the crater volume, i.e. approximately with the third power of the diameter. The cutoff at low energy is related to an observational cutoff in the TEM. The figure is unique in the way that it constitutes the only published data set for fluctuations in sputtering yields. It illustrates that fluctuations are

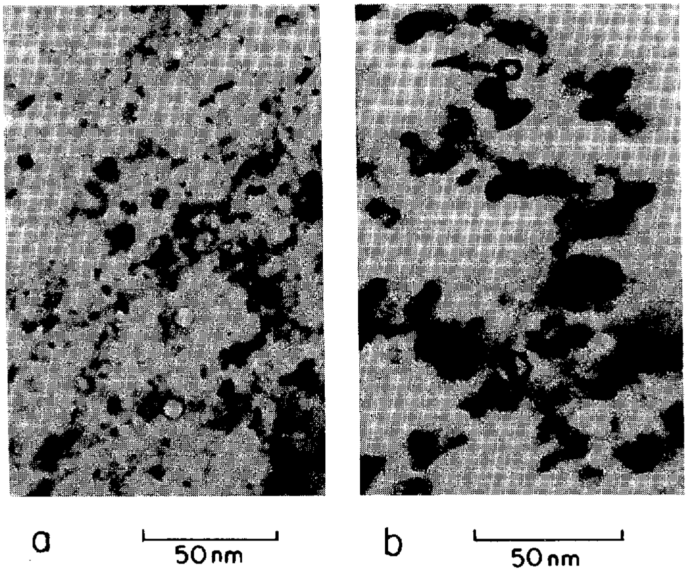

Figure 7. Faceted craters on a (100) Au surface (a) and a (111) surface (b) bombarded with Bi_2^+ ions. (From Merkle & Jäger, 1981).

substantially larger for dimer than for monomer irradiations. According to Merkle & Jäger (1981) this is thought to be related to the break-up of collision cascades into subcascades; a mechanism that will be more difficult under dimer than under monomer bombardment. If nonlinear effects exist for the system in question, they will be amplified by fluctuations, and the very large fluctuations may give some of the explanation for the large yield enhancement. Measurements of crater-size distributions are rather time-consuming. It is hence difficult to carry out systematic studies varying projectiles, targets and impact angles.

Beuhler & Friedman (1980, 1986) and Mathew et al. (1986) irradiated among other targets carbon with very large water clusters ($n \leq 150$) at 300 keV. Their results, partly also reported as TEM pictures, may to some extent be influenced by electronic energy deposition. It is interesting to note that yields are so large that the total ion energy is insufficient to atomize the sputtered carbon. Some of the TEM pictures by Mathew et al. from Pt-covered carbon look very much like the pictures published by Andersen et al. (1978) from Au-covered carbon foils bombarded with 15 MeV heavy ions, but there the irradiation conditions were clearly in the region dominated by electronic stopping.

A large number of papers (e.g. Hedin et al., 1989; Hunt et al., 1989; Thomas

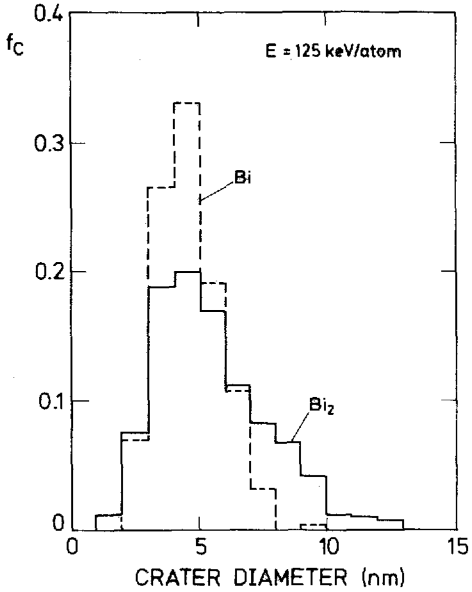

Figure 8. Crater size distributions for 125 keV Bi^+ and 250 keV bombardment of Au. (From Merkle & Jäger, 1981).

et al. 1985 and 1988; Salehpour et al., 1988 and 1989) report different sorts of yield enhancement under cluster bombardment in the electronic stopping region. Discussion of these results is considered to be outside the scope of the present review.

A particularly exciting cluster-enhanced yield involving nuclear collisions was introduced through the report of enhanced fusion rates under bombardment of metal targets with slow $(D_2O)_n$ clusters. (Beuhler et al., 1989, 1990, 1991). The results were heavily challenged experimentally (Fallavier et al. 1990, 1993; Vandenbosch et al., 1991, 1992) and finally withdrawn by the original authors (Beuhler et al., 1992). Meanwhile attention has been called to an interesting collision mechanism (Carraro et al., 1990) where a light atom (the deuteron) rattles to and fro between heavy atoms in the projectile cluster and the target (the so-called Fermi shuttle) and acquires a much larger energy than what might be transferred in a single collision, albeit with very low probability. The mechanism was not directly discussed by Sigmund in his 1989 review but implicitly present. Hautala et al. (1991) showed it to be incapable of explaining the yields originally published by Beuhler et al. (1989). The aspect which is interesting in this connection is whether

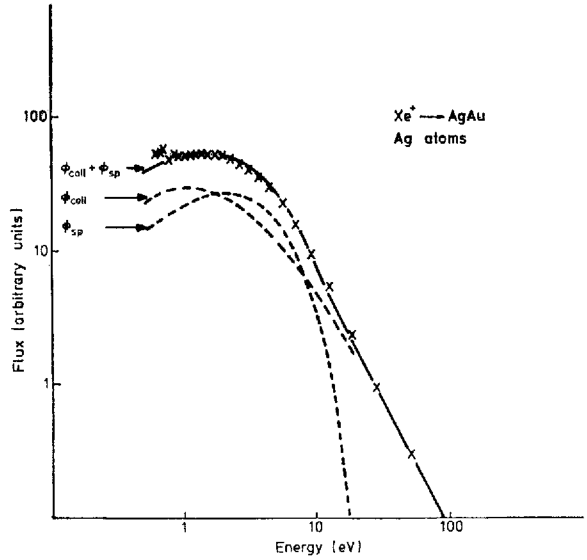

Figure 9. Energy spectra of silver atoms sputtered from an AgAu alloy by 6 keV Xe bombardment. A low energy spike component in the spectra is clearly seen. (From Szymonski et al., 1978).

the mechanism may give rise to sputtering effects. Sigmund (1989) suggests this may well be the case close to the sputtering threshold but experiments to confirm the idea will be difficult. Fallavier et al. (1993) find they are not able to lower their background sufficiently to measure fusion yields at the rate predicted by Hautala et al. and thus to confirm the feasability of the mechanism. They speculate whether other measurements might be performed. In spite of the possibility of making sputtering measurements, much more direct evidence appears to be obtainable from measurements of backscattering spectra, in particular because higher energy monomers or small-cluster beam-background components will have a lower scattering cross section than those looked for in contrast to what was the case for cluster-induced fusion. Pile-up in the spectra might, however, give rise to problems.

In the original paper on yield enhancement from dimers, Andersen & Bay (1974) concluded that if the enhancement was due to a spike mechanism, the 'extra' sputtered atoms must be expected to have very low energy. This prediction was tested through a measurement of the total reflected energy (also called sputtering efficiency), which is largely independent of surface-binding energy (Andersen, 1970). The experiment was performed with Se and Te monomers and dimers on lead. In spite of an expected yield enhancement of about a factor of 4 in the latter case, no enhancement in the reflected energy could be detected within the measuring accuracy of 10%. The extra sputtered atoms must hence have an average energy of only some percent of those sputtered by monomers. In spite of the fact that these results were reported in the original publication of nonlinear yields, they appear to have been largely forgotten.

Even more direct evidence for a low-energy component in the energy spectra of collisionally sputtered particles was presented later. Szymonski & de Vries (1977) bombarded Ag and Au with 6 keV Xe. Later (Szymonski et al. 1978) they also used an AgAu alloy as a target. Fig. 9 shows one of their energy spectra decomposed into a cascade part (fitting eq. (2) to the high energy part) and a low-energy Maxwell-Boltzmann-like part. From the cascade part surface-binding energies for the pure metals as well as the alloy components may be deduced. Ahmad et al. (1981) used 20 keV Ar and Xe on Ag[2]. While the spectrum found for Ar bombardment peaks at 2 eV, the maximum is found at 0.4 eV for xenon bombardment. Husinsky et al. (1978, 1980) used a very low binding energy target, viz. sodium. Again a clear low-energy spike component was seen. Measurements of velocity distributions of sputtered atoms in general were reviewed by Thompson (1987).

Oostra et al. (1988) performed an experiment that was the direct spectrum equivalent of the sputtering-efficiency measurement of Andersen & Bay (1974). They irradiated gold with 4 keV/atom iodine monomers and dimers. The spike component was, as expected, much stronger in the dimer than in the monomer case and a substantial yield enhancement was found. The surprising feature of the paper was, that through fits of a Maxwell-Boltzmann distribution to the low-energy part of the spectra, a higher temperature was deduced for the monomer than for the dimer case. A natural point of criticism would be that the model was strained too much through assuming a distribution corresponding to thermal equilibrium. Szymonski & Postawa (1990) showed that if the fit was instead made to the cascade part, the monomer spectrum showed a negative component at the lower energies. Szymonski & Postawa resolved the discrepancy by ascribing this artefact to a combination of uncertain background subtraction and very poor statistics for that part of the spectrum.

Closely coupled to a possible low-energy part of the energy spectra was the question of the influence of temperature on sputtering yields. In particular the very strong temperature dependence of noble-gas sputtering of silver found by Nelson (1965) was by many taken as clear evidence for spikes, until Besocke et al. (1982) and Hofer et al. (1983) showed that the temperature dependence was mainly due to background sublimation, not sputtering. Hofer et al. found only an approximate

---

[2] See also Ahmad et al. (1980) as another example of the work of M.W. Thompson and his group on sputtered energy spectra.

30% yield rise from 25°C to 775°C independent of whether irradiation was with 100 keV/atom Sb or Sb_2. In both the 1982 and 1983 publications the authors were very puzzled by the missing influence of target temperature on spike sputtering, but such evidence was also deduced from measurements of energy spectra from Cr and Ca by Husinsky et al. (1984, 1985). Sigmund & Szymonski (1984) showed from detailed analytical calculations that no strong influence should be expected, but that appears not to have influenced Hofer's viewpoint in his recent (1991) review on angular energy and mass distributions of sputtered particles.

Ion-induced electron emission is a phenomenon basically connected to the electronic stopping of the projectile ion although sometimes in a rather complicated way (Rothard et al. 1992). The question which has been raised several times is whether the much longer lifetime of the spike than that of the collision cascade proper will allow a sufficient coupling between atom and electron systems to cause enhanced electron emission. This hypothesis was tested by Thum & Hofer with V_n^+ and Nb_n^+ clusters ($n \leq 9$, $v < 4\times10^5$ m/s) incident on stainless steel. Absolutely no nonlinear effects were found. Other investigations (e.g. Hasselkamp & Scharmann, 1983; Kroneberger et al., 1989) showed molecular effects at much higher velocities. These are thought to be caused by nonlinearities in the electronic stopping.

Early results for enhanced ion yields from Si bombarded by Ne_2 and Ar_2 were published by Wittmaack (1979). Molecular effects on ion emission have also been studied more recently. While it is difficult to extract information relevant for the present purpose from the measurements of total emitted negative charge under $(H_2O)_n$ bombardment (Beuhler & Friedman, 1980, 1986) and from Reuter's (1987) measurements with CF_3^+ and O_2^+ irradiation, recent studies involving keV bombardment with $(CsI)_n^+$ and Au_n^+ (Blain et al., 1989; Benguerba et al., 1991) appear more promising. Firstly, their use of a liquid-metal ion source (LMIS) allows beams up to Au_5^+; presently only with energies up to approximately 30 keV, but when work to install a LMIS in a van de Graaff terminal will be finished shortly (Le Beyec, 1993) much higher energies and a much broader velocity region will be available. The LMIS has also been used successfully in a tandem accelerator, where the clusters have been transported through the charge-exchange system without breaking up (Schoppmann et al., 1993). This even further extends the energy range, still within the nuclear stopping region for heavy targets.

An example of the results of Benguerba et al. (1991) is shown as Fig. 10 displaying Au^- emission from gold bombarded with gold clusters. Very large enhancement factors are seen. For Au_4^+ at 10 keV/atom, a slight extrapolation of the data indicates a factor of 15. If the same enhancement factor holds for the total yield, that would bring the yield up to 300 for a 40 keV Au_4 cluster (c.f. fig. 1). If the involved atoms come out as single atoms – which they probably do not do – 30% of the incident energy would be consumed simply to overcome the sublimation energy.

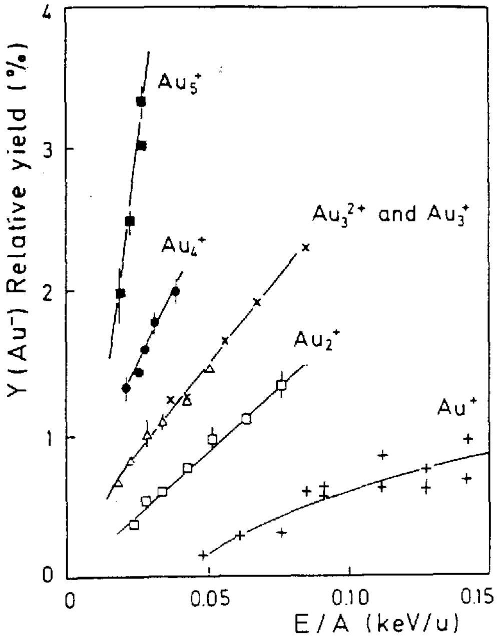

Figure 10. Au^- yield from a gold target as a function of primary ion energy per mass unit. The primary ions are Au_n^+ and Au_n^{++} with $n \leq 5$. (From Benguerba et al., 1991).

The question in such experiments is whether the ionization depends on the energy density of the spike. The Hofer & Thum results for electron emission discussed above indicate that not to be the case, but direct experimental evidence is entirely missing. Total yield measurements over a broad energy interval for Au_n impact on gold ought to be one of the first priorities when the new beams become available (della Negra et al., 1993, Demirev et al., 1991, Schoppmann et al., 1993, Le Beyec, 1993). A potential problem is to obtain mass and energy analyzed beams of heavy clusters. Beam lines are usually not equipped with bending magnets and focussing devices that allow handling of singly or doubly charged particles with masses of the order of 1000 to 2000 atomic mass units. It will be exceedingly difficult to measure absolute neutral sputtering yields on an event-by-event basis where the nature of the projectiles is identified by time-of-flight methods, which in other connections may be a convenient way to handle the indentification problem.

The Au-Au_2 negative ion yield enhancement factor at 15 keV/atom is found to be approximately 3.5. Johar & Thompson (1979) found the Bi-Bi_2 enhancement factor for the total gold sputtering yield to be 2.5 at 30 keV/atom and 3.9 at

45 keV/atom. This comparison seems to indicate that enhancement factors are substantially larger for Au^- ion yields than for total sputtering yields, further strengthening the case for measurements of both parameters.

Emission of clusters under cluster bombardment has been studied only on a few occasions. The crater measurements of Merkle & Jäger (1981) constitute circumstantial evidence for cluster emission but no direct proof. Beuhler & Friedman (1989) found emission of clusters up to C_{21}^+ from carbon bombarded with 240 keV $(H_2O)_{80}$ clusters and give detailed mass spectra, but similar spectra for single-molecule or small-cluster impact at the same energy per molecule are not available. Again, Benguerba et al. present interesting data. They conclude that 'cluster ions as projectiles are much more efficient than single atomic ions for ejecting complex secondary ions' a result that is in complete agreement with the circumstantial evidence from Merkle & Jäger. Further they conclude that 'our data support also a direct ejection mechanism of clusters under cluster impact'. This conclusion agrees well with the one reached by Andersen (1989) in his review of cluster emission in sputtering but less with the viewpoint of Hofer (1991) that tended to see sputtered clusters as created through a recombination mechanism. The two latter papers present general discussions of the field of cluster emission.

3 Computer Simulations

Simulations of sputtering through computer calculations were reviewed at length by Andersen (1987). It is not the idea here to repeat the classifications and conclusions of that paper nor to discuss any of the 400 references treated in the review. It is, however, amazing to note that virtually none of the papers discussed then treated cluster impacts in view of the number of papers on that subject that have appeared over the relatively short period since that review was completed.

The first group of papers treated here is concerned with cluster impact energies below the sputtering threshold: We are in the domain of cluster-beam deposition of films. The low energy makes possible rather detailed computer studies on small samples, but the general interest was very much triggered by the claim by Takagi & Yamada (1989) that the impact of large, ionized, low-energy clusters enhanced the epitaxial growth of high-quality crystal films. The claim was supported by the TEM observations of deposited discontinous films of Usui et al. (1989), but their films look very much like those described by Andersen et al. (1979) produced by simple evaporation. Silicon epitaxial deposition in particular was studied by Schneider et al. (1987) (not employing cluster impact), by Biswas et al. (1988) who gave some support for the Takagi conjecture and by Kwon et al. (1990) (the same group) who now were less enthusiastic. Kitazoe et al. (1984a,b) studied the impact of Al clusters on silicon and Cu on carbon. These programs were further developed by Yamamura (1990) for $(\mathrm{Ag})_n$ on carbon. In all cases the impacting clusters ($\sim$ 500 atoms and 6 - 10 eV/ atom) were found to flatten out on the substrate. No sputtering resulted. Xu et al. (1989) studied the impact of $(\mathrm{Ar})_n$ on Pt and found the impacting clusters to break up and individual atoms to be scattered nearly parallel to the surface. Hsieh & Averback (1990) and Averback et al. (1991) treated copper cluster impact on copper. At very low energy they found no particular effects from clusters. At higher energies, but still below the sputtering threshold, they found evidence for craters with a rim, rather like the pictures published by Mathew et al. (1986). Hence they saw no particular merit in large cluster beam deposition. Maybe that is rather fortunate as a closer inspection of the output of the Takagi source did not reveal the presence of large clusters in the beam (Brown et al., 1991).

A number of groups investigated cluster impacts on solids by means of computer simulations at energies where sputtering may occur. Molecular dynamics methods are used for the majority of these calculations. A Cambridge group looked at copper sputtering by SiCl_4 impact up to 1 keV (Park et al., 1987). Comparison to the yield of Ar atom impact showed no nonlinearities. For further details of their Ar sputtering studies, see also Stansfield et al. (1989). They returned to the $\mathrm{SiCl}_4 \rightarrow$ Cu(001) case (Broomfield et al., 1990) using ab initio calculated interatomic potentials and now did find significant nonlinearities. Very large nonlinearities were found by Yamamura (1988) who investigated $(\mathrm{Ar})_n$ impact on carbon ($10 < n < 200$, $E = 100$ eV/atom) using a binary-collision code. The enhancement factor of the yield was 80 for the largest clusters. Very strong nonlinearities were also found for the energy deposition. It is relevant here to mention that Yamamura & Muramoto (1992) found the reflected energy to show a slight enhancement for $(\mathrm{Al})_{500}$ on Ag and $(\mathrm{Ag})_{500}$ on Al. These results did not include the energy of the sputtered atoms. One of the basic ideas of the spike concept was confirmed by the simulations of de la Rubia et al. (1987) and Averback et al. (1991). Energy deposition of up to 5 keV in Cu and Ni caused local melting lasting some picoseconds. Most spectacular in this connection was the formation of craters surrounded by a rim without sputtering or with very little sputtering as also discussed above.

Shapiro & Tombrello have published a series of papers on simulation of cluster sputtering starting in 1990 with 1 keV/atom impact of Al_{32} and Al_{63} on aluminium and gold. They found the target to be compressed substantially by the impact. Sputtering was seen, but nonlinearities in the yield might not be discerned. These results are presented in more detail by Shapiro & Tombrello (1991 a). In their next (1991 b) paper Au (100) and (111) targets were simulated, irradiated by monomer and dimer Kr, Xe, Au and U at perpendicular incidence at 5 keV/atom. Dimer yield enhancement factors larger than 1 were found in all cases, but they were smaller for the heavy than for the light projectile constituents. The authors suggest this to be due to saturation, since a substantial nonlinear effect was suspected to be present already for the monomer impact. This sounds like the experimental saturation effects suggested by Benguerba et al. (1991) as discussed above. The simulated energy spectra show the enhancement to occur at surprisingly high ejection energies (1-10 eV). Even processes with a rather high-energy threshold like core excitations may display cluster effects (Shapiro & Tombrello, 1992).

Finally a group of cluster impact papers by Sigmund and coworkers will be discussed. They are to a rather limited extent concerned with cluster sputtering effects (mostly not with sputtering at all). Nevertheless they raise a number of questions important for the problems discussed in the present paper. Shulga et al. (1989) introduced the tool of switching on and off the interaction between target particles (and also later between cluster constituents) in the simulation. Two important mechanisms are disclosed through this process: The clearing-the-way and blocking-the-way effects which give rise to decreased or increased energy deposition (as earlier pointed out by Yamamura, 1988). These effects are discomforting in the present connection. We have regarded the Sigmund (1969) sputtering theory a sort of benchmark from which to judge nonlinear effects in monatomic sputtering. This attitude reflected the idea that deposited surface energy was strictly proportional to the nuclear stopping powers and that the stopping power of cluster components were additive. At energies close to threshold it now looks as if nonlinearities may as well be attributed to the stopping power as to the sputtering process. In this region the situation turns out to be as complicated as it is in the electronic-stopping region. In Shulga & Sigmund (1990) penetration of gold clusters through silicon is treated. Here the clearing-the-way effect dominates and stopping powers are lowered. In Pan & Sigmund (1990) the opposite situation is treated: carbon clusters on gold targets. Energy deposition is additive but carbon atoms may appear with high energies. This becomes even more pronounced if the clusters are mixed light and heavy (Hautala et al., 1991). Here we see the Fermi shuttle clearly demonstrated through Monte-Carlo and molecular-dynamics simulations as discussed in connection with cluster-induced fusion processes. Shulga (1991) finds lowered stopping powers for Cu clusters on copper as do Shulga & Sigmund (1992) for copper clusters on gold. In the latter case sputter-yield enhancement factors lower than one were calculated. Maybe the experimental data of Oliva-Florio et al. (1979) (see fig. 5 here) should really be extrapolated downwards to enhancement factors lower than one?

Johannessen (1993) studied Au (100) sputtering by 250 eV Xe and 500 eV Xe_2. He found only slight nonlinear effects, but when the dimers were oriented with their axis perpendicular to the surface, the clearing-the-way effect showed up.

4 Discussion

The aim of the present section is not to discuss which spike model best fits the experimental data. Experimental data are not sufficient nor covering a large enough energy interval to allow such an evaluation. The idea is rather to have a critical look at other alternative models that have been aired to see whether any of those could explain the experimental observations. We are hence for a brief moment neglecting the fact that the success of linear sputtering theory for moderate energy-deposition densities implies that spike effects must play a role for high densities due to the breakdown of the assumptions of linear theory.

Thompson (1981 a,b) implied that the mesoscopic roughening of the surface topography caused by high-yield events could explain part of the yield enhancement. Experimentally, such roughening has been clearly demonstrated (see Carter et al. (1981) for a review). Thompson made reference to the calculations of Littmark & Hofer (1978) indicating an increase of yield with increased surface roughening. Experimentally, the yield increase was seen by Besocke et al. (1982). Note in this connection that plenty of other high-dose effects may change the yields (Andersen & Bay, 1972, 1973; Andersen 1984). Thompson's conjecture, however, neglects the main virtue of the measuring technique employed by Andersen and Bay (1974, 1975): As seen from fig. 4 (and all the other data published by these authors), the enhancement factor is measured by comparing monomer and dimer yields at identical surface conditions. The measured enhancement factors must, therefore, be totally independent of dose even if strong dose effects are found for individual yields. The model was hence experimentally untenable before it was even proposed.

Johar & Thompson (1979) proposed an effect caused by a lowering of U_s due to radiation damage. As discussed below, surface-binding energies will depend on exactly from which sites at the surface sputtering takes place. Sputtering-yield measurements have probably never been made from a perfect surface. In reality eq. (1) as well as eq. (2) should hence contain a distribution of surface binding sites. The surface roughening caused by high-energy-density events is probably not very different from that caused by low-yield events due to surface diffusion, as long as we look on the atomic scale. Under high-yield conditions sputtering may occur through a two-step process where an atom is first moved to a low-energy site and later – within the same cascade – sputtered. A possibility in question is local surface melting. Such two-step processes will enhance the yields. By definition they are of a nonlinear nature. They are not thought to be particularly important.

Many authors proposed that the sputtering of clusters would lower the surface binding energy to be overcome (e.g. Merkle & Jäger (1981) and Beuhler & Friedman (1980, 1989)). The proposal is qualitatively appealing but has not been evaluated quantitatively. If the clusters are assumed to be hemispherical, a lot

Table I

fcc surface	(111)	(100)
Atom on plane	3	6
Corner on overlayer	6	6
Atom on ledge	7	7
Aton im plane	9	8

of different high-index crystal surfaces will be generated, and it is not clear what the binding energy will be. Here we shall present a much simplified model which, however, is easily quantified.

Calculations will be presented for close-packed clusters emitted from the (111) and (100) surfaces of an fcc lattice. Surface binding energies will be assumed to be proportional to the number of nearest neighbours which the emitted configuration of atoms had to the lattice left behind. As the lattice will only relax to a very limited extent during the emission process, the assumption is presumably quite justified.

An atom in an fcc lattice has 12 nearest neighbours. They are distributed differently in the (111) and (100) planes. An atom has 6 nearest neighbours within the (111) plane and 3 below and above. Within the (100) plane there are 4 neighbours while 4 are found below and above. Hence an atom expelled from the (111) plane leaves 9 nearest neighbours behind while an atom leaving the (100) plane only leaves 8: The (111) plane is hence expected to have a higher binding energy than (100). Within the present context this agrees with the fact that Hofer et al. (1983) found a lower enhancement factor for sputtering from the gold (111) surface than from (100).

Considering non-perfect surfaces we find the number of neighbours shown in table 1. Let us now look at planar triangular clusters expelled from the (111) surface. Let the edge length be n, the number of atoms in the cluster N and the number of nearest neighbours NN. For this particular configuration we find $N = n(n+1)/2$ and $\mathrm{NN} = 3n(n+5)/2$. Note that neighbours not only are found at the edges but also in the plane below. Fig. 11 shows NN and NN/8N as a function of N, i.e. normalization is chosen to an atom within the (100) plane.

Similarly, for the (100) plane, we find $N = n^2$ and $\mathrm{NN} = 4n(n+1)$. In the limit of very large plates, we find NN/8N to be 0.5 for the (100) surface and 3/8 for the (111) surface as shown in Fig. 11.

We now consider triangular pyramids extending inwards from the (111) plane. Beneath a surface triangle with side length n is removed a triangle with side length $(n-1)$ etc. In total, a regular tetrahedron limited by (111) faces is cut out. After

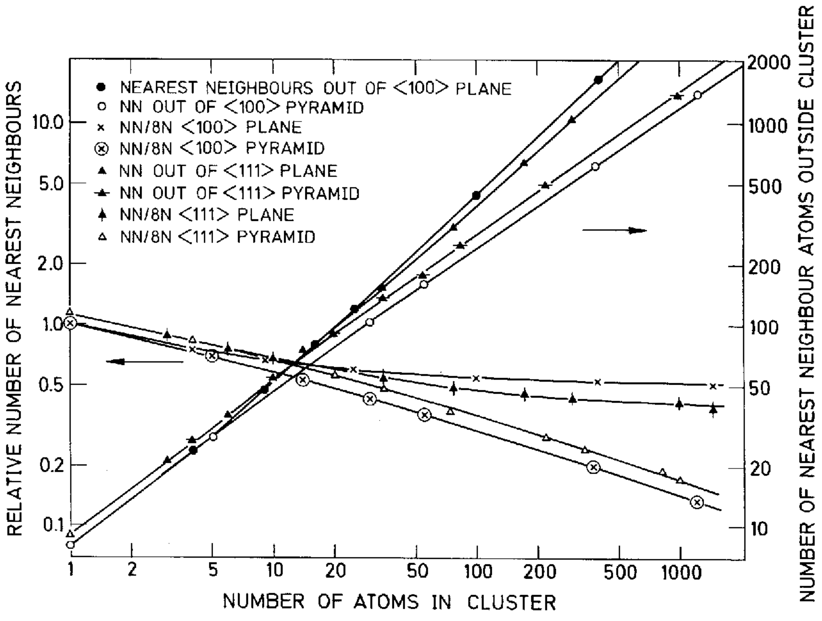

Figure 11. Nearest neighbours and relative number of neighbours of planar and pyramidal clusters from on (111) and (100) surfaces of an fcc lattice.

some calculations we find $N = n(n+1)(n+2)/6$ and $\mathrm{NN} = 9n(n+1)/2$. Note that a similar construction is not possible for an hcp lattice.

For the 4-sided pyramids on the (100) plane, we find $N = n(2n+1)(n+1)/6$ and $\mathrm{NN} = 2n(3n+1)$, again shown in Fig. 11. Again NN and NN/8N is shown as a function of N in fig. 11.

Note from the figure that significant differences between the surface energy saved for planar and volume clusters are not found before $N \geq 10$. Note also that the pyramids on the (100) face are ultimately the most energy-saving ones because their shape comes closer to a sphere than the (111) pyramids. Considering numbers, we note that a 2000 atom pyramid may be expelled at the cost of 200 individual emitted atoms.

The shapes postulated here are exactly the ones found for segregated inclusions in an fcc lattice (Johnson et al., 1992). They are also the shapes of the craters found by Merkle & Jäger (1981) as seen in fig. 8. This, however, does not tell whether the clusters were expelled in such a shape or whether the craters first obtained their equilibrium shape after the emission. Finally, it should be noted that the full lines of fig. 11 may not be used for interpolation. Intermediately-sized clusters will have binding energies above the lines because they must have a more regular shape. A similar argument for the continuum case has very recently been presented by Tersoff et al. (1993). Note that the abundance of clusters may not be judged either from time-of-flight or from laser fluorescence measurements of the energy spectra. In both cases energies per atom are measured. It is concluded that emission of clusters may play a non-negligible role for the high nonlinear yields. This is also related to the role played by fluctuations in the sputtering yields. If fluctuations are large, cluster emission will per se give rise to nonlinear yields, but both experimental and theoretical information is insufficient to judge this possibility.

As the last suggestion, Thompson (1981a,b) proposed that rather than considering the energy deposited within a thin layer at the surface, the energy deposited over the crater depth should be considered. He claims that if that be done, linear collision theory would still apply. It may be argued that if linear collision cascade theory gives the yields, it should also give the energy spectra and this is experimentally known not to be the case. Further, if it were, it might be shown that e.g. the 2000-atom yield found for 40 keV Bi_3 sputtering of gold would imply a kinetic energy of the sputtered atoms of some 70 keV with an average energy of 35 eV calculated from eq. (2). Hence the energy spectra must be different from eq. 2 simply because of energy conservation. Finally in standard linear collision cascade theory it is not possible to deplete a layer of atoms: There will always be a full layer to sputter from.

It is concluded that emission of clusters may play a non-negligible role in nonlinear effects but spike effects must carry the main load.

5 Conclusions and Recommendations

- Spike effects are the main cause for nonlinear effects in sputtering yields.
- Cluster emission may play a substantial role.
- The amount of existing systematic data does not allow to discern between different spike models.
- There is a substantial need for data on yields and energy spectra, to be taken over a very broad energy region with clusters containing different numbers of heavy atoms.
- The influence of spikes on the ionization probability (or electron attachment probability) should be studied.
- The influence of cluster impact on cluster emission should be studied.

References

Ahmad S, Farmery BW and Thompson MW, 1980: Nucl. Instrum. Methods **170**, 327

Ahmad S, Farmery BW and Thompson MW 1981: Phil. Mag. A **44**, 1387

Almen O and Bruce G, 1961: Nucl. Instrum. Methods **4**, 257

Andersen HH, 1970: Radiat. Eff. **3**, 51

Andersen HH, 1984: *Ion Implantation and Beam Processing.* eds. Williams JS and Poate JM, (Academic Press, Sydney) 127

Andersen HH, 1987: Nucl. Instrum. Methods **B18**, 321

Andersen HH, 1989: Vacuum **39**, 1095

Andersen HH and Bay HL, 1972: Radiat. Eff. **13**, 67

Andersen HH and Bay HL, 1973: Radiat. Eff. **19** 139

Andersen HH and Bay HL, 1974: J. Appl. Phys. **45**, 953

Andersen HH and Bay HL, 1975: J. Appl. Phys. **46**, 2416

Andersen HH and Bay HL, 1981: *Sputtering by Ion Bombardment. I.* ed. Behrisch R, (Springer, Berlin) 145

Andersen HH, Knudsen H and Møller Petersen P, 1978: J. Appl. Phys. **49**, 5638

Averback RS, Diaz de la Rubia T, and Hsieh H, 1991: Nucl. Instrum. Methods **B59/60**, 709

Balaji V, David, DE Maguera TF, Michl J and Urbassek HM, 1990: Nucl. Instrum. Methods **B46**, 435

Bay HL, Andersen HH, Hofer WO and Nielsen O, 1976: Nucl. Instr. Methods **132**, 301

Benguerba M, Brunelle A, Della Negra S, Depauw J, Joret H, leBeyec Y, Blain MG, Schweikert EA, Ben Assayag G, and Sudrane P, 1991: Nucl. Instr. Methods **B62**, 8

Besocke K, Berger S, Hofer WO, and Littmark U, 1982: Radiat. Eff. **66**, 35

Beuhler RJ and Friedman L, 1980: Nucl. Instrum. Methods **170**, 309

Beuhler RJ and Friedman L, 1986: Chem. Rev. **86**, 521

Beuhler RJ and Friedman L, 1989: Journ. de Physique **50**, C2, 127

Beuhler RJ and Friedman L, 1989: Phys. Rev. Letters **63**, 1292

Beuhler RJ and Friedman L, 1992: Phys. Rev. Letters **68**, 2101

Beuhler RJ, Chu YY, Friedländer G, Friedman L and Kunman W, 1990: J. Phys. Chem. **94**, 7665

Beuhler RJ, Chu YY, Friedländer G, Alessi JG, lo Destro V and Thomas JP, 1991: Phys. Rev. Letters **67**, 473

Biswas R, Grest GS and Soukoulis CM, 1988: Phys. Rev. **B38**, 8154

Bitensky IS and Parilis FS, 1987: Nucl. Instrum. Methods **B21**, 26

Blain MG, Della Negra S, Joret H, le Beyec Y and Schweikert EA, 1989: Phys. Rev. Letters **63**, 1625

Broomfield K, Stansfield RA and Clary DC, 1990: Surf. Sci. **227**, 369

Brown WL, Jarrold MF, McEachern RL, Sosnowski M, Takaoka G, Usui H and Yamada I, 1991: Nucl. Instrum. Methods **B59/60**, 182

Carraro C, Chen BQ, Schram S, and Koonin SE, 1991: Phys. Rev. **A42**, 1379

Carter G, 1979: Radiat. Eff. Letters **43**, 193

Carter G, Navinsek B and Whitton JL, 1981: *Sputtering by Particle Bombardment.II.* ed. Behrisch R, (Springer, Berlin) 232

David DE, Maguera TF, Tian R, Stulik D and Michl J, 1986: Nucl. Instrum. Methods **B14**, 378

de la Rubia T Diaz, Averback RS, Benedek R, and King WE, 1987: Phys. Rev. Letters **59** 1930

della Negra S, Brunelle A, le Beyec Y, Cureaudeau JM, Mouffron JP, Waast B, Håkansson P, Sundquist BUR and Parilis E, 1993: Nucl. Instrum. Methods **B74**, 453

Demirev P, Reimann CT, Axelson J, Kjellberg J, Håkansson P and Sundquist BUR, 1991: *Proc.Eighth Int.Conf. Secondary Ion Mass Spectrometry (SIMS VIII)*, eds. Benninghoven et al. (Wiley, Chichester), 33

Fallavier M, Kemmler J, Kirsch R, Poizat J-C, Remillieux J and Thomas J-P, 1990: Phys. Rev. Letters **65**, 621

Fallavier M, Kirsch R, Poizat J-C, Remillieux J, Rothard H and Thomas J-P, 1993: Phys. Rev. Letters **70**, 1022

Grønlund F and Moore JW, 1960: J. Chem. Phys. **32**, 1540

Harrison MR and Edwards PP, 1985: *The Metallic and Non Metallic States of Matter*, eds. Edwards, PP and Rao, NR, (Taylor and Francis, London), 389

Hasselkamp D and Scharmann A, 1983: Phys. Letters **96A**, 259

Hautala M, Pan Z and Sigmund P, 1991: Phys. Rev. **A44**, 7428

Hayashi C, 1987: Physics Today **44**

Hedin A, Håkansson P, Sundquist BUR and Johnson RE, 1989: Journ. de Physique **50**, C2, 215

Hofer WO, 1991: *Sputtering by Particle Bombardment III*, eds. Behrisch R and Wittmaack K, (Springer, Berlin-Heidelberg) 15

Hofer WO, Besocke K and Stritzker B, 1983: Appl. Phys. **A30**, 83

Hunt JE, Salehpour M, Fishel DL and Tou JC, 1989: Jour. de Physique 50, **C2**, 27

Hsieh H and Averback R, 1990: Phys. Rev. **B42**, 5365

Husinsky W, Bruckmüller R, Blum P and Viehböck F, 1978: Natl. Conf. *Interaction of Atomic Particles with Solids* (Minsk, USSR)

Husinsky W, Bruckmüller R and Blum P, 1980: Nucl. Instrum. Methods **170**, 287

Husinsky W, Betz G, and Girgis I, 1984: J. Vac. Sci. Technol. **A2**, 698

Husinsky W, Betz G and Girgis I, 1985: J. Vac. Sci. Technol. **B3**, 1543

Jäger W and Merkle K L, 1978: *Proc.Ninth Int.Conf.Electron Microscopy*, (El.Micr.Soc. Canada, Toronto) 378

Johannessen K, 1993: Nucl. Instrum. Methods **B73**, 481

Johar SS and Thompson DA, 1979b: Surf. Sci. **90**, 319

Johnson E, Hjemsted K, Schmidt B, Bourdelle KK, Johansen A, Andersen HH and Sarholt-Kristensen L, 1992a: Mat. Res. Soc. Symp. Proc. **235**, 485

Johnson E, Hjemsted K, Schmidt B, Bourdelle KK, Johansen A, Andersen HH and Sarholt-Kristensen L, 1992b: Electron Microscopy **2**, 267

Johnson RE, 1987: Int. J. Mass Spect. Ion Phys. **78**, 351

Johnson RE and Schou J, 1993: Mat. Fys. Medd. Dan. Vid. Selsk. **43** 403

Kitazoe Y and Yamamura Y, 1980: Radiat. Eff. Letters **50**, 39

Kitazoe Y, Sano M, Yamamura Y, Furutani H, and Yamamoto K, 1984a: Phys. Rev. **C29**, 828

Kitazoe Y, Gyalassi M, Daneilewicz P, Toki H, Yamamura Y, and Sano M, 1984b: Phys. Letters **B138**, 854

Kofmann R, Cheyssac P and Garrigos R, 1990: Phase Transitions **24-26**, 283

Kroneberger H, Rothard H, Burkhard M, Kemmler J, Koschar P, Heil O, Biedermann C, Leucinas S, Keller N, Lorenzen P, Hoffmann D, Clouvas A and Veje E, 1989: Journ. de Physique **50**, C2, 99

Kwon I, Biswas R, Grest GS and Soukoulis CM, 1990: Phys. Rev. **B41**, 3678

Le Beyec Y, 1993: Private communication

Littmark U and Hofer WO, 1978: J.Mater.Sci. **31** 2577

Matthew MW, Beuhler RJ, Ledbetter M and Friedman L, 1986: Nucl. Instrum. Methods **B14**, 448

Merkle KL and Jäger W, 1981: Phil. Mag. **44**, 741

Merkle KL and Pronko PP, 1974: J. Nucl. Mater. **53**, 231

Nelson RS, 1965: Phil. Mag. **11**, 291

Oliva-Florio AR, Alonso EV, Baragiola RA, Ferron J and Jakas MM, 1979: Radiat. Eff. Letters **50**, 3

Oliva-Florio A, Baragiola RA, Jakas MM, Alonso EV and Ferron J, 1987: Phys. Rev. **B35**, 2198

Oostra DJ, van Ingen RP, Haring A, deVries AE and Saris FW, 1988: Phys. Rev. Letters **61**, 1392

Pan Z and Sigmund P, 1990: Nucl. Instrum. Methods **B51**, 344

Park SC, Stansfield RA, and Clary DC, 1987: J. Phys. D: Appl. Phys. **20**, 880

Pelletier JD, Shapiro MH and Tombrello TA, 1992: Nucl. Instrum. Methods **67**, 296

Reuter W, 1987: Anal. Chem. **59**, 2081

Rol PK, Fluit JM and Kistemaker J, 1960: Physica **26**, 1000

Rothard H, Schou J, Koschar P and Groeneveld K-O, 1992: Nucl. Instrum. Methods **B69**, 154

Salehpour M, Fischel DL and Hunt JE, 1988: Phys. Rev. **B38**, 12320

Salehpour M, Fischel DL and Hunt JE, 1989: Journ. de Physique **50**, C2, 155

Schneider M, Schuller IK and Rahman A, 1987: Phys. Rev. **B36**, 1340

Schoppmann Ch, Wohlfart P, Brandl D, Saner M, Tamaschko CH, Voit H, Boussofiane K., Brunelle A, Chaurand P, Depauw J, Della-Negra S, Håkansson P and leBeyec Y., 1993: Nucl. Instrum. Methods (in press)

Schou J, Ellegaard O, Pedrys R and Sørensen H, 1992: Nucl. Instrum. Methods **B65**, 173

Shapiro MH and Tombrello TA, 1990: Phys. Rev. Letters **65**, 92

Shapiro MH and Tombrello TA, 1991a: Nucl. Instrum. Methods **B58**, 161

Shapiro MH and Tombrello TA, 1991b: Nucl. Instrum. Methods **B62**, 35

Shapiro HH and Tombrello TA, 1992: Nucl. Instrum. Methods **B66**, 317

Shulga VI, 1991: Nucl. Instrum. Methods **B58**, 422

Shulga VI and Sigmund P, 1990: Nucl. Instrum. Methods **B47**, 236

Shulga VI and Sigmund P, 1991: Nucl. Instrum. Methods **B62**, 23

Shulga VI, Vicanek M and Sigmund P, 1989: Phys. Rev. **A39**, 3360

Sigmund P, 1969: Phys. Rev. **184**, 383

Sigmund P, 1974: Appl. Phys. Letters **25**, 171

Sigmund P, 1975: Appl. Phys. Letters **27**, 52

Sigmund P, 1977: *Inelastic Ion Surface Collisions*, eds. Tolk NH et al. (Academic Press, New York) 121

Sigmund P, 1981: *Sputtering by Particle Bombardment I.*, ed. Behrisch R, (Springer, Berlin-Heidelberg) 9

Sigmund P, 1987: Nucl. Instrum. Methods **B27**, 1

Sigmund P, 1989: Journ. de Physique **50**, C2, 175

Sigmund P, 1993: Mat. Fys. Medd. Dan. Vid. Selsk. **43** 7

Sigmund P and Claussen C, 1981: J. Appl. Phys. **52**, 990

Sigmund P and Szymonski M, 1984: Appl. Phys. **A33**, 141

Stansfield RA, Broomsfield K and Clary CL, 1990: Phys. Rev. **B39**, 7680

Szymonski M, 1984: Nucl. Instrum. Methods **B2**, 583

Szymonski M. and de Vries AE, 1977: Phys. Letters **63A**, 359

Szymonski M and Postawa Z, 1990: Appl. Phys. **A50**, 269

Szymonski M, Bhattacharya RS, Overeijnder H and de Vries AE, 1978: J. Phys. D: Appl. Phys. **11**, 751

Takagi T and Yamada I, 1989: *Ion Beam Assisted Film Growth*, ed. Itoh T, (Elsevier, Amsterdam) 253

Tersoff J, Denier van der Gon, AW and Tromp RM, 1993: Phys. Rev. Letters **70**, 1143

Thomas JP, Filpus-Myuckx PE, Fallavier M and Schweikert EA, 1985: Phys. Rev. Letters **55**, 103

Thomas JP, Oladipo A and Fallavier M, 1988: Nucl. Instrum. Methods **B32**, 354

Thompson DA, 1980: *Proc.Symposium on Sputtering*, eds. Varga P et al. (Inst.allgem.Physik, Wien) 62

Thompson DA, 1981a: Radiat. Eff. **56**, 105

Thompson DA, 1981b: J. Appl. Phys. **52**, 983

Thompson DA and Johar SS, 1979: Appl. Phys. Letters **34**, 342

Thompson DA and Johar SS, 1981: Radiat. Eff. **55**, 91

Thompson MW, 1968: Phil. Mag. **18**, 377

Thompson MW, 1987: Nucl. Instrum. Methods **B18**, 411

Thum F and Hofer WO, 1979: Surf. Sci. **90**, 331

Townsend P D, 1983: *Sputtering by Particle Bombardment II.*, ed. Behrisch R, (Springer, Berlin-Heidelberg) 147

Urbassek HM and Michl J, 1987: Nucl. Instrum. Methods **B22**, 480

Usui H, Tanaka M, Yamada I and Takagi T, 1989: Nucl. Instrum. Methods **B37/38**, 886

Vandenbosch R, Trainor TA, Will DI, Neubauer J and Brown I, 1991: Phys. Rev. Letters **67**, 3567

Vandenbosch R, Ye D, Neubauer J, Will DI and Trainor T, 1992: Phys. Rev. **A46** (1992) 5741

Wittmack K, 1979: Surf. Science **90**, 557

Xu Guo-Qin, Holland RJ, Bernasek SL and Tully JC, 1989: J. Chem. Phys. **90**, 3831

Yamamura Y, 1988: Nucl. Instrum. Methods **B33**, 493

Yamamura Y, 1990: Nucl. Instrum. Methods **B45**, 707

Yamamura Y and Muramato M 1992: Phys. Rev. Letters **69**, 1463

Zalm PC and Beckers LJ, 1984: Philips Journ.Res. **39**, 11

Desorption Experiments on Organic Insulators with Low-Energy Particle Beams

By W. Ens
Department of Physics, University of Manitoba
Winnipeg, Canada R3T 2N2

Synopsis

Experimental investigations into the fundamentals of the desorption of thermally labile molecular ions by low-energy (~ keV) particle bombardment of organic solids or liquids are summarized, with some comparisons to high-energy (~ 100 MeV) bombardment. The influence of the primary-ion parameters and of the target properties on the mass spectrum, molecular-ion yield, and secondary-ion dynamics are considered. There is a remarkable similarity in the mass spectra and the degree of fragmentation for various bombarding conditions and for various types of target. At the same time higher molecular-ion yields and a higher mass range are observed for higher mass and energy of the incident particle. A higher mass range and less metastable decay is observed for samples dissolved in liquid glycerol or applied to nitrocellulose compared with samples applied to a metal substrate or with solid bulk sample. The damage resistance provided by a liquid matrix like glycerol is examined, and the importance of the high transmission provided by time-of-flight spectrometers in comparisons between liquid and solid (non-renewing) surfaces is emphasized.

Contents

1 Introduction

The application of mass spectrometry in analyzing non-volatile organic compounds has historically been limited by the difficulty in producing gas phase molecular ions from the compounds of interest. An important advance in this regard was realized by the application of energetic particle bombardment as a soft-ionization technique to eject molecular ions directly from the condensed phase. Particle induced desorption extended the accessible mass range in analytical mass spectrometry of biomolecules to a few tens of thousands of u. Variations of the method are now routinely applied in two distinctly different energy regimes: the particles may have energy on the order of 100 MeV (about 1 MeV/u) or on the order of 10 keV (near 100 eV/u). While new techniques like matrix-assisted laser desorption (Karas, 1993) and electrospray ionization (Fenn et al., 1990) are now more effective in the very-high-mass range, particle-induced desorption continues to play a role in the mass range up to a few thousand u.

The ejection of complex fragile molecules from a solid or liquid is a remarkable consequence of a high local energy density produced by energetic particle bombardment, and there is considerable interest in understanding the process. This paper summarizes the main experimental investigations of the fundamentals of organic molecular ion desorption with low-energy particle beams, but frequent reference is also made to relevant experiments with high-energy beams. The emphasis is on the results of physical measurements of the influence of various experimental parameters, with some discussion of their interpretation to unify the presentation. This summary focuses mainly on the desorption of biomolecules represented by peptides or amino acids although other types of organic compound are also considered.

There are a number of reviews concerning molecular-ion desorption by particle bombardment, and the proposed mechanisms involved (Sundqvist, 1991; De Pauw, 1986; De Pauw et al., 1991; Pachuta & Cooks, 1987; Colton et al., 1986; Benninghoven et al. 1987). In most of these, summaries of experiments with low-energy beams emphasize the effects of the target properties. Here experiments measuring the influence of the primary-ion properties on observables such as the mass spectrum, molecular-ion yield and secondary-ion dynamics are considered in some detail. The influence of some properties of the target, particularly its physical properties are then outlined.

2 Background

2.1 Historical Survey

In order to classify the various particle-induced desorption experiments, it is useful to give a brief account of the major developments that led to significant improvement in the mass spectrum obtainable by particle bombardment methods. The application of particle bombardment to produce molecular ions from non-volatile organic material was first demonstrated by Macfarlane and Torgerson (1976a; Torgerson et al. 1974) using fission fragments from ^{252}Cf ; i.e with high-energy particles of mass $\sim$ 100 u and energy of $\sim$ 100 MeV. Time-of-flight mass spectrometry was an essential component of that experiment (originally designed to measure the mass of short-lived radioactive atoms) because it offered high sensitivity to offset the practical limitations in the flux of the fission fragments. The use of time-of-flight proved to be fortuitous for organic mass spectrometry because it does not present a fundamental limitation in mass range, and the very early papers reported molecular ions desorbed from bulk samples of biomolecules with molecular mass close to 2000 u including vitamin B12 (1355 u) (Macfarlane and Torgerson, 1976b). The technique was named plasma desorption mass spectrometry (PDMS) because of the plasma associated with a fission fragment as it interacts with matter.

The mass range in PDMS with thick (multilayer) sample deposits on a conducting target foil, was gradually extended to more than 20 000 u by 1984 (Sundqvist et al., 1984). It was extended further and the signal-to-background ratio was improved with the introduction of an appropriate polymer as a substrate. Jordan et al. (1983) demonstrated improvement in the mass spectra obtained with PDMS when the sample was deposited onto nafion, and Jonsson et al. (1986) showed dramatic improvement in the mass spectra and mass range for proteins adsorbed to nitrocellulose. Molecular ions up to about 45 000 u have been observed with this method (Jonsson et al. 1989a).

Production of ions by fission fragment bombardment couples naturally with time-of-flight because it avoids two of the problems previously associated with time-of-flight. The fission process is well defined in time and the recoiling fragment may be used as a start signal, so the acceleration field may be held at a high, stable dc potential, instead of being pulsed. Secondly, since the ions are ejected directly from a solid equipotential surface, the energy and spatial spread is much smaller than for traditional gaseous ion sources. As a result PDMS contributed to a renewal of interest in time-of-flight relevant to other desorption methods including low-energy ion bombardment; the interest in time-of-flight continues to increase rapidly (Voress, 1992).

Soon after the observation of molecular-ion desorption induced by high-energy particle bombardment, Benninghoven et al. (1976) showed that for somewhat smaller molecules like amino acids, similar results could be obtained using secondary-ion mass spectrometry (SIMS) with primary particles of much lower energy. This technique was first demonstrated using 2 keV Ar^+ ions incident on thin layers (approximate monolayer equivalents) of sample on a metal substrate. The mass spectra were acquired with a magnetic-sector mass spectrometer. To avoid sample damage, which results in the loss of molecular-ion signal, it was necessary in those experiments to keep the primary ion current very low ($\sim$ nA/cm^2), in a method called static SIMS. This method however produces rather low secondary-ion current and the current becomes smaller for increasing molecular mass. Because of transmission losses and losses due to scanning the mass spectrum in sector-field instruments, the mass range was limited to biomolecules of a few hundred u.

To overcome the limitation imposed by the low secondary-ion current for larger molecules, groups at Manitoba (Chait & Standing, 1981) and Münster (Steffens et al., 1985) developed low-energy pulsed ion guns to take advantage of the high sensitivity and mass range of time-of-flight as had been demonstrated for PDMS. In 1980 the Manitoba group reported time-of-flight measurements of molecular ions of vitamin B12 ejected from a thick (bulk) sample by 5 keV Cs^+ bombardment (Standing et al., 1980; Ens et al., 1981). The highest mass polypeptide observed with this technique, using nitrocellulose as a substrate, is now about 14 000 for peptides (Ens et al., 1988a). A number of direct comparisons have shown that for an insulating target (either multilayer or nitrocellulose substrate) the spectra of many biomolecules like peptides obtained with keV ion bombardment are closely similar to spectra obtained with MeV bombardment (Ens et al., 1981; 1988a; 1988b; Lafortune et al., 1987).

A major advance in low-energy particle-induced desorption resulted from an alternative solution to the problem of low or transient secondary-ion currents. Barber et al. (1982a) demonstrated that high secondary molecular-ion currents could be sustained if the sample was dissolved in a viscous liquid like glycerol and bombarded with an incident-particle beam density typical of dynamic SIMS ($\gtrsim 10^{-5}$ A/cm^2). While the detailed mechanism is not understood, it is apparent that the matrix allows continuous renewal of the sample at the surface. The liquid matrix was introduced together with the introduction of a neutral atom gun (Surman & Vickerman, 1981; Barber et al., 1981) and the combined technique was called fast atom bombardment (FAB), though 'liquid SIMS' is often used, especially when the primary beam is charged. The neutral incident beam made coupling to existing sector-field and quadrupole spectrometers straight-forward, and the liquid matrix provided the sustained current required in such spectrometers. As a result FAB quickly became widespread as a routine method for organic mass spectrometry. The early results demonstrated a mass range up to about 3000 u (Barber et al., 1982a), and soon after, reports of the observation of molecular ions of insulin ($\sim$ 5700 u) appeared (Barber et al., 1982b; Dell & Morris, 1982); the largest molecular ion observed by FAB is trypsinogen (23 978 u) (Barber & Green, 1987). However, the very-high-molecular-mass compounds require rather specialized instruments and procedures so routine FAB analysis has been confined mainly to a mass range of a few thousand u.

2.2 Mass Spectrometry Methods

The survey above shows that the type of mass spectrometry used in desorption experiments can have important implications in the interpretation of the data. Of central importance is efficient transmission through the mass spectrometer because, in desorption from organic solids, there is usually a competition between sample damage and desorption of intact molecular ions. Other relevant properties include mass range, mass resolution and transit times. In the following a largely qualitative comparison of these properties, as relevant to the experiments summarized in this paper, is presented for magnetic-sector (deflection), quadrupole and time-of-flight mass spectrometers. Detailed treatment of the instrumentation in secondary ion mass spectrometry can be found in Benninghoven et al. (1987).

2.2.1 Scanning and Non-Scanning Instruments

Transmission efficiency is significantly limited in most mass spectrometers because the spectrum is acquired by scanning. A scanning mass spectrometer acts as a mass filter transmitting or detecting ions with a very narrow range of m/z at a given time; the instrument is adjusted to scan over the desired m/z range. The alternative to scanning is parallel detection, where in principle, all the ions (at least within a wide range of m/z) that enter the spectrometer are detected. The value of m/z for the detected ions is determined from their dispersion in space or time. A position sensitive detector (or photographic plate) used with a magnet-sector instrument is an example of parallel detection. The losses resulting from scanning the mass spectrum depend on the resolution and the mass range to be scanned; typically it is two to four orders of magnitude less efficient than parallel detection.

2.2.2 Deflection Instruments

The most common type of mass spectrometer used to analyze molecular ions desorbed by low-energy particle bombardment (mainly FAB) is the sector-field instrument, in a variety of geometries involving magnetic and electric fields. It normally provides unit mass resolution over the accessible mass range, and discriminates against background ions giving clean, easily interpreted spectra. As mentioned, the spectrum (or segments of it) can be acquired with parallel detection, but for practical reasons, nearly all commercial analytical instruments use scanning.

In addition to losses that result from scanning, the overall efficiency is limited by transmission losses in the spectrometer, particularly the source. There is a simple tradeoff between efficiency and resolution depending on the width of the principal (source) slit. Typically fewer than 1 % of the ions produced by desorption reach the detector plane.

The mass range of a sector-field instrument is determined by the maximum radius of the motion, R, (i.e. the size of the magnet), the magnetic field strength, B, and the acceleration voltage for the ions, V, according to the equation $m/q = R^2B^2/2V$. Commercial instruments designed for electron impact sources typically had a mass range of less than 1000 u at full (optimum) acceleration voltage. The mass range can be increased by reducing the voltage but at the expense of transmission and resolution. Detection efficiency also deteriorates at lower energies unless post-acceleration is used. Newer spectrometers used in FAB experiments are designed with larger, high-field magnets and typically have a mass range of $\sim$ 3000 u at full acceleration voltage; and up to 10 000 u with more expensive instruments.

Ions must remain intact throughout their transit through a magnetic- sector spectrometer ($\sim$ 100 μs) to be observed at the correct mass, so only relatively stable ions contribute. However, the extraction time from the source is relatively slow, so the mass spectrum represents ions formed on a rather long time scale ($\sim \mu$s) which could include product ions formed by metastable decay early in the source. The rate of metastable decay of the secondary ions can therefore have a strong influence on the mass spectrum (Ens et al., 1983).

Some of the disadvantages of a magnetic instrument are avoided with a Wien filter which can in a sense be considered a deflection instrument. It uses crossed magnetic and electric fields to select ions on the basis of velocity. The instrument provides high transmission and does not have a fundamental mass limit so high acceleration voltage can be used. Moreover, it provides mass dispersion over a small range so parallel detection can be used over a small segment of the spectrum.

2.2.3 Quadrupole Instruments

Quadrupole mass filters are compact, inexpensive instruments that use ac and dc quadrupole electric fields which allow stable trajectories for a narrow range of m/z; mass spectra must be acquired by scanning. The instrument typically gives modest mass resolution, and has low transmission ($< 10^{-3}$) for ion sources with dimensions $\sim$ 1mm. The mass range is usually restricted to $m/z \lesssim 1000$ in most instruments. For a given instrument mass resolution, mass range and transmission are strongly coupled; improvements in one aspect require compromises in the others. While quadrupole mass spectrometers are extremely common in applications with low m/z, they have not been widely used with particle bombardment sources (FAB) for analysis of organics.

2.2.4 Time-of-Flight

Time-of-flight (TOF) mass spectrometry has important advantages for studying desorption of molecular ions from solids. Since slits are not required, the instrumental transmission can be near unity, limited only by the transparency of a few grids. Also, parallel detection over the entire mass range is possible with readily available electronics. Thus the overall efficiency is better than that of scanning sector-field or quadrupole instruments by a factor of more than 10^4 . Secondly, there is no restriction on the mass range imposed by the spectrometer; only ion production and detection limit the mass range. Both high transmission and high mass range are realized in TOF without practical complications or compromise in other aspects of its performance.

In a simple linear spectrometer, ions need only remain intact during acceleration to contribute to the spectrum at their original mass; any decay after acceleration simply causes peak broadening. Metastable decay during acceleration causes a continuous background. In most instruments extraction from the source is fast ($\sim$ 100ns) so that the spectrum represents the ion population at a very short time after production. This is not the case in the instrument of Olthoff and Cotter (1987) which uses a low field and delayed extraction, allowing the use of a liquid matrix.

The lack of discrimination against background ions (including products of metastable decay) in a linear TOF instrument is its main disadvantage. The high background limits the dynamic range and reduces the efficiency. Peak broadening caused by metastable decay severely limits the resolution for most organic molecules larger than few hundred u . For smaller, stable ions (including small peptides) mass resolution is often limited by the axial velocity spread. The velocity spread of ions accelerated from a plane equipotential source is small compared to the velocity acquired from acceleration, and a resolution $M/\Delta M_{\mathrm{FWHM}} \sim 3000$ can be achieved in a linear spectrometer (Ens et al., 1986).

The axial velocity distribution can be largely compensated, and some discrimination against background ions (and neutrals) can be achieved with an elecrostatic mirror. (There are other methods of velocity compensation, but a mirror is the most common.) A number of groups have reported mass resolution higher than 10000 with reflecting TOF instruments, for small ions produced by particle-induced desorption (Niehuis et al., 1986; Tang et al., 1988, Brinkmalm et al., 1992); adjacent isotpic peaks can be resolved for organic molecular ions up to about 3000 u (Tang et al., 1989).

2.3 General Features of Molecular-Ion Desorption

In the subsequent sections, the influence of various experimental conditions on the desorption of molecular ions is summarized. Some basic characteristics of desorption with keV bombardment are outlined here to introduce some relevant concepts.

Mass spectra produced by keV bombardment of organic targets are characterized by peaks due to protonated or cationized positive molecular ions, or deprotonated negative molecular ions. For smaller molecules ($<$ 2000 u), characteristic fragment ion peaks are also observed but with considerably lower intensity. The molecular-ion yield (defined as the number of intact molecular ions desorbed from the surface per incident particle) for amino acids, is in the range of 0.1 - 10 % for 10 keV Cs^+ bombardment. The yield tends to decrease for larger sample molecules.

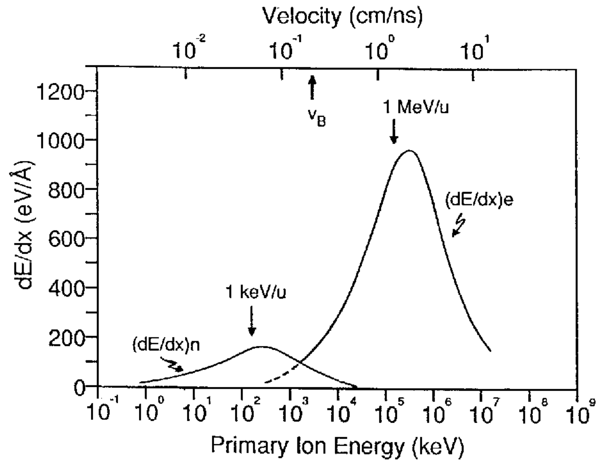

Figure 1. Nuclear and electronic stopping powers for ^{127}I on a solid of a model protein C_3H_5NO with a density of 1 g/cm^3 (Sundqvist, 1991; the nuclear energy loss was calculated using Eq. 2.2.1 in Sigmund (1969) with a Lenz-Jensen potential; the electronic stopping powers were taken from data tables (Ziegler, 1980)).

In addition to desorption, bombardment causes damage to the sample molecules and consequently a disappearance of the molecular-ion signal. The damage or disappearance cross-section, σ, is given by the equation $Y(\Phi) = Y(0)\exp(-\sigma\Phi)$ where $Y(\Phi)$ is the yield after an incident-particle fluence Φ (for low fluence). For a solid target, σ represents the area damaged by a single incident particle. The damage cross-section for amino acids bombarded by Ar^+ ions of a few keV is $\sim 10^{-14}$ cm^2 (Lange et al., 1984). Larger molecules tend to have larger damage cross-sections.

The sensitivity of mass spectrometric analysis depends on both the molecular-ion yield and the damage cross-section. The minimum amount of sample required to obtain a spectrum from peptides with mass $\sim$ 1000 u is in the range of 10 fmoles with a TOF spectrometer. In a scanning instrument, hundreds of pmoles are typically required. Since the damage cross-section increases with sample molecular mass, and the yield decreases with mass, the sensitivity rapidly becomes worse for larger molecules. The accessible mass range for samples in a glycerol matrix is about 24000 u; for a nitrocellulose substrate it is about 14000 u, with Cs^+ ion bombardment.

It is clear from the degree of metastable decay observed in time-of-flight instruments that molecular ions desorbed by particle bombardment are highly excited.

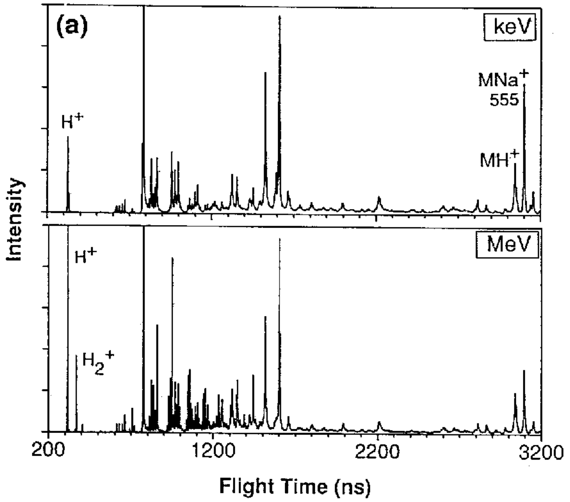

Figure 2a. Positive ion time-of-flight mass spectra of leucine enkephalin (555 u). The upper spectra were produced by 18 keV Cs^+ ion bombardment; the lower were obtained with ^{252}Cf fission fragment bombardment. In the MeV spectrum, the H^+ peak is off scale by a factor of about 3. The target was electrosprayed to give a multilayer sample. The spectra were acquired in the same spectrometer from the same target, without interrupting the vacuum between measurements. The data were acquired in a comparison experiment in Uppsala (Ens et al., 1988a).

Depending on the molecule and sample conditions, the number of molecular ions that decay during their flight time varies widely from a few per cent to nearly 100%. Kinetic energy distributions of small desorbed molecular ions are about 1 to 2 eV in width, considerably narrower than for desorbed atomic ions as might be expected.

3 Influence of the Incident-Particle Properties

Sputtering of material under particle bombardment is a rather mature field and the influence of incident-particle parameters such as mass, energy, charge state and angle of incidence has been studied in considerable detail (Behrisch, 1981; 1983; Behrisch & Wittmaack, 1991) ; many aspects of sputtering by particles in the keV energy range are well described by Sigmund's theory (1969, 1981). In contrast, systematic studies of the ejection of large molecular ions by keV particle bombardment as a function of bombarding conditions are scarce; studies of neutral molecule emission are scarcer still. Here the main results that have been obtained

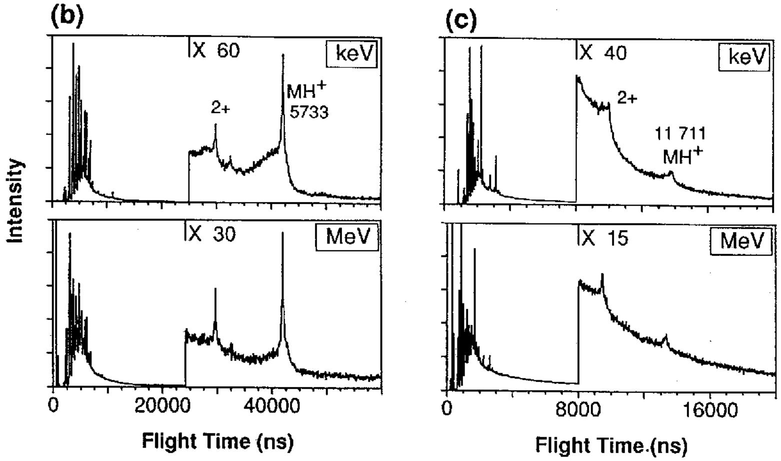

Figure 2b,c. Same as fig. 2a for (b) bovine insulin (5733 u) and (c) PSP (11711 u). The targets were prepared by depositing approximately one monolayer onto nitrocellulose.

in such experiments are summarized. Briefly, the nature of the mass spectrum is only weakly dependent on the incident-particle properties but the molecular-ion yield and the mass range have a strong dependence. The observation that the molecular-ion yield increases with the mass and energy of the incident particle, has given rise to the frequent assumption that the dependence of the molecular-ion yield on the bombarding conditions is similar to the dependence of the total sputtering yield.

The experimental results are often interpreted in terms of the energy loss of the incident particle per unit length, or the stopping power (dE/dx). The stopping power has two components which dominate in different velocity regimes above and below the Bohr velocity ($v_{\mathrm{B}} = 0.22$ cm/ns) as shown in Fig. 1. For low-energy bombardment typical of SIMS or FAB ($\sim$ keV/u) energy is lost mainly by nuclear stopping $(dE/dx)_{\mathrm{n}}$, whereas for high-energy bombardment typical of PDMS ($\sim$ MeV/u) electronic stopping $(dE/dx)_{\mathrm{e}}$ is dominant.

3.1 Secondary-Ion Mass Spectra

The dependence of the secondary-ion mass spectrum on the primary-ion mass and energy has been considered by various groups. Several experiments have shown that the amount of fragmentation decreases with increasing energy or mass of the incident projectile in the keV range (Barber et al. 1980; Standing et al., 1982; Buko et al., 1983; Amster et al., 1987; Winger et al., 1988; Hand et al., 1990; Hamdan et al., 1992). This appears to be the case, regardless of the type of target preparation used, and whether the target is liquid or solid. However, the effect is not dramatic, and as recently pointed out, a rather large change in the energy of Cs^+ projectiles from 2 to 35 keV in experiments with liquid targets, does not introduce different fragmentation channels and the relative intensities of different ions do not typically vary by more than a factor of two (Hamdan et al., 1992). In some cases, the observed mass spectrum was almost independent of primary-ion mass or energy (Kambara, 1982; Hoogerbrugge, 1988). No significant effects on the nature of the mass spectrum have been demonstrated for other primary ion parameters such as charge state and angle of incidence. The insensitivity of the mass spectrum to primary bombarding conditions is demonstrated dramatically in the comparisons of the mass spectra obtained with keV and MeV bombardment (Ens et al., 1981; 1988a; 1988b; Lafortune et al., 1987). Fig. 2 shows the mass spectra of leucine enkephalin (555 u), bovine insulin (5733 u) and PSP (pancreatic spaholytic peptide, 11711 u) obtained in Uppsala with high- and low-energy bombardment (Ens et al., 1988a). The mass spectra for the two bombarding energies were acquired in the same linear time-of-flight mass spectrometer using the same target without interrupting the vacuum between measurements. The relative intensities of the sample related ions are almost identical for the two bombarding energies. Moreover, even the background which is associated with metastable decay, is similar in the two cases. This similarity is remarkable considering that the dominant mode of energy loss for projectiles in the two energy ranges is fundamentally different as shown in Fig. 1. The difference in the energy loss mechanisms is reflected by the relative intensity of H^+ which is off-scale by about a factor of 3 in each of the MeV spectra in Fig. 2; H^+ emission is associated with electronic stopping power (Della-Negra et al., 1988). Similarly Fig. 3 shows a pronounced contrast in the relative intensity of atomic ions like H^-, C^-, O^- and F^- which are characteristic of nuclear sputtering compared to more complex ions like CN^- and $C_2H_7^-$ which are associated with electronic sputtering as well (Hunt et al., 1989; Salehpour et al., 1989). Not all organic compounds give mass spectra as similar for keV and MeV bombardment as the compounds studied by Ens et al. (1981; 1988a; 1988b) and Lafortune et al. (1987). For example crystal violet, coronene (Della-Negra et al., 1989) and some organic polymers (Hagenhoff et al., 1990) appear to behave differently, and moreover, the similarity in the spectra does not generalize to thin layers of sample deposited on metal substrates (Ens et al., 1988a). Still, the similarity in the mass spectra for many insulating organic targets under a wide range of bombarding conditions suggests that the desorption process is an indirect result of the primary excitation, and that a model of desorption ionization should accomodate these very different energy deposition conditions. A distinction is often made between surface

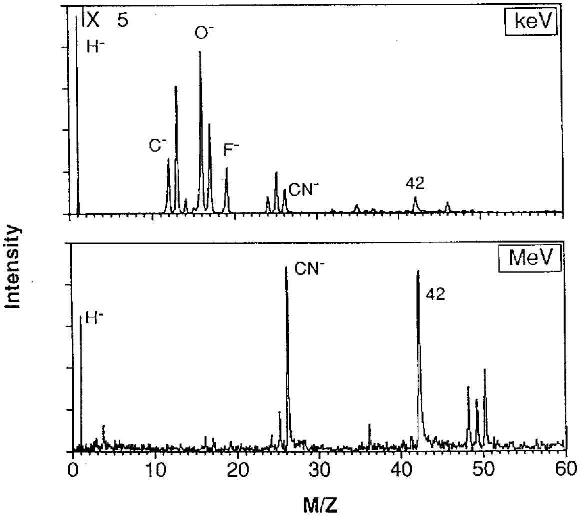

Figure 3. The low-mass range of negative ion time-of-flight mass spectra of leucine enkephalin (multilayer sample) obtained with 18 keV Cs^+ bombardment (upper) and with fission fragment bombardment (lower) (Ens et al., 1988a).

desorption mechanisms and bulk desorption mechanisms, identifying static SIMS with the former and liquid SIMS or FAB, and PDMS with the latter. However, it seems unlikely that fundamentally different mechanisms for static SIMS and PDMS could produce mass spectra with the degree of similarity demonstrated in Fig. 2.

3.2 Molecular-Ion Yields

3.2.1 Angle of Incidence

An increase in the angle of incidence from the normal, results in more energy deposited near the surface and in a higher sputtering yield (Andersen & Bay, 1981) as well as a higher molecular-ion yield (Martin et al., 1982). As the primary-particle direction approaches glancing incidence, the yield reaches a maximum and then decreases rapidly, because of an increase in the reflection coefficient, and because collision cascades near the surface are interrupted because of emission of high-energy recoils (Sigmund, 1969). For desorption of organic molecular ions from a glycerol matrix by 7 keV Xe bombardment, Martin et al. (1982) found a maximum yield for an incident angle of about 60° , although 70° degrees seems to be commonly used, presumably after optimization (Barber et al., 1982a). Szymcak & Wittmaack (1989) found an optimum angle of about 75° for desorption of vitamin

B1 from a solid multilayer target.

From a simple geometric argument, the amount of energy deposited in a given depth below a target surface, by an incident particle should have a $\cos^{-1}\theta$ dependence, for small angles of incidence, θ. A more detailed treatment by Sigmund (1969), taking account of energy transport of high-energy recoil atoms, indicates that for primary ions in the keV range the exponent varies from -1 to -2/3 depending on the target/ion mass ratio. The dependence of the molecular-ion yield on the angle of incidence can be used to gain some insight as to how the yield depends on the deposited energy. For solid multilayer samples of vitamin B1, the yield was found to have a $\cos^{-2}\theta$ dependence (Szymcak & Wittmaack, 1989).

3.2.2 Charge State of the Incident Particle

The technique introduced as 'fast atom bombardment' is distinguished mainly by the use of a liquid sample matrix such as glycerol, although initially the neutrality of the incident beam was emphasized (Surman & Vickerman, 1981; Barber et al., 1981). However, as widely expected, the presence of a single charge on the incident particle was not found to have an influence on the desorption process for organic molecular ions (Aberth et al., 1982), although a neutral beam has practical advantages.

Della Negra et al. (1988) have studied the influence of a wide range of charge states in keV bombardment of organic solids. No charge state dependence was observed for the yield of molecular ions of valine (or for most other positive ions) when bombarded with argon ions varying in charge state between 1^+ and 11^+. In contrast, the H^+ ion emission was found to be strongly dependent on the incident charge state. The results were interpreted as evidence that electronic processes do not play a significant role in the desorption of organic molecular ions by keV particles, but are largely responsible for H^+ emission. The charge state has a strong influence on molecular-ion yields from high-energy particle bombardment (e.g. Wien et al., 1987; Håkansson, 1993), where electronic sputtering is dominant.

3.2.3 Primary-Ion Mass and Energy

The yields of positive molecular ions of the amino acid alanine (desorbed from bulk sample) were measured by Standing et al. (1982) for incident alkali metal ions Li^+, Na^+, K^+ and Cs^+ in the energy range between 1 and 14 keV. The results, are shown in Fig. 4a plotted against the primary-ion energy. A number of other measurements in this energy range have been reported for ions or atoms incident on solids (Kambara, 1982; Benninghoven, 1983a; Amster et al., 1987; Hand et al., 1990; Zhou et al., 1992a) and liquids (Martin et al., 1982; Aberth & Burlingame, 1988; Yen et al., 1992). In general these results are qualitatively

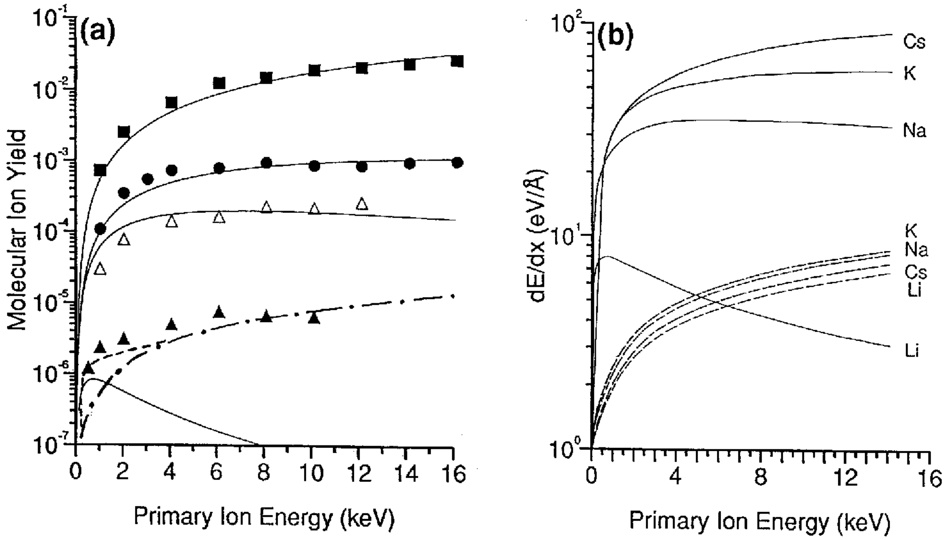

Figure 4. a) Yields of $[M + H]^+$ secondary ions from alanine produced by Cs^+ (filled squares), K^+ (filled circles), Na^+ (empty triangles) and Li^+ (filled triangles) primary ions at an incident angle of about 20° (Standing et al., 1982). The scale gives an upper limit on the absolute yield. The solid curves are proportional to $(dE/dx)_n^3$ with separate normalization for each projectile.The dot-dash curve is proportional to $(dE/dx)_e^2$ for Li. The dashed curve is a linear combination of $(dE/dx)_n^3$ and $(dE/dx)_e^2$. b) Calculations of the nuclear (solid curves) and electronic (dashed curves) stopping powers at the surface of an alanine target for incident alkali ions, using the "average" parameters quoted in Wilson et al. (1977). The curves were presented in Standing et al. (1982) but an error in the electronic stopping curves has been corrected here.

consistent with the results of Fig. 4a in that the yields increase with the mass and energy of the incident atomic ions and tend to saturate at higher incident energies. In particular, the strong dependence on the primary-particle mass in Fig. 4a, is in good agreement with the measurements of Martin et al. (1982) of the yield of molecular ions of leucine enkephalin and bradykinin from a liquid matrix. They found the yield with Xe bombardment to be about 30 times higher than with Ne bombardment at the same energy, although the spectrum did not change significantly. A similar factor is observed in Fig. 4 between the yields measured with Na^+ and Cs^+ bombardment. In one measurement of the molecular-ion yield as a function of primary energy, the yield was found to decrease for Cs^+ ion bombardment above about 20 keV (Aberth & Burlingame, 1988), but this appears to be inconsistent with the observation that the mass range is higher for 35 keV Cs^+ projectiles than for 10 keV projectiles (Barber & Green, 1987), and with a

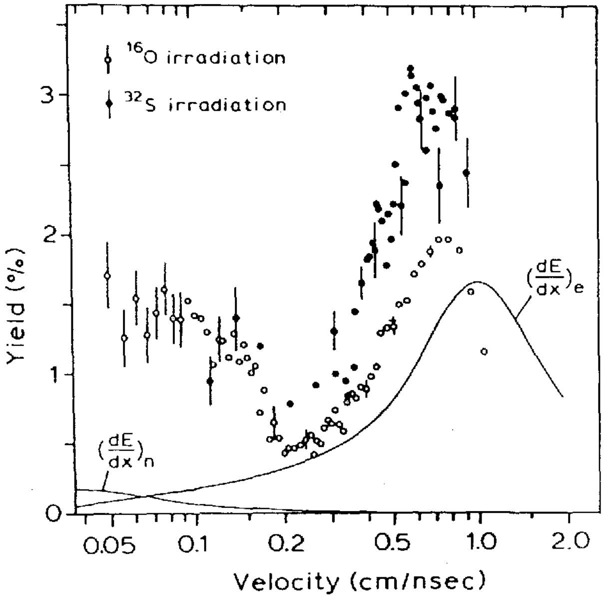

Figure 5. Yields of $[M + H]^+$ ions from a valine target as a function of the velocity of the primary ^{16}O and ^{32}S ions. Curves corresponding to the electronic and nuclear stopping powers are also shown (Albers et al., 1982).

recent comparison between 8 keV Cs^+ bombardment and 28 keV I^- bombardment which showed a dramatic enhancement by a factor of about 10 in the yield of bovine insulin with the higher energy I^- projectile (Zhou et al., 1992a).

Some comparisons of absolute molecular-ion yields for keV and MeV bombardment have also been made (Kamensky et al., 1982; Ens et al., 1988a; Della-Negra et al., 1989). The absolute yield in both methods depends strongly on the type of sample and target used, as described in section 4.4.3, and on the primary energy as described above. Here we mention only the dependence of the yield on the difference in primary energy for MeV and keV bombardment. Although the mass spectra are similar, the absolute molecular-ion yield for amino acids or small peptides (less than 1000 u) ejected from thick insulating targets is about an order of magnitude higher for bombardment with ^{252}Cf fission fragments (yield ~ 10%) than for typical primary bombardment conditions in SIMS (~ 10 keV Cs^+).

3.2.4 Molecular-Ion Yields and Stopping Power

It is well established that for high-energy particle bombardment, the electronic stopping power is responsible for the observed molecular ion desorption (Håkansson & Sundqvist, 1981; Dück et al., 1981; Håkansson et al., 1984; Becker et al., 1986; Della-Negra et al., 1987). The molecular-ion yields do not depend on the electronic stopping in any simple way, but for small molecules like valine, and for velocities below the maximum in stopping power, the yield scales rather closely with $(dE/dx)^2_{\mathrm{e}}$ (Becker et al., 1986).

In the case of low-energy bombardment the situation is less definite. The dependence of the molecular-ion yield on electronic stopping for MeV bombardment, and the similarity in the spectra for high- and low-energy bombardment have led to the suggestion that the desorption at low energy is related to the low-energy tail of the electronic stopping power curve. However some experimental results indicate that nuclear stopping is responsible at the lower energies.

Albers et al. (1982) have measured the positive secondary molecular ion yield for valine irradiated by ^{16}O and ^{32}S as a function of velocity in the region where the electronic and nuclear stopping curves cross. The results are shown in Fig. 5. The increase in the yield below 0.2 cm/s is interpreted as a result of the increasing nuclear stopping in that range. The velocity in these measurements is not typical of the velocity used in low-energy bombarding experiments, but they appear to indicate that both nuclear and electronic stopping can be effective in desorption of molecular ions, and that at least under some conditions nuclear stopping appears to be more effective than electronic stopping in this regard.

The results of Standing et al. (1982) shown in Fig. 4a for ion energies more typical of low-energy bombardment experiments, were compared to calculations of the nuclear and electronic stopping curves in that region (Fig. 4b). The curves were calculated using the Lindhard theory (Lindhard et al., 1963) as modified by Wilson et al. (1977). From the qualitative similarity of the yield dependence on projectle mass and the dependence of the nuclear stopping on mass, the authors concluded that nuclear stopping is primarily responsible for the desorption of molecular ions of alanine by the projectiles Na$^+$, K$^+$ and Cs$^+$ at keV energies.

The yield data for the 3 larger projectiles show a rather close fit to $(dE/dx)^3_{\mathrm{n}}$ shown as solid curves in Fig. 4a. The curves are normalized separately for each projectile but the normalizations are all within a factor of 2 of the average. In the case of the Li$^+$ projectile, the behaviour of the yield data is clearly described better by the electronic stopping than by the nuclear stopping as has been pointed out by Sundqvist (1991). However a linear combination of $(dE/dx)^3_{\mathrm{n}}$ and $(dE/dx)^2_{\mathrm{e}}$ gives a still better fit. Even so, the results suggest that when the magnitude of the nuclear and electronic stopping are comparable in this velocity range, electronic

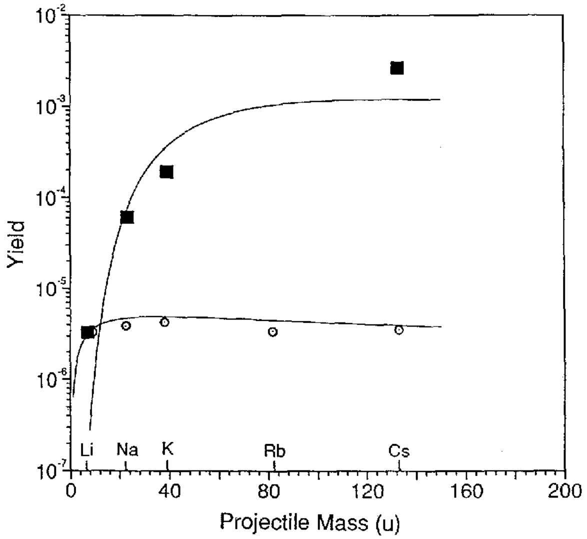

Figure 6. Measured yields of $[M + H]^+$ ions from alanine (filled squares) for 10 keV primary ions (Standing et al., 1982) and relative yields of electrons from Al_2O_3 (circles) for 21 keV primary ions (Mosshammer and Matthäus, 1989), as a function of the primary-ion mass of the incident alkali projectiles at a constant energy. The electron yields were normalized to coincide with the alanine yield for the Li^+ projectile. The curves are calculations of $(dE/dx)_n^3$ normalized at Na^+ and $(dE/dx)_e^2$ normalized at Li^+.

stopping is more effective, but for the projectiles typically used in SIMS, where nuclear stopping is strongly dominant, it is the nuclear stopping that accounts for the observed molecular ion yield.

This interpretation is more clearly illustrated by plotting the yield as a function of projectile mass for a given energy, as shown in Fig. 6 for 10 keV bombardment. Curves representing $(dE/dx)_n^3$ (normalized at Na^+) and $(dE/dx)_e^2$ (normalized at Li^+) are also shown in the figure. Since the electronic stopping is nearly constant with mass and actually decreases slightly with projectile mass above about 40 u, it cannot account for the dramatic increase in the observed molecular-ion yield. Electron emission is related to the electronic stopping power so the electron yield (renormalized at Li^+) for different incident alkali ions is also shown in Fig. 6. Electron yields were not measured by Standing et al. (1982) so the yields are taken from Moshammer & Matthäus (1989), for 21 keV incident ions and an Al_2O_3 surface. The conditions are different but the data illustrate the approximately constant effect of electronic stopping as a function of mass, for different alkali ions in this energy range.

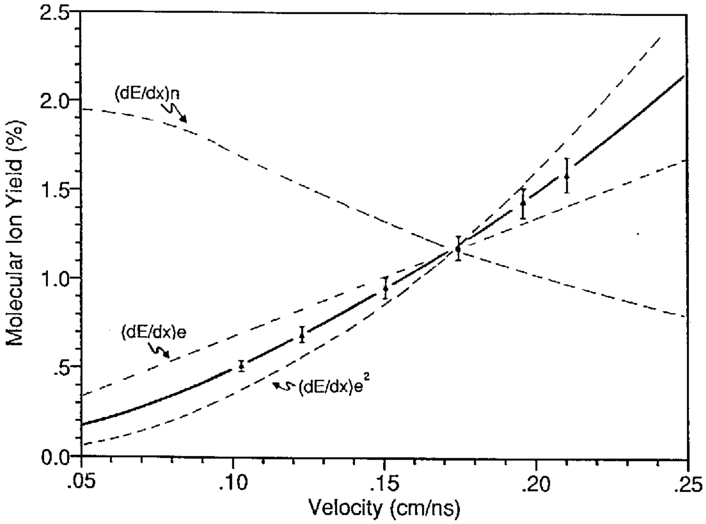

Figure 7. Yield of $[M - H]^-$ ions from valine as a function of the velocity of the incident Xe^+ ions. The dashed lines are calculations of $(dE/dx)_n$, $(dE/dx)_e$ and $(dE/dx)_e^2$ arbitrarily normalized to one of the data points (Salehpour et al.,1989).

More recent measurements of molecular-ion yields as a function of primary-ion velocity by Hunt et al. at Argonne (1989; Salehpour et al., 1989) appear at first to contradict the results of Albers et al. (1982) and those of Standing et al. (1982). The Argonne group reported yield measurements of the negative molecular ion of valine obtained with the projectiles Xe^+, Kr^+ and Ar^+ in the energy range 400 keV to 3.5 MeV where the nuclear and electronic stopping powers have comparable magnitude but opposite slope. In this velocity domain, no significant dependence of the yield on the primary-ion mass for a given energy was observed, in contrast to the situation at low energy (Standing et al., 1982; Martin et al., 1982) (Fig. 6). The independence of the yield on projectile mass, and the measured dependence of the yield on velocity, shown in Fig. 7, provide convincing evidence that in this energy range electronic stopping is mainly responsible for the desorption of negative molecular ions of valine. The data were fit to a function of the form $K(dE/dx)_e^n$, (Hunt et al., 1989; Salehpour et al., 1989) and based on the quality of the fit, the authors concluded that nuclear stopping contributed at most 5 % to the desorption of molecular ions. The values of n obtained in this fit were 1.6, 2.1 and 1.9 for Xe, Kr and Ar respectively. However the function is simply an empirical parameterization and a good fit to the data could also be obtained by assigning a value to n and allowing a contribution from the nuclear stopping power. In particular, if n = 2 is assumed, as is suggested by considerable experimental evidence (Becker et al., 1986), an appreciable contribution from nuclear stopping would be required to fit the data for Xe^+, the projectile for which the nuclear stopping is the highest. A curve proportional to $(dE/dx)_\mathrm{e}^2$ has been added to Fig. 7 to illustrate the required contribution from nuclear stopping in this case.

The stopping power (either nuclear or electronic) may not be the only (or even the main) parameter that determines the yield of molecular ions, and the dependence may well be different at substantially different velocities. Still, with the considerations mentioned above, the Argonne results (Hunt et al., 1989; Salehpour et al., 1989) (Fig. 7) are not inconsistent with the results of Standing et al. (1982) (Fig. 4). In the range where the nuclear and electronic stopping power have comparable magnitude, both experiments indicate that the electronic stopping power is more effective than nuclear stopping in the desorption of organic molecular ions. However, under typical SIMS conditions, nuclear stopping appears to be responsible for molecular-ion desorption.

It is more difficult to reconcile the results of Hunt et al. (1989; Salehpour et al., 1989), with those of Albers et al. (1982), which were obtained with a similar range of primary-ion velocity, but indicate that the nuclear stopping is more effective even when its magnitude is smaller than the electronic stopping. The discrepancy here may be related to the polarity of the molecular ions which was different in the two experiments. Significantly different dependence of the valine $[\mathrm{M + H}]^+$ and $[\mathrm{M - H}]^-$ yields on primary-ion velocity have been observed by Becker et al. (1986) in a somewhat higher velocity range.

The parameterization of the yields in Figs. 4 and 6 with $(dE/dx)_\mathrm{n}^3$ is simply an empirical fit to indicate a correlation. Recent results of Yen et al. (1992) show a quadratic dependence on the total stopping power. Theoretical interpretations of such scalings are difficult because only charged species are examined. Still, the results indicate that simple linear cascades do not likely make a significant contribution to the desorption yield, because they predict a linear dependence on the energy loss; high density bulk interactions such as a thermal spike or a pressure pulse are more likely to give such a steep dependence (Reimann, 1993).

3.3 Damage, Sensitivity, and Mass Range

For primary beam current densities of 10^{-9} A/cm^2 or greater, as is typically used for static SIMS in scanning mass spectrometers, the molecular-ion signal from solid targets decreases on the time scale required to obtain a spectrum because of sample damage.The damage cross-section has been measured by Lange et al. (1984) as $\sim 10^{-14}$ cm^2 for amino acids deposited onto Ag, bombarded with a $\sim$ 1 keV Ar^+ ions. With this cross-section, at currents typically required in quadrupole or magnetic mass spectrometers, the signal disappears in a few minutes.

The damage cross-section increases with primary-ion energy (Benninghoven, 1983a; Marien & De Pauw, 1982; Galera et al., 1991) but at least over a small range of energies, the dependence seems to be similar to the dependence of the yield on primary-ion energy (Benninghoven, 1983; Galera et al., 1991). Then if the integrated molecular-ion signal is limited by target damage, the sensitivity should not be strongly influenced by the primary-ion properties, since in that case it is determined by the the ratio of the molecular-ion yield to the damage cross-section.

Time-of-flight mass spectrometers use much lower average primary-ion current ($\sim 10^{-12}$ A/cm^2) than do scanning instruments. As such, the molecular-ion signal is often undiminished in the time it takes to acquire a spectrum, even for maximum sensitivity (Tang et al., 1990; 1991; Tang, 1991). In this case the sensitivity is limited by the signal-to-background ratio as progressively less sample is deposited onto the target surface. If the background has a similar dependence on the primary-ion properties that the molecular-ion yield has, then again the sensitivity should be independent of the properties of the primary ion. This has not been tested in a systematic way, but approximately the same sensitivity has been obtained for peptides in time-of-flight instruments using 10 keV Cs^+ (Tang et al., 1990; 1991), 30 keV In^+ (Katta et al., 1988) and 12 keV Ar^+ (Benninghoven et al., 1984). Typically, sufficient molecular-ion signal from peptides with molecular mass up to a few thousand u can be obtained from $\sim$ 10 - 50 fmoles of sample.

From the above considerations, one might expect that any difference in absolute yield for different bombarding conditions could be compensated by increasing the primary-particle flux. However, an important observation in the yield measurements described in section 3.2 is that under bombarding conditions for which the yield is higher, the mass range is also significantly increased. Thus for keV bombardment, a change from K^+ projectile to Cs^+ projectile gave an increase in the mass range for bulk samples from a few hundred to about 2000 (Ens et al., 1981), even though the mass spectra for lower-mass compounds are not significantly different. Similarly, a significant improvement in the mass range was reported when changing from $\sim$ 5 keV Xe bombardment to 30 or 35 keV Cs^+ bombardment. This resulted in the first liquid SIMS spectrum of lysozyme (14701 u) (Elliot et al., 1986), and a spectrum of trypsinogen (23978 u) (Barber & Green, 1987), still the largest peptide desorbed by keV particle bombardment.

An improved mass range associated with a higher yield is also demonstrated in the comparisons between keV and MeV bombardment. As mentioned before, for small peptides the yield is about an order of magnitude higher using MeV bombardment compared to 10 keV Cs^+ bombardment. In both cases the yield decreases with increasing molecular mass of the sample but the decrease is faster for keV bombardment. This general result was first reported by the Uppsala group

(Kamensky et al, 1982) and has since been confirmed under various conditions (Ens et al., 1988a; 1988b; Lafortune et al. 1988), as illustrated in Fig. 8. A similar decrease in the yield with molecular mass has been observed for polymers, and the decrease was found to be faster with incident Ne^+ ions compared to Ar^+ or Xe^+ ions (Niehuis, 1987). The faster decrease in the yield for lower energy or smaller projectiles is reflected in a higher mass range for MeV bombardment, by about a factor of 10 for multilayer samples, and a factor of 4 for samples deposited onto nitrocellulose. The observation can be reasonably understood by simple geometric considerations, where higher yield is presumed to be associated with a larger area of excitation (Håkansson et al. 1984).

3.4 Secondary-Ion Dynamics

The energy distributions, especially the internal energy or stability, of the desorbed organic molecular ions are known to have a strong dependence on the sample properties, considered in section 4.5. However at low bombardment energies there does not appear to be an influence on secondary-ion dynamics of the primary-ion properties. It has been mentioned that time-of-flight mass spectra of biomolecules are insensitive to the bombardment conditions; this applies to peak shapes, fragmentation patterns as well as metastable daughter-ion spectra (Poppe-Schriemer, 1993). Since a time-of-flight spectrum is strongly affected by the secondary-ion dynamics, this indicates already the insensitivity of dynamics to bombardment conditions.

In direct measurements of the metastable decay constant of phenylalanine desorbed from the bulk solid, Schueler et al. (1989) found no dependence on the primary Cs^+ energy from 3 keV to 13 keV although the yield changed considerably. Measurements by Hoogerbrugge & Kistemaker (1988) of the internal energy of sputtered neutral molecules of glycerol by photo-ionization mass spectrometry also showed no dependence on primary-ion species or energy; 900 to 3000 eV Xe and air ions were used as primary ions.

The kinetic energy of the secondary ions is difficult to measure but the spread in the axial energy ($1/2\; mv_a^2$, where v_a is the component of the velocity normal to the target surface) is $\lesssim 2$ eV for molecular ions up to at least several hundred u desorbed from solids, based on peak widths in linear time-of-flight measurements (Ens et al., 1986). Retarding voltage measurements in quadrupole instruments also show the spread in initial energy is $\lesssim 2$ eV for a wide variety of molecular-ion species (Hebert et al., 1986; Benninghoven, 1983a). The kinetic energy of the desorbed molecular ions is usually assumed to be independent of the primary ion energy and in fact similar distributions have been reported for some small molecular ions ejected by MeV bombardment of solid targets (Becker & Wien, 1986; Mosshammer et al., 1990). Van de Peyl et al. (1985) found that the spread in initial kinetic energy of organic ions sputtered from liquid glycerol was independent of primary Ar^+ ion energy between 160 eV and 3800 eV. A dependence of the secondary-ion energy on the incident energy for similar conditions was observed by Kelner & Markey (1984), but this is thought to be due to charging effects (van de Peyl et al., 1985).

In spite of the similarity in kinetic and internal energy distributions for most organic ions independent of primary-ion mass and energy in the keV range, a dramatic difference in the radial velocity distributions of larger molecular ions like insulin has been observed for keV and MeV bombardment (Ens et al., 1989a; 1989b; Håkansson, 1993). For MeV bombardment, the radial velocity distribution for molecular ions larger than a few hundred u is strongly correlated to the incident-ion direction. For normal incidence the radial velocity distribution for insulin has a pronounced minimum corresponding to normal ejection as shown in Fig. 9a which also shows the single-peaked symmetric distribution for a small fragment ion. The measurements were made by measuring the molecular-ion intensity in a linear time-of-flight spectrometer as a function of the deflection voltage applied to parallel plates in the flight tube. The results indicate that momentum perpendicular to the incident-ion track is imparted to the molecular ions of insulin, suggesting collective motion of the lattice rather than a thermal description of desorption (Bitensky & Parilis, 1987; Ens et al., 1989a; Johnson et al., 1989; Reimann, 1993).

Using the same geometry in the same apparatus, no such momentum transfer was observed for molecular ions of insulin desorbed by 18 keV Cs^+ ions (Ens et al., 1989b). In this case, the measured distributions for the molecular ions of insulin and for small fragment ions coincide. In measurements with improved angular resolution in another instrument a somewhat broader distribution is observed for molecular ions of insulin than for light ions (Fig. 9a). The contrast in the radial velocity distributions for MeV and keV bombardment is surprising in view of the similarity of the spectra obtained for insulin (Fig. 2b). The contrast may indicate different processes are involved or may simply reflect the different symmetries. The range of an incident keV ion is small so the energy dissipation may be expected to be roughly spherical about the mean damage depth (Sigmund, 1968). This is in contrast to the cylindrical symmetry about the track of an MeV particle.

It is unlikely the structure in the tails in Fig. 9b is significant but the insulin signal clearly persists to higher deflection voltage than does the signal from small fragments. This broader distribution for insulin may be an indication of a collective outward momentum transfer in keV bombardment (similar to the effect in MeV bombardment, but smaller), or it may just indicate a larger overall initial energy of large molecular ions.

4 Influence of Target Properties

Although the primary-ion energy has only minor influence on the nature of the mass spectrum, the nature of the target can have important implications on the spectra. Four different types target preparation for low-energy particle-induced desorption can be identified. (i) One method involves depositing thin layers of sample onto a metal substrate. Usually the substrate is first etched in nitric acid and the sample is deposited from solution with a microsyringe to give approximately one monolayer or sub-monolayer coverage. Other techniques including vacuum evaporation and Langmuir-Blodgett deposition have been used to produce more well-defined surfaces for fundamental studies. (ii) The sample may simply be deposited as bulk or multilayer solid. Following the example set in PDMS, the first time-of-flight SIMS experiments (Chait & Standing, 1981; Ens et al., 1981) used samples prepared by the electrospray method (McNeal et al., 1979). This essentially produces small thick islands of sample distributed randomly over the surface; an electrosprayed target can be regarded as a bulk sample. (iii) The sample can be deposited as a monolayer or sub-monolayer from solution onto a nitrocellulose film. The film of nitrocellulose is usually deposited onto a metal substrate by electrospray. In many cases the sample is then rinsed with water to remove contaminants. (iv) Lastly, the sample may be diluted in a suitable matrix, the most important type being a viscous liquid like glycerol. The main effects of the type of target preparation are summarized; the role of the chemical environment of the sample for a given method is considered briefly.

4.1 Damage and Renewal Processes, Mass Range, and Sensitivity

Sample damage was already considered in connection with primary beam parameters. Here sample damage and its implications in the context of target preparation are considered at the beginning of the discussion of target effects because of the importance of the liquid matrix in resisting damage. The other experimental results should be considered in this context.

4.1.1 Solid Targets

The Münster group has studied disappearance cross-sections under various conditions (Hagenhoff et al., 1990; Lange et al., 1984; Niehuis, 1987). For 3.5 keV Ar^+ bombardment of submonolayer coverage of amino acids on a silver substrate, they reported a disappearance cross-section for the $[M + H]^+$ ion from amino acids of about 4×10^{-14} cm^2; it is about 1×10^{-14} cm^2 for the $[M\text{-}H]^-$ ion. For non-

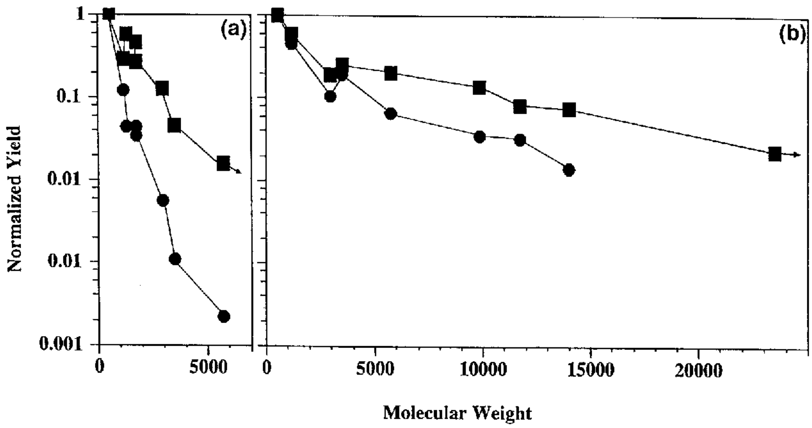

Figure 8. Molecular-ion yields (normalized to 1 for leucine enkephalin) obtained with 18 keV Cs+ bombardment (●) and fission fragment bombardment (□), for a series of peptides (a) electrosprayed (multilayer) and (b) adsorbed onto nitrocellulose (Ens et al., 1988a).

reactive metals or thick amino acid targets the dependence on the polarity is not present, and the cross-section for both ions is about 1 × 10^{-14} cm^2 (Lange et al., 1984). The cross-sections for larger peptides presumably increase in proportion to their size; for polymers, the cross-section was found to increases linearly with increasing mass (Hagenhoff et al., 1990).

As already mentioned, in scanning mass spectrometers, the lifetime of the molecular-ion signal from most solid targets is limited by sample damage. The problem is compounded for higher mass because the cross-section increases, and as illustrated in Fig. 8, within a class of compounds, the secondary molecular-ion yield decreases with increasing molecular mass. As a result the mass range available for solid sample SIMS of biomolecules is limited by sample damage in most scanning instruments. Mass spectra of peptides on solid targets obtained in scanning mass spectrometers are nearly all confined to molecular mass of a few hundred u.

For time-of-flight mass spectrometers, where sample damage does not usually limit the achievable molecular-ion signal, the mass range is considerably higher. For monolayers adsorbed to noble metals, or for bulk samples, the mass range for peptides is about 2000 u, although there are a few isolated reports of spectra of peptides with molecular mass up to about 3000 u (Ens et al., 1988a; 1988b; van Leyen et al., 1987), and there is evidence that molecular ions of insulin (5733 u) have been desorbed intact from bulk samples by 8 or 12 keV Cs^+ bombardment (Ens et al., 1988a, 1988b). The introduction of nitrocellulose as a substrate significantly increased the mass range for peptides to about 14000 u (Ens et al., 1988a) as

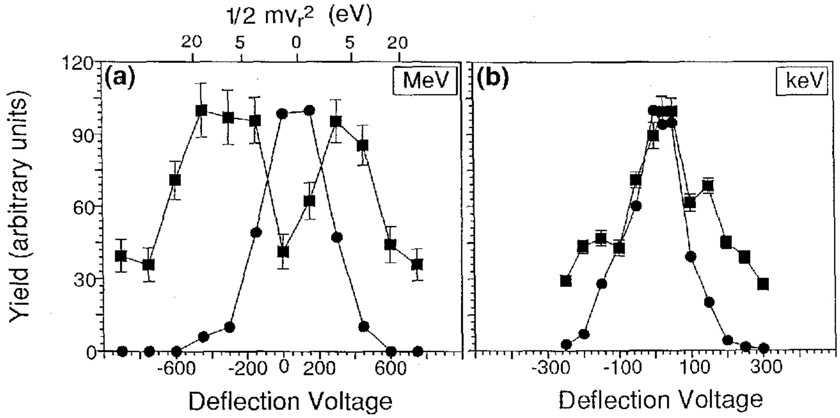

Figure 9. Yield of insulin molecular ions (□) and CH_3^+ ions (•) ejected from a multilayer target as a function of secondary ion deflection voltage for (a) ^{252}Cf fission fragments incident from behind and (b) 10 keV Cs^+ incident from the front at 20°. The measurements in (a) and (b) were made in different spectrometers. On the upper axis in (a), v_r is the radial velocity of an ion that strikes the centre of the detector at the corresponding deflection voltage (Ens et al., 1989b).

illustrated in Fig. 8; spectra of insulin and PSP are shown in Fig. 2. The adsorption of proteins and peptides to nitrocellulose allows the surface to be rinsed in order to remove low-mass contaminants like salts that can quench the molecular-ion yield. The improved spectra have also been attributed to favorable binding conditions with nitrocellulose that promote ionization of the proteins, and require less energy for ejection, compared to intermolecular bonds in bulk samples or to the bonds between the sample molecules and metal substrates (Jonsson et al., 1986; 1988; Chait, 1987).

4.1.2 Isolation in a (Liquid) Matrix

The advantages of isolating organic samples in a suitable matrix material has been demonstrated by Cooks et al. using ammonium chloride (Cooks & Busch, 1983; Liu et al., 1981; Unger et al., 1981; Busch et al., 1983; Hsu et al., 1983). Similar isolation of small nonpolar molecules in frozen rare gases has been demonstrated by Jonkman et al. (1978). Among the observed effects of the matrix is a significantly increased lifetime of the molecular-ion signal under particle bombardment, i.e. a reduction in the disappearance cross-section. Unger et al. (1981) and Hsu et al. (1983) reported that the molecular-ion signal was stable even for currents up to 10^{-6} A/cm^2, close to dynamic conditions. Significantly improved spectra of

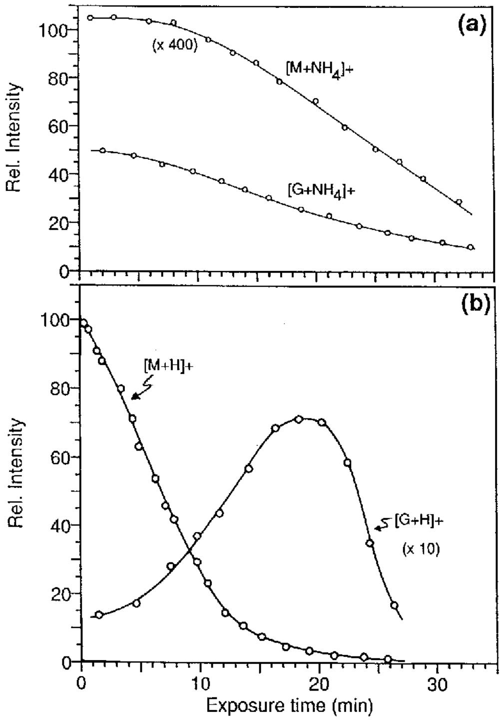

Figure 10. Variation of ion yields from (a) a mixture of stachyose (M), NH_4Cl and glycerol (G) and (b) a pentapeptide (M) in glycerol (G), as a function of irradiation dose from 6 keV Xe atoms at a flux of 10^{13} Xe atoms/cm^{2}s (Wong and Röllgen, 1986a).

organic salts, sugars, nucleotides and small peptides in ammonium chloride were obtained with a scanning instrument, with which a spectrum of sucrose on a metal backing had not been successful (Liu et al., 1981). In preliminary experiments at Manitoba with a time-of-flight instrument using low current density $\sim 10^{-12}$ A/cm^2, the use of the ammonium chloride matrix gave better spectra for organic salts but not for amino acids or peptides (Ens & Standing, 1982). Presumably a stable emission of undamaged material is possible at high currents if the volume of material removed in each sputtering event is comparable to the volume that sustains damage (Williams & Gillen, 1989). This condition is certainly not met in organic solids, but if the analyte is isolated in a matrix with properties that are nearer such a condition, some damage resistance could be expected.

The breakthrough with respect to damage resistance came with the introduction of the liquid matrix by Barber et al. (1982b). With the sample dissolved in glycerol, the ion or atom gun could be run at currents used in dynamic SIMS with only minimal loss of molecular-ion signal until the glycerol itself was depleted from the sample probe. Thus the disappearance cross-section is effectively eliminated indicating that a renewal process is occurring. This process has normally been attributed to the mobility of the liquid matrix, or high evaporation or sputtering rates, but there is no consensus on the detailed mechanism.

Analytes tend to concentrate at the surface of glycerol before bombardment so the initial molecular-ion signal decreases until some equilibrium is reached. Junack et al. studied the initial disappearance cross-section under static SIMS conditions (Junack et al., 1985) . For the cation from cetrimonium bromide, the measured cross-section under 3 keV Ar+ bombardment is about 3×10^{-14} cm^2; roughly the same cross-section for a monolayer deposited on Ag.

Investigation of the profile of ion emission as a function of dose under dynamic conditions has been performed for glycerol by Wong et al. (1985; Wong & Röllgen, 1986). After an initial rapid decrease, the molecular-ion signal for stachyose was observed to decrease gradually for nearly an hour until the glycerol was depleted (Fig. 10a). Chemical noise which was identified as products of radiation damage had nearly the same dependence so that the ratio of the molecular-ion signal to the noise signal is nearly constant. Similar results have been reported by Todd & Groenewald (1986). If the renewal process results from diffusion of fresh sample to the surface, an increase in the relative concentration of damage products would be expected as the glycerol becomes depleted. Thus the results suggest that the renewal process involves removal of the damage products rather than simply diffusion of fresh sample to the surface. Such a self-cleaning process may be related to a high sputter yield, considered in the next section, or a high evaporation rate (estimated to be ~ 50 nm/s), which may increase under dynamic bombardment conitions. If the renewal mechanism is largely 'sputter cleaning' (Wong et al., 1985; Wong & Röllgen, 1986a); the mobility of the sample may be only incidental. On the other hand, some experiments have shown considerable evidence for a concentration of radiation damage (Marien & De Pauw, 1982; Field, 1982; Todd, 1991). Moreover Wong and Röllgen (1986a) observed a profile for a pentapeptide different from that of stachyose (Fig. 10b), and found evidence for accumulated radiation damage, suggesting some contribution to the molecular-ion intensity from transport of molecules from the bulk. However, the time dependence does not fit a diffusion mechanism, and they suggest the possibility of ion migration for polar molecules like the pentapeptide.

Evidence for a gradual renewal occuring between particle impacts was also found by Olthoff & Cotter (1987) in time-of-flight experiments. A higher yield was observed for lower repetition rates allowing more time for the surface to renew. Similarly Junack et al. (1985) used static SIMS measurements in a time-of-flight

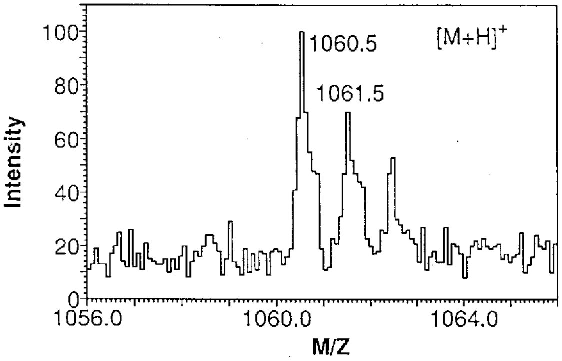

Figure 11. Molecular-ion region of the time-of-flight spectrum from 10 fmol bradykinin applied to a nitrocellulose target; ions were produced by 10 keV Cs^+ bombardment (Tang et al., 1991).

instrument to show that surface renewal requires $\sim$ 100 s. Using isotopically labelled surface layers, Ligon (1983) has shown that simple diffusion processes are too slow to account for surface renewal. Ligon & Born (1986; Ligon, 1983) argue that some transport of molecules from the bulk to the surface is necessary to explain the longevity of the signal in FAB, and suggest the possibility of macroscopic liquid flow driven by changes in the surface tension caused by particle bombardment.

In order to determine the role of the mobility of the matrix in renewal mechanisms, Williams & Gillen (1989) have studied damage profiles for frozen glycerol and compared it to ice and NH_4Cl. The behaviour of the three matrices was similar. The damage cross-section for low dose was found to be in the range 2 to 5×10^{-14} cm^2, similar to that of bulk sample or for a monolayer on a metal substrate. However, after a dose of about 5×10^{14} ions/cm^2 the disappearance cross-section decreased to about 10^{-6} cm^2. Even so, compared to a liquid surface, the signal was much weaker and decayed more quickly so conditions under which glycerol is a liquid are still clearly favored. This negative result for frozen glycerol doesn't resolve the question of the importance of the mobility. The liquid may be favorable because of a higher evaporation rate or sputtering yield, but some contribution from molecule transport is generally admitted.

With the problem of sample damage eliminated by the use of a liquid glycerol matrix, the mass range in scanning instruments is significantly improved. Peptide molecular ions up to mass 10 000 u are readily obtained in spectrometers with sufficient mass range, and with high primary-ion energy, a spectrum of trypsinogen (23 798 u) is possible (Barber & Green, 1987). This represents a dramatic increase in the mass range compared to that obtained with bulk samples or monolayers on Ag, even when these solid targets are analyzed by time-of-flight where damage is not a limitation. Thus, not only does glycerol provide a mechanism of sample renewal, but it is also a highly favorable matrix for desorption. Whether this is related to the liquid nature of the surface or some other properties of glycerol is not known. A very similar improvement in static TOF - SIMS of solids was realized by the introduction of nitrocellulose as a substrate. In that case the improvements are usually attributed to the binding properties of nitrocellulose, and similar considerations may apply to glycerol.

4.1.3 Sensitivity

The damage removal and surface regeneration provided by a liquid glycerol target is necessary to achieve the ion currents required by scanning mass spectrometers in the analysis of large organic molecules. However, a sample target that yields a mass spectrum without the need for surface renewal clearly has the potential for greater sensitivity. The best sensitivity has mainly been achieved with time-of-flight analyses of solid samples, giving complete spectra of peptides with molecular weight in the range of 1000 u from 5 to 50 fmol of sample applied to the target (Tang et al., 1991; Tang, 1991; Katta et al., 1988; Benninghoven et al., 1984); the molecular-ion region of the spectrum of bradykinin obtained with 10 fmol is shown in Fig. 11. A spectrum in this mass range from a liquid target acquired in a scanning instrument typically requires more than a pmol of sample, often closer to a nmole. Higher sensitivity has been achieved with a glycerol target by using a non-scanning Wien mass spectrometer equipped with a position-sensitive detector (Gibson et al., 1988; Aberth & Burlingame, 1988). Using low incident current and a cooled glycerol target (0 °C); Aberth & Burlingame (1988) obtained a small segment of the mass spectrum around the molecular ion from 10 fmol of methyl glucose polysaccharide (3514 u), with 15 keV Cs^+ bombardment.

4.2 Sputtering Yield

Much of the interpretation of the renewal mechanism and the desorption mechanism from liquid glycerol has been based on measurements of the sputtering yield. Yields have been measured using weight or volume loss techniques by Wong & Röllgen (1986a) for 8 keV Xe atom bombardment; by Barofsky et al. (1991) for 14 and 28 keV Ga, In and Bi bombardment; and by Todd & Groenewald (1986) for 5 keV Ar bombardment. The reported yield in each case is remarkably high: on the order of 1000 molecules of glycerol per incident particle were measured. This represents a yield of sputtered atoms one or two orders of magnitude higher than for condensed gases under similar conditions (David et al., 1986b). Each of the

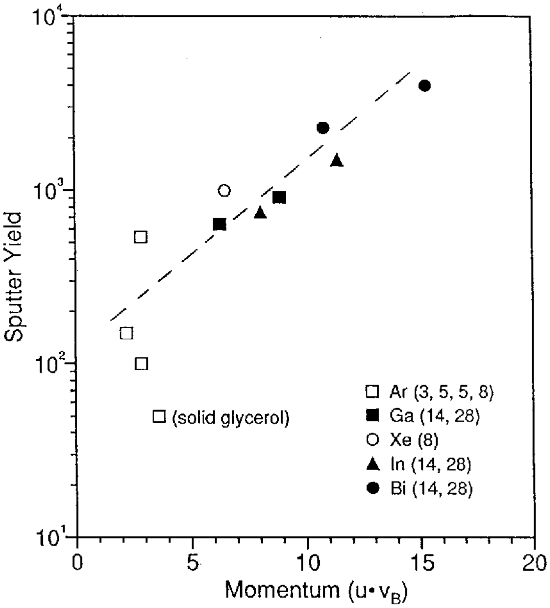

Figure 12. Various measurements of sputtering yield from glycerol in molecules of glycerol per incident particle, as a function of primary-particle momentum (product of the mass number and the velocity relative to the Bohr velocity, v_B).The incident particles and their energies in keV are indicated in the legend. References are given in the text.

groups mentioned above acknowledged the difficulty in the yield measurements, especially in correcting for evaporation which causes more weight loss than the sputtering does. The evaporation may be affected by the bombarding process, either by removing surfactants or by increasing the temperature, but this was not accounted for in the measurements. An increase in the evaporation rate during bombardment would cause an over-estimate of the sputtering yields.

Other estimates of the sputtering yield of glycerol for 3 and 5 keV Ar bombardment are considerably lower giving values of 140 (Junack et al., 1985) and 100 (Field, 1982) molecules of glycerol per incident particle. More controlled measurements of the sputtering yield for frozen glycerol have been made by Williams & Gillen (1989; Gillen et al., 1988), for 8 keV Ar bombardment. They measured a yield of 54±9 glycerol molecules using depth profiling techniques. A similar sputter yield was determined for ammonium chloride.

The various measurements of sputter yields from glycerol are summarized in Fig. 12 where the yields are shown as a function of the incident-particle momentum. There is considerable uncertainty in the measurements for liquid glycerol, but even

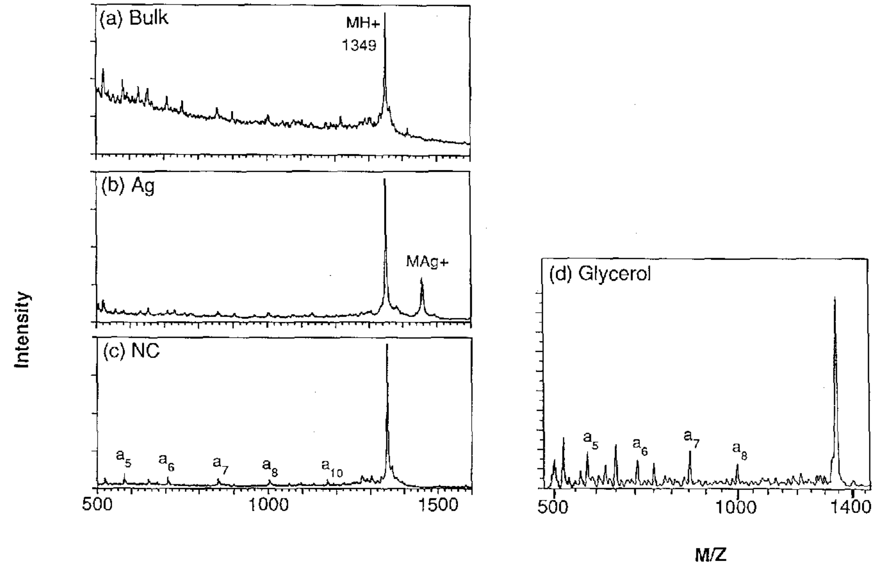

Figure 13. Time-of-flight mass spectra of substance P (1348 u) from (a) bulk sample, (b) a thin layer deposited onto etched Ag, (c) a thin layer on nitrocellulose and (d) a glycerol matrix. Each spectrum was acquired in a linear time-of-flight spectrometer. (a) - (c) were acquired at Manitoba with 10 keV Cs^+ bombardment; (d) is from Olthoff et al. (1988), acquired with 5 keV Xe^+ bombardment. Some fragment peaks are labelled using the nomenclature of Roepstorff & Fohlman (1984).

for frozen glycerol, the yield is high compared to the sputtering yields of 10 atoms or less from keV bombardment of metals (Andersen and Bay, 1981), but are typical of sputtering from ices (Brown and Johnson, 1986; David et al., 1986a; 1986b). The phase of glycerol is unlikely to affect the sputtering yield apart from the difference in sublimation energy, since on the time scale of the sputtering event, the atoms may be regarded as stationary in either phase (Andersen and Bay, 1981; Magee, 1983). However, strong temperature effects have been observed in sputtering from molecular gas solids (Chrisey et al., 1986). The primary mass and energy also have a strong influence on sputtering yields from condensed gases or ices (Brown & Johnson, 1986; David et al., 1986a; 1986b; Benit et al., 1987). With these considerations, many of the data may not be contradictory as Sundqvist (1991) has suggested.

While accurate sputter yields from liquid glycerol are still not known with confidence, they appear to be rather high and may contribute to its favorable desorption and renewal properties. The spraying mechanism of Wong and Röllgen

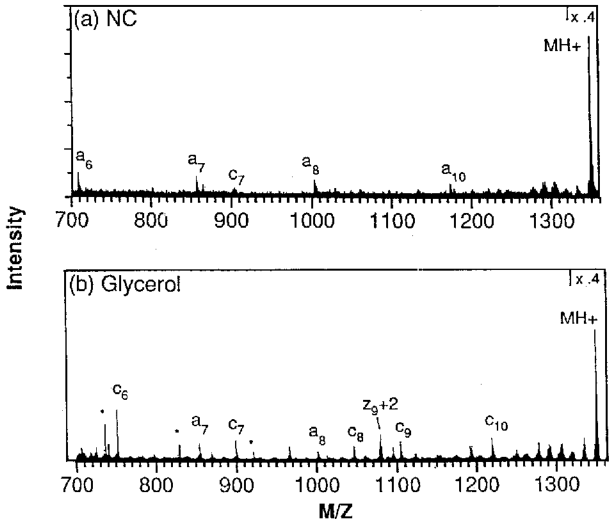

Figure 14. Mass spectra of substance P (1348 u) (a) from a sample deposited on nitrocellulose and analyzed with 10 keV Cs^+ bombardment in a reflecting time-of-flight mass spectrometer at Manitoba (Tang et al. 1989) and (b) from a sample dissolved in glycerol and analyzed with 6 keV Xe bombardment in a sector-field mass spectrometer (Martin and Biemann, 1987). The peaks marked with an asterisk are attributable to the glycerol matrix.

(1986a) or the phase explosion model of Sunner et al. (1988a) both assume high sputter yields. Desorption from nitrocellulose has similar properties to those of glycerol so the sputter yields from this polymer are of interest, but have not been measured.

4.3 Secondary-Ion Mass Spectra

The mass spectra obtained from organic targets by low-energy particle bombardment depend in detail on the type of target preparation and on chemical interactions with the substrate surface or matrix, but there are some general features. For most organic compounds that are tractable to the method, positive molecular ions are formed by protonation or attachment of available metal ions; negative molecular ions are formed by deprotonation. Such molecular ions usually give the most intense peak in their mass range although ordinary low-mass background may be more intense. For organic salts, the positive cation is the dominant peak. In addition to the parent-like signal, a number of peaks resulting from characteristic fragmentation are also observed in some cases.

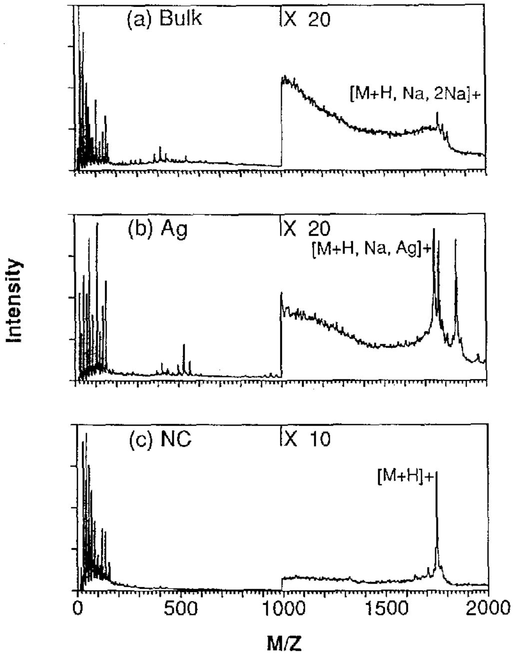

Figure 15. Time-of-flight mass spectra of a endorphin (1746 u) from (a) bulk sample, (b) a thin layer deposited on etched Ag, and (c) a thin layer on nitrocellulose. The spectra were acquired at Manitoba using 10 keV Cs^+ bombardment in a linear time-of-flight spectrometer.

4.3.1 Methods of Target Preparation

A comparison of spectra for the main types of target preparation (bulk, Ag substrate, nitrocellulose and glycerol) is presented here to give a sense of the most general features, such as the type of molecular ions, and their intensity compared to nearby background, to structural fragments and to the low-mass background. The appearance of the mass spectrum is affected by the type of mass spectrometer, and this must be accounted for in some of the comparisons. For the solid targets, time-of-flight spectra are necessarily used because of the problem of sample damage. Although higher-quality spectra are obtained in sector-field instruments or compensating time-of-flight spectrometers, comparisons of spectra in linear time-of-flight spectrometers are useful because the peak width and background are indicative of the degree of metastable decay and therefore the internal energy. The comparisons also depend on the molecular mass of the sample, and so spectra are shown for several different compounds in Figs. 13 to 17.

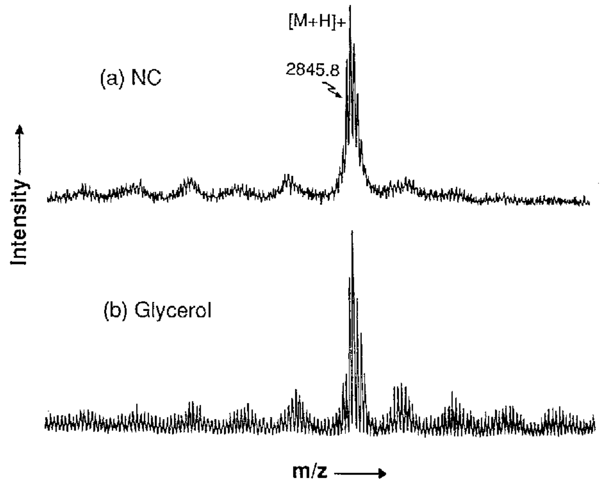

Figure 16. Molecular-ion region of mass spectra of melittin from (a) a solid sample deposited on nitrocellulose and analyzed with 10 keV Cs^+ bombardment in a reflecting time-of-flight mass spectrometer at Manitoba (Tang, 1991) and (b) from a sample dissolved in glycerol and analyzed with 6 keV Xe bombardment in a sector-field mass spectrometer (Barber et al., 1982c).

The main difference in the molecular-ion peaks is the presence of the metal adduct from the metal substrate, if present. Other adducts like alkali ions depend on the chemical environment, although with nitrocellulose it is possible to wash away salts, at least for larger peptides.

In the mass range below ~ 1000 u, the spectra from various surfaces all show intense molecular ions typical of the leu-enkephalin spectrum obtained from bulk sample shown in Fig. 2a. For larger molecules such as substance P, some differences in the signal-to-background ratio are apparent in time-of-flight spectra, as shown in Fig. 13. In this mass range, for most compounds, a Ag substrate demonstrates some advantage over bulk samples and gives spectra similar to those obtained with a glycerol or nitrocellulose target (Junack et al., 1985; Benninghoven, 1983b; Benninghoven et al., 1987). The spectrum obtained from glycerol in Fig. 13d was acquired by Olthoff et al. (1988) in a time-of-flight instrument; this was selected to make the comparison with the other time-of-flight spectra as direct as possible. However, FAB spectra are nearly always acquired in scanning instruments, so a comparison between a FAB spectrum taken in a sector-field spectrometer (Martin & Biemann, 1987), with a reflected time-of-flight spectrum obtained using a nitrocellulose substrate (Standing et al., 1990) is shown in Fig. 14. The low-intensity peaks in both spectra, examined in detail, can give considerable sequence informa-

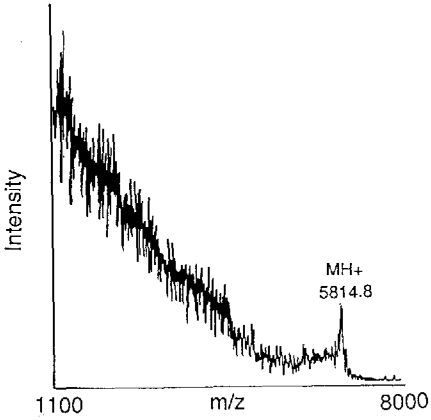

Figure 17. Wide-scan FAB mass spectrum of B29 porcine relaxin (5814 u) obtained in a sector-field mass spectrometer (Fenselau & Hyver, 1986).

tion (Tang et al., 1989; Standing et al., 1990; Tang, 1991; Martin and Biemann, 1987). The relative intensities of the fragments differ between the nitrocellulose target and the glycerol target (Tang, 1991), but compared on the same scale relative to the molecular ion, the extent of fragmentation is quite similar, with slightly more fragmentation appearing in the FAB spectrum.

For molecules larger than substance P, the spectrum deteriorates rapidly for bulk samples and to a lesser extent for Ag substrates as shown in Fig. 15. For some peptides like dynorphin A (2146 u), the spectra are better from a bulk target than from Ag but the situation shown in Fig. 15 is more typical. However, for nearly all peptides the spectrum is better using nitrocellulose (or glycerol) than either metal substrates or bulk sample, and beyond mass 2000 u peptide spectra from bulk or metal substrates are scarce. Fig. 15 also reveals the general trend that larger compounds yield spectra with less structural information although considerable sequence information can still be extracted from mass spectra of peptides in the mass range of about 2000 u (Poppe-Schriemer et al., 1991). A suitable FAB spectrum for comparison was not found for α-endorphin but in this mass range FAB spectra are similar to the nitrocellulose spectrum in Fig. 15c.

For molecular mass higher than $\sim$ 3000 u, mass spectra of biomolecules generated by low-energy bombardment are mainly obtained with liquid or nitrocellulose targets. In both cases the spectra have few features, as can be seen for insulin and PSP on nitrocellulose in Fig. 2. Published FAB spectra often show only the molecular-ion region so direct comparison is difficult. Fig. 16 shows that in the region immediately adjacent to the molecular ion of melittin, the spectra are similar in detail for the two types of target. For broad low-resolution scans in sector instruments, spectra of large peptides or proteins obtained with glycerol have a similar appearance to time-of-flight spectra of proteins adsorbed to nitrocellulose. An example of a wide scan FAB spectrum for a protein with molecular mass similar to insulin (see Fig. 2b) is shown in Fig. 17. Several other examples of wide scan FAB spectra for larger proteins, some with better signal-to-noise ratios, appear in Biemann et al. (1986), Fenselau & Cotter (1986), Naylor et al. (1988); Ashcroft et al. (1988), and Green & Bordoli (1991). Particle bombardment spectra of peptides with mass beyond a few thousand u are now interesting mainly from an academic point of view since much better spectra are obtainable by matrix-assisted laser desorption or electrospray ionization.

4.3.2 Chemical Environment

Secondary ion spectra are strongly affected by the chemical environment of the target or the solution from which the target is prepared. This is especially true for liquid targets where the mass spectrum is affected by many aspects of solution chemistry. The influence of the chemical environment in FAB mass spectra has been reviewed in considerable detail (De Pauw, 1986; Depauw et al., 1991; Fenselau and Cotter, 1987). Here the influence on ionization is considered briefly.

A strong correlation between charge state of the desorbed species and their precursors in solution or on a solid has been established. The dramatic difference in yield (by orders of magnitude) between reactive and non-reactive metal substrates (Lange et al., 1984) in the emission of protonated molecular ions was already discussed. The ion yield from organic salts is orders of magnitude higher than from compounds that form ions by protonation or cationization. The intensity of protonated- or deprotonated-molecular-ion yields is closely correlated to the pH of the sample solution (Hebert et al., 1986; Busch et al., 1982; Inchaouh et al., 1984). Electrochemical reactions have been used to produce ions in solution that are otherwise not seen in FAB spectra (Bartmess & Phillips, 1987; Phillips & Bartmess, 1989). Amine-characteristic secondary-ion intensities were found to be correlated to the amine concentration in a glycerol target (Todd, 1991). Ion pairing of preformed ions in solution has a strong influence on ion intensity (Reynolds & Cook, 1990). These observations are usually described in the context of the precursor model where ions already present on the target, either in the solid or liquid state, are ejected into the gas phase without modication by the desorption event (Benninghoven, 1983a; Cooks and Busch, 1983).

Alternatively, the ionization may occur during the desorption process itself, usually considered to occur by collisions in the gas phase. Sunner et al. (1986;

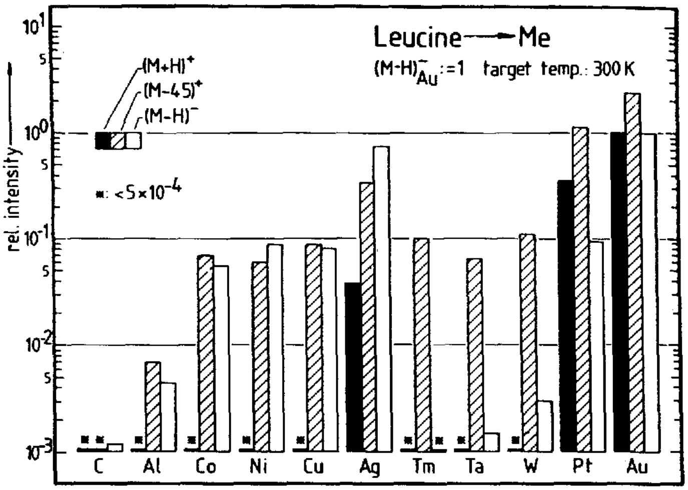

Figure 18. Relative secondary molecular-ion intensities from a monolayer of leucine deposited on various metal substrates (Lange et al., 1984).

1987) have demonstrated that gas-phase basicity is more closely correlated with the intensity of desorbed protonated species than the solution basicity. They also showed that the addition of salts to a liquid matrix significantly alters the spectrum with only a small change in the total ion current. Rouse & Allison (1993) observed potassium cationization of desorbed neutrals by injecting K^+ ions into the sample region during bombardment .

4.3.3 Temperature and Viscosity

The mass spectra obtained from liquid targets have been studied as a function of sub-ambient temperature by Katz et al. (1986; 1987), Morales et al. (1989), and Shiea & Sunner (1990) in scanning mass spectrometers. It was found that the spectrum degrades into chemical noise as the temperature is decreased. It has also been shown that the spectrum improves with elevated temperatures (Ackerman et al., 1987). The mass spectrum was also observed by Shiea and Sunner (1990) to have a similar dependence on viscosity which they controlled by the addition of sucrose. They showed that the temperature effect was also predominantly due to the change of viscosity. The measurements were intended to indicate the role of the liquid phase of glycerol in the desorption mechanism for large molecules. However, as the authors point out, it is very difficult in a scanning mass spectrometer to separate the effects of the surface renewal properties of a liquid target from its desorption properties. The temperature dependence was explained by changes in the transport processes and a gradual shift in the desorption mechanism (Shiea and Sunner, 1990). Similar experiments with static SIMS would be easier to interpret. The experiment of Aberth & Burlingame (1988) showed that mass spectra of methyl glucose polysaccharide (3516 u) and bovine insulin (5733 u) are readily obtained from cooled thioglycerol (0 °C) with low incident beam current in a Wien mass spectrometer equipped with a position-sensitive detector so scanning was not required.

Lange et al. (1984) have studied the temperature dependence of molecular-ion emission for thin layers of amino acids on metal substrates. The spectrum is approximately unchanged until about 320 K. Above this temperature, for non-reactive metals like Au and Pt, both protonated $[M+H]^+$ and deprotonated $[M\text{-}H]^-$ molecular ions disappear. Similar qualitative behaviour has been observed for cationized molecular ions of sucrose and adenosine deposited onto silver (Kambara & Hishida, 1981). On reactive metals like Cu, and Ni and including Ag, the protonated molecular ions have the same behaviour but the negative deprotonated molecular ion persists until about 450 K (Lange at al., 1984). The proposed explanation for the behaviour of the $[M\text{-}H]^-$ peak, is related to the formation of metal-anion complexes.

4.4 Molecular-Ion Yields

The molecular-ion yields from organic compounds vary by orders of magnitude depending on the type of compound, the type of target preparation and the detailed environment even for a given type of preparation. The relationships are complex and here only the main features are summarized.

4.4.1 Metal Substrates

The influence of the type of metal substrate on molecular-ion yields has been investigated by Benninghoven et al. (1982; Lange et al., 1983; 1984). Fig. 18 shows the measured intensity for the amino acid leucine deposited onto various metal surfaces. Emission of the positive molecular ion $[M+H]^+$ is clearly favored for the noble metals Au, Pt and Ag; it is not observed at all for the more reactive metals like Cu and Al. The emission of the negative molecular ion $[M\text{-}H]^-$ is much less sensitive to the nature of the metal, though still favored on noble metal surfaces. The observations can be understood if the molecules bind to reactive surfaces to form an anion-metal complex, but on noble metals both $[M\text{-}H]^-$ and $[M+H]^+$ are formed by proton exchange and are only loosely bound to the metal (Lange et al., 1984). Such a description suggests the ions are preformed on the surface before bombardment as proposed in the precursor model (Benninghoven, 1983a; Cooks

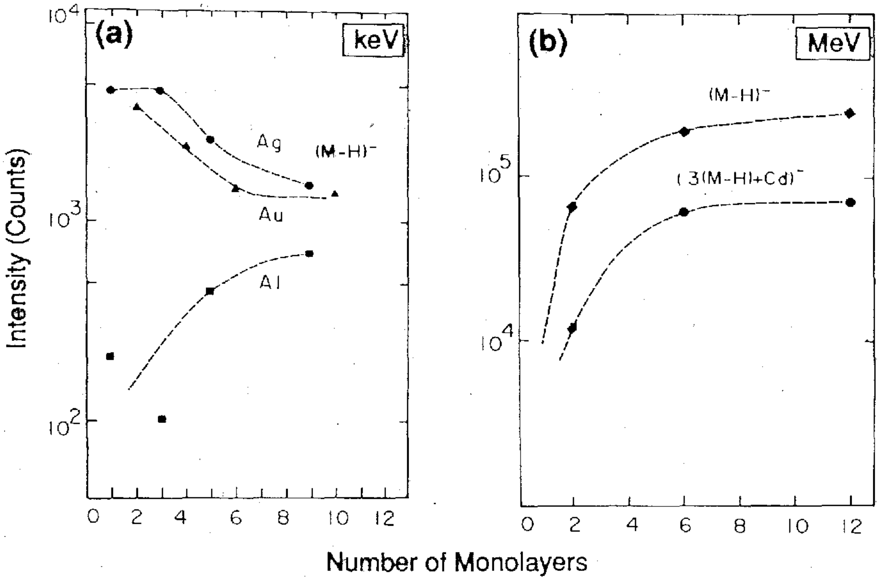

Figure 19 (a) Intensity of the $[M\text{-}H]^-$ ion peak as a function of the number of Cd stearate monolayers deposited on Al, Ag and Au substrates. Secondary ions were produced by 21 keV Cs^+ ion bombardment. (b) Intensity of the [M - H]- and $[3(M\text{-}H)+Cd]^-$ ion peaks as a function of the number of Cd stearate monolayers deposited on a Au surface. Secondary ions were produced by fission fragment bombardment (Bolbach et al., 1988).

and Busch, 1983). The most common metal substrate used for organic SIMS is Ag usually after it is etched in nitric acid.

4.4.2 Thickness Effects (Bulk Sample)

An effective comparison between desorption from bulk sample and from sample molecules in direct contact with various surfaces can be made by monitoring the molecular-ion signal as a function of sample thickness. After sufficient thickness,the surface no longer participates in the desorption process and the emission is characteristic of the bulk. Such experiments require a method of uniform deposition to be quantitative. Experiments have been done with samples prepared by vacuum evaporation and by the Langmuir-Blodgett technique.

Lange et al. (1984) have studied molecular-ion emission from amino acids deposited onto metal substrates by vacuum evaporation. In most cases the proximity of the metal substrate enhances the molecular-ion emission giving a maximum in signal intensity for a thickness of one or two monolayers. For thicker coverage the intensity decreases by more than an order of magnitude until it becomes characteristic of the bulk material. The exception to this behaviour is for the protonated molecular ion from reactive metals. In this case, the proximity of the metal surface inhibits positive-molecular-ion formation, and the signal increases with thickness.

Similar results have been obtained by Bolbach et al. (1988; 1992) for varying numbers of monolayers of Cd stearate on metal surfaces. As shown in Fig. 19a, for Ag and Au surfaces, maximum molecular-ion signal from 21 keV Cs^+ bombardment is obtained for one monolayer. For a reactive surface like Al the molecular-ion signal increases with thickness until about 10 monolayers. This is probably attributable to chemical effects (Bolbach et al., 1988).

For MeV bombardment of thin films on metal substrates, the behaviour as a function of thickness for biomolecules including amino acids (Säve et al., 1987a) or for Langmuir-Blodgett films (Bolbach et al., 1987; 1988; 1992; Säve et al., 1987a; 1987b), is very different from the behaviour for keV bombardment. For high-energy bombardment the molecular-ion signal increases with thickness in all cases until saturation is reached as illustrated for example in Fig. 19b. The difference between the MeV and keV results suggests that the proximity of the metal substrate in keV bombardment does not merely provide favorable binding conditions, since they would be equally advantageous in MeV bombardment. Rather it is likely that in keV bombardment the metal substrate enhances the desorption process because the nuclear stopping power is 4 to 5 times higher in the metal than in an organic solid. Desorption by MeV bombardment results from electronic stopping processes in insulators, so the presence of a metal substrate reduces the energy loss near the surface. These considerations may also explain why the close similarity in the mass spectra from multilayer insulators for keV and MeV bombardment (Ens et al., 1981; 1988a; 1988b; Lafortune et al., 1987) does not generalize to thin films on metal substrates; the yield for small peptides deposited as thin layers on Ag is higher for keV bombardment than for MeV bombardment (Ens et al., 1988a).

Experiments with Langmuir-Blodgett films of fatty acids showed evidence for ejected ions coming from below the surface by as many as 8 monolayers (~ 200 Å), for both keV and MeV bombardment (Bolbach et al., 1988; 1992; Säve et al., 1987c; Hagenhoff et al., 1992). On the other hand, recent measurements by Hagenhoff et al. (1992) with Langmuir-Blodgett layers of polymeric amphiphiles demonstrated almost complete quenching of ions from more than 3 monolayers below the surface for keV bombardment. This probably reflects a difference in the nature or the integrity of the surfaces. The fatty acid monolayers have a rather open structure which may collapse under ion bombardment. It is also possible that the monolayers of fatty acids were imperfect and had pinholes in them, but imperfections do not explain the results obtained with MeV bombardment where the ratio of ions from different depths changed with bombarding energy (Säve et al., 1987c).

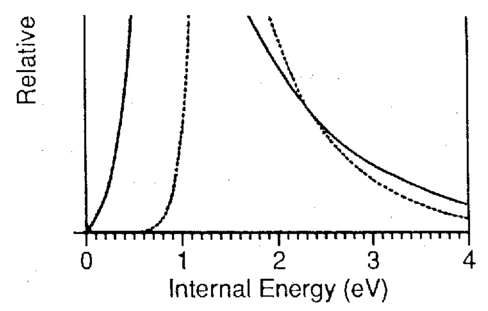

Figure 21. Internal energy of secondary ions in liquid SIMS (solid line) and solid (bulk) SIMS (dashed line) estimated on the basis of the fragmentation yield of substituted benzylpyridinium ions (De Pauw et al., 1991 (adapted from Derwa et al., 1990)).

peptides prepared on Ag, on nitrocellulose, in glycerol and in bulk have been made under static SIMS conditions in a compensating time-of-flight spectrometer by van Leyen et al. (1987). Some general observations can be made from these groups of measurements. For small organics like amino acids or small peptides, the molecular-ion yields from Ag substrates with ~ 10 keV Cs (or Xe) bombardment is on the order of a few percent. The yield from bulk sample is typically ten times smaller than that and the yields for glycerol and nitrocellulose fall in between, usually within a factor of two or three from those obtained with a Ag substrate. As the molecular weight increases, the yields decrease but at different rates for different surfaces. The rate of decrease for bulk samples is shown in Fig. 8a. It is about the same for Ag supported samples (Ens et al., 1988a) and represents a decrease in the yield by about 3 orders of magnitude for molecular mass ~ 3000 u compared to ~ 500 u (Ens et al., 1988a; van Leyen et al., 1987). A much slower decrease in the yield with molecular mass is observed for a nitrocellulose substrate as shown in Fig. 8b, so that beyond mass ~ 1000 u, the yield from nitrocellulose is higher than for either silver or bulk targets. The dependence of the yield on molecular mass for samples in a glycerol matrix is not known but from the similarity of the spectra and mass range with those obtained from nitrocellulose targets, the yield dependence on mass may be expected to be similar as well.

4.5 Secondary-Ion Dynamics

Although significant effects of the primary-ion properties for low-energy ions on the energy distributions of secondary organic molecular ions have not been demonstrated, some effects of target properties are clear. Metastable decay of particle-desorbed molecular ions was recognized early in time-of-flight measurements (Chait & Standing, 1981; Chait & Field, 1981). Chait & Field (1981) used retarding grids to demonstrate clearly that unimolecular decay causes considerable broadening and background in time-of-flight spectra. Decay patterns of selected parent ions can be determined using retarding grids (Chait & Field, 1984; Ens et al., 1983) or electrostatic mirrors (Della-Negra & LeBeyec, 1985; Standing et al., 1986; Tang et al., 1989), in methods analagous to tandem mass spectrometry. Thus it is clear that many of the desorbed molecular ions are highly excited as a result of the desorption and ionization processes. The introduction of nitrocellulose as a substrate for particle-induced desorption of organic molecules, resulted in mass spectra with sharper peaks and lower background compared to spectra obtained from bulk organic samples (Jonsson et al., 1986; 1989). Chait (1987) subsequently showed that molecular ions ejected from a nitrocellulose surface are cooler and undergo much less metastable decay than ions ejected from bulk sample. These measurements were made using fission fragment bombardment but they apply to low-energy bombardment as well for which nearly identical peak shapes are obtained, at least for smaller peptides (Fig. 2). In Fig. 20 the molecular-ion region is shown for time-of-flight mass spectra of insulin obtained from a bulk sample and from nitrocellulose by 12 keV Cs^+ bombardment (Lafortune et al., 1987). For the bulk sample there is some indication that molecular ions are desorbed intact, but mainly decay before they are fully accelerated. Presumably the difference between desorption from bulk sample and from nitrocellulose would also be reflected in the kinetic energy distributions of desorbed molecular ions. However, detailed comparisons to observe such a difference have not been made; qualitatively similar radial velocity distributions were observed for molecular ions desorbed by MeV bombardment from bulk sample and nitrocellulose (Ens et al., 1989a; Håkansson, 1993).

There is also evidence that molecular ions desorbed from an isolating matrix like ammonium chloride or liquid glycerol have less energy than those desorbed from bulk sample or from a metal substrate. Mass-analyzed ion kinetic-energy spectra of methadone show that the molecular ions undergo less metastable decay when desorbed from a glycerol matrix instead of a silver substrate (Campana et al., 1987). Wong and Röllgen (1986b) showed that the anomolies in CsI cluster distributions, which are caused by metastable decay (Ens et al., 1983), are less pronounced when the clusters are ejected from a glycerol target compared to a bulk solid. The internal energy of desorbed molecular ions has been estimated from fragmentation patterns assuming that the fragments arise from decay of desorbed molecular ions (Derwa & De Pauw, 1991; Derwa et al., 1990; Agnello et al., 1991; Hoogerbrugge et al., 1988), or from chemical considerations (Williams et al., 1987; Williams & Naylor, 1987). Hoogerbrugge et al. (1988) estimated the temperature of desorbed ions from glycerol to be considerably lower than that of the bulk, from photoionization experiments. It is generally agreed that the internal energy distributions are below about 3 eV, and that energy is lower for molecular ions desorbed from liquid matrices (De Pauw, 1986; Derwa et al., 1990; Blais et al., 1990) or from NH_4Cl (Busch et al., 1983) than from the bulk solid or from metal substrates, as illustrated in Fig. 21. Differences in fragmentation patterns have been observed depending on the nature of the liquid matrix as well (Takayama et al., 1990). Measurements of kinetic energy distributions for secondary molecular ions have also been made. Measurements for a tripeptide and an organic salt desorbed from glycerol and from a solid bulk sample were made by van der Pyle et al. (1985). Both the mean energy and the width of the energy distributions were lower for secondary ions ejected from the liquid surface. The full-width half maximum of the energy distributions for a glycerol target was usually in the range 0.3 - 0.7 eV, and about twice as high for solid targets. The kinetic energy distributions of various ions sputtered from liquid glycerol were measured by Hoogerbrugge et al. (1987). The asymptotic behaviour for the Na^+ ion and some glycerol ions showed evidence for the operation of a collision cascade mechanism in the emission of high-energy ions.

Compared to solid multilayer sample targets, or to thin sample layers on a metal substrate, liquid glycerol targets and solid nitrocellulose or NH_4Cl targets have been shown to reduce the amount of energy transferred to molecular ions of applied sample ejected from the surface by particle bombardment. Direct comparisons of the dynamics of molecular ions ejected from glycerol and nitrocellulose have not been reported, but from the similarity in the mass spectra and the mass range obtainable from the two surfaces, it seems reasonable that similar explanations for the cooler ejecta may apply. However, different explanations have been suggested in the two cases. Cooler ejecta from a nitrocellulose substrate are usually attributed to lower binding energies between the sample molecules (usually proteins) and the nitrocellulose compared to the intermolecular binding in the bulk solid or to a Ag substrate (Jonsson et al., 1986; 1988; Chait, 1987). The reduced energy transferred by an isolating matrix like glycerol or NH_4Cl is often ascribed to cooling effects in the gas phase, either by desolvation from larger ejected clusters, or collisional cooling with sputtered matrix molecules (Pachuta & Cooks, 1987; Wong and Röllgen, 1986a; Sunner et al., 1988a; 1988b). This description is analagous to the gas-flow model which has been used successfully to describe sputtering of condensed gases (Michl, 1983; Urbassek & Michl, 1987).

5 Concluding Remarks

The ejection and survival of thermally labile organic molecular ions following the violent collision of an energetic particle with a surface was not anticipated by the usual description of a sputtering event. Much of the experimental data addressing the mechanism is still largely qualitative; the response of the mass spectrum and to a lesser extent the relative molecular-ion yield to various experimental conditions.

The introduction of liquid matrices to secondary-ion mass spectrometry increased the mass range available in conventional scanning mass spectrometers from several hundred to several thousand u. The dramatic ease with which this increase became possible earned liquid targets a clear distinction from solid targets. There is little doubt that the liquid phase allows a target the mobility and possibly vapor pressure to permit surface renewal under high-flux particle bombardment. In addition, glycerol has proved to be a highly favorable matrix for the desorption process, and this has also been attributed to its liquid phase. In low-transmission scanning instruments the contributions from these two aspects of liquid targets cannot easily be distinguished, and the evidence that the liquid phase is important to the desorption mechanism is indirect, although the increased control of the chemical environment is clearly an advantage. In time-of-flight mass spectrometry a renewal mechanism is not required so solid targets can be used effectively. When time-of-flight spectra from solids are considered, especially with nitrocellulose as the substrate, the distinction between the liquid and solid phase blurs with respect to the desorption mechanism. A static SIMS analysis of frozen glycerol by time-of-flight would be a revealing experiment.

The results summarized in this paper indicate a remarkable insensitivity of the mass spectrum to diverse experimental conditions. In particular, although the yield of molecular ions increases strongly with the mass and energy of the bombarding particle, the mass spectrum remains largely the same. The molecular-ion yield for insulin is $\sim$30 times higher for fission fragment bombardment than for 18 keV Cs^+ bombardment, but the spectra, and metastable decay rates are nearly the same. The molecular-ion yield for peptides with molecular mass $\sim$ 1000 u changes by a factor of 30 between 7 keV Ne and 7 keV Xe bombardment but the fragmentation pattern is the same. The molecular-ion yield for small peptides is an order of magnitude higher from a silver substrate than from bulk sample, yet the degree of fragmentation is similar. Such similarity in the mass spectra in spite of widely varying molecular-ion yields suggests that gas phase interactions do not play a significant role in determining the pattern of fragmentation or in determining the ratio of observed fragments to the parent ion intensity.

On the other hand, there are also some fundamental aspects of the emission process that depend on the bombarding mass and energy, and on the type of target. Besides giving a higher molecular-ion yield, higher bombarding energy or mass also results in a higher mass range. Similarly the use of an appropriate matrix or substrate like glycerol or nitrocellulose, results in a higher mass range and cooler molecular ions compared to desorption from bulk samples or metal substrates. In both cases the increased mass range can be understood by considering an increased scale of the interaction, in one case because more energy is deposited near the surface, and in the other because of less energy required to cause ejection. The increased scale may correspond to a transition from a predominantly surface process to that of volume sputtering. A bulk sputtering mechanism is consistent with the high sputtering yields reported for glycerol and moreover, a desolvation mechanism or collisional cooling in an expanding gas is a plausible explanation for the lower internal energy.

A bulk sputtering mechanism involving a rapid phase change and gas expansion and/or the desorption of large clusters of matrix, is frequently invoked for desorption from glycerol (Wong and Röllgen, 1986a; Sunner et al., 1988a; 1988b), but is possibly relevant to a nitrocellulose substrate as well. Direct evidence for such a mechanism is scarce but it provides a possible explanation for the increase in mass range from $\sim$ 2000 u for peptides on a Ag substrate or in bulk to $\sim$ 20 000 u for peptides in glycerol or on nitrocellulose. However, a bulk desorption mechanism is not essential to a basic description of the desorption of fragile molecules like α endorphin (1746 u), still a remarkable phenomenon. As mentioned above, such molecules can be desorbed intact from a silver substrate with spectra not unlike those obtained from glycerol, and FAB spectra can be obtained from glycerol using incident Ne atoms for which the sputtering yield is presumably much lower. A gas expansion mechanism on a much larger scale has been applied to matrix-assisted laser desorption. In that situation, the description is manifested in a sharp irradiance threshold, a mass spectrum highly sensitive to the irradiance, a forward directed angular distribution (Ens et al., 1991), mass independent velocity distributions (Beavis & Chait, 1991) and energy deficits in high extraction fields (Zhou et al., 1992b). The scale of the process in keV particle bombardment is probably too small for similar direct evidence for a gas expansion, if present, to be observable.

Acknowledgements

Financial support at Manitoba is provided by the U. S. National Institute of Health (Institute of General Medical Sciences) and by the Natural Sciences and Engineering Research Council of Canada.

References

Aberth WH and Burlingame AL, 1988: Anal. Chem. **60**, 1426

Aberth W, Straub M and Burlingame AL, 1982: Anal. Chem. **54**, 2029

Ackerman BL, Holland J and Watson JT, 1987: Biomed. Environ. Mass Spectrom. **14**, 501

Agnello A, Derwa F and De Pauw E, 1991: in *Methods and Mechanisms for Producing Ions from Large Molecules*, Ed. K G Standing and W Ens, NATO ASI Series B: Vol. 269 (Plenum, New York) p. 117

Albers A, Wien K, Dück P, Treu W and Voit H, 1982: Nucl. Instrum. Methods **198**, 69

Amster IJ, Loo JA, Furlong JJP and McLafferty FW, 1987: Anal. Chem. **59**, 313

Andersen HH and Bay HL, 1981: in Behrisch (1981) and references therein

Ashcroft AE, Coles AD, Evans S, Milton DJ and Wright B 1988: in *The Analysis of Peptides and Proteins by Mass Spectrometery*, ed. C J McNeal, (Wiley, New York) 279

Barber M and Green BN, 1987: Rapid Commun. Mass Spectrom. **1**, 80

Barber M, Vickerman JC and Wolstenholme J, 1980: J. C. S. Faraday I **76**, 549

Barber M, Bordoli RS, Sedgwick RD and Tyler AN, 1981: J. Chem. Soc. Chem. Commun. 1981, p. 325

Barber M, Bordoli RS, Elliot GJ, Sedgwick RD and Tyler AN 1982a: Anal. Chem. **54**, 645A

Barber M, Bordoli RS, Elliot GJ, Sedgwick RD, Tyler AN and Green BN 1982b: J. Chem. Soc. Chem. Commun. 1982 p. 936

Barber M, Bordoli RS, Sedgwick RD, Tyler AN, Garner G V, Gordon DB and Tetler L W 1982c: Biomed. Mass Spectrom. **9**, 265

Barofsky DF, Jiang L, Barofsky E and Yen T, 1991: in *Methods and Mechanisms for Producing Ions from Large Molecules*, eds. K G Standing and W Ens, NATO ASI Series, Series B: Vol. 269, (Plenum, New York) p. 101

Bartmess JE and Phillips LR, 1987: Anal. Chem. **59**, 2014

Beavis RC and Chait BT, 1991: Chem. Phys. Lett. **181**, 479

Becker O and Wien K, 1986: Nucl. Instrum. Meth. B **16**, 456

Becker O, Della-Negra S, Le Beyec Y and Wien K, 1986: Nucl. Instrum. Methods B **16**, 321

Behrisch R, Ed., 1981: *Sputtering by Particle Bombardment I*, Topics in Applied Physics **47**, (Springer, Heidelberg)

Behrisch R, Ed., 1983: *Sputtering by Particle Bombardment II*, Topics in Applied Physics **52**, (Springer, Heidelberg)

Behrisch R and Wittmaack K, Ed., 1991: *Sputtering by Particle Bombardment III*, Topics in Applied Physics **64**, (Springer, New York)

Benit J, Bibring J-P, Della-Negra S, Le Beyec Y, Mendenhall M, Rocard F and Standing K, 1987: Nucl. Instrum. Meth. B **19/20**, 838

Benninghoven A, 1983a: in *Ion Formation from Organic Solids*, Springer Series in Chemical Physics 25, ed. A Benninghoven (Springer-Verlag, New York) p. 64

Benninghoven A, 1983b: Int. J. Mass Spectrom. Ion Processes **46**, 459

Benninghoven A, Jaspers D and Sichtermann W, 1976: Appl. Phys. **11**, 35

Benninghoven A, Lange W, Jirikowsky M and Holtkamp D, 1982: Surf. Sci. Lett. **123**, L721

Benninghoven A, Niehuis E, Friese T, Greifendorf D and Steffens P, 1984: Org. Mass Spectrom. **19**, 346

Benninghoven A, Rüdenauer FG and Werner W, 1987: *Secondary Ion Mass Spectrometry; Basic Concepts Instrumental Aspects, Applications and Trends*, (Wiley, New York) section 5.1.6

Biemann K, Martin SA, Scoble HA and Johnson RS, 1986: in *Mass Spectrometry in the Analysis of Large Molecules*, ed. C J McNeal, (Wiley, New York) p. 131

Bitensky IS, Parilis ES, 1987: Nucl. Instrum. Methods B **21**, 26

Blais JC, Viari A, Cole RB and Tabet JC, 1990: Int. J. Mass Spectrom. Ion Processes **98**, 155

Bolbach G, Della-Negra S, Deprun C, Le Beyec Y and Standing KG, 1987: Rapid Commun. Mass Spectrom. **1**, 22

Bolbach G, Beavis R, Della Negra S, Deprun C, Ens W, Le Beyec Y, Main D E, Schueler B and Standing KG, 1988: Nucl. Instrum. Meth. B **30**, 74

Bolbach G, Viari A, Brunot A and Blais JC, 1992: Int. J. Mass Spectrom. Ion Processes **112**, 93

Brinkmalm G, Håkansson P, Kjellberg J, Demiriv P, Sundqvist BUR, Ens W, 1992: Int. J. Mass Spectrom. Ion Processes **114**, 183

Brown WL and Johnson RE, 1986: Nucl. Instrum. Meth. B **13**, 295

Buko A, Phillips LR and Fraser BA, 1983: Biomed. Mass Spectrom. **7**, 408

Busch KL, Unger SE, Vincze A, Cooks RG and Keough T, 1982: J. Am. Chem. Soc. **104**, 1507

Busch KL, Hsu BH, Xie YX and Cooks RG, 1983: Anal. Chem. **55**, 1157

Campana JE, Ross MM and Callahan JH, 1987: Int. J. Mass Spectrom. Ion Processes **78**, 195

Chait BT, 1987: Int. J. Mass Spectrom. Ion Processes **78**, 237

Chait BT and Field FH, 1981: Int. J. Mass Spectrom. Ion Phys. **41**, 17

Chait BT and Field FH, 1984: J. Am. Chem. Soc. **106**, 1931

Chait BT and Standing KG, 1981: Int. J. Mass Spectrom. Ion Phys. **40**, 185

Chrisey DB, Boring JW, Phipps JA, Johnson RE and Brown WL, 1986: Nucl. Instrum. Meth. B **13**, 360

Colton RJ, Ross MM and Kidwell DA, 1986: Nucl. Instrum. Meth. B **13**, 259

Cooks RG and Busch KL, 1983: Int. J. Mass Spectrom. and Ion Physics **53**, 111

David DE, Magnera TF, Tian R, Stulik D and Michl J, 1986a: Nucl. Instrum. Meth. B **14**, 378

David DE, Magnera TF, Tian R and Michl J, 1986b: Radiat. Eff. **99**, 247

Dell A and Morris HR, 1982: Biochem. Biophys. Res. Commun. **106**, 1456

Della-Negra S and Le Beyec Y, 1985: Anal. Chem. **57**, 2035

Della-Negra S, Becker O, Cotter R, Le Beyec Y, Monart B, Standing KG and Wien K, 1987: J. Physique **48**, 261

Della Negra S, Depauw J, Joret H, Le Beyec Y and Schweikert EA, 1988: Phys. Rev. Lett. **60**, 948

Della-Negra S, Depauw J, Joret H and Le Beyec Y, 1989: J. de Physique **C2**, 63

De Pauw E, 1986: Mass Spectrom. Reviews **5**, 191

De Pauw E, Agnello A and Derwa E, 1991: Mass Spectrom. Reviews **10**, 10

Derwa F and De Pauw E, 1991: Org. Mass Spectrom. **26**, 117

Derwa F, De Pauw E, Galera R and Blais JC, 1990: Spectra 2000, **150**, 36

Dück P, Fröhlich H, Treu W and Voit H, 1981: Nucl. Instrum. Methods **191**, 245

Elliott G, Cottrell J S and Evans S, 1986: Proc. 34th ASMS Conf. on Mass Spectrom. Allied Topics, Cincinnati, OH, p. 880

Ens W and Standing KG, 1982: unpublished data

Ens W, Standing KG, Chait BT and Field FH, 1981: Anal. Chem. **53**, 1241

Ens W, Beavis R and Standing KG, 1983: Phys. Rev. Lett. **50**, 27

Ens W, Beavis R, Bolbach G, Main D, Schueler B and Standing K G, 1986: Nucl. Instrum. Meth. A **245**, 146

Ens W, Håkansson P, Sundqvist BUR, 1988a: *Secondary Ion Mass Spectrometry* SIMS VI, Ed. A M Huber, A Benninghoven, H W Werner and G Slodzian (Wiley, Chichester 1988) p. 623; and unpublished data from the same experiment

Ens W, Main D E, Standing KG and Chait BT, 1988b: Anal. Chem. **60**, 1494

Ens W, Sundqvist BUR, Håkansson P, Hedin A and Jonsson G, 1989a: Phys. Rev. B **39**, 763

Ens W, Sundqvist BUR, Håkansson P, Fenyö D, Hedin A, and Jonsson G, 1989b: J. de Physique **C2**, 9

Ens W, Mao Y, Mayer F and Standing KG, 1991: Rapid Commun. Mass Spectrom. 5, 117

Fenn JB, Mann M, Meng CK, Wong SF and Whitehouse CM, 1990: Mass Spectrom. Reviews **9**, 37

Fenselau C and Cotter RJ, 1986: in *Mass Spectrometry in the Analysis of Large Molecules*, ed. C J McNeal, (Wiley, New York) p. 89

Fenselau C and Cotter RJ, 1987: J. Chem. Rev. **87**, 501

Fenselau C and Hyver K, 1986: in *Ion Formation from Organic Solids IFOS III*, Springer Proc. in Physics 9, Ed. A Benninghoven, (Springer, Heidelberg) p. 109

Field FH, 1982: Anal. Chem. **86**, 5115

Galera R, Blais JC and Bolbach G, 1991: Int. J. Mass Spectrom. Ion Processes **107**, 53

Gibson BW, Yu Z, Burlingame AL and Aberth W, 1988: in *The Analysis of Peptides and Proteins by Mass Spectrometry*, ed. C J McNeal, (Wiley, New York) p. 217

Gillen G, Christiansen JW, Tsong IS T, Kimball B and Williams P, 1988: Rapid Commun. Mass Spectrom. **2**, 67

Green BN and Bordoli RS, 1991: in *Mass Spectrometry of Peptides*, Ed. D M Desiderio, (CRC Press, Boston), p. 109

Hagenhoff B, van Leyen D, Feld H and Benninghoven A, 1990: in *Ion Formation from Organic Solids IFOS-V*, eds. A Hedin, BUR Sundqvist and A Benninghoven, (Wiley, Chichester) p. 81

Hagenhoff B, Deimel M, Benninghoven A, Siegmund H and Holtkamp D, 1992: J. Appl. Phys. **25**, 818

Håkansson P, 1993, Mat. Fys. Medd. Dan. Vid. Selsk. **43**, 593

Håkansson P and Sundqvist BUR, 1981: Rad. Eff. **61**, 179

Håkansson P, Kamensky I, Salehpour M, Sundqvist B, and Widdiyasekera S, 1984: Rad. Eff. **80**, 141

Hamdan M, Curcuruto O, Franchi D and Tarzia G, 1992: Rapid Commun. Mass Spectrom. **6**, 712

Hand OW, Majumdar T K and Cooks RG, 1990: Int. J. Mass Spectrom. Ion Processes **97**, 35

Hebert N, Blais JC, Bolbach G and Inchaouh J, 1986: Int. J. Mass Spectrom. Ion Processes **70**, 45

Hoogerbrugge R and Kistemaker PG, 1988: in *Secondary Ion Mass Spectrometry SIMS VI*, eds. A Benninghoven, A M Huber, and H W Werner, (Wiley, Chichester) p. 631

Hoogerbrugge R, van der Zande WJ and Kistemaker PG, 1987: Int. J. Mass Spectrom. Ion Processes **76**, 239

Hunt JE, Salehpour M, Fishel DL and Tou JC, 1989: J. de Physique **C2**, 27

Hsu BH, Xie YX, Busch KL and Cooks RG, 1983: Int. J Mass Spectrom. Ion Physics **51**, 225

Inchaouh J, Blais JC, Bolbach G and Brunot A, 1984: Int. J Mass Spectrom. Ion Processes **61**, 153

Johnson RE, Sundqvist BUR, Hedin A and Fenyö D, 1989b: Phys. Rev. B **40**, 49

Jonkman HT, Michl J King RN and Andrade JD 1978: Anal. Chem. **50**, 2078

Jonsson GP, Hedin AB, Håkansson P, Sundqvist BUR, Säve G, Nielsen PF, Roepstorff P, Johansson KE, Kamensky I and Lindberg MSL, 1986: Anal. Chem. **58**, 1084

Jonsson G, Hedin A, Håkansson P and Sundqvist BUR, 1988: Rapid Commun. Mass Spectrom. **2**, 154

Jonsson G, Hedin A, Håkansson P, Sundqvist BUR, Bennich H and Roepstorff P, 1989a: Rapid Commun. Mass Spectrom. **3**, 190

Jordan EA, Macfarlane RD, Martin CR and McNeal CJ, 1983: Int. J. Mass Spectrom. Ion Phys. **53**, 345

Junack M, Sichtermann W and Benninghoven A, 1985: in *Ion Formation From Organic Solids IFOS III*, Ed. A Benninghoven (Springer-Verlag, Berlin) p. 96

Kambara H, 1982: Organic Mass Spectrom. **17**, 29

Kambara H and Hishida S, 1981: Anal. Chem. **53**, 2340

Kamensky I, Håkansson P, Sundqvist BUR, 1982: Nucl. Instrum. Methods **198**, 65

Karas M, 1993: Mat. Fys. Medd. Dan. Vid. Selsk. **43**, 623

Katta V, Grace L, Chaudary T and Chait BT, 1988: in Proc. 36th ASMS Conf. on Mass Spectrom. and Allied Topics, San Francisco, CA, p 413

Katz RN, Chaudhary T and Field FH, 1986: J. Am. Chem. Soc. **108**, 3897

Katz RN, Chaudhary T and Field FH, 1987: Int. J. Mass Spectrom. Ion Processes **78**, 85

Kelner K and Markey SP, 1984: Int. J. Mass Spectrom. Ion Processes **59**, 157

Lafortune F, Beavis R, Tang X, Standing KG and Chait BT, 1987: Rapid Commun. Mass Spectrom. **1**, 114

Lange W, Holtkamp D, Jirikowsky M and Benninghoven A, 1983: in *Ion Formation From Organic Solids*, ed. A Benninghoven (Springer-Verlag, Berlin) p. 124

Lange W, Jirikowsky M and Benninghoven A, 1984: Surf. Sci. **136**, 419

Ligon WV, Jr., 1983: Int. J. Mass Spectrom. Ion Phys. **52**, 183

Ligon WV, Jr. and Dorn SB, 1986: Int. J. Mass Spectrom. Ion Processes **78**, 99

Lindhard L, Scharff M and Schiøtt HE, 1963: Mat. - Fys. Medd. Dan. Vid. Selsk. **33**, no. 14

Liu LK, Busch KL and Cooks RG, 1981: Anal. Chem. **53**, 113

Macfarlane RD and Torgerson DF, 1976a: Science **191**, 920.

Macfarlane RD and Torgerson DF, 1976b: Int. J Mass Spectrom. Ion Processes **21**, 81

Magee CW, 1983: Int. J. Mass Spectrom. Ion Phys. **49**, 221

Marien J and De Pauw E, 1982: Int. J. Mass Spectrom. Ion Processes **43**, 233

Martin SA and Biemann K, 1987: Int. J. Mass Spectrom. Ion Processes **78**, 213

Martin SA, Costello CE and Biemann K, 1982: Anal. Chem. **54**, 2362

McNeal CJ, Macfarlane RD and Thurson EL, 1979: Anal. Chem. **51**, 2036

Michl J, 1983: Int. J. Mass Spectrom. Ion Phys. **53**, 255

Morales A, Kebarle P and Sunner J, 1989: Int. J. Mass Spectrom. Ion Processes **87**, 287

Moshammer R and Matthäus R, 1989: J. de Physique **C2**, 111

Moshammer R, Matthaäs R, Wien K and Bolbach G, 1990: in *Ion Formation from Organic Solids IFOS V*, eds. A Hedin, BUR Sundqvist and A Benninghoven, (Wiley, Chichester) p. 17

Naylor S, Moneti G and Guyan S, 1988: Biomed. Environ. Mass Spectrom. **17**, 393

Niehuis E, 1987: in *Secondary Ion Mass Spectrometry - SIMS VI*, eds. A Benninghoven, A M Huber and H W Werner, (Wiley, Chichester) p. 591

Niehuis E, Heller T, Feld H and Benninghoven A, 1986: in *Ion Formation from Organic Solids IFOS III*, Springer Proc. Phys. 9, ed. A Benninghoven, (Springer, Heidelberg) p. 198

Olthoff K and Cotter RJ, 1987: Nucl. Instrum. Meth. B **26**, 566

Olthoff JK, Lys IA and Cotter RJ, 1988: Rapid Commun. Mass Spectrom. **9**, 171

Pachuta SJ and Cooks RG, 1987: Chem. Rev. **87**, 647

Phillips LR and Bartmess JE, 1989: Biomed. Environ. Mass Spectrom. **18**, 878

Poppe-Schriemer N, 1993, PhD Thesis work, University of Manitoba, Winnipeg, Canada, (expected 1993)

Poppe-Schriemer N, Binding DR, Ens W, Mayer F, Standing KG, Tang X and Westmore JB, 1991: Int. J. Mass Spectrom. Ion Processes **111**, 301

Reimann CT, 1993: Mat. Fys. Medd. Dan. Vid. Selsk. **43**, 351

Reynolds JD and Cook KD, 1990: J. Am. Soc. Mass Spectrom. **1**, 233

Roepstorff P and Fohlman J, 1984: J. Biomed. Mass Spectrom. **11**, 601

Rouse JC and Allison J, 1993: J. Am. Soc. Mass Spectrom. **4**, 259

Salehpour M, Hunt JE, Fishel DL and Tou JC, 1989: Int. J. Mass Spectrom. Ion Processes **88**, 211

Säve G, Håkansson P and Sundqvist BUR, 1987a: Nucl. Instrum. Meth. B **26**, 571

Säve G, Håkansson P, Sundqvist BUR, Söderström E and Lindquist SE, 1987b: Int. J. Mass Spectrom. Ion Processes **78**, 259

Säve G, Håkansson P, Sundqvist BUR, Johnson RE, Sördeström E, Lindquist SE and Berg J, 1987c: Appl. Phys. Lett. **51**, 1379

Shiea JT and Sunner J, 1990: Int. J. Mass Spectrom. Ion Processes **96**, 243

Schueler B, Beavis R, Ens W, Main DE and Tang X, 1989: Int. J. Mass Spectrom. and Ion Processes **92**, 185

Sigmund P, 1968: Can. J. Phys. **46**, 731

Sigmund P, 1969a: Phys. Rev. **184**, 383; **187**, 768

Sigmund P, 1981: in Behrisch (1981) p. 9

Standing KG, Ens W, Chait BT and Field FH, 1980: presented at a symposium on *Ion Formation from Organic Solids*, Münster, Oct. 1980

Standing KG, Chait BT, Ens W, McIntosh G and Beavis R, 1982: Nucl. Instrum. Methods **198**, 33

Standing KG, Ens W, Beavis R, Bolbach G, Main D, Schueler B, Tang X and Westmore JB, 1986: in Ion Formation from Organic Solids IFOS III, Springer Proc. Phys. 9 (Springer, Heidelberg) p. 37

Standing KG, Ens W, Mayer F, Tang X and Westmore JB, 1990: in *Mass Spectrometry of Large Non-Volatile Molecules for Marine Organic Chemistry*, eds. E R Hilf and W Tuszynski, (World Scientific, New Jersey) p. 186

Steffens P, Niehuis E, Friese T, Greifendorf D and Benninghoven A, 1985: J. Vac. Sci. Technol. **A3**, 1322

Sundqvist BUR, 1991: in Behrisch and Wittmaack (1991) p. 257

Sundqvist BUR, Roepstorff P, Fohlman J, Hedin A, Håkansson P, Kamensky I, Lindberg M, Salephour M and Säve G, 1984: Science **226**, 696

Sunner JA, Kulatunga R and Kebarle P, 1986: Anal. Chem. **58**, 1312

Sunner J, Morales A and Kebarle P, 1987: Anal. Chem. **59**, 1378

Sunner J, Morales AM and Kebarle P, 1988a: Int. J. Mass Spectrom. Ion Processes **86**, 169

Sunner J, Ikonomou MG and Kebarle P, 1988b: Int. Mass Spectrom. Ion Processes **82**, 221

Surman DJ and Vickerman JC, 1981: J. Chem. Soc. Chem. Commun. **1981**, p. 324

Szymczak W and Wittmaack K, 1989: J. de Physique **C2**, 75

Takayama M, Fukai T, Nomura T and Nojima K, 1990: Int. J. Mass Spectrom. Ion Processes **96**, 169

Tang X, Beavis R, Ens W, Lafortune F, Schueler B and Standing K G, 1988: Int. J. Mass Spectrom. Ion Processes **85**, 43

Tang X, Ens W, Mayer F, Standing KG and Westmore JB, 1989: Rapid Commun. Mass Spectrom. **3**, 443

Tang X, Ens W and Standing KG, 1990:in Proc. 38th ASMS Conf. Mass Spectrom. and Allied Topics, Tucson, AZ p. 542

Tang X, Ens W, Poppe-Schriemer N and Standing KG, 1991: in *Methods and Mechanisms for Producing Ions from Large Molecules*, eds. KG Standing and W Ens, NATO ASI Series B: Physics Vol. 269, (Plenum, New York) p. 139

Tang X, 1991: PhD Thesis, University of Manitoba, Winnipeg, Canada

Todd P J, 1991: J. Am. Soc. Mass Spectrom. **2**, 29

Todd PJ and Groenewald GS, 1986: Anal. Chem. **58**, 895

Torgerson DF, Skowronski RP and Macfarlane RD, 1974: Res. Commun. **60**, 616

Unger SE, Day RJ and Cooks RG, 1981: Int. J. Mass Spectrom. Ion Physics **39**, 231

Urbassek HM and Michl J, 1987: Nucl. Instrum. Meth. B **22**, 480

van der Peyl GJQ, van der Zand e WJ, Hoogerbrugge R and Kistemaker PG, 1985: Int. J Mass Spectrom. Ion Processes **67**, 147 van Leyen D, Greifendorf D and Benninghoven A, 1987: in *Secondary Ion Mass Spectrometry SIMS VI*, eds. A Benninghoven, QM Huber and HW Werner, (Wiley, Chichester) p. 679

Voress L, 1993: Focus Column on the LeCroy Symposium on Instrumentation for Time-of-Flight Mass Spectrometry, Nov 1992, Anal. Chem. **65**, 75A

Wien K, Becker O, Guthier W, Della-Negra S, Le Beyec Y, Monart B, Standing KG, Maynard G and Deutsch C, 1987: Int. J. Mass Spectrom. Ion Processes **78**, 273

Williams DH and Naylor S, 1987: J. Chem. Soc. Chem. Commun. **1987**, p 1408

Williams DH, Findeis AF, Naylor S and Gibson W, 1987: J. Am. Chem. Soc. **109**, 1980

Williams P and Gillen G, 1989: in *Ion Formation from Organic Solids IFOS IV*, ed. A Benninghoven, (Wiley, Chichester) p. 15

Wilson WD, Haggmark LG and Biersack JP, 1977: Phys. Rev. B **15**, 2458

Winger BE, Hand OW and Cooks RG, 1988: Int. J. Mass Spectrom. Ion Processes **84**, 89

Wong SS and Röllgen FW, 1986a: Nucl. Instrum. Meth. B **14**, 436

Wong SS and Röllgen FW, 1986b: Int. J. Mass Spectrom. Ion Processes **70**, 135

Wong SS, Röllgen FW, Manz I and Przbylski M, 1985: Biomed. Mass Spectrom. **12**, 43

Yen TY, Barofsky E and Barofsky DF, 1992: presented at SPUT92, Copenhagen; Yen, T Y, PhD thesis (1992), Oregon State University, Corvalis Oregon

Zhou J, Ens W, Standing KG, Verentchikov A, 1992: Rapid Commun. Mass Spectrom. **6**, 671

Zhou J, Ens W and Standing KG, 1992: in Proc. 40th ASMS Conf. on Mass Spectrom. and Allied Topics, Washington DC, May 1992, p. 222

Ziegler JF, Ed., 1980: *Handbook of Stopping Cross-Sections for Energetic Ions in All Elements*, (Pergamon, New York)

Scanning Tunneling Microscopy Studies of Ion-Bombarded Surfaces

By I. S. T. Tsong
Department of Physics and Astronomy,
Arizona State University, Tempe, AZ 85287, U.S.A.
and
P. Bedrossian
Lawrence Livermore National Laboratory
Box 808, L-350 Livermore, CA 94550, U.S.A.

Synopsis

The recent results in atom-resolved scanning tunneling microscopy studies of semiconductor crystalline surfaces of Si(111)-(7 × 7) and Si(100)-(2 × 1) bombarded by energetic ions are reviewed. Low-fluence bombardment introduces surface damage consisting of random vacancies varying in size from single atom to multiple atoms. Annealing the bombarded Si(100) surface between 600°C and 850°C causes the random defects to order into vacancy lines perpendicular to the dimer rows. High-fluence experiments at elevated temperatures show nucleation of vacancy islands on Si(100) and Si(111) surfaces. With increasing temperatures and ion doses, step retraction occurs on the Si(100) and Si(111) surfaces, indicative of layer-by-layer sputtering. In the Si(100)-(2 × 1) case, a striking metastable single type-A domain is formed on the surface. For comparison, experiments of low-fluence bombardment of Au(111), and high-fluence bombardment of Pt(111) and $Pt_{25}Ni_{75}(111)$ surfaces are also briefly reviewed.

1 Introduction

A microscopic understanding of the interaction between energetic ions and solid surfaces became possible with the advent of the technique of scanning tunneling microscopy (STM). In this review, we will cover only those STM studies conducted in ultrahigh vacuum (UHV), i.e. where the base pressure of the experiment is at $\leq 1 \times 10^{-10}$ torr, because only at such vacuum are the starting surface and the tunneling conditions well-defined. There have been a number of STM studies of ion-bombarded surfaces of graphite or related materials carried out under atmospheric conditions. Unfortunately, the well-known anomalies observed in STM images of graphite in air (Albrecht et al., 1988; Colton et al., 1988; Kuwabara et al., 1990; Heckl & Binnig, 1992) were not addressed in these studies. Neither has there been any attempt to conduct definitive studies on the possible changes in tunneling response associated with enhanced adsorption of oxygen and other contaminants on the bombarded surface exposed to air. In view of these deficiencies and uncertainties, ambient STM studies of ion-bombarded graphite will not be included here.

The STM experiments carried out thus far are divided into two categories: (a) the low-fluence approach, in which the effects of individual ion impacts are examined; and (b) the high-fluence approach, in which sputtering of the surface is treated as the inverse of crystal growth. The surfaces studied are by necessity single-crystalline in nature so that the STM can clearly discern the initial ordering and defect density (if any) prior to ion bombardment. The bombardment is carried out in situ, i.e. in the same UHV chamber in which STM studies are being conducted, to avoid contamination of the surface. This is to ensure that any change in topography, defect density and atomic order observed by the STM must be the consequence of ion bombardment.

In this review, we present a detailed discussion of STM results of ion bombardment of semiconductor surfaces, specifically Si(111) and Si(100) surfaces, obtained over the past two years by the authors. STM studies of ion-bombarded surfaces of metals and alloys, primarily carried out by the research groups of Stanford, Jülich and Vienna, are also briefly discussed.

2 Low-Fluence Experiments

Prior to bombardment, the Si(111) and Si(100) surfaces were cleaned by flashing to 1200°C for ~20 seconds to eliminate the native oxide layer. The pressure in the UHV chamber was kept at or below 2×10^{-9} torr when the sample was at 1200°C. After the heat treatment, the atom-resolved STM images of these two surfaces would show the familiar Si(111)-(7 × 7) and Si(100)-(2 × 1) reconstructions. It is important to keep the defect density of the clean surface as low as possible since certain defects appear as vacancies or adclusters which may be confused as effects due to ion bombardment. Transition metal contamination is a main contributor to these defects, and in order to avoid this, all parts in contact or in the vicinity of the silicon samples are constructed in either tantalum or molybdenum.

The Si(111)-(7 × 7) and Si(100)-(2 × 1) reconstructions are easily contaminated by oxygen and the contamination produces surface features, e.g. the appearance of missing atoms, which could easily be mistaken as ion-bombardment damage (Liebsle et al., 1988; Avouris et al., 1991; Pelz & Koch, 1991; Kliese et al., 1992; Avouris & Cahill, 1992). To ensure that the STM was not imaging oxygen contamination, two tests were performed. The first was to leak the 99.9999% pure argon gas via the differentially pumped ion gun into the UHV chamber to a pressure higher than that used during ion bombardment for several minutes. It was confirmed by STM that the Si surfaces were not affected up to a pressure of 1×10^{-5} torr. The second test was to place the sample in the proximity of, but not actually in, the path of the Ar^+ ion beam for periods longer than that required to achieve a typical fluence. Once again STM images showed no sign of contamination of the silicon surfaces.

The clean Si(111) and Si(100) surfaces were bombarded by 3keV Ar^+ ions at normal incidence at fluences ranging from 7×10^{11} to 6×10^{12} ions cm^{-2}. 10^{12} ions cm^{-2} correspond to ~0.001 monolayer (ML) coverage. During bombardment, the pressure in the UHV chamber rose to 3×10^{-8} torr. Typical ion currents used were 5 - 10nA and the bombardment lasted a few seconds. The beam spot on the sample was 5mm in diameter.

The Si(111) and Si(100) surfaces before and after 3keV Ar^+ ion bombardment are shown in figs. 1 and 2 respectively. The defects created by ion bombardment are mainly in the form of missing atoms. These missing atoms tend to congregate to give the appearance of craters on the Si(111) and Si(100) surfaces. Usually in the vicinity of these craters, some bright spots are found. These are most likely adatoms or adclusters which originate from the sputtering process, perhaps due to atoms displaced from the nearby craters.

The appearance that the craters on the Si(111)-(7×7) surface are larger than those on the Si(100)-(2×1) surface can be easily understood from a consideration of the size of the 7×7 unit cell. The 7×7 has a unit cell edge of 27Å. The disappearance of four adjacent Si adatoms on the 7×7 surface would result in a pit of ~15Å × 15Å in area. Correspondingly, the disappearance of the same number of atoms on the 2×1 surface, e.g. two pairs of dimers on the same dimer row, would result in a pit area of only ~5Å × 5Å.

Over 200 STM images were taken by Zandvliet et al. (1992) on the ion- bombarded Si(111) and Si(100) surfaces and the results were remarkably consistent. From these images, we note that there are almost always more craters than the number of ion impacts. This means if we try to determine a sputtering yield from the number of missing atoms in the image, then the yield is always greater than 1 because each crater contains more than 1 missing atom. The sputtering yield determined by conventional methods (Zalm, 1988) for 3keV Ar^+ ions incident normally on Si is ~1. This suggests that at the very initial stages of sputtering, i.e. when the ion fluence is still insufficient to disturb the surface order, the sputtering yield may be higher than that measured at steady state, i.e. after the surface has been

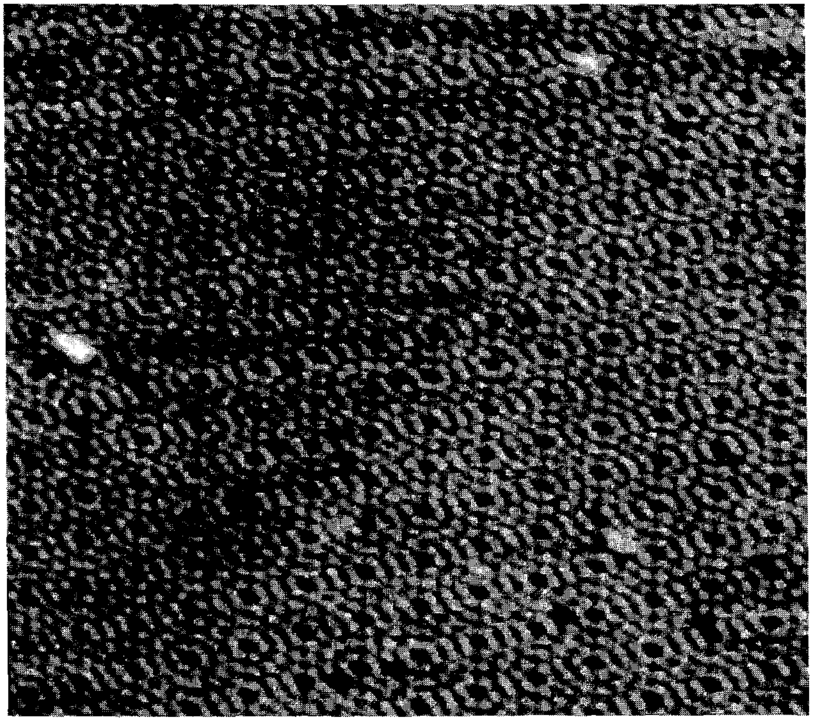

Figure 1a. STM image of Si(111)-(7 × 7) surface. Sample bias was 1.8V and tunnel current was 0.5nA. 40nm × 35nm scan of a clean surface showing the well-ordered 7× 7 reconstruction

impacted by high fluence and has become disordered. An observation of higher sputtering yield for an undamaged surface compared with a damaged surface has been reported for Ru(0001) by Burnett et al. (1989). On the other hand, the apparent large crater size observed in the images may not entirely be the result of sputtering. They could be the result of surface relaxation to relieve the strain produced by subsurface damage by the incoming ion as shown by Wilson et al. (1988). Classical molecular dynamics (MD) simulations by Feil et al. (1992) using a silicon microcrystallite consisting of 12 layers of 32 atoms each have reproduced some of the large craters observed on the Si(100) surface. Interestingly, however, in the same simulations, the number of atoms observed leaving the surface as sputtered atoms gives a sputtering yield of ~1. Thus the MD simulations support the notion that the observed craters are not exclusively due to sputtering.

Zandvliet et al. (1992) showed that on annealing, the ion-bombarded Si(111)

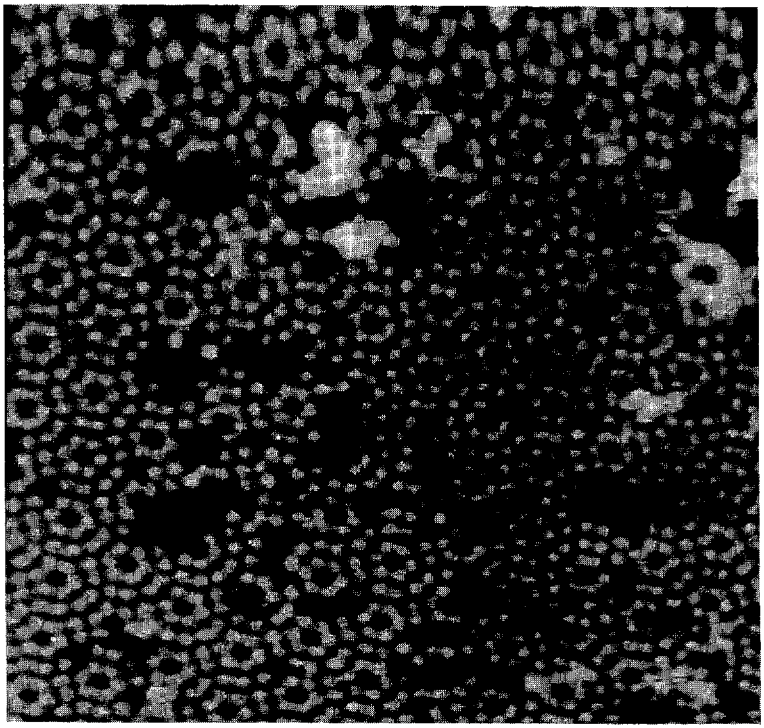

Figure 1b. Same as fig. 1a, but 25nm × 25nm scan of a surface bombarded by 3keV Ar^+ ions at a dose of $3 \times 10^{12}/cm^2$. A cratered appearance of the 7 × 7 structure is clearly visible.

and Si(100) surfaces produced contrasting results. The ion-bombarded defects or craters on the Si(111) surface disappeared totally when the surface was annealed at 750°C for 2 minutes and the 7 × 7 reconstruction was completely restored. The defects on the Si(100) surface, on the other hand, ordered into line defects perpendicular to the dimer rows as shown in fig. 3 upon annealing at temperatures between 600°C and 850°C for 2 minutes. When annealed at 950°C for 2 minutes, however, the line defects disappeared and the surface was restored to the original 2 × 1 state. No ordering of defects was observed at 500°C, indicating that the ordering threshold on the Si(100) surface was somewhere between 500°C and 600°C (Feil et al., 1992).

A likely mechanism for the ordering behavior on the Si(100) surface is that at elevated temperatures, the vacancies have preferential mobility along the dimer rows in addition to attractive interaction among themselves. When the vacancies

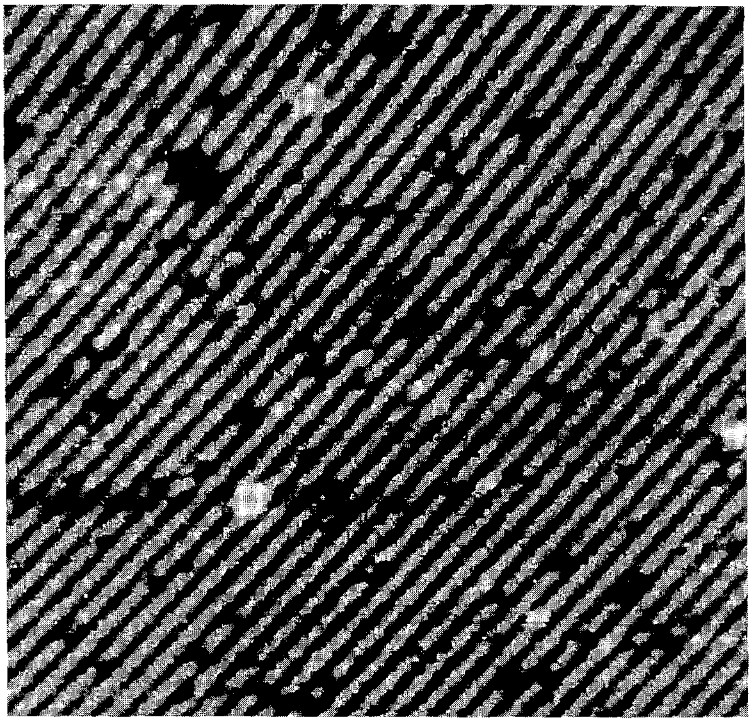

Figure 2a. STM image of Si(100)-(2 × 1) surface. Sample bias was -2.0V and tunnel current was 0.5nA. 20nm × 17nm scan of a clean surface showing the 2 × 1 reconstruction of dimer rows.

meet, they form the line defects observed in fig. 3. The question then arises on why the vacancies line up perpendicular to the dimer rows rather than parallel. Feil et al. (1992) performed quantum mechanical MD simulations using the ab initio real space tight-binding method of Sankey & Niklewski (1989) to seek an answer. In these simulations, the Si(100) surface was modeled by a five-layer slab repeated slab supercell, with the atoms in the bottom layer assigned huge masses and attached to hydrogen-like atoms to saturate their dangling bonds so that they were motionless and regarded as bulk atoms. Then a line of atoms (or dimers) was removed from the 2 × 1 surface and the atoms on the surface and in the exposed second layer were allowed to settle into their most favorable positions according to Newton's laws of motion. The total energies of the missing line perpendicular to the dimer rows and the missing line parallel to the dimer rows were then calculated and compared. Feil et al. (1992) found that the perpendicular case was favored by

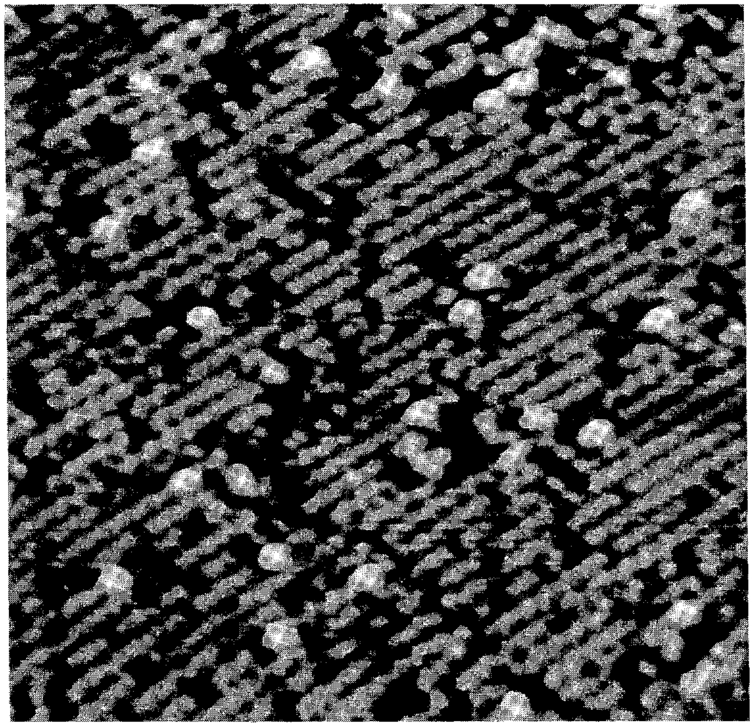

Figure 2b. Same as fig. 2a but 15nm × 22nm scan of a surface bombarded by 3keV Ar^+ ions at a dose of $3 \times 10^{12}/cm^2$. A pitted surface with missing dimers is observed.

having an energy lower by an amount of 0.011 eV/atom, in agreement with STM observations.

The depths of the sputtered craters on the Si(111) and Si(100) surfaces measured from the STM images are 2.1Å and 1.4Å respectively, suggesting that only the top layer surface atoms are missing or removed. This is not, however, conclusive evidence that sputtered atoms originate from the top layer because the observed craters or depressions may be a consequence of surface relaxation as discussed earlier. Due to the open structure of the silicon lattice, sputtering from second or deeper layers is conceivable as demonstrated by recent molecular-dynamics simulations by Smith et al. (1989) and experiments by Blumenthal et al. (1991). However, this may only be applicable to sputtering of an undamaged surface as high-fluence experiments in the next section provide convincing evidence of layer-by-layer sputtering.

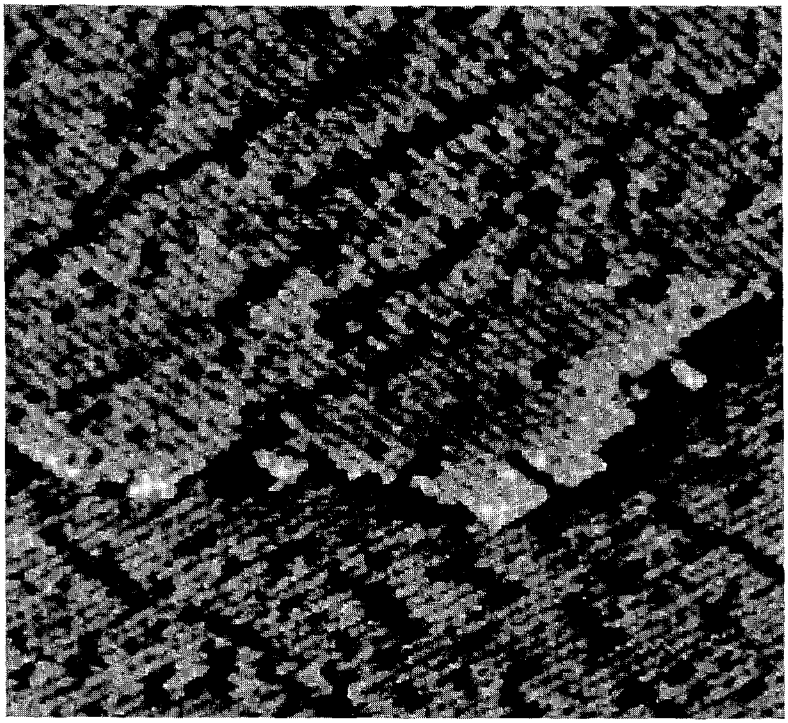

Figure 3. STM image of a bombarded Si(100)-(2 ×1) surface annealed at 750°C for 2 minutes. Scan area = 40nm × 40nm. Sample bias = -2.0V. Tunnel current = 0.5nA. The dimer vacancies ordered into lines perpendicular to the dimer rows on the type-B terrace (upper) and type-A terrace (lower) of the 2 ×1 surface.

STM studies of low-fluence Ne^+ ion bombardment at energies 3keV and 600eV on Au(111) surfaces under UHV conditions have been reported by Lang et al. (1991). They observed pits or craters on the Au(111) surface created by sputtering with a minimum diameter of 10Å, corresponding to approximately 10 atomic vacancies. Interestingly, the pit sizes showed an increasing trend with increasing ion fluence. The increase in pit size is probably due to the high mobility of vacancies on the Au surface even at room temperature, such that smaller pits tend to coalesce to form larger pits. This coalescent effect also explains why no pit sizes under 10Å were observed. Similar to the work of Zandvliet et al. (1992) on Si surfaces, the measured depth of the pits on Au(111) is 2.5Å, i.e. single atomic layer deep, suggesting that sputtering only removes the top-layer atoms.

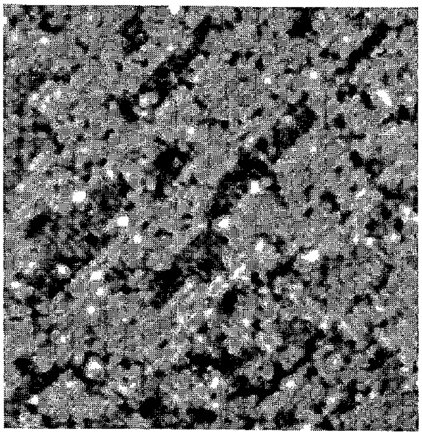

Figure 4. 360Å × 360Å STM image of Si(100)-2 ×1 following removal of ≈1/2 ML by 225eV Xe^+ sputtering with the substrate at 400°C. Anisotropic monolayer- deep depressions or vacancy islands (darker regions) are elongated parallel to the dimer rows of the top layer. The tip bias is +1.8V, so that occupied states are imaged.

3 High-Fluence Experiments

Bedrossian & Klitsner (1991, 1992) carried out STM studies of ion bombardment of Si(111)-(7 × 7) and Si(100)-(2 × 1) at high fluences ($>10^{15}$ ions/cm^2 and elevated temperatures. They showed that at sufficiently low ion energies, (≈200- 250eV) atomic-layer control of sputtering can be achieved. In an earlier study, Bedrossian et al. (1992) observed oscillations in reflection high-energy electron diffraction (RHEED) during glancing-angle, low-energy ion irradiation (200eV Xe^+) of Si(100)-(2 × 1) held at elevated temperatures, establishing that layer-by-layer removal from silicon can be accomplished under these conditions and implying that such a process may be described as the inverse of silicon homoepitaxial growth. Whereas the evolution of surface morphology during growth is mediated by mobile adatoms, which can either nucleate adatom islands or attach at step edges; layer-by-layer sputtering is found to be mediated by mobile surface vacancies which are created during sputtering and which can either nucleate monolayer-deep vacancy islands or annihilate at step edges. Monte Carlo simulations incorporating these processes have reproduced all of the RHEED observations (Chason et al., 1991).

STM has elucidated the kinetics and consequences of the signatures of layer-by-layer sputtering of silicon, vacancy island nucleation and step retraction. On Si(100), for example, one observes with increasing substrate temperature both a lower density and larger average size of vacancy islands for a given ion fluence,

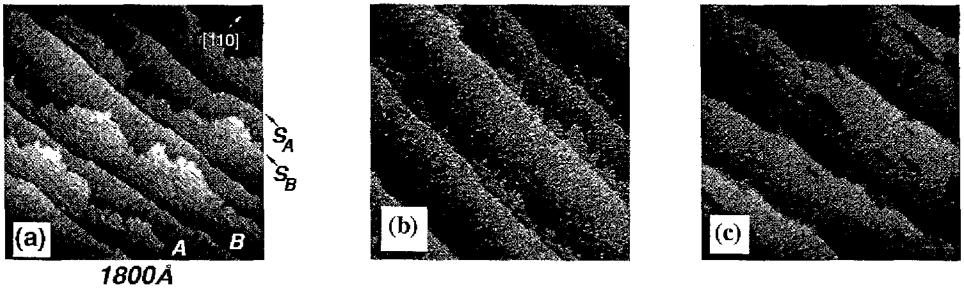

Figure 5. a) 1800Å x 1800Å image of 0.2°-offcut Si(100) showing predominantly straight S_A steps and wavy S_B steps on the 2 × 1 surface. b) 1800Å x 1800Å image following 225eV Xe^+ sputtering of $\approx 1/2$ ML at 450°C, showing depletion of the type-B domain. c) 1800Å x 1800Å image following Xe^+ sputtering of ≈ 1 ML at 450°C, showing almost complete depletion of the type-B domain and nucleation of depressions or vacancy islands in the type-A domain.

consequences of increasing vacancy mobility with temperature. Fig. 4 shows an example of vacancy island formation on Si(100) following removal of $\approx 1/2$ monolayer (ML) by 225eV Xe^+ ions incident at 75° from the surface normal, with the substrate held at 400°C. Because the dimer rows inside the vacancy islands are perpendicular to those in the outer layer, the vacancy islands are one monolayer deep (Chadi, 1987). The elongation of the depressions parallel to the dimer rows in the outer atomic layer indicates that mobile surface vacancies annihilate preferentially at the ends of dimer rows, just as the analogous elongation of growth islands along dimer rows has been ascribed to preferential sticking of adatoms at the ends of dimer rows (Hamers et al., 1989; Mo et al., 1989).

At still higher temperatures, a transition takes place from vacancy island nucleation to step retraction, analogous to step flow in epitaxial growth. For the case of Si growth on a substrate miscut towards the [110] direction, the preferential sticking of adatoms at the ends of dimer rows causes the S_B-step, which consists of the ends of dimer rows, to catch up with the S_A-step, which is parallel to a single dimer row, leading to a double-stepped, single-B-domain surface, on which all dimer rows lie perpendicular to the step edges (Sakamoto et al., 1987; Hoeven et al., 1987). Here, we use Chadi's notation (1987) for S_A and S_B steps. In the case of layer-by-layer sputtering, the preferential annihilation of vacancies at the ends of dimer rows leads to the retraction of the S_B-step relative to the S_A-step, as shown in fig. 5, resulting in a single-A-domain surface, a new surface phase of Si(100) which is not accessible by epitaxial growth. While the single-A-domain phase is not an equilibrium structure, it is stable at the temperature at which it was created. Its stability at typical growth temperatures therefore makes it a promising substrate

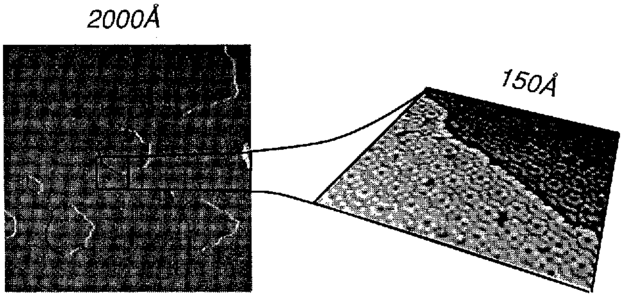

Figure 6. A 2000Å x 2000Å STM image and accompanying detail of a Si(111)-7 × 7 surface following 225eV Xe^+ bombardment at 580°C, showing monolayer- deep vacancy islands. The floor of the vacancy island in the enlarged image shows near-perfect 7 × 7 reconstruction. The tip bias is -1.8V, so unoccupied sample states are imaged.

for III/V-on-Si heteroepitaxy.

Layer-by-layer sputtering of Si(111) also proceeds via nucleation of vacancy islands, giving way to step retraction at elevated temperatures. In addition, one observes on this surface a second transition involving the surface periodicity itself. Layer-by-layer sputtering of Si(100) was found to preserve the 2 × 1 periodicity of that surface as low as 250°C. However, the Si(111) surface exhibits a transition from destruction to preservation of the 7 × 7 reconstruction with increasing substrate temperature (Bedrossian & Klitsner, 1991). Fig. 6 shows monolayer-deep vacancy islands formed after 225eV Xe^+ sputtering of Si(111)-7 × 7 at 580°C. As shown in the detail, the layer exposed by sputtering exhibits the 7 × 7 reconstruction.

In contrast, layer-by-layer sputtering at lower substrate temperatures can leave the exposed atomic layers with no long-range reconstruction. Fig. 7 shows the retraction of a step edge following an initial stage of sputtering of Si(111)-7×7 at 400°C. The material on the lower plane exposed by sputtering, immediately adjacent to the step edge, exhibits no long-range reconstruction. A sharp boundary separates this unreconstructed region from the fully reconstructed region. One may infer that the original step edge on the starting surface followed the path of this boundary. Purely physical sputtering can therefore not only induce the dereconstruction of the Si(111) surface, but can also cause selective dereconstruction adjacent to a step edge as in fig. 7.

STM studies of sputtering of Au(111) and Pt(111) surfaces by energetic ions at high fluence and at high temperatures have been conducted by the Jülich group (Michely et al., 1990; Michely & Comsa, 1991 a and b). In these experiments, sputtering acted essentially as a source of mobile monatomic vacancies, while lat-

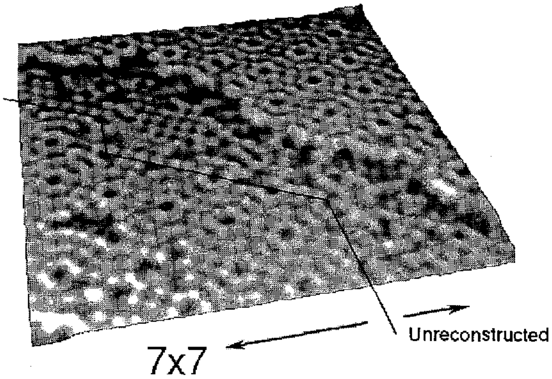

Figure 7. 150Å x 150Å image showing step retraction by 225eV Xe^+ sputtering of Si(111) at 400°C. The line separates the 7 ×7 region from newly exposed, unreconstructed material.

tice damaging effects were almost immediately annealed because of the elevated temperatures. Vacancy islands similar to those on silicon surfaces (Bedrossian & Klitsner, 1991 and 1992) were observed. Below 270°C, adatom islands were observed on Pt(111) in addition to vacancy islands. These adatom islands were formed by interstitials (of Frenkel pairs below the surface as a result of ion damage) diffusing to the surface layer forming adatoms which then coalesced to form islands. The adatom islands disappeared at or above 270°C leaving only vacancy islands. When the temperature was further increased to 350°C, the vacancy islands had an equilibrium hexagonal shape reflecting the symmetry of the (111) surface. As sputtering continued, STM images showed pits with depths of several monolayers. These pits consisted of hexagonal vacancy islands stacked one below another. The walls of each pit all had monolayer steps. The steps belonging to different layers generally did not touch and they maintained a constant pit slope. When sputtering was performed on Pt(111) at 440°C, the multi-layered pits were no longer observed. Instead, the STM images showed very large single-monolayer deep hexagonal vacancy islands. This surface morphology persisted even after the removal of 50 ML by sputtering and thus could be regarded as "steady-state" morphology attributable to layer-by-layer sputtering.

Schmid et al. (1992 a and b) have performed STM studies of preferential sputtering and recoil mixing of a $Pt_{25}Ni_{75}(111)$ alloy single crystal surface. Atom-resolved STM images of the sputtered surface annealed at 475°C clearly show dislocations which are attributed to sub-surface lattice mismatch dislocations reaching the surface. These mismatch dislocations are the result of preferential sputtering leading to platinum enrichment in the upper layers, which in turn increases the lattice constant in those layers.

4 Conclusions

Scanning tunneling microscopy (STM) has provided a new way of studying the effects of ion bombardment on surfaces on an atomic scale. The proper experimental procedure involves surface cleaning and in situ bombardment under UHV conditions. At low ion fluences, the defects in the form of missing atoms, pits and craters created by individual ion impacts can be examined in detail. The shapes and sizes of the ion- bombarded defects and their ordering at high annealing temperatures observed in STM images can be compared with molecular dynamics simulations. High-fluence bombardment of surfaces at room temperature generally results in a highly disordered surface and undulating surface topography. However, when bombardment is carried at elevated temperatures, formation of vacancy islands due to mobile vacancies is observed. Further bombardment at high temperatures results in annihilation of vacancies at step edges of Si(100) and Si(111) and steady-state monolayer deep hexagonal vacancy islands on Pt(111), confirming a layer-by-layer sputtering process. Other interesting phenomena in sputtering such as preferential sputtering in an alloy has also been studied by STM. The last two years have seen the beginning of atom- resolved STM studies of sputtered surfaces. Many more experiments are certain to follow and new insights will continue to be gained.

Acknowledgements

ISTT thanks J. D. Dow, H. B. Elswijk, H. Feil, M. H. Tsai, E. J. van Loenen and H. J. W. Zandevliet for their contributions and Philips Research Laboratories for the award of a van Houten Fellowship for this work. PB's work was performed at Sandia National Laboratories in collaboration with E. Chason, J. E. Houston, T. Klitsner, S. T. Picraux, and J. Y. Tsao and was supported by BES, Office of Materials Science, Contract No. DE-AC04-76DP00789, and at Lawrence Livermore National Laboratory under the auspices of the U.S. Department of Energy under Contract W-7405-Eng-48.

References

Albrecht TR, Mizes HA, Nogami J, Park SI and Quate CF, 1988: Appl. Phys. Lett. **52**, 362
Avouris Ph and Cahill D, 1992: Ultramicroscopy **42-44**, 838
Avouris Ph, Lyo IW and Boszo F, 1991: J. Vac. Sci. Technol. B **9**, 424
Bedrossian and P Klitsner T, 1991: Phys. Rev. B **44**, 13783

Bedrossian P and Klitsner T, 1992: Phys. Rev. Lett. **68**, 646

Bedrossian P, Houston JE, Tsao JY, Chason E and Picraux ST, 1991: Phys. Rev. Lett. **67**, 124

Blumenthal R, Caffey KP, Furman E, Garrison BJ and Winograd N, 1989: Phys. Rev. B **44**, 12830

Burnett JW, Pellin MJ, Calaway WF, Gruen DM and Yates Jr JT, 1989: Phys. Rev. Lett. **63**, 562

Chadi DJ, 1987: Phys. Rev. Lett. **59**, 1691

Chason E, Bedrossian P, Horn K, Tsao J and Picraux ST, 1991: Appl. Phys. Lett. **59**, 3533

Colton RJ, Baker SM, Driscoll RJ, Youngquist MG, Baldeschwieler JD and Kaiser WJ, 1988: J. Vac. Sci. Technol. A **6**, 349

Feil H, Zandvliet HJW, Tsai MH, Dow JD and Tsong IST, 1992: Phys. Rev. Lett. **69**, 3076

Hamers RJ, Kohler U and Demuth JE, 1989: Ultramicroscopy **31**, 10

Heckl WM and Binnig G, 1992: Ultramicroscopy **42-44**, 1073

Hoeven AJ, Lenssinck JM, Dijkkamp D, van Loenen EJ and Dieleman J, 1989: Phys. Rev. Lett. **63**, 1830

Kliese R, Röttger B, Badt D and Neddermeyer H, 1992: Ultramicroscopy **42-44**, 824

Kuwabara M, Clarke DR and Smith DA, 1990: Appl. Phys. Lett. **56**, 2396

Lang CA, Quate CF and Nogami J, 1991: Appl. Phys. Lett. **59**, 1696

Liebsle FM, Samsavar A and Chiang TC, 1988: Phys. Rev. B **38**, 5780

Michely T and Comsa G, 1991a: Surf. Sci. **256**, 217

Michely T and Comsa G, 1991b: Phys. Rev. B **44**, 8411

Michely T, Besocke KH and Comsa G, 1990: Surf. Sci. Lett. **230**, L135

Mo YW, Swartzentruber BS, Kariotis R, Webb MB, and Lagally MG, 1989: Phys. Rev. Lett. **63**, 2393

Pelz JP and Koch RH, 1991: J. Vac. Sci. Technol. B **9**, 775

Sakamoto T, Kawamura T, Nago S, Hashiguchi G, Sakamoto K and Kuniyoshi K, 1987: J. Cryst. Growth **81**, 59

Sankey OF and Niklewski DJ, 1989: Phys. Rev. B **40**, 3979

Schmid M, Biedermann A, Stadler H, Slama C and Varga P, 1992a: Appl. Phys. A **55**, 468

Schmid M, Biedermann A, Stadler H and Varga P, 1992b: Phys. Rev. Lett. **69**, 925

Smith R, Harrison DE and Garrison BJ, 1989: Phys. Rev. B **40**, 93

Wilson IH, Zheng NJ, Knipping U and Tsong IST, 1988: Appl. Phys. Lett. **53**, 2039

Zalm PC, 1988: Surf. Interface Anal. **11**, 1

Zandvliet HJW, Elswijk HB, van Loenen EJ, and Tsong IST, 1992: Phys. Rev. B **46**, 7581

Sputtering of Single Crystals: Experimental Evidence of the Ejection Process

By Nicholas Winograd
Department of Chemistry, Penn State University
152 Davey Laboratory, University Park, PA 16802, USA

Synopsis

The objective of this review is to summarize recent experimental evidence of the sputtering of atoms from single crystal targets. The information is extracted primarily from literature published within the last 10 years and is meant to compliment other recent reviews on single crystal sputtering. The emphasis of the discussion is on experiments that are performed on well characterized surfaces obtained under low-dose conditions. Because of this restriction, most of the experiments utilized laser postionization as the detection scheme. The discussion of experimental results is focused mainly toward comparison with results of molecular dynamics computer similations. The review includes a discussion of experimental techniques, a sampling of results obtained at normal incidence with keV Ar^+ ions, and others obtained at variable incident angles. In addition, energy and angular distributions of ground-state and excited-state sputtered atoms are compared in detail.

1 Introduction

Results of experimental studies of single crystals bombarded by keV particles offer a unique perspective on the fundamental processes underlying the scattering events associated with atom ejection. Since Wehner (1955) first observed his anisotropic emission - his famous 'spots' - there has been a lot of spirited discussion about the mechanisms of energy dissipation, particularly with regard to validating proposed theories. While in the early years single crystal sputtering was mainly of interest for its theoretical significance, later, single crystal effects became important in characterization of surface structure. Throughout this period, we have seen enormous advances in experimental technique and in the ability to quantitatively predict detailed information about the trajectories of ejected species. In this chapter, we review some of the important early studies and detail the recent strides in laboratory techniques which have helped to reveal experimental evidence for ejection processes associated with single crystal targets.

2 Historical Perspectives

The earliest systematic studies of the sputtering of single crystals date to 1955 and the pioneering work of Wehner (1955). These studies showed that W atoms ejected from single-crystal W targets bombarded by 150 eV Hg^+ions left the surface along preferred crystallographic directions. This anisotropy was in direct contradiction to many early theories of sputtering which suggested that the process was dominated by a thermal process or by sublimation (Von Hippel, 1926 and Townes, 1944) which would exhibit a yield with a cosine-like angular dependence. Wehner had convinced his peers by his use of single crystals that momentum transfer played a key role in the phenomenon.

During the 1960's many studies ensued which examined issues such as mass dependence, energy dependence and crystal face dependence of the sputtering yield. A few key observations emerged from many elegant experiments. For the fcc metals, for example, it was found that the preferred ejection generally occurs along the <110> bulk crystal direction (Anderson & Wehner, 1960). Single crystal effects were also observed for hcp and bcc metals (Nelson, 1963; Robinson & Southern, 1968). Interestingly, semiconductor crystals appeared much less anisotropic than metals (Southern et al., 1963). The reason for this early erroneous conclusion was primarily the more extensive damage suffered by these materials from the bombardment process.

Single crystal sputtering during the early period provided critical information for the theoreticians. As noted above, the evaporation models had to be discarded. An initial explanation of the anisotropies came from Silsbee (1957) who suggested that momentum could be focused along a row of equally spaced spheres if the distance between centers is less than twice the atomic diameter. This proposal inspired much more thinking about the problem from an atomic point of view. As the story goes, Wehner attempted to look for these Silsbee chains by constructing a model of a crystal with balls attached by strings to the ceiling. He then struck this crystal with a primary particle (ball) and photographed the event with a strobe lamp. The results were inconclusive but representative of how clever Wehner (1992) could be.

Computer simulations offered new hope to understanding single crystal sputtering. The modeling could be performed on a realistic crystallite since the lattice positions were known. Reasonable interaction potentials were becoming available in the mid-1960's and it was possible to solve Newton's equation of motion for a collection of atoms subject to an initial particle bombardment. Ironically, some of the early modeling studies supported the conclusions of Silsbee (Gibson et al., 1960). The calculations clearly revealed that focused collision sequences could contribute to sputtering. An early pioneer in computer modeling, Don Harrison, found that focused collision sequences were possible, but in fact were quite rare (Harrison et al., 1966, 1968). More importantly, he suggested that the sputtering event was dominated by near-surface collisions involving just the first couple of layers of the solid. We will discuss the significance of this important statement in later sections. Lehmann and Sigmund (1966) later also proposed that the surface structure dominated the angular distributions. They noted that when subsurface atoms attain a kinetic energy on the order of the surface binding energy, only head-on collisions can lead to emission of surface atoms. They also noted that subsurface atoms could be ejected through potential minima in the surface layer, created by gaps between atoms. These alternative explanations of the angular anisotropies helped to explain a number of problems with the focused collision sequence models associated with hcp crystals (Hofer, 1973). More importantly, however, they suggested that in order to establish a quantitative understanding of single-crystal sputtering, it would be essential for experimental data to be obtained from crystals with well-characterized surfaces.

There was much controversy about these ideas that broiled all the way through the 1970's. As knowledge of handling single crystals improved, experimental methods which required a lower dose of incident ions were presented. For example, Szymczak and Wittmaack (1980) developed a sensitive detection scheme for gold using Rutherford backscattering to analyze material collected on a plate. They concluded that for such high-Z metals as gold it might be necessary to include deep-layer focusing to explain the large anisotropies they observed. Hundreds of other articles on single crystal sputtering appeared during that time. Most of these have been thoroughly reviewed by Hofer (1991). He also provides a comprehensive list of important recent review articles. Most of this research effort produced a qualitative understanding of single crystal sputtering. For metals bombarded near normal incidence with keV heavy particles, the highest emission intensity is observed along open crystallographic directions in the plane of the surface. Other peaks may be observed in directions where it is easy for second-layer particles to escape. It was realized that a high bombardment dose could produce topographical features (Hauffe, 1991) that could lead to erroneous results. Moreover, surface cleanliness became an issue because of the proposal by Harrison, Lehmann and Sigmund that the sputtering mechanism involved mainly surface layers and hence would be influenced by adsorbed impurities. Energy distributions from single crystals were found to be qualitatively similar to those found from polycrystalline surfaces, although the peak in the energy distribution may not be the same as for

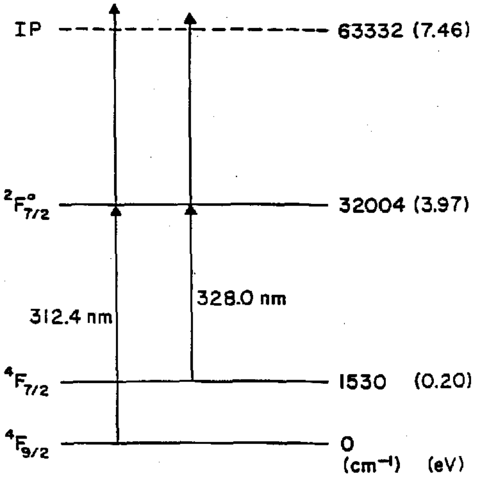

Figure 1. Partial energy level diagram for Rh. Ground-state Rh can be multiphoton ionized using two 312.4-nm photons. The first excited state can be probed by ionizing with two 328.0-nm photons.

amorphous systems and there may be structure in the distributions associated with direct recoils. (Reid et al., 1976)

More quantitative understanding of single crystal sputtering has been hampered by a number of factors. First, experimental techniques have not been generally available to examine bombarded single crystals at doses low enough ($<10^{14}$ ions/cm^2) to avoid artifacts. Secondly, the sputtering community has been slow to incorporate auxiliary surface characterization techniques such as low energy electron diffraction (LEED) and Auger electron spectroscopy (AES) into their apparatus. These methods show that the damage in single crystals is not removed unless the crystals are annealed well above their Debye temperature (Jenkins & Chung, 1971). Moreover, they show that even 'inert' metals such as copper and gold cannot be kept clean unless the vacuum is reduced to the 10^{-10} torr regime. Unless single crystal surfaces are prepared according to the rigors of modern surface physics, it is not possible to be sure that the resulting measurements can quantitatively be compared to proposed models and that data can even be quantitatively reproduced from lab to lab.

In this review, we examine the present status of experimental approaches to examining single-crystal sputtering. In general, the discussion will be restricted to experimental results obtained on well-characterized single crystal substrates obtained under low-dose conditions. The emphasis will be to present a limited data base, primarily from our own laboratory, where quantitative comparison to theory is possible. It is hoped that this review will not only encourage more experiments, but that the theory, now dominated by computationally intensive molecular dynamics calculations, can be reinvigorated with new analytical approaches.

3 Experimental Techniques

To fully characterize the sputtering event associated with single crystals, it is desirable to be able to vary the angle of incidence of the primary particle and to detect in a state-selective manner the sputtered flux with energy, angle and mass selection. It is also critical to obtain such data without damaging the crystal surface. During the 1970's there were many attempts to get at this problem. One idea involves postionization of the ejected species either by electron bombardment (Lundquist, 1978) or by a low energy plasma discharge (Oechsner & Gerhard, 1972). The ion which is formed is then detectable within single particle detection limits using a mass spectrometer. The work of Thompson and his group (1963, 1978) also stimulated much interest in the time-of-flight (TOF) technique. In general, these methods require an incident dose of more than 10^{17} particles/cm^2, at least 3 orders of magnitude beyond the damage threshold. Another approach involved the excitation of ejected atoms by a laser, followed by the measurement of the doppler-shifted fluorescent intensity (Hammer et al., 1976). This scheme allows individual electronic states to be detected. Unfortunately, the fluorescence techniques have not yet been systematically applied to angular distribution measurements and they require beam doses well in excess of 10^{16} particles/cm^2. Finally, an elegant experiment has been devised to collect a small amount of metal sputtered onto a detector using Rutherford backscattering spectroscopy (Szymczak & Wittmaack, 1980). Here, the dose could be kept in the range of 10^{15} particles/cm^2.

During the 1980's new laser techniques emerged which exhibited the necessary characteristics needed for efficient postionization. These include multiphoton resonance ionization (MPRI) (Winograd et al., 1982; Hurst & Payne, 1988), multiphoton nonresonance ionization (Becker & Gillen, 1984), and single-photon ionization (Schuhle et al., 1988). The MPRI method seems best from the point of view of maximizing sensitivity and state selection as pointed out by Hurst et al., (1979). Other schemes may prove viable as well in the future, although none have yet been applied to the study of the sputtering of single crystals. The MPRI approach for atoms can be employed by inspection of the electronic energy level diagram shown in Figure 1 for Rh, which will be used as a model system. There are a variety of electronic states that can be directly probed by an appropriate choice of the ionization wavelength. For example, the $^4F_{9/2}$ ground state can be ionized through

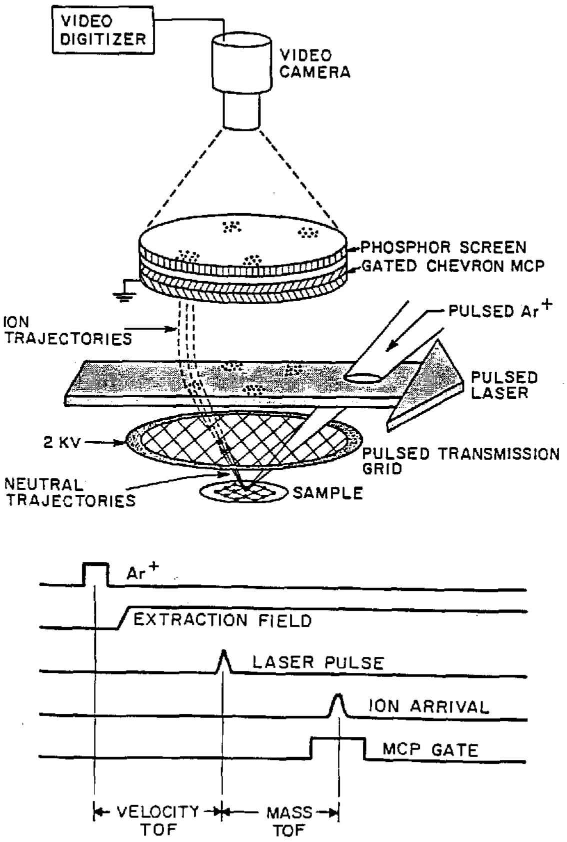

Figure 2. Detector for performing energy and angle-resolved measurements of neutral species desorbed from surfaces, along with the appropriate pulse sequences.

the $^2F_{7/2}$ state with two 312.4-nm photons. The $^4F_{7/2}$, $^4F_{5/2}$, and $^4F_{3/2}$ states lie within 1 eV of the ground state and can be ionized with two photons of slightly different energy (Moore, 1971). For this system $^4F_{9/2} \leftarrow {}^4F_{7/2}$ in the gas phase is a forbidden transition, so it is possible to make detailed measurements on both states and to directly compare the results.

The experimental geometry for such a scheme is shown in Figure 2 (Winograd et al., 1986). A pulsed ion beam of 200 ns serves to generate a burst of desorbed particles localized in space moving away from the target surface. At an appropriate time, a laser pulse tuned to an atomic resonance of the emitted particle is directed a few millimeters above and parallel to the target. As discussed by others (Hurst

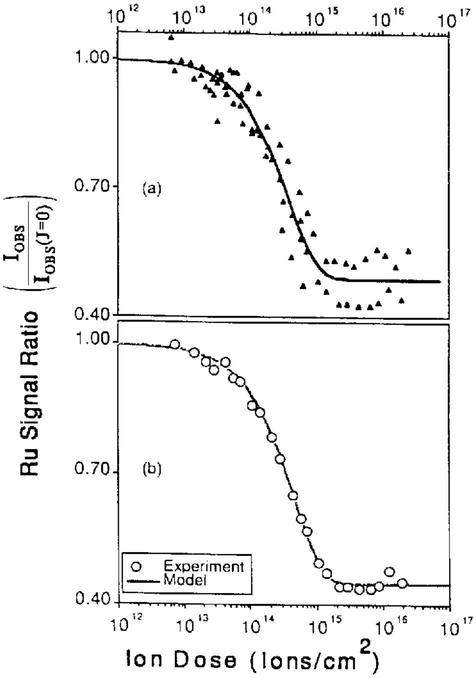

Figure 3. The Ru SNMS signal ratio, $I_{\mathrm{obs}}(J)/I_{\mathrm{obs}}(J=0)$, from the Ru(0001) surface plotted as a function of primary-ion dose, J. Results from four separate experiments are shown in (a) while results from a single experiment are shown in (b). The solid lines are the result of least-squares fits of the data by a proposed model (From Burnett et al., 1989).

& Payne, 1988), with sufficient laser power and excited-state lifetimes, all neutral species with excitations in resonance with the photon field and with appropriate ionization potentials are converted quantitatively into ions. Due to the pulsed nature of the experiment and the selective nature of the ionization process itself, the resulting ions may be efficiently counted by accelerating them with an external potential and measuring their TOF.

In this configuration the laser beam is focused in the shape of a ribbon 0.1 mm thick and 6 mm wide and directed 1 cm above and parallel to the target. Focusing allows ionization of those neutral species which are in a specific region of space. Hence, by varying the time difference between a 200-ns ion pulse and a 6-ns laser pulse, the velocity distribution of the neutral species is determined. Furthermore, the resulting ions may be imaged onto a microchannel plate which allows the position of the neutral species in the laser beam to be determined with respect to the position of the incident ion beam on the target. With knowledge of the nature of the extraction fields and instrumental factors associated with TOF measurements and position-sensitive detectors, it is feasible to calculate the take-off angles of the neutral species (Kobrin et al., 1986). This apparatus was also suitably equipped with LEED for surface crystallography measurements and AES for surface cleanliness monitoring. This energy- and angle-resolved neutral (EARN) detector is a powerful device for measuring neutral trajectories with enormous sensitivity. Typically, a full EARN measurement can be recorded with a dose of 10^{12} Ar^+ ions/cm^2.

4 Experimental Studies of Single Crystal Bombardment

4.1 Yield Measurements

Although extensive effort has been devoted to measuring the total yield of particles emitted from polycrystalline targets bombarded at normal incidence, not many of these measurements have been reported on single crystals since the 1960's (Magnuson & Carlston, 1963). These workers used a weight loss technique to determine that the yield of Cu{100} is 2.0 times the yield of Cu{110} and 0.7 times the yield of Cu{111}. This trend, generally supported by computer simulations (Harrison et al., 1979), follows the trend of surface atom density in these materials. In general, these measurements are quite variable due to the ill-defined experimental conditions and are of only qualitative value.

An important recent measurement using nonresonant laser postionization powerfully illustrates the necessity of using clean well-defined surfaces under low dose conditions. As shown in Figure 3 the yield from Ru(0001) decreases by a factor of two as the dose is increased above $\sim 10^{14}$ ions/cm^2 for bombardment with 3 keV Ar^+ at normal incidence (Burnett et al., 1989). Since most other techniques require at least 1×10^{15} particles/cm^2, it is clear that those studies are tainted by significant surface damage effects. For the Ru case, it is tentatively proposed that the decrease in yield arises from the primary ion going into defect sites created by previous bombardment. As seen in the Figure, this model fits well with the experimental data, although there are a number of adjustable parameters in it. This idea needs to be further tested since it does not seem likely, based on the results of recent molecular dynamics computer simulations (Harrison, 1988). It would be valuable to see similar studies on other materials and at various temperatures.

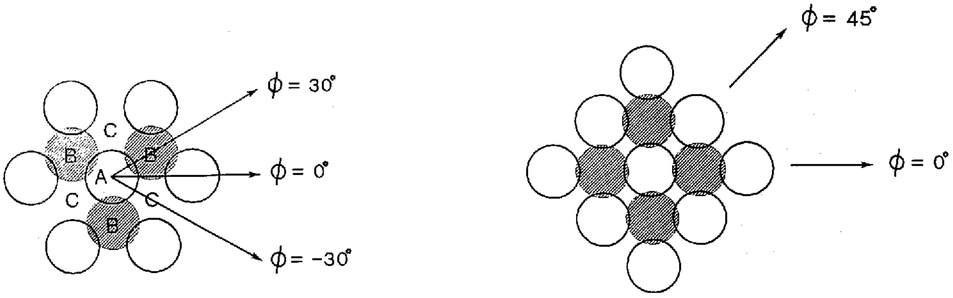

Figure 4. Schematic representation of our scheme for representing crystal directions for an fcc{111} and {001} face. A polar angle $\theta = 0^\circ$ is normal to the surface. Open circles designate first- layer atoms and shaded circles second-layer atoms. The letters A-C designate possible adsorption sites for oxygen atoms.

4.2 Depth of Origin of Emitted Particles from Single Crystals

In order to have a proper mechanistic view of the sputtering event, it is of course essential to be certain about from where the emitted particles originate. Controversy about this subject dates to the original model by Sigmund (1969) where it was implied that particles could be emitted from below the surface layers. Later, computer simulations (Harrison et al., 1978) showed that for copper single crystals >90% of the particles are emitted from the top layer. A corrected sputter depth has recently been given (Vicanek et al., 1989) which is consistent with simulations.

Experimental tests of this idea on monoelemental targets are not available. Ideally, it would be interesting to create a single crystal target with an isotope whose surface layer is different from the bulk and study it using laser postionization detection. Several workers have attempted to come close to accomplishing this goal. Prigge and Bauer (1980) measured the W^+ yield from W{110} covered with varying amounts of Cu, Ag and Pd. Although the results are subject to many artifacts, their studies show that the W^+ signal disappears between one and two monolayers of deposited overlayers.

The most definitive experiment on well-defined single crystals was carried out on Ru{0001} covered with known amounts of Cu (Burnett et al., 1988) and bombarded at normal incidence by 3.6 keV Ar^+ ions. The experiment is particularly nice since they employed low dose, LEED/Auger and used MPRI postionization for detection. Moreover, Cu is known to form two-dimensional rafts on Ru, rather than multilayer structures. The results clearly show that virtually all of the emitted particles arise

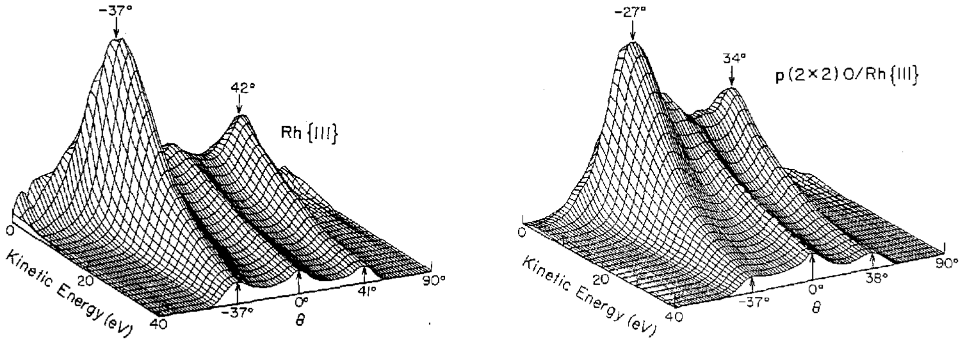

Figure 5. EARN intensity maps for clean Rh{111} and p(2×2) O Rh{111}. The plots are normalized to the highest intensity peak in both cases. The positive values of θ are recorded along $\phi = +30°$ and the negative values of θ are recorded along $\phi = -30°$ (From Winograd et al., 1986). Note that in the older spot notation, the [110] spot would occur at $\theta = 35.3°$ and $\phi = -30°$ and the [100] spot would occur at $\theta = 54.7°$ and $\phi = +30°$.

from the first layer.

Is this the final answer? No, there are a number of systems where the depth of origin is probably more than one layer. Computer modeling of Si{001}, for example, (Smith et al., 1989) clearly shows that particles can be emitted from the fourth or fifth layer. There is no direct experimental evidence for this prediction yet, but recent studies on GaAs{001} by Burnham et al. (1993) indicate that fourth layer Ga atoms can contribute significantly to observed angular distributions. Recent studies using the scanning tunneling microscope (STM) also suggest that deeper layers are exposed by single ion impacts on Si single crystals (Feil et al., 1992). If these results are correct, they may be important in understanding depth profiling in these commercially important materials.

4.3 Energy and Angular Distributions from Metallic Single Crystals

As was true during the time of Wehner's early experiments, accurate EARN distributions from well-defined surfaces are important for testing various theoretical models. Rhodium represents an important prototypical system for model studies. As seen in Figure 1, the electronic structure of Rh is well-suited for state-selected MPRI studies. Moreover, the surface chemistry of Rh has been extensively investigated by many techniques, and the surfaces are known to exhibit minimal surface relaxation or reconstruction that might complicate the analysis (Shepherd et al., 1978).

Let us first consider the {111} face bombarded at normal incidence by 5 keV Ar^+ ions (Winograd et al., 1986). The crystallographic definitions for this face are defined in Figure 4, and the EARN data are shown in Figure 5. Note that for this crystal face, the surface atoms exhibit six-fold symmetry. The three second-layer atoms, however, create bulk three-fold symmetry with characteristic directions along <111> ($\phi = 0°$ in our notation), <211> $\phi = -30°$, and <112>, $\phi = +30°$. Experimental EARN results for $\phi \pm 30°$ are shown in Figure 5. Note that the results are qualitatively similar to many of the early data taken under much more trying circumstances. In Wehner's nomenclature, there would be a set of 3 weaker spots (ϕ = 30°, 150° and 270°), 3 stronger spots (ϕ = -30°, 90° and 210°), as well as a very weak central spot. The intensity along the closest- packed line of atoms in the surface plane ($\phi = 0°$, 60°, $\cdots$) is not shown but exhibits a minimum in intensity. The energy distributions are clearly dependent on the take-off angle, suggesting that their final energies are influenced by surface-layer collisions.

This directional nomenclature is different from that previously associated with single crystal sputtering. The reason for this change is that the older notation was based on the assumption that the anisotropy arose primarily from focused collision sequences deep within the crystal. Therefore, it was natural to define the 'spots' using bulk crystallographic directions. Now, we know that surface processes are the main contributors to the angular anisotropies. It is essential, therefore, that we adopt a notation that reflects this process and is consistent with the notation employed by the surface physics community.

With present-day computers, it is possible to utilize molecular dynamics computer simulations to try to reproduce the experimental results shown in Figure 5. These calculations are important to carry out for two reasons. First, they tell us whether a molecular dynamics model is sufficient to describe the formation of the collision cascade and the subsequent trajectories of ejecting atoms. Second, they allow us to examine the microscopic mechanisms that give rise to the angular anisotropies. The comparison between theory and experiment provides a modern-day reality check.

The details of the molecular dynamics scheme in general are described elsewhere in this book (Robinson, 1993; Nieminen, 1993). The details of the procedure for calculating EARN distributions for Rh have been described in detail and will not be discussed here (Garrison et al., 1988; Foiles et al., 1986). As seen in Figure 6, however, it is clear that for Rh{111}, at least, the comparison between calculation and experiment is about as good as can be expected over a wide range of phase space.

The calculations tell us that the collision sequences are strongly dominated by

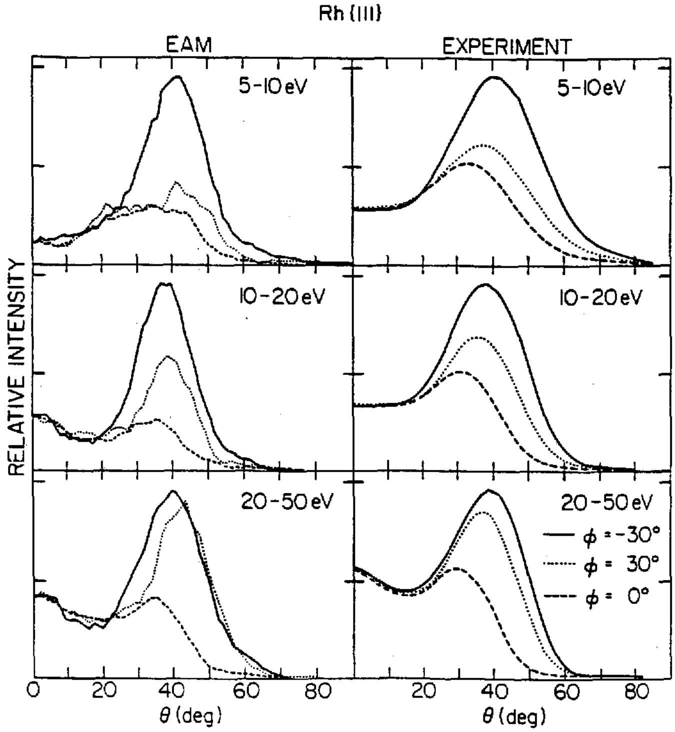

Figure 6. Polar angle distributions for various azimuthal angles for fixed secondary kinetic energy of the Rh atoms. In each frame the data are normalized to the ϕ = -30° peak intensity. The calculated data using the EAM potential are reported with a full width at half-maximum (fwhm) resolution of 15° in the polar angle. A constant solid angle is used in the histogramming procedure. The experimental resolution is also approximately 15°. The surface normal corresponds to $\theta = 0°$.

the alignment of atomic motions inside the solid. As these motions cause ejection of first-layer atoms, further focusing is caused by channeling or blocking by other first-layer atoms. Note that this type of channeling occurs at lower energies than that often associated with higher speed phenomena. For example, the highest intensity is observed along the open crystallographic directions ($\phi = \pm$ 30° in our case), and the minimum intensity is observed along the close-packed crystallographic direction (ϕ= 0°). If only the top surface layer was important, the peaks at θ = -37°, ϕ = -30° and θ = +42°, ϕ = +30° should be equal in intensity and not unequal as shown in Figure 5. The additional intensity at θ = -37°, ϕ = -30° arises mainly from the ejection of atom A by atom B (Figure 4) with first-layer focusing by other surface atoms. The peak at θ = +42° and ϕ = +30° is lower in intensity by a factor of

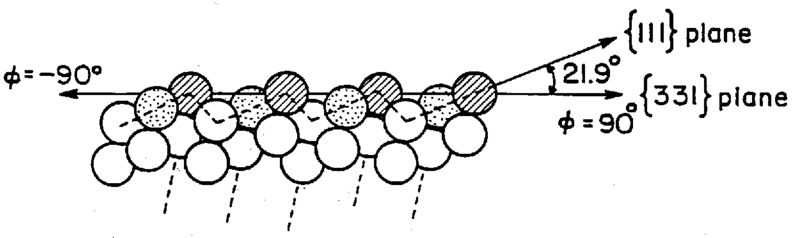

Figure 7. Cross-sectional view of the Rh{331} surface.

0.5 at low kinetic energy since no such mechanism is available along this azimuth. The peak at $\theta = 0°$ has a large component from ejection of the second-layer atom B which is focused upward by three surface atoms.

Many earlier experiments have been reported on {111} surfaces. Szymczak & Wittmaack (1980) found for 4 keV Ne^+ on gold, for example, that the peak along ϕ = -30° (the [011] spot in their notation) was at least 4 times the intensity of the peak along ϕ = +30° (the [100] spot). No intensity above a cosine background was observed at normal emission. The results are important since they show that the overall intensity directed into the spots is quite high, up to 50% in favorable cases. They are quantitatively different from the results found for Rh{111}, however, in that there is less of a difference found between ϕ = -30° and ϕ = +30° and there is a small amount of intensity found at normal emission for Rh{111}. It is unlikely that the distributions reported by Szymczak and Wittmaack could be reproduced by the computer modeling as these calculations would probably yield results very similar to those found on Rh{111}. Without further experiments and calculations, however, further hypothesizing about these differences would be mere speculation.

Another study of Ni{111} bombarded by 1.1 keV Ne^+ ions at normal incidence has recently been reported by Wucher et al. (1992). Their angular distributions, which are energy selected, are very similar to those found on Rh{111}. For example, they find that only the relatively high energy particles are emitted at normal incidence as shown in Figure 6. The major difference arises from the observation that the ϕ = +30° peak is several times more intense than the ϕ = -30° peak after the background is removed. Their computer modeling suggests these two features should be much closer in intensity as suggested by the data for Rh{111} shown in Figure 6. Since their experiments were not performed in the low-dose regime, it is difficult to speculate about the cause of this discrepancy.

How do these measurements and interpretations jive with earlier models of the production of angular anisotropies? This is a very tricky question. Mechanis-

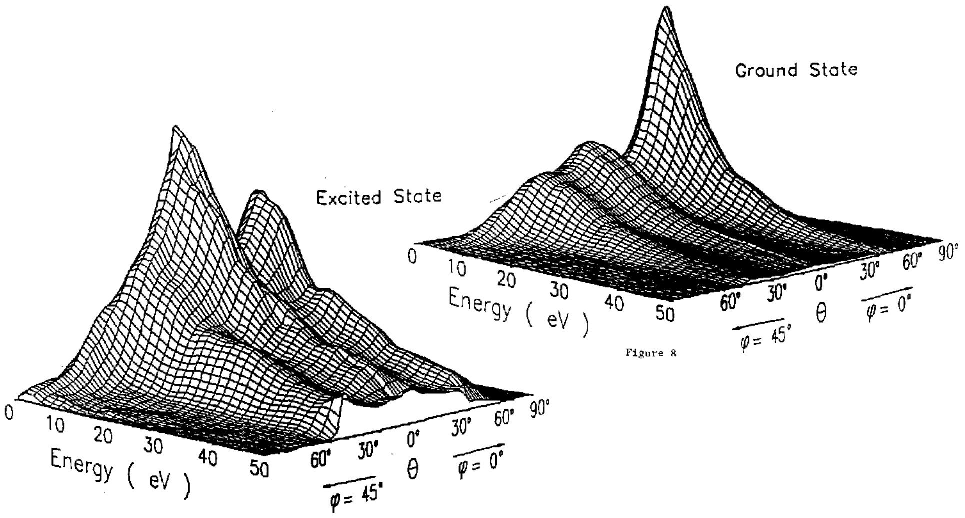

Figure 8. Energy- and angle-resolved distributions of Rh atoms in the ${}^4F_{7/2}$ excited state and ${}^4F_{9/2}$ ground state, ejected from 5 keV Ar$^+$ ion bombarded Rh{100}. The data correspond to ejection along $\varphi = 0^\circ$ (<100>) and $\varphi = 45^\circ$ (<110>) crystallographic directions, as defined in the inset. Due to the symmetry of the surface and the angular resolution (e.g., $\triangle\varphi = \pm\ 8^\circ$ at $\theta = 45^\circ$), the results represent the data over $\sim$ 50% of all space. Both plots are normalized to the maximum intensity peaks. See Figure 4 for definitions.

tic conclusions drawn from molecular dynamics calculations involve an analysis of thousands of trajectories in an attempt to extract the essential physics. As Harrison has often illustrated (1988), the atom ejection process is associated with a cataclysmic event. Although explanations of the angular anisotropies for Rh{111} arise from such an analysis, there are many other mechanisms which also contribute significantly to sputtering. It is often not possible to distill all this particle motion into simple pictures. The critical issue here is that the molecular dynamics calculations can, for the first time, provide quantitative agreement with experiment, at least for Rh{111}. The important mechanisms are embedded in the computer printouts and are available for the taking even though with considerable difficulty. This degree of certainty has never been available before.

Given this caveat, there appears to be a great deal of similarity between the notions originally presented by Harrison et al. (1966), by Lehmann and Sigmund (1966) and by the most recent studies - as long as you do not look too closely. The early work focused attention on mechanisms involving transparency effects, lens effects and specific force fields. Both Lehmann and Sigmund mechanisms are quite reasonable in light of the molecular dynamics studies, although they begin to break down when you ask questions about the energy dependence of the angular distributions. Their model would also predict that there should be no intensity in the $\phi = +30°$ direction. The key question, then, involves the generality of the mechanisms discussed above when applied to a variety of other systems.

If channeling and blocking in the first layer are important in controlling the angular distributions, there should be similar trends found on other crystal faces. Rh{331} is an interesting surface since it is a stepped structure with a (111) terrace that is three atoms wide. It is very similar to the {111} face except that it is tilted by 21.9° as shown schematically in Figure 7. The experimental results show that the ejection is strongly peaked along the $\phi = +90°$ azimuth, and that desorption along other crystallographic directions is considerably reduced (Reimann et al., 1989). Molecular dynamics calculations show that the $\theta = 15°$ peak arises from the same surface channeling mechanism operative for {111} corresponding to the $\theta = 37°$ peak along $\phi = 0°$. The reduced intensity along the other directions arises either from the presence of open channels in the crystal (near $\theta = 0°$) or from blocking due to the atomic step along $\phi = -90°$.

Similar anisotropies are observed for Rh atoms desorbed from ion-bombarded Rh{001} (Maboudian et al., 1990; El-Maazawi et al., 1991). The experimental EARN distribution for this surface is shown in Figure 8. The highest intensity is found along the open crystallographic direction, $\phi = 0°$, while a minimum intensity is observed along $\phi = 45°$. A comparison between the polar angle distributions for Rh{111} and Rh{001} reveals additional details about the surface channeling and blocking mechanisms. It turns out that the peak in the polar angle distribution in the 10-20 eV range is larger for {001} ($\theta_{\text{max}} = 40°$, $\phi = 0°$) than for {111} ($\theta_{\text{max}} = 37°$, $\phi = -30°$). This difference arises since the open channel is larger on {001}, allowing more grazing take-off angles. The polar angle intensity maxima along the close-packed directions, however, are nearly identical for both crystal surfaces ($\theta_{\text{max}} = 34°$ for {001} and $\theta_{\text{max}} = 32°$ for {111}). This result is important since the distance to the nearest-neighbor atom along the close-packed direction is identical for both surfaces. Thus, the polar angle distributions are determined by the extremely local interactions experienced by the desorbing atom, and can be predicted from the presence or absence of surface channeling directions.

Since crystal structure via surface channeling and blocking strongly influences the EARN distributions, it follows that adsorbate atoms or molecules on single-crystal substrates should systematically alter the trajectories of the desorbing underlayer species. The concept has been tested in detail for the p(2×2) O ordered overlayer on Rh{111} with the EARN experiment (Winograd et al., 1986; Reimann et al., 1989). For an atomic adsorbate of this sort, there are a number of possible high-symmetry binding sites including two different 3-fold hollow sites (often referred to as the **B** or hcp site and the **C** or fcc site) and an on-top site (or **A** site) as shown in Figure 4. The simplest idea is that adsorption of oxygen atoms at a **B** site should preferentially block Rh atoms desorbing along the ϕ = +30° azimuth, adsorption at a **C** site should alter Rh atoms leaving along ϕ = -30^0 while **A** site adsorption may have very little effect, except perhaps on the particles emitted at θ = 0°. Polar angle measurements as seen in the lower part of Figure 4 clearly show that the ϕ = -30° direction is preferentially reduced relative to either θ = 0° or ϕ = +30° strongly suggesting **C** site adsorption.

These results are quite interesting since they clearly show how sensitive the desorption angular distributions are to small overlayer coverages. In this case, in addition to the observed perturbations in the EARN distributions, the total ground state neutral Rh atom yield was observed to decrease by a factor of about 2 (Reimann et al., 1989). These observations further illustrate that trajectory measurements which are to be compared with theory must be performed on well-cleaned and characterized surfaces and under low-dose conditions.

4.4 Energy and Angular Distributions from Semiconductor Single Crystals

Angular anisotropies have also been observed for atoms ejected from ion-bombarded single crystal semiconductor surfaces. The earliest observations (Southern et al., 1963) indicated that the anisotropies were smaller than for metals. Later, however, it was discovered that the angular distributions were strongly temperature dependent, suggesting that crystal damage and thermal annealing were complicating the analysis (Anderson et al., 1963). Because of the technological importance of Si, GaAs and related materials, many studies of the topological changes that occur due to extensive bombardment have been reported (Carter et al., 1984). Only recently have well-defined surfaces prepared under UHV conditions been studied in detail. What emerges is a fascinating comparison between the dynamics of sputtering in metals with that found in the more open covalent lattice of semiconductors.

GaAs{001} represents an extraordinary model semiconductor surface. Depending upon how it is grown, the surface can be terminated with various coverages of As or Ga (Arthur, 1974; Neave & Joyce, 1978). It crystallizes with a zinc blende lattice, the same as Si, which means that the 001 plane exhibits alternating layers of As and Ga atoms. Moreover, the surfaces exhibit a well-defined rearrangement that has been characterized by scanning tunneling microscopy (Pashley et al., 1988) and by various diffraction techniques. The surfaces are normally prepared using molecular beam epitaxial growth (MBE) methodology (Arthur, 1974).

Molecular dynamics computer simulations have only recently been attempted for semiconducting materials (Stansfield et al., 1989; Smith et al., 1989). The calculations are more difficult in the sense that there is directional bonding which

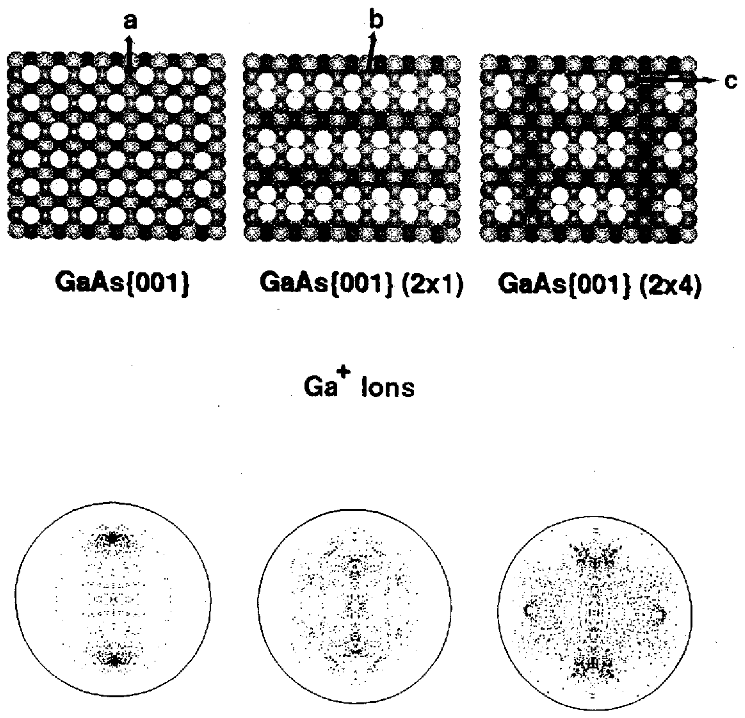

Figure 9. Top panel: Representations of three hypothetical GaAs{001} surfaces. The yellow balls represent surface As atoms. The purple balls represent second-layer Ga atoms and the green balls represent third layer As atoms. Bottom panel: calculated angular distributions of 10-30-eV Ga$^+$ ions desorbed by keV Ar$^+$-ion bombardment of the corresponding GaAs{001} surface given in the top panel. The <011> azimuthal crystal direction is parallel to arrow (c) in the figure. The polar angle of Ga$^+$-ion emission is proportional to the distance of a spot from the center of the circle. Ion ejection mechanisms (a), (b) and (c) are discussed in the text. (From Blumenthal et al., 1991).

requires the use of many-body potential functions. On the other hand, the lattices are much more transparent to the primary particle so that nuclear positions play a more dominant part in controlling the dynamics than the chemical bonding forces. The fact that the knowledge of the dynamics is not as extensive for semiconductors as it is for metals provides an added incentive for more effort in this area.

It is easy to examine the influence of the structure of the first atomic layer on the angular distribution of sputtered atoms from inspection of Figure 9. This figure shows on the left side a hypothetical unreconstructed GaAs{001} arsenic-terminated surface consisting of a square array of As atoms bonded to two Ga atoms

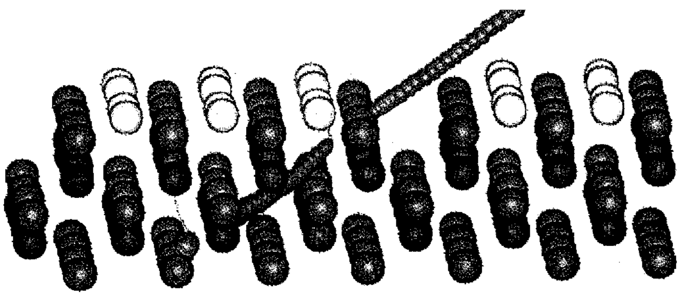

Figure 10. Top: The direct ejection mechanism which is responsible for the two dominant features in the GaAs{001}-(2×4) secondary ion distribution. The mechanism is characterized by a direct momentum transfer between a third layer As atom and a second layer Ga atom along their bond axis in the <110> direction. The Ga atom may eject over the channel between As$_2$ dimers or up through the As$_2$ dimers as pictured. Bottom: The desorption of a second layer Ga atom in the <110> direction across the missing dimer row. The pictured collision sequence shows a lower layer As atom channeling up through the crystal and transferring momentum to the Ga atom. The Ga atom may desorb at a high polar angle since it ejects across the missing dimer row. The momentum transfer in this direction is not as efficient as in the <110> direction which causes the desorbed ion intensity to be lower.

et al., 1983; Yarmoff et al., 1986).

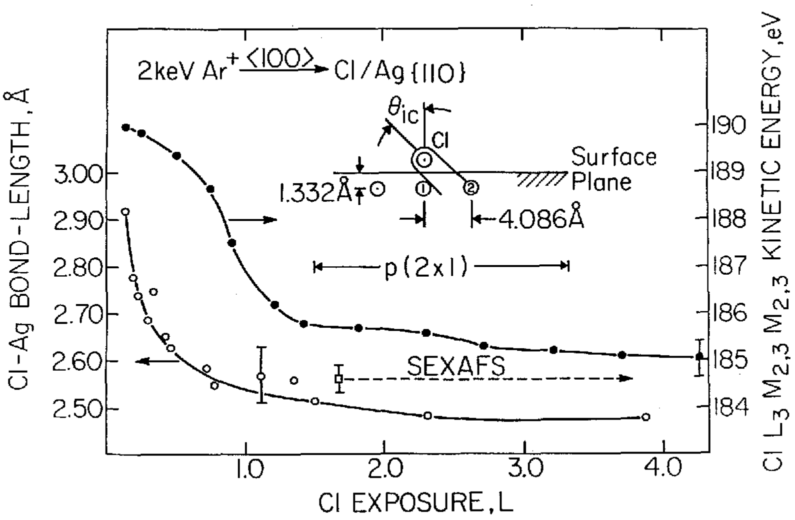

Figure 15. Ag-Cl bond-length change (○) and Auger Cl $L_3M_{2,3}M_{2,3}$ kinetic energy (●) as a function of Cl_2 exposure at 300 K. The reported value refers to the distance between the center of silver atom 1 and the Cl atom. The p(2×1) LEED pattern was observed in the exposure region as shown. The bond lengths from the SEXAFS experiments are associated with the LEED pattern; the same value was also obtained at a coverage beyond 4 L and associated with the c(4×2) LEED pattern. The shadow-cone induced desorption mechanism used to calculate the bond length is shown in the inset. The interplanar spacing refers to the relaxed clean-surface Ag{110} value. The shadow-cone shape was calculated using a Thomas-Fermi-Moliere potential with a scaling factor of 0.86. (From Winograd & Chang, 1989).

1989). The results for the shadow-cone experiments are shown in Figure 15. Of particular note is that at extremely low Cl coverages, the observed bond length is extended over that observed in the high coverage limit by nearly 0.4 Å. This change in length, accompanied by a change in the shape of the Auger electron emission spectra, has been explained as being due to a shift from highly ionic bonding at low coverage to more covalent bonding at high coverage. If the Ag-Cl interaction is highly ionic, the bond should have a significant dipole moment. Presumably dipole-dipole interactions between nearby Cl^- atoms force charge back into the Ag substrate. The absolute value of the bond length at high exposures agrees quite well with surface-EXAFS experiments obtained from the p(2×1) ordered overlayer (Holmes et al., 1987) as seen in Figure 15. The results are also consistent with the channeling and blocking experiments discussed previously, which suggest that the Cl adsorbate could more closely approach the surface at higher coverages (Moon

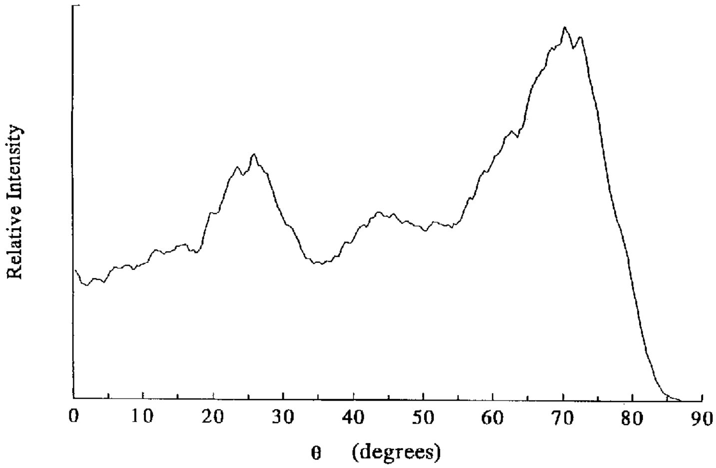

Figure 16. The relative intensity of 20-eV Ga^+ ions desorbed from the GaAs{001}(2×4) surface by 3-keV Ar^+-ion bombardment, plotted as a function of the ion-beam polar angle, relative to the surface normal. The ion beam is parallel to the <011> crystal direction. (From Xu et al., 1992).

et al., 1986).

These types of surface structure determinations are readily extended to more complex systems. Of special interest are compound semiconductor surfaces, not only because of their technological relevance, but also because they display a rich diversity of surface structures which need to be characterized. A good example is GaAs{001}-(2×4) which was examined earlier in this review with regard to its behavior under bombardment at normal incidence. The most straightforward objective of the shadow-cone experiments would be to determine the length of the As-As bond in the surface layer. This number is difficult to obtain by other methods, but is important for input into calculations aimed toward predicting the surface electronic structure (Chadi, 1987; Larsen & Chadi, 1988).

The results of this experiment (Xu et al., 1992) are shown in Figure 16. The crystal direction, <011>, corresponds to shooting the incident beam directly along the As_2 bond, in an azimuthal direction parallel to the missing row of As atoms. The spectrum consists of four major peaks at polar angles of $\theta_i = 70.1°$, $63.0°$, $44.5°$ and $25.8°$. There are many other distinguishable features in the spectrum which have been confirmed to be real structure, but their interpretation awaits future generations of research students (Burnham et al., private communication). The main peaks have been assigned on the basis of parallel molecular dynamics

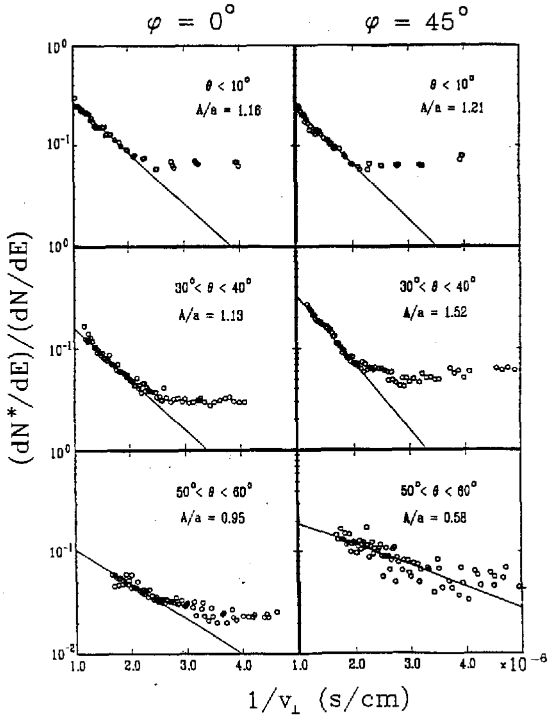

Figure 17. Ratio of intensities $(dN^*/dv/(dN/dv)$ vs $1/v_\perp$ for different angles of ejection. These data are direct ratios of the intensities given in Figure 1. The straight lines have been fit to the high velocity portion of the data and have a slope of A/a (in units of 10^6 cm/s) as displayed in each frame (From Shapiro & Fine, 1989).

calculations for Si (Xu et al., 1992). A summary of those results is given in Table I. Notice that the As_2 distance is determined from the small shoulder at 63° to be 2.73± 0.10 Å. The procedure for calculating the bond-length is identical to that described for the Ag{110} surface. This value of 2.73 ± 0.10 Å is within experimental error of a grazing-incidence x-ray diffraction value from GaAs{001} c(4×4) of 2.59 ±Å (Sauvage-Simkin et al., 1989). These numbers suggest that the dimer bond distance is much closer to the bulk As bond distance with threefold coordination than to a tetrahedral covalent As bond involving sp^3 hybridization (Kittel, 1986).

The fact that these simple angular distributions provide such microscopic information about surface structure is really remarkable from several points of view. Certainly, the primary beam is creating lots of damage to the surface, and yet it

Table I. Experimental and calculated results. Distances are expressed in Ångströms and angles in degrees. D_{11} is the first-layer As-As bond distance in a <011> direction; D_{22} the second-layer Ga-Ga distance along a <011> direction.

Crystal Direction	Peak	θ_i	D_{bulk}	D_{anal}	D
<011>	Peak 1	70.1	4.00	4.00 ± 0.10	D_{22}
	Peak 2	63.0	4.00	2.73 ± 0.10	D_{11}
	Peak 3	25.8	1.41	1.40 ± 0.10	D_{23}

seems possible to obtain accurate surface bond lengths. The experimental configuration is exceedingly straightforward, requiring only a simple ion source, quadrupole mass filter and polar angle rotation capabilities for the sample holder. The potential sensitivity of this approach to low concentrations of overlayers is indeed unprecedented. The three examples presented in this review are very promising ones, but much research remains to be accomplished in this area. It will be interesting to examine how the distributions change with shadow-cone radius and whether it will be possible to enhance certain desorption mechanisms by changing particle mass and energy. Perhaps the most important aspect of this experimental configuration, however, is that it allows an accurate description of the sputtering event to be performed without using molecular dynamics calculations. The angular distributions can be largely explained using only the details of the first encounter of the primary ion with the crystal surface.

6 Spectroscopic Studies of Single Crystal Sputtering

The laser techniques described in section III and IV are inherently state selective as illustrated in Figure 1. For example, the $^4F_{9/2}$ ground state can be ionized through the $^2F_{7/2}$ state with two 312.4 nm photons. The metastable $^4F_{7/2}$ state lies 0.2 eV above the ground state and can be ionized using two 328.0-nm photons. Since $^4F_{9/2} \leftarrow {}^4F_{7/2}$ is a forbidden transition, it is possible to make detailed measurements on both states and to compare the results directly. The comparison provides an unprecedented level of detail regarding the mechanistic aspects of energy excitation and quenching at surfaces.

A direct measurement of the complete EARN distribution for both the $^4F_{9/2}$ ground state and the $^4F_{7/2}$ excited state for Rh{100} has recently been completed (Winograd et al., 1992; Bernardo et al., 1992), and both maps are shown in Figure

8. Note that the intensity of the desorbed atoms in their ground state is very weak along the close-packed direction ($\phi = 45°$ as defined in Figure 3) due to blocking, as expected from the classical calculations. The open direction ($\phi = 0°$) largely arises from second-layer atoms being focused upward by first-layer atoms. The EARN map of the $^4F_{7/2}$ level is significantly different from the ground-state distribution. There is considerably more relative intensity observed at normal ejection ($\theta = 0°$). At low energies, only a shoulder exists along the $\phi = 45°$ azimuth (<110> direction). And finally, the falloff with energy is much slower for the excited state.

It is most likely that the population of the $^4F_{7/2}$ state is a direct measure of the excitation probability, uncomplicated by so-called cascading effects. This conclusion is derived from two important facts. First, the intensity of the ground-state signal is approximately 20 times the signal observed for the $^4F_{7/2}$ state. Second, the intensity of the next higher-lying excited state ($^4F_{5/2}$ with excitation energy of $\sim$ 0.3 eV above the ground state) is at least 2 orders of magnitude smaller than the $^4F_{7/2}$ state. Earlier studies by Young and co-workers (1984) using laser-induced fluorescence have shown that the population density for Fe decreases exponentially with the magnitude of the excited energy, roughly in accord with the observations for Rh. Similar results have been obtained using MPRI (Kimock et al., 1984). Hence, there are an insignificant number of excited Rh atoms in sufficiently high-lying excited states to contribute to the $^4F_{7/2}$ level by cascading from higher levels. Once these atoms reach the gas phase, then, it is unlikely that the population density is affected by decay from other excited states.

The interpretation of these energy and angle-resolved excitation probabilities are only now being sorted out. The general idea is to try to describe the dynamics of the excitation and deexcitation physics using known quantum mechanical phenomenon and then to examine the effects of this dynamics when it is coupled together with classical molecular dynamics (Bernardo et al., 1992). Several important concepts are emerging from these models. First, the form of the velocity dependence is strongly reminiscent of Hagstrum's (1954) original energy transfer ideas. A model which is consistent with this picture is currently being exploited by several groups and involves collisional excitation followed by nonradiative deexcitation (Bernardo et al., 1992; Shapiro & Fine, 1989). Both the excitation and deexcitation steps obviously depend upon the nature of the collision cascade as it evolves in the crystal and on the electronic properties of the material. For the data shown in Figure 17, note that the slopes of the change in the logarithm of the excited state fraction with $1/v_\perp$ depends on both polar and azimuthal angle. This effect is not predicted without including the influence of the cascade on the entire process (Winograd et al., 1992; Bernardo et al., 1992; Winograd, 1992). For example, if glancing collisions are important at high polar angles, the quenching rate will be appropriately higher.

Although there are many potential intricacies associated with these experiments, it is of interest here to conclude with one final observation. There is a region of the data shown in Figure 17 where the excited fraction is found to be independent of velocity. Although a number of factors contribute to this effect, the molecular dynamics calculations show that collisions of atoms over the surface are most important (Winograd et al., 1992; Bernardo et al., 1992; Winograd, 1992). With this mechanism, two independently ejected atoms undergo a hard collision over the surface and become reexcited. Because they are out of the electronic coupling range of the solid, the excitations are not quenched.

7 Conclusion and Prospects

The revolution in modern surface science has opened new opportunities for learning more details about single crystal sputtering than ever before. Moreover, new detection schemes have made it possible to essentially examine the collision dynamics on an event by event basis. The new data are now in quantitative agreement with results from sophisticated molecular dynamics calculations, at least for a limited number of model systems. This agreement allows one to extract the important energy dissipation mechanisms from the computer printouts and to have confidence in their validity.

Yet, there is much to be done. The computer simulations are complex and the experimentalists need simpler formulas by which to interpret their data. These formulae, however, should provide a quantitative prediction of the sputtering yield as a function of ejection energy and angle. Perhaps the shadow-cone approach, where the mathematics is easy, is a step in that direction. Spectroscopic studies of single crystal sputtering are only beginning and offer hope of disentangling the factors that go into inelastic energy loss. For example, the studies discussed here involved only electronic states that are part of the ground state manifold. Higher lying states will undoubtedly yield new surprises. And finally, there needs to be more work on molecular crystals, alloys or on insulating crystals in order to continue to elucidate the mechanistic differences associated with the sputtering of these disparate materials. Spectroscopic studies of neutral clusters emitted from single-crystals under low-dose conditions would provide interesting information about the vibrational and rotational excitations that occur in these species. There will certainly be many interesting new effects discovered with these substances. Their role is already becoming increasingly important in modern materials science.

Acknowledgements

The author greatly appreciates the critical reading of this manuscript by Barbara J. Garrison. He is also most grateful for the financial support of The National Science Foundation, The Office of Naval Research and The Department of Energy.

References

Anderson GS and Wehner GK, 1960: J. Appl. Phys. **31**, 2305

Anderson GS, Wehner GK and Olin HJ, 1963: J. Appl. Phys. **34**, 3492

Aono M, Oshima C, Zaima S, Otani S and Ishizawa Y, 1981: Jpn. J. Appl. Phys. **20**, L829

Aono M, Hou Y, Souda R, Oshima C., Otani S and Ishizawa Y, 1983: Phys. Rev. Lett. **50**,1293

Arthur JR, 1974: Surf. Sci. **43**, 449

Becker CH and Gillen KT, 1984: Anal. Chem. **56**, 1671

Bernardo DN and Garrison BJ, 1992: J. Chem. Phys. **97**, 6910

Bernardo DN, El-Maazawi M, Maboudian R, Postawa Z, Winograd N and Garrison BJ, 1992: J. Chem. Phys. **97**, 3846

Biegelsen DK, Bringams RD, Northrup JE and Swartz LE, 1990: Phys. Rev. **B41**, 5201

Blumenthal R and Winograd N, 1991: Phys. Rev. B15 **42**, 11027

Blumenthal R, Caffey KP, Furman E, Garrison BJ and Winograd N, 1991: Phys. Rev. B. **44**, 12830

Burnett JW, Biersack JP, Gruen DM, Jørgensen B, Krauss AR, Pellin MJ, Schweitzer EL and Yates Jr YT, 1988: J. Vac. Sci. Tech. **A6**, 2064

Burnett JW, Pellin MJ, Calaway WF, Gruen DM and Yates Jr JT, 1989: Phys. Rev. Lett. **63**, 562

Burnham JS, Goss SH and Xu C, 1993: private communication

Carter G, Navinsek B and Whitton JL, 1984: *Sputtering by Particle Bombardment II*, Ed., R. Behrisch, Springer-Verlag, Berlin, p. 231

Chadi DJ, 1987: J. Vac. Sci. Technol. **A5**, 834

Chang CC and Winograd N, 1989: Phys. Rev. B. **39**, 3467

Chang CC, Malafsky GP and Winograd N, 1987: J. Vac. Sci. Tech. A. **5**, 981

El-Maazawi M, Maboudian R, Postawa Z and Winograd N, 1991: Phys. Rev. B15 **43(14)**, 12078

Feil H, Zandvliet HJW, Tsai MH, Dow JD and Tsong IST, 1992: Phys. Rev. Lett. **69**, 3076

Foiles SM, Baskes MI and Daw MS, 1986: Phys. Rev. B **33**, 7983

Garrison BJ, Winograd N, Deaven DM, Reimann CT, Lo DY, Tombrello TA, Harrison Jr DE and Shapiro MH, 1988: Phys. Rev. **B37**, 7197

Gibson JB, Goland AN, Milgram M and Vineyard GH, 1960: Phys. Rev. **120**, 1229

Hagstrum HD, 1954: Phys. Rev. **96**, 6800

Hammer D, Benes E, Blum P and Husinsky W, 1976: Rev. Sci. Instrum. **47**, 1178

Harrison Jr DE, 1988: CRC Rev. in Sol. St. and Mat. Sci. **14**, S1

Harrison Jr DE, Johnson JP and Levy NS, 1966: Appl. Phys. Lett. **8**, 33

Harrison Jr DE, Levy NS, Johnson JP and Efron HM, 1968: J. Appl. Phys. **39**, 3742

Harrison Jr DE, Kelly PW, Garrison BJ and Winograd N, 1978: Surf. Sci. **76**, 311

Hauffe W, 1991: *Sputtering by Particle Bombardment III*, eds. R. Behrisch and K. Wittmaack, Topics in Applied Physics **64**, Springer-Verlag, Berlin, p. 305

Hofer WO, 1973: Rad. Effects **19**, 263

Hofer WO, 1991: *Sputtering by Particle Bombardment III*, Topics in Applied Physics **64**, Springer-Verlag, Berlin, p. 15

Holmes DJ, Panagiotides N, Barnes CJ, Dus R, Norman D, Lamble GM, Della Valle F and King DA, 1987: J. Vac. Sci. Technol. A **5(4)**, 703

Hurst GS and Payne MG, 1988: *Principles and Applications of Resonance Ionization Spectroscopy*, Adam Hilger, Philadelphia, PA

Hurst GS, Payne MG, Kramer SD and Young JP, 1979: Rev. Mod. Phys. **51**, 767

Jenkins LH and Chung MF, 1971: Surf. Sci. **29**, 125

Kimock FM, Baxter JP, Pappas DL, Kobrin PH and Winograd N, 1984: Anal. Chem. **56**, 2782

Kittel C, 1986: *Introduction to Solid State Physics*, 6th Ed., Wiley, New York, 76

Kobrin PH, Schick GA, Baxter JP and Winograd N, 1986: Rev. Sci. Instrum. **57**, 1354

Kuk Y and Feldman LC, 1984: Phys. Rev. **B30**, 5811

Larsen PK and Chadi DJ, 1988: Phys. Rev. **B37**, 8282

Lehmann C and Sigmund P, 1966: Phys. Stat. Solidi **16**, 507

Lindhard J, 1965: Dan. Vid. Sel. Mat. Fys. Medd. **34**, No. 14

Lundquist TR, 1978: J. Vac. Sci. Tech. **15**, 684

Maboudian R, Postawa Z, El-Maazawi M, Garrison BJ and Winograd N, 1990: Phys. Rev. B15 **42(12)**, 7311

Magnuson GD and Carlston CE, 1963: J. Appl. Phys. **34**, 3267

Moon DW, Bleiler RJ and Winograd N, 1986: J. Chem. Phys. **85**, 1097

Moore CE, 1971: *Atomic Energy Levels, U.S. Department of Commerce Report* NSRDS-NBS 35, Washington, DC

Neave JH and Joyce BA, 1978: J. Cryst. Growth, **44**, 387

Nelson RS, 1963: Phil. Mag. **8**, 693

Nieminen RM, 1993: Mat. Fys. Medd. Dan. Vid. Selsk. **43**, 81

Oechsner H and Gerhard W, 1972: Phys. Lett.**40A**, 211

Pashley MD, Habereen KW, Friday W, Woodall JM and Kirchner PD, 1988: Phys. Rev. Lett. **60**, 2176

Prigge S and Bauer E, 1980: In Advances in Mass Spectrometry, Vol. 8A, ed. Quale, A, Heyden, London, p. 543

Reid I, Farmery BW and Thompson MW, 1976: Nucl. Instrum. Methods **132**, 317

Reimann CT, El-Maazawi M, Walzl K, Garrison BJ and Winograd N, 1989: J. Chem. Phys. **90(3)**, 2027

Robinson MT, 1993: Mat. Fys. Medd. Dan. Vid. Selsk. **43**, 27

Robinson MT and Southern AL, 1967: J. Appl. Phys. **38**, 2969

Sauvage-Simkin M, Pinchaux R, Massies J, Calverie P, Jedrecy N, Bonnet and Robinson IK, 1989: Phys. Rev. Lett. **62**, 563

Schuhle U, Pallix JB and Becker CH, 1988: J. Am. Chem. Soc. **110**, 2323

Shapiro MH and Fine J, 1989: J. Nucl. Instrum. Methods **B44**, 43

Shepherd FR, Watson PR, Frost DC, Mitchell KAR, 1978: J. Phys. C. Solid State Phys. **11**, 4591

Sigmund P, 1969: Phys. Rev. **184**, 383

Sigmund P, 1987: Nucl. Instrum. Methods **B27**, 1

Silsbee RH, 1957: J. Appl. Phys. **28**, 1246

Smith R, Harrison Jr DE and Garrison BJ, 1989: Phys. Rev. **B40**, 93

Southern AL, Willis WR and Robinson MT, 1963: J. Appl. Phys. **34**, 3492

Stansfield RA, Broomfield K and Clary D, 1989: Phys. Rev. **B39**, 7680

Szymczak W and Wittmaack K, 1980: Nucl. Instrum. Methods **170**, 341

Thompson MW, 1963: Phys. Lett. **6**, 24

Thompson MW, Reid IH and Farmery BW, 1978: Philos. Mag. **38**, 727

Townes CH, 1944: Phys. Rev. **65**, 310

Tsong IST and Bedrossian P, 1993: Mat. Fys. Medd. Dan. Vid. Selsk. **43**, 209

Van der Veen JF, 1985: Surf. Sci. Rep. **5**, 199

Vicanek M, Jimenez-Rodriguez JJ and Sigmund P, 1989: Nucl. Instrum. Methods **B36**, 124

Von Hippel A, 1926: Ann. Physik **81**, 1043

Wehner GK, 1955: J. Appl. Phys. **26**, 1056

Wehner GK, 1992: private communication relayed to the author aboard the cruise ship Sjælland

Winograd N, 1992: J. Phys. Chem. **96**, 6880

Winograd N and Chang C-C, 1989: Phys. Rev. Lett. **62(21)**, 2568

Winograd N, Baxter JP and Kimock FM, 1982: Chem. Phys. Lett. **88**, 581

Winograd N, Kobrin PH, Schick GA, Baxter JP and Garrison BJ, 1986: Surf. Sci. Lett. **176**, L817

Winograd N, El-Maazawi M, Maboudian R, Postawa Z, Bernardo DN, and Garrison BJ, 1992: J. Chem. Phys. **96**, 6314

Wucher A, Watgen M, Mossner C, Oechsner H and Garrison BJ, 1992: Nucl. Instrum. Methods, **B67**, 531

Xu C, Caffey KP, Burnham JS, Goss SH, Garrison BJ and Winograd N, 1992: Phys. Rev. **B45**, 6776

Yarmoff JA, Cyr DM, Huang JH, Kim S and Williams RS, 1986: Phys. Rev.**B33**, 3856

Young CE, Calaway MF, Pellin MJ and Gruen DM, 1984: J. Vac. Sci. Technol.**A2**, 2782

Alloy and Isotope Sputtering

By Peter Sigmund
Physics Department, Odense University
DK-5230 Odense M, Denmark
and
Physics Division, Argonne National Laboratory
Argonne, IL 60439, USA
and
Nghi Q. Lam
Materials Science Division, Argonne National Laboratory
Argonne, IL 60439, USA

Synopsis

We present a summary of our current understanding of collisional sputtering from isotopic mixtures and alloys. In view of the large number of theoretical and experimental investigations reported in the literature, we made a considerable effort to provide precise definitions of pertinent physical parameters and a unified notation. This is fairly straightforward with regard to primary processes, i.e., the atomistics of the individual sputtering event which is in general preferential. In case of secondary processes, which address all compositional changes induced by ion bombardment and their influence on sputtering, we have tried to identify the common origin of two theoretical schemes that the present authors have been utilizing in the past, and to generate a unified version that also comprises several simpler treatments that were proposed in the literature. This goal has not yet been reached completely but we have come very close to it. The scheme allows for preferential sputtering from a nonvanishing depth of origin, collisional mixing treated beyond the diffusion picture, pressure relaxation, radiation-enhanced diffusion, as well as Gibbsian and radiation-induced segregation.

Progress in the understanding of primary sputter effects is reviewed, based upon transport theory, Monte Carlo and molecular-dynamics simulation, and measurements at low and high fluences. Available knowledge on secondary processes is summarized, based in part on theoretical and experimental work not addressing sputter phenomena directly. Quantitative comparison between theoretical predictions and experimental results is most feasible with respect to isotopic mixtures. The agreement is not yet perfect, and reasons for this are discussed. Many experimental results found on alloys under bombardment are well understood in qualitative terms, yet the number of unknown or uncertain parameters entering theoretical estimates is still too large to allow for theoretical predictions except for particularly simple systems. A list of open problems concludes the paper.

Contents

1 Introduction

The elementary event in sputtering is the emission of one or more atoms from the surface of some material, caused by the impact of an energetic particle. This elementary event is most often an intricate sequence of collision processes, i.e., a collision cascade involving a large number of target atoms. It is characteristic of the physicist's approach to science that initial studies of such a process are carried out on the simplest target materials. From a theoretician's point of view, elemental targets are simplest. Experimental studies are rarely if ever performed on truly monoatomic target materials. Real experiments deal with alloys, compounds, and mixtures with or without surface coverage because one or more of the following requirements are more or less violated: ultrapure, single-isotope starting material; clean surface; excellent vacuum in the target chamber; and self-bombardment by a high-purity, isotope-separated ion beam.

Sputter experiments on multicomponent materials show a much wider variety of processes. This increases the complexity but also allows extraction of more information in fortunate cases. For example, all reported experimental investigations on the depth of origin of sputtered atoms involve overlayers of some material deposited on a matrix. Most important, virtually all applications of sputtering involve multicomponent targets. Thus, understanding the different sputter properties of the components making up a given material is both necessary and major challenge.

This paper addresses isotopic mixtures, alloys, and some compounds, as opposed to molecular solids, biomolecular materials, and ionic crystals. The materials considered here are expected to show a sputter behavior typical of metals where collisional sputtering dominates and where the sputtered flux is composed primarily of neutral atoms and small molecules.

The key problem to be addressed is the preferential sputtering of the species present in the target material and the way how this manifests itself in experiments. Another question, frequently asked yet of less fundamental interest is the relation between the erosion rate of an alloy and the erosion rates of the pure constituent materials. Because of a variety of processes that lead to composition changes in alloys under ion bombardment that are only remotely related to sputter emission, a broad approach needs to be taken.

Composition changes under ion bombardment were discovered many years ago (Asada & Quasebarth, 1929). Theoretical studies were initiated much later (Andersen & Sigmund, 1974). A survey of the early history of the field has been given by Betz & Wehner (1983). Their chapter also offers a compilation of experimental data available at the time. An illuminating outline of the entire complex of problems, open questions, as well as available knowledge was given by Andersen (1984). Other reviews on more specific items will be mentioned in context.

In accordance with the title of this book, fundamental processes will be studied and very little will be said about applications. However, as indicated above, *all* application areas of sputtering are more or less affected by the processes that determine the sputtering of alloys and compounds. At this point we just list keywords such as ion beam analysis involving sputtering, ion beam modification of materials, sputter deposition of thin films, sputter cleaning and polishing, and plasma-wall interaction in fusion technology. Moreover, some control over sputter processes is demanded in virtually all experiments involving particle-solid interaction.

The experimental and theoretical literature in the field is extensive, yet there has been rather little systematic comparison between experimental findings and theoretical predictions, mostly due to the restricted range of validity of available quantitative predictions. An exception is the case of isotopic mixtures which will be discussed in sect. 3.

The mutually related topics of sputtering from a multicomponent target and compositional changes during ion bombardment will be discussed in general terms in sect. 2. An attempt has been made to outline a comprehensive scheme allowing to incorporate athermal and thermally-activated processes, flexible enough to allow for analytic or numerical input. The scheme is compatible with the seemingly different schemes used in previous work by each of the present authors, and it contains most existing phenomenological descriptions as special cases. An attempt has also been made to stick to a simple, comprehensive notation. In addition, sect. 2 summarizes simple estimates of sputter cross sections and partial sputter yields.

Section 4 addresses alloys. The processes that are thought to cause compositional changes under ion bombardment are discussed in physical terms, and simple quantitative estimates are given. The complex interplay between these processes and preferential sputtering is illustrated on a number of limiting cases, and the relation to measurable parameters is exemplified both schematically and by a survey of pertinent experiments.

A summary and outlook listing the most urgent needs for future effort concludes the chapter.

2 General Theory

2.1 General Considerations

Sputtering from a polyatomic mixture is a priori preferential: By this is meant that the behavior of a target atom with regard to sputtering is species-dependent. Therefore, measurable sputter parameters will generally not reflect the composition of the pertinent surface layer in a given material. This is a major handicap in surface analytical techniques involving sputtering; it is also a main motivation for fundamental studies of alloy sputtering.

Several factors determine preferential sputter behavior. First of all, binding forces acting on an atom at the surface or in the bulk are species-dependent. Differences may amount to an order of magnitude or more for hydrogen or noble gases in metals, to a factor of two for some metallic alloys, or perhaps a per mille for isotopic mixtures, but some difference will always exist. Secondly, in order to get sputtered, an atom must first be set in motion during the process of energy dissipation by primary radiation. The sharing of energy is species dependent through pertinent collision cross sections as well as conservation laws of momentum and energy. Finally, atoms may be ejected not only from the top surface layer of a solid or liquid but also from a shallow depth range underneath. Clearly, the ability of an atom to penetrate a number of overlayers is species dependent; this feature is well documented from the inverse process of ion implantation.

From a theoretical point of view, it is convenient to divide up the study of alloy sputtering into primary and secondary processes. Primary processes deal with the sputter behavior of a target with a given composition depth profile; they lead to nonstoichiometries in the sputtered flux even from a homogeneous target.

Secondary processes deal with changes in the target material due to a variety of effects initiated by the primary radiation.

Thus, the quantitative characterization of preferential sputter behavior is the main issue in the study of primary processes. Secondary processes are numerous, and at least five of them are important in the context of sputtering.

While a recoil cascade may give rise to sputtering only if it intersects the target surface, all recoil cascades generate disorder and transport atoms in the bulk. This causes compositional changes on several time scales. Collisional mixing proceeds concurrently with sputtering. At the end of the slowing-down cascade, major pressure gradients have normally built up which are thought to relax rapidly by collective motion of atoms from high-pressure to lower-pressure zones.

The concentration of point defects created in a cascade and surviving its cooling phase is usually higher than in equilibrium. These defects may be mobile at elevated temperatures and give rise to phenomena such as radiation-enhanced diffusion. Moreover, nonuniform production and/or annihilation of defects results in persistent defect fluxes. Preferential association of defects to particular alloy elements will couple a net flux of atoms of that component to the defect fluxes. This leads to radiation-induced segregation. In thermal equilibrium, Gibbsian segregation occurs, i.e., segregation to free surfaces and interfaces. This process reduces the free energy of an alloy system. In the absence of irradiation it would be frozen in at ambient temperature. It can be enhanced by diffusion of nonequilibrium defects during irradiation. The latter two secondary processes are preferential and may give rise to changes in target stoichiometry that are not necessarily related to sputtering.

In addition to initiating collision cascades, the implanted ion beam itself also changes the overall alloy composition. As a result, one may experience changes in chemical properties which may affect all processes described above. Finally, under certain bombardment conditions, nuclear transmutations may occur which, again, may result in chemical changes.

The study of radiation-induced compositional changes is complex and full of hidden surprises. One direct implication is the existence of several pertinent length scales. Sputter ejection and Gibbsian segregation are characterized by depth scales of the order of little more than an interatomic distance. The characteristic length in collisional mixing may be as large as the dimension of the pertinent collision cascade or subcascade, i.e., roughly the penetration depth of the incident ion beam. However, energy spectra in collision cascades are skew, with low energies and, hence, low relocation distances dominating. Activated processes may go over large distances since the target region that may be considered to be in an excited state will in general include atoms with energies that are too low to cause displacement.

An important limiting case in studies of alloy sputtering is the steady-state limit which may be reached after prolonged bombardment. A necessary condition for such a state to be reached by an eroding target is that the composition be initially homogeneous in the bulk. Another condition is that matter may not be transported over long distances; in other words, the thickness of the altered layer must be smaller than the total target thickness. If both conditions are fulfilled, the composition of the sputtered flux in the steady state must reflect the bulk composition of the target, unless atoms change identity by nuclear transformation. This is a direct consequence of the conservation of matter and an important test on any theory of compositional changes. This, however, does not preclude observable deviations from stoichiometry in differential quantities like energy spectra and angular distributions of sputtered particles.

2.2 Primary Processes

2.2.1 Fundamental Parameters

The primary quantity characterizing sputtering of a polyatomic mixture is a set of partial sputter yields, Y_i, defined as the mean number of sputtered i-atoms per incident beam particle. In the following, we shall assume the index i to include both the components that are initially present in an n-atomic target, $i = 1, 2 \ldots n$, and the implanted species, $i = 0$. Several techniques are available to measure partial yields, such as laser fluorescence or ionization, or collection of sputtered material and subsequent quantification by surface analytical techniques. Differential partial sputter yields such as the energy spectrum or angular distribution of i-atoms may also be measured. Such measurements may be demanding: In order to provide information on primary processes, they require low bombardment fluences.

Integral quantities may be measured such as the average mass change of the target per incoming beam particle due to sputtering,

$$\Delta m = \sum_i M_i Y_i, \tag{1}$$

where M_i is the mass of an i-atom, or the surface recession

$$w = \frac{dx}{d\Phi} = \sum_i \Omega_i Y_i, \tag{2}$$

where $d\Phi$ is the fluence [number of beam particles/area] necessary to erode a layer of thickness dx, and Ω_i is the effective atomic volume occupied in the target by an i-atom.

Measurable quantities like Δm or w may be converted into dimensionless effective sputter yields

$$Y_{\text{eff}}^{(M)} = \frac{1}{\overline{M}} \sum_i M_i Y_i \tag{3}$$

or

$$Y_{\text{eff}}^{(\Omega)} = \frac{1}{\overline{\Omega}} \sum_i \Omega_i Y_i, \tag{4}$$

which allow comparison with sputter yields of elemental target materials. Here, $\overline{M}$ and $\overline{\Omega}$ are the mean mass and mean atomic volume, respectively, per bulk atom. Evidently, the two effective sputter yields may differ for a given material in both magnitude and fluence dependence. In the older literature, a total sputter yield $Y_{\text{tot}} = \sum_i Y_i$ has frequently been introduced. This quantity is not measurable directly, and it is meaningful only in case of stoichiometric sputtering, where $Y_{\text{eff}}^{(M)} = Y_{\text{eff}}^{(\Omega)} = Y_{\text{tot}}$, as is easily verified.

In relating measurable quantities to theory one usually makes reference to a semi-infinite target with a plane surface. In view of the possible presence of microscopic and macroscopic surface roughness this idealization is not necessarily justified. On the other hand, this feature is presumably no more significant for multicomponent than for monoatomic targets, where that simplification is also quite common.

The partial sputter yield may be split into contributions from different depths,

$$Y_i = \int_0^\infty dx \sigma_i(x) N_i(x), \tag{5}$$

where $N_i(x)$ is the density [average number of i-atoms/volume] at depth x and $\sigma_i(x)$ is a quantity characterizing the sputter behavior of an i-atom as a function of depth. The target surface will always be assumed to coincide with the plane $x = 0$. This is appropriate for the standard backsputtering geometry.

The function $\sigma_i(x)$ has the dimension of an area and has therefore been termed sputter cross section (Sigmund et al., 1982). It depends on the environment, i. e., all densities $N_j(x)$ $(j = 0 \ldots n)$. For a uniform incident beam of fluence $d\Phi$, the probability for ejection of a given i-atom at depth x is $\sigma_i(x) d\Phi$. In general, $\sigma_i(x)$ will drop rapidly to zero with increasing depth x, dependent on the species.

If the target can be characterized by monolayers of a unique thickness, i.e., mostly for single crystals, an alternative description in terms of a discrete layer index l may be appropriate,

$$Y_i = \sum_{l=1}^{\infty} y_i^{(l)} c_i^{(l)}, \tag{6}$$

where $l = 1$ represents the top surface layer, $c_i^{(l)}$ the fraction of i-atoms in the lth layer, and $y_i^{(l)}$ a dimensionless quantity called the component yield of species

i from layer l. The component yields represent similar physical information as the sputter cross section. This discrete description, which is a special case of eq. (5), has been utilized mainly in conjunction with the assumption that only 1 (Betz & Wehner, 1983) or 2 (Lam, 1990) layers are depleted by sputtering. It is suitable for explicit incorporation of processes dealing with migrating lattice defects (vacancies, interstitials) but does not readily allow for changes in number density as a consequence of compositional changes. For nondilute alloys, this is a limitation.

As an example of a differential quantity characterizing sputter events consider

$$Y_i(\Theta)d^2\Omega = d^2\Omega \int_0^\infty dx \sigma_i(x,\Theta)N_i(x) \tag{7}$$

which represents the partial sputter yield differential in angle [mean number of i-atoms per beam atom ejected into a solid angle $d^2\Omega$ at a polar angle Θ against the outward surface normal]. Here, $\sigma_i(x,\Theta)d^2\Omega$ is the differential sputter cross section for ejection into a solid angle $d^2\Omega$ at a polar angle Θ from depth x, averaged over the distribution in energy and angle of the particle flux at depth x. With increasing depth x, the function $\sigma_i(x,\Theta)$ will reduce to an increasingly narrow peak around $\Theta = 0$. Therefore, the angular distribution of sputtered i-atoms will depend on the depth profile $N_i(x)$ (Sigmund et al., 1982). For a species enriched near the surface, the angular distribution will be broadened relative to that of a homogeneous sample, and vice versa. Similar considerations should apply to the energy distribution of sputtered atoms but do not seem to have been explored.

2.2.2 Theoretical Tools

We present a brief survey of theoretical methods that are available to predict preferential sputter behavior.

We address collisional sputtering, i.e., sputtering via cascades of elastic or quasi-elastic collisions. Calculations have been performed for random and crystalline targets. Analytic predictions are available only for random targets.

The standard system is a semi-infinite random target with a homogeneous composition. In analytic studies, the complexity may even be further reduced by operating with an infinite medium where sputtering is synonymous with the passage of target atoms through a reference plane at depth zero. For linear cascades, i.e., at low density of deposited energy, such a system is described by a linearized Boltzmann equation (Andersen & Sigmund, 1974; Watson & Haff, 1980) or, equivalently, a standard Monte Carlo code (Eckstein & Biersack, 1985; Vicanek & Urbassek, 1988). With suitable provisions about bulk and surface binding forces, particle fluxes extracted from analytic or numerical calculations may allow conclusions about preferential sputtering behavior.

The potential of Monte Carlo simulations may be extended to also comprise inhomogeneous composition profiles (Möller & Eckstein, 1984, 1985; Möller et al., 1988), provided that free flight paths are chosen small enough to make sure that the collision statistics is compatible with the local composition at any point. Also the Boltzmann equation approach can be applied to inhomogeneous composition profiles, but neither analytic nor numeric solutions have been determined this way, as far as we are aware.

Cascades are nonlinear in case of high density of energy deposition, but no unanimous agreement exists about pertinent processes even for monoatomic targets. Amongst several theoretical approaches that have been proposed for monoatomic targets, only the thermal model for the elastic-collision spike has been invoked to predict preferential sputtering (Sigmund, 1981).

In molecular-dynamics simulations the need to distinguish between linear and nonlinear cascades does not arise (Shapiro et al., 1988). All reported molecular-dynamics simulations operate with a target of initially homogeneous composition. Such codes are suited for studying preferential sputtering from both ordered and random alloys. Achieving adequate statistics is a notorious problem in molecular-dynamics simulations which is getting solved only gradually with ever more powerful hardware (Nieminen, 1993; Robinson, 1993). Studying disordered alloys requires care in setting up targets.

A common feature of all tools described in this section is that predictions on preferential sputtering can be made to emerge simultaneously with predictions on collisional mixing on the basis of compatible input.

2.2.3 Partial Sputter Yields

Analytic predictions of partial sputter yields have been provided on the basis of the theory of linear collision cascades in an infinite medium (Andersen & Sigmund, 1974; Sigmund, 1979). Two quantities were found relevant, the recoil density and the particle flux. The recoil density reflects the energy distribution of i-recoil atoms when set in motion. The particle flux reflects the energy distribution of i-atoms under steady-state conditions, i.e., under bombardment with a constant flux of primary radiation. While the recoil density is insensitive to the slowing-down behavior of recoiling atoms, the particle flux is, roughly, inversely proportional to the stopping power of an i-atom: The smaller the stopping power, the longer the slowing-down time and hence the greater the weight with which a given atom contributes to the particle flux under steady-state conditions.

Knowledge of the particle flux provides an estimate of the number of atoms passing through the surface plane at $x = 0$, provided that this plane is sufficiently close to the center of the collision cascade to be representative. This assumption, which also underlies conventional sputter theory for monoatomic targets (Sigmund, 1969a), has limitations. Quantitative studies of this particular aspect, both by analytic and numerical methods, have been performed for specific systems (Urbassek & Vicanek, 1988; Conrad & Urbassek, 1991).

Two more simplifications enter the theoretical treatment. Firstly, energy distributions are considered in the asymptotic limit where the ratio between particle energy and incident energy is $\ll 1$. Secondly, collisions between two target particles i, j are described by a power cross section of the form

$$d\sigma_{ij}(E,T) = C_{ij} E^{-m} T^{-1-m} dT, \tag{8}$$

where E is the energy of an i-atom before the collision, T the energy of a j- atom after the collision, m an exponent in the interval $0 < m < 1$, and C_{ij} a species-dependent constant. Both C_{ij} and m are determined by the interatomic potential that governs the collision. Moreover, the exponent m depends slightly on E. With this, the following result was obtained for the ratio of particle fluxes at energy ϵ in a binary, infinite, random medium,

$$\frac{\mathrm{flux}_1}{\mathrm{flux}_2} = \frac{N_1}{N_2} \frac{S_{21}(\epsilon)}{S_{12}(\epsilon)}, \tag{9}$$

where S_{ij} is the stopping cross section of an i-atom interacting with a j-atom,

$$S_{ij}(E) = \frac{1}{1-m} C_{ij} \gamma_{ij}^{1-m} E^{1-2m} \tag{10}$$

and $\gamma_{ij} = 4M_i M_j/(M_i + M_j)^2$.

Vicanek et al. (1993) derived eq. (9) without going over the power cross section (8) from a principle of detailed balance in the collision cascade where the flux of energy from the subsystem of i-atoms to the subsystem of j-atoms equals the opposite flux. That work also demonstrated that eq. (9) has certain limitations for widely different masses of the constituent atoms.

Eq. (9) shows that in this approximation, the ratio of particle fluxes is independent of the energy and the type of the incident radiation. This result hinges on the assumption that $\epsilon \ll E$.

It is also seen that the ratio of particle fluxes deviates from stoichiometry by the factor $S_{21}(\epsilon)/S_{12}(\epsilon)$ which, in the power approximation, is independent of ϵ. Since conventional screened-Coulomb interaction potentials are symmetric in i and j, the above ratio is independent of the atomic numbers, and all nonstoichiometry originates in a kinematic factor which, in the power approximation, reads

$$\frac{S_{21}(\epsilon)}{S_{12}(\epsilon)} = \left(\frac{M_2}{M_1}\right)^{2m} \tag{11}$$

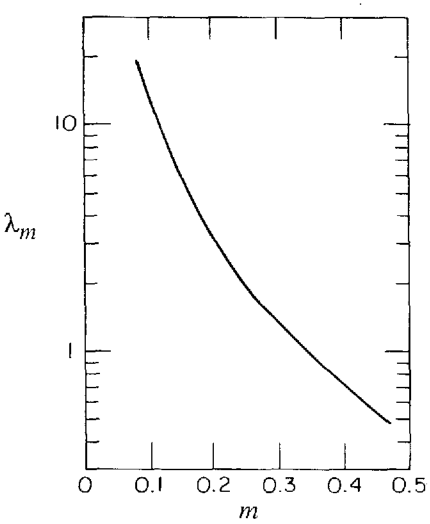

Figure 1. Numerical constant λ_m versus exponent m. The actual curve is not universal but somewhat dependent on the potential (here Born-Mayer potential). After Vicanek et al. (1989).

both for standard screened-Coulomb interaction (Lindhard et al., 1968; Ziegler et al., 1985) or for Born-Mayer-type interaction

$$C_{ij} = \frac{\pi}{2}\lambda_m a^2 \left(\frac{M_i}{M_j}\right)^m (2A_{ij})^{2m}, \tag{12}$$

which has been adopted for low-energy collisions (Sigmund, 1969a) with constants

$$A_{ij} \simeq 52eV(Z_iZ_j)^{3/4} \text{ and } a \simeq 0.219\text{Å} \tag{13}$$

according to Andersen & Sigmund (1965).

It is illuminating to analyze the physical origin of the preferential behavior expressed by eq. (9) in conjunction with (11). There are actually two intimately connected sources, each of which contributes a factor of $(M_2/M_1)^m$. Consider a j-isotope in the near-surface region, knocked on by some moving atom (another isotope or something else). The cross section for a knockon event at a given recoil energy is proportional to M_j^{-m} according to eq. (12). This accounts for one factor. Now, the fraction of recoil atoms able to leave the target is proportional to the total pathlength which a recoil is able to travel before coming to rest form a given initial energy. The stopping power of an i-atom is proportional to M_i^m according to eqs. (10,12). The pathlength is inversely proportional to the stopping power.

This accounts for the other factor. This argument is not restricted to a binary target (Sigmund, 1987a, 1993b).

The exponent m has in some applications been set equal to zero (Sigmund, 1969a). This approximation is acceptable for monoatomic targets but eliminates all collisional nonstoichiometry to first order (Watson & Haff, 1980). The value $m = 0.055$ adopted otherwise for not too light species at low energies (Sigmund, 1969a; Andersen & Sigmund, 1974) has been found to be a factor of two too small by comparison with accurate Born-Mayer scattering theory (Vicanek et al., 1989). For softer interaction potentials, m becomes even greater and can come close to $m \simeq 0.2$ (Biersack & Eckstein, 1984). The dependence of the dimensionless parameter λ_m on m is shown in fig. 1.

Not much definite information is available on potentials between atoms in solids governing collisions in the pertinent energy range (10 to 100 eV). The topic has been discussed by Robinson (1993) and Nieminen (1993) in this volume. It is conceivable that well-defined and well-analyzed measurements of preferential sputtering may provide as much information on low-energy collisions in solids as any of few other available sources.

The above equations for binary targets can be extended to polyatomic mixtures (Sigmund, 1987a; Urbassek & Conrad, 1993, Sigmund, 1993b). The particle flux in a ternary material with arbitrary mass ratios has been studied theoretically (Andersen & Sigmund, 1974). Their main result, expressed by their equations (29) and (30), can be written in the form

$$\frac{\mathrm{flux}_1}{\mathrm{flux}_2} = \left(\frac{N_1}{N_2}\right) \frac{N_1 S_{21} S_{31} + N_2 S_{21} S_{32} + N_3 S_{23} S_{31}}{N_1 S_{31} S_{12} + N_2 S_{32} S_{12} + N_3 S_{32} S_{13}}. \tag{14}$$

It is easily seen that for the conventional power cross section, eq. (8), numerator and denominator contain a factor that cancels out, with the result that the ratio of $\mathrm{flux}_1/\mathrm{flux}_2$ reduces rigorously to the prediction for the binary medium, i.e., eq. (9).

Eq. (14) was rederived by Urbassek & Conrad (1993), but allowance was made then for a species dependence of the exponent m, i.e., $m = m_{ij}$. Moreover, an analytic approach going beyond the power-law scattering cross section has been explored recently (Vicanek et al., 1993).

For a monoatomic medium, the energy-integrated particle flux is known to be $\propto U^{2m-1}$ (Sigmund, 1969a, 1981) where U is the surface binding energy, under the assumption that bulk binding energies can be ignored. This finding translates into a U_i^{2m-1}-dependence of the partial sputter yield of the i-th component in a random polyatomic target.

In summary, this form of simplified transport theory predicts the following ratio of partial sputter yields in a binary medium (Sigmund, 1981),

$$\frac{Y_1}{Y_2} = \frac{N_1}{N_2}\left(\frac{M_2}{M_1}\right)^{2m}\left(\frac{U_2}{U_1}\right)^{1-2m}, \tag{15}$$

which has frequently served as a standard of reference.

Experience from monoatomic targets suggests that the above picture will break down at low incident energies, where the precise meaning of 'low' is not well known but clearly dependent on the ion/target mass ratio. Some limitations have been analyzed for the specific case of isotopic mixtures (Conrad & Urbassek, 1991).

2.2.4 Surface Binding

The dependence on mass and surface binding energy shown in eq. (15) predicts large yields for small target mass and small surface binding energy. Since m is small for the energy range pertinent to sputtering the yield is more sensitive to variations in surface binding energy than in mass.

Early attempts to estimate pertinent surface binding energies were based on a pair-bonding model (Swalin, 1962). In such a model, the surface binding energy can be approximated by

$$U_i = Z_S\overline{U_{ik}}^k \tag{16}$$

where Z_S is an effective surface coordination number, U_{ik} is the bond strength between an i- and a k-atom, and the average is to be taken over nearest neighbors, weighted according to the surface composition. The validity of a pair-bonding model is undoubtedly dependent on the target material and somewhat questionable for metallic targets. Moreover, the pair-bonding model implies a statistical distribution of surface binding energies governed by the actual nearest-neighbor configuration. The above expression involves average surface binding energies. Since the sputter yield Y_i depends on a negative power of U_i, the range of validity of the above estimate must be limited to small variations of the U_{ik}. Nevertheless, eq. (16) leaves no doubt that U_i will vary as a function of bombardment time due to changing surface concentration.

Experimental evidence may be drawn from comparisons of sputtered-particle energy spectra for alloys of different composition with those of the corresponding pure materials. Such comparisons invoke the assumption of a peak position $\simeq U_i/2$. This relation stems from linear cascade theory (Thompson, 1968) and is well corroborated in case of elemental targets (Gruen et al., 1982). Within the range of validity of linear cascade theory, it should be equally well justified for alloys of homogeneous composition. Caution is indicated in the spike regime: In that case, the peak position becomes sensitive to bombardment parameters like

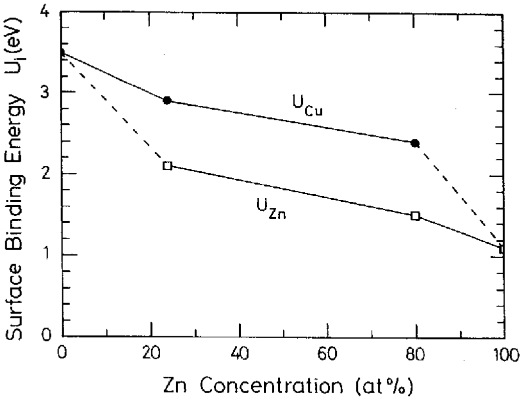

Figure 2. Compositional dependence of the surface binding energies U_{Cu} and U_{Zn} in Cu-Zn alloys. Curves drawn to guide the eye. After Szymonski (1980).

ion type and energy. Caution is also indicated after bombardment at high fluence: Here, composition gradients build up which will affect energy and angular spectra of sputtered atoms. Particularly in the presence of pronounced Gibbsian segregation, the peak position of the energy spectrum must be expected to change. Pertinent estimates are not available.

Experimental evidence suggests that surface binding energies indeed depend on alloy composition. Szymonski (1980) found U_{Zn} in Cu-Zn alloys to decrease with increasing Zn concentration toward the pure-Zn value, while U_{Cu} decreased from the pure-Cu value to a substantially smaller one (fig. 2). Similar composition dependences were observed in Au-Ag, Ni-W, and Cu-Li alloys by Szymonski et al. (1978), Oechsner & Bartella (1981), and Schorn et al. (1988), respectively. Noticeable matrix effects on the surface binding energy were also demonstrated for Cr atoms in different alloys (Husinsky et al., 1987).

Reliable values of static surface binding energies can now be calculated from standard codes on the basis of density functional and effective-medium theory for a given target configuration. Such values are implicit in molecular-dynamics simulations based on theoretical or empirical many-body potentials. For the present purpose, effective surface binding energies, valid under dynamic conditions, may be extracted from simulated energy spectra of sputtered atoms. Lam & Johannessen (1992) determined surface binding energies of Cu and Ni in a $\mathrm{Cu}_{0.5}$-$\mathrm{Ni}_{0.5}$ alloy dynamically and found $U_{\mathrm{Cu}} = 3.28 \pm 0.13$ eV and $U_{\mathrm{Ni}} = 3.97 \pm 0.17$ eV, which are lower than the heats of sublimation of pure Cu and Ni, i.e., 3.51 and 4.45 eV, respectively (Gschneidner, 1964).

Kelly (1978, 1980) related the bond strengths U_{ik} in eq. (16) to the heats of atomization of the pure components, $\Delta H_i \simeq (1/2)ZU_{ii}$, where Z is the bulk coordination number, and the heat of mixing of the alloy, ΔH_m. Since ΔH_m is usually much smaller than ΔH_i, one may approximate U_{ik} by

$$U_{ik} = \frac{1}{2}(U_{ii} + U_{kk}). \tag{17}$$

It was concluded that preferential sputtering estimated on the basis of the surface-binding-energy given by eqs. (16,17) was in most cases far smaller than experimental observations, the reason being that most measurements were affected by surface segregation (Kelly & Harrison, 1985).

2.2.5 Sputter Cross Sections

Sputter cross sections are determined via the recoil density. Let $F_i(\epsilon, \Theta, x)d\epsilon d^2\Omega dx$ be the number of i-atoms per incident particle recoiling from a layer (x, dx) with an energy $(\epsilon, d\epsilon)$ into an angular interval $d^2\Omega$ at some polar angle Θ against the surface normal. Moreover, let $P_i(\epsilon, \Theta, x)$ be the probability for such an i-atom to be ejected through the surface. Then the sputter yield reads

$$Y_i = \int_0^\infty dx \int d\epsilon \int d^2\Omega F_i(\epsilon, \Theta, x) P_i(\epsilon, \Theta, x), \tag{18}$$

from where $\sigma_i(x)$ can be extracted by comparison with eq. (5).

Recoil densities integrated over depth and direction of motion have been calculated for homogeneous polyatomic media within the approximation scheme applied to the particle flux (Andersen & Sigmund, 1974). They may be rendered differential by the assumptions of isotropy, constant energy spectrum over the pertinent depth range near the surface, and a depth distribution in accordance with the deposited energy. This yields

$$F_i(\epsilon, \Theta, x) \simeq \frac{1}{4\pi} K_i c_i' \frac{F_D}{\epsilon^2}, \tag{19}$$

where $F_D \simeq F_D(x{=}0)$ is the deposited energy per unit depth at the surface, c_i' a quantity closely related to, but not identical with an atom fraction (Andersen & Sigmund, 1974; Vicanek & Sigmund, 1994), and K_i a dimensionless factor called displacement efficiency. Actually, K_i is not identical with, but closely related to the quantity carrying the same name in conventional radiation damage theory. It is seen that K_i expresses the degree of preferentiality in the energy sharing of the collision cascade. Explicit results for the dependence of K_i on composition have been given by Andersen & Sigmund (1974). The range of validity of eq. (19) has been studied recently (Koponen, 1992).

Some discussion has been concerning the ejection probability $P_i(\epsilon, \Theta, x)$. While that discussion is not specific to polyatomic media, it deserves a comment here. Apart from the variables listed above, P_i must depend on the surface barrier as well as the cross sections for elastic and inelastic scattering. In early papers (Sigmund, 1969a; Falcone & Sigmund, 1981; Sigmund et al., 1982), P_i was determined from the continuous-slowing-down approximation, i. e., angular deflection was ignored and an atom was thought to be ejected if, after moving on a straight line toward the surface, it still had enough energy to overcome the barrier.

In subsequent work (Falcone, 1991, and earlier references quoted there), the ad hoc assumption was made that the ejection probability should be determined only by angular deflection while energy loss should be immaterial. This assumption ignores the fact that in the absence of energy loss, the ejection probability is either zero or one, dependent on whether the energy is above or below the barrier, independent of depth. In the case of dominating angular deflection and weak energy loss — which is relevant in electron emission (Sigmund, 1993a) — the pertinent escape depth becomes the geometric mean between the range and the transport mean free path Λ_t for angular deflection. This is in contrast with the claim made by Falcone (1991) that the escape depth should be identical with Λ_t. In sputtering, angular deflection is typically associated with substantial energy loss. Therefore, the limit of dominating angular deflection does not usually apply. Consequently, the dependence of the escape depth on Λ_t must be *even weaker* than $\sqrt{\Lambda_t}$.

We thus conclude, in agreement with quantitative results given by Vicanek et al. (1989), that for elemental targets, the escape function is governed primarily by energy loss while angular deflection is a perturbation which is noticeable only in accurate evaluations. The perturbation may become significant in polyatomic targets with very different masses where the light component may undergo wide-angle scattering events with only minor energy loss.

Within the continuous-slowing-down approximation, one finds

$$P = \begin{cases} 1 & \text{for } \left(1 - \dfrac{x}{R_i(\epsilon)\cos\Theta}\right)^{1/2m} > \dfrac{U_i}{\epsilon\cos^2\Theta} \\ 0 & \text{otherwise} \end{cases} \tag{20}$$

where $R_i(\epsilon)$ is the total pathlength of an i-atom of energy ϵ. This quantity can be found from the stopping power of an i-atom,

$$\left(\frac{d\epsilon}{dR}\right)_i = -\frac{1}{1-m}\sum_j N_j C_{ij}\gamma_{ij}^{1-m}\epsilon^{1-2m} = -A_i\epsilon^{1-2m}, \tag{21}$$

where the last step defines a stopping constant A_i.

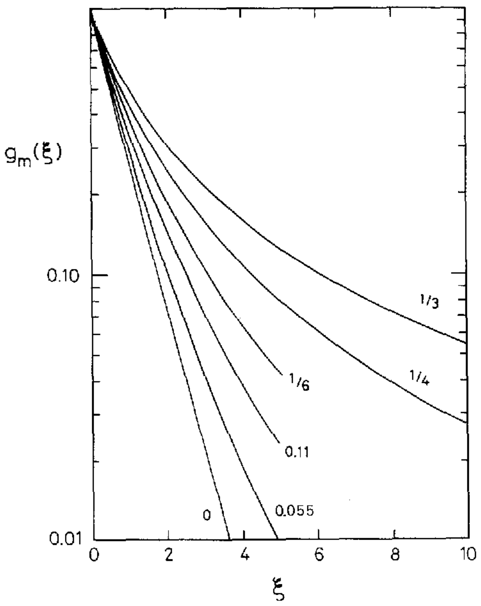

Figure 3. Depth dependence of the sputter cross section, eq. (20) for different values of the exponent m. The scale is specified by eq. (22).

Integration and comparison with eq. (18) yields (Sigmund et al. 1982)

$$\sigma_i(x) = \frac{K_i F_D}{6NU_i} g_m \left(\frac{A_i x}{U_i^{2m}} \right), \tag{22}$$

where

$$g_m(\xi) = \int_0^1 dt \frac{3t^2}{(1 + 2m\xi t^{4m-1})^{1/2m}}. \tag{23}$$

The functions $g_m(\xi)$ have been normalized such that $g_m(0) = 1$, and their halfwidth varies between $\xi_{1/2}$=0.5 and 0.75 for m running from 0 to 0.33 (fig. 3). Specifically, for $m = 0$, $g_0(\xi) = 3E_4(\xi)$, where $E_4(\xi)$ is an exponential integral in conventional notation (Abramowitz & Stegun, 1964).

The sputter cross section $\sigma_i(x)$ is preferential due to preferentiality of the displacement efficiency K_i and the surface binding energy U_i. The depth dependence expressed by the function $g_m(\xi)$ is also preferential in the sense that atoms with low stopping powers, i.e., low A_i, or high surface binding energy U_i, may emerge from deeper layers.

2.3 Secondary Processes

According to eq. (5), partial sputter yields of a multicomponent target are governed by sputter cross sections $\sigma_i(x)$ and densities $N_i(x)$. The physics of the sputter cross section is the subject of the theory of primary sputter processes. Secondary processes affect the behavior of densities as a function of depth and time.

In secondary processes it is appropriate to distinguish between two different time scales. For athermal processes, the rate-determing quantity is the ion fluence $d\Phi = J_0 dt$, where J_0 is the incident-ion current [number of ions/area/time] and dt a real-time interval. For thermally-activated processes, this direct correlation does not apply.

Pertinent athermal effects are 'prompt' processes in a collision cascade like sputtering, recoil mixing, and 'spike' phenomena (Sigmund, 1981). Also electronic sputtering, when present, and associated damage effects belong mostly into this category (Johnson & Schou, 1993). Moreover, pressure gradients building up in the material due to collisional rearrangement in a cascade must to some degree relax athermally on a time scale of the order of a lattice-vibrational period. This relaxation may even be affected by the energetics of Gibbsian segregation. Experimentally, athermal processes are identified by their dependence on ion fluence independent of the ion current density J_0.

Thermally activated processes like Gibbsian segregation in the conventional meaning, radiation-enhanced diffusion, and radiation-induced segregation, may be substantial during ion bombardment even at temperatures where they would be frozen in the absence of an ion beam. Once created, bombardment-induced point defects may migrate over distances that are large compared to the dimensions of an individual collision cascade. Therefore, bombardment-induced changes caused by migrating defects will depend on the density of ion current as well as on target temperature.

Thermal as well as athermal effects are governed by rate equations that are similar in structure but different in detail. The present introductory section is intended to show the gross features while specific processes will be treated in more detail in section 4.

2.3.1 Athermal Processes

In the absence of thermally activated processes, a full description of alloy sputtering must account for the compositional changes caused by primary effects of preferential sputtering, collisional mixing and ion implantation, as well as instantaneous relaxation of the target to a stable state. Numerous versions of the pertinent rate equations have been proposed. A general survey of work prior to 1981 was given by Betz & Wehner (1983). Existing treatments differ in the way how sputtering, mixing, and relaxation enter into the theoretical scheme, quite apart from the numerical input. The treatment given below should comprise the essentials of different schemes.

As a starting point we use a scheme proposed initially by Hofer & Littmark (1979) for a numerical treatment of collisional mixing in depth profiling by sputtering. In the original form, that scheme assumed stoichiometric sputtering and mixing, and ion implantation was disregarded. Proper generalizations followed subsequently. The scheme was condensed into a set of nonlinear kinetic equations (Sigmund et al., 1982). Although that set of equations in its original form disregarded ion implantation, it comes fairly close to a comprehensive description that allows incorporation of most pertinent processes including thermally activated ones (Sigmund & Oliva, 1993).

The key quantity characterizing the primary processes of collisional mixing and preferential sputtering is the relocation cross section $G_i(x,x')dx'$. This is an almost universally used quantity in mixing theory although names and notation vary slightly. Let $\delta\Phi G_i(x,x')dx'$ be the probability for a given target atom of type i to be relocated from an initial depth x into a layer (x',dx') by a small ion fluence $\delta\Phi$. In the absence of competing effects, this would result in the following kinetic equation for the composition profiles $N_i = N_i(x,\Phi)$,

$$\left(\frac{\partial N_i(x,\Phi)}{\partial\Phi}\right)_{\text{unrelaxed}} = \int_0^\infty dx' N_i(x',\Phi)G_i(x',x) - N_i(x,\Phi)\int_{-\infty}^\infty dx' G_i(x,x'). \tag{24}$$

A planar target surface is assumed in $x=0$. The first term on the right accounts for atoms relocated into depth x from some depth x' inside the target. The second term accounts for loss of atoms from depth x into some depth x' inside or outside the target.

Relocation into negative depths is synonymous with sputtering. The sputter cross section $\sigma_i(x)$ introduced in eq. (5) is related to the relocation cross section by

$$\sigma_i(x) = \int_{-\infty}^0 dx' G_i(x,x'). \tag{25}$$

It is convenient to abbreviate the right-hand side of eq. (24) by L_iN_i, where L_i is to be understood as an integral operator (Sigmund & Gras-Marti, 1981). The relocation cross section $G_i(x,x')dx'$ depends on the composition of the medium; hence, the relocation operator L_i will in general not be linear.

We may include the effect of ion implantation and expand eq. (24) into

$$\left(\frac{\partial N_i}{\partial\Phi}\right)_{\text{unrelaxed}} = \delta_{i0}f_0(x) + L_iN_i \tag{26}$$

with the relocation term

$$L_i N_i(x) = -N_i \sigma_i(x) + \int_0^\infty dx' [N_i(x') G_i(x', x) - N_i(x) G_i(x, x')]. \qquad (27)$$

Here, as frequently in the following, the Φ-variable has been suppressed for clarity. The index 0 denotes the implanted species, δ_{ij} is the Kronecker symbol (= 1 for $i = j$ and 0 otherwise), and $f_0(x)$ is the range profile of the primary beam normalized to $\int_{-\infty}^{\infty} dx f_0(x) = 1$. Implantation into negative depths is synonymous with ion reflection.

The integral on the right of eq. (27) represents the effect of collisional mixing, i.e., direct relocation of target atoms by beam ions ('recoil impantation') as well as relocation by cascade particles ('cascade mixing'). Due to the initial momentum of the beam particles, there is always a net transport of target atoms into the target. This leads to a pileup of matter in the region around the mean penetration depth of the beam and beyond, and a corresponding depletion in the near-surface region which adds to the loss by sputtering. The resulting pressure gradients are mechanically unstable and must relax instantaneously. In a molecular-dynamics simulation of a collision cascade, this relaxation will show up if the interatomic potential allows for a stable target configuration and if a cascade is followed over a sufficiently long time interval. Simulations of cascade processes by Monte Carlo or binary-collision codes as well as conventional analytic approaches do not incorporate this feature. Therefore it has to be superimposed separately.

A straightforward, although a bit schematic way of accounting for this relaxation is by letting the material relax homogeneously such as to satisfy a prescribed packing condition

$$\sum_{i=0}^{n} \Omega_i N_i(x) = 1, \qquad (28)$$

where Ω_i is the atomic volume of an i-atom. This criterion was adopted initially by Hofer & Littmark (1979) for a binary material with all atomic volumes being equal.

In order that eq. (28) be fulfilled, a relaxation term needs to be added on the right-hand side of eq. (26), as a result of which the rate equation reads

$$\frac{\partial N_i(x,\Phi)}{\partial \Phi} = \delta_{i0} f_0(x) + L_i N_i(x,\Phi)$$
$$- \frac{\partial}{\partial x} \left(N_i(x,\Phi) \sum_{j=0}^{n} \Omega_j \int_0^x dx' [\delta_{j0} f_0(x') + L_j N_j(x',\Phi)] \right). \qquad (29)$$

It is easily verified that the packing condition (28) is obeyed at any fluence if it is fulfilled initially.

Note that it is the imposition of a packing condition which causes the target surface to recede as a result of the loss of matter by sputtering. This recession has been taken into account in the explicit derivation of eq. (29) (Sigmund et al., 1982, Collins & Sigmund, 1992) by means of a coordinate transformation that ensures the surface always to be located at $x = 0$.

The above scheme is equivalent with the seminumerical scheme applied by Littmark mostly for mixing calculations (Littmark & Hofer, 1984). In addition, numerical schemes developed by Eckstein & Möller (1985) and by Roush et al. (1981) reflect more or less the same physical content.

2.3.2 Relation to Elementary Treatments

Eq. (29) contains most earlier treatments as special cases. This will be illustrated separately for the effects of sputtering, implantation, and mixing.

Eq. (27) identifies the effect of sputtering. That contribution to eq. (29) reads

$$\left(\frac{\partial N_i}{\partial \Phi}\right)_{\mathrm{sput}} = -\sigma_i(x)N_i(x) + \frac{\partial}{\partial x}\left(N_i(x)\sum_{j=0}^{n}\Omega_j\int_0^x dx'\sigma_j(x')N_j(x')]\right). \tag{30}$$

In many treatments, all depth dependence of sputtering is ignored, and atoms are considered to be sputtered only from the surface. Then the sputter cross section reduces to $\sigma_i(x) = \delta(x)Y_i/N_i(0)$ where $\delta(x)$ is the Dirac function, and eq. (30) to

$$\left(\frac{\partial N_i}{\partial \Phi}\right)_{\mathrm{sput}} = -Y_i\delta(x) + w\frac{\partial N_i}{\partial x}, \tag{31}$$

where w is the surface recession due to sputtering as defined by eq. (2). The term $w\partial N_i/\partial x$ is the familiar convection term from transport theory. Note, however, that w, which is usually treated as a constant material parameter, depends on fluence via the partial sputter yields Y_i. The term containing the Dirac function is equivalent with a boundary condition, $N_i(0) = Y_i/w$, ensuring the correct sputter current of each species through the surface.

The implant term in eq. (26) is of interest mostly for the buildup of the implanted species. It can be written in the form

$$\left(\frac{\partial N_i}{\partial \Phi}\right)_{\mathrm{impl}} = \left[\delta_{i0} - \Omega_0 N_i(x)\right] f_0(x) - u_0\frac{\partial N_i(x)}{\partial x}, \tag{32}$$

where

$$u_0 = \Omega_0\int_0^x dx' f_0(x') \tag{33}$$

represents the dilatation due to implanted ions. This term is frequently neglected in mixing calculations but is of central significance in estimates of ion collection efficiencies (Almén & Bruce, 1961; Titov, 1979).

The contribution from mixing is often written in the form of a diffusive term. The relation to the present notation is well established in transport theory but will be sketched here briefly. Diffusive motion implies motion in very small steps. In other words, the relocation cross section $G_i(x,x')dx'$ is nonvanishing only for x' close to x. The situation is simplest in case of translational invariance, i.e., for $G_i(x,x') = G_i(x'-x)$. Then, Tailor expansion of $N_i(x')$ around x yields

$$\left(\frac{\partial N_i}{\partial \Phi}\right)_{\text{mix,unrelaxed}} = -v_i \frac{\partial N_i(x)}{\partial x} + \hat{D}_i \frac{\partial^2 N_i(x)}{\partial x^2}. \tag{34}$$

with

$$v_i = \int_{-\infty}^{\infty} dx'(x'-x)G_i(x'-x) \tag{35}$$

and

$$\hat{D}_i = \frac{1}{2}\int_{-\infty}^{\infty} dx'(x'-x)^2 G_i(x'-x). \tag{36}$$

For a genuine random walk, the mean relocation rate v_i for species i vanishes, but in a collision cascade, the initial momentum of the beam causes preferential relocation into the beam direction and, hence, v_i to be positive. The quantity $\hat{D}_i$, as specified by eq. (36), differs from a genuine diffusion coefficient only by the conversion factor from time to fluence, i.e., $D_i = J_0\hat{D}_i$.

While there is little doubt about the accuracy of the diffusion approximation for genuine diffusive motion, caution is indicated in case of collision cascades. Firstly, long-range relocation is possible. This implies tails at large relocation depths which the diffusion approximation can handle reasonably only in the limit of high implant fluences. Secondly, the relocation cross section will generally vary with depth over the penetration depth of the beam. This generates an ambiguity with regard to which quantity the Taylor expansion in powers of the relocation depth should be applied to. Collins & Jimenez-Rodriguez (1982) suggested an expansion in which the product of the density and the relocation cross section is assumed to vary slowly with x. Despite some success (Collins et al., 1988), it is not obvious under what circumstances this is an improvement beyond straight expansion of $N_i(x')$ (Conrad & Urbassek, 1993). Thirdly, steep composition gradients may develop near the target surface both due to sputtering and recoil implantation which require additional attention, in particular with regard to the boundary conditions to be satisfied.

Existing theoretical treatments addressing the validity of the diffusion approximation in atomic mixing addressed mostly bulk mixing and sputter profiling. Preferential sputtering was treated by means of the diffusion approximation, based on eq. (29) without the implant term, by Oliva et al. (1986).

2.3.3 The High-Fluence Limit

A useful model system for experimental and theoretical studies of alloy and isotope sputtering is a material with a homogeneous composition in the bulk. In the absence of activated processes, such a system must reach a stationary state at high fluences where all species sputter stoichiometrically.

This emerges readily from eq. (29). In the stationary state, the derivative on the left must vanish. Integration over the x-variable over the half-space yields

$$0 = \delta_{i0} t_0 - Y_i - N_i(\infty) \sum_{j=0}^{n} \Omega_j (\delta_{j0} t_0 - Y_j), \tag{37}$$

where

$$t_0 = \int_0^\infty dx f_0(x) \tag{38}$$

is the retention coefficient for incident ions. Note that

$$\int_0^\infty dx L_i N_i(x) = -Y_i \tag{39}$$

by means of eq. (27). Splitting eq. (37) into beam and target species yields

$$Y_0 = t_0 \tag{40}$$

and

$$Y_i = N_i(\infty) \sum_{j=1}^{n} \Omega_j Y_j \quad \text{for} \quad i = 1 \ldots n \tag{41}$$

in the stationary state. Eq. (40) shows that the sputter rate for implant atoms balances the retained beam flux in the stationary state as it should be. Eq. (41) shows that the partial sputter yields of the target species are all proportional to the bulk concentration, i.e., the target sputters stoichiometrically.

While these results do not imply any assumptions on the nature and magnitude of atomic mixing effects, such information does enter into the absolute magnitude of the partial sputter yields for the target species. We note that it is essentially the effective sputter yield $Y_{\text{eff}}^{(\Omega)}$, eq. (4), that enters the asymptotic formula (41).

2.3.4 Activated Processes

The theoretical scheme described above for athermal processes can readily be extended such as to comprise thermally activated processes. Two items need to be considered. Firstly, such processes proceed in real time, i.e., fluence is insufficient as the sole time variable. Secondly, more species are involved in the transport of matter, especially point defects, i.e., vacancies and interstitials. In order to incorporate these two features, disregard relaxation for a moment and write

$$\begin{aligned}\left(\frac{\partial N_i(x,t)}{\partial t}\right)_{\text{unrelaxed}} &= J_0(t)\left(\delta_{i0}f_0(x)+\sum_{\nu=n+1}^{n+z}\delta_{i\nu}F_\nu(x)+\sum_{\nu=0}^{n}\delta_{i\nu}L_\nu N_\nu(x,t)\right)\\ &\quad+\Lambda_i N_i(x,t)-S_iN_i(x,t)\equiv Q_i(x,t). \qquad (42)\end{aligned}$$

Here, $N_i(x,t)$ denotes the density of implanted beam atoms for $i=0$, the density of target species for $i=1,\dots n$, and the density of i-type defects for $i=n+1,\cdots n+z$ if there are z different kinds of pertinent defects. The three terms in the brackets on the right-hand side of eq. (42) represent the implanted beam, the primary production of defects by the ion beam — $F_\nu(x)dx$ is the mean number of ν-defects generated per beam particle at depth (x,dx) — and primary relocation including sputtering, respectively. These processes are proportional to the beam current J_0 which may be time-dependent.

The fourth term, $\Lambda_i N_i(x,t)$, represents all transport processes which are not described by the relocation term L_iN_i. This term has a form analogous to eq. (27),

$$\Lambda_i N_i(x)=\int_0^\infty dx'[N_i(x')\Gamma_i(x',x)-N_i(x)\Gamma_i(x,x')] \qquad (43)$$

with the difference that there is no loss term due to sputtering. The relocation function $\Gamma(x,x')$ will in general be a functional of several of the pertinent densities, especially defect densities. On the other hand, the applicability of the diffusion approximation applied to $\Lambda_i N_i(x,t)$ will most often be granted. In sect. 4.5.1 this term will be written in a form that allows for linear coupling between different species. The above notation is meant to incorporate this feature symbolically.

Finally, the last term in eq. (42) represents most of all the loss of defects by annihilation, either via interaction with other migrating defect species or at stationary sinks such as dislocations, grain boundaries, and surfaces. However, also the loss of volatile atoms from the target surface may be included here. Again, the loss operator S_i may be a functional of several other densities. This will be made explicit in sect. 4.3.

Eq. (42) does not automatically obey a stability criterion. We now generalize the packing condition (28) such as to include not only beam and target particles but also defects so that a fixed volume Ω_ν is assigned to every ν-type defect,

$$\sum_{i=0}^{n+z}\Omega_i N_i(x)=1. \qquad (44)$$

With this, the comprehensive equation governing compositional changes reads

$$\frac{\partial N_i(x,t)}{\partial t} = \mathcal{Q}_i(x,t) - \frac{\partial}{\partial x}\left(N_i(x,t)\sum_{j=0}^{n+z}\Omega_j\int_0^x dx'\mathcal{Q}_j(x',t)\right), \tag{45}$$

$\mathcal{Q}_i(x)$ being defined by eq. (42). For constant atomic volume, this equation fulfills the packing condition at all times if it is fulfilled initially. The option of a composition-dependent atomic volume has been considered recently (Sigmund & Oliva, 1993).

In the following, an alternative version of eq. (45) will occasionally be used, which is easily verified by means of the packing condition (44),

$$\frac{\partial N_i}{\partial t} = \sum_{j=0}^{n+z}\Omega_j[N_j\mathcal{Q}_i - N_i\mathcal{Q}_j] - \frac{\partial N_i}{\partial x}\sum_{j=0}^{n+z}\Omega_j\int_0^x dx'\mathcal{Q}_j(x',t). \tag{46}$$

In the absence of concentration gradients — as may be the case at small irradiated fluences — this reduces to the simple expression

$$\frac{\partial N_1}{\partial t} = \Omega_2[N_2\mathcal{Q}_1 - N_1\mathcal{Q}_2] \tag{47}$$

if only two species are present. This illuminates the importance of the relaxation term: If relaxation were neglected, the right-hand side would just read $\mathcal{Q}_1$.

The main weakness of this description is its limitation to planar geometry. The real situation is unquestionably three-dimensional, at least in principle and most often in practice: An initially planar target surface does usually not retain its planar shape. The development of surface topography under sputtering has been an active area of investigation (Carter et al., 1983). It is also well documented that topography is sensitive to surface contamination. Despite this, the problem has apparently not been treated in conjunction with specific aspects of alloy sputtering.

2.3.5 The Stationary State

Several conditions must be expected to be fulfilled for a stationary state to develop in the presence of activated processes. An eroding target can reach a steady-state profile only if it has initially a homogeneous composition at least at great depths. The ion current J_0 must be reasonably constant. All pertinent sputter yields must be nonvanishing. All transport of matter must be limited to a finite depth range. If either of the two latter conditions is not fulfilled, one or more component will continue to be enriched or depleted, respectively.

While we are not sure whether a combination of these conditions makes up a sufficient criterion for the existence of a stationary state, we wish to briefly demonstrate the implications for sputtering when such a state does exist. Following the procedure applied in sect. 2.3.3, we set the left-hand side of eq. (45) equal to zero and integrate over all x. This yields

$$0=\int_0^\infty dx\mathcal{Q}_i(x)-N_i(\infty)\sum_{j=0}^{n+z}\Omega_j\int_0^\infty dx\mathcal{Q}_j(x). \tag{48}$$

The integral $\int_0^\infty dx\mathcal{Q}_i(x)$ receives five contributions according to eq. (42): The first and third one have been evaluated in sect. 2.3.3. The second and fifth contribution vanish for $i=0,1,\ldots n$, i.e., for i running over the target species and the beam particles. The fourth contribution is readily seen to vanish for arbitrary $G_i(x,x')$ by means of eq. (43). Therefore, we retain eq. (40) as was to be expected, and even eq. (41) remains strictly valid with the bounds on i and j as given: Again, sputtering proceeds stoichiometrically, independent of the quantitative input on either thermal or athermal processes. Again, the proportionality constant determining the absolute values does depend on that input.

2.3.6 Solving Equations

So far, no fully analytic solution of eq. (45) has been reported for any system. Selected numerical results will be given in sect. 4. Here a few schemes will be discussed briefly that allow to evaluate important limiting cases. While the choice of initial conditions is arbitrary within the limitations set by the packing condition (44), it is convenient – but of course not necessary – for calculations in the low-fluence limit to refer to a standard case where

$$N_i(x,0)=\mathcal{N}_i \tag{49}$$

and the $\mathcal{N}_i$ are the initial concentrations of atoms and defects in the material, taken as independent of depth and satisfying $\sum_{i=0}^{n+z}\Omega_i\mathcal{N}_i=1$. This allows for an initial (equilibrium) defect concentration but ignores an initial (equilibrium) segregation.

With this, we find the low-fluence behavior

$$\left(\frac{\partial N_i(x,t)}{\partial t}\right)_{t=0}=\sum_{j=0}^{n+z}\Omega_j\left[\mathcal{N}_j\mathcal{Q}_i(x,0)-\mathcal{N}_i\mathcal{Q}_j(x,0)\right]. \tag{50}$$

The initial concentration of beam particles, $\mathcal{N}_0$, will frequently be vanishing, and for many applications it is justified to ignore the initial, thermal defect concentrations $\mathcal{N}_{n+1}\ldots\mathcal{N}_{n+z}$ altogether. An additional term containing gradients of $\mathcal{N}_i$ would remain if the initial (equilibrium) segregation could not be neglected.

As did eq. (47), eq. (50) documents that the relaxation term cannot be ignored even at the lowest fluences. Indeed, in a binary material, a small ion fluence causes one component to be depleted and the other enriched near the surface due to sputtering. If relaxation were neglected, both components would appear depleted.

Next, consider the stationary state, assuming that all pertinent conditions be fulfilled for such a state to exist. In this case, the presence of an initial equilibrium segregation is immaterial. Dropping all time dependence and integrating over x from 0 to x and from x to ∞, respectively, leads to the following identities (Sigmund & Oliva, 1993),

$$N_i(x) = \frac{\int_0^x dx'\,\mathcal{Q}_i(x')}{\sum_j \Omega_j \int_0^x dx'\,\mathcal{Q}_j(x')} \tag{51}$$

and

$$N_i(x) = \mathcal{N}_i + \frac{\sum_j \Omega_j \int_x^\infty dx'[N_i(x)\mathcal{Q}_j(x') - N_j(x)\mathcal{Q}_i(x')]}{\sum_j \Omega_j \int_0^x dx'\,\mathcal{Q}_j(x')}. \tag{52}$$

Here, eq. (51) is useful to explore the analytic behavior of $N_i(x)$ in the vicinity of the surface. Eq. (52) can serve as the basis of an iteration scheme determining the stationary profile without computation at intermediate fluences. This scheme, involves $\mathcal{Q}_i(x)$ expressed by $N_i(x)$ through the definition, eq. (42), and an initial trial function for which eq. (49) is adequate.

Time-dependent solutions have been determined approximately by linearization of eq. (45) in terms of weak preferentiality (Sigmund et al., 1982; Jimenez-Rodriguez et al., 1992, Conrad & Urbassek, 1993). Here the assumption enters that profiles do not deviate significantly from the initial profile eq. (49), so that relocation operators can be expanded around a suitably chosen mean value. While the scheme turns out to deliver accurate profiles in the athermal case when the implanted species is left out of consideration, artefacts appear in the immediate vicinity of the surface (Sigmund & Oliva, 1993) that warrant caution in applications to sputtering.

Fully-numerical solutions have been provided by Falcone & Oliva (1984) and, more recently, by Wadsworth et al. (1990).

3 Isotopic Mixtures

3.1 General Considerations

Different isotopes of an element sputter preferentially. For solid hydrogen, under conditions of dominating electronic sputtering, large isotope effects have been found experimentally (Schou, 1992; Johnson & Schou, 1993). Under conditions of dominating collisional sputtering, measurements and theory suggest isotope effects to be small. While there has been discussion about the actual magnitude, there is little doubt that they do not exceed $\simeq \Delta M/2M$, where ΔM is the mass difference and M the mean mass. For a typical isotopic system with $\Delta M/M \leq 0.1$, this implies an effect of the order of 5% or less. This smallness requires high standards on the accuracy of sputter experiments even when only relative yields or spectra are asked for. It also implies stringent requirements regarding systematic and statistical errors in computer simulations undertaken to study isotope effects in sputtering. Conversely, analytical estimates benefit from the smallness of the effect because of the possibility of series expansion of pertinent physical quantities in terms of the relative mass difference. The main challenge there is the necessity to consider several small effects that might contribute to the overall picture.

Measurements of preferential sputtering from isotopic mixtures have been performed at high and low fluences. At high fluences the components sputter stoichiometrically, but their angular emission patterns need not be identical and, therefore, allow conclusions on preferential sputtering. At low fluences, partial sputter yields provide a direct measure of preferential sputtering.

It may be appropriate to discuss qualitatively a number of effects that compete with the mass dependence of the partial sputter yields discussed in sect. 2.2.3.

Firstly, according to eq. (15), the ratio of partial sputter yields is sensitive to differences in binding energy. Even though it may be justified to neglect a possible difference in the binding potential which keeps the atoms to their lattice sites, a difference in the effective binding energy arises due to the mass dependence of the zero-point energy. Hence, we may take

$$\frac{\Delta U}{U} \simeq \frac{3}{2}\frac{\hbar\omega_D}{U}\frac{\Delta M}{2M} \tag{53}$$

as a first approximation, where ω_D is a Debye frequency and $3\hbar\omega_D/2$ the zero-point energy. This implies that the lightest isotope has the smallest binding energy. In the absence of other effects, this gives rise to preferential sputtering of light isotopes according to

$$\frac{\Delta Y}{Y} \simeq -(1-2m)\frac{3}{2}\frac{\hbar\omega_D}{U}\frac{\Delta M}{2M} \tag{54}$$

in accordance with the dependence on surface binding in eq. (15).

Secondly, Gibbsian segregation has generally been ignored for isotopic systems. A small isotope effect must, however, occur essentially for the same reason as in case of the surface binding energy, i.e., the vibrational contribution to the free energy of an atom. If the surface modes are softer, the surface free energy will be smaller than the bulk free energy, and the $M_i^{-1/2}$-dependence of the vibration frequency will result in a negative segregation energy for the lighter isotopes (Foiles, 1992). Enrichment of the lighter species appears to be favored in thermal equilibrium.

Thirdly, there is a well-known isotope effect in diffusion (Peterson et al., 1973; Peterson, 1975). The relative difference in diffusivity between two isotopes results from the mass dependence of the jump frequency, i.e.,

$$\frac{\Delta D}{D} = -f \Delta K \frac{\Delta M}{2M}, \tag{55}$$

where f is the pertinent correlation factor (i.e., a geometric factor dependent only on the crystal structure and the atomic jump process) and ΔK an energy sharing factor. Eq. (55) implies that the isotope with the smallest mass diffuses most rapidly. This may give rise to a preferential coupling between the currents of radiation-produced defects (e.g., interstitials, at ambient temperature) and the lighter isotopes and may induce a surface enrichment of these isotopes during sputtering. Measurements of near-surface concentration profiles for different isotopes would be of interest.

Finally, light isotopes are recoil-implanted preferentially from the surface into deeper layers. It depends on the experimental technique whether this effect can be separated from that of preferential sputtering.

3.2 Theoretical Estimates: Primary Effects

Four groups of authors have been engaged in the theoretical study of isotope effects in sputtering. Since these groups worked rather independently we first discuss their contributions separately and subsequently try to summarize the current status.

3.2.1 Estimates of Sigmund and coworkers

The sharing of energy in linear collision cascades generated by high-energy primary ions in a homogeneous, infinite, polyatomic medium was studied by Andersen & Sigmund (1974) . The ratio between particle fluxes of two components 1, 2 was found to be given by eq. (9). For the specific case of power scattering, eq. (10), this reduces to eq. (11). The physical origin of this mass dependence has been described in sect. 2.2.3. Note in particular that eqs. (9) and (11) remain valid also between any two components of a medium containing more than two isotopes, and even in the presence of other elements.

Eq. (9) represents an asymptotic solution for the case of $E \gg \epsilon$. It is well established that anisotropy corrections need to be allowed for at moderate to low ratios of E/ϵ (Sigmund, 1981). For isotopic systems, such corrections have been explored recently (Sigmund & Sckerl, 1993).

According to conventional sputter theory, the composition of the sputtered-particle flux reflects the flux of atoms in the bulk, and the magnitude is determined by the depth distribution of deposited energy (Sigmund, 1969a). Within this picture, eqs. (9) and (11) represent an estimate of the ratio of partial sputter yields. This conclusion was implicit in the work of Andersen & Sigmund (1974) but was drawn only with considerable caution. The reason for this caution was the awareness of concentration gradients produced by preferential sputtering. Those gradients were assumed to be very pronounced at those fluences where measurements were available, since the feeding effect of collisional mixing was not yet established at the time.

A more explicit discussion of preferential sputtering, both for isotopic mixtures and alloys, based on the above results was presented subsequently (Sigmund, 1980, 1981). Here, eq. (11) was asserted to characterize the *primary* effect of preferential sputtering, at least in the limit of high ion energy. In that limit, the composition of the sputtered flux should be independent of ion type and energy.

Within this scheme, the key parameter governing preferential sputtering is the exponent m in the power cross section, eq. (10). That quantity was discussed briefly in sect. 2.2.3. The parameter depends on ejection energy and, somewhat, on M, but it may safely be set equal for all isotopes of a given element. The value of $m = 1/3$ valid for Thomas-Fermi interaction (Lindhard et al., 1963) is undoubtedly too large, and the value $m = 0.055$ adopted originally for Born-Mayer interaction (Sigmund, 1969a) turned up to be too small by comparison with an accurate numerical evaluation of the cross section and should have been set to $m = 0.11$ (Vicanek et al., 1989). Potentials utilized at present to describe repulsive interactions between atoms in the energy range in question include the Molière and Lenz-Jensen potential as well as the so-called KrC potential. Characteristic values of m lie around 0.15 – 0.20 for those potentials.

Allowing for uncertainties in the interatomic potential, one concludes that on the basis of bulk energy sharing and slowing-down, the deviation from stoichiometric sputtering is expected to be given by

$$\frac{\Delta Y}{Y} \simeq -k\frac{\Delta M}{M} \tag{56}$$

in the limit of high ion energy, with $k \sim 0.2 - 0.4$. The minus sign indicates that it is the low-mass component that sputters preferentially.

The leading correction term in an asymptotic expansion in terms of the ratio E/ϵ introduces a slight anisotropy into the particle flux and it modifies the magnitude of the enrichment factor. For heavy-ion bombardment at keV energies, the magnitude of that correction appears quite small (Sigmund & Sckerl, 1993).

3.2.2 Estimates of Haff, Tombrello, Shapiro and coworkers

A massive theoretical effort in the area was presented by collaborations inspired by Tombrello and colleagues.

In an early paper addressing binary compounds (Haff & Switkowski, 1976), energy sharing was treated by intuitive arguments. Sputtering was predicted to be stoichiometric in the absence of differences in surface binding energy, 'as observed experimentally'. In a related paper (Haff, 1977), a mass effect of the order of $(M_2/M_1)^{1/4}$ was predicted on the basis of arguments involving mean free paths and energy equilibration. Neither of these two papers addressed the item of isotope effects explicitly, but the arguments applied should be valid for those systems.

In a subsequent theoretical paper (Watson & Haff, 1980), energy dissipation was treated on the basis of transport equations equivalent to those analyzed by Andersen & Sigmund (1974). The cross section adopted for those calculations was simplified to the point where no preferentiality was allowed for, corresponding to $m = 0$ in eq. (8). A small isotope effect, quadratic in the mass difference, remained since the authors chose to analyze the recoil density instead of the particle flux. In agreement with a prediction on mass effects by Kelly (1978) but in contrast to all other earlier or later work, this isotope effect was predicted to be composition-dependent.

The conclusions of Watson & Haff (1980) formed the basis of extensive tabulations and predictions of isotope fractionation in minerals addressing the planetary-science community (Haff et al., 1981) and were utilized in the analysis of a most impressive set of experimental data (Russell et al., 1980). The predictions of Andersen & Sigmund (1974) — which clearly conflicted with that picture — were not mentioned.

Although the conclusions of Watson & Haff (1980) and Haff et al. (1981) were never withdrawn, it was apparently deemed necessary to reinvestigate the problem from the beginning by means of computer simulations (Shapiro et al., 1985, 1988; Lo et al., 1989) addressing elemental copper. The main challenge in the investigation of a small effect like preferential sputtering of isotopes by molecular dynamics is statistics. In order to achieve a tolerable signal-to-noise ratio, the authors worked with 'pseudo copper', i.e., targets containing isotopes with mass differences enhanced beyond those present in natural copper. While computational capacity was insufficient initially to provide adequate statistics, a reasonably clear picture has emerged subsequently.

Isotope effects were found to be linear in the mass difference and independent of concentration. Moreover, light isotopes were found to sputter preferentially. These features are in agreement with Andersen & Sigmund (1974) and in contrast to Watson & Haff (1980). Primary sputter effects turned out to depend on the emission angle and to differ for backward and forward sputtering. Moreover, the absolute magnitude of preferential sputtering was found to be fairly large in some simulations, corresponding to values of m in eq. (15) up to $\simeq 0.3$ (Shapiro et al., 1988).

However, caution is indicated in drawing fargoing conclusions from direct comparison between these results to either analytic predictions or experimental data:

Most simulations were done on single crystals (Shapiro et al., 1985, 1988) with the incident beam aligned along a low-index crystal direction. This has two important implications. Firstly, the angular emission characteristics are affected by formation of Wehner spots (Wehner, 1955). While questions regarding the mutual interference of spot formation and preferential sputtering have barely been asked, all existing knowledge of energy and angular spectra in elemental targets (Hofer, 1991) suggests that major or minor interferences exist. In the absence of at least a qualitative analysis, conclusions based on angular patterns of preferential sputtering from single crystals require considerable caution. Secondly, bombardment along low-index directions leads to substantial reductions in sputter yields due to the dominance of near-surface events in generating sputtering (Onderdelinden, 1968). Very little is known on how energy and angular distributions of sputtered atoms are affected even for monoisotope targets. It is evident, however, that these bombardment conditions are not representative for a polycrystal.

The above ambiguities were avoided in molecular-dynamics simulations on liquid copper (Lo et al., 1989). Here a two-isotope copper target with a mass difference of 25 atomic mass units, bombarded by 5 keV Ar, led to a 12.7 % difference in backward sputter yields, corresponding to $m = 0.16$ in eq. (11). The effect in the forward direction was found smaller by more than a factor of two. Thus, there does not seem to be a discrepancy in the magnitude of the predicted preferential sputter effects. This has been documented by a more detailed comparison (Sigmund & Sckerl, 1993).

A particular point in these simulations that deserves to be mentioned is the question of target setup. In the absence of segregation and ordering, the distribution of isotopes on the existing lattice sites must be taken as random, i.e., governed by Poisson's law. This assumption enters into cascade theory (Andersen & Sigmund, 1974) and into Monte Carlo simulations to be discussed below (Eckstein & Biersack, 1985). The assumption also entered initially into molecular-dynamics simulations by Shapiro et al. (1985). However, in the latter, one and the same initial target configuration was utilized in numerous runs. As a consequence, the total number of different target configurations was so small that concern arose as to whether the spectrum of isotopic compositions was representative. Therefore, the degree of preferential sputtering was evaluated not by comparison with the average target composition but with the actual composition. The validity of this correction was questioned (Sigmund, 1987a).

A straightforward response to the criticism would have been not to apply such a correction. After all, the situation encountered here accurately reflects the one that is met in an experiment: The number of i-atoms participating in any given collision cascade will, by necessity, be a fluctuating quantity, and in the absence of order, that number will be Poisson-distributed. Certainly, each ion meets its individual target configuration. Nevertheless, sputter yields will have to be recorded relative to the average composition. However, Shapiro et al. (1985) responded to the criticism by a modification of the algorithm so that the number of atoms of each species in a given target always reflected the nominal stoichiometry (Shapiro et al. 1988). This procedure is presumably justified in isotopic targets that exhibit long-range order but appears peculiar when applied to liquid targets (Lo et al., 1989). The associated numerical error is not known.

3.2.3 Estimates of Eckstein and Biersack

Monte Carlo simulations on isotopic mixtures of ^{10}B and ^{11}B were performed by Eckstein & Biersack (1985) in conjunction with a more comprehensive study of the sputtering of multicomponent targets. The physical picture underlying a Monte Carlo simulation resembles that of linear collision cascade theory. This is particularly true with regard to target setup and binary-collision dynamics. A distinct feature of the particular code used in these simulations is the assumption of a fixed free path as opposed to the common exponential distribution that follows from Poisson's law. This causes some peculiarities in the slowing-down of low-energy atoms (Sigmund et al., 1989) which give rise to results that differ from those of conventional Monte Carlo simulations but may in fortunate cases come closer to reality. The potential employed was the so-called KrC potential which leads to a low-energy cross section with $m \simeq 1/6$.

Most of the simulations performed in this work refer to genuine low-energy sputtering at an ion energy of 100 eV, where sputter phenomena are governed by single or double collisions (Winters & Sigmund, 1974). The significance of single-scattering events may even have been increased by carrying out most bombardments at an angle of incidence of 60^0. Typically, this results in preferential-sputtering phenomena that are governed by the 'mass mismatch' between ion and target (Taglauer & Heiland, 1978; Taglauer, 1982; Baretzky & Taglauer, 1985).

For heavy ions ($Z_0 = 10, 18, 36$, and 54) at an initial energy of 1 keV, preferential sputtering of the light isotope with a yield enhancement of 3.14 % was observed. This is in agreement with eq. (11) for $m = 1/6$. Much larger enhancements were found for He bombardment at E = 1 keV. Analytical estimates applying to this regime are not available.

3.2.4 Estimates of Urbassek and coworkers

Monte Carlo simulations of sputtering from an isotopic mixture of ^{92}Mo and ^{100}Mo were performed by Conrad & Urbassek (1991) with a code designed to accurately simulate the same physics on the basis of similar input as analytic transport theory. The validity of eq. (9) for the integrated particle flux in an infinite medium, integrated over all space and all directions of motion, was confirmed, and for the case of a semi-infinite medium only a minor correction was found. Simulations of an actual sputter event were carried out for bombardment with 5 keV Ar, stimulated by experimental results reported by Gnaser & Oechsner (1989, 1990).

The results of the simulation show an enrichment in the low-energy sputtered-particle flux of a magnitude very close to the one predicted by eq. (11). No substantial dependence on emission angle was found. A dramatically higher enrichment was observed in the upper parts of the energy spectrum. This enrichment exceeded what could be expected from the smooth dependence of the exponent m on ejection energy (Vicanek et al., 1989). The effect starts to be pronounced for atoms ejected at energies exceeding $\sim$ 100 eV. Such atoms do not contribute significantly to the sputter yield. Therefore, the overall enrichment of the sputter yield is only slightly larger than the value predicted by eq. (11).

In a subsequent paper (Urbassek & Conrad, 1992), these authors studied preferential sputtering for a wider class of cross sections where the exponent m in eq. (8) was allowed to be species-dependent, i.e., $m = m_{ij}$. This work extends the variety of solutions to the transport equations solved previously. However, new features emerge only for alloys of widely different masses. The impact of this work on isotopic mixtures is very minor.

A most important implication of this work is the confirmation of a significant dependence of the enrichment on the energy of ejected sputtered particles. Measurements on isotope sputtering do not necessarily record the total sputtered flux but may utilize an energy window (in addition to other windows such as ejection angle and charge state). In comparisons between theoretical predictions and experimental data, the adopted value of m needs to be the one applying to the energy window rather than the one representative for the overall energy spectrum of sputtered particles (Sigmund & Sckerl, 1993).

3.2.5 Summary

In an attempt to sum up a variety of theoretical predictions, it appears appropriate to follow the conventional scheme of classification into three regimes of sputtering by elastic collisions (Sigmund, 1981): the single-knockon regime, the linear-cascade regime, and the spike regime.

Several sets of experimental data sort under the heading of single-knockon regime (see below), while on the theoretical side, only Monte Carlo simulations have been performed (Eckstein & Biersack, 1985). Preferential sputtering may be caused by ion/target mass mismatch, i.e., light ions tend to cause preferential sputtering of the light component, and vice versa. At very low energies — of the order of $\sim$ 100 eV or less — surface processes of the type discussed by Winters &

Sigmund (1974) and invoked by Wehner (1977) may become important. In particular, preferential sputtering of the lighter component may be caused by direct knockon events where a light surface atom bounces off from a heavy atom in the second layer. The reverse process is impossible for kinematic reasons. Such events become exceedingly rare at keV energies (Winters & Sigmund, 1974). Moreover, recoil implantation is a very strong effect at low ion energy, in particular for heavy ions like Hg^+, and may introduce density gradients that could well account for the observed angular variations in the composition of the sputtered flux (Sigmund, 1987a).

In the linear-cascade regime, a very clear and consistent picture emerges from the work of all four groups mentioned above. For disordered media, the light species is sputtered preferentially, the deviation from stoichiometry depends insignificantly on composition and is almost independent of the angle of emission at the energies in question. It is well approximated by eq. (11), with the exponent m governed by the interaction potential. Some uncertainty prevails concerning the appropriate value of this exponent.

In arriving at this coherent picture, we have chosen to discard all claims made by Haff & Switkowski (1976), Haff (1977), Watson & Haff (1980), and Haff et al. (1981): There is a clear conflict between the first two references, and in the two latter studies, no preferentiality of the cross section was allowed for. Simulations on single crystals bombarded under channeling conditions (Shapiro et al., 1985, 1988) have also been disregarded. While such studies carry considerable intrinsic interest, the differences between the results and those for liquid targets under otherwise identical conditions (Lo et al., 1989) are very pronounced, both with regard to the magnitude of preferential sputtering and the sign of the angular variation. Although polycrystalline materials are not amorphous, there is usually a good correspondence between sputter parameters for the two groups of materials. Whether this is true for a given set of experimental data depends on the role of texture, i.e., the way how targets have been prepared.

In passing on, we recall that a minor preferential-sputtering effect is caused by the difference in surface binding energies, eq. (54).

Finally, for the spike regime, we recapitulate a result derived by Sigmund (1981)

$$\frac{Y_1}{Y_2} = \frac{N_1}{N_2}\sqrt{\frac{M_2}{M_1}}\exp\left(\frac{U_2 - U_1}{kT}\right), \tag{57}$$

where T denotes an effective spike temperature (Sigmund & Claussen, 1981), and

$$U_2 - U_1 = \frac{3}{2}\hbar(\omega_{D1} - \omega_{D2}) \tag{58}$$

in accordance with eq. (53). Eq. (57) can be said to reflect an effective m-value of

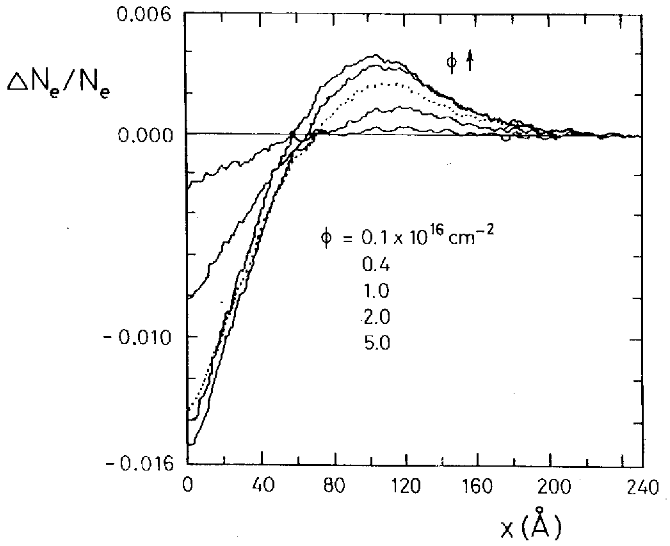

Figure 4. Calculated evolution of the concentration of a mixture of two Germanium isotopes under 5 keV argon bombardment. From Conrad & Urbassek (1992).

$m_{\text{eff}} = 0.25$ in eq. (15), but the dependence on surface binding energies is different when important.

3.3 Theoretical Estimates: Fluence Dependence and Stationary State

Theoretical results on the fluence dependence of preferential sputtering have become available recently (Jiménez-Rodríguez et al., 1992, Conrad & Urbassek, 1992). Numerical solution of eq. (29) in the limit of weak preferentiality yields predicted depth profiles of target stoichiometry *versus* ion fluence (fig. 4) as governed by collisional mixing and preferential sputtering on the basis of feasible input. In both studies it was found that the sputtered flux approaches stoichiometric composition only after an ion fluence of $\sim 10^{16}/\text{cm}^2$, i.e., after sputtering of many atomic layers. This is in accordance with experimental observations summarized below, and caused mainly by collisional mixing.

The two sets of profiles differ in the detailed behavior near the surface: The profiles calculated by Jiménez-Rodríguez et al. (1992) show a behavior that is reminiscent of segregation. This effect is caused by the flux of recoil atoms that are not energetic enough to overcome the surface barrier and hence get reflected. While the fate of such atoms needs to be considered, it appears questionable whether the description offered by Jiménez-Rodríguez et al. is adequate (Conrad & Urbassek, 1992).

Reliable profiles should provide pertinent input for theoretical predictions of angular emission patterns as well as energy spectra of sputtered species in the stationary state.

3.4 Experiments

Existing experimental data have been determined mainly by measurement of the composition of the sputtered flux, either by deposition on a collector and subsequent analysis or by means of secondary-ion (SIMS) or sputtered-neutral mass spectroscopy (SNMS). Measurements on the target have come up recently. While the energy resolution of conventional Auger spectroscopy may be insufficient for this, the potential of ion scattering spectroscopy has been pointed out (Ackermans et al., 1990a,b). Such data may be less affected by matrix effects of the type that SIMS or SNMS data suffer from.

Targets investigated include pure metals, with the natural composition or enriched with particular isotopes, or minerals. In the latter case, we recall that theoretical predictions for binary isotopic mixtures may readily be applied to polyatomic materials.

The presence of other components in the target than the isotopes under consideration will be disregarded in the following, in accordance with the conclusions of sect. 2.2.3.

3.4.1 Analysis of Collected Material

In one class of experiments, sputtered material is collected and subsequently analyzed by mass spectrometric techniques (Fluit et al., 1961; Wehner, 1977; Olson et al., 1979; Russell et al., 1980; Weathers et al., 1993). With the exception of the latest data (Weathers et al., 1993), these measurements required generously high bombardment fluences where the sputtered-particle current approached stoichiometry. Hence, reported deviations from stoichiometric sputtering, expressed in terms of yield ratios, must be suspected to underestimate the actual (low-fluence) effect. However, deviations from stoichiometric sputtering propagate into the angular distributions with increasing fluence, and those deviations survive into the stationary state. In the absence of segregation, this allows to extract a rough estimate of sputter preferentiality even from a high-fluence experiment.

Fluit et al. (1961) reported a 1.7 % enrichment of ^{6}Li over ^{7}Li in the sputter deposit after bombardment with 5 - 20 keV Ar$^+$ ions, corresponding to an m-value of 0.055 if this were a low-fluence result. Bombarding-ion fluences were not given explicitly, but it is evident that several monolayers must have been sputtered. For a light element like Li, a feasible value of m must be significantly greater than 0.11. Hence, these data do not contradict the theoretical prediction.

Wehner (1977) and Olson et al. (1979) observed very pronounced angular variations in the composition of the sputtered-particle current, up to 6 % for bombardment of Cu, Mo, W, and U with 60 - 100 eV Hg^+ ions. These variations may be caused by surface scattering events and/or recoil implantation as mentioned in sect. 3.2.5. Either explanation is consistent with the observation of much less pronounced variations (≤ 0.6 %) when the bombarding energy is raised to 300 eV. Quantitative theoretical estimates, either analytic or simulational, are missing.

Russell et al. (1980) found a 1.5 % angular variation of the isotopic ratio of ^{40}Ca over ^{44}Ca for high-energy (130 keV N^+ or 100 keV N_2^+) bombardment of Ca-containing minerals. Eq. (11) predicts an initial enrichment of 2.2 % for $m = 0.11$ or 3.3 % for $m = 1/6$. While the magnitude of the angular variation is not expected to be identical with the initial enrichment, there appears a sufficient margin to allow the conclusion that these data do not indicate more pronounced isotope effects than what can be accounted for theoretically. The same conclusion can be drawn from the fact that enrichments in the total deposit amount to up to 2 % for the lowest bombarding-ion fluences.

More recent data were reported by Weathers et al. (1993) for sputtering of Mo targets with 5 - 10 keV Ar^+ or Xe^+ ions. In the low-fluence limit, initial enrichments were large ($\sim 3 - 5\%$), corresponding to $m \sim 0.2 - 0.3$. Moreover, pronounced angular dependences were reported for part of the low-fluence data. Neither of these findings can be readily accounted for by existing theory. Since the sputtered material was analyzed by SIMS analysis of collectors, these measurements may be affected by preferential sputtering from the collector (Sigmund, 1993b). The significance of target texture has not been discussed in this context.

3.4.2 Analysis of the Secondary-Ion or Sputtered-Neutral Current

Measurements of the secondary-ion current show a pronounced isotope effect due to the dependence of the ionization probability of a sputtered particle on velocity rather than energy. Notwithstanding this, SIMS measurements may provide information on preferential sputtering if the current is measured as a function of fluence. At high fluence, the sputtered-particle current must be stoichiometric according to eq. (41). Hence, any nonstoichiometry in SIMS signals must be caused by different ionization probabilities. If the ionization probability does not change with fluence, any yield enhancement above the asymptotic value may be ascribed to preferential sputtering. While the behavior of the ionization probability was subjected to considerable scrutiny (Baumel et al., 1988), the point is central, and objections on purely experimental grounds are hard to reject totally.

Another point to be considered is the angular window in relative measurements. The fact that concentration gradients built up at high bombardment fluences introduce an enrichment in the heavy isotope of the sputtered-particle flux at oblique angles suggests that the relative variation in the enrichment factor *versus* fluence exceeds the average at oblique ejection and should be less than average at normal ejection (Weathers, 1993; Sigmund & Sckerl, 1993). Similar effects of the energy window may exist but have not been analyzed, and complete information on experimental geometry is rarely given in experimental papers because such artefacts may not have been expected.

Shimizu and Hart (1982) found a 0.6 % initial enrichment of ^{63}Cu over ^{65}Cu during bombardment with 13.2 keV O^- ions. While they did not ascribe this effect to preferential sputtering we note that an enrichment of 0.7 % would be predicted for $m = 0.11$.

Okano et al. (1985) reported an initial enrichment of the heavier species in measurements involving a series of metallic targets bombarded with 12 keV O_2^+ ions. While these effects were assigned tentatively to recoil implantation, the measurements clearly contradict all other existing experience. An independent attempt to reproduce these results has apparently not been reported.

Gnaser and Hutcheon (1988) observed enrichments for Li, Ti, Ga, and Mo isotopes under bombardment with 14.5 keV O^- ions which, when described in terms of eq. (11), require values of $m = 0.17$, $0.38 - 0.45$, 0.21, and 0.29, respectively. While the values for Li and Ga appear compatible with those characterizing feasible collision cross sections, those for Ti are outside the feasibility range. The value for Mo appears high but not excessive.

Measurements on B by Ar^+ and Ne^+ bombardment at 100 keV yielded enrichment of ^{10}B over ^{11}B by 4.6 to 5.2 % (Baumel et al., 1988), corresponding to an m-value of ~ 0.26 which is feasible for a light element.

Recent SNMS data, obtained by postionization of neutral atoms sputtered from Ge and Mo targets by 5 keV Ar^+ ions at low fluences (Gnaser & Oechsner, 1989, 1990), also showed large enrichments of the lighter isotopes (~ 5 %) corresponding to $m \sim 0.3 - 0.4$. These data are in good agreement with the collection data by Weathers et al. (1993) and in reasonable agreement with the SIMS measurements of Gnaser & Hutcheon (1988).

In a Monte Carlo simulation of preferential sputtering from a ^{70}Ge-^{76}Ge mixture, Conrad and Urbassek (1992) found that, by assuming a minor compositional gradient near the the surface, i.e., an 1.4 % increase in the ^{70}Ge concentration and a corresponding decrease in ^{76}Ge, the calculated magnitude and fluence dependence of the enrichment factor are in perfect agreement with these measurements.

Such a change in concentration, in order to be real, must be caused by equilibrium segregation. While direct evidence for the presence of segregation appears to be missing, Weathers et al. (1993) pointed out that the preferentiality in angular distributions of sputtered species, measured at low fluences, would have to have the opposite sign of what is found experimentally in Mo if segregation were the cause of discrepancy.

The above results indicate fair agreement with the linear-cascade prediction for Li, B, and Ga. The results for Mo and Ge can hardly be accounted for by this prediction alone, but a moderate spike component appears feasible for those heavy materials. According to eq. (57), evaporation from spikes predicts a more pronounced isotope effect. This could show up as a higher effective m-value. That assertion, however, does not apply to Ti which is too light to allow for a significant spike component (Sigmund, 1974; Cheng, 1990). It should be of interest to check the prevalence of this apparently most pronounced isotope effect by an independent measurement. In view of possible effects of target crystallinity, it appears to be crucial to check samples for texture in future experiments.

The present comparison between experimental findings and theoretical predictions is much more fargoing than what is currently possible in case of alloys. The reader is reminded, however, that the experimental yield ratios have not been measured directly but have been extracted from relative measurements, and thus are affected by secondary effects such as recoil implantation and alike (Sigmund, 1979; Sigmund & Sckerl, 1993).

4 Alloys

4.1 General Considerations

Eqs. (15) and (57) describe the preferential sputter behavior of a random alloy in the linear-cascade and spike regimes, respectively. In the former regime, the composition of the sputtered flux is insensitive to the bombarding-beam characteristics, i.e., the type, energy, and angle of incidence of the incoming ions. This prediction results from the assumption that cascades are fully developed and that the recoil velocity distribution within the cascades is well randomized. Measurements of 'true' preferential sputtering in alloys require quite low fluences and have been performed mainly by ions of fairly high energy (Andersen, 1984). The situation is different in the spike regime because the spike temperature depends on both beam and target parameters. Neither does eq. (15) apply to the energy range near the sputter threshold. Here the sputter preferentiality depends heavily on the type, energy, and angle of incidence of the bombarding ion (Taglauer & Heiland, 1978; Varga & Taglauer, 1981; Taglauer, 1982; Baretzky et al., 1987).

Molecular-dynamics simulations on the basis of realistic interatomic potentials provide another useful source of information on primary sputter properties. Preferential sputtering of Cu-Ni alloys was simulated by Lam & Johannessen (1992) on the basis of embedded-atom potentials given by Foiles (1985). Differential sputter parameters were calculated as functions of Ar^+ ion energy, alloy composition, and temperature. The sputtered flux was found to be slightly preferential in Cu, with a yield ratio ~1.2 depending weakly on ion energy and alloy composition. From the energy spectra of sputtered atoms, effective surface binding energies of the alloy components as well as an effective value of m were extracted. Simulations aiming at the same kind of information have been performed some time ago on the basis of Monte Carlo and binary-collision codes (Rosen & Bassel, 1984; Eckstein & Biersack, 1985; Eckstein & Möller, 1985). The relative merits of different types of simulation codes have been discussed in another contribution to this volume (Robinson, 1993).

In addition to preferential sputtering, several kinetic and thermodynamic processes, including collisional mixing, radiation-enhanced diffusion, Gibbsian segregation, and radiation-induced segregation can affect the near-surface composition of a material exposed to ion beams (Andersen, 1980, 1984; Betz & Wehner, 1983; Wiedersich, 1983, 1985; Lam & Wiedersich, 1981, 1987; Lam, 1990). These secondary processes have been investigated individually, experimentally and theoretically, at various levels of sophistication, often under conditions where sputtering was not an issue. Therefore, a reasonable understanding of several component processes including their dependences on irradiation and material variables has been achieved.

Conceptually, the phenomenon of bombardment-induced compositional changes is simplest when only athermal processes, i.e. preferential sputtering and collisional mixing, are operative. Then the thickness of the resulting altered layer is approximately equal to the ion range. However, very often at least one thermally-activated process is acting. In particular Gibbsian segregation, which can be accelerated by irradiation, is capable of causing substantial changes in the near-surface composition of an alloy during ion bombardment even in the absence of competing processes. Any component that segregates to the uppermost surface layer will be preferentially removed by sputtering, simply because more of it is located within the sputter depth. Thus, 'true' preferential sputtering may be hard to distinguish experimentally from Gibbsian segregation in the low-fluence limit. Radiation-enhanced diffusion may cause the altered layer to extend considerably beyond the penetration depth of the beam at elevated temperatures. Radiation-induced segregation, which is driven by gradients in the defect concentration, tends to drive the alloy system away from thermodynamic equilibrium and may cause significant redistribution. This process is quite effective in spreading changes in the alloy composition to large depths. It is the extension of the concentration gradient beyond the depth of origin of sputtered atoms that causes the long transients in the dependence of sputtered-flux composition on ion fluence.

We shall start by briefly characterizing pertinent individual processes. Firstly, sources and sinks will be specified, i.e., implant profiles and defect production as well as defect annihilation and entrapment. The discussion of collisional mixing will follow the conventional classification into cascade mixing and recoil implantation. Radiation-enhanced diffusion is a feeding mechanism with similar effects as cascade mixing except for the temperature dependence. Both tend to flatten concentration gradients. Gibbsian segregation acts only at the surface and thus interferes directly with preferential sputtering. Radiation-induced segregation is preferential, as is recoil implantation. The former gives rise to steep concentration gradients whereever there are persistent defect fluxes, e.g. near the bombarded surface. The latter leads to concentration changes of opposite sign at the near and far end of the damage depth. Consequently, both lead to a buildup of concentration gradients in the bulk. The relative importance of these processes depends on bombardment conditions and target parameters.

4.2 Diffusive Currents

Several of the processes to be discussed below may be characterized by diffusive currents. This section serves to compile a few relationships that are common to such processes.

Consider some transport process 'α' which contributes a term

$$Q_i^{(\alpha)} = \Lambda_i^{(\alpha)} N_i(x,t) \tag{59}$$

to the primary evolution of $N_i(x,t)$ according to eq. (42), with Λ_i to be specified by some expression of the type of eq. (43). Within the assumptions underlying the diffusion approximation (34), we may write $Q_i^{(\alpha)}$ in the form

$$Q_i^{(\alpha)} = \frac{\partial^2}{\partial x^2}\left(D_i^{(\alpha)} N_i\right) \tag{60}$$

with

$$D_i^{(\alpha)} = \frac{1}{2}\int_{-\infty}^{\infty} dx'(x'-x)^2 \Gamma_i^{(\alpha)}(x,x') \tag{61}$$

if the drift term vanishes. Allowance has been made here for depth-dependent diffusion coefficients. Such a dependence must be expected because of the finite penetration depth of the ion beam and many associated phenomena like primary defect production and collisional mixing.

The conventional diffusion picture, which was applied here, assumes small individual step size and requires bounds in the relocation integrals to be replaced by boundary conditions on the solution of the resulting differential equation.

Insertion of (60) into eq. (42) leads to

$$\left(\frac{\partial N_i(x,t)}{\partial t}\right)^{(\alpha)} = -\frac{\partial}{\partial x} J_i^{(\alpha)} \tag{62}$$

with

$$J_i^{(\alpha)} = -\frac{\partial}{\partial x}(D_i^{(\alpha)} N_i) + N_i \sum_j \left(\frac{\partial}{\partial x}(D_j^{(\alpha)} N_j) - \left[\frac{\partial}{\partial x}(D_j^{(\alpha)} N_j)\right]_{x=0}\right) . \tag{63}$$

Here the first term is a diffusion current of the common form (Manning, 1968). The second term represents a relaxation or Kirkendall current. Each current ($i = 0 \dots n+z$) obeys certain boundary conditions that are determined by the physical situation. For example, for a nonvolatile material, $J_i^{(\alpha)}$ has to vanish at the surface for $i = 1 \dots n$. This boundary condition implies that the second term in the brackets on the right-hand side of of eq. (63) drops out. By means of the packing condition, eq. (44), we may then write down eq. (63) in the more symmetric form

$$J_i^{(\alpha)} = \sum_j \Omega_j \left(-N_j \frac{\partial}{\partial x}\left(D_i^{(\alpha)} N_i\right) + N_i \frac{\partial}{\partial x}\left(D_j^{(\alpha)} N_j\right)\right) . \tag{64}$$

4.3 Sources and Sinks

For the purpose of theoretical modelling, either numerically or analytically, several pieces of input are needed which are more or less accessible. The present discussion is very brief and schematic.

Following the classification in eq. (42) we first need the penetration profile $f_0(x)$ of the ion beam. In principle, this is an intricate functional of the inhomogeneous composition profile in a polyatomic medium. The capability to follow this profile as a function of time is one of the strength points of the Monte Carlo technique (Roush et al., 1982; Möller & Eckstein, 1984). However, unless there are excessive compositional changes with increasing fluence throughout the penetration depth it will be justified to assume a constant penetration profile, evaluated for a homogeneous medium on the basis of standard range theory or tables with proper allowance for the multicomponent character of the medium. Caution is indicated with regard to the popular use of average atomic numbers and masses to approximate the target: The parameters governing energy loss and, in particular, angular scattering do not depend linearly on Z_2 and M_2. Therefore, straight interpolation between data for elemental targets is justified only in case of similar masses and atomic numbers. The shape of a penetration profile may often be approximated as a gaussian (Lindhard et al., 1963).

Similar considerations apply to the relocation operator L_i, in particular to the part covering deeply penetrating target atoms with high recoil energies. A recent study (Conrad & Urbassek, 1993) reports quantitative comparisons between mixing profiles evaluated on the basis of constant relocation cross sections (determined from the initial, homogeneous composition profile of the material) and cross sections that were continuously adjusted for compositional changes. Although the system (LuFe) exhibits pronouncedly nonstoichiometric behavior with regard to mixing and sputtering, calculated composition profiles were found to be insensitive to induced nonlinearities at all fluences.

Another piece of input is the rate of defect production $F_\nu(x)$ per unit depth. The spatial aspect of this quantity is closely related to the penetration profile (Winterbon et al., 1970). Most of the comments made on the latter apply correspondingly, with the exception that damage profiles are more pronouncedly nongaussian. The sharing of energy between the components of a polyatomic medium has been analyzed by the formalism describing preferential sputtering (Andersen & Sigmund, 1974). The most problematic part is the conversion between deposited energy and defect production. Conventional estimates may be based on the so-called modified Kinchin-Pease equation (Sigmund, 1969b,c), but major discrepancies are observed that depend on the material. This aspect will be touched upon in sect. 4.4.1. Providing feasible predictions in this area is one of the strengths of the molecular-dynamics technique.

Separate sections will be devoted to input on relocation cross sections and rates, i.e., operators L_i and Λ_i appearing in eq. (42).

Finally we need to specify sinks. Recombination between defects (e.g., vacancies and interstitials) is governed by the law of mass action,

$$\left(\frac{\partial N_\nu}{\partial t}\right)_{\text{loss}} = -\sum_{\mu=n+1}^{n+z} K_{\nu\mu} N_\nu N_\mu;\ \nu = n+1\ldots n+z \tag{65}$$

where $K_{\nu\mu}$ is a matrix of recombination rate constants with vanishing diagonal elements. Conversely, fixed sinks (dislocations, voids, etc.) lead to first-order annihilation kinetics of migrating defects, i.e., loss terms of the type of

$$\left(\frac{\partial N_\nu}{\partial t}\right)_{\text{loss}} = -K_\nu N_\nu N_s;\ \nu = n+1\ldots n+z \tag{66}$$

where K_ν is a rate constant and N_s the density of unsaturable sinks at depth x. The difference is important in the analysis of the time dependence of the approach to equilibrium.

The simple kinetic equations are valid if the mean separation between defects is larger than the mean distance between sinks. Interstitials and vacancies diffuse by random walk, the former significantly faster than the latter. Annihilation occurs instantaneously whenever the interstitial is sufficiently close to a vacancy, i.e., within the recombination volume.

The central recombination rate constant is defined by (Waite, 1957)

$$K_{\mathrm{IV}} = 4\pi r_{\mathrm{IV}}(D_{\mathrm{I}} + D_{\mathrm{V}}), \tag{67}$$

where r_{IV} is the recombination radius. Since the recombination volume is $\sim 10^2\Omega$ (Wollenberger, 1970), r_{IV} is of the order of two lattice constants. Defects that are eliminated by this reaction do not contribute to atomic diffusion. As a result, the rate of defect production used in the rate equations should correspond to the production of "free" defects that survive the recombination stage.

The loss term in eq. (66) implies that only one effective type of sink is present for each defect and that the sinks are inexhaustible and immobile. The annihilation rate constants are given by (Waite, 1957)

$$K_{\nu} = 4\pi r_{\nu} D_{\nu}, \tag{68}$$

where r_{ν} is the effective sink capture radius for a ν-type defect. The sink annihilation volume is generally $\sim 20\Omega$. Hence, r_{ν} is of the order of a lattice constant. For details, the reader is referred to Dienes & Vineyard (1957), Sharp (1969), and Lam et al. (1974).

The spatial and temporal dependence of the internal sink concentration during ion bombardment may also have to be considered. Steep gradients exist in both the defect and sink concentration distributions and the sink structure may evolve continously in the bombarded zone. To a first approximation, the spatial distribution of radiation-induced sinks may be assumed to be identical to that of the damage rate, and the peak density is allowed to build up linearly with time, reaching a saturation level depending on irradiation temperature (Lam & Leaf, 1986; Lam & Hoff, 1988).

For high concentrations, defects anneal by diffusion to extended sinks, in addition to mutual recombination and homogeneous sink annihilation, and hence the pertinent rate equations containing defect diffusion terms must be applied locally to each sink. Similarly, in the surface region, the diffusion of defects must also be taken into account explicitly. Then, the solution of these equations requires appropriate boundary conditions for the defect concentrations at the sink surface.

4.4 Collisional Mixing

4.4.1 Cascade Mixing

Moving atoms in a collision cascade do not only cause sputtering and defect production but also collisional mixing, i.e., compositional changes. The three effects are closely related but there are important quantitative differences which have been recognized only gradually. Collisional mixing can be roughly classified into recoil implantation and cascade mixing (Littmark & Hofer, 1980; Sigmund & Gras-Marti, 1981). The term 'recoil implantation' has been reserved for ion-impurity knockon events. This process is anisotropic and has a substantial preferential component because of potentially high recoil energies. Relocation by secondary and higher recoils is termed 'cascade mixing'. Although secondary recoils may have high energies and, therefore, may exhibit some anisotropy, the dominating events are low-energy recoils which are directed more or less isotropically. Theoretical aspects of collisional mixing have been reviewed by Littmark and Hofer (1984), and summaries of experimental studies on ion beam mixing are available (Matteson & Nicolet, 1983; Mayer & Lau, 1983; Averback, 1986; Cheng, 1990).

Cascade mixing has been studied as a contributing process in the generation of metastable material phases by ion bombardment (Mayer & Lau, 1983) and as a disturbing factor in sputter profiling (Andersen, 1979; Littmark & Hofer, 1980, 1984). In either case, experimental information can be drawn from measurements of the intermixing of adjacent layers of pure materials as a function of ion fluence or from the spreading of a thin marker layer in an otherwise homogeneous material. Accurate mixing rates may be determined experimentally by Rutherford backscattering analysis, provided that bombarding-beam energies are high enough to ensure penetration depths far in excess of the broadening of a marker layer. Information about mixing at lower energies needs to be drawn from sputter profiles. Because of the complexity of the phenomenon and the interference with surface and chemical effects (Fine et al., 1983; Marton et al., 1988,1989; Cheng et al., 1988; Wittmaack, 1991) that information is more indirect.

An estimate of the broadening of a marker layer may be found from eq. (19) which predicts the following mean square spreading per marker atom (Hofer & Littmark, 1979; Sigmund & Gras-Marti, 1980, 1981)

$$< \Delta x^2 >= \Delta\Phi \frac{1}{3} K_i \frac{F_D(x)}{N} \int \frac{d\epsilon}{\epsilon^2} \overline{R_i^2(\epsilon)} \qquad (69)$$

at depth x for a fluence increment $\Delta\Phi$. Here, $R_i(\epsilon)$ is the range of a recoil atom of energy ϵ. This estimate ignores relaxation.

The factor $1/\epsilon^2$ in eq. (69) demonstrates that cascade mixing is heavily dominated by low-energy events. It is also seen that cascade mixing is preferential.

While the preferentiality in the energy sharing, as expressed by K_i, is weak except for pronounced mass differences, the preferentiality implicit in R_i may be substantial. In view of the dominance of small relocation distances and the proportionality with fluence, eq. (69) is equivalent with a random walk characterized by a diffusion coefficient (Andersen, 1979; Matteson et al., 1981)

$$D_i = \frac{1}{6} < r_i^2 > \nu_i, \tag{70}$$

where $< r_i^2 >$ is the variance of the individual jump distance and ν_i an effective site-exchange frequency.

Measured mixing rates tend to be greater than those predicted from eq. (69), even for generous choices of the relocation distance $R_i(\epsilon)$ which is rather uncertain at low energies (Paine & Nicolet, 1983; Paine & Averback, 1985). This underestimate appears striking when compared with the observation in damage production, where a proper modification of eq. (19) was long ago found to overestimate the observed defect production. Several studies were devoted to tracing the origin of this discrepancy. Those cases where large discrepancies were observed — an order of magnitude or more — seem to be governed by replacement chains, as well as relocations in the cooling phase of a collision spike. While the former could be readily included in eq. (69) by suitable definition of the range (Andersen, 1979), the latter are clearly excluded. Roughly spoken, processes in the cooling phase of a collision spike cause annihilation of defects but increase disorder.

Illuminating observations on the behavior of collision cascades at low recoil energy were made in molecular-dynamics simulations on metallic targets under self-bombardment. At low primary energies (< 1 keV), most displacements were found to occur through sequences of near-neighbor atom replacements which create a vacancy at the origin of the chain and deposit an interstitial at the end. Long, linear replacement chains are rare, and frequently-observed sequences are short segments along different close-packed atomic rows; many of them close upon themselves with no net defect production. As a result, the number of atoms changing sites is significantly larger than that of Frenkel pairs created in a displacement event (Gibson et al., 1961, King & Benedek, 1983; Zhu et al., 1992; Gao & Bacon, 1993).

In more energetic cascades, extensive mixing occurs as a consequence of local structural disorder. Diaz de la Rubia et al. (1987) simulated a 5 keV displacement cascade and found that mixing takes place mostly in the region of the melt and during the cooling phase. Only a small fraction of the observed mixing effect took place in the collisional phase. Furthermore, structural disorder in the cascade center has an important effect on defect generation. The majority of defects are annihilated in the core of the cascade; only those interstitials that escape this region via replacement sequences survive mutual recombination. Consequently,

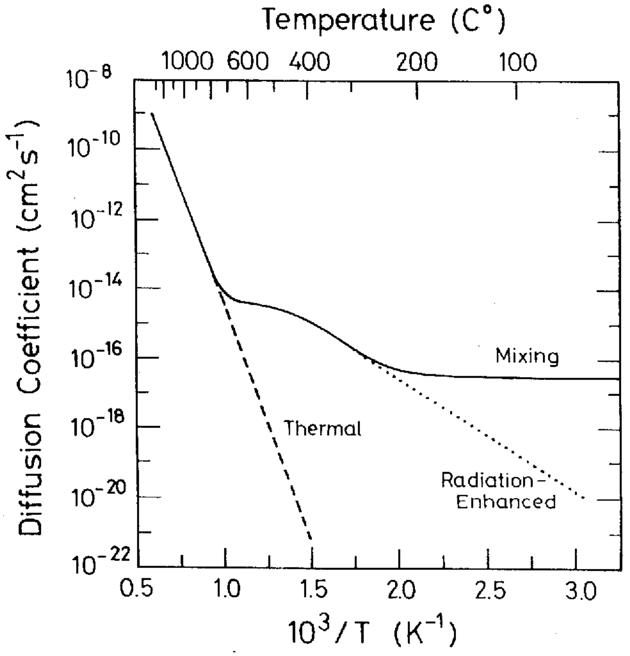

Figure 5. Temperature dependence of the steady-state diffusion coefficient calculated with physical parameters appropriate for Ni during bombardment at a typical displacement rate K $= 10^{-3}$ dpa/s. The contributions from displacement mixing, calculated from $D = \frac{1}{6}b^2\eta K$, radiation-enhanced diffusion, determined by eq. (76), assuming a moderate sink density, and thermal diffusion, are indicated.

the defect-production efficiency is quite low, typically ≤ 0.2 (Rehn & Okamoto, 1987) relative to the modified Kinchin-Pease estimate (Sigmund, 1969b,c).

In view of this state of affairs, parameters characterizing cascade mixing in the theory of compositional changes have been chosen semi-empirically, either on the basis of measured mixing rates in the low-temperature limit (Kim et al., 1985; Averback, 1986), simulation results for the effective number of replacements per displacement (King & Benedek, 1983; Zhu et al., 1992), or measured disordering rates in ordered alloys (Kirk & Blewitt, 1982; Zee et al., 1983). Alternatively, the effect of cascade mixing on sputter parameters has been studied by sampling different mixing rates over a range of feasible values (Sigmund & Oliva, 1993).

Specific estimates reported below have been performed on the basis of a diffusion coefficient of the form $D = b^2\eta K/6$ (Lam & Wiedersich, 1981, 1987), where b is the nearest-neighbor distance, K a defect production rate [number of displacements per

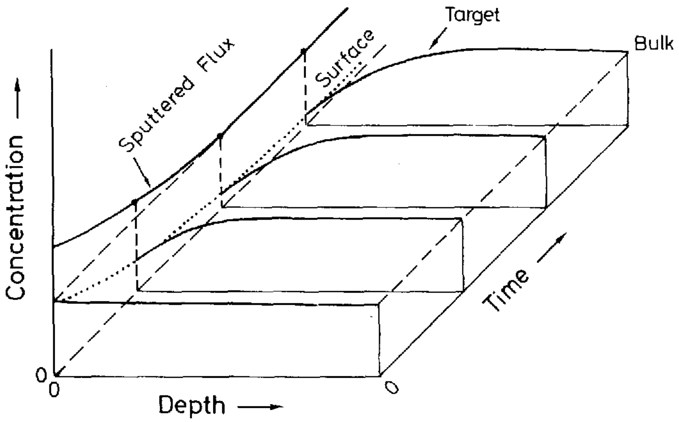

Figure 6. Schematic description of the effect of preferential sputtering on the development of the concentration profile and temporal evolution of the sputtered flux. The altered surface layer spreads into the target interior by displacement mixing and radiation-enhanced diffusion.

atom per time], and η an empirical parameter of the order of 10^2 - 10^3 representing the number of atomic replacements per displacement. By comparison with eq. (69), one notices that K must follow the depth dependence of F_D. In the presence of a significant spike component, a dependence like F_D^2 might be more appropriate (Cheng, 1990). All preferentiality has been excluded. Regardless of the specific model, cascade mixing is taken as temperature-independent.

Induced defect migration and recombination that take place during the cooling phase ($> 10^{-12}$ s) may be influenced by thermodynamic forces. Such 'quasi-thermal' diffusional processes within cascades may result in observed chemical effects in low-temperature ion-beam mixing. Thus, quantities like the heat of mixing and/or the chemical affinity can affect the intermixing rate (Cheng et al., 1984; d'Heurle et al., 1985; Averback et al., 1986; Peiner & Kopitzki, 1988; Cheng et al., 1992). Pertinent phenomenological theories have been proposed by Cheng et al. (1984), Kelly (1989a), Ma (1991), Kelly & Miotello (1991, 1992), and Koponen and Hautala (1992).

Cascade mixing is the dominant mechanism of atom transport during bombardment at low temperatures where vacancies are immobile, i.e., below $\sim 0.2\,T_m$ (T_m being the melting temperature). A typical estimate of D is given in fig. 5. This process can spread compositional changes induced in the uppermost atom layers to larger depths. Such spreading is confined to a region commensurate with the penetration depth of the ion beam.

The simultaneous effect of preferential sputtering and cascade mixing — which

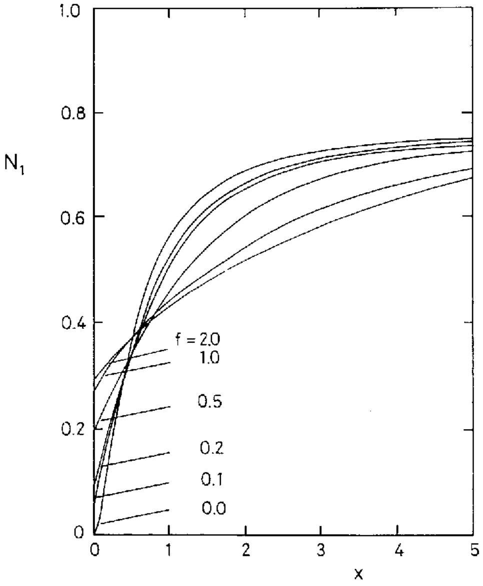

Figure 7. Calculated composition profile of a binary alloy under the action of preferential sputtering and preferential cascade mixing. The parameter f is a relative measure of the rate of cascade mixing at a fixed sputter rate. Schematic input. The length unit is the mean sputter depth. From Sigmund & Oliva (1993).

could also include the effect of radiation-enhanced diffusion to be discussed below — on the temporal evolution of the composition of the sputtered flux and the concentration profile in a binary alloy is illustrated schematically in fig. 6. The sputtered flux is initially enriched in 1-atoms. Gradually, the surface concentration decreases toward steady state, and the sputtered flux reflects the bulk composition. Under the action of displacement mixing and/or radiation-enhanced diffusion, compositional changes produced at the surface propagate into the bulk and form a relatively thick altered layer.

Fig. 7 shows steady-state profiles for different rates of atomic mixing. Here mixing is assumed preferential, in accordance with eq. (19). In this special case, the ratio of mixing rates is identical with the ratio of sputter cross sections. It is seen that the composition gradient is very steep in the absence of feeding by cascade mixing but flattens with increasing rate of mixing.

Andersen (1980, 1984) argued against cascade mixing as an effective feeding mechanism for preferential sputtering. His argument was based on the fact that both sputtering and cascade mixing are governed by eq. (19) and identical range-energy relations. In view of the very small depth of emergence of sputtered atoms, it was thought that this could not be consistent with an altered-layer depth of the order of an ion range or more, as found experimentally. This argument ignores the magnitude of the composition gradients involved. Even if the fact that eq. (19) underestimates the mixing rate while predicting correct sputter rates is ignored, fig. 4 demonstrates that characteristic fluences may come out right if only preferential sputtering and collisional mixing are taken into account.

4.4.2 Recoil Implantation

Unlike cascade mixing, recoil implantation is by and large a single-collision phenomenon. On a relative scale, the effect tends to be particularly important at low ion energies where cross sections get large. This is particularly true at energies close to the sputter threshold where significant disordering may take place within an ordered layer that erodes only very slowly (Sigmund, 1987a). This is also the regime where 'negative recoil implantation', i.e., sputter events induced by direct ion-atom interaction, becomes significant (Winters & Sigmund, 1974; Kelly, 1978).

Recoil implantation depends significantly on ion and target masses and is thus heavily preferential. Its role in the understanding of preferential sputtering has been recognized early (Kelly & Sanders, 1976a,b; Sigmund, 1979), although achieving a unified picture has shown up to be more complex a task than anticipated originally. Roughly, the cross section for generation of a primary recoiling target atom of some given energy increases with decreasing mass/atomic number of a hit target atom; the total pathlength travelled by a target recoil of a given energy increases with decreasing mass/atomic number of that atom; the maximum energy transfer from an ion to a target atom depends on the mass mismatch; finally, the penetration depth of a light target atom in a substrate containing heavy components is substantially smaller than its pathlength because of angular scattering. All this results in a fairly complicated situation, where different computer codes simulating nominally the same physical situation were able to produce predictions of recoil implant profiles that even differed in sign (Möller & Eckstein, 1984; Roush et al., 1982, 1983; Goktepe et al., 1986). The origin of these discrepancies has been traced to angular scattering (Sigmund, 1988), but even the most recent results indicate a surprising sensitivity of predictions on recoil implantation to details of the input regarding interatomic potentials, cutoff radii, binding energies, and alike (Konoplev & Gras-Marti, 1993; Conrad & Urbassek, 1993).

Recoil implantation tends to shift the centroid of a thin, planar marker layer in the beam direction or opposite to it, depending on the mass/atomic number of marker and matrix. Motion opposite to the beam is expected when matrix atoms are implanted more efficiently than marker atoms (Andersen, 1979; Sigmund &

Gras-Marti, 1981). Matrix relocation is an effect that cannot be accounted for unless a relaxation term is included in the basic rate equation, cf. the low-fluence solution eq. (47). So far, predicted absolute marker shifts have been found to be in better agreement with theory than the broadening predicted for cascade mixing. Broadening by recoil implantation is also predicted but affects mostly the deeply penetrating tails that may be observed at low implant fluences.

The fact that recoil implantation is both anisotropic and preferential implies a depletion of the preferentially-implanted species in the surface region which may be mistaken for being caused by sputter depletion (Sigmund, 1979). This feature is well established in the related field of monolayer desorption (Winters & Taglauer, 1987). A similar degree of understanding in alloy sputtering has been halted by lacking command over the sign of recoil implantation, but the qualitative significance of the effect at not too high ion energies is unquestioned.

4.5 Processes Assisted by Defect Migration

4.5.1 General Considerations

Eq. (64) represents diffusional currents in the absence of thermodynamic forces. In order to incorporate the latter, we need to go backward for a moment and characterize diffusion currents by gradients in a chemical potential rather than composition gradients. This is necessary to properly characterize Gibbsian segregation as well as preferential coupling of certain species to certain types of defects. This section serves to provide the necessary general background. Specific migrational processes wil be discussed subsequently.

Existing notation in the field (Lam & Wiedersich, 1981) is adapted to alloys where atomic rearrangement does not cause noticeable local density changes. Therefore, atomic volumes enter mainly to straighten up dimensions, and the conserved quantity is the number of lattice sites. Presently we aim at a unified description of collisional and migrational phenomena, and the alloys considered are not generally dilute. For both reasons we shall keep to the notation adopted above, i.e., try to fulfill the requirement of volume conservation also in the description of migrational phenomena. This implies that conservation of lattice sites is not an issue. We note, however, that all existing quantitative calculations ignore the effects of different atomic volumes of the species present.

A general starting point to describe diffusional motion in the presence of forces may be taken to be Darken's equations (Shewmon, 1963; Manning, 1968)

$$J_i = -\sum_j \mathcal{M}_{ij} X_j ;\ i,j = 0 \dots n+z, \tag{71}$$

where the $X_j = -\partial \mu_j / \partial x$ are thermodynamic forces and the μ_j are chemical potentials. The coefficients $\mathcal{M}_{ij}$ have to obey the Onsager relations

$$\mathcal{M}_{ij} = \mathcal{M}_{ji}, \tag{72}$$

and the total volume current must vanish in the absence of a change in coordinate system due to sputter erosion, i.e., $\sum_i \Omega_i J_i = 0$. For the latter to be satisfied independent of the specific chemical potential chosen, we must have

$$\sum_i \Omega_i \mathcal{M}_{ij} = 0. \tag{73}$$

This relation is fulfilled automatically if $\mathcal{M}_{ij}$ is written in the form

$$\mathcal{M}_{ij} = \mathcal{M}^*_{ij} - N_i \sum_k \Omega_k \mathcal{M}^*_{kj} \equiv \sum_k \Omega_k (N_k \mathcal{M}^*_{ij} - N_i \mathcal{M}^*_{kj}), \tag{74}$$

where the second term represents the Kirkendall current and the coefficients $\mathcal{M}^*_{ij}$ describe the 'direct' coupling between the different species. Eqs. (72,73) reduce the number of independent coefficients $\mathcal{M}_{ij}$ or $\mathcal{M}^*_{ij}$ from $(n+z+1)^2$ to $\frac{1}{2}(n+z)(n+z+1)$.

While it is conceivable to calculate *all* parameters $\mathcal{M}_{ij}$, whether independent or not, from first principles, it is more common to determine some of them by fitting experimental data. For that purpose, further reduction of the number of free parameters is desirable. A reasonable simplification is to neglect the coupling between different types of atomic species and the coupling between different types of defect, i.e.,

$$\mathcal{M}^*_{ij} = 0 \text{ for } i \neq j = 0 \ldots n \text{ and for } i \neq j = n+1 \ldots n+z. \tag{75}$$

With this, the number of free parameters reduces to $(n+1)z$. If vacancies are the only defect present, this implies that there is one independent diffusion coefficient for each atomic species. If there are two categories of defect (vacancies and interstitials), there are two independent diffusion coefficients per species, etc.

4.5.2 Radiation-Enhanced Diffusion

At sufficiently elevated temperatures, point defects become mobile. Free defects that escape homogeneous annihilation diffuse toward extended sinks such as grain boundaries and surfaces. Between ~ 0.2 and $\sim 0.6T_m$, their concentrations can exceed those present in thermodynamic equilibrium by many orders of magnitude. Therefore, diffusion is strongly enhanced by irradiation.

The simplest model for radiation-enhanced diffusion is a 3-species system consisting of one atomic species, vacancies, and interstitials. If the coupling between vacancies and interstitials is neglected, there are only two free parameters to describe the motion of all three species, and the diffusion coefficient for atoms will be determined by the parameters governing the motion of defects, i.e.,

$$D = \frac{1}{6} b^2 Z(\nu_\mathrm{I} c_\mathrm{I} + \nu_\mathrm{V} c_\mathrm{V}), \tag{76}$$

where $c_\nu = \Omega_\nu N_\nu$, ν_ν are jump frequencies, indices $\nu = \mathrm{V}, \mathrm{I}$ refer to vacancies and interstitials, respectively, and b is the nearest-neighbor distance. Moreover,

$$\nu_\nu = \nu_\nu^0 \exp\left(-H_\nu^m / kT\right), \ \nu = \mathrm{V}, \mathrm{I} \tag{77}$$

where ν_ν^0 is the attempt frequency and H_ν^m the defect migration enthalpy.

In early theoretical studies of radiation effects (Lomer, 1954; Dienes & Damask, 1958; Damask & Dienes, 1963; Sharp, 1969; Wiedersich, 1972), defect concentrations were calculated under the assumption that defect diffusion to extended sinks was negligible and, hence, that defect distributions were uniform throughout the irradiated solid. In subsequent work (Foreman, 1972; Rothman et al., 1973; Lam et al., 1974; Seeger, 1975), defect flow to a surface was included. Steady-state defect diffusion profiles in a semi-infinite solid can be estimated analytically (Lam et al., 1974; Seeger, 1975).

A typical temperature dependence of D for radiation-enhanced diffusion is included in fig. 5. In the absence of defect sinks or in the lower end of the pertinent temperature range, the concentrations of excess point defects are mainly limited by mutual recombination. Then the diffusion coefficient is proportional to the square root of the ion current J_0, and the slope of the Arrhenius plot corresponds to $H_\mathrm{V}^m/2$. Annihilation of defects at sinks gains importance at higher temperatures, and D becomes temperature independent and directly proportional to J_0. The characteristics of radiation-enhanced diffusion have been summarized by Adda et al. (1975), Lam & Rothman (1976), Sizmann (1978), and Rothman (1983).

Diffusion in a binary alloy is characterized by a minimum of four independent parameters. As a matter of convention, the preferential part of radiation-enhanced diffusion will be treated separately under the heading of radiation-induced segregation, and the parameters entering eq. (76) will be taken to be suitable averages.

At higher temperatures, above $\sim 0.6\,T_m$, the equilibrium concentration of thermal vacancies is larger than that of radiation-induced defects, and consequently, thermal diffusion is dominant. The contribution from interstitials to the diffusion coefficient according to eq. (76) can be ignored, and c_V becomes the equilibrium concentration of vacancies.

Eq. (76) only provides a simple account of radiation-enhanced self-diffusion within the 'Lomer' model. In real alloy systems, the diffusion kinetics can be influenced by many factors (Sizmann, 1978; Rothman, 1983; Wollenberger, 1987), including defect aggregation, defect-impurity binding, defect concentration gradients,

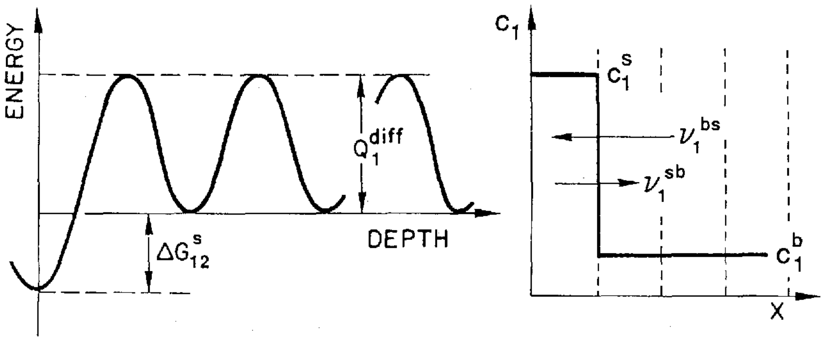

Figure 8. Schematic description of the energetics of Gibbsian segregation and its effect on near-surface concentration of 1-atoms. Pertinent jump frequencies are indicated.

and chemical effects like atomic ordering and clustering, heat of mixing, mutual solid solubility, and precipitation. The contribution of, e.g., mobile vacancy clusters to radiation-enhanced diffusion can destroy the symmetry between interstitial and vacancy, and affect the simple time and temperature dependence of D (Lam, 1975). The presence of an impurity atom changes the defect mobility in its proximity to an extent which depends on the strength of the defect-impurity interaction and the geometry of the lattice (Manning, 1968; Robrock, 1983). Strong defect-solute binding is also the physical origin of impurity segregation. A comprehensive treatment of atomic diffusion in defect gradients was given by Manning (1968, 1981). The defect concentration gradients provide additional driving forces for diffusion which must be included in eq. (71). In addition, the effects of limited mutual solubility or immiscibility should be accounted for in the analysis of the temperature dependence of intermixing and radiation-enhanced diffusion (Averback, 1986; Rehn & Lam, 1987; Marton et al. 1988). Atomic clustering and precipitation create compositional inhomogeneitites and interfaces which, if incoherent in nature, can serve as extended sinks for points defects.

The development of compositional profiles as a result of preferential sputtering and radiation-enhanced diffusion has been treated theoretically by Pickering (1976), Ho (1978), and Collins (1978). The qualitative behavior is very similar to what was shown for cascade mixing in fig. 6.

4.5.3 Gibbsian Segregation

Gibbsian segregation tends to modify concentrations of alloy components at surfaces and interfaces such as to minimize the surface free energy. As a rough rule, it is the weakly-bound species that segregate, and those also tend to sputter preferentially. Thus, the effects of sputtering and segregation most often go into opposite directions. It is important, therefore, to study the interplay of the two effects.

In a very simple layer model, the equilibrium configuration in the absence of bombardment can be characterized by atom fractions c_i^{b} in the bulk and c_i^{s} in the top surface layer so that (Wynblatt & Ku, 1979; Hofmann, 1990; du Plessis, 1990)

$$\frac{c_i^{\mathrm{s}}}{c_j^{\mathrm{s}}} = \frac{c_i^{\mathrm{b}}}{c_j^{\mathrm{b}}} \exp\left(-\frac{\Delta G_{ij}^{\mathrm{s}}}{kT}\right), \tag{78}$$

where $\Delta G_{ij}^{\mathrm{s}}$ is a segregation free energy (fig. 8).

For the purpose of studying compositional changes under ion bombardment, a model is needed that describes the kinetics of Gibbsian segregation. This is by itself a topic under active investigation (Hofmann, 1990; du Plessis, 1990). A few ad hoc models have been designed for use in sputtering studies, all of which may appear somewhat schematic.

Lam & Wiedersich (1981) used the following ansatz to characterize the net current of 1-atoms from the bulk to the surface in a binary alloy,

$$\frac{\Omega}{\zeta} J_1 = \nu_1^{\mathrm{bs}} c_1^{\mathrm{b}} c_2^{\mathrm{s}} - \nu_1^{\mathrm{sb}} c_1^{\mathrm{s}} c_2^{\mathrm{b}} , \tag{79}$$

where Ω and ζ are an effective atomic volume and atomic layer thickness, respectively, and ν_1^{bs} and ν_1^{sb} are the jump frequencies of 1-atoms from the bulk into the surface layer and vice versa (fig. 8). With this, equilibrium is achieved in accordance with eq. (78) if the jump frequencies are defined in accordance with the relation

$$\nu_1^{\mathrm{sb}} = \nu_1^{\mathrm{bs}} \exp\left(\frac{\Delta G_{12}^{\mathrm{s}}}{kT}\right) \tag{80}$$

for a binary system. Eq. (79) — which has been generalized to ternary alloys (Yacout et al., 1989) — hinges on a well-defined separation of the material into a surface layer and the bulk. This is consistent with a model of a solid composed of discrete atom layers, and it provokes the occurrence of the parameter ζ which would otherwise not be needed.

Products of atom fractions appear in eq. (79) since the probability for, e.g., a 1-atom from the bulk to replace a 2-atom in the surface layer depends on both the bulk concentration of 1-atoms and the surface concentration of 2-atoms.

The key parameter determining the segregation rate is the jump frequency ν_1^{bs}. It depends on the bulk concentrations and jump frequencies of defects. Therefore, Gibbsian segregation can be strongly enhanced by irradiation in the temperature regime where point defects are mobile.

At low irradiation temperatures where thermally-activated diffusion processes are insignificant, atomic motion occurring within displacement cascades may also contribute to Gibbsian segregation (Andersen et al., 1982, 1983; Li et al., 1982, 1983). This process, which will be called 'bombardment-enhanced Gibbsian segregation', may be taken into account by inclusion of a temperature-independent term representing the mixing-induced jump frequency (of the order of ηK) on the right-hand side of eq. (80).

Alternative schemes have been proposed. Swartzfager et al. (1981) and du Plessis et al. (1989a,b) used standard theory of diffusion in a force field where the diffusion current is given by

$$J_i = -\mathcal{M}_i N_i \frac{\partial \mu_i}{\partial x}, \tag{81}$$

with mobilities $\mathcal{M}_i$ and chemical potentials μ_i. Numerical calculations were carried out in layer models similar to the one used by Lam & Wiedersich (1981). Sigmund & Oliva (1993) applied an *ansatz*

$$(J_i)_{\text{unrelaxed}} = -\frac{\partial}{\partial x}\left[N_i D_i(x)\right], \tag{82}$$

with

$$D_i(x) = \tilde{D}_i \exp\left(\frac{V_i(x)}{kT}\right). \tag{83}$$

This provides both an ordinary diffusion term and a segregation term of the type of eq. (81), governed by some segregation potential $V_i(x)$.

The latter three models are not bound to a layer model of the solid and can be incorporated into a more comprehensive description by adoption of an appropriate segregation potential.

However, relaxation effects need to be accounted for. In eq. (79), atom jumps come in pairs. Therefore, within the assumption of a species-independent atomic volume, target stability will not be affected by segregation currents. Conversely, eq. (82) was employed in connection with eq. (29) which incorporates relaxation.

A distribution of jump distances, and consequently a more flexible segregation model, can be accounted for by adoption of a suitable transport kernel $\Gamma_i(x,x')$ in eqs. (42,43) such as

$$\Gamma_i(x,x') = \exp\left(\frac{V_i(x)}{kT}\right)\Gamma_i(|x'-x|) \tag{84}$$

which induces segregation solely via a position-dependent jump frequency. The same is true, mutatis mutandis, for eq. (80). In conjunction with the diffusion

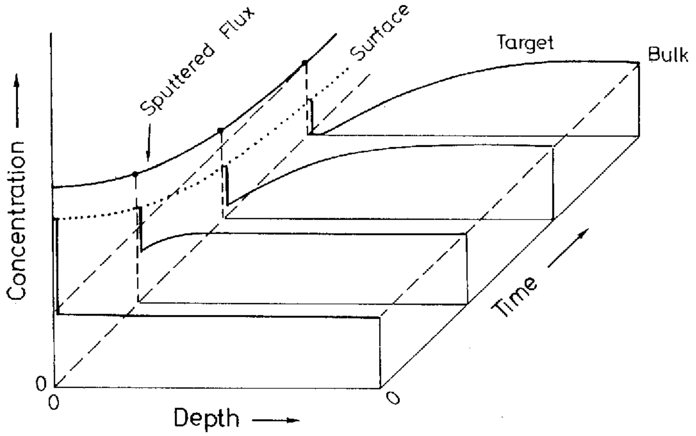

Figure 9. Schematic representation of the simultaneous effects of Gibbsian segregation and preferential sputtering on the development of the concentration profile and the time evolution of the composition of the sputtered flux.

approximation (60), eq. (84) leads to a segregation current of the form (82) with

$$\tilde{D}_i = \frac{1}{2}\int dx'(x'-x)^2\Gamma_i(|x'-x|). \tag{85}$$

This current needs to be corrected for relaxation by means of eq. (29). As a result, one finds

$$J_i = \sum_j \Omega_j N_i N_j \left(\frac{\partial D_j}{\partial x} - \frac{\partial D_i}{\partial x}\right) + \sum_j \Omega_j \left(N_i D_j \frac{\partial N_j}{\partial x} - N_j D_i \frac{\partial N_i}{\partial x}\right), \tag{86}$$

where

$$D_i = \tilde{D}_i \exp\left(\frac{V_i(x)}{kT}\right) \tag{87}$$

Here, the first term on the right-hand side is the segregation current which is a generalized form of eq. (79). The second term is governed by concentration gradients. It is nonvanishing even in the absence of a segregation potential, as follows already from the *ansatz* eq. (82). This term could be included in the ordinary diffusion current.

The interplay of Gibbsian segregation and preferential sputtering in affecting the concentration profiles in a binary alloy and the sputtered-atom flux is shown schematically, based on the two-layer description eq. (79), in fig. 9. Here it is assumed that 1-atoms are sputtered preferentially and that all sputtered atoms

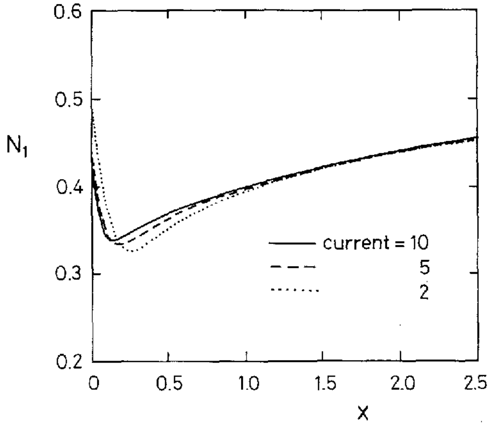

Figure 10. Stationary depth profile illustrating segregation due to preferential sputtering and Gibbsian segregation of component 1. Schematic input. The length unit is the average sputter depth. From Sigmund & Oliva (1993).

originate from the outermost atom layer. Furthermore, in the presence of Gibbsian segregation, the starting concentration of 1-atoms in the surface layer is larger than its bulk value, $c_1^{(1)} > c_1^{\mathrm{b}}$. This initial condition gives rise to initially-enhanced preferential sputtering of 1-atoms. With increasing fluence, the sputtered flux and the concentration profiles approach their steady-state values.

Fig. 10 shows stationary composition profiles under the influence of preferential sputtering and Gibbsian segregation, calculated in the continuum model based on eq. (82). This graph illustrates how the effect of segregation decreases with increasing ion current density.

Figs. 9 and 10 both demonstrate that the deviation of the surface composition from the equilibrium value, caused by preferential loss of 1-atoms, results in a reduction in the concentration of these atoms in subsurface layers as the alloy system attempts to approach equilibrium. At elevated temperatures, the steady-state subsurface depletion of the surface-segregating component can be quite severe. An example is given in fig. 11 for a Pd-20 at % Au alloy bombarded by 2 keV Ne^+ ions at several temperatures (Swartzfager et al., 1981). A gold spike is formed at the surface as a result of Gibbsian segregation, and the near-surface depleted layer extends deeper into the sample interior with increasing temperature.

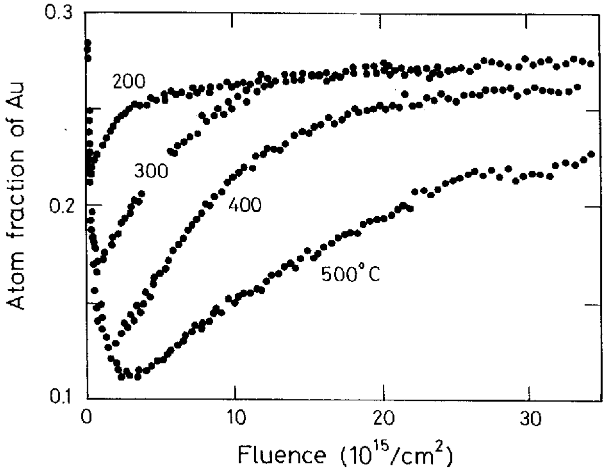

Figure 11. Depth profiles of altered layers produced in a Pd-20 at % Au alloy by sputtering with 2 keV Ne^+ at various temperatures. The bulk concentration of Au is seen to be larger than 20 at % because of preferential sputtering of Pd during the ion scattering analysis. From Swartzfager et al. (1981).

4.5.4 Radiation-induced Segregation

Among the processes that alter the stability of alloy phases during irradiation, radiation-induced segregation was found to have the most profound effect. In contrast to radiation-enhanced diffusion, which accelerates the approach to thermodynamic equilibrium, radiation-induced segregation tends to destabilize and to produce concentration gradients. This process results from two combined effects: persistent defect fluxes into or out of certain spatial regions and a preferential coupling between particular alloy components and these fluxes (Johnson & Lam, 1976; Wiedersich et al., 1979; Wiedersich & Lam, 1983; Martin et al., 1983).

Elimination of point defects at extended sinks such as grain boundaries and free surfaces is a common cause of persistent defect fluxes. Spatial nonuniformity in the defect production is another one that is particularly important in ion bombardment. Since the defect flow is always associated with fluxes of atoms, any preferential association of defects with a particular alloy component, and/or preferential participation of a component in defect diffusion will couple a net flux of the alloying element to the defect fluxes. If the defect fluxes persist in time, then this preferential defect-solute coupling leads to changing composition profiles within an initially uniform alloy phase. Theoretical descriptions of radiation-induced segregation in dilute alloys (Johnson & Lam, 1976, 1978), concentrated binary (Wiedersich et al, 1979; Wiedersich & Lam, 1983) and ternary (Lam et al., 1982) alloys are available as well as summaries of experimental observations (Okamoto & Rehn, 1979; Rehn, 1982; Rehn & Okamoto; 1983; Ardell & Janghorban, 1983). A generalized treatment of the phenomenon in multicomponent systems was proposed by Chen (1983).

A simple formalism for non-dilute alloys was developed by Wiedersich et al. (1979). Following eq. (71), total defect fluxes consist of partial fluxes that occur by exchange with different alloy components, and similarly the total atom fluxes can be partitioned into those taking place via vacancies and interstitials. In their notation,

$$\begin{aligned} J_{\mathrm{V}} &= \alpha N_{\mathrm{V}} \sum_{j=1}^{n} \mathcal{M}_{j\mathrm{V}} \frac{\partial N_j}{\partial x} - D_{\mathrm{V}} \frac{\partial N_{\mathrm{V}}}{\partial x} \,, && (88) \\ J_{\mathrm{I}} &= -\alpha N_{\mathrm{I}} \sum_{j=1}^{n} \mathcal{M}_{j\mathrm{I}} \frac{\partial N_j}{\partial x} - D_{\mathrm{I}} \frac{\partial N_{\mathrm{I}}}{\partial x} \,, && (89) \\ J_i &= -N_i \mathcal{M}_{i\mathrm{I}} \frac{\partial N_{\mathrm{I}}}{\partial x} + N_i \mathcal{M}_{i\mathrm{V}} \frac{\partial N_{\mathrm{V}}}{\partial x} - \alpha D_i \frac{\partial N_i}{\partial x}, \; i = 1 \ldots n, && (90) \end{aligned}$$

where α is a thermodynamic factor which differs from unity for a non-ideal alloy, and $\mathcal{M}_{i\mathrm{I}}$ and $\mathcal{M}_{i\mathrm{V}}$ are diffusive coupling coefficients introduced above, satisfying Onsager's relations (72). Defect fluxes are thus driven by gradients in atom and defect concentration, and atom fluxes are induced by the gradients in defect concentration and chemical potential. The sums on the right-hand side of eqs. (88) and (89) represent the Kirkendall currents from vacancy and interstitial diffusion in accordance with eq. (74). They have opposite signs because the vacancy flux generates a flux of atoms in the opposite direction.

Eqs. (88 - 90) allow predictions of trends in segregation in a quasi-steady state. Since attainable defect concentrations are lower than concentrations of component atoms by many orders of magnitude, diffusion coefficients of alloying elements are significantly smaller than those of defects. Hence, the defect profile reaches a quasi-steady state much more quickly during irradiation than the composition profile of the alloy components. Under this condition (i.e., $J_{\mathrm{V}} = J_{\mathrm{I}}$), the following expression can be derived for the total flux of 1-atoms in a binary alloy (Wiedersich & Lam, 1983)

$$J_1 = -D' \frac{\partial}{\partial x} N_1 - D^* \left(\frac{\mathcal{M}_{1\mathrm{I}}}{\mathcal{M}_{2\mathrm{I}}} - \frac{\mathcal{M}_{1\mathrm{V}}}{\mathcal{M}_{2\mathrm{V}}} \right) \frac{\partial}{\partial x} N_{\mathrm{I}} \,, \tag{91}$$

with

$$D' = \frac{\mathcal{M}_{1\mathrm{V}} N_1 D_2 + \mathcal{M}_{2\mathrm{V}} N_2 D_1}{\mathcal{M}_{1\mathrm{V}} N_1 + \mathcal{M}_{2\mathrm{V}} N_2} \tag{92}$$

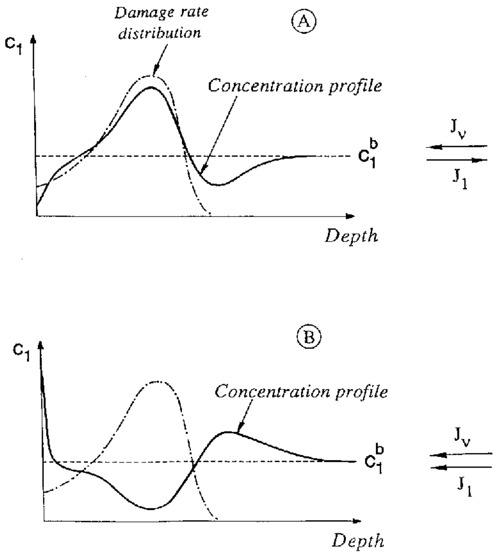

Figure 12. Schematic description of the solute concentration profile resulting from radiation-induced segregation via vacancy (A) and interstitialcy (B) mechanisms during ion bombardment.

$$D^* = \frac{\mathcal{M}_{2V}\mathcal{M}_{2I}N_1D_2}{\mathcal{M}_{1V}N_1+\mathcal{M}_{2V}N_2} . \tag{93}$$

At low fluence, $\partial N_1/\partial x$ in an initially homogeneous alloy is small; therefore, the direction and magnitude of J_1 are controlled by the last terms in eq. (91). If $\mathcal{M}_{1I}/\mathcal{M}_{2I} > \mathcal{M}_{1V}/\mathcal{M}_{2V}$ or $\nu_{1I}/\nu_{2I} > \nu_{1V}/\nu_{2V}$, the flux of 1-atoms will be in the same direction as the defect fluxes, and the 1-component will be enriched in any region where there exists an influx of defects. Conversely, if $\nu_{1I}/\nu_{2I} < \nu_{1V}/\nu_{2V}$, the net 1-atom flux will go opposite to the defect fluxes, and the 1-component will be depleted at defect sinks. The current J_1 has its maximum when 1-atoms migrate exclusively via an interstitial mechanism and 2-atoms via vacancies.

The shapes of the solute concentration profiles that develop during ion bombardment at elevated temperature are more complex because of additional effects of defect flows from the peak-damage region (Lam et al., 1978a; Marwick et al., 1979). This is shown schematically in fig. 12. For segregation via vacancy diffusion, solute enrichment in the peak-damage region is observed at the expense of solute depletion on both sides of the peak, in addition to strong solute depletion near the bombarded surface. The opposite effect will be measured for segregation via interstitialcy diffusion. Furthermore, if vacancies interact strongly with a particular alloy component, forming tightly-bound but mobile atom-vacancy complexes, atom

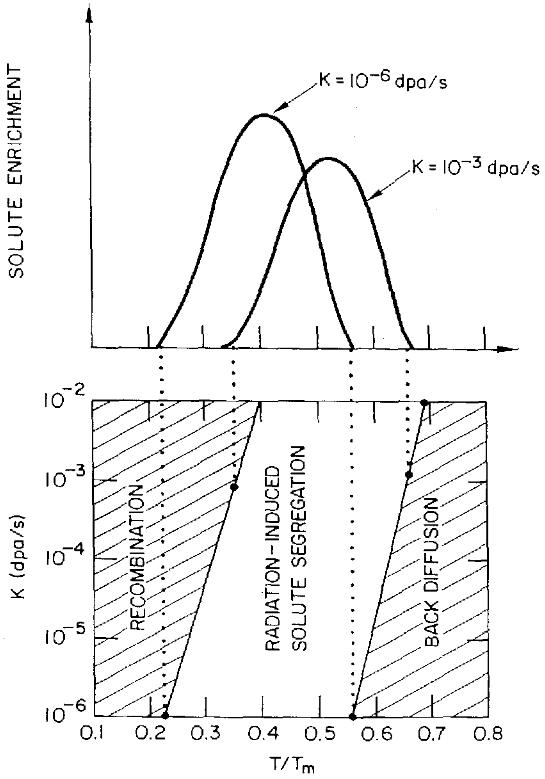

Figure 13. Schematic representation of the damage-rate and temperature dependence of radiation-induced segregation.

and defect fluxes will go in the same direction (Lam et al., 1978b; Gupta & Lam, 1979). As enrichment or depletion of the 1-component occurs, a concentration gradient will be set up which will oppose further influx of 1-atoms. Eventually, a steady-state composition profile will be reached.

At a given displacement rate, radiation-induced segregation is significant only at intermediate temperatures where sink annihilation dominates. This is shown schematically in fig. 13. At lower temperatures, high concentration and low mobility of point defects favor mutual recombination, suppressing long-range migration. Segregation is then unimportant. At high temperatures, on the other hand, concentrations and mobilities of thermal vacancies are high and effective solute back-diffusion prevents the buildup of concentration gradients. Therefore, radiation-induced segregation is small again.

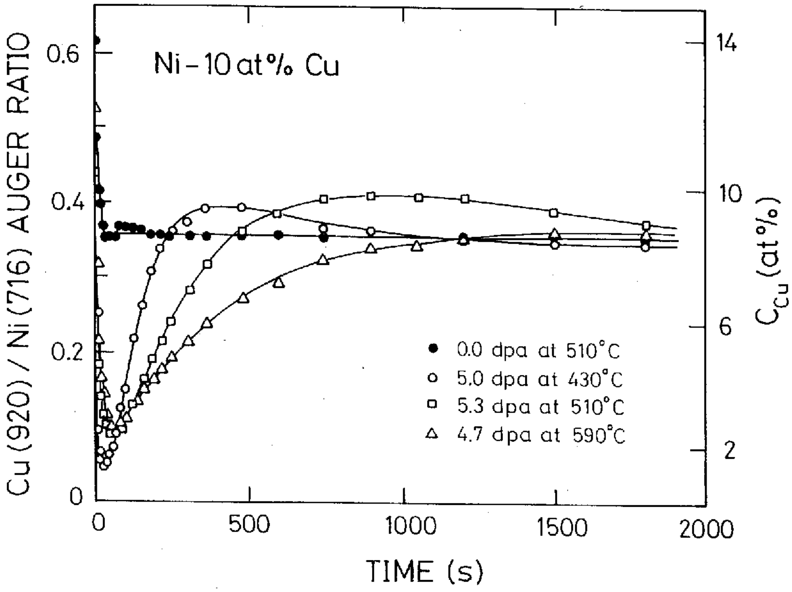

Figure 14. Depth profiles of the Cu concentration in a Ni-10 at % Cu alloy bombarded with 3 MeV Ni^+ ions to a dose of ~5 dpa at various temperatures, along with the depth profile of an unirradiated control specimen. Since Auger electrons of the transitions used for the analysis have a mean escape depth of ~1.5 nm, the compositions indicated on the right-hand ordinate represent an average over several atom layers. Consequently, a steady-state Auger ratio representing ~8.5 at % Cu was obtained for the bulk concentration in a Ni-10 at % Cu alloy. From Wagner et al. (1983).

Radiation-induced segregation and Gibbsian segregation may or may not occur in the same direction, depending on the alloy. In Ni-Si alloys, Si enrichment at the surface can result from either Gibbsian segregation (Lam & Hoff, 1988) or radiation-induced segregation (Lam et al., 1978a; Piller & Marwick, 1978; Wagner et al., 1982; Rehn, 1982; Rehn & Okamoto, 1983), whereas in Ni-Cu alloys, Gibbsian segregation gives rise to Cu enrichment at the surface (Brongersma et al., 1978; Ng et al., 1979, Lam et al., 1985b; Rehn et al., 1986), but radiation-induced segregation causes surface and subsurface Cu depletion (Wagner et al., 1983). Measurements of Cu profiles in a Ni-10 at % Cu alloy are shown in fig. 14. Upon heating of the alloy to an elevated temperature prior to irradiation, a thin Cu-rich layer was produced at the surface. Conversely, bombardment of the alloy by 3 MeV Ni^+ ions at the same temperature resulted in a severe Cu depletion. In general, the thickness of the layer affected by radiation-induced segregation is considerably (possibly orders of magnitude) larger than the layer affected by Gibbsian segregation. Moreover, radiation-induced segregation can be more effective than radiation-enhanced diffusion in altering the alloy composition at large depths during sputtering (Rehn et al., 1985).

4.6 Sputter Depth

Pronounced changes of the alloy composition in the near-surface region can affect the differential properties of alloy sputtering. Hence we need to have an idea about the depth of origin of sputtered atoms, or sputter depth, which received considerable attention some time ago. The quantity is of special interest in connection with the depth resolution of sputter-based surface-sensitive analytical techniques.

The sputter depth x_i of an i-atom needs to be distinguished from the saturation depth which is a minimum target thickness for which the sputter yield attains its infinite-thickness value, i.e., the depth in which those collision events take place which eventually may lead to sputtering (Sigmund 1969a). While x_i should depend mainly on target parameters, the saturation depth depends also on bombarding conditions and is in general a sizable fraction of the penetration depth of the beam. Failure to recognize this difference resulted in excessively large estimates of x_i given in the older literature (Onderdelinden, 1968).

Most theoretical estimates of x_i refer to elemental targets while experiments aiming at x_i were all performed on multicomponent systems.

The fact that the energy spectrum of sputtered atoms exhibits a maximum at energies of a few eV ($\sim 0.5U_i$) implies that most sputtered atoms originate from a rather shallow depth. Conversely, there is no doubt that some fraction of the emitted atoms making up the high-energy tail must come from great depths. Fig. 3 indicates an approximately exponential decay of the sputter cross section with increasing depth. Hence, for a homogeneous target, x_i is close to the decay length characterizing the sputter cross section, cf. eq. (5). This suggests that

$$x_i \simeq U_i^{2m}/A_i \sim (1-m)\frac{U_i^{2m}}{\sum_j N_j C_{ij}\gamma_{ij}^{1-m}}, \tag{94}$$

which implies x_i to be preferential. For elemental copper, the magnitude of the sputter depth was given as 4.8 Å (Sigmund, 1969a) for $m = 0$. The exponential decay of the sputter cross section was found later (Falcone & Sigmund, 1981).

While the above value of the sputter depth was smaller than any available estimate in the literature at the time it was published, subsequent work showed that it was about a factor of two too large. Information was drawn from binary collision (Robinson, 1983; Rosen et al., 1983; Rosen & Bassel, 1984) and molecular-dynamics (Harrison, 1983; Shapiro et al., 1985) simulations which all indicated that a very large fraction of sputtered atoms originate in the topmost two monolayers. The main reason for this difference was found much later to lie in an underestimate of the Born-Mayer scattering cross section at low energies (Vicanek et al., 1989).

Kelly & Oliva (1986a) extracted a value of the mean sputter depth of 0.8 ± 0.1 atom layers by inspection of published experimental and simulation data on a variety of materials. In response to this astonishingly small error margin, major differences were pointed out between the predictions of various simulation codes regarding the sputter depth, some of which predicted values that considerably exceeded the analytic estimate (Sigmund, 1987b). A round-robin computer simulation of a specific ejection probability was undertaken for the purpose of a direct comparison between the predictions of different codes (Sigmund et al., 1989). Six molecular-dynamics codes, four binary-collision lattice simulation codes, and eight Monte Carlo codes were applied to simulate the ejection of a low-energy Cu recoil ($5 \leq E \leq 50$ eV) from a certain depth interval ($0 \leq x \leq 5$ nm) within a Cu target. After elimination of obvious errors in some of the codes, substantial differences remained which were due first of all to different assumptions on surface binding and the statistics of free-flight paths, and secondly to sources of discrepancy like different assumptions concerning interaction potentials, cutoff radii, and electronic stopping. All molecular-dynamics and binary-collision simulations indicated that, for an intact crystalline Cu target, atoms with an initial energy up to 50 eV are sputtered largely from the outermost two layers. Monte Carlo simulations showed deeper tails.

Measurements were performed on a number of alloys. Dumke et al. (1983) reported 85 % and 70 % of the sputtered species as originating from the first atom layer during 15 keV and 25 keV Ar^+ bombardment, respectively, of a liquid Ga-In eutectic alloy. This sensitivity of the sputter fraction to the ion energy was unexpected. Repeating this experiment over a wider energy range (25 - 250 keV), Hubbard et al. (1989a,b) found ~87 % of the sputtered-atom flux to originate in the first layer, independent of the projectile energy within the range indicated. At 3 keV, the fraction was observed to increase to 94 %. This is expected to occur at low penetration depths of the ion beam (Harrison, 1983; Robinson, 1983; Biersack, 1987; Yamamura & Muraoka, 1989; Lam & Johannessen, 1992).

Less direct evidence was drawn from the temperature dependence of the surface composition of alloys in the steady state. ~65 % of the sputtered atoms were reported to originate from the outermost layer in 3 keV Ne^+ bombarded Ni-Cu (Lam et al. 1985b), ~50-65 % in Ni-Au (Lam et al. 1985a), ~55 % in Ni-Ge (Hoff and Lam 1988), ~70 % in Ni-Pd (Tang and Lam 1989), and ~95-100 % in Ni-Si alloys (Lam and Hoff 1988).

Measurements of Burnett et al. (1988) indicated that ~66 % of the sputtered-atom flux stems from the first layer in the Cu-Ru system. In addition, experimental observations of sputtering from overlayered targets, including C/Ni (Morita et al., 1983, 1984), Li/Cu (Krauss et al., 1984a), and O/Ti (Pellin et al., 1985), all suggested that the majority of sputtered atoms originated from the outermost atomic layer.

No information has been deduced from existing experimental data on the preferentiality of the sputter depth.

4.7 Angular Distributions of Sputtered Atoms

Compositional gradients within the depth of origin of sputtered atoms affect the angular distributions of the individual sputtered species (Sigmund et al., 1982). As a rough rule, the emission pattern narrows for those species for which a relatively large fraction of sputtered particles originates from greater depth. This implies that in a binary alloy, the species that is enriched at the surface will have a flatter angular distribution than the depleted one. The situation is more complex when composition profiles are governed by both sputtering and segregation, acting on similar length scales.

An angular variation of the composition of the sputtered flux was first observed by Olson et al. (1977, 1979). They found that sputtering of Ag-Au, Cu-Ni, and Fe-Ni alloy targets by Hg^+ or Ar^+ ions at energies below 300 eV caused the lighter elements to be preferentially ejected in the direction normal to the surface. These authors suggested that sputtering of surface atoms bouncing back from subsurface atoms played a role in this phenomenon. It is well established that such events are significant in monolayer desorption studies at low beam energies (Winters & Sigmund, 1974). With increasing ion energy, the observed enrichment decreased rapidly. At 1 keV, preferential ejection of Au from Ag-Au and Ni from both Cu-Ni and Fe-Ni alloys along the surface normal was observed. The observed behavior of the angular distribution is readily understood on the basis of steep compositional gradients at the surface. In fact, Ag, Cu and Fe are known to be enriched at the surface of these respective alloys by Gibbsian segregation (Mazurowski & Dowben, 1990).

Similar effects were reported for Cu-Pt alloys under Ar^+ bombardment by Andersen et al. (1982). At ion energies above 20 keV, they found preferential ejection of Pt in the forward direction, and they interpreted this in terms of surface-directed segregation of Cu. The effect was independent of temperature over the range from -196 to 300 C. Above 300 C, the composition of the sputtered flux was significantly enriched in Cu and independent of emission angle. These measurements were performed before a steady state had been attained. The time to reach steady state is longer at high temperatures (Andersen et al., 1984a). In other experiments carried out on AgAu, Cu_3Au, Ni_5Pd, and NiPt, the weaker-bound component was found to segregate to the surface even at 77 K (Andersen et al., 1983).

The effect of segregation on angular distributions of atoms sputtered from Cu-Ni, Co-Ni and Fe-Ni alloys under 3-keV Ar^+ bombardment at room temperature and 300 C was investigated by Ichimura et al. (1984). Preferential ejection of Ni in near-normal directions was observed during sputtering of Cu-Ni alloys at both temperatures. In Co-Ni alloys, Co atoms were ejected preferentially in the forward direction only at 300 C. For Fe-Ni, no difference in the angular distributions of the two components was discerned. The latter result differs from the behavior at lower energies observed by Olson et al. (1979).

Kang et al. (1983) measured angular distributions of Au and Cu sputtered from a Au-Cu alloy under 3 keV Ar^+ bombardment at room temperature. They found practically no difference in these distributions, although their ISS measurements (Kang et al., 1982) revealed that ion bombardment caused a strong Au enrichment in the outermost atom layer and depletion in the subsurface region. Gold segregates at the surface of Au-Cu alloys (Wynblatt & Ku, 1979; Li, 1988). An attempt to check the reproducibility of this result has not been reported.

Dumke et al. (1983) and Hubbard et al. (1989a,b) measured the angular distribution of sputtered atoms from a liquid Ga-In eutectic alloy. In this system, Gibbsian segregation gives rise to an outermost atom layer that is virtually pure In. Their data for Ar^+ sputtering showed that In atoms sputtered from the first surface layer had a nearly-normal $\cos^\chi \theta$ distribution with $\chi = 1.8 \pm 0.1$ independent of ion energy. The angular distribution of Ga atoms was significantly sharper with $\chi = 3.2 \pm 0.2$ at energies ranging from 15 to 250 keV and $\chi = 4.9 \pm 0.3$ at 3 keV. The increase in the value of χ at this low energy was accompanied by an increase in the contribution of the uppermost atomic layer to the sputtered-atom flux as a result of a decrease in the energy of higher-order recoil atoms (Hubbard et al. 1989a).

Angular distributions of atoms sputtered from Co-Au, Cu-Be, Cu-Zn, and W-Si alloys during Ar^+ bombardment at 0.25 and 2 keV were investigated by Wucher & Reuter (1988). For low bombarding energy, the two distributions differed significantly; this difference, which was most pronounced for Cu-Be, seemed to scale with the atomic mass in the way that the lighter particles were sputtered preferentially along the surface normal. For 2 keV, however, all angular distributions looked alike, following essentially a $\cos^3 \theta$ law. Forward-peaked distributions were observed for Co atoms sputtered from Co-Au alloys, Cu from Cu-Zn, Be from Cu-Be, and W from W-Si. No information on the properties of Gibbsian segregation in these alloys has been reported in the literature. However, the light, undersized solute Be is known to segregate to the surface of Cu-Be alloys during irradiation (Rehn & Okamoto, 1983). In this case the observed preferential ejection of Be along the surface normal appears to be inconsistent with the general prediction. It should be of interest to repeat the measurement on Cu-Be alloys in an independent experiment.

In summary, the angular distributions of species sputtered from an alloy can provide useful information about compositional gradients within the first few surface layers. In fact, this information was used to demonstrate the presence of a segregated layer (Andersen et al., 1982, 1983, 1984a) as well as to identify the surface-segregating element in an alloy (Andersen et al. 1984b, Sarholt-Kristensen et al., 1992).

4.8 Theoretical Estimates

While the system of nonlinear rate equations, eq. (45), accomodates all effects that are thought to govern partial sputter rates and composition profiles versus time, temperature, and ion current density, no comprehensive solution, analytic or numerical, is available at this time for any system. One good reason for this is the fact that the equation in the present form was only found during the writing of this review. Quite apart from this, a considerable amount of reliable input is needed. Moreover, finding reliable and accurate solutions for a given input may not be a trivial matter. The present subsection serves to present a brief survey of calculations that have been performed on systems that have been simplified in one way or another and to study the interplay and synergistics of some of the important effects. The following section, dealing with measurements, will serve a very similar purpose.

Early models by Pickering (1976), Haff (1977), Ho (1978), Collins (1978), Webb et al. (1978), and Chou & Shafer (1980) considered the effects of preferential sputtering and radiation-enhanced diffusion. The analytical model of Ho (1978), in particular, has been frequently applied to analyze depth profiles in bombarded alloys. All these models operate with linear differential equations since matter transport is characterized by diffusion coefficients and sputtering by boundary conditions at the target surface. In the work of Lam et al. (1980), the interplay of preferential sputtering and radiation-induced segregation was investigated. The interplay between preferential sputtering from a nonvanishing sputter depth and collisional mixing was studied on the basis of eq. (29) (Sigmund et al., 1982, and references given below). Measurements of sputtering at elevated temperatures by Rehn et al. (1979) indicated the need to include Gibbsian segregation as an effective mechanism for feeding atoms of certain alloy components into the surface layer. Theoretical models of Swartzfager et al. (1981), Itoh & Morita (1984), Kelly (1985), Kelly & Oliva (1986b), and Koshikawa & Goto (1987) included the simultaneous effects of preferential sputtering, radiation-enhanced diffusion and Gibbsian segregation on concentration profiles. The model of Lam & Wiedersich (1981, 1982a,b, 1987) included also radiation-induced segregation and cascade mixing. Although this model is the most comprehensive one evaluated up till now, it treats collisional mixing by means of a stoichiometric diffusion current and ignores long-range events. Sputtering is modelled by a two-layer model.

The simplest nontrivial case is that of preferential sputtering in the presence of a nonpreferential diffusive current and a vanishing sputter depth. Here, eqs. (29,31,34) lead to

$$\frac{\partial N_i}{\partial \Phi} = w\frac{\partial N_i}{\partial x} + \bar{D}\frac{\partial^2 N_i}{\partial x^2} \tag{95}$$

as well as the boundary condition

$$wN_i + \bar{D}\frac{\partial N_i}{\partial x} = Y_i \text{ at } x = 0 \tag{96}$$

and the initial condition $N_i = \mathcal{N}_i$ for $\Phi = 0$. These are the equations underlying the treatment of Ho (1978).

It is seen from eq. (96) that sputtering is necessarily stoichiometric for $\bar{D} = 0$, i.e., if there is no feeding mechanism to compensate for a preferentially sputtered species.

For a nonvanishing diffusion coefficient $\bar{D}$, a closed-form solution can be found in principle but is fairly complex because both Y_i and w depend on fluence via $N_i(0)$. However, in the high-fluence limit, one obtains the appealing result

$$N_i(x) = \mathcal{N}_i + [N_i(0) - \mathcal{N}_i]e^{-x/\beta}, \tag{97}$$

where β is the effective altered-layer thickness, $\beta = \bar{D}/w$, and $N_i(0) = \gamma_i Y_i$ with some species-dependent factor γ_i.

The case of a nonvanishing sputter depth in the absence of transport has been treated recently (Sigmund & Oliva, 1993). Very steep concentration gradients were found to develop near the surface, and the concentrations of all components except the one with the lowest value of $\sigma_i(0)$ (where $\sigma_i(x)$ is the sputter cross section) approached 0 at the surface.

Numerical evaluations of fluence-dependent composition profiles under the influence of sputtering and collisional mixing have been performed by Sigmund et al. (1982), Falcone & Oliva (1984), Oliva et al. (1986), Peinador et al. (1990, 1991), Jiménez-Rodríguez et al. (1992), and Urbassek & Conrad (1992, 1993). The three early papers were based on schematic input. The most important conclusion that emerges from the other three papers — which address overlayer desorption, isotopic mixtures, and an alloy with widely different masses, respectively — is the fact that the approach to equilibrium appears over a range of fluence that is comparable with that observed experimentally.

Figure 10 illustrates the synergistics of preferential sputtering and Gibbsian segregation for schematic input. It shows the composition profile of a species that sputters preferentially and segregates. The composition spike near the surface is the more pronounced the smaller the ion beam current density.

Rate equations allowing for thermally activated effects as well as cascade mixing in the diffusion picture and preferential sputtering via boundary conditions were solved numerically by a finite-difference scheme (Lam & Wiedersich, 1981). Thermodynamic equilibrium defined the initial state as well as the boundary conditions at $x = \infty$. Since Gibbsian segregation was included via atom exchange between the two upper surface layers, these layers were treated discretely (Lam & Wiedersich, 1982a; Yacout et al., 1989).

Taking into account all the five basic processes in the model requires a large number of physical parameters in the calculations (Lam & Wiedersich 1981, 1987). For binary alloys, three parameters were utilized to determine preferential sputtering, two component sputter yields for the top layer and a sputter fraction for the second atom layer that was assumed to be the same for both components. Displacement mixing was characterized by two parameters, the number of replacements per Frenkel pair and the defect-production efficiency. The damage rate and distribution were calculated by TRIM simulation (Biersack & Haggmark, 1980). Gibbsian segregation was likewise specified by two parameters, the enthalpy and entropy of segregation. These two quantities have been measured for many alloy systems. Quantifying radiation-enhanced diffusion and radiation-induced segregation requires information on diffusivities of vacancies and interstitials and of defect-solute complexes. That is, pre-exponential defect jump frequencies, defect migration energies, and defect-solute binding energies must be provided. In addition, the effective defect formation energies and the concentration of radiation-induced sinks are needed.

The computed time evolution of the concentration profiles in Ni-40 at % Cu and Ni-9.5 at % Si alloys during 3 keV Ne^+ bombardment at 500 C is shown in fig. 15. Both Cu and Si are initially enriched at the surface due to Gibbsian segregation (Lam et al. 1985b, Lam & Hoff 1988). These concentrations decrease gradually as a result of preferential sputtering and finally attain steady-state values. The shapes of the Cu and Si concentration profiles and the thicknesses of altered layers differ noticeably because of different radiation-induced segregation behavior, i.e., Si atoms segregate toward the surface whereas Cu atoms move away from the surface during irradiation (Rehn & Okamoto 1983). This example demonstrates that detailed information about the synergistic effects of pertinent processes on compositional changes can be obtained using this model. The fitting of model

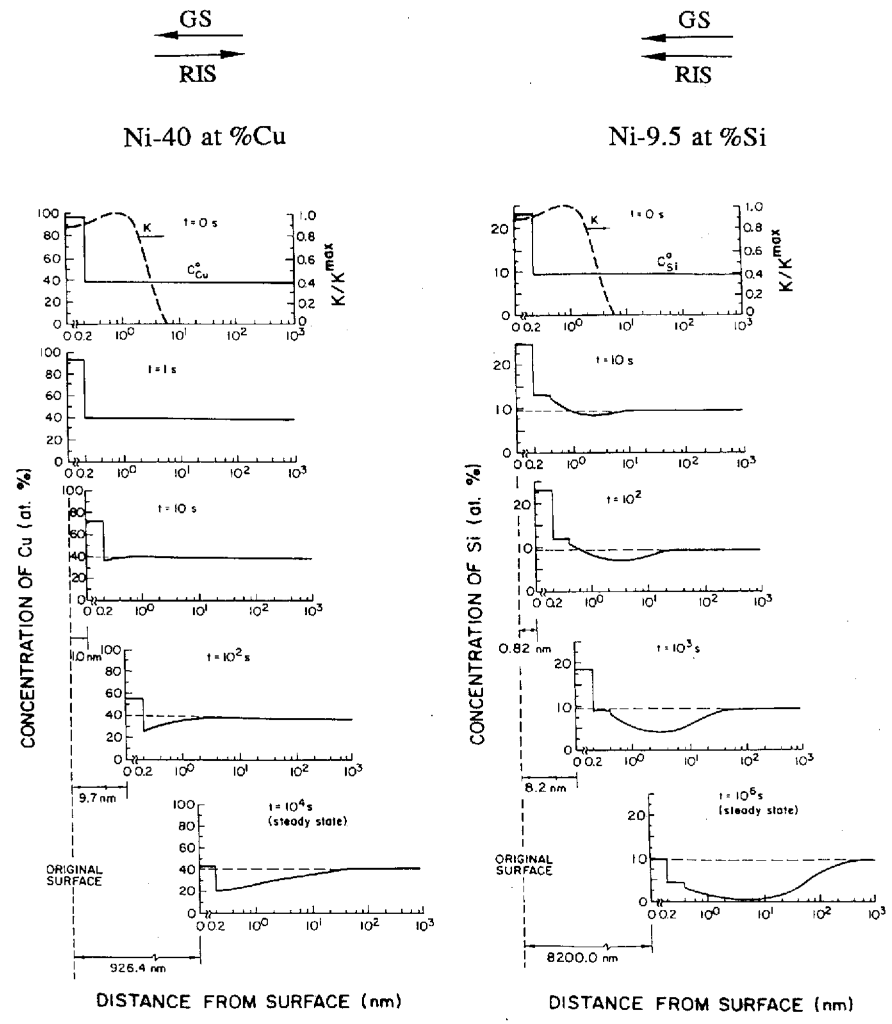

Figure 15. Development of the Cu concentration profile in a Ni-40 at % Cu alloy and of the Si concentration profile in a Ni-9.5 at % Si alloy during 3 keV Ne$^+$ bombardment at 500 C. The spatially-dependent damage rate K is shown by the dashed curve in the top portions, and the thicknesses of sputtered layers are indicated for various times. From Lam (1990).

calculations to experimental data has provided useful information on properties of point defects and defect-solute interactions in bombarded alloys (Lam & Hoff 1988, Hoff & Lam 1988, Tang & Lam 1989). Similar calculations were performed for near-surface composition modifications in ternary systems (Yacout et al. 1989; Tang et al., 1990).

4.9 Measurements

Bombardment-induced changes in surface composition have been measured in numerous alloy systems. Tabulations may be found in reviews by Betz & Wehner (1983), Andersen (1984), and Shimizu (1987). Mainly data published after 1987 have been summarized in this section. In order to elucidate synergistic effects of the pertinent processes, special emphasis will be laid on temperature-dependent sputtering of alloys.

4.9.1 Experimental Methods

A comprehensive review of various experimental techniques for surface and depth analysis based on sputtering, their principles, advantages and limitations has been given recently by Wittmaack (1991).

Compositional changes have been measured most often by Auger electron spectroscopy (AES). For an extensive survey cf. Betz & Wehner (1983). Because of variations in alloy composition near the surface, Auger transitions of several different energies have usually been employed in the analysis. Low-energy Auger electrons (~100 eV) have mean free paths ~4 Å, while for high-energy electrons (~1 keV), mean free paths lie around 15-20 Å. Low-energy Auger lines thus trace an average composition in the uppermost few surface layers. As a result, low-energy AES can detect the general effect of Gibbsian segregation but is not very suitable to characterize the interplay between this process and preferential sputtering. Recently, Li et al. (1991) showed that detailed composition profiles can be deduced from angle-resolved Auger spectroscopy. X-ray photoelectron spectroscopy (XPS) was also used in several studies (Thomas & Ralph, 1983; Hetzendorf & Varga, 1987; Lawniczak-Jablonska et al., 1989). The depth information is similar to that obtained from high-energy AES. In addition, information regarding phase transformations in the subsurface region may be derived.

Numerous measurements have been made with low-energy ion scattering spectroscopy (ISS). This technique is sensitive to the composition in the uppermost surface layer but does not yield information about the composition and extent of the altered layer. In studies of bombardment-induced composition changes, the same ions that are used to sputter the alloy are also employed to collect the ISS signals (Swartzfager et al., 1981; Lam et al., 1985a,b).

While SIMS has been used routinely for depth profiling multicomponent materials and for studying preferential sputtering from isotopic mixtures (sect. 3.4), it has not been widely employed to investigate bombardment-induced surface alterations.

SNMS (secondary neutral mass spectrometry) has been applied in the determination of sputter yield and surface composition of binary alloys (Gnaser & Oechsner, 1993). With this technique, problems involving the matrix dependence of ionization/excitation process may be less severe. Since neutral atoms constitute the majority of the sputtered flux, information about compositional modifications at low fluences may be obtained.

Bombardment-induced surface alterations are unavoidable during analyses of the sputtered-flux composition. Furthermore, implantation of beam particles such as O or Cs may give rise to chemically-induced Gibbsian segregation in some alloy systems (Andersen et al., 1983).

Rutherford backscattering spectroscopy (RBS) has also been employed to determine compositional changes and thickness of the altered layer caused by high-energy ion bombardment (Liau et al., 1977, 1978; Affolter et al., 1985) or at elevated temperatures (Harper et al. 1992; Hong & Harper, 1992). Because of relatively poor mass resolution, the technique can only be employed to systems with sizable differences in mass such as metal silicides. Further, the depth resolution of RBS is inadequate for revealing compositional gradients in the near-surface region.

4.9.2 Low Temperatures

Low-energy AES measurements of Li et al. (1982, 1983, 1985) demonstrated the development of a Au spike at the surface and a depleted subsurface layer in Au-Cu alloys during Ar^+ bombardment at temperatures as low as -120 C. These data offered insight into the role of thermodynamic variables in collisional mixing. Although the results have been widely accepted, they did raise a number of concerns. Firstly, the small variations ($1 - 4$ at %) of the alloy composition over a short distance (~10 Å) from the surface raised a question regarding the experimental accuracy. Shimizu (1987) examined the quantitative correction procedure used by Li et al. under the analysis of the raw data and noted that the accuracy of the reported depth profiles was far beyond that expected on the basis of the experimental data input. Secondly, the dependence of the altered-layer composition on ion current density at -120 C was found difficult to understand (Rehn & Lam, 1987). The size of the observed altered layer indicated that Gibbsian segregation of Au atoms to the surface played an important role. Since normal radiation-enhanced diffusion is negligible in this temperature regime, segregation must be fed by collisional mixing. However, cascade overlap must play a role, since a dependence on ion current density was observed. Rehn & Lam (1987) estimated that under the experimental conditions, pertinent dynamic events within cascades had to occur over durations of $\sim 10^{-4}$s after the initial knockon event. This is about seven orders of magnitude longer than the lifetime of a cascade.

Koshikawa (1985) measured the effect of 2 keV ion bombardment on the composition of Au-Cu alloy thin films prepared by co-evaporation of the pure metals onto a W substrate. Both low- and high-energy AES were utilized, and no composition changes were found at the surface at -120 C. Noticeable effects (i.e., Au enrichment in the near-surface region) were only observed during bombardment at room temperature. Such an enrichment was reported earlier by Kang et al. (1984) for keV Ar^+ bombardment and ISS analysis.

Qu & Xie (1988) used AES to monitor the time evolution of the near-surface composition of several homogeneous binary alloys (Au-Cu, Au-Ni, Au-Pd, Cu-Ni, and Cu-Pd) during Ar^+ bombardment at different energies. Fresh surfaces were prepared by scraping specimens inside the vacuum chamber before sputtering. Near the surface, the evolution toward steady state, measured by low-energy AES, was found to depend on ion energy. Many profiles showed complex variations in the transients. Qu & Xie attributed these variations to the synergistics of Gibbsian segregation and preferential sputtering. The stationary surface compositions obtained were consistent with component sputter yields $y_i^{(1)}$ equal to the sputter yields of the pure elements. Cu was sputtered preferentially from Cu-Ni and Cu-Pd, and Au was sputtered preferentially from Au-Pd, Au-Cu, and Au-Ni alloys.

Sputtering from Cu-Pd alloys was assessed by ISS (Ackermans et al., 1990b). Their experimental results and conclusion appear conflicting: Preferential sputtering of Cu was said to occur during 2 and 3 keV Ne^+ bombardment, yet the measurements showed virtually no deviations of the Cu concentration in the topmost surface layer from the bulk concentration. These authors stated that it was impossible in these experiments to distinguish between preferential sputtering and radiation-induced segregation. This claim is hardly justified because the steady-state surface composition is only dictated by preferential sputtering. Radiation-induced segregation should affect only the transient behavior of the surface composition and the evolution of the subsurface concentration profile.

Changes in the near-surface composition of a FeSi single crystal under bombardment by Ne^+, Ar^+, and Kr^+ ions in the energy range 0.3 - 3 keV were studied via low-energy AES by Castro & Ballesteros (1988). Si was always sputtered preferentially, and the effect was most pronounced at low ion energies. Ratios of partial sputter yields were similar for all three projectiles below 0.5 keV but became quite different at higher energies. As expected, the steady-state surface composition depended on the type and energy of the bombarding ions at energies above ~ 1 keV.

Kurokawa & Shimizu (1987) assessed the composition profile of the altered layer formed in an Al-Mg alloy under 3 keV Ar^+ bombardment by ISS, AES and EELS (electron energy loss spectroscopy). Sputtering and radiation-enhanced Gibbsian segregation of Mg resulted in a Mg composition spike at the surface, followed by Mg-depleted layers extending over a depth of ~150 Å. A slight enrichment in Mg of the uppermost atom layer (65 at % compared to 60 at % in the bulk) revealed by ISS may reflect the effect of surface segregation of Mg during post-bombardment ISS analysis with He^+ ions.

Du Plessis et al. (1989b) measured surface and subsurface composition changes in Pd-Pt alloys after 1 keV Ar^+ bombardment by ISS and AES and concluded that during irradiation, Pd segregated to the alloy surface where it was sputtered preferentially. This resulted in a relatively high concentration of Pd on the surface and a strong Pd depletion in subsurface layers. Experimental data were fitted to model calculations to derive the Gibbsian segregation energy and the radiation-enhanced diffusion coefficient.

Lawniczak-Jablonska et al. (1989) used XPS to measure the changes in subsurface composition of Ni-Mo alloys during 1 keV Ar^+ bombardment. The time required to reach steady state in the altered layer and the magnitude of the composition change were found larger for two-phase alloys than for solid solutions. The ratios of the extracted component sputter yields depended strongly on the bulk compositions. Note, however, that sputter yield ratios deduced from XPS or high-energy AES measurements cannot be reliable.

Bombardment-induced compositional changes in Cu-Pt alloys were investigated previously by Andersen et al. (1982, 1983, 1984a). Li et al. (1990) studied this alloy system by means of different Auger transitions. In agreement with the results of Andersen et al., the steady-state Cu profiles could be characterized by the synergistics of radiation-enhanced Gibbsian segregation of Cu to, and preferential sputtering from, the alloy surface during $0.2 - 2$ keV Ar^+ bombardment at room temperature. These profiles were also found consistent with that obtained subsequently by angular-resolved AES for 2.8 keV Ar^+ ions (Li et al., 1991). The latter profile showed more details of changes in the near-surface composition. The observed changes were higher than those created by bombardment at lower energies. Li et al. interpreted this observation in terms of decreasing mass effect with increasing ion energy.

Steady-state enrichment of Cu in the near-surface region of Cu-Zn alloys under 4 keV Ar^+ bombardment was reported by Marchetti et al. (1990), in agreement with earlier observations by Ferron et al. (1983) and Hammer & Shemenski (1984). Marchetti et al. interpreted this as a result of preferentially sputtering Zn. Caution is indicated since composition changes were monitored with high-energy Auger lines.

Preferential sputtering of InP was reviewed and revisited by Malherbe & Barnard (1991). Surfaces of InP wafers bombarded by 0.5 - 5 keV Ar^+ ions were investigated by medium-energy Auger transitions. P was found to be sputtered preferentially, leaving In-enriched surfaces. The steady-state near-surface composition depended on the angle of incidence but was found independent of both ion energy and crystal orientation. The mass difference between In and P was asserted to be the major factor determining preferential sputtering of P while surface binding was thought to be of secondary importance.

Preferential sputtering of Ni leading to Pt enrichment at the surface of Ni-Pt alloys has been observed by several groups (Andersen et al., 1983; de Temmermann et al., 1986, 1987; Weigand et al., 1992; Schmid et al., 1992). ISS measurements revealed that this effect was independent of surface orientation (Weigand et al., 1992), similar to results obtained for InP (Malherbe & Barnard, 1991). The synergistic effect of radiation-enhanced Gibbsian segregation which occurred even at 77 K was reported by Andersen et al. (1983). Surface enrichment in Pt caused an increase in the lattice constant of the upper atom layers. This resulted in the formation of subsurface lattice-mismatch dislocations, which were characterized recently by Schmid et al. (1992) by means of scanning tunneling microscopy.

From AES measurements of composition changes in CdTe, HgTe and HgCdTe during bombardment with 0.6 - 3 keV Ar^+ ions, Stahle & Helms (1992) assessed the sputter preferentiality of alloy components. It was suggested that preferential sputtering from these materials was controlled by the dominant effect of chemical bonding. Sputtering of Cd from CdTe was weakly preferential, whereas Hg sputtering was highly preferential from both HgTe and HgCdTe. The effects of defect-assisted processes appeared unimportant at room temperature because steady state was reached within a very short time.

Van Wyk et al. (1991) bombarded amorphous Cu-Ti alloys of different compositions with 2 keV Ar^+ ions and measured surface and subsurface compositions with ISS and AES. It was found that Cu segregated to the surface where it was sputtered preferentially. The thickness of the altered layer was estimated to be ~40 Å, i.e., equal to the damage depth. By fitting the experimental data with their kinetic model which includes the effects of radiation-enhanced Gibbsian segregation and preferential sputtering, they also derived the segregation energy and the radiation-enhanced diffusion coefficient as functions of alloy composition. The accuracy of these calculated parameters was limited mainly due to the intricate interplay between Gibbsian segregation and preferential sputtering. An excessively large sputter-yield ratio equivalent to $y_{\mathrm{Cu}}^{(1)}/y_{\mathrm{Ti}}^{(1)} = 6$ was necessary for the best possible fit of the results. Note that point defects are ill-defined in amorphous materials (Adda et al., 1987). Therefore, the concept of radiation-enhanced segregation in these media requires some clarification.

4.9.3 Elevated Temperatures

The first study of bombardment-induced alterations of surface composition at elevated temperatures was carried out on Cu-Ni alloys by Shimizu et al. (1975). Alloys were sputtered at temperatures within the range 100-600 C, and AES analysis of near-surface compositions was performed after samples had been cooled down to room temperature. The interpretation of these measurements was somewhat complicated by effects arising during specimen cooling. Nevertheless, a strong effect of irradiation temperature on near-surface composition changes was observed. Subsurface compositional profiles were not measured. Since sputter yields of metals are insensitive to temperature up to near the melting point, the temperature dependence observed was an indication of the importance of thermally-activated processes in alloy sputtering. A ratio of partial sputter yields was deduced from the composition ratio in steady state. Cu was found to sputter preferentially with a yield ratio ~1.9 at room temperature. Considerably larger yield ratios were found for bombardment at elevated temperatures. This implied bombardment times too short to reach steady state and/or changes in the composition of the sputtered surface during the post-bombardment cooling to ambient temperature.

Simultaneous AES measurements of composition changes in a Cu-40 at % Ni alloy during 5 keV Ar^+ sputtering at temperatures between 50 and 600 C were reported by Rehn et al. (1979, 1980). Two Auger transitions were used for each alloying element: Cu transitions at 106 and 920 eV, and Ni transitions at 102 and 716 eV. Low-energy measurements showed that the Cu concentration in the uppermost atom layers rapidly approached a steady-state value of ~40 at %, and this value was practically independent of temperature over the range investigated. Cu was found to sputter preferentially with a yield ratio ~2. High-energy measurements revealed that above 300 C, Cu depletion in the subsurface region was more pronounced than in the outermost layers, and no steady state was yet reached after 2 hours of bombardment. Indeed, both the time to reach steady state and the degree of Cu depletion in the subsurface region increased with increasing temperature. The extent of compositional change in the subsurface region was also determined by depth profiling of the bombarded specimen after cooling down to room temperature. These measurements demonstrated that Gibbsian segregation and radiation-enhanced diffusion of solute elements played important roles in the formation of the altered layer. Deviations from the bulk composition occurred up to remarkably large depths.

Swartzfager et al. (1981) carried out a similar study on Cu-Ni, Ag-Au and Au-Pd alloys via ISS. Alloys were bombarded by 2 keV Ne^+ ions at temperatures between 200 and 500 C, and compositional changes in the outermost atom layer were probed in situ with the same ions. Sputtering was found to be nonpreferen-

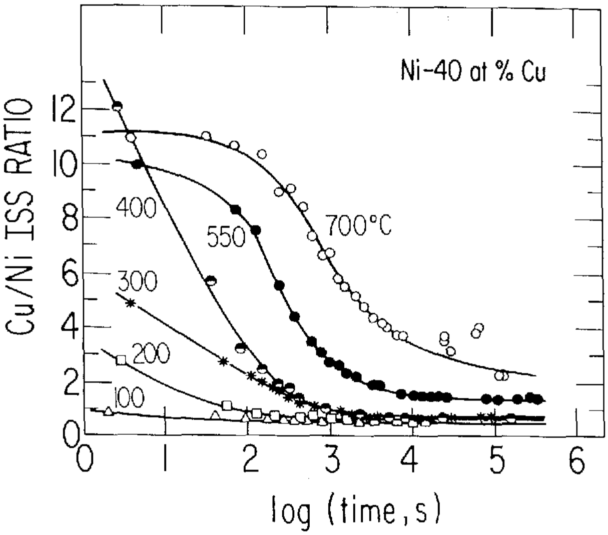

Figure 16. Time dependence of Cu/Ni ISS intensity ratio measured during 3 keV Ne^+ bombardment of a Ni-40 at % Cu alloy with a flux of 3.75 10^{13} ions/cm^2s at various temperatures. After Lam et al. (1985b).

tial in Cu-Ni and Ag-Au alloys (in seeming disagreement with AES results), while Pd was sputtered preferentially from Au-Pd. Similar to what was found in AES studies, pronounced alterations of the alloy composition were observed in the near-surface region. These measurements were interpreted in terms of synergistic effects of sputtering, radiation-enhanced diffusion, and Gibbsian segregation. Steady-state concentration profiles were analyzed by means of the model of Ho (1978), eq. (95). This model includes preferential sputtering and radiation-enhanced diffusion and describes the steady-state alloy composition in the altered layer by Ho's equation (97), which indicates that the logarithm of the concentration change in this layer should depend linearly on the distance from the surface with a slope of $-1/\beta$ within the region where radiation-enhanced diffusion dominates. Analyzing their concentration profiles in this way, Swartzfager et al. estimated β and D for several temperatures. The altered-layer thickness was found to be independent of the ion current J_0 and to rise sharply with temperature from ~400 C in Cu-Ni alloys. Extracted diffusion coefficients varied between 10^{-16} and 10^{-15} cm^2/s, virtually independent of temperature below ~400 C. This suggests that in this regime, radiation-generated point defects annihilate mainly at extended sinks. Note, however, that segregation was not considered in Ho's model.

ISS measurements on Ni-40 at % Cu alloys by Lam et al. (1985a) confirmed the results of Swartzfager et al.. The data for steady-state surface composition changes during bombardment at room temperature indicated that sputtering of this alloy system was nonpreferential. For bombardment above ~400 C, a noticeable temperature dependence was found (fig. 16). This effect was interpreted in terms of a significant contribution of the second atom layer to the sputtered flux. The same observations were also made on other Ni-based alloys (Lam et al., 1985b; Lam & Hoff, 1988; Hoff & Lam, 1988; Tang & Lam, 1989).

Morita et al. (1981) employed RBS to investigate compositional changes in self-supporting films of Ni-Si and Ni-Au alloys undergoing 5 keV Ar^+ bombardment at elevated temperatures. They found that above ~500 C, overall solute concentrations decreased rapidly with increasing fluence, the depletion being more severe in the near-surface region than deeper inside the specimen. The temperature dependence of solute depletion by sputtering was stronger in Ni-Si than in Ni-Au films.

Compositional changes in Ni-12.7 at % Si alloys bombarded by 5 keV Ar^+ ions at temperatures between 30 and 700 C were also reported by Rehn et al. (1983). Significant loss of Si from the specimen subsurface during bombardment at elevated temperature was detected by AES. This observation was supported by ISS measurements (Lam & Hoff, 1988). In addition, Rehn et al. (1983) found that very near the surface, the composition analyzed by low-energy (~100 eV) Si and Ni Auger signals remained equal to that of the bulk below ~650 C due to near-stoichiometric sputtering.

Li (1988) bombarded Au-Cu alloys by 2 keV Ar^+ ions between 30 and 700 C and performed AES depth profiling at room temperature to investigate the temperature dependence of steady-state redistribution. It was found that depletion of Au near the surface was most pronounced at ~300 C. Above this temperature, the altered layer extended deeper into the bulk and the surface concentration of Au increased steadily. The latter behavior suggested that steady state was not attained during bombardment at the upper end of the temperature range, i.e., above 450 C.

Li (1989) also measured composition changes in Au-Cu alloys during bombardment by 0.2 - 2 keV N^+ ions in the temperature range 25 - 300 C. The results were compared with those obtained for Ar^+ bombardment. There was no difference at 25 C, yet as the temperature increased, bombardment-enhanced Gibbsian segregation became effective, and differences between depth profiles became more apparent. Indeed, the subsurface Au depletion was more pronounced for N^+ bombardment. Li explained this observation in terms of differences in the partial sputter yields and damage depths in the two cases.

Near-surface compositional changes resulting from 2 keV Ar^+ bombardment in Ni-Cr alloys at temperatures between 30 and 600 C were reported by Jeng &

Holloway (1990). In this alloy system, Gibbsian segregation of Ni to the surface was found to be very weak (Jeng et al., 1988). Low-energy Auger measurements revealed that the steady-state Cr/Ni composition ratio increased continuously from 200 to 400 C due to preferential sputtering of Ni atoms transported to the surface by radiation-enhanced Gibbsian segregation. Above 400 C, the same ratio decreased with increasing temperature. This temperature dependence had been measured (Rehn & Wiedersich, 1980) and modeled (Lam & Wiedersich, 1982a) previously for Cu-Ni alloys.

The same behavior was also observed in ternary Fe-18Cr-3Mo alloys during 1 keV Ar^+ bombardment (Schiffman & Polak, 1986). Under steady-state conditions, the Cr/Fe concentration ratios, as monitored by both low- and high-energy Auger lines, showed significant temperature dependence above ~250 C. They reflected significant Fe depletion in the near- and subsurface regions, which increased gradually to maximum values at ~550 C and then decreased. A similar temperature dependence was obtained in phenomenological modeling (Yacout et al., 1989). Schiffman & Polak (1986) also noticed that the presence of small amounts of CO in the target chamber during bombardment caused inversion of this trend. That is, chemically-induced segregation of Cr resulted in surface enrichment of this element, and continuous sputtering of Cr from the surface led to its depletion in the underlying layers.

Chemically-driven segregation can also be triggered by implantation of certain incident-ion species. For example, O^+ bombardment of Ni_5Pd gave rise to surface segregation of Ni (the element with the stronger bond), in contrast to segregation of Pd (the element segregating in thermal equilibrium) during Ar^+ bombardment (Andersen et al., 1983). Similar reversal of segregation trends was also observed in Cu_3Au.

Effects of bulk impurities, such as O and C, on bombardment-induced near-surface composition modifications at elevated temperatures were observed in V-Cr alloys by Dawson & Hu (1985, 1986). Bombardment by Ar^+ ions at ambient temperature depleted the surface in Cr, whereas bombardment at 525 C increased the surface Cr concentration. This Cr enrichment at the alloy surface resulted from co-segregation of V and O or V and C to the surface — this is only possible at high temperature — and simultaneous, preferential removal of V by sputtering.

Compositional changes in binary alloys of heavy and light elements, like Cu-Li and Al-Li, during elevated-temperature sputtering were measured and modeled by Krauss et al. (1984b, 1985, 1988). They found that dilutions of Li in these metals produced surfaces covered with nearly pure Li upon heating. During bombardment above ~300 C, the Li-rich overlayer remained stable; in fact, the surface concentration of Li increased with increasing temperature. Efficient surface segregation processes during irradiation and the low sputter yield of Li play a key role in the maintenance of the Li overlayer.

Several studies of bombardment-induced compositional changes have been carried out on metal silicides. In general, the development of compositional profiles was found to be controlled by radiation-activated segregation and preferential sputtering of Si. Affolter et al. (1985) bombarded thin films of $CoSi_2$ and $NbSi_2$ on Si substrate by Xe^+ ions in the energy range 200 to 260 keV at different temperatures and analyzed the composition change in the irradiated materials by RBS. Preferential sputtering of Si was demonstrated, and partial sputter yields for the two silicides were shown to be comparable. The amount of sputtered species increased almost linearly with ion fluence until intermixing of the silicide with the underlying Si became appreciable. This occurred at lower fluences during bombardment at temperatures above room temperature. A Si-depleted subsurface layer was observed, the spatial extent of which was found comparable with the Xe range after bombardment at ambient temperature in $CoSi_2$, but significantly smaller after bombardment at 200 C. Marked differences between the results of sputtering at low and high temperature were rationalized in terms of radiation-enhanced diffusion across the silicide film in the presence of an underlying Si substrate.

Compositional modifications of $CrSi_2$ and Cr_3Si induced by 2 to 5 keV Ar^+ sputtering between -80 and 370 C were investigated by Ottaviani & Valeri (1987) using AES. Concentration profiles were measured over a depth of a few nanometers below the surface by simultaneous analysis of low- and high-energy Auger lines. Surface enrichment in Cr was found in both compounds at room temperature, the enrichment being stronger at lower ion energy and in the Si-rich silicide. In addition, elemental concentrations derived from low- and high-energy Auger lines were practically identical, suggesting that the altered layer was formed by preferential sputtering of Si and collisional mixing. Only at temperatures significantly higher than room temperature do thermally-activated processes become dominant in Cr-silicides. In fact, with increasing temperature, a transition to a Si-richer surface composition was observed at $\sim$250 C. During thermal annealing, the same transition occurred at higher temperature. This transition was attributed to the formation of the stable CrSi phase which can be enhanced during bombardment.

Ion beam effects on the near-surface composition of $TaSi_2$ were studied by the same group (Valeri et al., 1991). Steady-state sputtering of this silicide with Ar^+ ions below $\sim$410 C resulted in Si depletion at the surface and, much more severe, in the subsurface region. Preferential sputtering and radiation-enhanced segregation of Si were believed to be responsible for the development of such a compositional profile. Above 410 C, diffusional processes became efficient, progressively reducing the concentration gradients within the altered layer. Furthermore, the subsurface composition measured at room temperature showed a noticeable dependence on ion energy, in agreement with the results reported for other silicides (Wirth et al., 1984, 1986; Clement et al., 1990).

Recently, Harper et al. (1992) and Hong & Harper (1992) studied the temperature dependence of preferential sputtering of Si by 300 eV Ar^+ ions from $TiSi_2$ and $CoSi_2$, respectively. Compositional changes in the silicide were recorded by RBS and AES. In the case of $TiSi_2$, room-temperature bombardment caused a normal, linear decrease in silicide thickness due to loss of both Ti and Si. As the temperature was increased to 500 - 700 C, the thickness and composition of the silicide remained almost unchanged during bombardment. Since the Ti RBS peak area was almost constant in specimens bombarded at high temperature, this effect was attributed to preferential sputtering of Si being continuously compensated by rapid diffusion of Si from the substrate beneath the silicide layer. Compared with room-temperature values, the partial sputter yield of Ti decreased by a factor of 5 at 500 - 700 C while the yield of Si increased by a factor of 2. This implies that the sputtered flux was close to 100 % Si. Almost the same observations were made on $CoSi_2$ (Hong & Harper, 1992): The sputtering rate of this silicide, when deposited on Si, decreased significantly above 400 C. However, on SiO_2 substrates, the sputtering rate of $CoSi_2$ was nearly constant, independent of bombardment temperature.

4.9.4 Conflicting Characterizations

Some discussion is indicated here of conflicting experimental results published in the literature on preferential sputtering. In the typical case of Cu-Ni alloys, researchers using AES to probe near-surface compositional changes reported preferential sputtering of Cu (Betz & Wehner, 1983, and references therein; Qu & Xie, 1988). Experiments involving ISS led to opposite conclusions. Okutani et al. (1980) studied sputtering of Ni-48 at % Cu alloys by 3 keV Ar^+ ions and found Ni to be sputtered preferentially. Swartzfager et al. (1981) and Lam et al. (1985a) found ISS intensity ratios measured on the sputtered surfaces virtually identical to bulk concentration ratios. This suggested that sputtering of Cu-Ni alloys by Ne^+ ions was nonpreferential. Kamiya et al. (1988) reported that their ISS measurements on dilute Cu-Ni targets showed preferential sputtering of Ni in low-Ni alloys and of Cu in low-Cu alloys - an effect which cannot be understood on the basis of eq. (15). The discrepancy between ISS and AES data can be reconciled in terms of near-surface compositional gradients and the respective depth resolutions of these analysis techniques. The disagreement amongst ISS measurements is, however, difficult to explain; differences in sample preparation, residual gas in the target chamber, and calibration may be important influencing factors.

Discrepancies between AES and ISS measurements should be anticipated for most multicomponent systems, except for some cases where near-surface compositions remain unchanged during bombardment as a result of near-stoichiometric sputtering and negligible surface segregation. The Ni-Co alloy system is a good example. Several compositional characterizations have been performed on this system over the past decade because of the technological importance of Ni-Co alloy films in the areas of magnetic storage and catalysis. Therefore, a direct comparison of several results can be made.

Tanaka et al. (1983) studied composition changes in these alloys by Auger lines Ni(859 eV) and Co(656 eV) after sputter cleaning with a 5 keV Ar^+ beam. They found that the near-surface concentrations of Ni and Co differed only very slightly from the bulk composition. AES work by Kurokawa et al. (1989b) on Ni-Co alloys under Ar^+ bombardment confirmed these findings. No apparent synergistic effects of preferential sputtering and surface segregation could be detected from both low- and high-energy Auger signals. Since the accuracy of the low-energy Auger signals was rather poor (affected by stray magnetic fields resulting from the ferromagnetic properties of the alloying elements), Kurokawa et al. (1989a) extended their earlier measurements using both ISS and AES. They found that surface and subsurface compositions were the same as in the bulk.

Fujita et al. (1990) and Sethuraman et al. (1990, 1991) used several techniques to characterize Ni-Co films of varying composition. The results of AES depth profiling indicated spatially-uniform film composition, in agreement with previous observations of nonpreferential sputtering from Ni-Co alloys. For this reason, and because of negligibly small corrections for matrix effects, the Ni-Co alloy system has been proposed as a reference material for surface chemical analysis by AES (Fujita et al., 1990).

Among several available analytical techniques, ISS appears to be the most suitable for demonstrating the interplay between Gibbsian segregation and preferential sputtering because it provides, in principle, direct information on the composition in the outermost atom layer. However, since this information comes from the conversion of ISS intensity ratios to compositions, an accurate calibration is required. Most calibrations reported were obtained from sputter-cleaned surfaces and, consequently, affected by preferential sputtering. Reliable calibrations must be performed on fresh surfaces, created in ultrahigh vacuum by, e.g., scraping or fracture (Betz, 1980). Simultaneous analyses with AES (or XPS) and laser-induced fluorescence can be a good complement because the former provides useful information about subsurface composition changes while the latter yields the composition of the sputtered flux (Bay, 1987).

5 Summary and Outlook

Although we have tried to summarize a broad spectrum of problems within the field of alloy and isotope sputtering, we have put emphasis on some aspects and deemphasized others. The primary focus has been on preferential sputtering and related aspects. Information on absolute sputter yields is implicit in much of the discussion but comes rarely to the surface. If pressed to make an explicit statement on the latter point we would have to say that rough estimates can be made by simple reasoning and precise predictions are unavailable.

We tried to focus on precise definitions of those parameters which we believe are important in the understanding of preferential sputter effects, and to stick to a clear and unambiguous notation, flexible enough to accomodate both continuum and discrete descriptions. It is shown that sputter cross sections and component yields are two ways of describing the same physics when combined properly with particle densities and atom fractions, respectively. Explicit introduction of species-dependent atomic volumes allows to incorporate density changes along with compositional changes. Conversely, the assumption of a species-independent atomic volume is equivalent with that of a fixed lattice structure independent of composition. Either description allows inclusion of defects.

During the decade that passed since the appearance of the review by Betz & Wehner (1983), there has been progress in the theory of primary and secondary sputter processes as well as in experiment. Predictions on the dependence of preferential sputtering on mass and surface binding energy have long been available but have been strengthened, clarified, and numerically modified along with increasing experience from numerical simulation. This has led in particular to a fairly clear and consistent theoretical picture of preferential sputtering from isotopic targets. Nevertheless, discrepancies prevail in that area between theoretical predictions and experimental data, and there are also differences between different experimental data on similar systems. Key points are the existence or nonexistence of a pronounced angular variation in the isotopic composition of the sputtered flux and the absolute magnitude of the overall enrichment of this flux at low bombardment fluences. Similar discrepancies are present in alloy sputtering. They are larger in absolute terms, but they tend to receive less attention because of a wider variety of possible disturbing factors.

Much progress has happened in the understanding of secondary effects, namely the role of collisional mixing and thermally-activated processes. This development started little more than a decade ago. The proper mathematical formalism has developed gradually, and numerical results, based on schematic or realistic input, have been emerging with increasing intensity. When starting this project we felt there was an urgent need to reconcile numerous available descriptions of matter transport in the target during sputtering, developed by different groups at different times and rather independent of each other. With the emergence of our eq. (45) in conjunction with relations like eqs. (42,44), this goal has essentially been achieved. There are still a few open ends, but closing those is not expected to invoke major problems.

The number of uncertain or unknown parameters that govern secondary processes is quite large. Thus, comprehensive quantitative predictions are not likely to emerge in the near future. This does not preclude quantitative predictions with a more limited scope, such as on the fluence dependence of isotope enrichment where the first results have appeared as reported in sect. 3. Moreover, well-planned measurements on alloy sputtering allow to extract pertinent parameters by comparison with numerical simulations on secondary effects. Several examples have been mentioned in sect. 4.

We like to conclude this survey with a list of important problems.

- Absolute measurements on isotope sputtering (composition of target and/or sputtered flux).
- Estimates of energy spectra of sputtered atoms from targets containing strong composition gradients near the surface.
- Quantitative theory of the effect of composition gradients on angular distributions of sputtered particles.
- Quantitative predictions on absolute erosion rates and partial sputter yields.
- Clarification of the role of preferential sputtering and recoil implantation in low-energy alloy and isotope sputtering.
- Experimental studies of preferential sputter depths for materials with widely different constituents.
- Predictions on preferential sputtering from high-density cascades on the basis of a variety of models proposed to describe collision spikes.
- Analytical relationships (scaling laws) describing fluence-dependent preferential sputtering, composition gradients, and altered-layer depths in different regimes of temperature and ion current density. Establishing quantitative criteria for the limits of these regimes.
- Systematic experiments testing scaling laws governing secondary processes.
- Experimental and/or theoretical studies of the interplay between compositional and topographical changes.

Acknowledgements

Our experience in the main topic of this chapter has been acquired over a long time period in cooperation with a number of friends and colleagues, in particular N. Andersen, R. Collins, A. Gras-Marti, K. Johannessen, R. A. Johnson, A. R. Krauss, P. R. Okamoto, A. Oliva, L. E. Rehn, S. J. Rothman, M. W. Sckerl, R. Sizmann, H. Wiedersich, H. F. Winters, and A. Yacout. Numerous aspects have been discussed in the Danish Sputter Club, in particular with H. H. Andersen, F. Besenbacher, J. Bøttiger, J. J. Jiménez-Rodríguez, J. Onsgaard, J. Schou, S. Tougaard, H. M. Urbassek, and M. Vicanek, as well as with D. M. Gruen, R. Kelly, and G. K. Wehner. In addition, H. H. Andersen, R. A. Baragiola, H. M. Urbassek, and M. Vicanek provided useful comments and suggestions on a preliminary manuscript. We wish to express our sincere gratitude to all of them. One of us (PS) would like to acknowledge the hospitality of the Physics Division at Argonne, especially D. S. Gemmell and G. H. Berry, during his tenure of an Argonne Distinguished Fellowship. This work was supported by the U. S. Department of Energy, Office of Basic Energy Sciences, under Contract no. W-31-109-ENG-38 and by a grant from the Danish Natural Science Research Council (SNF).

References

Abramowitz M and Stegun IA, 1964: *Handbook of Mathematical Functions with Formulas, Graphs, and Mathematical Tables* (U.S. Government Printing Office, Washington, D.C.)
Ackermans PAJ, Creuwels MAP, Brongersma HH and Scanlon PJ, 1990a: Surf. Sci. **227**, 361
Ackermans PAJ, Krutzen GCR and Brongersma HH, 1990b: Nucl. Instrum. Methods B **45**, 384
Adda Y, Beyeler M and Brebec G, 1975: Thin Solid Films **25**, 107
Adda Y, Brebec G, Gupta RP and Limoge Y, 1987: Mater. Sci. Forum **15-18**, 349
Affolter K, Hamdi AH and Nicolet MA, 1985: Appl. Phys. A **37**, 19
Almen O and Bruce G, 1961: Nucl. Instrum. Methods **11**, 257
Andersen HH, 1979: Appl. Phys. **18**, 131
Andersen HH, 1980: *The Physics of Ionized Gases (SPIG 1980)*, ed. M. Matic (Boris Kidric Institute of Nuclear Sciences, Beograd) 421
Andersen HH, 1984: *Ion Implantation and Beam Processing*, ed. J. S. Williams and J. M. Poate (Academic Press, Sydney) 127
Andersen HH and Sigmund P, 1965: Riso Report no. **103**
Andersen HH, Chernysh V, Stenum B, Sørensen T and Whitlow HJ, 1982: Surface Sci. **123**, 39
Andersen HH, Stenum B, Sørensen T and Whitlow HJ, 1983: Nucl. Instrum. Methods **209/210**, 487
Andersen HH, Stenum B, Sørensen T and Whitlow HJ, 1984a: Nucl. Instrum. Methods B **2**, 623
Andersen HH, Stenum B, Sørensen T and Whitlow HJ, 1984b: Nucl. Instrum. Methods B **2**, 601
Andersen N and Sigmund P, 1974: Mat. Fys. Medd. Dan Vid. Selsk. **39**, no. 3
Ardell AJ and Janghorban K, 1983: *Phase Transformations during Irradiation*, ed. F.V. Nolfi, Jr. (Applied Science Publishers, London) 291
Asada T and Quasebarth K, 1929: Z. Phys. Chem. A **143**, 435
Averback RS, 1986: Nucl. Instrum. Methods B **15**, 675

Averback RS, Peak D and Thompson LJ, 1986: Appl. Phys. A **39**, 59

Baretzky B and Taglauer E, 1985: Surf. Sci. **162**, 996

Baretzky B, Möller W and Taglauer E, 1987: Nucl. Instrum. Methods B **18**, 496

Baumel LM, Weller MR, Weller RA and Tombrello TA, 1988: Nucl. Instrum. Methods B **34**, 427

Bay HL, 1987: Nucl. Instrum. Methods B **18**, 430

Betz G, 1980: Surface Sci. **92**, 283

Betz G and Wehner GK, 1983: *Sputtering by Particle Bombardment II.* Top. Appl. Phys. **52**, ed. R. Behrisch.(Springer-Verlag, Berlin) 11

Biersack JP, 1987: Nucl. Instrum. Methods B **27**, 21

Biersack JP and Eckstein W, 1984: Appl. Phys. A **34**, 73

Biersack JP and Haggmark LG, 1980: Nucl. Instrum. Methods **174**, 257

Brongersma HH, Sparnaay MJ and Buck TM, 1978: Surface Sci. **71**, 657

Burnett JW, Biersack JP, Gruen DM, Jørgensen B, Krauss AR, Pellin MJ, Schweitzer EL, Yates JT and Young CE, 1988: J. Vac. Sci. Technol. A **6**, 2064

Carter G, Navinsek B and Whitton JL, 1983: *Sputtering by Particle Bombardment II*, Top. Appl. Phys. **52**, ed. R. Behrisch (Springer-Verlag, Berlin) 231

Castro GR and Ballesteros A, 1988: Surf. Sci. **204**, 415

Chen I-W, 1983: J. Nucl. Mater. **116**, 249

Cheng YT, 1990: Mater. Sci. Repts. **5**, 45

Cheng YT, Van Rossum M, Nicolet MA and Johnson WL, 1984: Appl. Phys. Lett. **45**, 185

Cheng YT, Dow AA and Clemens BM, 1988: Appl. Phys. Lett. **53**, 1346

Cheng YT, Simko SJ, Militello MC, Dow AA, Auner GW, Alkaisi MH and Padmanabhan KR, 1992: Nucl. Instrum. Methods B **64**, 38

Chou NJ and Shafer MW, 1980: Surf. Sci. **92**, 601

Clement M, Sanz JM and Martinez-Duart JM, 1990: Surf. Interf. Anal. **15**, 440

Collins R, 1978: Rad. Effects **37**, 13

Collins R and Jiménez-Rodríguez JJ, 1982: Radiat. Eff. Lett. **68**, 19

Collins R and Sigmund P, 1992: J. Appl. Phys. **72**, 1993

Collins R, Jiménez-Rodríguez JJ, Wadsworth M and Badheka R, 1988: J. Appl. Phys. **64**, 1120

Conrad U and Urbassek HM, 1991: Nucl. Instrum. Methods B **61**, 295

Conrad U and Urbassek HM, 1992: Surf. Sci. **278**, 414

Conrad U and Urbassek HM, 1993: Nucl. Instrum. Methods B, submitted

Damask AC and Dienes GJ, 1963: *Point Defects in Metals* (Gordon and Breach, New York)

d'Heurle F, Baglin JEE and Clarke GJ, 1985: J. Appl. Phys. **57**, 1426

Dawson PT and Hu MP, 1985: Surf. Sci. **163**, 198

Dawson PT and Hu MP, 1986: J. Nucl. Mater. **139**, 198

de Temmermann L, Creemers C, van Hove H, Neyens A, Bertolini JC and Massardier J, 1986: Surf. Sci. **178**, 888

de Temmermann L, Creemers C, van Hove H and Neyens A, 1987: Surf. Sci. **183**, 565

Diaz de la Rubia T, Averback RS, Benedek R and King WE, 1987: Phys. Rev. Lett. **59**, 1930

Dienes GJ and Damask AC, 1958: J. Appl. Phys. **29**, 1713

Dienes GJ and Vineyard GH, 1957: *Radiation Effects in Solids* (Interscience Publishers, New York) 138

Dumke MF, Tombrello TA, Weller RA, Housley RM and Cirlin EH, 1983: Surf. Sci. **124**, 407

du Plessis J, 1990: Solid State Phenomena **11**, 1

du Plessis J and van Wyk GN, 1989a: J. Phys. Chem. Solids **50**, 237

du Plessis J, van Wyk GN and Taglauer E, 1989b: Surf. Sci. **220**, 381

Eckstein W and Biersack JP, 1985: Appl. Phys. A **37**, 95

Eckstein W and Möller W, 1985: Nucl. Instrum. Methods B **7/8**, 727

Falcone G, 1991: Phys. Lett. A **160**, 189
Falcone G and Oliva A, 1984: Appl. Phys. A **33**, 175
Falcone G and Sigmund P, 1981: Appl. Phys. **25**, 307
Falcone G, Aiello D, Forlano L, Piperno F, 1991: Phys. Lett. A **160**, 189
Ferron J, De Bernardez LS, Goldberg EC and Buitrago RH, 1983: Appl. Surf. Sci. **17**, 241
Fine J, Andreadis TD and Davarya F. 1983: Nucl. Instrum. Methods **209/210**, 521
Fluit JM, Friedman L, Boerboom AJH and Kistemaker J, 1961: J. Chem. Phys. **35**, 1143
Foiles SM, 1985: Phys. Rev. B **32**, 7685
Foiles SM, 1992: personal communication
Foreman AJE, 1972: Radiat. Eff. **14**, 175
Fujita D, Tanaka A, Goto K and Homma T, 1990: Surf. Interf. Anal. **16**, 183
Gao F & Bacon DJ, 1993: Phil. Mag. A **67**, 289
Gibson JB, Goland AN, Milgram M and Vineyard GH, 1961: Phys. Rev. **120**, 1229
Gnaser H and Hutcheon ID, 1988: Surf. Sci. **195**, 499
Gnaser H and Oechsner H, 1989: Phys. Rev. Lett. **63**, 2673
Gnaser H and Oechsner H, 1990: Nucl. Instrum. Methods B **48**, 544
Gnaser H and Oechsner H, 1993: Phys. Rev. B **47**, 14093
Goktepe OF, Andreadis TD, Rosen M, Mueller GP and Roush ML, 1986: Nucl. Instrum. Methods B **13**, 434
Gruen DM, Pellin MJ, Young CE, Mendelsohn MH and DeWald AB, 1983: Phys. Scr. **T6**, 42
Gschneidner KA, 1964: Solid State Physics **16**, 275
Gupta RP and Lam NQ, 1979: Scripta Metall. **13**, 1005
Haff PK, 1977: Appl. Phys. Lett. **31**, 259
Haff PK and Switkowski ZE, 1976: Appl. Phys. Lett. **29**, 549
Haff PK, Watson CC and Tombrello TA, 1981: J. Geophys. Res. **86**, 9553
Hammer GE and Shemenski RM, 1984: J. Vac. Sci. Technol. A **2**, 1132
Harper JME, Motakef S and Moy D, 1992: Appl. Phys. Lett. **60**, 1196
Harrison DE, 1983: Rad. Effects **70**, 1
Hetzendorf G and Varga P, 1987: Nucl. Instrum. Methods B **18**, 501
Ho PS, 1978: Surf. Sci. **72**, 253
Hofer WO, 1991: *Sputtering by Particle Bombardment III*, Top. Appl. Phys. **64**, ed. R. Behrisch and K. Wittmaack (Springer-Verlag, Heidelberg) 15
Hofer WO and Littmark U, 1979: Phys. Lett. **71A**, 457
Hoff HA and Lam NQ, 1988: Surf. Sci. **204**, 233
Hofmann S, 1990: *Surface Segregation Phenomena*, ed. P.A. Dowben and A. Miller (CRC Press, Boca Raton, Florida) 107
Hong QZ and Harper JME, 1992: J. Appl. Phys. **71**, 4527
Hubbard KM, Weller RA, Weathers DL and Tombrello TA, 1989a: Nucl. Instrum. Methods B **36**, 395
Hubbard KM, Weller RA, Weathers DL and Tombrello TA, 1989b: Nucl. Instrum. Methods B **40/41**, 278
Husinsky W, Wurz P, Strehl B and Betz G, 1987: Nucl. Instrum. Methods B **18**, 452
Ichimura S, Shimizu H, Murakami H and Ishida Y, 1984: J. Nucl. Mater. **128 & 129**, 601
Itoh N and Morita K, 1984: Rad. Effects **80**, 163
Jeng SP and Holloway PH, 1990: Surf. Sci. **227**, 273
Jeng SP, Batich CD and Holloway PH, 1988: Surf. Sci. **193**, L63
Jiménez-Rodríguez JJ, Conrad U, Urbassek HM, Abril I and Gras-Marti A, 1992: Nucl. Instrum. Methods B **67**, 527
Johnson RA and Lam NQ, 1976: Phys. Rev. B **13**, 4364
Johnson RA and Lam NQ, 1978: J. Nucl. Mater. **69 & 70**, 424-433

Johnson RE and Schou J, 1993: Mat. Fys. Medd. Dan. Vid. Selsk., Mat. Fys. Medd. Dan. Vid. Selsk. **43**, 403

Kamiya I, Buck TM, Sakurai T and Patterson CH, 1988: Nucl. Instrum. Methods B **33**, 479

Kang HJ, Shimizu R and Okutani T, 1982: Surf. Sci. **116**, L173

Kang HJ, Matsuda Y and Shimizu R, 1983: Surf. Sci. **127**, L179

Kang HJ, Kawatoh E and Shimizu R, 1984: Surf. Sci. **144**, 541

Kelly R, 1978: Nucl. Instrum. Methods **149**, 553

Kelly R, 1980: Surf. Sci. **100**, 85

Kelly R, 1985: Surf. Interf. Anal. **7**, 1

Kelly R, 1989a: Mater. Sci. Eng. A **115**, 11

Kelly R, 1989b: Nucl. Instrum. Methods B **39**, 43

Kelly R and Harrison DE, 1985: Mater. Sci. Eng. **69**, 449

Kelly R and Miotello A, 1991: Nucl. Instrum. Methods B **59/60**, 517

Kelly R and Miotello A, 1992: Surf. and Coatings Technol. **51**, 343

Kelly R and Oliva A, 1986a: Nucl. Instrum. Methods B **13**, 283

Kelly R and Oliva A, 1986b: *Erosion and Growth of Solids Stimulated by Atom and Ion Beams*, ed. G. Kiriakidis et al., NATO ASI Series, no. **112** (Nijhoff, Dordrecht) 41

Kelly R and Sanders JB, 1976: Surf. Sci. **57**, 143

Kelly R and Sanders JB, 1976b: Nucl. Instrum. Methods **132**, 335

Kim SJ, Nicolet MA, Averback RS and Baldo P, 1985: Appl. Phys. Lett. **46**, 154

King WE and Benedek R, 1983: J. Nucl. Mater. **117**, 26

Kirk MA and Blewitt TH, 1982: J. Nucl. Mater. **108/109**, 124

Konoplev V and Gras-Marti A, 1992: Phys. Rev. B **46**, 13713

Koponen I, 1991: Nucl. Instrum. Methods B **59/60**, 41

Koponen I and Hautala M, 1992: Nucl. Instrum. Methods B **69**, 182

Koshikawa T, 1985: Appl. Surf. Sci. **22/23**, 1985

Koshikawa T and Goto K, 1987: Nucl. Instrum. Methods B **18**, 504

Krauss AR, Gruen DM and DeWald AB, 1984a: J. Nucl. Mater. **121**, 398

Krauss AR, Gruen DM, Lam NQ and DeWald AB, 1984b: J. Nucl. Mater. **128** & **129**, 570

Krauss AR, DeWald AB, Gruen DM and Lam NQ, 1985: Rad. Effects **89**, 129

Krauss AR, Gruen DM, Lam NQ, DeWald AB, Valentine MG, Sagara A and Kamada K, 1988: J. Scanning Microscopy **2**, 1365

Kurokawa A and Shimizu R, 1989: Surf. Sci. **207**, 460

Kurokawa A, Shimizu R, Kubota Y and Kang HJ, 1989a: Surf. Interf. Anal. **14**, 388

Kurokawa A, Tezuka M, Takegoshi K, Kudo M and Shimizu R, 1989b: Nucl. Instrum. Methods B **39**, 57

Lam NQ, 1975: J. Nucl. Mater. **56**, 125

Lam NQ, 1990: Scanning Microscopy Supplement **4**, 311

Lam NQ and Hoff HA, 1988: Surf. Sci. **193**, 353

Lam NQ and Johanessen K, 1992: Nucl. Instrum. Methods B **71**, 371

Lam NQ and Leaf GK, 1986: J. Mater. Res. **1**, 251

Lam NQ and Rothman SJ, 1976: *Radiation Damage in Metals*, ed. N.L. Peterson and S.D. Harkness (American Society for Metals, Metals Park, Ohio) 125

Lam NQ and Wiedersich H, 1981: J. Nucl. Mater. **103/104**, 433

Lam NQ and Wiedersich H, 1982a: Mater. Res. Soc. Symp. Proc. **7**, 35

Lam NQ and Wiedersich H, 1982b: Rad. Effects Lett. **67**, 107

Lam NQ and Wiedersich H, 1987: Nucl. Instrum. Methods B **18**, 471

Lam NQ, Rothman SJ and Sizmann R, 1974: Rad. Effects **23**, 53

Lam NQ, Okamoto PR and Johnson RA, 1978a: J. Nucl. Mater. **78**, 408

Lam NQ, Okamoto PR and Wiedersich H, 1978b: J. Nucl. Mater. **74**, 101

Lam NQ, Leaf GK and Wiedersich H, 1980: J. Nucl. Mater. **88**, 289

Lam NQ, Kumar A and Wiedersich H, 1982: *Effects of Radiation on Materials - 11th Conference, ASTM STP782*, ed. H.R. Brager and J.S. Perrin (American Society for Testing and Materials, Philadelphia) 985

Lam NQ, Hoff HA and Régnier PG, 1985a: J. Vac. Sci. Technol. **A3**, 2152

Lam NQ, Hoff HA, Wiedersich H and Rehn LE, 1985b: Surf. Sci. **149**, 517

Lawniczak-Jablonska K, Heinonen M and Sulyok A, 1989: Surf. Sci. **222**, 129

Li RS, 1988: Surf. Sci. **193**, 373

Li RS, 1989: Appl. Surf. Sci. **35**, 409

Li RS and Koshikawa T, 1985: Surf. Sci. **151**, 459

Li RS, Koshikawa T and Goto K, 1982: Surf. Sci. **121**, L561

Li RS, Koshikawa T and Goto K, 1983: Surf. Sci. **129**, 192

Li RS, Li CF and Zhang WL, 1990: Appl. Phys. A **50**, 169

Li RS, Li CF, Liu G, Zhang XS and Bao DS, 1991: J. Appl. Phys. **70**, 5351

Liau ZL, Brown WL, Homer R and Poate JM, 1977: Appl. Phys. Lett. **30**, 626

Liau ZL, Mayer JW, Brown WL and Poate JM, 1978: J. Appl. Phys. **49**, 5295

Lindhard J, Scharff M and Schiøtt HE, 1963: Mat. Fys. Medd. Dan. Vid. Selsk. **33**, no. 14

Lindhard J, Nielsen V and Scharff M, 1968: Mat. Fys. Medd. Dan. Vid. Selsk. **36**, no. 10

Littmark U and Hofer WO, 1980: Nucl. Instrum. Methods **168**, 329

Littmark U and Hofer WO, 1984: *Thin Film and Depth Profile Analysis*, Top. Appl. Phys. **37**, ed. H. Oechsner (Springer-Verlag, Berlin) 159

Lo DY, Tombrello TA and Shapiro MH, 1989: Nucl. Instrum. Methods B **40/41**, 270

Lomer WM, 1954: UKAEA Report AERE T/R **1540**

Ma E, 1991: Nucl. Instrum. Methods B **58**, 194

Malherbe JB and Barnard WO, 1991: Surf. Sci. **255**, 309

Manning JR, 1968: *Diffusion Kinetics for Atoms in Crystals* (van Nostrand, Princeton)

Manning JR, 1981: *Phase Stability during Irradiation*, ed. JR. Holland et al. (The Metallurgical Society of AIME, New York) 3

Marchetti F, Dapor M, Girardi S, Cipparrone M and Tiscione P, 1990: Vacuum **41**, 1706

Martin G, Cauvin R and Barbu A, 1983: *Phase Transformations during Irradiation*, ed. F.V. Nolfi, Jr. (Applied Science Publishers, London) 47

Marton D, Fine J and Chambers GP, 1988: Phys. Rev. Lett. **61**, 2697

Marton D, Fine J and Chambers GP, 1989: Mater. Sci. Eng.. **A115**, 223

Marwick AD, Piller RC and Sivell PM, 1979: J. Nucl. Mater. **83**, 35

Matteson S and Nicolet MA, 1983: Ann. Rev. Mater. Sci. **13**, 339

Matteson S, Paine BM and Nicolet MA, 1981: Nucl. Instrum. Methods **182/183**, 53

Mayer JW and Lau SS, 1983: *Surface Modification and Alloying*, ed. J.M. Poate et al. (Plenum, New York) 241

Mazurowski J and Dowben PA, 1990: *Surface Segregation Phenomena*, ed. P.A. Dowben and A. Miller (CRC Press, Boca Raton, Florida) 365

Möller W and Eckstein W, 1984: Nucl. Instrum. Methods B **2**, 814

Möller W and Eckstein W, 1985: Nucl. Instrum. Methods B **7/8**, 645

Möller W, Eckstein W and Biersack JP, 1988: Comp. Phys. Commun. **51**, 355

Morita K, Nakamura H, Hayashibara M and Itoh N, 1981: J. Nucl. Mater. **103 & 104**, 1373

Morita K, Tsuchiya T, Hayashibara M and Itoh N, 1983: J. Nucl. Mater. **116**, 63

Morita K, Ohno H, Hayashibara M and Itoh N, 1984: Nucl. Instrum. Methods B **2**, 596

Ng YS, Tsong TT and McLane SB, 1979: Phys. Rev. Lett. **42**, 588

Nieminen R, 1993: Mat. Fys. Medd. Dan. Vid. Selsk. **43**, 81

Oechsner H and Bartella J, 1981: *Proc. 7th Intern. Conf. on Atomic Collisions in Solids*, 1977, Moscow (Moscow State University Publishing House, USSR) **2**, 55

Okamoto PR and Rehn LE, 1979: J. Nucl. Mater. **83**, 2

Okano J, Ochiai T and Nishimura H, 1985: Appl. Surf. Sci. **22/23**, 72

Okutani T, Shikata M and Shimizu R, 1980: Surf. Sci. **99**, L410

Oliva A, Kelly R and Falcone G, 1986: Surf. Sci. **166**, 403

Olson RR and Wehner GK, 1977: J. Vac. Sci. Technol. **14**, 319

Olson RR, King ME and Wehner GK, 1979: J. Appl. Phys. **50**, 3677

Onderdelinden D, 1968: Can. J. Phys. **46**, 739

Ottaviani G and Valeri S, 1987: Nucl. Instrum. Methods. B **19/20**, 97

Paine BM and Averback RS, 1985: Nucl. Instrum. Methods B **7/8**, 666

Paine BM and Nicolet MA, 1983: Nucl. Instrum. Methods **209/210**, 173

Peinador JA, Abril I, Jiménez-Rodríguez JJ and Gras-Marti A, 1990: Nucl. Instrum. Methods B **48**, 589

Peinador JA, Abril I, Jiménez-Rodríguez JJ and Gras-Marti A, 1991: Phys. Rev. B **44**, 2061

Peiner E and Kopitzki K, 1988: Nucl. Instrum. Methods B **34**, 173

Pellin MJ, Young CE, Gruen DM, Aratono Y and DeWald AB, 1985: Surf. Sci. **151**, 477

Peterson NL, 1975: *Diffusion in Solids - Recent Developments* (Academic Press, New York) 115

Peterson NL, Barr LW and Le Claire AD, 1973: J. Phys. C **6**, 2020

Pickering HW, 1976: J. Vac. Sci. Technol. **13**, 618

Piller RC and Marwick AD, 1978: J. Nucl. Mater. **71**, 309

Qu Z and Xie TS, 1988: Surf. Sci. **194**, L127

Rehn LE, 1982: Mat. Res. Soc. Symp. Proc. **7**, 17

Rehn LE and Lam NQ, 1987: J. Mater. Eng. **9**, 209

Rehn LE and Okamoto PR, 1983: *Phase Transformations during Irradiation*, ed. F.V. Nolfi, Jr. (Applied Science Publishers, London) 247

Rehn LE and Okamoto PR, 1987: Mater. Sci. Forum **15-18**, 985

Rehn LE and Wiedersich H, 1980: Thin Solid Films **73**, 139

Rehn LE, Danyluk S and Wiedersich H, 1979: Phys. Rev. Lett. **43**, 1764

Rehn LE, Boccio VT and Wiedersich H, 1983: Surf. Sci. **128**, 37-50

Rehn LE, Lam NQ and Wiedersich H, 1985: Nucl. Instrum. Methods B **7/8**, 764

Rehn LE, Hoff HA and Lam NQ, 1986: Phys. Rev. Lett. **57**, 780

Robinson MT, 1983: J. Appl. Phys. **54**, 2650

Robinson MT, 1993: Mat. Fys. Medd. Dan. Vid. Selsk. **43**, 27

Robrock KH, 1983: *Phase Transformations during Irradiation* ed. FV. Nolfi, Jr. (Applied Science Publishers, London) 115

Rosen M and Bassel RH, 1984: Nucl. Instrum. Methods B **2**, 592

Rosen M, Mueller GP and Fraser WA, 1983: Nucl. Instrum. Methods **209/210**, 63

Rothman SJ, 1983: *Phase Transformations during Irradiation*, ed. F.V. Nolfi, Jr. (Applied Science Publishers, London) 189

Rothman SJ, Lam NQ, Sizmann R and Bisswanger H, 1973: Radiat. Eff. **20**, 223

Roush ML, Andreadis TD and Goktepe OF, 1981: Radiat. Effects **55**, 119

Roush ML, Goktepe OF, Andreadis TD and Davarya F, 1982: Nucl. Instrum. Methods **194**, 611

Roush ML, Davarya F, Goktepe OF and Andreadis TD, 1983: Nucl. Instrum. Methods **209/210**, 67

Russell WA, Papanastassiou DA and Tombrello TA, 1980: Radiat. Eff. **52**, 5

Sarholt-Kristensen L, Andreev A, Johansen A, Andersen HH and Johnson E, 1992: Nucl. Instrum. Methods B **68**, 258

Schiffman B and Polak M, 1986: Surf. Interf. Anal. **9**, 151

Schmid M, Biedermann A, Stadler H, Slama C and Varga P, 1992: Appl. Phys. A **55**, 468

Schorn RP, Zaki Ewiss MA and Hintz E, 1988: Appl. Phys. A **46**, 291

Schou J, 1992: Dr. Sci. Thesis, Odense University

Seeger A, 1975: Phys. Stat. Sol. A **28**, 157

Sethuraman AR, 1991: Nucl. Instr. and Meth. B **54**, 513

Sethuraman AR, Reucroft PJ, De Angelis RJ, Kim DK and Okazaki K, 1990: J. Vac. Sci. Technol. A **8**, 2255

Shapiro MH, Haff PK, Tombrello TA and Harrison DA, 1985: Nucl. Instrum. Methods B **12**, 137

Shapiro MH, Tombrello TA and Harrison DE, 1988: Nucl. Instrum. Methods B **30**, 152

Sharp JV, 1969: UKAEA Report AERE-R **6267**

Shewmon PG, 1963: *Diffusion in Solids* (McGraw-Hill, New York)

Shimizu H, Ono M and Nakayama K, 1975: J. Appl. Phys. **46**, 460

Shimizu N and Hart SR, 1982: J. Appl. Phys. **53**, 1303

Shimizu R, 1987: Nucl. Instrum. Methods B **18**, 486

Sigmund P, 1969a: Phys. Rev. **184**, 383; **187**, 768

Sigmund P, 1969b: Appl. Phys. Lett. **14**, 114

Sigmund P, 1969c: Rad. Effects **1**, 15

Sigmund P, 1979: J. Appl. Phys. **50**, 7261

Sigmund P, 1980: J. Vac. Sci. Technol. **17**, 396

Sigmund P, 1981: *Sputtering by Particle Bombardment I*, Top. Appl. Phys. **47**, ed. R. Behrisch (Springer-Verlag, Heidelberg) 9

Sigmund P, 1987a: Nucl. Instrum. Methods B **18**, 375

Sigmund P, 1987b: Nucl. Instrum. Methods B **27**, 1

Sigmund P, 1988: Nucl. Instrum. Methods B **34**, 15

Sigmund P, 1993a: *Ionization by Heavy Charged Particles*, ed. R.A. Baragiola, NATO ASI Series (Plenum Press, New York) 59

Sigmund P, 1993b: Nucl. Instrum. Methods B, **82**, 192

Sigmund P and Claussen C, 1981: J. Appl. Phys. **52**, 990

Sigmund P and Gras-Marti A, 1980: Nucl. Instrum. Methods **168**, 389

Sigmund P and Gras-Marti A, 1981: Nucl. Instrum. Methods **182/183**, 25

Sigmund P and Oliva A, 1993: Nucl. Instrum. Methods B **82**, 242

Sigmund P and Sckerl MW, 1993: Nucl. Instrum. Methods B **82**, 269

Sigmund P, Oliva A and Falcone G, 1982: Nucl. Instrum. Methods **194**, 541; B **9** (1985) 354

Sigmund P, Robinson MT, Baskes MI, Hautala M, Cui FZ, Eckstein W, Yamamura Y, Hosaka S, Ishitani T, Shulga VI, Harrison DE, Chakarov IR, Karpuzov DS, Kawatoh E, Shimizu R, Valkealahti S, Nieminen RM, Betz G, Husinsky W, Shapiro MH, Vicanek M and Urbassek HM, 1989: Nucl. Instrum. Methods B **36**, 110

Sizmann R, 1978: J. Nucl. Mater. **69 & 70**, 386

Stahle CM and Helms CR, 1992: J. Vac. Sci. Technol. A **10**, 3239

Swalin RA, 1962: *Thermodynamics of Solids* (Wiley, New York), ch. 9

Swartzfager DG, Ziemecki SB and Kelley MJ, 1981: J. Vac. Sci. Technol. **19**, 185

Szymonski M, 1980: Appl. Phys. **23**, 89

Szymonski M, Bhattacharya RS, Overeijnder H and de Vries AE, 1978: J. Phys. D **11**, 751

Taglauer E, 1982: Appl. Surf. Sci. **13**, 80

Taglauer E and Heiland W, 1978: Appl. Phys. Lett. **33**, 950

Tanaka A, Takemori M and Homma T, 1983: J. Elect. Spect. Rel. Phen. **32**, 277

Tang S and Lam NQ, 1989: Surf. Sci. **223**, 179

Tang S, Lam NQ and Yacout A, 1990: Surf. Sci. **231**, 253

Thomas MP and Ralph B, 1983: Surf. Sci. **124**, 129

Thompson M, 1968: Phil. Mag. **18**, 377

Titov VV, 1979: Zh. Tekh. Fiz. **49**, 844 (Sov. Phys. J. Tech. Phys. **24**, 488)

Urbassek HM and Conrad U, 1992: Nucl. Instrum. Methods B **69**, 413

Urbassek HM and Conrad U, 1993: Nucl. Instrum. Methods B **73**, 151
Urbassek HM and Vicanek M, 1988: Phys. Rev. B **37**, 7256
Valeri S, di Bona A, Ottaviani G and Procop M, 1991: Nucl. Instrum. Methods. B **59/60**, 98
van Wyk GN, du Plessis J and Taglauer E, 1991: Surf. Sci. **254**, 73
Varga P and Taglauer E, 1981: J. Nucl. Mater. **111/112**, 726
Vicanek M and Sigmund P, 1994: To be published
Vicanek M and Urbassek HM, 1988: Nucl. Instrum. Methods B **30**, 507
Vicanek M, Jiménez-Rodríguez JJ and Sigmund P, 1989: Nucl. Instrum. Methods B **36**, 124
Vicanek M, Conrad U and Urbassek HM, 1993: Phys. Rev. B **47**, 617
Wadsworth M, Armour DG, Badheka R and Collins R, 1990: Int. J. Numerical Modelling **3**, 157
Wagner W, Rehn LE and Wiedersich H, 1982: Philos. Mag. A **45**, 957
Wagner W, Rehn LE, Wiedersich H and Naundorf V, 1983: Phys. Rev. B **28**, 6780
Waite TR, 1957: Phys. Rev. **107**, 463
Watson CC and Haff PK, 1980: J. Appl. Phys. **51**, 691
Weathers DL, Spicklemire SJ, Tombrello TA, Hutcheon ID and Gnaser H, 1993: Nucl. Instrum. Methods B **73**, 135
Webb R, Carter G and Collins R, 1978: Rad. Effects **39**, 129
Wehner GK, 1955: J. Appl. Phys. **26**, 1056
Wehner GK, 1977: Appl. Phys. Lett. **30**, 185
Weigand P, Novacek P, van Husen G, Neidhart T, Mezey LZ, Hofer W and Varga P, 1992: Nucl. Instrum. Methods B **64**, 93
Wiedersich H, 1972: Radiat. Eff. **12**, 111
Wiedersich H, 1983: *Surface Modification and Alloying*, ed. J.M.Poate et al. (Plenum, New York) 261
Wiedersich H, 1985: Nucl. Instrum. Methods B **7/8**, 1
Wiedersich H and Lam NQ, 1983: *Phase Transformations during Irradiation*, ed. F.V. Nolfi, Jr. (Applied Science Publishers, London) 1
Wiedersich H, Okamoto PR and Lam NQ, 1979: J. Nucl. Mater. **83**, 98
Winterbon KB, Sigmund P and Sanders JB, 1970: Mat. Fys. Medd. Dan. Vid. Selsk. **37**, no. 14
Winters HF and Sigmund P, 1974: J. Appl. Phys. **45**, 4760
Winters HF and Taglauer E, 1987: Phys. Rev. B **35**, 2174
Wirth Th, Atzrodt V and Lange H, 1984: phys. stat. sol. A **82**, 459
Wirth Th, Procop M and Lange H, 1986: Vacuum **36**, 433
Wittmaack K, 1991: *Sputtering by Particle Bombardment III*, Top. Appl. Phys. **64**, ed. R. Behrisch and K. Wittmaack (Springer, Heidelberg) 161
Wollenberger HJ, 1970: *Vacancies and Interstitials in Metals*, ed. A Seeger et al, (North-Holland, Amsterdam) 215
Wollenberger HJ, 1987: Mater. Sci. Forum **15-18**, 1363
Wucher A and Reuter W, 1988: J. Vac. Sci. Technol. A **6**, 2316
Wynblatt P and Ku RC, 1979: *Interfacial Segregation*, ed. W. C. Johnson and J. M. Blakeley (American Society for Metals, Metals Park, Ohio) 115
Yacout AM, Lam NQ and Stubbins JF, 1989: Nucl. Instrum. Methods B **42**, 49
Yamamura Y and Muraoka K, 1989: Nucl. Instrum. Methods B **42**, 175
Zee RH, Guinan MW and Kulcinski GL, 1983: J. Nucl. Mater. **114**, 190
Zhu H, Lam NQ, Devanathan R and Sabochick MJ, 1992: Mat. Res. Soc. Symp. Proc. **235**, 533; and to be published
Ziegler JF, Biersack JP and Littmark U, 1985: *The Stopping and Range of Ions in Solids* (Pergamon, New York)

Theoretical Models for Sputtering and Desorption of Bio-Organic Molecules under Collisional and Electronic Excitation by Ion Impact

By C.T. Reimann
Division of Ion Physics, Department of Radiation Sciences
Uppsala University, Box 535, S-751 21 Uppsala, Sweden

Synopsis

Particle-beam excitation of materials composed of thermally labile bio-organic molecules causes sputtering into the gas phase of intact molecules as well as their fragments. The desorbed ionic components, easily detected, form the basis for mass spectrometric applications. Keen interest in understanding desorption phenomena has been driven by the prospects for measuring increasingly higher molecular masses. The key question is: How can a fragile bio-organic molecule be desorbed intact by an inherently destructive incident energetic ion? In this paper, several prominent desorption theories are reviewed. Models involving 'collective' motion, such as the 'pressure pulse' model, seem most effective at explaining how large molecules acquire enough momentum to be desorbed without simultaneously acquiring enough internal energy to be dissociated. Weaknesses in the current state of our knowledge are identified. In particular, a lack of comprehensive knowledge on ejection of neutral molecules strongly impedes the validation of theoretical models.

Contents

1 Introduction

It is well known that sputtering of bio-molecular ions may be induced by energetic particle impacts on organic targets. Reports on MeV-fission-fragment-induced desorption were first published by Torgerson et al. (1974) and Macfarlane & Torgerson (1976). Meanwhile, Benninghoven et al. (1976) observed that keV atomic ions can also induce desorption of biomolecular ions. Finally, scattered works have appeared on keV cluster- and molecular-ion-induced desorption of molecules from organic targets. Recent examples include the works of Ledbetter et al. (1987), Mahoney et al. (1991), Kaufmann et al. (1992), and Martens et al. (1992).

In a generic ion impact desorption experiment, energetic projectiles impinge on an organic solid composed of bio-molecules which are bound together by hydrogen, ion-pair, and van der Waals bonds. A typical cohesive binding energy is of the order of a few electron volts (eV) per molecule. Close to the projectile path through the solid, the deposited energy density is extremely high and causes extensive fragmentation of target molecules. But over time, locally deposited energy diffuses outwards from the initially excited region. Eventually, several different kinds of species are desorbed from the target, including neutral and charged fragments and whole molecules. The observation of intact bio-molecule ejection has proved particularly interesting in view of the inherently damaging nature of the incident energetic projectiles. The readily detected desorbed ions form the basis of powerful mass spectrometric techniques applicable in the biological sciences.

A desorption event in response to an energetic projectile impact is the end result of a large number of processes, all of which are in principle amenable to theoretical treatment. One would begin by modelling energy deposition and the creation of kinetic energy in the excited solid. In the case of keV atomic and cluster projectile impact, target particle motion is directly excited, but in the case of MeV atomic projectiles, target particles are set in motion indirectly through relaxation of electronically deposited energy. This conversion occurs via relaxation of repulsive electronic states (as in the case of a Coulomb explosion, for example), molecular expansion after vibrational excitation, or chemical energy release. One would next model what could be referred to as 'direct' desorption processes in which a particular molecule is ejected due to its own repulsive interactions with neighbouring molecules. One would then proceed to model what could be referred to as 'indirect' desorption processes which reflect the spatial evolution of energy to regions quite far beyond that in which energy is initially deposited. Finally, one would model the further evolution that may take place in energized species during and after desorption. Such further evolution may modulate the charge state and degree of clustering or fragmentation, determining critically what species is eventually detected far away from the sample.

A brief consideration of salient experimental results provides strong indications that indirect desorption mechanisms are of dominant importance for desorption of organic materials under particle beam excitation. Consider first the case of MeV atomic ions incident on organic solids. A typical example is 90 MeV $^{127}\mathrm{I}^{14+}$ incident on a leucine target (MW 131 u). The electronic stopping power $(dE/dx)_\mathrm{e}$ of the ions in this target is about 1000 eV/Å; approximately half of the ion energy is deposited within an 'infratrack' of radius 5.6 Å (Brandt & Ritchie, 1974), giving an energy density there of about 5.1 eV/Å^3. The volume occupied per leucine molecule is approximately 125 Å^3, meaning that each leucine molecule in the infratrack receives 640 eV of energy. Since the total internal molecular binding energy of leucine is only about 100 eV, molecules in the infratrack will be completely fragmented. Because energetic secondary electrons leave the infratrack and cause additional modifications to surrounding target material, the radius 5.6 Å can be considered to be a lower limit on the size of the region which is completely damaged by the incident ion. Salehpour et al. (1986) have examined the fluence dependence of the desorbed leucine ion signal, which they have used to extract 'damage radii' of around 30 Å. Because the ion yield may not be representative of the much larger neutral yield, the interpretation of the ion fluence dependence in terms of damage is tentative, and 30 Å should be regarded as a rough upper limit on the size of the region which is completely damaged by the incident ion. Salehpour et al. (1986) have also measured the neutral ejection yield of leucine molecules to be about 1200 leucine molecules per incident ion. If the desorbed volume is assumed to be a half-sphere, then the radius of this volume is around 40 Å, larger than the above estimates of the damaged area around the ion track and much larger than the size of the primary excited region of the ion track. Thus, a large number of ejected intact molecules come from outside the region of the target which is directly excited and damaged by the incident energetic particle.

Consider next the case of keV atomic projectiles incident on an organic material. Such ions slow down mainly by undergoing screened elastic nuclear collisions which set target atoms in motion. (A small fraction of the projectile energy is lost in ionization events as well.) Whitlow et al. (1987) have performed computer simulation studies of the slowing down of 10 keV Xe ions in a biomolecular target (relative atomic composition: C_3H_5NO, 71 u). In these simulations, although the range of this projectile into the target is 200 Å, at a distance of only 10 Å laterally away from the ion track the deposited energy density is already an order of magnitude less than it is at the impact point. Wong et al. (1985) measured the absolute sputtering yield of 6 keV Xe ions incident on liquid glycerol (92.09 u) and found it to be in excess of 1000 glycerol molecules per incident ion. If the desorbed material is assumed to come from a contiguous volume in the form of a half-sphere, then the diameter of this volume is at least 80 Å, quite a bit larger than the apparent radial extent of the collision cascade. Even the assumption that the whole energized region of the target is ejected as a gas jet would only account for about half of the observed ejection yield. Again, one concludes that a large number of ejected intact molecules come from outside the region of the target which is directly excited by the incident energetic particle.

Finally, consider the case of keV and MeV clusters impacting organic targets. Ledbetter et al. (1987) have bombarded tobacco mosaic virus with energetic water clusters such as 275 keV $(H_2O)_{200}H^+$. The impact of such an ion on this organic target generally removed a 160 Å long 'slice' of the 180 Å diameter cylindrical virus, the slice being perpendicular to the long cylindrical axis. The water cluster ions employed in the virus bombardment study are thought to be 'ice balls' rather than 'snow flakes', meaning that their diameters range from 23 to 50 Å depending on their exact shape. Each oxygen atom in the projectile has a kinetic energy of about 1.2 keV, and neglecting cluster effects, such an atom would deposit its energy in a volume of diameter 30 to 40 Å based on simple stopping power considerations and a primitive collision cascade picture. Comparing the volume of the initially energized region of the virus to the volume of the impact-induced crater, it is seen that 90 to 95% of the desorbed molecules come from outside the initially energized region.

Johnson (1987) performed an extensive review of theoretical models extant at that time, and Sundqvist (1991) and Johnson & Sundqvist (1992) have given short summaries of the current experimental and theoretical status of biomolecular desorption. However, there does not seem to exist any extensive and comprehensive current review of theories of particle impact induced organic molecule desorption. In this article, such a review is attempted. The main theories which are covered are: collision cascade; ion track; evaporative thermal spike; bulk desorption (gas-flow); shock wave; and pressure pulse. In each case, the theory is described in some detail, and its validity in various arenas of applicability is specified. Because currently available experimental evidence suggests that ejected molecules come from relatively far away from the region that is initially energized, it is concluded that ejection mechanisms characterized by 'indirectness' or 'collective motion imparted at a distance' are currently the most satisfactory. Consequently, bulk desorption,

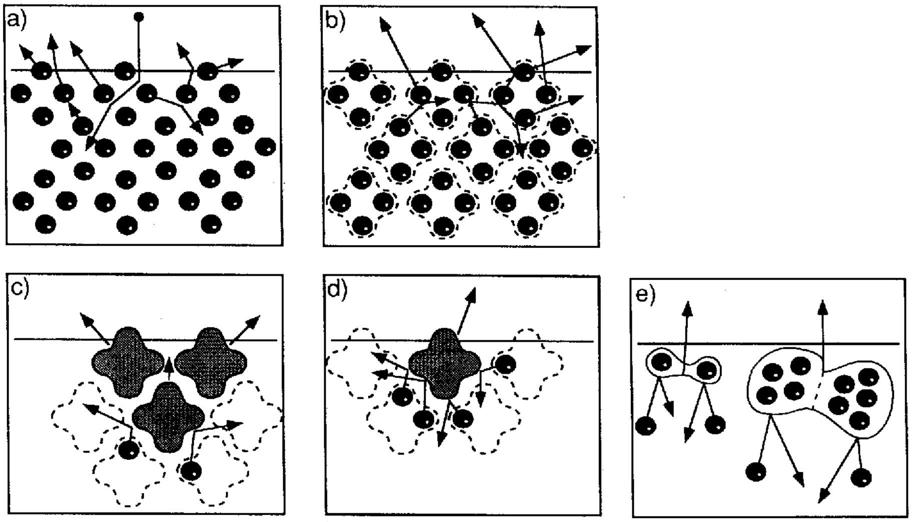

Figure 1. Schematic diagrams of collision cascade sputtering of atoms and molecules. a) Collision cascade in an atomic solid. Five atoms are sputtered. b)-d) Collision cascades in an organic solid. b) At early times, the cascade has an atomic character. c) At late times, the cascade has a molecular character. d) One molecule being ejected by several atoms impacting from below. e) Schematic diagram of statistical models. Left, model of Haring et al. (1987). Right, model of Hoogerbrugge & Kistemaker (1987).

shock waves, and pressure pulses describe the widest range of data, though other models discussed are not without their regimes of applicability. Molecular dynamics simulation results are included as theory and are discussed where applicable, and it is seen that well-designed simulations provide crucial insight into both experimental and analytical theoretical results. It is finally noted that the lack of comprehensive data on ejection of neutral bio-organic molecules is a strong impediment to evaluating the validity of theoretical models. Therefore, experimentalists are directed to devote more effort to probing the neutral ejecta.

2 Collision-Cascade Desorption

The collision cascade model is considered to be germane mainly for cases in which keV atomic ions are incident on solid matter. In this 'low velocity' regime, the projectile velocity v_0 is less than the Bohr velocity v_{Bohr}, and the incident ion energizes atoms in the target through screened elastic nuclear collisions. Target atoms, set into motion, undergo subsequent collisions, setting a second generation of atoms into motion. The total ensemble of energized atoms is referred to as a 'collision cascade' as long as the energy density is not 'too high'. The energy density is considered to be too high if most of the atoms in the collisionally energized region of the target are in motion, or if moving atoms tend to collide with other moving atoms rather than with atoms at rest. A schematic diagram of an atomic collision cascade is shown in fig. 1a.

Collision cascade theory for atomic solids is well-established and has been described at length by Sigmund (1969, 1969a, 1981). A Boltzmann integral equation approach is employed with its underlying assumption of 'molecular chaos' and randomization of the particle coordinates and velocities after each collision according to some statistical distribution function. Solution of the Boltzmann integral equation leads to the conclusion that, inside the solid, the distribution of recoil atoms is isotropic and is characterized by a kinetic energy spectrum $N(E) \propto E^{-2}$. This is the result of a series of two-body collisions between moving and stationary atoms. Taking into account energy lost by atoms moving towards the surface and the surface barrier, total and differential sputtering yields are calculated. For rather low incident particle kinetic energies and high desorbed atom kinetic energies, the desorbed atom kinetic energy spectrum scales as E^{-2}. The peak in the energy distribution is located at $U/2$, where U is the surface binding energy. The sputtering yield is proportional to the nuclear stopping power, $(dE/dx)_{\rm n}$. This model describes quite well the sputtering of metal targets by keV atomic ions. Falcone (1987, 1990) has presented additional comments on collision cascade theory.

The question of how collision cascade theory should be generalized to the case of a molecular solid is in detail a complex one. Hoogerbrugge and Kistemaker (1987) have pointed out that the initial, more energetic portion of the collision cascade can be described by the atomic collision cascade model, but that 'in a later, low energy, stage of the cascade the presence of relatively strong bonds forces the complete molecules to take part in the collisions and the atomic picture loses its value.' Schematic diagrams showing the situations at these extremes in time are shown in fig. 1b,c. One theoretical approach to collision cascade sputtering of molecules is a 'statistical' model in which a point of view intermediate to the atomic and molecular pictures is taken. In this model, a molecule at the surface is assumed to be impacted from below by a number of atoms, and these impacting atoms are assumed to have a kinetic energy distribution given by the atomic collision cascade picture, $N(E) \propto E^{-2}$. This simplified situation is shown in fig. 1d.

Haring et al. (1987) have calculated kinetic energy and angular distributions of desorbed diatomic molecules using the statistical model, and they have generalized their results to the cases of larger polyatomic molecules. Their model is based closely on a similar model due to Können et al. (1975), which describes the desorption of clusters formed from separate atoms on the surface. Briefly, each atom ('target atom') in the polyatomic molecule to be desorbed is assumed to be impacted by a moving atom from the substrate below. The target atom is assumed to gain kinetic energy as though it were a participant in a collision cascade; that is, after the collision, it is characterized by an isotropic velocity distribution and kinetic energy spectrum $N(E) \propto E^{-2}$. The momenta acquired by the target atoms are assumed to be uncorrelated. The resulting distribution in total momentum and internal energy is given as an integral over a product of the single atom momentum distribution functions $\chi(p)$ with the proviso that the total internal energy must not exceed the binding energy of the molecule. The final desorbed molecule parameters are calculated as in standard collision cascade theory. The chief result of this theory is as follows: for a polyatomic molecule consisting of m atoms, each of which is impacted by one recoil atom from a collision cascade in the substrate, the desorbed molecule kinetic energy spectrum for large kinetic energies scales as $E^{0.5-2.5m}$. For $m = 1$, the kinetic energy distribution for high kinetic energies reduces to the usual form, which is proportional to E^{-2} for the atomic collision cascade. The steeper energy distribution for polyatomics is related to the possibility for fragmentation if the internal energy is too great. Urbassek (1987) has made additional comments on the sputtering of molecules by a collision cascade.

Hoogerbrugge & Kistemaker (1987) have extended the model of Haring et al. (1987) in the sense that a polyatomic molecule containing $m > 2$ atoms is considered to be impacted by exactly two atoms originating in a collision cascade. Each atom from below is assumed to collide with a portion, or 'sub-unit', of the molecule to be desorbed. A schematic diagram of the proposed idea is shown in fig. 1e. Each sub-unit is considered to receive a correlated momentum as a whole, but the momenta of the two sub-units are assumed to be uncorrelated. For a molecule composed of two sub-units, momentum space analysis yields an asymptotic kinetic energy spectrum which is the same as that predicted by Haring et al. (1987) for a diatomic molecule impacted by two collision cascade atoms. That is, the desorbed molecule kinetic energy distribution is proportional to $E^{-4.5}$ for high kinetic energies.

Garrison (1983) has employed a classical dynamics simulation to demonstrate that collision cascade sputtering of organic molecules is indeed feasible. The simulated situation was that of a 1 keV Ar^+ incident upon a Ni(001) crystal on the surface of which had been adsorbed flat organic molecules as large as $C_{24}H_{12}$ (300.4 u). The simulation results suggest that a cascade in the underlying solid is capable of ejecting large organic admolecules from the surface. However, such admolecules have to be struck simultaneously by two or three atoms from the underlying solid in order for ejection of the intact molecule to take place. This is a good example of what appears to be a general principle: desorption of a large molecular moiety with sufficiently low internal energy to avoid fragmentation requires some kind of 'collective' desorption process, in this case a fortuitous push in the same general direction by several atoms colliding from below.

Well-designed classical dynamics simulations may be employed in order to gain an intuitive feel for the validity of statistical models in describing molecular desorption during collision cascades. Shapiro & Tombrello (1992) have reported results of classical dynamics studies of ejection of dimers and larger clusters from ion bombarded Cu. Those authors judge that statistical models even of dimer ejection are too simplistic to adequately describe the cluster ejection process. In particular, the surface is not well-defined when cluster ejection occurs, and each atom in the cluster undergoes multiple (and probably correlated) collisions with various underlying and neighbouring atoms. The possible parallels between cluster desorption and molecule desorption, exploited to generate the statistical models discussed above, are obvious but have not yet been validated extensively. Probably classical dynamics simulations are an important key to understanding collision cascade desorption of molecules from surfaces.

In the general arena of bio-organic molecule desorption, collision cascade theory has mostly been applied to the case of sputtering of molecular ions from glycerol, a commonly employed fast atom bombardment (FAB) matrix. Typically, no consideration is given to the fact that one detects desorbed ions but compares the measurements with results of theories of neutral particle ejection. One focus of experimental work has been on measuring the desorbed ion kinetic energy distribution in the limit of large kinetic energies. Generally, asymptotic power laws of the form E^{-x} are observed. A good example of this work is that of Hoogerbrugge et al. (1987) who have studied the emission of ions like Na^+, $GlyNa^+$, and $(NaCl)_2Na^+$ from a glycerol matrix. The theoretical results of Haring et al. (1987) and Hoogerbrugge & Kistemaker (1987) were generalized to obtain the number of 'hits' necessary to desorb an ion: $m = (x + 0.5)/2.5$. For the ions listed above, $m = 1.0$, 2.1, and 3.3 were respectively obtained. In general, m was rather close to being an integer, supporting its interpretation as a number of 'hits'. Since some of the molecular ions contained more than three atoms, a 'hit' is considered to involve a group or 'sub-unit' of atoms in the molecule.

Even though collision cascade desorption probably does occur for these glycerol liquid matrices, the model does not account for the dominant fraction of the yield. Yen et al. (1992) and Yen (1992) have studied the ion yield from pre-formed analyte molecular ions bound to the surface of a glycerol liquid drop by a surfactant. The ion sputtering yield scales as $[(dE/dx)_\mathrm{n} - C]^2$, where $(dE/dx)_\mathrm{n}$ is the nuclear stopping power and C is a threshold parameter. By contrast, the collision cascade model predicts linear scaling in $(dE/dx)_\mathrm{n}$. Also, Kelner & Markey (1984) show clear evidence that the peak in the kinetic energy spectrum of desorbed poly (ethyleneglycol) ions (133 u) varies by more than a factor of two as the Ar^+ projectile energy varies from 2 to 4 keV, also at odds with the predictions of the collision cascade model. It is widely suspected that low energy desorbed molecular ions from keV ion-bombarded glycerol are produced by a thermal 'bulk desorption' type mechanism or a pressure pulse, and that only the high energy sputtered particles reflect a collision cascade that occurs early on before the surface is catastrophically disrupted. The ideas of bulk desorption and pressure pulses are discussed below.

Studies have been performed by Standing et al. (1982) and Ens (1992) on bombardment of solid organic samples by 1 to 16 keV primary alkali ions. For the heavier alkali ions, Na^+, K^+, and Cs^+, ion sputtering yields scale as $(dE/dx)_{\mathrm{n}}^3$, which is at variance with the predictions of simple collision cascade theory. For the relatively light Li^+ projectile, the electronic energy loss also plays a role, since $(dE/dx)_{\mathrm{e}}$ and $(dE/dx)_{\mathrm{n}}$ are comparable. Even so, the sputtering yield in this case scales as a linear combination of $(dE/dx)_{\mathrm{n}}^3$ and $(dE/dx)_{\mathrm{e}}^2$. For solid organic targets, it also seems that collision cascades do not play a dominant role in the ejection of bio-organic molecules.

3 Hit Theory Description of Desorption

The 'hit theory' approach to organic molecule desorption is designed for cases in which incident MeV atomic ions are responsible for the initial excitation. Such ions deposit energy electronically according to the electronic stopping power, $(dE/dx)_{\mathrm{e}}$. About half of the deposited energy appears in a cylindrical 'infratrack' of radius of the order of 5 Å, and the other half of the deposited energy appears in a cylindrical 'ultratrack', which is of considerably larger radius. The chief means of depositing energy in the ultratrack is by energetic secondary electrons ('delta rays'), which emanate from the infratrack and create additional electronic excitation and ionization events in the surrounding material. The central idea of hit theory is that if a molecule near the surface receives at least i_{min} hits, i.e. if at least i_{min} secondary electrons interact with it, then the molecule is desorbed, possibly as an ion. Hit theory has been employed to account for the observed $(dE/dx)_{\mathrm{e}}$ dependence of the ion desorption yield. The general idea of hit theory was introduced by Katz (1968). The application of hit theory to desorption, giving the ion track model, was introduced by Hedin et al. (1985) and has been recapitulated by Johnson (1987).

A schematic diagram of an organic molecule bound to a surface is shown in fig. 2. Both inter- and intra-molecular bonds are shown. The molecule is assumed to be bathed in a flux of secondary electrons due to the nearby passage of an MeV atomic ion through the material. The desorption of the intact molecule under these conditions requires the preservation of all internal bonds and the breaking (excitation to an anti-bonding state) of some of the external bonds. The charge of the

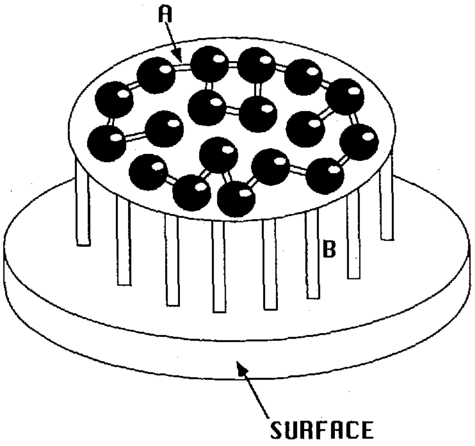

Figure 2. Schematic diagram of an organic molecule showing both internal bonds (A) and bonds to surrounding molecules in the surface (B). Successful desorption requires breaking all the bonds B while leaving all bonds A intact. Ionization will require some additional bonding adjustments.

desorbed species, if not predetermined, depends on some additional adjustments in bonding. Hit theory is basically a statistical description of these bonding modifications. In deriving the hit theory desorption model, the average number of hits experienced by a molecule must be calculated. Let $\eta_{\mathrm{F}}(r)$ be the average number of internal bonds broken in a molecule located a perpendicular distance r from the incident ion track. Correspondingly, $\eta_{\mathrm{D}}(r)$ will be the average number of external bonds broken. One may write:

$$\eta_{\mathrm{F}}(r) = \frac{\varepsilon(r)}{n_{\mathrm{M}} W_{\mathrm{F}}}; \; \eta_{\mathrm{D}}(r) = \frac{\varepsilon(r)}{n_{\mathrm{M}} W_{\mathrm{D}}} \tag{1}$$

where $\varepsilon(r)$ is the energy density deposited by secondary electrons at a distance r from the ion track, n_{M} is the molecular number density, and W is a bond breaking energy. The nature of $\varepsilon(r)$ was discussed by Hedin et al. (1985). They pointed out that the detailed nature of secondary electron energy loss and the kinetic energy distribution of the secondary electrons give rise to a simple approximation for $\varepsilon(r)$:

$$\varepsilon(r) \propto \frac{(dE/dx)_{\mathrm{e}}}{r^2}. \tag{2}$$

Next a key assumption is made: The number of hits experienced by a molecule is described by the Poisson distribution. Then, if the average number of hits is η, the

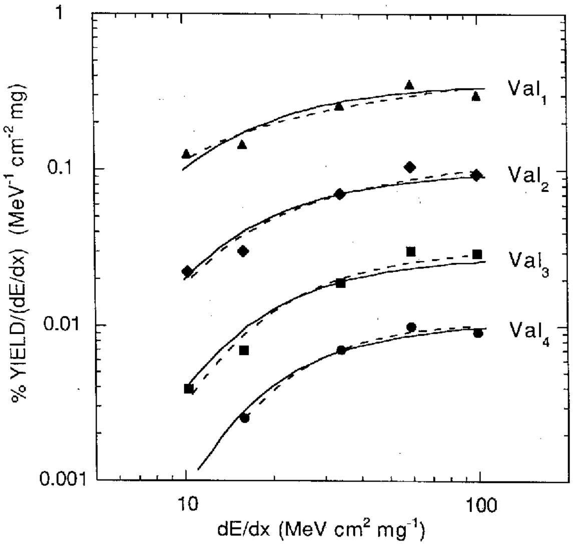

Figure 3. Ion sputtering yield divided by electronic stopping power $(dE/dx)_e$ vs. $(dE/dx)_e$ for valine monomers and clusters from MeV-heavy-atomic-ion-excited valine. For experimental details, see Hedin et al. (1985). The solid lines represent the results of the ion track model of Hedin et al. (1985). In the order from monomer to tetramer, the number of hits required to fit the data is 4, 5, 6 and 7 respectively. The dashed lines represent the results of an evaporative thermal model by Lucchese (1987). Both of these models are discussed in the text.

probability of a molecule experiencing exactly i hits is:

$$\mathrm{Pr}(i) = \frac{\eta^i}{i!}e^{-\eta} \tag{3}$$

An expression for the desorption yield of molecular ions can then be written. It assumes that only molecules receiving no damage hits are desorbed intact, and that desorption requires at least i_{min} hits of the desorptive type. Two details are specified as proportionality constants: the probability that the molecule is desorbed as an ion is P_{ion}, and the average depth from which ion desorption occurs is Z_{avg}. The desorption yield is then given as an integral over the surface of the sample with the ion track located at the center:

$$Y = P_{\mathrm{ion}} Z_{\mathrm{avg}} n_{\mathrm{M}} \int_{r_{\mathrm{d}}^2}^{\infty} \pi d(r^2) e^{-\eta_{\mathrm{F}}(r)} \sum_{i=i_{\mathrm{min}}}^{\infty} \frac{\eta_{\mathrm{D}}^i(r)}{i!} e^{-\eta_{\mathrm{D}}(r)}. \tag{4}$$

The lower integration limit, r_{d}, takes into account that a direct collision between the incident ion and the target molecule causes complete fragmentation; r_{d} is roughly

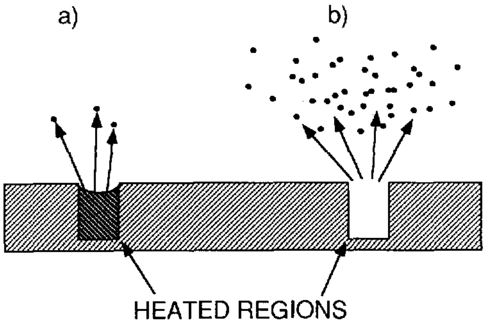

Figure 4. Schematic diagrams of thermal desorption mechanisms. a) Activated desorption (i.e. evaporation); b) Bulk desorption after an irreversible transition to the gas phase.

equal to the radius of the target molecule. The integral diverges for $i_{\mathrm{min}} = 1$, but in practice, fits to data have yielded $i_{\mathrm{min}} > 1$. For large $(dE/dx)_{\mathrm{e}}$, the predicted stopping power scaling is $Y \propto (dE/dx)_{\mathrm{e}}$. This scaling stems from the dependence of $\varepsilon(r)$ on r and $(dE/dx)_{\mathrm{e}}$, as shown in eq. 2 above. For smaller $(dE/dx)_{\mathrm{e}}$, a steeper scaling is predicted, $Y \propto (dE/dx)_{\mathrm{e}}^n$, with $n > 1$.

Hedin et al. (1985) successfully employed hit theory and the ion track model to account for the $(dE/dx)_{\mathrm{e}}$ dependencies of ion yields for a number of organic substances. Shown in fig. 3 is a plot of the $(dE/dx)_{\mathrm{e}}$ dependence of the desorption of ions of valine monomers (117 u) and clusters (up to the tetramer). The ion yield is divided by $(dE/dx)_{\mathrm{e}}$ and plotted against $(dE/dx)_{\mathrm{e}}$. The rising and saturating behavior with respect to $(dE/dx)_{\mathrm{e}}$ occurs just as predicted by the ion track model. If the minimum number of hits causing desorption, i_{min}, is employed as a fitting parameter, then it turns out that the larger the cluster, the larger i_{min}. The conclusion is that more massive target molecules require a greater number of hits in order to be desorbed.

Despite the success of the ion track model in describing ion yield scaling with $(dE/dx)_{\mathrm{e}}$, the general usefulness of the model seems limited. It does not account for the asymmetric ion emission patterns observed by Ens et al. (1989) in off-normal MeV ion incidence experiments. The model makes reference to ionization only through a proportionality constant, so it cannot account for the observation by Hedin et al. (1987) that the yield of small neutral biomolecules obeys a cubic scaling law, Y $\propto (dE/dx)_{\mathrm{e}}^3$ (for bulk desorption, a possible dependence of Z_{avg} on $(dE/dx)_{\mathrm{e}}$ could be considered, however). The similarity noted by Ens et al. (1989a) and others between secondary ion mass spectra from keV and MeV atomic-ion-bombarded organic samples must be regarded as a mystery from the standpoint of the ion track model, considering that very few secondary electrons are emitted in keV atomic ion impacts. Finally, the most useful aspect of the ion track model is that it may be regarded as a description of the small amount of ionization which occurs along with the dominant desorption of neutrals. However, it may be anticipated that the neutral desorption process will modulate the ionization and neutralization processes, and the ion track model fails to address this issue.

4 Thermal Models of Desorption

Thermal models of desorption, which may be important in a variety of types of particle-surface interactions, are easily described qualitatively. After an ion impact, energy is deposited locally within a small volume. As a result of either collisions or coupling of electronic energy into the nuclear coordinates, target particles receive a certain amount of kinetic energy. If nearly every particle in the energized region acquires significant kinetic energy, then the energized region is referred to as a 'thermal spike' or 'elastic spike' and may be characterized by a temperature T. Once created, a thermal spike evolves spatially over time due to heat conduction: $T = T(\mathbf{r}, t)$. The energized region becomes wider but also cools, finally diluting completely.

Two mechanisms by which desorption occurs in response to a thermal spike are shown schematically in fig. 4. The first mechanism is activated desorption, or evaporation from the heated region on a molecule-by-molecule basis. The second mechanism is bulk desorption, in which the energized region of the target spontaneously vaporizes and is emitted all at once. Below, these two desorption mechanisms are described along with their possible areas of applicability.

4.1 Thermally Activated Desorption

The evaporative approach to desorption begins with the heat conduction equation:

$$\nabla \cdot \{\kappa(T)\nabla T\} = C(T)\frac{\partial T}{\partial t}. \tag{5}$$

Here, $\kappa(T)$ is the thermal conductivity and $C(T)$ is the specific heat of the target material. In principle, both quantities may be a function of temperature, and in turn the temperature will be a function of space and time: $T = T(\mathbf{r}, t)$. For a cylindrical track geometry, appropriate to the case of an MeV atomic ion impacting on an organic target and depositing energy electronically, Mozumder (1969) has given an often utilized solution to the heat conduction equation:

$$T(r,t) = \frac{T_0}{1 + 4\delta t/r_0^2} \exp\left\{\frac{-r^2}{r_0^2 + 4\delta t}\right\}. \tag{6}$$

In this solution, r is the perpendicular distance from the axis of the track, t is the elapsed time after incidence of an ion, $\delta = \kappa/C$ is the thermal diffusivity, and both κ and C are assumed to be independent of temperature. A spatially narrow Gaussian distribution in initial temperature is assumed with initial temperature at the center of the ion track T_0 and initial width r_0. T_0 and r_0 are related as follows:

$$T_0 = \frac{1}{\pi \rho C_\mathrm{v} r_0^2} \left(\frac{dE}{dx} \right)_\mathrm{e} . \tag{7}$$

In this formula, ρ is the mass density of the target, $\mathrm{C_v}$ is the unit mass heat capacity, and $(dE/dx)_\mathrm{e}$ is the electronic stopping power. The general nature of the solution shown in eq. 6 is that, away from the region of initial excitation, there is a temperature 'pulse' which then decays as the heat energy flows to infinity.

A general expression for the evaporative desorption yield due to a thermal spike is written as a surface integral:

$$Y = \int_0^\infty dt \int_0^\infty 2\pi r dr \Phi[T(r,t)]. \tag{8}$$

Here, Φ is the thermally activated flux of particles evaporating from the surface, which depends on the local temperature. A typical choice for Φ is the expression for the flux of an ideal gas evaporating at constant density across a planar surface barrier, calculated from the Maxwell-Boltzmann law:

$$\Phi = \frac{n_\mathrm{M} kT}{\sqrt{2\pi MkT}} \exp\left(-\frac{U}{kT} \right) . \tag{9}$$

But sometimes the simpler Arrhenius form is employed: $\Phi \propto \exp(U/kT)$. U is the surface binding energy, n_M is the number density of molecules, M is the molecular mass, and k is the Boltzmann constant. The scaling of Y with $(dE/dx)_\mathrm{e}$ is discussed generally by Johnson & Evatt (1980) and Johnson (1987). When a 'delta function' or narrow initially energized region is assumed (r_0 and U/kT_0 small), then the central result of the cylindrical thermal evaporation model is $Y \propto (dE/dx)_\mathrm{e}^2$. On the other hand, if the track has a larger initial width, then $Y \propto (dE/dx)_\mathrm{e}^2$ only at high values of $(dE/dx)_\mathrm{e}$; at lower values, Y is a more rapidly varying function of $(dE/dx)_\mathrm{e}$.

The above solutions pertain to the special case of cylindrical tracks (usually associated with energy deposition by MeV atomic ions) and temperature-independent κ and C. However, solutions assuming spherical geometry and/or temperature-dependent κ and C have also been presented by Vineyard (1976), Johnson & Evatt (1980), Sigmund & Claussen (1981), Urbassek & Sigmund (1984), and many others. As noted for example by Sigmund (1974), the gradients in the energy density deposited by an incident ion can be so large that the concept of local thermodynamical equilibrium is not valid. In response to this objection, Johnson et al. (1991) have given an elastic spike formalism which does not assume local thermodynamical equilibrium. In this case, instead of a local temperature $T(\mathbf{r},t)$, a local energy density $\varepsilon(\mathbf{r},t)$ is employed in the diffusive description. A modified expression for the evaporative flux must be employed, but $Y \propto (dE/dx)_\mathrm{e}^2$ scaling still results.

Lucchese (1987) has presented an alternative thermal desorption model, based on a cylindrical initial excitation, which gives a different high $(dE/dx)_\mathrm{e}$ scaling law: $Y \propto (dE/dx)_\mathrm{e}^1$. The main modifications to the above theory are that a rate equation approach is employed, and that only molecules from the first monolayer are assumed to be capable of being thermally desorbed. If $F(\mathbf{r},t)$ is the fraction of first monolayer molecules remaining at distance r and time t, then one may write the following activated rate equation which comes from transition state theory:

$$\frac{dF(r,t)}{dt} = -\frac{\Omega_0}{2\pi}\exp\left\{-\frac{U}{kT(r,t)}\right\}F(r,t). \tag{10}$$

Ω_0 is the frequency characterizing the molecule-surface bonding. Employing one of the standard expressions for $T(\mathbf{r},t)$, eq. 10 can be integrated in order to find the values of F after the thermal spike has dissipated. The predicted desorption yield is given by the following surface integral:

$$Y = \sigma\int_0^\infty 2\pi r dr\{1 - F(r,t{=}\infty)\} \tag{11}$$

where σ is the surface number density of molecules. The ion yield is modelled by an additional multiplicative factor which is the fraction of desorbed molecules leaving in the ionized state. Lucchese (1987) has extended this model in several respects, but the key point is as follows. The combination of an assumption of only surface monolayer molecules being desorbed and the exponentially activated nature of the desorption together mean that: for each ion impact, there will be a relatively abrupt boundary between the region in which nearly all surface molecules have been desorbed and the region in which almost no surface molecules have been desorbed. Thus, a 'platter' or 'raft' of molecules is desorbed. If one performs a dimensional analysis of the heat diffusion equation, eq. 5, and takes cognizance of eq. 7, one may see that the platter area turns out to be roughly proportional to $(dE/dx)_\mathrm{e}$ (for large enough $(dE/dx)_\mathrm{e}$), and therefore so does the desorption yield: $Y \propto (dE/dx)_\mathrm{e}^1$. Unfortunately, no reason is given why it should be anticipated that thermal desorption of ions and/or neutrals would take place only from the surface monolayer.

One key objection to the thermal spike model with evaporative desorption is this: If the excited region is in local thermal equilibrium, then by the time a molecule acquires enough translational thermal energy in order to evaporate, it has also acquired more than enough internal energy to dissociate. This problem has been discussed by Williams & Sundqvist (1987) and others. Although it is not clear if this objection can be successfully overcome, Lee & Lucchese (1989) have attempted to show that thermal desorption with 'cool' internal modes can occur. They have calculated stochastic classical trajectories of a model system in response to a temperature pulse such as that described by eq. 6. The model system consisted of a linear molecule bound perpendicularly to a surface. The molecule consisted of 40 'units' arranged in a linear chain, each unit with mass 15 u, and with the bottom unit representing the surface. Binding among the top 39 units was strong compared with the binding between the surface (first unit) and the adsorbed molecule (via the second unit); the surface bond was also characterized by a low vibrational frequency. The surface unit was subjected to a stochastic force of magnitude and duration in accordance with the thermal spike model, and the internal energy of the top 39 units was monitored as a function of time. The internal energy of the adsorbed molecule remained low and was seen to increase only slowly on the time scale of complete dissipation of the thermal spike.

Lee & Lucchese (1989) employed a very similar model setup in order to monitor the center-of-mass motion of the adsorbed molecule with respect to several atoms representing the substrate. During thermal excitation, the substrate was evidently perturbed by large fluctuations which succeeded in 'pushing away' and eventually desorbing the molecule. The authors conclude that if molecules are bound to a substrate by relatively weak, low frequency bonds, coupling to the translational desorption mode takes place efficiently while coupling to the internal modes takes place only inefficiently. They argue that desorption of a molecule by thermal means is possible without significant fragmentation, as long as equilibrium between translational and internal modes is never achieved on the timescale of desorption.

Applications of activated desorption thermal spike models are many and varied, and it is difficult to give a comprehensive list of appropriate references. However, a few highlights can be mentioned. For example, Ollerhead et al. (1980) proposed a simple thermal spike model to account for MeV ion-induced desorption from solid Xe, and Seiberling et al. (1980) employed the thermal spike model to account for MeV-ion-induced desorption of UF_4. The latter authors suggested a specific mechanism for the initial production of localized heating: a Coulomb explosion, occurring over some time during which ions are left mutually exposed in the infratrack. The thermal spike model can explain much of the data on sputtering of frozen small-molecule gases, as summarized by Johnson (1987, 1990) and Johnson & Sundqvist (1992).

Considering MeV atomic ion bombardment of organic insulators, Macfarlane (1982, 1982a) and Macfarlane & Torgerson (1976, 1976a) were among the first to suggest that a thermal spike mechanism might be involved in the observed desorption phenomena. These authors also correctly pointed out that the applicability of the thermal spike mechanism depended strongly on the prospect that the internal modes of the desorbed molecules would fail to be in thermal equilibrium with the translational modes, so that fragmentation would not be overwhelming.

The observed stopping power dependencies for both ion and neutral small molecule desorption yields, as far as these are known, can be compared favourably to the predictions of evaporative thermal spike models. Lucchese managed to generate a thermal model which accounted for the $(dE/dx)_\mathrm{e}$ dependence of positive ion yields (and in one case negative ion yields too). The model, discussed above, gave a stopping power dependence $Y \propto (dE/dx)_\mathrm{e}^1$ for high $(dE/dx)_\mathrm{e}$, and the excellent fits which were achieved are shown in fig. 3 for monomers and clusters of the amino acid valine. For lower $(dE/dx)_\mathrm{e}$, both data and model show a steeper than linear stopping power scaling. For the amino acid leucine, Hedin et al. (1987) have reported a neutral sputtering yield stopping power scaling $Y \propto (dE/dx)_\mathrm{e}^3$. Since the generality of this result is not known, it may turn out that the leucine neutral yield data are also described by the evaporative thermal spike model. If this is true, however, one would predict that for higher but so far untested values of $(dE/dx)_\mathrm{e}$, $Y \propto (dE/dx)_\mathrm{e}^1$ for neutral leucine desorption. Of course, the general applicability of the evaporative thermal spike model in explaining MeV atomic ion induced desorption of small organic molecules requires that the different measured stopping power scaling of ionic and neutral yields over the same $(dE/dx)_\mathrm{e}$ range be convincingly explained. This seems difficult, unfortunately, since these models do not specifically address the ionization mechanism except through an overall proportionality factor.

MeV atomic-ion impact-induced ejection of larger organic molecules, such as proteins, is not well described by the evaporative thermal spike model. This follows mainly from measurements of radial velocity and ejection angle distributions for ions. Evaporative thermal spike models predict an approximate $\cos\theta$ polar angular distribution, whereas Ens et al. (1989), Moshammer et al. (1990) and Moshammer (1991) have found many instances in which both positive and negative large desorbed molecular ions are ejected strongly in off-normal directions. Off-normal ejection is more easily explained employing a pressure-pulse model, discussed below. Unfortunately, it is not known experimentally whether the neutral molecular sputtering yields display similar angular ejection patterns to those of the ion sputtering yields, though the molecular dynamics simulations of Fenyö et al. (1990) based on the pressure-pulse idea seem to suggest that this would be so.

Evaporative thermal spike ideas have been successfully employed to rationalize features of keV to MeV heavy cluster ion bombardment of carbon and organic insulators. Matthew et al. (1986) have employed a thermal spike model in an attempt

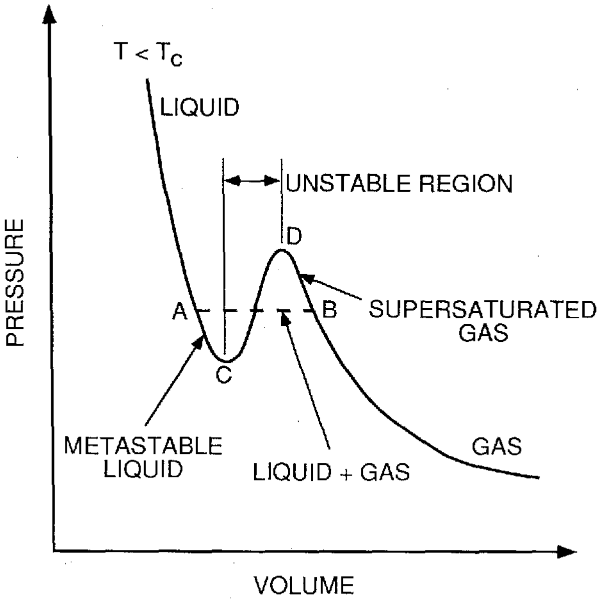

Figure 5. Pressure-volume curve for a material exhibiting a liquid-to-gas phase transition. Segment A-C represents a metastable liquid; segment D-B represents a supersaturated gas; and segment C-D represents an absolutely unstable state of the liquid, characterized by an irreversible transition to the vapor phase.

to understand the formation of craters in thin carbon films under impact of cluster ions of the form $(H_2O)_nH^+$, where n ranges from 25 to 150. Typical impact kinetic energies were 100 to 300 keV. Briefly, an impacting cluster was assumed to deform into a flat 'disc' upon impact, and, assuming a constant cluster stopping power $(dE/dx)_c$, the initial temperature profile of an approximately cylindrical thermal spike was calculated. The heat diffusion equation was employed to calculate the spatial and temporal dilution of heat energy, and the evaporative model described above was used to calculate the number of evaporated carbon atoms. The volume of excavated material was compared to the observed crater volume. One important uncertainty in this model is the value of the stopping power suitable for describing the interaction of an impacting cluster with the target. However, the values of $(dE/dx)_c$ required to explain the observed crater size were within a factor of two of a simple estimate of cluster stopping power based on a simple atomic picture. Some subtleties that enter into the determination of the stopping power of a cluster are discussed by Sigmund (1989).

Ledbetter et al. (1987) bombarded a sample composed of tobacco mosaic virus

(TMV) with cluster ions of the form $(H_2O)_nH^+$. Typical impact kinetic energies were 100 to 300 keV. By employing transmission electron microscopy, the orderly excision and complete disappearance of 'slices' of TMV with no accompanying leftover debris whatsoever was observed. The edges of the excised slices appeared to be flat and were perpendicular to the axis of the cylindrical TMV. The authors pointed out that the structure of TMV consists of a number of slice-like 'gyres' which are relatively more weakly bound to each other than they are internally bonded. The material that had taken up the volume of a typical crater had been composed of up to six gyres, whereas the size of the impacting cluster is only a fraction of the size of one gyre. The central idea that emerges is as follows: Cluster impact produces a local high temperature thermal spike of restricted spatial extent; the thermal energy diffuses much more efficiently within a gyre than across the boundary between gyres. Consequently, evaporation proceeds efficiently, even across several gyres, until the thermal energy diffusing up to one gyre-gyre boundary is suddenly reduced below a certain threshold. Thereafter, very little energy is transmitted, and the evaporation abruptly ceases with the result that the final crater shape is determined by the shape of the gyre-gyre boundary. The evaporative thermal spike model may thus serve as an effective rationalization for the formation of craters in cluster-ion bombarded TMV.

4.2 Thermally Induced Bulk Desorption

The term 'bulk desorption' refers generally to events in which locally deposited energy causes an abrupt transition of a volume of solid or liquid to the gas phase, after which the gassified material escapes from the surface. This desorption mechanism is sometimes referred to as 'gas-flow' or 'phase-explosion' desorption. A number of approaches have been taken to modelling bulk desorption processes. Sunner et al. (1988) have employed a simple thermodynamic picture; Urbassek & Waldeer (1991) and Shiea & Sunner (1991) have employed molecular dynamics simulations; and several authors have performed analytical treatments of adiabatic expansion, for example: David et al. (1986), Urbassek & Michl (1987), and Kelly (1990). These treatments are reviewed here, although applications of these theories to desorption from organic targets are sparse.

The simple thermodynamical picture of bulk desorption begins with a pressure-volume (PV) diagram for a material which exhibits a liquid-gas phase transition. A schematic PV diagram is shown in fig. 5. For temperatures below the critical temperature, T_c, as the pressure is decreased by increasing the volume, there is a range of volumes for which the pressure remains constant (denoted by the dashed line in fig. 5). At this stage, due to heterogeneous nucleation (i.e. the presence of some dust or other impurities in the liquid), the liquid evaporates (boils) as the

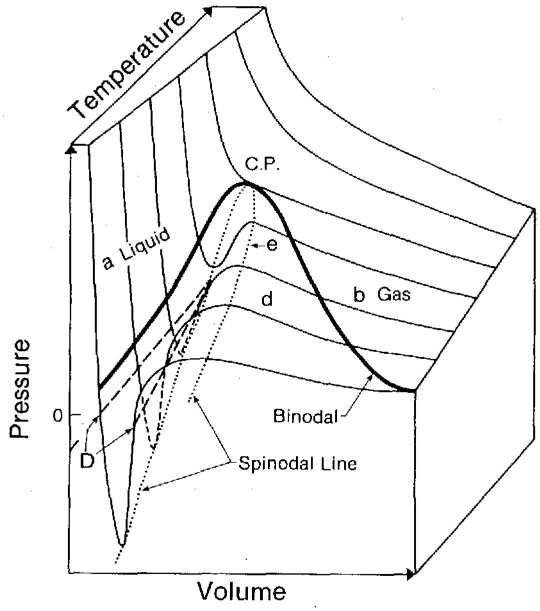

Figure 6. Pressure-volume-temperature surface showing all thermodynamic states available to a simple one-component system. The surface includes the metastable thermodynamic states. The spinodal line encloses the states which are unstable and lead to spontaneous vaporization. The phase explosion model states that an ion impact drives the system from the left-most point of D to the spinodal, leading to vaporization and bulk desorption. Reprinted from Sunner et al. (1988) by permission.

volume increases, keeping the pressure constant. When all the liquid has evaporated, the pressure again decreases as the volume increases. A reverse behavior occurs upon compression of the gas.

In the absence of heterogeneous nucleation, a different behavior occurs. Overexpansion past the volume at which the liquid normally would have begun to evaporate fails to induce evaporation, giving a metastable liquid. Overcompression past the point at which the gas normally would have begun to condense fails to induce condensation, giving a metastable or supersaturated gas. As shown in fig. 5, there is a bit of 'forbidden' PV curve which joins the metastable liquid and supersaturated gas states. This connecting piece, shown in fig. 5 as segment C-D, is characterized by the following relation:

$$\left(\frac{\partial P}{\partial V}\right)_T \geq 0. \tag{12}$$

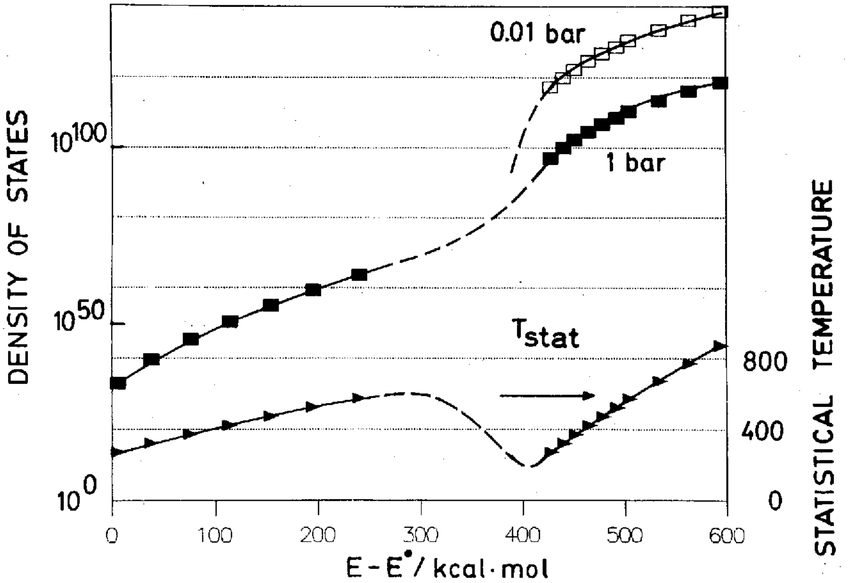

Figure 7. DOS and $T_{\rm stat}$ plotted against internal energy for ten H_2O molecules. A region of log(DOS) characterized by positive curvature is unstable by entropy considerations and undergoes a spinodal transition to vapor and clusters. Reprinted from Sunner (1990) by permission.

According to this relation, the liquid is absolutely mechanically unstable, and a spontaneous phase transition occurs to the 'spinodal' form consisting of a combination of vapor and clusters. This scenario is discussed by Zeldovich & Todes (1940).

Sunner et al. (1988) show a typical pressure-volume-temperature (PVT) surface characterizing a single component system. An example of such a PVT surface is shown schematically in fig. 6. They consider the case of liquid glycerol, a commonly employed matrix for FAB (keV atom impact). Under vacuum conditions, glycerol is a metastable liquid which only very slowly evaporates. It is argued that an incident atomic particle deposits energy, driving up the local temperature. If the heated material reaches the spinodal line at which the liquid becomes unstable against vaporization, the resulting gas is ejected into vacuum, entraining any analyte molecules that have been dissolved in the glycerol and delivering these to the gas phase as well. Pre-formed ions in the solution, ions charged statistically during desorption, and neutral analyte molecules charged during gas phase interactions with matrix ions in the selvedge, are all available for detection in FAB secondary ion mass spectroscopy. The sudden decompression of the gas during ejection gives rise to a strong cooling effect, and a low degree of internal energy and low fragmentation are expected in the desorbed molecules. Sunner et al. (1988) suggest that the duration of high temperature conditions is at most of the order of 10^{-9} sec. The overall scenario thus parallels that which is thought to occur during matrix-assisted laser desorption.

Two criticisms may be levelled at the above treatment. First, the use of PVT diagrams is only valid for systems in thermal equilibrium, whereas the desorption system may be far from equilibrium. Second, the desorption system may be too small for the principles of bulk thermodynamics to be valid. In response to these criticisms, Sunner (1990) has provided an alternative treatment based on statistical thermodynamics. In this case, the density of states (DOS) for a microscopic ensemble of ten water molecules is back-calculated from entropy and enthalpy values for bulk water. The curve DOS vs. E (total energy) is plotted semi-logarithmically in fig. 7. At the left and right of the plot are the water liquid and gas phases respectively, and for each phase, the statistical temperature (inverse slope of a log(DOS) vs. E plot) increases with increasing total energy. However, there is a range of energies for which the log(DOS) vs. E curve would clearly have a positive curvature, displaying a decreasing temperature as the total energy increases. This is the mechanically unstable region discussed above in connection with a PVT diagram, but now the instability can be understood through an entropy argument. Since log(DOS) is the entropy, then at a point at which the log(DOS) vs. E curve has a positive curvature, the entropy always increases if the system breaks up into part gas phase and part liquid phase. Therefore, the break-up is spontaneous, and for a certain total energy density, liquid water vaporizes and ejects clusters in a spinodal transition. Sunner (1990) also points out that, during the phase explosion, energy may flow from internal vibrational states of water (which molecules are individually stable independently of the stability of the phase in which the molecules reside) to the translational modes, resulting in 'cooler' molecules and clusters, and faster (but more directed) ejection.

Molecular dynamics simulations have also been employed to gain insight into bulk desorption processes. Such methods have the advantage that, in principle, only microscopic interaction details need be specified, and the conditions of equilibrium or lack thereof can be demonstrated by sampling the internal kinetic energy distribution as a function of time. Unfortunately, classical dynamics simulations tend to be limited to the cases of solids composed of atoms and small molecules.

Urbassek & Waldeer (1991) and Waldeer & Urbassek (1993) have performed classical dynamics simulations on a condensed argon solid collisionally energized by a 1 keV argon atom. Results of their study are shown in figs. 8 and 9. The state of the system is monitored by noting in what form material escapes, and by sampling the kinetic energy spectra of atoms in the solid as a function of time.

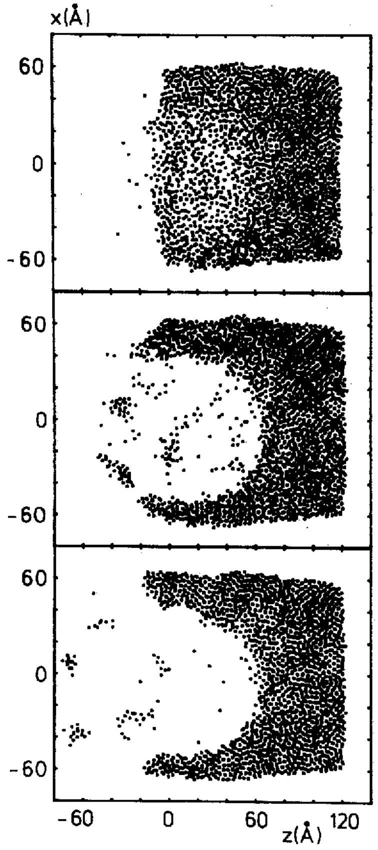

Figure 8. Crater formation in an argon solid after incidence of a 1 keV argon ion. Top frame: 3.2 psec after impact. Middle frame: 13.8 psec. Bottom frame: 24.7 psec. Extensive clustering is apparent. Reprinted from Urbassek & Waldeer (1991) by permission.

At very early times after the ion impact, the internal kinetic energy distribution is mainly the same low temperature Maxwell-Boltzmann distribution which characterized the solid just before the ion impact, but with an added collision cascade 'tail' at high energies displaying the usual E^{-2} scaling. For slightly later times, but still before many atoms have left the target, the kinetic energy spectrum indicates that the system is far from equilibrium. This spectrum cannot be fit even by a summation of two Maxwell-Boltzmann models. At comparatively late times, after hundreds of atoms have been sputtered, the internal kinetic energy distribution is again a relatively low temperature Maxwell-Boltzmann distribution. The max-

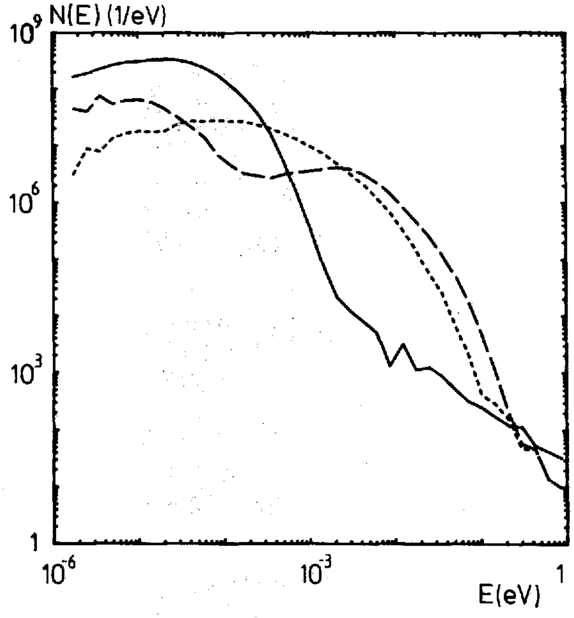

Figure 9. Kinetic energy spectrum of argon atoms in the solid shown in fig. 8. Solid line: 0.14 psec after impact. Dashed line: 3.2 psec. Dotted line: 24.7 psec. Note marked lack of equilibrium at 3.2 psec. Reprinted from Urbassek and Waldeer (1991) by permission.

imum temperature during the whole desorption process is never even as high as the critical temperature of liquid argon, and the condition of high kinetic energy density lasts only about 10 psec. The extensive clustering observed in the sputtered plume is indicative of rather low internal energies of sputtered particles. Although a thermodynamical picture does not hold in detail throughout the desorption event, the classical dynamics and thermodynamics pictures yield the same conclusions: a large portion of the target is vaporized and ejected as a gas, with marked clustering accompanying the gas expansion. Although the simulation is aimed at assessing the role of bulk desorption in the case of particle-excited rare gas solids, there is no reason in principle why the same concepts should not be applicable to a variety of organic targets as well.

Shiea & Sunner (1991) have also performed classical dynamics simulations of bulk desorption. They considered a very low energy projectile incident on an two-dimensional atomic lattice and made plots of kinetic energy density as a function of time and space. They plotted an internal energy ('temperature') history for a region of the solid near the incident ion impact point. Just after projectile impact, there is a temperature pulse lasting less than 1 psec, and this is attributed to the passage of a shock wave through the lattice. Next a slower temperature pulse lasting 2 or 3 psec is observed and this evidently causes a weak spinodal transition of the sort which was predicted by thermodynamic theory and discussed above: a transformation of the lattice to an assortment of isolated atoms and 'filaments' of atoms, or clusters. If molecules are included in the lattice, some of these are ejected intact.

A number of authors have attempted analytical descriptions of the dynamics of bulk desorption, although again these treatments are aimed at clarifying sputtering mainly of atomic solids. Urbassek & Michl (1987) have modelled the bulk desorption process in terms of collision-free molecular flow in three dimensions, a procedure they claim is a good approximation to the correct description in terms of unsteady adiabatic expansion. Noting that the collision-free molecular flow formalism cannot possibly model the dissipation of energy by thermal conduction, they add a nonconservative force field to simulate this heat dissipation. Finally, the possibility of recondensation is included by halting the gas flow out of the crater when the temperature falls below a certain critical value, taken arbitrarily to be the sample boiling point. The derivations of and resulting expressions for the sputtering yield and the axial kinetic energy spectrum are given but they are detailed and are not repeated here. The model axial kinetic energy spectra, when fitted with parameters suitable for describing the spatial extent of collisional excitation by a keV atomic ion incident on a solid rare gas target, were able to account for the low kinetic energy sputtered atom yield, which is typically much higher than can be accounted for by the simple collision cascade model. As noted above, these same concepts may well also be applicable to organic targets.

Balaji et al. (1990) have given a simplified derivation of the total desorption yield calculated by Urbassek & Michl (1987). They employ the evaporative thermal spike yield equation, eq. 8, with an expression for the flux appropriate to the situation of an ideal gas passing across a plane with no binding potential: $\Phi(T) \propto T^{1/2}$. They then assume that the temperature drops in time according to eq. 6 but with the exponential part held at exactly one, i.e. they consider only regions of the sample very close to the ion impact track and assume a constant initial track radius as did Sigmund & Claussen (1981). The time integral in eq. 8 is then effectively simplified and parametrized in terms of temperature, and upon including a critical condensation temperature, an expression for the sputtering yield is obtained which is the same as that obtained by Urbassek & Michl (1987).

Kelly (1990) has adapted the analytical solution for one-dimensional unsteady adiabatic expansion to the case of keV atomic ions incident on various frozen gases. The modelled situation is that of a 'plug' of hot material. The size and temperature of the plug are determined by the parameters of the material and the impacting ion. If the temperature of the plug exceeds the critical temperature, the material turns into a hot dense gas which escapes. The situation in which a gas is suddenly released from a hole or cavity is described by equations governing adiabatic expansion in the continuum limit, which have been specified and solved. The essence of the solution is that, at some point in time, the density of the escaping gas has decreased to the point at which collision-free molecular flow occurs. At this point, the dominant fraction of the gas has a number of well-defined properties. In particular, the temperature of the gas is uniform, and its flow speed is linear in distance from the bottom of the evacuated plug but achieves a well-defined maximum value. The axial kinetic energy spectrum consists of the Maxwellian form, superimposed on a flow, and integrated over the entire range of flow velocities in the plume. The analytic result for the energy spectrum is complex but is similar in form to a single Maxwellian velocity distribution superimposed on a single flow velocity. Sputtering yields predicted in this gas flow model greatly exceed the yields predicted from collisional sputtering. It is suggested that, though the present model is one-dimensional in nature, in a three-dimensional measurement additional information is available from measurements of the angular distributions of sputtered particles, and the higher the gas flow velocity, the narrower the angular distributions are likely to be. Although these ideas have been applied mainly to the case of ion-bombarded frozen gases, it is likely that application to certain organic targets could also be fruitful and should be considered.

For applications, the case of keV atomic particles incident on glycerol is first considered. Glycerol is a commonly employed matrix material for FAB secondary ion mass spectroscopy measurements. The sputtering yield of glycerol under keV atomic ion bombardment is thought to be high, although admittedly the technical problem of accounting for evaporation during the measurement is a taxing one. Barofsky & Barofsky (1986) and Barofsky et al. (1991) have measured sputtering yields in the range 1000 to 4000 for a variety of ions incident on liquid glycerol, for example 10 to 30 keV Bi^+, In^+, and Ga^+. Wong et al. (1985) have measured comparable sputtering yields for 6 to 10 keV Xe atoms incident on glycerol. A bulk-desorption or gas-flow model provides an attractive rationalization for such high sputtering yields.

Just as the use of a matrix material revolutionized the technique of laser desorption for biomolecular mass analysis (Karas & Hillenkamp, 1988), so did the use of matrix materials like liquid glycerol revolutionize the technique of FAB mass analysis (Barber et al. 1981, de Pauw, 1986). Compared to solid matrices, the use of liquid matrices can yield mass spectra characterized by greater intensity and a lower degree of fragmentation. Part of this improvement is due to renewal effects absent for solid targets: in the liquid, ion-induced damage at the surface is in effect 'rinsed away' into the bulk of the liquid. However, another part of the improvement may be caused by the gentle ejection of analyte molecules entrained in a plume of desorbing matrix molecules. Significant cooling occurs, as discussed above, and this results in lower fragmentation rates. This cooling has been observed by Hoogerbrugge et al. (1988), who performed photo-ionization measurements on sputtered glycerol molecules. By monitoring fragmentation patterns and comparing to similar patterns measured for heated glycerol gas, they concluded that the desorbed glycerol molecules have considerably lower internal energy then they had in the liquid phase prior to sputtering. Such cooling effects are consistent with the operation of a bulk desorption mechanism in the case of liquid matrices excited by incident ions.

Sunner et al. (1988, 1988a) and Shiea & Sunner (1990) have also employed bulk desorption ideas to explain a number of observations that they have made in connection with FAB. For example, Sunner et al. (1988a) acquired FAB spectra of a variety of matrix substances, listed in order of mass: water, methanol, ethanol, 2-propanol, n-butanol, n-octanol, and glycerol. While extensive clustering is observed in the case of water (and also nitrogen) matrices, the clustering propensity sharply decreases in the order listed. The authors explain this trend in terms of an enthalpy argument. In the case of water, the enthalpy content at the spinodal state is less than what is required to guarantee the creation of an homogeneous vapor phase. Consequently, extensive clustering is observed in the FAB spectra. For 2-proponal, by contrast, it turns out that the enthalpy content of the spinodal state is sufficient to guarantee complete vaporization. In this case, a smaller degree of clustering was observed in the FAB spectra. The applicability of thermodynamic concepts to the FAB desorption process is taken to be in favor of the validity of phase-explosion and bulk desorption ideas.

Shiea & Sunner (1990) monitored FAB spectra as they varied the viscosity of the matrix material by means of changes in temperature and modifications to the matrix solution. They noted that, for a sufficiently great increase in the viscosity, the FAB spectra deteriorated, displaying a large degree of fragmentation and chemical noise. The authors offered the following rationalization for this effect. They assumed that the material in the core region of the collision-cascade induced spike is gassified and is characterized by high internal energy and a high degree of fragmentation. In the case that the surrounding material is characterized by a high viscosity, they supposed that the hot gas is promptly ejected, resulting in poor FAB spectra. In the case that the surrounding material is characterized by a low viscosity, however, they supposed that the surrounding material 'yields' to the increased pressure, delaying the ejection of the hot 'spike' material. Consequently, more of the surrounding material is heated up to the spinodal state and participates in the phase explosion. The result is that a large number of intact, low internal energy molecules are ejected. Under these conditions, excellent FAB

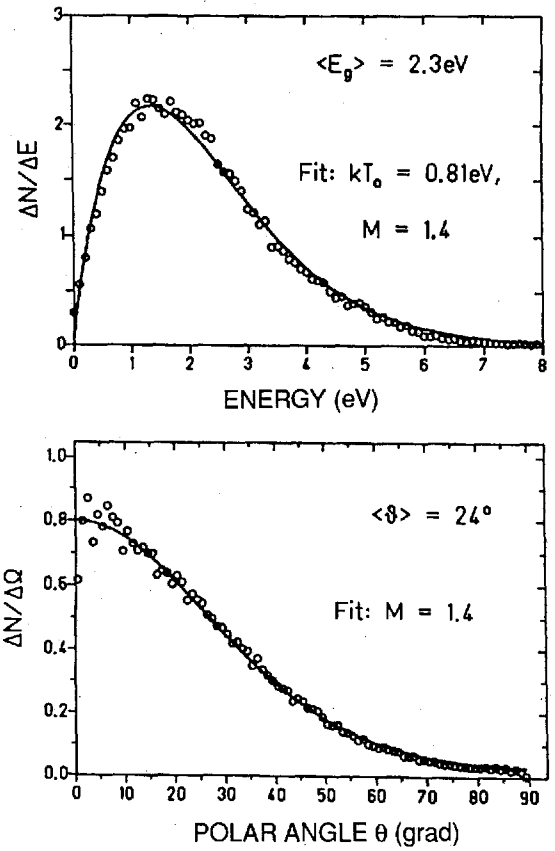

Figure 10. Kinetic energy and ejection polar angle distributions of the M = 30 u fragment of valine. Excitation is by ^{252}Cf fission fragments. The solid line is a fit to a Maxwellian velocity distribution with a gas flow velocity superimposed along the surface normal. Reprinted from Moshammer (1991) by permission.

spectra characterized by low noise and strong molecular peaks are obtained.

Much of the discussion of bulk desorption of organic materials revolves around liquid targets. Is a liquid matrix necessary for the occurrence of bulk desorption phenomena for FAB and keV atomic ion irradiation? The answer is not totally clear, but it is possible that bulk desorption could occur in solids. Several items of theory discussed above were based on model solids, after all, and one may suspect that these theories are also applicable at least to solids composed of small organic molecules. Also, there are cases for which SIMS on analytes in the solid phase and

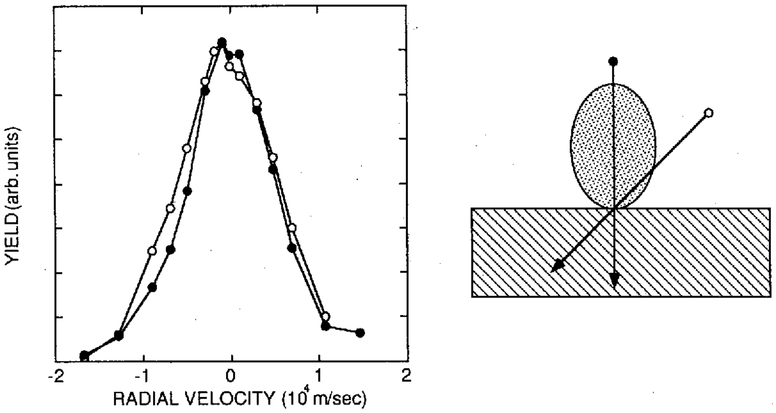

Figure 11. Radial velocity distributions for the $M = 15$ u fragment of insulin, for 0° and 45° angles of incidence. Excitation is by 72.3 MeV ^{127}I ions. The resulting distributions are the same. Adapted from Fenyö et al. (1990a).

in a matrix liquid yielded similar spectra and ion count-rates to within a factor of 10 (see Junack et al., 1986). Finally, solid targets can be a source of rather massive ions, with $M > 10000$ u, suggesting that these ions are ejected gently and with sufficient vibrational cooling to avoid fragmentation.

Although the bulk desorption models provide a qualitative explanation of various features of sputtering by FAB, there is some room for debate whether the model is truly applicable. As discussed in the introduction, it may be suggested that a large fraction of the ejected intact molecules and major fragments are likely to be ejected from outside the region of the target directly excited by the incident ion. An alternative theory of liquid matrix FAB has been offered by Wong & Röllgen (1986), and this theory is discussed below, under the heading 'pressure-pulse sputtering'.

In the area of MeV atomic ion impacts on organic targets, Moshammer (1991) has measured energy- and angle-resolved ejection distributions of fragments of valine ejected by ^{252}Cf fission fragments. The results are displayed in fig. 10. The observed distributions are well accounted for by a Maxwellian superimposed on a supersonic flow characterized by Mach number 1.2, consistent with a simple gas-flow 'ansatz'. The MeV ions, however, create a cylindrical track, and if the gas-flow model is applicable, then there should be evidence of fragments being ejected backwards along the ion track direction in a 'jet-effect'. However, Fenyö et al. (1990a) have noted that this jet effect is conspicuously absent, at least for the CH_3^+ fragment measured, as shown in fig. 11. As the angle of incidence of the impacting ions

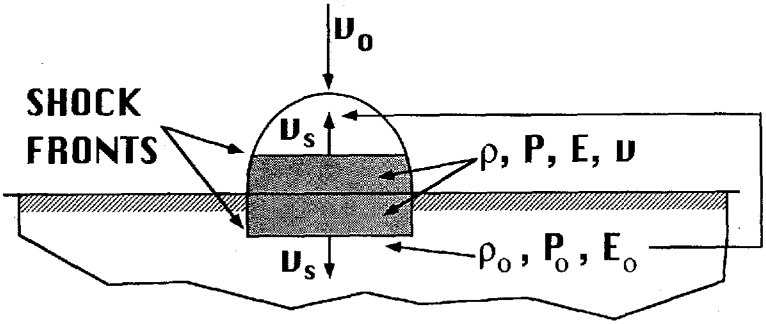

Figure 12. Schematic diagram of shock wave fronts produced as a glycerol cluster impacts a glycerol matrix. For simplicity, a one-dimensional viewpoint is taken. v_0 is the speed of the initial cluster; the other symbols are defined in the text.

was switched between 0° and 45°, no change in the radial velocity distributions was observed. In fact, no jet-effect has ever been observed for pre-existing organic species desorbed from a surface, and consequently it is doubtful that the gas flow model plays a strong role in MeV ion-induced desorption of organic molecules.

5 Shock-Wave Models of Desorption

The incidence of energetic particles onto surfaces can lead to extremely high deposited energy densities. One possible consequence of high energy density and high energy density gradient conditions is that a 'shock wave' may be created which propagates outward from the region of excitation into the surrounding material. Desorption may be caused in several ways. For example, if a shock wave reflects off the surface (vacuum interface) from below, material may be 'mechanically ablated' or 'spallated' by being in effect left behind during the unloading wave. Also, it is possible that shock wave energy may be focused into defects or narrow protrusions sticking off the surface, also leading to direct desorption of a piece of the solid. Finally, after a shock wave passes through a region of a material, this region is left in a heated state, and the excess thermal energy may cause desorption through evaporation or bulk desorption or through response to the energy density gradient (see pressure-pulse discussion below). There is a large body of literature concerning shock wave and hydrodynamic theory (Zel'dovich & Raizer, 1967; Landau & Lifshitz, 1959).

The complex details of the theory are outside the scope of this paper, and thus a qualitative definition of a shock wave is given here. Loosely speaking, a shock

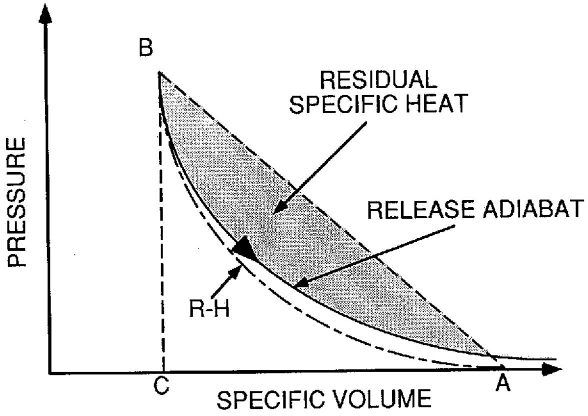

Figure 13. Equation of state for a shocked material. Point A represents the rest or normal state. Points on the Hugoniot, curve R-H, represent final states of the material that can be reached by shock excitation. If the system is excited to point B and subsequently undergoes an adiabatic release or unloading process, then a residual specific heat (heat energy per unit mass) is left whose magnitude is represented by the shaded area shown in the figure. Drawn by Jörgen Ahlbom, Uppsala University.

wave is a relatively narrow propagating mechanical disturbance across which there are distinct changes in thermodynamical parameters like pressure, temperature, and material density. Terms like 'relatively narrow' and 'considerable' are hard to pin down precisely, but narrow means that the width is no more than a few lattice spacings of the material. The shock wave itself propagates with a speed exceeding that of sound in the medium. Supersonic propagation of a mechanical disturbance is a sufficient condition for deducing that the disturbance has a shock-like character.

One shock wave model of desorption is based on the idea that a passing shock wave leaves the material in a heated state. Mahoney et al. (1992) have observed desorption of analyte molecular ions from a glycerol matrix under massive glycerol cluster impacts at three times the speed of sound. The impacting cluster is regarded as a piston which compresses a plug of target material. Shock wave fronts propagate both into the target and back into the incident cluster. These authors have carried out a simple hydrodynamic analysis, utilizing known thermodynamic data on glycerol, to justify that shock wave heating can account for the observed desorption. Their treatment begins with the Rankine-Hugoniot equations applied to the one-dimensional picture of the collision event shown in fig. 12. The Rankine-Hugoniot equations result from applying the principles of conservation of

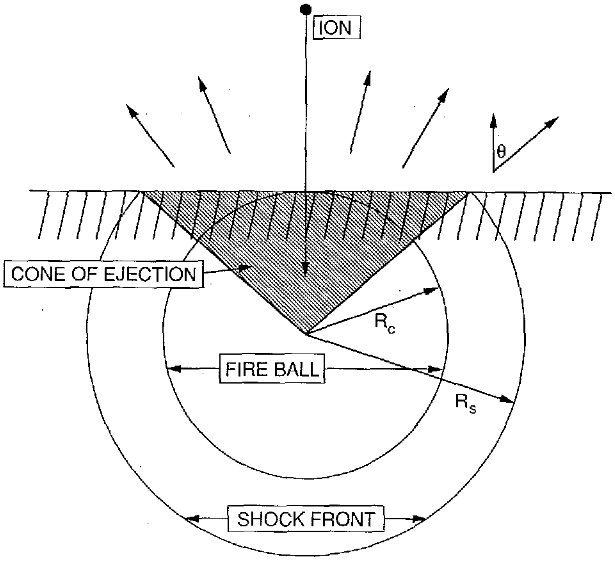

Figure 14. Schematic diagram of a spherical shock wave initiated by a critical energy deposition within a sphere of radius R_c. Based on an ejection criterion discussed in the text, a cone-shaped plug of material, shown in the figure as the shaded volume, is ejected. Adapted from Kitazoe et al. (1981).

momentum, mass, and energy across a shock wave front:

$$\begin{aligned} P - P_0 &= \rho_0 v v_s \\ \frac{V}{V_0} &= \frac{v_s - v}{v_s} \\ E - E_0 &= \frac{1}{2}(P + P_0)(V_0 - V). \end{aligned} \tag{13}$$

In the region behind the shock wave, the pressure is denoted by P, the volume per unit mass is denoted by V, and the energy per unit mass is denoted by E. Corresponding quantities in the unshocked region of the sample are denoted respectively by P_0, V_0, and E_0. The mass density in the unshocked region is $\rho_0 = V_0^{-1}$. v_s is the shock wave speed, and v is the speed of glycerol molecules in the shocked region. (Here and in fig. 12, E and V represent specific energy and specific volume respectively, rather than energy and volume as employed elsewhere in this paper.)

An equation of state for shocked material is shown schematically in fig. 13. In the case of glycerol, the shock wave and molecular speeds are known as a function of density under shock conditions, and by employing the first two Rankine-Hugoniot equations, an equation of state curve called the Hugoniot may be constructed. Consider initial state A and final state B on the Hugoniot. The area under the straight line segment AB is the shock-induced change in the energy per unit mass. This follows from the form of the third Rankine-Hugoniot equation. The system at state B then undergoes a 'release adiabat' during which compressional potential energy is released. The shaded area shown in fig. 13 represents the leftover specific thermal energy after passage of the shock wave and relaxation of the material. Using the Hugoniot itself as an approximation to the release adiabat, it turns out that for glycerol, the leftover residual specific heat is of the order of magnitude required to vaporize the region of the target excited by cluster impact. Both evaporative thermal spike and bulk desorption mechanisms could be active.

Kitazoe et al. (1981) have performed an analytic hydrodynamical analysis of non-linear sputtering yields for the case of heavy atomic ion bombardment of high-Z materials, again regarding energy dissipated by the shock wave as a cause of sputtering. The geometry treated is shown in fig. 14. The incoming ion is assumed to scatter at some depth R_c, whereupon the scattered atom(s) set up a dense collision cascade or elastic spike. The resulting 'fire ball' has radius R_c. Within this radius, the average energy per volume is approximately

$$\varepsilon \approx \frac{2R_c(dE/dx)}{\frac{4}{3}\pi R_c^3} = \frac{3(dE/dx)}{2\pi R_c^2}. \tag{14}$$

Here, dE/dx is the appropriate stopping power. If $\varepsilon > \varepsilon_c$, a critical value of energy density, then a shock wave is assumed to be created. An expression for the energy per particle, E, behind the shock wave front is given by Landau & Lifshitz (1959) for spherical symmetry. Taking into account energy deposited both as heat and plastic deformation,

$$E(R) \cong \frac{\dfrac{\varepsilon}{n_\mathrm{A}}\left(\dfrac{R_c}{R}\right)^2}{1+\dfrac{3}{2}\sqrt{\dfrac{2\varepsilon}{Mc^2 n_\mathrm{A}}}\log\left(\dfrac{R}{R_c}\right)}. \tag{15}$$

Here, R is the distance from the center of the fire ball, M is the target particle mass, n_A is the number density of atoms, and c is the speed of sound. Because of the highly compressed nature of the fire ball, $E(R)$ is characterized by a strongly radial macroscopic velocity component, so that the following criterion is employed for ejection:

$$E(R_\mathrm{s})\cos^2\theta = U. \tag{16}$$

R_s is the radial distance from the center of the fire ball to the outermost point on the surface at which ejection can take place, U is the surface binding energy, and

θ is the angle defined in fig. 14. The final ejected volume is assumed to be the conical-shaped volume shown in fig. 14, so that, from geometrical considerations along with eq. 14, the sputtering yield scales as

$$Y \propto R_c^3 \propto \left(\frac{dE}{dx}\right)^{3/2}. \tag{17}$$

The absolute magnitude of the sputtering yield of course depends on θ through eqs. 16 and 15. If the predicted sputtering yield is comparable to or less than the yield predicted by the collision cascade sputtering model, then the shock wave heating model is considered not to be relevant (i.e. the shock is too weak or nonexistent). However, the authors identify a number of cases involving atomic ion bombardment of metal targets for which the model appears to have some validity. Carter (1983) has debated against the relevancy of shock phenomena in describing sputtering from dense elastic collisional spikes, although he admitted the possibility of 'some unspecified collective hydrodynamic motion' occurring early in the spike formation process.

A generally similar viewpoint to the above is taken by Gol'danskii et al. (1975) and Demirev (1988) in describing the interaction of MeV heavy atomic ions with water or organic targets. Solutions are given to equations governing a cylindrically expanding shock wave, appropriate to the geometry of MeV ion interactions with solids. The solutions include expressions for the position of and pressure behind the shock wave front as a function of time. Demirev (1988) noted that for times up to about 50 psec after excitation, and for a radius of 600 Å around the initial track, the resulting pressures correspond to a volume energy density sufficient to desorb typical protein molecules bound by hydrogen or van der Waals bonds.

Bitensky & Parilis (1987) have generated a theory in order to describe desorption of clusters and organic molecules under the influence of spherical and cylindrical shock waves. These authors assume that sputtering occurs by spallation, and they employ a pressure criterion to define the point at which sputtering occurs. Referring again to fig. 14, a conical chunk of material is assumed to be desorbed if

$$P(R_\mathrm{s}) \cos\theta = P_\mathrm{cr} \tag{18}$$

where P(R_s) is the residual overpressure at radius R_s and P_cr is some critical pressure. If the molecules have radius r_m, then for the molecules to be ejected separately but intact, the following additional conditions must be met:

$$\frac{P_\mathrm{d}}{2r_\mathrm{m}} \geq |\boldsymbol{\nabla} P(r)| \geq \frac{P_\mathrm{cr}}{2r_\mathrm{m}}. \tag{19}$$

In this inequality, the 'pressure' in the molecular volume is related implicitly to the internal energy by hydrodynamical equations, and P_d is related to some internal

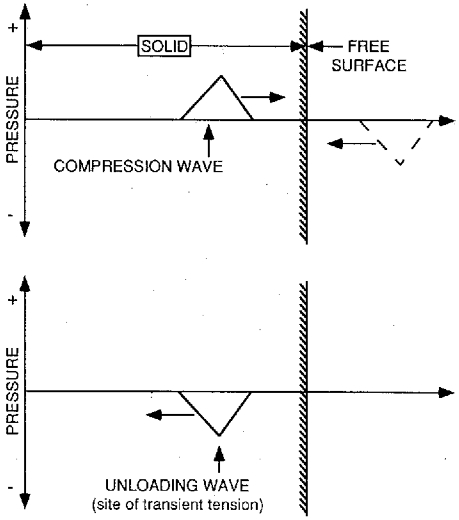

Figure 15. Schematic diagram of an acoustic-like weak shock wave reflecting from the free surface of a solid. A virtual leftward-propagating unloading wave is required in order to preserve the boundary condition that the pressure at the surface be zero at all times. As the compression wave interacts with the free surface, the virtual unloading wave becomes real and causes the solid to experience a transient tensile stress as it propagates into the bulk. The solid may crack or blister and pieces may be ejected. Adapted from Zel'dovich & Raizer (1967).

pressure sufficiently high to cause dissociation of the molecules. As in the treatment of Kitazoe et al. (1981), owing to geometry, the sputtering yield turns out to scale as $Y \propto (dE/dx)^{3/2}$ for sufficiently high (dE/dx).

In the model of Bitensky & Parilis (1987), dissipation is ignored by assuming simple scaling laws for the pressure. (This is analogous to ignoring the logarithmic term in the denominator of eq. 15 so that $E(R)$ obeys a simple geometrical scaling law.) The overpressure then is regarded as causing spallation of a finite-sized chunk of matter from the surface. The concept is illustrated schematically in fig. 15. A weak, acoustic-like shock wave characterized by a pulse-like spatial pressure profile moves towards the free surface. The boundary condition at the surface is that the pressure there is negligible for all time, so the solution to the wave equation involves a counter-propagating negative pressure pulse which is positioned such that this boundary condition is satisfied. Therefore, after the shock wave reaches the surface, an unloading wave characterized by negative pressure propagates down into the solid. Negative pressure is interpreted as a tensile stress, and if this stress is sufficiently large, the material may fracture and the loose pieces of material may be ejected. These concepts are discussed by Zel'dovich & Raizer (1967).

The detailed scaling law derived by Bitensky and Parilis (1987) was successfully employed to fit the MeV-ion-induced molecular ion desorption results of Hedin et al. (1985), but this scaling law is not consistent with the scaling observed for neutral desorbed molecules by Hedin et al. (1987), $Y \propto (dE/dx)_e^3$. Therefore, ways of improving the performance of the model have been discussed by Bitensky et al. (1989, 1990, 1991) and Parilis et al. (1993). In particular, an alternative assumption about how shock waves arise is considered. If the shock wave is assumed to originate when the energy flux through the boundary defining the originally excited region exceeds a critical value, then $R_S \propto dE/dx$ and the sputtering yield will have a cubic dependence on dE/dx. However, note that an energy flux is directly related to an energy gradient. Thus, the improved version of the shock wave model resembles quite closely the pressure pulse model discussed in the next section. In fact, the Bitensky et al. (1991) expressions for the normal and radial components of 'pressure' and those given by Fenyö & Johnson (1992) for the momentum acquired by a molecule under the action of an energy density gradient are essentially the same. For MeV atomic ions incident on organic targets, calculated spatial distributions of sputtered molecules (Bitensky et al., 1991) are in excellent qualitative agreement with measured spatial distributions of desorbed molecular ions (Moshammer et al., 1990).

Molecular dynamics simulations may profitably be exploited to examine or model shock wave phenomena on a microscopic scale. For example, Holian et al. (1980) have modeled piston-driven shock waves in Lennard-Jones fluids like liquid argon. Robertson et al. (1991) have simulated a steady split shock wave in a solid which undergoes a phase transition. And Wagner et al. (1992) have simulated spallation at high strain rates under shock wave excitation. In all cases tested so far, good agreement is obtained between the simulation results and results from macroscopic continuum mechanics theory. This is remarkable considering that the simulations are based on a microscopic description of the interactions between the particles making up the system.

The use of molecular dynamics simulations for understanding shock effects after excitation of a target by an incident ion does not yet seem to be highly developed. Therefore, only three examples are briefly discussed here. Again the simulation by Shiea and Sunner (1991) is mentioned. They considered an atomic particle incident on a Lennard-Jones matrix. A temperature spike occurring around 0.5 psec after particle excitation was attributed to the passage of a shockwave. It seems that a second temperature spike occurring at 1.5 psec could be attributed to thermal energy remaining after unloading at the surface begins to proceed (in a manner similar to that shown in figs. 13 and 15 but probably differing in some details), but this interpretation is by no means clear. Another example is provided by Fenyö &

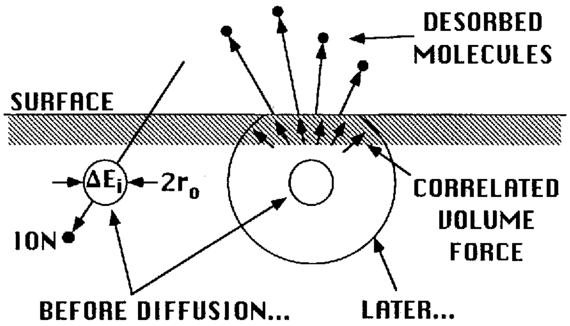

Figure 16. Left: an incident ion creates a localized region of kinetic energy excitation. Right: the motional energy diffuses collisionally. As energy reaches the surface, desorption may occur either by evaporation or in response to the correlated volume force, $\nabla\varepsilon(\mathbf{r},t)$.

Johnson (1992), who model a Lennard-Jones solid excited by depositing potential energy in a cylindrical core or 'track'. A disturbance propagating to the boundary in less than 2 psec is regarded as being the remnant of a shock wave which was diluted after travelling a distance of only 20 Å. Excess energy is left in the central excited region of the track, and this energy diffuses collisionally, causing pressure pulse desorption after about 5 psec as described below. It is possible that some fraction of the energy initially confined to the track region was due to shock heating. However, in this case it seems hard to rigorously define a shock wave given a space of only 20 Å. Finally, one may refer again to the results of Waldeer & Urbassek (1993), who modeled the sputtering caused by the incidence of an argon ion on an argon lattice. The authors clearly observed shock waves in their simulations but claimed that they did not contribute to the sputtering process.

In the absence of work designed to investigate deliberately and carefully the role played by shock waves in particle desorption, one must regard the concept of shock induced sputtering as being not well developed for geometries in which the shock waves, if they exist, are rapidly degraded to weak acoustic waves. The question of the role of shock waves in particle desorption is still very much open to discussion, and new models are appearing, such as the soliton sound-shock model of Hilf et al. (to be published).

6 Pressure-Pulse Models of Desorption

The highlights of a pressure pulse model of desorption of organic molecules have been presented by Johnson et al. (1989). The essential aspects of the model are

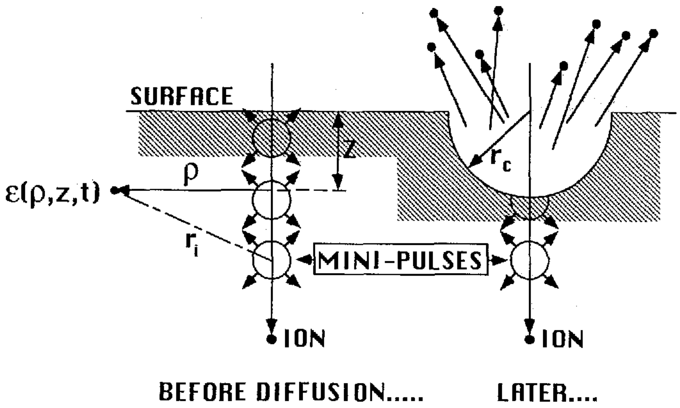

Figure 17. Pressure pulse model applied to a cylindrical ion track. Left: the cylindrical ion track is regarded as being composed of a series of "mini-pulses" spaced by a distance λ. Right: under the action of the correlated volume force, $-\nabla\varepsilon(\mathbf{r},t)$, a half-sphere of the target is ejected. r_c scales linearly with $\Delta E/\lambda \approx dE/dx$.

reviewed here. To start with, an ion traversing a solid is assumed to deposit kinetic energy ΔE_i in a small spherical volume of radius r_0. The kinetic energy could be the result either of a collisional interaction or of an electronic interaction with partial conversion of the electronically deposited energy into kinetic energy. The assumed geometry is shown in fig. 16. The energy is assumed to propagate according to a simple diffusion equation:

$$\nabla \cdot [\kappa \nabla \varepsilon(\mathbf{r},t)] = \frac{\partial \varepsilon(\mathbf{r},t)}{\partial t}. \tag{20}$$

In this equation, κ is the diffusivity, and $\varepsilon(\mathbf{r},t)$ is the volume energy density as a function of spatial coordinates and time. The solution of eq. 20 is:

$$\varepsilon(\mathbf{r},t) = \frac{\Delta E_i}{\pi^{3/2}(r_0^2+4\kappa t)^{3/2}} \exp\left(-\frac{r^2}{r_0^2+4\kappa t}\right). \tag{21}$$

If $\varepsilon(\mathbf{r},t)/kn_M$ is identified as a local temperature $T(\mathbf{r},t)$, then the result is the thermal spike formalism discussed above but for a spherical geometry. An evaporative desorption yield could be calculated using eqs. 8 and 9.

The existence of a gradient in $\varepsilon(\mathbf{r},t)$ gives rise to a 'volume force': -$\nabla\varepsilon(\mathbf{r},t)$ is the net force per unit volume on a region of material containing energy density $\varepsilon(\mathbf{r},t)$. The temporally transient nature of the solution for $\varepsilon(\mathbf{r},t)$ given in eq. 21 means that -$\nabla\varepsilon(\mathbf{r},t)$ is closely related to a sort of 'pressure pulse'. The idea is

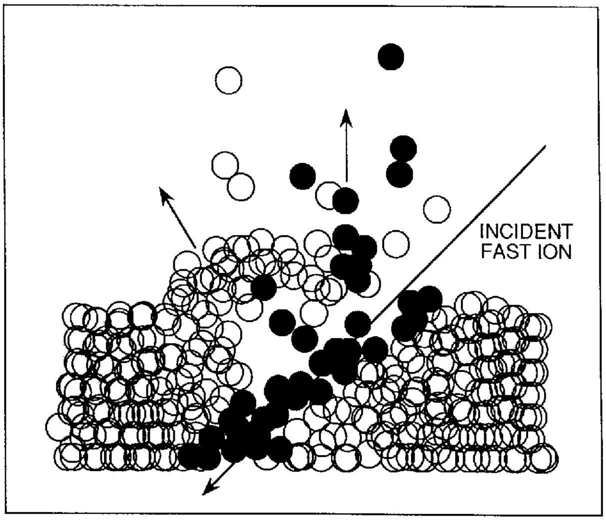

Figure 18. Molecular dynamics simulation of pressure pulse desorption due to depositing potential energy in a cylindrical track by expanding the molecules there. (o) unexpanded molecules; (•) expanded molecules. Expanded molecules are ejected directly in a "popcorn" type effect. Unexpanded molecules eject away from the track direction in response to the correlated volume force. Horizontal scale is roughly 300 Å. Adapted from Fenyö et al. (1990).

applied to the sputtering of organic molecules. The momentum acquired by a molecule experiencing the pressure pulse is:

$$\boldsymbol{p}(\mathbf{r}) = \frac{\beta}{n_{\mathrm{M}}} \int_0^\infty dt[-\boldsymbol{\nabla}\varepsilon(\mathbf{r},t)]. \tag{22}$$

Here, β is a thermodynamical proportionality constant describing the fraction of the energy in the solid which appears as translational kinetic energy rather than as internal energy of molecules. Desorption occurs when a molecule acquires a critical normal momentum which is related to the surface binding energy U:

$$p_\perp \geq p_c = \sqrt{2MU}. \tag{23}$$

The ejection of molecules by a correlated volume force is shown schematically in fig. 16.

The pressure pulse model has been applied to the case of cylindrical ion tracks, which are regarded as a collection of evenly spaced 'mini-pulses' (average spacing λ). The geometry is shown in fig. 17. At depth z, radial distance ρ, and time t,

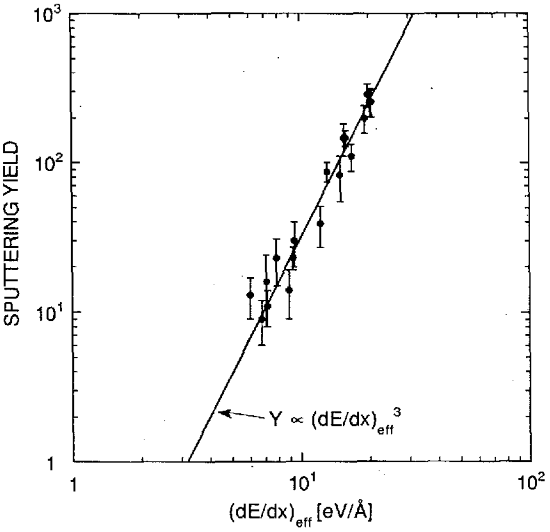

Figure 19. Simulated pressure pulse molecular sputtering yield versus dE/dx. The stopping power scaling is approximately $Y \propto (dE/dx)^3$. Adapted from Fenyö et al. (1990).

the energy density is:

$$\begin{aligned} \varepsilon(\rho, z, t) &= \sum_{i=0}^{\infty} \varepsilon_i(r_i, t) \approx \int_0^{\infty} \varepsilon(\sqrt{\rho^2 + (z' - z)^2}, t) \frac{dz'}{\lambda} \\ &= \frac{\Delta E_{\mathrm{i}}}{\lambda \pi \xi^2(t)} \exp\left(-\frac{\rho}{\xi^2(t)}\right) \frac{1 + \mathrm{erf}[z/\xi(t)]}{2} \end{aligned} \tag{24}$$

where

$$\xi^2(t) = r_0^2 + 4\kappa t \tag{25}$$

The term $(1 + \mathrm{erf}[z/\xi(t)])]/2$ decreases in magnitude as z approaches zero, showing that there is an energy gradient at and near the vacuum interface. The surface on which the ejection criterion eq. 23 is satisfied is a half-sphere of radius r_{c}, also shown in fig. 17. The theory does not assert anything on the form in which the material is ejected, but since the gradient is largest at the surface, it may be supposed that molecules are ejected sequentially starting at the surface and then proceeding downwards into the bulk. Identifying the quantity $\Delta E_{\mathrm{i}}/\lambda$ with the stopping power dE/dx, it turns out that r_{c} and the sputtering yield Y scale as follows with dE/dx:

$$r_{\mathrm{c}} \propto \frac{1}{n_{\mathrm{M}}^{2/3} U} \frac{dE}{dx}; \; Y \propto \left(\frac{1}{U} \frac{dE}{dx}\right)^3 . \tag{26}$$

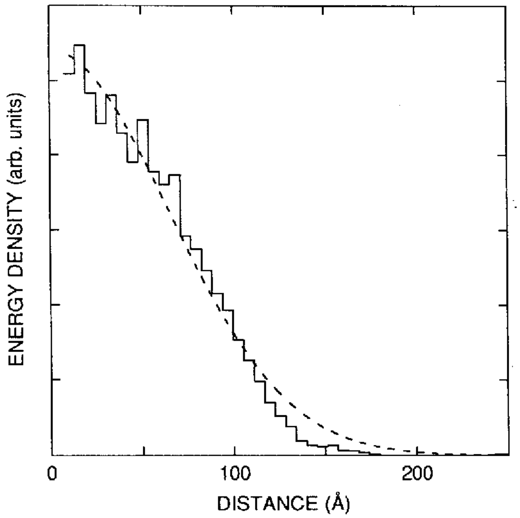

Figure 20. Radial dependence of the energy density from a pressure pulse classical dynamics simulation. The dotted line shows a comparison to the results of the energy diffusion equation. After about 4 psec, the molecular dynamics results and the diffusion equation results are completely consistent. Adapted from Fenyö & Johnson (1992).

For a cylindrical ion track oriented normal to the surface, ejection from the surface is estimated as being about 45° away from the normal direction. If ions are incident at some angle with respect to the surface normal, than the ejection is predicted to be closer to the normal than 45°. In the limit of grazing incidence, then ejection in the plane determined by the ion incidence vector and the surface normal would tend to be along the surface normal.

Fenyö et al. (1990) have performed molecular dynamics simulations of pressure pulse sputtering. Their model solid consisted of a collection of incompressible and structureless 'molecules' of mass 10^4 u which were bound together by a Lennard-Jones potential. An excited 'ion track' was created by depositing potential energy in a narrow cylindrical region of the target. This 'deposition' was performed by 'expanding' the molecules, i.e. by increasing the internuclear separation which yields the minimum potential energy between two neighbouring molecules. As shown in fig. 18, a number of the 'expanded' molecules are directly ejected close to the normal direction. These particles are ejected directly in the 'popcorn' fashion suggested by Williams & Sundqvist (1987). However, a considerable quantity of 'unexpanded' molecules are also ejected in a direction away from the direction of incidence of the impacting ion. These molecules are ejected in response to the

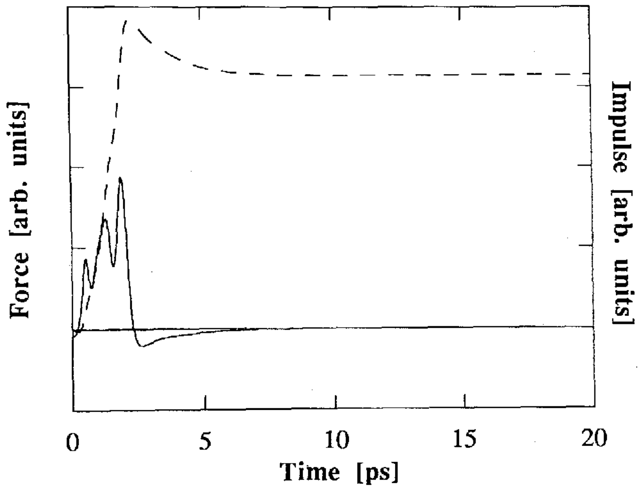

Figure 21. Force (solid line) and impulse (dotted line) experienced by a surface atom as a function of time under the influence of a pressure pulse; from a classical molecular dynamics calculation. In less than 5 psec, the atom in question is desorbed. Adapted from Fenyö & Johnson (1992).

pressure pulse ejection mechanism, as predicted by the analytical pressure pulse model described above. As shown in fig. 19, the yield of desorbed particles per excited track scales very nearly as $Y \propto (dE/dx)_e^3$, again showing consistency with the analytical pressure pulse model.

Fenyö & Johnson (1992) have used the detailed information available in classical dynamics simulations to examine whether a diffusion equation truly describes events occurring in the material surrounding an energized core region created by locally deposited energy. According to their results, the following events occur. First, over 2 to 3 psec, the core potential energy is converted into kinetic energy in the surrounding material. As shown in fig. 20, by 4 psec, the energy density is described diffusively by eq. 24. As shown in fig. 21, some molecules relatively near the center have acquired enough momentum to be desorbed, after a time less than 5 psec, and these are the pressure-pulse desorbed molecules. For times greater than 5 psec, the diffusion equation approach still describes the evolution of energy in the system, but an energy-dependent thermal diffusivity must be taken into account. Johnson et al. (1989) have noted that the conclusions from their analytic pressure pulse model 'will be similar for κ not constant'. As discussed above, the role played by shock waves in the simulation was unclear but appeared to be limited to defining the profile of deposited energy before collisional diffusion sets in. It is interesting that the classical dynamics simulation, although utilizing only detailed

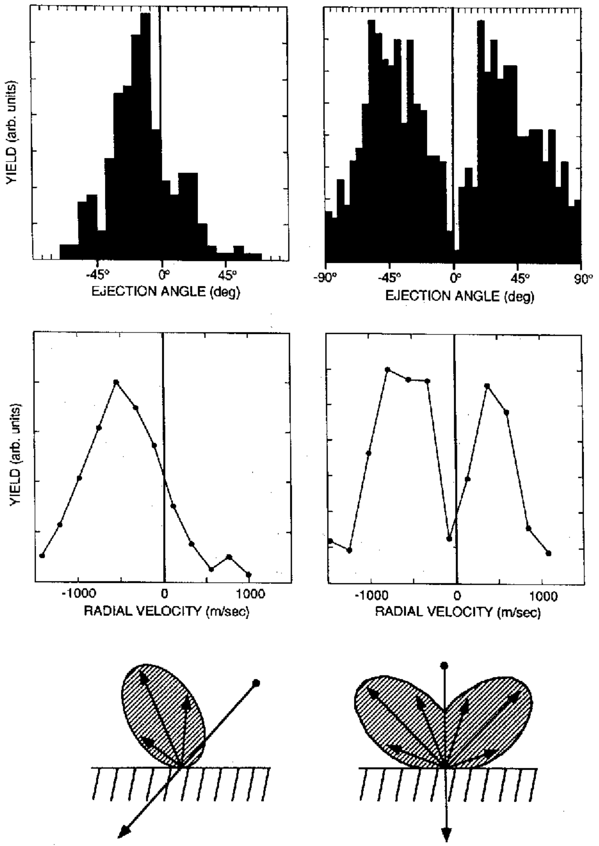

Figure 22. Top: classical molecular dynamics results, ejection angular distributions for off-normal and normal incident ions. Middle: radial velocity distributions for desorbed insulin ions for off-normal and normal incident ions. Bottom: schematic diagram of the sputtered plumes in the two cases. Adapted from Fenyö et al. (1990).

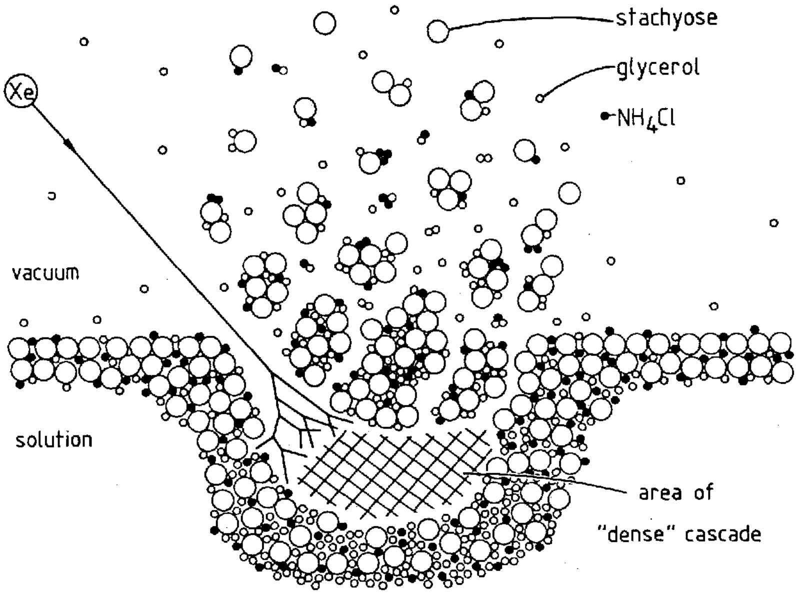

Figure 23. Schematic diagram of pressure pulse desorption due to a keV atomic ion incident on glycerol. Reprinted from Wong & Röllgen (1986) by permission.

'local' or microscopic information on how molecules interact, gives results which are largely consistent with the macroscopic diffusion equation approach which makes no reference whatsoever to the detailed structure of an organic molecular solid.

For the case of MeV atomic ions incident on organic targets, the pressure pulse model quite convincingly accounts for several important observations. For example, the model specifically refers to the dominant neutral molecule ejection yield and predicts a stopping power scaling $Y \propto (dE/dx)_e^3$. This result is consistent with the only known measurement of the neutral desorbed particle yield scaling, performed by Hedin et al. (1987) for the amino acid leucine. The magnitude of the yield, typically of the order of 1000 desorbed molecules per incident ion, is approximately accounted for. Qualitative agreement has also been obtained between the molecular-dynamics-predicted ejection angular distributions and radial velocity distributions obtained by Ens et al. (1989) for desorbed insulin ions. A comparison between these quantities is shown in fig. 22 for two different angles of incidence: 0° (i.e. normal incidence) and 45°. Not surprisingly, the neutrals show a less pronounced off-normal angular ejection pattern but with a similar sense.

Although agreement between the pressure pulse theory and MeV atomic ion induced desorption results is impressive, caution is still required in assessing the validity of the theory. For example, it is not known experimentally whether the $Y \propto (dE/dx)_{\mathrm{e}}^3$ scaling law holds in general. Also, the angular distributions of desorbed neutral particles have not yet been measured, meaning that only qualitative comparisons may be made between experiment and theoretical predictions. Since the pressure pulse model does not address the complex issue of ionization/neutralization, the different stopping power scaling laws for positive and negative desorbed ion yields remain unexplained. As Ens et al. (1989) and Moshammer et al. (1990) have shown, the angular distributions of ions from various organic samples can differ remarkably from one another in a way that is not clearly accounted for by the pressure pulse model. For example, amino acid monomer ions do not show off-normal ejection under excitation by normally incident ions, although their neutral desorption yield scales as $Y \propto (dE/dx)_{\mathrm{e}}^3$ as predicted by the pressure pulse model. Possibly the ejection of small organic molecules, the only case for which relatively detailed neutral ejection data is available, is best described by thermal models, which can also scale steeply with $(dE/dx)_{\mathrm{e}}$ over a limited range of $(dE/dx)_{\mathrm{e}}$.

Another area in which the pressure pulse concept could be applicable is that of FAB of liquid matrices containing organic analyte molecules. Wong & Röllgen (1986) wrote: 'A concerted momentum transfer to molecules by surrounding atoms or molecules is probably the only mechanism which leaves large, fragile molecules intact in the desorption process'. Their concept for desorption is shown schematically in fig. 23. The authors argue that an incident keV Xe ion penetrates 50 to 100 Å into the matrix, creating a dense cascade and stimulating a vaporization process. A high pressure builds up, ejecting overlying material in the form of clusters of analyte and solvent molecules. During desolvation, vibrationally 'cold' analyte molecules result. Considering remarks made in the introduction and in the section on thermal models concerning the size of the excited region of the target in comparison to the ejected volume, it is considered that the pressure pulse model must be taken seriously as a potential explanation of aspects of keV atom or ion bombardment of liquids.

Yen et al. (1992) have performed an experiment which can be interpreted as corroborating the pressure pulse idea for keV atomic ion bombardment of glycerol matrices. They deployed a charged HDPA surfactant on the surface of glycerol to define a layer of a preformed ionic analyte, dAMP, just below the surface. keV Ga^+, In^+, Bi^+, as well as ionic dimers and trimers of Bi and Au, were used to bombard this system, and the ion yield of dAMP was observed to scale as follows with the nuclear stopping cross section S_{n}: $Y \propto (S_{\mathrm{n}} - \mathrm{thresh})^2$. Assuming that the detected species may only come from the surface of the glycerol-surfactant system, the desorption geometry is strictly two dimensional. Referring to eq. 26, it can be seen that the pressure pulse model would predict approximately square-law stopping power scaling ($Y \propto r_c^2 \propto S_\mathrm{n}^2$), in qualitative agreement with the experimental observation. (By analogy with the simulation result of Whitlow et al. (1987), the excitation geometry may be considered to be approximately cylindrical.) Standing et al. (1982) have measured the primary ion energy dependence of alkali ion induced sputtering of ions from solid alanine. Ens (1992) has shown that, particularly for the heavier alkali ions, the ion yield is well described by the relation $Y \propto S_\mathrm{n}^3$. If it may be assumed that ions are emitted from the bulk as well as the surface for the case of the solid analine, then this result is also qualitatively consistent with the pressure pulse model. Ens et al. (1989) also measured radial velocity distributions for insulin ions desorbed by keV Cs^+ and MeV $^{252}\mathrm{Cf}$ fission fragments. Secondary ion mass spectra were surprisingly similar, but Cs^+ bombardment did not produce pronounced off-normal ejection, as might have been expected if there is pressure pulse desorption such as is considered to occur for MeV $^{252}\mathrm{Cf}$ fission fragment excitation. Perhaps the excitation geometries are not sufficiently alike, or perhaps insulin and analine targets give different results for other reasons. More work is needed to ascertain whether the pressure pulse concept may be applied to keV ion induced sputtering of organics, but there is clearly some promise that it does.

7 Concluding Remarks

In this review, a number of theoretical desorption models have been discussed and evaluated as to their ability to describe energetic particle beam induced desorption of large, thermally labile bio-organic molecules. The following models were discussed: collision cascade; ion track; evaporative thermal spike; bulk desorption; shock wave; and pressure pulse. Although the models as expressed have a degree of generality, they each tend to refer only to a part of the overall process that starts with projectile impact and ends with the detection of an ionic or neutral desorbed particle. Also, experimental situations considered were quite varied, including both solid and liquid organic targets and bombardment by keV and MeV atomic and cluster ions. Given the wide range of situations that it is desirable to model and the limited scope of each theory, it is not surprising that no one model can be found that describes everything. In some cases, it is quite plausible that two or more models apply simultaneously. For example, in the case of keV atomic ion bombardment of liquid organic matrices commonly employed in FAB mass spectroscopy, evidence of collision cascade sputtering can be seen along with the dominant bulk desorption mechanism. As another example, the precise role of shock waves in causing desorption is rather uncertain. The role of a shock wave could be merely to heat a region of a target, after which bulk desorption may occur.

In the case of cluster ion bombardment of organic targets, the operative desorption mechanism is unknown, but evaporative thermal spike, bulk desorption, pressure pulse, and shock wave mechanisms have all been convincingly invoked to rationalize the observations.

The desorption of a large bio-organic molecule without significant fragmentation requires a considerable impulse without significant accompanying internal energy. 'Volume forces' and 'collective' motion of the lattice can satisfy these requirements and lead to desorption of intact molecules relatively far from the area of initial excitation. Consequently, the bulk desorption, shock wave, and pressure pulse models are most appealing as candidates for describing large molecule desorption. Possibly the pressure pulse model may be considered to be the most general model that has been proposed so far. This model is roughly consistent with much of the body of data on MeV-atomic-ion-induced desorption of organic molecules and can be employed to rationalize many features of keV atomic- and cluster-ion bombardment of organic targets as well. Molecular dynamics simulations, based on a purely microscopic interaction picture, give results consistent with the analytical pressure pulse model and its macroscopic viewpoint of assumed diffusion of energy density with no reference to detailed structure and interactions. This impressive agreement is a further indication that ejection of whole molecules by an energy gradient volume force is a feasible desorption mechanism.

Although bulk desorption and the pressure pulse/shock wave models are most able to explain the desorption of large molecules under particle impact, there are cases for which the other models considered, such as the collision cascade, ion track, and evaporative thermal spike models, have some validity. For example, evaporative models may provide an adequate explanation for MeV ion-induced desorption of small organic molecules, and the collision cascade model describes the high kinetic energy component of molecules desorbed from liquid matrices under keV atomic ion bombardment.

Several directives for future work should be considered. For example, nearly every theory makes predictions concerning sputtered neutral molecules, whereas nearly every experiment is based on the detection and analysis of sputtered ions. This discrepancy is a serious one that hinders comparisons between data and theory. It is therefore recommended that theorists perform more detailed analyses of ionization and neutralization processes, and that experimentalists make serious efforts to measure neutral molecule yields and kinetic energy- and angle-resolved ejection distributions. Atomic force microscopy imaging of ion impact 'craters' and multiphoton ionization probes of neutral ejecta would be two effective means of extending our knowledge on the behavior of neutral desorbed molecules. Also, it is noted that well-designed computer 'gedanken experiments' provide powerful insight into the response of matter to energetic particle excitation. As has been convincingly demonstrated by a number of workers, molecular dynamics is a powerful tool for investigating the link between microscopic interactions and macroscopic behavior. However, current simulations of ion impacts on organic targets regard the target molecules as point particles, and it would be a significant advance if the internal structure of the molecular target particles could be also taken into account. This would lead to a better analysis of conditions under which varying amounts of internal excitation of desorbed molecules occurs, a subject which has not yet been thoroughly investigated.

The overall conclusion of this account is that some very impressive models of bio-organic molecule ejection have been generated. The pressure pulse model of ejection seems to be the most generally applicable model available at this time, but one must be aware of certain subsets of the observations that may require invoking other desorption models in order to be adequately explained. With appropriate extensions of existing experimental, theoretical, and calculational art, the prospects for attaining a thorough understanding of macromolecular desorption are quite promising.

Acknowledgments

The author expresses his gratitude towards a number of individuals for their help in understanding the theoretical models and experimental background discussed herein, including Jörgen Ahlbom, Iosif Bitensky, Plamen Demirev, Jan Eriksson, David Fenyö, Per Håkansson, and Robert E. Johnson. He also thanks Bo U.R. Sundqvist for many useful discussions and for the opportunity to be a part of the Ion Physics Group at Uppsala where much work in the field of ion-induced desorption of biomolecules is carried out. He is also appreciative of P. Sigmund for the opportunity to participate in the SPUT92 conference. Finally, the author is grateful for the financial support provided by the Swedish Research Council for Engineering Sciences.

References

Balaji V, David DE, Magnera TF, Michl J and Urbassek HM, 1990: Nucl. Instrum. Meth. B **46**, 435

Barber M, Bordoli RS, Sedgewick RD and Taylor AN, 1981: J. Chem. Soc., Chem. Commun., 325

Barofsky DF and Barofsky E, 1986: *Ion Formation from Organic Solids (IFOS III)*, ed. Benninghoven A, Springer-Verlag, Berlin, 86

Barofsky DF, Ilias AM, Barofsky E and Murphy JH, 1984: *32nd Ann. Conf. Mass Spectrom. and Allied Topics*, San Antonio, Book of Abstracts, 186

Barofsky DF, Jiang L-F, Barofsky E and Yen T-Y, 1991: *Methods and Mechanisms for Producing Ions from Large Molecules*, eds. Standing KG and Ens W, Plenum Press, New York, 101

Benninghoven A, Jaspers D and Sichtermann W, 1976: Appl. Phys. **11**, 35

Bitensky IS and Parilis ES, 1987: Nucl. Instrum. Meth. B **21**, 26

Bitensky IS, Goldenberg AM and Parilis ES, 1989: J. de Physique C **2**, 213

Bitensky IS, Goldenberg AM and Parilis ES, 1990: *Ion Formation from Organic Solids (IFOS V)*, eds. Hedin A et al., John Wiley and Sons, New York, 205

Bitensky IS, Goldenberg AM and Parilis ES, 1991: *Methods and Mechanisms for Producing Ions from Large Molecules*, eds. Standing KG and Ens W, Plenum Press, New York, 83

Brandt W and Ritchie RH, 1974: *Physical Mechanisms in Radiation Biology*, eds. Cooper RD and Wood RD, USEC Technical Inf. Center, Oak Ridge, Tennessee, 20

Carter G, 1983: Nucl. Instrum. Meth. **209/210**, 1

David DE, Magnera TF, Tian R, Stulik D and Michl J, 1986: Nucl. Instrum. Meth. B **14**, 378

Demirev PA, 1988: Adv. in Mass Spect. **11A**, 460

Ens W, 1992: Mat. Fys. Medd. Dan. Vid. Selsk. **43**, 155

Ens W, Sundqvist BUR, Håkansson P, Hedin A and Jonsson G, 1989: Phys. Rev. B **39**, 763

Ens W, Sundqvist BUR, Håkansson P, Fenyö D, Hedin A and Jonsson G, 1989a: J. de Physique C **2**, 9

Falcone G, 1987: Surf. Sci. **187**, 212

Falcone G, 1990: La Rivista del Nuovo Cimento, 1

Falcone G, Sroubek Z, Sindona G and Uccella N, 1988: Int. J. of Mass Spect. and Ion Phys. **83**, 223

Fenyö D and Johnson RE, 1992: Phys. Rev. B **46**, 5090

Fenyö D, Sundqvist BUR, Karlsson BR and Johnson RE, 1990: Phys. Rev. B **42**, 1895

Fenyö D, Hedin A, Håkansson P and Sundqvist BUR, 1990a: Int. J. of Mass Spectrom. and Ion Proc. **100**, 63

Garrison BJ, 1983: Int. J. of Mass Spect. and Ion Phys. **53**, 243

Gol'danskii VI, Lantsburg EYa and Yampol'skii PA, 1975: JETP Lett. **21**, 166

Haring RA, Roosendaal HE and Zalm PC, 1987: Nucl. Instrum. and Meth. B **28**, 205

Hedin A, Håkansson P, Sundqvist BUR and Johnson RE, 1985: Phys. Rev. B **31**, 1780

Hedin A, Håkansson P, Salehpour M and Sundqvist BUR, 1987: Phys. Rev. B **35**, 7377

Holian BL, Hoover WG, Moran B and Straub GK, 1980: Phys. Rev. A **22**, 2798

Hoogerbrugge R and Kistemaker PG, 1987: Nucl. Instrum. Methods B **21**, 37

Hoogerbrugge R, Van der Zande WJ and Kistemaker PG, 1987: Int. J. of Mass Spect. and Ion Proc. **76**, 239

Hoogerbrugge R, Bobeldijk M, Kistemaker PG and Los J, 1988: J. Chem. Phys. **88**, 5314

Johnson RE, 1987: Int. J. of Mass Spectrom. and Ion Proc. **78**, 357

Johnson RE, 1990: *Energetic Charged-Particle Interactions with Atmospheres and Surfaces*, Springer-Verlag, Berlin

Johnson RE and Evatt R, 1980: Rad. Eff. **52**, 187

Johnson RE and Sundqvist BUR, 1992: Physics Today, March, 28

Johnson RE, Sundqvist BUR, Hedin A and Fenyö D, 1989: Phys. Rev. B **40**, 49

Johnson RE, Pospieszalska M and Brown WL, 1991: Phys. Rev. B **44**, 7263

Junack M, Sichtermann W and Benninghoven A, 1986: *Ion Formation from Organic Solids (IFOS III)*, ed. Benninghoven A, Springer-Verlag, Berlin, 96

Karas M and Hillenkamp F, 1988: Anal. Chem. **60**, 2299

Katz R, 1968: Nuclear Track Detection **2**, 1

Kaufmann R, Kirsch D, Rood H-A and Spengler B, 1992: Rap. Comm. in Mass Spect. **6**, 98

Kelly R, 1990: Nucl. Instrum. Meth. B **46**, 441

Kelner L and Markey SP, 1984: Int. J. of Mass Spect. and Ion Proc. **59**, 157

Kitazoe Y, Hiraoka N and Yamamura Y, 1981: Surf. Sci. **111**, 381

Können GP, Tip A and de Vries AE, 1975: Rad. Eff. **26**, 23

Landau LD and Lifschitz EM, 1959: *Fluid Mechanics*, Reading, Massachussetts

Ledbetter MC, Beuhler RJ and Friedman L, 1987: Proc. Natl. Acad. Sci. USA **84**, 85

Lee S-L and Lucchese RA, 1989: J. de Physique C **2**, 231

Lucchese RR, 1987: J. Chem. Phys. **86**, 443

Macfarlane RD, 1982: Acc. Chem. Res. **15**, 268

Macfarlane RD, 1982a: Nucl. Instrum. and Methods **198**, 75

Macfarlane RD and Torgerson DF, 1976: Science **191**, 920

Macfarlane RD and Torgerson DF, 1976a: Phys. Rev. Lett. **36**, 486

Mahoney JF, Perel J, Ruatta SA, Martino PA, Husain S and Lee TD, 1991: Rap. Comm. in Mass Spect. **5**, 441

Mahoney JF, Perel J, Lee TD, Martino PA and Williams P, 1992: J. Am. Soc. Mass Spectrom. **3**, 311

Martens J, Ens W, Standing KG and Verentchikov A, 1992: Rap. Comm. in Mass Spect. **6**, 147

Matthew MW, Beuhler RJ, Ledbetter M and Friedman L, 1986: Nucl. Instrum. Meth. B **14**, 448

Moshammer R, 1991: Thesis, Institut für Kernphysik, Techn. Hochschule Darmstadt, Germany

Moshammer R, Matthäus R, Wien K and Bolbach G, 1990: *Ion Formation from Organic Solids (IFOS V)*, eds. Hedin A et al., John Wiley and Sons, New York, 17

Mozumder A, 1969: Adv. Radiat. Chem. **1**, 1

Ollerhead RW, Bøttiger J, Davies JA, L'Ecuyer J, Haugen HK and Matsunami N, 1980: Rad. Eff. **49**, 203

Parilis ES, Kishinevsky LM, Turaev NYu, Baklitzky BE, Umarov FF, Verleger VKh, Nizhnaya SL and Bitensky IS, 1993: *Atomic Collisions on Solid Surfaces*, Elsevier Science Publishers, Amsterdam, 339

dePauw E, 1986: Mass Spectrosc. Rev. **5**, 191

Robertson DH, Brenner DW and White CT, 1991: Phys. Rev. Lett. **67**, 3132

Salehpour M, Håkansson P, Sundqvist BUR and Widdiyasekera S, 1986: Nucl. Inst. Meth. B **13**, 278

Seiberling LE, Griffith JE and Tombrello TA, 1980: Rad. Eff. **52**, 201

Shapiro MH and Tombrello TA, 1992: Unpublished presentation at *SPUT92*

Shiea JT and Sunner J, 1990: Int. J. of Mass Spect. and Ion Proc. **96**, 243

Shiea JT and Sunner J, 1991: *Methods and Mechanisms for Producing Ions from Large Molecules*, eds. Standing KG and Ens W, Plenum Press, New York, 147

Sigmund P, 1969: Phys. Rev. **184**, 383

Sigmund P, 1969a: Phys. Rev. **187**, 768

Sigmund P, 1974: Appl. Phys. Lett. **25**, 169

Sigmund P, 1981: *Sputtering by Ion Bombardment, Vol. I*, ed. by Berisch R, Springer, Berlin, 8

Sigmund P, 1989: J. de Physique C **2**, 175

Sigmund P and Claussen C, 1981: J. Appl. Phys. **52**, 990

Standing KG, Chait BT, Ens W, McIntosh G and Beavis R, 1982: Nucl. Instrum. and Methods B **198**, 33

Sundqvist BUR, 1991: *Sputtering by Particle Bombardment Vol. III*, eds. Behrisch R and Wittmaack K, Springer-Verlag, Berlin, 257

Sunner J, 1990: *Ion Formation from Organic Solids (IFOS V)*, eds. Hedin A et al., A, John Wiley and Sons, New York, 175

Sunner J, Morales A and Kebarle P, 1988: Int. J. of Mass Spect. and Ion Proc. **86** 169

Sunner J, Ikonomou MG and Kebarle P, 1988a: Int. J. of Mass Spect. and Ion Proc. **82**, 221

Torgerson DF, Skowronski RP and Macfarlane RD, 1974: Biochem. Biophys. Res. Commun. **60**, 616

Urbassek HM, 1987: Nucl. Instrum. Meth. B **18**, 587

Urbassek HM and Michl J, 1987: Nucl. Instrum. Meth. B **22**, 480
Urbassek HM and Sigmund P, 1984: Appl. Phys. A **35**, 19
Urbassek HM and Waldeer KT, 1991: Phys. Rev. Lett. **67**, 105
Vineyard GH, 1976: Rad. Eff. **29**, 245
Wagner NJ, Holian BL and Voter AF, 1992: Phys. Rev. A **45**, 8457
Waldeer KT and Urbassek HM, 1993: Nucl. Instrum. Meth. B **73**, 14
Whitlow HJ, Hautala M and Sundqvist BUR, 1987: Int. J. of Mass Spectrom. and Ion Proc. **78**, 329
Williams P and Sundqvist BUR, 1987: Phys. Rev. Lett. **58**, 1031
Wong SS and Röllgen FW, 1986: Nucl. Instrum. Meth. B **14**, 436
Wong SS, Röllgen FW, Manz I and Przybylski M, 1985: Biomed. Mass Spectrom. **12**, 43
Yen TY, 1992: Thesis, Dept. of Agricultural Chemistry, Oregon State University
Yen TY, Barofsky E and Barofsky DF, 1992: Poster presented at SPUT92, Copenhagen
Zel'dovich YaB and Raizer YuP, 1967: *Physics of Shock Waves and High-Temperature Hydrodynamic Phenomena*, eds. Hayes WD and Probstein RF, Academic Press, New York
Zel'dovich Ya and Todes OM, 1940: Zh. Eksp. Fiz. **10** 1441

Sputtering of Inorganic Insulators

By R.E. Johnson
Engineering Physics, Thornton Hall,
University of Virginia, Charlottesville, VA 22903, U.S.A.
and
J. Schou
Association Euratom-Risø National Laboratory,
Physics Department, DK-4000 Roskilde, Denmark

Synopsis

Results for knock-on and electronic sputtering of inorganic insulators are summarized. Knock-on sputtering of room-temperature insulators can be treated using standard sputtering theory at low fluences. Since these materials are mostly chemical compounds, the treatment is roughly analogous to that for alloy sputtering. Whereas data are available only for one elemental room-temperature insulator, sulfur, a number of studies have been performed for low-temperature condensed gases for which nonlinear effects are observed even at low excitation densities.

The impressive development in electronic sputtering of inorganic insulators during the last decade is also described. Solid-state electronic transport and relaxation processes, which occur following the production of electronic excitations in a solid by charged particles and photons, can be studied by sputtering and luminescence measurements combined with molecular dynamics calculations. For the rare-gas solids the dynamics of exciton transport, trapping, and relaxation are reasonably well described, with the primary energizing process being a repulsive interaction of an atom within an excimer or with the lattice. Aspects of the nonradiative electronic transitions leading to electronic sputtering for solid nitrogen and oxygen are similarly understood, since the sputtering yields are linear in excitation density at low excitation densities. These yields, like those for other low-temperature condensed gases, become quadratic at higher excitation densities, consistent with the 'thermal spike' ejection. Because of the richness of possible electronic relaxation processes, there is no universal mechanism in electronic sputtering. However, for incident charged particles the efficiency of electronic sputtering of all inorganic insulators is determined both by the size of the nonradiative relaxation energy released compared to the surface binding energy and by the size of the excitation density deposited, with nonlinear dependencies on excitation density predominating.

Contents

1 Introduction

Inorganic insulators comprise a class of materials with widely differing properties. This includes highly refractory materials, some metallic oxides, as well as the most volatile materials, the frozen gases, which are solids only at very low temperatures. In addition, the electrical conductivity can differ by many orders of magnitude throughout this class of insulators, and the composition varies from simple structures of pure elements to complicated chemical compounds.

The physical processes leading to the sputtering of insulators are knock-on collisions and electronic excitations. For knock-on sputtering a comprehensive data base and a number of theoretical treatments exist for elemental metals, alloys, and refractory solids (Andersen & Bay, 1981; Sigmund, 1981; Betz & Wehner, 1983; Townsend, 1983; Kelly, 1984a,b; Lam, 1990; Falcone, 1990; Sigmund & Oliva, 1993). Therefore, to extend knock-on sputtering to inorganic insulators means that the sputtering of multicomponent and of volatile solids must be described. The treatment of electronic sputtering is different as it is induced by incident electrons and photons as well as by ions and does not occur in metals, except, possibly, at very high excitation density when a significant density of inner shell excitations is created.

The emphasis in this article is on electronic sputtering of inorganic insulators for which the most dramatic advances have occurred over the last fifteen years, particularly for the low-temperature condensed gases. The interest in such solids was stimulated in part by the first systematic studies of sputtering of water ice by W.L. Brown, L.J. Lanzerotti and coworkers which gave unexpectedly large sputtering yields (Brown et al., 1978). These experiments were performed in response to the Voyager spacecraft observations, which showed that the icy objects in the outer solar system were exposed to energetic plasma-ion bombardment (Brown et al., 1982; Johnson, 1990).

The low-temperature condensed gases are also ideal systems for basic studies of the differences in electronic relaxation processes between gases and solids. Because the lattice binding energies vary over an order of magnitude, such solids provide a means for exploring the efficiency of processes leading to sputtering and the dependence on excitation density. Electronic sputtering of these solids is closely related to photon, electron, and ion-stimulated desorption of adsorbed species (DIET, 1983-1993). Therefore, the classical MGR-desorption mechanism (Menzel & Gomer,1964; Redhead, 1964) has often been invoked to describe the non-radiative, electronic transitions leading to sputtering.

Immediate applications of electronic sputtering are the particle release from cryopanels during bombardment by stray particles in accelerators (Benvenuti et al., 1987), and lithography by radiation-induced alterations of solids (Brown, 1984). Knock-on sputtering of insulators has been studied much less systematically than electronic sputtering, but is also of considerable interest for planetary science (Johnson, 1990). This trend contrasts with the rapid developments occurring in sputter deposition, which was the dominant production method for epitaxial thin films of metal oxides and other refractory solids up to 1990 (Harper, 1990; McClanahan & Laegreid, 1991; Geerk et al., 1989). In spite of the wide use of sputter deposition, almost no systematic data are available at present for many oxides including high T_c-superconductors.

The content of this chapter has overlap with that in a number of other chapters in this issue, particularly the chapters on desorption/sputtering of biomolecules by heavy-ion beams and laser pulses (Reimann, 1993; Håkansson, 1993) and the chapter on sputtering of alkali-halides (Szymonski, 1993). We first review the concepts behind knock-on sputtering of inorganic insulators. This includes consideration of both linear and nonlinear sputtering processes. Although this discussion is brief, it lays the ground work for the discussion of electronically-induced sputtering and the resulting material alterations. Alterations occur because of the lack of stoichiometry in sputtering of room-temperature insulators, which are mostly chemical compounds (Betz & Wehner, 1983), and because chemical processes can be induced in such materials (Roth, 1983). We then describe sputtering in response to electronic excitations produced by fast ions, electrons, or photons, with the emphasis on ion-induced sputtering, and we include the results of relevant molecular dynamics calculations. This is followed by a brief review of the experimental methods used to study electronic sputtering. Finally, recent experimental results are presented for both knock-on and electronic sputtering of inorganic insulators.

Before proceeding we note that sputtering can be separated into three, roughly separate physical processes. First, the incident radiation produces a distributed source of momentum transfer events. An event may be a direct momentum transfer to a target atom, by an incident ion or by a nuclear fragment from a radioactive decay, or it may be momentum produced by a non-radiative relaxation process following an electronic excitation. Second, for excitations of species at some depth into the solid, the possibility of momentum transport to the surface can be described by an approximation to the Boltzmann transport equations, such as the linear collision cascade, diffusion or hydrodynamic equations. Finally, either for an excitation at the surface or for momentum transported to the surface, escape is determined by the binding of atoms and molecules to the solid.

2 Stopping Power Concepts

Since sputtering is determined by the local energy density deposited in the solid, for incident fast ions and electrons an important quantity is the stopping power dE/dx, the energy loss per unit path length. This quantity is described in reviews by Sigmund (1975a) and Ziegler et al. (1985) for ions and by Inokuti (1971) and Schou (1988) for electrons.

The total stopping power for fast ions is usually expressed as a sum of the electronic and nuclear-elastic contributions,

$$dE/dx = (dE/dx)_{\mathrm{e}} + (dE/dx)_{\mathrm{n}}.$$

The second term gives the energy deposited which is known to lead to knock-on sputtering, whereas the first term gives the contribution that in some materials can lead to electronic sputtering. Although there can be synergism between electronic and knock-on processes for ions with keV/amu energies (e.g., Matsunami, 1990; Varga et al., 1991), we ignore this here. A quantity that, to first order, is

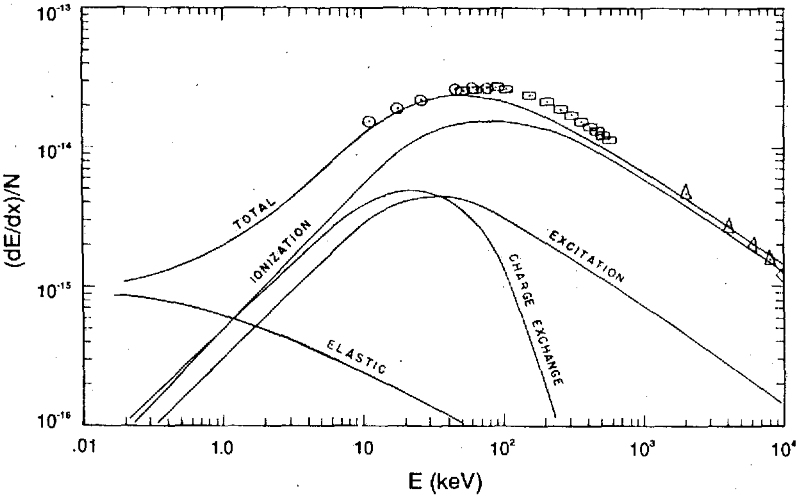

Figure 1a. Semi-empirical stopping cross sections, S, for water vapour where $dE/dx = N_{\mathrm{mol}}S$ with N_{mol} the molecular density. S is given as a sum of its constituents S_{n} (elastic or knock-on) and S_{e} (a sum of ionization, excitation and the charge exchange cycle); data points and curves from Miller and Green (1973).

independent of the material density N is also used,

$$S(E) = \frac{1}{N}\frac{dE}{dx}$$

called the stopping cross section, shown for water in fig. 1a. The yield of molecules ejected per incident ion by these two processes is also assumed to be roughly additive, as suggested by the structure of the measured sputtering yields for protons incident on low temperature solid H_2O in fig. 1b. The electronic component of the stopping power in fig. 1a. is, in turn, a sum of different excitation processes, making electronic sputtering of insulators a richer and more complex phenomenon.

In the description of measured yields, stopping powers obtained directly or extrapolated from measurements are used. Since sputtering is a surface process, it is important to remember that the value of the stopping power at the entrance surface can differ from the value measured: the average stopping power after passage through a thin sample, called the 'equilibrium charge state' stopping power. This fact has often hampered comparisons of measured yields to models. Ion beams can be prepared in a variety of charge states, but the effective charge state of the ions moving inside the material can change from that of the incident ions. This change occurs over a distance determined by the electron capture and loss cross sections

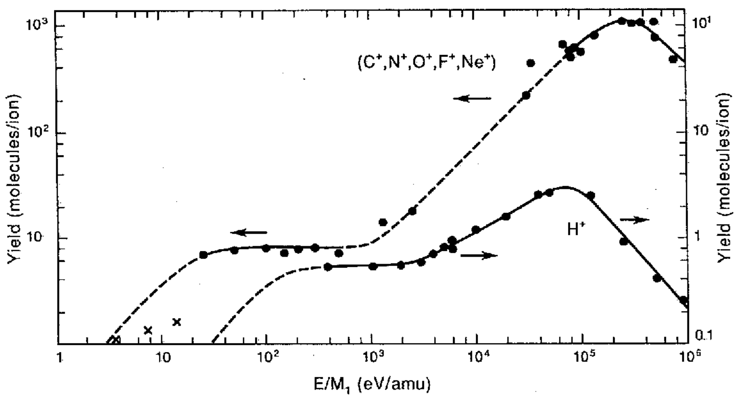

Figure 1b. The sputtering yield of water ice (< 77 K) vs. E/M_1 (ion energy/ion mass) by incident H^+ and medium mass ions (C^+, N^+, O^+, F^+, Ne^+): experimental points •, and molecular dynamics calculations, ×, from Johnson (1990).

(Allison, 1958; Maynard & Deutsch, 1987). Although the electronic sputtering yield is found to be sensitive to the incident ion charge state, few attempts have been made to use a non-equilibrium charge state stopping power for interpreting sputtering (e.g., Johnson & Brown, 1982; Nieschler et al., 1984; Wien et al., 1987). Therefore, to facilitate comparisons with theory, equilibrium charge state beams can be prepared for fast ions by having the beam first penetrate a thin carbon foil, since the equilibrium charge is expected to be roughly independent of the material penetrated. Use of molecular projectiles provides an additional control over the energy deposition near the surface (Andersen & Bay, 1974; Oliva-Florio et al., 1979; Brown et al., 1980b; Ellegaard et al., 1993a) by creating overlapping regions of excitation. Because the components of the incident molecule gradually scatter, the overlap decreases with distance into the solid, allowing a test of the effective depth for energy deposition leading to ejection.

3 Theory: Knock-on Sputtering

When an incident particle strikes a target particle in the surface or in the near surface layers of a solid, the struck particle may have sufficient momentum and the appropriate direction to overcome the binding forces. It can escape either directly or after scattering from a neighbor, as in fig. 2a. If it does not escape directly, the struck particle will collide with another target particle setting up a cascade of collisions which can transport momentum to the surface and lead to particle

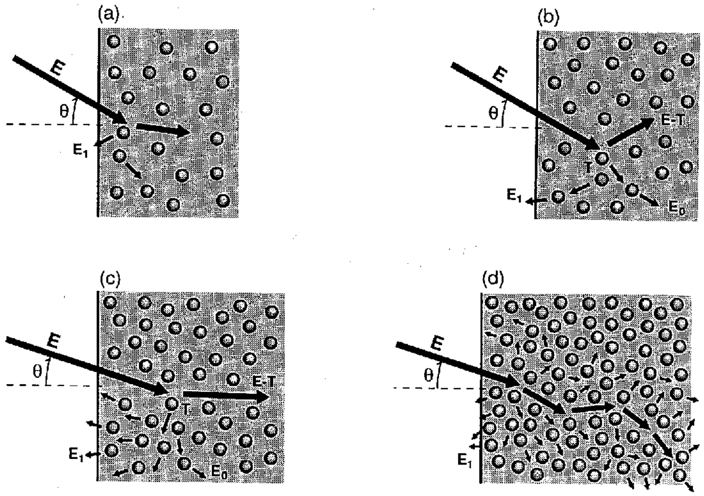

Figure 2. a) Incident ion ejects an atom from the solid in a direct knock-on; b) incident ion strikes an atom and initiates a cascade which leads to an ejected atom; c) a cascade in a volatile solid; d) a high density of cascades giving a cylindrically energized region and a nonlinear sputtering yield.

ejection.

An important aspect in sputtering is the density of atoms set in motion near the surface as indicated in figs. 2a-d. It affects both the description of the momentum transport in the solid and whether species in a molecular insulator are ejected as atoms or molecules. In addition, the cascades produced act separately when the number per unit volume is small (linear sputtering regime), as in fig. 2b or 2c, or cooperatively when the density of cascades is high (nonlinear sputtering regime) as in fig. 2d. Finally, if the energy deposited does not dissipate sufficiently fast, the ambient temperature of the target can increase, leading to beam-induced sublimation. In the following, we treat each of these contributions separately.

3.1 Single-Collision Ejection

The probability of direct ejection by a knock-on event is calculated from the collision cross section $d\sigma(\vec{p};\vec{p}_1,\vec{p}_2)$, where $\vec{p}$ is the momentum of the incident ion, with the direction generally given relative to the surface normal, and $\vec{p}_1$ and $\vec{p}_2$ are the momenta of the incident and recoiling target particle after the collision. The probability per unit path length for a collision is obtained from $N d\sigma$, where N is the number of atoms per volume. We write $P_{\rm es}(\vec{p}_2,x)$ as the probability of a target particle of momentum $\vec{p}_2$ to escape from a depth x where it is set in motion by the collision (Oliva et al., 1987; Sigmund et al., 1989). If the mean free path for an energetic collision, λ_c, determined from $N d\sigma$, is much greater than the average thickness of a monolayer, ℓ, then the single collision sputtering yield is calculated as a product of the probability of producing an energetic recoil and the escape probability,

$$Y^s = \int\int P_{es}(\vec{p}_2, x) \frac{N d\sigma}{\cos\theta} dx \tag{1}$$

where θ is the angle of incidence with respect to the surface normal. Y^s varies steeply with θ near $\theta = 0$, but for large θ it becomes $\sim \ell/(2\lambda_c \cos\theta)$, since ejection occurs predominantly from the surface layer, and since roughly half the directions are outward. λ_c^{-1} can be estimated by integrating $N d\sigma$ over energy transfers greater than the displacement energy of the solid. For sputtering of refractory solids at large θ, Y^s is an important or even dominant fraction of the total sputtering yield evaluated below.

3.2 Collision Cascades

In addition to direct ejection, a primary recoil set in motion below the surface can initiate a cascade of collisions which can transport momentum to the surface, as in fig. 2b (Sigmund, 1969, 1972, 1981; Kelly, 1984b). The Boltzmann transport equation for moving particles colliding with nearly stationary particles provides the energy distributions of recoils, which only weakly depend on the interaction forces (Sigmund, 1969). In a solid composed of identical atoms, the number of recoils set in motion with energy between E_0 and $E_0 + dE_0$ by a primary recoil of energy T is

$$G(T, E_0) dE_0 \approx \Gamma \frac{T}{E_0^2} dE_0 \text{ for } T \gg E_0. \tag{2}$$

When recoil energy is also lost to electronic and vibrational excitation, that amount of energy is removed from T in eq. (2). Only the quantity Γ in eq. (2) is determined by the interatomic potential, and it is of the order of unity. Calculating the angular distribution is more complicated, but in the limit $T \gg E_0$, i. e., after a number of generations of recoils, it approaches an isotropic distribution.

The probability of escape for a recoil approaching the surface is $P_{es}(\vec{p}_0, x)$, where $E_0 = p_0^2/2M$. Since the production of secondary recoils is determined by the quantity $N d\sigma$, the cascade contribution to sputtering has a form like that in eq. (1), but includes momentum transport,

$$Y^c \approx \alpha \int\int\int\int P_{es}(\vec{p}_0, x) G(T, E_0) dE_0 \frac{d\Omega}{4\pi} N d\sigma dx. \tag{3}$$

Here $d\Omega/4\pi$ comes from the assumed isotropic production of recoils, and the transport coefficient α, which corrects for this, includes the dependence on incident angle θ (Sigmund, 1969). The total yield, to which experiment is compared, is $Y = Y^{\mathrm{s}} + Y^{\mathrm{c}}$; near threshold Y^{s} dominates. For isotropically produced primary recoils, resulting from radioactive decay or electronic excitations, the transport correction is not needed and it is possible to replace $G(T, E_0)$ in eq. (3) by $G(T, E_0) + \delta(T - E_0)$, so that eqs. (1) and (3) can be combined.

The variables in eq. (3) can be separated and the integrals carried out. At energies much larger than the threshold energy for initiating sputtering (Andersen & Bay, 1981), the resulting yield is often written

$$Y = Y^{\mathrm{s}} + Y^{\mathrm{c}} \approx \Lambda_{\mathrm{c}} F_{\mathrm{D}}(E, 0). \tag{4}$$

The quantity $F_{\mathrm{D}}(E, x)$, which depends also on θ, is the distribution of recoil energy per unit depth as obtained from a Boltzmann transport equation. Because $F_{\mathrm{D}}(E, x)$ is not uniform with depth the surface value, $F_{\mathrm{D}}(E, 0)$, is used in eq. (4). This includes the source function and transport (Sigmund, 1969), whereas Λ_{c} is an ejection efficiency, which contains the averaged escape probability.

To relate the discussion above to electronically stimulated sputtering we note that, if the spatial dependence of the cascade is known, a yield, $Y(T, x)$, can be constructed for a primary recoil produced at a depth x with energy T. A sputter-weighted depth describing transport and escape for a uniform excitation density (Cui et al., 1988) can be defined[1]:

$$\overline{\Delta x}(T) = \int Y(T, x) dx. \tag{5a}$$

The total yield $(Y^{\mathrm{s}} + Y^{\mathrm{c}})$ is obtained by integrating over the primary recoil distribution $N d\sigma$,

$$Y = \int \overline{\Delta x}(T) \frac{N d\sigma}{\cos\theta} dx \approx \frac{\overline{\Delta x_{\mathrm{c}}}}{\lambda_{\mathrm{c}} \cos\theta}. \tag{5b}$$

This is equivalent to the result in eq. (4), and can be written using the mean depth $\lambda_{\mathrm{c}} \cos\theta$ between the production events of two energetic primary recoils and $\overline{\Delta x_{\mathrm{c}}}$, a sputter-weighted depth.

Sigmund (1969) approximately solved the transport equations for a steeply varying, Born-Mayer-like, interaction, giving $\Gamma \approx 6/\pi^2$ in eq. (2), and determining the dependence of α on the ion/target atom mass ratio. He treated both planar and spherical surface binding. For atomic ejection subject to planar binding of

---

[1] $\overline{\Delta x}(T)$, as defined by eq. (5a), may considerably exceed the maximum depth of origin of sputtered particles, i.e., the depth range over which $Y(T, x)$ is nonvanishing.

magnitude U,

$$\Lambda_\mathrm{c} = \frac{\Gamma/4}{N\overline{\sigma}_\mathrm{d}U} \tag{6a}$$

where $(N\overline{\sigma}_\mathrm{d})^{-1}$ is the effective mean-free-path for escape, and $\overline{\sigma}_\mathrm{d}$ is the diffusion (momentum-transfer) cross section averaged over the spectrum of escape energies[2]. Since particles are predominantly ejected from the surface layer (Sigmund et al., 1989), $(N\overline{\sigma}_\mathrm{d})^{-1}$ is approximately the thickness of a monolayer

$$\ell = N^{-1/3}. \tag{6b}$$

Then, the quantity in eq. (4) becomes

$$\Lambda_\mathrm{c} = \frac{\Gamma}{4}\frac{\ell}{U}. \tag{6c}$$

In addition, the sputtering yield in eq. (4) is often written using

$$F_\mathrm{D}(E,0) = \alpha(dE/dx)_\mathrm{n} \approx \alpha(0)\frac{NS_\mathrm{n}}{\cos^q\theta}, \tag{7}$$

applicable at small angles, where S_n is the nuclear stopping cross section (fig. 1a) and the exponent q depends weakly on the incident ion to target atom mass ratio (Sigmund, 1969; Oliva-Florio et al., 1979). For normal incidence, Andersen & Bay (1981) have determined the quantity $\alpha\Gamma/4\overline{\sigma}_\mathrm{d}$. Although the traditionally assumed values of Γ and $\overline{\sigma}_\mathrm{d}$ have to be altered (Vicanek et al., 1989), the value typically used for $\alpha\Gamma/4\overline{\sigma}_\mathrm{d}$ at normal incidence is close to that derived experimentally by Andersen & Bay.

From the recoil distribution G in eq. (2), the energy spectrum of the ejecta for planar binding can be obtained. A particle escapes when the component of energy normal to the surface is greater than that of the barrier U. This gives

$$\frac{1}{Y}\frac{dY}{dE_1} = \frac{2UE_1}{(U+E_1)^3}, \tag{8a}$$

where E_1 is the energy of the ejected particle. For spherical binding the energy of the escaping particle must be greater than U and the direction outward. This gives

$$\frac{1}{Y}\frac{dY}{dE_1} = \frac{U}{(U+E_1)^2}, \tag{8b}$$

and the yield parameter in eq. (6a) doubles in size. The quantity U typically used for comparison with data is the cohesive energy, equal to the average sublimation energy. This is appropriate for experiments in which a number of layers of material are removed. For crystalline surfaces and sub-monolayer yields, the actual surface binding energy is appropriate.

---

[2] $\overline{\sigma}_\mathrm{d} = 2C_0 = \pi\lambda_0 a_\mathrm{BM}^2$ in Sigmund's (1969) notation.

4 Theory: Nonlinear Effects

In the above it was assumed that a recoil always struck a nearly stationary atom and the collisions were binary. A breakdown in the latter assumption does not affect the above expressions significantly (Cui et al. 1988, 1989a,b,c). However, when the first assumption breaks down and recoils strike atoms already set in motion, nonlinear effects occur in sputtering. For instance, the energy spectrum of a primary recoil cascade is not proportional to the energy transfer, T, generating the cascade, as in eq. (2), and the energy spectrum of the ejecta will exhibit an enhancement at low energies over that in eq. (8a). Such a cascade is often referred to as a 'thermal spike', or just a 'recoil spike', as thermodynamic equilibrium is generally not attained. If these spikes are well separated spatially or in time then the calculated yield is still linear in the quantity λ_c^{-1} , as in eq. (5c): proportional to the number of energetic primary recoils set in motion per unit path length. However, when λ_c is of the order of or less than the cascade radius, as in fig. 2d, then recoils in one cascade can strike those in another (Andersen & Bay, 1974; Sigmund, 1974, 1975b). In this case, even if the ion flux is low, so the sample is not heated, the sputtering yield can vary faster than linearly with λ_c^{-1}, and a quasi-thermal equilibrium can occur (Sigmund, 1977). Whereas eq. (2) applies for the prompt recoils having large energies, the motion of the majority of the particles is generally calculated from the equations of continuum mechanics, often under the assumption that the local energy spectrum is nearly Maxwellian. Recent sputter results for volatile solids and the improvements in molecular dynamics calculations have led to increased interest in nonlinear sputtering.

4.1 Continuum Mechanics

Molecular dynamics calculations are useful for obtaining a quantitative description of the ejecta in this regime. The models described below can often approximate this. They are obtained by reducing the nonlinear Boltzmann transport equation (Sigmund, 1981) to the equations of continuum mechanics: the continuity, momentum, and energy equations, and an equation of state (e.g., Urbassek et al., 1993),

$$\frac{\partial N}{\partial t} + \nabla \cdot (N\vec{v}) = 0 \tag{9a}$$

$$\frac{\partial (N\vec{v})}{\partial t} + \nabla \cdot (N\vec{v}\vec{v}) = -\nabla P/M + \text{viscous terms}, \tag{9b}$$

$$\frac{\partial (NE)}{\partial t} + \nabla \cdot (N\vec{v}E) = -P\nabla \cdot \vec{v} + \nabla \cdot (\kappa N \nabla E). \tag{9c}$$

Here the atoms of mass M have a local average velocity, $\vec{v}$, and a distribution of velocities around the average, determined by a mean energy E. Also, $N\vec{v}$ is the local flux of material, $NM\vec{v}\vec{v}$ is the momentum flux of a local volume element, and $N\vec{v}E$ is the energy flux. The quantity $-\nabla P$ in eq. (9b) is the volume force, where P is the local pressure, and κ in eq. (9c) is the 'thermal' diffusivity. The mean energy per particle, E, in eq. (9c) is often written as the specific heat at constant volume times a temperature. The quantities E, N, and P are related by the equation of state of the material, which is complicated for a solid experiencing large temperature gradients (Zel'dovich & Raizer, 1967).

For a given excitation distribution, the starting point is the flux of escaping particles at the surface, Φ_s, the number per unit area per unit time crossing the surface after the time t from the ion impact. The yield produced by a single incident ion is calculated from an expression of the form,

$$Y = \int\int \Phi_s(\vec{\rho}, t) d^2\rho \, dt \tag{10}$$

where ρ is the radial distance from the point of penetration. In a yield calculation, two principal excitation geometries are considered: spherical, representing the case for which a gaussian-like distribution of energy has been deposited, and cylindrical, in which a track of atoms of initial root-mean-square radius $\overline{\rho}$ has been energized.

Although the linear cascade yield can also be calculated from eq. (10), here we apply it only to the nonlinear regime. Johnson et al. (1991) describe the statistics of the transition from low to high excitation density. Generally, this is ignored and the nonlinear yield is added to the linear yield as indicated in fig. 3. All of the nonlinear models exhibit a 'threshold' dependence at low values of the deposited energy density relative to the cohesive energy density, or $\ell(dE/dx)/U \approx 1$ in fig. 3 (Sigmund & Claussen, 1981; Johnson, 1987). The threshold dependence for the nonlinear contribution is not easily observed in atomic ejection by knock-on sputtering. It has been seen for molecular ejection from organic insulators (Håkansson, 1993) and for electronic sputtering of an inorganic insulator (Torrisi et al., 1988).

Unfortunately, calculating the sputter flux, Φ_s, from eqs. (9) is not straightforward, so that various approximations are used. Assuming diffuse transport gives the thermal spike model: i.e., flow is neglected, $\vec{v} = 0$ in eqs. (9), and eq. (9c) is solved for E. On the other hand, in most 'hydrodynamic' models diffuse transport is neglected, $\kappa = 0$, and $\vec{v}$ and E are computed from eqs. (9). For example, since the times for energy deposition and the evolution of cascades are short compared to acoustic transport times, a weak 'shock' may be generated, so that 'shock-wave' solutions to eqs. (9) have been applied (Yamamura, 1982).

To clarify the dE/dx dependence of the models, we write the yield in eq. (10)

in terms of the net volume V_s of material which is sputtered,

$$Y = NV_s = N\pi\rho_s^2\,\overline{\Delta x}_s, \tag{11}$$

where ρ_s is the radial extent of the sputtered volume and $\overline{\Delta x}_s$ is the sputter depth (Johnson, 1987). Note the difference between the quantities, $\overline{\Delta x}_c$ in eq. (5b) and $\overline{\Delta x}_s$ in eq. (11). The former is determined by the depth from which the initially deposited energy contributes to ejection of surface species, whereas $\overline{\Delta x}_s$ above is the mean depth of the ejected volume. The dependence of ρ_s and $\overline{\Delta x}_s$ on dE/dx is given below for approximate solutions to eq. (9).

4.2 Thermal Spike Sputtering

The most frequently applied estimate of Φ_s is that obtained from the 'thermal spike' model. Φ_s in eq. (11) is assumed to depend on $\vec{\rho}$ and t only via the local energy at the surface, $E_s(\vec{\rho}, t)$: i.e.,

$$\Phi_s(\vec{\rho}, t) \to \Phi_s[E_s(\vec{\rho}, t)], \tag{12}$$

where E_s is obtained by solving eq. (9c) in the diffusion approximation ($v = 0$). Analytic forms for the yield are obtained for thermal diffusivity, $\kappa \propto E^n$ (Johnson & Evatt, 1980), assuming that molecules individually make the transition to the gas phase, by analogy with normal sublimation. This is well understood for $E_s \ll U$, however, the model is occasionally applied at high dE/dx, $E_s \gg U$, to describe situations in which flow must occur. To account for this, the surface at which Φ_s and E are described can be allowed to evolve, forming a crater, and the energy transported away by the sputter flux accounted for in eq. (9c) (Urbassek & Sigmund, 1984).

Generally, the vapor pressure–flux relationship is used for the surface flux in eq. (12),

$$\Phi_s \approx \frac{P_s(kT_s/U)}{\sqrt{2\pi M k T_s}}, \tag{13a}$$

where $c_v kT_s = E_s$, with c_v the specific heat at constant volume (dimensionless here). The effective vapor pressure is often written,

$$P_s\left(\frac{kT_s}{U}\right) \approx P_s^0\left(\frac{kT_s}{U}\right)^m \exp\left(-\frac{U}{kT_s}\right),$$

explicitly indicating the effect of the barrier to escape, U. Using this and analytic expressions for E_s, sputtering yields are obtained [Mozumder, 1969; Vineyard, 1976; Johnson & Evatt, 1980; Sigmund & Claussen, 1981; Claussen, 1982; Sigmund

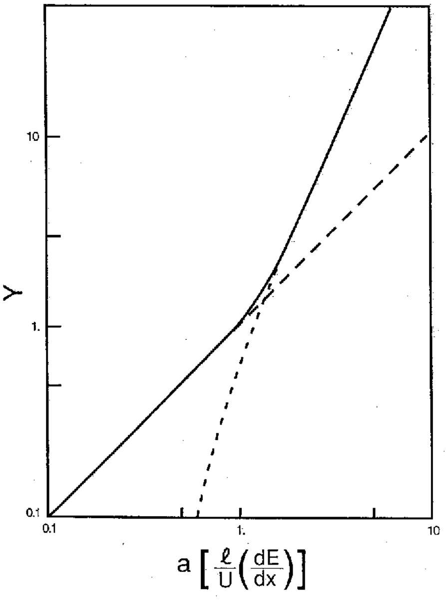

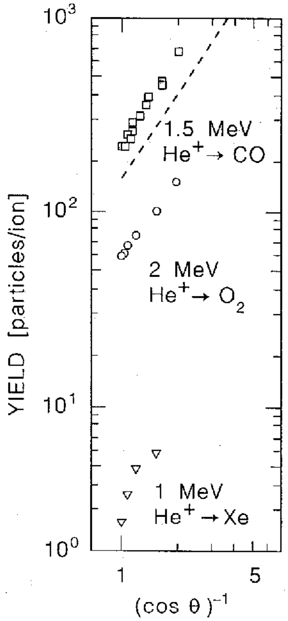

Figure 3. Schematic drawing of a yield versus scaled energy deposition: linear yield at low dE/dx and nonlinear at high dE/dx [here a quadratic yield based on cylindrical thermal spike model in eq. (14) at high dE/dx]. The parameter a is of the order of $(\ell/\overline{\rho})^2$ in this model, where $\overline{\rho}$ is the root mean square width of the cylindrical region and ℓ taken from eq. (6b).

Figure 4. The yield as a function of the reciprocal cosine of the angle of incidence, θ: (squares) Brown et al. (1984); (circles) Gibbs et al. (1988); (triangles) Ollerhead et al. (1980); (dashed-line) $(\cos\theta)^{-1.64}$ in eq. (16a).

& Szymonski, 1984]. Since sputtering is not sublimation-like and local thermal equilibrium is usually not achieved, a simpler approximation to the ejected flux is

$$\Phi_s \approx \frac{1}{4} N v_s G_s. \tag{13b}$$

Here v_s is the mean speed of surface molecules, obtained from E_s, so that $Nv_s/4$ is the flux to the surface, and G_s is a barrier function. Johnson et al. (1991) use $G_s = (1 - U/E_s)\Theta(E_s - U)$, where $\Theta(x)$ is the step function. This assumes that the molecules in the solid have a delta function distribution in energy at the mean local energy E_s.

It is found for an initially narrow cylindrical spike that the yield has the form

$$Y \approx c_s \left(\frac{\ell}{U}\frac{dE}{dx}\right)^2 g_s(\theta), \tag{14}$$

where c_s is a model-dependent constant, and the angular dependence is contained in $g_s(\theta)$ (Johnson, 1987; Johnson et al., 1991). This applies beyond the threshold region ($\ell(dE/dx)/U \gg 1$) and is obtained for Φ_s from either eq. (13a) or eq. (13b).

To clarify the dependence on dE/dx in eq. (14), we define a critical radius, $\rho_c \gg \overline{\rho}$, at which the uniformly distributed energy density equals the cohesive energy density, NU,

$$\frac{dE/dx}{\pi\rho_c^2} = NU. \tag{15}$$

First, the area $\pi\rho_c^2$ is proportional to dE/dx by eq. (15), and the area $\pi\rho_s^2$ in eq. (11) can be set equal to $\pi\rho_c^2$. Second, we assume that the sputter depth in eq. (11) can be written as the mean transport speed times the decay time of the spike, $\overline{\Delta x_s} \approx \overline{v}_s\Delta t$. For an average diffusivity $\overline{\kappa}$, the time for decay of the spike is $\Delta t \approx \pi\rho_c^2/\overline{\kappa}$. Substituting these into eq. (11), we obtain the dependence on dE/dx in eq. (14) if the ratio $\overline{v_s}/\overline{\kappa}$ is independent of the energy density. The onset of the threshold region in fig. 3 is $\overline{\rho} \approx \rho_c$.

Using a constant diffusivity, in which case the cylindrical track of energy transfer events can be treated additively, and including the truncation of the excitation region at the surface, we obtain

$$g_s(\theta) = \frac{4q}{\pi}\tan^{-1} q \text{ for } q = \cos^{-1}\theta \tag{16}$$

for $g_s(\theta)$ in eq. (14), or

$$g_s(q) \approx q^x, x = 1 + 2/\pi \text{ for } q \to 1. \tag{16a}$$

(Johnson, 1989). The approximation in eq. (16a) is in good agreement with the measured angular dependence shown in fig. 4. In addition, spike models lead to ejected particle energy distributions which peak at energies lower than and decay more rapidly at high energies than the result in eq. (5a) (Sigmund & Claussen, 1981).

When the penetration depth is comparable to the mean radial extent of the energy deposition, $\overline{\rho}$, sputtering is produced by a roughly spherical spike of total energy E. If the center of the spike is at the surface and $\overline{\rho}$ is small, so the geometry is hemispherical, then a critical radius, r_c, is obtained by spreading the energy over $(2\pi r_c^3/3)$. That is,

$$\frac{E}{2\pi r_c^3/3} = NU.$$

This gives $r_c \propto E^{1/3}$, so that $\rho_s^2 \propto E^{2/3}$ in eq. (11). Using the diffusive estimate above, $\overline{\Delta x_s} \approx \overline{v_s}\pi r_c^2/\overline{\kappa}$, one obtains the yield in eq. (11) in the form $Y \propto E^{4/3}$ (Vineyard, 1976; Johnson & Evatt, 1980; Claussen, 1982).

An incident ion with a large mean-free path for collisions may create recoil spikes which are well separated along the track of the ion, as in fig. 2c. Ellegaard et al. (1990, 1992) called these subspikes, since for a small mean-free path, λ_c, they can merge to a cylindrical spike, as in fig. 2d. As stated earlier, the yield for non-overlapping recoil spikes is linear in λ_c^{-1}, but the expression in eq. (5a) becomes $\overline{\Delta x}(T) \propto T^{5/3}$ (Johnson & Brown, 1982; Johnson et al., 1991) for spherical 'subspikes' with centers randomly distributed in depth along an ion's track. In addition, the energy spectrum of the ejecta exhibits an enhancement at low energies (Claussen, 1982), which O'Shaughnessy et al. (1988a) approximated using eq. (8b).

4.3 Hydrodynamic Sputtering

In contrast to spike models, most other models based on eqs. (9) are referred to as hydrodynamic in that they roughly account for the momentum and continuity equations, as well as the energy equation. We briefly compare these models, which are also discussed in Reimann (1993), and we assume that the same effective U applies in each model.

In 'shock' models the energy left at the surface by the passing shock wave is typically considered (Yamamura, 1982; Carter, 1983). The yield is then calculated as in the spike model, giving an effective ejection area in eq. (11), $\pi\rho_s^2 \propto dE/dx$. By scaling arguments the sputter depth, $\overline{\Delta x}_s$, is also proportional to ρ_s, so that the yield in eq. (11) varies as

$$Y \approx c_{\mathrm{sh}} \left[\frac{\ell}{U} \frac{dE}{dx} \right]^{3/2} \tag{17}$$

written in dimensionless form (Bitensky & Parilis, 1987). Similarly, $Y \propto E^{3/2}$ for a spherically excited volume (Yamamura, 1982).

Since the flux of ejecta is a momentum transport quantity it is sensible to use eq. (9b) to describe Φ_s. The outward component of the momentum transferred to a volume element in the solid can be estimated from

$$N v_x \approx -\frac{1}{M} \int \frac{\partial P}{\partial x} dt \tag{18a}$$

where P is the local pressure in eq. (9b). This applies under the assumption that the density changes are small, even for relatively large pressure gradients (Johnson et al., 1989). At the surface this momentum can couple into particle motion. The criteria for ejection are: the x-component of the momentum transferred to a particle must exceed a critical momentum, $Mv_x > p_c$, where p_c is a minimum momentum for escape, and the particles between it and the surface must also escape

(Bitensky et al., 1990). A yield is then obtained (Johnson et al., 1989) using eq. (18a) and assuming the energy is deposited in a narrow cylindrical track, the energy in the overlapping cascades is treated additively, and the diffusivity in eq. (9c) is a constant. Ignoring dissipation of energy to other processes, the sputter radius and depth are found to be proportional to dE/dx. Substituting $\rho_\mathrm{s} \propto dE/dx$ and $\overline{\Delta x_\mathrm{s}} \propto dE/dx$ into eq. (11), one obtains

$$Y \approx c_\mathrm{p} \left(\frac{\ell}{U} \frac{dE}{dx} \right)^3 g_\mathrm{p}(\theta), \tag{18b}$$

where c_p is model dependent (Fenyö & Johnson, 1992). Bitensky et al. (1990) obtained a similar expression modifying the shock model to account for the momentum flux and obtained a form for $g_\mathrm{p}(\theta)$. The threshold region was also recently described (Fenyö, 1993).

Urbassek & Michl (1987) assumed that, in a highly energized cylindrical region produced by heavy keV ions, emptying by 'gas flow' into the vacuum along the track direction occurs much faster than radial transport. Therefore, they used a flux like that in eq. (13b) with $G_\mathrm{s} = \Theta(E_\mathrm{s} - U)$ (Balaji et al., 1990). They assumed that the effective sputter radius in eq. (11), ρ_s, approximately equals the average initial radius of the energized, cylindrical region, $\bar{\rho}$. They then calculated the depth of ejection, $\overline{\Delta x_\mathrm{s}}$, as in the spike model, so that $\overline{\Delta x_\mathrm{s}} \propto dE/dx$ for $\rho_\mathrm{c} \gg \overline{\rho}$. This results in a slower dependence of the yield on dE/dx:

$$Y = c_\mathrm{g} \frac{\ell}{U} \frac{dE}{dx} \left(\frac{\overline{\rho}}{\ell} \right)^2 ,$$

with c_g again a model dependent constant and where U in their model is determined by the gas condensation temperature. The effective dE/dx in their calculation was obtained by considering the shape of the recoil cascade for these incident low energy ions.

Because of the difficulties in describing both the evolution of energy and momentum and the phase transformation that occurs at the surface associated with particle ejection, molecular dynamics simulations have been performed, as will be discussed. For typical dE/dx, a 'weak shock' is usually seen propagating out of the high excitation density region, but only depositing small amounts of energy across the solid (Urbassek & Waldeer, 1991; Fenyö & Johnson, 1992). This shock may be responsible for promptly ejecting weakly attached surface species. What remains is a transiently pressured volume which produces a radial compression of the material and an outward expansion (Johnson & Sundqvist, 1992). The competition between the pressurized driven flow and the radial energy transport out of the region, determines the properties of the ejecta (Urbassek & Waldeer, 1991;

Urbassek et al., 1993). This establishes an exciting connection between sputtering and hydrodynamic processes at the atomic level.

4.4 Beam Heating

For ion sputtering a large fraction of the deposited energy goes to heat the sample. For sufficiently well conducting solids, this energy is effectively dissipated. For relatively high beam fluxes, for which the cooling is too slow, an increase in the surface temperature of the sample can occur giving rise to enhanced surface loss (Sigmund & Szymonski, 1984). In this case, a heating term is added to eq. (9c); in equilibrium this heat is dissipated by sublimation, radiative cooling, and/or conduction. If ϕ is the incident ion flux then, ignoring sublimation and radiative cooling, the heating has negligible effect on the yield if the equilibrium energy density achieved is much less than the cohesive energy density

$$\phi EL/\kappa \ll NU \tag{19a}$$

where L is the penetration depth. When there is a contribution to sputtering it is characterized by a Maxwell-Boltzmann energy distribution for escaping particles (Haring et al., 1984a),

$$dY/dE_1 \propto \frac{E_1 e^{-E_1/kT_\mathrm{s}}}{(kT_\mathrm{s})^2}, \tag{19b}$$

where T_s is the target surface temperature, a function of $\phi(E)$.

4.5 Overview

The events associated with erosion of a solid by the collisional (knock-on) energy deposited can be roughly ordered in time so that the contributions to the yield are treated additively (Sigmund, 1977; Kelly, 1979; Sigmund & Szymonski, 1984). Direct ejection is followed by a collision cascade in which fast particles collide with much slower particles resulting in an E_1^{-2} component to the high energy part of the energy spectrum. Subsequently, particles with similar speeds begin to collide, either in an individual cascade or in overlapping cascades. This can contribute an enhanced low energy component to the sputter ejecta. The yield and energy spectrum for this contribution are partially explained by elastic-collision spike models. Finally, an increase in the ambient temperature can produce sublimation (a late effect) which is characterized by a Maxwell-Boltzmann energy distribution. As the cascade energy degrades in a molecular solid, molecules may dominate the ejecta and, eventually, chemical effects can occur, also a late effect. We consider the latter after discussing electronically stimulated sputtering.

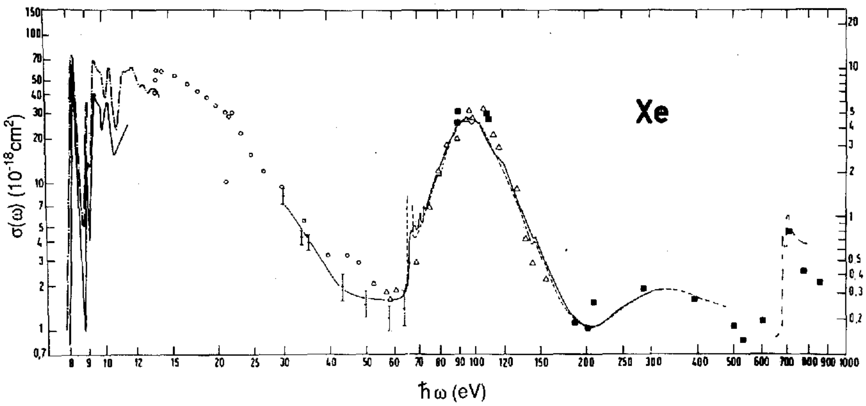

Figure 5. Absorption cross section for solid Xe versus $\hbar\omega$, photon energy. Dashed lines and symbols are for absorption in a gas; solid lines only are solid state absorption determined by reflectance. From Sonntag (1977).

5 Theory: Electronic Sputtering

The electronic energy deposited by a fast ion has also been shown to lead to sputtering. This process is closely related to photon and electron-stimulated desorption. However, that subject usually implies ejection of adsorbed species primarily as ions, whereas a description of the dominant neutral ejecta is emphasized here for bulk species. Electronic sputtering was first studied extensively for the alkali halides (Townsend, 1983; Szymonski, 1993). A parallel development for more refractory materials was stimulated by Haff (1976). He pointed out that the electronic relaxation processes, which produce tracks in dielectrics, could also produce sputtering.

Whereas the principal problems in knock-on sputtering are the description of momentum transport and escape, electronic sputtering is a more complex phenomenon, requiring also an understanding of the conversion of electronic energy into atomic motion. The incentive for understanding this is high, however, as electronically-induced ejection provides one of the few measures of the non-radiative relaxation processes occurring in solids. The unraveling of the sputtering process is complicated by the fact that, in addition to any nonlinearities in transport and ejection discussed above, the energy conversion processes themselves can change with excitation density.

In order to characterize electronic sputtering and to identify the linear and nonlinear regimes, we use the mean depth for producing an excitation, λ_e. The deposition of electronic energy is determined by the absorption spectrum of the material $\sigma_{\rm abs}(\omega)$, given in fig. 5 for gaseous and solid xenon, and the frequency spectrum of the exciting radiation. Therefore, for absorption of an incident photon of energy $\hbar\omega$ to a sputtering precursor state,

$$\lambda_{\rm e}^{-1} = N\sigma_{\rm abs}(\omega). \tag{20a}$$

A charged particle, on the other hand, produces a track of ionizations and excitations along its path through the solid. Therefore, $\lambda_{\rm e}$ is often estimated from the electronic stopping power, fig. 1a,

$$\lambda_{\rm e}^{-1} \propto f_{\rm e}(dE/dx)_{\rm e}, \tag{20b}$$

where $f_{\rm e}$ is the fraction of the electronic energy converted into atomic motion which can lead to sputtering. The physics of transport and escape then leads to expressions for the yield like those for knock-on sputtering. That is, one replaces $(dE/dx)_{\rm n}$ or $\lambda_{\rm c}$ by $f_{\rm e}(dE/dx)_{\rm e}$ or $\lambda_{\rm e}$, respectively, in the yield expressions above. For instance, when sputtering occurs in response to individual excitations which are uniformly distributed in depth, one can write

$$Y = \frac{\overline{\Delta x_{\rm e}}}{\lambda_{\rm e}} = \Lambda_{\rm e}\left(\frac{dE}{dx}\right)_{\rm e} \tag{20c}$$

as in eqs. (5b) and (4). Similarly, the quantity $\ell f_{\rm e}(dE/dx)_{\rm e}/U$ would be used in eqs. (14), (17), and (18b).

5.1 Electronic Energy Deposition

For a fast charged particle, electronic excitations are produced in two ways. The incident particle makes a close collision with an electron in a binary encounter, transferring sufficient kinetic energy to cause ionization, or a fast charged particle passing some distance from an atom produces a time varying field. The frequency components of this field can be absorbed according to $\sigma_{\rm abs}(\omega)$, producing dipole excitations and ionizations.

For fast ions or electrons with $v \gg v_0$, where v_0 is the Bohr velocity, dipole excitations dominate, but the close collision component produces more energetic ionizations and, consequently, ionization cascades. The weighted spectrum of energy deposition is similar to $\hbar\omega\sigma_{\rm abs}(\omega)$ in fig. 5. Peaks are seen for inner shell excitations and ionization is the dominant energy deposition process for fast ions or electrons. The amount of energy exceeding the ionization energy for a shell (or band gap energy in a solid) goes into secondary electron kinetic energy. From the spectrum in fig. 5 the distribution of secondary electron energies is seen to be broad and extends to very high energies.

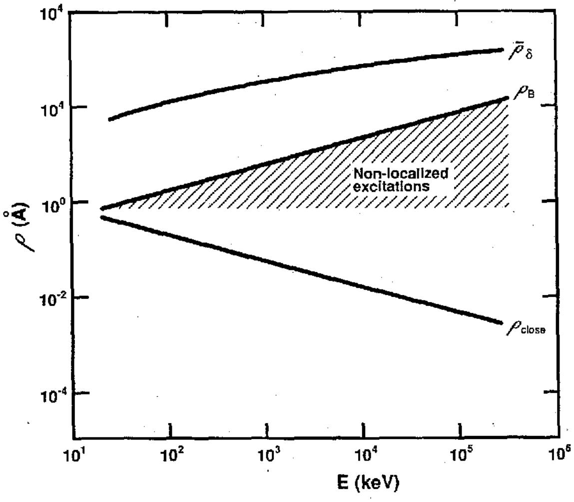

Figure 6a. The 'track' structure for a fast light ion: $\overline{\rho}_\delta$ is the average distance for secondary electron ejection perpendicular to a track, ρ_B is the Bohr adiabatic radius, ρ_close is the distance of closest approach in a head-on collision with an electron. Brandt & Ritchie (1974).

5.1.1 Primary Excitation

Useful quantities are the number of primary ionizations per unit path length, dJ/dx, and the electronic energy lost per unit path length $(dE/dx)_\mathrm{e}$ in fig. 1a. For a bare ion of charge $Z_1 e$ and speed $v \gg v_0$, where v_0 corresponds to the average velocity of the electrons in the outer orbitals, incident on a target having Z_2 electrons per atom (Inokuti, 1971),

$$\frac{1}{N}\frac{dJ}{dx} = \int_{\hbar\omega > I} \sigma(v,\omega)d\omega \approx 4\pi \frac{(Z_1 e^2)^2}{m_\mathrm{e} v^2}\frac{2m_\mathrm{e}\overline{z^2}}{\hbar^2} \ln \frac{2m_\mathrm{e}v^2}{I''} \tag{21a}$$

$$\frac{1}{N}\left(\frac{dE}{dx}\right)_\mathrm{e} = \int \hbar\omega\sigma(v,\omega)d\omega \approx 4\pi \frac{(Z_1 e^2)^2}{m_\mathrm{e} v^2} Z_2 \ln \frac{2m_\mathrm{e}v^2}{I'}. \tag{21b}$$

In eq. (21a), $\sigma(v,\omega)$ is a cross section differential in ω, and $\overline{z^2}$ a ground state matrix element giving the extent of the electron cloud. The integration in eq. (21a) is over all ionizations, whereas the integration in eq. (21b) is over all excitations and is weighted by the energy of excitation $\hbar\omega$. The expressions on the right of eqs. (21) are the Bethe-Bohr expressions for fast ions, where I' and I'' are averaged 'ionization' energies determined from the energy absorption spectrum. Whereas the quantity dJ/dx is dominated by dipole excitations, the close collision contribution

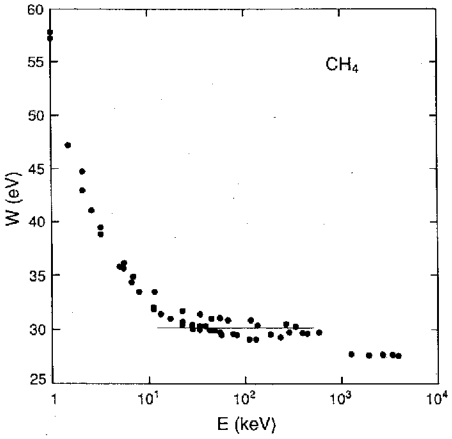

Figure 6b. W-value versus E for protons on gas phase CH_4: horizontal line is the ICRU value (30.5 ± 1.0 eV); points: data from Srdoč et al. (1993).

to $(dE/dx)_e$ is comparable to the dipole contribution because of the larger $\hbar\omega$ (e.g Lindhard & Winter, 1964; Fano, 1963). For fast ions these two contributions to $(dE/dx)_e$ have roughly the same dependence on v, a result of the Coulomb interaction between a bare ion and an electron.

The similarity in the energy dependence of the two expressions in eqs. (21a) and (21b) at large v leads to the useful result that their ratio, $(dE/dx)_e/(dJ/dx)$, is slowly varying in energy for fast particles with $v \gg v_0$. This ratio is the average energy expended per ionization produced by the incident particle, which for 1 MeV H^+ on a number of materials is $\sim$ 60 eV, increasing slowly with increasing v.

In a condensed material the same description applies but the absorption spectrum $\sigma_{\rm abs}(\omega)$ changes. The principal change is for the outer shell electrons and is, therefore, small for the weakly bound rare-gas solids, as seen in fig. 5. When the electron clouds from neighbors overlap significantly either in the initial or final state, then the spectrum shifts and collective effects occur. In metals, the conduction band is formed and the absorption is dominated by a broad plasma-like state associated with the classical plasma frequency, $\omega_p = (4\pi e^2 N_e/m_e)^{1/2}$, where N_e is the density of free electrons in the conduction band.

5.1.2 Secondary Electrons

Those energetic electrons which are not produced by inner shell decay are forward directed and travel some average distance from the ion track, which we write as $\overline{\rho}_\delta$. The subscript comes from the often-used term delta-rays for energetic secondary

Table I

SOLIDIFIED GASES							
Species	Sublimation energy, U (meV/part.)	Ionization energy I (eV)	Density, molecule or atom ($10^{22}/\mathrm{cm}^3$)	W (eV)	Bulk yield for incident		
					2keV e^-	6keV H_2^+	1MeV He^+
Ne	19.6	21.56	4.54	39.3	28	107	
Ar	80	15.76	2.67	26.6	2.7	26	$48^{b)}$
Kr	116	14.00	2.22	23.0		15	
Xe	164	12.13	1.73	20.5			$8.1^{e)}$
D_2	12.65	15.46	3.03	$36.5^{a)}$		$209^{j)}$	
N_2	78	15.6	2.21	37.0	1.1	12.6	$32^{i)}$
O_2	90	12.2	2.28	32.5	2.4	37	$140^{c)}$
CO	88	14.0	2.2	34.5	$1.7^{g)}$	$36^{f)}$	$300^{h)}$
H_2O	532	12.6	3.3	30.0			$10^{d)}$

W, gas phase values for fast protons; I, gas phase. a) electron value. b) Reimann et al. (1988). c) Johnson et al. (1991). d) Bøttiger et al. (1980). e) Ollerhead et al. (1980). f) Schou (unpubl.). g) Schou et al. (1985). h) Chrisey et al. (1990). i) Rook et al. (1985). j) Stenum et al. (1990). All other yields for electron and hydrogen ion bombardment from Schou (1991).

electrons. This distance is compared in fig. 6a to the maximum distance for dipole excitations, the Bohr adiabatic radius, a dynamic screening length, $\rho_{\mathrm{B}} \approx v/\overline{\omega}$, where $\hbar\overline{\omega} \approx I'$ in eq. (21b) is the mean energy of the outer shell electrons. For a close collision with an electron at a target atom, a binary collision distance is shown in fig. 6a. These lengths are used to define the structure of the ionization track; the inner (infra-)track, $\rho < \rho_{\mathrm{B}}$, and the outer (ultra-)track, $\rho_{\mathrm{B}} < \rho < \overline{\rho}_{\delta}$. Because energetic secondary electrons produced near the surface can be scattered and ejected, aspects of the energy spectrum in the solid can be studied (Baragiola, 1993a). These electrons typically deposit their energy over distances $\sim$ 10-20Å, with the tail of the distribution extending to $\overline{\rho}_{\delta}$ (Dubus et al., 1987). The most energetic electrons efficiently produce additional ionization and excitations. In this decay process resonant excitations may produce important differences between solids (Inokuti, 1991). Measurements in the gas phase and calculations both indicate that the distribution in excitation density decays beyond the Bohr radius, ρ_{B}, as $\sim \rho^{-2}$ out to the radius determined by the maximum energy transfer to the electrons, $\overline{\rho}_{\delta}$.

The often-used quantity W is defined as the average energy expended per ionization or electron-hole pair produced by an ion or an electron stopping in a material (Table I): W is equal to the incident ion energy, E, divided by the number of ion-electron pairs produced (ICRU, 1979). Because W is only slowly varying with v at $v \gg v_0$, the value in a given depth is approximately equal to W, except close to the surface. Therefore, the mean depth between two ionization events in eq. (20b) is

$$\lambda_e^{-1} \approx (dE/dx)_e/W. \tag{21c}$$

The value of W is about half $(dE/dx)_e/(dJ/dx)$ at high velocities, implying that for every primary ionization an additional ionization is produced (Paretzke et al., 1986). On the other hand, W increases with decreasing energy at low energies, fig. 6b, approaching the average energy per primary ionization after nuclear energy loss is accounted for. Because excitations below the ionization threshold become more important at low ion energies, W may not be the appropriate quantity to use in an estimate of λ_e from $(dE/dx)_e$ at all energies, as suggested by fig. 1a. In addition, at high velocities, secondary electron transport lowers the effective $(dE/dx)_e$ (i.e., the density of deposited energy) at the surface (Schou, 1980; Johnson et al. 1991). These differences, combined with the change in the radial distribution indicated in fig. 6a, can cause a difference in the sputtering yield measured above and below the maximum in $(dE/dx)_e$, referred to later as two branches.

W has three contributions for fast incident ions or electrons (Platzman, 1961): the fraction of the net energy deposited in the formation of electron-hole pairs, the fraction deposited in excitation, and that fraction of the secondary electron energy transfered to the lattice. The fraction of energy deposited in electron-hole pairs is (I/W) where I is the ionization energy. For an atomic material most of the energy is in electron-hole pair recombination energy ($\sim$ 65% for Ar), whereas in a molecular material it becomes $\sim$ 40% of the total, as low energy excitations are efficiently produced. Therefore, W/I is smaller for atomic ($\sim$1.5) than molecular gases ($\sim$ 2.5), Table I. Although results are sparse, W is roughly proportional to the band gap energy for a solid. In the solid state both holes and excited states (excitons) are produced by a fast incident ion. The secondary electrons produced for the most part remain in the solid, and therefore each hole has, on the average, an associated electron. Since most sputtering experiments are not able to distinguish between excitons and electron-hole pairs, we use the word exciton in the following discussion unless we are specifically referring to the behavior of holes.

5.2 Electronic Energy Conversion

Below the electronic excitation threshold, the secondary electrons can heat the lattice or cause vibrational excitations in a molecular solid. The energy so expended is of the order of 10-30% of the initial energy deposited for fast, light ions with energies above the maximum in the electronic stopping power, depending on the material. This can lead to sputtering only at very high excitation densities

Table II

	Electronic Relaxation Processes	
1	$A^+ + B + M \rightarrow AB^+ + M + \Delta E$	Ion-molecule reaction
2	$A^* + B + M \rightarrow (AB)^* + \Delta E + M$	Dimerization
3	$AB^+ + e \rightarrow (AB)^* + \Delta E$	Recombination
4	$(AB)^* \rightarrow A + B + \Delta E$	Repulsive Decay
5	$A^* + \text{lattice} \rightarrow A^* + \text{lattice} + \Delta E$	Lattice Relaxation
6	$AB(v) + M \rightarrow AB(v') + M + \Delta E$	Vibrational Relaxation
7	$A^+ + B^+ \rightarrow A^+ + B^+ + \Delta E$	Coulomb Repulsion
8	$A^{++} + B \rightarrow A^+ + B^+ + \Delta E$	Charge Exchange
9	$A^+ + e + e \rightarrow A^* + e$ (hot)	Dielectronic Recombination
10	$A^{**} + e \rightarrow A^* + e$ (hot)	Collisional Deexcitation
11	$A^* + A^* \rightarrow A^* + A^+ + e$ (hot)	Excited State Fusion
12	$A + A(v) \rightarrow A + A(v') + \Delta E$	Vibrational Quenching

(Williams & Sundqvist, 1987; Ritchie & Claussen, 1982), as it occurs in small energy increments, vibrations and phonons. A large fraction of the electronic energy is tied up as electron-hole pairs or excitons, involving larger increments of energy in large band-gap materials. The relaxation (decay) of these states is discussed below following concepts outlined earlier (Johnson & Brown, 1982).

Two classes of relaxation processes are described. At low excitation density, the excitonic regime, the effects are primarily due to individual exciton decay processes. In certain frozen gases, processes analogous to gas-phase processes, not surprisingly, determine the creation of atomic or molecular motion, Table II. At high excitation density, processes (7-12) in Table II are enhanced in the track core. The latter involve multiple excitations or ionizations: pairs of electrons, holes or excitons. In addition, cooperative processes occur. This is the track regime, to be discussed later. Initially, only certain special decay routes were thought to lead to damage and sputtering. However, almost all contributions to the relaxation process lead to an effect at sufficiently high excitation density in some material (Johnson, 1993).

5.2.1 Low Excitation Density

It is seen from the excitation spectrum in fig. 5 that outer shell and inner shell excitations are produced. In both the gas and solid phase the inner shell excitations typically relax by an Auger transition, $(A^+)^* \rightarrow A^{++} + e$, in less than 10^{-13} sec, leading to a multiply ionized species and an additional, energetic secondary electron (Baragiola, 1993a, 1993b). Such processes in condensed matter are evident in the secondary electron spectrum, and can result in the transfer of an electron to a

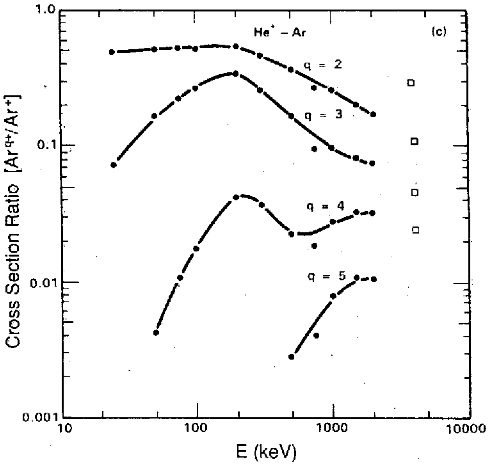

Figure 7. Ionization cross sections for gas phase Ar by He^+ vs. E: total ionization produced in multiply-ionizing processes divided by single ionization cross section

neighbor (~10^{-14} sec), $A^{++} + A \rightarrow A^+ + A^+$, producing two closely spaced holes. This also occurs via inner shell electron transfer from a neighbor (Knotek & Feibelman, 1978). The Coulomb repulsion of trapped, neighboring holes has been suggested to account for a number of phenomena observed in defect and track formation in dielectrics, as well as in electronic sputtering (e.g., Itoh et al., 1985).

Multiple ionization occurs also by the excitation of shallow core holes (2s electron in oxygen), shake-off, capture plus ionization, etc. (Rudd et al., 1992). These processes can have surprisingly large cross sections below the peak in the stopping cross section, as indicated for argon in fig. 7. By the above processes, low energy electrons dominate the secondary electron spectrum and excitations exceeding the band gap eventually relax to electron-hole pairs at the band gap. Because the electrons are much more mobile than the holes, the mobility of the holes controls the density of events in this regime.

For a hole at the band gap, relaxation occurs by photon emission or by a nonradiative process. In the gas phase, dissociative recombination (3 and 4 in Table II) is a dominant recombination and heating route. In a van der Waals bonded molecular solid this also occurs. A relaxation scheme for solid argon, based on the gas phase (Johnson and Inokuti, 1983) is shown in fig. 8 in terms of the pair potentials between an ion, Ar^+, or an excited argon, Ar^*, and a neighbor. A hole combines with a neighbor to form a vibrationally excited Ar_2^+. While relaxing vibrationally, this dimer can recombine with a cool electron into an electronic state

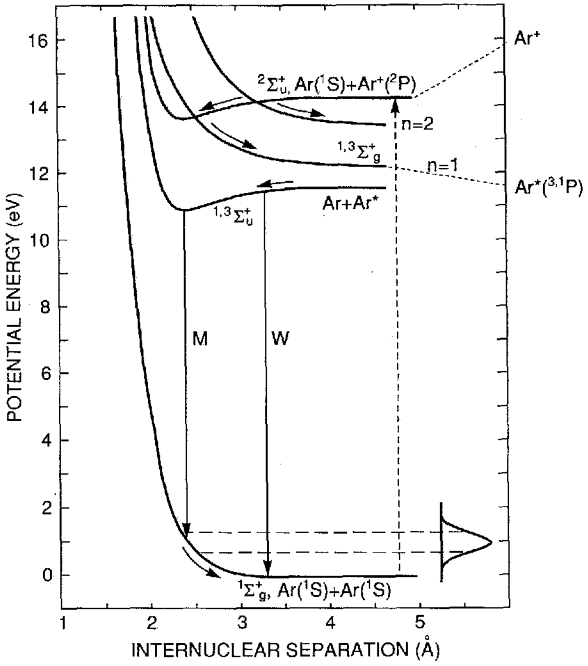

Figure 8. Potentials for Ar-pairs in solid Ar. The excited state, Ar* $n = 1$, which leads to the $[(3p)^5\ 4s)]$ state is indicated. This splits into singlet and triplet states. There is, of course, an ensemble of repulsive and attractive states associated with higher states indicated, e. g. n=2, and these are both Σ and Π states. The luminescence bands M and W are indicated. The W band is an ejected dimer (Reimann et al., 1988). Vertical dashed line indicates excitation to a hole state. Other dashed line indicates transition to gas phase on ejection. The solid arrows indicate a relaxation pathway (i.e., vibrational relaxation followed by dissociative recombination and repulsive decay).

with a repulsive interaction, causing the two argon atoms to separate energetically,

$$\mathrm{Ar}_2^+ + \mathrm{e} \rightarrow \mathrm{Ar} + \mathrm{Ar}^* + \Delta E, \quad \Delta E \approx 1\mathrm{eV}. \tag{21c}$$

If occurring at the surface, an excited Ar may be ejected as the sublimation energy is only 0.08 eV. If the excited species is not ejected, it also can react with a neighbor forming an excimer. Since this potential energy curve does not 'cross' the ground state energy, the excimer decays by emission of a photon. Since this takes $> 10^{-9}$ sec, the excimer typically relaxes to a low vibrational state prior to photon emission, except in solid neon for which the vibrational-lattice interaction is extremely weak. Emission from the relaxed state gives the M-band luminescence indicated in fig. 8, while unrelaxed, ejected dimers account for the W-band also indicated. Because the internuclear separation in the relaxed excimers is much smaller than that for two ground state neighbors, repulsive potential energy is again released (Reimann et al., 1988),

$$\mathrm{Ar}_2^* \rightarrow \mathrm{Ar} + \mathrm{Ar} + \hbar\omega + \Delta E, \quad \Delta E \approx 1eV.$$

Repulsive decay of internal states of molecules or between excited dimers can be an important source of kinetic energy in excited insulators (Børgesen et al., 1982).

5.2.2 Exciton/Hole Dynamics

It has been pointed out often that electrons in the conduction band of a dielectric usually are mobile with a high diffusivity ($\sim$ 1000 cm^2/sec). The holes can also be mobile but much less so ($\sim$1 cm^2/sec) (Schwentner et al., 1985; Brown, 1993). Therefore, it may at first seem puzzling that electronic sputtering can occur, since the electrons and holes rapidly 'neutralize'. In a metal, neutralization is equivalent to recombination, whereas in a dielectric or a semi-conductor recombination can lead to release of the band-gap energy either radiatively or non-radiatively. Therefore, the band gap energy may be available for sputtering (Brown, 1984). The competition between hole diffusivity and the electron cooling rate (Johnson & Inokuti, 1983) determines the dilution of the energy density in the 'track' at the time of recombination and sputter ejection, affecting the efficacy of events (7-12) in Table II.

In a crystalline material the mobile holes and free excitons are waves distributed over many lattice sites. However, it is useful in the following to think of holes and excitons as localized entities which hop between the atomic or molecular constituents. This is the Frenkel picture of holes and excitons: electron exchange can occur between a hole and a neighbor

$$\mathrm{Ar}^+ + \mathrm{Ar} \rightarrow \mathrm{Ar} + \mathrm{Ar}^+$$

resulting in transport. For a typical spacing in solid argon ($\sim$ 3.4 Å), overlap integrals (Johnson, 1970) give a time for exchange with each neighbor ($\tau_{\mathrm{ex}} \approx 10^{-14}$ sec) leading to a hole diffusivity of $\sim$ 1 cm^2/sec. For the larger atoms, Kr and Xe, the hopping times are shorter (Fugol', 1988) because of larger electron overlap. On the other hand, for the $n = 1$ state in solid argon (fig. 8) the exchange time is longer ($\sim 10^{-13}$ sec), since two electrons are involved, leading to a lower exciton diffusivity $\sim$ 0.1cm^2/sec (Schwentner et al., 1985; Tarrio & Schnatterly, 1992).

Such holes or excitons can diffuse until they trap at a defect, grain boundary, or a surface. In a carefully prepared, large, and very good crystal they may diffuse long enough to emit a photon (free exciton emission) or until a random lattice

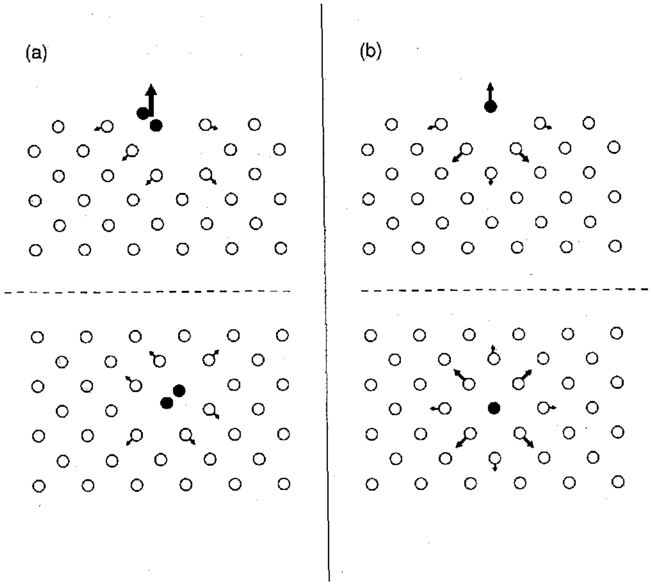

Figure 9. a) Trapped dimer (e.g. Ar_2^* in fig. 8) in bulk: leads to M-band emission in fig. 8; at surface: leads to ejection in Ne and Ar, in a vibrationally excited state; W-band in fig. 8. b) Trapped atomic exciton in bulk. At the surface it ejects an Ar (see fig. 8). In Ne it has sufficient energy to eject a number of atoms.

disturbance leads to self-trapping: the lattice distorts localizing the hole. For solid xenon a shift in the principal luminescence feature between excitons trapped at intrinsic defects and self-trapped excitons is observed (Varding et al., 1993). All trapped species formed diffuse much more slowly ($\ll 0.1\text{cm}^2/\text{sec}$).

In atomic rare-gas solids such effects are well studied and trapping occurs to two principal end states, which are indicated schematically in fig. 9. Either the lattice distorts symmetrically forming an atomic, trapped exciton, which is dominant for solid neon, or the excited species interact strongly with a particular neighbor forming a molecular, trapped exciton (an excimer), dominant for typical laboratory samples of argon, krypton, and xenon (Schwentner et al., 1985; Zimmerer, 1987). The latter is indicated in the potential energy diagram in fig. 8. This dimerization process occurs in all the dielectrics of interest and is seen clearly by the M-band luminescence, fig. 8. Although these are typical end states, cluster-like states may occur: Ar_n^+ , for a highly damaged lattice or surface (Baba et al., 1991).

Assuming that 'recombination' awaits the trapping process, and ignoring the net field in an ion track, one may roughly describe excitation transport by a field

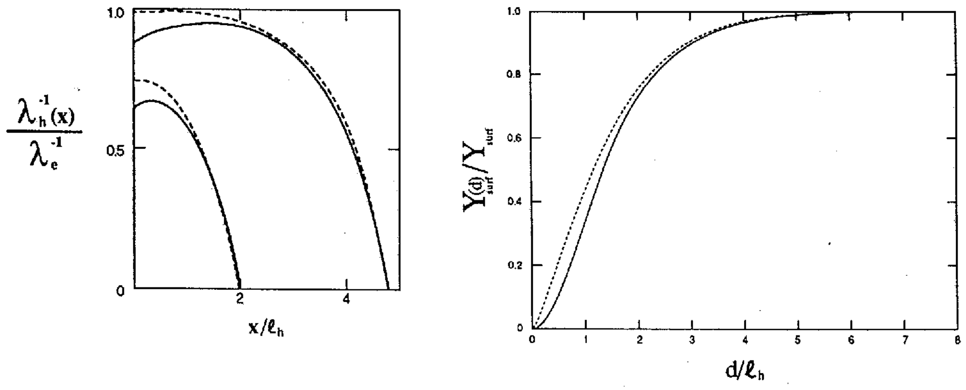

Figure 10. a) The distribution , eq. (24), of trapped excitons versus depth for two sample depths, $d = 2\ell_h$ and $5\ell_h$ and for $\Delta = 0$, dashed curves, and $\Delta = 0.1$, full curves: $\Delta = \tau_h \ell / \tau_h^s \ell_h$. For latter the increase in surface trapped species not shown. (See also, Reimann et al., 1988). b) The change in the surface layer contribution to the yield (including enhanced trapping) for $\Delta = 0.1$ and 10. The lack of sensitivity of shape to enhanced trapping allows extraction of ℓ_h from experiment.

free diffusion equation. For mobile holes with local density, N_h,

$$\frac{\partial N_h}{\partial t} = D_h \nabla^2 N_h - \frac{1}{\tau_h} N_h - k_{hh} N_h^2 - k_i N_h. \tag{22a}$$

Here D_h is the hole diffusivity, τ_h^{-1} is a trapping rate, k_{hh} describes the hole-hole interaction, and k_i represents quenching by impurities (Reimann et al., 1988). The effect of the free electrons from the background on hole transport can be roughly included in D_h, τ_h and k_{hh}.

Ignoring the surface effects discussed, the initial condition for a fast incident ion is approximated as a narrow cylindrical track

$$\lambda_e^{-1} \frac{\exp(-\rho^2/\bar{\rho}^2)}{\pi \bar{\rho}^2}$$

with $\lambda_e^{-1} \approx (dE/dx)_e/W$. Under the assumption of a constant diffusivity, the holes are non-interacting ($k_{hh} = 0$), a reflecting surface, and a solid without impurities ($k_i = 0$), the distribution of trapped holes becomes

$$N_h(t \to \infty, \rho) = \lambda_e^{-1} \frac{\exp(-\rho^2/\ell_h^2)}{\pi \ell_h^2} \tag{22b}$$

for $0 \ll x \ll d$, where d is the sample thickness, and ℓ_h is the average diffusion length: $\ell_h = (D_h \tau_h)^{1/2}$. For enhanced trapping at the vacuum interface, a term of the form, - $(\ell/\tau_\mathrm{h}^\mathrm{s})\delta(x)N_\mathrm{h}$, can be added or appropriate boundary conditions be given (Reimann et al., 1984b, 1988). Here, the layer thickness is $\sim \ell$, eq. (6b), and $(\tau_\mathrm{h}^\mathrm{s})^{-1}$ is the increase in the surface trapping rate (Reimann et al., 1988). The quantity $\ell/\tau_\mathrm{h}^\mathrm{s}$ is called the recombination velocity as it gives the recombination rate at a surface. For a sample thickness $d \gg \ell_\mathrm{h}$, the enhancement in the number of the excitons trapped in the surface layer is given by the multiplicative factor

$$R_\mathrm{s} = \frac{1+\Delta(\ell_\mathrm{h}/\ell)}{1+\Delta},$$

$$\Delta \equiv \tau_\mathrm{h}\ell/\tau_\mathrm{h}^\mathrm{s}\ell_\mathrm{h}. \tag{23}$$

Here the first part, $1/(1+\Delta)$, accounts for the reduction of species in the layer due to diffusion (see fig. 10a), and the second part gives the increase due to surface trapping (Boring et al., 1989)[3].

Surface trapping can occur also at the substrate. For a perfectly quenching substrate (recombination velocity infinite at $x = d$) and for a vacuum interface which does not trap preferentially (recombination velocity zero at $x = 0$) the radially integrated density, $\lambda_\mathrm{h}^{-1}(x) \equiv \int_0^\infty N_\mathrm{h}\pi d\rho^2$, gives the mean depth between trapped holes, λ_h. From eq. (22a) this gives

$$\lambda_\mathrm{h}^{-1}(x) = \lambda_\mathrm{e}^{-1}\left(1 - \frac{\cosh(x/\ell_\mathrm{h})}{\cosh(d/\ell_\mathrm{h})}\right) \tag{24}$$

where λ_e^{-1} is the initial excitation density, assumed independent of depth for a fast incident ion traversing a thin sample. If $\ell_\mathrm{h} \gg \ell$, then even for a large surface trapping efficiency the depth dependence of the trapped hole distribution, shown in fig. 10a, does not change significantly. For $\ell_\mathrm{h} = 60\ell$, typical for fast ion or electron sputtering of argon (Reimann et al., 1988), the changes seen in fig. 10a correspond to a factor of six increment in the trapping rate in the surface layer:

$$\Delta = (\tau_\mathrm{h}\ell/\tau_\mathrm{h}^\mathrm{s}\ell_\mathrm{h}) = 0.1.$$

A hole trapped at depth x can, on recombination, lead to a yield, $Y(\Delta E, x)$, due to energy release ΔE from one or more of the repulsive decay processes in fig. 8. The subsequent energy transport and escape are determined by molecular dynamics. The total yield is obtained from the trapped hole distribution as in eq. (24). If dx/λ_h is the probability of a hole being trapped between x and $x + dx$, then the average yield is

$$Y(d) = \int Y(\Delta E, x)\frac{dx}{\lambda_\mathrm{h}(x)}. \tag{25a}$$

---

[3] Note: eq. (23) differs from eq. (4.2) in Reimann et al. (1988).

Below we look at bulk and surface contributions separately. The M-band (bulk) and W-band ('surface') luminescence were treated in a similar manner (Reimann et al., 1988).

When only surface trapped species lead to ejection the yield in eq. (25a) becomes,

$$Y_{\mathrm{surf}} = Y(\Delta E, 0)\frac{\ell}{\lambda_{\mathrm{e}}} R_{\mathrm{s}} \tag{25b}$$

for $d \gg \ell_h$. For a uniform excitation density, a quenching substrate, and no enhanced trapping at the surface ($R_{\mathrm{s}} = 1$), the yield vs. thickness due to surface-trapped species is

$$\frac{Y_{\mathrm{surf}}(d)}{Y_{\mathrm{surf}}} = 1 - \frac{1}{\cosh(d/\ell_{\mathrm{h}})} \tag{25c}$$

(Reimann et al., 1988; Ellegaard et al., 1988). Including even a large increase in the surface trapping rate, for example, $\Delta = 0.1$ and 10 for $\ell_{\mathrm{h}} = 60\,\ell$, which corresponds to increases of 6 and 600 times, does not change the thickness dependence of the surface component of the yield, as seen in fig. 10b. However, it can significantly affect the size of the yield, giving $R_{\mathrm{s}} = 6.4$ and 54.6 respectively in eqs. (23) and (25b). Finally, when the depth from which an energy release leading to ejection of an argon atom, $\overline{\Delta x}(\Delta E)$ from eq. (5a), is much smaller than the diffusion length, ℓ_h, then the bulk contribution to the yield in eq. (25a) for $R_{\mathrm{s}} = 1$ becomes

$$\sim \lambda_{\mathrm{e}}^{-1}\frac{\overline{\Delta x}(\Delta E)}{1+\Delta},$$

resembling the first part of eq. (23).

There are some important assumptions in the above description. We have replaced a distribution in grain boundaries and impurities by the diffusion length, ℓ_h, ignored fields, and the electron 'recombination' times are assumed to be much larger than the hole trapping times, τ_h. Grain size and quenching by impurities, k_i in eq. (22a), simply changes ℓ_h (Reimann et al., 1988). Although it is clear that interactions between excitons must play an increasingly important role in determining the electronic sputtering yield with increasing excitation density, and $\lambda_{\mathrm{e}}^{-1}$ is a few per monolayer for 1 MeV He$^+$ in argon, the holes are assumed to be non-interacting in eq. (22a), $k_{\mathrm{hh}} = 0$. Itoh et al. (1985,1987) point out that holes can attract, via lattice polarization, and trap close together. A related process is the fusion of excitons to produce holes, $\mathrm{A}^* + \mathrm{A}^* \rightarrow \mathrm{A}^+ + \mathrm{A} + \mathrm{e}$ (process 11) seen even in molecular clusters (Schriver et al., 1987). However, ionized or excited atoms interact with neighbors by both repulsive and attractive states. Typically, there are more states leading to repulsion than to attraction, producing a net, weakly-repulsive interaction. This can lead to scattering of holes, affecting the diffusion constant, D_h, or τ_{h} can be modified if this interaction enhances trapping.

5.2.3 Track Core Processes

The understanding of nonlinear yields has been a dominant aspect of electronic sputtering since the water ice measurements of Brown et al. (1978). The ejection due to Coulomb repulsion between two randomly produced ionizations near the surface gives a nonlinear yield (Haff, 1976; Johnson & Brown, 1982, 1983). In addition, as the excitation density, λ_e^{-1}, increases, the energy releases in mini-cascades from a density of randomly distributed excitations can overlap. As described for knock-on sputtering, this also can produce nonlinear yields. One replaces λ_c by λ_e, or dE/dx by $f_e(dE/dx)_e$ in eqs. (14), (17), and (18b), where f_e is the fraction of the electronic energy participating in sputtering. Therefore, above some threshold excitation density (Johnson, 1987) thermal spike sputtering gives a yield quadratic in $(dE/dx)_e$ (viz. fig. 3). Including the statistics of the transition from a linear to a quadratic sputtering regime results in a yield that differs from that obtained by addition which was used in fig. 3 (Johnson et al., 1991).

As the excitation density increases alternate electronic relaxation pathways can occur. For instance, the Coulomb explosion model of track formation (Fleischer et al., 1975) has been applied to sputtering. Counting only primary ionization, dJ/dx in eq. (21a), the repulsive energy density in a narrow track is

$$\left(\frac{dE}{dx}\right)_{\mathrm{coul}} \propto \frac{e^2}{\epsilon}\left(\frac{dJ}{dx}\right)^2 \tag{26a}$$

where e is the electron charge and ϵ an effective dielectric constant. If $(dE/dx)_{\mathrm{coul}}$ in eq. (20c) is used to calculate direct ejection gives $Y \propto (dJ/dx)^2$ (Haff, 1976). This can also be used to energize a thermal spike (Seiberling et al., 1980, 1982), using eq. (26a) in eq. (14), giving $Y \propto (dJ/dx)^4$, or to produce shock ejection (Bitensky & Parilis, 1987), using eq. (26a) in eq. (17), which would give $Y \propto (dJ/dx)^3$. The latter authors used $(dE/dx)_e$ for the driving energy, instead of $(dE/dx)_{\mathrm{coul}}$. This results in a yield proportional to $(dE/dx)_e^{3/2}$ (Reimann, 1993).

The release of energy during the decay of the hot plasma in the track core can clearly lead to enhanced sputtering, but a good description is waiting. The electrons cool to the lattice, by scattering from neutrals and ions, while the high density of incompletely screened holes produces repulsion after trapping. Using the total, rather than primary ionization, the net coulomb energy can roughly be written (Johnson & Brown, 1982)

$$\left(\frac{dE}{dx}\right)_{\mathrm{coul}} \approx \frac{e^2}{\epsilon}\left(\frac{(dE/dx)_e}{W}\right)^2 \ln\left(\frac{\overline{\rho}^2+\overline{\rho}_-^2}{2\overline{\rho}\,\overline{\rho}_-}\right) \tag{26b}$$

which must be less than $(dE/dx)_e$. Here $\overline{\rho}$ and $\overline{\rho}_-$ are the root-mean-square radii of the hole and electron distributions during Coulomb repulsion and ejection. $\overline{\rho}_-$

is, therefore, a rapidly decaying function of time.

Watson & Tombrello (1985) treated the plasma decay and calculated an average $\overline{\rho}$. They used the net repulsive potential in the track to energize the lattice, calculating escape via eq. (13a). Recently Ritchie et al. (1989) gave a description of the hot plasma decay, including ambipolar diffusion for positive and negative charges along with the hydrodynamic equations, eqs. (9). The principal problem is the complexity of the atomic processes which determine cooling, recombination, and repulsion.

Not only can hole repulsion heat the lattice, but so can electron cooling via collisions with the neutrals and holes in the lattice. In a dense plasma, electron-electron collisions will enhance the de-excitation and recombination rates (processes 9 and 10, Table II), converting the band gap energy into secondary electron kinetic energy (Ritchie & Claussen, 1982). The energized electrons can lose their kinetic energy to lattice motion, producing a thermal spike (Klaumünzer et al. 1986; Houpert et al., 1989). In a molecular solid, the energized electrons would instead excite molecular vibrations, leading to material expansion. A sufficiently rapid expansion, due to high excitation density, has been suggested as a cause of material ejection (Williams & Sundqvist, 1987).

5.3 Molecular Dynamics

5.3.1 Solid-State Potentials

When energy is deposited in the lattice by an energetic exothermic process, it can be transported to the surface by collisions, viz. eq. (2). Therefore, energy release in the bulk as well as at the surface can lead to sputtering, eq. (5a). This transport of energy through the solid can be described by molecular dynamics, MD (Hoover, 1986; Nieminen, 1993; Robinson, 1993). In this method the interaction of each particle with all neighbors in a sample, not necessarily pair-wise, is calculated at each time step. Therefore, knowing the potentials and using the position and momentum at the beginning of the time step, new positions and momenta are obtained and the atomic motion can be followed.

Whereas ground state potentials in many solids are available, for the electronic processes occurring in Table II the interaction potentials between a localized, excited species and its neighbors are poorly known. Unlike the ground-state atoms and molecules, which are often closed-shell structures, an excited atom or molecule in the field of neighbors interact via an ensemble of potentials. For the simple case of an Ar^+ interacting with one Ar neighbor, this involves, ignoring spin-orbit splitting, two Σ states (zero angular momentum along the internuclear axis) and two doubly degenerate Π states (one unit of angular momentum) (Herzberg, 1950).

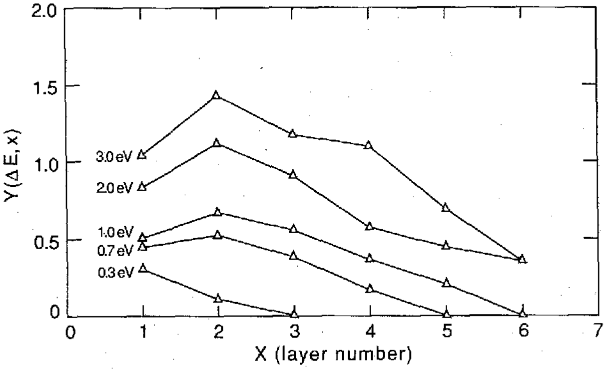

Figure 11. Yield versus depth due to energy release in crystal Ar, (100) face: ΔE indicated (Cui et al., 1988).

The differences between these interactions have to do with the shape of their electron distribution relative to the intermolecular axis. The potentials for these states evolve to the polarization potential at large separation, and the splitting between the two Σ states and that between the Π states determines the electron exchange rate with a neighbor (e.g., Johnson, 1982). Pair potentials for some Σ states are shown in fig. 8. There is, of course, an ensemble of repulsive and attractive excited states with each having a width in the solid.

When there are a number of neighbors, linear combinations of the wave functions associated with the excited argon atom can be used to diagonalize the interaction matrix. For an excited atom in a symmetric distribution of neighbors the resulting wave function has the symmetry properties of the field. Therefore, for the trapped atomic exciton in fig. 9b, the potential is approximated by a linear combination of the six potentials (Boursey et al., 1977 ; Cui et al., 1989a), and the net interaction is weakly repulsive (viz. fig. 8). Using these potentials in a MD calculation, the trapping of an atomic exciton at an undamaged vacuum surface was found to lead to ejection (Cui et al., 1989a), as predicted by Coletti et al. (1985) and as indicated in fig. 9b.

For the dimer in fig. 9a, the lowest excited state is described by the attractive $^{1,3}\Sigma_u^+$ potential acting between the two atoms (Schwentner et al., 1985), as indicated in fig. 8. Each of these atoms also interacts with the neighbors by an average made up of the other five potentials (Cui et al., 1989b). Such simple schemes have, of course, limited applicability, especially as the symmetry is broken at a surface and at defects. Also, when the radius of the electron cloud exceeds the interatomic radius, the increased distortion requires many body interactions.

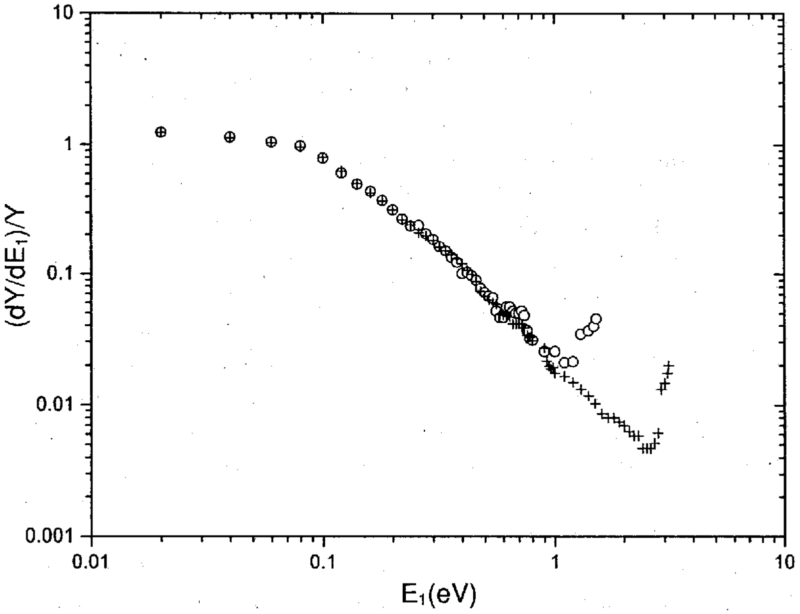

Figure 12. Energy spectra of ejected O_2 from solid amorphous O_2 for $\Delta E = 3.2$ eV (+) and 1.6 eV (o). O_2 given a kinetic energy in random direction at all depths. Decay as E_1^{-2} seen: spectra resembles eqs. (8a) and (8b) with the single event ejection added, as discussed in text. (Liu & Johnson, 1993).

5.3.2 Calculations: Single Events

To represent an energetic nonradiative relaxation event, an atom or molecule can simply be set in motion, or a pair interaction can be changed from attractive to repulsive to represent excitation to a repulsive state. In a crystal focussed collision sequences can occur (Robinson, 1981; Townsend, 1983; Cui et al., 1988), but when ΔE significantly exceeds the sublimation energy, U, the expression in eq. (2) with $T = \Delta E$ roughly applies for both crystalline and amorphous solids, even though the binary collision approximation breaks down (Garrison and Johnson, 1986; Cui et al., 1988, 1989c). $Y(\Delta E, x)$ is given in fig. 11 for a cascade in crystalline argon initiated by a randomly oriented momentum transfer event.

For sputtering by photons or when surface effects are important, eq. (25a), this is averaged over the distribution of excitations with depth. For a uniform distribution, using the definition of $\overline{\Delta x}$ in eq. (5a), the integration of $Y(\Delta E, x)$ gives

$$\overline{\Delta x}(\Delta E) \sim c\ell(\Delta E - U)/U \tag{27}$$

which is seen to be linear in ΔE. By contrast a diffusive cascade would give, $\overline{\Delta x}(\Delta E) \propto \Delta E^{5/3}$ (Johnson & Brown, 1982), as discussed earlier. Because of the linear dependence on ΔE in eq. $(27)^4$, the quantity f_e in eq. (20b) has the form $f_\mathrm{e} \approx \Delta E/W$, when electron-hole pair formation is a precursor to electronic sputtering.

By application of molecular dynamics to a number of condensed gases, the quantity c in eq. (27) was found to be about 0.15 for atomic and molecular solids (Johnson et al., 1991) roughly consistent with $c \approx \Gamma/4$ and $(N\overline{\sigma}_\mathrm{d})^{-1} \approx \ell$ as in eq. (6c). The calculated energy spectrum of sputtered atoms directly reflects the recoil energy spectrum discussed earlier, $G(\Delta E, E_0) + \delta(\Delta E - E_0)$, as seen in fig. 12 for O_2 molecules set in motion in a random direction and at random depths in solid oxygen (Liu & Johnson, 1993). The E_1^{-2} dependence in eqs. (8a) and (8b) over a range of energies $U < E_1 < \Delta E$ is remarkably well reproduced, implying that binary collisions are not a necessary requirement for such a dependence (Cui et al., 1988). Since the statistics of the low-energy ejecta was poor, the absence of the maximum in fig. 12 like that in eq. (8a) at $U/2 \approx 0.04$ eV is not certain. The fraction of ΔE dissipated to internal degrees of freedom is ~ 10% at these energies and no dissociation occurs. Excitation to a repulsive dissociating state of O_2 leads to a similar spectrum for the O_2 ejecta without the peak at large E_1, and, of course, O atoms were also ejected (Banerjee et al., 1991b); note that O_3 could not form easily for the potentials used.

5.3.3 Calculations: Tracks

A number of molecular dynamics calculations have been carried out for a track of excitations. Cui & Johnson (1989) and Banerjee et al. (1991a) treated vibrationally excited molecules in a cylindrical track in an amorphous solid of van der Waals bonded O_2 molecules. Although the excitation was rapid, no ejection occurred unless the molecules in the track were excited above the dissociation limit because of the large average spacing between molecules. When the internal molecular well structure was artificially modified so that the atoms in the vibrating molecule experienced larger excursions, a stronger vibrational-lattice interaction was produced. The rate of transfer of the internal energy to center of mass energy of the neighboring molecules was now seen to increase with excitation density as shown in fig. 13. Therefore, the total energy transfer to lattice motion, which we will call $(dE/dx)_\mathrm{eff}$, also increased. This manner of excitation resulted in a calculated yield which depended roughly on $(dE/dx)^3_\mathrm{eff}$ over the narrow range of $(dE/dx)_\mathrm{eff}$ studied. Earlier such a dependence was found for massive molecules, intended to represent biomolecules which were excited by vibrational expansion (Fenyö et al., 1990). Assuming $(dE/dx)_\mathrm{eff} \approx f_\mathrm{e}(dE/dx)_\mathrm{e}$, these early MD cal-

---

[4] For a variety of decay routes, an average $\overline{\Delta E}$ can be used

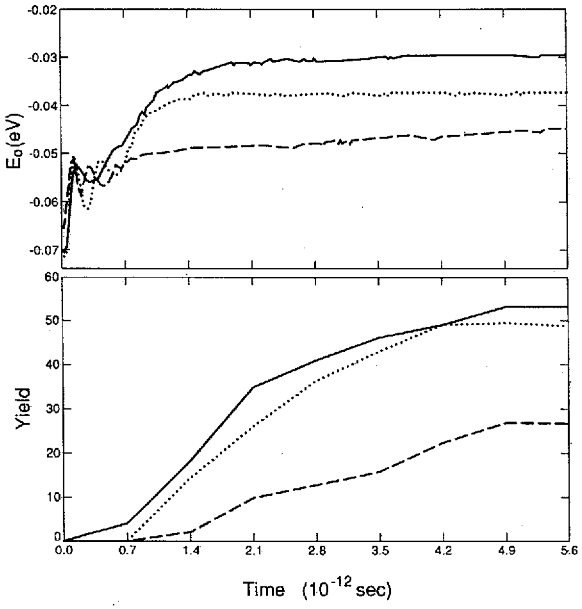

Figure 13. Time dependence of the average center-of-mass energy of molecules in a cylindrical volume of a sample of a diatomic solid: mass same as O_2, interatomic energy smaller than O_2 and separation larger. Molecules are initially excited vibrationally for three different values of internal vibrational energy per molecule. The transfer of vibrational energy to center of mass energy, E_0, is seen vs. time, as in the accumulated ejection yield, Y. From Banerjee et al. (1991a).

culations were suggestive for developing the so-called pressure pulse model given in eqs. (18a) and (18b) (Johnson et al., 1989; Reimann, 1993). Since then, MD calculations have been used to test this model (Fenyö & Johnson, 1992; Fenyö, 1993).

Recently, Urbassek et al. (1993) excited a cylindrical volume of atoms in an argon solid by giving them kinetic energy in a random direction. Such an excitation might be the result of a Coulomb explosion in the track or some other 'track' process. At the lowest $(dE/dx)_{\text{eff}}$ the yield also exhibited a cubic dependence. Surprisingly, at larger $(dE/dx)_{\text{eff}}$ the yield became nearly linear for the ejection times, up to 10^{-11} sec, and for initial energies and sample conditions studied. This result occurred because the radial diffusion of energy was slow compared to the transport by flow of gas from the transiently pressurized track.

6 Theory: Molecular Solids and Compositional Changes

6.1 Preferential Ejection

Because the sputter yield depends inversely on the cohesive energy, U, the more volatile elements of a mixed material are sputtered preferentially at low fluences. In the linear cascade regime the description of sputtering from an alloy or a chemical compound has been treated by a number of authors resulting in approximate analytic expressions for the yield of each species (Andersen & Sigmund, 1974; Haff & Switkowski, 1976; Andersen, 1984; Sigmund & Lam, 1993). For knock-on sputtering, an approximate yield ratio for two species, Y_i and Y_j, is (Sigmund, 1981)

$$\frac{Y_i}{Y_j} \approx \frac{c_i}{c_j}\left(\frac{M_j}{M_i}\right)^{2m}\left(\frac{U_j}{U_i}\right)^{1-2m}, \tag{28a}$$

where c_i is the relative concentration of species i in the surface region, U_i is the average surface binding energy of species i, and m is a number determined by the interaction potential. For a steeply repulsive potential $m \approx 0$. For thermal spike sputtering, eqs. (12) - (16), under the assumption of a cylindrical region of excitation,

$$\frac{Y_i}{Y_j} \approx \frac{c_i}{c_j}\frac{M_j}{M_i} g(U_i, U_j) \tag{28b}$$

where

$$g = \begin{cases} (U_j/U_i)^2 & \text{(Kelly, 1979)} \\ \exp\left(\dfrac{U_j - U_i}{kT}\right) & \text{(Sigmund, 1981)} \end{cases}$$

At very low fluences the surface concentrations, c_i, are generally equal to the bulk concentrations, c_i^0 , but they change with fluence, since the more volatile elements are depleted more rapidly. Because diffusion occurs along the damage path of an ion, the extent of this depleted region can approach the ion penetration depth (Kelly 1984; Sigmund & Oliva, 1993). Although the sputtering is initially non-stoichiometric, the yield ratio can become stoichiometric at high fluences, $(Y_i/Y_j) \approx (c_i^0/c_j^0)$, as the concentrations in the surface region change according to either eq. (28a) or (28b). These expressions should only be used as a guide to understanding compositional alteration by sputtering.

6.2 Sputtering of Molecules

In a molecular material, atoms or molecules may be ejected. Based on the above discussion, the relative yields will depend on the relative sizes of the cohesive energy of the molecular solid, U, the dissociation energy, E_b, and the removal energy, U_a, for a particular atomic species (Kelly, 1987).

In addition, the relative yields are extremely sensitive to the spatial extent of the momentum distribution at the surface. The likelihood of molecular ejection is enhanced if correlated events occur at the surface (Urbassek & Hofer, 1993). Therefore, molecular ejection becomes relatively more important when a volume element at the surface has a net directed momentum, figs. 2c and 2d (Johnson et al., 1989; Reimann, 1993). For a typical high excitation density, the initiating events often lead to fragmentation and fragment ejection, whereas the later, correlated energy transport can lead to molecular ejection (Bitensky & Parilis, 1987; Johnson & Sundqvist, 1992). Although it can be useful to roughly characterize the relative amounts of atomic and molecular species by an average temperature, ejection is, in general, a nonequilibrium process.

Let us consider a low-density collision cascade in a low temperature solid of condensed, homonuclear diatomic molecules (solid O_2 or N_2). If the energy transfer, T, to either atom of a molecule is much greater than $\sim 2E_\mathrm{b} + U_\mathrm{a}$, atomic ejection is dominant. The energy transfer to the atom must be at least $2E_\mathrm{b}$ for dissociation since half the energy transferred to one atom goes to motion of the center-of-mass of the molecules. For lower values of binary collision energy transfer molecular ejection dominates. Because the recoil number density in eq. (2) grows at low recoil energies, a large number of molecules can be ejected as $U \ll E_\mathrm{b} + U_\mathrm{a}$ in these solids.

Since electronic relaxation events typically release small energies, electronic sputtering at low excitation densities leads to atomic ejection only by repulsive dissociation at the surface. Below the surface these events can lead to ejection of molecules by momentum transfer to the surface, as discussed. The residual atoms in the bulk are radicals which are difficult to sputter as they have relatively large binding energies to the solid, U_a. Therefore, with increasing fluence they accumulate and react, so that chemical processes can eventually control sputtering, as discussed below.

6.3 Chemical Sputtering

In knock-on and electronic sputtering of molecular material, the deposited energy will lead to broken bonds, formation of radicals, and preferential ejection. This can eventually lead to chemical reactions occurring, as the radical species bind efficiently to the sample. In addition, for electronic sputtering, an excited species can directly react with a neighbor, with again the possibility of new species forming. Such reactions can affect the erosion rate of the solid in two ways. First, the reacting species may release sufficient energy in an exothermic reaction to directly cause ejection or to increase the local temperature enhancing sputtering (Johnson & Brown, 1982; David & Michl, 1989). Second, any newly formed species may have a lower or higher volatility than the molecules in the solid. This can change the effective cohesive energy, U, and, thereby, the sputtering yield. Such effects were treated for knock-on sputtering of refractory solids by Roth (1983).

When the new species are formed from radicals produced in the track of a single ion, the effect on the yield is independent of fluence. When a newly formed radical reacts with a background of previously produced radicals, the effect on the yield is fluence and temperature dependent (Reimann et al., 1984a). A typical reaction rate between two radical species would be written, $\kappa(T')N_iN_j$, where $\kappa(T')$ is the reaction rate constant and N_i and N_j are the local densities of the reacting species. This is one term of a set of rate equations which would include diffusion. T' is used to indicate that the reaction may be driven by the kinetic energy of one of the newly formed species, a 'hot atom' reaction (Matsuura et al., 1984; Adloff et al., 1992) or by the ambient temperature, T_a. In the latter case the ejection yield depends on the activation energy for the reaction, ΔE_a (Kelly, 1977; Johnson & Brown, 1982), so that the yield for a formed species would be proportional to $\exp(-\Delta E_\mathrm{a}/kT_\mathrm{a})$ (Brown et al., 1982; Reimann et al., 1984a).

As a final issue, the implanted ion itself may be reactive: H, C, O, S, etc. In a refractory material with low sputtering yield, as for C^+ on a silicate grain or H^+ on graphite, more volatile species may form after a large fluence enhancing the sputtering yield: CO (Rocard & Bibring, 1982) and CH_4 (Roth, 1983) respectively. The second process is of interest in fusion devices, whereas the first process was of interest for solar wind sputtering of lunar soil at the time of the Apollo missions (Taylor, 1982). Such a process is also of interest at Europa, a moon of Jupiter where sulfur, ejected from the neighboring moon Io, is ionized, accelerated, and implanted into Europa's icy surface, producing an SO band seen in UV-reflectance (Sack et al., 1993). In the following we review first the experimental methods and then summarize the data available.

7 Experimental Methods

The study of sputtering of insulators involves a number of methods well known in other fields as well as some new techniques. In the standard setup shown in fig. 14, an insulating target is placed in a vacuum chamber with a pressure typically 10^{-8} torr or below. Beam particles (ions, electrons, or photons) impinge on the target causing a loss of material. Important properties to be measured are the sputtering yield, Y, the energy distribution dY/dE_1, angular and mass distributions of the ejected particles, the composition of the residual target, and the luminescence from the target or from escaping particles. Measurements of the angular and mass distributions of the ejected particles, as well as systematic studies of the yields and energy distributions have been performed only in few cases.

Key parameters are the primary energy, E, the type of incident particle, and the angle of incidence, θ. However, based on the theoretical discussion, it is often advantageous to plot the results versus dE/dx or the corresponding stopping cross section, S. For experiments on frozen gases the thickness of the film and the temperature of the substrate are also important. For incident ions, varying the charge state and using molecular ions can be helpful, as discussed.

When irradiating films of frozen gases on a cryogenic substrate, the possibility of easily varying the thickness is a particular advantage. Because of the simplicity of producing low-temperature samples of condensed-gases in situ, systematic measurements have been carried out in a number of laboratories. Targets of sulfur, the only elemental room-temperature insulator studied (Chrisey et al., 1988; Torrisi et al., 1988), were also produced by in situ film deposition. This is in contrast to measurements on other room-temperature insulators, in which the samples have to be inserted into the vacuum system and cleaned by heating or sputtering prior to measurements.

7.1 Yield Measurements

The sputtering yield is measured in a variety of ways. For room-temperature insulators or refractory materials, the methods are similar to those applied to metals (Andersen & Bay, 1981), but typically with reduced beam currents to reduce sample heating and charging. Yields have been determined by weight-loss, film thickness change, profilometry of the sputtered volume, and interference micrographs (Bach, 1988). The only yield for electron-induced sputtering of alkali halides was determined by measuring the crater dimensions (Szymonski et al., 1985).

Because the yield can depend on the thickness of the target, integral and differential measurements of the yield can differ. In the former case, the yield is evaluated from the number of particles necessary to remove an insulating layer of known thickness completely. The erosion continues until a clear signal from the substrate is detected (Schou et al., 1984). The methods below are differential.

7.1.1 Mass Loss: Rutherford Backscattering

Rutherford backscattering (RBS) measures the absolute number of atoms per unit area (the column density) at any time, and, therefore, it can be used to determine both the sputtering yield (Brown et al., 1978, 1986; Ollerhead et al., 1980; Besenbacher et al., 1981) and the changing composition of the target (Brown et

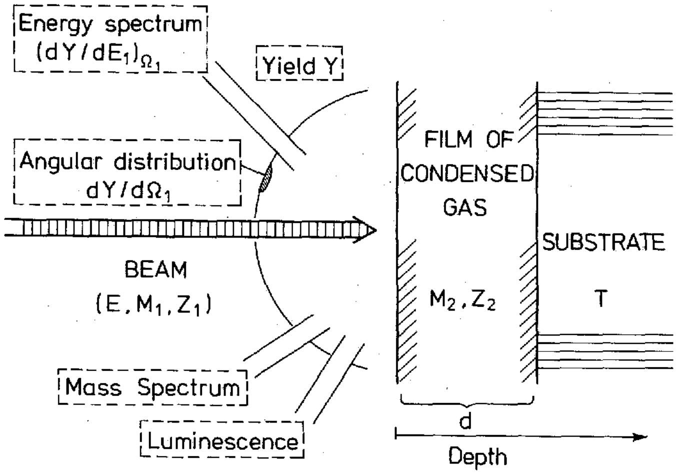

Figure 14. Schematic survey of the experimentally studied quantities in an erosion experiment with a frozen gas (From Schou, 1987).

al., 1984). A simultaneous monitoring of beam current, area of beam spot, and change in column density gives the yield, fig. 15. The precise determination of the change in column density may be carried out from the shift of the position of a thin heavy marker (typically a 50 Å thick gold layer deposited on beryllium) or from the reduction of the total number of film atoms detected in the backscattered peak. The ions responsible for probing the thickness can be different from those eroding the film. The agreement in the yield determined from the marker shift or the peak reduction is usually good, but the marker shift is generally used. Potential disadvantages are that the erosion produced by the probing beam, often 1 - 1.5 MeV He^+ ions, has to be subtracted, and species lighter than the probing beam can not be detected. Typically, the achievable sensitivity corresponds to the removal of a monolayer of argon from solid argon (Reimann, 1992).

Ion beam analysis of a foil on which sputtered atoms have been collected has been carried out for a few materials. This procedure requires a primary eroding beam and an analyzing beam, or the ability to change the beam setting from the target to the collector foils. Qui et al. (1982) used forward scattering of, typically, 4 MeV F^+ ions to study refractory solids.

7.1.2 Mass Loss: Energy Loss from Substrate Source

A method related to RBS is the determination of energy loss for helium ions originating from a thin radioactive layer deposited on the substrate. The column density

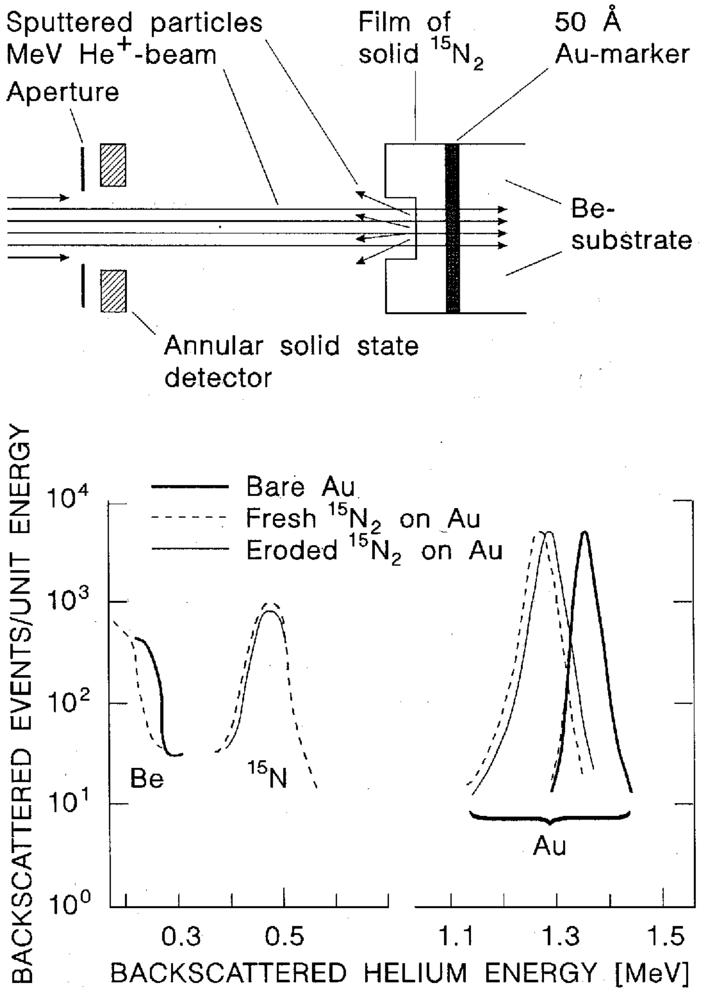

Figure 15. Schematic survey of the geometry (upper part) and the data curves (lower part) in an erosion experiment on solid $^{15}N_2$ with Rutherford Backscattering Spectrometry (RBS). (Modified from Brown et al., 1986).

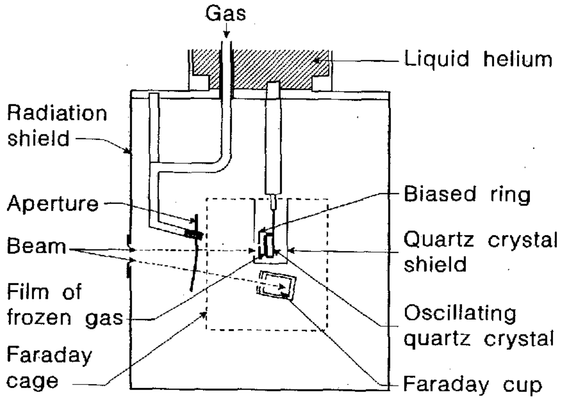

Figure 16. Schematic survey of the geometry for a typical erosion experiment with a frozen gas deposited on a quartz crystal (Modified from Schou et al., 1984).

can be evaluated from the energy loss of the emitted alpha particles traversing the film obtained from a solid state detector. Although care must be taken not to bombard the radioactive source, the method is simple and easy to apply, but because of the low dE/dx the sensitivity is less than in RBS experiments (Chrisey et al., 1988).

7.1.3 Mass Loss: Microbalance

The mass loss from a frozen-gas target by particle irradiation may be determined by a quartz crystal microbalance on which a cryogenic sample is deposited, fig. 16. This method has a high sensitivity and the mass loss is obtained from the linear change in frequency as the film is removed by sputtering (Schou et al., 1984; David & Michl, 1989). Two demands pose a problem for low-temperature erosion experiments with a quartz crystal microbalance: the crystal has to oscillate freely in a holder and the thermal conduction from the cryogenic area to the crystal electrode, on which the film is deposited, must be sufficiently good. The typical sensitivity corresponds to the removal of one monolayer of argon from solid argon. A reference quartz crystal can also be mounted in thermal contact with the target crystal (David & Michl, 1989), providing a large improvement in sensitivity, $\sim$ 0.1-10^{-3} monolayer of argon (Baragiola, 1993c). With a microbalance the control of film deposition is particularly easy. A complicating feature is the measurement of the primary current on a high-frequency electrode.

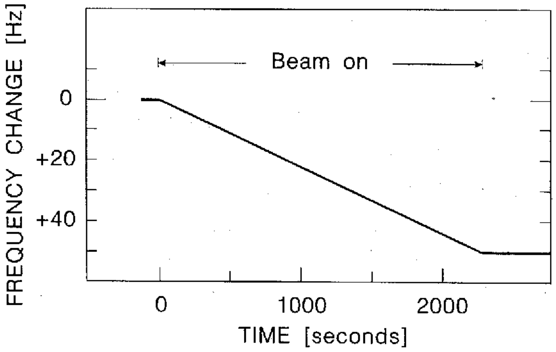

Figure 16, cont'd. Schematic survey of the frequency change curve for a typical erosion experiment with a frozen gas deposited on a quartz crystal (Modified from Schou et al., 1984).

7.1.4 Quadrupole Mass Spectrometry

A frequently used method for obtaining a relative yield is the detection of the sputtered species by a mass spectrometer. One of the first sputtering measurements of relevance to this chapter was carried out by Erents & McCracken (1973) with quadrupole mass spectrometry (QMS). The method is fast and can give absolute yields when calibrated. The spectrometer is directed toward the target, which is irradiated by a pulsed beam so that background subtraction is possible (Brown et al., 1986). An additional advantage is the ability to determine the composition of the ejecta. The relative sensitivity under typical beam currents is about 0.01 monolayers of argon (Reimann, 1992).

7.2 Energy Distributions

The energy distribution of the emitted particles can directly reflect the energetics of the ejection processes as discussed. For alkali halides this has also been decisive in identifying the erosion processes (Szymonski, 1993). The energy distributions of particles sputtered from insulating targets have almost exclusively been studied using time-of-flight (TOF). In general, the distribution is measured for a small solid angle around the target normal, whereas the angle of incidence differs between experiments [0° (Hudel et al., 1991), 45° (O'Shaughnessy et al., 1988a,b; Pedrys et al., 1988) or 60° (Haring et al., 1984a)]. A pulsed beam strikes the insulating target and generates a pulse of eroded particles that passes through a quadrupole equipped with an ionizer. The kinetic energy of each species can be determined from the time interval between the impact of the beam particles and the arrival of the sputtered particles, for energies from 10^{-3}eV up to about 10 eV. The problem of obtaining good statistics for the rare ejection of particles with more than 1 eV was overcome using a correlation method (Overeijnder et al., 1978).

Mechanical TOF-spectrometers were used by Tombrello and coworkers (Griffith et al., 1980; Seiberling et al., 1980). The sputtered particles emitted normal to the target surface were collected on a rotating aluminum wheel and then exposed to neutron activation analysis. This gave accurate energy spectra for uranium atoms sputtered from room-temperature insulators, UF_4 and UO_2. A particularly refined setup that combines TOF-spectrometry and angular resolved spectrometry of metastable neutrals has been developed by Sanche and coworkers (Leclerc et al., 1990, 1992).

7.3 Mass and Luminescence Spectra

Measurements of the masses of emitted particles are useful for detecting clusters ejected from elemental targets and radicals, new chemical species, or clusters ejected from chemical compounds. The masses are typically determined using a QMS, with the beam pulsed or continuous.

Simultaneous measurements of luminescence and sputter ejecta have been important for identifying the energy release events for frozen gases and alkali halides (Reimann et al., 1984a, 1988; Szymonski, 1993). Occasionally, the change in luminescence intensity during particle irradiation has been utilized to estimate the erosion rate (Coletti & Debever, 1983) or to study the excited states of sputtered atoms (Kloiber et al., 1988) and molecules (Reimann et al., 1991).

7.4 Target Analysis

The particle or photon bombardment can cause preferential sputtering and modification of the target. It is sometimes possible to carry out an external macroscopic chemical analysis, if the amount of residual material is sufficient and is non-volatile. A common in situ analysis of atomic composition is Rutherford backscattering. For instance, absolute loss rates of carbon from frozen methane were obtained in this manner by Lanzerotti et al. (1987), whereas for the deuterium loss from CD_4 they used the ^{3}He(d,p)^{4}He nuclear reaction in the deuterated sample. A common in-situ analysis of molecular composition is infrared (IR) absorption spectroscopy (Benit et al., 1987; David et al., 1986; David & Michl, 1989). For instance, this has helped in the interpretation of the temperature dependence exhibited in water ice sputtering (Rocard et al., 1986; Spinella et al., 1991). In addition, mass spectrometers are used to monitor the change in character of the ejecta with irradiation time (SIMS or neutral SIMS), which is indicative of the changing target composition. This has also been used to monitor the change in water ice by loss of H_2 (D_2) and

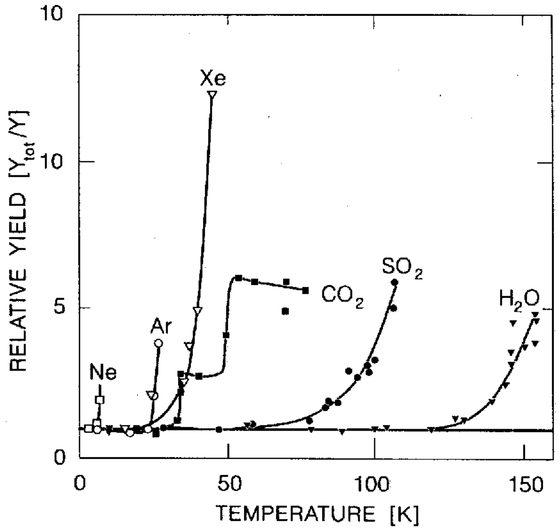

Figure 17. The relative yield Y_{tot}/Y is plotted versus the substrate temperature. Y_{tot}; total yield; Y, low-temperature yield. Ne-data, Schou et al. (1986); Ar-data, Besenbacher et al. (1981); Xe-data, Ollerhead et al. (1980); CO_2-data Brown et al. (1982); SO_2-data, Boring et al. (1984); H_2O, Brown et al. (1980a). From Schou (1987).

O_2 (Brown et al., 1982, 1984).

7.5 Selective State Excitation

Using laser or synchrotron light (Kloiber et al., 1988; Feulner et al., 1987; Menzel, 1990) selective excitation of the solid can be made to test particular electronic states that might lead to sputtering. Recently, Runne et al. (1993) selectively excited Kr atoms in the surface of solid argon to the $n = 1$ state, which can not migrate. In this way an excitation at the surface is known to decay at the point of absorption. Selective excitations of solids have been preformed with low energy electrons as well (Kloiber & Zimmerer, 1989; Hourmatallah et al., 1988; Leclerc et al., 1992).

8 Experimental Data

The solid inorganic insulators may be divided into the following classes according to their general properties and behavior during sputtering:

A) elemental solid insulators (e.g. deposited S_8)
B) oxides and related solid compounds (e.g. SiO_2, Al_2O_3)
C) frozen gases (e.g. N_2, Ar, H_2O)
D) alkali halides and related materials (e.g. $MgCl_2$)

The latter group is treated by Szymonski (1993). Whereas knock-on sputtering of insulators is similar to that of metals, electronic sputtering occurs in most insulators and only occurs in semiconductors and metals at extremely high excitation densities (Johnson, 1993; Brown, 1993). In addition, since frozen gases and elemental insulators are much more volatile than metals, beam-induced evaporation may play a larger role.

8.1 Beam-Induced Evaporation

The heating of the solid, externally or directly by a beam of high current, can lead to surface loss as discussed earlier. There is a threshold below which the yield is independent of the ambient temperature for a typical current density, whereas for higher temperatures or intensities the yield increases rapidly with temperature (Lanzerotti & Brown, 1983). For the rare-gas solids for a typical low ion current density the threshold temperature increases with increasing sublimation energy (Schou, 1987, 1991), as seen in fig. 17. This temperature, approximately $0.02U/k$, is somewhat below the melting temperature. In contrast to this, the increasing yield with temperature seen in fig. 17 for CO_2, SO_2, and H_2O (Brown et al, 1982; Boring et al., 1983) is due to formation of volatile products to be discussed; enhanced ejection due to heating occurs at much higher temperatures.

At high current densities the yield is beam current dependent (Besenbacher et al., 1981; Schou et al., 1984; Sigmund & Szymonski, 1984; Schou 1991). The erosion yield for electron-bombarded solid neon increased by more than two orders of magnitude as a result of a current density increase from 10 $\mu A/cm^2$ up to 35 $\mu A/cm^2$ (Schou et al., 1984). For the most volatile material which exists in equilibrium with laboratory vacuum, namely solid hydrogen, yield measurements could be carried out only for current densities below 0.2 $\mu A/cm^2$ (Stenum et al., 1991). Beam-induced evaporation is indicated by an enhancement in the energy spectrum at very low energies, eq. (19b) (Haring et al., 1984a; Ellegaard et al., 1993b). Pedrys et al. (1984) observed that ejection energies for F_2 emitted from electron-bombarded solid sulfur hexafluoride could be described by a Maxwell-Boltzmann function using a macroscopic target temperature. Sputtering of solid methane resulted in an energy spectrum for emitted hydrogen which could be similarly described (Pedrys et al., 1986). In contrast, for the ejected SF_6 and CH_4 molecules, the energy spectra were independent of the beam current since

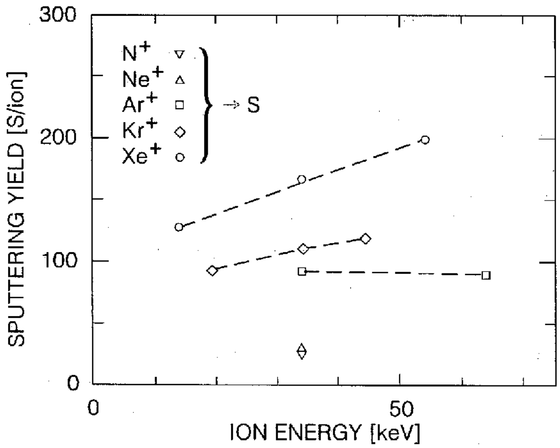

Figure 18. Sputtering yield for medium mass ions incident on sulfur. The yield is given in S-atoms per ion, but the ejected species are frequently polyatomic molecules. Data from Chrisey et al. (1988). Dashed curves to guide the eye only.

the molecular emission is determined by the energetic release processes. For solid sulfur, a strong beam-induced evaporation ($\sim 10^4 \mathrm{S/He}^+$) was seen if the target was not cooled (Fink et al., 1984). This yield is orders of magnitude larger than that at low temperatures (Torrisi et al., 1986).

The alkali halides show the remarkable feature that direct electronic sputtering takes place for the halide component alone. The surface becomes gradually enriched with the alkali atoms and the erosion may eventually cease, unless the temperature (for example, produced by a high beam current density) is high enough that the alkali atoms evaporate as fast as the halogen atoms are sputtered. At low temperatures the sputtering is controlled largely by the evaporation rate of the metal, which leads to a Maxwell-Boltzmann distribution for the ejecta (Overeijnder et al., 1978, Szymonski, 1980, 1993, Szymonski et al., 1990).

8.2 Knock-on Sputtering

Knock-on sputtering of insulators is similar to that of metals, as discussed earlier, except for the volatility and chemical composition. Low volatility means that many atoms are set in motion at each impact on the frozen gases. In addition, the molecular frozen gases show considerable chemical activity, and many refractory insulators are also multicomponent targets. For example, sputtering of the latter oxides resembles that of metallic alloys, although the anion may be chemically

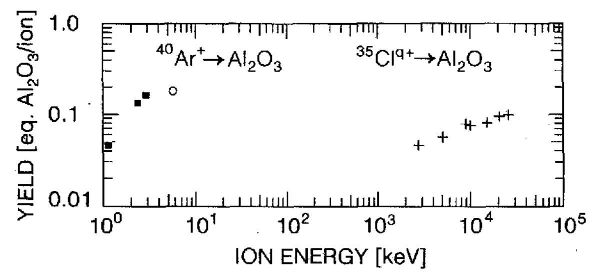

Figure 19. Knock-on and electronic sputtering yield for heavy ions incident on Al_2O_3, expressed as Al_2O_3 molecules/ion, even though the majority of the ejected particles may be atoms.+, electronic sputtering yield from Qui et al. (1982). Knockon sputtering yields, full squares from Davidse & Maissel (1966) and o from Bach (1988).

active in insulators.

8.2.1 Sulfur

Sulfur is the only elemental room-temperature insulator that has been investigated. It has been studied primarily because of its interest at Io (Johnson, 1990). The yield from low-temperature sulfur bombarded by medium mass ions in fig. 18 increases strongly with the mass of the primary ion, but the variation with ion energy is relatively small. The size of the experimental yield agrees roughly with that predicted by linear collision-cascade theory using an assumed average sublimation energy per atom, U, and an atomic interaction cross section, $\overline{\sigma}_d$, in eq. (6a) (Chrisey et al., 1988).

The sulfur atoms in the parent molecules, S_8 are bound much stronger to their neighbors (2.7 eV) than the unit species, S_8, is to the lattice (1.1 eV). Because of the size of S_8 and the strong S-S bond, the sulfur is ejected predominantly as diatomic molecules rather than as S_8 or other large molecules S_6 and S_7. The relative distribution of ejected masses depends very little on the incident ion mass. Chrisey et al. (1988) measured the energy distribution for S_1, S_2 and S_3 ejected as a result of 44 keV Ar^+ ion bombardment. The high-energy part of the tail for the two lightest species is consistent with knock-on sputtering (Urbassek & Hofer, 1993). The effective binding energy, U, inferred from the peak in the energy spectra, 100 and 50 meV for S_1 and S_2 respectively, is lower than that determined from the yield measurements. Even though the low-energy part of these spectra depends strongly on the background subtraction, one may interpret the spectra to be the result of linear collision-cascades in a damaged material of loosely bound sulfur fragments.

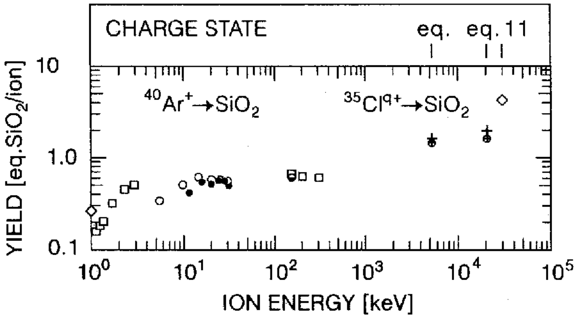

Figure 20. Knock-on and electronic sputtering yield for heavy ions incident on SiO_2. Knock-on yields: ◇, Cantagrel and Marchal (1973); ○, Bach et al. (1974); •, Edwin (1973); half-filled circles, Schroeder et al. (1971); □, Jacobsson and Holmén (1993). Electronic yields: +, fused and, ⊕, crystalline, Qui et al. (1983); ◇, Sugden et al. (1992). The ^{35}Cl charge states are indicated above the yield figure, ‘eq.means equilibrium charge state.

8.2.2 Refractory Materials

Oxides have been studied comprehensively within the last twenty years (Betz and Wehner, 1983). Oxygen is often sputtered preferentially as atoms or in molecular species. Therefore, an enrichment of the heaviest elements occurs in the surface region, which is partly compensated for by diffusion (Lam & Sigmund, 1993). The sputtering yield from oxides is comparable to that from metals except for MgO and Al_2O_3 (Betz & Wehner, 1983). For SiO_2, recent measurements by Jacobsson and Holmén (1993) demonstrate that the total yield does not deviate too much from the corresponding atomic yield from silicon. However, if metals are bombarded in an oxygen atmosphere, so that oygen atoms are continuously available, the yield of the metal atoms falls drastically as the oxygenation of the surface increases (Kelly, 1987).

Results for aluminum oxide bombarded by keV argon ions are shown in fig. 19. The total yield is given in equivalent Al_2O_3 molecules ejected, even though the ejection is primarily as atoms. This yield increases up to a plateau with a net ejection equivalent to about 0.2 Al_2O_3/ion at 5-10 keV . There are no data points above 10 keV, but the general trend should follow the nuclear stopping power until electronic sputtering becomes dominant. For silicon dioxide the energies 1-300 keV are fairly well investigated (fig. 20). These data show that there is a plateau from 5 to 300 keV similar to that at comparable velocities in fig. 1b for water.

Theoretical comparisons are difficult for the oxides since the magnitude of the effective surface barrier, U, is not known accurately. Kelly (1987) and Bach (1988) have used the atomization energy instead of the sublimation energy in order to

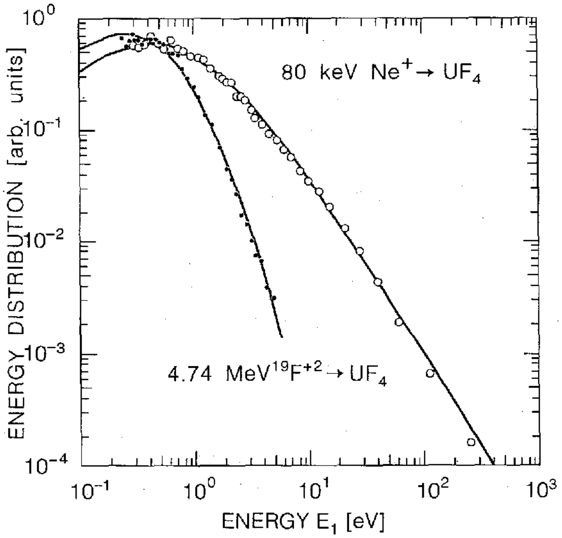

Figure 21. Energy spectra of sputtered U-atoms from UF_4 at medium mass ion bombardment (Griffith et al., 1980). The lines are a fit to $E/(E+U)^n$. For Ne^+ ion bombardment, $n = 2.6$ and $U = 12.0$ eV. For F^{+2} ion bombardment, $n = 6.1$ and $U = 0.71$ eV.

evaluate the yield, as discussed. This is the sum of the formation enthalpy for the oxide, the sublimation energy of the metal atom, and the dissociation energy for oxygen. Essentially, one divides the ejection process into subprocesses: the molecule is split into its gas-phase constituents, the metal atom is evaporated from the solid, and the oxygen molecule is dissociated. This gives an average value for U, although different values should be used for the ejected oxygen and metal atoms, because the forces at any surface site depend on the atom and on the atomic environment.

Sputtering of uranium atoms from uranium tetraflouride was studied by Griffith et al. (1980) with keV as well as MeV medium mass ions. The yield of uranium atoms, obtained from neutron activation analysis, was about 0.2 per ion for 100 keV-ions, which corresponds to a surface binding energy of 2.5 eV.

A study on low energy sputtering of tantalum oxide by argon and helium ions was recently reported (Baretzky et al., 1992). Preferential sputtering was shown to be governed by collision processes rather than by diffusion and segregation. Sputtering of the high T_c-superconductors has so far not been studied systematically, although the partial yields obviously play a key role in the thin-film deposition by sputtering. A complicating feature is the expected strong directional dependence because of the anisotropy of the crystal structure (Geerk, 1993).

Energy spectra of metal atoms from oxygen-covered surfaces have been studied comprehensively (Betz, 1987; Dullni, 1984; Kelly, 1987). The energy distributions of the metal atoms are broadened compared with the emission from pure metal surfaces. Usually, this is characterized by a fitting parameter that replaces the sublimation energy in the energy distribution in eq. (8a). This parameter is often a factor of 2-3 larger than the sublimation energy. The relevance to regular oxides is not certain. The energy distribution of sputtered uranium atoms from uranium tetraflouride by 80 keV Ne-ions (Griffith et al., 1980) is typical of a linear collision-cascade (fig. 21). At high ejection energies (100 eV) the distribution shows a tail $E_1^{-1.6}$, close to the E_1^{-2}-tail in eq. (8a). The position of the maximum is at 0.35 eV, which is much lower than that inferred from the yield measurements by use of eqs. (4) and (6a).

8.2.3 Frozen Gases

Generally, the sputtering of the most volatile frozen gases shows the most pronounced deviation from the linear collision-cascade description. The energy spectra of the emitted particles, the energy dependence of the sputtering yield, and, in some cases, the dependence on incident angle have been studied.

Frozen gases often exhibit energy spectra with an E_1^{-2} high-energy tail, indicating that the linear collision-cascades dominate at an early stage of the sputtering process, as in eqs. (8a) and (8b). However, the maximum of the energy distribution, if seen, is usually substantially below one-half of the sublimation energy (Brown & Johnson, 1986), appropriate for eq. (8a). Even at low collisional excitation density, large λ_c, the effective surface binding energy deduced using eq. (8a) is below the sublimation energy (O'Shaughnessy et al., 1988a; Pedrys et al., 1985; Pedrys, 1990, 1993). At small λ_c the nonlinear behavior of the collision cascades enhances the low-energy ejecta, which is seen for solid xenon bombarded by xenon ions at 1-30 keV (Pedrys, 1990; O'Shaughnessy et al., 1988a).

The results for the total yields show the trend predicted from linear collision-cascade theory (eqs. (4) and (6a)) if the collisional excitation density, λ_c^{-1}, is small and/or the sublimation energy large. The best agreement for frozen gases is found for medium-mass ions incident on solid krypton and xenon (Stevanovic et al., 1984; Boring et al., 1987; O'Shaughnessy et al., 1988a). For the water ice results at low values of the stopping cross section S in fig. 1b (Christiansen et al., 1986; Bar-Nun et al., 1985), very rough agreement with the linear collision-cascade theory has been reported, even though the yield is controlled in part by formation and reaction of radicals, so that sputtering from this material is a complex process.

Generally, the agreement with the linear collision-cascade theory is fair for the

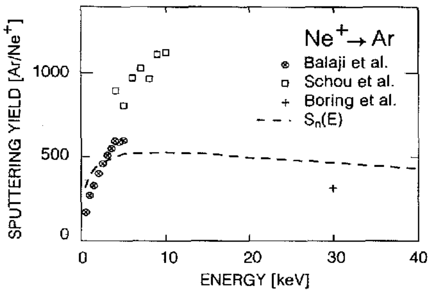

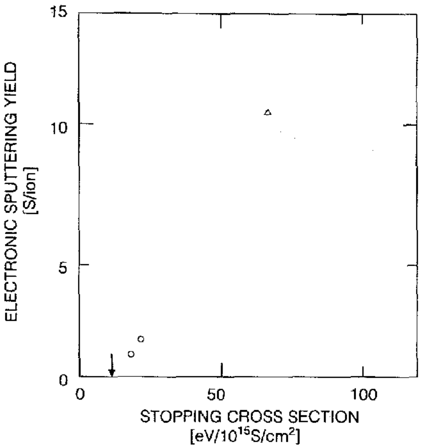

Figure 22. Sputtering yield for Ne$^+$ions incident on solid Ar. ⊗, Balaji et al. (1990); □, Schou et al. (1992); +, Boring et al. (1987). Dashed line, the nuclear stopping cross section, calculated from Schou (1988) and normalized to the yield at $E = 2.75$ keV.

Figure 23. The electronic sputtering yield of sulfur as a function of the electronic stopping cross section, $(dE/dx)_e/N$, Δ, 1 MeV He$^+$ from Torrisi et al. (1986); o, 49 keV and 33 keV H$^+$ from Chrisey et al. (1988). For MeV H$^+$, no sputtering was obtained; arrow indicates the rough threshold of dE/dx for which no erosion was measurable.

total yield up to much higher primary energies and for much higher collisional densities than for the energy distribution. The reason for the discrepancy is not known. It is possible that the energy distributions, which in all setups are measured for a limited solid angle around an exit angle perpendicular to the surface and for ions at non-normal incidence, may not be representative of all exit directions and of normal incidence. There is also a relatively low dE/dx threshold for nonlinear effects in the condensed gas solids, as discussed, and a linear region exhibiting spike effects can occur (Ellegaard et al., 1990, 1992). An example of a 'spike' regime, characterized by a strongly nonlinear dependence of the yield on the nuclear stopping power, is shown in fig. 22 for neon ions incident on solid argon. A similar trend is observed for neon ions on neon (Schou et al., 1992). Balaji et al. (1990) show that the yield for solid rare gases in general increases very strongly at low incident ion energies, whereas the point obtained by O'Shaughnessy et al. (1988a) shows that the yield decreases at high ion energies. The very large yield from such systems means that atoms are not individually ejected from an intact surface, as discussed.

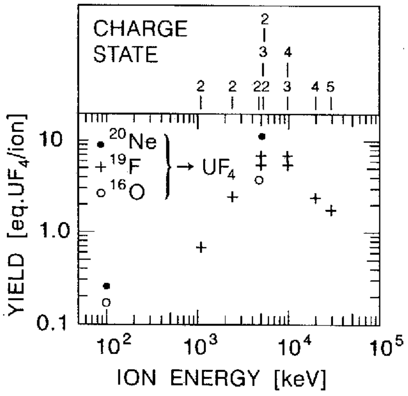

Figure 24. Knock-on and electronic sputtering yield from UF_4 in units of equivalent molecules per ion. Data points from Griffith et al. (1980). The charge state of the incident ion is shown above the yield figure.

9 Electronic Sputtering

9.1 Sulfur

As for knock-on sputtering, sulfur is the only elemental solid room-temperature insulator that has been investigated. Only, the three data points and a threshold value for the total yield shown in fig. 23 were obtained at low temperature (Torrisi et al., 1986; Chrisey et al., 1988). The trend observed for a number of other low-temperature frozen gases, to be discussed, suggested that this yield also is roughly quadratic in the stopping power above threshold, consistent with the thermal spike result in eq. (14), for the most common fragment, S_2 (Chrisey et al., 1988). The empirical efficiency for knock-on sputtering, Λ_c in eq.(4), is found to be about three times higher than that measured for electronic sputtering, Λ_e in eq. (20c). Such a difference is consistent with the results for other frozen gases.

An interesting feature of electronic sputtering of sulfur is the formation of a sputter-resistant residual layer. The material, which is primarily produced at low excitation densities, is probably polymerized sulfur. Because of its size, S_8 is not ejected efficiently by light ions so that the threshold seen in fig. 23 is associated with the competition between the formation and ejection of S_2, and the polymerization of sulfur which increases the effective U.

9.2 Refractory Materials

Electronic sputtering of refractory inorganic insulators occurs for high energy medium and heavy mass ions. Because the yields are small, sensitive methods are required so that these materials have not been studied as comprehensively as, for example, the alkali halides. The observation by Biersack & Santner (1976) that the sputtering yield of potassium chloride follows the electronic stopping power rather than the nuclear one stimulated the investigations of oxides, nitrides and other refractory materials (Betz & Wehner, 1983). Ion production by high-energy ions is summarized by Wien (1989, 1992) and Håkansson (1993). The luminescence spectra and defect formation are comparatively complex for these materials. It is known that luminescence and defect formation in silicon dioxide are correlated (Itoh et al., 1990), but the implications for sputtering of this material and other refractory materials are not clear.

Uranium tetrafluoride has been comprehensively studied. The yield was obtained for fluorine and chlorine ions from 1 to 30 MeV (Griffith et al., 1980; Meins et al., 1983) (fig. 24). The sputtered uranium atoms were detected by neutron activation analysis. Since there was no indication of preferential sputtering, the yield is given in equivalent molecules/ion. The yield as a function of incident ion energy follows the electronic stopping power (Seiberling et al., 1982), estimated from Ziegler's (1980) tables using Bragg's rule (Sigmund, 1975a). The yield decreased with stopping power above the peak much faster than linearly. At the stopping power peak $Y = 7$ molecules/ion for incident fluorine, an impressive value since that for knock-on sputtering is more than one order of magnitude lower (fig. 24).

Griffith et al. (1980) also investigated the effect of the primary ion type and charge state. For oxygen, fluorine, and neon ions, of the same charge state and energy per mass, shown in fig. 24, they found that the yield increased by a factor of 3, although the nuclear charge of the incident ion increased by only 25 percent. An increase of the charge state from 2 to 3 also led to a 30 percent enhancement of the yield. For a charge-equilibrated chlorine beam, the sputtering yield exceeded 100 molecules/ion (Meins et al., 1983). In contrast to this, the yields for bombardment of uranium tetrafluoride with 1 to 4 MeV helium ions were barely measurable, suggesting there is a threshold excitation density.

The energy distribution of uranium atoms emitted from uranium tetrafluoride during bombardment by 4.74 MeV F^{+2} had a maximum at about 0.3 eV (Griffith et al., 1980). Above this maximum the energy distribution decreased rapidly, exhibiting an asymptotic behavior close to E_1^{-5} in contrast to that for knock-on sputtering described earlier. Seiberling et al. (1980) interpreted this to be a thermal distribution with an effective temperature around 4100 K. A similar distribution induced by 13 MeV Cl-ions led to an effective temperature of $\sim$ 5200 K. The authors argued that the trends may be described by a thermal spike model, eqs. (12)-(15), in which the lattice is heated by Coulomb repulsion, as discussed earlier. This group also obtained the only experimentally determined angular distribution for electronic sputtering. The data points for emitted uranium atoms from a film bombarded by 4.75 MeV $^{19}F^{+3}$-ions are well approximated by a cosine-function, consistent with the spike model.

The yield of uranium atoms from uranium dioxide under bombardment of 5 to 30 MeV chlorine ions with charge states from $q = 3$ to 6 was more than three orders of magnitude less than the corresponding one for uranium tetrafluoride (Meins et al., 1983).

Qui et al. (1982) measured the electronic sputtering yields from sapphire (Al_2O_3) and lithium niobate ($LiNbO_3$) with chlorine ions at energies between 3 and 25 MeV. The yield, determined by forward Rutherford scattering, varied from about 0.05 to 1.0 Al_2O_3/ion (fig. 19) and 0.06 to 0.12 $LiNbO_3$/ion. The data points lie on the low-energy side of the stopping power peak for both materials and vary nearly linearly with the electronic stopping power. Although they noted that lithium niobate is a much softer material than sapphire, and the latter has a higher thermal diffusivity than the former, these differences had no obvious influence on the yield.

Qui et al. (1983) also studied the sputtering of silicon and its compounds in the electronic stopping regime with chlorine ions at 5 and 20 MeV. Silicon showed a very low yield, probably without any electronic component. The yield from crystalline and fused silicon dioxide was measured for chlorine ions in the equilibrium charge state at 5 and 20 MeV (fig. 20). The average values for fused silicon dioxide were about ten percent larger than those for crystalline quartz, even though the authors consider this difference to be insignificant. They observed that a thickness of more than three monolayers of the oxide film is required for electronic sputtering. This effect has been confirmed by Sugden et al. (1992), who did not observe any electronic sputtering for a thin native oxide layer ~ 0.1 nm. According to the latter group the threshold thickness is about six monolayers. They also found that silicon dioxide is sputtered stoichiometrically, and the yield for perpendicular incidence, measured by a nuclear reaction technique, was almost twice as high as that measured by Qui et al. (1983), partly explained by a higher charge state. At 20 MeV the yield induced by equilibrium charge state chlorine, ($q = 11$) and angle of incidence of $\theta = 70°$, was about a factor of 2 larger than that for $q = 6$ (Sugden et al., 1992). They also found the yield varied with the angle of incidence as $(\cos\theta)^{-1.7}$. This is surprisingly similar to the result in eq. (16), also seen for frozen gases.

The processes that lead to electronic sputtering in these materials are not known, although trapping of excitons is accompanied by defect production (Gris-

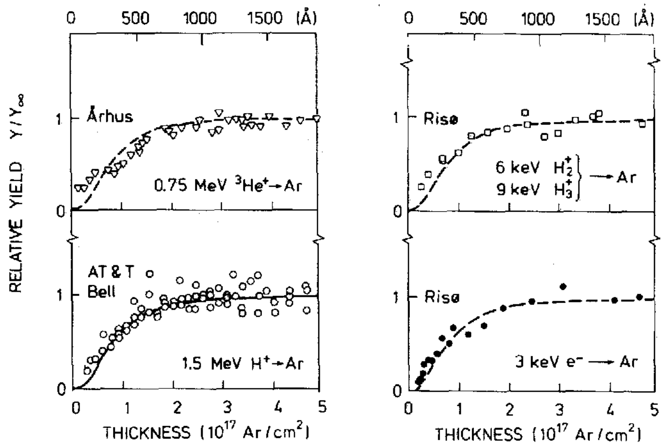

Figure 25. The thickness-dependence of electronic sputtering from solid argon for different projectiles. The relative yield is plotted versus thickness. All yields have been normalized to the thick-film yield $Y_\infty = 1$. Solid and dashed lines, eq. (25c) with $\ell_h = 210$ Å. Solid line from Reimann et al. (1984b) as reference. ^{3}He$^+$, from Besenbacher et al. (1981); 3 keV e$^-$, from Ellegaard et al. (1988); hydrogen ions from Schou et al. (1987). (From Schou, 1987).

com, 1989). Fiori and Devine (1984) observed that laser irradiation created defects and oxygen deficiency in thin, amorphous silicon dioxide layers. Helium ions were more efficient in depleting the surface of oxygen than heavy-rare gas ions (Thomas & Hoffmann, 1985), and low energy neon ions are more efficient than neon neutrals of the same energy (Mizutani, 1991). Even though the low-energy results involve electronic excitations, the relaxation processes can be very different from those initiated by fast ions.

One oxide frequently studied is titanium oxide. Unfortunately, measurements have been made mainly for the emitted ions (Knotek & Feibelman, 1978; Kurtz, 1986; Kurtz et al., 1986). This desorption process has also been correlated with defect structures.

A strong yield dependence on the stopping power was observed for europium oxide bombarded by heavy rare gas and uranium ions with an energy between 0.5 and 1 MeV/amu (Guthier, 1986). The yield was roughly proportional to the stopping power cubed, which is suggestive either of threshold behavior for a thermal spike (fig. 3) or a hydrodynamic model, eq. (18b) (Wien, 1992; Reimann, 1993). Although obtained with unsatisfactory vacuum conditions, these yields represent the highest primary energy studied.

9.3 Frozen Gases

The group of the frozen gases is the most comprehensively studied for electronic sputtering:

A) the samples are relatively easy to handle and the yields are large,

B) the yield dependence on film thickness may be easily measured

C) for the elemental gases, the energy release processes in the gas phase are largely known,

D) many of the irradiated gases show strong luminescent features from which the excited states in the solid may be identified.

The group of frozen gases is divided into the rare gas solids, solid elemental molecular gases, and solid heteronuclear molecular gases. Early experiments suggested condensed gases were efficiently sputtered by electronic processes (Erents & McCracken, 1973, 1975), but systematic studies began in 1978.

9.3.1 Solid Rare Gases: Argon

Sputtering yields for the rare gas solids all exhibit a pronounced thickness dependence. This is suggested as being caused by transport of the deposited electronic energy either as mobile excitons or holes. In addition, the luminescence from these solids during charged-particle or photon bombardment is well known (Schwentner et al., 1985; Zimmerer, 1987), and many of the emitted bands can be assigned to identified excited states. Among the rare gas solids, argon has become the standard system.

The dependence of the yield on argon film thickness is shown in fig. 25, resembling that in fig. 10b. The figure includes data from three laboratories and four types of projectiles. The thickness dependences are similar, giving a characteristic diffusion length, ℓ_h in eq. (25c), of about 200 Å (Schou, 1987). This suggests that mobile excitons or holes generated within this depth are quenched at the substrate (Reimann et al., 1984b). Because the excitations are mobile they can also reach the surface and contribute to sputtering as described, eqs. (24) and (25b). Similar data for 0.2 keV electrons (Hudel et al., 1991) show a faster increase to saturation, indicating that the range of the electrons is smaller than the diffusion length.

The value $\ell_h = 210$ Å obtained by Reimann et al. (1984b) is used as a common reference in fig. 25, although reevaluation gave $\ell_h = 230$ Å (Reimann et al., 1988). The simultaneous measurements of the luminescence and sputtering yield as a function of argon film thickness were decisive for understanding the sputtering process. The similarity of the extracted diffusion lengths and the description of the two emission phenomena by the same diffusion equations was a strong argument

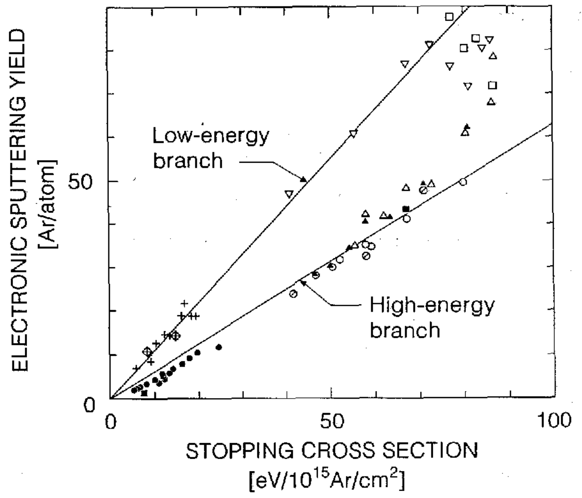

Figure 26. The electronic sputtering yield from solid Ar as a function of the electronic stopping cross section, $(dE/dx)_e/N$ for Ar. Data from Reimann et al. (1988); •, H^+ (QMS); ○, $^4He^+$ (QMS); ⊘, $^3He^+$ (QMS); filled squares, He^+, H^+ (RBS). Data from Besenbacher et al. (1981); filled triangles, $^3He^+$, $^4He^+$ (high velocity) (RBS); ▽, $^4He^+$ (low velocity) (RBS); □, He^{2+} (RBS). Data from Schou et al. (1988); +, H^+ , crossed diamond, He^+. The solid lines represent the high-energy and low-energy branches. Stopping cross section are from Andersen and Ziegler (1977) and Ziegler (1977).

that the same mobile excitations are responsible for photon emission and sputtering (Reimann et al., 1984b). Further, since impurities both trap and quench excitations (eq. (22a)) ℓ_h varied with oxygen impurity concentration (Reimann et al., 1988).

The agreement between diffusion lengths obtained by traditional optical methods (Schwentner et al., 1985; Zimmerer, 1987) and those obtained by particle bombardment is not good. The results produced with light MeV ion bombardment involve a constant energy deposition along the path of the ion through the thin film. Since this geometry requires few assumptions to interpret the data, these diffusion lengths appear to be firmly established. The data for low-energy ion or keV electron impact are more difficult to disentangle, since the profile of the deposited energy changes, because of either a varying stopping power for the ions or backscattering of the primary electrons.

Films which have been utilized to obtain fig. 25 are produced either using a jet of gas onto a cold target or emitting gas through the channels of a microchannel plate to obtain a more uniform solid. These are polycrystalline films with a considerable defect density (Zimmerer, 1987). In a few cases improved crystal quality has led

Table III

Diffusion Length in Solid Rare Gases at Charged-Particle Bombardment

Material	Ref.	Primary Particle	Length (Å)	Film growth temp. (K)
Ne	Schou et al. 86	2 keV e^-	230 1)	6
	Hourmatallah et al. 88	24 eV e^-	252 1)	8
Ar	Schou et al. 87	9 keV H_3^+ 6 keV H_2^+	190	7
	Ellegaard et al. 88	2 keV e^-	200-300	7
	Besenbacher et al. 81	0.75 MeV $^3He^+$	270 2)	8
	Hourmatallah et al. 88	24 eV e^-	310	10
	Reimann et al. 84	1.5 MeV H^+ 1.5 MeV He^+	190 3)	12
	Reimann et al. 88	1.5 MeV H^+ 1.5 MeV He^+	230 3)	12
	Hourmatallah et al. 88	24 eV e^-	383	17
	Hourmatallah et al. 88	24 eV e^-	436	22
	Hourmatallah et al. 88	24 eV e^-	845	25
Kr	Schou et al. 87	9 keV H_3^+ 6 keV H_2^+	300	7
Xe	Ollerhead et al. 80	1 MeV He^+	500 4)	25

Concerning the accuracy consult the references. 1) Absorbing-like boundary conditions for the surface. 2) Evaluated by Reimann et al. (1984b). 3) Same experimental points. Improved evaluation in Reimann et al. (1988). 4) The length evaluated by Schou (1987).

to an enhanced diffusion length (Table III) (Hourmatallah et al., 1988); therefore, the measured diffusion length can depend on the fluence of the primary particle (Varding et al., 1993).

Three studies with photon irradiation have demonstrated that particle ejection takes place via exciton production. Feulner et al. (1987) and Kloiber & Zimmerer (1989, 1990) showed that selective photon excitation of the surface or bulk states induces sputtering. A strong enhancement of the yield for excitation energies above the energy gap was observed by Kloiber & Zimmerer (1989). The dominant mobile carrier of the excitation has not yet been identified, although it is thought to be an atomic hole or a free, highly excited exciton, as suggested by Reimann et al. (1984b) for MeV ion excitation of argon. The carrier can, of course, depend on the excitation process: e.g., ions produce excitons and holes with large wave numbers.

Yields for ion bombardment of thick solid argon films are shown in fig. 26. These have been obtained at three laboratories using several methods. For the two low-energy He-ions points the yields have been corrected for knock-on sputtering (Schou et al., 1988); otherwise, it is ignored. These yields lie on a common curve having two 'branches', and the data from different laboratories smoothly merge together. The branches roughly correspond to values on each side of the electronic stopping power peak (viz. fig. 1a). The yields on the low-energy side are ~1.7 times those on the high energy side at the same stopping power. Each branch may be approximated as a linear function of the electronic stopping cross section up to ~ 70 eV/10^{15} Ar/cm^2. Using eq. (20c) and (21c) gives, $\overline{\Delta x_e} \approx 17$ and $29\ \ell$ respectively, or using $(dE/dx)_e$, $\Lambda_e \approx 2.4$ and 4.1 Å/eV respectively.

Differences in yield for the same value of the equilibrium stopping power, $(dE/dx)_e$, can occur for four reasons (Johnson & Brown, 1982):

(1) non-equilibrated charge states;

(2) a difference in the character of the excitations at different velocities (fig. 1a); and

(3) differences in the radial distribution of the deposited energy (fig. 6a), leading to increased excitation density at low velocity,

(4) difference in surface excitation density due to secondary excitation transport.

In the sputtering of refractory materials (Griffith et al., 1980) and solid oxygen (Gibbs et al., 1988), increasing ion charge state leads to an enhanced yield. The charge state and radial distribution are not expected to be as important for the solid rare gases as they are for other solids, since charge equilibration distances and mean radial distributions of secondaries are typically smaller than the diffusion length (Reimann et al., 1988). Therefore, the enhancement observed at low ion velocities is likely to be due to the changing character of the excitation spectrum, suggested

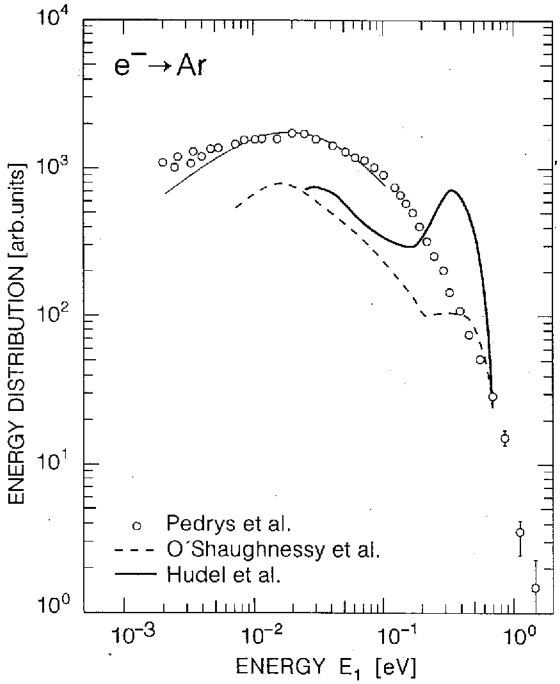

Figure 27. Energy spectra of Ar-atoms from electron-irradiated solid Ar. The three data sets have been place arbitarily relative to each other. The solid line through the points from Pedrys et al. (1988) is a fit with eq. (8a) for $U = 60$ meV. Pedrys et al. (1988), 0.5 keV e^-, $\theta = 45°$, $\theta_1 = 0°$. O'Shaughnessy et al. (1988), 2.5 keV e^-, $\theta = 45°$, $\theta_1 = 0°$. Hudel et al. (1991), 0.2 keV e^-, $\theta = 0°$, $\theta_1 = 0°$.

by figs. 1a and 7. However, Besenbacher et al. (1981) found, in the transition region, that the sputtering yield of argon is about 20 per cent larger for doubly charged helium ions than for singly charged ions, a change not unlike that for solid oxygen.

The dimerization process described earlier produces kinetic energy that ultimately leads to particle ejection. The mobile holes become trapped at the surface or in the bulk, forming Ar_2^+. The repulsive decay scheme then follows that described by Johnson & Inokuti (1983) (see fig. 8), although the recent observations of a resonant state which can lead to energy release is intriguing (Michaud et al., 1993). Since the mobile electrons are not trapped efficiently in argon (Sowada et al., 1982), the trapped holes will eventually capture an electron. The resulting repulsive dissociative recombination may liberate up to ~ 1 eV to the two atoms (eq. (21c)). If this occurs in the surface layer, a ground state or excited atom is ejected. If in the bulk, the electronically excited atom then can form a molecular exciton which decays radiatively to the repulsive ground-state, releasing ~ 1.1 eV. Since these energies are much larger than the cohesive energy of solid argon, a low energy collision cascade is generated [viz. eq. (27) and fig. 11] leading to ejection of ground state atoms. This relaxation sequence has been extensively discussed (Reimann et al. 1984b, 1988; Brown & Johnson, 1986; Schou, 1987, 1991). Quite remarkably, the luminescence and sputtering yields for fast penetrating ions are only slightly modified when an outside field is applied producing a large secondary electron yield (Grosjean & Baragiola, 1993).

The energy distributions of the ejected particles, combined with molecular dynamics calculations using the gas-phase ground-state pair potentials, have led to a definitive identification that the ground-state repulsion leads to ejection. The energy distributions shown in fig. 27 have either a peak around 0.5 eV (Hudel et al., 1991) or a shoulder (O'Shaughnessy et al., 1988b, Pedrys et al. 1988). Since the peak size depends on film purity, film structure, and, possibly, angle of detection, the conditions in each experiment are not completely comparable. The peak is due to the excimer emission, $\mathrm{Ar}_2^*\ (^{1,3}\Sigma_u^+) \rightarrow \mathrm{Ar}_2\ (^1\Sigma_\mathrm{g}^+) + \hbar\omega$, with the peak width determined by the ground vibrational state of Ar_2^* decaying to the repulsive part of the ground-state potential, as indicated in fig. 8 (O'Shaughnessy et al., 1988b). Therefore, the area under the peak was used to estimate the surface vs. the bulk trapping probability using eq. (23): i.e. $(\tau_\mathrm{h}/\tau_\mathrm{h}^\mathrm{s}) \approx 4.7$ in the films studied (Boring et al., 1989). All three curves have a distinct low-energy peak due to low-energy, cascades following a repulsive decay below the surface [eq. (27) and fig. 11], again confirmed by molecular dynamics calculations (O'Shaughnessy et al., 1988b). A comparison to the linear collision cascade energy spectrum is made for one data set using an effective surface binding, $U = 60$ meV in eq. (8a).

Excited ejected atoms are clearly observed in the luminescence spectra as these exhibit narrow atomic lines. For photon and electron excitation at low kinetic energy, metastable neutrals $\mathrm{Ar}^*\ ^3P_0$ and $^3P_2$ were detected by Arakawa et al. (1989), Arakawa & Sakurai (1990), Kloiber & Zimmerer (1990), and Leclerc et al. (1990, 1992). The maximum value kinetic energy, ~ 40 meV, originates from the repulsive interaction associated with cavity formation occurring around the atomic exciton (figs. 8 and 9b). This ejection process occurs in addition to dimer decay, as suggested by Coletti et al. (1984) and as corroborated by molecular dynamics calculations (Cui et al., 1989a, Reimann et al. 1990, 1991). The measurements of the energy distribution of metastable neutrals ejected by 200 eV electrons showed the low-energy peak around 40 meV and a high-energy feature (Arakawa et al., 1989). The studies with 14.5 eV electrons have resolved the low-energy peak into three components (Leclerc et al., 1992) which are characterized by the numbers of nearest neighbors in accordance with the studies of molecular dynamics (Cui et al., 1989a). The high-energy peak had a maximum around 0.35 eV and a full-width of half maximum of 0.19 eV (Leclerc et al., 1992). This peak, partly embedded in the ground state peak in fig. 27, suggests that about 0.7 eV, on the average, is liberated by the upper state transition in fig. 8, Eq. (21c), a dissociative recombination predicted by Johnson & Inokuti (1983). Therefore, a dominant solid-state, electron-hole recombination pathway has been identified from particle ejection studies.

The well known W-band in the luminescence spectrum was shown to be a surface feature as adsorbed atoms could quench it but not the M-band (Roick et al., 1984). It was later shown to be due to luminescence from ejected electronically-excited dimers in high vibrational states (Reimann et al., 1988, 1990, 1991). The kinetic energy of these excited dimers is low, about 60 meV, suggesting they originate from cavity ejection (Cui et al., 1989b). However, a distribution of vibrational states is seen, including the ejection of Ar_2^* in low vibrational states but with higher kinetic energy, $\sim$ 100 meV. Because of the inefficiency of transfer of vibrational energy into lattice motion, the origin of more energetic dimers in low vibrational states is not clear. Three-body interactions involving an energetic, excited argon atom from a dissociative recombination, or recombination involving Ar_3^+, might be precursors of energetic-relaxed excimers Ar_2^* (Reimann et al., 1991, 1992).

For photon and electron excitation, thresholds are exhibited for ion emission (Dujardin et al., 1990; Baba et al., 1991; Schwabenthan et al., 1991; Menzel, 1990). Again, gas phase cross sections are instructive. For example, simultaneous excitation of two 3p-excitons in adjacent atoms was used to explain a threshold around 24 eV in the emission of Ar^+ and Ar_2^+ induced by low-energy electrons (Baba et al., 1991).

9.3.2 Solid Rare Gases: Neon, Krypton and Xenon

Solid neon is much more volatile than argon, whereas the heavy rare gas solids are correspondingly less volatile. The sublimation energy varies from 20 meV for neon up to 164 meV for xenon (Table I). The atomic excitons are important primarily for solid neon and argon, and formation and vibrational relaxation of the molecular excitons occurs more efficiently with increasing atomic number (Zimmerer, 1979, 1987). The luminescence in neon originates from atomic rather than molecular excitons, and the molecular excitons have not yet been observed in the vibrational ground state. Although the energy release following emission from the molecular exciton in the vibrational ground state decreases with increasing atomic number, the exciton in neon decays from a vibrationally excited state. Therefore, the average energy release is $\sim$ 200 meV, compared with $\sim$ 1.1 eV for solid argon.

The electron-induced sputtering yield from solid neon is almost an order of magnitude larger than that from argon consistent with the small sublimation energy

(Table I) (Schou et al., 1986). It appears that the net conversion of electronic energy into atomic motion from all channels is about as efficient for solid neon as for argon based on low energy keV hydrogen ion bombardment of neon. The diffusion length of excitons in solid neon irradiated by electrons from 0.8 to 3 keV was determined to be ~ 230 Å (Schou et al., 1986)[5] consistent with ~ 250 Å using 24 eV-electrons (Hourmatallah et al., 1988, see Table III).

Neon atoms are also ejected due to VUV-photon irradiation. Mass spectroscopy studies (Kloiber & Zimmerer, 1989) and luminescence studies (Coletti & Debever, 1983) were used to show that neutral desorption occurs for incident electrons with energies below the band gap. The results from Kloiber et al. (1988) and Kloiber & Zimmerer (1989) demonstrate that the excitation of the $n' = 1$ excitons leads to a yield that is almost as large as that from photons just above the energy gap. These experiments did not provide any clear evidence on the type of the mobile excitation, an atomic hole or a highly excited free exciton. Ellegaard et al. (1986a) noted the absence of a thickness dependence during bombardment by keV hydrogen ions. Comparing the ionization cross sections (Rudd et al., 1985) to stopping cross sections, they conclude these ions largely produce excitations below the ionization threshold of neon, implying the mobile excitation is an atomic hole.

Although the yield of excited neutrals is about one-tenth of the total yield (Kloiber et al., 1988), a rich structure is exhibited. For instance, exciton trapping below the surface can lead to ejection of the excited species as well as ejection of ground state atoms (Coletti et al., 1985; Hourmatallah et al., 1988; Laasch et al., 1990). This occurs because the sublimation energy is low but lattice distortion energy is large and differs for trapping at the surface or in the bulk, as indicated by the shifts in the luminescence spectra. The distribution of kinetic energy of the emitted $^3P_2$ and $^3P_0$ atoms was measured by Kloiber & Zimmerer (1990) and Weibel et al. (1993). The most probable value of the energy of these atoms ranged from 0.16 eV up to 0.25 eV depending on the excitation energy (Fugol' et al., 1988; Belov et al., 1989; Kloiber & Zimmerer, 1990). According to Fugol' et al. (1988) the trapping of a $3p$-exciton leads to an energy release of 0.8 eV which is responsible for the ejection of the $3p$- atoms. A diffusion length before trapping of the order of a few hundred Å is again extracted from these luminescence data.

Charged-particle bombardment of solid krypton has been studied systematically for keV hydrogen ions (Schou et al., 1987). The diffusion length is ~ 300 Å, slightly larger than that for argon, consistent with theory (Fugol', 1988). The yield is smaller than that for argon, in agreement with the larger sublimation energy of solid krypton, eqs. (20c) and (27).

The energy release following M-band emission is about 0.8 eV and the fraction

---

[5] The data points from Børgesen et al. (1982) were not corrected for energy-dependent beam broadening.

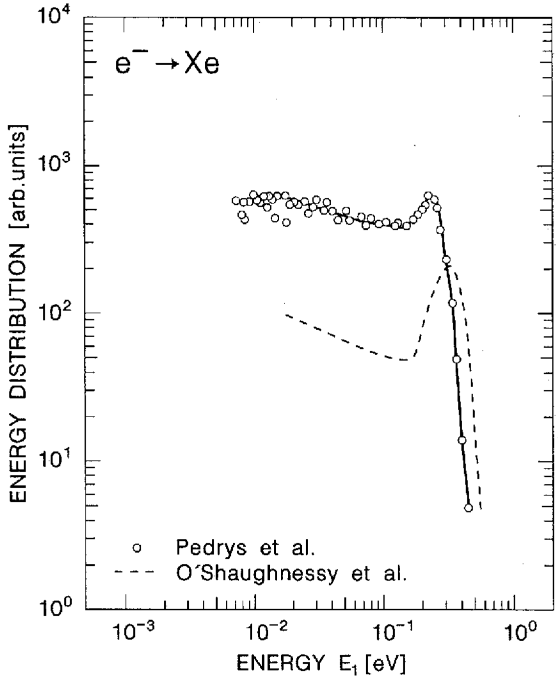

Figure 28. Energy spectra of Xe-atoms, see fig. 27. The line through the data points of Pedrys et al. (1988) has been drawn merely to guide the eye.

of the ejecta associated with surface trapped species was shown to be larger than that for solid argon (Boring et al., 1989) with $(\tau_\mathrm{h}/\tau_\mathrm{h}^\mathrm{s})$ in eq. (23) about 6.5 for the films studied. Arakawa et al. (1989) observed excited neutrals with energy up to more than 0.7 eV, presumably from dissociative recombination, and Mann et al. (1992) observed metastable neutrals under bombardment with eV electrons. Low energy metastable krypton atoms resulting from trapping at the surface were not seen (Arakawa et al., 1989), consistent with molecular dynamics calculations (Buller & Johnson, 1991), since the cavity-forming, repulsive interaction is not as strong as in argon (Kloiber and Zimmerer, 1989). The total yield of the metastable atoms increased with thickness up to about 100 atomic layers consistent with the diffusion length determined from the total yield due to hydrogen ion bombardment. Because the metastable neutrals originate via recombination (fig. 8), the atomic hole is the dominant mobile excitation.

For solid krypton irradiated by photons, there is a substantial sputtering for photon energies that coincide with the lowest excitonic levels, but ejection also

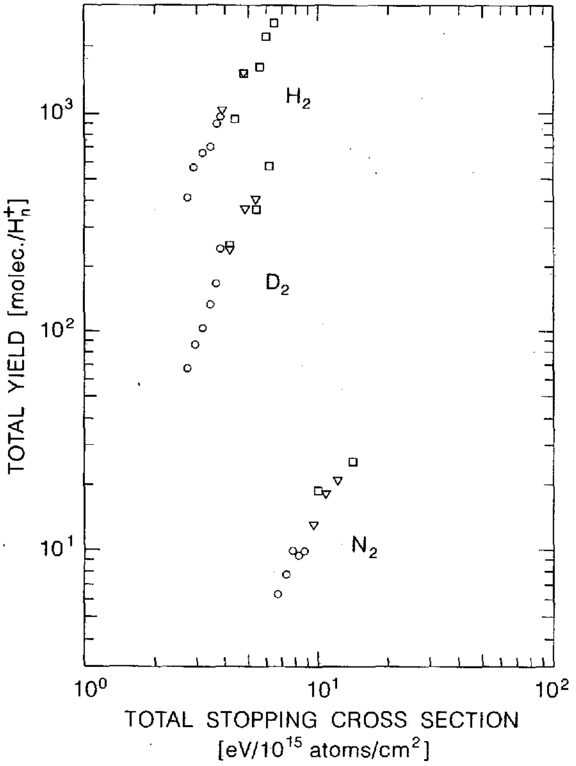

Figure 29. The yield as a function of the sum of the stopping cross sections of the atoms in the hydrogen ions. ○, H+; ▽, H_2^+; □, H_3^+. Nitrogen data from Ellegaard et al. (1993a), deuterium data from Stenum et al. (1990), hydrogen data from Stenum et al. (1991) and Schou (unpublished).

occurs for photon energies above the band gap (Feulner et al., 1987; Kloiber & Zimmerer, 1989, 1990). In particular, the yield increases strongly for photon energies above the threshold for electron-electron scattering.

Electronic sputtering yields for solid xenon by light ions, 0.2 MeV - 2 MeV, were originally interpreted as thermal spike sputtering (Ollerhead et al., 1980). However, the few data are consistent with a yield versus stopping power, $(dE/dx)_e$, with two branches which depend linearly on the stopping power (Schou, 1987). The ratio of the yield divided by the electronic stopping cross section, Y/S_e, is about a factor of five lower for xenon than argon, because of the higher sublimation energy and the smaller energy release after M-band emission. This energy is clearly indicated by the peak at ~ 0.3 eV in the energy distribution of emitted xenon atoms from electron-bombarded xenon (fig. 28). Since this energy is comparable to the

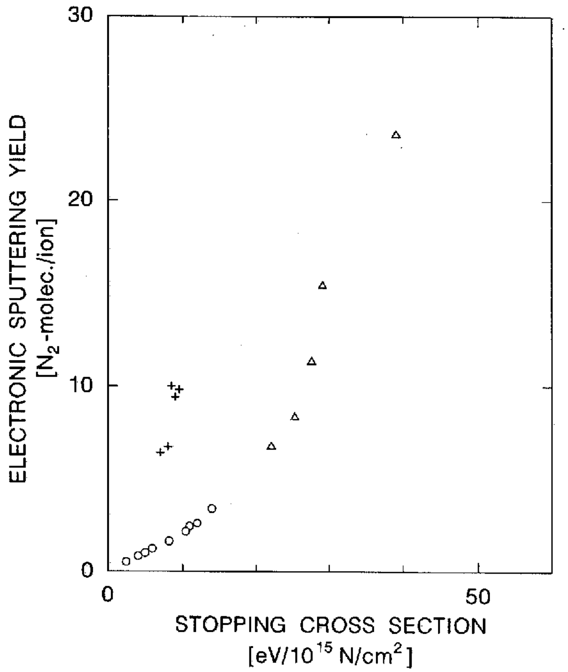

Figure 30. The electronic sputtering yield from solid N_2 as a function of the electronic stopping cross section, $(dE/dx)_e/N$, for N_2. Data from Johnson et al. (1991), ○, H^+; Δ, He^+. Data from Ellegaard et al. (1993a), +, H^+.

sublimation energy, no clear low-energy peak due to decay below surface is seen in the xenon spectra for incident keV electrons (O'Shaughnessy et al., 1988b; Pedrys et al., 1989). Here enhanced surface trapping of excitons dominates sputtering, with (τ_h/τ_h^s) in eq. (23) about 3.9 for the films studied (Boring et al., 1989), but no metastables have been observed (Mann et al., 1992).

The yield due to 1 MeV He^+-ions was measured as a function of xenon film thickness (Ollerhead et al., 1980). This gives a rough estimate of the diffusion length of ℓ_h = 580 Å (Schou, 1987), consistent with the expected trend with the atomic number. The existing measurements do not indicate the predominant mobile excitation. Photon-induced ejection from solid xenon occured for excitation energies at the excitonic levels as well as for energies above the band gap (Kloiber & Zimmerer, 1989, 1990). However, the relative yield decreases with increasing photon energy up to the largest energies studied, around 17 eV.

9.3.3 Solid Elemental Molecular Gases

In addition to frozen S_8, sputtering has been investigated for solid nitrogen, oxygen and hydrogen and its isotopes. The yields for the latter are shown in fig. 29. Like the rare gas solids these van der Waals solids have low cohesive energies, but the sputtering yield does not appear to be controlled by significant exciton mobility. No photon-induced neutral particle emission has been studied, in contrast to the many contributions on photon-stimulated ion emission (e.g., Rocker et al., 1990; Hellner et al., 1990).

Deexcitation processes in solid nitrogen are fairly well known and the optical emission from electronically excited states has been studied (Oehler et al., 1977; Coletti & Bonnot, 1977; Poltoratskii & Fugol', 1979; Zumofen et al., 1984; M. Kühle et al., 1985; Pan et al., 1987). The dominant emission process seen in the luminescence spectrum, $[\mathrm{N}(^2\mathrm{D}) \rightarrow \mathrm{N}(^4\mathrm{S})]$, gives the green line and clearly indicates that dissociation can drive sputtering (Rook et al., 1985), leaving stable radicals in solid nitrogen. The sputtering yield for light ions is shown in fig. 30 versus the stopping cross section exhibiting two branches. The increase in the yield for the low-energy ions over that for the MeV-ions with equal stopping powers is more pronounced than for light ion bombardment of solid argon, probably due to the lack of significant excitation transport. In contrast to argon, these results exhibit both a clear linear and quadratic dependence on the stopping cross section. The electron-induced yield points, not shown in the figure, comprise a curve that lies slightly above the linear part of the lower branch below $S_e = 10\ \mathrm{eV}/(10^{15}\ \mathrm{atoms/cm^2})$ in fig. 30. Using MeV H^+ and He^+, Brown et al. (1986) mapped the transition from the linear dependence, first observed using keV electrons (Ellegaard et al., 1986b), to the quadratic dependence, first observed using MeV He^+ ions (Rook et al., 1985).

Sputtering is produced by energy deposited in the first four to five monolayers (Banerjee et al., 1991b) for solids without significant excitation transport. Therefore, electronic sputtering by an incident molecular ion is determined by the total stopping power of the constituent atoms in a bombarding molecule (fig. 29). This gives a yield in the quadratic regime for incident H_2^+ which is four times the yield due to an H^+ at the same velocity, in contrast to the results for solid argon (Brown et al., 1982).

Since the excited state mobility is only a few monolayers (Johnson et al., 1991), the changing dependence of the yield seen in fig. 30 can be a result of the increasing excitation density, λ_e^{-1}, going from isolated relaxation processes to closely spaced processes (fig. 3 and eqs. (20c) and (14)). The yields in the transition region can be explained by assuming the electronic relaxation processes do not change with excitation density, but the energy release from individual events acts additively:

overlapping spikes (Johnson et al., 1991). Using the yields in the linear regime and molecular dynamics estimates of $\Delta\overline{x}$ in eq. (27) then $f_\mathrm{e} \approx 0.1$, corresponding to energy release $\Delta E \approx$ 2eV - 3eV.

The energy distributions of particles emitted from solid nitrogen have been measured for keV electrons (Pedrys et al., 1988, 1993a; Hudel et al., 1992) for hydrogen ions (Ellegaard et al., 1993a) and for helium ions (Ellegaard et al., 1993b). The dominant particle in the emission flux is the parent molecule, N_2, but atoms and polyatomic molecules with up to four atoms have also been observed. The fraction of monatomic neutrals is considerable, but the polyatomic molecules comprise less than one percent of the diatomic ejecta. The spectrum of the diatomic molecules has no pronounced features, but exhibits a maximum around 20 meV, decreasing steeply at higher energies.

The most obvious recombination process for an intrinsically molecular species is that which is dominant in the gas phase, $N_2^+ + e \rightarrow N + N^*$, (Fox & Dalgarno, 1983). This is clear from the green luminescent feature associated with the $N(^2D)$ radical in solid nitrogen (Rook et al., 1985). For outer shell ionization, such processes deposit a few eV (Oehler et al., 1977), consistent with the energy release extracted from the yield data in the linear regime. However, since there was no distinct high-energy tail of N-atoms in the energy distribution of electron-irradiated solid nitrogen, Pedrys et al. (1993a) suggested that the dimerization process identified in solid argon might also occur efficiently in solid nitrogen,

$$\mathrm{N}_2^+ + \mathrm{N}_2 + \mathrm{e} \rightarrow (\mathrm{N}_2)_2^+ + \mathrm{e} \rightarrow \mathrm{N}_2^* + \mathrm{N}_2, \quad \Delta E \approx 1 - 3.7\,\mathrm{eV}.$$

In fact, the interaction between an excited and ground state molecule leading to dimerization has been identified in the luminescence spectrum of a number of materials.

The electronic sputtering yield of solid oxygen has a dependence on $(dE/dx)_\mathrm{e}$ which is similar to that of nitrogen, fig. 30. However, there are some differences between these materials which effect the size of the sputtering yield (Rook et al., 1985; Ellegaard et al., 1986; Brown et al., 1986; Schou, 1991). Solid oxygen is known not to luminesce as efficiently and is more active chemically following irradiation. Therefore, the conversion of excitation energy into motion is more efficient than in nitrogen, since other parameters such as the sublimation energy, the number density and the W-value are similar (see Table I). The yield data indicate that $f_\mathrm{e} \approx 0.2$ and $\Delta E \approx 4 - 6$ eV (Johnson et al., 1991), of the order of twice that for N_2.

The electron-induced kinetic energy distributions of emitted O_2 (Hudel et al., 1992; Pedrys et al., 1993b) also resembles that for nitrogen, except that the distribution falls off more steeply above 1 eV and the maximum is slightly higher. The energy distribution of oxygen molecules from bombardment by keV hydrogen ions is similar to that obtained from electron bombardment (Ellegaard et al., 1993a). Ozone formation can play an important role by quenching the excited radicals created by dissociative excitation or recombination (David & Michl, 1989). Since there is no activation threshold, the reaction does not depend on background temperature. By this process 1.1-6 eV may be eventually liberated, depending on whether the oxygen atom is in the ground or an excited state (Pedrys et al., 1993a). However, the contribution of this energy to the yield is unknown, as is the contribution from processes such as attachment (Sanche, 1984).

The influence of the initial charge state has been investigated. The yield induced by charge-equilibrated 2 MeV He ions with the charge state $q = 1.75$ is a factor of 1.2 larger than that of singly charged ions (Gibbs et al., 1988). This result is, surprisingly, similar to that for argon. These authors also found that the yield $Y(\theta)$ as a function of angle of incidence behaves similarly for the singly charged and the charge-equilibrated ions, and closely fits the thermal spike expression in eq. (16) (fig. 4). These measurements demonstrate that hole production by charge-exchange at the surface is not a dominant channel for electronic sputtering of oxygen.

Electronic sputtering of solid hydrogenic targets deviates in several respects from that of the less volatile solid nitrogen and oxygen. The sublimation energy is extremely low, ranging from 8.7 meV/molecule for hydrogen up to 14.8 meV/molecule for solid tritium. The yield for very thin films of hydrogen or its isotopes is found to be strongly enhanced on all substrates. Even though this effect has been observed during electron as well as ion bombardment (Erents & McCracken, 1973; Børgesen & Sørensen, 1982; Stenum et al., 1990), the origin of the enhancement is not known. A similar enhancement is seen in most condensed gas films at the few monolayer level (Rook et al., 1985; Hudel et al., 1991).

Very few studies of luminescence from solid hydrogen isotopes exist. A relatively strong continuum with a maximum around 800 nm, probably generated by association of neutral atoms, was observed by Forrest et al. (1992). In contrast, very weak features were observed in the visible or ultraviolet region (Schou, 1991; Stenum et al., 1993) suggesting non-radiative relaxations dominate. This combined with the low sublimation energy leads to high sputtering yields. Using 10 keV protons, the yield ranges from about 200 molecules for deuterium and up to about 800 molecules for solid hydrogen per proton (Stenum et al., 1991).

For incident molecular and atomic hydrogen ions the dependence of the yield on the sum of the stopping powers is roughly quadratic for the most volatile molecules, hydrogen and hydrogen deuteride, and cubic for the least volatile molecule, deuterium (Stenum et al., 1991). This nonlinearity shows up also in the dependence on the cohesive energy, U. Sputtering of solid hydrogen is electronic at these velocities since incident deuterium and hydrogen ions of equal velocity produce equivalent sputtering yields and the nuclear stopping power has a different dependence on the ion energy than does the yield.

Sputtering of solid deuterium by keV electrons deviates strongly from that produced by ions in that the yield decreases, passes through a minimum and then increases with increasing thickness (Erents & McCracken, 1973; Børgesen & Sørensen, 1982; Schou et al., 1984; Ellegaard, 1986). The minimum is typically located at thicknesses that exceed the electron range. The enhancement for thick films was suggested to be due to charging (Schou, 1991). For the solid hydrogen isotopes, the relaxation events determining sputtering are uncertain, although transitions from the repulsive triplet ($b^3\Sigma_u^+$) state to the ground state are a possibility, liberating up to 7 eV (Celiberto et al., 1989).

9.3.4 Solid Heteronuclear Molecular Gases: Water Ice

Electronic sputtering of water ice has been extensively studied because of its importance in the outer solar system and the interstellar medium (Johnson, 1990; Greenberg & Pirronello, 1991). This link to astrophysical and planetary problems was the reason that water ice was the first material for which electronic sputtering was studied systematically (Brown et al., 1978, 1980a, 1980b). These early experiments showed that electronic sputtering was a general process, occurring for materials other than alkali halides. The yield data from water ice during hydrogen ion and medium light ion bombardment versus energy, E, are shown in fig. 1b. The knock-on contribution dominates at low energies, whereas for energies above about 1 keV/amu the dependence clearly resembles that of the electronic stopping power. The measured yields induced by hydrogen and helium ions are large in view of the large sublimation energy, $U = 0.53$ eV. Whereas the yield is about 20 H_2O/He^+ for ion energies close to the stopping power peak, the yield from solid nitrogen for the same dE/dx is only a factor 2 larger although the sublimation energy is almost an order of magnitude smaller.

The yields for hydrogen and helium ion bombardment also exhibit higher yields for the same stopping power below the stopping power peak than those above the peak (Brown et al., 1980b). This effect was in part attributed to the use of the equilibrium charge state stopping power, as discussed earlier, rather than the actual stopping power for the non-equilibrated ions (Johnson and Brown, 1982). The yield as a function of the stopping power at high velocities is well approximated by a quadratic function down to below 10^{-14}eVcm^2/H_2O. The yield induced by high-energy fluorine ions also correlated with the electronic stopping power, and reducing the incident charge state reduced the yield (Cooper & Tombrello, 1984).

The temperature dependence of the yield of emitted species, fig. 31, has been critical for understanding the sputtering of water ice. The RBS-measurements of the sputtering of water ice by 1.5 MeV He^+-ions from Brown et al. (1980a)

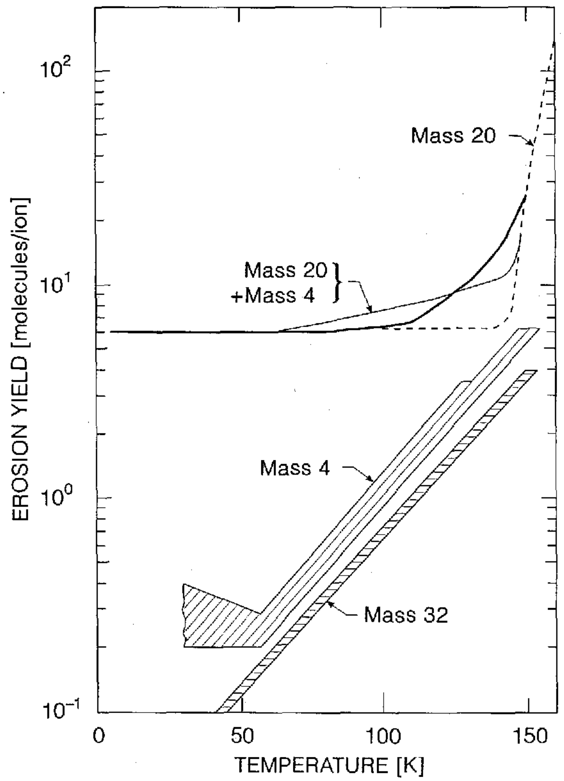

Figure 31. The temperature dependence of partial and total yields. Total and partial erosion yield from solid D_2O bombarded by 1.5 MeV He^+ ions. Details of normalization procedure described in the text or by Brown et al. (1984) Thick solid line, absolute yield of D_2O (RBS); thin solid line, sum of partial yields of D_2O and D_2 (QMS); dashed line, D_2O (QMS); hatched area for D_2 and O_2 includes the scattering of the data points (QMS).

showed that the total yield was independent of temperature at low temperatures and increases with increasing temperature above ~ 120 K. The existence of a temperature independent yield was confirmed by Cooper and Tombrello (1984) and Bar-nun et al. (1985). The onset of the temperature dependent contribution depends on the ion energy, implying that the temperature independent and temperature dependent contributions depend differently on the electronic stopping power, $(dE/dx)_e$ (Brown et al., 1980a). The surface composition, however, appears to remain roughly stoichiometric, a 2:1 ratio of hydrogen to oxygen atoms.

Heavy water, D_2O, was used to obtain a substantial improvement in the signal-to-background ratio of the measurements of the ejected species in fig. 31 (Brown et al., 1984). Primarily D_2O, D_2 and O_2 were seen. The mass spectra were normalized to the RBS yield at low temperatures, whereas the sum of deuterium and heavy water molecules has been adjusted to the RBS-yield at 150 K. The oxygen yield has been normalized to a value one-half of that for the deuterium molecules, so that the stoichiometry is preserved. The yield of oxygen and deuterium molecules varies with temperature even at temperatures below the liquid nitrogen temperature. Using IR spectroscopy Rocard et al. (1986) and Benit et al. (1987) observed the disappearance of water molecules due to heavy ion bombardment at liquid-nitrogen temperature. They suggested that at very high excitation densities erosion may be affected by hydrogen atom migration to the surface.

The ejecta reflect considerable chemical activity in the irradiated solid. Although D_2 can be formed by direct excitation, oxygen molecules are not present in the film, but have to be formed before the ejection (Reimann et al., 1984a). The ejected flux determined by Haring et al. (1984c) also contained a number of radicals up to mass 37 even for hydrogen and helium ion bombardment. For 1.5 MeV Ne^+-ions Benit and Brown (1990) demonstrated using hydrogen and oxygen isotopes that new molecules are formed that involve considerable diffusion before particle ejection.

Energy spectra for oxygen molecules sputtered from water ice by He^+-ions at 6 keV (Haring et al., 1984b) and 0.5 keV incident electrons (Pedrys et al. 1993b) exhibit a maximum at an ejection energy of $\sim$ 10 meV. However, there is no clear indication of an E_1^{-2}-tail above 0.1 eV. For emitted D_2O ice at 12 K energies observed from 0.1 eV up to 1 eV suggest the existence of an E_1^{-2}-tail for 1.5 MeV He^+-ion bombardment (Brown et al., 1984).

Experiments in radiation chemistry demonstrate that irradiation of water by light MeV ions or keV electrons primarily leads to the production of electron-hole pairs and excited water molecules. The excited molecules dissociate to H + OH or H_2 + O, and the charged species, e and H_2O^+, recombine and dissociate releasing $\sim$ 1-2 eV (Spinks & Woods, 1990; Turner et al., 1983, 1988; Dixon, 1970). Certain electronic relaxation processes have been identified from luminescence measurements from water ice irradiated by MeV electrons (Quickenden et al., 1991; Vernon et al., 1991; Trotman et al., 1986). A feature at 385 nm is associated with dissociative excitation of water. This leads to OH and H with up to 2 eV, with H receiving (17/18) of the energy. Because the products are radicals their binding to the solid is increased over that of H_2O. Therefore, the yield of OH is small, but H atoms are ejected from the surface. By a three-body reaction, the association of H and OH to either H_2 or H_2O can gradually release approximately 5 eV.

Although the net energy released in a single excitation can be larger than the sublimation energy, 0.53 eV for water molecules in ice, most of the energy is transferred to the lightest species, H_2 or H, so that ejection of an H_2O in a single event is unlikely (Johnson, 1990). Therefore, the quadratic dependence seen for low temperature ice (< 77 K) at very low stopping powers, $(dE/dx)_e$, is sensible. Since the average bond energies of the hydrogen and oxygen molecules to the surface are small, such species can diffuse to the surface and are easily ejected. For this reason yields at higher temperatures should be linear after a threshold fluence (Brown et al., 1980a). For 1.5 MeV He^+-ion bombardment, two ion-electron pairs are produced per Å along the track, and the quadratic dependence of the yield on the stopping power persists, consistent with the other molecular condensed gases.

The total yield did not depend on film thickness for thicknesses between 0.8 and $90 \times 10^{17} H_2O/cm^2$ at 77 K (Brown et al., 1980b) and at 10 K (Cooper and Tombrello, 1984). The yield of deuterium as well as oxygen molecules increased with film thickness during 1.5 MeV neon-ion bombardment (Reimann et al., 1984a), suggestive either of diffusion along the track (Benit et al., 1987; Rochard et al., 1986) or that the thickness may affect the storage time of the radicals prior to reaction.

The temperature dependence of the yield of a newly formed species is determined by the mobility of the radicals and the energy barrier for the reaction. At the lowest temperatures (below 20 K), the hydrogen atoms are fairly immobile, but around 30 K the mobility increases (Hudson & Moore, 1992). The hydroxyl radical is immobile up to liquid-nitrogen temperature, but the radicals become increasingly mobile from 90 K up to the temperature 140 K, around which they disappear (Spinks & Woods, 1990). The electrons can be trapped at low temperatures and become mobile with increasing temperature. The trapping mechanism depends on the crystal and defect structure of the ice (Buxton et al., 1977).

The diffusion of radicals and the reactions are activated processes. The temperature dependent part of the yield of water molecules suggests an activation energy of 50 meV at low temperatures for 0.9 MeV proton bombardment and an activation energy of 300 meV at temperatures between 120 and 160 K, for 1.5 MeV He^+-ion bombardment (Brown et al., 1980a). The temperature dependence of the molecular-oxygen-yield transient leads to activation energies around 50 and 70 meV under 1.5 MeV neon ion bombardment (Reimann et al., 1984a).

The net erosion of water ice can be influenced by the morphology of the ice. Hudson & Moore (1992) recently found that a transition from amorphous to crystalline ice, induced by irradiation with 0.7 MeV protons, is accompanied by a sudden release of hydrogen and water molecules as well as hydroxyl radicals. Beam-induced amorphorization of crystalline water ice also occurs for light ion and electron bombardment (Strazzulla et al., 1992). Sample structure clearly influences electronic sputtering via the mobility of the radicals, but details are not understood yet.

9.3.5 Other Solid Heteronuclear Molecular Gases

Electronic excitation of the solid heteronuclear molecular gases results in sputtering in a manner similar to that for water ice. The solids are modified and decomposed during light-ion or electron bombardment. Chemical compounds that initially were not present in the solid may be generated (de Vries et al., 1984) and those with lower binding energy are easily released. Conversely, higher binding energy products remain, so that involatile residues also form. The details of the processes that lead to particle ejection are largely unknown, but repulsive relaxation (dissociative recombination) can provide energetic fragments and chemical activity both of which can heat the lattice and lead to sputtering. Generally, luminescence studies from these solids have not yet been particularly helpful because sputtering involves prompt processes ($< 10^{-11}$ sec) whereas luminescence is delayed ($> 10^{-9}$ sec).

Solid carbon monoxide is the only heteronuclear diatomic species that has been studied systematically. This solid is perhaps the simplest non-elemental insulator, since many of the molecular properties are similar to those of solid nitrogen and oxygen. The electronic sputtering yield for MeV ion incidence was measured by Brown et al. (1984) and later extended to keV ion bombardment by Chrisey et al. (1990). The yield is quadratic in the stopping power for MeV ion bombardment and significantly exceeds that for solid nitrogen and oxygen, even though the sublimation energy is comparable (Table I). Even at the lowest values of the stopping power there is no evidence of a linear regime (Chrisey et al., 1990). Adsorbed CO is known to efficiently lose O in a single excitation (Leung et al., 1977); therefore, single events can lead to sputter loss of neutrals or even negative ions (Sanche, 1984). However, the size of the yield suggests that these events are dominated by quadratic processes. Although, the yield for helium ions below the stopping power peak lies somewhat above those from energies above the stopping power peak, this is not the case for the low-energy hydrogen points which apparently are similar above and below the electronic stopping power maximum.

The sputtering yields due to 2 keV-electron bombardment (Schou et al., 1985) and relative yields for 1 to 3.5 keV electrons (Brown et al., 1984) were normalized to the MeV ion data and were found to follow the high-energy ion branch very closely (Chrisey et al., 1990). This agreement requires that the surface value of the deposited energy is $\sim 1.6(dE/dx)_e$, because of backscattered primaries (Ellegaard et al., 1986b). Even though this choice is standard for materials of atomic numbers from 6 up to 10 (Valkealahti et al., 1989), agreement between ion and electron data only occurs for carbon monoxide. For solid nitrogen the yields induced by electrons and high-energy ions disagree by a factor of 2 for the same value of the energy deposited at the surface.

Energy distributions for species sputtered from solid carbon monoxide during ion bombardment have been determined by Haring et al. (1984b) and Chrisey et al. (1990). The latter group compared the spectrum of emitted CO induced by argon ion bombardment with that induced by helium bombardment. Even though the first type of ion produces dominantly knock-on sputtering and the second type electronic sputtering, the spectra were similar. Both showed a pronounced E_1^{-2}-tail up to almost 1 eV, and a low-energy peak around 15 meV.

The processes that convert excitational energy into kinetic energy are less established than those for the elemental molecular gases. Dissociation of an excited or ionized carbon monoxide molecule and dissociative recombination of a molecular ion are seen in radiation chemistry. These processes typically release about 1 eV, sufficient to initiate displacement cascades since $U = 0.08$ eV (Chrisey et al., 1990). Reactions among fragments may be important as well since the yield is quadratic even at low stopping powers: e.g., C_2 and O_2 form as well as CO_2, C_2O, and O_3 (Haring et al., 1984b; Pedrys et al., 1985; Chrisey et al., 1990). The reactions lead to the production of a non-volatile residue (Haring et al., 1984c; Schou et al., 1985; Chrisey et al., 1990). For MeV He^+ RBS analysis indicates that the stoichiometric composition is approximately C_3O (probably polymerized) corresponding to $\sim$ 2-5 percent of the original film, (Chrisey et al., 1990).

Electronic sputtering of solid sulfur dioxide has been studied by Lanzerotti et al. (1982), Boring et al. (1984), and Moore (1984) because of its interest at Io. The yield for MeV protons and helium ions is roughly quadratic in stopping power. No thickness dependence was observed between thicknesses 3.9 to 4.9×10^{17} SO_2/cm^2, but mass 80 (either S_2O or SO_3) was observed to be fluence dependent (Boring et al., 1983). Large yields were found by Lepoire et al. (1983) for fluorine ion bombardment up to 8000 SO_2/F, for energies between 1.6 MeV and 25 MeV and charge states from 2 to 5. Their yield for 1.5 MeV He^+-ion at 30° is about three times larger than that obtained by Boring et al. (1984) at 0°. Based on eq.(16) a factor of $\sim$ 1.3 is expected ignoring charge-state equilibrium effects. The yield for the fluorine ion bombardment varies faster than the stopping power squared. A residue is observed which is enriched in oxygen, but had a low sputtering yield (Lepoire et al., 1983; Moore, 1984). However, details of the sputtering process are not understood.

Methane, though not inorganic has erosion properties related to the other condensed gases. It is a simple hydrocarbon and is found in condensed form in fractional concentrations on Pluto and Triton. Light-ion bombardment leads immediately to modification of the solid, so the yield depends on the fluence in addition to the usual parameters (Lanzerotti et al., 1987). At low fluence the yield is around 100 molecules for 900 keV-helium ion. The decomposition of the methane leads to emission of hydrogen, so that the sample progresses from an initially pure methane film towards a carbon-rich polymer (Lanzerotti et al., 1987). These authors observed that the bond breaking starts immediately under keV proton and helium ion bombardment of deuterated methane, but the yield of the deuterium molecules remains small until a fluence threshold has been reached. Above this threshold the yield of deuterium increases by an order of magnitude, until it decreases as the film is depleted in deuterium. At these temperatures (12-28 K) the diffusivity of deuterium is low, so the threshold is a percolation threshold for which a sufficient fraction of the methane is made porous. This is consistent with finding that the hydrogen (deuterium) emission was accompanied by an enhanced light scattering (Strazzulla et al., 1988) and the net loss is proportional to film thickness for these ions which penetrate to the substrate (Lanzerotti et al., 1987). The chemical modification of the methane by light ion bombardment has been studied by several groups. Large hydrocarbon ions are observed in the sputtered flux (Pedrys et al., 1986) as well as high mass neutrals (Foti et al., 1987). Benit et al. (1987) observed the formation of new carbon-hydrogen bonds with infrared absorption spectroscopy.

The energy distribution of methane molecules emitted during 6-8 keV hydrogen or helium ion bombardment falls off steeply above 0.1 eV for large fluences. Pedrys et al. (1986) approximated the spectra by a Maxwell-Boltzmann distribution with a temperature of 203 K. Although formation of hydrogen and hydrocarbon polymer can provide the energy, the processes that lead to particle ejection are not known.

Ariyansinghe et al. (1989) studied C_2H_2 and C_2H_4 and Foti et al. (1987) studied benzene, C_2H_6. The results showed largely the same trends as for methane: hydrogen depletion and formation of an involatile residue. A heavy residue was generated in C_2H_2, but not in C_2H_6 in which the bonds are saturated, when low energy ions are used.

One of the most complicated solidified gases that has been sputtered is frozen sulfur hexafluoride (Pedrys et al., 1984). The sputtered flux during keV electron bombardment consisted of sulfur flourides, which at high fluences exhibit energy distributions which fall off steeply above 0.1 eV. Only the distribution of SF_5^+, which originates in part from post ionized sulfur hexafluoride, shows a distribution with an E_1^{-2}-tail. The distribution of diatomic fluorine molecules can be approximated with a Maxwell-Boltzmann distribution corresponding to the actual target temperature. As with $H_2(D_2)$ in methane, the diatomic molecules are, apparently, formed and ejected in events uncorrelated with the ejection of the sulfur fluorides.

10 Summary

Results for knock-on sputtering of inorganic insulators by incident ions and electronic sputtering by incident ions, electrons and photons were summarized. Knock-on sputtering of room-temperature insulators, with surface binding energies for constituent atoms comparable to that of metals, can be roughly treated on the basis of standard sputtering theory at low fluences. However, the molecular character of room-temperature insulators adds a complication, especially at high fluences. There is some analogy for these with the sputtering of metallic alloys, except that efficient molecular ejection can occur, which is not understood quantitatively. Unfortunately, sputtering data are available for only one room-temperature elemental insulator, sulfur. The most important new studies for knock-on sputtering are for the volatile, frozen gases, for which nonlinear effects are observed in the yield and/or the ejected particle energy spectra even at relatively low excitation densities. Although this has been known for some time the nonlinear effects are not understood quantitatively.

The most exciting results and ideas described in this review concern electronic sputtering, since the relaxation processes which follow the electronic excitation of a solid can be studied via detecting the sputtered species. In this manner a clear picture has emerged of the electronic relaxation processes which lead to sputtering in the rare-gas solids. The physics of the sputtering of solid argon is the best known for these materials, although there are a number of important outstanding questions regarding differences in the yield above and below the stopping power maximum, on the mechanism for dimer ejection and vibrational cooling, and on the relationship of the large secondary electron yields to sputtering and luminescence. Certain aspects of nonradiative electronic relaxation in a few molecular solids have also emerged, particularly for solid nitrogen and oxygen. However, the details of the decay processes leading to sputtering of these materials are not well understood, and often quite complicated chemical processes can affect sputtering of the heteronuclear molecular condensed gases.

An essential parameter in electronic sputtering of inorganic insulators is the excitation density, which determines the nature of the transport and ejection processes. At low excitation densities, excitonic processes occur which ultimately lead to particle ejection in the condensed gases: migration of excitons, trapping, and relaxation and energy transfer to target atoms. There are, however, very few studies of these processes as a function of sample crystal quality or impurity content. For high excitation densities, the volatile solids exhibit nonlinear yields and even refractory solids may be sputtered electronically. Although these are not understood quantitatively, the magnitude of the stopping power and the surface binding energy control the electronic sputtering yield, as is the case for knock-on sputtering. In addition, for high velocity ions, the W-value is important. Therefore, most experimental results can be analyzed using the quantity $f_{\mathrm{e}}\ell(dE/dx)_{\mathrm{e}}/U$, where f_{e} is the fraction of the electronic energy released in energetic non-radiative processes. Here, $f_{\mathrm{e}} \approx \Delta E/W$, is of the order 0.1-0.3 in a number of condensed gases for fast light ions, and f_e appears to increase with decreasing ion velocity The increasing ability to carry out detailed experiments, combined with molecular dynamics calculations, will allow one to obtain a high level of detail about the electronic relaxation processes which lead to sputtering of a number of low-temperature, molecular condensed gases.

Acknowledgements

The authors would like to thank G. Zimmerer, C. Reimann, R.A. Baragiola, H.H. Andersen, and P. Sigmund and one anonymous referee for extensive comments on the manuscript.

References

Adloff JP, Gaspar PP, Imamura M, Maddock AG, Matsuura T, Sano H and Yoshihara Y, 1992: *Handbook of Hot Atom Chemistry*, Kodanska, Tokyo
Allison SK, 1958: Rev. Mod. Phys. **30**, 1137
Andersen HH, 1984: in *Ion Implantation and Beam Processing*, eds. Williams JM and Poate JM, Academic, Australia, 127
Andersen HH and Bay HL, 1974: J. Appl. Phys. **45**, 953
Andersen HH and Ziegler JF, 1977: *Hydrogen Stopping Powers and Ranges in All Elements*, Pergamon, NY
Andersen HH and Bay HL, 1981: in *Sputtering by Particle Bombardment I*, ed. Behrisch, R, Springer, NY, 145
Andersen N and Sigmund P, 1974: Mat. Fys. Medd. **39**, no. 3
Arakawa I, Takahashi M and Takeuchi K, 1989: J. Vac. Science Techn. **A7**, 2090
Arakawa I and Sakurai M, 1990: in *Desorption Induced by Electronic Transitions, DIET IV*, eds. Betz G and Varga P, Springer, NY, 246
Ariyasinghe WM, McElroy RD and Powers D, 1989: Nucl. Instrum. Methods B **44**, 61
Baba Y, Dujardin J, Feulner P and Menzel D, 1991: Phys. Rev. Lett. **66**, 3269
Bach H, Kitzmann I and Schröder H, 1974: Rad. Effects **21**, 31
Bach H, 1988: J. Non-Cryst. Solids **102**, 36
Balaji V, David DE, Magnera TF, Michl J and Urbassek HM, 1990: Nucl. Instrum. Methods B **46**, 435
Banerjee S, Johnson RE, Cui ST and Cummings PT, 1991a: Phys. Rev. B **43**, 12707
Banerjee S, Liu M and Johnson RE, 1991b: Surf. Sci. Lett. **255**, L504
Baragiola RA, 1993a: in *Low Energy Ion-Surface Interactions*, ed. Rabalais JW, Wiley, NY
Baragiola RA, 1993b: *Ionization of Solids by Heavy Particles*, Plenum, NY
Bargiola RA, 1993c: Unpublished communication
Baretzky B, Møller W and Taglauer E, 1992: Vac. **43**, 1207
Bar-nun A, Herman G, Rappaport ML and Mekler Yu 1985: Surf. Sci. **150**, 143
Belov AG, Svishchev VN and Fugol' Ya, I, 1989: Sov. J. Low Temp. Phys. **15**, 34
Benit J and Brown WL, 1990: Nucl. Instrum. Methods B **46**, 448
Benit J, Bibring J-P, Della-Negra S, Le Beyec Y, Mendenhall M, Rocard F and Standing K, 1987: Nucl. Instrum. Methods B **19-20**, 838
Benit J, Bibring J-P and Rocard F, 1988: Nucl. Instrum. Methods B **32**, 349

Benvenuti C, Calder R and Gröbner O, 1987: Vacuum 37, 699: Erratum Vacuum **38**, 145

Besenbacher F, Bøttiger J, Graversen O, Hansen JL and Sørensen H, 1981: Nucl. Instrum. Methods **191**, 221

Betz G and Wehner GK, 1983: in: *Sputtering by Particle Bombardment II*, ed. Behrisch R., Springer, 11

Betz G, 1987: Nucl. Instrum. Methods B **27**, 104

Biersack JP and Santner E, 1976: Nucl. Instrum. Methods **132**, 229

Bitensky IS and Parilis ES, 1987: Nucl. Instrum. Methods B **21**, 26

Bitensky IS, Goldenburg AM and Parilis ES, 1990: in *Ion Formation from Organic Solids V (IFOSV)*, eds Hedin A et al. Wiley, Chichester, 205

Boring JW, Johnson RE, Reimann CT, Garret JW, Brown WL and Macantonio KJ, 1983: Nucl. Instrum. Methods **218**, 707

Boring JW, Garrett JW, Cummings TA, Johnson RE and Brown WL, 1984: Nucl. Instrum. Methods B **1**, 321

Boring JW, O'Shaughnessy DJ and Phipps JA, 1987: Nucl. Instrum. Methods B **18**, 613

Boring JW, Johnson RE and O'Shaughnessy DJ, 1989: Phys. Rev. B **39**, 268

Boursey E, Castex MC and Chandrasekharan V 1977: Phys. Rev. B **16**, 2858

Brandt W and Ritchie RH, 1974: in *Physical Mechanisms in Radiation Biology*, eds. Cooper RD and Wood RW, US Dept. of Commerce, Wash. D.C., 20

Brown WL, 1993: in *Ionization in Solids by Secondary Electrons* ed. Baragiola RA, Plenum, N.Y. 395

Brown WL, 1984: in *Ion Implantation and Beam Processing*, eds. Williams, JM and Poate MJ, Academic, Australia (Acad. Press. N.Y.) 99

Brown WL, Lanzerotti LJ, Poate JM and Augustyniak WM, 1978: Phys. Rev. Lett. **40**, 1027

Brown WL, Augustyniak WM, Lanzerotti LJ, Johnson RE and Evatt R, 1980a: Phys. Rev. Lett. **45**, 1632

Brown WL, Augustynik WM, Brody E, Cooper B, Lanzerotti LJ, Ramirez A, Evatt R and Johnson RE 1980b: Nucl. Instrum. Methods **170**, 321

Brown WL, Augustyniak WM, Marcantonio KJ, Simmons EH, Boring JW, Johnson RE and Reimann CT, 1982: Nucl. Instrum. Methods B **1**, 307

Brown WL, Augustyuniak WM, Marcantonio KJ, Simmons EH, Boring JW, Johnson RE and Reimann CT, 1984: Nucl. Instrum. Methods B **1**, 307

Brown WL and Johnson RE, 1986: Nucl. Instrum. Methods B **13**, 295

Brown WL, Lanzerotti LJ, Marcantonio KJ, Johnson RE and Reimann CT: 1986: Nucl. Instrum Methods B **14**, 392

Buller WT and Johnson RE, 1991: Phys. Rev. B **43**, 6118

Buxton GV, Gillis HA and Klassen NV, 1977: Can. J. Phys. **55**, 2385

Børgesen P and Sørensen H, 1982: Phys. Lett. **90 A**, 319

Børgesen P, Schou J, Sørensen H and Claussen C, 1982: Appl. Phys. A **29**, 57

Bøttiger J, L'Ecuyer J, Matsunami N and Ollerhead R, 1980: Rad. Effects **49**, 119

Cantagrel M and Marchal M, 1973: J. Mat. Science **8**, 1711

Carter G., 1983: Nucl. Instrum. Methods **209/210**, 1

Celiberto R, Cacciatore M and Capitelli M, 1989: Chem. Phys. **133**, 369

Chrisey DB, Boring JW, Phipps JA, Johnson RE and Brown WL 1986: Nucl. Instrum. Methods **13**, 360

Chrisey DB, Boring JW, Johnson RE and Phipps JA, 1988: Surf. Sci. **195**, 594

Chrisey DB, Brown WL and Boring JW, 1990: Surf. Sci. **225**, 130

Christiansen JW, Carpini D Delli and Tsong IST, 1986: Nucl. Instrum. Methods B **15**, 218

Claussen C, 1982: Nucl. Instrum. Methods **194**, 567

Coletti F and Bonnot AM, 1977: Chem. Phys. Lett. **45**, 580

Coletti F and Debever JM, 1983: Solid State Comm. **47**, 47

Coletti F, Debever JM and Zimmerer G, 1984: J. Physique Lett. **45**, L 467

Coletti F, Debever JM and Zimmerer G, 1985: J. Chem. Phys. **83**, 49

Cooper BH and Tombrello TA, 1984: Rad. Effects **80**, 203

Cui ST, Johnson RE and Cummings PT, 1988: Surf. Sci. **207**, 186

Cui ST and Johnson RE, 1989: Int. J. Quant. Chem: Quant. Chem. Symp. 23, 575; Errata, 1991: I.J.Q.C. **41**, 383

Cui ST, Johnson RE and Cummings PT, 1989a: Phys. Rev. B **39**, 9580

Cui ST, Johnson RE, Reimann CT, Boring JW, 1989b: Phys. Rev B **39**, 12345

David DE, Magnera TF, Tian R, Stulik D and Michl J, 1986: Nucl. Instrum. Methods B **14**, 378

David DE and Michl J, 1989: Prog. Solid St. Chem. **19**, 283

Davidse PD and Maissel LI, 1966: J. Vac. Sci. Techn. **4**, 33

DIET I, 1983: Springer Ser. in Chem. Phys. **24**, eds. Tolk NH et al. Springer, Berlin

DIET II, 1985: Springer Ser. in Surf. Science **4**, eds. Brenig W and Menzel D, Springer, Berlin

DIET III, 1988: Springer Ser. in Surf. Science **13**, eds. Stulen RH and Knotek ML, Springer, Berlin

DIET IV, 1990: Springer Ser. in Surf. Science **19**, eds. Betz G and Varga P, Springer, Berlin

DIET V, 1993: Springer Ser. in Surf. Science **31**, eds. Burns AR et al. Springer, Berlin

Dixon RS, 1970: Rad. Res. Rev. **2**, 237

Doke T, Hitachi A, Kubota S, Nakamoto A and Takahashi T, 1976: Nucl. Instrum. Methods **134**, 353

DuBois RD, Toburen LH and Rudd ME, 1984: Phys. Rev. A **29**, 70

Dubus A, Devooght J and Dehaes JC, 1987: Phys. Rev. B **36**, 5110

Dujardin G, Hellner L, Besnard-Ramage MJ and Azria R, 1990: Phys. Rev. Lett. **64**, 1289

Dullni E, 1984: Nucl. Instrum. Methods B **2**, 610

Edwin RP, 1973: J. Phys. **D6**, 833

Ellegaard O, 1986: PH.D. Thesis Risø-M-2617, Risø National Laboratory

Ellegaard O, Schou J and Sørensen H, 1986a: Nucl. Instrum. Methods B **13**, 567

Ellegaard O, Schou J, Sørensen H, 1986b: Surf. Sci. **167**, 474

Ellegaard O, Pedrys R, Schou J, Sørensen H and Børgesen P,1988: Appl. Phys. A **46**, 305

Ellegaard O, Schou J and Sørensen H, 1990: Europhys. Lett. **12**, 459

Ellegaard O, Schou J, Stenum B, Sørensen H and Pedrys R, 1992: Nucl. Instrum. Methods B **62**, 44

Ellegaard O, Schou J, Stenum B, Sørensen H, Pedrys R, Oostra DJ, Haring A and De Vries AE, 1993a: to be published

Ellegaard O, Schou J, Sørensen H, Pedrys R and Warczak B, 1993b: Nucl. Instrum. Methods B **78**, 192

Erents SK and McCracken GM, 1973: J. Appl. Phys. **44**, 3139

Erents SK and McCracken GM, 1975: in *Atomic Collisions in Solids* eds. S. Datz and C.D. Moak Plenum, N.Y. 625

Falcone G and Sigmund P, 1981: Appl. Phys. **25**, 307

Falcone G, 1990 Riv. di Nuov. Cimento **13**, 1

Fano U, 1963: Ann. Rev Nucl. Sci. **13**, 1

Fenyö D, 1993: Phys. Rev. B (in press)

Fenyö D, Sundqvist BUR, Karlsson BR and Johnson RE, 1990: Phys. Rev. B **42**, 1895

Fenyö D and Johnson RE, 1992: Phys. Rev. B **46**, 5090

Feulner P, Müller T, Puschmann A and Menzel D, 1987: Phys. Rev. Lett. **59**, 791

Fiori C and Devine RAB, 1984: Phys. Rev. Lett. **52**, 2081

Fink D, Biersack JP, Städele M, Tjan K, Haring R and de Vries AE, 1984: Nucl. Instrum. Methods **B 1**, 275

Fleischer RL, Price PB and Walker RM, 1975: *Nuclear Tracks in Solids*, Univ. of Calif. Press, Berkeley

Forrest JA, Brooks RL, Hunt JL, Stenum B, Schou J, Sørensen H, Gürtler P, Magnotta F, Mapoles ER, Souers PC and Collins GW, 1992: Phys. Rev. B **46**, 13820

Foti G, Calcagno L, Zhou FZ and Strazzulla G, 1987: Nucl. Instrum. Methods B **24-25**, 552

Fox JL and Dalgarno A, 1983: J. Geophys. Res. **88**, 9027

Fugol' I Ya, 1978: Adv. Phys. **27**, 1

Fugol' I Ya, 1988: Adv. Phys. **37**, 1

Fugol' I Ya, Belov AG and Svishchev VN, 1988: Solid State Comm. **66**, 503

Garrison BJ, 1983: Int. J. Mass. Spec. and Ion Physics **53**, 243

Garrison BJ and Johnson RE, 1984: Surface Science **148**, 388

Geerk J, 1993: Private communication

Geerk J, Linker G and Meyer O, 1989: Mat. Science Rep. **4**, 19

Gibbs KM, Brown WL and Johnson RE, 1988: Phys. Rev. B **38**, 11001

Greenberg JM and Pirronello V, 1991: eds. *Chemistry in Space*, NATO-ASI series C Vol. 323

Griffith JW, Weller RA, Sieberling LE and Tombrello TA, 1980: Rad. Effect **51**, 223

Griscom DL, 1989: Phys. Rev. B **40**, 4224

Grosjean DE and Baragiola RA, 1993: in *Ionization of Solids by Heavy Particles*, ed. Baragiola RA, Plenum, N.Y., 381

Guthier W, 1986: Proc. in Physics **9**, Springer, 17

Håkansson P, 1993: Mat. Fys. Medd. Dan. Vid. Selsk. **43**, 593

Haff PK, 1976: Appl. Phys. Lett. **29**, 473

Haff PK and Switkowski ZE, 1976: Appl. Phys. Lett. **29**, 549

Haring RA, Pedrys R, Haring A and de Vries AE, 1984a: Nucl. Instrum. Methods B **4**, 40

Haring RA, Pedrys R, Oostra DJ, Haring A and de Vries AE, 1984b: Nucl. Instrum. Methods B **5**, 483

Haring RA, Pedrys R, Oostra DJ, Haring A and de Vries AE, 1984c: Nucl. Instrum. Methods B **5**, 476

Harper J, 1990: *Plasma-Surface Interactions and Processing of Materials*, eds. Auciello O et al. NATO ASI Series-No. E 176, Kluwer Academic, Dordrecht, 251

Hellner L, Besnard-Ramage MJ, Dujardin G and Azria R, 1990: in: *Desorption Induced by Electronic Transitions, DIET IV*, eds. Betz G. and Varga P. Springer, 240

Herzberg G, 1950: *Spectra of Diatomic Molecules*, Van Nostrand-Reinhold, Princeton

Hoover WG, 1986: *Molecular Dynamics*, Springer-Verlag, Berlin

Houpert C, Stader F, Groult D and Toulemonde M, 1989: Nucl. Instrum. Methods B **39**, 120

Hourmatallah A, Coletti F and Debever JM, 1988: J. Phys. C. **21**, 1307

Hudel E., Steinacker E and Feulner P, 1991: Phys. Rev. B **44**, 8972

Hudel E, Steinacker E and Feulner P, 1992: Surf. Sci. **273**, 405

Hudson RL and Moore MH, 1992: J. Phys. Chem. **96**, 6500

ICRU, 1979: *Average Energy Required to Produce an Ion-Pair*, Internat. Commission on Radiation Units and Measurements Report **31**

Inokuti M, 1971: Rev. Modern Phys. **43**, 297

Inokuti M, 1991: Appl. Radiat. Inst. **42**, 979

Itoh N, 1987: Nucl. Instrum. Methods B **27**, 155

Itoh N, Nakayama T and Tombrello TA, 1985: Phys. Lett. **108A**, 480

Itoh C, Suzuki T and Itoh N, 1990: Phys. Rev. B **41**, 3794

Jacobsson H and Holmén G, 1993: Nucl. Instrum. Methods B **82**, 291

Johnson RE, 1970: J. Phys. B **3**, 539

Johnson RE, 1982: *Introduction to Atomic and Molecular Collisions*, Plenum, N.Y.

Johnson RE, 1987: Int. J. Mass Spec. Ion Proc. **78**, 357

Johnson RE, 1989: J. de Physique Coll. **C2**, 251

Johnson RE, 1990: *Energetic Charged Particle Interactions with Atmospheres and Surfaces*, Springer-Verlag, Berlin

Johnson RE 1993: in *Ionization of Solids by Heavy Particles*, ed. Baragiola RA, Plenum, N.Y. 419

Johnson RE and Evatt R, 1980: Radiat. Effects. **52**, 187

Johnson RE and Brown WL, 1982: Nucl. Instrum. Methods **198**, 103

Johnson RE and Brown WL, 1983: Nucl. Instrum. Methods **209/210**, 469

Johnson RE and Inokuti M, 1983: Nucl. Instrum. Methods **206**, 289

Johnson RE, Sundqvist BUR, Hedin A and Fenyö D, 1989: Phys. Rev. B. **40**, 49

Johnson RE, Pospieszalska M and Brown WL, 1991: Phys. Rev. B **44**, 7263

Johnson RE and Sundqvist BUR, 1992: Phys. Today, **45(3)**, 28

Kaiser RI, Mahfouz RM and Roessler K, 1992: Nucl. Instrum. Methods B **65**, 468

Kelly R, 1977: Rad. Effects. **32**, 91

Kelly R, 1979: Surf. Sci. **90**, 280

Kelly R, 1984a: Rad. Effects. **80**, 273

Kelly R, 1984b: in *Ion Bombardment Modification of Surfaces*, eds. Aucello O. and Kelly R., Elsevier, N.Y. 27

Kelly R, 1987: Nucl. Instrum. Methods B **18**, 388

Kelly R, 1990: Nucl. Instrum. Methods B **46**, 441

Klaumünzer S, Hou M-D and Schumacher G, 1986: Phys. Rev. Lett. **57**, 850

Kloiber T, Lasch W, Zimmerer G, Coletti F and Debever JM, 1988: Europhys. Lett. **7**, 77

Kloiber T and Zimmerer G, 1989: Rad. Eff. Def. Solids **109**, 219

Kloiber T and Zimmerer G, 1990: Phys. Scr. **41**, 962

Knotek ML and Feibelman PJ, 1978: Phys. Rev. Lett. **110**, 964

Kühle H, Bahrdt J, Fröhling R, Schwentner N and Wilcke H, 1985: Phys. Rev. B **31**, 4854

Kurtz RL, 1986: Surf. Sci. **177**, 526

Kurtz RL, Stockbauer R and Madey TE, 1986: Nucl. Instrum. Methods B **13**, 518

Laasch W, Hagedorn H, Kloiber T and Zimmerer G 1990: Phys. Stat. Sol. **b 158**, 753

Lam NQ, 1990: Scan. Micr. Suppl. **4**, 311

Lanzerotti LJ and Brown WL, 1983: J. Geophys. Res. **88**, 989

Lanzerotti LJ, Brown WL, Augustyniak WM and Johnson RE, 1982: Astrophys. J **259**, 920

Lanzerotti LJ, Brown WL, Marcantonio KJ, 1987: Astrophys. J. **313**, 910

Leclerc G, Bass AD, Michaud M and Sanche L, 1990: J. Elec. Spec. Rel. Phen. **52**, 725

Leclerc G, Bass AD, Mann A and Sanche L, 1992: Phys. Rev. B **46**, 4865

Lepoire DJ, Cooper BH, Melcher CL and Tombrello TA, 1983: Rad. Effects **71**, 245

Leung C, Steinbrüchel Ch and Gomer R, 1977: Appl. Phys. **14**, 79

Lindhard J. and Winther Aa, 1964: Mat. Fys. Medd. **34** no. 4

Liu M and Johnson RE, 1993: submitted

Mann A, Leclerc G and Sanche L, 1992: Phys. Rev. B **46**, 9683

Matsunami N, 1990: Nucl. Instrum. Methods B **46**, 452

Matsuura T, 1984: *Hot Atom Chemistry*, Elsevier, Amsterdam.

Maynard G and Deutsch C, 1987: Lecture Notes in Physics **269** ed. by Hilf ER et al., Springer, 94

McClanahan ED and Laegreid N, 1991: *Sputtering by Particle Bombardment III*, eds. Behrisch R and Wittmaack K, Springer, Berlin-Heidelberg, 339

Meins CK, Griffith JE, Qiu Y, Mendenhall MH, Seiberling LE and Tombrello TA, 1983: **71**, 13

Menzel D, 1990: Appl. Phys. A **51**, 163

Menzel D and Gomer R, 1964: J. Chem. Phys. **42**, 886

Michaud M, Cloutier P and Sanche L, 1993: Phys. Rev. B **47**, 4131

Miller JH and Green AES, 1973: Rad. Res. **54**, 354

Mizutani 1991: Jap. J. Appl. Phys. **30**, L628

Moore MH, 1984: Icarus **59**, 114

Mozumder A, 1969: Adv. Radiat. Chem **1**, 1

Nieschler E, Nees B, Bischof N, Fröhlich H, Tiereth W and Voit H, 1984: Rad. Effects **83**, 121

Oehler O, Smith DA and Dressler K, 1977: J. Chem. Phys. **66**, 2097

Ollerhead RW, Bøttiger J, Davies JA, L'Ecuyer J, Haugen HK and Matsunami N, 1980: Rad. Eff. **49**, 203

Oliva A, Kelly R and Falcone G, 1987: Nucl. Instrum. Methods B **19/20**, 101

Oliva-Florio A, Alonso EV, Baragiola RA, Ferron J and Jakas MM, 1979: Rad. Eff. Lett **50**, 3

O'Shaughnessy DJ, Boring JW, Phipps JA and Johnson RE, 1988a: Surf. Sci. **203**, 227

O'Shaughnessy DJ, Boring JW, Cui S and Johnson RE, 1988b: Phys. Rev. Lett. **61**, 1635

Overeijnder H, Szymonski M, Haring A and de Vries AE, 1978: Rad. Eff. **36**, 63

Pan SL, Zumofen G and Dressler K, 1987: J. Chem. Phys. **87**, 3482

Paretzke HG, Turner JE, Hamm RN, Wright HA and Ritchie RH, 1986: J. Chem. Phys. **84**, 3182

Pedrys R, 1990: Nucl. Instrum. Methods B **48**, 525

Pedrys R, 1993: Unpublished communication

Pedrys R, Haring RA, Haring A and de Vries AE 1984: Nucl. Instrum. Methods B **2**, 573

Pedrys R, Oostra DJ and de Vries AE, 1985: in *Desorption Induced by Electornic Transitions, DIET II*, eds. Brenig W and Menzel D, Springer, Berlin, 190

Pedrys R, Oostra DJ, Haring RA, Calcagno T, Haring A and de Vries AE, 1986: Nucl. Instrum. Methods B **17**, 15

Pedrys R, Oostra DJ, Haring A, de Vries AE and Schou J, 1988: Nucl. Instrum. Methods B **33**, 840

Pedrys R, Oostra DJ, Haring A, de Vries AE and Schou J, 1989: Rad. Eff. Def. Solids **109**, 239

Pedrys R, Warczak B and Schou J, 1993a: to be published

Pedrys R, Warczak B, Schou J and Ellegaard O, 1993b: to be published

Platzmann RL, 1961: Int. J. Appl. Rad. Inst. **10**, 116

Poltorataskii YuB and Fugol' Ya, I, 1979: Sov. J. Low Temp. **5**, 439

Qui Y, Griffith JE and Tombrello TA, 1982: Rad. Eff. **64**, 111

Qui Y, Griffith JE, Meng WJ and Tombrello TA, 1983: Rad. Effect. **70**, 231

Quickenden TI, Matich AJ, Bakker MG, Freeman CG and Sangster DF, 1991: J. Chem. Phys. **95**, 8843

Redhead PA, 1964: Can. J. Phys. **42**, 886

Reimann CT, 1992: Unpublished communication

Reimann CT, 1993: Mat. Fys. Medd. Dan. Vid. Selsk. **43**, 351

Reimann CT, Boring JW, Johnson RE, Garret JW, Farmer KR, Brown WL, Marcantonio KJ and Augustyniak WM, 1984a: Surf. Sci. **147**, 227

Reimann CT, Johnson RE and Brown WL, 1984b: Phys. Rev. Lett. **53**, 600

Reimann CT, Brown WL and Johnson RE, 1988: Phys. Rev. B **37**, 1455

Reimann CT, Brown WL, Nowakowski MJ, Cui ST and Johnson RE, 1990: in *Desorption Induced by Electronic Transitions DIET IV*, eds. Betz G and Varga P, Springer-Verlag, Berlin, 226

Reimann CT, Brown WL, Grosjean DE, Nowakowski MJ, Buller WT, Cui ST and Johnson RE, 1991: Nucl. Instrum. Methods B **58**, 404

Reimann CT, Brown WL, Grosjean DE and Nowakowski MJ, 1992: Phys. Rev. B **45**, 43

Ritchie RH and Claussen C, 1982: Nucl. Instrum. Methods **198**, 133

Ritchie RH, Gras-Marti A and Ashley JC, 1989: in *Proc. 12th Werner Brandt Workshop*, ed. Ritchie RH, Oak Ridge Nat. Lab, Oak Ridge, Tenn, 595

Robinson MT, 1989: in *Sputtering by Particle Bombardment I*, ed. Behrisch R, Springer-Verlag, Berlin, 73

Rocard F and Bibring JP, 1982: Phys. Rev. Lett. **38**, 1763

Rocard F, Benit J, Bibring JP, Ledu D and Meunier R, 1986: Rad. Effects **99**, 97

Rocker G, Feulner P, Scheuerer R, Zhu L and Menzel D, 1990: Phys. Scr. **41**, 1014

Roessler K, 1992: Nucl. Instrum. Methods B **65**, 55

Roick E, Gaethke R, Gürtler P, Woodruff TO and Zimmerer G, 1984: J. Phys. **C17**, 945

Rook FL, Johnson RE and Brown WL, 1985: Surf. Sci. **164**, 625

Roth J, 1983: In *Sputtering by Particle Bombardment II*, ed. Behrisch R, Springer, NY, 1991

Rudd ME, Kim YK, Madison DH and Gallagher JW, 1985: Rev. Mod. Phys. **57**, 965

Rudd ME, Kim YK, Madison DH and Gay TS, 1992: Rev. Mod. Phys. **64**, 441 73

Runne M, Becker J, Laasch W, Varding D, Zimmerer G, Liu M and Johnson RE, 1993: Nucl. Instrum. Methods B **82**, 301

Sack N, Johnson RE, Boring JW and Baragiola RA, 1993: Icarus **100**, 534

Sanche L, 1984: Phys. Rev. Lett. **53**, 1638

Sanche L, 1990: J.Phys. B **23**,1597

Schou J, 1980: Phys. Rev. B **22**, 2141

Schou J, 1987: Nucl. Instrum. Methods B **27**, 188

Schou J, 1988: Scan. Micr. **2**, 607

Schou J, 1989: in *Structure-Property Relationships in Surface-Modified Ceramics*, eds. McHargue C et al. (Kluwer Academics) 61

Schou J, 1991: Dr. Scient. thesis, Risø-report R-591 (EN), Risø National Laboratory

Schou J.: 1993: Unpublished communication

Schou J, Sørensen H and Børgesen P, 1984: Nucl. Instrum. Methods B **5**, 44

Schou J, Ellegaard O, Børgesen P and Sørensen H, 1985: in *Desorption Induced by Electronic Transitions, DIET II*, eds. Brenig W and Menzel D, Springer, Verlag, Berlin, 170

Schou J, Børgesen P, Ellegaard O, Sørensen H and Claussen C, 1986: Phys. Rev. B **34**, 93

Schou J, Pedrys R, Ellegaard O and Sørensen H, 1987: Nucl. Instrum. Methods B **18**, 609

Schou J, Ellegaard O, Sørensen H and Pedrys R, 1988: Nucl. Instrum. Methods B **337**, 808

Schou J, Ellegaard O, Pedrys R and Sørensen H, 1992: Nucl. Instrum. Methods B **65**, 173

Schriver KE, Hahn MY and Whetten RI, 1987: Phys. Rev. Lett. **59**, 1986

Schroeder JB, Dieselman HD and Douglass JW, 1971: Appl. Opt. **10**, 295

Schwabentahn P, Scheurer R, Hudel E and Feulner P, 1992: Sol. State. Comm **80**, 773

Schwentner N, Koch EE and Jortner J, 1985: *Electronic Excitations in Condensed Rare Gases*, (Springer)

Seiberling LE, Griffith JE and Tombrello TA, 1980: Rad. Eff. **52**, 201

Seiberling LE, Meins CK, Cooper BM, Griffith JE, Mendenhall MH and Tombrello TA, 1982: Nucl. Instrum. Methods **198**, 17

Shiea JT and Summer J, 1991: in *Methods and Mechanisms for Producing Ions from Large Molecular*, eds. Standing K and Ens W, Plenum, N.Y. l47

Sigmund P, 1969: Phys. Rev. **184**, 383

Sigmund P, 1972: Rev. Roum. Phys. **17**, 969 and 1079

Sigmund P, 1975a: in *Radiation Damage Processes in Materials*, ed. Dupuy CHS, (Noordhoff, Leyden) 3

Sigmund P, 1975b: Appl. Phys. Letts. **27**, 52

Sigmund P, 1977: in *Inelastic Ion-Surface Collisions*, eds. Tolk NH et al. Academic, NY, 121

Sigmund P, 1981: in *Sputtering by Particle Bombardment I*, ed. Behrisch R, (Springer Verlag), 9

Sigmund P, 1987: Nucl. Instrum. Methods B **27**, 1

Sigmund P and Claussen C, 1981: J. Appl. Phys. **52**, 990

Sigmund P and Szymonski M, 1984: Appl. Phys. A **33**, 141

Sigmund P, Robinson MT, Baskes M, Hautala M, Cui FZ, Eckstein W, Yamamura Y, Hosaka S, Ishitani T, Shulga VI, Harrison Jr DE, Charakov IR, Karpuzov DS, Kawatoh E, Shimizu R, Valkealahti S, Nieminen RM, Betz G, Husinsky W, Shapiro MH, Vicanek M and Urbassek HM, 1989: Nucl. Instrum. Methods B **36**, 110

Sigmund P and Oliva A, 1993: Nucl. Instrum. Methods B **82**, 269

Sigmund P and Lam NQ, 1993: Mat. Fys. Medd. Dan. Vid. Selsk. **43**, 255

Sonntag B, 1977: in *Rare Gas Solids II*, ed. Klein ML and Venables JA, Academic Press, Inc. N.Y., 1021

Sowada V, Warman JM and Deltas MP, 1982: Phys. Rev. B **25**, 3434

Spinella F, Baratta GA and Strazzulla G, 1991: Rev. Sci. Instr. **62**, 1743

Spinks JWT and Woods RJ, 1990: *Introduction to Radiation Chemistry*, John Wiley, NY

Srdoč D, Inokuti M and Krajear-Bronić I, 1993: in *Atomic and Molecular Data for Radiotherapy (IAEA CRP)* in press

Stenum B, Ellegaard O, Schou J and Sørensen H, 1990: Nucl. Instrum. Methods B **48**, 530

Stenum B, Schou J, Ellegaard O, Sørensen H and Pedrys R, 1991: Phys. Rev. Lett. **67**, 2842

Stenum B, Schou J, Sørensen H and Gürtler P, 1993: J. Chem. Phys. **98**, 126

Stevanovic DV, Thompson DA and Davies JA 1984: Nucl. Instrum. Methods **B1**, 315

Strazzulla G, Torrisi L and Foti G, 1988: Europhys. Lett. **7**, 413

Strazzulla G, Baratta GA, Leto G and Foti G, 1992: Europhys. Lett. **18**, 517

Sugden S, Sofield CJ and Murrell MP, 1992: Nucl. Instrum. Methods B **67**, 569

Szymonski M, 1980: in *Symposium on Sputtering*, eds. Varga P et al. Techn. Univ. Wien, Austria, 761

Szymonski M, Ruthowski J, Poradzisz A, Postawa Z and Jørgensen B, 1985: in *Desorption Induced by Electronic Transitons, DIET II*, eds, Brenig W and Menzel D, Springer-Verlag, Berlin, 160

Szymonski M, Czuba P, Dohnalik T, Jozefowski L, Karawajczyk A, Kolodziej J, Lesniak R and Postawa Z, 1990: Nucl. Instrum. Methods B **48**, 534

Szymonski M, 1993: Mat. Fys. Medd. Dan. Vid. Selsk. **43**, 495

Tarrio C and Schnatterly SE, 1992: J. Phys. Chem. Solids **53**, 1013

Taylor SR, 1982: it Planetary Science: A Lunar Perspective, Lunar and Planet. Inst., Houston

Thomas JH, III and Hoffmann S, 1985: J. Vac. Sci. Techn. **A 3**, 1921

Torrisi L, Coffa S, Foti G and Strazzulla G, 1986: Rad. Effects **100**, 61

Torrisi L, Coffa C, Foti G, Johnson RE, Chrisey DB and Boring JW, 1988: Phys. Rev. B **38**, 1516

Townsend PC, 1983: in *Sputtering by Particle Bombardment, II*, ed. Behrisch R, Springer-Verlag, Berlin, 147

Trotman SM, Quickenden TI and Sangster DF, 1986: J. Chem. Phys. **85**, 2555

Turner JE, Magee JL, Wright HA, Chatterjee A, Hamm RN and Ritchie RH, 1983: Rad. Res. **96**, 437

Turner JE, Hamm RN, Wright HA, Ritchie RH, Magee JL, Chatterjee A and Bolch WE, 1988: Rad. Phys. Chem. **32**, 503

Urbassek HM and Sigmund P, 1984: Appl. Phys. A **35**, 19

Urbassek HM and Michl J, 1987: Nucl. Instrum. Methods B **22**, 480

Urbassek HM and Waldeer T, 1991: Phys. Rev. Lett. **67**,105

Urbassek HM and Hofer WO, 1993: Mat. Fys. Medd. Dan. Vid. Selsk. **43**, 97

Urbassek HM, Kafemann H and Johnson RE, 1993: Phys. Rev. B in press

Valkealahti S, Schou J and Nieminen RM, 1989: J. Appl. Phys. **65**, 2258

Varding D, Becker J, Frankenstein L, Peters B, Runne M, Schröder A and Zimmerer G, 1993: Fiz. Nizh. Temp. **19**, 600

Varga P, Diebold U and Wutte D, 1991: Nucl. Instrum. Methods B **58**, 417

Varma MN and Baum JW, 1980: Radiat. Res. **81**,335

Vernon CF, Matich AJ, Quickenden TI and Sangster DF, 1991: J. Phys. Chem. **95**, 7313

Vicanek M, Jimenz Rodriguez JJ and Sigmund P, 1989: Nucl. Instrum. Methods B **36**, 124

Vineyard GH, 1976: Rad. Effects. **29**, 245

de Vries AE, Haring RA, Haring A, Klein FS, Kummel AC and Saris FW, 1984: J. Phys. Chem. **88**, 4510

Watson CC and Tombrello TA, 1985: Rad. Effects. **89**, 263

Watson WD, 1976: Rev. Mod. Phys. **48**, 513

Weibel DE, Herayama T and Arakawa I, 1993: Surf. Sci. **283**, 204

Weller RA and Weller MR, 1982: Nucl. Instrum. Methods **194**, 573

Wien K, 1989: Rad. Eff. Def. Solids **109**, 137

Wien K, 1992: Nucl. Instrum. Methods B **65**, 149

Wien K, Becker O, Guthier W, Della Negra S, LeBeyec Y, Monart B, Standing KG, Maynard G and Deutsch C, 1987: Int. J. Mass Spectrom Ion Proc. **78**, 273

Williams P and Sundqvist BUR, 1987: Phys. Rev. Lett. **58**, 1031

Yamamura Y, 1982: Nucl. Instrum. Methods **194**, 515

Zel'dovich YaB and Raizer YuP, 1967: *Physics of Shock Waves and High Temperature Hydrodynamic Phenomena* Vol. I & II, eds. Hayes WP and Probstein RP, Academic Press, N.Y.

Ziegler JF, 1980: *Handbook of Stopping Cross Section for Energetic Ions in All Elements*, Pergamon, New York

Ziegler JF, Biersack JP and Littmark U, 1985: *The Stopping and Range of Ions in Solids*, Pergamon, New York

Zimmerer G, 1979: J. Lum. **18-19**, 875

Zimmerer G, 1987: in *Excited State Spectroscopy in Solids*, ed. M. Manfredi (XCVI Corso, Soc. Italiana di Fisica, Bologna, Italy) eds. Grassano UM and Terzi N, North-Holland, Amsterdam, The Netherlands, 37

Zumofen G, Sedlacek J, Taubenberger R, Pan SL, Oehler O and Dressler K, 1984: J. Chem. Phys. **81**, 2305

Electronic Sputtering of Alkali Halides

By Marek Szymonski
Institute of Physics, Jagellonian University
ul. Reymonta 4, PL-30-059 Krakow, Poland

Synopsis

Inelastic interactions of energetic charged particles and photons with surfaces of alkali halides result in sputtering of various particles such as ions, atoms and molecules. A dominant fraction of this emission is in the form of halogen and alkali atoms characterized by a thermal (Maxwellian) spectrum of translational energies. For several alkali halides, however, a significant part of the halogen atoms is ejected with nonthermal energies, i.e. energies of the order of 0.1 eV. At first, a brief review of old experimental data is given and previously proposed mechanisms of electronic halogen sputtering, due to non-radiative decay of the self-trapped exciton in the bulk of the crystal, are critically discussed. Subsequently, recent systematic studies of angular-resolved kinetic-energy distributions of the emitted particles are presented and current views on the electronic mechanisms of sputtering are described. In particular, it is shown that the widely accepted bulk excitonic mechanism (often called 'the Pooley-Hersh mechanism') cannot explain new experimental findings about the emission of nonthermal halogen atoms. Instead, some recently proposed concepts of electronic sputtering are described and compared with the experimental data.

1 Introduction

A charged particle slowing down in an ionic insulator, in addition to displacing atoms from their lattice positions, creates electronically excited states (excitons and electron-hole pairs). These initially delocalized excitations can interact with a lattice to form localized excited states, so-called 'self-trapped holes' and 'self-trapped excitons'. Such localized excitations can subsequently decay nonradiatively leading to defect production in the bulk of the crystal and/or particle emission from the surface. In the particular case of an impinging low-energy electron, the elastic part of the interaction can be neglected due to a highly unfavorable mass ratio between the projectile and the target atom. Similar electronic sputtering (desorption) phenomena have been observed for UV or X-ray photon irradiation. Such processes provide a unique opportunity to study the electronic transitions

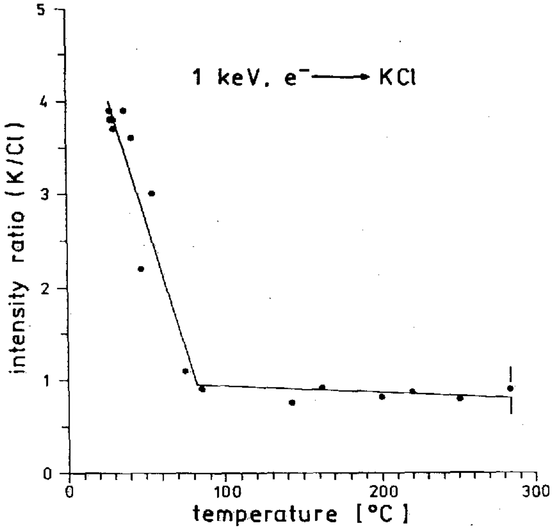

Figure 1. Composition changes in the (100) KCl surface induced by bombardment with a 1 keV electron beam. The K LMM 252 eV and Cl LMM 181 eV steady-state Auger intensity ratios are plotted as a function of the sample temperature. Due to Szymonski et al. (1992a).

responsible for transfer of the excitation energy deposited primarily in the electronic system of the solid into the energy of atomic motion leading to surface sputtering.

Interactions of charged particles and photons with alkali halides have been studied for several decades. In the early stages of these investigations a problem of defect production and radiolytic decomposition in the bulk of the crystal was observed (Crawford, 1968; Royce, 1967). Later, Palmberg & Rhodin (1968) and Townsend & Kelly (1968), reported on the efficient emission of particles from electron bombarded surfaces of alkali halides. Similar sputtering phenomena were also observed for photon irradiated surfaces (Townsend & Elliott, 1969; Brinciotti et al., 1991). In an extensive review Townsend (1983) concluded that electronic sputtering (ES) of alkali halides can be adequately understood in terms of what he called 'the Pooley-Hersh model', primarily used for explanation of Frenkel-pair formation in the bulk of alkali halides (Pooley, 1966; Hersh, 1966). Now, 10 years later, it appears that neither the primary defect structure and evolution in the bulk, nor the surface emission phenomena were sufficiently known. In this last decade, considerable theoretical development of self-trapped excitons and related defect formation in the bulk has been made (for reviews see: Williams & Song, 1990; Itoh & Tanimura, 1990; Song & Williams, 1993). But new, much more sophisticated experiments, performed recently, have provided new insight into the basic mechanisms involved in the electronic sputtering of alkali halides. It is the purpose of this review to summarize the most important experimental findings in this field over the last two decades and to outline possible electronic processes leading to sputtering from alkali halide surfaces.

Generally, such electronic sputtering processes are of fundamental importance and, to a large extent, they should be observed for various ionic insulators such as halides, oxides and oxidized surfaces. Alkali halides can be used as model systems for studying these electronic interactions since they have simple and well-known crystallographic and electronic structures, and because electronic sputtering in these materials is very efficient.

2 First Experimental Findings on Electronic Sputtering of Alkali Halides

In the very first experimental investigations of alkali halide electronic sputtering two methods were used: (1) investigations of the surface composition cha nges induced by prolonged electron bombardment and (2) measurements of the accumulated sputtered material on the collector disc. The first experiment by Palmberg & Rhodin (1968), followed by some others (Cota Araiza & Powell, 1975; Friedenberg & Shapira, 1979) belonging to group (1), resulted in a very important observation. Alkali halide surfaces subjected to prolonged electron bombardment at room temperature showed a significant deficiency in the halogen component as measured by Auger Electron Spectroscopy. Temperature-dependent studies revealed that the apparent enrichment of the alkali component vanishes with increasing surface temperature at a rate related to its thermal evaporation properties. An example of such temperature dependence taken from recent work by Szymonski et al. (1992) is presented in fig. 1. The most significant conclusion was that the ES occurred due to the activation of the halogen sublattice only, whereas the alkali component was neutralized and evaporated thermally from the surface. This last finding is consistent with the work of Townsend et al. (1976) who measured a cosine angular distribution for Na atoms desorbed from NaCl with a 'hot-wire' detector.

In an early attempt by Elliott & Townsend (1971) to detect halogen emission, angular scans were made with a quartz crystal oscillator to measure the sputtered mass. The results for NaCl and KI samples showed a smooth cosine-like background with a superimposed maximum at 45° with respect to the <100> direction. This maximum became much more apparent when the sample temperature was raised from 250 to 350°C. Later, Townsend et al. (1976) used a silica disc to collect the particles desorbed from a (100) NaCl crystal. Despite some degradation of the

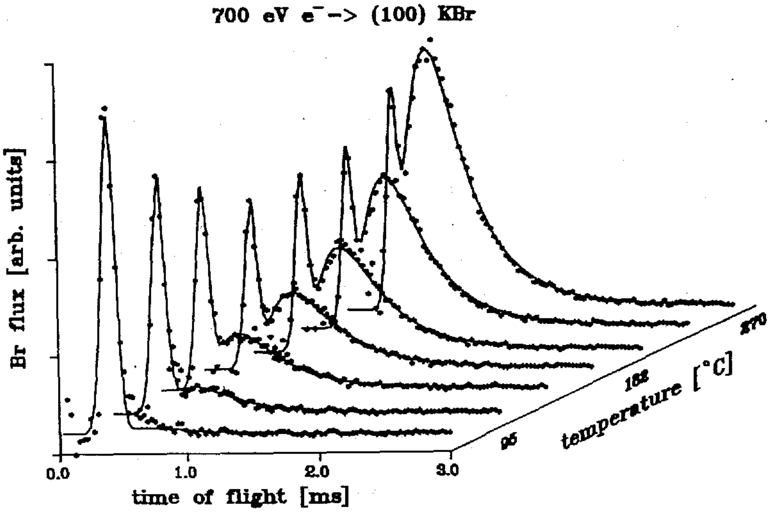

Figure 2. A set of angular-resolved time-of-flight distributions of Br atoms leaving a (100) surface of KBr at temperatures from 95 to 270°C. The observation angle was 0° . The distributions were normalized to reproduce the temperature dependence of the total intensity. Due to Kolodziej et al. (1992a).

deposit when it was exposed to the atmosphere for analysis, the authors were able to observe a rather complex pattern. It consisted of a central star feature with eight arms obtained on 'all occasions' and additional <011>, <112> and <133> spots found under what the authors called 'controlled conditions'. Although the appearance of the <011> spots was discussed in terms of the so called 'Pooley model' described below, the origin of the central pattern and the other spots was left unexplained. In fact, we should note at this point that the interaction of the backscattered primary electrons (Marklund & Andersson, 1966; Egelhoff 1984 & 1987; Ascolani et al. 1991) with the deposit might account for some if not all of its features observed in the work of Townsend et al. (1976). The authors noted that the collector plate was cooled to 77 K in order to inhibit previously observed resputtering by the reflected primary electrons, but even at this low temperature ES of non-thermal chlorine atoms from a thin NaCl deposit is expected to occur, leaving behind areas of higher contrast containing colloidal sodium. Furthermore, the collector technique does not provide any information about either the mass or charge of the different sputtered species that arrive at the collector plate and stick with various probabilities.

Directional features along the <110> and <112>axes with the collector technique were also measured by Schmid et al. (1975) under multiphoton laser ablation of NaCl, KBr and KCl at room temperatures and in vacuum of 10^{-6} Torr. In this laser experiment only the lowest excitonic states could be excited with the available photon energy, and in contrast to Townsend's experiments the central spots were not observed. In order to find the nature of this directional emission Schmid et al. used microchannel plate detectors and a miniature Mattauch-Herzog mass spectrometer. Well-localized emission of negative ions was observed with the microchannel detectors from KBr and KCl with a narrow angular distribution around the <110> and <112> directions. Also strong emission of neutral halogen atoms was registered but its angular distribution could not be measured with the available mass spectrometer.

The observed anisotropies in the emission patterns registered on the collector deposits were used as a major argument for the so-called 'Pooley-Hersh mechanism' proposed by Townsend for explanation of the electronic sputtering of alkali halides (Elliott & Townsend, 1971; Townsend et al., 1976). The Pooley-Hersh mechanism will be described in more detail in section 6.2. At this point it should be noted, however, that this model predicted directional emission of halogen atoms along the <110> direction of the crystal. Therefore, it would only account for some of the observed spots in the collector experiments.

3 Time - of - Flight Spectroscopy of Desorbed Halogen Atoms

The first time-of-flight (TOF) measurements for electron sputtered alkali halides were performed by Overeijnder et al. (1978a, b) for compressed powder samples. The most important result of these investigations was that the TOF spectra of halogen neutral atoms sputtered with 540 eV electrons from RbCl, KBr, RbBr, KI and RbI samples were characterized by a two-component velocity distribution. This type of distribution is indicative of two distinct mechanisms causing the emission of halogen atoms. Recently, it has been shown that the absolute sputtering yield as well as the relative ratio between the thermal and non-thermal halogen component is strongly dependent on the sample impurity content and the electron current density of the primary beam (Kolodziej et al., 1992b). Neither of these factors were controlled in the experiments by Overeijnder et al., thus we will not report further on that work.

The first published energy distributions for halogen atoms sputtered from single-crystal material were obtained by Postawa & Szymonski (1989) and Postawa et al. (1989). Later, such spectra were measured for well prepared surfaces, characterized with LEED and Auger Electron Spectroscopy (Szymonski et al., 1991a, b;

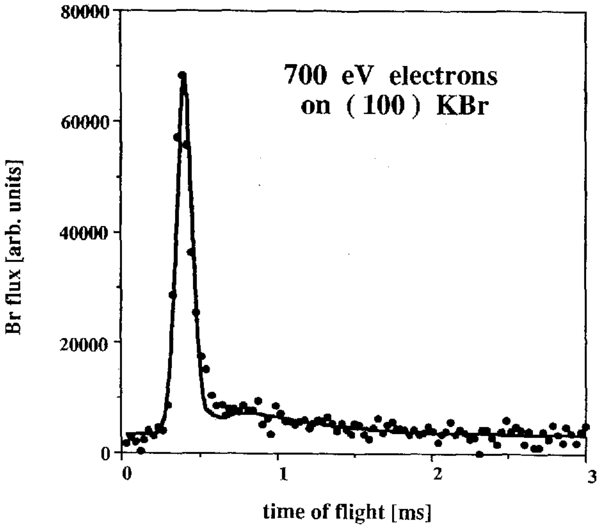

Figure 3a. Br atoms sputtered from a (100) KBr surface with 700 eV electrons. The surface temperature was 95°C and the observation angle was 0° . The solid curves were drawn to guide the eye. Time-of-flight distribution of the Br atoms. Due to Szymonski et al. (1991).

Szymonski et al., 1992). Examples of the temperature-dependent TOF spectra taken along the surface normal for (100) KBr (Kolodziej et al., 1992) are shown in fig. 2; similar spectra have also been measured for (100) KCl, RbCl, RbBr, KI, and RbI. These neutral halogen atom spectra consist of both a broad peak that has a temperature-dependent maximum and a narrow, higher velocity peak whose energy (at peak maximum) is temperature-independent. The broad peak can be fitted by a Maxwellian energy distribution that is representative of the specimen temperature and is due to thermally emitted particles. The differential flux, $\Phi(E)$, of such thermally evaporating particles can be expressed by the formula:

$$\Phi(E) \sim E e^{-E/k_{\mathrm{B}}T}, \tag{1}$$

where k_{B} is the Boltzmann constant and T is the temperature of the surface.

The narrow peak, whose maximum corresponds to a kinetic energy of 0.25 eV in KBr, is due to the ejection of hyperthermal halogen atoms. The lack of any apparent broadening of this hyperthermal peak on the low energy side of the distribution (see figs. 3a,b), suggests that these hyperthermal atoms do not originate in the bulk of the crystal. If they were emitted from inside the crystal, then their distribution should include energy loss processes involved in getting to the surface. Such loss processes were not observed suggesting that hyperthermal

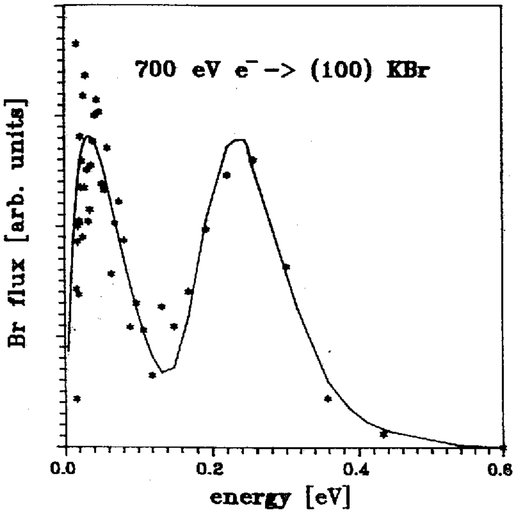

Figure 3b. Same as figure 3a. Energy distribution of Br atoms. Due to Szymonski et al. (1991).

halogen atoms were emitted from the surface directly.

Angular-resolved measurements of the thermal and nonthermal distributions show that they have markedly different angular distributions. The thermal particles can be described by a cosine-like function; in contrast, the nonthermal halogen atoms have a strikingly more peaked angular dependence. In fig. 4, the angular distributions of the nonthermal Br signal are shown for the (100) and the (110) surfaces of the KBr crystal respectively. Note that in the case of the (110) surface the <100> axis forms an angle of ± 45° with the surface normal in the (001) plane. Accordingly, two peaks are seen in fig. 4b, centered at + 45° and -45° with respect to the surface normal. From the above data, it is clear that emission of nonthermal halogen atoms from alkali halide surfaces is strongly collimated along the <100> axis of the crystal.

There is also a basic difference in the temperature dependence of these components. As is shown on the Arrhenius plot in fig. 5 (Kolodziej et al., 1992 a), the nonthermal emission decreases with an increase in the target temperature. At the same time, the yield of thermally evaporated atoms increases. It is seen, however, that the thermal Br component can not be described by a single rate equation process and a linear fit can only be made for temperatures above 160°C. There, the least squares fit gives an activation energy of 0.19 ± 0.04 eV. Accordingly, Dou & Lynch (1992) have found 2 temperature regions in the Arrhenius plots for NaCl

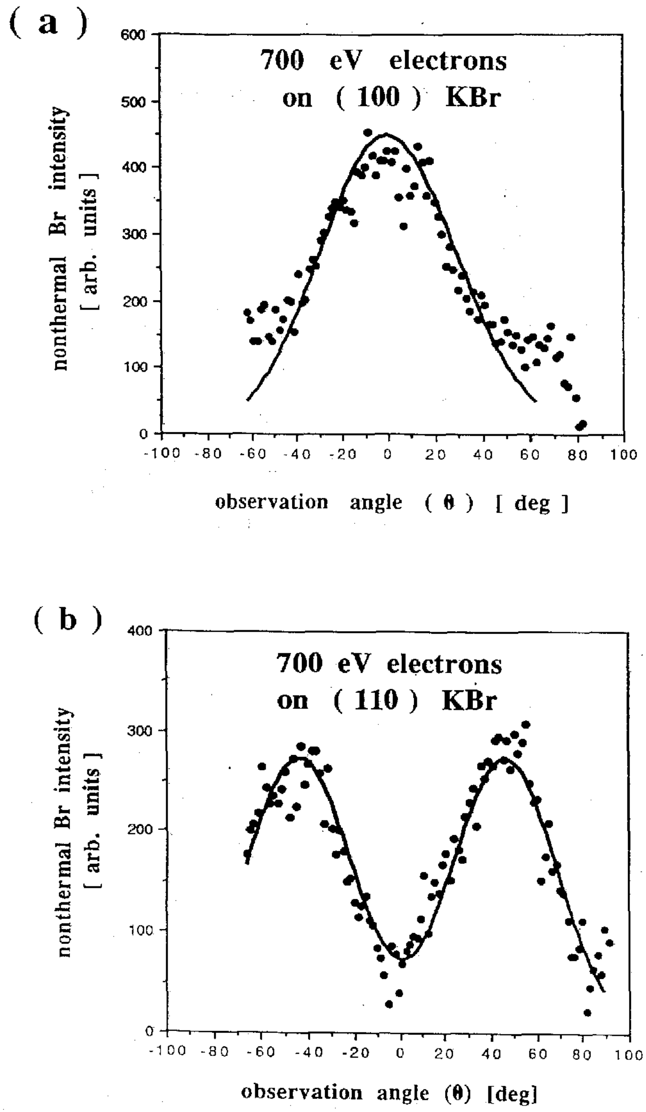

Figure 4. Angular distributions of nonthermal Br atoms sputtered from a KBr crystal at 140 °C. a) The distribution measured in a (010) plane of the (100) KBr crystal. b) The distribution measured in a (001) plane of the (110) KBr crystal. Due to Szymonski et al. (1991).

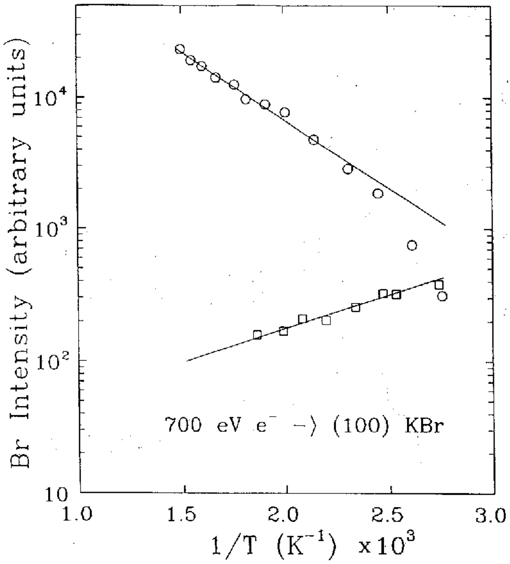

Figure 5. Arrhenius plot of the temperature dependence of the thermal (circles) and nonthermal (squares) yields of Br atom desorption from (100) KBr. The upper solid line was fitted to the experimental points above 160°C and has a slope corresponding to the activation energy of 0.19 eV. The lower line fits the nonthermal experimental points. Due to Kolodziej et al. (1992a).

and KCl crystals. The high temperature region activation energies (temperatures at which thermal sputtering dominates) were 0.07 eV and 0.12 eV for NaCl and KCl respectively. Low temperature values were much larger (0.29 and 0.27 eV, respectively) and they were interpreted as due to a partial surface metallization occurring at low temperatures. In contrast, the nonthermal component of the Br flux sputtered from KBr surface closely follows a straight line dependence on the Arrhenius plot (see fig. 5) but with a positive slope. The 'negative' activation energy in this case is 0.09 ± 0.02 eV (Kolodziej et al. 1992a).

The target temperature is not the only parameter determining the yield. In fig. 6 we present the energy dependence of the thermal and nonthermal partial yields for Br atom desorption from (100) KBr (Postawa et al., 1993a). The nonthermal signal increases steeply at low electron energies, reaches a maximum around 900 eV, and then drops. On the other hand, the thermal yield component at first decreases with the electron energy up to about 2.5 keV and then it starts to rise. A different behavior has been observed for Cl atom sputtering from a (100) NaCl sample, as presented in fig. 7. In this last case, the nonthermal component of the energy spectrum is not found and the dependence of the Cl atom yield on the electron

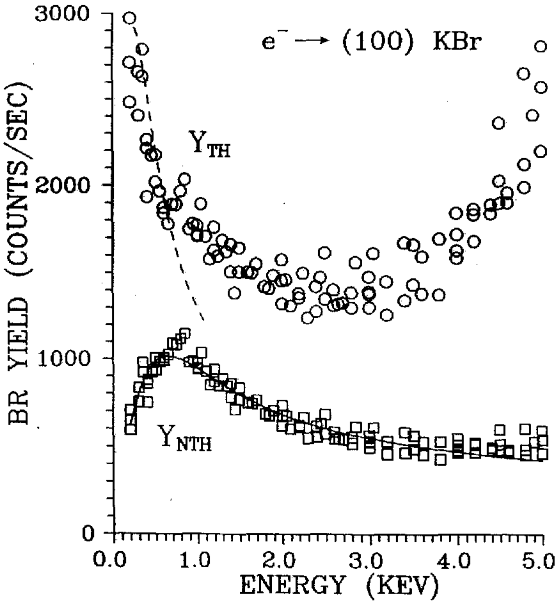

Figure 6. The dependence of thermal (circles) and nonthermal (squares) Br atoms sputtered from (100) KBr on the electron beam energy. The solid line was calculated theoretically as described in the text. Due to Postawa et al. (1993a).

beam energy is not pronounced. It is clear, however, that the character of this dependence changes with the target temperature.

Intense nonthermal emission has only been observed in some alkali halides, namely the chlorides, bromides and iodides of potassium and rubidium. In the other halides, either both the halogen and the alkali emission is thermal over the whole investigated temperature range, or a small contribution due to nonthermal halogen atoms is observed at room temperature (NaF and NaCl). A comparison of the relative yield ratio of the thermal component to the nonthermal one is shown in Table I (Kolodziej et al., 1992c). Since this ratio is strongly dependent on the sample temperature, the beam energy, and the electron current density, the numbers presented in Table I were obtained under exactly the same experimental conditions.

Recently, Kolodziej et al. (1992b) have been able to study the dependence of ES processes on the electron beam current density for the two velocity components of the sputtered flux. It appears that the yield of thermally emitted atoms decreases with an increase of electron current density, especially at low current densities (see

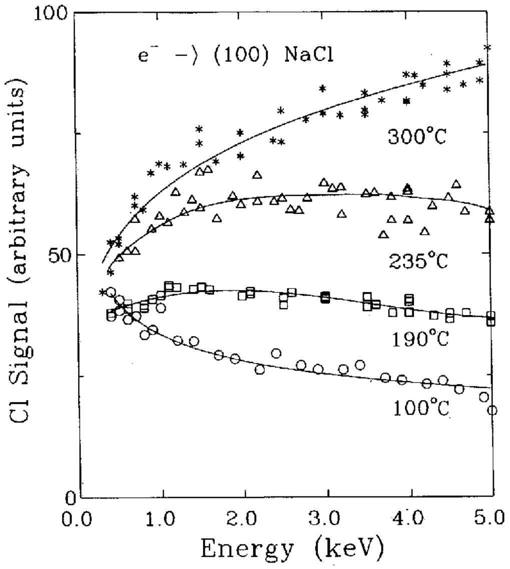

Figure 7. The dependence of the yield of Cl atoms desorbed from (100) NaCl on the primary electron energy at various surface temperature. Due to Postawa et al. (1993b).

fig. 8). The change in the nonthermal yield is negligible and within the experimental error that part can be considered as constant. The current density dependence of the thermal component indicates that electron sputtering measurements have to be performed under carefully controlled current density conditions. Unfortunately, many older experimental reports do not specify such conditions at all.

4 Thermal Desorption of the Alkali Component

The behavior of the complementary alkali component which is emitted appears to be different in character from that which has been seen for the halide. The angular distribution of K atoms for a (100) KCl at 140°C, shown in fig. 9, was easily fitted by a cosine dependence. There is no evidence of any preferential angular emission as there was for Cl. The same cosine-like angular distributions were observed for alkali atoms sputtered electronically from other alkali halides (Townsend et al., 1976; Szymonski et al., unpublished data).

The energy distributions for alkali atoms sputtered from single crystal alkali halides are always Maxwellian, eq. (1), as already reported by Szymonski et al. (1984). An example of such distributions obtained for a (100)NaCl at various

Table I. Comparison of yield ratio of nonthermal to thermal component for different alkali halides bombarded with a 1-keV electron beam at a surface temperature of 150°C.

Sample	Yield Ratio
KCl	0.37
KBr	0.67
KI	0.29
RbCl	0.49
RbBr	0.93
RbI	0.65

surface temperatures is reproduced in fig. 10 (from the work by Postawa et al. (1989)). These distributions are shown in a semi-logarithmic plot where $\Phi(E)$ is divided by E and presented as a function of E. In such a diagram, formula (1) is represented by a straight line with a slope determined by $1/T$. It can be seen that the energy distributions for sodium atoms shown in fig. 10 are purely thermal for all target temperatures. The shape of the distributions did not depend on the angle of observation. Temperatures obtained from a fit of formula (1) were equal to within 10% to the target temperature, measured with a thermocouple attached close to the sample surface. Measurements for single crystals generally agree with an earlier study for compressed powders by Overeijnder et al. (1978), except that Overeijnder had measured the thermal distribution as proportional to $\sqrt{E}$, rather than to E as in formula (1). It has been shown, however, that this observation of a $\sqrt{E}$ factor was caused by a technical problem with the slit width used in the time-of-flight spectrometer (Szymonski & de Vries, 1981). The Maxwellian energy distributions of alkali atoms emitted from electron bombarded alkali halides have also been confirmed using a Doppler-Shifted Laser-Induced Fluorescence (DSLIF) technique (Husinsky et al., 1988; Czuba et al., 1991). We would, therefore, conclude that the emission of alkali atoms must be due to thermal processes which take place after the electronic sputtering of halogen atoms occurs: the residual alkali ions left behind on the surface are neutralized and simply evaporate.

There have been several papers published in recent years reporting on alkali component emission from surfaces substantially modified by electron bombardment (Betz et al., 1990; Sarnthein et al., 1991; Seifert et al., 1991). These measurements were performed at relatively low sample temperatures, so that the alkali component could not balance the fast sputtering of halogen and accumulated in a form of islands, agglomerates and metal-like overlayers. A favorite sample for such a study was LiF since Li has the lowest vapor pressure of all alkalis. A closely related

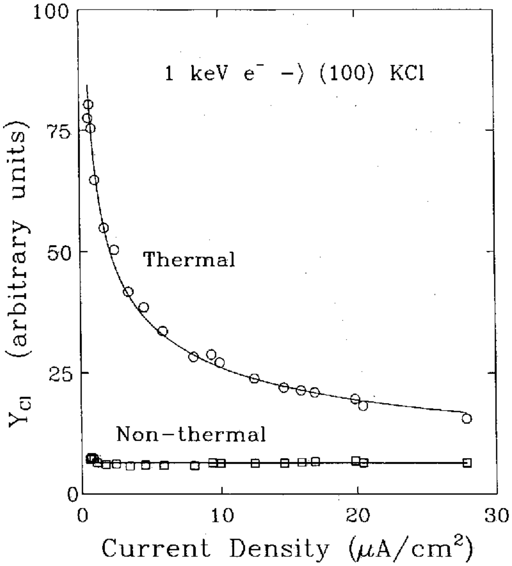

Figure 8. The dependence of thermal (circles) and nonthermal (squares) Cl atoms desorbed from (100) KCl on the electron beam current density. Due to Kolodziej et al. (1992b).

phenomenon seemed to be a delayed emission of alkali atoms from LiF (Green et al., 1987; Betz et al., 1990) and recently from KI (Brinciotti et al., 1993). Since this review is focused on the fundamental mechanisms of electronic sputtering which occur for stoichiometric, unperturbed crystals, topics related to alkali enrichment are not covered in detail.

5 Photon-Induced Sputtering of Alkali Halides

While electron-induced sputtering of alkali halides has been studied extensively over the past two decades, a review of the literature of photon-stimulated sputtering/desorption (PSD) does not reveal many experimental data. Parks and coworkers have observed desorption of positive halogen and alkali ions from a NaF crystal as the Na(1s) absorption edge was traversed in a synchrotron experiment and from LiF for photon energies near the F(2s) and Li(1s) edges (Parks et al., 1983 and 1984). The magnitudes of the positive-ion yields were rather small (3 ions per 10^8 photons absorbed) but the ion yield dependence on the X-ray energy closely resembled that of the total yield of secondary electrons generated by the same core-level excitations.

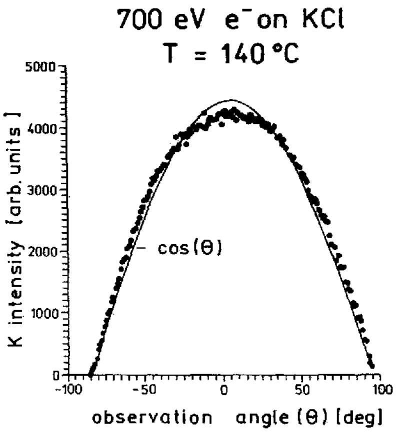

Figure 9. Angular distribution in a (010) plane of K atoms leaving a (100) surface of KCl at 140°C. The solid line represents a cosine function fitted to the experimental data.

There are only a few reports on PSD of neutrals from alkali halides, mostly due to valence excitations (Townsend & Elliott, 1969; Taglauer et al., 1986; Haglund et al., 1988). The early work on ground-state neutral sputtering yields reported that there was either no correspondence with the X-ray absorption spectrum or there was only a few percent enhancement in the yield of ground state Li atoms desorbed from LiF at the Li(1s) core excitation energy (Husinsky et al, 1988). The first systematic studies of PSD obtained by excitation of a KI single crystal in the fundamental absorption region up to 10 eV were performed by Brinciotti et al. (1991). They provided crucial information on the threshold excitation energies required for sputtering of neutral halogen atoms to occur. The results of their work are reproduced in fig. 11a,b. Al though we selected the halogen component data only, the dependences for the potassiu m component are essentially the same. We can clearly see an onset at about 5. 3 eV, followed by a band peaked at about 5.6 eV and dependent on the temperature. This structure can be related to the well-known optical absorption features of potassium iodide (Eby et al., 1959). The optical transition to the lowest excitonic state occurs at 5.6 eV at room temperature. The transition energy moves towards lower energies and broadens as the temperature increases. Thus, the band at 5.6 eV in the yield spectra of both K and I arise from the nonradiative decay of the exciton in its lowest excited state formed at those excitation energies. The subsequent slow increase in the yield spectra, starting at about 5.9 eV, can be correlated with the onset of the band-to-band fundamental absorption in potassium iodide. The photon absorption in this region produces

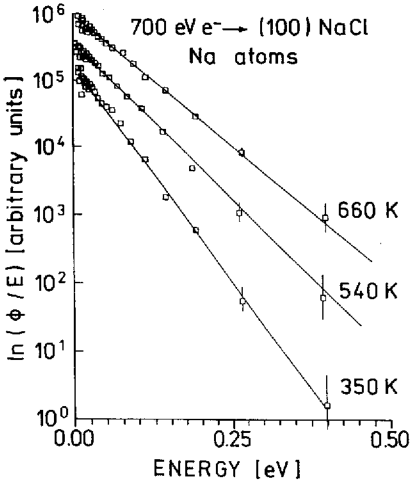

Figure 10. Energy distributions, $\Phi(E)$ divided by E, of Na atoms leaving a (100) NaCl target at three different target temperatures under bombardment of 700 eV electrons. A solid lines represent the best fits of the formula (1) to the experimental points. Temperatures measured with the thermocouple were 335 K, 525 K and 630 K respectively. Due to Postawa et al. (1989).

electron-hole pairs. Further increase of the excitation energy results in a fast rise in the desorption yield, due to transitions to higher excitonic and ionized states. The most important conclusion of this work is that the valence electronic excitation is sufficient for electronic sputtering of alkali halides. Since in the case of low energy electron bombardment these valence excitations are produced with the highest cross section, this type of energy loss process is therefore, the most important one for electron sputtering.

Sputtering of neutral sodium atoms from the (100) surface of single-crystal NaCl following Cl(1s) core-level excitation with synchrotron radiation has been observed by Szymonski et al., (1992). It was found that the bulk NaCl crystal shows significant sputtering at and above th e Cl K-edge, and that the dependence of the Na atom yield on X-ray energy has the same threshold and gross features as the total electron yield spectrum (see fig. 12). However, desorption from a 20 Å thick NaCl layer deposited on Si(100) could not be detected. This implies that accumulation of the decaying products of primary excitations over a considerable depth of bulk NaCl is required in order to account for the appreciable Na atom sputtering yield observed from the bulk crystal and the absence of any Na atom desorption from the thin film. Furthermore, the temperature dependence observed in this experiment suggests that the final steps in the Na sputtering process are

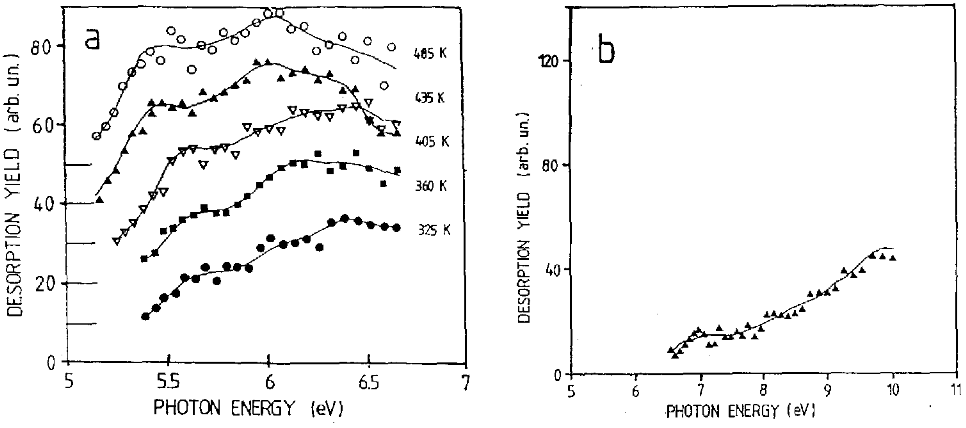

Figure 11. Desorption yield of iodine atoms emitted from (100)KI as a function of exciting photon energy. a) Measured at different sample temperatures in the 5.2 - 6.7 eV photon energy range. b) Measured at 393 K in the 6.5 - 10 photon energy range. Due to Brinciotti et al. (1991).

very similar to those occurring in electron bombarded alkali halides. It is very plausible, therefore, that even at these high photon energies the sputtering process is driven by valence electron-hole pairs created by fast secondary electrons from photoexcitation and Auger decay of the primary core-excitons.

There is still another very recent, important experiment on photon-stimulated ejection of atoms from alkali halide nanocrystals (Li et al., 1992). Interband excitation of single alkali halide nanocrystals, in the form of mass-selected $M_{n\pm1}X_n^{\pm}$ beams (M = K, Cs and X = Br, I), by ultraviolet radiation leads exclusively to halogen-atom emission with a large cross section. Beyond the cross section, it was significant that the halogen-emission process was certainly not the lowest energy fragmentation channel and that it could not be observed in thermally activated clusters (Hwang et al., 1990).

6 Current Views on the Mechanisms of Electronic Sputtering

6.1 Primary Excitations in Alkali Halides

As I have already mentioned, electrons incident on crystalline alkali halides create excitons and electron-hole pairs. In fact the most important electronic transitions leading to these excitations are from the valence band (formed by outermost p-

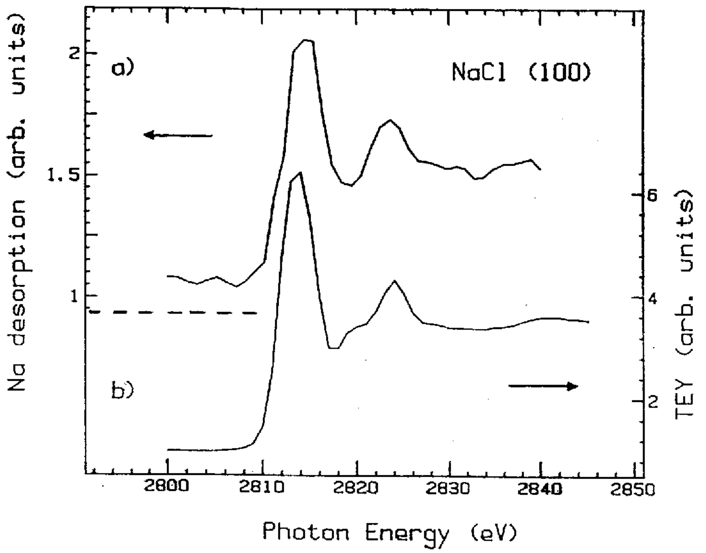

Figure 12. Synchrotron radiation in the energy region of the Cl K-edge interacting with a NaCl(100) crystal kept at 430 K. a) Na atom signal from a quadrupole mass spectrometer is plotted against photon energy. The dashed line indicates the background level of Na atom signal. b) Total electron yield spectrum. Due to Szymonski et al. (1992b).

type electrons of halogen atoms) to the conduction band of the crystal (Brinciotti et al., 1991). The resulting electrons and holes are free to move in the crystal; they also can form coulombically bound pairs, the excitons. Direct transitions to such excitonic states within the band gap are also possible.

A valence hole in an alkali halide quickly localizes (self-traps) on a covalently bonded pair of lattice halide ions, where the binding is induced by the hole's occupancy of an antibonding orbital (Williams & Song, 1990). The two bonded halide ions relax toward each other symmetrically along <110> in NaCl-type alkali halides (Kabler, 1972). A self-trapped exciton results when an electron becomes bound to the site of the self-trapped hole or so called V_k center (Song & Williams, 1993). Such self-trapping occurs on a sub-picosecond time-scale (Williams, 1989). The STEs can decay, with the emission of polarized light. This decay scheme appears to dominate at low temperatures (Kabler, 1964).

According to Pooley (1966) and Hersh (1966) the lowest state of the STE can decay nonradiatively forming a pair of separated Frenkel defects, i.e. an electron trapped in the halogen vacancy (an F-center) and an interstitial halogen atom (H-center) that is removed by a chain of replacement collisions along the <110>

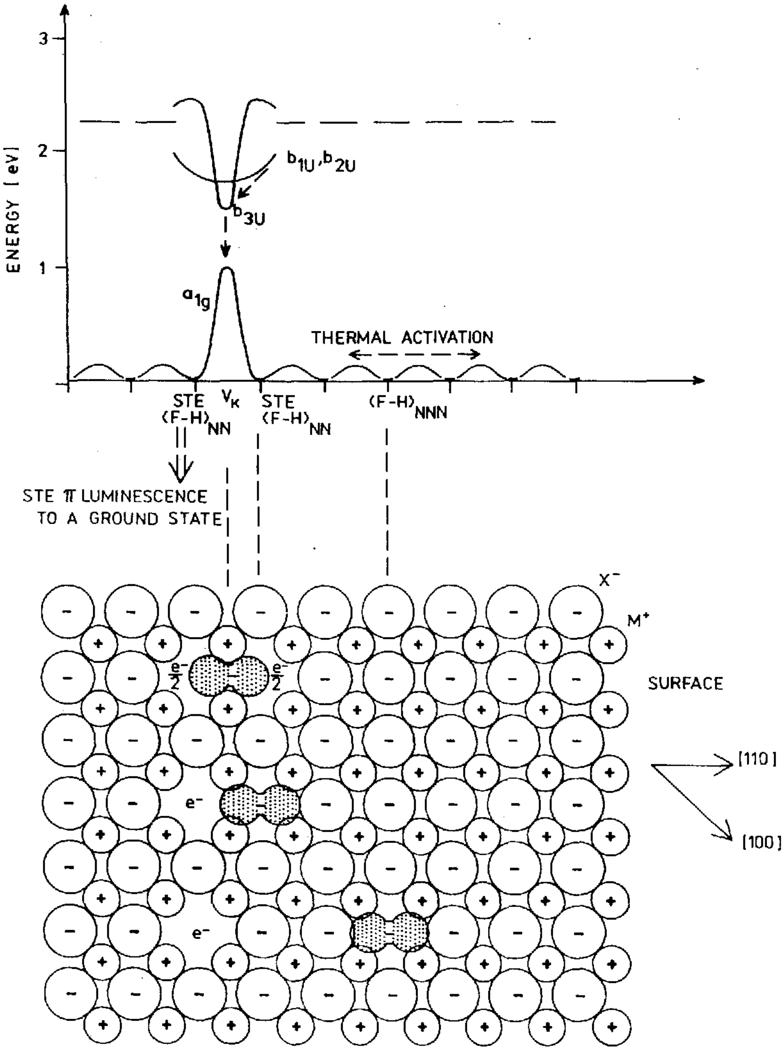

Figure 13. The change of the lattice energy relative to the perfect lattice of KCl versus the translational coordinate along the <110> axis. The STE states are designated by the electron orbitals. In the lower part of the figure, pictorial representations of lattice configurations for the 'on-center' and 'of-center' STE and F-H pair in a next nearest-neighbor position are shown. Due to Williams et al. (1986).

axis of the crystal. More recently Williams (1989) has distinguished two types of F-H pair production: a diffusive, thermally activated process and a dynamic one. The diffusive channel starts from the lowest STE electronic state which is unstable against a shift along the <110> axis to an 'off-center' equilibrium position. The adiabatic potential energy diagram (Williams et al., 1986) is shown in fig. 13. It is seen that the F- and H-center separation can occur by thermally-assisted diffusion of a halogen atom out of the relaxed STE in its lowest, π-luminescent state. Thermally activated motion of the halogen can also cause a recombination of the F-H pair into the STE with the subsequent emission of a π-luminescence photon (Szymonski, 1990). Consequently, the probability for achieving a sufficient separation of the F and H center so that they would not be able to recombine by competing processes is increasing with the sample temperature.

In the dynamic process, the energy for F-H pair formation and separation is derived from the energy of higher electronic states of the STE (Itoh & Saidoh, 1973; Williams et al., 1986). As indicated in fig. 13, the STE, relaxing through these higher levels, should cross into the lowest a_{1g} potential surface near the configuration with 'on-center' (V_k -like) symmetry. Since the a_{1g} surface at this point is unstable, the H center may be ejected at sufficient velocity to continue on for several lattice spacings along <110> direction of the crystal before thermalizing (Williams et al., 1986). The proposed mechanism of the dynamic F-H center pair formation is constrained to those specific crystals for which the energy drop associated with translation of the H-center along <110> from the 'on-center' position is relatively high allowing for stable F-H separation (Williams, 1989).

6.2 Nonthermal Emission of Halogen Atoms

Townsend et al. (Elliott & Townsend, 1971; Townsend et al., 1976) suggested that the Pooley-Hersh (PH) model could be used to describe ES processes in alkali halides. Should the STE decay within the range of the replacement collision sequence below the surface, hyperthermal halogen atoms could be ejected at the expense of the energy stored in the STE. Since then many modifications to the Pooley model have been made. Perhaps the most significant alteration suggests that the energy for dynamic F-H pair formation and for separation by the <110> focused replacement sequence is derived from the energy of higher excitonic states of the STE (Williams et al., 1986). A schematic visualization of the PH model is given in fig. 14. Because of the geometric orientation of the STE, the H center, and the direction of the halogen replacement collision sequence, all of which are oriented along the <110> direction, the hyperthermal halogen species would be preferentially ejected from the surface along this <110> direction. This is in contrast to recent observations (see section 3). For instance, it is clearly visible in

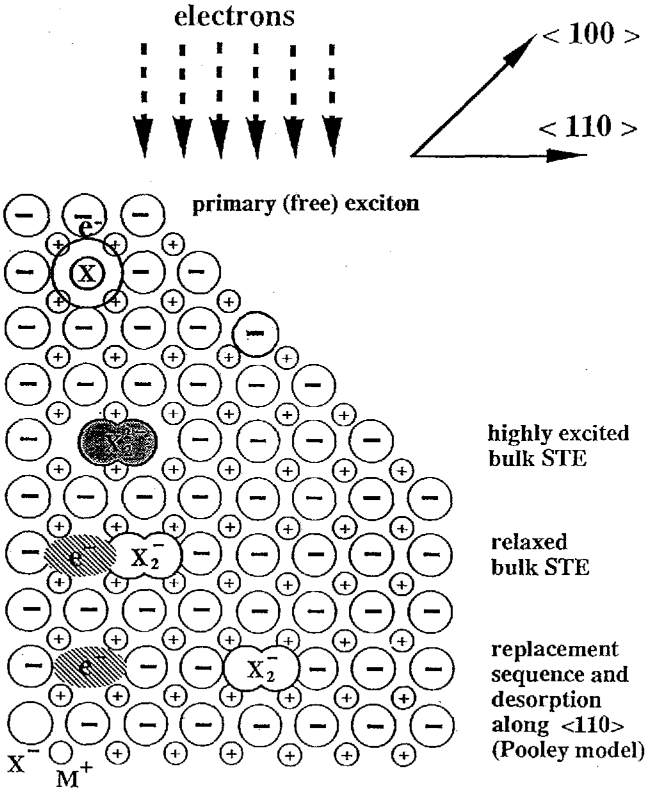

Figure 14. A schematic view of the lattice excitations in alkali halides leading to desorption via the focused replacement sequences (Pooley-Hersh model). X denotes a halogen and M an alkali atom.

fig. 4 that non-thermal Br atoms are predominantly emitted from both the (100) and the (110) surfaces of KBr crystal, along the <100> crystallographic axis.

This and other experimental findings described in the previous subsection clearly contradict the predictions of the PH model and indicate the need for a new theoretical approach to explain the nonthermal emission from alkali halides. Any new model should address the following observations:

- Nonthermal halogen atoms are emitted with a well-defined energy spectrum (not broadened at the low-energy side) in the range between 0.1 - 1 eV. The lack of broadening suggests that the nonthermal atoms are emitted from the surface directly. If they have to migrate from inside of the crystal, the energy spectrum should reflect energy loss processes encountered in this migration.

- Emission is strongly collimated along the <100> direction of the crystal.
- The yield of hyperthermal atoms is relatively large, suggesting that electronic excitation from considerable depths of the solid must be contributing to this emission. Therefore, an efficient transport of this excitation energy from the bulk to the surface is required.
- The nonthermal halogen flux has been found to decrease slowly with increasing temperature of the sample.
- The yield of nonthermal emission has a well-defined maximum for primary electron energy equal to about 1 keV (in KBr).

In recent publications a new model has been proposed (Szymonski et al., 1991, 1992) which is based on the concept of excited, 'hot', conduction electron - valence hole pairs created within the penetration range of the incident electrons (Elango et al., 1976; Kadchenko & Elango, 1978; Green et al., 1990). Hot holes could be created in the valence band of alkali halides with a rather wide distribution of initial kinetic energies, corresponding to the valence band density of states (Elango et al., 1976). For example, in KBr the width of the valence band is about 2.6 eV (Kowalczyk et al., 1974) so that, on average, the holes could have as much as 1.3 eV excess energy. This high initial energy acquired in primary excitation makes the hot holes very mobile: they can migrate over distances of several hundred Å, thus providing very efficient transport of the energy deposited in the bulk of the crystal to the surface. The diffusion of holes has been described by Reimann et al. (1988) in relation to electronically stimulated desorption of rare gas solids. Postawa et al. (1993a) have used essentially the same formalism and solved the following diffusion equation:

$$D_+ d^2 n_+ / dx^2 - n_+ / \tau_+ + I_0 H_+ = 0, \tag{2}$$

where $n_+(x)$ is the hole density radially and temporally averaged over many incident electron trajectories, D_+ is the diffusion coefficient of holes, and τ_+ is the trapping lifetime of a hole. The source function of holes, $I_0 H_+(x)$, can be approximated using the model of Al Jammal & Townsend (1973) for the depth distribution of the deposited energy, $H(x)$ (see fig. 15a). I_0 is the flux of incident electrons. The hole diffusion length is given by $L^2 = D_+ \tau_+$. With the help of the above equation one can transform the profile of the primary deposited energy, $H(x)$, into the depth distribution of the hot holes (see fig. 15b). It has been shown by Postawa et al. (1993a) that the best agreement between the experimental results for KBr and the model calculations can be obtained if $L = 100$Å. The value of L is not affected

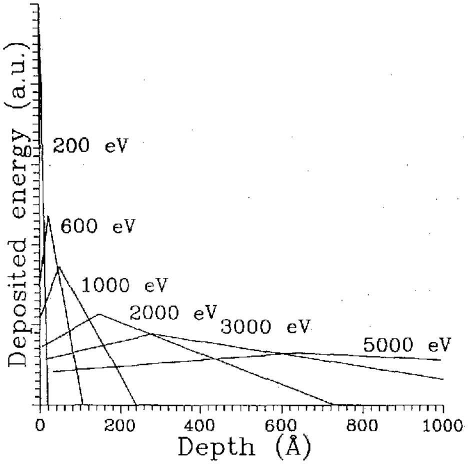

Figure 15a. The depth distribution of energy deposited in the (100) KBr crystal by different energy primary electrons. The distribution function $H(x)$ was calculated as proposed by Al Jammal & Townsend (1973) with the total electron range values taken from Bronstein & Procenko (1970).

by the state of the surface, i.e. whether the surface is reflecting or absorbing. The absolute sputtering yield, however, is strongly dependent on the surface reflectivity. The solid line in fig. 6 represents the result of the model calculations for $L = 100$Å and a totally absorbing surface, i.e. every electron-hole pair arriving at the surface could potentially lead to emission of a nonthermal halogen atom.

The final precursor state at the surface responsible for this emission is not known yet with any certainty. Szymonski et al. (1991) postulated that the hot hole arriving at the surface can be transiently localized at a surface halogen ion (within a fraction of a vibrational period). Such a suddenly-neutralized halogen ion would find itself in the repulsive potential of neighboring alkali ions and it would perhaps be ejected with hyperthermal energy. In order to understand the nature of this repulsive interaction we make the following consideration. The most commonly used potential for halides is the one due to Rittner (1951) who, starting from classical arguments, proposed that the interaction energy between the ions M^+ and X^- of an alkali halide is given by (all in atomic units):

$$V(R) = Ae^{-aR} - \frac{1}{R} - \frac{\alpha_+ + \alpha_-}{R^4} - \frac{2\alpha_+\alpha_-}{R^7} - \frac{C_6}{R^6}, \tag{3}$$

where α_+ and α_- are the polarizabilities of the positive and the negative ions. Here, the first term represents the short range Born-Mayer type repulsion energy, with adjustable parameters A and a. The second term is the Coulomb attraction

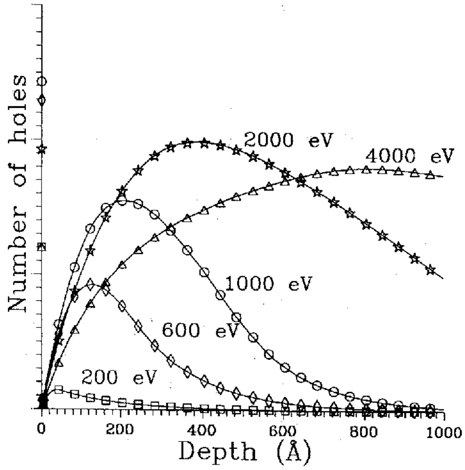

Figure 15b. Same as fig. 15a. Depth distributions of holes calculated from the solution of eq. (2) for a totally absorbing surface and with the diffusion length L = 100 Å.

between the two ionic charges. The third term gives the interaction between the charge of one ion and the induced dipole moment of the other ion, while the fourth term provides the interaction between the two induced dipoles. The last term is the dispersion force, in which the van der Waals coefficient C_6 can be obtained by standard techniques. A detailed discussion and further refinement of equation (3) is given by Patil (Patil, 1987). Neutralization of a surface halogen ion by a suddenly-arriving hole would result in cancellation of the attractive term $-1/R$. Consequently, the surface halogen ion + hole complex could experience a repulsive, short-range potential initiating the ejection. In fact, molecular-dynamics calculations by Green et al. (1989) have shown that the net potential of a neutral F atom approaching an alkali cation at the (100) NaF surface is positive for distances equal to or smaller than the anion-cation distance of the regular NaF lattice; thus the interaction is repulsive. For ionic NaCl-type surfaces, the surface halogen's five nearest alkali neighbors (four in the plane of the surface and one below the surface halogen) are all positive ions. The net initial repulsive force would then be directed between the sub-surface alkali ion and the surface halogen (see fig. 16); this direction is along the <100> axis and is consistent with the nonthermal emission observed.

At larger M^+-X^0 distances, however, the long-range forces related to multipolar polarizabilities of the halogen atom by the neighboring surface ions start to dominate over the short range repulsion. The resulting interaction is attractive and the

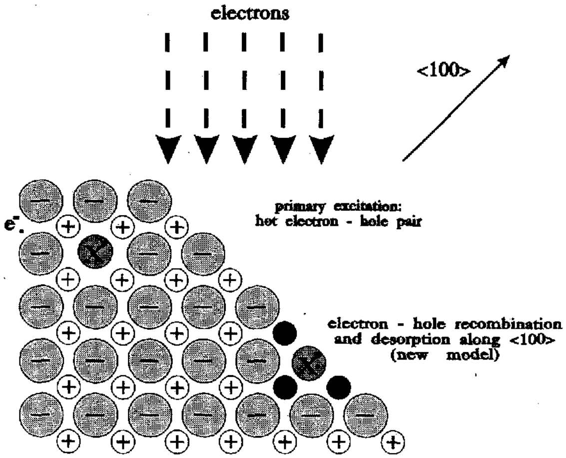

Figure 16. A schematic view of the new model proposed for explanation of ES of energetic halogen atoms. Hot electron-hole pairs created in the bulk of the crystal can diffuse and recombine at the surface. The surface halogen ejection is initiated by the repulsive interaction between the surface halogen, neutralized by the arriving hole and the neighboring alkali ions sharing an extra electron.

atom can be bound above the surface (Green et al., 1989). It has been pointed out by Itoh (Itoh, 1992) that the energy acquired due to short-range repulsion among the alkali ions and the halogen atom alone is not sufficient to overcome the long-range attraction. Also Song & Chen (Song & Chen, 1993), in a very recent theoretical work concluded that no halogen atom escape could be obtained when only the hole was present on the surface. The situation might be quite different, however, if we realize that the primary excitation process produces electron-hole pairs rather than isolated holes. It is likely, therefore, that the hole arriving at the surface halogen site is surrounded by a delocalized electron charge shared by the neighboring alkali ions. Partial neutralization of these ions should reduce the attractive forces preventing the halogen from ejection, initially driven by the short range repulsion between X^0 and M^+. Furthermore, the surrounding lattice and the electron may transform into the F-center configuration facilitating the final desorption of nonthermal X^0.

Essentially the same surface ejection mechanism has been proposed recently by Li et al. (1992) in order to explain photon-stimulated ejection of halogen atoms from alkali-halide nanocrystals. The emission process was illustrated on the calculated potential energy diagram reproduced in fig. 17. The repulsion following the vertical excitation process (due to UV-photon irradiation in that work) results in

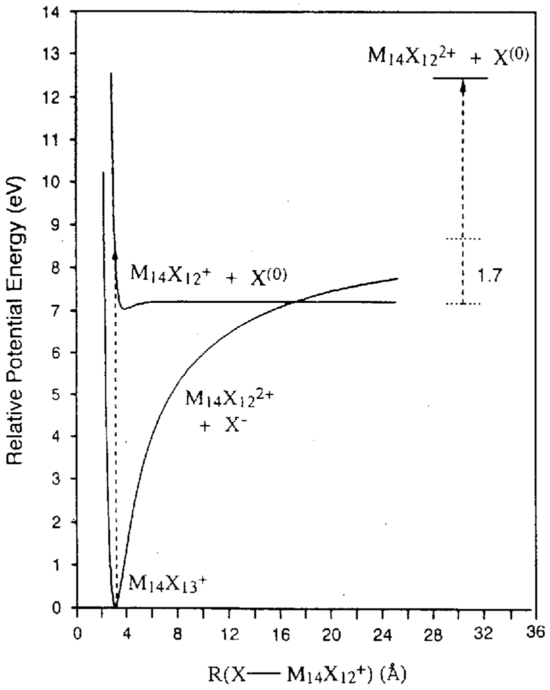

Figure 17. The relative potential energy curves for the halogen atom emission from the surface of the cubic $M_{14}X_{13}^{+}$ cluster. (The energy and distance axes are appropriate for the homolog M=Na, X=F and so must be scaled for KBr or other halides). The ionic curve (lower) is a Born-Mayer potential and the neutral curve for $X^{(0)}$ loss (upper) is a Lennard-Jones 6-12 potential fitted to asymptotic energies for $M_{14}X_{13}^{+}$, $M_{14}X_{12}^{2+}$ and $M_{14}X_{12}^{+}$. The asymptotic difference is 1.7 eV. Due to Li et al. (1992).

a gain in kinetic energy of about 1 eV for the neutral halogen which is sufficient to overcome the weaker attractive interactions. At long distance, where the neutral surface meets the ionic surface (see fig. 17) a (non)crossing occurs allowing for further separation along the neutral surface, if the velocity of the ejected atoms is sufficiently high (Li et al., 1992). Simultaneously, the neighboring cations and the electron relax into the F-center geometry. At reduced velocity, the trajectory may cross to the ionic surface, leading to recombination of an electron-hole pair and relaxation.

Lately, Puchin et al., (1992) have performed theoretical studies of atomic emission caused by electronic excitation at the (100) surface of NaCl. In particular, they calculated adiabatic potential energy surfaces (APES) that described the relaxation of the lowest triplet excited state and the ground (singlet) state of the electron-hole pair localized on the Cl site in the top surface layer. The excited state consist of a hole localized on the Cl p-orbital and an electron distributed over the nearest cations and outermost (diffuse) s-orbital of Cl. This situation is quite similar to the one treated by Li et al. and shown in fig. 17. Thus, Puchin et al. (1992) confirmed that an electron-hole pair localized on a surface halogen can lead to the prompt ejection of a nonthermal halogen atom.

It is the personal opinion of the present author that surface electron-hole recombination with direct ejection of the nonthermal halogen atom along the <100>, such as described by Li et al. (1992) and Puchin et al. (1993), represents the most plausible scenario for the final surface step in ES of nonthermal halogen.

In the same work Puchin et al. (1993) have also calculated the APES for an H-center near the surface as a function of its distance from the top surface layer. It has been shown that the H-center approaching the surface tends to be oriented along a direction which is only about 20° ±10° away from the <100> direction perpendicular to the surface. This is in contrast to the bulk orientation of the H-center which is along the <110> axis. The reoriented surface H-center can decompose into a halogen ion on the lattice site and an emitted Cl atom. However, it has been found that there is no stable relaxed atomic configuration corresponding to the self-trapped exciton located in the first two layers of the surface. Puchin et al. postulated, therefore, that the self-trapped excitons formed below the surface can decay producing H-centers which subsequently become reoriented towards the <100> and decomposed with emission of energetic halogen atoms.

Very similar results have been obtained recently by Song & Chen (1993) for the potential energy surface of the STE created on and near the (100) surface in NaBr, KBr and RbBr. In all three samples the energetic halogen desorption is described as due to the STE instability. A resulting neutral halogen atom is driven toward the surface with about 1 eV energy along <110> initially. Near the surface, the ejected atom starts to reorient along <100> axis as described above.

We note at this point very recent, important experiments by Meise et al. (1993). These authors have shown that in KBr, at 4 K, the dynamically created F-H pairs are the 4th nearest neighbours. This effectively means that the kinetic energy, derived from the STE instability, is used up after about 4 anion separations along <110>. If the maximum energy available initially is about 1 eV, the minimum energy to continue the replacement sequence is about 0.1 eV. Thus, according to Song and Chen (1993), the expected energies of dynamically emitted halogen range from 1.0 eV to 0.1 eV, depending on the place of origin of the STEs. This expectation is compatible with the experimental data (Kolodziej et al., 1992a).

6.3 Thermally Assisted Desorption of Halogens

Nonradiative decay of the STEs in near-surface layers or deeper in the crystal will form pairs of separated F and H centers as described in subsection 6.1. At temperatures of interest for this paper, H-centers can migrate inside the crystal, arrive at the surface and desorb thermally as proposed by the present author (Szymonski, 1980). The rate of the process should increase with temperature. Halogens that diffuse to the surface and evaporate would come off with a cosine-like angular distribution.

At room temperature, the H-centers are known to form interstitial aggregates, as was recently observed for iodides (Allen & Comins, 1990 and 1992). At elevated temperatures there will be a temperature-dependent competition between coagulation and free diffusion of interstitials. We believe that our observation of the thermal Br signal, which does not follow a single rate equation but sharply increases in the temperature range below 160 °C (see right hand side of fig. 5) may reflect the temperature dependent enhancement of the number of interstitial halogen atoms (H-centers) available for diffusion towards the surface. Only above 160°C does the diffusive mechanism dominate over the coagulation and the desorption of thermal Br then follows an Arrhenius dependence. At this high temperature limit, the yield of desorbing Br can be described by (Kelly, 1979):

$$S_{\mathrm{th}} \cong \frac{E_0}{E^*} C_{\mathrm{H}}^{\mathrm{diff}}(0) \lambda_{\mathrm{th}}, \tag{4}$$

where E is the incident electron energy, E^* is the energy consumed per created interstitial halogen atom, λ_{th} is the diffusion range and $C_{\mathrm{H}}^{\mathrm{diff}}(0)$ is the spatial distribution of the interstitial halogen atoms prior to diffusion, which is assumed to be uniform over a range much larger then λ_{th} . For thermally activated motion the diffusion range depends exponentially on 1/T. From the least- squares fit to the upper part of such dependence in fig. 5 it appears that the activation energy for this motion equals to 0.19 eV. This value is considerably higher than the activation energies for translation and rotation of an isolated H-center in KBr which are known to be 0.09 eV and 0.037 eV (Bachman & Kanzig, 1968; Dienes & Smoluchowski, 1976).

The yield of thermally emitted halogen atoms depends not only on the diffusion range of the interstitial halogen atoms but also on the depth of deposited energy. At low electron energies, the penetration of primary projectiles is usually smaller than the mean migration range of H centers. In this limit, the number of emitted halogens should increase with the energy of the incident electrons because more and more energy is deposited in the volume of the crystal contributing to the desorption. However, once the migration range of H centers is exceeded, the fraction of the primary electron energy deposited in the 'active' subsurface region will decrease and the desorption yield should drop. Such behavior is indeed visible in our data at low temperatures. Moreover, since the mean diffusion range increases with the target temperature, the maximum in the yield-energy dependence shifts toward higher energies. This is reflected in the the energy dependent curves taken at high surface temperatures (upper part of fig. 7).

As seen in fig. 8 the yield of thermal halogen atoms decreases with the current density, especially at low currents. It is plausible that the range of diffusing interstitial halogen can be reduced in a crystal damaged by high current density electron irradiation. The density of the created defects, such as vacancies, dislocations, etc. should increase with the current density and consequently cause a quenching of the halogen diffusion. The coagulation of the H-centers into interstitial aggregates should also be strongly current density dependent, particularly at low temperatures. This effect could further reduce the fraction of interstitial halogen atoms able to diffuse to the surface under high current density conditions. This interesting phenomenon needs further experimental investigations.

6.4 Thermal Desorption of Alkali Atoms

Since the electronic transitions lead to the selective desorption of halogen atoms, the alkali component should simply evaporate thermally from the halogen-deficient surface, provided that the remaining alkali ions will be efficiently neutralized and the alkali vapor pressure at the sample temperature is sufficiently high. The expected angular distribution in this case is cosine-like.

The problem of charge neutralization of originally positive alkali ions in the altered surface layers was discussed by Green et al. (1987). It has been suggested that the F-centers must diffuse from their place of origin to the surface, neutralizing metal atoms, which then may thermally desorb. The authors argued that this model could explain the considerable delays in emission of ground state alkali atoms as observed experimentally for LiF crystal by Loubriel et al. (1986). In general, the F-centers are rather immobile compared to H-centers, but they might be created much closer to the surface than was previously thought (see subsection 6.2). In addition, Puchin et al. (1993) in their theoretical work, calculated that a ground state F-center arriving at the surface cannot cause emission of the neighboring alkali atom. The same conclusion holds for two F-centers formed at the surface by diffusion. Instead, it is suggested that formation of the F-center clusters and/or alkali metal clusters in the near-surface layers might be required to explain the delayed alkali emission. On the other hand, it should be noted that electronic sputtering of alkali halides at sufficiently elevated temperatures and low-to-moderate electron current densities results in stoichiometric emission of both alkali and halogen components (Szymonski et al., 1992).

Until now, there has been no experimental evidence that alkali atoms could be emitted from electron bombarded alkali halide surfaces with nonthermal energies. This indicates that emission processes based on Coulomb repulsion of positive ions created by Auger de-excitation of core-level excitons (Feibelman & Knotek, 1978; Knotek & Feibelman, 1978) or alkali atom emission due to its interaction with an excited F-center at the surface (Puchin et al., 1993) does not contribute significantly to electronic sputtering from surfaces of alkali halides.

7 Concluding Remarks

Electronic sputtering of alkali halides has been studied experimentally and theoretically for several decades. A careful analysis of the experimental data accumulated over the years allows the following conclusions:

- The flux of sputtered particles consists mainly of alkali and halogen atoms in their electronic ground states. Emission of halogen neutral dimers, positive and negative ions as well as excited alkali atoms has also been reported but amounts to only a small fraction of the sputtered flux and has not been discussed in the present review.

- Photon-induced-sputtering experiments have shown that the valence electronic excitations are most important for emission of halogen and alkali neutrals.

- A significant fraction of the halogen atom emission from electron-sputtered surfaces of chlorides, bromides and iodides of potassium and rubidium has a nonthermal spectrum of translational energies (in the energy range 0.1 - 1.0 eV). A remaining part of the halogen atoms and all alkali atoms evaporate from the surface with a Maxwellian spectrum of kinetic energies characterized by the macroscopic surface temperature. The emission of neutrals from alkali halides other than those listed above was only thermal, except NaCl and NaF at the room temperature where some indications of small nonthermal emission were registered.

- The nonthermal halogen atoms are ejected from the surface preferentially along the <100> crystallographic directions.

- Electronic sputtering yields of alkali halides are of the order of 1-10 per incident electron of 1 keV energy. Since the total range of such electrons is of the order of 100 nm, an efficient, long range transport mechanism of the deposited energy from the bulk to the surface is required. It has been shown that fast hot-hole diffusion can supply a significant fraction of the electron-hole excitations to the near-surface layers. Such a large number of surface excitations is necessary in order to explain the high sputtering yields.

- A new model has been discussed for the ejection of energetic halogen atoms. This model is based on recombination of the electron-hole pair, transiently localized on the surface halogen ion, with direct ejection of the nonthermal halogen atom along the <100> direction of the crystal. The model is supported by the results of recent cluster calculations and is consistent with current experimental observations. Alternatively, a model based on near-surface ejection of an H-center due to the STE instability, reoriented at the surface along the <100> prior to emission, has been proposed.
- The emission of thermal halogen atoms is consistent with a model in which interstitial halogen atoms and/or aggregates are produced in the bulk of the crystal from decaying self-trapped excitons. Subsequently, halogen interstitial atoms can diffuse thermally to the surface and then evaporate.
- The origin of the alkali atom component can be described by the neutralization and subsequent thermal evaporation of excess alkali atoms from the halogen deficient surface.

Acknowledgements

Many of the experimental results presented in this paper were obtained in a very pleasant collaboration with P. Czuba, J. Kolodziej, P. Piatkowski, A. Poradzisz and Z. Postawa from my group at the Jagellonian University, and J. Fine, V. Kempter, and N. Tolk. Many fruitful discussions with G. Betz, N. Itoh, V. Puchin, A. Shluger, K.S. Song and R. Williams, on basic mechanisms of alkali halide sputtering, are gratefully acknowledged. The financial support for this work was provided by the Polish Committee for Scientific Research under Contract No. BP 2603.

References

Al Jammal Y, Pooley D and Townsend, PD, 1973: J. Phys. C.: Solid State Phys. **6**, 247
Allen AMT and Comins JD, 1990: Nucl. Instr. Meth. B **46** 240
Allen AMT and Comins JD, 1992: J. Phys. Condens. Matter. 4, 2701
Ascolani H, Guraya MM and Zampieri G, 1991: Phys. Rev. B **43**, 5135
Bachmann K and Kanzig W, 1968: Phys. Kondens. Mater. **7**, 284
Betz G, Sarnthein J, Wurz P and Husinsky W, 1990: Nucl. Instr. Meth. B. **48**, 593
Brinciotti A and Piacentini M, 1992: private communication
Brinciotti A, Zema N and Piacentini M, 1991: Radiat. Eff. Def. Sol. **119-121**, 559

Brinciotti A, Piacentini M and Zema N, 1993: Int. Workshop on *Electronic Excitations at Surfaces of Halides*, Book of Abstracts, Krakow, to be published in Rad. Eff. Def. Sol.

Bronshteyn IM and Protsenko N, 1970: Radio Eng. Electron. Phys. **15**, 677

Cota Araiza LS and Powell BD, 1975: Surf. Sci. **51**, 504

Crawford JH, 1968: Adv. Phys. **17**, 93

Dienes GJ and Smoluchowski R, 1976: J. Phys. Chem. Solids **37**, 95

Dou Q and Lynch DW, 1992: To be published

Eby JE, Teegarden KJ and Dutton DB, 1959: Phys. Rev. **116**, 1099

Egelhoff WF, 1987: Phys. Rev. Lett. **59**, 559

Elango MA, Kadchenko VN, Saar AM and Zhurakovski AP, 1976: J. Luminescence **14**, 375

Elliott DJ and Townsend PD, 1971: Phil. Mag. **23**, 249

Feibelman PJ and Knotek ML, Phys. Rev. B. **18**, 6531

Friedenberg A, Shapira Y, 1979: Surf. Sci. **87**, 581

Green TA, Loubriel GM, Richards PM, Tolk NH and Haglund RF, Jr, 1987: Phys. Rev. B **35**, 781

Green TA, Riley ME and Coltrin ME, 1989: Phys. Rev. B **39**, 5397

Green TA, Loubriel GM, Richards PM, Hudson LT, Savundararaj PM, Albridge RG, Barnes AV and Tolk NH, 1990: in *Desorption Induced by Electronic Transitions*, ed. by G. Betz and P. Varga (Springer, Berlin) 281

Haglund RF Jr, Mendenhall MH, Tolk NH, Betz G and Husinsky W, 1988: Nucl. Instr. Meth. B **32**, 321

Hersh HN, 1966: Phys. Rev. **148**, 928

Husinsky W, Wurz P, Mader K, Wolfrum E, Strehl B, Betz G, Haglund RF Jr, Barnes AV and Tolk NH, 1988: Nucl. Instr. Meth. B **33**, 824

Hwang H-J, Sensharma DK and El-Sayed MA, 1990: Phys. Rev. Lett. **64**, 808

Itoh N, 1992: private communication

Itoh N and Tanimura K, 1990: J. Phys. Chem. Sol. **51**, 717

Kabler MN, 1964: Phys. Rev. **136**, A 1296

Kabler MN, 1972: in *Point Defects in Solids*, eds. Crawford JH, and Slifkin LM, Plenum, New York, vol. 1, chap. 6

Kadchenko VN and Elango M, 1978: Phys. Stat. Sol. a **46**, 315

Kelly R, 1979: Surf. Sci. **90**, 280

Kim YS and Gordon RG, 1974: J. Chem. Phys. **60**, 4332

Knotek ML and Feibelman PJ, 1978: Phys. Rev. Lett. **40**, 964

Kolodziej J, Czuba P, Piatkowski P, Poradzisz A, Postawa Z, Szymonski M and Fine J, 1992a: Nucl. Instr. Methods B **65**, 507

Kolodziej J, Czuba P, Kempter V, Piatkowski P, Postawa Z and Szymonski M, 1992b: Vacuum, in press

Levine JL and Mark P, 1966: Phys. Rev. **144**, 751

Li X, Beck RD and Whetten RL, 1992: Phys. Rev. Lett. **68**, 3420

Loubriel GM, Green TA, Richards PM, Tolk NH, Albridge RH, Haglund RF, Snowdon KJ, Hudson LT, Cherry DW, Cole RK, Mendenhall MH, Newns DM and Savundararaj PM, 1986: Phys. Rev. Lett. **57**, 1781

Marklund I and Andersson S, 1966: Surf. Sci. **5**, 197

Meise W, Rogulis U, Koschnick FK and Spaeth J-M, 1993: in *ICDIM-92*, Book of Abstracts, Nordkirchen, to be published in Proc. by World Scientific

Mentzel D and Gomer R, 1964: J. Chem. Phys. **41**, 3311

Overeijnder H, Szymonski M, Haring A and de Vries AE, 1978 a: Radiat. Eff. **36**, 63

Overeijnder H, Szymonski M, Haring A and de Vries AE, 1978 b: Radiat. Eff. **38**, 21

Palmberg PW and Rhodin TN, 1968: J. Phys. Chem. Sol. **29**, 1917

Parks CC, Hussain Z, Shirley DA, Knotek ML, Loubriel G and Rosenberg RA, 1983: Phys. Rev. B **28**, 4793

Parks CC, Shirley DA and Loubriel G, 1984: Phys. Rev. B **29**, 4709

Patil SH, 1986: J. Chem. Phys. **86**, 313

Pooley D, 1966: Proc. Phys. Soc. **87**, 245

Postawa Z and Szymonski M, 1989: Phys. Rev. B **39**, 12950

Postawa Z, Czuba P, Poradzisz A and Szymonski M, 1989: Radiat. Eff. Def. Sol. **109**, 189

Postawa Z, Kolodziej J, Czuba P, Piatkowski P, Poradzisz A, Szymonski M and Fine J, 1993a: in Springer Series in Surface Sciences, vol. **31** (Springer, Berlin) 299

Postawa Z, Kolodziej J, Czuba P, Piatkowski P, Szymonski M, Bielanska E, Camra J, Ciach T, Faryna M, Rakowska A, 1993b: Nucl. Instr. Methods Phys. Res. B **78**, 314

Puchin VE, Shluger AL and Itoh N, 1993: Phys. Rev. B **47**, 10760

Redhead PA, 1966: Can. J. Phys. **42**, 886

Reimann CT, Brown WL, Johnson RE, 1988: Phys. Rev. B **37**, 1455

Rittner ES, 1951: J. Chem. Phys. **19**, 1030

Royce BSH, 1967: Prog. Solid State Chem. **4**, 213

Sarnthein J, Wurz P, Husinsky W and Betz G, 1991: Surf. Sci. **241**, 6

Schmid A, Braunlich P and Rol PK, 1975: Phys. Rev. Lett. **35**, 1382

Seifert N, Husinsky W and Betz G, 1991: Phys. Rev. B. **43**, 6723

Song KS and Chen LF, 1993: Int. Workshop on *Electronic Excitations at Surfaces of Halides*, Book of Abstracts, Krakow, to be published in Radiat. Eff. Def. Sol.

Song KS and Williams RT, 1993: *Self-Trapped Excitons* (Springer, Berlin)

Szymonski M, 1980: Radiat. Eff. **52**, 9

Szymonski M, 1990: Nucl. Instr. Methods B **46**, 427

Szymonski M, Rutkowski J, Poradzisz A, Postawa Z and Jorgensen B, 1984: DIET II, Springer Series in Surface Sciences, vol. **4** (Springer, Berlin) 160

Szymonski M, Poradzisz A, Czuba P, Kolodziej J, Piatkowski P and Tolk NH, 1991a: Nucl. Instr. Methods B **58**, 485

Szymonski M, Kolodziej J, Czuba P, Piatkowski P, Poradzisz A, Tolk NH and Fine J, 1991b: Phys. Rev. Lett. **67**, 1906

Szymonski M, Poradzisz A, Czuba P, Kolodziej J, Piatkowski P, Fine J, Tanovic L and Tanovic N, 1992a: Surf. Sci. **260**, 295

Szymonski M, Tyliszczak T, Aebi P and Hitchcock AP, 1992b: Surf. Sci. **271**, 287

Taglauer E, Tolk NH, Riedel R, Colarita E, Margaritondo G, Gershenfeld H, Stoffel N, Kelber JA, Loubriel G, Bommahavar AS, Bakshi M and Huric Z, 1986: Surf. Sci. **169**, 267

Townsend PD, 1983: in *Sputtering by Particle Bombardment II*, ed. Behrisch R (Springer, Berlin) 147

Townsend PD and Elliott DJ, 1969: Phys. Lett. A **28**, 587

Townsend PD and Kelly JC, 1968: Phys. Lett. A **26**, 138

Townsend PD, Browning R, Garland DJ, Kelly JC, Mahjoobi A, Michael AJ and Saidoh M, 1976: Radiat. Eff. **30**, 55

Walkup RE, Avouris Ph and Ghosh AP, 1987: J. Vac. Sci. Technol. **B5**, 1423

Williams RT, 1989: Radiat. Eff. Def. Sol. **109**, 175

Williams RT and Song KS, 1990: J. Phys. Chem. Sol. **51**, 679

Williams RT, Song KS, Faust WL and Leung CH, 1986: Phys. Rev. B **33**, 7232

Electronic Processes in Sputtering by Laser Beams

By Richard F. Haglund, Jr.
Department of Physics and Astronomy
Vanderbilt University, Nashville TN 37235 USA
and
Roger Kelly
Dipartimento di Fisica, Universit'a degli Studi di Trento
I-38050 Povo (Trento), Italy

Synopsis

Electronic processes play a significant role in the sputtering of solid surfaces by laser beams. This role is especially prominent in the interactions of laser light with nonmetallic targets and with the plume of sputtered material, but also extends to the interaction of the plume with the target surface. These electronic processes include: light emission following single- and multi-photon excitation; defect formation, excitation and relaxation; excitation and ionization of desorbing atoms and molecules; cluster emission; laser-induced photochemistry both in the plume and in the target itself; and gas-surface and plasma-surface interactions. At low fluence or intensity, laser irradiation modifies the composition and structure of non-metallic surfaces; the kinetics of particle removal are mainly determined by the density of electronic excitation and by the strength of the electron-lattice coupling. Above a characteristic fluence threshold, high-yield sputtering of the surface appears to arise in virtually all materials from bond-breaking around surface defects, such as vacancies and asperities, which are either pre-existing or are created by prior laser-induced desorption. This picture provides the basis for a kinetic model of sputtering of non-metallic solids by intense laser beams which is based on electronic excitation and relaxation mechanisms, rather than on thermal processes.

Contents

1 Introduction and Motivation

Notwithstanding its rapidly growing applications in many areas of technology and medicine, the physical mechanism of sputtering initiated by intense laser light has been an open challenge for some two decades. Laser ablation now plays an essential role in many areas (Miller & Haglund, 1991), including microlithography for integrated circuits (Ehrlich & Tsao, 1989); pulsed-laser deposition of thin films (Hubler & Chrisey, 1992); surface cleaning and defect removal (Allen et al., 1992, Tam et al., 1992); and laser surgery (Puliafito et al., 1987). While empirical studies have produced many important developments, a deeper understanding of the kinetics and dynamics of laser ablation will be required to further extend its potential for technological application.

Table I. Comparison of Ion Sputtering Phenomenology with that of Laser Ablation

Characteristic	Ion Sputtering (E $<$ 10 keV)	Ion Sputtering (E $>$ 1 MeV)	Laser Ablation
Energy-absorption mechanism	Mainly nuclear collisions	Mainly electronic excitation	Electronic followed by vibrational excitation
Particle-ejection mechanism(s)	Collisional and electronic, possibly thermal	Collisional and electronic	Electronic, thermal, thermomechanical
Residual damage	Collisional damage which can be annealed	Electronic damage which can be annealed (e.g., fission tracks)	Electronic, or thermal, or thermomechanical or none.
Material removal efficiency	$\approx$ 1 atom per 100 eV	Zero	$\approx$ 1 atom per 100eV eV
Density of electronic excitation	Consistently low	Consistently high	Variable depending on ratio of photon to bandgap energy
Role of electronic excitation	Small perturbation on collisional process	Dominant, as with fission tracks	Essential feature for all non-metallic solids

Sputtering processes initiated by intense photon beams from pulsed lasers can be viewed as comprising four phases:

(i) absorption of laser light by both single- and multi-photon processes;

(ii) transformation of photon-beam energy in radiative and non-radiative processes;

(iii) ejection of particles - atoms, molecules and ions - from the solid surface; and

(iv) formation and expansion of a plume of ejecta above the surface.

The first and second phases are governed by the optical physics of the irradiated solid and by the physical conservation laws; it is fair to say that these are well understood. The third phase is much better understood for collisionally induced sputtering than for the electronic processes discussed here. The fourth has no analog in sputtering by either ions or energetic electrons. Thus its existence is a further reason to separate sputtering by intense photon beams into two qualitatively different regimes: laser-induced desorption, and laser ablation.

Table II. Operating parameters of lasers frequently used for ablation

LASER	Wavelength	Laser-Pulse Duration	Laser-Pulse Energy	Repetition Frequency	Photon Flux ($m^{-2}s^{-1}$)
Nd:YAG	1064 nm	5-7 ns	500 mJ	5-10 Hz	10^{30}-10^{35}
Nd:YAG (2ω)	532 nm	3-5 ns	200 mJ	5-10 Hz	10^{29}-10^{34}
Nd:YAG/Dye	550-650 nm	5 ns	10 mJ	1-5 Hz	10^{25}-10^{30}
XeCl/Dye	350-600 nm	5 ns	20 mJ	2-50 Hz	10^{26}-10^{31}
XeCl excimer	308 nm	15-20 ns	300 mJ	up to 1 kHz	10^{29}-10^{34}
KrF excimer	248 nm	12-15 ns	500 mJ	up to 1 kHz	10^{29}-10^{34}
ArF excimer	193 nm	10 ns	100 mJ	1-50 Hz	10^{28}-10^{33}
F_2 excimer	157 nm	10 ns	10 mJ	1-20 Hz	10^{26}-10^{31}

In this paper, laser ablation refers to a high-yield photon sputtering process exhibiting all of the following characteristics: (1) material removal, possibly non-stoichiometric, at rates ranging from a small fraction of a monolayer to a few monolayers per pulse; (2) a particle yield which is a power function of the density of electronic excitation; and (3) a threshold photon flux below which only particle emission, without destruction of the surface, is observed. For sufficiently large removal rates, typically half a monolayer or more per pulse (NoorBatcha et al., 1987, 1988), formation of a plume above the surface is observed. This plume exhibits extremely complex gas- dynamic and/or plasma behavior. We have chosen not to discuss those hydrodynamical or thermomechanical processes, such as exfoliation, which result in emission of macroscopic fragments or droplets. These have been reviewed, for example, by Rothenberg & Kelly (1984).

Closely related to laser ablation is the phenomenon of laser-induced desorption which is a low-yield sputtering process. Below the characteristic threshold for ablation, laser-induced desorption results in the ejection of atoms, molecules or ions from isolated surface sites. However, the surface is disturbed so little that any residual disorder is highly localized and cannot be detected by such average surface-analytical techniques as low-energy electron diffraction. In the desorption regime, plasma or collisional effects on the emitted particles are generally insignificant. Although material removal rates are small, changes in surface structure and composition due to laser-induced desorption can significantly affect the course of ablation.

Like sputtering by ions or energetic electrons, laser ablation causes rapid removal of surface material, and may combine thermal and collisional with electronic effects. As shown in Table I, laser ablation also differs in significant respects from heavy-particle sputtering. Whereas the primary events in heavy-particle sputtering include both nuclear collisions (for ion energies in the keV range) and electronic

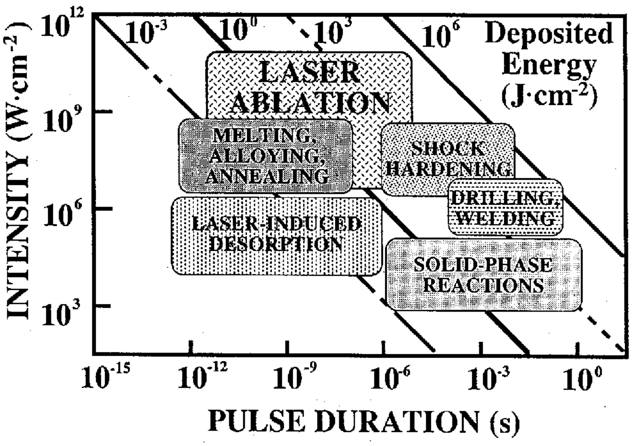

Figure 1. Schematic showing laser-solid interactions important in materials processing as a function of laser pulse duration and laser intensity, for the nanosecond pulsed lasers listed in Table II.

excitation (for ions at and above MeV energies), the primary event in laser ablation is an electronic excitation leading to formation of electron-hole (e-h) pairs.

In this review, we summarize theoretical and experimental observations about the four phases of sputtering by intense beams from nanosecond pulsed lasers with wavelengths ranging from the ultraviolet to the near-infrared. We find that one critical parameter for desorption and ablation, the local density of electronic excitation, can be estimated from a simple model for multiphoton absorption. We demonstrate that the interactions of photons with metals, semiconductors and insulators are also differentiated by a fundamental materials property, the electron-lattice coupling strength. The gas-dynamic behavior of the ablation plume, plasma characteristics and ambient gas effects are then described. In conclusion, we consider how electronic processes influence the kinetics of laser-induced desorption and ablation in insulators, semiconductors and polymers.

2 Energy Deposition and Transformation in Laser Ablation

Intense photon beams from lasers are characterized by a photon energy, pulse duration, and any of three analogs for current density in an ion beam: fluence, or pulse energy per unit area, often denoted by $F(\mathrm{J/cm^2})$; intensity, denoted by I and equal to the power per unit area ($\mathrm{W/cm^2}$); and flux, denoted by Φ, the number of photons per unit area (cm^{-2}). This usage is different from that applied to particle beams, where only the incident flux measured in ions/cm^2 is specified. Technologically interesting laser-solid interactions occur over a wide range of intensities and pulse durations, as shown in figure 1. The initial result of the laser-solid interaction is always the creation of electron-hole pairs. For long pulses or relatively low intensities, relaxation of these electron-hole pairs may produce surface modifications - such as phase transformation, melting, hardening or mixing - without significant material removal. Laser-induced desorption and ablation, in contrast, require short pulses and relatively high intensities as shown in the figure.

In principle, an intense laser pulse can eject surface atoms or ions into the gas phase either by heating the surface above the thermodynamic critical temperature $T_{\rm tc}$ to cause vaporization, or by initiating electronic processes which induce localized lattice instability and bond-breaking. We shall emphasize ablation by nanosecond-pulsed lasers operating from the ultraviolet to the near- infrared region of the spectrum, mainly because an enormous share of the fundamental studies, and virtually all technical applications, of laser ablation fall in this regime. Typical nanosecond-pulsed lasers used in ablation have photon energies ranging from 7.9 eV (157 nm, as for the F$_2$ excimer laser) to 1.17 eV (1064 nm, for the Nd:YAG laser); operating parameters are listed in Table II.

The process of laser ablation involves a variety of feedback effects which must be taken into account in any attempt to model the phenomenon. In nonmetallic solids, for example, laser irradiation can generate color centers or optically active defects which change the absorption characteristics, and thus the deposition of laser energy, for subsequent pulses, or even for photons late in the same pulse. Surface-conditioning or incubation effects occur even at interpulse spacings which are much longer than characteristic thermal diffusion times. As the plasma plume forms during ablation, resonant absorption processes in the plasma may decouple laser light from the target. In the light of this complex phenomenology, we have elected to focus initially on electronic processes leading to the ejection of atoms, molecules and ions into the gas phase both below and above the ablation threshold.

The initial event in laser ablation of any solid surface, is the creation of an electron-hole pair by an optical transition from a filled state (e.g., in the valence band or in a defect state) to an empty state (which might be in the conduction band or likewise be an empty defect or surface state). The probability of creating electron-hole pairs in a nonmetallic solid depends on the intensity of the laser light as a function of depth, $I(z)$:

$$I(z) = I_0 \cdot e^{-(\sigma^{(1)}n_1+\sigma^{(2)}n_2\Phi+\cdots)z} = I_0 \cdot e^{-(\alpha+\beta I+\cdots)z} \tag{1}$$

where I_0 is the incident intensity, $\sigma^{(k)}$ is the k-photon absorption cross section, the n_k are the number densities of absorbers participating in the kth-order process, and α and β are, respectively, the one- and two-photon absorption coefficients. The intensity and photon flux are denoted by I and Φ, respectively. The ellipsis in eq. (1) refers to progressively higher-order absorption processes. When only one-photon processes are important, eq. (1) reduces to the familiar Beer's law giving exponential attenuation of the light with depth. When the laser photon energy $h\nu$ is greater than the bulk band-gap energy E_G, light is strongly absorbed by one-photon transitions near the surface. If $h\nu$ is less than E_G, on the other hand, the solid is highly transmissive at that wavelength. The laser may induce either one-photon transitions between surface or defect states and the conduction band, in accordance with Beer's law, or multiphoton transitions between valence and conduction bands. Typical nanosecond lasers produce ablation in essentially all nonmetallic solids by one-, two-, three- or four-photon transitions.

The initial dynamics of laser sputtering are governed by the density of electronic excitation created in a solid by the laser pulse. This density, essentially the spatial density of electron-hole pairs, depends on the ratio of energy required to create an electron-hole pair to the laser photon energy. For a one-photon transition - say, for a single-photon transition from a filled valence-band state to an empty surface state, or to the conduction band - this ratio is simply unity. For multiphoton transitions between the valence and conduction bands of transparent solids, it is the smallest integer k such that k equals or exceeds the ratio $E_G/h\nu$. Either the single-photon or the multiphoton absorption characteristics may be changed by the formation of transient defects during a laser pulse, or by the accumulation of defects with successive laser pulses.

The probabilities for optical transitions with photon multiplicity k can be estimated from a simple physical picture (Andrews, 1984). The intensity I (in W/cm^2) of the laser in a cubical cell of material with a linear dimension L

$$I = \text{mean photon number} \cdot \frac{\text{energy/photon}}{\text{transit time}} \cdot \frac{1}{\text{area}} = m \cdot \frac{hc/\lambda}{L/(c/n)} \cdot \frac{1}{L^2} \tag{2}$$

where m is the mean number of photons in the designated volume and n is the index of refraction. Hence, the mean photon number in an atomic volume irradiated by the laser at intensity I is

$$m = \frac{nIL^3\lambda}{hc^2}. \tag{3}$$

Assuming that laser photons obey Poisson statistics, the probability of k photons simultaneously being in a volume having a mean photon number m is

$$P_k = \frac{m^k}{k!}e^{-m} \cong \frac{m^k}{k!} \propto I^k \quad (m \ll 1). \tag{4}$$

This model is useful for estimating the number of electron-hole pairs produced by laser excitation in a given solid. However, more detailed considerations re-

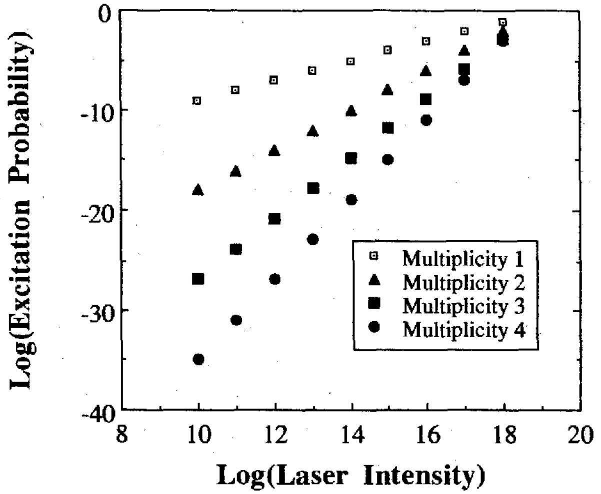

Figure 2. Probability of creating an electron-hole pair (vertical axis) as a function of laser intensity (in units of W/cm^2). We have assumed an hypothetical solid with a band-gap energy of 4 eV in which valence- to conduction-band electronic transitions are generated by means of one-, two-, three- and four-photon excitation.

quire a knowledge of the actual k-photon optical cross sections. The cross sections for single-photon band-to-band transitions are on the order of atomic dimensions, 10^{-16}-10^{-19} cm^2. Multiphoton cross sections are correspondingly smaller; for transparent solids, for example, measured two- photon cross sections range from 10^{-34} - 10^{-50} cm^4/s, with the larger cross section for resonant, the smaller for non-resonant transitions.

Some typical order-of-magnitude estimates of excitation probability for single- or multi- photon transitions as a function of laser intensity are shown in figure 2. For example, for a XeCl laser irradiating the alkali halide KCl, the band-to-band excitation needed to create an e-h pair requires $k = 2$, and, for an intensity typical of such excimer lasers, we find $P_2 \approx 10^{-7}$. For an incident laser pulse of 100 mJ in 20 ns, containing some 10^{18} photons, this would create some 10^{11} electron-hole pairs in the irradiated volume. Thus, even at the highest intensities typical of ablation experiments, the spatial density of electronic excitation remains low in a transparent material, not much greater than that found in irradiation of these solids with much weaker synchrotron-light sources. In semiconductors, by way of contrast, electron-hole pairs can be created by many lasers via one-photon transitions. For instance, a 100 mJ pulse from a Q-switched Nd:YAG laser incident on a silicon surface, for example, can create electron-hole pairs with probability P_1

Table III. Grouping of Nonmetallic Solids by Type of Electronic Relaxation.'X' stands for one or more of F, Cl, Br but not I. Adapted from Nakai et al. (1991), and Itoh (1993). Values of α from Kittel (1986) and from Hayes & Stoneham (1985).

Type	Electron-Lattice Coupling Strength	Characteristics	Examples
1	Weak α=0-0.9	Neither excitons nor holes are self-trapped in the bulk. Two-hole or Anderson (negative-U) localization is possible.	Si, Ge, III-V and II-VI semiconductors. TlX, CuX, AgBr, ZnO.
2	Intermediate α=0.5-2	Polaronic response with varying degrees of localization according to degree of ionicity	MgO, CaO, c-SiO_2, Al_2O_3, $LiNbO_3$ $KNbO_3$, LiI, NaI, KI, RbI, CsI, possibly "YBCO"
3	Strong α=2-4	Either excitons or holes are self-trapped (localized) in the bulk. Localization by lattice distortion.	LiX, NaX, KX, RbX, AgCl, MgF_2, CaF_2, SrF_2, BaF_2, BaFCl, $RbMgF_3$, a-SiO_2.

$\approx 10^{-3}$ during a pulse duration of 10 ns. Thus the probability of e-h pair creation can vary from one material to another by many orders of magnitude, even though the laser parameters are virtually the same.

In order for either desorption or ablation to occur, electron-hole pairs generated by the initial laser-solid interaction must ultimately induce a lattice instability leading to motion of the atomic constituents of the surface. Since this instability must result from relaxation by electron-lattice coupling, the mechanisms of laser-induced desorption and ablation also depend strongly on the electron-lattice coupling strength (Table III). For instance, in strong-coupling solids such as alkali halides, self-trapped excitons (STE) are formed by the strong Coulomb interactions of laser-generated electron-hole pairs with the crystal lattice. The relaxation of these STEs into vacancy-interstitial defect pairs imparts kinetic energy to the interstitial atoms, kinetic energy which near the surface may be sufficient to eject atoms or ions from the surface. In solids with weak coupling, on the other hand, such as compound semiconductors and some oxides, there is no self-trapping of excitons, and both radiative and nonradiative electronic processes (e.g., Auger decay) compete for the energy of the electron-hole pairs. Most oxides have intermediate coupling strength, and excitons in some large-bandgap oxides may be self-trapped.

While it is clear that electron-lattice coupling plays a definitive role in desorption and ablation of nonmetals, no quantitative criterion has yet been established for either regime. However, coupling strength is at least a qualitative indicator of the relative dominance of radiative and non- radiative processes which compete for the energy poured into a laser-irradiated solid. This coupling strength is conventionally defined (Kittel, 1986; Hayes & Stoneham, 1985) to be

$$\alpha = \frac{1}{2}\left(\frac{1}{\varepsilon_\infty} - \frac{1}{\varepsilon_0}\right)\frac{e^2}{r_\mathrm{p}}\frac{1}{\hbar\Omega_\mathrm{LO}} = \frac{\text{average deformation energy}}{\text{average phonon energy}} \tag{5}$$

where the dielectric constants ε_0 and ε_∞ are, respectively, the values with ionic screening and electronic screening only; Ω_LO is the frequency of the longitudinal optical phonon, and the polaron radius r_p is defined by

$$r_\mathrm{p}^2 = \frac{\hbar^2}{2m_\mathrm{p}^*}\frac{1}{\hbar\Omega_\mathrm{LO}},$$

with m_p^* the effective polaron mass. Intuitively, α is a measure of the number of phonons (vibrational quanta) 'dressing' an electron as it moves through a deformable lattice. The parameter α is also correlated with the ionicity of the bonds; it is large in ionic materials, small in covalently bonded materials, and vanishes for metals. Coupling strengths in Table III were computed from eq. (5).

In nonmetallic solids, electron-lattice coupling is critical to localization of the incident laser energy on a single atom or small group of atoms for a time scale on the order of a few vibrational periods. In solids with strong coupling, such localization can occur even in perfectly crystalline material and at low densities of electronic excitation. In solids with weak coupling, on the other hand, it appears that energy can be localized only at defects (Hattori et al., 1992) or at very high densities of electronic excitation in the perfect lattice (Koo et al., 1992). Hence localization is the final key to the desorption and ablation mechanism.

To summarize, we can say that the phenomenology of laser-induced desorption and laser ablation depend in an essential way on both the density of electronic excitation and on the electron-lattice coupling strength, and the way these two parameters interact to produce energy localization and lattice instabilities. The density of electronic excitation depends on the band-gap energy and on the laser used to induce the lattice instability; the typical lasers we have in mind for this review produce only low densities of electronic excitation in wide band-gap solids, but very high densities in semiconductors. The electron-lattice coupling strength is a function of the ionicity of the material. Since many wide-bandgap materials are also highly ionic, we expect most transparent insulators to have large values of α, while covalent semiconductors have small values of a. With these criteria in mind, we display in figure 3 the range of electronic-excitation densities and electron-lattice coupling strengths in which laser ablation occurs in non-metallic solids.

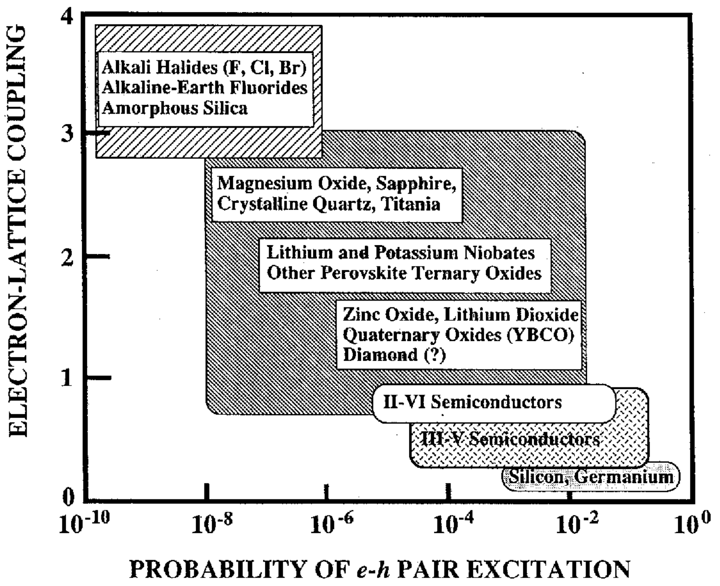

Figure 3. Laser ablation of various nonmetallic solids as a function of electron-lattice coupling strength a defined in eq. (5) (vertical axis) and of the probability of band-to-band electronic excitation using eq. (4) (horizontal axis).

3 Laser Ablation from Metallic Solids in Vacuum

While this review is primarily concerned with laser ablation in nonmetals, it is useful to begin with a survey of ablation from metal surfaces. This is partly because pulsed-laser deposition of metal films, stripes and ribbons is an increasingly important area of microelectronics technology, as in interconnect fabrication (Liu, 1992). In addition, however, ablation of metals also furnishes important illustrations of the themes of energy deposition, localization and transformation, and provides clear contrasts with sputtering of metals by ion beams. We note at the outset that it is problematical whether ideas and terminology developed mainly from a study of nonmetals, namely 'desorption' and 'ablation', can be applied to metals.

Laser ablation of metals was studied soon after the development of the laser (Ready, 1964). Irradiation by laser light produces an extremely high density of electronic excitation in metals within a skin depth ($\approx$ 500-1000 nm) of the surface, while electron lattice coupling is essentially zero: There is complete long-range dielectric screening of the ions by the electrons, with the result that freely moving electrons excited by the laser scatter off the lattice ions until the electron energy is completely thermalized, on a subpicosecond time scale. Following this line of reasoning, Ready used the formalism of one- and two-dimensional heat transfer to predict the temperature rise and the total amount of material vaporized. More recent treatments of ablation from semi-infinite metal surfaces continue to follow Ready's basic prescription, applying a steady-state, one-dimensional model based on the idea that the incident laser lights heats the metal substrate first to the melting point and then to vaporization temperature. The major correction to this treatment is the inclusion of gas-dynamic effects at the vapor-liquid interface (Chan & Mazumder, 1987). In many cases of technological interest, the irradiated material is in the form of a thermally thin substrate, and the heat-conduction equations for the semi-infinite case must be modified accordingly (Imen et al., 1989).

The question of electronic processes in laser ablation from metals requires that we get at the dynamics of the fundamental process of energy deposition and relaxation following the laser pulse. Recent measurements of transient reflectivity on metal surfaces with picosecond (Yen et al., 1982) and femtosecond (Fujimoto et al., 1985) lasers have confirmed subpicosecond thermalization times for photoexcited electrons in metals. Thermal modulation measurements of the transmission of thin Nb films, again with femtosecond laser pulses, give an electron-phonon relaxation time of 360 fs (Yoo et al., 1990); on Cu films, the relaxation times range up to 4 ps at high intensities (Elsayed-Ali et al., 1987). The electron-lattice coupling strength defined in eq. (5) does not apply to metals because polarons are not formed. Instead, the relaxation of the initial photoexcitation in metals is described by an electron-phonon coupling constant, defined as the quantity g appearing in the following coupled equations (Anisimov et al., 1975):

$$C_{\mathrm{e}} \frac{\partial T_{\mathrm{e}}}{\partial T} = \kappa \nabla^2 T_{\mathrm{e}} - g(T_{\mathrm{e}} - T_{\mathrm{l}}) + S(r,t) \tag{6a}$$

$$C_{\mathrm{l}} \frac{\partial T_{\mathrm{l}}}{\partial T} = g(T_{\mathrm{e}} - T_{\mathrm{l}}). \tag{6b}$$

Here, the subscripts 'e' and 'l' refer to the electron and lattice, respectively, the T_i are temperatures, the C_j are heat capacities, and $S(r,t)$ is the source (laser) term. If one assumes a model for heat transfer by absorption in the sample, these equations can be used to fit experimental transmission or reflectivity data with the electron-phonon coupling constant g as a parameter, and give magnitudes for g ranging from $2{\cdot}10^{12}$ $\mathrm{Wcm^{-3}K^{-1}}$ for Nb (Yoo et al., 1990) down to 10^{11} $\mathrm{Wcm^{-3}K^{-1}}$ for Cu (Elsayed-Ali et al., 1987). Electron-phonon relaxation times of the right order-of-magnitude can be estimated from Drude theory (Ashcroft & Mermin, 1986)

Of direct relevance to laser ablation is an interesting experiment by Corkum et al. (1989) in which laser ablation measurements for laser pulses ranging from 100 ns to 3 ps duration were used to estimate both the relaxation time and the electron-phonon coupling constants of bulk copper and molybdenum in the form of high-quality mirror surfaces. As criteria for surface melting, the experimenters used the appearance of a damaged spot (evidence of gross material removal) and the appearance of a visible spark (plasma formation), which fit our criteria for laser ablation. Their measurements show that the threshold fluence for damage is independent of pulse duration below 1 ns. The use of the coupled rate equations (6) to extract the electron-phonon coupling constant gives values of g much smaller than those measured for thin films: 10^{10} Wcm^{-3}K^{-1} for Cu and $2{\cdot}10^{10}$ Wcm^{-3}K^{-1} for Mo. There has been some debate among the various researchers as to the origin of these differences (Corkum et al., 1990); it is quite possible that g depends on the precise morphology of a given sample. However, the interesting point is that ablation is apparently associated with reduced coupling efficiency to the phonon bath. This may be evidence for nonthermal mechanisms of localization in the ablation process.

The difficulty seems to lie in the (usually) unspoken assumption that heating to the point of vaporization must be the primary process of laser sputtering in metals. Certainly, recombination of e-h pairs and transfer of the absorbed photon energy to delocalized lattice-vibration modes is so rapid in metals that, on a nanosecond time scale, the laser-surface interaction appears to be a thermal process (Hicks et al., 1988). Measurements of Cu^0, Cu^+ and Cu_2 sputtered from pure bulk Cu by XeF (λ = 351 nm) and ArF (λ = 351 nm) lasers also show thermal behavior at fluences of order 1-2 Jcm^{-2} (Dreyfus, 1991). The use of a laser-induced fluorescence probe made it possible to follow the yield as a function of fluence for all three species simultaneously. The data show that the yield of Cu^0 and of Cu_2 are proportional to $\exp(-1/T)$ throughout this low-fluence range, with kinetic energies consistent with a surface temperature up to 4000 K. However, above approximately 2-3 Jcm^{-2}, the Cu^+ ions have energies up to ten times that temperature, indicating that non-thermal processes have been initiated. These high kinetic energies are almost certainly due to photoionization and collision phenomena in the ablation plume. Thus we may infer that, at least at low fluences, there are circumstances in which ablation from metal surfaces is a thermal process.

This, however, most assuredly does not mean that ablation from metal surfaces is inevitably a thermal process. This is because desorption and ablation involve localized lattice modes with sufficient energy to break bonds in the lattice, while the thermal modes of the lattice are by definition delocalized. Desorption or ablation can only occur by a thermal process when there is enough energy in some delocalized mode, in a statistical sense, for bond-breaking to occur, or when the energy deposited in the delocalized lattice modes exceeds the critical thermodynamic temperature T_{tc} at which a phase transformation from solid or liquid to the gas phase occurs instantaneously on the time scale of the laser pulse.

Moreover, experimental evidence with metals suggests that, despite the rapid thermalization of the incident laser energy in the surface, there are non-thermal effects in desorption and ablation. Helvajian & Welle (1989), for example, observed Ag ions ablated by 351 nm and 248 nm laser light from clean, high-purity, single-crystal surfaces with kinetic energies approaching 9±1 eV, corresponding to temperatures far above T_{tc}. There was only a slight wavelength dependence in the ablation threshold in the intensity range 1-12 MW/cm^2; the ion yield showed an intensity dependence of I^{13} for 248 nm laser irradiation and I^{18} for 351 nm irradiation. Kim & Helvajian (1991a, 1991b) have shown that this is a general phenomenon, with similar high-energy-ion ejection occurring from Al (1991a) and W(100) surfaces (1991b, 1993). The experiments on tungsten surfaces show that the threshold for ion ejection is lowered by adsorption of oxygen, hydrogen and fluorine, suggesting that adsorbates can help to localize the photoexcitation producing desorption. This mechanism is likely to be especially effective at surface defect sites, such as vacancies or steps.

A host of other experiments give similar evidence that desorption and ablation from metals occurs by athermal mechanisms connected with surface properties. Arakawa and co-workers showed that Al atoms could be desorbed from thin aluminum films deposited on a glass prism and excited by an internally reflected laser beam (Lee et al., 1989). Ablation experiments on roughened Ag showed one group of thermal-energy ions ($\approx$ 0.5 eV) and a second non-thermal ion group (typical energies 3.6 eV); similar results are observed in laser ablation of a variety of other metals, including Mg, Bi, Pd, Al, Cu and Au (Shea & Compton, 1993). The clear connection between spatial localization of the laser energy and desorption has been shown by Träger and his coworkers. In their experiments, Na atoms were desorbed by continuous-wave laser irradiation from Na clusters adsorbed on alkali-halide surfaces even at laser intensities in the mW/cm^2 range (Hoheisel et al., 1988; Vollmer et al., 1989). At these laser intensities, it is impossible to induce a significant temperature rise in the clusters.

The puzzle is, what then is the mechanism of energy localization? One possibility suggested by the experiments is excitation of the surface plasmon resonance in small metal particles. This process has been computed in standard quantum-mechanical perturbation theory by Ritchie et al. (1991) as the evaporative decay by ion emission of a surface plasmon. The results predict that the ion yield should increase with the third power of the laser intensity, in general agreement with the experiments of Shea & Compton. The relative ion-production efficiency - roughly 10^{-8} ions per incident photon - is also in reasonable agreement with these calculations. However, while the surface-plasmon resonance is clearly one possible mechanism of energy localization leading to desorption, it is by no means the only possibility, since the wavelength dependence characteristic of the surface plasmon is not always found in desorption yields.

Indeed, it may well be possible that any small inhomogeneities in a metal surface - such as asperities, defects or dislocations - can serve as initiation sites for ablation. If, in fact, such defects play a pivotal role, then the problem of ideas and terminology to which we have earlier alluded, would be largely overcome. Localization of the incident laser energy might occur in a variety of ways - such as localization by plasmon resonances, at such surface geometrical imperfections as steps and vacancies, or at the sites of adsorbates or impurities - but the terminology of excitation, localization and relaxation would remain appropriate. Laser sputtering of metals would then be formally equivalent to laser ablation of nonmetals and both processes would properly be designated as ablation in the limit of high yields.

4 Laser Ablation from Non-Metallic Solids

A physical understanding of the dynamics of ablation is greatly complicated by the presence of gas-surface interactions if the ablated surface is not in vacuum, and by plume-surface interactions at high ablation yields. In this section, we summarize pertinent observations about laser ablation of solids with different electron-lattice coupling strengths, primarily in high or ultra- high vacuum and generally without reference to the plume. These observations will form the basis for modeling the kinetics of particle ejection in both laser-induced desorption and laser ablation.

4.1 Laser Ablation of Solids with Strong Electron-Lattice Coupling

The mechanisms of laser-induced desorption in alkali halides and of both laser-induced desorption and ablation in strong-coupling solids have been discussed by Matthias & Green (1990) and by Haglund & Itoh (1993), respectively. The use of laser ablation in growing thin films of strong-coupling materials for applications to optical technology are summarized by Cheung et al. (1992). As listed in Table III, solids with strong electron-lattice coupling include the alkali halides and alkaline-earth fluorides, and possibly some of the more ionic oxides (e.g., MgO) and amorphous SiO_2. However, for convenience, we have treated a-SiO_2 and MgO in the next section as the extreme cases of the intermediate electron-lattice coupling strength typical of other oxides.

In a strong-coupling solid, laser photons generate electron-hole pairs by Franck-Condon transition, that is, a so-called 'vertical' transition to an electronically excited state so rapid that there is only a negligible change in the radial (or other appropriate configuration) coordinates of the electron until after the excitation.

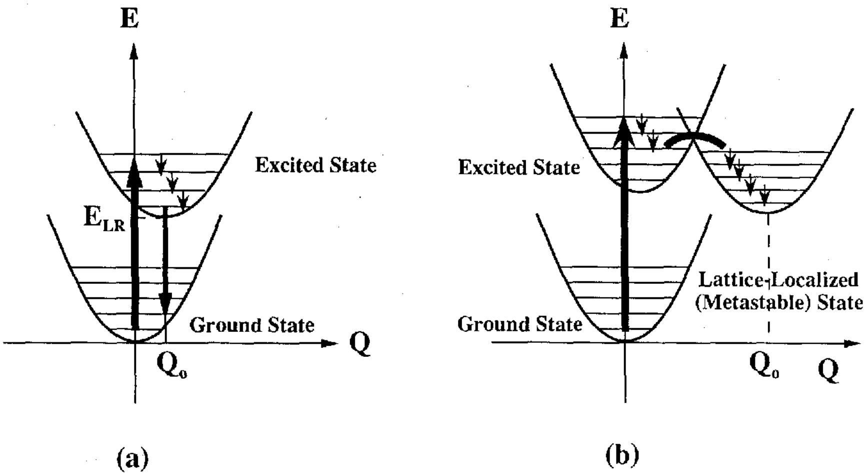

Figure 4. Schematic representation of electronic potential energy surfaces and vibrational energy levels for (a) weak and (b) strong electron-lattice coupling. Adapted from Hayes & Stoneham (1975).

This Franck-Condon transition is followed by a relaxation to a potential energy surface whose minimum is displaced with respect to the ground state potential-energy surface of the solid, as shown in figure 4 (adapted from Hayes & Stoneham, 1985). The magnitude of the displacement in the configuration coordinate marking the minimum of the lattice-localized state is a measure of the strength of the electron-lattice coupling. This as a manifestation of the empirical rule that in strong-coupling solids the ions tend to follow the motion of electrons and holes. Because of the strong coupling, relaxation by non-radiative processes, which can lead to defect production, desorption and ablation, compete favorably with luminescence transitions.

In the alkali halides, it is generally accepted that self-trapping of the photogenerated hole forms the so-called V_k center depicted in fig. 5. Subsequent capture of an electron leads to the formation of a self-trapped exciton usually within a picosecond. The decay of this exciton produces a Frenkel defect (vacancy-interstitial pair) consisting of an F-center and an H-center (bottom panel in figure 5). We note that the F-center is an electron trapped at an anion vacancy, and that an H-center could be defined either as a relaxed neutral halogen interstitial or an interstitial X_2^- molecule. As lattice relaxation occurs following decay of the STE, the vacancy (F-center) and interstitial (H-center) separate from each other by a few

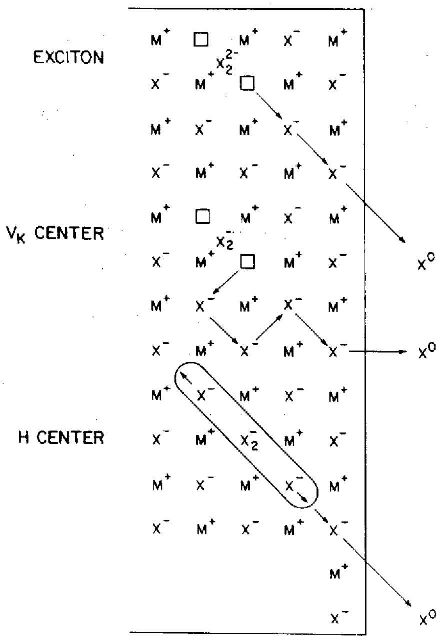

Figure 5. Schematic of laser-induced desorption from a strong-coupling solid. (a) Formation of self- trapped hole. (b) Formation of self-trapped exciton. (c) Decay of self-trapped exciton to form F-center and H-center. (d) Separation of F-center from H-center. (e) Desorption of H-center by dissociation of halogen negative molecular ion.

lattice spacings to reach their lowest-energy configuration (Williams et al., 1986). Although this picture is generally true for the alkali halides, and probably also holds for most alkaline-earth fluorides, recent femtosecond-laser studies of self-trapping in alkali iodides sho that under some circumstances, the self-trapped excitons are found before the V_k center develops (Iwai et al. 1994).

In the bulk, vacancy-interstitial pairs can modify the optical absorption of the solid. Near the surface, the decay of the F-H center pair leads to energetic expulsion of the halogen neutral; the F-center, following diffusion to the surface, can neutralize a surface metal ion, leading eventually to thermal desorption of a neutral metal atom. These events result in desorption yields proportional to the nth

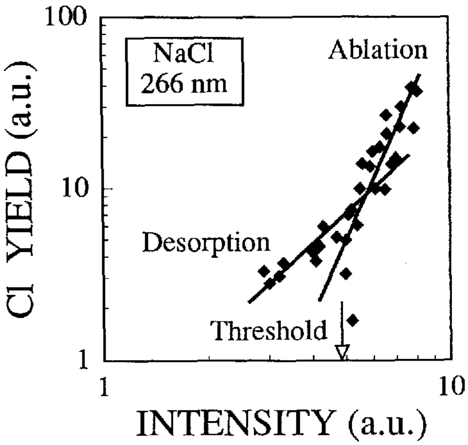

Figure 6. Yield of Cl atoms, detected by a quadrupole mass spectrometer, from laser irradiation of an NaCl crystal using the fourth harmonic of a Nd:YAG laser (266 nm). Each data point comes from a single laser shot on a pristine sample site. The sharp break and steepened yield curve in the middle fluence range signal the onset of ablation. Adapted from Schmid et al. (1975).

power of the laser intensity for an n-photon excitation producing the band-to-band transition, or to the first power of the density of electron-hole pairs. This proportionality between yield and electronic excitation density underlies the expression 'linear regime' as applied to laser sputtering below the ablation threshold. This mechanism has been verified not only for desorption from perfect surfaces, but also for desorption induced by multiphoton defect excitation in KCl and NaCl (Schmid et al. 1975) for desorption induced by vacuum-ultraviolet single-photon transitions in LiF and KCl (Bunton et al., 1992), and for ultraviolet-laser-induced desorption from NaCl clusters (Li et al., 1992).

Above the ablation threshold, weakly-bonded atoms near vacancies produced in this linear regime, as well as those near defects in the near-surface bulk, are more easily ejected from the surface than those at perfect lattice sites. This leads to a rapid increase in the yield as a function of laser intensity. Thus the most characteristic feature of laser ablation in pure strong-coupling solids in vacuum is a change in the slope of the yield vs fluence or intensity for neutral atoms at the threshold for ablation, as shown in figure 6 for the case of Cl atoms from NaCl undergoing laser ablation at 266 nm. This sharp break in the yield curve is observed both for the metal and non-metal atoms and ions expelled from the surfaces of strong-coupling solids, and typically has a dependence of n^{2-3}, where n is the order of the multiphoton process. For this reason, laser ablation is sometimes

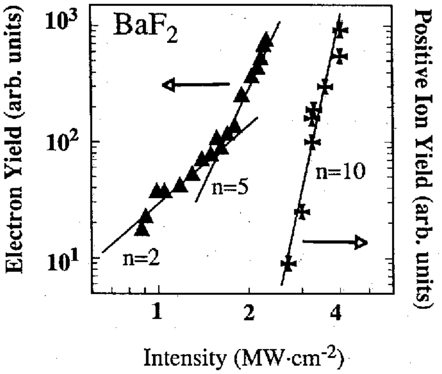

Figure 7. Yields of ions and photoelectrons emitted from the surface of BaF$_2$ under pulsed laser irradiation by the second harmonic of Nd:YAG, 532 nm. The sharp break and steep increase in yield as a function of intensity again signals the onset of ablation or the regime of nonlinear yield vs intensity. Adapted from Reif (1989).

said to occur in the 'nonlinear regime' of electronic excitation density. Similar behavior has been seen in photoelectron yields from the surface of BaF$_2$ (fig. 7), suggesting a common underlying mechanism (Reif, 1989). Note the extremely high yield dependence for the ablated ions.

There are at least two possible reasons for the onset of the nonlinear dependence on the density of electronic excitation above the ablation threshold. One is the growth of vacancy clusters in the surface and in the near-surface bulk due to laser-induced desorption of isolated atoms in the linear regime. Atoms near the vacancy are less strongly bonded and thus more readily ablated; in addition, the removal of an atom adjacent to a vacancy cluster enlarges the cluster, thus geometrically increasing the number of weakly-bound atoms which can be ejected by subsequent excitation. The second reason for the onset of the nonlinear regime is the change in the linear bulk absorption coefficient due to the formation of defects. Studies of nonlinear processes in ultraviolet optical materials, such as CaF$_2$, MgF$_2$ and LiF, showed the growth of color centers after several hundred laser pulses from a 280-fs KrF laser (Hata et al., 1990). The color centers are typically formed by two-photon excitation, as observed from the F-center-luminescence vs laser intensity curve and have absorption bands in the 5 eV region. This effectively increases the cross section for ablation, because what, for example, initially required a two-photon excitation then requires only a single photon. Since both the formation rate for these centers and the absorption depend strongly on laser intensity, we can expect the ablation rate to rise rapidly as absorption, transfer of energy to the lattice, and defect excitation begin to contribute to the yield.

This increase in absorption due to defects can also be affected by the density of excitation, as shown by Tanimura & Itoh (1988). In their experiment, RbI - in which vacancy-interstitial pairs are not formed by excitons at low temperature - was irradiated by an excimer laser at fluences between 10 and 100 $\mathrm{mJ/cm^2}$ to create self-trapped excitons following two-photon excitation of electron-hole pairs. Luminescence intensity from self-trapped excitons and optical absorption were measured as a function of laser intensity; the absorption showed a transient component proportional to the square of the excitation density (fourth power of the laser intensity). While this experiment was not designed to observe desorption or ablation, the clear implication of the work is that the interaction of laser-induced excitons is possible at excitation densities attainable even in transparent solids.

Another possible mechanism for producing nonlinear yield functions is enhanced electron-hole pair generation and ablation by resonant multiphoton ionization involving intermediate defect states. Electron and metal-ion ablation yields of metal fluorides measured by Reif (1989) exhibit a resonant enhancement attributable to the involvement of excited intermediate states, suggesting a correlation between the intensity dependence of the yields and the number of photons required to reach these surface states. Earlier cluster calculations on the alkaline-earth halides MgF_2, CaF_2 and BaF_2 by Rosén (Reif et al., 1987) showed a high density of unoccupied surface electronic states accessible by multiphoton transitions. The relatively defect-free surfaces of MgF_2 and CaF_2 have much lower multiphoton-excitation cross sections and correspondingly higher laser ablation thresholds. This qualitative agreement should not obscure the fact that the calculation of the cluster surface states is not easy (Westin et al., 1990), so that detailed comparison of experiment and theory may still be premature.

Extrinsic defects can also influence the course of laser ablation in strong-coupling solids, as shown in recent experiments which measured photoacoustic beam deflection near the point of laser irradiation of dielectrics in air (Reif et al., 1989). On relatively defect-free surfaces of strong-coupling solids, such as MgF_2 and CaF_2, the extremely rapid rise of the photoacoustic energy during ablation was attributed to the onset of avalanche ionization or dielectric breakdown at perfect lattice sites. On the other hand, in materials with greater intrinsic defect density, such as BaF_2, or with enhanced extrinsic defect density, such as mechanically rough CaF_2 and LiF, a different photoacoustic yield vs intensity relation seemed to implicate multiphoton excitation of surface or defect states as the operative mechanism.

4.2 Desorption and Ablation in Intermediate-Coupling Solids: Oxides

The oxides constitute the largest family of materials with intermediate electron-lattice coupling strength, and a potentially rich and largely unexplored field for fundamental studies of laser-induced desorption and ablation. Laser interactions with oxide materials are also critical to various optical, electronic and superconducting technologies. Laser ablation is already used, for example, to drill holes (called 'vias') in oxide layers between different levels in microelectronic circuits, for thin-film deposition of high-T_c superconductors, and for machining ceramics.

One possible reason for the paucity of fundamental laser ablation studies in oxides is the complex nature of optical excitations in these materials. Apart from amorphous silica and possibly MgO, self-trapped excitons probably do not form in oxides, so that the strong-coupling model of section 4.1 is not an appropriate description. In these materials, it is more appropriate to consider the optical response as due to the formation of the polaron - an elementary excitation consisting of the excited electron and its associated lattice-strain field (Kittel, 1986). Optically excited solids with intermediate electron-lattice coupling exhibit a broad range of polaron responses, including the formation of excitons which are not self-trapped, as well as large-polaron formation and relaxation. Because oxide band-gap energies range from around 10 eV (in Al_2O_3) to zero (e.g., in Ti_2O_3), it is also possible to study a range from low to high density of electronic excitation with conventional nanosecond-pulsed lasers.

The broad range of polaronic responses results from the greatly varying energy width of the bands in oxide materials. When an electron is excited by an optical transition, it can lower its energy either by delocalizing in a band state or by forming a localized excitation, such as a polaron. The path followed in any specific case depends on whether the energy gained by localization exceeds the energy width of the conduction band. In transition-metal oxides, for example, the width of the optically important *d*-band arises from metal-oxygen-metal interactions, and varies with the connectivity between oxide structural units (Cox, 1992). The diverse electronic and structural characteristics of oxides lead to a great variety of desorption and ablation phenomena, as indicated by experiments which we now survey.

4.2.1 Crystalline Sapphire

Both laser-induced desorption and ablation have been studied in sapphire (Al_2O_3). There is still some controversy about self-trapping of excitons in this material (Valbis & Itoh, 1990). Dreyfus and co-workers (1986a,b) observed steady-state ablation of sapphire with a 248-nm KrF laser, using laser-induced fluorescence to detect

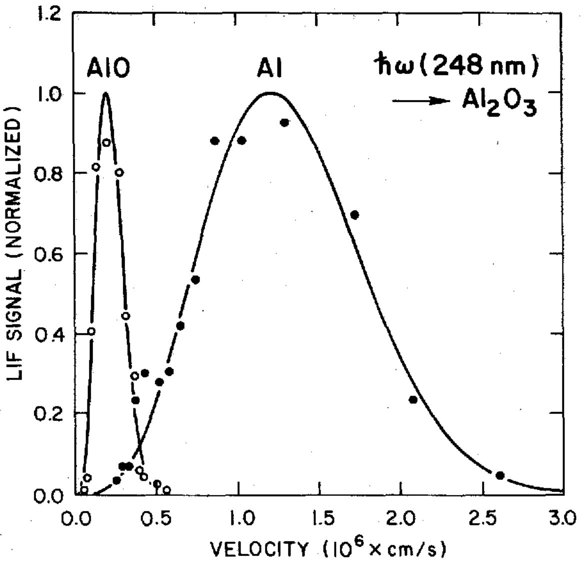

Figure 8. Velocity distributions of Al and AlO neutrals from a sapphire (Al_2O_3) surface. The distributions are non-Maxwellian, are not identical, and are consistent with most probable energies of 4 and 1 eV, respectively. Adapted from Dreyfus et al. (1986).

both Al atoms and AlO molecules. A fluence threshold of 0.6 J/cm^2 was found for ablation. Above threshold, the velocity distributions of both Al and AlO, shown in figure 8, were measured by time-of-flight spectrometry; the internal energy distributions for the AlO were extracted by fitting the observed rotational spectra. The velocities of the Al atoms did not fit a Maxwellian distribution and exhibited some fluence dependence, with most probable translational energies (E_{trans}) ranging from 4 eV near threshold to nearly 20 eV at 3 J/cm^2, far above the thermodynamic critical temperature T_{tc}. On the other hand, rotational energies (E_{rot}) of AlO, shown in figure 9, were much lower (corresponding to $\approx$ 500-600 K) than the translational energies and can reasonably be identified with a surface temperature T_{tc}. The situation in which ablated molecules have high translational energies, yet are internally cold, is a 'fingerprint' for a non-thermal mechanism of ablation.

Observation of the inequality $E_{\mathrm{trans}} \gg E_{\mathrm{rot}}$ showed that the emission of the AlO molecules was not consistent with surface vaporization, but instead with an electronic ablation mechanism. In confirmation, photothermal deflection measurements showed a temperature rise far too small to account for the observed high kinetic energies of AlO and Al (Dreyfus et al., 1987). Ablation of a thin oxide

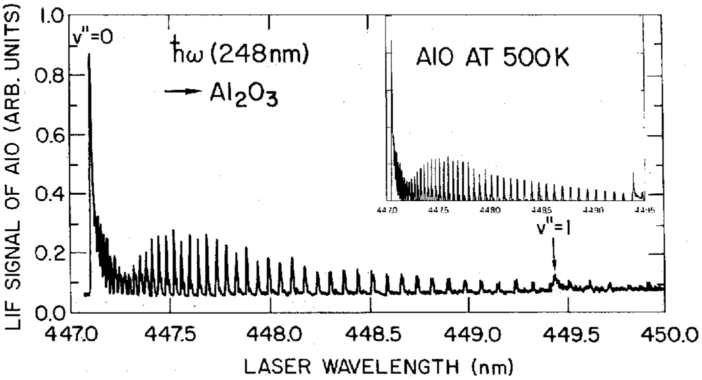

Figure 9. Measured and calculated rotational energy spectra of AlO desorbed from sapphire (Al_2O_3) at fluences above the ablation threshold of 0.6 J/cm^2. The rotational temperature inferred from the measurement is 600 K, far below the effective translational temperature deduced from time-of-flight measurements. Adapted from Dreyfus et al. (1986).

film on an aluminum metal substrate showed that, even though the estimated temperature rise in the film differed significantly from bulk Al_2O_3 samples, energy and velocity distributions of the ablation products remained similar, suggesting a common electronic mechanism as had been previously conjectured on the basis of electron microscope scans (Rothenberg & Kelly, 1984).

Chase and his collaborators have also studied ablation of Al_2O_3 (Chase et al., 1991), paying particular attention to changes in the surface stoichiometry. At the fundamental wavelength of the Nd:YAG laser ($h\nu = 1.17$ eV), laser irradiation induces a surface reconstruction; presumed ejection of oxygen atoms or ions (not observed) is accompanied by emission of Al^+ ions with a typical energy of 8 eV. Schildbach & Hamza (1992) suggest that this high energy results from exciton decay. Electron energy loss (EELS) spectra of the irradiated Al_2O_3 surface show the growth of surface states in the bandgap which could be created by one- or two-photon excitation. Electrons could be promoted from filled surface states into the conduction band by one-photon transitions; ions would be produced by an inter-atomic Auger decay. Sequential excitation by a pulsed 80-ps Nd:YAG laser showed an ablation threshold for Al_2O_3 consistent with single-photon excitation, and an ablation mechanism with a relaxation time of order 200 ps. Such a time constant is consistent with the thermally constrained relaxation of a surface electronic excitation.

Ablation of sapphire has also been studied in air and low vacuum using a picosecond laser (4th harmonic of Nd:YAG, $\lambda = 266$ nm, nominal laser-pulse duration

30 ps) at fluences of order 10 J/cm^2, far above the threshold for ablation (Brand & Tam, 1990). The depth of the ablation crater was found to vary linearly with exposure (or number of laser pulses), and showed negligible dependence on ambient pressure. Spherical, apparently amorphous, sapphire particles were ejected from the surface, as observed by scanning electron microscopy. The experimenters suggest 'hydrodynamic sputtering' rather than 'electronic sputtering' as the mechanism. However, at extremely high fluence, the electronic processes which change the optical properties of the surface during laser irradiation are effectively masked. Moreover, because of the significant penetration depth of 266-nm light into the sapphire, the laser-irradiated volume is relatively deep and narrow. Thus the explosive release of droplets observed in the experiment may well be strongly constrained by the geometry of the ablation crater.

4.2.2 Silicon Oxides and Silicate Glasses

Fused silica and silicate glasses have enormous practical importance in many technologies, and their physical and optical properties have been studied in great detail. The bandgap energy for a-SiO_2 – 7.6 eV – is comparable to many alkali halides; however, the tetrahedral covalent structure of SiO_2 gives its electron-lattice coupling a distinctive character. Both amorphous and crystalline SiO_2 support the self-trapping of excitons, but only in a-SiO_2 do these STEs relax to form Frenkel pairs. In silica, the E' center (oxygen vacancy) and non-bridging-oxygen hole center are the analog of the F- and H-centers in the alkali halides. Defect creation related to the self-trapped exciton has been studied in bulk a-SiO_2 by a number of groups. Tsai et al. have shown (1988) that 6.4 eV photons from an ArF laser produce the E' center in fused silica by nonradiative decay of neutral excitons (1988). Devine has reported (1989) that the density of E' centers in amorphous silica (Spectrosil W1) scales with the number of two-photon absorption events induced by an ArF laser at 193 nm (6.4 eV). The scaling shows the same dependence on excitation density for the case of 4.8 eV lasers (KrF at 248 nm) and for γ irradiation, for which the number of electron-hole pairs can likewise be calculated reliably. This seems to show that the creation of these point defects has an excitonic origin. Studies on thin silica films under ultraviolet plasma irradiation also show that the E' center is created by ultraviolet light with wavelengths around 250-300 nm, possibly by an excitonic mechanism (Devine et al., 1991). The creation of optically absorbing defects in fused silica by 193 nm laser irradiation has also been observed, again via two-photon absorption (Rothschild et al., 1989). The two- and three-photon kinetics of the STE have recently been mapped out by tracking the STE luminescence in the well-known 2.8 eV band (Joosen et al., 1992) following excitation by a sixty-femtosecond laser pulse.

In a study of the long-term effects of ultraviolet laser irradiation on fused silica, Tam and co-workers observed permanent, irreversible changes in both physical and optical properties of fused silica after $6{\cdot}10^7$ pulses from a KrF laser at a fluence of approximately 400 mJ/cm^2 and a pulse repetition frequency of 300 Hz (Leung et al., 1991; Leclerc et al., 1991). Among the changes observed in this work were a compaction in both front and back surfaces of the laser-irradiated area, and an exposure-dependent change in transmission of the sample. The transmission loss was found to recover somewhat twelve to fourteen hours after laser irradiation ceased, incidating very long-term defect-annealing processes at work. It is also intriguing that these changes are not found to occur in crystalline quartz. This may be connected to the fact that excitons are self-trapped in amorphous fused silica (see, for example, Itoh et al. 1989), but not in crystalline quartz.

Laser ablation of fused silica has also been studied with an Ar excimer laser operated at a wavelength of 126 nm (9.8 eV) having a pulse length of 5 ns. In this case, ablation is initiated by one-photon band-to-band transitions (Takigawa et al., 1990). The SiO_2 surface was the back reflector in the Ar excimer laser, and had a reflectivity of order 0.15 in the vacuum ultraviolet. Single-shot ablation of the silica surface was observed by topographic scanning with a non-contact profiler at a fluence of 280 mJ/cm^2. Measurements of vacuum ultraviolet reflectivity using a synchrotron light source showed that the SiO_2 surface was virtually devoid of Si-O bonds, and indicated significant increases in reflectivity in the 5-6 eV region due to generation of E' centers.

Fused silica films have been grown by laser ablation using an ArF laser ($\lambda = 193$ nm) to irradiate both silicon monoxide and silicon dioxide substrates (Fogarassy et al., 1990, Fogarassy et al., 1991 and Slaoui et al., 1992). Because SiO has a one-photon absorption coefficient α at approximately $5{\cdot}10^5$ cm^{-1} at 193 nm, the laser energy is deposited within a few wavelengths of the surface. Interestingly, however, the threshold measured for Si, SiO and SiO_2 substrates varies by less than 50% from 1 J/cm^2 even though the linear absorption varies by two orders of magnitude. This suggests that electronic mechanisms other than simple absorption may play a role. One possibility suggested by these authors is that strong surface heating might change the surface composition by the thermal reaction $2{\cdot}SiO \longrightarrow SiO_2 + Si$ or by electronic processes involving defects (Fogarassy et al., 1988).

Ablation of thin SiO_2 films grown by electron-beam evaporation on borosilicate glass (BK-7) substrates using 70-ps pulses from a Nd:YAG laser (1064 nm) was observed by Chase et al. (1992). Particle yields near threshold, measured by a quadrupole mass spectrometer, were dominated by Si and O neutral atoms with energies of several eV. By using time-delayed pairs of pulses and assuming both a power-law absorption and a simple exponential relaxation (Chase et al., 1990), the ablation yields near threshold were shown to arise from linear absorption processes,

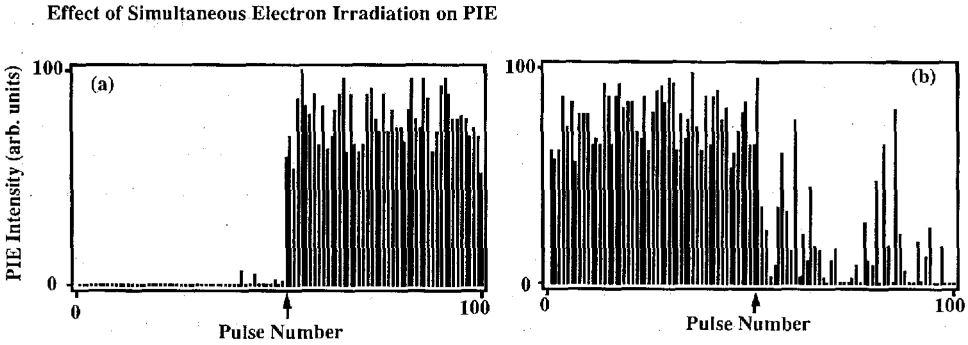

Figure 10. Total positive-ion yields (PIE) from sodium trisilicate glass irradiated by an electron beam and a KrF laser. In the top panel, total PIE is shown for the case where a 1500-eV electron beam, with a current density J = 6 mA/cm^2, is turned on at the arrow after approximately fifty laser pulses. In the lower panel, the electron beam and the laser irradiate the sample simultaneously at the start; the electron beam is turned off after the same number of laser pulses. From Dickinson et al. (1990).

consistent with a free-electron heating mechanism (Arnold & Cartier, 1992). The same double-pulse technique applied to polished surfaces of the borosilicate glass, however, showed a behavior more nearly consistent with electron-hole-pair creation by five-photon excitation for a laser wavelength of 580 nm.

Picosecond laser ablation has been studied in α-quartz by the group of Petite & Agostini (Petite et al., 1991), using a oscillator-amplifier laser system capable of delivering significant pulse energies using multiple, sum or difference frequencies of the Nd:YAG oscillator wavelength. The nominal pulse duration was selectable between 50 and 150 ps. Ion desorption only of impurity ions was observed below 10^9 W/cm^2 intensity, but significant Si and O ion emission was seen above that threshold. In the same experiment, electron emission was measured as a function of laser wavelength for photon energies equal, respectively to 1.98, 2.34 and 3.51 eV. Valence electrons could be ejected from SiO_2 by four-, five- or six-photon transitions at these wavelengths; however, the intensity dependence of the electron yields was about half the expected values, indicating that the electron emission probably comes from surface and/or defect states, particularly in view of the strong dependence of the yield on surface temperature (Petite et al., 1985).

Surface electronic defects have a dramatic effect on the ablation threshold in silicate glass (Dickinson et al., 1990). A sodium trisilicate glass [$Na_2O{\cdot}3SiO_2$] with a bulk band-gap energy of 8.5 eV, was irradiated by a KrF laser (λ = 248 nm, $h\nu$ = 5 eV). Ablation was detected by monitoring the intense positive-ion emission accompanying ablation, using a channel electron multiplier without amplification.

At a fluence of 1 J/cm^2, no positive ion emission was detected for the first fifty pulses, as shown in the upper frame of figure 10. At the fifty-first laser pulse, a 1500-eV electron beam with a current density of 6 mA/cm^2 was directed at the target, at which point the positive-ion emission abruptly jumped to a value consistent with rapid etching of the surface. When both the laser and electron beam were turned on initially, strong positive-ion emission was observed, as shown in the lower panel of fig. 10. When the electron beam was turned off after the fifty-first laser pulse, positive ion emission occurred only in intermittent bursts. Since the KrF laser can produce defects by two-photon absorption processes in this glass, it appears that surface defect density plays a significant role, with the electron beam producing large defect densities, the laser producing smaller defect densities consistent with the lower probability of band-to-band excitation by two-photon absorption. This is consistent with earlier reports of 'induction' or 'incubation' behavior in these same materials (Eschbach et al., 1989); Negative-ion spectra from the same material show the presence of electrons and several negative-ion species, in all probability formed by electron attachment to neutral atoms and molecules in the plume (Langford et al., 1990). Apart from the potential uses of this 'dual-beam' or 'electron-seeded' ablation as a technique for high-resolution photolithography, this work clearly establishes a correlation between the existence of electronic or structural defects and ablation in the silicates.

4.2.3 Laser Ablation in Other Binary Oxides and Chalcogenides

Irradiation of ZnO, a solid with weak electron-lattice coupling, by laser beams capable of generating band-to-band transitions, has been shown to produce ablation products which do not have a simple Maxwell-Boltzmann velocity distribution (Nakayama et al., 1982). The same general behavior, with a sharp fluence threshold for ablation and a non-thermal velocity distribution, was observed in TiO_2 (Nakayama, 1983). Laser ablation of HfO_2 films grown by electron-beam evaporation on borosilicate-glass (BK-7) substrates was studied by Chase et al. (1992) using the double-pulse technique cited earlier. Below the threshold for macroscopically visible surface damage, particle emission with very high energies is observed. The measured relaxation time for the initial excitation appeared to be in the few-ns range, although the scatter in the data make this estimate somewhat problematical.

MgO has a wide bandgap and is very ionic, but band-to-band excitation does not produce electronic defects. Studies of laser ablation at 248 nm in neutron- and gamma-irradiated MgO shows that the introduction of displacement defects dramatically lowers the ablation threshold (Webb et al., 1993). Even above the plasma threshold (roughly, for $\Phi > 2$ J/cm^2), an incubation effect consistent with accumulation of defects affected the rate of material removal. The defects could also be induced by KrF laser; their local density was also dependent on the prior cleavage or polishing history of the surface, suggesting a link to mechanical defects. Scanning electron microscopy data showed that the surface of the crystal began to fracture before ablation and rapid material removal. At fluences of 1-3 J/cm^2, laser irradiation of freshly cleaved surfaces produced a pattern of conical microscopic penetrations of the surface; in these 'microholes', magnesium-rich droplets accumulated, testifying to localized decomposition of the surface (Dickinson et al., 1993a). Interestingly, laser irradiation at high fluence in MgO also removes some types of surface defects, suggesting that laser processing could be used to stabilize surfaces under certain conditions.

Laser-induced desorption and ablation have been studied in the chalcogenide semiconductor ZnS under ultrahigh vacuum conditions, using an XeCl laser at a wavelength of 308 nm (Arlinghaus et al., 1989). Since the interband absorption edge of ZnS is at 325 nm, electron-hole pairs are created by one-photon excitation under these conditions. Velocity distributions were measured by two-photon laser-induced fluorescence. At fluences of 20-55 mJ/cm^2, corresponding to intensities of 0.66-1.83 MW/cm^2 for the 30-ns XeCl laser pulse, velocity distributions are Maxwellian and the yield of Zn atoms follows an Arrhenius relation with an activation energy of 2.5 eV, consistent with the heat of vaporization of ZnS. Above 60 mJ/cm^2, however, the temperature inferred from the velocity distributions rises from 2000 to 9000 K – a value clearly inconsistent with any reasonable surface temperature. This suggests that a nonthermal mechanism is operative, possibly the interaction of the ablation plasma with the surface. Chase (1994) has also suggested, based on the results of double-pulse experiments with 70-ps pulses, that free-electron heating may be responsible.

4.2.4 Laser Ablation in Ternary Ferroelectric Oxides

Laser ablation from the surfaces of ternary oxide ferroelectrics is emerging as an important factor in the application of these materials in nonlinear optics where laser intensities are high; in the use of $KNbO_3$ as a diode laser material; in micromachining, for example, for direct writing to form optical circuits and optical interconnects with silica fibers; and in thin-film deposition by laser ablation for nonvolatile memories where other methods are impossible to apply.

The optical response and the character of the laser ablation for oxide ferroelectrics change depending on the relationship between laser wavelength and optical gap. The bulk conduction-band edge of $LiNbO_3$ lies almost exactly 4 eV above the bulk valence-band edge. Earlier work has shown that ultraviolet laser irradiation near the band edge produces emission of various ground-state and excited-state

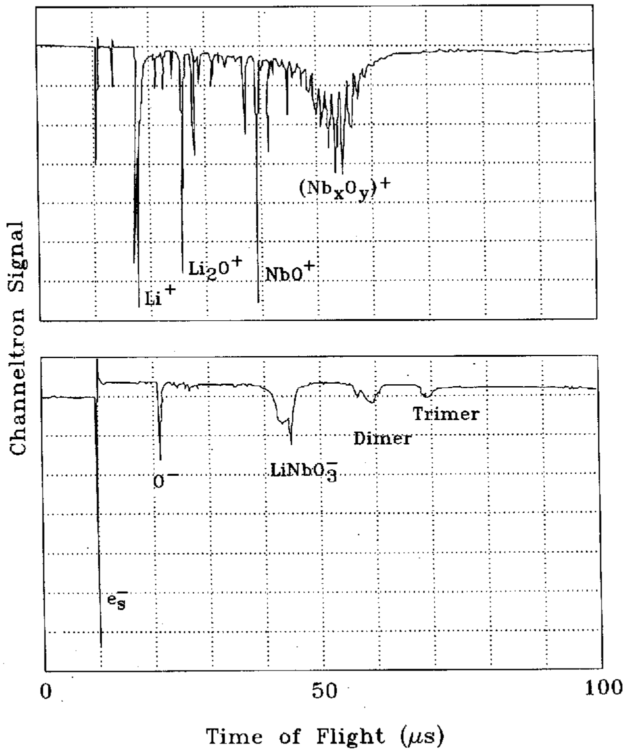

Figure 11. Time-of-flight spectra of (a) positive and (b) negative ions from $LiNbO_3$ irradiated by the fourth harmonic of a Nd:YAG laser at 266 nm. Each spectrum comes from a single laser pulse incident on a fresh surface site. The major peak in the positive-ion spectrum is Nb_2O_x, with the central peak at Nb_2O_5, the maximally valent oxide. Note the peaks corresponding to the dimer and trimer of $LiNbO_3$ and the two-component time-of-flight distribution.

atoms, molecules and ions (Haglund et al., 1991). Laser ablation from $LiNbO_3$ and $KNbO_3$ shows some of the same features as the experiments in strong-coupling materials: metallization of the surface, for example, apparently from preferential emission of oxygen atoms and ions. As in the strong-coupling case, there appears to be a linear regime, as detected by the rate of change of emission of excited metal atoms from the surface at moderate fluences (Haglund et al., 1992a). Translational velocities of emitted atoms and diatomic molecules are consistent with a nonthermal ablation mechanism. In contrast to ablation in the alkali halides, however, the ablation regime in $KNbO_3$ is characterized by a reduction in the power-law dependence of the yield of excited atoms on laser fluence.

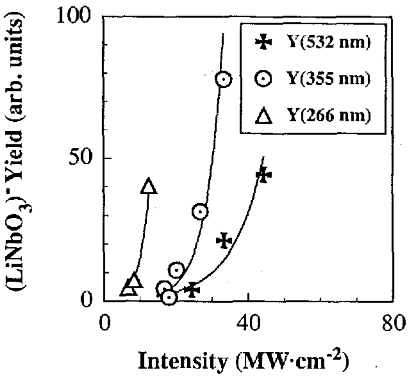

Figure 12. Yields of the LiNbO$_3^-$ molecular ion as a function of laser intensity for three different laser wavelengths. Each point is obtained by averaging over several time-of-flight spectra such as those shown in Fig. 11. The band-to-band transition is excited by either the 266 nm or 532 nm transition by single or two-photon transitions, respectively; defect states just below the conduction-band edge are excited by one-photon transitions at 355 nm. The curves are only guides for the eye.

Near the ablation threshold but below the fluence required to form a visible plasma, there is also evidence of neutral and ionic molecular clusters with masses up to 600 a.m.u., though it is by no means clear whether these are ejected intact from the surface or are formed by condensation in the plume. Molecules in both ground and excited states - some no doubt formed in the ablation plume - are observed at intensities below 10^8 W/cm^2 under ultraviolet laser (XeCl, $\lambda = 308$ nm) irradiation (Haglund et al., 1993). Time-of-flight spectra for both positive and negative ions desorbed at the fourth harmonic of the Nd:YAG laser (266 nm) are shown in the two panels of figure 11; the negative-ion spectrum includes dimers and trimers (Haglund et al., 1992b). Molecular-ion emission is also observed for laser desorption with 532-nm and with 355-nm light. However, as shown in figure 12, the intensity dependence of the ablation yields varies for the three wavelengths. The steepest yield *vs* intensity curve is for ablation at 266 nm, initiated by single-photon band-to-band transitions. At 355 nm, excitation of surface states or surface defects can also create electron-hole pairs by single-photon transitions. At 532 nm, on the other hand, a two-photon transition is required to generate each electron-hole pair, and the density of excitation in the solid, at least initially, is correspondingly lower. This apparently leads to a yield of lithium niobate negative ions which varies much less steeply with fluence. These results demonstrate that either excitation of surface defects or band-to-band transitions can lead to ablation, but that one-photon band-to-band transitions give the highest yield at a specified fluence, and

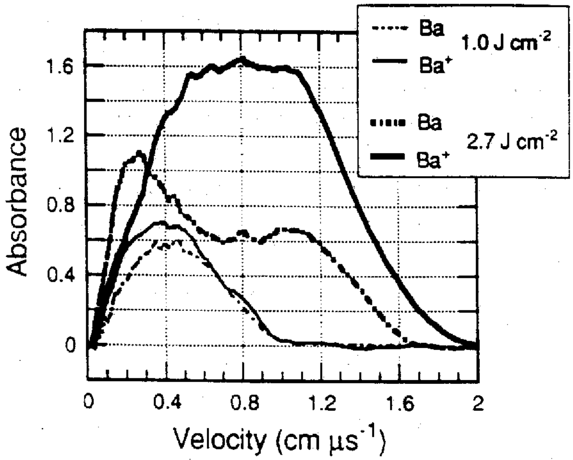

Figure 13. Absorbance of a laser ablation plume as a function of time-of-flight velocity of ablated Ba ions and atoms, measured at a distance of 1 cm above the surface of a $YBa_2Cu_3O_{7-\delta}$ pellet. The target was irradiated in moderate vacuum for fluences of 1.0 Jcm^2 and 2.7 J/cm^2, respectively, using a KrF laser. Note the growth of the high-velocity components at the higher fluence. From Geohegan (1991).

likewise have the lowest threshold.

4.2.5 Quaternary Perovskite Superconductors

The current demand for high-quality thin films of high-temperature superconducting materials has produced a rich outpouring of literature on the relationship of ablation parameters to thin-film quality, but rather less work on fundamental mechanisms. The optical bandgap of these materials is typically in the far-infrared region of the spectrum, so that any infrared, visible or ultraviolet laser can cause efficient laser ablation by initiating band-to-band excitations. There are clear signs of nonthermal ablation mechanisms operative in these materials. However, the literature on ablation in high or ultrahigh vacuum, where one might hope to observe the primary processes of particle emission and ablation, is rather sparse.

Among relevant fundamental studies is the work of Wiedeman & Helvajian (1991), who measured the product and kinetic-energy distributions for atoms, molecules and ions desorbed and ablated from a sintered $YBa_2Cu_3O_{6+x}$ target at laser wavelengths of 351, 248 and 193 nm. The fluence range covered in the experiments ranged from 50 mJ/cm^2, the threshold for desorption, to 800 mJ/cm^2, the plasma formation threshold and also, presumptively, the ablation threshold.

The relative populations of metal atoms and metal-oxygen diatomics showed significant wavelength variation, as did the distribution of products. In addition, the velocity distributions are clearly nonthermal, with mean kinetic energies in excess of 3 eV. However, it is not clear whether the nonthermal velocity distributions themselves should be taken as evidence of the electronic character of the ablation process, since multiple collisions in the evolving laser plume above the surface, even in vacuum, can also produce the same effect (Kelly & Dreyfus, 1988; Nogar et al., 1991).

In ablation experiments on $YBa_2Cu_3O_{7-\delta}$ at low fluences (≈ 0.1 J/cm^2), high-sensitivity absorption spectroscopy on atoms and ions (Geohegan & Mashburn, 1989) shows nearly Maxwellian velocity distributions, and a ratio of Ba^+/Ba^0 of order 5:1. At higher fluences (of order 1 J/cm^2), absorption due to Ba^+ increases, coming largely from the leading edge of the ablation plume. At higher intensities, the Ba neutral-atom and ion velocity distributions begin to include a fast non-thermal component, as illustrated in figure 13. Debye screening lengths in the ablation plume are larger than 10 μm, however, showing that the plume is overwhelmingly composed of neutral atoms. Total ion emission shows a sharp break as a function of fluence near $F \approx 0.4$ J/cm^{2,} changing from a $F^{7.4}$ to a $F^{1.5}$ dependence above this critical value (Geohegan, 1991). A corresponding change in ion velocity on the leading edge and at the peak number density of the plume occurs at nearly the same fluence, suggesting the onset of plume-surface interactions. Note the contrast to the case of the alkali halides (figures 6 and 7) where the onset of ablation is accompanied by a steepening of the yield vs intensity curve.

Measurements of ion and molecule mass and optical-emission spectra as a function of laser intensity have been carried out for several high-T_c materials (Chen, Phillips and McCann, 1993; Chen & Phillips, 1991; Chen, Murphy & Phillips, 1990). These spectral measurements on atom, ion and molecule sputtering from $YBa_2Cu_3O_{7-\delta}$, $Bi_2Sr_2CaCu_2O_{8+x}$ and Tl-CaBa-Cu-O substrates cannot be described by the Saha-Langmuir equation even in the regime where the plume is well-formed. This suggests that thermionic emission cannot account for the ablation mechanism. Photography of laser-ejected particles from $YBa_2Cu_3O_{7-\delta}$ surfaces also shows particles with suprathermal velocities (Kelly et al., 1992). Thus, even though the high-T_c materials have small bandgaps and rapid relaxation times, non-thermal, presumably electronic processes make their influence unmistakable. No thermal process can account for ablation products with translational energies in the 1-10 eV range, because the temperature T of the surface must satisfy the condition $T \leq T_{tc}$.

Clusters containing thousands to millions of atoms have also been observed in laser ablation plumes from $YBa_2Cu_3O_{7-\delta}$ irradiated by the combined fundamental and second-harmonic laser irradiation from a Nd:YAG laser (Becker & Pallix, 1988). A number of authors have reported mass spectrometric and optical measurements of low-mass particles from direct desorption processes both below and above the threshold for visible plasma production (see the above references from the Chen group, also Saenger, 1989). Cluster formation, on the other hand, has been seen only at intensities just below those required for the development of the visible plume, presumably because of fragmentation by energetic ions or electrons in the plume. The fact that the clusters do not appear at threshold suggests that the clusters are not directly desorbed or ablated, but instead condensed by multiple collisions in the plume once it reaches some critical mass density. The largest clusters observed might properly be called 'macroclusters', with diameters approaching 60 Å. With increasing dose, ridges or channels developed on the irradiated target, and increased condensation of clusters in the plume was observed, suggesting that plume-surface interactions may play a role in the condensation process.

4.3 Laser Ablation in Weak-Coupling Solids

Laser ablation in semiconductors (Dubowski, 1988) and laser-induced desorption and ablation in weak-coupling solids (Haglund & Itoh, 1993) have recently been reviewed. In weak-coupling solids, excitons are not self-trapped, and ablation is only one outcome of the competition between radiative and such nonradiative relaxation processes as Auger recombination. Early studies with nanosecond lasers reported 'thermal ablation' of Si (Brown, 1980). However, ablation of Si by a picosecond Nd:YAG laser at fluences up to 3.5 $\mathrm{J/cm^2}$ showed most probable velocities of atoms and ions greater than those corresponding to the temperature T_{tc} (Liu et al., 1982). It now appears likely that ablation is also at least partly electronic in all weak-coupling solids. For example, an inter-atomic Auger charge transfer mechanism has been proposed to explain energetic-ion ablation of Si (Wu, 1990).

The ablation thresholds of both elemental and compound semiconductors were measured by Namiki et al. (1988) using a pulsed nitrogen laser ($\lambda = 337$ nm) and shown to decrease as one moves from Group IV to III-V and II-VI materials.

More recent studies of GaN, GaP and GaAs ablation yields (Namiki et al., 1991) led to thresholds of 150 ± 50, 55 ± 10 and 75 ± 15 $\mathrm{mJ/cm^2}$, respectively, and also suggest that gas-dynamic effects play a significant role in ablation from these materials. (See section 5.1 below.) Angle-resolved time-of- flight spectra of ejected Ga and X_2 neutrals, where X is variously N, P and As, were used both to study the gas-dynamic effects, which exhibit strong variations with angle of ejection, and the velocity distributions. These authors found that it was impossible to fit the ablation yields to a shifted Maxwellian distribution typical of a thermal ablation process; in addition, the translational temperatures ranged from $5\cdot 10^3$ to 10^4 K, far too high to be attributed to thermal ablation. Namiki et al. (1987) propose that this high energy comes, instead, from inelastic collisions which occur at the first stages of desorption, feeding on the internal energy of the X_2 molecules formed by the dimerization.

Another study of laser-surface interactions in the III-V semiconductors by Long et al. (1992) has shown that surface decomposition occurs in GaAs irradiated by 5-ns high-repetition-rate (6 kHz) copper-vapor laser ($\lambda = 510$ nm) pulses at fluences as low as 1 mJ/cm^2, far below the ablation threshold. As int the work of the Namiki group, the photon energy in this case is well above the bandgap energy, thus assuring efficient production of electron-hole pairs. At this high pulse repetition frequency, long-term relaxation effects may also be induced. However, the electronic character of the process is assured, since the temperature rise due to photon absorption is less than 13 K. Time-resolved photoemission measurements show the growth of a Fermi-level feature related to the formation of Ga islands; scanning electron microscopy shows the Ga islands to have diameters as large as 100 Å. This surface decomposition is attributed to the desorption of As atoms, and is thus reminiscent of the decomposition by release of the non-metallic component one expects in strong-coupling solids.. However, Long et al. (1992) suggest, based on the growth rate of Ga islands with laser fluence, that the As desorption and concomitant aggregation of Ga atoms is the result of a two-step process. The first step is bond rearrangement at a surface kink site; if the site is excited a second time, desorption results, otherwise the site relaxes to its original configuration. Thus the first step would involve direct photoexcitation, the second a nonradiative transition, possibly thermally activated.

Neither of these two measurements used a sensitive technique to detect directly the products of desorption; the quadrupole mass spectrometer, for example, cannot 'see' anything less than a substantial fraction of a monolayer of sputtered material. More sensitive detection techniques, such as laser-induced fluorescence and resonance ionization mass spectroscopies, have been employed recently to study laser-induced desorption and ablation from GaP, a weak-coupling material with an unoccupied surface state just below the bulk conduction-band edge. The Itoh group has pioneered extremely-high-sensitivity studies of Ga atoms detected by resonance-ionization mass spectroscopy. Desorption and ablation are initiated by excitation of the surface state without any bulk absorption, thus guaranteeing the absense of thermal effects. Typical examples of the yield-fluence relation for Ga^0 sputtered from GaP at fluences both below and above the ablation threshold at an incident laser wavelength of 600 nm is shown in fig. 14 (from Hattori et al., 1991). Noteworthy here is the existence of two thresholds for desorption of Ga^0 below the threshold for ablation of Ga metal atoms with concomitant rapid destruction of the surface. Other studies by the same group, showing the striking effects of temperature variation on desorption yields and of the excitation of surface states in

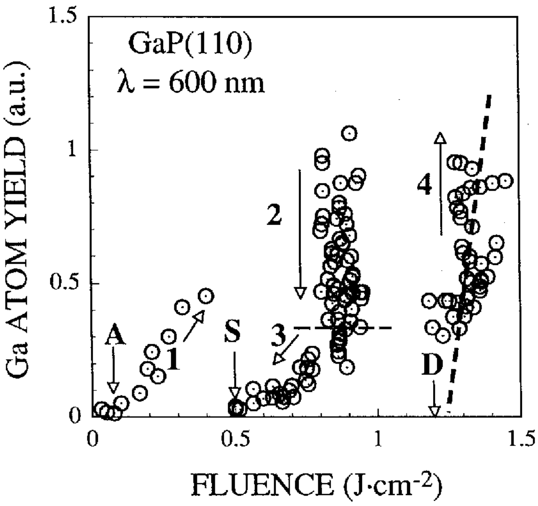

Figure 14. Comparison of the differing behavior of desorption and ablation yield vs shot number for Gao desorbed or ablated from Ga^0, as measured by resonant multiphoton ionization spectrometry. Data 1 are for a series of shots at gradually increasing laser fluence. Data 2 result from shots at a constant fluence of 0.85 J/cm^2 (I_2), below the ablation threshold; note the decreasing yield with shot number. Data 3 are for decreasing laser fluence (I_S). Data 4 were taken above the threshold for defect-initiated ablation. The laser fluence was held constant at 1.35 J/cm^2 (I_4); note that the yields are increasing sharply with shot number. From Hattori et al. (1991).

the conduction band have recently been reported for GaAs (Kanasaki et al., 1993).

In weak-coupling solids, ions and neutral atoms are desorbed by laser irradiation, the yield of the former increasing more rapidly than the latter as fluence increases (Nakayama, 1983). Ablation yield above threshold increases much more rapidly as a function of laser fluence in compound semiconductors than in alkali halides. The ablation threshold can be determined not only from the fluence dependence of the yield but from modification of the LEED pattern (GaP, Kumazaki et al., 1987a, b). Dispersive X-ray analysis (XDS), and Auger electron spectroscopy (AES) show that the ablated surface is not stoichiometric. Photoelectron emission from InP exhibits nearly the same dependence on the fluence as the ion emission yields (Moison & Bensoussan, 1982).

There is much evidence which associates both desorption and ablation with defect formation. For example, chemically-etched GaAs etched surfaces were found to have much lower ablation thresholds than untreated surfaces (Sardar et al., 1987). Adatom and step sites show low desorption thresholds in GaP (Hattori et al., 1991). Structural defects introduced by Ar-ion irradiation also reduced threshold levels (Hattori et al., 1992). However, these defects apparently are not accumulated as they are in strong-coupling solids. For example, the ablation threshold determined by LEED patterns was changed only slightly after irradiation by 1, 100 and 1000 laser shots (Hattori et al., 1991).

The II-VI compound semiconductors are of increasing technological interest and laser ablation is now being studied as a means of modifying surface epitaxy. Recent experiments by Brewer and co-workers (1990) showed that the surface composition of CdTe can be modified reversibly by excimer (KrF, $\lambda = 248$ nm) laser irradiation. The experiments were carried out in high vacuum, and the removal rates ranged from less than 0.1 nm/pulse to approximately 10 nm/pulse. At the highest rates of material removal which occurs for fluences above 65 mJ/cm^2, ablation and irreversible surface damage occur, and photoionization of neutral atoms and molecules in the plume becomes significant. Above a laser fluence of 40 mJ/cm^2, a metal-enriched surface is observed; at lower fluences, stoichiometry can be restored by laser irradiation. The translational energies and kinetic temperatures deduced from the velocity distributions of the Cd, Te and Te$_2$ desorption products are all consistent with the measured sample surface temperatures of 380 to 400 C. However, the rates for laser-induced desorption are more than six orders of magnitude higher than those for vacuum sublimation in the same temperature range, indicating that the process is not purely thermal (Brewer et al., 1991). The results may be the outcome of a competition between two thermally activated processes, under the assumption that the kinetics of Cd desorption is linked to the kinetics of Te$_2$ formation.

4.4 Laser Ablation of Polymers

A discussion of laser ablation would be incomplete without mentioning polymers because of their importance in both semiconductor technology, where they are used as photoresists (Phillips et al. 1991), and in medicine, where tissues can often be treated in zeroth-order approximation as biopolymers. The bonds between monomers, as in the polyimides (Kapton) and poly(methylmethacrylate) (PMMA), are strong and covalent. The forces between polymers, on the other hand, are typically an order of magnitude weaker (Srinivisan, 1986). Ultraviolet light is sufficient to break the covalent bonds by an electronic transition, separating the polymer into monomers (Garrison & Srinivasan, 1985). Polymer ablation was initially assumed to result from an electronic process described as photochemical ablation. However, polymer ablation exhibits complex dependence on laser wavelength, pulse duration and intensity which may show both electronic and thermal features (for example, Davis & Gower, 1987).

For laser wavelengths below 260 nm, efficient one-photon absorption by a $n-\pi^*$

state produces an excited-state with a lifetime of microseconds (Srinivasan et al., 1987); hence, multiple-photon excitation leading to bond-breaking and efficient ablation is possible within the duration of a single 10- 20-ns pulse. Photochemical decomposition of the polymer by nanosecond pulses at from KrF or ArF lasers results in a sudden volume change and the launching of a photoacoustic wave from the laser-irradiated surface into the bulk (Dyer & Srinivasan, 1986). By comparison, 160-fs pulses from an XeCl laser ($\lambda = 308$ nm) ablate PMMA efficiently and without collateral thermal damage by a two-photon transition leading directly to bond-breaking (Srinivasan et al., 1987). Ablation of poly(tetrafluoroethylene) (Teflon) by 300-fs pulses from a KrF laser likewise shows efficient ablation at fluences as low as 0.5 J/cm^2 (Küper and Stuke, 1989a). In contrast to nanosecond-pulse ablation at this wavelength, ultrashort-pulse ablation introduces no collateral thermal effects.

In addition to some intrinsic absorption leading to direct bond-breaking, exposure to ultraviolet light at fluences below the ablation threshold produces increased absorption, so that ablation at 308 nm is possible after a number of incubation pulses. Infrared absorption studies implicate a variety of ester groups with infrared absorption bands at 1643 cm^{-1} (C=C stretch) and 3078 cm^{-1} (C = C - H stretch) in the changed ultraviolet absorption; an additional absorption band at 2104 cm^{-1} has also led to speculation that CO or ketene photoproducts also accumulate during this incubation period (Küper & Stuke, 1989b). There is evidence that the absorption of polyimide saturates at fluences above threshold under KrF irradiation, thus modifying the radiation transport into the surface during the ablation pulse (Pettit & Sauerbrey, 1991). ArF-laser-irradiated polyimide also exhibits a transient reflectivity change due to the creation of highly excited species; recovery to the pre-ablation value of reflectivity requires nearly 1 ms (Ediger & Pettit, 1992). It is not yet established how these modifications of optical properties are related to observed laser-induced changes in surface conductivity (Feurer et al., 1993) and surface structure (Phillips et al., 1993).

Much effort has been devoted to characterizing the state of the ablation products from polymer surfaces. Picosecond ablation experiments on polymers show that there is a finite (≈ 20 ps) delay as the vibrational and electronic excitation is converted into translational motion (Kim et al., 1989). Time-of-flight mass spectrometry on the neutral ejecta has been carried out by nonresonant post-ionization using picosecond (Larciprete & Stuke, 1987) and nanosecond (Hansen, 1989a) lasers; a coherent vacuum-ultraviolet laser beam ($\lambda = 118.4$ nm) has also been used to achieve 'soft' photoionization of neutral ablation products (Feldman et al., 1987). The observations from these experiments may be summarized as follows:

- The neutral monomer is the dominant product in most cases, but relative

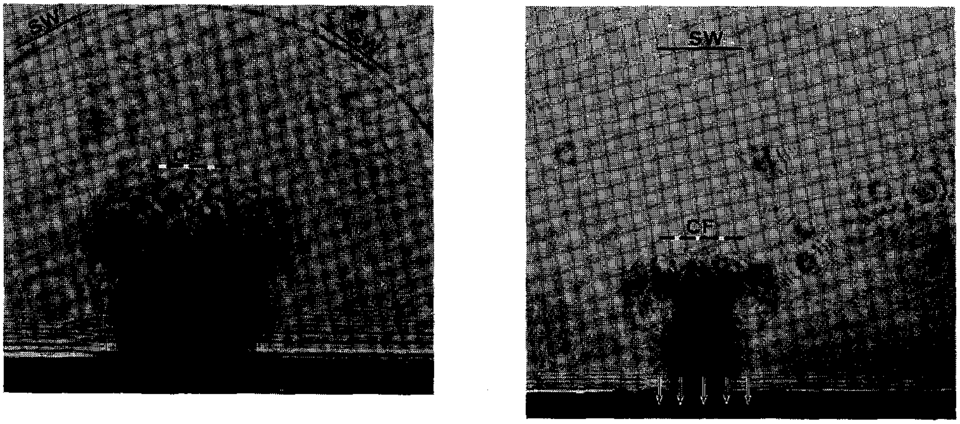

Figure 15. Shock-wave from a polymethylmethacrylate target exposed to five laser pulses (248 nm, pulse duration 20 ns, diameter 700 μm, $F = 2.1$ J/cm^2) in air. Heavy particles and the shock wave at fixed time delays after the ablation pulse are indicated by SW. The contact front of the heavy particles is indicated by CF. (a) Delay of 2.9 μs; (b) delay of 4.9 μs with a photographic reduction in magnification by 0.61. The arrows represent the recondensation process. From Kelly & Miotello (1993).

monomer abundance shows strong fluence, wavelength and time-delay effects. In poly(tetrafluoroethylene), the monomer may be produced by a thermally activated 'unzipping' process (Dickinson et al., 1993b).

- At higher fluences, decay products of masses lower than the monomer become increasingly prominent, indicating the opening of fragmentation channels.
- Decay products of masses higher than the monomer are also observed late in the ablation process, suggesting complex photochemical activity in the plume.

When PMMA targets were exposed to five pulses from a KrF laser (248 nm, pulse duration 20 ns, beam-spot diameter 700 μm, fluence 2.1 J/cm^2) in air, sustained photoreactions above the laser-irradiated surface were also observed (Kelly et al., 1992). Emitted heavy particles and the shock wave initiated by the ablation of low-mass particles were photographed by firing parallel to the target surface a second laser (596 nm, 1 ns pulse duration) at fixed time delays with respect to the ablation pulse. The outer boundary of the plume of ejected particles is called the contact front. In this experiment, however, the contact front, located at about 0.75 of the distance to the shock-wave boundary, is not imaged. Although the initial laser-PMMA interaction is by necessity electronic, the actual release of particles into the gas phase persists far beyond the ablating pulse (in this case, $6 \pm 2\mu$s, while the contact front velocity implies a plume temperature of roughly 500 K. This situation is in some respects analogous to that observed in the alkali halides, where electronic excitation in the halogen sublattice leads to expulsion of energetic halogen atoms on a nanosecond time scale, while the metal atoms are vaporized in a thermal process dictated by the surface temperature and defect diffusion times.

5 Plasma and Plume Effects in Laser Ablation

As we observed at the outset, one of the distinguishing features of laser ablation compared to sputtering by ion beams is the development of a plume of neutral and ionized particles.

The plume may be formed either in vacuum or in a gaseous atmosphere. Indeed, a significant technological advantage of laser ablation compared to ion sputtering is that the former need not take place in a vacuum. It is precisely this characteristic which has made possible pulsed-laser deposition of thin films - a laser assisted epitaxial-growth process which is sometimes (as with the high-temperature superconductor $\mathrm{YBa_2Cu_3O_{7-\delta}}$) more effective in a gas atmosphere than in vacuum. In other cases, such as the laser ablation of polyimide, the fact that one can work in a normal atmosphere is not essential to the process but is more convenient in an industrial setting. In this section, we briefly consider the ablation plume as formed both in gaseous atmospheres and in vacuum, and the gas-dynamic and plasma effects observed in that plume.

In the plume, plasma, collisional and photochemical effects, all either electronic in origin or having consequences for the electronic states of particles in the plume, present major complications to understanding the dynamics of laser ablation.

There are several criteria which characterize the dividing line between laser-induced desorption, low-density ablation regime, and the gas-dynamic regime in which the ablation plume is fully formed. As we shall see, one of the simplest is the spatial distribution of the ablation products: in laser-induced desorption, the emitted particles have a $\cos\vartheta$ distribution unless crystallographic effects intervene; in low-density laser ablation, the ejecta have a $\cos^4\vartheta$ distribution; and in the gas-dynamic regime, the angular distribution is approximately proportional to $\cos^n\vartheta$, with n larger than 4. Each of these three regimes is associated with a class of readily identifiable electronic processes.

5.1 Summary of Gas-Dynamic Effects

One important aspect of the ablation plume is related solely to its gas dynamics. It is out of context to review in detail the role of gas dynamics in laser ablation (Kelly et al., 1992), but a brief statement is still in order. We have made the point in the present work that the laser-sputtering phenomenon has two distinctive regimes: that appropriate to low fluences which we have termed desorption and that appropriate to high fluences, termed ablation. These regimes are separated by a threshold as shown in figures 6 and 7. Gas-dynamic effects can be expected to set in gradually somewhat above this threshold, the details depending on the removal rate. The critical removal rate is approximately 0.5 monolayers/pulse for a typical 30-ns pulse (NoorBatcha et al. 1987). In order to be explicit in the discussion, we shall assume that the release of particles from the surface is purely thermal; the gas dynamics must, of course, be modified if we admit the existence of suprathermal-velocity atoms or ions in the plume, as is typical in ablation.

Gas-dynamic effects on the spatial distribution of ejected particles provide a convenient way to differentiate laser-induced desorption from both the threshold region where the plume density is low and the ablation regime in which the ablation plume is fully formed. As we shall now show, particles emitted in the desorption regime have a $\cos\theta$ distribution unless crystallographic effects intervene; in the low-plume-density regime around threshold, the ejecta have a $\cos^4\theta$ distribution, and in the ablation regime, the angular distribution is very nearly proportional to $\cos^n\theta$, where n is larger than 4. Each of these three gas-dynamic regimes is associated with a distinctive set of electronic processes.

At sufficiently low yield, the particles emerging from the target surface will go immediately into free flight. The velocity distribution of these particles is therefore the well known Maxwellian with, however, only positive velocities normal to the surface (x-direction):

$$f_{\mathrm{s}}^{+} d^3v \propto \exp\left(-\frac{E_I + (m/2)\left(v_x^2 + v_y^2 + v_z^2\right)}{k_{\mathrm{B}}T_{\mathrm{s}}}\right) d^3v \;; v_x \geq 0 \tag{7}$$

where v_i is a velocity component and T_{s} is the surface temperature. Assuming a planar, semi-infinite surface appropriate to most desorption and ablation experiments, the number of particles traversing an element of area dA parallel to the physical surface in a time dt is proportional to $f_{\mathrm{s}} v \cos\theta dt dA$. Note that this formulation implicitly assumes that there are no interactions which alter the velocity v. Hence, in the desorption regime, the angular distribution of ejected particles follows a cosine law.

At high intensities and for yields on the order of 0.5 monolayer/pulse, the ongoing effusion of particles from the surface leads to the formation of a Knudsen layer

(KL) which, in turn, feeds an unsteady adiabatic expansion of the plume (Kelly & Braren, 1991; Braren et al., 1991; Kelly, 1990). This Knudsen layer changes both the energies and the angular distributions of ablated particles. Failure to take the Knudsen layer properly into account has sometimes led to misinterpretations of the mechanism of particle ejection, as pointed out by Kelly & Dreyfus (1988). In the Knudsen layer, the particles come to thermodynamic equilibrium; negative values of v_x develop and the velocity distribution takes on a form normally approximated as a shifted Maxwellian:

$$\begin{aligned} f_{\mathrm{K}}^{\pm} d^3 &\propto \exp\left(-\frac{E_I + (m/2)\left((v_x - u_{\mathrm{K}})^2 + v_y^2 + v_z^2\right)}{k_{\mathrm{B}} T_{\mathrm{s}}}\right) d^3v; \\ -\infty &\leq v_x \leq +\infty \end{aligned} \tag{8}$$

Here ''K' stands for 'Knudsen layer', T_{K} is a new temperature which is typically 20-30% lower than T_{s}, u_{K} is the flow velocity given by

$$u_{\mathrm{K}} = a_{\mathrm{K}} = \sqrt{\lambda k_{\mathrm{B}} T_{\mathrm{K}}/m},$$

a is the speed of sound, and γ is the heat capacity ratio, C_V/C_p. The same argument which for particles obeying eq. (7) led to a signal scaling as $\cos\vartheta$ now leads to a TOF signal of more complicated form:

$$\text{signal} \propto \cos\vartheta \cdot f(\cos\vartheta)$$

which can be shown, however, to be similar in angular dependence to $\cos^4\vartheta$. If the primary release process is not thermal, eq. (7), of course, ceases to be valid, but eq. (8) should still be acceptable.

If still more collisions occur, the velocity distribution retains the form of eq. (8) but with u_{K} replaced by u_M and T_{K} by T_M, where $M = u/a > 1$ stands for Mach number. We therefore have $u_M - Ma_M = M\sqrt{\lambda k_{\mathrm{B}} T_M/m}$. T_M, the new temperature, can be very much lower than T_{s}, depending on how many collisions occur before the particles have such a low density that they once again go into free flight. An alternative representation of particles showing $M > 1$ is, not in terms of a velocity distribution as in eq. (8), but in terms of solutions of the flow equations (Kelly, 1990; Kelly & Braren, 1991). The simplest solutions are for a non-terminating expansion with a KL as the surface boundary condition:

$$a = u_{\mathrm{K}}\left(1 - \frac{\lambda - 1}{\lambda + 1}\frac{x}{u_{\mathrm{K}}t}\right) \tag{9}$$

$$u = u_{\mathrm{K}}\left(1 + \frac{2}{\lambda + 1}\frac{x}{u_{\mathrm{K}}t}\right). \tag{10}$$

Here T is obtained from a^2, the gas density from $a^{2/(\gamma-1)}$, and the gas pressure from $a^{2\gamma/(\gamma-1)}$. Eq. (9) shows that a decreases linearly towards $a = 0$, while (10) shows that u increases linearly towards .

$$u = u_{\mathrm{K}} \frac{\gamma+1}{\gamma-1}.$$

These limiting values are, of course, not normally realized in practice since the particles finally go into free flight (Saenger, 1983; Kelly, 1990).

In laser ablation, the release of particles from the surface finally terminates. At that moment, there is a catastrophic drop in particle density at the target surface, followed by a region of increasing density, and terminated by a region furthest from the surface in which Eqs. (9) and (10) remain applicable. The existence of a low density at the surface is evident in fig. 15. In fact, it is from a series of such photographs that the duration of the release process with polymethylmethacrylate (PMMA) was estimated to be 6±2 μs (Braren et al., 1991; Kelly et al., 1992).

5.2 Experimental Observations of Gas-Dynamic Effects

The ablation plume created in vacuum at intensities typical of the experiments we have described is a weakly ionized (1% - 10%) plasma; the intensity threshold for ablation is typically at 10^8 W/cm^2. Thus ablation plumes differ significantly from the fully-ionized laser plasmas produced in inertial-confinement fusion experiments; of course, these are generated at much higher intensities ($I > 10^{12}$ W/cm^2). Relatively few measurements of these plasmas have been carried out, however, since most experimenters simply report being able to see a visible plasma plume. At that point, of course, the plasma is likely to be already quite highly ionized and many important laser-induced photochemical effects are likely to occur at lower ionization levels. The conclusion to be drawn is that visibility of a plume is not a necessary condition for its existence.

Some quantitative studies of the electron and gas density in ablation plumes have been carried out by interferometric and photographic techniques. Walkup and collaborators have shown that a Michelson interferometer permits measurements of electron density in ablation plumes from sapphire surfaces (Walkup et al., 1987). Picosecond measurements on ablation plumes from polymers show not only the expected generation of a shock wave ahead of the plasma, but also of self-focusing of the laser light in the plume, which could also enhance the rate of ablation (Zyung et al., 1989). Since plasmas as a rule exhibit a significant third-order optical susceptibility, self-focusing and related phenomena may be significant in nanosecond pulse experiments as well.

Recent studies combining photographic, spectroscopic and holographic diagnostics in novel ways are portentous for greater quantitative understanding of gas-

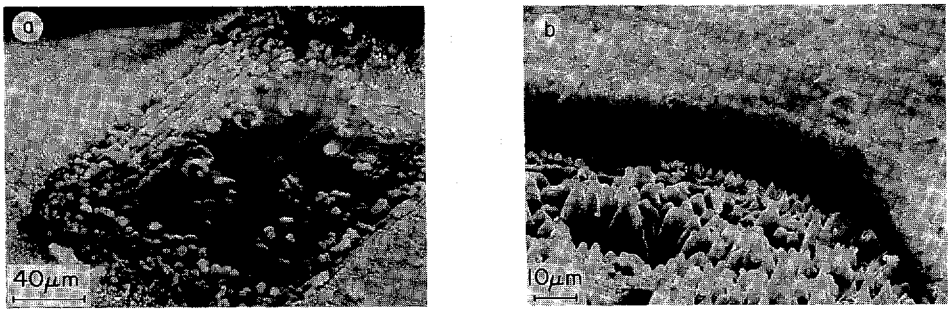

Figure 16. Possible plasma-etched features in Al_2O_3 viewed by scanning electron microscopy. (a) A linear feature with a spacing of approximately 1.2 μm, made above the plasma threshold in vacuum. (b) An irregular pattern of cones, created by laser irradiation of Al_2O_3 in air above the plasma threshold. From Kelly et al. (1985).

dynamic processes in ablation. In a study of poly(ethyleneteraphthalate) (PET) and poly(methylmethacrylate) ablation by a KrF laser (248 nm), pulsed schlieren photography and photothermal laser deflection measurements were combined to show that the ejecta from the surface may have undergone partial combustion when ablation was carried out in ambient air (Ventzek et al., 1990). Photothermal deflection spectroscopy in air has been used to estimate the initial temperature of benzene ejecta from a PET surface irradiated at fluences near 10 J/cm^2 (Ventzek et al., 1991). A pulsed dye laser has been used for resonance absorption photography of plumes from Al (Gilgenbach & Ventzek, 1991) and from polymers (Ventzek et al., 1992), yielding species-specific and gas-dynamic information simultaneously. Holographic interferometry of plumes ablated by a KrF laser from Al surfaces in vacuum and in gaseous environments shows that it is possible to extract absolute line-density information on selected species (Lindley et al., 1993). Clearly the deployment of these sophisticated techniques in the future will reveal much about the detailed gas-dynamics of laser ablation at high fluences.

The effects of surface-plasma interactions in ablation are likewise poorly understood. The formation of cones and craters is one possible effect of plasma-surface etching during ablation, as seen in figure 16 for the surface of Al_2O_3 irradiated by a KrF laser (248 nm) (Kelly et al., 1985). These unusual changes in surface morphology have long been known in ion sputtering, and result from the fact that ions scatter from cones as depicted schematically in figure 17 (Auciello & Kelly, 1982). For the same reason, photon scattering from surface asperities may lead to evolution of cone-shaped structures in the ablated region of the surface. It is also possible that there are effects from the acceleration of ions and electrons to modest imaging techniques (Zyung et al., 1989). Computational modeling of laser-plume interactions has recently been initiated by Vertes (1992); the initial results suggest that the temperature of the plume changes dramatically during and after the laser pulse, and that ions are formed with particular effectiveness in the plume by multiphoton ionization. Thus both experiment and theory suggest that it is necessary to take into account not only gas dynamics but also photochemistry in assessing the effects of the plume on the dynamics of ablation.

6 Electronic Models of Laser Ablation

As pointed out in section 1, the ablation process involves four distinct phases: (i) the deposition of electronic energy at the surface; (ii) transformation of this electronic energy into other forms by radiative and non-radiative processes; (iii) ejection of a plume of atoms, ions, and possibly molecules from the surface; and (iv) interactions of the plume with the surface, of the laser light with the plume, and of the plume particles with each other. The coupling of laser light into the surface and into the ablation plume can be predicted for monatomic solids with reasonable confidence (Phipps et al., 1988). However, the electronic interactions which lead to particle ejection and plume formation are poorly understood. In this section, therefore, we consider how the phenomena of laser-induced desorption and ablation can be incorporated into models for ablation kinetics.

6.1 Electron-Avalanche and Free-Electron-Heating Models

Some of the earliest models for laser ablation were based on field emission (or electron-avalanche) and free-electron-heating models. The inadequacies of the field-emission model have been documented in a number of recent papers. Free-electron-heating is important in bulk laser damage to solids, but its effect at surfaces remains an open question at the present time.

The field emission model assumes that energetic electrons are created through multiphoton excitation and field ionization at regions where the field is enhanced, such as in the neighborhood of inclusions, inhomogeneities and surface or interfacial regions. This model, proposed and elaborated by Bloembergen (1974), assumed that destruction of the surface occurs by electron avalanches initiated by the high electric field of the laser at impurity inclusions and mechanical imperfections in surfaces or optical coatings. While it successfully explained the failure of optical components due to poor quality coatings, the field-emission model cannot explain desorption or ablation from high-quality, high-purity materials. This model, recently summarized by Smith (1978), now seems best suited to describing ablation due to extrinsic defects.

Recent work on the mechanism of bulk laser damage in ultrapure materials for laser wavelengths such that $h\nu$ is less than E_{gap} has shown conclusively that free-electron heating, following multiphoton excitation, rather than avalanche breakdown, is the intrinsic bulk damage mechanism in most optical materials (Shen et al., 1988). The damaged volume is heated, and ultimately expanded beyond its yield stress, by the temperature 'spike' in the free-electron gas (Kelly et al., 1985). Of great relevance to laser ablation are the observations by Soileau et al. (1989) that suggest that self-focusing effects must also be properly taken into account when dealing with extrinsic laser-induced damage - a category which should include ablation. The relevant self-focusing effects might occur either in the plasma, as noted in section 5.2, or in the solid surface.

Recent quantum-mechanical transport calculations predict significant laser-induced free-electron heating of bulk SiO_2 at laser wavelengths ranging from 250 nm to 10 μm. In the calculations, electron-hole pairs are assumed to be created by multiphoton excitation across the bulk band gap. At very high local electric fields, in excess of 2 MV/cm, it is found that scattering by longitudinal-optical phonons no longer balances the acceleration of free-electrons (Arnold et al., 1992). For electric fields in excess of 7 MV/cm, even acoustic phonons are no longer able to 'stabilize' the hot electrons, and electron-hole-pair creation by electron impact is energetically possible. Temperature rises predicted by the calculation are consistent with the experimental data for the alkali halides (Jones et al., 1988). Laser intensities at which the free-electron heating occurs are of order 10^{11}-10^{12} W/cm^2, consistent with bulk laser-damage thresholds, but far in excess of ablation thresholds at the surface which are typically 10^8 - 10^9 W/cm^2. It is therefore not yet clear that this mechanism will be important in the laser sputtering regime.

6.2 Thermal Ablation Models

Thermal ablation might be expected given that nanosecond laser pulses are long compared to typical thermal diffusion times for many materials. In fact, modeling of ablation plumes usually begins with the assumption that the particles in the plume are evaporated from a surface in local thermodynamic equilibrium, so that the particles are ejected into the plume with velocity distributions and in electronic or vibrational states typical of that thermodynamic equilibrium. The reviews of experimental data presented above should have made it clear that nothing could be further from the truth, even for the surfaces of pure metals.

True thermal ablation can probably occur on the time scale of the laser pulse with all materials systems provided there is rapid heating of the target to the thermodynamic critical temperature T_{tc} (Martynyuk, 1983). At this temperature, the phase transition from solid to gas or liquid to gas occurs almost instantaneously.

In particular cases, true thermal ablation can also arise by ordinary vaporization, in which the mass loss per unit area $\Delta M/A$ is the sum of the thermal yields of the N component species of the target, integrated over the time duration τ_p of the incident laser pulse (Dreyfus et al., 1986a):

$$\frac{\Delta M}{A} = \sum_{j=1}^{N} \int_0^{\tau_\mathrm{p}} \frac{m_j \alpha_j(t) p_j(t)}{\sqrt{2\pi m_j k_\mathrm{B} T(t)}} dt \tag{11}$$

Here the α_j are the vaporization coefficients, $p_j(t)$ are the vapor pressures and T is the absolute temperature. Where the particles are evaporated thermally, the mass loss should follow eq. (11) evaluated at $p = p_\mathrm{c}$ and $T = T_\mathrm{c}$, while the velocity distributions will be Maxwellians appropriate to that temperature. While this expression follows in straightforward fashion from classical thermal physics, it seems to fit almost no experimental situations except long-pulse laser ablation of metals, nanosecond laser ablation of carbon (Dreyfus et al. 1987) and, possibly, ablation of elemental semiconductors. Rather, the measured velocity distributions of ablated ions, atoms and molecules normally exhibit kinetic energies corresponding to temperatures much greater than T_tc, so that eq. (11) cannot be applicable. This implies that the particles in most cases are either released through electronic or explosive mechanisms, or that gas-dynamic, photochemical or plasma mechanisms intervene between the ablated surface and the point at which the particles are detected.

Closely related to the thermal models in spirit is the idea of ablation induced by a structural phase change, such as melting or dimerization, in elemental or compound semiconductors (Namiki et al., 1987; Ichige et al., 1988). The model is an intellectual descendant of Van Vechten's idea (1978) that the dense electron-hole plasma created by one-photon excitations in semiconductors weakens the average binding energy. The key observation is that the ablation threshold decreases with increasing ionicity f_i in compound semiconductors. Phillips showed (1973) that the ratio κ_VFF of the bond-bending to the bond-stretching valence-force-field constants scales as $\kappa_\mathrm{VFF} = 0.29(1-f_i)$. Namiki proposed that the structural instability which produces ablation results from dimerization of non-metallic elements at adjacent sites in the perfect lattice, an interaction which becomes progressively attractive as the local density of holes increases. This, in turn, reduces the bond-bending force so much that the ionicity f_i rises above the value 0.785 at which the tetrahedral lattice is unstable. The laser intensity at which ablation ensues will thus be lower for the more ionic III-V and II-VI semiconductors than for the covalently bonded group IV elements – in agreement with experiment.

However, this mechanism can be effective only in ablation and not in desorption. Repeated irradiation of the same spot on a GaP (110) surface at fluences above the ablation threshold - as determined by the modification of the LEED pattern - produces an increase of ablation yield as a function of shot number. Below the threshold, on the other hand, yield decreases with shot number even at a detection sensitivity of 10^{-4} monolayer. This result can be explained in two ways: if laser ablation is accompanied by a phase change or if ablation is initiated at defect sites, near which atoms are more weakly bound and where energy can be localized (section 4.1). By contrast, laser-induced desorption eliminates, rather than creates, some kinds of defects (Hattori et al., 1992).

6.3 Ablation Models for Nonmetallic Solids

As we have seen, laser-induced desorption phenomena in nonmetallic solids vary substantially with electron-lattice coupling strength (Table III). In solids with strong coupling, desorption proceeds through a complex series of localization and dissociation steps which may be triggered by multiphoton or sequential, multiple-photon excitation followed by relaxation through coupling to localized, anti-bonding vibrational modes. In solids with weak coupling, desorption probably stems from two-hole localization or from two-step radiative-nonradiative transitions at defect sites. Yields measured as a function of intensity show various behaviors depending on whether desorption reduces or increases the population of defect sites.

Measurements of laser ablation, on the other hand, exhibit remarkable generic similarities which suggest a common ablation mechanism. One such is the strong family resemblance of yield vs intensity curves above the ablation threshold; these frequently have a roughly sigmoidal shape showing rapid growth above threshold followed by saturation. Another is the relatively narrow range of ablation thresholds - typically of order 10^9 W/cm^2 - over a wide range of strong- and weak-coupling materials. Yet another is the rapid loss of surface stoichiometry in nonmetallic solids under intense laser irradiation. We now consider the possibility that electronic excitation of weakly bonded atoms in the vicinity of surface vacancies and vacancy clusters is the operative ablation mechanism for all nonmetallic solids, as proposed by Hattori et al. (1991) for the compound semiconductor GaP.

Atoms surrounding surface vacancies are weakly bound to the lattice and thus more likely to be ejected by pulsed-laser irradiation. Moreover, desorption increases the size of vacancy clusters on the surface layer, thus accelerating the rate of particle emission. Finally, as vacancy clusters evolve in the top layer, vacancies in the second layer are either exposed or can be readily created, and multiplication of vacancies in subsurface layers commences. In the vacancy model, the ablation threshold is that laser fluence at which the probability of ejecting weakly bonded atoms near vacancies approaches unity. Since the desorption mechanism - and hence the defect accumulation phase - differs for solids with strong and weak electron-lattice

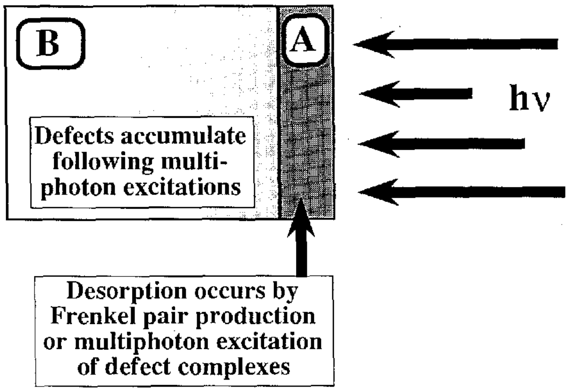

Figure 18. Schematic of a laser-irradiated solid with strong electron-lattice coupling, showing Region A in which desorption occurs (near-surface layers) and Region B in which defects created by multiphoton excitation are accumulated.

coupling, the mechanisms of defect-accumulation, vacancy production and ablation for these two types of solids are also necessarily distinct. We now consider how this model can be applied to nonmetallic solids with varying electron-lattice coupling.

6.4 Kinetics of Defect-Induced Laser Ablation

As we have seen, the laser-solid interaction always results in the creation of electron-hole pairs and/or excitons. Below the ablation threshold, the mechanisms of ion and atom desorption depend in detail on the electron-lattice coupling. For strong coupling, the excitons are self-trapped, leading to desorption from the decay of Frenkel (vacancy-interstitial) defect pairs. In solids with weak coupling, desorption occurs at defect sites, since electron-hole pairs are not self-trapped and Frenkel pairs are therefore not produced by band-to-band transitions. In intermediate-coupling solids, of course, features of both extremes may be represented. Defect formation almost certainly plays a pivotal role in effects which have been variously described as due to 'incubation' or 'surface conditioning' (section 4). We now consider how these insights from experiment can be applied to the kinetics of ablation in strong- and weak-coupling solids.

6.4.1 Laser-Ablation Kinetics in Strong-Coupling Solids

Desorption and ablation experiments on solids with strong electron-lattice coupling show that atom yields depend linearly on the density of electronic excitation (that is, on the kth power of the intensity for a solid in which a k-photon transition is required to create an electron-hole pair) for low fluence or intensity. The yields then increase to a higher-power function of the density of excitation above threshold. Three possible sources of emitted atoms and ions in near-surface sites have been suggested by the experiments: The first is F- and H-centers (Frenkel pairs) generated by nonresonant multiphoton absorption at perfect lattice sites. The second is Frenkel pairs or trapped-hole complexes at surface defect sites which can be excited by resonant multiphoton excitation. The third possibility is optical absorption at bulk defect sites created by nonresonant multiphoton transitions which are exposed as the surface is progressively eroded by ejection of atoms into the gas phase. As ablation proceeds, these bulk defects - which include but are not limited to F- or H-centers - may also diffuse to the surface from the (interior of the) bulk solid, or grow by aggregation to form multiple-defect centers (e.g., M or R centers) with still more complex, possibly resonant, optical responses.

With these arguments in mind, we consider the interaction of a single laser pulse of intensity I with a perfect, strong-coupling, initially transparent, crystal, divided into two regions, as in figure 18: Region A comprises the topmost three or four atomic layers, from which particles are ejected by any of the three mechanisms enumerated above. In Region B Frenkel defects and, at higher intensities, possibly other more complicated defects, are created by nonresonant multiphoton absorption and are either accumulated in or diffuse into Region A. As the surface is eroded during a single laser pulse, there is no longer a 'perfect' surface; at later stages of the pulse, the exposed surface region includes more and more of these accumulated or diffused defect complexes.

This process can be described by an appropriate set of rate equations. We denote the number density of perfect surface lattice sites on the surface as n_{P} per unit area; in addition, there are near-surface Frenkel pairs or multiple-hole complexes with number density n_{SD} per unit volume, and bulk defect sites with a number density n_{BD} per unit volume. The number density of halogen atoms n_{e} ejected from the surface is governed by a rate equation which includes the contributions of all three constituents:

$$\frac{dn_{\mathrm{e}}}{dt} = \eta_{\mathrm{p}}\sigma_{\mathrm{NR}}^{(k)}\Phi^{k}n_{\mathrm{p}} + \eta_{\mathrm{SD}}\sigma_{\mathrm{R}}^{(\ell)}\Phi^{\ell}n_{\mathrm{SD}} + \eta_{\mathrm{BD}}\sigma_{\mathrm{NR}}^{(m)}\Phi^{m}n_{\mathrm{BD}}, \tag{12}$$

where the η_i are quantum efficiencies; $\sigma_i^{(k)}$ is the k-photon excitation cross section for photoinduced emission by process i ('NR' and 'R' for nonresonant and resonant multiphoton excitation, respectively, and 'SD' and 'BD' for surface and bulk defect excitation). This rate equation describes three competing processes which depend in different ways on the photon flux Φ. The first term represents 'direct' emission from perfect surface-lattice sites by non-resonant multiphoton transitions; the sec-

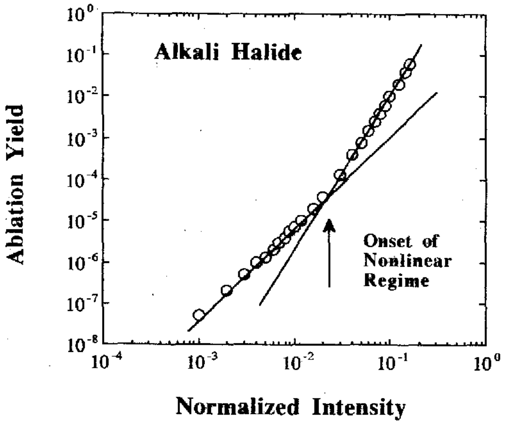

Figure 19. Schematic of ablation yields as a function of normalized laser intensity from an optically thin sample of a strong-coupling solid in which ablation can occur at and near the surface (Region A) while defects can be generated simultaneously by multiphoton processes in Region B. The 'kink' in the middle of the curve corresponds to the ablation threshold; its origin is explained in the text.

ond term represents 'indirect' emission by resonant, multiple-photon transitions on surface defects; and the third term represents emission from bulk-like defects which either diffuse to Region A from Region B, or which are exposed as the surface is eroded. Furthermore, the time variations in the number density of perfect surface-lattice sites and bulk-defect sites which have diffused to the surface are correlated with the average desorption rate:

$$\left\langle \frac{dn_{\mathrm{e}}}{dt} \right\rangle = -\left\{ \frac{dn_{\mathrm{P}}}{dt} + \frac{dn_{\mathrm{BD}}}{dt} \right\} \tag{13}$$

where the angular brackets denote the average rate of atom emission. Given information about the cross sections and number densities, these rate equations can be integrated over the duration of the laser pulse. Calculations for realistic cross sections in alkali halides have been presented elsewhere (Haglund & Itoh, 1993).

The qualitative results one expects are shown schematically in figure 19. The desorption yield at low intensity or fluence is proportional to Φ^k or I^k, because the only sites from which particle emission can occur initially are the perfect sites; in the desorption regime, these are by definition isolated from each other because the crystallographic structure of the surface remains intact. As the ejection of atoms produces surface defect complexes with significant density of states in the bandgap, resonant multiphoton processes and enhanced absorption at bulk-defect sites which have been exposed by erosion of the surface begin to contribute relatively more to

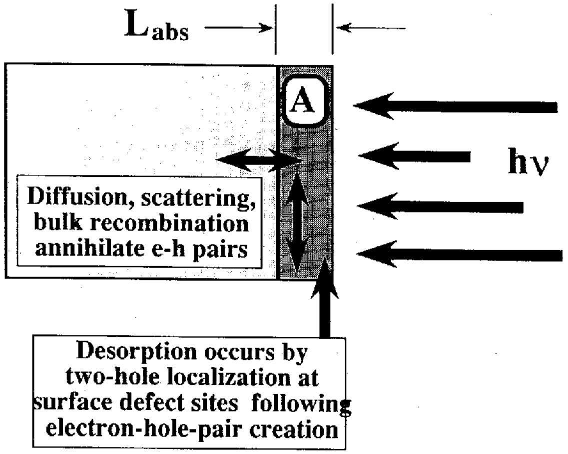

Figure 20. Diagram of the ablation zone in a solid with weak electron-lattice coupling. Because there are no permanent defects created in the subsurface layers, electron-hole pairs can only participate in desorption by being localized at a defect. Otherwise, electron-hole pairs are annihilated by Auger recombination at the surface or in the bulk.

overall emission yield. The simple kinetic model described here reproduces the most characteristic feature of the yield-fluence relation in a strong-coupling solid - the threshold seen in figs. 6, 7 and 8. The threshold occurs at that intensity at which there has been a significant accumulation of either hole complexes or one-photon-absorbing defects in the bulk solid. That number can in principle be computed using the formalism for the electronic excitation density induced in the solid by the relevant multiphoton transitions. More importantly, there are no 'thermal' parameters in this model; only formation and decay rates, all in principle deducible from optical-absorption measurements.

6.4.2 Laser-Ablation Kinetics in Weak-Coupling Solids

In solids with weak electron-lattice coupling, neither excitons nor holes are self-trapped, and localization of two holes at a given lattice site is necessary to produce excitation to an anti-bonding potential energy surface. However, the energy required for particle emission is prohibitively large at perfect lattice sites. Thus laser-induced desorption almost certainly arises primarily from defect sites, such as adatoms, steps or kinks, and antisites. In many weak-coupling materials, these defects produce Jahn-Teller lattice distortions with symmetry properties which differ from those of perfect sites; often they are also optically active. As in the strong-coupling solids, ablation begins at a fluence threshold where significant numbers of surface and sub-surface defects have been accumulated; however, in the weak-coupling solids, these must be vacancies resulting from previous desorption events. The form of the yield vs fluence curves for desorption and ablation strongly resemble each other because both grow exponentially with defect population.

Because photoexcited electron-hole pairs do not form long-lived defects in weak-coupling materials, there is no analog to Region B (compare figure 18 with figure 20) in strong-coupling solids, in which defects accumulate as ablation progresses. Instead, electron-hole pairs are created throughout that portion of the solid in which the laser light is totally absorbed, say to a depth of $L_{\rm abs} = 3/\alpha$, where α is the absorption coefficient. It should be noted that $L_{\rm abs}$ may be only a single monolayer in depth, as in the case where excitation of surface electronic states in GaP is known to produce desorption at wavelengths for which the bulk solid is transparent. From the irradiated volume of depth $L_{\rm abs}$, photo-excited electron-hole pairs trapped at defect sites lead to desorption with some probability which depends on the details of the site and of the desorption mechanism. The remaining e-h pairs eventually recombine, principally by Auger processes.

For simplicity, we assume that desorption occurs at a single kind of site with number density $n_{\rm D}$. Although both surface and bulk electron-hole pairs are created by the laser pulse, the high recombination rates and the efficiency for trapping holes in the bulk generally mean that only those electron-hole pairs which are trapped by surface defects survive long enough to cause desorption or ablation. The rate at which atoms are emitted from these surface defect sites can be written as

$$\frac{dn_{\rm e}}{dt} = \sigma^{(\ell)}\Phi^{\ell} n_0(\eta_{\rm trap}\eta_{\rm des} - \eta_{\rm recom}) \tag{14}$$

where the light is absorbed by a transition of order ℓ; σ is the cross section; and the density of absorbers is $\eta_{\rm recom} n_0$. The quantum efficiencies for hole trapping at defect sites, desorption and recombination are denoted by $\eta_{\rm trap}, \eta_{\rm des}$, and $\eta_{\rm recom}$, respectively. For III-V semiconductors irradiated by nanosecond pulses, the number ℓ ranges from 2 to 6. The quantum efficiencies are strong functions of the density of excitation; the trapping efficiency for two holes at a single defect site, for example, depends on the electron-hole-plasma screening radius which is an exponentially rising function of the local e-h pair density (Itoh et al. 1985), as well as on defect type. Electron-hole recombination in weak-coupling materials is dominated by Auger processes which are proportional to the third power of the electron-hole density (Yoffa, 1980); numerical estimates are given by Nakai et al. (1991).

Thus the physics of excitation and relaxation in the weak-coupling solid leads to a kinetic equation for the desorption yield with a structure quite different from the strong-coupling case. Unlike eq. (12), this expression clearly has a threshold at that value of the intensity for which the term in brackets vanishes. Below this threshold, there is no desorption because the electron-hole pairs recombine before being trapped at defect sites. It is to be explicitly noted that the existence of the threshold does not indicate ablation unless the other conditions for ablation (section 1) are met. An example of this situation is shown in figure 14, in which ultrasensitive detection of Ga atoms desorbed from a clean GaP(110) surface in ultrahigh vacuum reveals two different thresholds for desorption from specific defect sites below the ablation threshold (around 1.2 J/cm^2) at which gross damage to the surface occurs after only a few laser pulses (section 4.3).

The desorption yield can be expected to depend on a very high power of photon flux or laser intensity immediately above threshold, in qualitative agreement with the experimental data of figure 14. This is primarily due to the fact that the recombination rate has a cubic dependence on electron-hole pair density - that is, on the density of electronic excitation induced by the laser - and any process leading to atom or ion emission from the surface must first overcome the recombination.

The form of eq. (14) is appropriate for any surface defect; however, the quantum efficiencies will vary according to the specific type of defect. Thus, if more than one type of defect can trap holes and generate desorption, there will be a different threshold and different yield vs fluence relation for each type of defect, as noted already in conjunction with the data of fig. 14. Unlike the situation in strong-coupling solids, the surface defects on the surfaces of weak-coupling solids may be eliminated with progressive laser irradiation. As desorption occurs from adatom or step sites, for example, the number of these defects is progressively reduced, the former rapidly because of the small adatom defect density on a smooth surface, the latter at a relatively constant rate (Nakai et al., 1991).

In a strong-coupling solid, the transition from desorption to ablation results from growth in the number of accumulated surface defects. Since defects are not accumulated in weak-coupling solids, the transition between desorption and ablation must have another origin. Experiment points to ablation by photoexcitation of weakly-bound atoms near vacancies. Under this assumption, the rate at which the atoms are emitted is given by

$$\frac{dn_{\mathrm{e}}}{dt} = \eta_{\mathrm{WBA}} \sigma^{(k)} \Phi^k n_{\mathrm{WBA}}, \tag{15}$$

where I is the laser intensity, $n_{\mathrm{WBA}}(\mathrm{t})$ is the number of weakly bound atoms near vacancies and vacancy clusters at time t, k is the photon multiplicity required to break the bond for the WBAs, and $\sigma^{(k)}$ is the k-photon excitation cross section. For small vacancy clusters, emission of one atom produces one new vacancy and

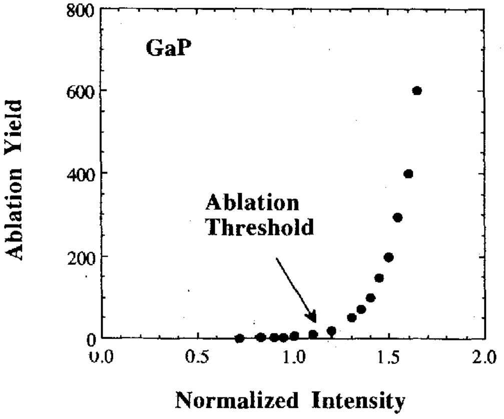

Figure 21. Schematic of the ablation yield as a function of normalized laser intensity from an optically thick sample of a weak-coupling solid. In this case ablation is produced by a single-photon or multiphoton band-to-band transition involving defect states, but no electronic defects are created below the absorption zone.

one more weakly bonded atom on average; thus

$$n_{\mathrm{WBA}}(t) = n^0_{\mathrm{WBA}} + \int_0^{\tau_{\mathrm{p}}} \frac{dn_{\mathrm{e}}}{dt} dt. \tag{16}$$

An exact calculation of the ablation rate requires a detailed model of the way in which the number of vacancies grows. A Monte Carlo calculation, for example, showed that the rate of growth in the number of atoms ablated from vacancy sites changes from an exponential to a power-law dependence during the laser pulse (Okano et al., 1993). The ablation yield as a function of laser intensity based on this Monte Carlo calculation is shown in figure 21 (from Haglund & Itoh, 1993). In contrast to the desorption threshold – the magnitude of which depends in detail on the trapping, desorption and recombination processes – the ablation threshold in a vacancy-initiated model is that intensity at which the probability of desorbing weakly bonded atoms approaches unity. Thus we have $\sigma^{(k)}\Phi^k n_{\mathrm{WBA}}\tau_{\mathrm{p}} \approx 1$ at threshold. There is no 'kink' in the ablation yield, as in figure 6, because there is no accumulation of defects in the bulk which move from subsurface layers into the emission zone by either diffusion or erosion of the surface, as sketched in figure 20.

6.4.3 Laser-Ablation Kinetics in Polymers

The discovery of efficient ablation of polymers and biological tissues by Srinivasan (1985) led to a number of attempts to explain the phenomenon. An early molecular dynamics simulation reported by Garrison and Srinivasan (1986) showed that the dramatic forward peaking of the polymer yields observed experimentally could be reproduced by assuming the breaking of monomer bonds in the ablation volume. This calculation might be criticized, however, on the grounds that it probably used too narrow an aspect ratio at the target. In such a 'gun-barrel' geometry, forward peaking need not come from an electronic or photochemical effect; it may simply be the result of the narrow, deep zone in which the laser energy is deposited. It is more reasonable to view forward peaking as a gas-dynamic effect, as discussed in section 5.1, which can occur even in situations where laser energy is deposited in a relatively wide, shallow zone. The strong forward-peaking in the 'gun-barrel' geometry arises from the existence of a flow velocity u normal to the target surface which can greatly exceed the sound speed.

The crucial problem in polymer photoablation is the existence of a threshold and the physical basis of its magnitude for various polymers. One general attempt to explain the threshold phenomenon is a multiple-hit model for the ablation process (Kiss & Simon, 1985). The model assumes that photon absorption is stochastic, and that a monomer is ablated once the number density of photons reaches a certain critical value n_c. If the polymer has N_m units and the number of photons absorbed by the polymer is $N_{h\nu}$, then the probability of ablation of a monomer unit is

$$P = \sum_{j=n_c}^{N_{h\nu}} \frac{N_{h\nu}}{j} \cdot (N_m - 1) \tag{17}$$

Of course, such a model contains essentially no information on the physics of ablation without an attempt to explain the origin of the critical value n_c.

Mahan has proposed a model which incorporates the idea of residual bond-breaking density, thus allowing for an estimate of physical parameters which determine the critical number of absorbed photons (Mahan et al., 1988). This model also starts from the assumption that bond-breaking occurs whenever a threshold is exceeded, in this case, a threshold value for the broken-bond density n_T. Garrison and Srinivasan have also suggested that polymer ablation occurs when the density of excitation exceeds a critical value. Although their model does not treat the physical origin of the critical concentration, it is in principle equivalent to Mahan of the multiple-hit models. All these models assume a simple Beer's-law absorption profile, and predict an ablation rate which depends on the number of laser pulses or absorbed dose (J/cm^2) but is independent of the linear absorption. This is an important check on the model, since ablation yields for polymers show a variation of only about a factor 2 even though the linear absorption coefficient α varies by factors of nearly 300, for both 193 nm and 248 nm laser radiation.

Several experimental groups have proposed rate-equation models which give a more detailed picture of the kinetics of polymer ablation, assuming that one has a way of measuring or computing the threshold level of broken bonds. All are based on coupled rate equations which take into account not only the changes in the volume density of absorbing chromophores in the polymer, but also the effects of absorption of laser light in the polymer and in the plume. If one assumes that one- and two-photon absorption in the polymer and one-photon absorption in the plume are the relevant absorption processes, then the number density of chromophores $n(x, t)$ at a time t following laser irradiation and a depth x is (Sauerbrey & Pettit, 1989)

$$\frac{\partial n}{\partial t} = (n_0 - n)(\sigma^{(1)}\Phi + \sigma^{(2)}\Phi^2) \tag{18}$$

where the $\sigma^{(k)}$ are the k-photon absorption cross sections and Φ is a function of both x and t. The companion rate equation describes the evolution with depth of the photon flux:

$$\frac{\partial \Phi}{\partial x} = -(n_0 - n)\left(\sigma^{(1)}\Phi + \sigma^{(2)}\Phi^2\right) - \sigma_P^{(1)}\Phi. \tag{19}$$

The time-integrated photon flux as a function of penetration depth is

$$S(x) = \int_0^T \Phi(x, t)dt. \tag{20}$$

By integrating eq. (20) over an appropriate time T, and eq. (19) from the surface where $S(x) = S_0$ up to the threshold value S_{th}, one can determine the depth of the ablation crater per incident laser pulse, the principal quantity of interest in many technological applications of polymer ablation. In the special case of single-photon absorption and low photon flux, Eqs. (18-20) may be solved exactly to yield

$$d_1 = \frac{1}{n_0}(S_0 - S_{\text{th}}) + \frac{1}{\alpha}\ln\left(\frac{1 - e^{-\sigma^{(1)}S_0}}{1 - e^{-\sigma^{(1)}S_{\text{th}}}}\right) \tag{21}$$

For moderate fluences and reasonable cross sections, the argument of the exponential is small and eq. (21) reduces to the well-known form, first derived by Jellinek & Srinivasan (1984), in which the value of d_1 is proportional to the fluence ratio $\ln(F/F_{\text{th}})$. It is precisely the threshold value S_{th}, of course, which describes the physics of the complex incubation processes that lead to ablation. The relative change in etch depth assuming one- and two-photon absorption is shown in fig. 22 which displays femtosecond ablation data (Küper & Stuke, 1989a) together with calculations by Sauerbrey & Pettit (1989).

Two important corrections to this kinetics model should be mentioned. First, depending on the laser pulse length and pulse repetition frequency, explicit account

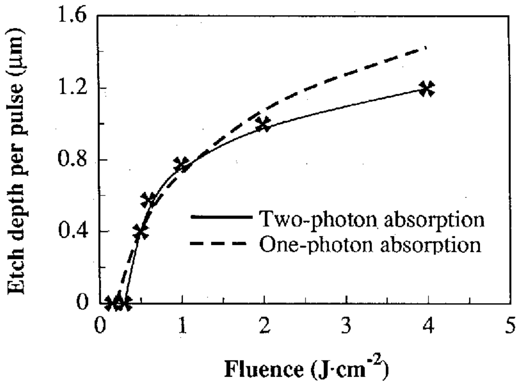

Figure 22. Etch depth per pulse achieved by femtosecond laser ablation (crosses, from Küper and Stuke, 1989b). The dashed line is the calculation resulting from eq. (20) including only one-photon absorption; the solid-line is the same calculation with two-photon absorption. From Sauerbrey & Pettit (1989). Note that no plume forms in this case because of the ultrashort laser pulse.

must be taken of thermal diffusion. Cain et al. (1992) have shown that threshold fluence and some details of the material-removal rate per laser pulse are significantly affected by both electronic (multiphoton transitions and saturation) and thermal (nonradiative relaxation and diffusion) effects. Second, we note that what is discussed in this section relates only to the initial laser-polymer interaction. The ultimate release of particles was proposed by Kelly et al. (1992) to be thermal, or at least thermally constrained (sect. 4.4). For very long-pulse ultraviolet-laser irradiation, in fact, this is clearly the case (Srinivasan, 1991).

7 Summary and Outlook for the Future

Sputtering by intense pulsed laser beams is strongly affected by electronic processes which occur both in ejecting atoms, molecules and ions from the surface, and in the plume above the surface. These electronic processes are manifested in surface-incubation and defect-generation phenomena occurring prior to sputtering; velocity distributions of ejected particles corresponding to temperatures far above the thermodynamic critical temperature T_{tc}; non-equilibrium distributions among different degrees of freedom in molecular species; the creation of excited atoms and molecules; energetic-ion production; and unusual surface topologies sculptured by plasma-surface interactions.

In the search for fundamental understanding of these processes, laser-induced desorption experiments are central to understanding the mechanisms of energy deposition, localization and transformation to kinetic energy of ejected particles. It will be particularly crucial to do more experiments in which all desorbed species are observed, as almost no 'kinematically complete' experiments of this type have yet been done. This is at least partly due to the challenge inherent in the detection of neutral non-metallic atoms, whether one chooses multiphoton resonance ionization or multiphoton laser-induced fluorescence spectroscopies. However, since the nonmetallic species is usually the one released in the primary process of desorption, the dynamics of laser-induced desorption will remain unresolved without this information. In this context, further experimentation on oxides might be particularly fruitful, because of the possibility of covering a wide range of electron-lattice coupling strengths and of electronic excitation densities. Studies of desorbed particles need also to be accompanied by more detailed information about changes in surface structure and composition which define the precursor conditions of laser ablation. These studies are difficult, particularly on insulating surfaces, but the tools for carrying them out - such as scanning-probe microscopy - are growing rapidly in sophistication. Indeed, observation of a single picosecond-laser-induced defect on a surface has been conjectured by Williams et al. (1992) on the basis of atomic-force microscopy of an alkali halide surface.

The second area crying out for more experimentation is ablation in the impulse limit in which energy deposition occurs on a time scale short compared to the operative electronic and vibrational relaxation processes. Ultrafast laser desorption experiments have thus far been applied primarily to molecular adsorbates on metal surfaces (for example, Misewich et al., 1992), where high temporal resolution has made it possible to distinguish the role of multiple, successive excitations in desorption. Clearly, picosecond or femtosecond laser excitation at pulse energies sufficient to initiate desorption would be of great interest in determining the dynamics of desorption from solid surfaces, particularly in ascertaining the role played by such multiple excitations. One experiment has already been carried out on the surface of KI by Williams and co-workers, using the ultraviolet output of a 100-fs Ti:sapphire laser; desorption products were observed, and atomic-force microscope pictures indicated metallization of the surface (Pendleton et al., 1993).

The time for modeling the kinetics and dynamics of laser-induced desorption has clearly arrived. By identifying the fundamental mechanisms of electronic excitation and relaxation, it is now possible to establish kinetic equations for desorption based on fundamental electronic properties of materials rather than on average thermodynamic parameters. The dynamics of some of these mechanisms are not yet fully understood, but by focusing on electronic processes it is possible to isolate these mechanisms and measure the appropriate rate constants. New approaches to modeling, based on molecular dynamics, may also provide insight deeper than simple 'rate-equation' models. However, the incorporation of electronic excitation poses significant challenges to the molecular dynamicists.

If, indeed, ablation turns out to be strongly determined by surface and subsurface vacancies, a rich additional field of theoretical and computational study will be opened up. Calculations of the growth of vacancies and vacancy clusters from the desorption to the ablation limits would be particularly instructive. The dynamics of such growth processes are model-dependent, as pointed out in section 6, and few comparisons among different models have been carried out to date. In addition to standard Monte Carlo and statistical techniques, new tools in the form of percolation calculations based on fractal geometries, as well as cellular automaton models, might prove useful and extremely interesting.

The development of free-electron lasers operating in the mid- to far-infrared region of the electromagnetic spectrum (Brau, 1989) is likely to influence profoundly our understanding of the relationships between thermal and electronic processes in laser ablation. The primary event in free-electron-laser excitation of solids is vibrational excitation of the solid. In the first experiments, there is solid evidence that these lasers produce significant wavelength-sensitive effects on irradiated solids (Schwettman, 1993). Picosecond free-electron lasers can impart vibrational energy to the solid on a time scale short compared to vibrational relaxation times, illuminating the ways in which selective excitation of vibrational modes produces lattice instabilities leading to desorption and ablation. These studies will form an interesting contrast to experiments done at visible and ultraviolet wavelengths where the primary excitations are purely electronic.

Finally, process throughput requirements in technological applications of nanosecond laser ablation are pushing laser operation toward the kHz regime. The effects of these high repetition rates on desorption and ablation are scarcely understood at all, but are clearly important in areas ranging from damage to laser optics to changes in surface stoichiometry during film deposition. Evidence thus far suggests that the cumulative effects of defect formation are significant. If this is indeed the case, it may be, for example, that trading lower intensity for higher pulse repetition frequency may lead to interesting and useful effects.

There is clearly no shortage of exciting research in prospect on the electronic aspects of laser desorption and ablation. Just as clearly, laser ablation will be an important area of research for years to come, for, as Thorsten Veblen observed, 'the outcome of any serious research can only be, to make two questions grow where only one grew before.' (Veblen, 1919)

Acknowledgement

Research at Vanderbilt University was partially supported by the Office of Naval Research through the Vanderbilt Free-Electron Laser Program, Contract Number N00014-91-C-0109. One of us (RH) owes a special dept to prof. Noriaki Itoh, Nagoya University, for extended dialogues on the fundamental mechanisms of laser ablation, an opportunity partially supported by a grant from the Division of International Programs, National Science Foundation. It is also a pleasure to thank Prof. Franz Hillenkamp, Universität Münster, for stimulating discussions during the preparation of this review.

References

Allen SD, Lee SJ and Imen K, 1992: Optics and Photonics News **3**, 29 and references therein.
Anisimov SI, Kapeliovich BL and Perel'man TL, 1975: Sov. Phys. JETP **39**, 375
Andrews DL, 1984: Am. J. Phys. **53**, 1001
Arlinghaus H, Calaway WF, Young CE, Pellin MJ, Gruen DM and Chase LL, 1989: J. Appl. Phys. **65**, 281
Arnold D, Cartier E and DiMaria DJ, 1992: Phys. Rev. B **45**, 1477
Arnold D and Cartier E, 1992: Phys. Rev. B **46**, 15 102
Ashcroft NW and Mermin ND, 1976: *Solid-State Physics* (Philadelphia: Saunders College)
Auciello O and Kelly R, 1982: Rad. Effects **66**, 195
Becker CH and Pallix JB, 1988: J. Appl. Phys. **64**, 5152
Bloembergen N., 1974: IEEE J. Quantum Electron. **QE-10**, 375
Bozhevolnyi SI and Potemkin IV, 1993: J. Phys. D (in press)
Brand JL and Tam AC, 1990: Appl. Phys. Lett. **56**, 883
Braren B, Casey KG and Kelly R, 1991: Nucl. Instr. Meth. B **58**, 463
Brau C, 1989: Science **243**, 1795
Brewer PD, Zinck JJ and Olson GL, 1990: Appl. Phys. Lett. **57**, 2526
Brewer PD, Zinck JJ and Olson GL, 1991: in Miller JC & Haglund RF (1991), 96-105
Brown WL, 1980: in *Laser and Electron-Beam Processing of Materials*, eds. White CW and Peercy PS (Academic Press, New York), 20
Bunton PH, Haglund RF Jr., Liu D and Tolk NH, 1992: Phys. Rev. B **45**, 4566
Cain SR, Burns FC and Otis CE, 1992: J. Appl. Phys. **71**, 4107
Chan CL and Mazumder J, 1987: J. Appl. Phys. **62**, 4579
Chase LL, Lee HWH and Hughes RS, 1990: Appl. Phys. Lett. **57**, 443
Chase LL, Hamza AV and Lee HWH, 1991: in Miller JC & Haglund RF (1991) 193
Chase LL, Hamza AV and Lee HWH, 1992: J. Appl. Phys. **71**, 1204
Chase LL, 1994: Nucl. Instrum. Methods B, to be published
Chen CH, Murphy TM and Phillips RC, 1990: Appl. Phys. Lett. **57**, 937
Chen CH and Phillips RC, 1991: J. Appl. Phys. **70**, 4643
Chen CN, Phillips RC and McCann MP, 1993: J. Appl. Phys. **73**, 922
Cheung JT, Sankur H and Chang T, 1992: Optics and Photonics News **3**, 24
Corkum PB, Brunel F, Sherman NK and Srinivasan-Rao T, 1988: Phys. Rev. Lett. **61**, 2886
Corkum PB, Brunel F, Sherman NK and Srinivasan-Rao T, 1990: Phys. Rev. Lett. **64**, 1847 in response to a critique by H. E. Elsayed-Ali on the preceding page

Cox PA, 1992: *Transition Metal Oxides: An Introduction to their Electronic Structure and Properties* (Oxford: Clarendon Press) Ch. 3

Davis GM and Gower MC, 1987: Appl. Phys. Lett. **50**, 1286

Devine RAB, 1989: Phys. Rev. Lett. **62**, 340

Devine RAB, Francou J-M, Inard A and Pelletier J, 1991: Appl. Phys. Lett. **56**, 1549

Dickinson JT, Langford SC, Jensen LC, Eschbach PA, Pederson LR and Baer DR, 1990: J. Appl. Phys. **68**, 1831

Dickinson JT, Jensen LC, Webb RL, Dawes ML and Langford SC, 1993a: J. Appl. Phys., in press

Dickinson JT, Shin J-J, Jiang W and Norton MG, 1993b: J. Appl. Phys., in press

Dreyfus RW, Kelly R and Walkup R E., 1986a: Appl. Phys. Lett. **49**, 1478

Dreyfus RW, Walkup RE and Kelly R, 1986b: Rad. Eff. **99**, 199

Dreyfus RW, Kelly R and Walkup RE, 1987: Nucl. Instrum. Meth. B **23**, 557

Dreyfus RW, McDonald FA and von Gutfeld RJ, 1987: Appl. Phys. Lett. **50**, 1491

Dreyfus RW, 1991: J. Appl. Phys. **69**, 1721

Dubowski J, 1988: Chemtronics **3**, 67

Dyer PE and Srinivasan R, 1986: Appl. Phys. Lett. **48**, 445

Ediger MN and Pettit GH, 1992: J. Appl. Phys. **71**, 3510

Ehrlich D J and Tsao J Y., 1989: *Laser Microfabrication: Thin-Film Processes and Litho- graphy* (New York, Academic Press)

Elsayed-Ali HE, Norris TB, Pessot MA and Mourou GA, 1987: Phys. Rev. Lett. **58**, 1212

Eschbach PA, Dickinson JT, Langford SC and Pederson LR, 1989: J. Vac. Sci. Technol. A **7**, 2943

Feldmann D, Kutzner J, Laukemper J, MacRobert S and Welge KH, 1987: Appl. Phys. B **44**, 81

Feurer T, Sauerbrey R, Smayling MC and Story BJ, 1993: Appl. Phys. A **56**, 275

Fogarassy E, White CS, Slaoui A, Fuchs C, Siffert P and Pennycook SJ, 1988: Appl. Phys. Lett. **53**, 1720

Fogarassy E, Fuchs C, Slaoui A and Stoquert JP, 1990: Appl. Phys. Lett. **57**, 664

Fogarassy E, Fuchs C, Slaoui A and Stoquert JP, 1991: in Miller JC & Haglund RF (1991), 38

Fujimoto JG, Liu JM, Ippen EP and Bloembergen N, 1984: Phys. Rev. Lett. **53**, 1837

Garrison BJ and Srinivasan R, 1985: J. Appl. Phys. **57**, 2909

Geohegan DB and Mashburn DN, 1989: Appl. Phys. Lett. **55**, 2345

Geohegan DB, 1991: in Miller JC & Haglund RF (1991), 193

Gilgenbach RM and Ventzek PLG, 1991: Appl. Phys. Lett. **58**, 1597

Haglund RF Jr, Arps JH, Tang K, Niehof A and Heiland W, 1991: Mat. Res. Soc. Symp. Proc. **201**, 507

Haglund RF Jr., Tang K, Affatigato M, Niehof A and Heiland W, 1992a: Nucl. Instr. Meth. B **65**, 206

Haglund RF Jr., Tang K and Chen CH, 1992b: Mat. Res. Soc. Symp. Proc. **243**, 405

Haglund RF Jr., Affatigato M, Tang K and Chen CH, 1993: Submitted to Appl. Phys. Lett.

Haglund RF Jr. and Itoh N, 1993: in *Principles and Applications of Laser Ablation*, JC Miller, ed., (Heidelberg, Springer), to be published

Hansen SG, 1989a: J. Appl. Phys. **66**, 1411

Hansen SG, 1989b: J. Appl. Phys. **66**, 3329

Hata K, Watanabe M and Watanabe S, 1990: Appl. Phys. B **50**, 55

Hattori K, Okano A, Nakai Y, Itoh N and Haglund RF, Jr., 1991: J Phys.: Condens. Matter **3**, 7001

Hattori K, Okano A., Nakai Y and Itoh N, 1992: Phys. Rev. B **45**, 8424

Hayes W and Stoneham AM, 1985: *Defects and Defect Processes in Nonmetallic Solids* (New York: Wiley)

Helvajian H and Welle R, 1989: J. Chem. Phys. **91**, 2616

Hicks J M, Urbach LE, Plummer EW and Dai H-L, 1988: Phys. Rev. Lett. **61**, 2588

Hoheisel W, Jungmann K, Vollmer M, Weidenauer R and Träger F, 1988: Phys. Rev. Lett. **60**, 1649

Hubler GK and Chrisey D, 1992: *Pulsed Laser Deposition* (New York: Hilger)

Ichige K, Matsumoto Y and Namiki A., 1988: Nucl. Instr. Meth. B **33**, 820

Imai S, Shibata T, Tokizaki T, Tanimura K, Nakamura A, Schluger A and

Imen K, Lin JY and Allen SD, 1989: J. Appl. Phys. **66**, 488

Inam A, Wu XD, Venkatesan T, Ogale SB, Chang CC and Dijkkamp D, 1987: Appl. Phys. Lett. **51**, 1112

Itoh N, 1994: Nucl. Instrum. Methods B, to be published

Itoh N, Nakayama K and Tombrello TA, 1985: Phys. Lett. **108A**, 480

Itoh C, Tanimura K, Itoh N and Itoh M, 1989: Phys. Rev. B **39**, 183

Jellinek H and Srinivasan R, 1984: J. Phys. Chem. **88**, 3048

Joosen W, Guizard S, Martin P, Petite G., Agostini P, Dos Santos A, Grillon G, Hulin D, Migus A and Antonetti A, 1992: Appl. Phys. Lett. **72**, 1234

Kanasaki J, Okano A, Ishikawa K, Nakai Y and Itoh N, 1993: Phys. Rev. lett. **70**, 2495

Kelly R and Dreyfus RW, 1988: Nucl. Instr. Meth. B **32**, 341

Kelly R and Braren B, 1991: Appl. Phys. B **53**, 160

Kelly R, Cuomo JJ, Leary PA, Rothenberg JE, Braren BE, and Aliotta CF, 1985: Nucl. Instr. Meth. B **9**, 329

Kelly R, 1990: J. Chem. Phys. **92**, 5047

Kelly R, Miotello A, Braren B, Gupta A and Casey K, 1992: Nucl. Instr. Meth. B **65**, 187

Kelly R and Miotello A, 1993: Appl. Phys. A (in press)

Kim H, Postlewaite JC, Zyung T and Dlott DD, 1988: J. Appl. Phys. **64**, 2955

Kim H, Postlewaite JC, Zyung T and Dlott DD, 1989: Appl. Phys. Lett. **54**, 2274

Kim HS and Helvajian H, 1991a: J. Phys. Chem. **95**, 6623

Kim HS and Helvajian H, 1991b: in Miller JC & Haglund RF (1991), 87

Kim HS and Helvajian H, 1993: J. Vac. Sci. Technol., to be published

Kiss LB and Simon P, 1988: Sol. State Comm. **65**, 1253

Kittel C, 1986: *Introduction to Solid-State Physics*, Sixth Edition (New York: Wiley)

Kumazaki Y, Nakai Y and Itoh N, 1987a: Phys. Rev. Lett. **59** 2883

Kumazaki Y, Nakai Y and Itoh N, 1987b: Surf. Sci. Lett. **184**, L445

Küper S and Stuke M, 1989a: Appl. Phys. Lett. **54**, 4

Küper S and Stuke M, 1989b: Appl. Phys. A **49**, 211

Larciprete R and Stuke M, 1987: Appl. Phys. B **42**, 181

Langford SC, Jensen LC, Dickinson JT and Pederson LR, 1990: J. Appl. Phys. **68**, 4253

Leclerc N, Pfleiderer C, Wolfrum J, Greulich K, Leung WP, Kulkarni M and Tam AC, 1991: Appl. Phys. Lett. **59**, 3369

Lee I, Parks JE, Tallcott TA and Arakawa ET, 1989: Phys. Rev. B **39**, 8012

Leuchtner RE, Horwitz JS and Chrisey DB, 1992: Mat. Res. Soc. Symp. Proc. **243**, 525

Leung WP, Kulkarni M, Krajnovich D and Tam AC, 1991: Appl. Phys. Lett. **58**, 551

Li X, Beck RD and Whetten RL, 1992: Phys. Rev. Lett. **68**, 3420

Lindley RA, Gilgenbach RM and Ching CH, 1993: Appl. Phys. Lett. **63**, 888

Liu JM, Yen R, Kurz H and Bloembergen N, 1982: Mat. Res. Soc. Symp. Proc. **4**, 29

Liu YS, 1992: Optics and Photonics News **3**, 10 and references therein

Long JP, Goldenberg SS and Kabler MN, 1992: Phys. Rev. Lett. **68**, 1014

Mahan GD, Cole HS, Liu JYS and Phillipp HR, 1988: Appl. Phys. Lett.**53**, 2377

Martynyuk MM, 1983: Russ. J. Phys. Chem. **57**, 494

Matthias E and Green TA, 1990: in *Desorption Induced by Electronic Transitions DIET IV*, eds. Betz G and Varga P (Berlin, Heidelberg: Springer), 112

Miller JC and Haglund RF Jr., eds., 1991: *Laser Ablation: Mechanisms and Applications* (Heidelberg: Springer), Springer Tracts in Modern Physics 389

Miller JC, ed., 1993: *Physics and Applications of Laser Ablation* (Berlin, Heidelberg: Springer) in press

Misewich JA, Heinz TF and Newns DM, 1992: Phys. Rev. Lett. **68**, 3737. See also related experimental work listed in the references

Moison JM and Bensoussan M, 1982: J. Vac. Sci. Tech. **21**, 315

Nakai Y, Hattori K, Okano A, Itoh N and Haglund RF, Jr., 1991: Nucl. Instrum. and Methods B **58**, 452

Nakayama T, Ichikawa H and Itoh N, 1982a: Surf. Sci. Lett. **123**, L693

Nakayama T, Itoh N, Kawai T, Hashimoto K and Sakata T, 1982b: Rad. Eff. Lett. **67**, 129

Nakayama T, 1983: Surf. Sci. **133**, 101

Namiki A, Cho S and Ichige K, 1987: Japan. J. Appl. Phys. **26**, 39

Namiki A, Katoh K, Yamashita Y, Matsumoto Y, Amano H and Akasaki I, 1991: J. Appl. Phys. **70**, 3256

Nogar NS, Dye RC, Estler RC, Foltyn SR, Muenchausen RE and Wu XD, 1991: in Miller JC & Haglund RF (1991), 3-11

NoorBatcha I, Lucchese RR and Zeiri Y, 1987: J. Chem. Phys. **86**, 5816

NoorBatcha I, Lucchese RR and Zeiri Y, 1988: J. Chem. Phys. **89**, 5251

Okano A, Matsuura AY, Hattori K, Itoh N and Sign J, 1993: Appl. Phys. Lett., to be published

Ong CK, Khoo GS, Hattori K, Nakai Y and Itoh N, 1991: Surf. Sci. Lett. **259**, L787

Otis CE and Dreyfus RW, 1991: Phys. Rev. Lett. **67**, 2102

Otis CE, Gupta A and Braren B, 1993: Appl. Phys. Lett. **62**, 102

Pendleton WE, Wilson RM, Reed RK, Zhang Y, Liu H and Williams RT, 1993: International Workshop on *Electronic Excitations at the Surfaces of Halides*, Krakow, Poland, May 3-5, 1993. To be published in Rad. Eff. Def. Sol.

Petite G, Agostini P, Boiziau C, Vigouroux JP, Le Gressus C and Duraud JP, 1985: Opt. Comm. **53**, 189

Petite G, Martin P, Trainham R, Agostini P, Guizard S, Jollet F, Duraud JP, Böher K and Reif J, 1991: in Miller JC & Haglund RF (1991) 224

Pettit GH and Sauerbrey R, 1991: Appl. Phys. Lett. **58**, 793

Phillips JC, 1973: *Bonds and Bands in Semiconductors* (New York: Academic Press)

Phillips HM, Callahan DL, Sauerbrey R, Szab and Bor Z, 1991: Appl. Phys. Lett. **58**, 2761, and references therein

Phillips HM, Smayling MC and Sauerbrey R, 1993: Microelectron. Eng. **20**, 73

Phipps CR Jr., Turner TP, Harrison RF, York GW, Osborne WZ, Anderson GK, Corlis XF, Haynes LC, Steele HS, Spicochi KC and King TR, 1988:J. Appl. Phys. **64**, 1083

Puliafito C., Deutsch TF and Parrish J, 1987: J. Quant. Electron. **QE-15**, 1357

Ready JF, 1971: *Effects of High-Power Laser Radiation* (New York: Academic Press)

Reif J, Nielsen HB, Semmler O, Matthias E, Westin E and Rosén A, 1987: J Vac. Sci. Tech. B **5**, 1415

Reif J, Petzoldt S, Elg AP and Matthias E, 1989: Appl. Phys. A **49**, 199

Reif J, 1989: Opt. Eng. **28**, 1122

Ritchie RH, Manson JR and Echenique PM, 1991: in Miller JC & Haglund RF (1991) 239

Rothschild M, Ehrlich DJ and Shaver DC, 1989: Appl. Phys. Lett. **55**, 1276

Rothenburg JE and Kelly R, 1984: Nucl. Instrum. Meth. B **1**, 291

Saenger KL, 1983: J. Chem. Phys. **79**, 6043

Saenger KL, 1989: J. Appl. Phys. **66**, 4435

Sardar DK, Becker MF and Walser RM, 1987: J. Appl. Phys. **62**, 3688

Sauerbrey R and Pettit GH, 1989: Appl. Phys. Lett. **55**, 421

Schildbach MA and Hamza AV, 1992: Phys. Rev. B **45**, 6197

Schmid A, Bräunlich P and Rol PK, 1975: Phys. Rev. Lett. **35**, 1382

Schwettman HA, 1993: *Free-Electron Laser Spectroscopy in Biology, Medicine and Materials Science*, SPIE Symp. Proc. **1852**

Shea MJ and Compton RN, 1993: Phys. Rev. B **47**, 9967

Shen XA, Braunlich P, Jones SC and Kelly P, 1988: Phys. Rev. B **38**, 3494

Slaoui A, Fogarassy E, Fuchs C and Siffert P, 1992: J. Appl. Phys. **71**, 590

Smith WL, 1978: Opt. Eng. **17**, 489

Soileau MJ, Williams WE, Mansour N and Van Stryland EW, 1989: Opt. Eng. **28**, 1133

Srinivasan R, 1986: Science **234**, 559

Srinivasan R, Sutcliffe E and Braren B, 1987: Appl. Phys. Lett. **51**, 1285

Srinivasan R, Braren B and Casey KG, 1990: J. Appl. Phys. **68**, 1842

Srinivasan R, 1991: in Miller JC & Haglund RF (1991), 123

Takigawa Y, Kurosawa K, Sasaki W, Yoshida K, Fujiwara E and Kato Y, 1991: J. Non- Cryst. Solids **116**, 293

Tam AC, Leung WP, Zapka W and Ziemlich W, 1992: J. Appl. Phys. **71**, 3515

Tanimura K and Itoh N, 1988: Phys. Rev. Lett. **60**, 2753

Tsai TT, Griscom DL and Friebele EJ, 1988: Phys. Rev. Lett. **61**, 444

Valbis J and Itoh N, 1991: Rad. Eff. and Def. in Solids **116**, 171

Van Vechten A, Tsu R and Saris FW, 1979: Phys. Lett. **74A**, 422

Veblen TB, 1919: *The Place of Science in Modern Civilization and Other Essays* (New York: BW Huebsch). Cited in The MacMillan Dictionary of Quotations (New York: Macmillan, 1987), P 484

Ventzek PLG, Gilgenbach RM, Sell JA and Heffelfinger DM, 1990: J. Appl. Phys. **68**, 965

Ventzek PLG, Gilgenbach RM, Heffelfinger DM and Sell JA, 1991: J. Appl. Phys. **70**, 587 (1991)

Ventzek PLG, Gilgenbach RM, Ching CH and Lindley RA, 1992: J. Appl. Phys. **72**, 1696

Vertes A and Gijbels R, 1993: in *Laser Ionization Mass Analysis*, eds. Vertes A et al., (New York: Wiley) Chapter 3

Vollmer M, Weidenauer R, Hoheisel W, Schulte U and Träger F, 1989: Phys. Rev. Lett. B **40** 12509

Webb RL, Jensen LC, Langford SC and Dickinson JT, 1993: J. Appl. Phys., to be published

Westin E., Rosén A and Matthias E, 1990: in *Desorption Induced by Electronic Transitions - DIET IV*, eds. Betz G and Varga P (Heidelberg: Springer). Volume 19 of the Springer Series in Surface Science

Wiedeman L and Helvajian H, 1991: J. Appl. Phys. **70**, 4513

Williams RT, Song KS, Faust WL and Leung CH, 1986: Phys. Rev. B **33**, 7232

Williams RT, Wilson RM and Liu H, 1992: Nucl. Instrum. Meth. B **65**, 473

Wu Z, 1990: in *Desorption Induced by Electronic Transitions - DIET IV*, eds. Betz G and Varga P (Heidelberg: Springer-Verlag, 1990). Volume 19 of the Springer Series in Surface Science

Yen R, Liu JM, Bloembergen N, Yee TK, Fujimoto JG and Salour MM, 1982: Appl. Phys. Lett. **40**, 185

Yoffa EJ, 1980: Phys. Rev. B **21**, 2415

Yoo KM, Zhao XM, Siddique M, Alfano RR, Osterman DP, Radparvar M and Cunniff J, 1990: Appl. Phys. Lett. **56**, 1908

Zyung T, Kim H, Postlewaite JC and Dlott DD, 1989: J. Appl. Phys. **65**, 4548

Desorption Experiments on Organic Insulators with High Energy Particle Beams

By Per Håkansson
Division of Ion Physics, Department of Radiation Sciences
Uppsala University, Box 535, S-751 21 Uppsala, Sweden

Synopsis

Fast heavy ions can electronically sputter or cause desorption from many different kinds of insulating materials like water ice, condensed gases, alkali halide salts and organics. In this paper a summary of experiments on electronic sputtering of biomolecules with MeV energy particle beams will be given. Recent results on formation of 'buckyballs' when a certain polymer is irradiated with fast heavy ions will also be described.

1 Introduction

When an energetic particle hits a surface, atoms or molecules can be sputtered from the surface. In the case of slow heavy ions with keV energies a series of screened Coulomb collisions occurs, refered to as a collision cascade in the material. This can lead to ejection of surface atoms according to the established theory for nuclear elastic sputtering by Sigmund (1969). The sputtering yield is proportional to the nuclear elastic part of the stopping power of the primary ion. This means that above the maximum in the nuclear stopping power function, see figure 1, the sputtering yield will decreases with increasing primary ion energy, but it will always be present. This sputtering mechanism is effective in all materials.

Also fast heavy ions with MeV energies can cause sputtering. For conductors like metals the few data on total sputtering yields and the energy dependence of ion yields show that a large fraction of the particle yield is associated with nuclear elastic sputtering (see e.g. Wien, 1989). However, the energy spectra of some metal ions sputtered by fast heavy ions (Matthäus et al. 1993) as well as the high total Au yield sputtered from an Au foil with 1.3 GeV ^{238}U ions (Cheblukov et al. 1992) indicate that electronic excitations in the track of the incident particle contribute to sputtering even in metals.

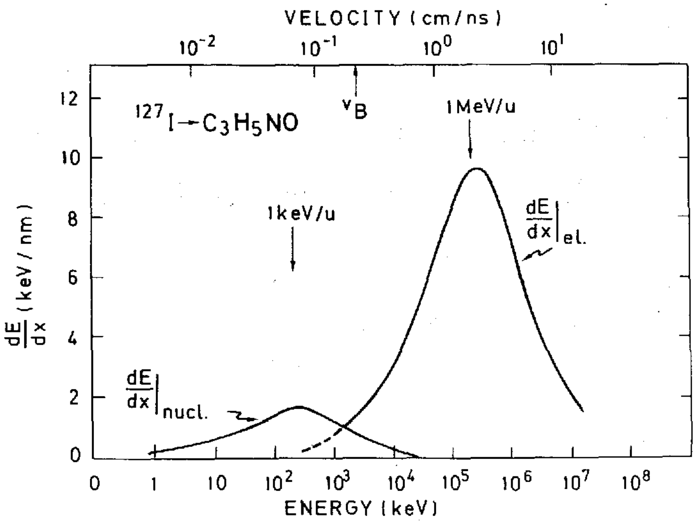

Figure 1. The nuclear and electronic stopping powers as a function of the primary ion energy (velocity). The values are for ^{127}I ions bombarding a target of C_3H_5NO. The Bohr velocity, $v_B = 0.22$ cm/ns, separates approximately the velocity regimes where, respectively, nuclear and electronic stopping dominate and thus also the two corresponding sputtering processes nuclear elastic sputtering and electronic sputtering.

In the case of many insulators, much higher sputtering yields have been measured for fast heavy ions than expected from nuclear elastic sputtering. As will be described in this paper, this new sputtering process in insulators is connected to the electronic part of the stopping power of the primary ion and is therefore called electronic sputtering to distinguish it from the nuclear sputtering process mentioned above. Fast heavy ions can sputter many different types of insulators (Wien, 1989), including water ice, metal oxides, condensed gases, alkali halide salts and biomolecules. Electronic sputtering is also called 'desorption' in the literature. Desorption and sputtering are often used interchangeably but 'desorption' generally applies to ejection of an adsorbed species, usually as an ion.

The Bohr velocity, $v_B = 0.22$ cm/ns, is the velocity of the electron in the hydrogen atom in Bohr's semiclassical atomic model. This velocity is often used to distinguish the two velocity regimes where either nuclear elastic stopping power or electronic stopping power dominates. Therefore it can also be used to roughly separate the corresponding processes, nuclear elastic sputtering from electronic sputtering, see figure 1. In this paper slow ions have a velocity $v < v_B$ whereas fast ions have $v > v_B$.

The fact that intact biomolecules can be sputtered as ions from a surface due to bombardment with fast heavy ions was discovered by Macfarlane and coworkers at Texas A&M University (Torgerson et al. 1974). Fission fragments from a radioactive source, ^{252}Cf, were used as primary ions. The electronic sputtering effect was exploited in an ion source using a new type of mass spectrometer in which the masses are determined by the time-of-flight technique. This form of mass spectrometry is called plasma desorption mass spectrometry, PDMS, by the inventors (Macfarlane & Torgerson, 1976). Both positive and negative ions can be analyzed. The remarkable finding is that large, non-volatile and thermally labile biomolecules, like peptides and proteins, can be studied with PDMS. The technique is now an important mass spectrometric tool for biological research of proteins (Sundqvist & Macfarlane, 1985; Roepstorff 1990). The largest observed molecular ions so far are from ovalbumin which has a molecular weight of 45 000 u (Jonsson et al. 1989). The important applications of electronic sputtering in the biosciences have over the years been a strong driving force in the attempts to elucidate the underlying physical desorption process.

1.1 Conversion of Energy into Molecular Motion

A central problem in electronic sputtering is to understand how the deposited energy can be converted to molecular motion which then leads to desorption (Johnson, 1987). How can a fast heavy ion, losing nearly 1 keV/Å in the target material, desorb intact proteins which are held together by rather weak bonds? The first suggested conversion mechanism was the Coulomb explosion of the positively charged infratrack (Haff, 1976). If the conductivity of the material is low enough there may be time enough to cause atomic and molecular motion due to the Coulomb repulsion before the track is neutralized. However, it has been claimed that even in insulators there may not be time enough for the Coulomb force to act due to the increased conductivity of the excited track core (Watson & Tombrello, 1985). Another possibility of the conversion of the deposited energy into atomic and molecular motion that has been suggested is excitation of the molecules to repulsive states with subsequent separation of the molecule (Johnson & Sundqvist, 1983; Watson & Tombrello, 1985). Furthermore, Williams & Sundqvist (1987) have suggested that an excitation to vibrational states by the flux of low-energy secondary electrons also will lead to larger separation between the molecules. The common idea with these mechanisms is that an expansion of the material will take place around the ion trajectory leading to molecular motion.

1.2 Desorption Mechanisms

Over the years many different desorption models have been proposed. To illustrate some different approaches to the problem a few models will be briefly described below. For more details the reader is referred to the review article in this volume by Reimann on desorption models. Common features for the described models below are the lack of an ionization mechanism and that a region around the point of impact of the primary ion is assumed to have too high energy density to allow desorption of intact molecules. From this region only molecular fragment and low-mass ions are assumed to be desorbed. However, recent experiments (see section 10) indicate that fullerenes can be formed in the central part of the ion track when a certain polymer is irradiated.

In the ion track model by Hedin et al. (1985) a statistical treatment is performed of the flux of secondary electrons that is generated by the primary ion when it is slowed down in the material (see section 3). These electrons propagate in the material and deposit energy when they are slowed down. The energy deposition at a certain point is approximately proportional to the flux of electrons at that point. In the model, which is a multihit model based on Poisson statistics, a molecule is desorbed if it is hit by a certain minimum number m of electrons. This is equivalent to requiring that a certain amount of energy must be deposited in the molecule for desorption to occur. The model can reproduce some general observations made by Håkansson et al. (1984) when the yield of large biomolecules is measured as a function of the electronic stopping power.

In the thermal model by Voit et al. (1989) the thermal flow is calculated to annular elements around the point of impact of the primary ion on the target surface from a number of sources of thermal energy along the trajectory of the primary ion. This energy is transferred from the kinetic energy of the primary ion through the electronic stopping power. The desorption probability is proportional to $\exp(-U_0/E_\mathrm{s})$ where U_0 is the surface binding energy and E_s the energy available at the molecular site. The yield is obtained by a summation over all time intervals, all sources and all annular elements weighted by the corresponding probability. The model is able to reproduce the dependence of measured secondary ion yields on the energy and initial charge state of the primary ions for light mass molecules like the amino acid valine (117 u).

In the continuum mechanical model or pressure pulse model by Johnson et al. (1989) the primary ion creates sources of impulses along its track through the solid. The energy from the individual sources spreads diffusively in the solid. In the case of a fast heavy ion with a large energy loss in the solid the sources act cooperatively and the energy density at any time is obtained by adding the contributions from the different sources. The resulting energy density gradient will cause a volume force

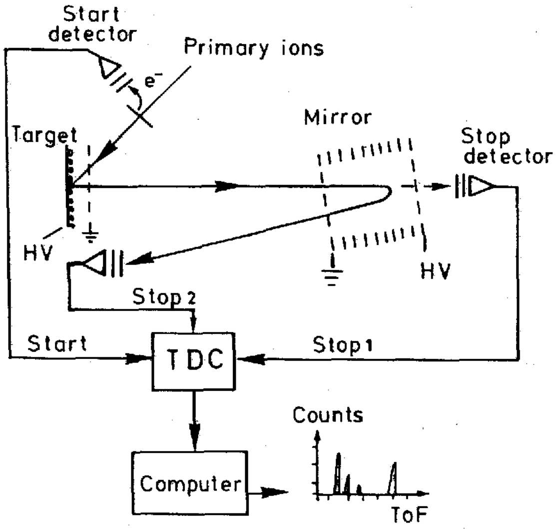

Figure 2. The principle of a time-of-flight, ToF, spectrometer with a single-stage mirror. Fast heavy ions from an accelerator (or fission fragments from a ^{252}Cf source) bombard the target on high voltage (HV). When the primary ions pass through a thin carbon foil in the start detector, a start signal for the ToF measurement is generated. The desorbed secondary ions are accelerated through a grid on earth potential into a field-free region. If the mirror voltage is off, the ions will continue into the straight stop detector and generate a stop signal. The time differences between the start and stop signals are converted into flight times by a time-to-digital converter, TDC. These are stored in a spectrum by a micro computer. With the mirror voltage on, only secondary ions will be reflected by the mirror into the second stop detector and no neutral decay products. This will improve the signal-to-noise ratio in the spectra. Furthermore, the mirror compensates for the initial axial velocity distributions of the ions and an improvement in time resolution and thus mass resolution will be obtained.

on the surrounding material, and by integrating this force over time the net impulse transferred to a volume element can be obtained. A molecule will be desorbed if the z-component of this impulse is larger than a critical impulse determined by the cohesive energy of the material. For a molecule on the surface one can show that the ejection will be at a certain angle relative to the nuclear track. The same directional ejection can also be obtained from a similar shock wave model introduced by Bitensky & Parilis (1987). The principal differences between these models are the description of the energy transport and the criterion for ejection (Fenyö & Johnson, 1992).

It is always difficult to justify the validity of a certain model based on a fit to a particular subset of experimental data. However, as will be shown in this paper, some basic electronic sputtering experiments on large biomolecules can only be explained by expansion models like the pressure pulse model (Johnson et al. 1989) and the modified shock wave model (Bitensky et al. 1991).

Wien (1989) has reviewed the field of electronic sputtering in general and from insulators (Wien, 1992). Sundqvist (1991) has reviewed desorption of organic molecules induced by particle impact. This summary paper covers mainly experiments of electronic sputtering from organic insulators.

2 Experimental Methods

Electronic sputtering of ions can conveniently be studied with the time-of-flight (ToF) technique. This has been described in detail elsewhere (Macfarlane & Torgerson, 1976; Le Beyec, 1989; Sundqvist, 1991), and therefore only some basic facts will be described here. A schematic drawing of a ToF spectrometer is shown in figure 2. The target, which usually is at a potential of 10 - 15 kV, is bombarded with fast heavy ions from an accelerator. The desorbed and ionized molecules are accelerated through a grid on earth potential into a field-free drift region where they finally are stopped in a pair of microchannel plates. There, a shower of secondary electrons is created that generate a stop signal for the ToF measurement. The start signal is usually generated from a shower of secondary electrons produced when the primary ion is passing a thin carbon foil before hitting the target.

A common spectrometer design (Torgerson et al. 1974) where fission fragments from a ^{252}Cf source are used to bombard the target is the following. In the spontaneous fission of a ^{252}Cf nuclei two, almost collinear, fragments are created. One is then used to desorb the molecules on the target while the other is used to give a start signal for the ToF measurement.

In terms of desorption yield there is no difference between fission fragments from a ^{252}Cf source and an accelerator beam of ^{127}I ions with an energy around 80 MeV. However, in contrast to the fission fragments, the accelerator beam is well defined in energy, type of ion, angle of incidence and charge state, a prerequisite in many experiments. The time difference between start and stop signals is measured with a time-to-digital converter (TDC) and stored in a spectrum where the time scale is proportional to the square-root of the mass divided by the charge state of the ion. The data are recorded in event-by-event mode, which means that for each primary ion giving a start signal the corresponding stop signals are recorded. Usually a primary ion desorbs several secondary ions per impact so the TDC must be able to handle several stops per start.

Sometimes biomolecular ions are metastable and decay in flight. If this happens in the field-free region in the spectrometer it will lead to a broadening of the ToF peak. One way to get rid of neutrals and other decay products and thus to improve the signal- to-noise ratio in the spectrum is to reflect the secondary ions in an electrostatic mirror. This will also make sure that a certain experiment is performed with stable ions. The mirror will compensate for the initial axial velocity distribution of the secondary ions and thereby improve the time resolution, and hence the mass resolution in a ToF spectrum. This was first demonstarted by Mamyrin et al. (1973) with a two-stage, second order compensating, mirror.

Today, mirrors are frequently used by many groups, and several different designs and applications exist. Here only a few will be mentioned. Tang et al. (1988) have compared the performance of a single-stage and two-stage mirror in SIMS-measurements. Della-Negra et al. (1987b) have developed an axial symmetric system with an annular microchannel plate stop detector that also is a two-stage mirror (Brunelle et al. 1991). A gridless mirror has been developed by Walter et al. (1986) for laser multiphoton postionization work. Brinkmalm et al. (1992b) have analyzed large biomolecules in a PDMS instrument with a single-stage mirror.

One common technique for preparing a target for a desorption experiment is to electrospray the molecules onto a metallic backing (McNeal et al. 1979). In the case of peptides and proteins, the technique used today is to adsorb the molecules to a polymer backing, usually a film of electrosprayed nitrocellulose (Jonsson et al. 1986).

3 Basic Ion-Track Concepts

When the nuclear sputtering yield is measured as a function of the primary ion energy, it first passes a maximum but is thereafter a continuously decreasing function for increasing primary ion energy. This is because the yield follows the nuclear stopping power (Sigmund 1969), see figure 1. However, it was independently found at Erlangen (Dück et al. 1980) and Uppsala (Håkansson et al. 1981b) that the yield for organics desorbed by fast heavy ions increased with increasing primary ion energy. This is also the case for the electronic stopping power function in this energy range. We therefore deal with electronic sputtering. Fundamental for the understanding of electronic sputtering is the concept of an ion track, and therefore some basic concepts are described below.

The energy loss of a fast heavy ion penetrating an insulator with a velocity above the Bohr velocity is dominated by electronic excitations and ionizations. Very little energy goes into nuclear collisions, which play no significant role in desorption from insulators at these incident particle energies. Along the path of the ion a cylindrical region with intense ionizations and excitations is produced due to direct Coulomb interactions, see figure 3. This region is called the infratrack (Brandt & Ritchie, 1974), and its radius scales with the velocity of the primary ion

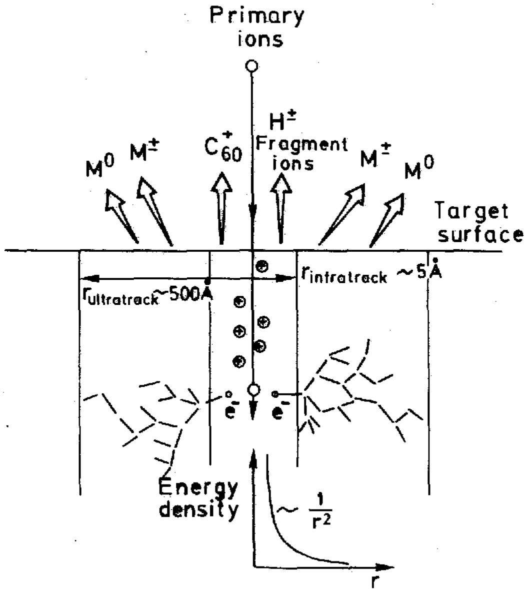

Figure 3. When a fast heavy ion passes through an organic target it will lose energy in a cylindrical region with intense ionizations and excitations due to direct Coulomb interactions. This region is called the infratrack and will become positively charged for a short time. The δ-electrons carry the excitation far out into the material and produce new generations of secondary electrons. This outer part of the track is called the ultratrack. The energy density of the deposited energy falls off like $1/r^2$ from the track centre. Light ions like H^+ and H^- are believed to be desorbed close to the track centre and so promptly that they feel the positively charged track core. Fragment ions are assumed to be created in the hot central part of the track region and desorbed closer to the track centre than molecular ions. Further out neutrals are desorbed. The molecular ions are desorbed with a strong directional correlation caused by the radially expanding track. In the case of a poly(vinylidene difluoride) target fullerenes are created in the hot central part of the track and ejected due to the axially expanding track.

(Sundqvist, 1993) :

$$r_{\text{infratrack}} \approx 6.7 \times (E/M)^{\frac{1}{2}} \text{Å} \qquad (1)$$

where E is the kinetic energy of the particle in MeV and M is the mass of the particle in u. Due to the direct interaction between the primary ion and target electrons, high energy δ-electrons are produced. These carry the excitation far out into the material and produce new generations of secondary electrons. This outer part of the track is called the ultratrack (Brandt & Ritchie, 1974). Its radius, which is determined by the projected range of the δ-electrons, scales as the square of the

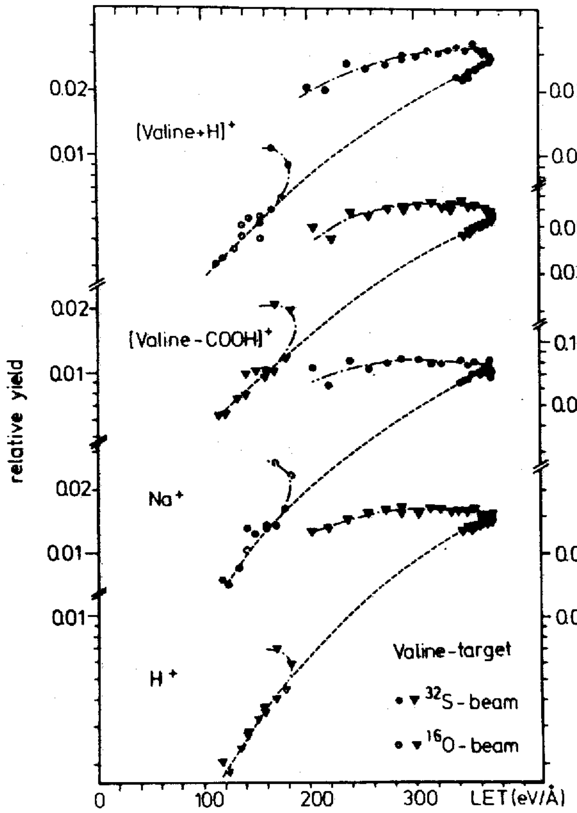

Figure 4. The yield of some different secondary ions from a valine target as a function of the linear energy transfer, LET, of the primary ions. (LET is the same as 'stopping power'). The target was bombarded with MeV energy ^{16}O ions (unfilled symbols to the left) and ^{32}S ions (filled symbols to the right). The same stopping power value can in certain cases be obtained with two different primary ion energies but the corresponding desorption yields are not necessarily the same. For each set of data points the lower branch corresponds to the high energy side and the upper branch to the low energy side of the stopping power function. The lines are guides for the eye, (Dück et al. 1980).

velocity of the primary ion (Sundqvist, 1993) :

$$r_{\mathrm{ultratrack}} \approx 830 \times E/(\rho M)\text{Å} \qquad (2)$$

Here ρ is the density of the material in g/cm^3. For 72 MeV ^{127}I ions, which is a typical fast heavy ion used in desorption experiments with biomolecules, these radii are approximately 5 and 500 Å respectively. The total energy loss per path length for such an ion is about 1 keV/Å and about 75 % (Kraft et al. 1992) of the deposited energy is converted into kinetic energy of the secondary electrons. The track zones are established within 10^{-15} s and the energy density falls off like $1/r^2$ (Kobetich & Katz, 1968) from the track centre.

4 Scaling of Yields with Electronic Stopping Power

In the literature, quite a lot of measurements can be found on how the yield of a certain biomolecular ion depends on the electronic stopping power of the primary ion. The data demonstrate the coupling of the sputtering process with the electronic rather than the nuclear part of the energy loss function. However, many of the yield vs. dE/dX curves exhibit a peculiar double-branch yield which make the interpretation of the data complex. This was shown already in the first accelerator experiments on electronic sputtering of biomolecules, namely valine desorbed by ^{16}O and ^{32}S beams by Dück et al. (1980), see figure 4.

The reason for the double branches is that the yield is a function of the deposited energy density in the track rather than a function of the total energy loss. When the primary particle energy is changed the track dimensions are also changed, as described in the previous paragraph. As a consequence the deposited energy per volume unit can decrease even if the total deposited energy increases. In a more well-defined experiment it is therefore important to keep the velocity of the primary ions constant, so the yield is measured as a function of the energy density rather than the electronic stopping power (Håkansson et al. 1984).

In the same paper Håkansson et al. also showed that when the yield of biomolecules is measured as a function of the electronic stopping power (energy density), the dependence on the stopping power will be steepest for low stopping power values and large molecules. This result has been confirmed both by Becker et al. (1986a) and Brandl et al. (1991). For large stopping power values the dependence will be approximately linear. There is also a threshold in energy density below which no molecular ions are observed. The larger the molecule the larger is this threshold. A 10 MeV ^{16}O beam will for example not desorb any molecular ions

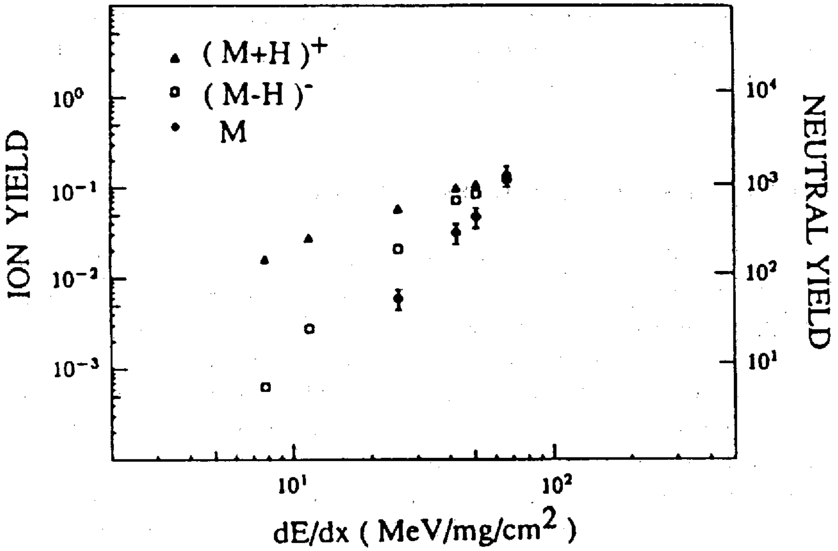

Figure 5. Absolute yields of intact neutral molecules (right scale) and normalized yields for positive and negative molecular ions (left scale) of the amino acid leucine as a function of the electronic stopping power of the primary ions. The energies of the different primary ions were chosen so the velocity was kept constant which means that the stopping power is proportional to the energy density in the ion track. The different scaling of the yields with energy density probably reflects different desorption mechanisms for neutrals vs. ions and indicates how far out from the track different species originate, (Hedin et al. 1987a).

from an electrosprayed target of insulin but it will produce a rather good spectrum of an amino acid (Hedin et al. 1987b).

There still exists only one complete set of data on the scaling of the yield for the neutral ejecta as well as the charged-particle ejecta with the electronic stopping power (energy density). That is for the amino acid leucine studied by Hedin et al. (1987a). The target was bombarded with beams of 20 MeV ^{32}S, 36 MeV ^{59}Ni, 49 MeV ^{79}Br and 78 MeV ^{127}I ions in charge-state equilibrium and with the same velocity for all the primary particles. The method used to measure the neutral yield will be described in the next section. The neutral yield was found roughly to follow a cubic dependence on the electronic stopping power (energy density). Including the primary ion beams 7 MeV ^{12}C and 10 MeV ^{16}O the scalings for positive and negative leucine molecules were found to be approximately linear and quadratic, respectively, as shown in figure 5. This is in agreement with recent results by Brandl et al. (1991) for the amino acid valine. The differences in scaling probably reflect different desorption mechanisms for neutrals vs. ions and indicate how far out from the track different species originate (Johnson & Sundqvist 1992). Brandl et al. (1991) discuss the different scalings for positive and negative ions in terms of different ionization mechanisms.

5 Neutral-Yield Measurements

Because of the difficulties in measuring absolute total sputtering yields for biomolecular solids very few measurements are available. This is at present a problem in the comparison between experimental data and theoretical models, because so far most models contain no description of the ionization process.

In the two neutral yield measurements described in this paper the sputtered molecules were collected on clean pieces of silicon. To obtain the relative amount of material on the collector, it was rotated in the chamber to become a target in a small ToF spectrometer and analyzed with the PDMS technique. This was done in situ for the scaling experiment described above. To obtain the absolute amount of material on the collector, it was taken out from the chamber and analyzed with state-of-the-art amino acid analyzing technique.

The latter method was used by Salehpour et al. (1986) who irradiated a multilayer target of the amino acid leucine (131 u) with a beam of 90 MeV ^{127}I ions. Under the assumption of a $\cos\theta$ distribution for the sputtered molecules the yield of intact leucine molecules was found to be 1200 ± 200. The yield of positive ions of intact leucine molecules is only 13 % which gives a neutral-to-ion ratio of 10^4. With a molecular weight of 131 u and assuming a volume of $5\times5\times5$ Å^3 for leucine the neutral yield corresponds to a total mass sputtered of nearly 160 000 u. This corresponds to a volume of a half sphere with a radius of 42 Å being removed (Sundqvist et al. 1989).

In a similar experiment with the collector method but performed under ultra high vacuum conditions, Nees (1988) has measured extremely high neutral yields from a testosterone hormone (274 u) and a derivate of it (428 u). The absolute yield of intact molecules sputtered by a 30 MeV ^{16}O^{5+} beam and determined with a biochemical method was found to be about 10^6 for both samples.

At present only these two measurements are available on the total sputtering yield, and it is not clear if the large difference in the numbers are an experimental fact or due to some artifacts. One can notice that the total yield in the pressure-pulse model (Johnson et al. 1989) is inversely proportional to the cohesive energy to the third power which could be very different for these two kinds of targets. This is consistent with the fact that refractory solids with large cohesive energies, like Al_2O_3, have very small total yields (Qiu et al. 1983). However, even with the lower value of the total sputtering yield for organics one can conclude that the total

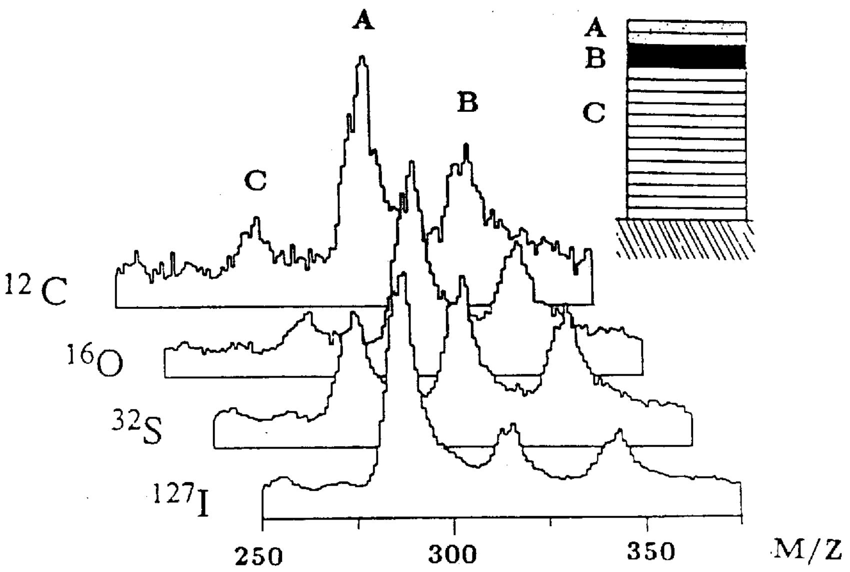

Figure 6. A Langmuir-Blodgett film was built up by 13 layers of stearic acid (C), 2 layers of behenic acid (B) and 2 layers of arachidic acid (A). Each layer had a thickness of 25 Å. The figure shows negative time-of-flight spectra around the molecular ion region for 4 different heavy ion beams. These have the same velocity which means that the corresponding stopping power values are proportional to the energy density in the ion track. The systematic change in the relative peak heights with energy density indicates crater formation. In the case of ^{127}I ions, secondary ions are observed from layers well below the surface indicating a sputtering depth of around 150 Å, (Säve et al. 1987a).

ejection is dominated by neutral molecules for these kinds of multilayer samples and molecules.

6 Electronic Sputtering from Langmuir-Blodgett Films

With the Langmuir-Blodgett technique it is possible to build targets of uniformly oriented organic molecules layer by layer. The films can be made very homogeneous and with well-defined thickness. The PDMS technique can be used to characterize the films, e.g. to discover incomplete salt formation or replacement of the original counter-ion by ions from the substrate surface (Schmidt et al. 1990). With spontaneous-desorption mass spectrometry (Della-Negra et al. 1985) defects in the films, e.g. pinholes built in during the preparation, can be detected (Schmidt et al. 1991a).

Säve et al. (1987b) used such films to study the sample film thickness dependence in electronic sputtering and found that the yield saturates around 125 - 150 Å. By using different Cd-stabilized fatty acids with the only difference being the number of CH_2 groups in the hydrocarbon chain, one can make films with marked layers suitable for measurements of the desorption depth. In such an experiment (Säve et al. 1987a), a target of 13 layers of stearic acid (C) followed by 2 layers of behenic acid (B) and on top of that 2 layers of arachidic acid (A) was constructed, see figure 6. Each layer had a thickness of 25 Å. Analysis of the target with 78 MeV ^{127}I ions showed that the most intense molecular-ion peak was from the bottom layers, indicating a sputtering depth of around 150 Å. The systematic change of the spectra with lower energy density beams excludes the possibility of inhomogenous films and indicates crater formation. The same conclusion was obtained in similar experiments by the Orsay group (Bolbach et al. 1987) and also recently by the Erlangen group (Schmidt et al. 1991b).

To get an idea of the radius of the crater one can use the damage cross section measurements for 78 MeV ^{127}I ions on arachidic acid (Sundqvist et al. 1989). That radius is 80 Å which means that a rather large crater is formed in the case of ^{127}I ions if one assumes that the damage radius is close in size to a removal radius. The number of molecules sputtered from this volume is of the same order of magnitude as the neutral yield obtained for leucine described above. Both Bolbach et al. (1987) and Schmidt et al. (1991b) have developed crater models where the shape of the craters for different beams is discussed. Della-Negra et al. (1990) have measured the dependence of the yield from Langmuir-Blodgett films on the charge state and the angle of incidence of the primary ion. One result from that study is that the strong dependence of the charge state for normal angle of incidence vanishes for grazing angles in agreement with the assumption of a large interaction depth. The general trend in the data can be reproduced with a modified version of the shock wave model (Bitensky & Parilis, 1987).

When using the information obtained from Langmuir-Blodgett experiments one should keep in mind that the oriented Langmuir-Blodgett films could be a rather special case where the film structure promotes sputtering from deep layers and formation of ions from layers below the surface.

7 Energy and Angular Distributions of Secondary Ions

7.1 Axial-Velocity Measurements

The axial velocity component of a secondary ion refers to the component in the direction of the spectrometer axis. The velocity distribution of this component for a certain ion, or corresponding energy distribution, can be obtained from the shape of the corresponding mass line if the acceleration voltages and distances for a straight time-of-flight spectrometer are known with high accuracy (Fürstenau et al. 1977). Becker & Wien (1986) have developed one method for such measurements based on a double acceleration grid arrangement. Macfarlane et al. (1986) and Widdiyasekera et al. (1988) have developed other methods using one grid. For large molecular ions like insulin (5733 u) and LHRH (1801 u) the energies were found by Widdiyasekera et al. to be 3-4 eV, in qualitative agreement with similar measurements by Macfarlane et al. (1986). For the lightest ions H^+ and H_2^+ the initial energies are typically 10 eV but depend on the sample thickness. These light ions are desorbed close to the impact of the primary ion and experience a repulsive force due to the positive charge remaining in the infratrack. This charging effect has also been observed by Macfarlane & Jacobs (1989) when studying H^+ and H_2^+ emission from nitrocellulose films. The 'axial energy' distributions were shifted towards higher values compared to those where the films were covered with an Au layer. Moshammer et al. (1990) have also shown that the positively charged track increases the 'axial energy' for H^+ ions and even reduces it for H^- ions from an organic target compared to a contaminated Au film. An influence of the positively charged track core on the initial radial velocity distributions for H^+ and H^- ions has also been found by Fenyö et al. (1993).

7.2 Radial-Velocity Measurements

The radial velocity component of a secondary ion refers to the component perpendicular to the spectrometer axis. The corresponding velocity distribution can be measured by changing the voltage over a set of deflection plates in the field-free region in a straight time-of-flight spectrometer and measuring the corresponding secondary ion yield, see insert in figure 7. The first experiment of this type was reported by Ens et al. (1989), using fission fragments from a ^{252}Cf source at normal incidence on an insulin target. This experiment gave the surprising result that there is a minimum in the molecular ion yield in the track direction. This is in contrast to the light fragment ion CH_3^+ which has a symmetric distribution whith its maximum along the normal to the surface, see figure 7.

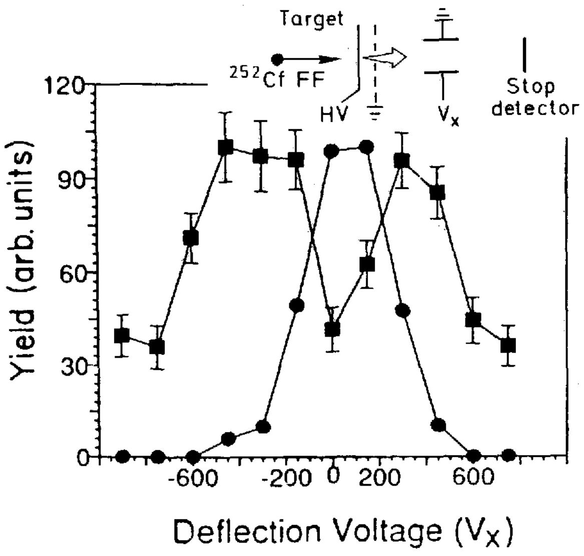

Figure 7. The insert in the figure shows how the radial velocity distribution of secondary ions can be measured in a straight time-of-flight spectrometer. The beam is deflected over the stop detector and the corresponding yield is measured as a function of deflection voltage. The figure shows the result of such a measurement for fission fragments (FF) from a ^{252}Cf source at normal angle of incidence on an insulin target. The fragment ions CH_3^+ (dots) have a distribution around zero deflection voltage corresponding to desorption around the normal to the surface. In contrast to the fragments, the molecular ions of insulin (squares) have an emission minimum in the track direction and are desorbed in a cone out from the target surface. The distributions are normalized to each other, (Ens et al. 1989).

More detailed experiments were performed by Fenyö et al. (1990b) using a small time-of-flight spectrometer that could be rotated around the point of impact of an accelerator beam aimed from behind at a target of renin substrate (1801 u). Results of experiments performed at four different angles are shown in figure 8. The light fragment ions like CH_3^+ have all a symmetric radial velocity distribution around the normal to the target surface, independent of the angle of incidence, and are therefore not shown in the figure. However, the molecular ions of renin substrate have a minimum in the yield with one maximum on each side for perpendicular incidence. When the spectrometer is tilted one of the maxima disappears. Note that for the largest angle (60°) the distribution is closer to ejection along the normal to the surface than for 45° angle of incidence.

The interpretation of the data is that large molecular ions like renin substrate or insulin are ejected at an angle from the surface correlated with the direction

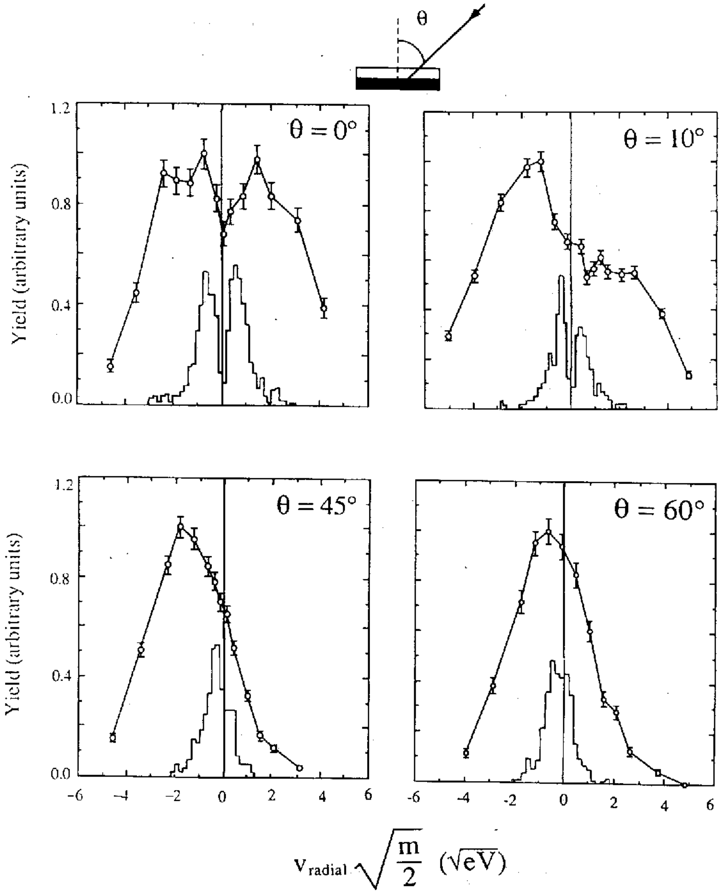

Figure 8. The data points are the measured radial velocity distributions of molecular ions from a renin substrate sample desorbed by 72 MeV ^{127}I ions at four different angles of incidence. The vertical line in each figure denote the centroid of the corresponding distribution for the fragment ion CH_3^+. This ion has the same forward peaked emission pattern independent of the angle of incidence unlike the molecular ions. Compare with figure 7. For each angle of incidence is also shown the corresponding distribution from classical molecular-dynamics simulations of the sputtering event. See text for details, (Sundqvist et al. 1991).

of the incoming primary ion. With the help of the initial axial velocity measurements mentioned above one can estimate an angle of ejection for renin substrate. The results are 43° and 84° with respect to the direction of the primary ion for perpendicular and 45° angle of incidence respectively. These experimental findings strongly support the expansion model by Johnson et al. (1989) and the shock wave model by Bitensky & Parilis (1987) and seem to rule out thermal models in the case of large molecular ion ejection. Both models predict ejection angles of 45° and 67.5° for the two cases in qualitative agreement with the experimental findings. One should however keep in mind that the measurements are for secondary ions and the calculations in the models are for neutral molecules ejected from the surface layer.

The lower curves in figure 8 show the results of classical molecular-dynamics simulations of the sputtering event. The simulations are described elsewhere (Fenyö et al. 1990c; Fenyö & Johnson, 1992) but in brief the basic idea is the following: At time zero a certain number of molecules around the track of the primary ion starts to expand due to e.g. a Coulomb explosion. A Lennard Jones potential is assumed for the interaction between the molecules. By solving the equation of motion for each molecule in time steps, ejection is obtained of molecules. These have a radial velocity distribution in qualitative agreement with the experimental data. One possible explanation for the lack of quantitative agreement in figure 8 between molecular-dynamics simulations and experiment could be that intact ions only leave from adsorbed surface sites (Fenyö 1991).

7.3 Angular-Distribution Measurements

The Darmstadt group has developed a sophisticated position-sensitive stop detector for angular and energy measurements of secondary ions. For each secondary ion the time-of-flight and the position of impact in the detector plane are recorded. The radial and axial velocities as well as the emission angle can then be calculated (Moshammer et al. 1990). Figure 9 shows such measurements by Moshammer (1991) for fission fragments from a ^{252}Cf source at normal incidence on a valine and an alpha-cyclodextrine target respectively. For the latter case an emission minimum for a large negative molecular ion is also demonstrated which rules out the possibility that the emission pattern is caused by the positively charged nuclear track. The same conclusion was also drawn by Fenyö et al. (1990a) who found the same value on the radial velocity component for negative, positive, and also doubly charged molecular ions of bovine insulin desorbed by 72 MeV ^{127}I ions at 45° angle of incidence.

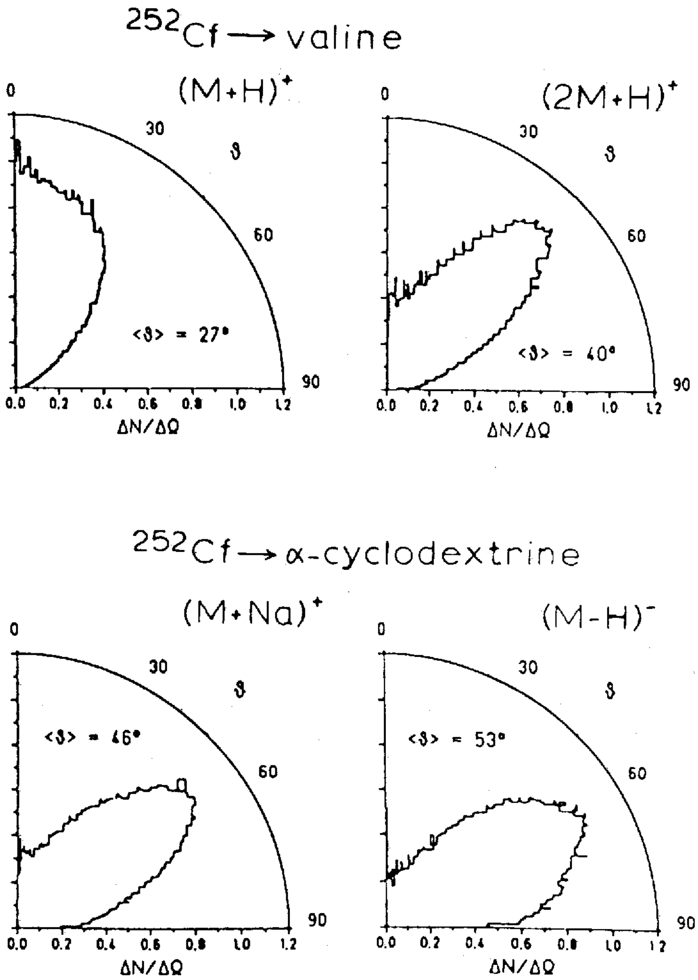

Figure 9. Polar diagrams of angular distributions measured with a position sensitive stop detector of molecular ions from targets of valine and α-cyclodextrine desorbed by fission fragments from a ^{252}Cf source at normal angle of incidence. The molecular ion of valine, $(M+H)^+$, has a forward peaked distribution almost like a $\cos\theta$ distribution unlike the dimer of valine, $(2M+H)^+$, which has an emission minimum in the track direction. In the case of a-cyclodextrine such a minimum is found both for the positive quasi molecular ion, $(M+Na)^+$ and the negative molecular ion, $(M\text{-}H)^-$. The latter observation rules out the possibility that the emission pattern is caused by the positively charged ion track. Compare with figure 7 and 8, (Moshammer, 1991).

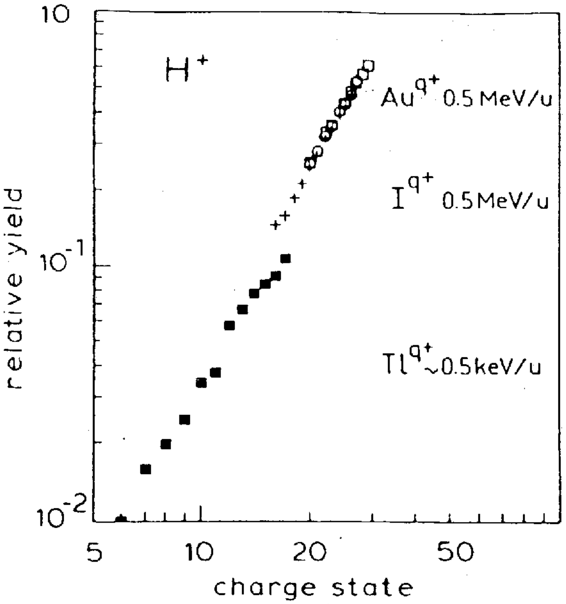

Figure 10. The H^+ yield as a function of the incident charge states of ^{127}I and ^{197}Au ions at 0.5 MeV/u. The yield scales approximately as the incident charge state to the third power. The target is a carbon foil and the H^+ ions have been shown to come from surface contaminants of water and hydrocarbons. The fact that the yield only depends on the incident primary-ion charge state and not on atomic number for constant ion velocity is in marked contrast to what is found for other secondary ions. This indicates that the H^+ emission takes place promptly close to the point of impact of the primary ion. Under the same experimental conditions it has also been found that the H^+ yield for slow heavy ions, ^{208}Tl ions at 0.5 keV/u, scales approximately as the charge state to the third power, (Benguerba et al. 1991b).

8 Emission of Hydrogen Ions

8.1 Hydrogen Emission Induced by MeV Ions

In general, the secondary ion yield in electronic sputtering depends strongly on the charge state (Håkansson et al. 1981a; Becker et al. 1986b; Della-Negra et al. 1987a) and the atomic number of the primary ion (Håkansson & Sundqvist, 1982; Becker et al. 1986a). The yield data have been analyzed in terms of the charge exchange cycle between the primary ion and the solid down to around 100-200 Å. From a description of this cycle it appears that the yield depends on the integrated deposited energy down to that depth (Wien et al. 1987). For the emission of H^+ ions the situation is, however, completely different. Della-Negra et al. (1987c) have shown that, for constant projectile velocity, the yield of H^+ ions from a carbon foil

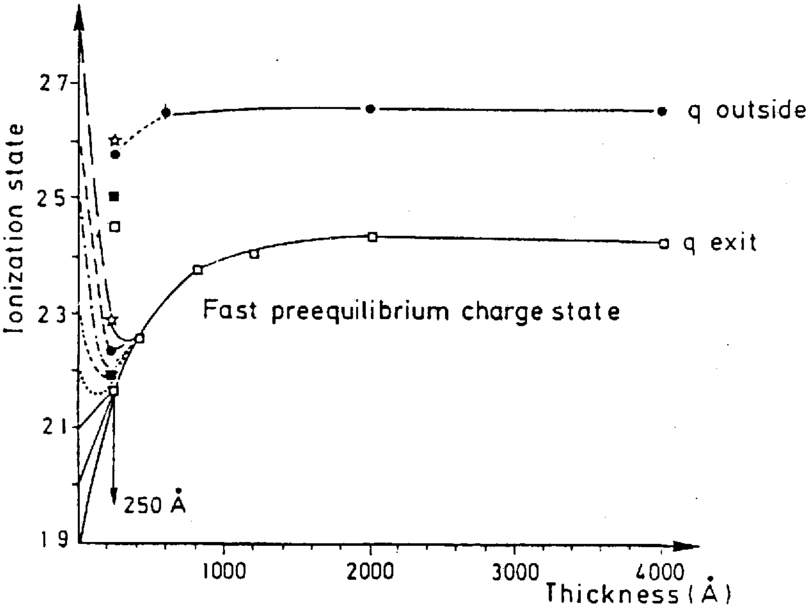

Figure 11. By using the experimental fact that the H^+ yield only depends on the charge state of the heavy ion when it crosses the surface (see figure 10) of the target, the ionization state of the ion inside the foil can be determined. The figure shows the variation of the ionization state of 127 MeV ^{127}I ions as a function of the thickness of different carbon foils traversed. Independent of the incident charge state the ions first reach a preequilibrium charge state which is lower than the final equilibrated charge state (curve (q exit)). This charge state is in turn lower than the charge state obtained 40 ns after the ions have left the foil due to postionization Auger effects (curve 'q outside'), (Benguerba et al. 1991a).

depends only on the primary ion charge when it crosses the surface and not on the atomic number of the primary ion. One such experiment (Benguerba et al. 1991b) was performed employing 0.5 MeV/u ^{197}Au ions ($22 < q < 29$) and ^{127}I ions ($15 < q < 27$). The yield of H^+ ions was found to have almost a cubic dependence on the charge state, independent of the type of ion as shown in figure 10. The emitted H^+ ions were shown to originate from surface contaminants of water and hydrocarbons. The hydrogen emission is thus not dependent on the total energy loss in the foil but rather on the high-energy density deposition in the surface close to the point of impact at an early stage of the energy dissipation.

8.2 Hydrogen Emission Induced by keV Ions

The Orsay group (Benguerba et al. 1991b) has also found the same, almost cubic, charge state dependence for H^+ emission from a carbon foil bombarded with 0.5 keV/u ^{208}Tl ions ($5 < q < 18$) obtained from a radioactive source as shown in figure 10. In this energy range no other ions exhibit a charge-state dependence, not even H^- (Brunelle et al. 1989a). One possible explanation for the emission is that the highly charged primary ion sets up a strong electric field that causes electron emission from the surface before the impact of the ion. The H^+ emission is assumed to be a secondary effect of the electron emission (Della-Negra et al. 1988).

8.3 The Concept of Preequilibrium Charge State

The charge-state dependence of H^+ emission can also be used to determine the mean charge of fast heavy ions inside a foil (Benguerba et al. 1991a). Figure 11 shows the result of such a measurement. Carbon foils of thicknesses between 250 Å and 4000 Å were bombarded with ^{127}I ions at 1 MeV/u. First a calibration curve was established by measuring the H^+ yield from the front side as a function of the charge state. Then the spectrometer was rotated and by measuring the H^+ yield at the exit surface, and by use of the calibration curve the charge state could be determined of the ions just when they left the surface. The finding is that independent of the initial charge state the ions quickly, already at 250 Å, reach a 'preequilibrium charge state'. The full equilibration is reached for much larger film thicknesses and this charge state is found to be lower than the equilibrated charge state measured 40 ns after the ions have left the surface due to postionization Auger effects (Brunelle et al. 1989b).

9 Electronic Sputtering of Small Secondary Ions

For sputtering of intact large biomolecules where a clear nonsymmetric angular distribution has been established, any kind of diffusive model must be excluded. That is however not the case for the fragment ions probably emanating from the hot zone close to the track, the so called infratrack where direct primary ionizations and excitations take place. Moshammer (1991) assumes that from this region, a gaseous flow of particles comes out in the direction of the track. With a simple gas-dynamic model, very good fits can be performed to measured energy and angular distributions. Figure 12 shows such distributions for a positive fragment ion (30 u) of valine ejected for bombardment at normal incidence with a beam of ^{134}Xe ions at 1.4 MeV/u. The gas temperature in this case is 9400 K, and the flow velocity

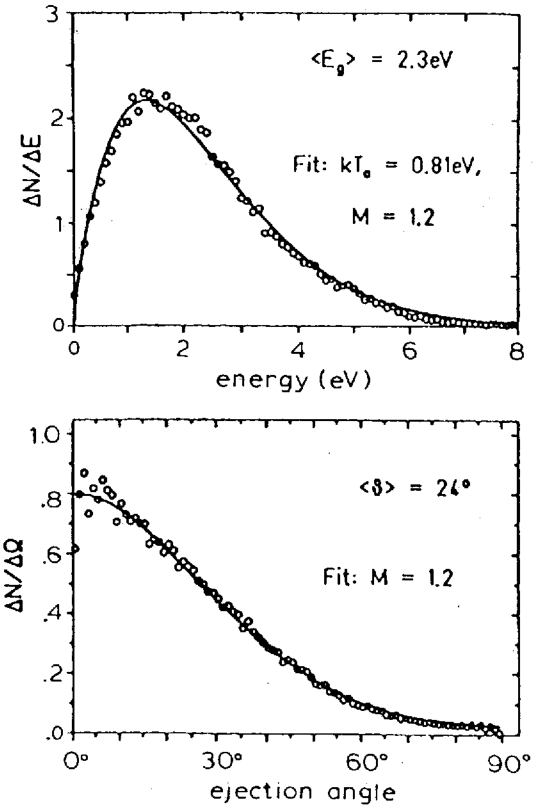

Figure 12. Total energy distribution (upper curve) and angular distribution (lower curve) of a fragment ion (30 u) of valine desorbed by a 1.4 MeV/u ^{134}Xe beam at normal angle of incidence. The fragment ions are believed to be created in the hot central part of the ion track and to be evaporated from the target surface due to a thermal process. The solid lines are calculated in a gas-flow model with the fitting parameters being T_0, the gas temperature and M, the gas flow velocity. In the figure T_0 corresponds to 9400 K and M to 1.2 times the velocity of sound, (Moshammer, 1991).

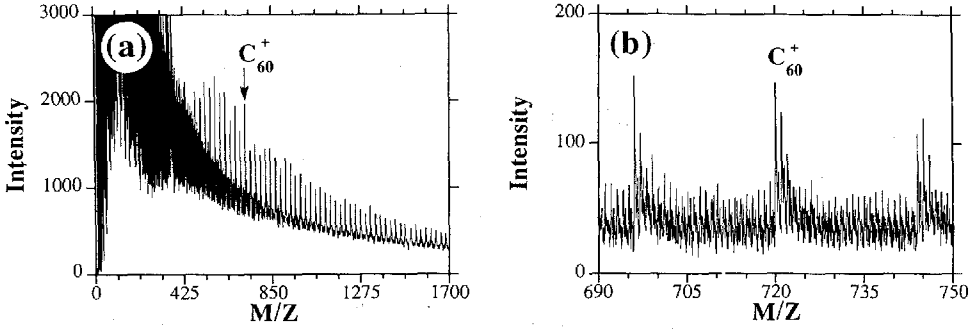

Figure 13. a) When the polymer PVDF, poly(vinylidene difluoride), is irradiated with fast heavy ions even numbered carbon clusters C_n, fullerenes, are promptly formed in the ion track. The figure shows a time-of-flight spectrum of such positive ions with $40 < n < 138$ desorbed by 72 MeV ^{127}I ions. There is an intensity enhancement for the C_{60}^+ (buckyball) ion. b) Expanded view of the region around the C_{60}^+ ion peak from the same spectrum. Due to the ^{13}C isotope each fullerene ion peak splits into several. There is also a peak at every integer mass unit corresponding to different combinations of hydrogenated carbon clusters, (Brinkmalm et al. 1992a).

is 1.2 times the velocity of sound.

However, in the measurements at Uppsala by Fenyö et al. (1990b) of the radial velocity distributions for different angles of incidence of low-mass fragment ions, no indications have been obtained so far of a gas 'jet' of particles going in a direction correlated with that of the incoming primary ion. All angular distributions for low-mass fragment ions measured so far are peaked around the normal to the surface independent of the angle of incidence. Of course, this observation does not rule out other types of thermal processes for the desorption of low-mass fragment ions.

10 Formation of Fullerenes in the Ion Track

When the polymer poly(vinylidene difluoride), PVDF $(CH_2 - CF_2)_n$, is irradiated with fast heavy ions, even-numbered carbon cluster ions are formed (Feld et al. 1990; Brinkmalm et al. 1992a). As shown by Brinkmalm et al. the ions are formed promptly as a consequence of single ion impact, and there is an intensity enhancement for the famous C_{60}^+ (buckyball) ion (Kroto et al. 1985). Arguments that the clusters really consist of only carbon are the systematic trend in the intensity variation of the ^{13}C isotope peaks in the spectra and the accurate determination of their masses. Figure 13 shows a spectrum of positive ions from a PVDF target bombarded with 72 MeV ^{127}I ions. The spectrum is recorded in a time-of-flight spectrometer, see figure 2, equipped with an electrostatic mirror. The latter is

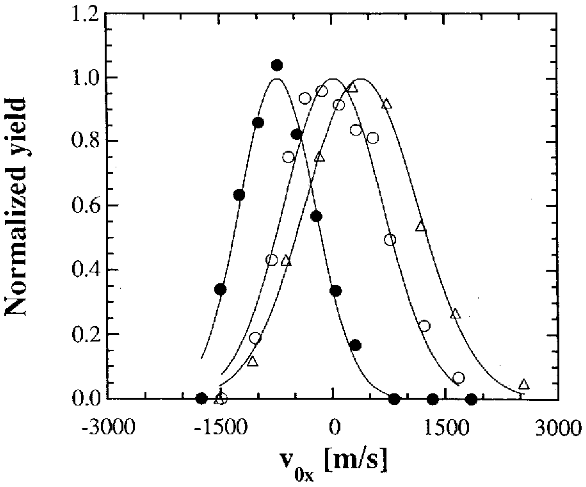

Figure 14. Radial velocity distributions for molecular ions from leu-enkephaline (left curve), C_{60}^+ ions from a synthetic fullerene sample (central curve) and C_{60}^+ ions from a PVDF target (right curve) when bombarded with 72 MeV ^{127}I ions at 45° angle of incidence. The distributions are peak-normalized to the distribution of $C_2H_3^+$ ions which are desorbed symmetrically around the normal to the surface in each case. With respect to the primary ion direction the distributions correspond to ejection angles $> 45°$ for leu-enkephaline, 45° (i.e. ejection normal to the surface) for C_{60}^+ ions from a synthetic fullerene sample and $< 45°$ for C_{60}^+ ions from a PVDF sample. The last case is indicating that the fullerenes are formed in the hot central part of the ion track and ejected due to the axially expanding track, (Brinkmalm et al. 1993).

necessary to use in order to resolve the cluster ions due to extensive metastable decays and, presumably, a broad initial axial velocity distribution of the cluster ions. The clusters are separated by 24 mass units and the pattern extends up to about mass 4000 u. The spectrum also contains peaks at every integer mass unit indicating many combinations of hydrogenated carbon clusters. However, no mixed fluorohydrocarbon ions can be seen in the spectra. From the nearly symmetric peak shapes of the cluster ion peaks one might rule out the possibility that the clusters are formed as decay products of a fullerene precursor that cools down by evaporation in the acceleration region in the spectrometer. It should be noted that no carbon clusters have been observed under irradiation of teflon $(CF_2\text{-}CF_2)_n$ or graphite (which is a conductor) under the same experimental conditions.

The ion-induced fullerene formation is a new phenomenon observed in the field of electronic sputtering of organic molecules. On a very short time scale a considerable atomization occurs followed by mixing and condensation of atoms, leading to the ejection of new molecules completely different from the target material. The

C-C bond is so energetically favoured that the target material locally collapses. The volume occupied by 60 carbon atoms in a vibrationally relaxed C_{60} molecule is eight times smaller than in the original target material (Johnson & Sundqvist, 1992). As will be shown below, there are experiments indicating that this formation takes place in the hot central part of the ion track, a region that so far only has been assumed to eject fragment and atomic ions.

Figure 14 shows a summary of three different measurements of initial radial velocity distributions (Brinkmalm et al. 1993). The peptide leu-enkephalin (555 u), synthetic fullerenes made according to the recipe by Krätschmer et al. (1990) and a film of PVDF were bombarded by 72 MeV ^{127}I ions at 45° angle of incidence. In the figure, the distributions are peak-normalized to the low-mass fragment ion $C_2H_3^+$ which is ejected normal to the surface. The shift of the distribution for molecular ions from leu-enkephalin (left curve) corresponds to an ejection angle larger than 45° away from the direction of the incoming primary ion. This is believed to be a consequence of the radially expanding track as was earlier discussed for other peptides. The distribution for C_{60}^+ ions from the synthetic fullerene sample (central curve) shows no shift compared to the low-mass fragment ion indicating ejection normal to the surface. However, the distribution for the C_{60}^+ ions from the PVDF target (right curve) is shifted in such a way that the ions are desorbed in a direction between the normal to the surface and the direction of the incoming primary ion. This is the first time ejection has been observed in a 'backward' direction, and it is an indication that the fullerenes are formed in the hot central part of the track and that they are desorbed into vacuum from the axially expanding track.

11 Conclusions

To summarize, we have the following picture of an electronic sputtering event in a bioorganic material (compare with figure 3). The fast heavy ion deposits energy along its trajectory in the sample through ionizations and electronic excitations. Light ions like H^+ and H_2^+ are promptly desorbed from regions close to the point of impact at an early stage of the energy dissipation. The emission of these secondary ions serves as a probe of the track before it starts to expand. In the central part of the track the energy density is very high, causing extensive fragmentation of the molecules. These fragments are probably evaporated away from the surface due to some thermal process. As the track starts to expand, a pressure pulse is created that propagates radially and sputters the large molecular ions or neutrals when intersecting the surface with a strong directional correlation. It is supposed that the molecular ions come from regions closer to the central part of the track than the neutrals (Johnson & Sundqvist, 1992).

Central experiments like the scaling to the third power of the neutral yield with the electronic stopping power and the directional correlation are roughly explained by the pressure-pulse model (Johnson et al. 1989), the modified shock-wave model (Bitensky et al. 1991) and by the molecular-dynamics simulations (Fenyö et al. 1990c; Fenyö & Johnson, 1992). However, only when the ions are assumed to come from the surface can these models give agreement with the measured radial velocity distributions. One should keep in mind that almost all experimental data are for ions, and only Bitensky et al. (1991) have attempted to include the ionization step in their theoretical model. Unfortunately the neutral-yield scaling measurement of leucine is the only one performed so far, and this experiment should be repeated for other cases.

Although a large body of experimental information is available today there is still a need for more measurements, especially on total neutral-molecule yields and data related to the ionization processes.

The ion-induced fullerene production from a polymer film is an example of a completely new form of electronic sputtering of organic insulators. Extensive atomization/condensation processes take place promptly upon ion bombardment in the hot central part of the ion track. This leads to the formation of new molecules from an area that so far only has been considered creating fragments and atomic ions. The fullerene production seems to probe the hot core of the axialy expanding track. However, to be able to calculate an ejection angle, measurements on the initial axial velocity distributions are needed.

This paper has described some desorption experiments on organic insulators induced by high energy particle beams. These ions have large stopping power values, up to about 1000 eV/Å. However, the discussed electronic sputtering process also scales down to low stopping power values, about 40 eV/Å , (Salehpour et al. 1989). The relative contributions of electronic and nuclear stopping in the keV energy region to the sputtering yield of organics are however not fully understood as discussed in a review article by Ens in this volume.

Acknowledgements

The author acknowledges the support from the Swedish Natural Science Research Council, the Swedish Research Council for Engineering Sciences and valuable comments on the manuscript by B. U. R. Sundqvist, R. E. Johnson and C. T. Reimann.

References

Becker O and Wien K, 1986: Nucl. Instr. Meth. **B16**, 456
Becker O, Della-Negra S, Le Beyec Y and Wien K, 1986a: Nucl. Instr. Meth. **B16**, 321

Becker O, Guither W, Wien K, Della-Negra S and Le Beyec Y, 1986b: Springer Proc. in Physics 9, Springer Verlag, p. 11

Benguerba M, Brunelle A, Della-Negra S, Depauw J, Joret H, Le Beyec Y, Da Silveira E and Maynard G, 1991a: *Methods and Mechanisms for Producing Ions from Large Molecules*, eds. KG Standing and W Ens, Plenum Press, New York, p. 19

Benguerba M, Della-Negra S, Joret H and Le Beyec Y, 1991b: Int. J. Mass Spectrom. Ion Processes **107**, R11

Bitensky IS and Parilis ES, 1987: Nucl. Instr. Meth. **B21**, 26

Bitensky IS, Goldenberg AM and Parilis ES, 1991: *Methods and Mechanisms for Producing Ions from Large Molecules*, eds. KG Standing and W Ens, Plenum Press, New York, p. 83

Bolbach G, Della-Negra S, Deprun C, Le Beyec Y and Standing KG, 1987: Rapid Commun. Mass Spectrom. **1**, 22

Brandl D, Schoppmann Ch, Schmidt R, Nees B, Ostrowski A and Voit H, 1991: Phys. Rev. **B43**, 5253

Brandt W and Ritchie RH, 1974: *Physical Mechanisms in Radiation Biology*, eds. RD Cooper and RD Wood, USEC Technical Inf. Centre, Oak Ridge, Tennessee, p. 20

Brinkmalm G, Barofsky D, Demirev P, Fenyö D, Håkansson P, Johnson RE, Reimann CT and Sundqvist BUR, 1992a: Chem. Phys. Lett. **191**, 345

Brinkmalm G, Håkansson P, Kjellberg J, Demirev P, Sundqvist BUR and Ens W, 1992b: Int. J. Mass Spectrom. Ion Processes **114**, 183

Brinkmalm G, Demirev P, Fenyö D, Håkansson P, Kopniczky J and Sundqvist BUR, 1993: Phys. Rev. B **47**, 7560

Brunelle A, Della-Negra S, Depauw J, Joret H and Le Beyec Y, 1989a: Nucl. Instr. Meth. **B43**, 586

Brunelle A, Della-Negra S, Depauw J, Joret H, Le Beyec Y and Wien K, 1989b: Nucl. Instr. Meth. **B43**, 484

Brunelle A, Della-Negra S, Depauw J, Joret H and Le Beyec Y, 1991: Rapid. Commun. Mass Spectrom. **5**, 40

Cheblukov YN, Koshkarev DG, Peuto AR, Rudskoygh IV, Vasiliev NA, Nazarov VM, Bock R, Hoffmann DHH, Müller RW and Vetter J, 1992: Particle Accelerators **37/38**, 351

Della-Negra S, Le Beyec Y and Håkansson P, 1985: Nucl. Instr. Meth. **B9**, 103

Della-Negra S, Becker O, Cotter R, Le Beyec Y, Monart B, Standing K and Wien K, 1987a: J. Physique **48**, 261

Della-Negra S, Deprun C and Le Beyec Y, 1987b: Rapid. Commun. Mass Spectrom. **1**,10

Della-Negra S, Le Beyec Y, Monart B, Standing K and Wien K, 1987c: Phys. Rev. Lett. **58**, 17

Della-Negra S, Depauw J, Joret H, Le Beyec Y and Schweikert EA, 1988: Phys. Rev. Lett. **60**, 948

Della-Negra S, Depauw J, Joret H, Le Beyec Y, Bitensky IS, Bolbach G, Galera R and Wien K, 1990: Nucl. Instr. Meth. **B52**, 121

Dück P, Treu W, Fröhlich H, Galster W and Voit H, 1980: Surf. Sci. **95**, 603

Ens W, 1993: Mat. Fys. Medd. Dan. Vid. Selsk. **43**, 155

Ens W, Sundqvist BUR, Håkansson P, Hedin A and Jonsson G, 1989: Phys. Rev. **B39**, 763

Feld H, Zurmühlen R, Leute A and Benninghoven A, 1990: J. Phys. Chem. **94**, 4595

Fenyö D, 1991: Thesis at the Faculty of Science, no 321, Uppsala University, Uppsala, Sweden

Fenyö D and Johnson RE, 1992: Phys. Rev. **B46**, 5090

Fenyö D, Hedin A, Håkansson P, Johnson RE, and Sundqvist BUR, 1990a: *Ion Formation from Organic Solids (IFOS V)*, eds. A Hedin, BUR Sundqvist and A Benninghoven, J. Wiley & Sons, p. 33

Fenyö D, Hedin A, Håkansson P and Sundqvist BUR, 1990b: Int. J. Mass Spectrom. Ion Processes **100**, 63

Fenyö D, Sundqvist BUR, Karlsson BR and Johnson RE, 1990c: Phys. Rev. **B42**, 1895

Fenyö D, Håkansson P and Sundqvist BUR, 1993: Nucl. Instr. Meth. B, in press

Fürstenau N, Knippelberg W, Krueger FR, Weiss G and Wien K, 1977: Z. Naturforsch. **32A**, 711

Haff PK, 1976: Appl. Phys. Lett. **29**, 473

Hedin A, Håkansson P, Sundqvist B and Johnson RE, 1985: Phys. Rev. **B31**, 1780

Hedin A, Håkansson P, Salehpour M and Sundqvist BUR, 1987a: Phys. Rev. **B35**, 7377

Hedin A, Håkansson P and Sundqvist BUR, 1987b: Nucl. Instr. Meth. **B22**, 491

Håkansson P and Sundqvist B, 1982: Rad. Eff. **61**, 179

Håkansson P, Jayasinghe E, Johansson A, Kamensky I and Sundqvist B, 1981a: Phys. Rev. Lett. **47**, 1227

Håkansson P, Johansson A, Kamensky I, Sundqvist B, Fohlman J and Peterson P, 1981b: IEEE Trans. Nucl. Sci. **NS-28**, 1776

Håkansson P, Kamensky I, Salehpour M, Sundqvist B and Widdiyasekera S, 1984: Rad. Eff. **80**, 141

Johnson RE, 1987: Int. J. Mass Spectrom. Ion Processes **78**, 357

Johnson RE and Sundqvist B, 1983: Int. J. Mass Spectrom. Ion Phys. **53**, 337

Johnson RE and Sundqvist BUR, 1992: Physics Today, **March**, 28

Johnson RE, Sundqvist BUR, Hedin A and Fenyö D, 1989: Phys. Rev. **B40**, 49

Jonsson G, Hedin A, Håkansson P, Sundqvist BUR, Säve G, Nielsen P, Roepstorff P, Johansson KE, Kamensky I and Lindberg M, 1986: Anal. Chem. **58**, 1084

Jonsson G, Hedin A, Håkansson P, Sundqvist BUR, Bennich H and Roepstorff P, 1989: Rapid Commun. Mass Spectrom. **3**, 190

Kobetich EJ and Katz R, 1968: Phys. Rev. **170**, 391 and 405

Kraft G, Kraemer M, Scholz M, 1992: Rad. Environ. Biophys. **31**, 161

Kroto HW, Heath JR, Brien SCO, Curl RF and Smalley RE, 1985: Nature **318**, 162

Krätschmer W, Lamb LD, Fostiropoulos K and Huffman DR, 1990: Science **347**, 354

Le Beyec Y, 1989: *Advances in Mass Spectrometry*, Volume 11A, ed. P Longevialle Heyden & Sons Ltd., p. 126

Macfarlane RD and Jacobs DL, 1989: *Ion Formation from Organic Solids (IFOS IV)* , ed. A Benninghoven, J. Wiley & Sons, p. 71

Macfarlane RD and Torgerson DF, 1976: Int. J. Mass Spectrom. Ion Phys. **21**, 81

Macfarlane RD, Hill JC, Jacobs DL and Phelps RG, 1986: *Mass Spectrometry in the Analysis of Large Molecules*, ed. CJ McNeal, J. Wiley & Sons, p. 1

Mamyrin BA, Karataev VI, Shmikk DV and Zagulin VA, 1973: Sov. Phys.-JETP **37**, 45

Matthäus R, Moshammer R, v Hayn G, Wien K, Della Negra S, and Le Beyec Y, 1993: Int. J. Mass Spectrom. Ion Proc. **126**, 45

McNeal CJ, Macfarlane RD and Thurston EL, 1979: Anal. Chem. **51**, 2036

Moshammer R, 1991: Thesis, Institut für Kernphysik, Techn. Hochschule Darmstadt, Germany

Moshammer R, Matthäus R, Wien K and Bolbach G, 1990: *Ion Formation from Organic Solids (IFOS V)*, eds. A Hedin, BUR Sundqvist and A Benninghoven, J. Wiley & Sons, p. 17

Nees B, 1988: Thesis, Physikalisches Institut der Universität Erlangen-Nürnberg, Germany

Qiu Y, Griffith JE, Meng WJ and Tombrello TA, 1983: Radiat. Eff. **70**, 231

Reimann, CT: Mat. Fys. Medd. Dan. Vid. Selsk. **43**, 351

Roepstorff P, 1990: *Mass Spectrometry of Peptides*, ed. DM Desiderio CRC - press, Boca Raton, p. 65

Salehpour M, Håkansson P, Sundqvist B and Widdiyasekera S, 1986: Nucl. Instr. Meth. **B13**, 278

Salehpour M, Hunt JE, Fishel DL and Tou JC, 1989: Int. J. Mass. Spectrom. Ion Processes **88**, 211

Schmidt R, Brandl D, Schoppmann CH, Voit H, Kröhl T, Johannsmann D and Knoll W, 1990: Int. J. Mass Spectrom. Ion Processes **99**, 223

Schmidt R, Nees B, Schoppmann CH, Brandl D, Ostrowski A, Voit H, Johannsmann D and Knoll W, 1991a: Thin Solid Films **195**, 307

Schmidt R, Schoppmann CH, Brandl D, Ostrowski A, Voit H, Johannsmann D and Knoll W, 1991b: Phys. Rev. **B44**, 560

Sigmund P, 1969: Phys Rev **184**, 383

Sundqvist BUR, 1991: *Sputtering by Particle Bombardment, part III*, eds. R Behrisch and K Wittmaack, Springer Verlag, p. 257

Sundqvist BUR, 1993: Int. J. Mass Spect. Ion Proc. **126**, 1

Sundqvist BUR and Macfarlane RD, 1985: Mass Spectrom. Rev. **4**, 421

Sundqvist BUR, Ariyaratne A, Ens W, Fenyö D, Hedin A, Håkansson P, Jonsson G and Widdiyasekera S, 1989: *Ion Formation from Organic Solids (IFOS IV)*, ed. A Benninghoven, J. Wiley & Sons, p. 51

Sundqvist BUR, Håkansson P, Hedin A, Fenyö D, Brinkmalm G, Roepstorff P and Johnson RE, 1991: *Methods and Mechanisms for Producing Ions from Large Molecules* eds. KG Standing and W Ens, Plenum Press, New York, p. 7

Säve G, Håkansson P, Sundqvist BUR, Johnson RE, Söderström E, Lindqvist SE and Berg J, 1987a: Appl. Phys. Lett. **51**, 1379

Säve G, Håkansson P, Sundqvist BUR, Söderström E, Lindqvist S-E and Berg J, 1987b: Int. J. Mass Spectrom. Ion Processes **78**, 259

Tang X, Beavis R, Ens W, LaFortune F, Schueler B and Standing KG, 1988: Int. J. Mass Spectrom. Ion Processes **85**, 43

Torgerson DF, Skowronski RP and Macfarlane RD, 1974: Biochem. Biophys. Res. Com. **60**, 616

Voit H, Nieschler E, Nees B, Schmidt R, Schoppmann CH, Beining P and Scheer J, 1989: J. de Physique **C2**, 237

Walter K, Boesl U and Schlag EW, 1986: Int. J. Mass Spectrom. Ion Processes **71**, 309

Watson CC and Tombrello TA, 1985: Rad. Eff. **89**, 263

Widdiyasekera S, Håkansson P and Sundqvist BUR, 1988: Nucl. Instr. Meth. **B33**, 836

Wien K, 1989: Rad. Eff. Defects in Solids **109**, 137

Wien K, 1992: Nucl. Instr. Meth. **B65**, 149

Wien K, Becker O, Guthier W, Della-Negra S, Le Beyec Y, Monart B, Standing KG, Maynard G and Deutsch C, 1987: Int. J. Mass Spectrom. Ion Processes **78**, 273

Williams P and Sundqvist B, 1987: Phys. Rev. Lett. **58**, 1031

Fundamental Aspects of Matrix-Assisted Laser Desorption Ionization Mass Spectrometry

By Michael Karas
Institute for Medical Physics and Biophysics, University of Münster,
Robert-Koch-Str. 31, D-4400 Münster, Germany

Synopsis

Matrix-assisted laser desorption ionization forms one of the major break-throughs in modern mass spectrometry. It allows today the desorption of intact ions of biomacromolecules in the mass range of up to 400,000 Dalton. Especially for peptides and proteins it is becoming a routine technique for determination of the molecular mass. Basic understanding of the underlying desorption and ionization mechanisms, however, is still very rudimentary. This can be attributed to the fact that a successful desorption of macromolecule ions is the result of a complex set of physico-chemical and experimental parameters. With regard to the matrix, these are the ability to incorporate macromolecules in the preparation step, to absorb energy upon irradiation with a short laser pulse and undergo a phase transition from solid to gas and to yield a high number of charged analyte ions by photochemical processes. Measurements of the properties of the desorbed ions show a strongly forwarded emission, a mass-independent initial velocity and an energy deficit which is increasing both with mass and laser fluence. These ion characteristics can be rationalized by a supersonic expansion of a vaporized surface layer and collisions in the acceleration step. A more refined understanding of the desorption process has to be gained by future work in order to enable systematic choice of matrix compounds and to optimize the experimental conditions for an improved mass spectrometric performance.

1 Introduction

The development of matrix-assisted laser desorption ionization mass spectrometry.

Even though lasers have unique properties, they have so far found limited use as desorption ionization sources in organic mass spectrometry. Laser light can easily be focused to yield very high power and energy densities at a sample surface, but irradiation of large fragile biomolecules with continous-wave lasers and lasers emitting pulses with durations above 1μs resulted in extensive thermal degradation rather than in the desired emission of intact molecule ions. Short-pulse lasers, either $C0_2$-lasers emitting at 10.6 μm in the infrared or frequency-multipled Nd-YAG-lasers (266 or 355nm) have been used with better results, but the analytical performance achieved either with respect to the accessible mass range, broad applicability, or sensitivity was not satisfying enough to spread out the technique. Only in specialized areas, such as in fourier-transform ion-cyclotron-resonance mass spectrometers or in laser microprobe instruments, lasers are routinely used.

The use of a matrix was proposed by the authors in the mid 80s to circumvene fundamental problems limiting the application of pulsed UV-lasers as a desorption ionization source in organic mass spectrometry. The main drawbacks were that the technique was not generally applicable to different classes of organic compounds and that the accessible mass range was limited to about 1500 Dalton in most favourable cases. Investigations into the laser desorption ionization (LDI) of small organic compounds revealed the underlying reasons. Sample absorption at the laser wavelength was found to be the most relevant factor (Karas et al., 1985); it was therefore concluded that energy coupling into the irradiated sample by resonant excitation of analyte molecules plays a key role in UV-LDI. This was in strong contrast to the general picture of the laser desorption process. Until then, a fast heating of the sample mediated by an absorbing substrate had been regarded to be the underlying mechanism, and any influence of the laser wavelength and sample absorption had therefore been disregarded.

Energy from a UV-laser beam may be deposited into a solid (or liquid) organic sample either by resonant electronic excitation - provided the sample contains a chromophore, usually an aromatic π-electron system - or at sufficiently high laser irradiances (W/cm^2) by non-linear multiphoton absorption. In a typical instrumental configuration, samples are prepared as thin layers dried from solution onto a metallic substrate which in case of a transparent sample may serve as the absorber of the laser energy. It was, however, found in a series of experiments undertaken for small organic compounds, such as amino acids and dipeptides, that - with respect to a soft and reproducible desorption of molecule ions - a high sample absorption at the laser wavelength is required (Karas et al, 1985). The necessary laser irradiance (W/cm^2) was inversely proportional to the absorption coefficient of the sample. It was furthermore found that this soft desorption ionization exhibits a steep threshold behaviour and is only possible in a narrow irradiance range at or slightly above this threshold irradiance. The value determined for this threshold was in the range of 10^7 W/cm^2. Provided the life time of the excited electronic states is short compared to laser pulse time (typically 3 to 10 ns) - which can reasonably be assumed for an organic solid-linear absorption processes are dominating and enable a controllable energy deposition into the sample by careful attenuation of the laser pulse energy. Beer's law can be used for a calculation of the energy deposited and the penetration depth of the laser light. The energy absorbed per molecule in the uppermost layer was found to be in the range of 5 to 10 eV, corresponding to the absorption of one or more than two photons per molecule (photon energy at 266 nm: 4.6 eV); penetration depths were calculated to be 100 to 300 nm, respectively. The energy deposited per unit volume suffices to overcome the solid state cohesion forces (sublimation energy) of typical hydrogen-bonded non-volatile organic compounds. Within the given set of experimental parameters, little energy is lost from the excited volume by heat conduction. Therefore, energy is channeled efficiently into desorption. The upper limit of the usable irradiance is set by an increasing (photo)fragmentation of the organic molecules. This competing fragmentation channel is also regarded to be the reason for the observed mass range limit. With these results a qualitative model was proposed which described the desorption process as an explosive vaporization of a microvolume induced by an electronic excitation of individual chromophores and fast relaxation of the energy into vibrational excitation of the molecular lattice (exciton-phonon-coupling).

Careful inspection of the UV-LDI mass spectra showed that simple models based on solution chemistry, such as (de)protonation or the emission of preformed ions, or gas-phase cationization by alkali ions do not allow for a coherent explanation of the observed ion species. Besides the expected (de)protonated molecules, often high-abundance radical molecular ions show up as well as product ions of (multiple) hydrogen addition or abstraction reactions. It was therefore proposed that the key process in ionization of strongly absorbing compounds is their photoionization. This may be initiated either by a two-photon absorption or by a bimolecular reaction of two singly-excited molecules (energy pooling). The ion species finally registered in the mass spectrum are the products of (photo)chemical reactions of usually reactive radical molecular ions and neutrals taking place in the condensed phase or in the expanding high-density material plume (Ehring et al., 1992).

2 Matrix Idea and Concept

With the above results and considerations it is obvious that UV-LDI suffers from severe and systematic restrictions which prevent its widespread use as a desorption ionization technique in mass spectrometry of bioorganic compounds. On the other hand, the well-defined desorption ionization characteristics of small highly-absorbing compounds and the characterization of the LDI-process as a collective event inducing ablation of a sample volume, gave a guideline for a new approach: provided an analyte is only present at a high dilution in a suitable compound - hence a matrix - it should be possible to set free analyte molecules and possibly molecule ions by UV-LDI of the excess matrix (Karas et al., 1986, 1987, 1988a,b, 1989a,b). Intimate mixing of matrix and analyte was therefore regarded to be a crucial point. Nicotinic acid was chosen as a test compound in the initial matrix experiments; it exhibits a high molar absorption at the wavelength of 266 nm and possesses both an acidic and basic functional group which was regarded to facilitate the embedding of polar peptide and protein molecules (Karas et al., 1988a, 1988b, 1989). The principal features of the matrix techniques have been worked out in the mid 80s in the author's lab, and its feasibility has been shown for medium-size peptides. Application to proteins above 10 kDa was initiated by reports documenting the possibility to desorb intact protein ions by a laser desorption technique; a different matrix approach had been followed, i.e. solving the sample in slurry of a non-volatile liquid, such as glycerol, and small metal particles functioning as absorption centers for the incident laser light (Tanaka et al., 1988). This matrix technique, however, has not found any further impact in analytical chemistry until now.

3 Experimental Techniques

The principal investigations for MALDI have been performed on a laser microprobe instrument, equipped with a Q-switched ND-YAG laser at a wavelength of 266 nm. Short-pulse lasers are required to induce the desired desorption process, therefore time-of-flight (TOF) mass analyzers, allowing for registration of virtually all ions formed and posing no mass limitations, are best suited. Today several dedicated laser TOF instruments are available for MALDI. These are firstly linear TOF instruments (Beavis & Chait, 1989a) using ion acceleration to high kinetic energies (up to 40 keV) to allow for a sufficiently high mass resolution also for ions of considerable initial ion energy spread (see below). Due to the conceptual simplicity, they are bench-top-type instruments. Secondly, reflectron TOF instruments are used allowing for an improved mass resolution; some of these include microscopic observation of the sample by a video-camera system and allow for a selection of the sample area irradiated which showed to be advantageous. All pulsed UV-lasers, such as Nd-YAG (266 or 355 nm) or Excimer-lasers (248, 308, 351 nm), can be used, but small, easy-to-run and inexpensive nitrogen lasers emitting at 337 nm are the most widespread ones. The laser beam is focused to the sample surface by simple quartz lenses to some 100μm in diameter, the laser intensity at the sample is controllable by fine attenuation. Ions are detected by conventional secondary electron multipliers, but due to the relatively low velocity of macromolecule ions even for high initial or post-acceleration, detection efficiency considerably decreases with mass. Furthermore, it is known today (Spengler et al., 1990; Kaufmann et al., 1992) that secondary ions formed by the impact of the large ions may considerably contribute to ion detection, but cause time resolution problems in a TOF system. The development of improved ion detection systems thus is a highly interesting area. For signal registration fast A/D conversion by transient recorders is required. Their technical performance (sampling rate and memory) considerably improved in the last years allowing today for ns-time resolution and up to 1 million data points to be stored.

The required intimate mixture of analyte molecules in the matrix is practically achieved in a very simple preparation procedure. Small aliquots (0.5 to $1\mu l$) of matrix (ca. 50 mM) and analyte solution (typically $\leq 10\mu M$) in widely variable solvents and solvent mixtures are mixed on a metallic support, dried in air and then transfered to the vacuum chamber of the mass spectrometer. The following matrix compounds have proven to be most useful analytically (the laser wavelengths typically used are given in brackets) :

- 2,5-dihydroxybenzoic acid (337, 355 nm) (Strupat et al., 1991)
- sinapinic acid (3,5-dimethoxy-4-hydroxycinnamic acid) and caffeic acid (337, 355 nm) (Beavis & Chait, 1989b),
- 4-hydroxy- α-cyanocinnamic acid (337, 355nm) (Beavis et al., 1992)

Nicotinic acid has been replaced by these compounds in practical applications due to undesired features, especially formation of adduct ions between analyte and matrix. In the IR range best results have been obtained with an Er-YAG laser emitting at 2.94 μm (Overberg et al., 1990). Due to the resonant absorption into OH- and NH-stretching vibrations a large variety of compounds can be used as absorbing matrices. IR-MALDI on the other hand, is so far used only in few laboratories, but may provide some significant developments and advantages in the future.

Usually single laser shots clearly show molecule ion signals, mass spectra are typically accumulated from 10 to 100 single laser shots yielding a better signal-to-noise ratio. The whole procedure including preparation and first evaluation takes only a few minutes.

Figure 1 summarizes graphically the development from LDI to MALDI; it shows the limited accessible mass range both for UV- and IR-LDI and accounts for the restriction of UV-LDI to strongly absorbing samples. The spectra show the direct UV-laser mass spectrum of a pentapeptide (left) with only low molecular ion signals besides a high unspecific background, the MALDI mass spectrum of the same peptide (top) with a prominent protonated molecule and the UV-MALDI mass spectrum of a large protein, a monoclonal antibody (IgG) of ca. 150,000 Dalton (right).

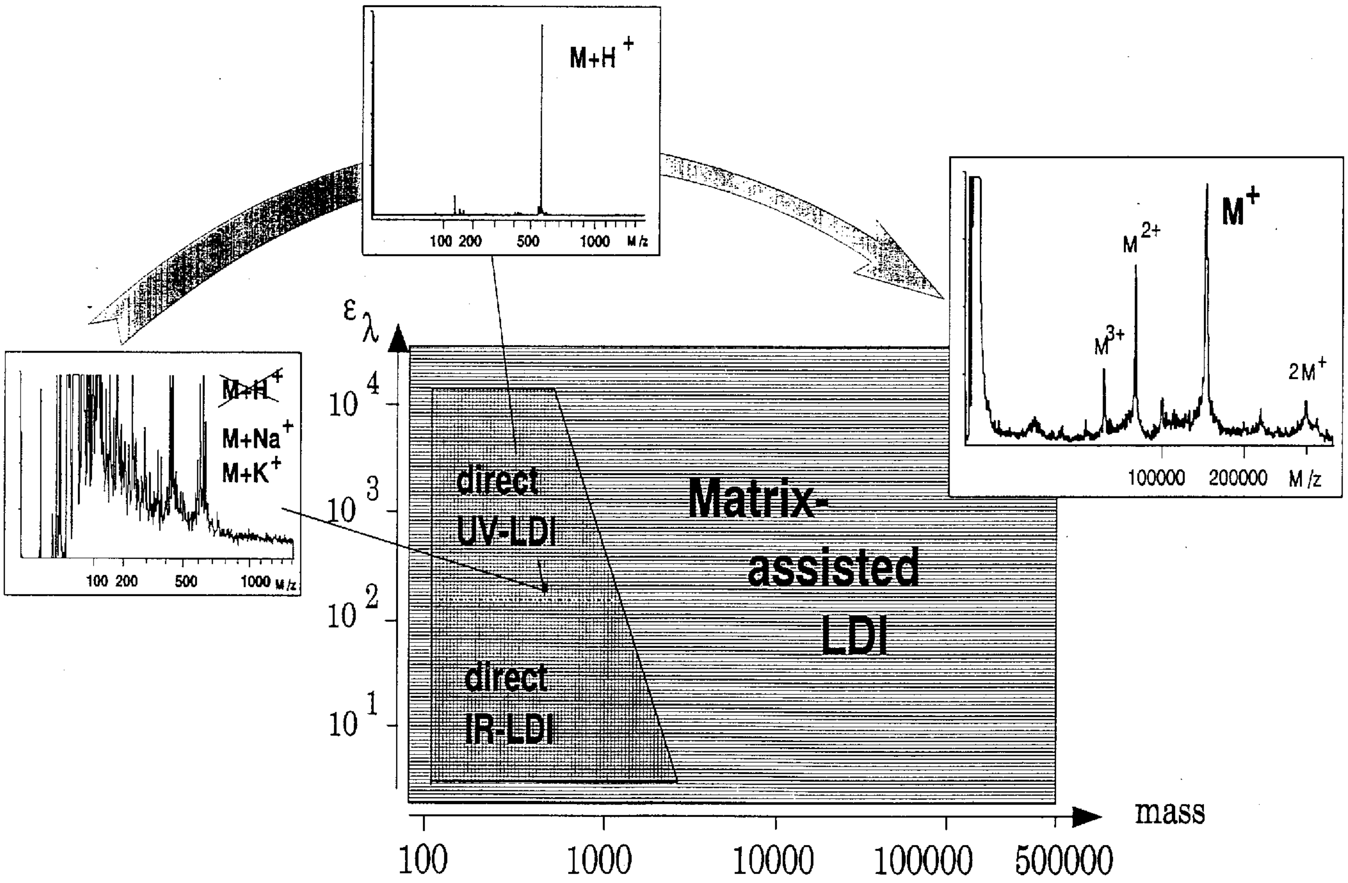

Figure 1. Schematic summary of the development from LDI to MALDI; the extention of the accessible mass range is exemplified by three mass spectra: a) direct UV-LDI mass spectrum of a pentapeptide (left), b) the improvement obtained by use of a matrix for the same

4 Current Analytical Status

Peptides and proteins can be analyzed in the mass range between 500 and 500 000 Dalton (Hillenkamp et al., 1991; Chait et al., 1992). The lower mass limit is usually determined by intense interfering matrix signals. The actual mass limit in the range of some hundreds kDa seems to be rather determined by the currently available ion detectors than by the ion desorption process. MALDI has an excellent sensi- tivity, typical sample loads are $\leq$ 1 pMol (Karas & Hillenkamp, 1989b), 1 femtomol suffices under favourable conditions (Strupat et al., 1991). Furthermore, virtually the whole sample can be regained after analysis, because the amount of material consumed for analysis is much less than the amount loaded. The greatest analytical strength of MALDI seems to be that it can be applied to proteins, independent of their primary, secondary or tertiary structure, of their widely-varying solution phase properties and functional modifications by e.g. glycosylation and phoshorylation (Beavis & Chait, 1990a). Due to the formation of essentially singly- or doubly-charged molecule ions only, mixture analysis and data interpretation is straightforward, also for rather complex natural protein mixtures e.g. milk or saliva, or for cleaved peptides obtained by enzymatic or chemical digestion of proteins (Beavis & Chait, 1990a).

Another important feature of the MALDI technique is that it tolerates even relatively high concentrations of inorganic and organic contaminants (Beavis & Chait, 1990a, Strupat et al., 1991). Salt at physiological concentration and buffers as normally used in biochemical procedures do not deteriorate signal quality, which is unique as compared to other mass spectrometric ionization techniques. This feature also enables the use of the technique in direct combination with biochemical reactions, such as enzymatic digestions. C-terminal sequencing of peptides by carboxypeptidases or determination of the carbohydrate content of a glycoprotein by enzymatic cleavage and MALDI mass determation of the intact and deglycosylated protein may serve as examples.

Mass determination accuracy obtainable is in the 0,01% range provided suitable calibration by well-defined proteins is used (Beavis & Chait, 1990b). Above 30 kDa signals of the analyte containing a matrix adduct are no longer resolvable from the protonated analyte signal. Increased mass resolution is therefore highly desirable, but due to not fully understood reasons reflectron TOF instruments, though capable to achieve sufficiently high mass resolution (up to 4000) for peptides up to 10 kDa, have not been able to yield relevant improvements in the high mass range. Nevertheless, MALDI is a valuable tool for protein analysis also in the higher mass range. For chemically heterogeneous proteins such as glycoproteins the average molecular mass is determined, the width of the molecule ion signal can be used as a semi-quantitative measure for the heterogeneity of the carbohydrate moiety. As a further example, the determination of chelator- and anticancer drug-load to monoclonal antibodies by measuring the mass shift between conjugated and non-conjugated antibody molecules has been reported (Siegel et al., 1991).

MALDI is moreover not only applicable to peptides and proteins, but also to other classes of biopolymers such as oligosaccharides (Stahl et al., 1991), glycoconjugates, e.g. glycolipids, and oligonucleotides (Parr et al., 1992; Nordhoff et al., 1992), but currently the quality of the mass spectra and the accessible mass range has not yet reached the level as routinely achievable for proteins. Further work is undoubtedly needed in these areas, focussing on new matrices and optimized sample preparation procedures.

5 Current Status of Understanding

The most obvious question is what makes a material function as a matrix. Besides some physico-chemical prerequisites, such as vacuum stability, its solubility in solvents usable also for the analytes and the lack of chemical reactivity with analyte compounds, a strong absorption at the laser wavelength is the first important issue. A high absorption cross section enables to deposit energy into the matrix and to optimize the desorption process by careful control of the applied laser irradiance. Absorption spectra usually determined in solution may be used in a practical first approach, but one has to keep in mind that the absorption coefficients and the shape of the absorption curve for a solid are expected to be different from solution; this has been exemplified for sinapic acid showing a broadening of the absorption band and a shift of the absorption maximum to higher wavelengths (Hillenkamp et al., 1992).

Two further important functions can be attributed to the matrix, but cannot yet be deduced from the chemical structure of a matrix candidate or its physicochemical properties. These are the ability to form a solid solution of analyte molecules in the host matrix and the ability to ionize analyte molecules within the desorption process. Two elegant experiments revealed the surprising ability of two matrices, 2,5-DHB and sinapic acid, to incorporate protein molecules into matrix host crystals when the solvent is slowly evaporated. For 2,5-DHB mm-size crystal were grown in a controlled way, cytochrome c was added as the analyte protein at a low concentration. The undisturbed x-ray diffraction pattern of 2,5-DHB could be observed as well as a uniform distribution of a test protein; nearly identical MALDI spectra were obtained with a laser microprobe instrument by irradiating either the surface or inner parts of the crystal (Strupat et al., 1991). Furthermore the concentration of the protein in the crystal was measured by redissolving them and using chromatographic separation and spectrophotometric determination; the

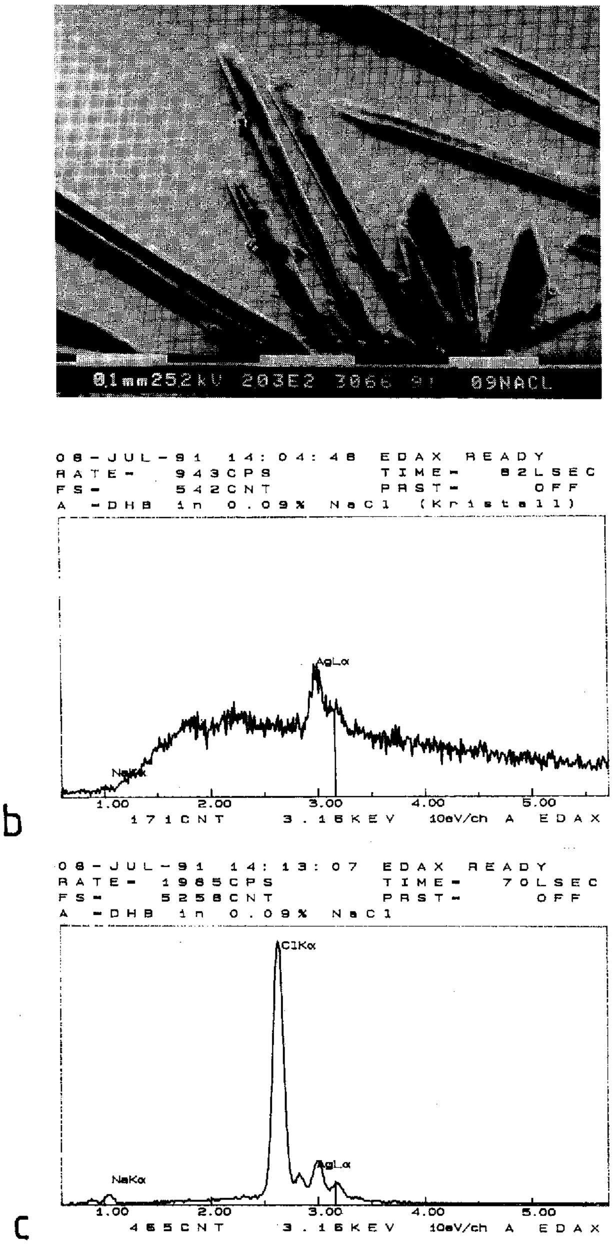

Figure 2. a) Electron micrograph of a 2,5-dihydroxybenzoic acid preparation, containing 0.9% NaCl in the starting solution b) and c) show x- ray microanalysis spectra of b) long 2,5-DHB needles and c) a small crystalline particle sticking to a 2,5-DHB needle.

Figure 3. Electron micrograph of a part of a dried droplet of 2,5-dihydroxybenzoic acid (the matrix) containing cytochrome c as an analyte.

protein concentration was found to be directly proportional to the concentration in the starting solution. For sinapinic acid, incorporation into matrix crystals was investigated by using stained proteins. This matrix crystallizes into extended sheets and the specific staining pattern obtained showed that proteins are incorporated into a crystal by a specific interaction with one crystal surface (Beavis & Bridson, 1992). This formation of a solid solution can also explain the tolerance towards ubiquitous contaminants such as salts and buffers as an in-situ cleaning step which incorparates analyte and excludes contaminants upon crystallization. Figure 2 shows a electron micrograph of a 2,5-dihydroxybenzoic-acid-matrix preparation out of a solution containing physiological (0.9%) salt (NaCl) concentration; x-ray microanalysis revealed that the large crystal needles of DHB (and analyte) are essentially salt-free (a), whereas the small crystal particles sticking to the needles consist of sodium chloride (b).

The shape of the crystals is depending on the individual matrix used, it varies from large crystalline needles extending from the rim of the dried droplet into

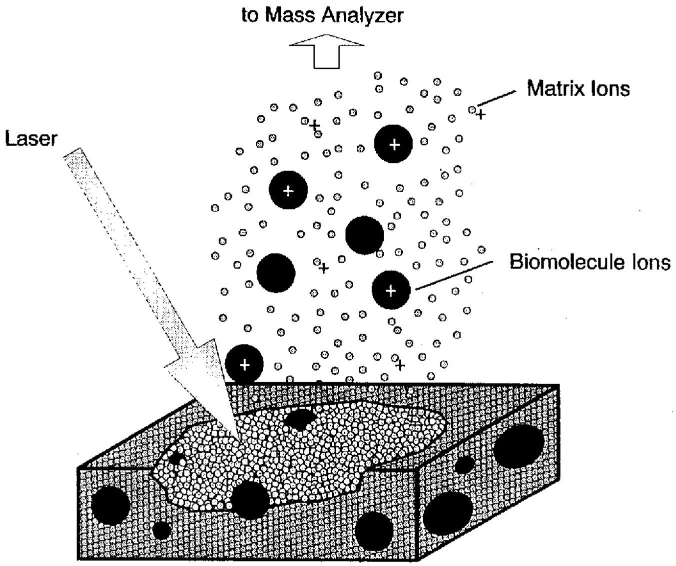

Figure 4. Schematic view on the MALDI process.

the inner area (2,5-DHB) (see figure 3) to finely dispersed microcrystals. At any rate, the light microscopic control of the crystalline structure can be used as a first inspection for a successful preparation step. A too high analyte concentration will alter the crystallization and may therefore deteriorate the MALDI performance. It is furthermore clear that the presence of contaminations which prevent the matix-analyte solution from crystallizing, such as high-vapor-pressure liquids (dimethylsulfoxide and glycerol), are detrimental (Beavis & Chait, 1990a).

The active role of the matrix in ionization has been deduced from the fact that, despite the low relative and absolute concentration of the analyte, molecular ion signals are registered at comparable or even higher intensities than those of the matrix (Ehring et al., 1992). Chemical ioniza- tion by proton transfer reactions between matrix ions and analyte neutrals is regarded to be the underlying mechanism. The ability of a matrix to function as a protonating agent is documented in the respective UV-LDI mass spectrum of the matrix compounds. The presence of both radical and even-electron species in the positive or negative ion mass spectra of all usable matrix compounds may be regarded as an indication for their inability to form stable (non-reactive) ion species and hence their photochemical reacitivity.

The currently discussed models for MALDI are still very rudimentary and far away from giving a satisfactory description of the desorption ionization process or from giving directions for its optimization.

In the 'pressure pulse' model (Johnson et al, 1991), originally developed for fast-ion-induced ejection, a pressure gradient is set up perpendicular to the surface by the energy deposited; if that exceeds a threshold value molecules gain a net expansion velocity. The authors point out that the interpretation of ion yield as a function of fluence may be misleading, because ionization itself may be depend on fluence in a different way than the ablation. The model also predicts an increase of the expansion velocity with increasing laser fluence, which has actually not been observed in postionization experiments. In these experiments the velocity of the desorbed neutrals is determined by a variable time delay between the desorption and the ionizing laser (Dreisewerd et al., 1990). Alternatively, in a sublimation-like model molecules would leave the surface due to a local surface temperature, but an effective threshold would be observed as the yield rapidly increases over a small range of fluences. This was assumed in the 'bottleneck' model (Vertes et al., 1990) but emphasis is put on the question how, despite the high temperatures calculated, fragile large biomolecules can survive desorption to be detected as intact molecule ions in a time- of-flight mass spectrometer. Model discussion has until now concentrated on the desorption process, desorption and ionization is therefore separately discussed in the following. Figure 4 tries to visualize the MALDI process.

In the meantime, a considerable amount of data has been accumulated illuminating some relevant characteristics of the desorption process and properties of the desorbed species.

This is firstly a very steep threshold behaviour in ion desorption as a function of the applied laser pulse energy (under otherwise constant conditions, such as focus diameter) which has been reported already in the original papers and has been clearly confirmed by single-ion counting experiments (Karas et al, 1985, and 1989a; Ens et al., 1991). This holds for the neutrals, as shown in postionization experiments (Spengler et al., 1988), as well as for the ions, which for the examples examined show a somewhat higher threshold energy. These thresholds were regarded as a proof for a collective process involving a microvolume of the sample, but the true physical origin of these thresholds is still unclear. Therefore it is an open question whether a threshold irradiance (W/cm^2) or a threshold fluence (J/cm^2) is the relevant physical parameter (Karas et al. 1987; Beavis, 1992). It is furthermore noteworthy that the actual values given by the different groups differ by more than an order of magnitude. Irradiance has been used in the original papers to account for the fact that short-pulse lasers have been used and that the respective desorption process cannot be induced by conventional heating. Provided that the laser pulse is short enough and heat conduction to the surrounding sample layer or substrate is negligible (see below), fluence or irradiance can be used equivalently for the calculation of the deposited energy. First results on the influence of the laser pulse time have been reported and seem to indicate that for shorter laser pulses the laser energy stays constant (and thus the irradiance increases) (Demirev et al., 1992)). Under the assumption of an essentially linear absorption process and using the absorption coefficient from solution, Beer's law can be used for an estimate of the energy deposited as well as for the penetration depth of the laser into the condensed-phase sample (Karas et al., 1985). Typical values are in the range of 2 eV (photon energy: 3.7 eV at 337 nm) per molecule in the uppermost layer. This would provide enough energy to sublime the upper layers of the irradiated volume. It is, however, interesting to note that the observed steep rise of the threshold curve can be rationalized by a simple geometric consideration, i.e. the increase of the surface area exposed to an irradiance/fluence above a threshold value in a gaussian laser beam of increasing pulse energy (Beavis, 1992). A possible explanation could be that only a very shallow surface layer (much thinner than the absorption depth) is ablated in the threshold regime. At this point in time, the threshold phenomena still need further investigation, e.g. by variation of laser pulse time, spot size and beam profile. As Johnson and Sundqvist pointed out, it may be misleading to directly interpret the data obtained from ion yield vs. fluence measurements.

Initial velocities of desorbed matrix and analyte ions have been investigated by measuring the flight-time differences between prompt and a 'two-stage' extraction with an initial field-free region (Beavis & Chait, 1991; Zhou et al., 1992). Results show a high initial velocity in the range of 700 m/s for analyte ions, irrespective of their mass, and hence an initial energy proportional to the ion mass, and a slightly higher velocity for matrix ions. To account for these high initial velocities, the phase transition of a matrix layer to a high-pressure fluid and its adiabatic expansion into the vacuum, forming a supersonic jet, has been proposed (Beavis & Chait, 1991). The strongly forwarded emission characteristics has been confirmed by measurement of the radial kinetic energy which is the range of 2.4 eV for insulin compared to 17 eV (Ens et al., 1991) of axial energy.

Despite this directional emission and high initial velocities, ions exhibit kinetic energy deficits, a typical value for positive molecule ion of insulin was determined to be 24 eV. The size of the deficit increases both with the intensity of the signal and the molecule ion mass; it is also larger for negative ions (Zhou et al., 1992). Two processes may be responsible for this feature of the desorbed ions. The first is an impediment of the ion acceleration by collisions in the expanding material plume above the surface, the second is a delayed ion formation by charge(proton)-transfer reactions taking place by collisions of neutrals and ions above the surface and thereby at lower electrical potentials. It is expected that both effects contribute; and it can be anticipated that further research into these processes will become highly relevant for an improvement of matrix-LDI and will have strong influence on optimized instrumental concepts.

The time scale of the desorption event is essentially confined to the laser pulse length of some ns. This can be deduced from the minimal peak width of the observable ion signals which was found to be in the range of 5 ns for peptides in a reflector instrument (Ingendoh et al., 1993). Prolonged ion emission which would not be compensated for in a reflector TOF instrument can thus be excluded.

The electron-microscopic inspection of the irradiated matrix/analyte preparations confirms that only a very shallow surface layer is ablated in matrix-LDI with UV-lasers (Strupat et al., 1991). Visible ablation and the formation of craters happens only at considerably higher irradiances, far above the useful irradiance range. On one hand, the observation of a minute sample ablation agrees well with the small penetration depth of the laser light, as estimated with the assumption of linear absorption processes. This also explains the very high number of LDI mass spectra obtainable from one sample spot. On the other hand, ablation does not proceed uniformly on a microscopic scale. Slight local roughening can be observed within the irradiated area, as well as small spherical structures which indicate melting of the sample; the latter accumulate at edges or cracks in the matrix-analyte crystals. These observations have been done with 2,5-dihydroxybenzoic acid which crystallizes into large structures. Whether these observations can be applied also to other matrices needs to be investigated.

The initial statement that MALDI produces exclusively intact quasimolecular ions has in the mean time been replaced by a more refined picture. Fragment ions have indeed been observed for peptides and proteins (Spengler et al., 1991; Hill et al.,1991). For proteins, they mainly arise from loss of small neutral molecules, such as ammonia, water and CO_2. A strong influence of the residual gas pressure indicates that bimolecular collision-induced fragmentation is a major source for these fragment ions. Furthermore, a smaller, matrix-dependent 'thermal load' resulting in metastable fragmentation is stemming from the desorption process (Spengler et al., 1992a). The strong effect of gas phase collisions indicates that also the 'matrix contribution' is due to collisional activation in the dense desorbing material plume and not to direct laser excitation. If time spreads due to postacceleration to the detector can be neglected, these fragmentations do not show up in a linear TOF instrument, and result in resolved peaks or tailing respectively in reflectron instruments. If confirmed by further investigations, these effects set clear boundary conditions for the ion source design. If controllable, the decay of ions may, on the other hand, be a further and highly-useful feature of MALDI, because it provides structural information, e.g. for peptide sequencing (Spengler et al., 1992b).

With regard to a more refined description of the LDI process, the energy deposited into the matrix is the first important factor. Because of the moderate irradiance values in the threshold regime, linear (classical) absorption processes seem to give a satisfying number for the energy absorbed per absorbing molecule; due to the usually short lifetime of the excited states both multiphoton absorption or bleaching should be negligible. The incident laser energy has to be corrected for reflection losses - which may be hard to do because of the microscopic structure of the sample. The same holds for the energy reemitted by fluorescense. Heat conduction into the surroundings has to be considered as a further loss mechanism. For typical irradiation conditions, i.e. penetration depth is much smaller than the focus diameter, the contribution of the essentially one-dimensional heat conduction can be estimated by the determination of the thermal diffusion depth, $dt_L = \sqrt{4kt_L}$ [k: thermal diffusivity, t_L: laser pulse time][1]. This value describes the thickness of the layer to which heat is transported within the laser pulse time. For typical UV-MALDI conditions this value is in the range of 100 nm, which is comparable to the laser penetration depth. On the other hand, experiments using shorter laser pulses showed that the pulse energy stays essentially constant - which indicates that energy loss due to heat conduction is not essential already at ns-pulses -, longer pulses where this condition is no longer valid have not been investigated yet. It is moreover important to keep in mind, that the intensity profile of the laser at the sample may be a further critical parameter. It is usually assumed to be gaussian, but irradiance or fluence values are calculated for a homogenous (=flat-top) profile.

Within the relatively long laser pulse time, energy deposited into electronic excitation of matrix molecules is expected to be thermalized leading to heating of the organic molecular lattice with a temperature distribution both laterally and in-depth. Two main questions arise:

1) Is a direct phase transition solid-gas taking place or is intermediate melting possible and essential for the process ?
2) Does the MALDI ablation process proceed uniformly, more comparable to an adiabatic expansion of a vaporized surface layer, or is the ablation confined to highly localized areas within the irradiated spot.

The latter is supported by the EM inspection, which shows changes within the irradiated areas on the μm- and sub-μm scale, such as individual minicraters and regions which appear to have melted into spherically shaped structures. An intermediate liquid phase - presumably at highly localized regions in the irradiated spot and preferentially formed at local protrusions and crystal imperfections and boundaries - would become unstable when heated up close to the critical temperature and undergo a phase explosion (Sunner et al., 1988). This may furthermore

---

[1] Note from your editor: This is inconvenient notation because t cannot be a length and a time at the same time. I suggest you replace dt_L by a length such as x_L. Note also that the differential is inappropriate.

give a new access to the explanation of the threshold behaviour. Intermediate formation of a liquid and the reduced heat conduction of a liquid would result in a steep rise of the deposited excitation energy and favor localized emission centers.

If the fundamental process is a fast laser heating of a defined volume, the next question would be: how can large fragile macromolecules survive? Is there a mechanism which would supply a lower excitation of analyte molecules compared to the absorbing matrix molecules and/or a source of cooling and confining the high temperature to a very short time period? The first case has been discussed proposing a bottleneck for the energy flux within the matrix/analyte system (Vertes et al., 1990). On the other hand, one has to consider that these large molecules have a huge amount of degrees of freedom and may be stable even if heated to relatively high temperatures at least for the time period to be detected in a time-of-flight instrument (McKeown & Johnston, 1991). Adiabatic expansion will result in a cooling of internal degrees of freedom, even though cooling is much more pronounced for the translational energy. The phase explosion as an instantaneous phase transition of a liquid volume is expected to result in the emission of a broad distribution from gas molecules to larger clusters. The shrinking of the clusters by evaporation of matrix molecules would provide a cooling of a 'hot' analyte molecule ion. However, some of these considerations may be futile and misleading. The main objection is that they are based on the strongly enhanced fragmentation observed for the ions with increasing irradiance and simply assume that the same holds for the neutrals. This can only be done if ions and neutrals are excited by the same source of energy, i.e. heating. As discussed above, there is, however, strong evidence that fragmentation is induced by collisions within the field-free drift region and reasonably also in the ion acceleration region. This is further substantiated by an observation done in a laser (neutral) desorption/postionization experiment; postionized intact molecules were still registered at irradiances up to a factor of 10 higher than those applicable for direct laser desorption of molecule ions (Spengler et al, 1988).

All the above-mentioned experimental results and their discussion show that the basic understanding of the desorption (ablation) event is still at a very early stage. Moreover, the above discussion focuses on one part of the desorption ionization process, i.e. the ablation. It is obvious that the ionization of the analyte molecules forms the second equally important step of the LDI process. For the ionization, however, a more elaborate model is available today which covers qualitatively most of the features of the observed ion spectra (Ehring et al., 1992). The starting point for this model has been the careful inspection of the UV-LDI mass spectra of numerous small organic compounds. An active role of the matrix ions is deduced from the fact that high-intensity analyte ions are observed, even though they are present only at a high molar dilution in the matrix-analyte mixture. Cationization, i.e. the adduct ion formation between alkali ions and neutral molecules, is only of minor importance for peptides and proteins. Desorption of preformed ions would result in a strong influence of the chemical properties of the peptides which is actually not observed. Formation of ion pairs by a disproportionation reaction is energetically unfavorable as can be deduced from simple thermodynamic considerations.

The basic idea of the ionization model is that ionization is initiated by photoionization of the matrix molecules, either by absorption of a second photon, by an excited-state molecule, or by reaction of two singly-excited molecules. Thus, a radical (positive) molecular ion as well as a solvated electron or a radical anion ,respectively, are formed initially. These reactions will occur at the early phase of the desorption ionization event, i.e. within the laser-pulse time and still in the solid or the high-density expanding material plume. The ionic species finally observed are products of (photo)chemical reactions between ions and neutrals and reflect the chemical reactivity of the radical ion precursors. Compounds which are able to form stable radical or protonated or deprotonated species should therefore have a low tendency to transfer their charge to analyte molecules. The ionizing reactivity of a matrix is expressed in the positive and negative ion mass spectra of the matrix compounds by the presence of both radical and even-electron species and further uncommon species such as high-abundance $[M + 2H]^+$ - or $[M - H]^+$-ions, and indeed all matrix compounds found usable so far show this behaviour. These reactions may furthermore become highly probable if they happen within desorbed clusters of matrix containing one analyte molecule.

6 Conclusion

MALDI is a relatively young desorption ionization technique which has considerably extended the useful mass range for mass spectrometry. It has already found widespread analytical use. This is also expressed by the fact that several commercial instruments have become available in a short time after the introduction of the technique. It is noteworthy that with the introduction of the technique new fundamental problems and questions arise; the most important are the phenomena of large-ion impact on surfaces which are highly relevant for the detection of high-mass ions by conventional ion detectors. It is typical that progress has so far been mainly obtained empirically. Improved basic understanding of the LDI process will not only improve practical aspects such as the choice of the new matrices, but is expected to have direct impact on the instrumental design and its optimization. IR-MALDI whose feasibility has been shown in the author s lab both for Er-YAG (2.94 μm) (Overberg et al., 1990) and for CO_2-lasers (10.6 μm) (Overberg et al., 1991) and which yields mass spectra of comparable characteristics will open a new field with regard to the elucidation of the underlying fundamental processes. Preliminary results indicate that the energy deposited by vibrational excitation is below that required for vaporization or even melting. It therefore appears that new concepts both for the ablation process and for the ionization have to be developed.

References

Beavis RC, 1992: Org. Mass Spectrom. **27**, 864
Beavis R and Bridson JN, 1992: J. Phys. D, submitted
Beavis RC and Chait BT, 1989a: Rapid Commun. Mass Spectrom. **3**, 233
Beavis RC and Chait BT, 1989b: Rapid Commun. Mass Spectrom. **3**, 432
Beavis RC and Chait BT, 1990a: Proc. Nat. Acad. Sc. **87**, 6873
Beavis RC and Chait BT, 1990b: Anal. Chem. **62**, 1836
Beavis RC and Chait BT, 1991: Chem. Phys. Lett. **181**, 479
Beavis BC, Chaudhary T and Chait B T, 1992: Org. Mass Spectrom. **27**, 156
Chait BT and Kent SBH, 1992: Science **257**, 1885
Demirev P, Westman A, Reimann CT, Håkannson P, Barofsky D, Sundqvist BUR, Cheng YD, Seibt W and Siegbahn K, 1992: Rapid Commun. Mass Spectrom. **6**, 187
Dreisewerd K, Bahr U and Hillenkamp F, 1990: Inst. Phys. Conf. Ser. No 114: Section II, 447
Ehring H, Karas M and Hillenkamp F, 1992: Org. Mass Spectrom. **27**, 472
Ens W, Mao Y, Mayer F and Standing KG, 1991: Rapid Commun. Mass Spectrom. **5**, 117
Hill JA, Annan RS and Biemann K, 1991: Rapid Commun. Mass Spectrom. **5**, 395
Hillenkamp F, Karas M, Beavis RC and Chait BT, 1991: Anal. Chem. **63**, 1196A
Hillenkamp F and Ehring H, 1992: *Mass Spectrometry in the Biological Sciences*, M Gross (ed.), Kluwer Acad. Publ., 165
Ingendoh A, Karas M and Hillenkamp F, to be published
Johnson RE and Sundqvist BUR, 1991: Rapid Commun. Mass Spectrom. **5**, 574
Karas M, Bachmann D and Hillenkamp F, 1985: Anal. Chem. **57**, 2935
Karas M, Bachmann D and Hillenkamp F, 1986: *Advances in Mass Spectrom.* **10B**, JFJ Todd (Ed.), J. Wiley & Sons, Chichester, 969
Karas M, Bachmann D, Bahr U and Hillenkamp F, 1987: Int. J. Mass Spectrom. Ion Proc. **78**, 53
Karas M and Hillenkamp F, 1988a: Advances in Mass Spectrom. **11A**, 354
Karas M and Hillenkamp F, 1988b: Anal. Chem. **60**, 2299
Karas M, Bahr U and Hillenkamp F, 1989a: Int.J. Mass Spectrom. Ion Proc. **92**, 231
Karas M, Ingendoh A, Bahr U and Hillenkamp F, 1989b: Biomed. Environm. Mass Spectrom. **18**, 841
Kaufmann R, Kirsch D, Rood H-A and Spengler B, 1992: Rapid Commun. Mass Spectrom. **6**, 98
McKeown PJ and Johnston MV, 1991: J. Am. Soc. Mass Spectrom. **2**, 103
Nordhoff E, Ingendoh A, Cramer R, Overberg A, Stahl B, Karas M, Hillenkamp F and Crain P.F., 1992: Rapid Commun. Mass Spectrom. **6**, 771
Overberg A, Karas M, Bahr U, Kaufmann R and Hillenkamp F, 1990: Rapid Commun. Mass Spectrom. **4**, 293
Overberg A, Karas M and Hillenkamp F, 1991: Rapid Commun. Mass Spectrom. **5**, 128
Parr GR, Fitzgerald MC and Smith LM, 1992: Rapid Commun. Mass Spectrom. **6**, 369
Siegel MM, Hollander IJ, Hamann PR, James JP, Hinman L, Farnsworth APH, Phipps A, King DJ, Karas M, Ingendoh A and Hillenkamp F, 1991: Anal. Chem. **63**, 2470

Spengler B, Bahr U, Karas M and Hillenkamp F, 1988: Anal. Instrum. **17**, 173

Spengler B, Kirsch D, Kaufmann R, Karas M, Hillenkamp F and Giessmann U, 1990: Rapid Commun. Mass Spectrom. **4**, 301

Spengler B, Kirsch D and Kaufmann R, 1991: Rapid Commun. Mass Spectrom. **5**, 198

Spengler B, Kirsch D and Kaufmann R, 1992a: J. Phys. Chem., submitted

Spengler B, Kirsch D, Kaufmann R and Jaeger E, 1992b: Rapid Commun. Mass Spectrom. **6**, 105

Stahl B, Steup M, Karas M and Hillenkamp F, 1991: Anal. Chem. **63**, 1463

Strupat K, Karas M and Hillenkamp F, 1991: Int. J. Mass Spectrom. Ion Proc. **111**, 89

Sunner J, Ikonomou MG and Kebarle P; 1988: Int. J. Mass Spectrom. Ion Proc. **82**, 221

Tanaka K, Waki H, Ido Y, Akita S, Yoshida Y and Yoshida T., 1988: Rapid Commun. Mass Spectrom. **2**, 151

Vertes A, Gijbels R and Levine RD, 1990: Rapid Commun. Mass Spectrom. **4**, 228

Zhou J, Ens W, Standing KG and Verentchikov A, 1992: Rapid Commun. Mass Spectrom. **6**, 671

Sputtering and Surface Science

By E. Taglauer
Max-Planck-Institut für Plasmaphysik, EURATOM Association,
Boltzmannstr. 2, D-85748 Garching bei München, Germany

Synopsis

Sputtering and surface science are intimately related, both historically and scientifically. While the knowledge and techniques which have been acquired in the discipline of surface science have been helpful and indispensable in understanding fundamental processes in the sputtering of elemental and multicomponent material, sputtering phenomena themselves have had a decisive share in the dramatic boom in surface science in the last decades. Sputtering has become an ubiquitous tool in experimental surface science work for cleaning, microsectioning, depth profiling etc. Powerful methods for the analysis of surface composition and crystalline surface structures are based on sputtering processes. Moreover, the sputtering of solids and the concurring surface phenomena have become an active field of research in their own right. Via sputtering new routes can be followed in fundamental surface research, e.g. by using atomic resolution microscopy techniques to study the kinetics and processes by which a (sputtered) surface relaxes to its thermodynamic equilibrium. Several aspects demonstrating the importance of sputtering for surface science are discussed.

1 Introduction

Sputtering and surface science are intimately related to each other in the sense that sputtering is both goal and vehicle in surface research. Sputtering, i.e. the release of atoms from a surface due to ion bombardment, is important in a vast field of applications as well as for basic understanding of dynamical processes on solid surfaces (Behrisch, 1981). Some of these aspects are discussed in the following.

In a typical situation in this context a surface is bombarded by Ar^+ ions with a kinetic energy of about one keV whereby atoms are set in motion in a near-surface region through a collision cascade.

Such an ion has a projected range in the solid of the order of 10 nm and the resulting collision cascade typically extends to dimensions of about 20 nm (Winterbon et al., 1970; Eckstein, 1991). The lifetime of the cascade is of the order

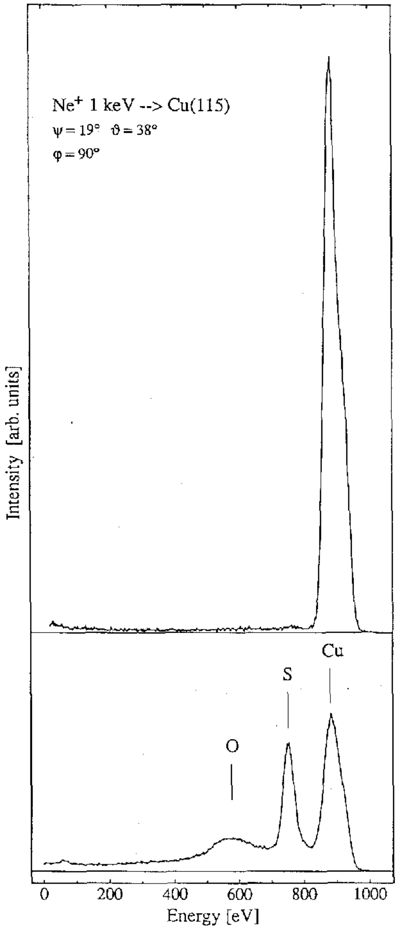

Figure 1. Ne$^+$ ion scattering signal before (bottom) and after (top) sputter-cleaning of a Cu(115) surface (Liegl, 1992).

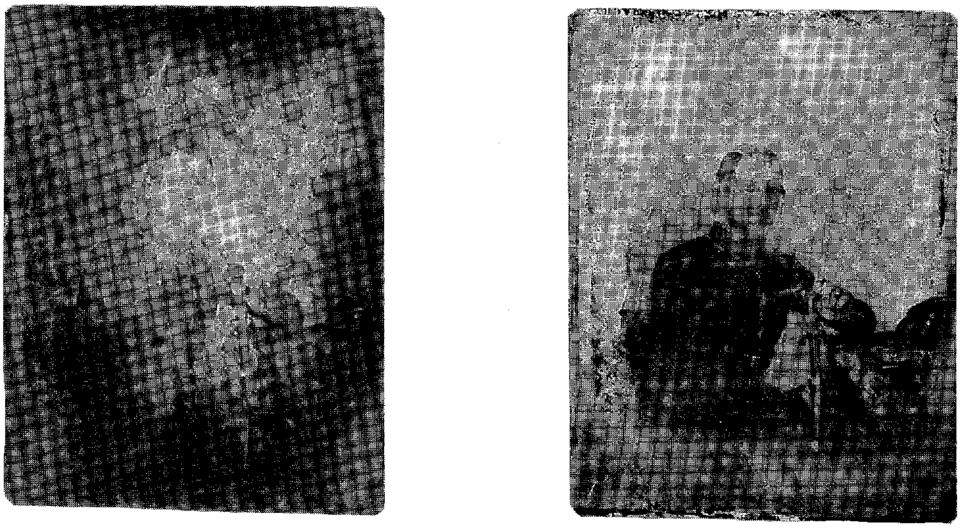

Figure 2. Daguerrotype photograph before (a) and after (b) cleaning in a glow discharge by 'physical' and 'chemical' sputtering (courtesy of W. Poschenrieder).

of 1 ps and only a small fraction of the atoms within a cascade are in motion at any time, i.e. in the situations considered here we are in the linear cascade regime (Sigmund, 1981). Those atoms which are eventually ejected from the surface as a result of the collision process originate predominantly from the first and second atomic layer (Sigmund et al., 1989; Harrison, 1983). This whole scenario demonstrates the surface sensitivity of the sputtering process. Consequently, sputtering is important in various surface related aspects, such as

- surface preparation which includes surface cleaning and preparation of non-equilibrium surfaces,
- surface etching, i.e. the generation of sputter-depth profiles and the sputtering of adlayers,
- surface analysis by detecting sputtered particles, either ions or neutrals including directly recoiling particles, and
- the investigation of surface interactions such as preferential sputtering of compound material, radiation enhanced diffusion and segregation, and annealing kinetics of bombarded surfaces.

2 Surface Preparation

The surface cleaning effect of the sputtering process has first been observed by Wehner (1957) in a glow discharge and has been introduced specifically to studying well defined surfaces by Farnsworth et al. (1958). Since then, sputter-cleaning of surfaces has become a standard procedure in any kind of surface investigation (Taglauer, 1990). Quite frequently, 1-3 keV Ar^+ ion beams with current densities of microamps/cm^2 are used and allow the removal of many surface contaminants within a reasonable time, i.e. in the order of some 10^3 seconds.

A typical situation is shown in fig. 1, in which a surface contamination of about half a monolayer of O and S on Cu(115) is reduced to less than a hundredth of a monolayer after 20 min Ne^+ bombardment (Liegl, 1992). Situations as shown in fig. 1 are familiar to every experimentor in this field. It has to be mentioned that the radiation damage on the surface caused by sputtering generally has to be removed by annealing, a procedure which can again lead to surface contamination due to segregation. As a result, repetitive cycles of sputtering and annealing have been adopted in most cases in order to prepare clean surfaces. Recoil implantation is another process which can considerably reduce the cleaning effect of sputtering, particularly for heavier overlayers on light substrates (Tarng and Wehner, 1972).

An enhanced cleaning effect can occur when in addition to the physical sputtering processes chemical reactions can take place. This occurs in glow discharge sputtering if reactive species such as hydrogen ions are involved. Such a combination is used in conditioning the inner walls of large fusion devices (Dylla, 1980) or also in semiconductor fabrication (Winters and Coburn, 1992). There is also an interesting application for cleaning precious silver objects, such as ancient altar figurines or Daguerrotype photographs (Roidl et al., 1987). Figure 2 shows the cleaning effect of a hydrogen glow discharge on such an early photograph. On these very thin and sensitive silver layers only little physical sputtering can be tolerated and this is controlled by operating close to the sputtering threshold (which is about 100 eV for H on Ag). In addition, chemical reactions like

$$\begin{aligned} \mathrm{Ag_2S + 2H \rightarrow 2Ag + H_2S} \\ \mathrm{MeO + 2H \rightarrow Me + H_2O} \end{aligned}$$

take place (here MeO stands for any metal oxide). With the same procedure also 17th century angel figurines of the altar in Tschenstochau (Poland) were restored.

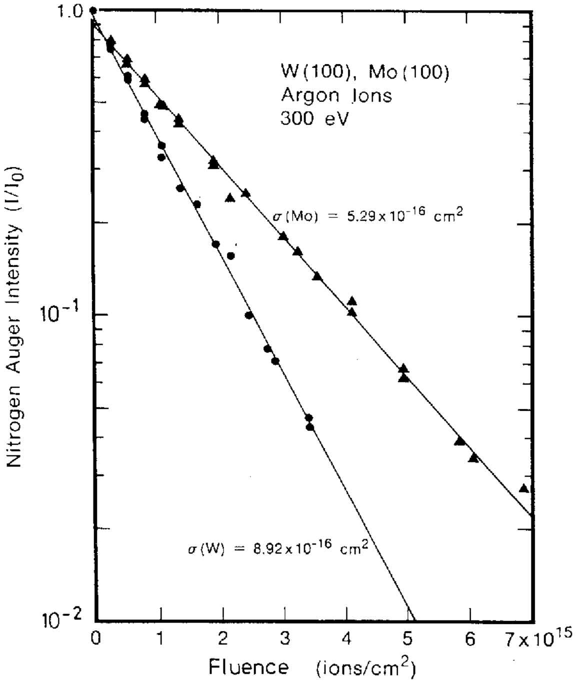

Figure 3. Sputter removal of nitrogen from W and Mo single crystal surfaces. Initial coverage about half a monolayer (Winters & Taglauer, 1987).

3 Sputtering of Adsorption Layers

For well defined adsorption layers (in contrast to the uncontrolled contamination layers considered in the previous section) the relevant physical sputtering processes have been studied in detail and experimental results can be well reproduced by theoretical estimates. Under the influence of an ion flux F the surface density of an adsorption layer, N_A, decreases according to the relation

$$\frac{dN_\mathrm{A}}{dt} = -\sigma \cdot F \cdot N_\mathrm{A} \tag{1}$$

in which σ is the sputtering cross section. For the purpose of comparison σ can be related to a sputtering yield Y through the monolayer density N_ML, $\sigma = Y/N_\mathrm{ML}$. The exponential decrease following from eq. (1) has been observed for some adsorption systems, an example is given in fig. 3 (Winters and Taglauer, 1987). Here, the sputtering of N from single crystalline Mo and W surfaces is well represented by an exponential decay. Frequently, a deviation from the initial slope is observed

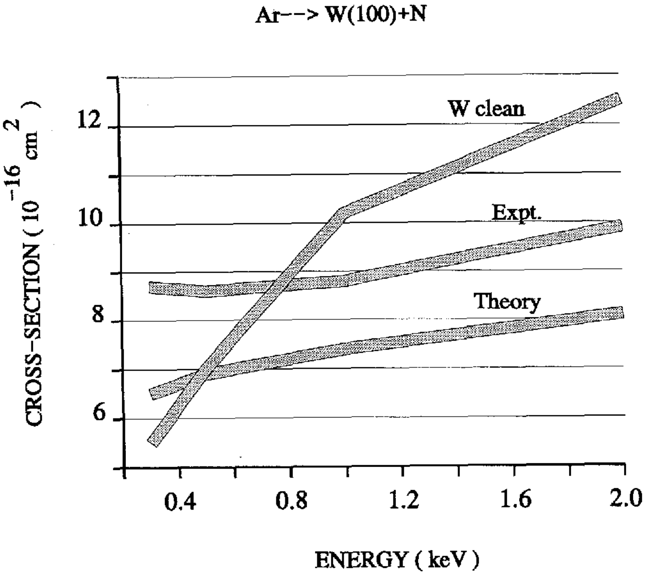

Figure 4. N-Sputter cross sections for Ar^+ in bombardment of W(100) + N and W-sputter cross section for clean W (data from Winters & Taglauer, 1987).

after sputtering of about 90% of the adsorption layer, this deviation is attributed to recoil implantation. Obviously this is not the case for the system shown in fig. 3. Probably recoil implanted N segregates back to the surface. The slope of the straight lines in the figure yields the sputtering cross section. Such cross sections were calculated by Winters and Sigmund (1974) and in more detail by Yamamura and Kimura (1987). Important parameters in these calculations are the surface binding energy of the adsorbate, the reflection coefficient for the primary projectiles and the total energy transfer to the substrate lattice which determines the substrate sputtering yield. Figure 4 shows the comparison of these calculations with experiments for N on W(100) and also the sputtering yield for Ar on clean W. Without a fitting parameter the theory reproduces the experimental data quite well, particularly also the fairly flat energy dependence which deviates from the much steeper metal sputtering yield. It also shows that for low energies the adlayer sputtering yield can significantly surpass the substrate sputtering.

The removal of the surface adlayers by sputtering brings the second (and following) atomic layers to the surface and thus quite naturally allows the analysis of the layering of the various constituents of a multicomponent structure by using appropriate surface analytical techniques. Therefore sputter-etching of surfaces has

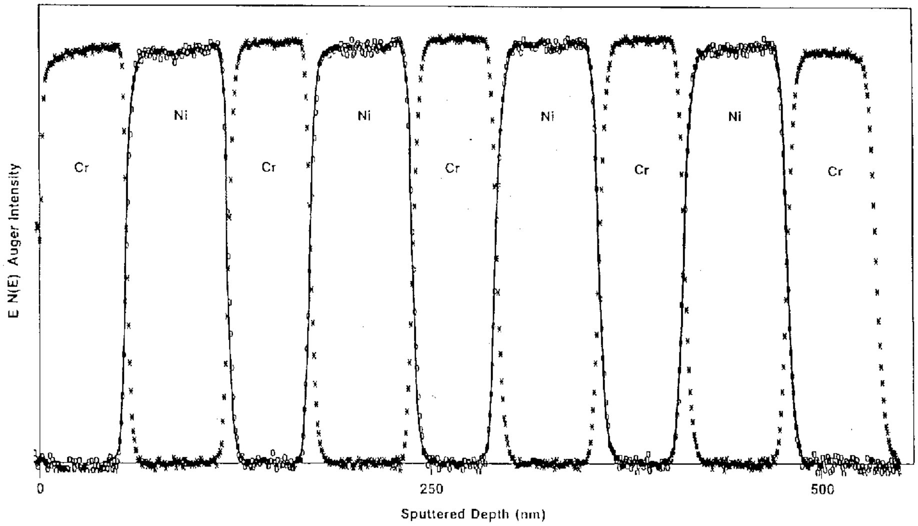

Figure 5. Sputter depth profile of a Ni-Cr multilayer structure using a 1 keV rastered argon ion beam. The average film thickness is 50nm for Cr and 63nm for Ni (Fine & Navinsek, 1985).

become a very common method for determining concentration depth profiles. For coverages of the order of a monolayer, i.e. the situation described above, this application is e.g. important for the analysis of supported catalyst systems (Brongersma & van Leerdam, 1991; Taglauer, 1991). These catalysts consist of high surface area supports (e.g. transition metal oxides) that carry the active components. For the performance of the catalyst (activity, selectivity etc.) the geometric position of the outermost atomic layers is decisive and 'monolayer depth profiles' are therefore very helpful in studying catalysts.

In many cases the depth distribution of the constituing elements is of interest to much larger depths, say several hundred nanometers. This is a range which is not usually comprised in the field of surface science, but the analytical techniques, i.e. ion or electron spectroscopies are quite often taken from the surface science arsenal. A nice example is given in fig. 5 which shows the result of a Ni-Cr multilayer structure, sputtered with 1 keV Ar^+ ions and analysed by Auger electron spectroscopy (AES) (Fine & Navinsek, 1985). Up to the ninth layer a sharp interface was obtained here. This raises the question of the limitations of sputter depth profiling, i.e. to which extent does the experimental result really represent the initial concentration profile? This question has been investigated by many researchers and can only be marginally touched here. The examined sample

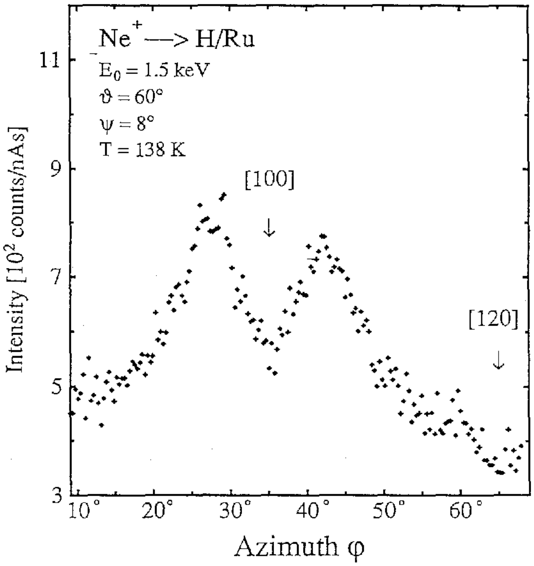

Figure 6a. Azimuthal distribution of H^+ recoils from Ru(001) under Ne^+ bombardment: Experiment (Schulz et al., 1992).

is changed by the impinging ion flux mainly due to atomic mixing (i.e. relocation of sample atoms due to collision processes), there is no 'layer-by-layer' removal of atoms and therefore a broadening of the depth distributions must be expected. Furthermore, different atomic species have different sputtering yields and therefore the flux of sputtered particles leaving the surface has an elemental composition that differs from that of the surface. This preferential sputtering effect (Betz & Wehner, 1983) has important consequences on depth profiling. The analysis of the sputtered particle flux or the surface composition can lead to quite different results (Coburn, 1976). The relevance of the various effects of course depends on the experimental parameters, i.e. mass, energy and angle of incidence of the probing particles and also the target properties such as chemistry, temperature, roughness, etc. (Wittmaack, 1968). Figure 5 nevertheless demonstrates that very satisfactory results can be obtained by sputter etching.

4 Surface Analysis

One of the major connections of sputtering to surface science is that it offers the possibility of determining the chemical composition and the structure of surfaces

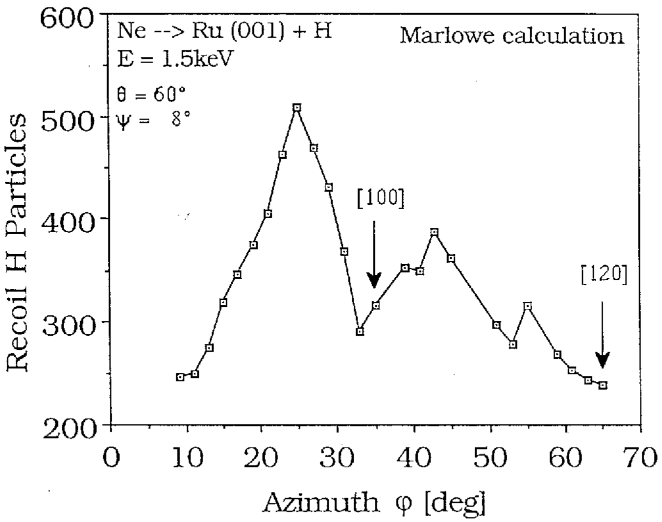

Figure 6b. Same as figure 6a: MARLOWE calculation

by analyzing sputtered particles. For instance, understanding of adsorbates can be gained if directly recoiling species are detected from the bombarded surface (Rabalais, 1991; Niehus et al., 1993). These recoils can be identified by their kinetic energy and thus by variation of bombardment and detection geometry a mass specific, structure dependent signal is obtained.

Figure 6 shows as an example the azimuthal distribution of H^+ recoils from a H/Ru(001) surface sputtered with 1.5 keV Ne^+ ions (Schulz et al., 1992). From the azimuthal distribution it can be deduced that hydrogen adsorbs in a threefold coordinated position on this surface, about 1 Å above the top Ru layer. These findings are corroborated by numerical simulations using the binary collision code MARLOWE (Robinson & Torrens, 1974). In this program only collisional but no charge exchange processes are taken into account. The similarity between experiment and calculation proves that H^+ species are representative for all recoils under these conditions. In the calculation the adsorbed H was only placed in fcc lattice sites, and the resulting asymmetry on both sides of the [100] direction is more pronounced than in the experiment. This is probably due to domain formation.

A related technique is the angle resolved secondary ion mass spectrometry (Winograd & Garrison, 1991) in which the structural information again arises from the detection geometry but the sputtered species are identified with a mass spectrometer. With such measurements e.g. detailed analyses of Cl on Ag (100) were

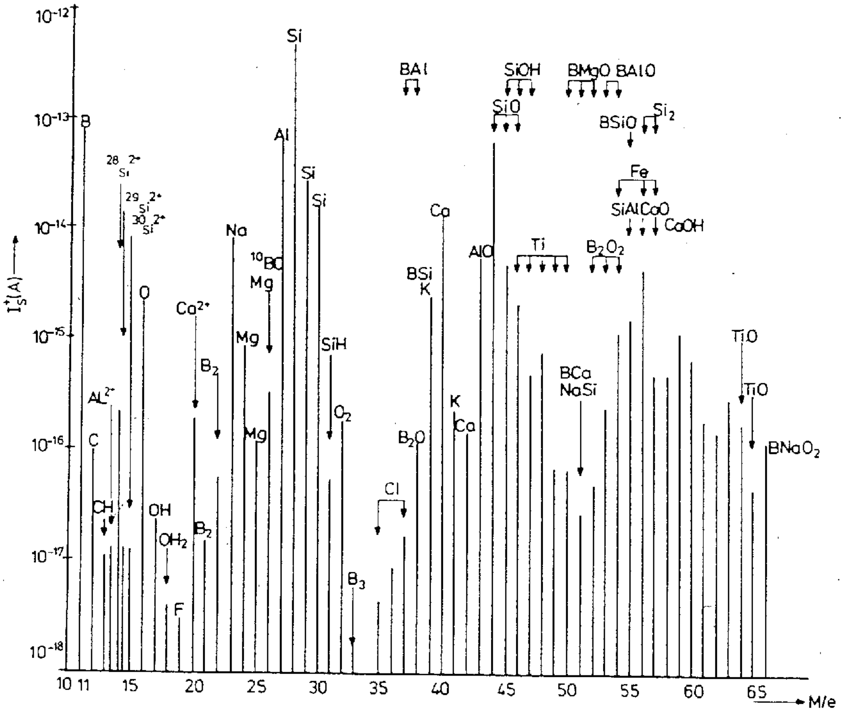

Figure 7. Positive SIMS spectrum from a glass standard (NBS 93) using 14.5 keV O^- ions, 0.2 μA (Morgan & Werner, 1987).

obtained.

Secondary ion mass spectrometry (SIMS) is certainly the most widespread surface analysis technique related to sputtering (for a comprehensive reference see e.g. Benninghoven et al. (1987)). In this technique secondary ions (positive or negative) emerging from a bombarded surface are analyzed using a mass spectrometer. It is thus possible to analyze elemental and molecular species, their depth distribution (by sputter etching) and their lateral distribution (on a micrometer scale) using scanning or imaging techniques. The main advantages of the technique are the excellent mass resolution, the possibility to detect molecular species (from hydrogen to large organic molecules) and the high sensitivity which also results in an extraordinary dynamical range of the detection signal. Some of these features can be observed in fig. 7 which shows a positive-ion mass spectrum from a glass bombarded with 14.5 keV O^- ions (Morgan & Werner, 1987). The spectrum exhibits a large variety of ionic species which can be exploited for information about the surface chemistry, but they also make quantitative analysis difficult. The spectrum also indicates the high sensitivity for trace analysis, which is in the ppm range for SIMS, and a dynamical range of about six orders of magnitude. As already mentioned, the main limitation of SIMS lies in the quantification problem. This is not only due to the multielemental molecular species but even more so due to the large variations in ion yields, which sensitively depend on the chemical composition of the surface (matrix effect). The secondary ion yield Y^+ (secondary ion/primary ion) can vary by orders of magnitude if the surface composition changes, experimental values for 3 keV Ar^+ bombardment are e.g. 0.02 for clean Al and 2.0 for oxidized Al; 3×10^{-4} for clean Si and 10^{-2} for oxygen covered Si. These problems can partly be compensated by using electronegative species (oxygen ions or gas stream) for positive SIMS and electropositive ions (Cs^+) for negative SIMS, but this is not always compatible with the analytic situation. Another approach consists in post-ionization of sputtered neutrals (consequently abbreviated by SNMS) either by an electron beam, a plasma discharge or laser radiation (see e.g. Benninghoven et al., 1987). These methods require a large technical effort and are not yet as widespread as SIMS, but they are under rapid development and offer substantial new analytical possibilities.

5 Surface Interactions

The effects of ion bombardment on near-surface compositional changes are of fundamental interest and also important for many applications such as depth profiling, ion implantation and material modification. Particulary preferential sputtering effects on metallic alloys have obtained considerable attention, also in view of the

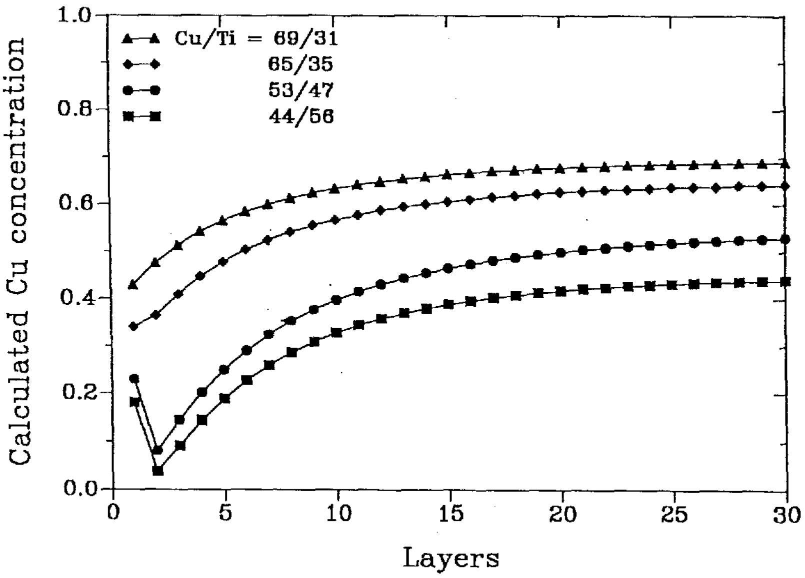

Figure 8. Calculated steady state Cu concentration profiles (using ISS and AES data) for bombardment of various CuTi alloys with 2 keV Ar^+ ions (van Wyk et al., 1991).

concurring effects of surface segregation and radiation-enhanced diffusion (Betz & Wehner, 1983; Lam & Wiedersich, 1987). Preferential sputtering results in an altered layer below the surface, whose composition is different from the bulk due to the difference in sputtering yields of the components. The depth of this altered layer corresponds to the range in which the kinetic energy of the primary ions is deposited (Baretzky et al., 1992). The depletion of one constituent can be counteracted by surface segregation if this minimizes the surface free energy (Kelly, 1985). Segregation is a true surface phenomenon, leading to a concentration jump between the top and the second atomic layer. Analyis of these effects therefore requires methods with appropriate information depths, as e.g. given by ion scattering spectroscopy (ISS) with an exclusive first-layer sensitivity (Niehus et al., 1993) and AES with an information depth of about 5 atomic layers. From the combination of both methods the near-surface concentration profile can be deduced. In steady state the sputtered flux is balanced by the diffusion flux and thus the segregation energy and the radiation-enhanced diffusion coefficient can be obtained from such measurements. Figure 8 shows as an example steady-state concentration profiles calculated with ISS and AES data for various amorphous CuTi alloys bombarded with 2 keV Ar^+ ions (van Wyk et al., 1991). The depth of the altered layer corre-

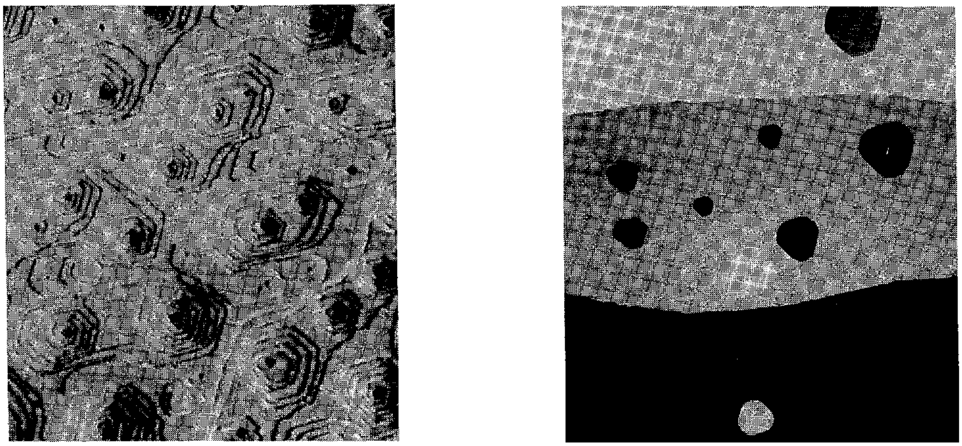

Figure 9. STM micrograph (825 Å × 825 Å) of a Pt(111) surface sputtered at 625 K (a) and at 910 K (b) (3300 Å× 3300 Å) with 600 eV Ar^+ ions (courtesy of Michely & Comsa).

sponds to the range of the defect distribution caused by the argon ions.

Sputtering of surfaces is generally associated with the development of a variety of surface structures (Carter et al., 1983). From the basic physics point of view, structural studies with high lateral resolution are of particular interest. Early investigations with atomic resolution were performed with field ion microscopy (e.g. Vernickel, 1966). The recent development of the scanning tunneling microscope (STM) opened new possibilities for obtaining real-space information about sputtered surfaces and their annealing behavior. This is of basic interest concerning the equilibrium morphology of surfaces. A beautiful example in this context is a study of the sputtering of a Pt(111) surface with 600 eV Ar^+ ions at various temperatures (Michely & Comsa, 1991). Figure 9a shows an STM micrograph for sputtering at 625 K. Ordered pit formation on the surface can clearly be seen, up to ten terraces or more can be distinguished. This result indicates that under these conditions intralayer diffusion obviously takes place (hexagonal pits) but interlayer diffusion is prohibited. This occurs at higher temperatures and results in a quasi layer-by-layer removal of surface atoms as shown in fig. 9b. On one terrace only vacancy clusters (dark hexagonal structures) with monoatomic depth or equivalent adlayer islands (bright structures) are found. The apparent rotation of these two structures can be understood from the crystallographic orientation of <110>/{111} steps and <110>/{100} steps. Application of the Wulff construction to this equilibrium form allows the determination of the ratio of the free energies of these steps. It could also

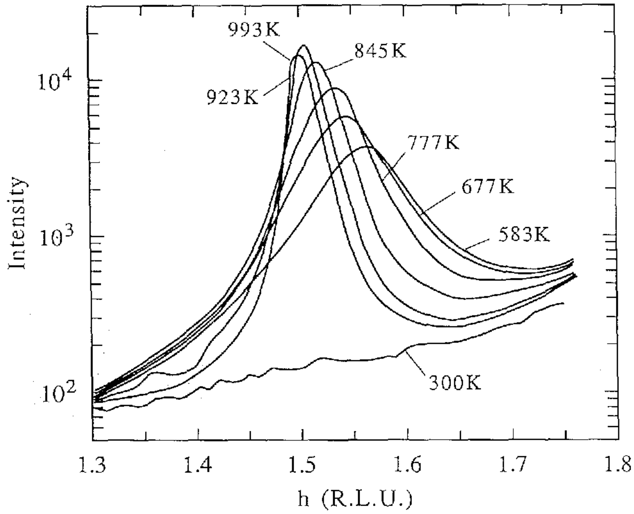

Figure 10. Half-order diffraction peaks of a sputter-roughened Pt(110) surface after annealing at various temperatures. The direction of *h* (in reciprocal lattice units) is along the [001] surface direction (Kern et al., 1992).

be shown that temperature-dependent equilibrium morphology of sputtered metal surfaces (pit formation, layer-by-layer removal; vacancy islands) is analoguous to crystal layer growth (3D island growth; layer-by-layer growth; adatom islands). A further example along these lines is the investigation of the 'smoothening' kinetics of a sputter-roughened surface by time-resolved X ray diffraction (Kern et al., 1992). The interest is the expectation that the kinetic behavior of various systems can be classified by universality classes analoguous to equilibrium phase transitions. In a study of a sputter-roughened Pt(110) surface the roughness was characterized by the step density measured by the shift (and broadening) of a half order diffraction peak, see fig. 10. Flattening of this surface proceeds with a power law dependence on time, the exponent depending on the temperature. A detailed theoretical understanding of this behavior is presently not yet available.

The purpose of showing these examples is that sputtering, apart from its very important and widely used application as an indispensable means of surface analysis and etching, also has a decisive role in research activities concerning the fundamental behavior of solid surfaces. Thus, particularly at the advent of new techniques and applications sputtering will certainly continue to be an important aspect of surface investigations.

References

Baretzky B, Möller W and Taglauer E, 1992: Vacuum **43**, 1216

Behrisch R (Editor) 1983: *Sputtering by Particle Bombardment*, Springer Verlag, Berlin

Benninghoven A, Rüdenauer FG and Werner HW, 1987: *Secondary Ion Mass Spectronomy*, John Wiley & Sons, New York

Betz G and Wehner GK, 1983: in Behrisch (1983), Vol.II, p. 11

Brongersma HH and van Leerdam GC, 1991: in *Fundamental Aspects of Heterogeneous Catalysis Studied by Particle Beams*, Brongersma HH and van Santen RA, editors, Plenum Press, New York, p. 283

Carter G, Navinsek B and Whitton JL, 1983: in Behrisch (1983), Vol.II, p. 231

Coburn JW, 1976: J. Vac. Sci. Technol. **13**, 1037

Dylla HF, 1980: J. Nucl. Mater. **93, 94**, 61

Eckstein W, 1991: *Computer Simulation of Ion-Solid Interactions*, Springer, Berlin

Farnsworth HE, Schlier RE, George TH and Burger RM, 1958: J. Appl. Phys **29**, 1150

Fine J and Navinsek B, 1985: J. Vac. Sci. Technol. **A3**, 1408

Harrison DE Jr, 1983: Radiat. Eff. **70**, 1

Kelly R, 1985: Surf. Interf. Anal. **7**, 1

Kern K, Robinson IK and Vlieg E, 1992: Surf. Sci. **261**, 118

Lam NQ and Wiedersich H, 1987: Nucl. Instrum. Methods B **18**, 471

Liegl A, 1992: Doctoral Thesis, Technical University Vienna

Michely T and Comsa G, 1991: Surf. Sci **256**, 217

Morgan AE and Werner HW, 1987: in Benninghoven et al. (1987), p. 985

Niehus H, Heiland W and Taglauer E, 1993: Surf. Sci. Rep. **17**, 213

Rabalais JW, 1991: J. Vac. Sci. Technol. **A9**, 1293

Robinson MT and Torrens IM, 1974: Phys. Rev. **B9**, 5008

Roidl E, Brunnert S and Poschenrieder W, 1987: Labor 2000, 128

Schulz J, Taglauer E, Feulner P and Menzel D, 1992: Nucl. Instrum. Methods B **64**, 558

Sigmund P, 1981: in Behrisch, Vol. I, p. 9

Sigmund P, Robinson MT, Baskes MI, Hautala M, Cui FZ, Eckstein W, Yamamura Y, Hosaka S, Ishitani T, Shulga VI, Harrison DE, Jr, Chakarov IR, Karpuzov DS, Kawatoh E, Shimizu R, Valkealahti S, Nieminen RM, Betz G, Husinsky W, Shapiro MH, Vicanek M and Urbassek HM, 1989: Nucl. Instrum. Methods B **36**, 110

Taglauer E, 1990: Appl. Phys. **A51**, 238

Taglauer E, 1991: in *Fundamental Aspects of Heterogeneous Catalysis Studied by Particle Beams*, Brongersma HH, and von Santen RA, editors, Plenum Press, New York, p. 301

Tarng M and Wehner GK, 1972: J. Appl. Phys. **43**, 2268

Vernickel H, 1966: Z. Naturf. **21**, 1308

Wehner GK, 1957: Phys. Rev. **108**, 35

Winograd N and Garrison BJ, 1991: in *Ion Spectroscopies for Surface Analysis*, Czanderna AW and Hercules DM, editors, Plenum Press, New York, p. 45

Winterbon KB, Sigmund P and Sanders JB, 1970: K. Danske Vid. Selsk. Mat. Fys. Medd. **37**, 14

Winters HF and Coburn JW, 1992: Surf. Sci. Rep. **14**, 161

Winters HF and Sigmund P, 1974: J. Appl. Phys. **45**, 4760

Winters HF and Taglauer E, 1987: Phys. Rev. **B35**, 2174

Wittmaack K, 1986: J. Vac. Sci. Technol. **A4**, 1662

van Wyk GN, du Plessis J and Taglauer E, 1991: Surf. Sci. **254**, 73

Yamamura Y and Kimura H, 1987: Surf. Sci. **185**, L475

Sputtering in Planetary Science

By T. A. Tombrello
California Institute of Technology
Pasadena, California 91125, USA

Synopsis

The interaction of energetic atoms and molecules with solid materials occurs in a variety of astrophysical environments: molecular clouds; stellar atmospheres; forming planetary systems; and satellite surfaces and atmospheres. It should, therefore, be no surprise that sputtering phenomena take place and often play important roles in the evolution of the materials involved. In this review I shall endeavor not only to show the ubiquity of sputtering in such situations but also to indicate how laboratory experiments, molecular dynamics simulation, and theory can be used together to understand better the astrophysical and planetary processes themselves. It is also important to consider that it now may be possible that the atoms/ions sputtered from planetary surfaces by the solar wind may allow remote mapping measurements of planetary surface compositions.

1 Introduction

The existence of stellar winds, magnetospheric trapping, and energetic shock fronts provides many environments in the universe where energetic ions, atoms, and molecules can be accelerated sufficiently to cause sputtering. A decade ago I was asked to review how sputtering was involved in solar system processes (Tombrello, 1982); this paper is intended to update and extend that report. In several ways, however, this paper will have a somewhat different emphasis. Generally, I shall concentrate on collisional sputtering; there has been a recent review of electronic excitation induced desorption/sputtering that should give the reader adequate references to the role played by such processes for the Jovian and Saturnian satellites (Johnson & Sundqvist, 1992).

A large part of my previous review was devoted to the description of how solar wind erosion of a planetary atmosphere unshielded by a magnetic field or ionosphere could gradually change the atmospheric composition (Haff et al., 1978). Examples were given for the ^{4}He budget of Venus (Watson et al., 1980) and the erosion and

Table I. Sputtering in shock fronts. A shock velocity of 100 km/sec implies a proton energy of 50 eV and an alpha particle energy of 200 eV; at 200 km/sec these energies quadruple, i.e., 200 and 800 eV, respectively. The sputtering yield data were taken from Roth et al., (1979).

Substance	$S_p(50\text{ eV})$	$S_p(200\text{ eV})$	$S_\alpha(200\text{ eV})$	$S_\alpha(800\text{ eV})$
C	$4\cdot10^{-3}$	$9\cdot10^{-3}$	0.07	0.09
Fe	-	$3\cdot10^{-3}$	0.05	0.15
Al_2O_3	-	$4\cdot10^{-3}$	0.01	0.17
SiC	$4\cdot10^{-4}$	$6\cdot10^{-3}$	0.08	0.13
SiO_2	10^{-3}	$1\cdot10^{-2}$	0.03	0.13
ZrC	-	$3\cdot10^{-5}$	0.01	0.05
Mo	-	10^{-5}	0.02	0.05

differentiation of the Martian atmosphere (Haff et al., 1978; Watson et al., 1980; Haff & Watson, 1980). Although this phenomenon seems to be very far afield from our usual picture of sputtering, it represents a straightforward application of the original ideas of Thompson (1968) and Sigmund (1969), in which the surface binding energy is replaced by the gravitational potential energy (Haff et al., 1978). Since there have been few significant advances in this area, this topic will not be discussed in greater detail herein.

The moon's surface is virtually unshielded from solar wind bombardment; thus, solar wind implantation and sputtering is a significant factor in lunar surface modification (Wehner et al., 1963). One should, however, note that here (as well as on all planetary satellites) the effect of micrometerites is usually greater (Schneider et al., 1973). Thus, it is important to understand that only when sputtering, electronic desorption, uv ionization, volcanic outfall (e.g, on Io), and meteoritic impact are put together into a comprehensive model are we likely to provide a realistic picture of planetary surface modification. Since this has not been attempted I shall deal in sect. 3 with solar wind sputtering in a more limited sense - the opportunity it may provide for surface elemental analysis from orbit.

The greatest advance that has occurred during the decade has been the unambiguous identification of grains from meteorities that show clearly their formation in stellar atmospheres (section 2.2.2). Their exposure there and subsequently in the interstellar medium to ion/atom bombardment is an important factor in determining their survival probability. For that reason, the next section will be devoted to presenting that material in detail.

2 Irradiation Effects on Extraterrestrial Grains

2.1 Formation and Destruction of Grains

It seems well established that grains are formed in the mass loss processes of red giant stars (Knapp & Morris, 1985) and novae (Gehrz et al., 1980). In the case of the former the total mass of grain production is about equally divided between oxygen-rich red giants (where silicate grains are thought to be formed (Lafont et al., 1982)) and their less common carbon-rich relatives (where carbon or SiC grains are created (Thaddeus et al., 1984)). Supernovae are also conjectured as producing grains, but this is not yet confirmed to be competitive with the red giant and nova sources (Dwek & Werner, 1981). All the known circumstellar grain creation processes (which is not expected to be a complete list) can reproduce the amount of observed interstellar dust in 3×10^9 y (Dwek & Scalo, 1980). This material is likely to be a mix of carbon and carbide grains and refractory silicates, Al_2O_3, and $MgAl_2O_4$ particles. These may have acquired mantles of deposited/accreted material, which in some cases are adsorbed or implanted C, N, H species and in others are composed of more refractory material that was condensed sequentially during the later stages of grain formation (Draine, 1984; Greenberg, 1984).

The subsequent history of such grains involves their exposure to supernova-generated shock fronts of the neutral gas in the interstellar medium that may destroy them before they have an opportunity either to be added to newly forming stars or perhaps to become larger solid bodies in a planetary system (Draine & Salpeter, 1979).

Sputtering from gas-grain interactions in shocks is thought to be the main destruction mechanism; the effect of grain-grain collisions has not been studied in as much detail (Seab & Shull, 1983; Seab & Shull, 1985[1]; Seab, 1987). Typical shock fronts that are violent enough to destroy grains have velocities between 30 and 400 km/sec (Seab & Shull, 1983; Seab & Shull, 1985; Seab, 1987); at velocities much above 100 km/sec Fe and Si in the shocked volume are observed to have cosmic abundances, i.e. virtually all the grains must be destroyed (Cowie, 1978). A relative velocity of 100 km/sec corresponds to sputtering at 50 eV/atomic mass unit. Thus, it is clear that the hydrogen plays only a small role in the sputtering ($\lesssim 10\%$) and the ^{4}He dominates (Seab & Shull, 1983; Seab & Shull, 1985; Seab, 1987) (see table I). It is estimated that shocks of this magnitude (orginating in supernovae) are encountered by a grain on the average every 10^8 years (McKee & Ostriker, 1977). This result creates for us a dilemma – why are there any grains around that preserve details of their formation if they are created an order of magnitude more slowly [$\sim 3\times10^9$y, (Dwek & Scalo, 1980)] than they are destroyed? Below I list the evidence

---

[1] this ref. will appear often, abbreviated hereafter as IACIID

that leads one to suspect that some grains do indeed survive and carry with them the clear mark of their creation sites.

2.2 Preservation of a Prior History of Stellar Grain Creation that is Indicated by the Observation of Isotopic Fractionation and Anomalies in Meteorites

The presence of significant deviations from terrestrial isotopic abundance patterns in meteoritic materials shows that they preserve information about a previous period of processing. There are clear radioactive parent-daughter associations, especially ^{26}Al-^{26}Mg, that point at an episode of nucleosynthesis just before the solar system formed as well as to the preservation of the signatures of stellar element formation earlier (Kerridge, 1985; Lee, 1979; Niederer & Papanastassiou, 1984).

These heterogeneities give us both insights about and constraints upon the sites where nuclear synthesis occurs. They also may preserve evidence of other types of solar system processes involving, for example, sputtering (Russell et al., 1980; Esat & Taylor, 1986) or molecular reactions (Thiemens & Heidenreich, 1983; Heidenreich & Thiemens, 1985; Bhattacharya & Thiemens, 1989) that affect isotopic distributions. In either case, these anomalies give us many clues about the formation of the solar system that we have begun to untangle, although it is certainly no exaggeration to note that so far no unique scenario has been suggested by these data (Wood, 1985).

Below I list several examples of meteoritic components that, as shown by such isotopic heterogeneities, preserve traces of their history as stellar-produced grains.

2.2.1 Calcium-Aluminum-Rich Inclusions (CAIs)

In meteorites one finds inclusions that have the Ca-Al-rich compositions that one would expect from the first materials to condense out of an initially-hot solar nebula (Grossman & Larimer, 1974). However, detailed study has shown that these inclusions cannot be simply accounted for by a single gas-solid fractionation process, but involved a number of stages of reprocessing (Kerridge & Bunch, 1979; Ireland, 1988; Armstrong, 1989; Keller & Buseck, 1989); some have been melted - many have been exposed to secondary lower-temperature alterations. For example, the fact that the rare earth elements have abundance patterns associated with their relative volatilities (rather than their ionic sizes as in terrestrial materials) attests to such complex processing (Kornacki & Fegley, 1986; Ireland et al., 1988). The inclusions show that at least some parts of the solar nebula were hot, but despite the evidence of a 'classical' cooling, well-mixed solar nebula, variations in the pattern of isotopes show that hetrogeneities from earlier periods are preserved, although the original interstellar materials may not have survived intact. These minerals include hibonite, perovskite, melilite, spinel, Ti-rich pyroxene, and anorthite. They contain an extremely rich (albeit confusing) assortment of isotopic heteogeneities that show unusual isotopic fractionation as well as unmistakeable evidence for nucleosynthetic processes (Kerridge, 1985; Lee, 1979; Niederer & Papanastassiou, 1984).

One of the first and perhaps the most widely visible heterogeneity is in the isotopic fractionation of the oxygen isotopes. On a three isotope plot there is a unit slope for $[^{17}O/^{16}O]$ versus $[^{18}O/^{16}O]$ as opposed to the ~ 0.5 slope exhibited by the typically fractionated terrestrial samples (Clayton, 1978; Clayton & Mayeda, 1989). Most isotopic fractionation processes observed in nature are linear in the mass difference; thus, ^{17}O is usually fractionated half as much as ^{18}O when both are compared to the most abundant isotope, ^{16}O. This deviation from what is typical for terrestrial materials has commonly been interpreted as reflecting a reservoir (whose material form is still unspecified) of virtually pure ^{16}O as well as at least two other distinct (though also unspecified) solar system oxygen reservoirs (Clayton et al., 1985). The 'pure' ^{16}O could be a relic of an oxygen-rich red giant star or perhaps a supernova source based on the evolution of one (Clayton, 1975; Cameron & Truran, 1977).

Two Allende inclusions show Nd and Sm isotope distributions that reflect stellar r- and p-process material (sample, EK-1-4-4) and p-process material alone (sample, C-1) that seem to indicate a super nova origin (Lugmair et al., 1978; Wasserburg et al., 1979). (The r-process involves rapid neutron capture relative to beta decay; the p-process involves proton-induced nuclear reactions.)

Also seen in Ca-Al-rich inclusions are strong mass-dependent fractionations of the Si, Mg, and Ca isotopes (Niederer & Papanastassiou, 1984) as well as excesses of ^{50}Ti (Niemeyer & Lugmair, 1984), ^{54}Cr excesses that are correlated with the ^{50}Ti (Birck & Allegre, 1984), and deficits of ^{47}Ti (Niemeyer & Lugmair, 1984). It is curious that the presence of these anomalies occurs in the presence of a normal Mg isotopic distribution.

Another dramatic clue in these inclusions has been the discovery of ^{26}Mg excesses that are associated with the ^{27}Al concentration. In many cases the excess ^{26}Mg is in a single mineral phase; thus, it can conceivably be attributed to relic ^{26}Mg from previous ^{26}Al decay (Gray & Comston, 1974). However, ^{26}Mg excesses have also been found that correlate with ^{27}Al in a number of coexisting phases within the inclusion. This is best explained by the in situ decay of ^{26}Al that must have been produced less than 3×10^6 years before its incorporation into the inclusion (Lee et al., 1977). That the effect was locally heterogeneous is shown by the fact that ^{26}Mg deficits also occur (Kerridge, 1985; Lee, 1979; Niederer & Papanastassiou, 1984). One should note that gamma rays that follow the decay of ^{26}Al have been observed in the direction of the galactic center; thus, this apparent novae-produced ^{26}Al could have been responsible for the incorporation of either 'live' ^{26}Al or its relic ^{26}Mg into the solar system early in its history (Mahoney et al., 1984; Share et al., 1985).

2.2.2 Bulk and Acid-Resistant Residues from Carbonaceous Chondrites

Neon data from carbonaceous chondrites was one of the earliest indications that there were heterogeneities in the isotopic patterns of some elements. In this case a neon component (Ne-E) that was virtually pure ^{22}Ne was identified (Black, 1972). This material may be due to the very short lived parent ^{22}Na ($T_{1/2} \sim 2.5$ years) perhaps produced by proton irradiation; however, there has been no association of the Ne-E component with a Na mineral, so the path by which this isotope arrived in its meteoritic home is so far totally unspecified (Eberhardt et al., 1981).

Probably the clearest and most dramatic association of a meteoritic mineral fraction with a specific stellar origin is provided by Xe. By subjecting a carbonaceous chondrite to a sequence of acid dissolution steps, one is left with an acid-insoluble residue. Two of its components bear the unmistakable signatures of their origin. One is carbon in the form of diamond which has a Xe isotope pattern (Xe-HL) that is enriched in both the lightest and the heaviest isotopes, i.e. p- and r-process Xe that would have come from a supernova (Tang et al., 1988; Anders et al., 1989).

Although its designated source is more ubiquitous, the other component, SiC, is no less significant. The Xe in the SiC has an s-process Xe isotopic pattern, a big Ne-E component (^{22}Ne), enrichments in ^{29}Si and ^{30}Si, as well as depletions of ^{12}C and ^{14}N. (The s-process involves neutron capture reactions that are slow compared with beta decay.) Thus, the origin of the SiC in a carbon-rich red giant (with perhaps proton irradiation and even supernova components as well) seems unavoidable. There is apparently a ^{21}Ne excess, which if it is cosmic ray produced, indicates that the material was incorporated into the meteorite within 40My (Anders et al., 1989; Lewis et al., 1990). It is indeed a puzzle how so many noble gas atoms could be implanted into a grain without causing its destruction. Thus, one can only surmise that these atoms were incorporated simultaneously with the accretion of the grain.

Unlike isotopic heterogeneities associated with the calcium-aluminum rich inclusions, both the diamond and SiC thus seem to have been delivered to us in a pristine condition - despite the fact that we expect such grains to have been destroyed (or at least appreciably modified - thereby losing the Xe and Ne). Some SiC grains have been large enough to be analyzed individually and show uniform C, N, Si compositions with depth. These grains could be products from a single star,

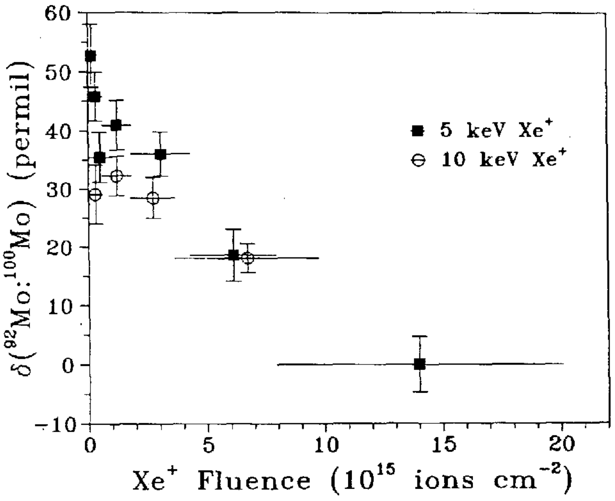

Figure 1. Isotopic fractionation of the Mo flux sputtered into near-normal directions ($\theta \simeq 17°$) vs. the bombarding fluence for Xe^{+} projectile. Each symbol is plotted at the midpoint of the fluence range used for the corresponding collection; the horizontal bar through each symbol indicates this range. Uncertainties indicated by the vertical error bars are $\pm 2\sigma$. Taken from Weathers et al. (1992).

but to be confident of this interpretation, knowledge of grain destruction lifetimes is required.

2.2.3 Interplanetary Dust Particles (IDPs)

Our information about grains in the neighborhood of the sun comes not only from their observation in the scattering of electromagnetic radiation (as for their interstellar cousins) (Mathis, 1985) but also from their detailed study as micrometeorites that are collected in sediments and the statosphere (interplanetary dust particles/IDPs/Brownlee particles), in space, and perhaps as constituents of meteorites (Walker, 1985). We, of course, are close to the point where we shall have an even greater supply of these small objects from the space station and perhaps a cometary-sample-return mission. The IDPs have a variety of forms; some are compact with densities near 2 g/cm^3; others are porous/fluffy. Their compositions/structure can be associated with 'olivine', 'pyroxene', and 'layer lattice silicates' (Walker, 1985). It is not unreasonable to assume that they are at least in part the building blocks from which some of the larger meteorites formed, and their optical properties have already been shown to be similar to those of comets (Sandford & Walker, 1985). So far none of these objects has a strong resemblence

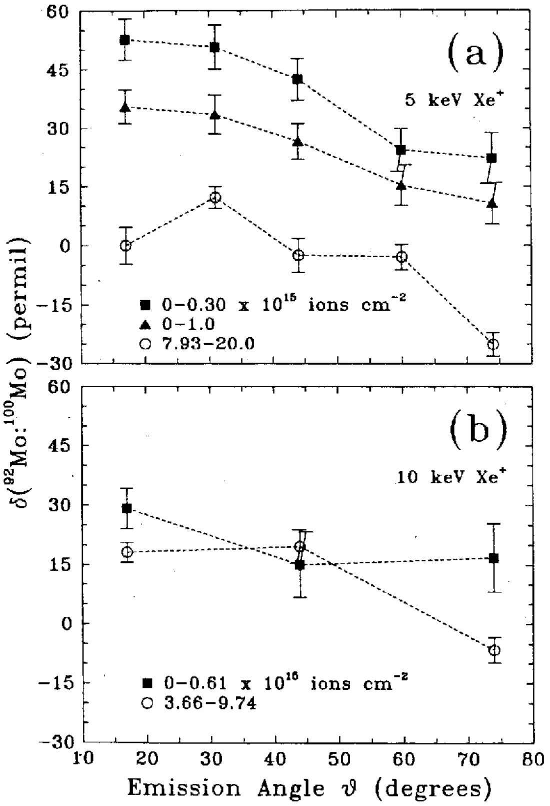

Figure 2. Isotopic fractionation of sputtered Mo vs. emission angle measured from the target normal for different indicated fluence ranges of (a) 5 keV Xe^+ and (b) 10 keV Xe^+ projectiles. Indicated uncertainties are $\pm 2\sigma$. Taken from Weathers et al. (1992).

to the interstellar grains that we briefly surveyed above, e.g. no refractory cores (Tomecka & Buseck, 1984); however, many contain carbon (mostly amorphous) compounds (Christofferson & Buseck, 1983; Rietmeijer & Mackinnon, 1985). Most of the objects at hand seem to have been formed by vapor phase condensation (Bradley et al., 1983). They have been exposed to intense ion bombardment in the early stages of the formation of the solar system as well as more recently to the solar wind. Because of their small size this irradiation may have been especially significant in altering their elemental and isotopic compositions.

Generally, the small size of these objects has precluded the use of the full arsenal of isotopic measurements that have been done on meteorites. Deuterium has large enrichments ($\sim$ 25%) which are variable on a few-micron scale. This excess seems to be associated with carbon but not with OH. The carbon isotopic ratios are constant over a given grain but vary from grain to grain. Mg and Si isotopes show terrestrial ratios (Walker, 1985). ^{16}O-rich oxygen has been found in a few IDPs but with enrichments within the range of other meteoritic materials. The grains probably have too few noble gas atoms for isotopic analyses to be performed on individual grains.

2.3 Basic Questions about Grain Sputtering that Need to be Answered

We see from the examples in the previous section that although grains coming from stellar sources are exposed to sputter erosion, some individual grains apparently survive having preserved a clear signature of stellar nucleosynthetic processes. Better knowledge of sputtering is, therefore, important in two respects. First, we need reliable estimates of what types of grain materials are likely to survive and the statistical lifetimes involved. Second, we need to know to what extent sputtering, which is known to produce elemental and isotopic fractionation itself, has distorted the image that is retained by the surviving grains.

2.3.1 Sputtering Yields and Fractionation

Although there is much data on the sputtering yields from ion bombardment (sputtered atoms/ion) for elemental metallic targets, there is much less for compounds and virtually none for refractory minerals of the types discussed in section 2.2.1 (Kaminsky, 1965; Behrisch, 1981,1983). Generally, yields can vary substantially and the role of adsorbed layers or overlying mantles can modify the yields. One must also note that preferential sputtering is important in the context discussed herein because it can lead to altered surface layers on the grains that have very different properties than those of the bulk material. Such selective effects obviously lead to the preferential destruction or preservation of particular grain types. (See table I for examples of sputtering yields in order to get a feeling for the range of values for different materials (Roth et al., 1979).) In addition to obtaining more complete laboratory data there is also a clear need to improve the molecular dynamics simulations that can both give us better intuition about preferential sputtering processes and also allow extrapolations to situations not possible in the laboratory, e.g. sputtering of small objects, rough surface effects, coating layers, etc. Such simulations have already had a major impact on our knowledge of isotopic fractionation by sputtering (Shapiro et al., 1985; Shapiro et al., 1988; Lo et al., 1989).

Early measurements by our group for Ca minerals showed enrichment of 1-2% in the total yield of $^{40}Ca/^{44}Ca$ at moderate fluences and a 1.5-2% fractionation between ejection normal and oblique to the surface even at large fluences where the material removed overall was in isotopic equlibrium, i.e. equivalent to the bulk value (Russell et al., 1980). Simulations to understand these data at a more fundamental level showed that the observed fractionations should have been much larger ($\sim$ 10%) (Shapiro et al., 1985; Shapiro et al., 1988; Lo et al., 1989); the Ca effects had been diluted by too large a bombarding fluence. Subsequent data for secondary ions of Mo, Li, etc. (Gnaser & Hutcheon, 1988) and of boron (Baumel et al., 1988) showed large effects that agreed with the simulations. These prompted our examination of the sputtering of neutral atoms from Mo, which was chosen because it represented a low sputtering yield typical of interstellar grain materials (see table I) and because we could conveniently make a pure metallic target of 50% ^{92}Mo-50% ^{100}Mo to give an easily visible effect for comparison with the molecular dynamics simulations. Examples from these data are shown versus ion fluence in Figure 1 and versus angle from the surface normal in Figure 2; one observes that the effects are enormous both at low fluences ($\sim$ 6%) and across the range of ejection angles ($\sim$ 2%) independent of fluence (Weathers et al., 1989; Weathers et al., 1993). Other recent isotopic fractionation data are given in table II (Gnaser & Hutcheon, 1988; Baumel et al., 1988; Weathers et al., 1989; Weathers et al., 1992; Gnaser & Oechsner, 1989; Gnaser & Oechsner, 1990).

In our Ca experiment we showed that $^{43}Ca/^{44}Ca$ was fractionated linearly relative to $^{40}Ca/^{44}Ca$, although the precision ($\sim$ 0.1%) was not as good as one would like due to the low abundance of ^{43}Ca (Russell et al., 1980). It is especially important to determine if sputtering produces effects that are linear in the mass difference; if it does not (as suggested by Esat and Taylor (1986)) then it is possible that some anomalies attributed to nucleosynthetic processes may arise from a more prosaic source.

Since sputtering is expected to play a significant role in the processing of every interstellar grain, we should have quantitative data about how this processing modified the elemental and isotopic composition of what survives. To do this properly suggests that data be obtained for relevant materials (e.g., C, SiC, and CAI minerals) that give overall erosion yields as well as establishing the degree of fractionation that can arise. One might also consider the co-deposition of noble gas atoms with Si and C to determine whether the SiC grains observed by Lewis et al. (1990) could have been formed in this way. These data should be tied together by molecular dynamics (MD) simulations, and careful modeling of sputtering in shocks should be repeated using these data. Examples of the relevant shock and grain history models are Seab & Shull, (1983) and Liffman & Clayton, (1988); Seab et al., (1985); Liffman, (1990), respectively.

Table II. Low-fluence iostopic fractionation data from other experimental studies. In the upper group of measurements, intensities of positive secondary ions were observed; in the lower group, intensities of sputtered neutrals were observed. In all cases, the lowest bombarding fluences were $\sim 1 \cdot 10^{15}$ ions/cm^2. Taken from Weathers et al. (1993).

Ref.	Projectile	θ(deg)[a]	Fluence to Steady State (ions/cm^2)	Target	Isotope Pair	Mass Ratio M_H/M_L	θ(deg)[b]	δ(°/oo)[c]
f)	14.5 keV O^-	~ 10	$\sim 5 \cdot 10^{16}$	TiO_2	$^{46}Ti^+$:$^{50}Ti^+$	1.0869	$\lesssim 15$	63 ± 13
"	"	"	NA[d]	Natural Mo	$^{92}Mo^+$:$^{100}Mo^+$	1.0870	$\lesssim 15$	49 ± 4.3
g)	100 keV Ar^+	30	$\sim 3 \cdot 10^{17}$	Natural B	$^{10}B^+$:$^{11}B^+$	1.0995	0	51.8 ± 1.8
g)	100 keV Ne^+	"	$\sim 2 \cdot 10^{18}$	"	"	"	0	46.1 ± 2.4
h)	5 keV Ar^+	30	$\sim 6 \cdot 10^{16}$	Natural Mo	^{92}Mo:^{100}Mo	1.0870	0	51 ± 4
h)	"	0	"	"	"	"	30	65 ± 14
h)	"	30[e]	"	"	"	"	60	57 ± 12
i)	5 keV Ar^+	30	$\sim 2 \cdot 10^{16}$	Ge (100) Crystal	^{70}Ge:^{76}Ge	1.0858	0	52 ± 5

a) Projectile angle of incidence, measured from the target normal.

b) Angle of ejection of the sputtered material, measured from the target normal.

c) Isotopic fractionation measured at the lowest bombarding fluences, normalized to the steady-state isotope ratio at the same ejection angle, indicated uncertainties are $\pm 2\sigma$. δ given in parts per thousand (°/oo)

d) Not available.

e) The direction of incidence was such that the angle betweeen the projectile path and the emission direction of the analyzed material was also 30°.

f) Gnaser and Hucheon (1988).

g) Baumel et al. (1988).

h) Gnaser and Oechsner (1989).

i) Gnaser and Oechsner (1990).

2.3.2 Grain-Grain Collisions

Although one might not automatically make the connection, the collisions of small grains in the interstellar medium are not really very different from the impacts of large molecular ions (cluster ions) on surfaces. This topic has become an exciting area in ion-solid interactions both because it represents an extreme case of non-linear energy deposition and because of its technological applications.

It has not only been possible to do experiments with such ions, it has also been possible to simulate the gross features of such impacts by molecular dynamics models. These simulations show that at the bombarding energies corresponding to an interstellar shock front (~ keV/atom), the grains are expected to be completely destroyed in such collisions (Shapiro & Tombrello, 1990, 1991). However, at low energies (~eV/atom), where the simulations were performed to guide thin film deposition attempts, there was a high probability for their sticking together (Hsieh & Averback, 1990). Obviously, at intermediate velocities one expects to find to an increasing degree crater formation, fragmentation, etc. (Hsieh & Averback, 1990; Pelletier et al., 1992).

This area of simulation appears to have the potential for improving our intuition about such grain collision phenomena. For example, to what degree are the volatile mantle materials evaporated, ablated, etc. in soft collisions (eV/atom)? This is important because the grain surfaces may serve as sites for the formation of some types of organic molecules that are observed in the interstellar medium (Watson, 1976). It is also suggested from the simulations that the heating induced even in the softer collisions may also cause substantial alteration of the grain-core composition itself.

3 Using Solar Wind Sputtering for Remote Planetary Surface Analysis

Because the moon's surface is virtually always exposed to bombardment by the solar wind, surface atoms are always being sputtered. There have been several proposals to detect the neutral atoms (Tombrello & Neugebauer, 1990) or the ions (Elphic et al., 1991; Johnson & Baragiola, 1991) from lunar orbit.

At the earth's orbit the solar wind consists mainly of hydrogen and helium ions. The flux is about 3×10^8 protons/cm^{2}sec having energies of ~ 1 keV and 10^7 alpha particles/cm^{2}sec with energies of ~ 4 keV (Feldman et al., 1977). The sputtering yields (ejected atoms per incident ion) on typical lunar surface materials will be like those of SiO_2 or Al_2O_3, which are of the order of 0.02 for the protons and 0.1 for the alphas (Roth et al., 1979). Thus, the exposed lunar surface yields $\sim 7 \times 10^6$

atoms/cm^{2}sec from these solar wind components. Although the heavier ions in the solar wind have higher sputtering yields, their lower abundances cause their contributions to the overall ejected atom yield to be $\sim$ 10% of that from hydrogen and helium. The energy spectrum (Thompson, 1968) of atoms sputtered by keV projectiles has the approximate form

$$\frac{E}{(E+B)^3}, \qquad (1)$$

where B is the surface binding energy of an atom in the target material. Typically, B $\sim$ 5 eV, so that the peak of this spectrum, which occurs at B/2, is at $\sim$ 2.5 eV. The escape velocity for the moon is 2.37 x 10^5 cm/sec; for oxygen atoms this corresponds to 0.5 eV, while for Si, 0.8 eV. The ability to escape depends also on the direction of motion of the sputtered atom, but most are expected to escape or at least reach spacecraft altitude (100 km for the proposed Lunar Observer Mission (Nash, 1990)). The angular distribution of sputtered atoms from a smooth surface is $\cos^n \theta$, where θ is measured from the normal to the surface and n is 1-2, although surface roughness tends to make $n \lesssim 1$. In addition, the angular distribution seen from a spacecraft will be affected by the large-scale topography of the planet. As a result of the long-term solar wind irradiation, lunar soil surfaces are expected to have reached steady state with respect to sputtering; thus, the relative fluxes of sputtered atoms give the composition directly.

The intent of these proposals is to explore the feasibility for a flight instrument on the orbiter which will measure the atom/ion composition sputtered from the lunar surface. Such an instrument would give a SIMS-like analysis of the lunar surface that would complement the planned γ-ray and x-ray fluorescence measurements since the sputtered atoms would come mainly from the major surface constituents, whereas the x-rays only provide information on the light elements Mg, Al, and Si and the γ-rays come mainly from radioactive elements (natural and produced by energetic cosmic ray and solar flare particles) that lie within $\sim$ 1 m of the surface and only provide information on a subset of heavier elements. Generally, the sputtered atom distributions should allow the determination of the basic lithology of the surface (e.g., rock and mineral types) for the major elemental constituents down to $\sim$ 1% levels - instrumental and spacecraft background permitting. It should also be possible to obtain information on minor components as well, but those would be averaged over much larger areas of the surface. Thus, one would get information on all major elements present (such as Ca, which is not determined from the x- and γ-rays), and we would be consistently analyzing the surface material.

Much photo-geologic evidence suggests that certain fairly extensive dark mantling deposits on the moon are products of volcanic fire fountains (Hawke, 1990).

Laboratory study of homogeneous lunar glass spherules thought to be representative of such fire fountain material show surface enrichments of a number of elements including K, halogens, S, and Zn (Meyer, 1990). This suggests the interesting possibility that a mass spectroscopic instrument such as those being considered could identify and map pyroclasic deposits. This takes advantage of the fact that since sputtered atoms come primarily from the surface atomic layer of the material, these thin surface deposits might be detected.

4 Conclusions

It was not my intention in this review to cover all possible ways in which sputtering can affect the properties of planetary materials. In the case of the interstellar grains that may have been an ingredient in the formation of our solar system, I have tried to provide a systematic introduction for the reader who may be interested in learning more about this subject. This story is certainly one of the most exciting that has arisen recently, i.e., that we can see the clear signs of the stellar origins of some of this material, preserved in what seems to be nearly pristine form. How this observation can be reconciled with the high probability for the sputter-destruction or modification of such grains should provide us with many research topics.

In the case of solar wind sputtering of planetary surfaces I have attempted to show the yet untested potential for such observations to provide remote analyses of planetary surfaces. Overcoming the obvious technical difficulties of these proposals will not be easy; however, the technique offers a unique opportunity that is well matched to low-cost space missions that should not be ignored. Here we need first to explore carefully the limitations of the technique in the laboratory as a prelude to designing flight instruments.

In my desire to hold this review to within reasonable limits, I have managed to slight the role played by sputtering in many other planetary contexts. In addition to those other topics listed in the introduction (e.g., atmospheric sputtering and electronic excitation mediated desorption) one obviously could add many more - the endless variety of environments in the universe provides so many opportunities for energetic particle bombardment. I can only assume that if I am asked to do this again in a decade hence, that paper will look as different from this one as this does from its predecessor.

Acknowledgements

I would like to acknowledge the contributions to this work not only of the many students and visitors to my group that are cited in the text but also to decades of tutorial education from my close friends and associates, D. S. Burnett and R. M.

Housley. This work was supported in part by the National Aeronautics and Space Administration [grant NAGW-2279].

References

Anders E, Lewis RS, Tang M and Zinner E, 1989: IAU Symposium 135, NASA-Ames Research Center, California, July 1988

Armstrong JT, 1989: Lunar Planet. Sci.**XX**, 23

Baumel LM, Weller MR, Weller RA and Tombrello TA, 1988: Nucl. Instrum. Methods B **34**, 427

Behrisch R (ed.), 1981: *Sputtering by Particle Bombardment I*, Top. Appl. Phys. **47**, (Springer Verlag, NY)

Behrisch R (ed.), 1983: *Sputtering by Particle Bombardment II*, Top. Appl. Phys. **52**, (Springer Verlag, NY)

Bhattacharya SK and Thiemens MH, 1989: Lunar and Planet. Sci. **XX**, 71

Birck JL and Allegre CJ, 1984: Geophys. Res. Lett. **11**, 943

Black DC, 1972: Geochim. Cosmochim. Acta **36**, 377

Bradley JP, Brownlee DE and Veblen DR, 1983: Nature **301**, 473

Cameron AGW and Truran JM, 1977: Icarus **30**, 447

Christofferson R and Buseck PR, 1983: Lunar Planet. Sci. **XIV**, 411

Clayton DD, 1975: Astrophys. J. **199**, 765

Clayton RN, 1978: Ann. Rev. Nucl. Part. Sci. **28**, 501

Clayton RN and Mayeda TK, 1989: Lunar Planet. Sci. **XX**, 169

Clayton RN, Mayeda TK and Molini-Velsko CA, 1985: *Protostars and Planets II* (Univ. of Arizona, Tucson), p. 755

Cowie LL, 1978: Astrophys. J. **225**, 887

Draine BT, 1984: *Protostars and Planets II*, ed. T. Gehrels (Univ. Ariz. Press, Tucson)

Draine BT and Salpeter EE, 1979: Astrophys. J. **231**, 438

Dwek E and Scalo JM, 1980: Astrophys. J. **239**, 193

Dwek E and Werner MW, 1981: Astrophys. J. **248**, 138

Eberhardt P, Jungck MHA, Meyer FO and Niederer FR, 1981: Geochim. Cosmochim. Acta **45**, 1515

Elphic RC, Funsten HO III, Barraclough BL, McComas DJ, Paffett MT, Vaniman DT and Heiken G, 1991: Geophys. Res. Lett. **18**, 2165

Esat TM and Taylor SR, 1986: Lunar Planet. Sci. **XVII**, 208

Feldman WC, Asbridge JR, Bame SJ and Gosling JT, 1977: *The Solar Output and its Variation*, O. R. White, ed. (Colorado Associated University Press, Boulder) pp. 351-382

Gehrz RD, Grasdalen GL, Hackwell JA and Ney EP, 1980a: Astrophys. J. **237**, 855

Gehrz RD, Hackwell JA, Grasdalen GL, Ney EP, Neugebauer G, Sellgren K, 1980b: Astrophys. J. **239**, 570

Gnaser H and Hutcheon ID, 1988: Surface Sci. **195**, 499

Gray CM and Comston W, 1974: Nature **251**, 495

Greenberg JM, 1984: *Laboratory and Observational Infrared Spectroscopy of Interstellar Dust* (Royal Obs., Edinburgh) p. IV

Grossman L and Larimer JW, 1974: Rev. Geophys. Space Phys. **12**, 71

Haff PK and Watson CC, 1980: J. Geophys. Res. **82**, 8436

Haff PK, Zwitkowski ZE and Tombrello TA, 1978: Nature **272**,803

Hawke BR, 1990: *Lunar Volcanic Glasses: Scientific and Resource Potential*, J. W. Delano and G. H. Heiken, eds. (Lunar and Planetary Inst., Technical Report 90-02) pp. 34-40

Heidenreich JE and Thiemens MH, 1985: Lunar Planet. Sci. **XVI**, 335

Hsieh H and Averback RS, 1990: Phys. Rev. **B42**, 5365

Ireland TR, 1988: Geochim. Cosmochim Acta **52**, 2827

Ireland TR, Fahey AJ and Zinner EK, 1988: Geochim. Cosmechim. Acta **52**, 2841

Johnson RE and Baragiola R, 1991: Geophys. Res. Lett. **18**, 2169

Johnson RE and Sundqvist BUR, 1992: Phys. Today **45**, 28

Kaminsky M, 1965: *Atomic and Ion Impact Phenomenon Metal Surfaces* (Springer, Berlin)

Keller LP and Buseck PR, 1989: Lunar Planet. Sci. **XX**, 512

Kerridge JF, 1985: IACIID, p. 71 (refer to Seab & Shull, 1985 for complete description of this reference source)

Kerridge JF and Bunch TE, 1979: *Asteroid* (Univ. of Arizona, Tucson), p. 745

Knapp GR and Morris M, 1985: Astrophys. J. **292**, 640 [also see erratum (1986) Astrophys. J. **303**, 521

Kornacki AS and Fegley B, Jr., 1986: Earth Planet. Sci. Lett. **79**, 217

Lafont S, Lucas R and Omont A, 1982: Astr. & Astrophys. J. . **106**, 201

Lee T, 1979: Rev. Geophys. Space Phys. **17**, 1591

Lee T, Papanastassiou DA and Wasserburg GJ, 1977: Astrophys. J. Lett. **201**, L107

Lewis RS, Amari S and Anders E, 1990: Nature **348**, 293

Liffman K, 1990: Astrophys. J. **355**, 518

Liffman K and Clayton DD, 1988: Proc. Eighteenth Lunar and Planetary Sci. Conf., p. 637

Lo DY, Tombrello TA and Shapiro MH, 1989: Nucl. Instr. Meth. **B40/41**, 270

Lugmair GW, Marti K and Scheinin NB, 1978: Lunar Planet. Sci. **IX**, 677

Mahoney WA, Ling JC, Wheaton WA and Jacobson S, 1984: Astrophys. J. **286**, 578

Mathis JS, 1985: IACIID p. 29 (refer to Seab Shull, 1985 for the complete description of this reference source)

McKee CF and Ostriker JP, 1977: Astrophys. J. **218**, 148

Meyer C, 1990: *Lunar Volcanic Glasses: Scientific and Resource Potential*, J. W. Delano and G. H. Heiken, eds. (Lunar and Planetary Inst., Technical Report 90-02) pp. 50-51

Nash DB, ed., 1990: *Lunar Observer: An Essential Robotic Mission to Prepare for Human Exploration of the Moon*, (JPL), draft

Niederer FR and Papanastassiou DA, 1984: Geochim. Cosmochim. Acta **48**, 1279

Niemeyer S and Lugmair GW, 1984: ibid, 1401

Pelletier JD, Shapiro MH and Tombrello TA, 1992: Nucl. Instr. Meth. **B67**, 296

Rietmeijer FJM and Mackinnon IDR, 1985: Nature **315**, 733

Roth J, Bohdansky J and Ottenberger W, 1979: *Data on Low Energy Light Ion Sputtering*, IPP 9/26 (Max-Planck-Inst. für Plasmaphysik, Garching bei Munchen)

Russell WD, Papanastassiou DA and Tombrello TA, 1980: Radiat. Eff. **52**, 41

Sandford S and Walker RM, 1985: Astrophys. J. **291**, 838

Schneider E, Sturzer D, Hartung JB, Fechtig H and Gentner W, 1973: Geochim. Cosmochim. Acta Suppl. **4** 3277

Seab CG, 1987: Interstellar Processes, eds. D. J. Hollenbach and H. A. Thronson, Jr. (Reidel Publ. Co., Boston) p. 491

Seab CG and Shull JM, 1983: Astrophys. J. **275**, 652

Seab CG and Shull JM, 1985: *Interrelationships Among Circumstellar, Interstellar and Interplanetary Dust*, eds. J. A. Nuth and R. E. Stencel (NASA Conf. publications 2403) p. 37

Seab CG, Hollenbach DJ, McKee CF and Tielens AGGM, 1985: IACIID, p. A-28

Shapiro MH and Tombrello TA, 1990: Phys. Rev. Lett. **65**, 92

Shapiro MH, Haff PK, Tombrello TA and Harrison DE, Jr., 1985: Nucl. Instr. Meth. **B12**, 137

Shapiro MH, Tombrello TA and Harrison DE, Jr., 1988: Nucl. Instr. Meth. **B30**, 152

Share GH, Kinzer RL, Kurfess JD, Forrest DJ, Chupp EL, and Rieger E, 1985: Astrophys. J. **292**, L61

Sigmund P, 1969: Phys. Rev. **184** 383

Tang M, Lewis RS, Anders E, Grady MM, Wright IP and Pillinger CT, 1988: Geochim. Cosmochim. Acta **52**, 1235

Thaddeus P, Cummins SE and Linke RA, 1984: Astrophys. J. Lett. **283**, L45

Thiemens MH and Heidenreich JE, 1983: Science **219**, 1073

Thompson MW, 1968: Phil. Mag. **18**, 377

Tombrello TA, 1982: Rad. Eff. **65**, 149

Tombrello TA and Neugebauer MM, 1990: Proposal to the Caltech President's Fund, unpublished

Tomeoka K and Buseck PR, 1984: Lunar Planet. Sci. **IV**, 858

Walker RM, 1985: Ibid, p. 55

Wasserburg GJ, Papanastassiou DA and Lee T, 1979: *Les Elements et Leurs Isotopes dan l'Univers*, (Liege) p. 203

Watson CC, Haff PK and Tombrello TA, 1980: Geochim. Cosmochim Acta (Proc. Lunar Sci. Conf. 11th, Houston, TX) p. 2479

Watson WD, 1976: Rev. Mod. Phys. **48**, 513

Weathers DL, Hutcheon ID, Gnaser H, Tombrello TA and Wasserburg GJ, 1989: Lunar Planet. Sci. **XX**, 1185

Weathers DL, Spicklemire SJ, Tombrello TA, Hutcheon ID and Gnaser H, 1993: Nucl. Instr. Meth. B **73**, 135

Wehner GK, Kennight C and Rosenberg DL, 1963: Planet. Space Sci. **11**, 885

Wood JA, 1985: (working group chm.) IACIID, p. W6-33

Submitted to the Academy June 1993.
Published December 1993.